ICCC 2023 - Guidelines for citation and reuse

Please cite the conference proceedings as following:
Thailand Concrete Association, Ed. *Further Reduction of CO2 -Emissions and Circularity in the Cement and Concrete Industry, 16th International Congress on the Chemistry of Cement 2023 - ICCC2023* (Bangkok 18.-22.09.2023). Bangkok, 2023. Available at: https://www.iccc-online.org/archive/

Please cite individual papers as following:
Author. Title. In: Thailand Concrete Association, Ed. *Further Reduction of CO2 -Emissions and Circularity in the Cement and Concrete Industry, 16th International Congress on the Chemistry of Cement 2023 - ICCC2023* (Bangkok 18.-22.09.2023). Bangkok, 2023. Available at: https://www.iccc-online.org/archive/

Organized by

TCA
สมาคมคอนกรีตแห่งประเทศไทย
Thailand Concrete Association

THE 16TH INTERNATIONAL CONGRESS ON THE CHEMISTRY OF CEMENT
ICCC 2023
BANGKOK THAILAND

ICCC 16th 2023

INTERNATIONAL CONGRESS ON THE CHEMISTRY OF CEMENT

CONGRESS PROCEEDING VOLUME IV

Further reduction of CO_2-emission and circularity in the cement and concrete industry

SEPTEMBER 18-22, 2023

CENTARA GRAND & BANGKOK CONVENTION CENTRE @CENTRALWORLD

Co-Sponsor by

aci American Concrete Institute Always advancing

SEADMA

gcca

ASTM INTERNATIONAL

Contact infomation :
Email: iccc2023.tca@gmail.com
Website : https://www.iccc2023.org/

PREFACE

The International Congress on the Chemistry of Cement (ICCC) is the renowned global platform that summarizes the state of the art of cement chemistry as well as major trends in cement application. Since the first International Congress on the Chemistry of Cement started in London in 1918, it has provided a strong and fruitful link between the academic world and the cement industry. It has always stimulated scientific exchanges and discussions between researchers, students, and those who have already gained working experience in many fields of chemistry relevant to cement production and its use in concrete and mortar. The ICCC is the venue to present cement and environmental development together with meeting worldwide and renowned experts from all over the world who come to present their works at the congress.

This proceeding collects the papers submitted to the 16th International Congress on the Chemistry of Cement (ICCC 2023), which was held in Bangkok, Thailand between September 18-22, 2023, and organized by Thailand Concrete Association on the theme of "further reduction of CO2-emission and circularity in the cement and concrete industry". The ICCC 2023 attracted more than 565 papers and more than 800 delegates and students from 49 countries.

The scientific program covers the topics of the newest and the most important research and development describing the new dimensions in clinker production, advances in hydration chemistry, enhancing clinker substitution and supplementary cementitious materials, advances in characterization methods and modelling, new low carbon cement and carbonatable binders, new findings in admixture & rheology, new technology for quality concrete, durability & reactive transport, sustainability, circular economy, waste processing and recycling, and standardization of cement and concrete.

The Organizing Committee and the Scientific Committee believe that our participants will be most satisfied with the congress and will gain the knowledge to improve their professional works in the future.

Prof.Thanakorn Pheeraphan
Chairman of the Organizing Committee

Prof.Somnuk Tangtermsirikul
Chairman of the Scientific Committee

Steering Committee Members

The Steering Committee is comprised of 26 members.

1. Prof. Dr. Mark G. Alexander, University of Cape Town, South Africa
2. Prof. Dr. Alexandra Bertron, INSA Toulouse, France
3. Prof. Dr. Shashank Bishnoi; Indian Institute of Technology Delhi, India
4. Prof. Dr. Leon Black, University of Leeds, United Kingdom
5. Dr. Cesar Constantino; Titan America LLC, USA
6. Jesper Sand Damtoft, Aalborg Portland A/S, Denmark
7. Prof. Dr. Jan Deja; Stowarzyszenie Producentów Cementu – PCA, Poland
8. Dr. Wolfgang Dienemann, HeidelbergCement AG, Germany
9. Daniel Duque, Cementos Argos S.A., Columbia
10. Ing. Jan Gemrich, Czech Cement Association, Czech Republic
11. Prof. Dr. Frederik Paul Glasser, University of Aberdeen, Scotland
12. Prof. Dr. R. Doug Hooton, University of Toronto, Canada
13. Prof. Dr. Vanderley M. John, Escola Politécnica da USP, Brasil
14. Prof. Dr. Kimberly Kurtis, Georgia Institute of Technology, USA
15. Christophe Levy, Lafarge Holcim Innovation Center (Chairman), France
16. Prof. Dr. Ippei Maruyama, Nagoya University Furocho, Japan
17. Dr. Bibekananda Mohapatra, Director General of the National Council for Cement and Building Materials, India
18. Dr. Marta Palacios, Instituto Eduardo Torroja, Spain
19. Prof. Dr. Angel Palomo, Instituto Eduardo Torroja, Spain
20. Prof. Dr. Thanakorn Pheeraphan, Thailand Concrete Association (Deputy-Chairman), Thailand
21. Prof. Dr. Martin Schneider, VDZ e.V., Research Institute, Germany
22. Prof. Dr. Karen Scrivener, École Polytechnique Fédérale de Lausanne – EPFL, Switzerland
23. Prof. Dr. Caijun Shi, Hunan University, China
24. Prof. Dr. Sui Tongbo, Sinoma International Engineering Co., Ltd., China
25. Prof. Dr. Jannie S. J. Van Deventer, Zeobond Pty Ltd, Australia
26. Dr. Kazuo Yamada, National Institute for Environmental Studies, Japan

Dr. Joerg Rickert, VDZ (Permanent Secretariat of ICCC), Germany - (Without the right to vote)

Organizing Committee Members

Advisory committee members

1. Dr. Wonchalerm Chalodhorn, Siam City Cement Co. Ltd.
2. Prof.Dr. Chai Jaturapitakkul, King Mongkut's University of Technology Thonburi
3. Prof.Dr. Parinya Jindaprasert, KhonKaen University
4. Mr. Ferdinand Leopolder, The South East Asia Drymix Mortar Association SEADMA,
5. Assoc.Prof.Dr. Pichai Nimityongskul , 1st President of Thailand Concrete Association
6. Mr. Chakporn Oonjitt, Construction Institute of Thailand
7. Mr. Wanchai Phanomchai, Thai Industrial Standards Institute
8. Mr. Chana Poomee, Thai Cement Manufacturers Association
9. Dr. Phirun Saiyasitpanich, Office of Natural Resources and Environmental Policy and Planning
10. Mr. Manasit Sarigaphuti, The Siam Cement Group Public Company Limited
11. Assoc.Prof. Anek Siripanichgorn, Engineering Institute of Thailand
12. Prof.Dr. Boonchai Stitmannaithum, Chulalongkorn University
13. Prof.Dr. Piti Sukontasukkul, King Mongkut's University of Technology North Bangkok
14. Mr. Sumate Surabotsopon, Italian-Thai Development Public Company Limited
15. Prof.Dr. Somnuk Tantermsirikul, Sirindhorn International Institute of Technology
16. Dr. Saranyu Viriyavejakul, Neighboring Countries Economic Development Cooperation Agencies
17. Prof.Dr. Pennung Warnitchai, Asian Institute of Technology
18. Mr. Boonyanit Wongrukmit, Electricity Generating Authority of Thailand

Organizing Committee members

1. Prof.Dr. Thanakorn Pheeraphan, Thailand Concrete Association and NavamindaKasatriyadhiraj Royal Air Force Academy (Chairman)
2. Asst.Prof. Dr. Chuchai Sujivorakul, King Mongkut's University of Technology Thonburi (Deputy Chairman)
3. Mr. Boonrawd Kuptitanhi, The Concrete Products and Aggregate Co., Ltd. (Treasurer)
4. Asst.Prof.Dr. Nattapong Magaratat , King Mongkut's University of Technology North Bangkok (Secretariat)
5. Dr. Praveen Chompreda, K.C.S. & ASSOCIATES. Co., Ltd.
6. Assoc.Prof.Dr. Phongthorn Julphunthong, Naresuan University
7. Miss Sunkamol Khongsawatvorakul, Saint-Gobain Thailand.
8. Mr. Sumet Kiatmetha, Hilti (Thailand) Ltd.
9. Gp.Capt. Nuth Limsuwan, Office of Civil Engineering Royal Thai Armed Forces.
10. Dr. Nontapat Nimityongskul, Asia Cement Public Company Limited.
11. Assoc.Prof. Panuwat Joykad, Srinakharinwirote University
12. Dr. Yut Panitanwong, Concrete Product and Aggregate Co.,Ltd.
13. Mr. Suwatchai Puwapattanachat, SIKA (Thailand) Ltd.
14. Mr. Narin Sayanwisuttikam, KAO Industrial (Thailand) Co., Ltd.
15. Dr. Kritsada Sisomphon, The Siam Cement Group Public Company Limited.
16. Mr. Chalermwut Snguanyat, The Siam Cement Group Public Company Limited.
17. Mr. Pakorn Sutthiwaree, Siam City Cement Public Company Limited.
18. Assoc.Prof.Dr. Weerachart Tangchirapat, King Mongkut's University of Technology Thonburi
19. Asst. Prof. Dr. WarangkanaSaengsoy, Construction and Maintenance Technology Research Center, SIIT
20. Prof.Dr. Wanchai Yodsudjai, Kasetsart University

Scientific Committee Members

1. Prof.Mark Alexander, South Africa
2. Prof.Carmen Andrade, Spain
3. Prof.Sergio Angulo, Brazil
4. Dr.Mohsen Ben Haha, Germany
5. Prof.Susan Bernal Lopez, UK
6. Prof.Alexandra Bertron, France
7. Prof.Shashank Bishnoi, India
8. Prof.Maria Blanco, Spain
9. Prof.Jeff Bullard, USA
10. Prof.Maria Alba Cincotto, Brazil
11. Prof.Jan Deja, Poland
12. Prof.Donguk Choi, South Korea
13. Prof.Josee Duchesne, Canada
14. Mr.Wilmar Echeverri, Colombia
15. Prof.Ivan Escalante, Mexico
16. Dr.Duncan Herfort, Denmark
17. Prof.Bruno Huet, France
18. Prof.Jason Ideker, USA
19. Prof.Edgardo Irassar, Argentinia
20. Prof.Zhengwu Jiang, China
21. Prof.Maria Juenger, USA
22. Dr.Marios Katsiotis, Greece
23. Prof.Shiho Kawashima, USA
24. Prof.Paula Kirchheim, Brazil
25. Prof.Jiaping Liu, China
26. Mr.Federico Lopez, Mexico
27. Prof.Barbara Lothenbach, Switzerland
28. Prof.Horst Ludwig, Germany
29. Prof.Ippei Maruyama, Japan
30. Prof.Thomas Matschei, Germany
31. Mr.Mike McDonald, South Africa
32. Dr.Sean Monkman, Canada
33. Prof.Paulo Monteiro, USA
34. Mr.Carlos Orozco, Colombia
35. Dr.Marta Palacios, Spain
36. Prof.Martin Palou, Slovakia
37. Dr.César Pedrajas, Spain
38. Prof.Rafael Pileggi, Brazil
39. Prof.Kedsarin Pimraksa, Thailand
40. Prof.John Provis, UK
41. Prof.Francisca Puertas, Spain

Scientific Committee Members

42.Prof.Jueshi Qian, China
43.Prof.Aleksandra Radlinska, USA
44.Dr.Nailia Rakhimova, Russia
45.Prof.Matteo Romano, Italy
46.Prof.Nicolas Roussel, France
47.Dr.Kwesi Sagoe-Crentsil, Australia
48.Prof.Manu Sanathanam, India
49.Prof.Miguel Sanjuán, Spain
50.Prof.Caijun Shi, China
51.Dr.Denise Silva, USA
52.Prof.Somnuk Tangtermsirikul, Thailand (Chairman)
53.Dr.Theodor Staněk, CZ
54.Prof.Arezki Tagnit-Hamou, Canada
55.Mr.Antonio Telesca, Italy
56.Dr.Paul Tennis, USA
57.Prof.Michael Thomas, Canada
58.Prof.Jorge Tobon, Canada
59.Prof.Sandro Torres, Brazil
60.Prof.Matthieu Vandamme, France
61.Dr.Yury Villagrán Zaccardi, Argentina
62.Prof.Fazhou Wang, China
63.Prof.Zhang Wensheng, China
64.Prof.Claire White, USA
65.Dr.Frank Winnefeld, Switzerland
66.Dr.Hong Wong, UK
67.Dr.Kazuo Yamada, Japan
68.Prof.Cheng Yu, China
69.Prof.Doug Hooton, Canada
70.Peter Kruspan, Switzerland

Contents

	Topics	Page
	Preface	i
	Committees	
	- Steering Committee Members	ii
	- Organizing Committee Members	iii
	- Scientific Committee Members	v
	Papers	
PA0003	Self-healing concrete using special biological materials	1
PA0018	3D Printed Prefabricated Prefinished Volumetric Construction for Sustainable Construction	6
PA0023	The First 3D Printed 2-storey Building in Thailand	10
PA0031	Outline of NEDO Moonshot Project "Calcium Carbonate Circulation System in Construction"	14
PC0004	Effects of different calcined kaolinite clays on the sulfate demand of LC^3 cements	18
PC0005	Monitoring of nucleation and growth of C-S-H phases by analytical ultracentrifugation and ICP-OES	22
PC0006	Effect of Temperature on Performance of Calcium Aluminate Cement Based Accelerator	26
PC0009	Effect of mixing conditions on the rheology and microstructure of silicate-activated slag mixtures	30
PC0018	Effect of Formulation Process of An Alkali-free Liquid Accelerator on Hydration and Properties of Portland Cement	35
PC0030	Hydration of Blended Pastes at Later Age under Different Curing Conditions: Insights into the Rate Limiting Mechanism	40
PC0045	Activation of prehydrated CAC during curing at 20℃ using micro- sized $CaCO_3$	45
PC0057	Effect of Zn retention in alite on the hydration of cementitious systems	49
PC0061	Organic additive´s influence on M-S-H formation	53
PC0069	Modifications on the early hydration stages of a Portland cement paste induced by polydimethylsiloxane (PDMS)	58
PD0004	Challenges and opportunities of limestone calcined clays cements with less than 50% clinker	62

Contents

	Topics	Page
	Papers	
PD0011	Monitoring The Impact Of Accelerators On The Reactivity Of Model Blended Cements	67
PD0013	Using Calcined Clay and Calcium Chloride to Enable Aluminium Reinforced Concrete	71
PD0024	Critical Investigations on Two-Stage Mixing to Increase Early Strength of Cements with Slag and Limestone	75
PD0032	Using blast furnace slag from iron ore “green briquette” on cements – Part 1: chemical and mineralogical characterization	79
PD0038	On the synergies among supplementary cementitious materials	83
PD0039	Comparison of composite cements with limestone filler, fly ash, and calcined clays	88
PD0041	Using blast furnace slag from iron ore “green briquette” on cements - Part 2: physical-mechanical characterization	92
PD0047	Microstructure characterization of (A/F) H 3phases with different alkali concentrations based on calcium sulfoaluminate cement	97
PD0051	PCE Superplasticizers for a Green Binder Containing Calcined Clay	101
PD0058	Impact of C-S-H seeding on hydration and strength of slag blended cement	105
PD0060	Comparison and optimization of calcination processes towards using clays as Supplementary Cementitious Materials	109
PD0064	Electrification of Calcined Clay Systems in the Cement Industry – Technical, Economic and Environmental Potentials	113
PD0066	Modelling of clay calcination: Rotary kiln versus flash calciner	117
PD0072	Assessing the viability of incoperating granite dust as a partial cement replacement in concrete	121

Contents

	Topics	Page
	Papers	
PD0075	Performance Evaluation and Beneficiation of Fly Ash Co-mingled with Flue Gas Desulfurization Products for Use in Concrete	125
PD0076	Pozzolanic Reactivity and Characterization of Natural Pozzolans	129
PD0077	Transformation of Bauxite Residue into a Reactive Supplementary Cementitious Material	133
PD0088	Reducing the clinker factor in vitrified bauxite residue-containing ternary blended cements	139
PD0092	Use of synthetic-SCMs in blended cements and hybrid alkaline cements	144
PD0094	Influence of burning level on calcined clay reactivity - Experience from a rotary field trial up to RMX application	148
PD0098	A tailored supplementary cementitious material based on Calcined Clay technology for Ready Mix production	152
PD0100	Influence of dregs and grits on the hydration of Portland cement pastes	156
PD0102	The Assessment of SCMs Reactivity in Thailand	161
PD0106	Performance of concretes with ternary blended cements containing limestone filler and calcined illitic clay	165
PD0114	Determination of calcined clay minerals impact on strength and carbonation of Portland cement mortars using k-value concept	169
PD0120	A preliminary study on pozzolanic activity and reaction kinetics of coal gasification slag	173
PE0026	Low-Cost and Reliable Contact Angle Goniometry for Cementitious Materials	177
PE0030	C-S-H sorption under temperature and relative humidity changes	181
PE0032	Behavior of water in C-S-H	185
PE0038	Determination of amorphous silica and alumina fractions in metakaolin using X-ray diffraction and PONKCS method	189

Contents

	Topics	Page
	Papers	
PE0039	Luminescent-based method for monitoring pH and chloride ingress in cementitious systems	194
PF0003	Alkaline materials based on pulverized recycled concrete and waste glass	199
PF0012	Microstructural modifications of alkali-activated fly ash cement pastes by the presence of calcium hydroxide	203
PF0017	High-performance eco-cement synthesized from municipal solid waste incineration bottom ash and recycled concrete fine	207
PF0022	Valorization of a low-grade magnesia as a precursor in the preparation of MKPCs	212
PF0027	Effect of organic ligands in AAM binders	216
PF0034	Utilization of carbonated steel slag powder in cementitious materials	220
PF0065	Evolution of products in CO_2 surface treated cement	224
PF0066	CO_2 utilization for ready mixed concrete production: development, challenges and scale up	228
PF0073	Amine-CO_2 treatment of cement slurry and its effect on Portland cement-fly ash-slag ternary system	232
PF0082	Synthesis of Giorgiosite [$Mg_5(CO_3)4(OH)_2 \cdot 5–6H_2O$], further light on a new hydrated magnesium carbonate for MgO-based cement	236
PF0083	Limitations of isothermal calorimetry for sulfate optimization of Limestone Calcined Clay Cements (LC3)	240
PF0096	Chemical and structural evolution of magnesium silicate hydrate	244
PF0110	Utilization of biochar as a carbon sink in low carbon concrete	248
PF0111	Effect of carbonated phases on the performance of different MgO- based formulations	252

Contents

	Topics	Page
	Papers	
PF0117	Phase formation and CO_2 absorption of reactive magnesium oxide (MgO) cement (RMC) with additive under various curing regimes	256
PF0120	Development of Calcium Sulfoaluminate-Belite Cement Using Low Grade Limestone	262
PF0121	Composition-Reactivity Relationship of Indian Biomass Ash	266
PF0129	Transforming lignite fly ash into a carbon negative SCM through mineral carbonation	270
PG0019	Synthesis of polycarboxylate ether (PCE) polymer superplasticizers and the study of their interaction with cement´s main clinker phases	274
PG0024	A New Class of Admixtures for Low Carbon Concrete	278
PG0029	Chemical Admixtures Used in 3D Printing	282
PG0030	Novel PCE Superplasticizers for Low Carbon and Zero Clinker Binders	286
PG0032	Investigation into A Novel Starch-based Superplasticizer for Alkali-activated Slag	290
PG0038	Rheology of superplasticized limestone calcined clay cements	294
PG0052	Synergy effect of TEA as cement additive and PCE on rheological and hydration kinetics of limestone cementitious materials	298
PG0056	The Effect of Crystalline Morphology on the Rheology of Ettringite Suspensions in Presence of Admixtures	303
PG0062	A study on early strength development of fly ash-GGBS geopolymer concrete admixed with inhibiting admixtures	307
PH0013	Preliminary study of cementitious composite as a self-healing material in concrete structures	312
PH0028	Thermal stability of UHPC based on alkali-activated slag and metakaolin	316

Contents

	Topics	Page
	Papers	
PH0037	Sprayable Glass Bubble Insulation for Sustainable and Energy Efficient Building Insulation	320
PH0041	Preparing energy conservation self-levelling mortar via fly ash cenospheres/paraffin using in floor radiant heating	324
PI0003	Experimental study on ion penetration in concrete under the condition of competitive adsorption	328
PI0010	Crack reactivity of ultra-high performance fibre reinforced concrete under the flowing impact of geothermal water	332
PI0022	Durability of concrete with low temperature belite binder (LTBB)	337
PI0042	Insight on Chloride Ions Solidification Mechanism in Layered Double Hydroxides Designed with Different Cations both from First Principles Calculation and Experimental Work	341
PI0045	Sulphate Attack of Concrete in Sewer System	346
PI0055	Effects of Mixed salt in Saline Soil on the Microstructural Evolution of Cement Paste	350
PI0057	Physicochemical stability of calcium aluminate cement and hemihydrate-based material exposed to deep sea	354
PI0062	Influence of carbonation on chloride Resistance of low clinker cements	358
PI0073	Towards the Development of Prescriptive-Based Specifications for Non-Traditional SCMs to Prevent Alkali-Silica Reaction	362
PI0077	Influence of elevated environmental temperatures on passivation and corrosion risk of steel reinforcement	366
PJ0010	Ultra-green concrete: a technological breakthrough to save 800 Mt of CO_2 per year	370
PJ0012	Cement-Based Radiative Coolers for Photovoltaics: Towards a Practical Design	376
PJ0018	Capability of traditional and geopolymer cementitious systems for the immobilization of a thermally treated ion exchange resin	380

Contents

	Topics	Page
	Papers	
PJ0024	Influence of Waste Glass Powder and Silica Flour on Compressive Strength and Permeability of Cement Pastes at HTHP	384
PJ0035	Valorization of Calcium Sulfate Residues by Adding Accelerating Admixture in Portland cement	388
PJ0038	Effect of calcination temperature on paper mill lime sludge as an activator for GGBFS based cementless UHPC	392
PJ0039	Utilizing paper mill lime mud as fine aggregate for sustainable high- strength mortar	396
PJ0042	Relationship between the chemical composition of cementitious materials and their radioactivity	401
PJ0043	Effects of post-fire water curing on strength recovery of thermally damaged mortar from 800 ℃	405
PJ0054	Strength performance of recycled aggregate concretes with different qualities of recycled aggregates	410
PJ0061	Study on the Deterioration Mechanism of Cementitious Waterproofing Membrane (Part II: Microstructural Evolution)	414
PJ0070	Influence of Hardened Cement Paste (HCP) Particle Size on Their Reuse in Fresh Cement Paste	418
PJ0076	Investigation of Properties of Recycled Fine Aggregate Carbonated by Different Methods in Air or Water	422
PJ0079	Develop new concepts of Two Stage Concretes (TSC) achieving carbon neutral society	426
PJ0099	The Cement Sector and Life Cycle Assessment: Insights from a Systematic Literature Review	430
PJ0100	Estimating carbon uptake at building level: insights from a bottom-up approach	434
PJ0101	Calcium sulfoaluminate clinker production from sulfidic mine tailings	438

Contents

	Topics	Page
	Papers	
PJ0104	Recommendations of the French National project FastCarb about accelerated carbonation of recycled concrete	442
PJ0109	Preparation and hydration of steel slag-based cementitious material	446
PK0006	Recent advances on European cement standards prepared by CEN TC51 for more sustainable products	450

The 16th International Congress on the Chemistry of Cement 2023 (ICCC2023)
"Further Reduction of CO_2 -Emissions and Circularity in the Cement and Concrete Industry"
September 18–22, 2023, Bangkok, Thailand

Self-healing concrete using special biological materials.

Néstor Isaías Quintero Mora[1*], Carlos Castillo[2], José Julián Morales[3]

[1] *CEMEX, Monterrey, Mexico*

Email: nestorisaias.quintero@cemex.com
[2] *CEMEX, Monterrey, Mexico*

Email: carlos.castillol@cemex.com

[3] *CEMEX, Monterrey, Mexico*

Email: josejulian.morales@cemex.com

ABSTRACT

Ready-mix concrete represents one of the most resistant materials used in the construction industry. However, hardened concrete is also very susceptible to cracking due to several factors, for example shrinkage, lack of control joints, freezing / thawing cycles, or mechanical fatigue. Without adequate treatment, such cracks and microcracks tend to propagate affecting the integrity of the structure, thus favoring external agents like oxygen, water, chloride, or other chemicals to penetrate the concrete structure through the cracks networks and start corroding the metal reinforcement, leading a rapid deterioration of the mechanical resistance of the reinforced concrete. The present work describes the efforts from CEMEX to design a self-healing concrete using a porous aggregate, where this material contains a biological agent in the form of bacteria spores, with at least a calcium source and a carbon source, to enable a self-healing process of microcracks or cracks that form in the hardened concrete.

KEYWORDS: *Self-healing concrete, Cement Innovation, Bio-cements, B.pseudofirmus.*

1.Introduction

These failures in concrete structures translate into millions dollar of losses Calvo et all (2021), for this reason the self-repair technology originated with the purpose of reducing the costs derived from the continuous maintenance and where alternatives of self-repair have been proposed through physical, chemical, and biological methods. It is known that concrete-based materials can show autogenous healing of cracks due to the unreacted cement in the concrete that is exposed to moisture on the crack surface.

Until now, self-healing technologies have focused primarily on physical, chemical, and recently biological methods. The physical methods consist mainly of the use of discontinuous fibers of materials such as PVA, polyethylene and polypropylene of high tenacity Paul et al (2020). The repair achieved through the physical processes could be more due to a process of autogenous repair of the cement than to an effect of the fibers.

The described aggregate aims to provide a cost effective industrial solution (using bioproducts as raw material) overcoming the disadvantages of high costs and long term performance, The project aims at the use of a high strength cement based on artificial aggregate with controlled porosity to be able to immobilize bacteria/spores, calcium and carbon sources, several ways are mentioned relating to the manufacture of artificial porous aggregate media that reduce the risk of leaching of bacteria/spores when exposed to fresh cement paste Saifan(2016).

The technology aims to achieve a level of curing that inhibits the arrival of external water through the microcracks to the steel reinforcement of the concrete, avoiding its corrosion and degradation since as mentioned by François & Arliguie., (1999) those microcracks are one of the main causes of the exposure of the steel reinforcement. The technology involves the preparation of a porous micro-concrete to produce dry porous micro-concrete (carrier), which will be impregnated (immobilized) with biological compounds, to be used as a curing agent, in the production of a self-healing concrete.

The micro-concrete is produced using cement as the main binder with controlled porosity, the impregnation material comprises a carbon source, a calcium source and bacteria, the carbon source represents the source of nutrients for the growth and propagation of the bacteria. The integrated bacteria were *Bacillus pseudofirmus* which is among the microorganisms of Microbiologically Induced Calcite Precipitation (MICP), a phenomenon in which the environmental conditions and the metabolism of these MICP allow the generation of calcium carbonate structures in a natural way Garcia J. et al (2017).

2.Laboratory Tests - Preparation of the micro concrete based porous aggregates (carrier).

2.1. Design of the micro-concrete mix.

Cement type according to ASTM C150 with dosages between 280kg/m³ and 350Kg/m³. Fine aggregates typically from 0.5mm to 1.0mm with dosages between 580kg/m³ and 640Kg/m³. Water/cement ratio between 0.3% and 0.6% by weight % cement. Air entrained (cationic type) with dry solids content between 0.03% and 0.12% by weight % cement.

Porous micro-concrete samples were prepared with different air contents, from 15 % by volume to 25 % by volume. The air contents ranged from 0.03 to 0.12 wt.% to 25 wt.%, corresponding to air dosages (dry solids content) of 0.03 to 0.12 wt.% of cement. The air content of aggregates ranged from 35% to 45%.

Table 1: Typical concrete mix design for 1m³ of porous micro concrete to produce porous aggregates.

Element	Micro concrete 1	Micro concrete 2
Ordinary Portland Cement	300 Kg/m^3	300 Kg/m^3
Fine aggregates (0.55-0.84 mm)	587 Kg/m^3	587 Kg/m^3
H2O	121 L/m^3	121 L/m^3
Air Entrainer	240 g/m^3	240 g/m^3
NaCl additions	600 g/m^3	0 g/m^3

2.2. Measurement of aggregate pores.

The size (diameter) of the air voids (pores) in the porous micro-concrete was measured by scanning electron microscopy by measuring 5 to 10 pores in 10 fields at 500 to 1000x magnification. For each sample, at least 10 different zones or fields were selected, and 5 to 10 pores were measured at magnifications of 500x to 1000x. The sizes of the measured voids/pores ranged from 15 µm to 150 µm, with an average of 90 µm where a desired pore size between 20 and 150 µm is sought at a density of 2.4 g/cm3.

2.3. Production of porous aggregates (carriers) from micro-concrete.

Micro concrete samples were crushed with a jaw crusher and sieved to obtain aggregate particles ranging in size from 0.5 mm to 12 mm.

2.4. Bacteria cultivation and preparation

Bacillus pseudofirmus bacteria was cultured using the following procedure: Crude molasses were diluted with water to form a solution with a dry solids content of molasses between 0.05 and 3 wt.%. The pH was adjusted with a basic 4N sodium hydroxide solution to a pH of 10.5, at which the strain reacts best, but activity is observed from a pH of 9, at which it is best suited to the concrete conditions at a pH of 10.5. The sterilization of the molasse solution was done by autoclaving using a known sterilization process at a temperature of 121°C for 30 minutes at 1.03 bar. The inoculation of the molasses solution was performed with 100 µl of Bacillus pseudofirmus at 10^7—10^9 CFU per mL of molasses solution and an incubation period of 24h at 30 °C with an agitation of 200 rpm. The solution passed then through a centrifugation process for 10 min at 6000 rpm between 4 °C and 10 °C to gather the bacterial pellet (cell mass).
For spore generation, we used a standard culture broth where 100% sporulation was achieved within 72h.

2.5. Calcium and carbon sources and their impregnation in the aggregate

The calcium source was selected from inorganic calcium salts such as calcium chloride. A water solution with calcium source concentration between 0.1M and 0.3M. The organic carbon source was selected from raw molasses that were diluted with water to form a solution with dry solid content of molasses located between 0.08 and 2.5 weight %. The micro concrete aggregates were impregnated with the calcium source solution, carbon source solution and the solution containing the bacteria in two separate steps:

Step 1: The micro concrete was impregnated with a solution A containing the carbon source solution and the calcium source solution.

Step 2: The material (micro concrete) was encapsulated in a cartridge-like column, the bacteria/spore's solution B (with concentration of 10^9 — 10^{11} CFU per ml) was then poured slowly for impregnation.

Table 2: Mix design of the variousconcrete prepared, dosages in Kg or volume per m^3 of final concrete.

Fc'300												
Material	Reference Mix		Mix 1		Mix 2		Mix 3		Mix 4		Mix 5	
	Weight (kg)	Volume (m3)	Weight (kg)	Volume (m3)	Weight (kg)	Volume (m3)	Weight (kg)	Volume (m3)	Weight (kg)	Volume (m3)	Weight (kg)	Volume (m3) [NFRFI] [NFRF2] [NFRF3] [NFRF4] [NFRF5]
Portland Cement	300	0.095	300	0.095	300	0.095	300	0.095	300	0.095	300	0.095
Gravel 9 - 25 mm	734	0.274	723	0.27	723	0.27	723	0.27	723	0.27	723	0.27
Sand 0.25 4.5 mm	1112	0.421	1096	0.415	1096	0.415	1096	0.415	1096	0.415	1096	0.415
Expanded Clay	-	-	8.14	0.0096								
Porous aggregates from micro concrete 1							24	0.0096			24	0.0096
Porous aggregates from micro concrete 2					24	0.0096			24	0.0096		
Water	190	0.19	190	0.19	190	0.19	190	0.19	190	0.19	190	0.19
Molasses (%)									0.5		0.5	
CaCl2 (M)									0.24		0.24	
Bacteria (CFU/g of micro concrete)									1.0E+07		1.0E+07	

2.6. Preparation of a final concrete containing the self-healing agent.

Final concrete samples were prepared by mixing the constituents listed below normally for 4 to 5 minutes according to the protocol used for concrete mixing, using a conventional concrete mixer, after which representative final concrete samples were prepared as described in table 2.

According to the project and with respect to the reference mix part of the dense aggregates was replaced by porous aggregates. In mix 1 the porous aggregates were expanded clay, in mix 2 the porous aggregates were non-impregnated micro-concrete 2 (table 2) porous aggregates (carrier), in mix 3 the porous aggregates were non-impregnated micro-concrete 1 (table 2) porous aggregates (carrier), in mix 4 the porous aggregates were impregnated micro-concrete 2 (table 2) porous aggregates (curing agent), in mix 5 the porous aggregates were impregnated micro-concrete 1 (table 2) porous aggregates (curing agent). impregnated micro concrete 1 (table 2) porous aggregates (curing agent).

Some examples of final concrete mix designs are presented in Table 2. In the examples, the rate of replacement of course and sandy aggregates (with respect to the Reference Mix) by porous micro-concrete aggregates in mix1, mix 2, mix 3, mix 4, and mix 5 remained constant at 1.4 % volume.

3.Results

The final cured concrete specimens prepared according to the example mix designs in Table 2 were pre-cracked at 28 days of curing using a hydraulic press at a rate of 0.35 N/mm2*sec until cracks were visible (visible to the naked eye). On average, 15 surface cracks with a width of between 200 μm and 2 mm and a length of between 5 and 10 cm were observed per sample. The pre-cracked samples were stored for 100 days at 22+2°C and 95% to 100% relative humidity.

The healing rate of each sample after 100 days was calculated by averaging the percent repair (total crack coverage achieved) of 10 cracks (length: 1.5-2 cm and width:100- 700 μm) in a sample.

Table 3 presents the average results for the different final concrete prepared with the mix designs described on table 2.

Table 3: Compressive strength of the diferent samples

Compressive strenght	Reference Mix	Mix l	Mix 2	Mix 3	Mix 4	Mix 5
7 days (MPa)	24.2	19.9	23.4	24.5	24	24.3
28 days (MPa)	29.8	24.5	29.4	30.2	30. l	30.4

From Table 4, taking the reference mix at 100 days (healing rate 36.5%), the substitution of 1.4% by volume of dense aggregates with porous aggregates impregnated with micro-concrete without the addition of alkaline salts (micro-concrete 2) resulted in an increase in the healing rate of 40% (mix 4). From Table 4, taking as a reference the reference mix at 100 days (healing rate 36.5%), the substitution of 1.5.

Table 4: Healing rate at 100 days for the final concrete prepared with the mix designs of table 2

Mixes	Reference Mix	Mix l	Mix 2	Mix 3	Mix 4	Mix 5
Healing Rate (%)	36.5	n.a.	36.8	36	5 l	71.46

The substitution of 1.4 % of dense aggregates by porous micro-concrete impregnated aggregates with additions of alkaline salts (Micro concrete 1) resulted in an increase in the healing rate of 96% (Mixture 5).

In general, it can be admitted that the healing rate was strongly related to the bacteria/spores.

Colony Forming Units (CFU) active in the final hardened concrete. The comparison between the curing rate of the final concrete prepared respectively with mixes 4 and 5 showed that the presence of the alkaline salt in the mix design to prepare the porous concrete microaggregates positively influenced the survival rate of bacteria/spores.

In concrete samples prepared with mix design 5, the alkaline salt will be present in the porous concrete micro-aggregates and, when exposed to the final concrete cement paste during the mixing process, will accelerate the setting of the final concrete cement paste on the surface of the porous micro-aggregates.

The follow-up of the repair was carried out following the longitudinal repair with photography and reference rule measuring with the ImageJ software what would represent 100% of the total of the crack and as the crack sealing is observed the percentage of repair is calculated, examples of the repairs can be seen in the Figure 1 where the repair of a reference crack with a maximum opening of 0.230 mm and in the case of the specimen with the impregnated aggregate with a maximum opening of 0.310 mm can be observed.

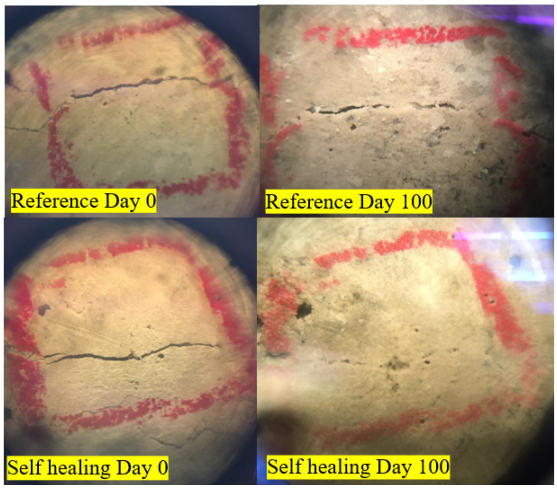

Figure 1. Example of initial cracks vs. at the end of 100 days where the repair is observed in the reference and impregnated aggregate specimens.

4. Conclusions

The healing rate, on the other hand, remained constant at 69% to 72% for dosages of the healing agent of 5 volume %, 10 volume %, 15 volume % and 20 volume % and 30 volume % of the total aggregates of the final concrete.

From an industrialization (manufacturing capability, storage capacity, separate silo for the healing agent) and cost (manufacturing cost of the healing agent is higher compared to normal aggregates), it is preferable to use a low dosage of the healing agent while ensuring the maximum healing capability.

The healing agent according to the research thus provides important advantages with respect to the prior art. According to the research, high healing rates, above 70%, can be achieved with low dosages of the healing agent 0.5 to 5 volume % of the total volume dense aggregates and the mechanical properties of the final concrete containing the healing agent are not negatively affected by the presence of said healing agent.

References

Calvo Valdés, A., Medeiros, M. H. F., and Macioski, G. (2021). "Corrosion sensor for monitoring reinforced concrete structures: Tests on reinforced concrete specimens", *Revista ALCONPAT*, 11(3): 64-87

François R., and Arliguie G. (1999). "Effect of micro cracking and cracking on the development of corrosion in reinforced concrete members", *Magazine of concrete research*, 51(2) 143-150

García J., Rodriguez D., Wang J., De Belie N., Moran J.M., Guerra M.I., and Valdés A.J., (2017). "Quality improvement of mixed and ceramic recycled aggregates by bio deposition of calcium carbonate", *Construction and building materials*. 154. 1015-1023

Paul, S., van Zijl, G., and Šavija, B. (2020). "Effect of Fibers on Durability of Concrete: A Practical Review", *Materials*, 13(20): 4562

Seifan, M., Samani, A.K. and Berenjian, A. (2016) "Bioconcrete: next generation of self-healing concrete", *Applied Microbiology and Biotechnology*, 100 (6): 2591-2602

The 16th International Congress on the Chemistry of Cement 2023 (ICCC2023)
"Further Reduction of CO_2 -Emissions and Circularity in the Cement and Concrete Industry"
September 18–22, 2023, Bangkok, Thailand

3D Printed Prefabricated Prefinished Volumetric Construction for Sustainable Construction

K. Pongpaisanseree[1*], P. Jongvisuttisun[2], P. Jiramarootapong[3], K. Meemuk[4], P. Chaiyapoom[5] and C. Snguanyat[6]

SCG Cement Co.,Ltd., CPAC, Bangkok, Thailand
[1] *Email: kittispo@scg.com,* [2] *Email: passarij@scg.com,* [3] *Email: patipatj@scg.com*
[4] *Email: kornravm@scg.com,* [5] *Email: phattarc@scg.com,* [6] *Email: chalerms@scg.com*

ABSTRACT

The construction industry is struggling with many problems, such as skilled labor shortage, poor productivity, lack of construction safety, and high waste and pollution generation. As a result, many construction technologies have been invented to solve problems. Much research on 3D printing for construction has proven that 3D printing is a viable solution. By using automation and machines to work instead of people, one can use less construction labor and reduce the accident rate on the construction site while increasing the construction speed. Moreover, 3D printing provides a high level of design freedom.

Prefabricated Prefinished Volumetric Construction (PPVC), a modular construction, is another approach for reducing problems in the construction industry. Since modules are produced and finished from the factory and delivered to the site for installation, only a short period is required on-site. Thus, the quality is controlled and construction time is significantly reduced.

This project demonstrated the integration of 3D printing technology with a PPVC approach. 3D printing enhanced the production process by allowing freedom of operation when producing modules. A prototype 3D-printed PPVC building with two stories was constructed. The total useable area of the building was 68 square meters. The building was divided into four modules with different wall textures. From the study, 3D-printed PPVC reduced the construction time and waste from the construction site, and also improved embodied carbon from construction stage compared with the conventional construction.

KEYWORDS: *3D Printing, PPVC, Modular Construction*

1. Introduction

The construction industry worldwide is facing various problems, including a shortage of construction labor, safety issues on construction sites, waste and pollution from construction, and long construction times. Therefore, new construction technologies have been developed to solve these problems, one of which is Additive manufacturing for construction or 3D construction printing. This technology has been widely studied and developed because it uses automation and machinery to replace human labor, thereby significantly addressing the problem of construction labor shortage. In addition, this technology offers many advantages for the construction industry, such as reducing waste from construction, increasing efficiency and accuracy, reducing errors, reducing accidents on construction sites, and increasing design flexibility (Warszawski and Navon (1998), Sakdanaraseth et al (2016), Li et al (2017)).

Another construction technology to mitigate problems in the construction industry is PPVC, which uses the Design for Manufacturing and Assemble (DfMA) principle. This construction technique is prevalent in many countries, especially in Singapore. PPVC uses engineering knowledge to simplify the structure and manufacture building components in an industrial factory apart from the construction site (off-site). By using modular construction process, modules are produced with architectural finishes and MEP systems. These modules are then transported to the construction site and assembled to form a building, like building Lego blocks (Liew et al. (2019)). This process significantly reduces the time, the amount of labor required to work on-site, the waste and pollution from construction, and provides better quality control of construction qualities.

Based on the advantages above, this project combined the PPVC construction system with 3D Printing technology, which we defined as "Prefabricated Prefinished 3D Printed Volumetric Construction (PP3DVC)". This process improves the efficiency of module production and overall construction, and provides more flexibility in building design. The project involved designing and constructing a two-story residential building, shown in Figure 1, with a total area of 68 square meters which is the world's first 2-storey 3D printed building constructed with prefabricated prefinished volumetric construction approach. In addition, the modules' weight was reduced by the design of floor system and the development of lightweight 3D printing mortar. This work also studied the performance and impacts of the construction of PP3DVC in different dimensions, including construction time, waste generated from the construction, and total embodied carbon from construction.

2. Design of 3D printed prefabricated prefinished volumetric construction

2.1 Concept design

3D printing technology has a significant advantage in allowing more design freedom than conventional techniques. Therefore, each 3D-printed building can have unique characteristics that differentiate it from others. Thus, this prototype 2-story building was designed with a unique shape and curved wall to highlight the design advantages. In addition, the exterior walls were designed with parametric design principles to have different patterns on each module. The structure comprised four prefabricated modules, each with different sizes and functions. Each module was manufactured and finished inside a factory. The modules were constructed using the prefabricated prefinished volumetric construction approach. Construction modules are shown in Figure 1. Another critical factor to consider in designing was the weight of each module which impacts the difficulty of construction. In this project, the weight of each module was limited to at most 10 tons to facilitate transportation and installation.

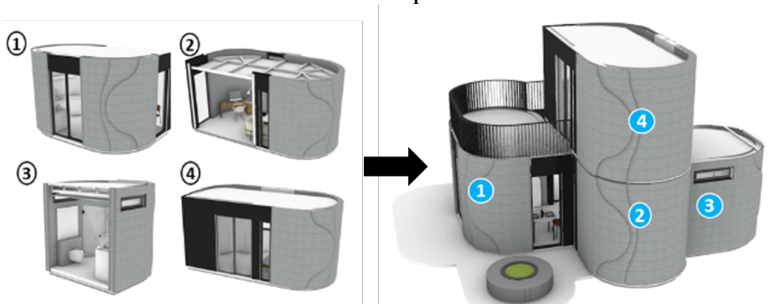

Figure 1: Concept design of "Prefabricated Prefinished 3D Printed Volumetric Construction" building

2.2 Structural design

The building structure is designed for residential building purpose, with a live load of 150 kg/m^2. The structure of each module is composed of a steel frame with steel sections connected by welding. The modules are assembled using a dry joint system, and the completed structure is a moment-resisting frame. Due to the weight limitations of the module, we designed it using a steel frame in combination with a lightweight floor system and 3D printing wall, which has been developed to reduce weight.

Due to the hybrid structure of the building, consisting of steel and 3D-printed walls, a structural analysis of both the steel structure and the 3D-printed walls was conducted. While the steel structure was analyzed using Autodesk Robot software, the 3D-printed walls were analyzed using finite element analysis (FEA) based on the behavior of 3D-printed walls from previous research (Jiramarootapong et al. (2020), Tanapornraweekit et al. (2022)). Results from both analyses were used to consider the structural behaviors in lifting, transportation, construction, and use stages to ensure performance and safety.

2.3 Connection joint

In PPVC construction, modules must be assembled, so the performance of connection joints is crucial to the building. Joints in the PP3DVC building were designed based on strength, leakage prevention, ease of assembly, and aesthetics. Research from Chen et al. (2018) was also studied and applied to the design of structural connections used in the building.

3. Lightweight 3D printing mortar

In modular construction systems, the weight of the modules is another critical factor to consider as it impacts transportation and installation. Generally, Reinforced Concrete (RC) PPVC modules are heavier than Steel PPVC modules. Since the project used cement-based mortar for 3D printed walls, a lightweight 3D printing mortar was developed to reduce the weight of 3D printed walls. The density of the lightweight 3D printing mortar is 1,600 kg/m^3, which is 16% lighter than that of normal-weight 3D printing mortar (1,900 kg/m^3), but the compressive strength of both formulas is comparable. The properties of the lightweight 3D printing mortar used are shown in Table 1.

Table 1 Properties of lightweight 3D printing mortar

Properties	Standard	Value	
Water requirement (percent per dry mortar)	-	25.5	%
Time of setting, initial	ASTM C807	110-150	minute
Density at 28 days	ASTM C642	1,600	kg/m^3
Compressive strength at 28 days	ASTM C109	40	MPa
Flexural strength at 28 days	ASTM C348	7.4	MPa

From the development of a lightweight module system using a steel frame in combination with a light floor and lightweight 3DP wall system, we were able to reduce the weight of each module to no more than 10 tons. The total weight of each module is 6.58, 7.64, 5.71, and 7.5 tons, respectively.

4. Manufacturing and construction process

Construction of the PP3DVC building was divided into three parts:

1. Site preparation: This involved preparing the construction site and foundation work parallel to module production. The total duration for this stage was 22 days.
2. Factory fabrication: This stage involved the production of 4 modules, including floor fabrication, 3D wall printing, installation of steel structures, and off-site finishing work, which included architectural and MEP work in the factory, as shown in Figure 2. The total time for this stage was 48 days.
3. On-site installation and finishing: This involved transporting the pre-fabricated modules for construction and completing all finishing work on-site. The jobs completed on-site were module jointing, concrete slab placement for the balcony, roofing, and external staircase, as shown in Figure 3. The total duration for this stage was 8 days.

Figure 2: Factory fabrication

Figure 3: On-site Installation and Finishing

The total construction period was 60 days, from August 2022 to October 2022, with 62% of the construction work off-site and 38% on-site. When comparing 3D Printed PPVC with traditional masonry construction (brick-and-mortar) and precast concrete construction, the construction time was reduced by 64 days or 51%, and 20 days or 25%, respectively. The comparison of total construction time is shown in Figure 4. The exterior and interior of the building are shown in Figure 5.

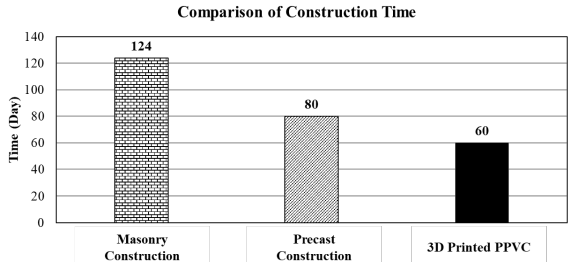

Figure 4: Comparison of construction time between 3D printed PPVC and traditional construction

Figure 5: The exterior and interior of the building

5. Construction wastes and embodied carbon

When calculating the amount of waste generated from the construction, the waste generated from construction of the building using the 3D printed PPVC approach building was less than that of using the masonry construction approach by up to 95%, equivalent to embodied carbon reduced to approximately 3,700 kg CO_2e in terms of waste materials. When calculating the total amount of embodied carbon from materials, production processes, transportation, and installation of the building (cradle-to-practical operation), it was found that the PP3DVC building has an embodied carbon of 294 kg CO_2e/m^2, which is less than that of the same-sized building constructed with masonry construction, which has an embodied carbon of 323 kg CO_2e/m^2.

6. Conclusions

The construction of the PP3DVC building demonstrates the advantages of both 3D printing and PPVC technologies, including:

1. Design: 3D printing technology helps increase freedom in designing building shapes to be unique.
2. Construction efficiency: It can reduce construction time by focusing on off-site construction of completed modules from the factory. Quality control can be managed without rework. This building was constructed in just only 60 days.
3. Environmental friendliness: It reduces pollution from construction activities on-site, including dust, noise, and waste. Additionally, it reduces the amount of embodied carbon produced throughout the construction process.

References

Warszawski, A. and Navon, R. (1998) “Implementation of robotics in buildings: current status and future prospects”, *J. of Construc. Eng. Manage.*, 124: 31-41

Sakdanaraseth, T., Prasittisopin, L. and Horayangkura, V. (2016) “Design and construction of curvilinear geometry architecture of 3D printing technology incorporating cement-based material – case study: A multi-purpose pavilion”, *5th Intern. Conf. Sustain. Energy. Green Arch., Smart Technology and Built Environment (SEGA-05)*

Li, X., Qureshi, A. and Al-Hussein, M. (2017) “Developing a BIM-based integrated model for CAD to CAM building production automation”, *34th Intern. Symp. Automat. Robot. Construc. (ISARC)*

Liew, J.Y.R., Chua, Y.S. and Dai, Z (2019) “Steel. concrete composite systems for modular construction of high-rise buildings”, *Structures*, Volume 21: 135-149

Jiramarootapong, P., Prasittisopin, L., Snguanyat, C., Tanapornraweekit, G. and Tangtermsirikul, S. (2020) "Load Carrying Capacity and Failure Mode of 3D Printing Mortar Wall Panel Under Axial Compression Loading.", Edited by F., Lucas, S., Wolfs, R., Salet, T. Bos. *Second RILEM International Conference on Concrete and Digital Fabrication.* DC 2020

Tanapornraweekit, G., Jiramarootapong, P., Paudel, S., Tangtermsirikul, S. and Snguanyat, C. (2022) "Experimental and Numerical Investigation of 3d Printed Mortar Walls Under Uniform Axial Compression.", *Construction and Building Material*, Volume 360

Chen, A.W., Hao, W., Bi, H. and Lacey, K. (2018) “Structural response of modular buildings – An overview.” *Journal of Building Engineering* Volume 16: 45-46

The 16th International Congress on the Chemistry of Cement 2023 (ICCC2023)
"Further Reduction of CO_2 -Emissions and Circularity in the Cement and Concrete Industry"
September 18–22, 2023, Bangkok, Thailand

The First 3D Printed 2-storey Building in Thailand

P. Jiramarootapong[1 *], P. Jongvisuttisun[2], K. Pongpaisanseree[3], K. Meemuk[4], P. Chaiyapoom[5] and C. Snguanyat[6]

SCG Cement Co.,Ltd., CPAC, Bangkok, Thailand
[1] *Email: patipatj@scg.com,* [2] *Email: passarij@scg.com,* [3] *Email: kittispo@scg.com*
[4] *Email: kornravm@scg.com,* [5] *Email: phattarc@scg.com,* [6] *Email: chalerms@scg.com*

ABSTRACT

3D printing technology has become one of the most popular construction methods worldwide due to its advantages over traditional construction, such as reducing waste on construction sites, solving labor shortage problems, and, one of the most well-known advantages, reducing total construction time, As demonstrated in 2020, SCG (Siam Cement Group) has constructed the first 102 square meters of 3D-printed building in Thailand within one month. The structure is a one-story with non-load bearing parametric 3D printed walls. The printed wall area is 270 square meters, and the printing time took only seven days. In 2022, this project, SCG, combines 3D printing technology with traditional construction method to construct a 345 square meters 2-storey medical center building in Saraburi, Thailand. The building includes 2-storey non-load bearing 3D printed walls and 1-storey load bearing 3D printed walls. The building was designed to resist the seismic load. The behaviors of 3D-printed walls were modeled using finite element analysis with the boundary condition from the primary structure behavior. The seismic load was superimposed as a horizontal load along the height of 3D-printed walls. The analyzed results of the 3D printed wall were compared with SCG-SIIT 3D printing research criteria. First cracking strain and interfacial properties were used as criteria for the analysis. The analysis showed that the safety factor of 3D printed walls being at least four based on critical first cracking strain criteria.

KEYWORDS: 3D printing construction; Mortar; Structural response

1. Introduction

The population growth rate around the world is rising steadily. Therefore, the increase in the need for means of subsistence, such as accommodation, is inevitable. At the same time, the construction industry also struggles with the shortage of construction workers and working skills (L. Reiter, T. Wangler (2018)). Therefore, research on digital construction is studied extensively to overcome such problems. In the modern industry, 3D printing, one of the most outstanding technological advancements in additive manufacturing, has been widely used in various applications such as health care, aerospace, and architecture, due to the benefit of technology in reducing the number of operation workers to control the quality of the outcome. Based on this benefit, 3D printing technology is a popular solution for solving the labor shortage situation in the construction industry worldwide. Besides, the benefits of technology for construction in unique design and waste reduction have also been demonstrated in many countries. As in Thailand, in 2020, SCG constructed a 1-story 3D printed building with a 102 square meter co-working area in Saraburi, Thailand. The design's unique aesthetically textured walls and structural functionality were accounted for in the design through various digital programming software such as parametric modeling.

In recent years, SCG has continued researching 3D printing construction to leverage construction 3D printers to fabricate increasingly large, detailed, and ambitious buildings. Therefore, in 2022, we constructed the ASEAN's first 2-story 3D printed building with a 1-story 3D printed load-bearing structure, "SCG health center", as a prototype to demonstrate the potential of combining 3D printing construction technology with traditional construction techniques for building a large commercial area building. Located in Saraburi, Thailand, the building is a medical center for SCG employees and subcontractors around

Kheng Khoi. This paper presents the key concept of designing and constructing the building. The project's challenges, such as construction planning and analysis of structural behaviors, are also illustrated.

2. Manufacturing procedure

2.1 Concept design

Figure 1a. Shows the final concept design of the building. The entire building space is 345 square meters to accommodate six functional roles, including an examination room, trauma room, recovery room, pharmacy, conference room, and breastfeeding room. The exterior walls of the building are 3D printed with two 3D-printed construction techniques. One is a 2-story non-load bearing 3D printed facade, while another is a 1-story load bearing 3D printed wall. The 2-story non-load bearing wall's texture was designed to provide continuity along the height to represent the "curtain," as shown in Figure 1b. The interior walls inside the building are lightweight panels to reduce the weight of the whole structure.

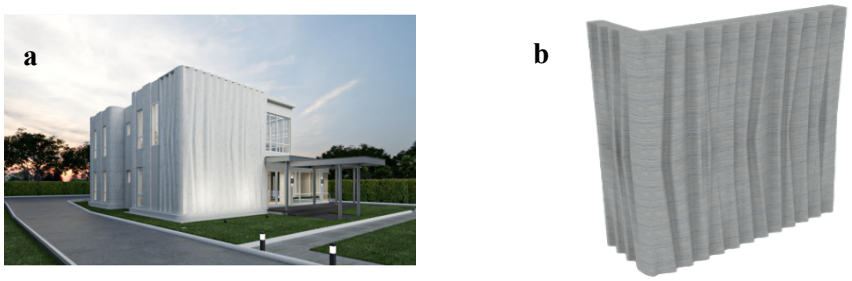

Figure 1: a. Final design of "SCG Health center" building b. The texture of 2-storey non-load bearing 3DP panel

The non-load-bearing 3D-printed walls are combined with prefabricated columns and beams. The construction solution for precast construction with 3D printing as a non-load-bearing wall was studied and applied in this building. The total printed 2-story wall area is 240 square meters, and the maximum printed size at 6.25 meters long and 6.8 meters high. The average thickness of the wall is about 30 centimeters. In this building, one room with a usable area of 20 square meters was designed as a 1-storey load-bearing 3D printed structure. The bearing wall was designed to carry the vertical load from the precast slab. The specifications of the 3D printing panel, both non-load and load bearing, including the dimension of the printing path, the thickness of the 3D printed wall, and the intensity of the infill shell, were designed based on analysis from the finite element method to ensure that the 3D printing panels can transfer all forces and loads safely.

2.3 Materials

The materials used in this project were two 3D printing mortar classes based on the bearing capacity requirement. The properties of the 3D printing material are shown in Table 1.

Table 1: Properties of 3D printing material

Property	Standard	Load bearing (High strength)	Non-load bearing (Low strength)
		NN550	NN250
Setting time (min)	ASTM C807	110-150	110-150
Compressive strength, MPa	ASTM C109	≥80	≥35
Split tensile strength, MPa	ASTM C496	2.1	1.4
Flexural strength, MPa	ASTM C348	12	8

3. Design and analysis concept for the 3D printed structures

The main load-carrying structure for this building is the skeleton of the precast column and beam members. The non-load bearing 3D printed wall panel was designed to support the lateral force, including wind and seismic loads. The lateral load must be transferred from the 3D-printed non-load-bearing walls to the skeleton structure. The load-bearing 3D printed panel was designed to carry lateral and vertical loads from the upper slabs with the live load requirement of 100 kg/m2. The significant challenge in this building was constructing a 3D-printed one-story load-bearing wall structure. The solution for construction, such as bearing reinforcements and connections with other members, is based on the load-bearing masonry code requirements (TMS 402: Building Code Requirements for Masonry Structures, formerly designated as TMS 402/ACI 530/ASCE 5). In addition to design code for 3D-printed walls, both non-load and load-bearing, the structural analysis based on knowledge from 3D printing research was performed to ensure structural safety. All 3D printed walls were designed and calculated with the criteria from a previous study about the large-scale testing of 3D printing panels (P. Jiramarootapong(2020) and G.Tanapornraweekit, P.Jiramarootapong (2022)).

Since the building was designed to resist the seismic load, the structural integrities of 3D printed walls, both load-bearing and non-load-bearing walls, were modeled with the boundary conditions from the complete structural analysis from Autodesk Robot. The seismic load was superimposed as a horizontal load along the height. The study showed that the safety factor of 3D printed walls being at least four based on critical first cracking strain criteria. The models of a non-load-bearing structure and a load-bearing structure are shown in Figures 4a and 4b, respectively.

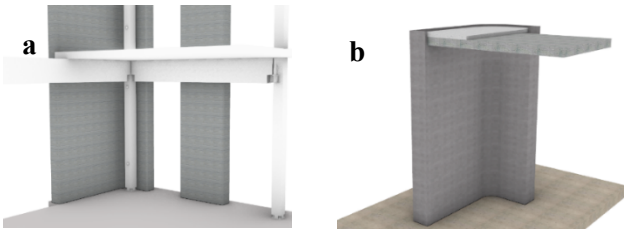

Figure 4 a. Non-load bearing structure b. Load bearing structure

4. 3D printing construction process

The overall building construction process began with the pre-construction phase, during which the architectural and structural designs needed to be clarified. CPAC BIM software was used as a construction management tool since the pre-construction phase to optimize the 3D printing time, construction sequence, and detailed engineering. The 3D printing construction took place for 108 working hours to print 240 square meters of wall area and required nearly 80 tons of cement. After that, the building's structural elements, such as its beams and precast columns, were installed. The last step was the completion of the architectural, mechanical, electrical, and pumping work. Figure 5 and Figure 6 present the flow of the working process and the overall appearance of the building before interior finishing, respectively. By using CPAC BIM technology, the 3D printing time and construction sequence were optimized. The main structural members of the building was based on traditional construction, which includes precast beams, columns, and shear walls with 2-story non-load bearing 3D printed walls. This method reduced the total construction time by 20 percents.

Figure 5: The working process

Figure 6: The 3D printed 2-story building

5. Conclusions

The study presents the advantages of combining 3D printed technology with traditional construction methods and also the advantage of load-bearing 3D printing construction over non-load-bearing 3D printing construction, which include:

1. **Design:** Compared to traditional construction, 3D printing technology allows designers to create more uniqueness through increased flexibility in design and construction.
2. **Construction speed:** This project's printing speed was 2.2 square meters per wall panel per hour. Also, with CPAC BIM technology, the construction sequence was foreseen. Both technologies reduced the total construction time by 20 percent
3. **Construction efficiency**: The quality of the wall's construction was controlled by the 3D printed machine.
4. **Larger usable area:** No extra structural elements are needed for a load-bearing 3D printed structure.
5. **Environmental friendliness:** It lessens dust, noise, and trash pollution caused by construction activities on the construction site.

Acknowledgements

The authors would like to acknowledge Prof. Somnuk Tangtermsirikul and Assoc. Prof. Ganchai Tanapornraweekit, Construction and Maintenance Technology Research Center (CONTEC), for their consultation on developing this project's construction solution. Also, to the C-insight company limited, which has given valuable comments on structural behavior analysis and connection details configuration.

References

Wangler T., Roussel R., Bos F.P, Salet T.A.M., and Flatt R.J., "Digital Concrete: A Review", *Cement and Concrete Research*, 2019 (123)

Everett H. "THAILAND'S SCG 3D PRINTS CO-WORKING BUILDING DESIGNED BY PARAMETRIC MODELING", [cited 2021 Oct 12]. Available from: https://3dprintingindustry.com/news/thailands-scg-3d-prints-co-working-building-designed-by-parametric-modeling-184368/

Jiramarootapong, P., Prasittisopin, L., Snguanyat, C., Tanapornraweekit, G., Tangtermsirikul, S. (2020). Load Carrying Capacity and Failure Mode of 3D Printing Mortar Wall Panel Under Axial Compression Loading. In: Bos, F., Lucas, S., Wolfs, R., Salet, T. (eds) Second RILEM International Conference on Concrete and Digital Fabrication. DC 2020. RILEM Bookseries, vol 28. Springer, Cham. https://doi.org/10.1007/978-3-030-49916-7_65

Tanapornraweekit G., Jiramarootapong P., Paudel S., Tangtermsirikul S., Snguanyat C.,"Experimental and numerical investigation of 3D-printed mortar walls under uniform axial compression", *Construction and building materials,* 2022(360)

The 16th International Congress on the Chemistry of Cement 2023 (ICCC2023)
"Further Reduction of CO_2 -Emissions and Circularity in the Cement and Concrete Industry"
September 18–22, 2023, Bangkok, Thailand

Outline of NEDO Moonshot Project "Calcium Carbonate Circulation System in Construction"

T. Noguchi[1*], I. Maruyama[2], R. Kitagaki[3], M. Kanematsu[4], M. Tamura[5], S. Fujimoto[6], M. Tsujino[7], H. Nakazawa[8], Y. Kuroda[9], H. Hirao[10], H. Hyodo[11], and T. Masuo[12]

[1] *The University of Tokyo, Tokyo, Japan*
Email: noguchi@bme.arch.t.u-tokyo.ac.jp
[2] *The University of Tokyo, Tokyo, Japan*
Email: i.maruyama@bme.arch.t.u-tokyo.ac.jp
[3] *Hokkaido University, Sapporo, Japan*
Email: ryoma@eng.hokudai.ac.jp
[4] *Tokyo University of Science, Noda, Japan*
Email: manabu@rs.tus.ac.jp
[5] *Kogakuin University, Tokyo, Japan*
Email: masaki-t@cc.kogakuin.ac.jp
[6] *Utsunomiya University, Utsunomiya, Japan*
Email: fujim@cc.utsunomiya-u.ac.jp
[7] *Shimizu Corporation, Tokyo, Japan*
Email: m.tsujino@shimz.co.jp
[8] *Shimizu Corporation, Tokyo, Japan*
Email: nakazawa.h@shimz.co.jp
[9] *Shimizu Corporation, Tokyo, Japan*
Email: y.kuroda@shimz.co.jp
[10] *Taiheiyo Cement, Sakura, Japan*
Email: Hiroshi_Hirao@taiheiyo-cement.co.jp
[11] *Taiheiyo Cement, Sakura, Japan*
Email: Hikotsugu_Hyoudou@taiheiyo-cement.co.jp
[12] *Masuo Recycle, Tokyo, Japan*
Email: taka.m@masuo-group.com

ABSTRACT

Cement concrete is an indispensable construction material, but its production uses a large amount of limestone, which is a finite natural resource, and emits a large amount of CO_2. To fundamentally solve these problems, Ca in cement concrete accumulated as a construction is regarded as a potential unused resource capable of capturing CO_2. By developing a technology to regenerate cement concrete demolition waste and CO_2 in the air as calcium carbonate concrete (CCC), a new resource recycling system called "C^4S", Calcium Carbonate Circulation System for Construction will be realized. This paper outlines a status of the project. An efficient crushing method and an efficient CO_2 capture and storage method for waste concrete are being developed. After crushing, the powders are used to produce calcium bicarbonate solution and the large particles are densely packed with pressure in a container as aggregate. Calcium bicarbonate solution is flowed or impregnated between the aggregate particles, and calcium carbonate crystals are precipitated by controlling temperature and evaporation rate. The calcium carbonate crystals bond the aggregate particles to form CCC. In addition, various studies are being conducted to implement C^4S in society, including studies on structural design, optimum recycling scenario, and analysis of $LCCO_2$ reduction effect. With the realization of C^4S, global warming will be greatly suppressed in the future.

KEYWORDS: *Calcium carbonate, Precipitation, Waste concrete, CO_2, Circulation*

1. Introduction

To solve CO_2 emission and limestone depletion at the same time, Ca in concrete structures is regarded as a potential resource absorbing CO_2. An innovative technology is being developed to regenerate waste concrete and CO_2 in the atmosphere as calcium carbonate concrete (CCC). As shown in Figure 1, the C^4S project is aimed to develop technology for rapid carbonation of demolished waste concrete, technology for production of highly concentrated calcium bicarbonate solution from carbonated waste concrete and atmospheric CO_2, technology for structural CCC production using carbonated waste concrete and calcium bicarbonate solution, and technology and system for implementation of CCC in construction.

2. Manufacturing of CCC raw materials

2.1 Production of carbonated raw materials

High humidity accelerates carbonation of cement paste powder (CPW). On the other hand, carbonation of coarse CPW with a certain particle size (e.g., 0.6 to 1.18 mm) progresses in initial stage but is suppressed after a few days due to $CaCO_3$ barrier formation. Therefore, for practical application of CO_2 absorption into waste concrete, it is essential to develop direct air capture (DAC) acceleration into coarse CPW, improving gas permeability of crushed waste concrete. Experiments on DAC acceleration are underway, focusing on a wet-heat cycle with natural ventilation. Figure 2 shows that carbonation of coarse CPW can be accelerated when exposed to cyclic RH60-80% rather than constant RH60% or RH80%.

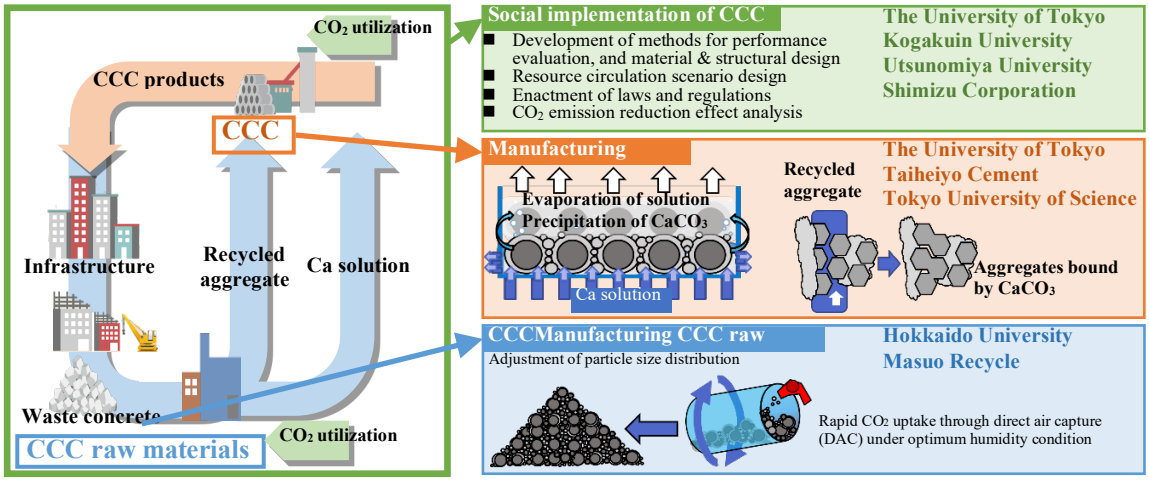

Figure 1. Overview and organization of C^4S reserach and development project

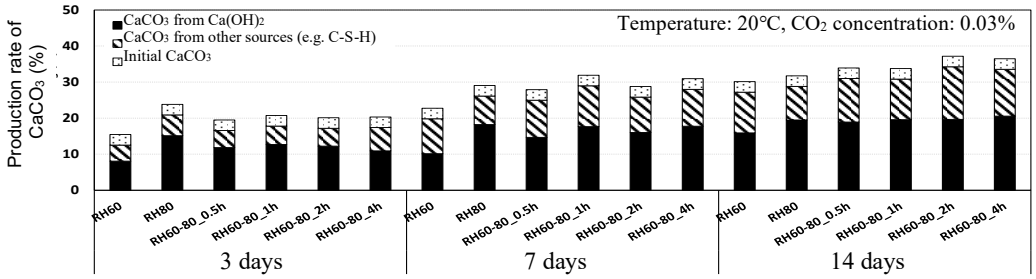

Figure 2. Calcium carbonate production rate by each source of calcium

2.2 Production of bicarbonate solution

Calcium bicarbonate solution for CCC manufacturing is produced by blowing CO_2 into water in which substances containing Ca has been added. Ca solubility in calcium bicarbonate solution highly depends on temperature (Kojima et al (1992)), and the rate of increase in Ca solubility is affected by the particle size of solid containing Ca. Ion-exchanged water was placed in a container and cooled to 5°C or 20°C and stirred while CO_2 gas was blown into the container for 18 hours, after which the carbonated cement paste

and mortar were added and the changes in Ca^{2+} concentration and pH were measured over time. As expected, Ca solubility was higher at 5°C than at 20°C as shown in Figure 3. The smaller the grain size, the greater the dissolution rate of Ca and the higher the Ca solubility.

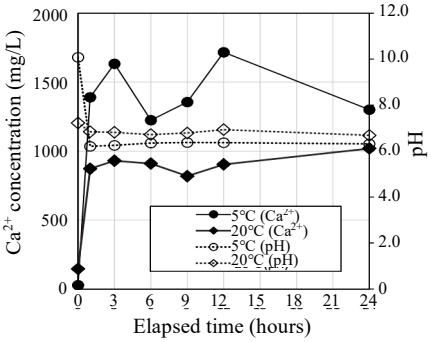

Figure 3. Effect of temperature on Ca

3. Manufacturing of CCC

The carbonated waste concrete particles are packed in a container, and the calcium bicarbonate solution is poured between the particles and the container is heated. Since the solubility of Ca decreases with increasing temperature, $CaCO_3$ precipitates when the container is heated. This precipitation forms a cross-linked structure between the particles, which gives strength to CCC. When $CaCO_3$ precipitates from calcium bicarbonate solution, CO_2 is generated again. To capture and utilize this CO_2 efficiently, it is desirable that some of the filled particles have hydrates with uncarbonated Ca contributing to further carbonation. Therefore, even if the waste concrete is not fully carbonated, the process of wet carbonation can efficiently carbonate Ca in the waste concrete. Since the production process currently under development involves heating, the dominant precipitating phase of $CaCO_3$ is aragonite (Tai and Chen (1998)), as shown in Figure 4. Previous studies by Maruyama et al. (2021) have shown that the precipitation of aragonite is useful in the development of CCC strength.

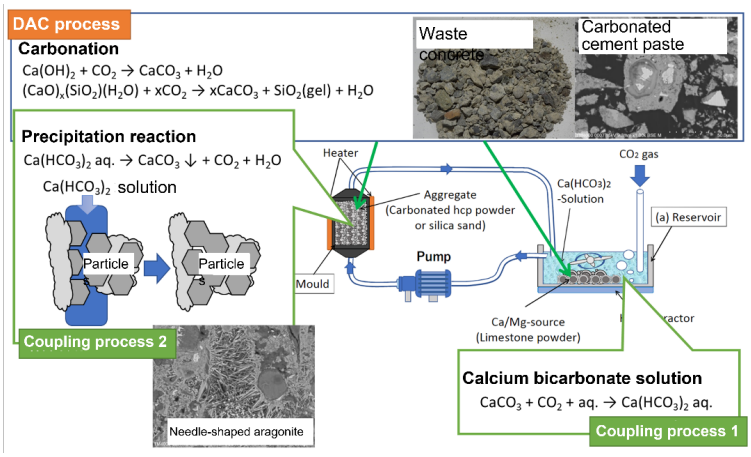

Figure 4. Precipitation method for CCC manufacturing

Another manufacturing method for CCC is to apply pre-loading to waste concrete particles packed in a mold as shown in Figure 5. CCC raw material, carbonated mortar powder of 0.6 mm or less, is mixed with its 10-15% water, packed in a mold, and loaded at 10 MPa. The mold is removed, and the specimen is immersed in a calcium bicarbonate solution with Ca^{2+} concentration of 0.5 g/L and total carbonate concentration of 1.3 g/L for 2 hours, and then dried for at least 12 hours to form a CCC hardened body. Compressive strength of up to 56 MPa has been obtained with φ10x20 mm specimen because of increased mortar powder filling rate and precipitated calcium carbonate content. The addition of magnesium sulfate or seawater during immersion in the calcium bicarbonate solution also contributed to the increase in strength up to 56 MPa. Currently, optimization of the manufacturing process is underway with the aim of increasing the size of CCC specimens.

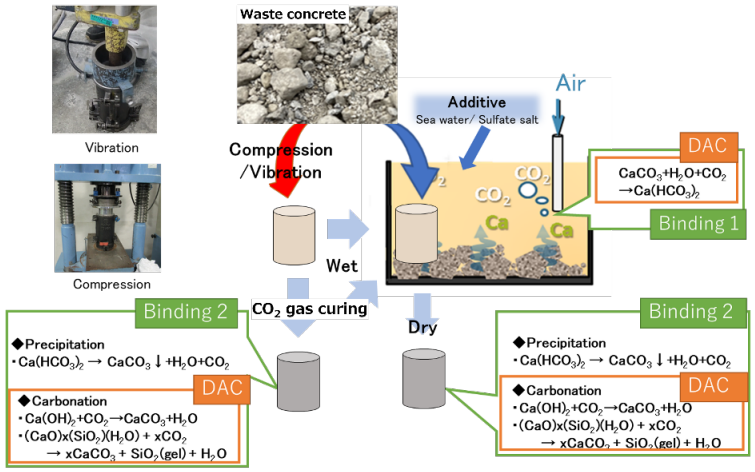

Figure 5. Pre-loading method for CCC manufacturing

4. CCC structural members

A possible form of structural CCC member is to manufacture unit members filled with CCC in a thin-walled steel tube and connect them by tensioning rods as shown in Figure 6. Toward realization of this form, experiments were conducted on simulated members filled with low-strength concrete in thin-walled steel tubes. Even when the strength of concrete was 5 MPa, the steel tube provided a confining effect, resulting in a

strength of 10 MPa or higher, and the relation between the strength and the restrained steel ratio was linear. Therefore, the strength of CCC member is estimated from the strength of CCC and the thickness of steel tube.

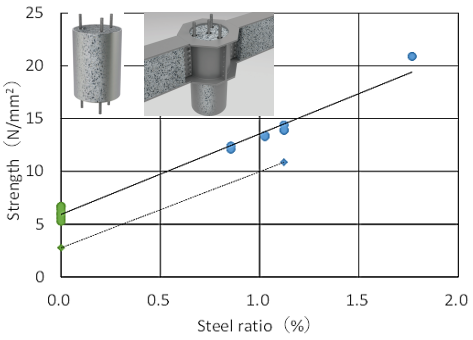

Figure 6. Confining effect on strength

5. Social implementation of CCC structures

5.1 Resource circulation

To stably manufacture CCC in the future, a stable supply of waste concrete generated by demolition of structures is needed. Therefore, based on various statistical information, the amount of waste concrete from building demolition in Japan was estimated. The results are shown in Figure 7. It is also known that the amount of waste concrete generated from civil engineering structures is about 80% of that from buildings. Taking this into account, the total amount of waste concrete generated in Japan by 2050 is expected to be about 6.9 billion tons, which can be effectively used as raw materials for CCC.

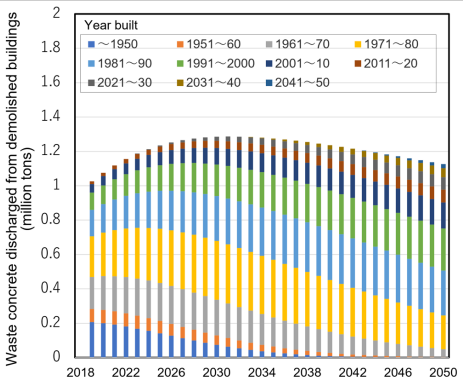

Figure 7. Waste concrete generation

5.2 CO_2 emission and sequestration

In manufacturing CCC raw materials and CCC, CO_2 is emitted during waste concrete crushing, rapid carbonation, pressure molding, and cooling and heating of calcium bicarbonate solutions. On the other hand, crushed waste concrete absorbs a large amount of CO_2. Ideally, the sum should be negative. The balance of CO_2 emission and absorption in manufacturing CCC raw materials and CCC at current laboratory level and in plants in the future is shown in Figure 8. Carbon negative CCC can be achieved by large scale production, improving the thermal efficiency in CCC production, using low-temperature waste heat and natural cooling, and increasing the carbonation rate of the CCC raw material.

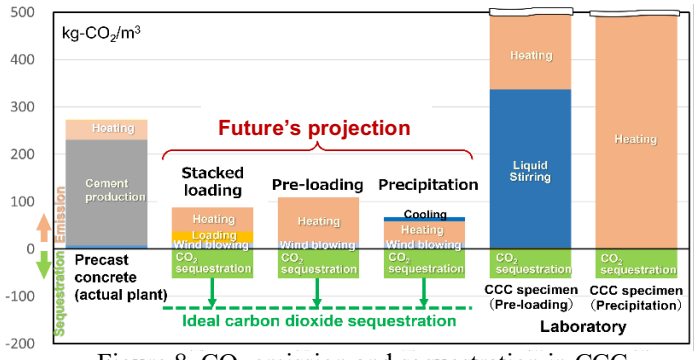

Figure 8. CO_2 emission and sequestration in CCC

6. Conclusions

Since CCC is a structural material that is completely different from conventional concrete, it is necessary to establish guidelines for CCC manufacturing methods, as well as design, construction and maintenance methods for CCC structures, to promote CCC widely in the world. Furthermore, if CCC is to be applied to the main structural components of buildings, it is essential to investigate the legalization of CCC. In ancient times, hundreds of millions of years ago, CO_2 was fixed in the process of raising the Himalayas and the Alps, creating a cool earth where living organisms could live. There are great expectations for the project, which is a grand attempt to reproduce this event in modern civilized society and save the earth.

References

Kojima, Y. et al (1992) "Control of Crystal Shape and Modification of Calcium Carbonate Prepared by Precipitation from Calcium Hydrogencarbonate Solution", *Journal of Ceramic Society of Japan*, 100(1165): 1145-1153

Maryama, I. et al (2021) "A New Concept of Calcium Carbonate Concrete using Demolished Concrete and CO_2", *Journal of Advanced Concrete Technology*, 19(10): 1052-1060

Tai, C.Y. and Chen, F.B. (1998) "Polymorphism of $CaCO_3$, precipitated in a constant-composition environment", *AIChE Journal*, 44: 1790-1798

The 16th International Congress on the Chemistry of Cement 2023 (ICCC2023)
"Further Reduction of CO_2 -Emissions and Circularity in the Cement and Concrete Industry"
September 18–22, 2023, Bangkok, Thailand

Effects of different calcined kaolinite clays on the sulfate demand of LC^3 cements

Lucas Goldenberg Py[1a], José da Silva Andrade Neto[1b], Márlon Longhi[1c], Ana Paula Kirchheim[1d]

[1] *Laboratory of Innovation in Eco-efficient Cement, Federal University of Rio Grande do Sul (UFRGS), Porto Alegre, Brazil*

[a] *lucasgpy@gmail.com*
[b] *josedasilvaandradeneto@gmail.com*
[c] *marlonlonghi@gmail.com*
[d] *anapaula.k@gmail.com*

ABSTRACT

Calcined clays and limestone filler arise as an alternative to lower the clinker content and reduce carbon dioxide emissions in the cement industry, given their wide availability worldwide. In recent years, limestone calcined clay cement (LC^3) has been studied as a promising cement to achieve net zero. However, LC^3 cements present different sulfate demand -in terms of the amount of calcium sulfate needed to reach optimum properties- when compared to Portland cement (PC), and the factors influencing the sulfate demand of the LC^3 cements are not yet well understood. This study aimed to evaluate sulfate balance and hydration kinetics of LC^3 using two calcined clays with different kaolinite content and superficial specific area (78.2 wt.% and 34.3 m^2/g *vs*. 46.1 wt.% and 77.7 m^2/g). Mixes of PC and LC^3 cements, varying the amount of calcium sulfate in the blend (from 2.0 to 5.5%), were studied. Isothermal calorimetry, thermogravimetric analysis, and compressive strength tests were conducted. It was observed in the calorimetric tests a wide difference in the early hydration between the ternary cements and OPC. The finer calcined clay, despite having a much lower kaolinite content, resulted in higher sulfate demand. This probably occurred due to the acceleration of the C-S-H precipitation caused by the filler effect. Both calcined clays, due to the high surface areas and therefore enhanced reactivity consumed all portlandite formed at 3, 7 and 28 days.

KEYWORDS: *LC^3, sulfate balance, cement, hydration, calcined clay.*

1. Introduction

The cement industry is a significant source of greenhouse gas emissions. The primary source of these emissions is the chemical process used to produce cement, called the "calcination" process. This process releases high amount of carbon dioxide (CO_2) in the atmosphere. Overall, the cement industry is responsible for approximately 7-8% of global carbon dioxide emissions, making it a significant contributor to climate change according to Nie et al (2022).
Limestone Calcined Clay Cement (LC^3) is a type of cement that is made by combining Portland clinker, limestone, calcined clay, and gypsum. LC^3 is designed to have a lower carbon footprint than traditional Portland cement by replacing a significant portion of the clinker with calcined clay and limestone. Scrivener et al (2018). The use of calcined clay in this cement can help to reduce the amount of CO_2 emissions from cement production by up to 30% compared to traditional Portland cement.
The presence of aluminates in calcined clay and the presence of gypsum in the cement are both important for the pozzolanic reaction to occur. However, according to Andrade Neto, De la Torre and Kirchheim (2021), more ettringite is formed by the presence of additional Al ions in calcined clays calcium sulfate is consumed faster. The balance between aluminium and calcium sulfate in the cement plays an important role in the hydration kinetics of the cement. By controlling this balance, the setting time and strength of

the cement can be adjusted to meet the specific needs of the project. This study aimed to evaluate sulfate balance and hydration kinetics of limestone calcined clay using two different sources of metakaolin.

2. Materials and methods

Two calcined clays were mixed with clinker, limestone filler and gypsum to produce ternary blended cements. One clay with a high amount of kaolinite (HMK) and other with a medium amount of kaolinite (MMK). The clays were calcined in a stationary kiln at 650 °C and 750 °C for 2 hours, respectively, and then grounded in a disk mill. The calcination temperatures were defined according to preliminary tests, which determined the temperatures needed to reach a complete dehydroxylation of kaolinite.
BET Superficial specific area (SSA) of the materials was determined using a Micromeritics (model Gemini VII) apparatus. XRD measurements were conducted in zero background holders, using a X'Pert Pro PANalytical diffractometer equipped to X'Celerator detector, operated at 45 kV and 40 mA with CuKα radiation in a step size 0.0167° 2θ equivalent to 60 min per scan from 7° to 70° 2θ. Thermogravimetry analysis was assessed by Mettler Toledo TGA 2 aparatus, between 40 °C and 1000 °C range, with a heating rate ramp of 20 °C/min at airflow with a purge of nitrogen.
The HMK presented a BET SSA of 34.3 m²/g, while the MMK presented a much higher BET SSA equal to 77.7 m²/g. The higher SSA obtained in MMK is explained by Jovanovic et al (1992). Figure 1 shows thermogravimetric analysis on the left and XRD diffractograms on the right, of the raw and thermally activated clays.

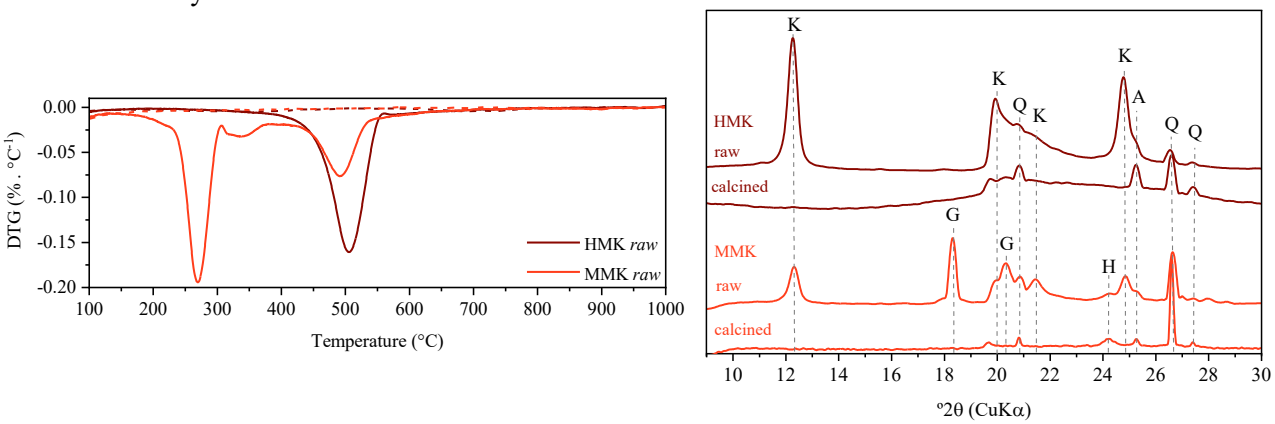

Figure 1. TGA of the raw clays (continued lines) and clacined clays (dashed lines) on the left; XRD of the raw and calcined clays. K- kaolinite, G- gibbsite, H-hematite, A-anatase, Q-quartz on the right.

Two mass losses event between 150 °C and 400 °C were observed in MMK clay, which corresponds to gibbsite transformation into amorphous alumina, as observed in the XRD diffractogram of the raw and calcined sample. Between 400 °C and 650 °C, dehydroxylation of kaolinite was observed for both clays. From the weight loss between 400 and 650 ºC, it was possible to estimate the kaolinite content of the raw clays: 78% and 46% for HMK and MMK, respectively. Comparing the DTG curves of the raw and calcined clays, a complete dihydroxylation of kaolinite was obtained for both clays, which was confirmed by the XRD results.
In addition, R³ tests using isothermal calorimetry (at 40 °C) were performed to evaluate calcined clays' reactivity as prescribed by Avet et al (2016). The total heat released after 36 hours of reaction was 689.5 J/g of calcined clay for the HMK, and 384.9 J/g of calcined clay for the MMK, indicating the much higher reactivity of the HMK. Cement pastes were prepared within a mix proportion of 95-5% of clinker and gypsum for OPC; LC^3 pastes were prepared in a 55 wt.% of clinker+gypsum and 45 wt.% of of calcined clay: limestone (2:1 ratio). Sulfate adjustment was conducted, varying the total $\%SO_3$ content from 2.0 to 5.5.
To evaluate hydration kinetics, a TAM air microcalorimeter was used at 22 °C in cement pastes at a w/b ratio of 0.6. In addition, the cement hydration was stopped by isopropanol exchange at 3, 7 and 28 days, and thermogravimetry analysis of the cement pastes were performed, using the same equipment and following the same procedure described before for the kaolinite clays.

3. Results and discussion

Figure 2 shows sulfate optimization by calorimetry analysis with different sulfate levels. The so-called optimum sulfate content is the one that allows the alite reaction to occur before the sulfate depletion and the renewed aluminate reaction. In this sense, the OPC cement show optimum content between 3.5 and 4.0 $\%SO_3$ – which the shoulder peak occurs a few hours after the silicate peak. For the HMK, the optimum sulfate level is between 3.0 and 4.0 $\%SO_3$. However, the MMK exhibits a much higher sulfate demand. Up to 3.0 $\%SO_3$, one can note that the sulfate depletion occurs before the main silicate peak, which retards and supress the alite reaction. For proper sulfation, a sulfate content between 4.5 and 5.5 $\%SO_3$ is needed. It is important to highlight that these content are higher than the allowed by standards (usually up to 4.0 – 4.5%), as it can result in durability problems with delayed ettringite formation (DEF). The higher sulfate demand of the MMK, despite its lower kaolinite content compared to HMK, is probably due to much higher BET SSA (77.7 vs. 34.3 m^2/g). The higher SSA results in an enhanced filler effect, with a higher C-S-H precipitation rate, which adsorbs more sulfate ions, accelerating sulfate depletion, as previously observed by Zunino and Scrivener (2019).
Comparing the optimum sulfate mixes, one can note that the OPC mix releases a much lower amount of heat per g of clinker (3 vs. 6 – 6.5 mW/g of clinker at the peak of silicate peak and 250 vs. 500 J/g of clinker at 72 hours), which indicates a much fast clinker reaction in the LC^3 cements due to the filler effect, as also observed by Zunino and Scrivener (2019) and Avet and Scrivener (2018).

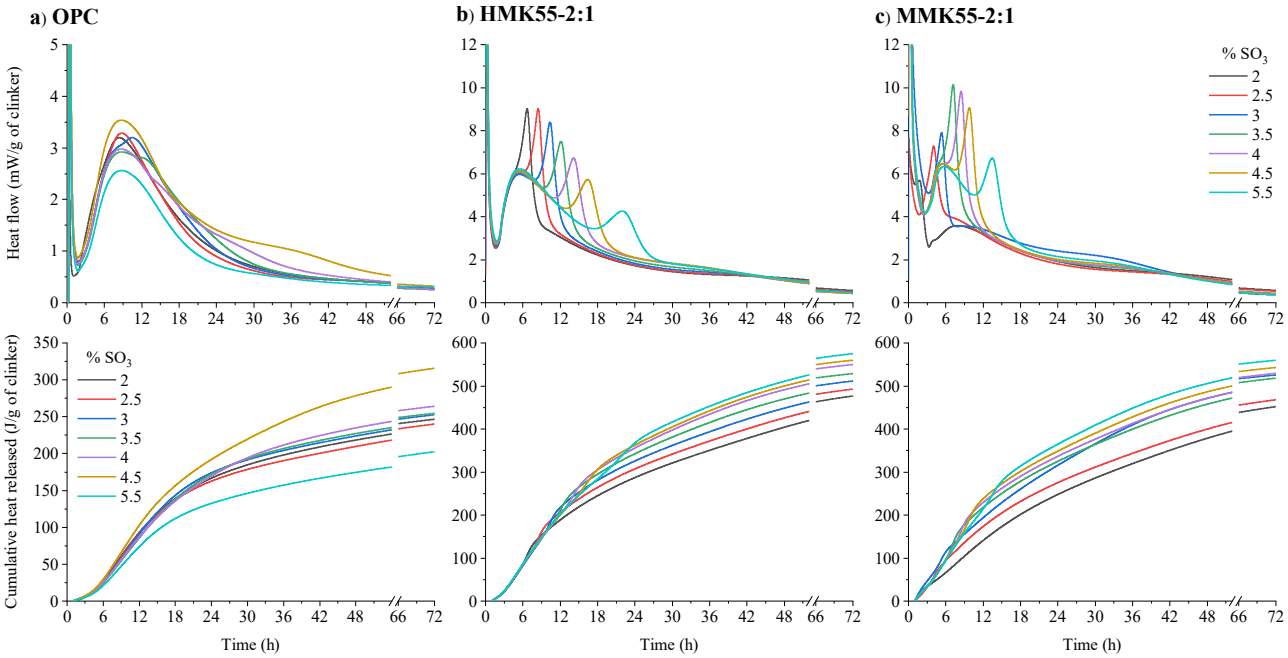

Figure 2. Calorimetry analysis of cement pastes with different SO_3 levels; heat flow (1st row) cumulative heat released (2nd row).

Figure 3 presents the Portlandite and combined water content, determined by TGA, and compressive strength at 3, 7, and 28 d.

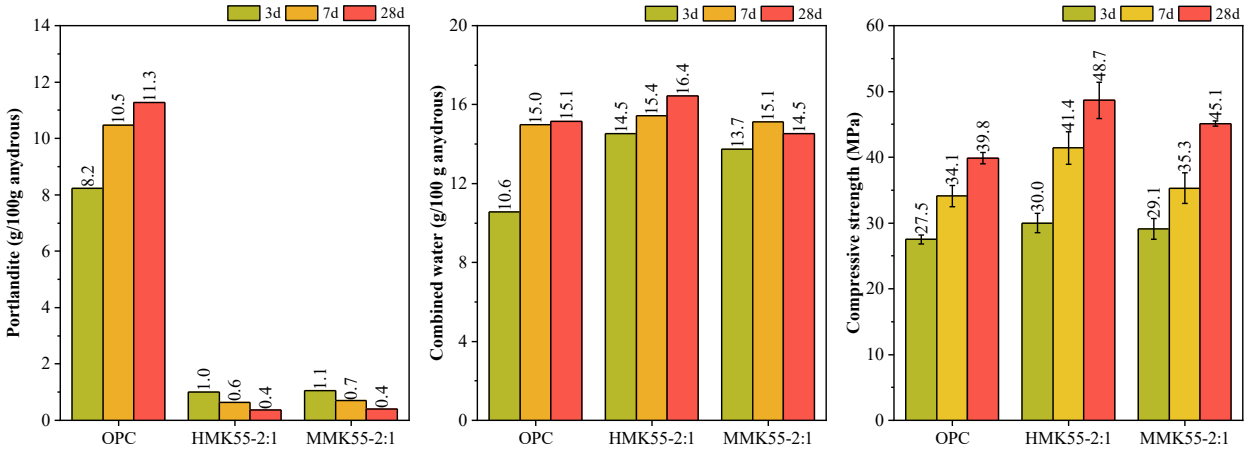

Figure 3. Portlandite content, combined water and compressive strength.

Calcium hydroxide content was extremely lower in LC^3 systems compared to OPC due to the lower amount of clinker and pozzolan effect. The LC³ cements presented similar compressive strength of OPC at 3 days, and exhibited higher compressive strength at 28 days (22.4% and 13.3% higher for HMK and MMK cements, respectively). The similar strength at 3 days, despite the much lower clinker content, is explained by the enhancement of clinker reaction due to the filler effect, as observed by calorimetry. The higher strength at later ages results from the pozzolanic reaction and the pore refinement, as observed by Avet and Scrivener (2018).

3. Conclusions

It was observed that the superficial specific surface area of the MMK clays had a great effect on the sulfate balance and hydration kinetics of the blends. The higher surface area resulted in early sulfate depletion even with lower kaolinite amounts. Both ternary blended cements consumed higher amounts of calcium hydroxide and showed higher compressive strength results compared to OPC, with only clinker and gypsum in its composition.

References

Andrade Neto, J. da S., De la Torre, A. G. and Kirchheim, A. P. (2021) 'Effects of sulfates on the hydration of Portland cement – A review', *Construction and Building Materials*, 279, p. 122428.

Avet, F. *et al.* (2016) 'Development of a new rapid, relevant and reliable (R3) test method to evaluate the pozzolanic reactivity of calcined kaolinitic clays', *Cement and Concrete Research*. 85, pp. 1–11.

Avet, F. and Scrivener, K. (2018) 'Investigation of the calcined kaolinite content on the hydration of Limestone Calcined Clay Cement (LC3)', *Cement and Concrete Research*, 107, pp. 124–135.

Jovanovic, et al. (1992) "Properties of activated alumina obtained by flash calcination of gibbsite", *Journal of Colloid and Interface Science*, 150, pp36-41.

Nie, S. *et al.* (2022) 'Analysis of theoretical carbon dioxide emissions from cement production: Methodology and application', *Journal of Cleaner Production*, 334, p. 130270

Scrivener, K. *et al.* (2018) 'Calcined clay limestone cements (LC^3)', *Cement and Concrete Research*, 114, pp. 49–56.

Zunino, F. and Scrivener, K. (2019) 'The influence of the filler effect on the sulfate requirement of blended cements', *Cement and Concrete Research*, 126, p. 105918.

The 16th International Congress on the Chemistry of Cement 2023 (ICCC2023)
"Further Reduction of CO_2 -Emissions and Circularity in the Cement and Concrete Industry"
September 18–22, 2023, Bangkok, Thailand

Monitoring of nucleation and growth of C-S-H phases by analytical ultracentrifugation and ICP-OES

T. Sowoidnich[1*], C. Rößler[2], H.-M. Ludwig[3] and H. Cölfen[4]

[1] *Bauhaus-Universität Weimar, Finger-Institute for Building Materials, Weimar, Germany*

Email: thomas.sowoidnich@uni-weimar.de

[2] *Bauhaus-Universität Weimar, Finger-Institute for Building Materials, Weimar, Germany*

Email: Christiane.roessler@uni-weimar.de

[3] *Bauhaus-Universität Weimar, Finger-Institute for Building Materials, Weimar, Germany*

Email: horst-michael.ludwig@uni-weimar.de

[3] *University of Konstanz, Department of Physical Chemistry, Konstanz, Germany*

Email: helmut.coelfen@uni-konstanz.de

ABSTRACT

The pathway of nucleation and growth of C-S-H is important for understanding the hydration kinetics of Portland cement and subject of the present work. Therefore, analytical ultracentrifugation (AUC) is used to characterize the nucleation of C-S-H in aqueous environments with a detection capability ranging from ions to sub-micron particles. Complementary, the chemical composition of the aqueous phase is investigated by means of inductively coupled plasma-optical emission spectroscopy (ICP-OES). Combination of AUC and ICP-OES allows a clear distinction between formation of nanoscale particles and development of ion concentration.

The experiments were designed with the aim at producing C-S-H from C_3S hydration without portlandite and calcite. Therefore, the C_3S hydration was conducted in diluted continuously stirred suspensions with special designed reaction control.

Results from the aqueous phase composition prove that both pH and calcium ion concentrations are nearly constant, signaling that portlandite has not formed, and that silicon concentration varies within 24 hours of hydration with known assignments of C-S-H precipitation. Thus, the used experimental setup is suitable for the investigation of C-S-H crystallization from C_3S hydration without formation of portlandite.

In parallel to ICP-OES, the aliquots were examined by AUC regarding the sedimentation coefficient, which refers to the velocity of sedimentation; larger values correlate with increased species size or density. The experimental data prove that the aqueous phase contains in the majority ions, but also clusters with variable sizes/densities, and species that are larger than atom clusters. These are assumed to be nano-scaled particles. The sedimentation coefficient of the clusters varies broadly, which may reflect variation in composition / water content. In conclusion, the present work shows that the nucleation of C-S-H originated from hydrating C_3S occurs via pre-nucleation clusters.

KEYWORDS: *C-S-H, Hydration, Prenucleation, Non-Classical Nucleation*

1. Introduction

During the hydration of tricalcium silicate (C_3S) and dicalcium silicate (C_2S) calcium-silicate-hydrate (C-S-H) phases and portlandite are formed. The pathway of nucleation and growth of C-S-H is important for understanding the hydration kinetics of Portland cement. The present work focuses on the early stages of C-S-H nucleation by applying analytical ultracentrifugation (AUC) and inductively coupled plasma-optical emission spectroscopy (ICP-OES) to analyse the aqueous phase of C_3S suspensions. The

experiments were designed with the aim to precipitate C-S-H with high Ca/Si from C_3S hydration without portlandite and calcite or the presence of foreign ions (e.g. Na, K, Cl). Therefore, the C_3S hydration was conducted in diluted, continuously stirred suspensions using a special designed reaction control according to Lecoq (1993), which was slightly modified to allow extraction of aliquots. After different time-steps an aliquot of the suspension was extracted, filtrated and immediately investigated by means of AUC and ICP-OES.

2. Materials and methods

Triclinic C_3S was prepared by burning a mixture of calcium carbonate ($CaCO_3$, Merck, p.a.) and amorphous silica (SiO_2, Merck, p.a.) several times at 1550°C with milling procedures in between. The chemical analysis of the C_3S was determined by chemical wet analysis. The following composition was determined (wt.-%): LOD=0.0, LOI=0.2, CaO=73.0, SiO_2=26.2, Al_2O_3=0.0, Fe_2O_3=0.0, MnO=0.0, MgO=0.0, Na_2O=0.01, K_2O=0.01, SO_3=0.1. The free lime content was 0.1. Calcium hydroxide (Merck, p.A.) was mixed with purified water for the preparation of the starting solution (saturated calcium hydroxide solution). The suspension experiments were started by adding C_3S to the saturated calcium hydroxide solution. All preparation steps were conducted at 25 °C in N_2 atmosphere to prevent carbonation.

The aqueous phase extracted from the hydrated C_3S suspensions was subjected to AUC and ICP-OES. For AUC, the aqueous phase was filled into 12 mm Ti double sector cells (Nanolytics, Potsdam, Germany) with sapphire windows. MilliQ water was used in the reference sector. These measuring cells were put into an An-60 Ti rotor in an analytical ultracentrifuge (AUC, Beckman-Coulter XL-I), which was operated at 20 °C. The sedimentation of the particles was assessed by means of an advanced Rayleigh interference optics developed by Nanolytics at 60,000 rpm. For the determination of time-dependent development of the species dispersed in the aqueous phase, at first short measuring intervals of 20 s for a duration of 49.5 min were applied. Each sample was measured in four-plicate. The filled rotor with the cells was tempered to 20 °C for 1 h before the start of the experiment. The data was evaluated using two-dimensional spectrum analysis (2DSA) with 50 Monte Carlo (MC) iterations (Brookes et al. (2010)) in UltraScan III version 4.0, revision 6577 for Linux. From the 2DSA-MC evaluation method, the sedimentation coefficient (s) and diffusion coefficient (D), the hydrodynamic diameter obtained from the diffusion coefficient (d_D) and the density of the hydrated sedimenting species (ρD) has been calculated.
The ICP-OES measurements were conducted to determine the ion concentrations of the aqueous phase in a Horiba ActivaM (Jobin Yvon). At λ=317.933 and 373.690 nm the concentration of Ca and at λ=251.611 nm the concentration of Si were analysed. The limit of detection was 0.07 µmol/L for Si, and the limit of quantification was 0.2 µmol/L for Si.

3 Results

Results from the aqueous phase composition in Figure 1 prove that both pH and calcium ion concentrations are nearly constant (pH=12.58±0.03; [Ca]=22.8±1.4 mM) and silicon concentration varies within 24 hours of hydration. A first increase of Si to 40-45 µM is observed after 10 min of C_3S hydration, which is followed by a minimum after 1 h of hydration. Thereafter a slight increase in silicon concentrations is detected, which is followed by a decrease that ends up in a constant low value (plateau) until 24 h of hydration. The variation of silicon concentration assigns the formation of C-S-H (Barret (1980)). The typical drop of calcium ion concentration and pH caused by portlandite precipitation is not observed because the critical supersaturation with respect to portlandite ([Ca]=30-36 mM (Barret (1997))) has not been reached. Thus, the used experimental setup is suitable for the investigation of C-S-H crystallization from C_3S hydration without formation of portlandite.

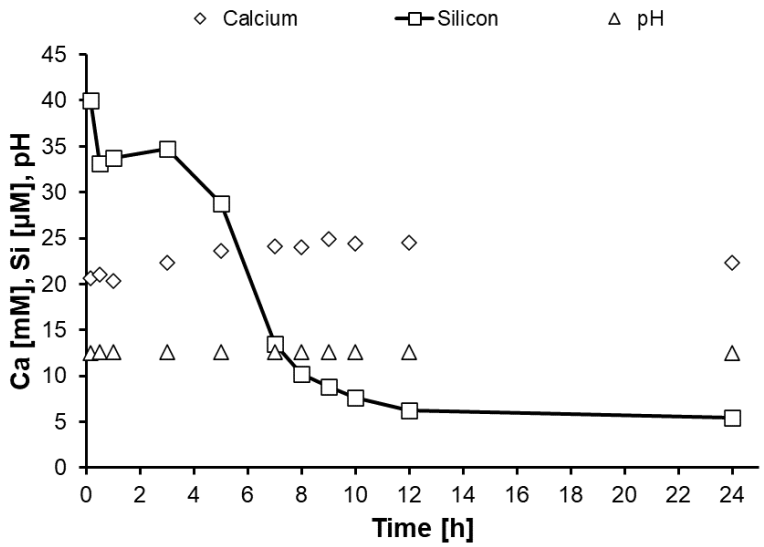

Figure 1. Time-dependent development of the calcium, silicon and hydroxide (as pH) concentration of the aqueous phase of C_3S-suspension with reaction control.

In parallel to the investigation of the ion composition of the aqueous phase via ICP-OES, the aliquots were examined by AUC. Results of the obtained sedimentation coefficients are shown in Figure 2.

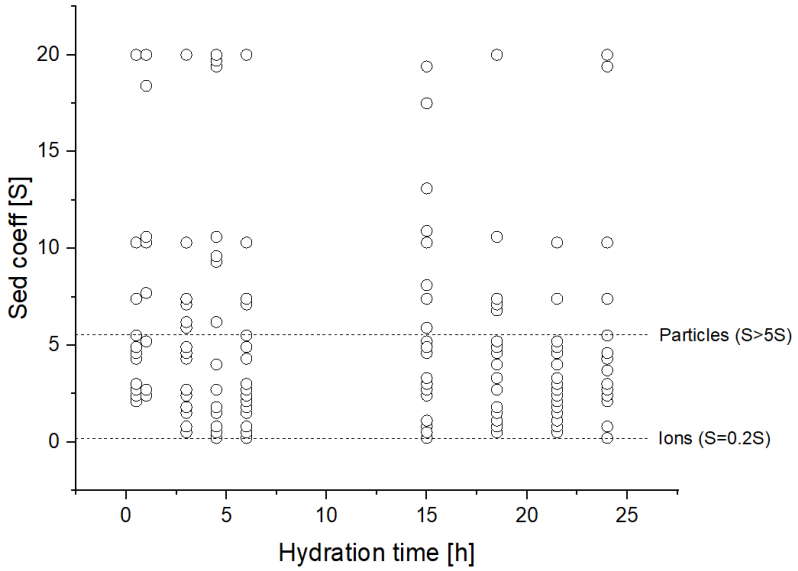

Figure 2. Time-dependent development of the sedimentation coefficient. The regions of ions, cluster and particles are sketched in the figure by dashed lines.

Results in Figure 2 demonstrate that, except for the first 30 min of hydration, in all samples identical species are detected by AUC. The value of the sedimentation coefficient refers to the velocity of sedimentation, larger values correlate with increased species size or density (Gebauer (2008)). Limits for sedimentation coefficients of ions and particles (Gebauer (2008)) are indicated by dashed lines in Figure 2. Therefore, the experimental data prove that the aqueous phase contains not only ions and particles, but also clusters with variable sizes/densities (region between ions and particles). The sedimentation coefficient of the clusters varies broadly, which may reflect variation in composition / water content.
The water content in the clusters can be estimated from the frictional ratio f/f0, which reflects the deviation of the shape of a species from a sphere and its hydration (association with water molecules). A sphere has a f/f0 ratio of 1.0, and all deviating shapes (other shapes, association with water molecules) have higher f/f0 ratios as 1.0. (Dong (2021)) The f/f0 distribution over the sedimentation coefficient is shown in Figure 3 for the sample hydrated for 1 hour.

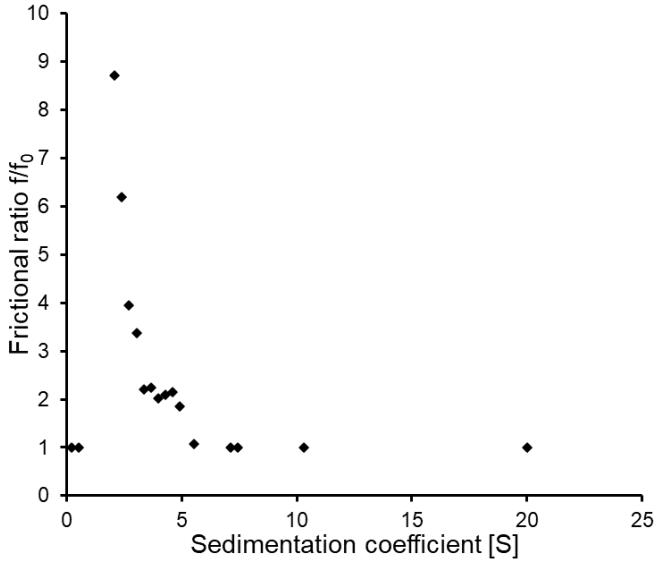

Figure 3. Frictional ratio of species in dependence on their sedimentation coefficient distribution at 1 hour of hydration.

Results in Figure 3 show that the detected species with sedimentation coefficient between approx. 2 to 6 S have a f/f0 higher than 1, which indicates that these species are intermediates of species that have different concentrations of water molecules (Dong (2021)).

3. Conclusions

The present work shows that the nucleation of C-S-H originated from hydrating C_3S occurs via pre-nucleation clusters with sedimentation coefficients that are typical for such clusters. These pre-nucleation clusters were found after 10 min of hydration with high reproducibility in all investigated samples up to 24 hours of C_3S hydration. It was further shown that the smaller clusters contain water molecules.

Acknowledgements

The Deutsche Forschungsgemeinschaft (DFG) is acknowledged for financial support of this project (401097244).

References

Lecoq, X. (1993): ´Étude de l'hydratation à concentration contrôlée du silicate tricalcique Ca3SiO5 et des caractéristiques de ses produits de réaction´, PhD-Thesis, University of Bourgogne, Dijon, France.

Brookes, E., Cao, W., and Demeler, B. (2010): "A two-dimensional spectrum analysis for sedimentation velocity experiments of mixtures with heterogeneity in molecular weight and shape", Eur Biophys J, 39, 405-14 (2010).

Barret, P. and D. Ménétrier (1980): ´Filter dissolution of C3S as a function of the lime concentration in a limited amount of lime water´, Cem. and Concr. Res., 1980. 10(4): p. 521-534.

Barret, P. and D. Bertrandie (1997): ´Importance of the liquid to solid weight ratio in the powdered solid-liquid reactions: Example drawn from cement constituent hydration´, Sol. St. Ion., 1997. 101-103(Part 1): p. 359-365.

Gebauer, D., A. Volkel, and H. Colfen (2008): ´Stable Prenucleation Calcium Carbonate Clusters´, Science, 2008. 322(5909): p. 1819-1822.

Dong, L., et al. (2021): ´Highly Hydrated Paramagnetic Amorphous Calcium Carbonate Nanoclusters as a Superior MRI Contrast Agent´, 2021, Research Square.Leung, C.K.Y. and Cao, Q. (2010) “Development of Pseudo-ductile Permanent Formwork for Durable Concrete Structures”, *RILEM Materials and Structures*, 43(7): 993-1007.

The 16th International Congress on the Chemistry of Cement 2023 (ICCC2023)
"Further Reduction of CO_2 -Emissions and Circularity in the Cement and Concrete Industry"
September 18–22, 2023, Bangkok, Thailand

Effect of Temperature on Performance of Calcium Aluminate Cement Based Accelerator

Arnesh Das[*1], Jean Noel Bousseau[2], Nicolas Maach[3] and Robert J. Flatt[4]

[1] *ETH Zurich, Zurich, Switzerland*
Email: dasa@ethz.ch
[2]*Imerys Technology Center, Lyon, France*
Email: jeannoel.bousseau@imerys.com
[3]*Imerys Technology Center, Lyon, France*
Email: nicolas.maach@imerys.com
[4] *ETH Zurich, Zurich, Switzerland*
Email: flattr@ethz.ch

ABSTRACT

Digital Casting Systems (DCS) can be a potential solution to the challenge of rising demand for producing concrete elements. An important aspect for the successful execution of DCS lies in the acceleration of cement hydration. Calcium aluminate cement (CAC) based accelerators have been successfully used for such processes but there is a question of robustness of performance of such accelerators at different temperatures. In this study, the effect of temperature on the accelerating performance of two different types of CAC based accelerator – one, crystalline based and another, amorphous was investigated. Strength build-up and hydration studies are done at different temperatures. It is concluded that the amorphous based CAC is more suitable for using at low temperatures (below 16^0C) while the crystalline one is more appropriate at higher temperatures.

KEYWORDS: *Digital Casting System (DCS), acceleration, temperature, crystalline, amorphous.*

1. Introduction

The ever-increasing world population has meant that there is also a rising demand for construction. Concrete is the most used construction material due to its versatility and low-cost, but it also accounts for up to 8% of man-made CO_2 emissions. Therefore, there is also a need to reduce the construction related carbon footprint. Digital Casting System (DCS) is a potential solution to these issues. It is based on a unique chemical acceleration and digital process control of cement hydration that enables faster fabrication of concrete elements. It also allows using structurally optimized thin formworks, which use significantly less material compared to existing solutions, (Lloret et al., 2022). An important aspect of the successful execution of DCS lies in the acceleration of cement hydration. A calcium aluminate cement (CAC) based accelerator has been successfully used for DCS as well as for 3D concrete printing processes (Reiter et al., 2020; Das et al., 2022a). For instance, with such an accelerator, it has been possible to demold cast elements at 4 hours instead of the usual 8-10-hour period that is needed for non-accelerated standard concrete mixes (Lloret et al., 2022).

The accelerating performance of CAC is quite robust as the mechanism of its action is independent of the ingredients of the concrete mix or presence of other chemical admixtures (Das et al., 2022a). However, one factor against which it is not robust is temperature. The open time of the CAC accelerator before its addition to ordinary Portland cement (OPC) is also an important factor that needs to be considered for such digital fabrication processes. In this study, we investigate the performance (strength build-up in the first hour and open time before OPC addition) of two different types of CAC over a practice-relevant

range of temperature. Conclusions are then drawn about which grade of CAC is more appropriate for DCS at a given temperature.

2. Materials and Methods

The OPC used for this study was a CEM I 52.5R (Holcim Normo 5R). The first accelerator (CrysCAC) studied was a paste of CAC (Ciment Fondu, Imerys France) and calcium sulfate anhydrite (C$; Francis Flower). The CAC to C$ ratio was 2:1. The most dominant and reactive phase in this CAC was crystalline CA (about 50% by weight of CAC). The second type of accelerator (AmpCAC) studied was a paste of an amorphous based CAC (Imerys, France) that has a commercial name LEAP FIT. Such an accelerator already has the C$ added to it, the ratio of amorphous CAC to C$ being 1:1.

The OPC and CAC pastes were prepared using an IKA mixer that was run at 500 rpm for 2 minutes. The water to cement ratio of the mixes was 0.38. Pertaining to the requirements of DCS, a delayed addition of the accelerator was done. The OPC and CAC pastes were prepared one after another and then the CAC paste accelerator was added to the OPC paste, 15 minutes later. They were then mixed at 500 rpm for 1 minute. While the mixing happened in the normal lab temperature (~20^{0}C), the all the raw materials were preconditioned in a water bath set to the different temperatures of testing. Tartaric acid (TA) was used as the retarder to ensure the open time of the CAC pastes (0.1% and 0.3% by weight of binder for 23^{0}C and 35^{0}C respectively).

The strength build-up achieved after acceleration was studied using a rotational rheometer with parallel plate geometry. The test was started immediately after mixing with accelerator was finished. The test protocol followed was in accordance with Reiter et al. (2016). After an initial period of pre-shearing, the material is subjected to very small strain amplitude (0.0005%), and it measures the evolution of storage modulus (G') over a period of 20 minutes. The measurement was done at different temperatures ranging from 5^{0}C to 35^{0}C.

Isothermal calorimetry was used to study the progress of hydration of the various mixes using a TAMAir calorimeter. The measurements were done at temperatures of 10^{0}C, 23^{0}C and 35^{0}C.

3. Results and Discussion

The rheometry measurement essentially follows 'strength build-up at rest' given the very small strain amplitude. Fig. 1 shows a comparison of the evolution of storage modulus (G') for CrysCAC and AmpCAC at 10^{0}C. At 5% dosage, AmpCAC initially shows a faster increase but the final G' value at the end of 20 minutes is similar to that obtained with CrysCAC. It is to be noted that the final value obtained with AmpCAC could likely even be smaller, had the test been run beyond 20 minutes. Based on previous analysis conducted, it was found that at these dosages, the system usually runs out of CAC only around the end of the first hour (Das 2022b). The observation at 10% dosage is however much different, with AmpCAC showing a much faster evolution and much higher final G' value. A very similar observation was made at 23^{0}C (data not reported here).

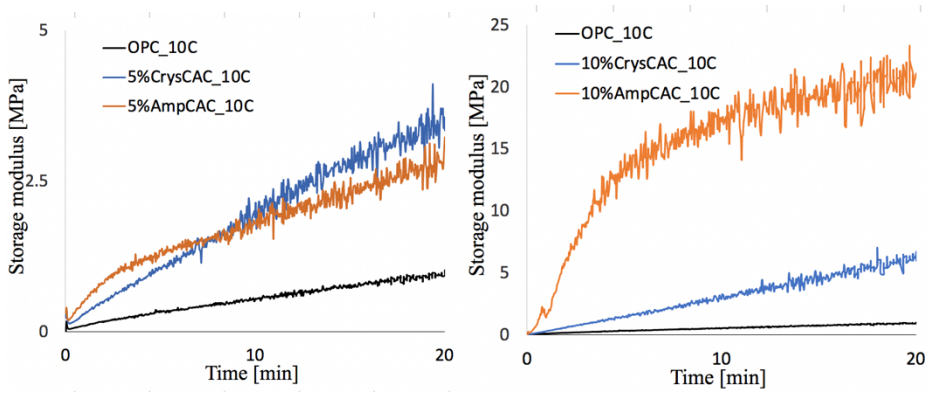

Fig. 1 Evolution of storage modulus for CrysCAC and AmpCAC at 10^{0}C at 5% (left) and 10% (right) dosage.

Fig. 2 shows the storage modulus (G') at the end of 20 minutes measured for OPC paste as well as various dosages of the two types of CAC accelerator at different temperatures. The OPC paste shows a consistent value of G' up to 23^{0}C and a slightly larger value at higher temperatures. For CrysCAC, it seems the evolution of storage modulus at different temperatures is dosage dependent as it appears linear for 2.5% dosage and exponential for 5% dosage. With AmpCAC, the G' value is much more consistent at low temperature (5^{0}C to 16^{0}C), irrespective of dosage. For a dosage of 2.5%. the values are higher from 23^{0}C to 35^{0}C but still quite consistent between each other. This is however not the case for 5% dosage whereby the evolution can be approximated by an exponential.

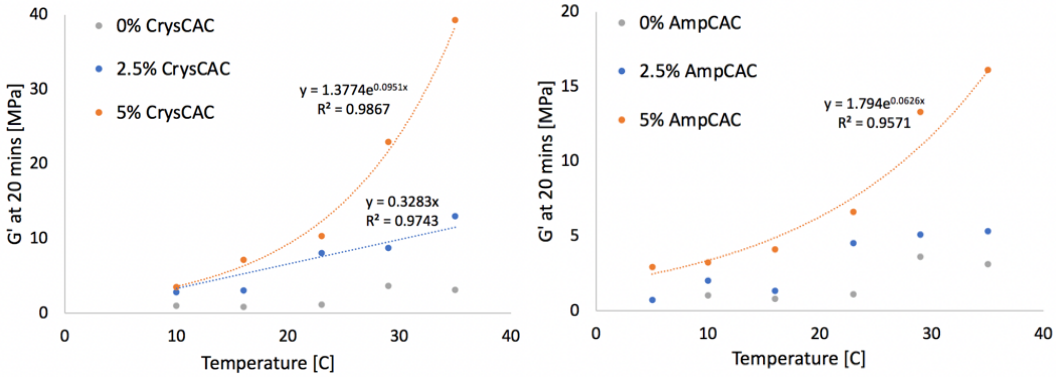

Fig. 2 Evolution of storage modulus at different temperatures for CrysCAC (left) and AmpCAC (right)

Fig. 3 shows the isothermal calorimetry for OPC paste as well as for 5% dosage of CrysCAC and AmpCAC at 10^{0}C and 23^{0}C (left), and CrysCAC and AmpCAC with TA as retarder at 23^{0}C and 35^{0}C (right). A notable difference that can be seen is in the onset of acceleration period of the mixes at 10^{0}C (6 hours) and 23^{0}C (2 hours). However, CrysCAC and AmpCAC at a particular temperature show the onset of acceleration period around the same time as the OPC paste. The peak of heat rate at the two temperatures is also significantly different. Next, with TA as retarder, it seems that CrysCAC has a much longer open time compared to AmpCAC, at both 23^{0}C and 35^{0}C. Therefore, they should remain processable for long periods without showing much change in rheology.

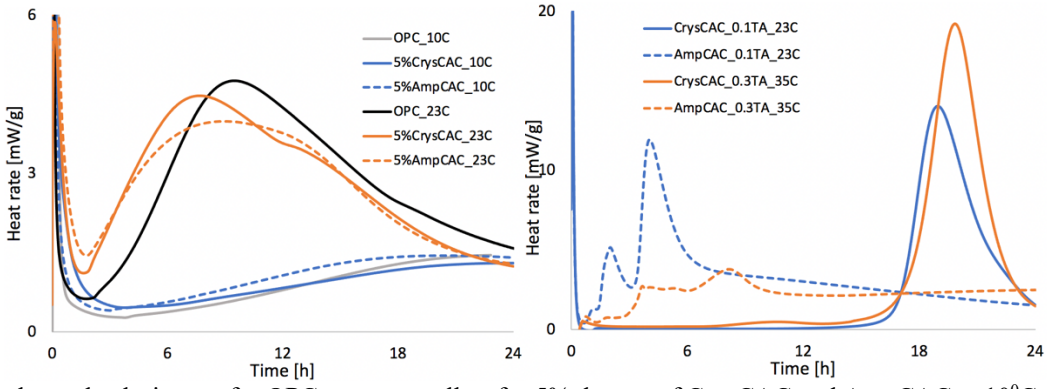

Fig. 3 Isothermal calorimetry for OPC paste as well as for 5% dosage of CrysCAC and AmpCAC at 10^{0}C and 23^{0}C (left), and CrysCAC and AmpCAC with TA as retarder at 23^{0}C and 35^{0}C (right).

To summarize the main results, AmpCAC being more reactive, shows a faster initial evolution of strength compared to CrysCAC. An additional advantage of AmpCAC is that it shows robust performance at low temperatures (5^{0}C to 16^{0}C). Since it is amorphous, its dissolution rate is not much affected by temperature (Berger et al., 2022), giving a relatively robust performance in relation to temperature, even if the accelerator dosage has a major effect. A major issue of working with AmpCAC at temperatures above 23^{0}C is its very short open time, even with high dosage of TA as retarder. Hence, CrysCAC is more appropriate for use at such temperatures while AmpCAC delivers the needed additional speed at temperatures below 16^{0}C.

From an application point of view for DCS, the major challenge lies in achieving the required strength performance when working at low temperature. The CAC can only give a certain amount of strength depending on the dosage used and one cannot go beyond a certain CAC amount, keeping in mind

the cost and the associated carbon footprint. For instance, if there is a certain strength requirement at 4 hours for demolding and transporting the cast element, it would be essential that silicate hydration from OPC also contributes. Based on previous studies, it was found that mortars accelerated with AmpCAC had higher compressive strength at 4 hours compared to those accelerated with CrysCAC (Berger et al., 2022). This was attributed to higher ettringite and bound water content for the former. The AmpCAC was also found to have a more positive influence on the degree of C_3S hydration, thus showed better long-term strength performance (7 and 28 days) compared to the CrysCAC (Berger et al., 2022).

At such low temperatures, other accelerating admixtures such as lithium carbonate and sodium carbonate could also potentially be used to enhance the performance of CAC. They could be added to the OPC in the beginning so that they do not interfere with the open time of CAC and later, on mixing OPC with the CAC, these admixtures can enhance performance. Lithium is a known accelerator for AH_3 formation, which releases OH^- ions, which can then be used for the fast precipitation of ettringite (Nalet et al., 2022). Concerning the use of sodium carbonate in OPC, it would precipitate calcite and thus deplete calcium ions from the pore solution, thereby enhancing the dissolution of CAC. However, the robust performance of all these admixtures needs to be validated by doing further experiments/analysis.

4. Conclusions

In this study, the effect of temperature on the accelerating performance of two different types of CAC based accelerator was investigated. AmpCAC was found to show robust performance, particularly at low temperatures. The dosage of accelerator used strongly influences the strength that can be obtained due to CAC reaction alone. Also, at a given dosage of TA, CrysCAC was found to have a much longer open time, therefore, such an accelerator would be the preferred option at temperatures above 16^0C. In order to enhance performance at low temperature, the option of using other admixtures such as lithium carbonate and sodium carbonate should be investigated.

Acknowledgments

This work was conducted as part of an Innosuisse project titled “Digital Casting System: Increased Productivity in Prefabrication”, in collaboration with Dr. Ena Lloret-Fritschi, Assistant Professor, USI, Switzerland and Muller-Steinag Holding AG. The authors would like to thank Prof Lloret-Fritschi and Cedric Domon (Director, Research and Development, Muller Steinag group) for the useful discussions about Digital Casting.

References

Lloret-Fritschi E., Quadranti E., Scotto F., Fuhrimann L., Demoulin T., Mantellato S., Unteregger L., Burger J., Pillegi R., Gramazio F., Kohler M., Flatt R.J, “Additive Digital Casting: From Lab to Industry” *Materials* (2022).

Reiter L., Wangler T., Anton A., Flatt R.J, “Setting on demand for digital concrete – principles, measurements, chemistry, validation”, *Cement and Concrete Research 132* (2020).

Das A., Reiter L., Mantellato S., Flatt R.J., “Early-age hydration and rheology control of ternary binders for 3D printing applications” *Cement and Concrete Research 162* (2022).

Reiter L., Wangler T., Roussel N., Flatt R.J, “Distinguishing flocculation and hydration effects on the thixotropy of cement pastes”, *8th International RILEM Symposium on Self-Compacting Concrete, Washington DC, USA* (2016).

Das A., “3D concrete printing: early-age strength build-up and long-term durability”, *PhD Thesis, ETH Zurich* (2022).

Berger S., Tourlakis D., Perrot S., “Ettringite accelerator in portland cement dominated systems: a comparison of different calcium aluminate technologies”, *International Conference on Calcium Aluminates, Cambridge, UK* (2022).

Nalet C., Maach N., Charpentier E., Berger S., Fryda H., “Accelerating calcium aluminate cements with lithium salt: new insights on the hydration mechanism and on the properties”, *International Conference on Calcium Aluminates, Cambridge, UK* (2022).

The 16th International Congress on the Chemistry of Cement 2023 (ICCC2023)
"Further Reduction of CO_2 -Emissions and Circularity in the Cement and Concrete Industry"
September 18–22, 2023, Bangkok, Thailand

Effect of mixing conditions on the rheology and microstructure of silicate-activated slag mixtures

Y. Sun [1*], Y. Tao [2], G. Ye [3], and G. De Schutter [4]

[1, 2, 4] *Department of Structural Engineering and Building Materials, Ghent University, 9052 Ghent, Belgium*
Email: yubo.sun@ugent.be; yaxin.tao@ugent.be; geert.deschutter@ugent.be.
[3] *Faculty of Civil Engineering and Geosciences, Delft University of Technology, 2628 CN Delft, the Netherlands*
Email: g.ye@tudelft.nl.

ABSTRACT

The current study aims to assess the effect of mixing conditions on the rheological and microstructural properties of silicate-activated slag pastes. It was found that rheological parameters were significantly improved with longer mixing times. After arresting activation reactions, the size distribution of precursor particles/agglomerates was measured with laser diffraction to reveal the particle dispersion by applying different mixing conditions. In the meantime, the phase evolution along the early-stage reactions was characterized by thermogravimetric analysis (TGA), X-ray diffraction (XRD), and Fourier-transform infrared (FTIR) spectroscopy. It was found that a longer mixing time has led to finer particles and a slight increase in the early reaction products, which might fill the interstitial voids to lubricate. Meanwhile, no apparent variations in the crystalline phases and the Al/Si-O bonds were detected in early reaction products by extending the mixing time.

KEYWORDS: *AAMs, Blast furnace slag, Rheology, Microstructure, Characterization.*

1. Introduction

Alkali-activated material (AAM) is developed as a class of sustainable alternative binders to substitute Portland cement (PC) in concrete. However, the rheology control of AAMs has been problematic. In particular, the flash setting has been frequently reported in alkali-activated slag (AAS) mixtures prepared with silicate activators (Palacios et al. (2021)). It was found that the water-reducing admixtures developed for PC materials become much less effective in AAMs due to interactions with the activator (Lu et al. (2021)). Accordingly, there is still a lack of proper methods to regulate the flow of fresh AAMs. Existing literature suggests that extending the mixing time appears to be an effective approach to improve the workability of AAMs (Palacios and Puertas (2011)), whereas the longer mixing time may also contribute to better mechanical properties (Mahmood et al. (2021)). However, the underlying fluidizing mechanism behind it is not yet well-understood.

Therefore, the main objective of this study is to investigate the mixing conditions on the rheology and microstructure of silicate-activated slag mixtures. By using different mixing protocols, the rheological behavior of AAS pastes was first evaluated. The solid fraction in fresh AAS paste was further characterized to investigate the effect of longer mixing time on the particle size and early reaction products. Results may assist in better understanding the fluidizing mechanism in silicate-activated slag mixtures by applying an extended mixing time.

2. Materials and methods

2.1 Materials

Ground granulated blast furnace slag (BFS) used in this study was provided by Ecocem Benelux B.V.. Chemical compositions detected by X-ray fluorescence (XRF) spectroscopy are presented in Table 1.

Table 1. Chemical composition of BFS measured by XRF.

Precursor	CaO	SiO_2	Al_2O_3	MgO	SO_3	TiO_2	K_2O	Fe_2O_3	MnO	ZrO_2	Other
BFS	40.9	31.1	13.7	9.16	2.31	1.26	0.69	0.40	0.31	0.12	0.05

Sodium hydroxide and sodium silicate were used in this study to prepare the activator solution. Reagent-grade sodium hydroxide anhydrous pearls (>99%) were provided by Brenntag N.V., and the sodium silicate solution (15% Na_2O, 30% SiO_2, and 55% water) was provided by PQ Corporation.

2.2 Mixture proportion

The mixture proportion of the AAS paste used in this study is presented in Table 2. Sodium hydroxide, sodium silicate, and tap water were blended one day before mixing to reach a target composition with 4% Na_2O by weight of slag and the Ms (molar ratio between SiO_2 and Na_2O) of 1. The water to binder (w/b) ratio was fixed at 0.3 (Note: binder refers to the sum of slag and solid activators).

Table 2. Mixture proportion of the AAS paste used in this study.

BFS (g)	NaOH (g)	Sodium silicate (g)	Extra water (g)	Na_2O	Ms	w/b
100	2.58	13.33	25.24	4%	1	0.3

2.3 Test on fresh AAS pastes

Three mixing protocols were designed as illustrated in Fig. 1. AAS pastes were prepared with a Hobart planetary mixer by blending 500 g slag with corresponding activators, and the activator solution was gradually added in 10 seconds. By following P1, P2, and P3 with different mixing times, AAS mixtures were mixed at 140 rpm for 3, 5, and 10 min, respectively. AAS pastes obtained were collected for further tests.

Fig. 1. Mixing protocols used in this study.

The rheological tests were performed with an Anton Paar MCR 102 rheometer (fitted with a 6-blade vane, 22mm in diameter, and 16 mm in height). The fresh AAS paste was loaded into a cylindrical cup (27.6 mm inner diameter and 75 mm depth), and the temperature was controlled at 20 ± 0.5 °C with a water bath system. Before each measurement, the paste was subjected to a 60 s pre-shear at 100 s^{-1} to reach a reference state (Alnahhal et al. (2021)), and then rested for 120 s. The stress growth was conducted with a shear rate of 0.1 s^{-1} for 60 s until an equilibrium state. The maximum stress occurred along the stress growth test was recorded as the static yield stress (τ_0), and the average shear stress of the last 10 s was denoted as the equilibrium shear stress (τ_e). The degree of thixotropy was assessed through the difference between τ_0 and τ_e (τ_0-τ_e) (Puertas et al. (2018)). Afterwards, the fresh paste was subjected to another pre-shear at 100 s^{-1} for 60 s to eliminate the structuration and reach a steady state. During flow curve tests, the shear was applied with stepwise increase and decrease in rotational speeds, ranging between 20 s^{-1} and 100 s^{-1} by 5 steps. Each step was conducted for 30 s, and the average response of the last 5 seconds was recorded to derive the flow curves. Downward portions of flow curves were fitted with the Herschel-Bulkley model to derive the dynamic rheological parameters (Feys et al. (2008)). Rheological tests were performed on 3 replicate samples, and the results presented are the most representative or average of 3 measurements.

In the meantime, the bulk solid fraction in fresh AAS pastes was characterized to study the effect of mixing conditions on the reaction products. The size distribution of solid particles/agglomerates was measured with laser diffraction. In specific, 2 g of fresh paste was dispersed in 500 mL isopropanol by applying electromagnetic stirring at 500 rpm for 3 min. By following the same dispersing process, the particle size distribution of solid fractions in fresh AAS mixtures was measured with laser diffraction (average of 5 measurements). Moreover, the activation reaction was terminated at 10 min by using the solvent replacement technique (Palacios et al. (2021)). The solid fraction collected by filtration was vacuum dried and ground to pass a 63 μm sieve for further characterization. Thermogravimetric analysis (TGA) was performed with a TG-449-F3-Jupiter instrument from 40 to 900 °C at 10 °C/min in argon atmospheres to assess the reaction products, and the mass evolution as a function of temperature was recorded. X-Ray diffraction (XRD) tests were conducted using a Bruker D8 Advance diffractometer with Cu-Kα radiation (λ = 1.54 Å). XRD patterns were recorded at the range between 5° and 70° with a step

size of 0.02°. Fourier transform infrared (FTIR) spectroscopy was detected with a Spectrum TM 100 Optical ATR-FTIR spectrometer from 400 to 1300 cm^{-1} with a resolution of 1 cm^{-1}.

3. Results and discussion

3.1 Rheology of AAS pastes

Results of stress growth and flow curves on fresh AAS pastes are shown in Fig. 2, and the rheological parameters obtained are summarized in Table 3. By extending the mixing time, the yield stress and consistency factor of AAS significantly reduced, indicating better fluidity in both static and dynamic states. Meanwhile, τ_0-τ_e declined with longer mixing time, which suggests that the early-age thixotropic build-up in AAS was progressively eliminated. Further, a longer mixing time also resulted in a less pronounced shear thickening behavior (indicated by the flow index).

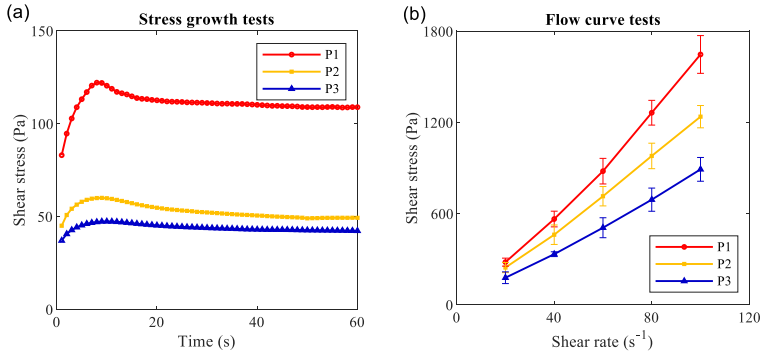

Fig. 2. Results of rheological tests (a) stress growth tests; (b) flow curve tests.

Table 3. Rheological parameters obtained by using different mixing protocols.

	Stress growth test		Flow curve test			
	Static yield stress (Pa)	Degree of thixotropy (Pa)	Dynamic yield stress (Pa)	Consistency factor (Pa·s^n)	Flow index	R^2
P1	122.09	13.21	93.03	5.74	1.31	0.9998
P2	60.02	10.78	62.19	3.68	1.22	0.9996
P3	47.33	4.86	58.18	2.99	1.16	0.9999

3.2 Particle size distribution

The particle size distribution curves of solid particles/agglomerates are presented in Fig. 3. Compared to the starting slag particles, results show that the solid particles are interconnected to assemble large agglomerations at early ages, leading to the rapid structuration by using sodium silicate activators in AAS. With the increase in mixing time, it was found that the particle size of agglomerations progressively declined, and the amount of fine particles around 1 μm significantly increased. It has been suggested that fine particles may fill in the interstitial voids to release more free water and lubricate (Lu et al. (2021)). In the meantime, the particle packing in the system is optimized with the smaller particles, and better mechanical properties are achieved with a denser microstructure. Instead, the larger agglomerates could not be effectively broken down with declined mixing time to act as fillers, which lead to negative effects on the rheology of the paste due to the adsorption of free water content (Sargam and Wang (2021)).

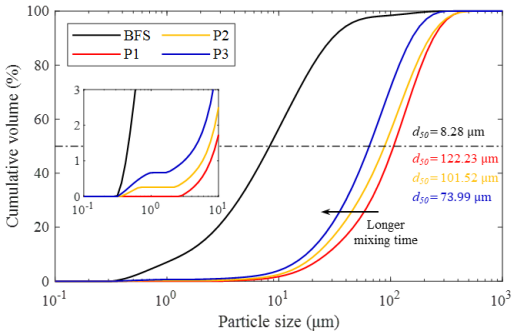

Fig. 3. Particle Size distribution of solid particles and agglomerates in fresh AAS.

3.3 Characterization of reaction products

The solid fraction in fresh AAS was characterized to study the effect of mixing conditions on the reaction products. As shown in Fig. 4 (a), the DTG peak below 200 °C is associated with C-(A)-S-H phases formed in AAS (Kapeluszna et al. (2017)). It is indicated that the amount of early reaction products slightly increased with a longer mixing time. It might be attributed to a more thorough contact between slag and activators by the extra mixing process, which promoted the dissolution and thus resulted in more early reaction products. In addition, as shown in Fig. 4 (b) and (c), the solid content in AAS pastes was further assessed by XRD and FTIR. Results suggest that a longer mixing time did not result in significant variations in the crystalline phases and the vibration feature of Al/Si-O bonds in early reaction products.

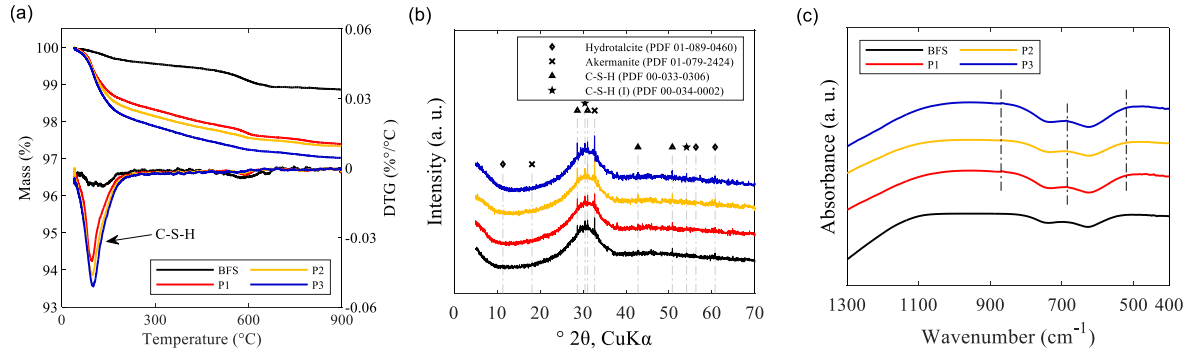

Fig. 4. Characterization of early reaction products in early-age AAS by using different mixing conditions (a) TGA; (b) XRD patterns; (c) FTIR spectra.

3. Conclusions

In this study, the rheological performance of silicate-activated slag pastes has been studied by using different mixing conditions. It was found that a longer mixing time has led to finer particles and a slight increase in the early reaction products, which might fill the interstitial voids to provide a fluidizing effect. Meanwhile, no apparent variations in the crystalline phases and the Al/Si-O bonds were detected in early reaction products by extending the mixing time. Results indicate that the fresh property of silicate-AAS could be improved by appropriately controlling the particle size of early reaction products.

Acknowledgements

This paper presents the research results from the DuRSAAM project. The financial support from the European Union's Horizon 2020 research and innovation programme (ETN DuRSAAM – H2020-MSCA-ITN-2018-813596) is gratefully acknowledged.

References

Alnahhal, Mohammed Fouad, Taehwan Kim, and Ailar Hajimohammadi. 2021. "Distinctive Rheological and Temporal Viscoelastic Behaviour of Alkali-Activated Fly Ash/Slag Pastes: A Comparative Study with Cement Paste." Cement and Concrete Research 144(October 2020): 106441.

Feys, Dimitri, Ronny Verhoeven, and Geert De Schutter. 2008. "Fresh Self Compacting Concrete, a Shear Thickening Material." Cement and Concrete Research 38(7): 920–29.

Kapeluszna, Ewa, Łukasz Kotwica, Agnieszka Różycka, and Łukasz Gołek. 2017. “Incorporation of Al in CASH Gels with Various Ca/Si and Al/Si Ratio: Microstructural and Structural Characteristics with DTA/TG, XRD, FTIR and TEM Analysis.” Construction and Building Materials 155: 643–53.

Lu, Cuifang et al. 2021. “Rheology of Alkali-Activated Materials: A Review.” Cement and Concrete Composites 121(April): 104061.

Mahmood, Aziz Hasan, Stephen J Foster, and Arnaud Castel. 2021. “Effects of Mixing Duration on Engineering Properties of Geopolymer Concrete.” Construction and Building Materials 303: 124449.

Palacios, M et al. 2021. “Cement and Concrete Research Early Reactivity of Sodium Silicate-Activated Slag Pastes and Its Impact on Rheological Properties.” Cement and Concrete Research 140(October 2020): 106302.

Palacios, Marta, and Francisca Puertas. 2011. “Effectiveness of Mixing Time on Hardened Properties of Waterglass-Activated Slag Pastes and Mortars.” ACI Materials Journal 108(1): 73.

Puertas, F. et al. 2018. “Alkali-Activated Slag Concrete: Fresh and Hardened Behaviour.” Cement and Concrete Composites.

Sargam, Yogiraj, and Kejin Wang. 2021. “Influence of Dispersants and Dispersion on Properties of Nanosilica Modified Cement-Based Materials.” Cement and Concrete Composites 118: 103969.

The 16th International Congress on the Chemistry of Cement 2023 (ICCC2023)
"Further Reduction of CO_2 -Emissions and Circularity in the Cement and Concrete Industry"
September 18–22, 2023, Bangkok, Thailand

Effect of Formulation Process of An Alkali-free Liquid Accelerator on Hydration and Properties of Portland Cement

Y.F. Wang[1], L. Lei[2*], and C.J. Shi[3*]

1 *Technische Universität München, Chair for Construction Chemistry, 85747, Garching, Lichtenbergstraße 4, Germany*
Email: yifei1.wang@tum.de
2 *Technische Universität München, Chair for Construction Chemistry, 85747, Garching, Lichtenbergstraße 4, Germany*
Email: lei.lei@tum.de
3 *Key Laboratory for Green & Advanced Civil Engineering Materials and Application Technology of Hunan Province, College of Civil Engineering, Hunan University, Changsha 410082, P. R. China*
Email: cshi@hnu.edu.cn

ABSTRACT

Alkali-free powder and liquid accelerators are commonly used in sprayed concrete. Revealing the effect of formulation process of liquid accelerator on hydration and properties of Portland cement is beneficial to better use of powder and liquid accelerators. In this study, an aluminum sulfate-based alkali-free accelerator was formulated. Thereafter, the effect of formulation process was investigated by setting time, compressive strength, heat evolution, X-ray diffraction (XRD) and thermogravimetry (TG). Results indicate that the formulation process contributes to further decrease of setting time as much higher initial hydration rate (initial reaction period) occurred and more ettringite (AFt) formed at early stages. Also, the formulation process benefits to higher early strength at 1 d due to higher hydration rate within several hours. It can be concluded that the formulation process enhanced the acceleration effect of this alkali-free accelerator and higher dosages are needed for powder accelerator without formulation process to achieve satisfactory acceleration effect.
KEYWORDS: *Alkali-free accelerator; Formulation process; Acceleration*

1. Introduction

Accelerators are widely used in spayed concrete to achieve fast setting, high early strength and certain stickiness of concrete, contributing to constructions of support engineering such as tunnel initial and slope stability supports [1]. Currently, liquid and powder forms of accelerators both exist in the market and in most cases accelerating chemicals used in powder forms can also be used in liquid forms. For example, alkali-containing accelerators such as aluminates, silicates and carbonates and alkali-free accelerators such as aluminum salts can be used in liquid and powder forms for wet- and dry mix shotcreting, respectively.
Compared to powder accelerators or dry-mix shotcreting, liquid accelerators or wet-mix shotcreting causes less dust pollution and mixing uniformity problems, exhibiting huge market potential. Investigation into the formulation process of liquid accelerators on hydration and properties of Portland cement is of significance for the application of these two types of accelerators and better understanding of the acceleration effect. Considering that alkali-free accelerators have advantages on more environmentally friendly, higher later strength and less durability problems of shotcrete than alkali-containing accelerators, an aluminum sulfate based alkali-free accelerator (AMD) was formulated in this research and comparison of this liquid accelerator and all raw materials of this accelerator on hydration and properties of Portland cement was conducted in this research by setting time, compressive strength, heat evolution, XRD and TGA.

2. Materials and methods

2.1 Materials

Portland cement complying with Chinese standard GB175-2007 was used in the research. Distilled water was used to prepare all pastes and mortars. Aluminum sulfate, magnesium sulfate, diethanolamine (DEA), phosphoric acid, polyphenylamide were used to formulate the AMD accelerator.

2.2 Formulation of AMD accelerator

According to exploration experiments, the formulation process of the AMD accelerator is as follows: At first, DEA was mixed with water in a laboratory reactor for 5 min to prepare TEA solution. Aluminum sulfate was added to this solution and stirred for 40 min to ensure complete dissolution of aluminum sulfate. During this process,

dissolution and complexation occurred. Thereafter, magnesium sulfate was added and stirred for 30 min. Finally, small amounts of phosphoric acid and polyphenylamide were added to the solution and stirred for 30 min to stabilize the solution and increase the viscosity of accelerator. The final product, named AMD accelerator, was a paleyellow liquid with pH value of 4 and solid content of 48.8%. During the formulation, the temperature was kept around 50 ℃ and the stirring speed was maintained at 150 r/min.

2.3 Test methods

The initial and final setting times were tested every 10 seconds until initial and final setting. Specific experiments were conducted following GB/T 35159-2017. Compressive strengths of mortars at 1 and 28 d were conducted according to standard GB/T 50081-2002 by using a RONG JI DA (Shanghai, China) 300 kN servo-hydraulic testing machine. For molding of mortars in mold of 40*40*160 mm, considering that mortars lose fluidity rapidly, all mortars were molded by using a mortar vibrating table. For An 8-channel isothermal calorimeter (Thermometric TAM Air) operated at 20 ℃ was used to measure the heat of hydration of Portland cement pastes within 72 h with AMD accelerator and its raw materials. Mineral phase composition of cement pastes was tested by using the X-ray diffraction method by using Philips X-ray diffractometer, with a Cu Ka source, a scanning range of 5-70° and a scanning speed of 2° per minute. DTG analysis is used to further quantify and identify cement products such as C-S-H gel, AFm, ettringite and portlandite, which was proceeded by using a TGA instrument type of Netzsch STA 409 PC from 20 to1000 °C at temperature rate of 10 °C / min and nitrogen atmosphere.

3. Results and discussion

3.1 Setting time

Fig. 1 shows the initial and final setting times of Portland cement pastes with different dosages of this accelerator (AMD) and its raw materials (un-AMD). As can be seen, the AMD accelerator dramatically decreased setting time of cement pastes at proper dosages. The initial and final setting times decreased from 153 and 185 minutes to 2.5 and 5 minutes at the dosage of 8 %. However, cement pastes with raw materials of AMD accelerator presents much longer setting time at all dosages, with initial and final setting times at 9 and 16 minutes at the dosage of 8 %. Therefore, it can be concluded that formulation process of AMD accelerator is beneficial to the setting time reduction.

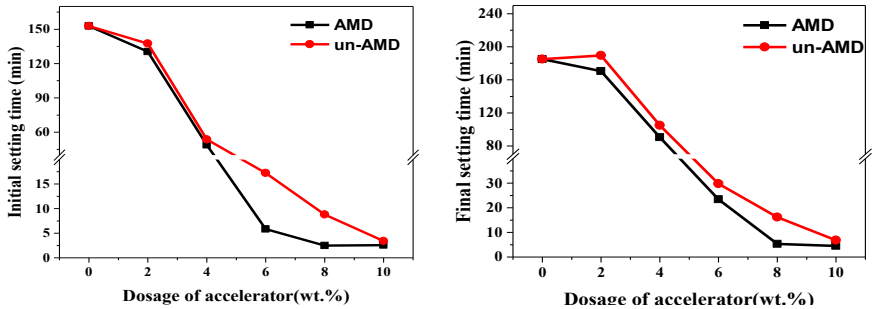

Fig. 1. Initial and final setting times of cement pastes with different dosages of AMD accelerator and its raw materials.

3.2 Compressive strength

Compressive strengths of Portland cement mortars with different dosages of AMD accelerator and its raw materials (un-AMD) are shown in **Fig. 2**. At 1 d, all samples with AMD accelerator and its raw material gained higher compressive strength than reference cement paste, with the highest compressive strength of samples with AMD accelerator at 6 % and the highest compressive strength of samples with its raw materials at 8 %. At dosages below 8 %, samples with AMD accelerator always gained higher compressive strength than that with raw materials of this accelerator, indicating the formulation process is also beneficial to early strength development. The lower strength of sample AMD10 than sample un-AMD10 can be attributed to the excessive rapid setting of sample AMD10. At 28 d, samples also gained higher compressive strength with AMD accelerator and its raw material, although the increase was relatively limited. There is no obvious rule to be followed on 28 d compressive strength of cement pastes with AMD accelerator or raw materials of AMD, indicating that the formulation process of AMD accelerator exhibited limited effect on long-term strength development.

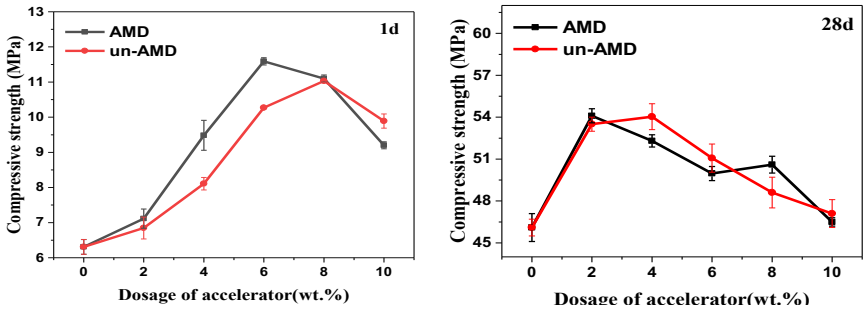

Fig. 2. Compressive strength at 1 and 28 d with different dosages of AMD accelerator and its raw materials.

3.3 Heat evolution

The effect of AMD accelerator and its raw materials on cement hydration was monitored by isothermal calorimetry, as is shown in **Fig. 3**. As can be seen, the initial reaction peak enhanced with AMD accelerator and its raw materials, and the formulation process contributes to higher initial reaction peak, which is consistent with setting time. Compared to reference sample, samples AMD8 and un-AMD8 presented lower and/or narrower main hydration peaks, which means the somewhat retarded C_3S hydration at early stages. However, these samples presented higher cumulative heat due to the enhanced initial reactions or the accelerated aluminates hydration and higher hydration rate after several hours (about 20 h). Notably, reference sample had an exothermic shoulder after the main hydration peak, which is due to the second hydration of aluminate phase after the complete consumption of gypsum to form AFm. This peak disappeared in samples AMD8 and un-AMD8 due to the additional SO_4^{2-} amounts. It can be concluded that the formulation process of this accelerator has positive effect on early hydration of cement.

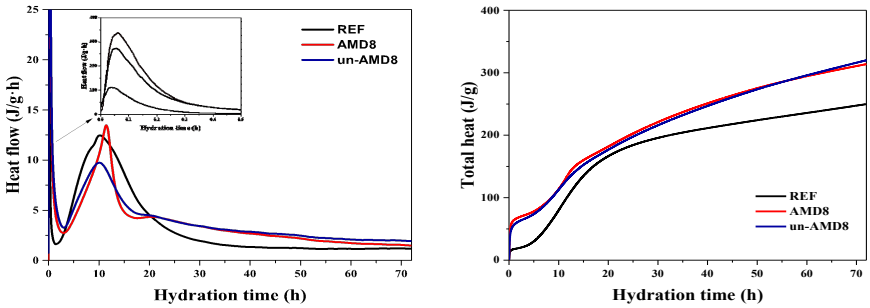

Fig. 3. Hydration heat flow (left) and total heat of Portland cement pastes with AMD accelerator and its raw materials.

3.4 XRD analysis

Fig. 4 shows XRD patterns of samples with AMD accelerator and its raw materials at hydration ages of 30 min, 1 d and 28 d. Compared to reference sample, samples AMD8 and un-AMD8 exhibited stronger characteristic peaks of ettringite but higher peak intensities of C_3S and C_2S at 30 min and 1 d, indicating that this accelerator accelerated the formation of ettringite but retarded that of silicates, which can be attributed to negative interaction between silicates hydration and ettringite formation, as concluded by Wang et al. [2].

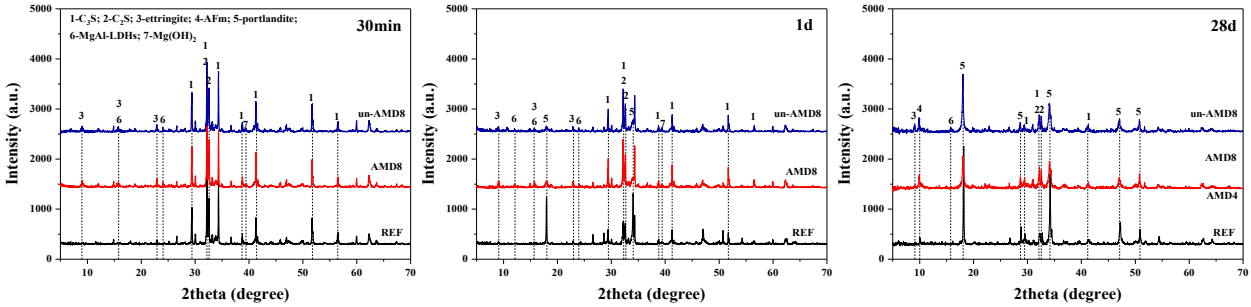

Fig.4. XRD patterns of cement pastes with AMD accelerator and its raw materials at different ages.

Also, peak intensity of ettringite in AMD8 sample was much higher than that with un-AMD8 sample at 1 d, suggesting that the formulation process is beneficial to ettringite formation at early ages. It was reported that the rapid setting and hardening can be achieved by large amounts of ettringite formation [3]. However, peak intensity

of ettringite in AMD8 sample was comparable to that of un-AMD8 sample at 30 min, which contradicts the result that setting time of AMD8 sample was much shorter than that of un-AMD8 sample. A possible explanation to this phenomenon is that ettringite formed much faster in AMD8 sample due to the faster diffusion of ions. Thus, the formation of ettringite might present a lower degree of crystallinity that could not be detected by XRD analysis. Glasser [4] also observed a gel-like structure of ettringite at early ages. Besides, alite hydration proceeded to a larger extent in un-AMD sample at 1 and 28 d, with the consequent production of larger amount of portlandite, which indicates that the formulation process had negative effect on alite hydration.

3.5 DTG analysis

Fig. 5 shows DTG curves of cement pastes with 8 % of AMD accelerator and its raw materials at different hydration ages. At 30 min, the endothermal peak of C-S-H + AFt was traced within 200 °C and CH could not be detected in both AMD8 and un-AMD8 samples. Therefore, the peaks within 200°C of AMD8 and un-AMD8 samples can be mainly attributed to degradation of ettringite due to the almost no hydration of silicates and formation of C-S-H at 30 min. The corresponding mass loss of AMD8 sample was greater than that of un-AMD8 sample, which also verified that the formulation process of this accelerator is conducive to the formation of ettringite, thus leading to the faster setting and hardening. At 1 d, the peak of C-S-H + AFt and a shoulder peak of AFm can be detected in both AMD8 and un-AMD8 samples and their fitted results are shown in **Fig. 5 (right)**. As can be seen, AMD8 sample presents higher peak of AFm, indicating that the formulation process of this accelerator promoted aluminates hydration and the transformation of AFt to AFm. Besides, degradation of CH was first detected at 1 d. At 28 d, the peak shape within 200 °C is widened and a distinct shoulder of AFm can be seen in both samples. A reasonable explanation is that large amounts of C-S-H gel formed at 28 d. From XRD analysis at 28 d, ettringite was almost undetectable, which means the mass loss below 300 ℃ is mainly due to the decomposition of C-S-H gel and AFm.

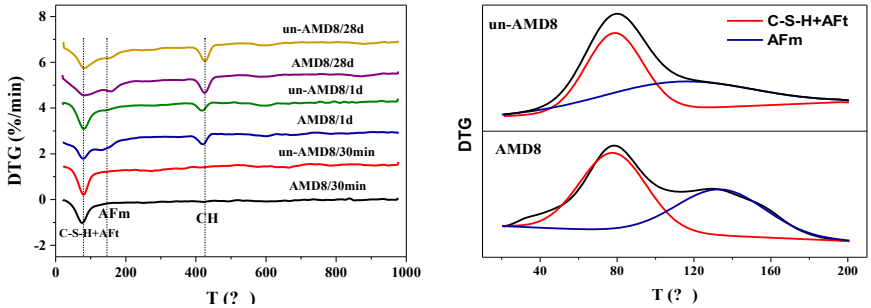

Fig. 5. DTG curves of cement pastes with AMD accelerator and its raw materials at different hydration ages (left) and the DTG fitted results of AMD8 and un-AMD8 samples at 1 d (right).

4. Conclusion

In this study, the following conclusions can be obtained:

1) Both the alkali-free accelerator and its raw materials can significantly accelerate the setting and enhance the early strength of Portland cement at appropriate dosages. The formulation process exhibits advantages on setting time reduction and early strength enhancement.
2) The accelerated aluminates hydration and ettringite formation are the main reason for accelerated setting and hardening. The formulation process led to faster aluminates hydration and ettringite formation, as verified by the initial reaction peak and the XRD results.
3) Generally, the formulation process provides a more efficient alkali-free accelerator. For the application of such accelerators without the formulation process or the powder accelerators, higher dosages should be considered to achieve satisfactory acceleration effect.

References

[1] Prudencio Jr.L.R. (1998) "Accelerating admixtures for shotcrete", *Cement and Concrete Composites*, 20: 213-219.
[2] Wang, Y.F., Shi, C.J., Ma Y.H., Xiao, Y.C. and Liu, Y. "Accelerators for shotcrete-Chemical composition and their effects on hydration, microstructure and properties of cement-based materials", *Construction and Building Materials*, 2021, 281: 122557.
[3] Wang, Y.F., Shi, C.J., Lei, L., Ma, Y.H., Liu, J.H. and Hu, X. "Formulation of an alkali-free accelerator and its effects on hydration and mechanical properties of Portland cement". *Cement and Concrete Composites*, 129: 104485.

[4] Glasser, F.P. “The stability of ettringite. International RILEM Workshop on Internal Sulfate Attack and Delayed Ettringite Formation”. *RILEM Publications SARL*, 2004.

The 16th International Congress on the Chemistry of Cement 2023 (ICCC2023)
"Further Reduction of CO_2 -Emissions and Circularity in the Cement and Concrete Industry"
September 18–22, 2023, Bangkok, Thailand

Hydration of Blended Pastes at Later Age under Different Curing Conditions: Insights into the Rate Limiting Mechanism

Liming Huang[1*], Luping Tang[2], and Zhenghong Yang[3]

[1] *Department of Architecture and Civil Engineering, Chalmers University of Technology, 41296 Gothenburg, Sweden*
School of Materials Science and Engineering, Tongji University, Shanghai 201804, PR China
Email: limingh@chalmers.se

[2] *Department of Architecture and Civil Engineering, Chalmers University of Technology, 41296 Gothenburg, Sweden*
Email: tang.luping@chalmers.se

[3] *School of Materials Science and Engineering, Tongji University, Shanghai 201804, PR China*
Email: tjZHY92037@163.com

ABSTRACT

The hydration of supplementary cementitious materials (SCMs) is critical for the long-term performance of the sustainable cement-based materials. The mechanism of the later age hydration still lacks a clear understanding. This study aims to provide some insights into the later age hydration of cement-based pastes with fly ash and slag. The blended pastes were cured up to 600 days under different conditions (by the sealed curing at room temperature, elevated temperature and in water). The hydration degree has been characterized by the chemically bound water. The microstructure of hardened pastes was measured by N_2 sorption isotherms. Hydration at later age is only able to occur in pores within a certain range of size. The effect of pore size and temperature on nucleation rate of hydration products has been assessed to understand the mechanisms of hydration at later age.

KEYWORDS: *Hydration, Later age, SCMs, Microstructure, Nucleation*

1. Introduction

Substituting Portland cement with supplementary cementitious materials is the most efficient way to lower the clinker content in cement (Monteiro et al., 2017). SCMs significantly influence both the hydration of ordinary Portland cement and the microstructure of hardened cement-based materials. Hydration of cement blended with SCMs is an interaction between water and these binders. This process is involved with the dissolution of minerals and the followed precipitation of hydration products from pore solution. There are several reviews from the previous ICCCs to update the recent understanding of hydration mechanism of cement-based materials (Scrivener et al, 2015; Scrivener et al., 2019). However, a comprehensive understanding of the rate-limiting mechanism for later age hydration is yet to be fully established. Therefore, this study performed a detailed investigation of the microstructure in the blended pastes after a long-term curing.

2. Experimental procedure

2.1 Materials and curing regimes

Binders in this study include Portland cement (CEM I 52.5R), fly ash from Cementa and slag from Thomas Cement. The detailed chemical composition and particle size distribution were presented in (Huang, 2022).
Portland cement was substituted with 35% fly ash (P145) or slag (P245) by weight to make a binary binder system. The pastes were mixed with a *w/b* of 0.45. The mixing protocol of the paste was described

in (Huang, 2022). The pastes were cured under three different regimes (see Figure 1). Some freshly prepared paste was cast in polypropylene tubes and sealed with lips. One batch of the tubes was cured under a constant temperature with 20 ±1 ℃ for 600 days. The other batch of tubes were move into an oven with 50 ℃ after 390-day of 20 ℃ curing. Some paste was cast into zip bags and rolled to a uniform thickness of approximately 1 mm prior to the sealing. After one week of sealed curing, these samples were crushed into particles < 1 mm and cured in water in a 1 L container up to 600 days.

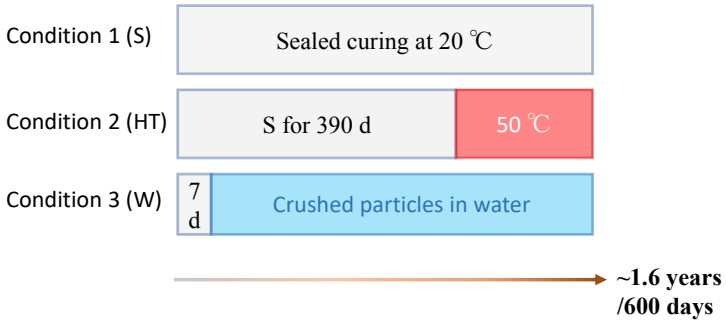

Figure 1. Three different curing regimes for the blended pastes.

2.2 Test methods

The inner relative humidity (RH) of the sealed samples was measured to evaluate the size of pores containing liquid water. After 600 days of curing, the sealed sample was quickly crushed into pieces and then sealed in a double layer zip bag with a humidity meter inside (Testo 174H). The zip bags were put in a sealed box to ensure a quick equilibrium between sample and stagnant air. The meter continuously records the temperature and the RH inside the bags every hour.

The particle samples were immersed into the isopropanol for 3 days. Afterwards, the residue sample was rinsed by diethyl ether and then vacuum dried at 30 ℃ for 24 h. The dried samples were sealed in 5 ml tube for Thermogravimetric and N_2 sorption measurement. A BET instrument (TriStar3000, Micromeritics) was used to measure the N_2 sorption isotherm of sample.

Samples were ground into powder for thermogravimetric analysis with instrument (SDT Q600, TA Instruments). Test was set with a heating rate of 10 °C/min under a continuous nitrogen flow (100 cm^3/min) from 20 to 1000 °C.

3. Results

3.1 TGA of paste

Figure 2 shows the differential mass change of the fly ash and slag blended pastes cured with different regimes. Pastes cured in water has the highest bound water losing between 20 and 250 ℃. It means that compared with the other two curing regimes, pastes cured in water has the highest amount of hydration products, including C-S-H, ettringite or AFm, whose decomposition occurs in this range (Scrivener et al., 2018). The bound water from portlandite (420–500 ℃) is much lower in fly ash paste cured in water compared with the sealed curing samples. A similar trend is observed in the slag pastes cured in water compared with the sealed curing. The elevated temperature seems to have few effects on the bound water losing below 350 ℃, but it increases the loss in 350–420 ℃. The bound water of portlandite in fly ash paste is reduced while that in slag pastes is increased by the elevated temperature curing after 390 days.

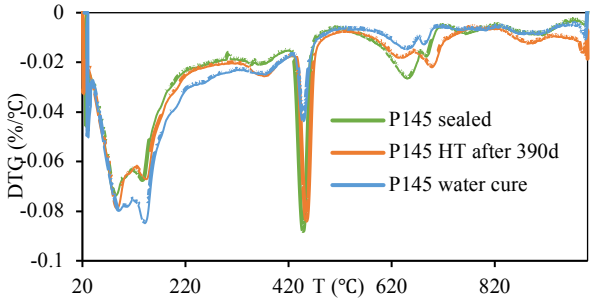

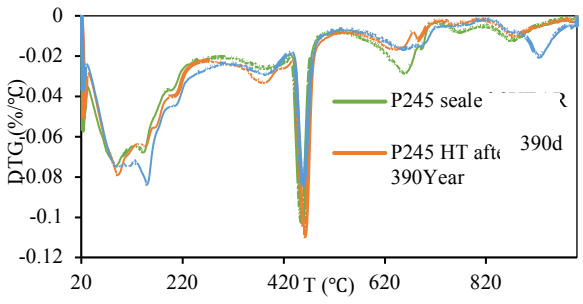

Figure 2. Differential thermogravimetric mass change of the fly ash and slag blended pastes.

Water curing provides sufficient water for later age hydration of both fly ash and slag to inhibit the precipitation of portlandite and to increase the amount of C-S-H and calcium aluminate hydrates. An increase in curing temperature after 390 days minorly enhances the hydration of fly ash to reduce portlandite content, and it activates the hydraulic reaction of slag to increase the content of portlandite.

3.2 N_2 sorption

Figure 3 presents the N_2 sorption of fly ash and slag blended pastes cured under different regimes. Water cured pastes have a much higher sorption of N_2 gas at the initial pressure condition, which indicates a much higher specific surface in hardened pastes. The cavitation-induced hysteresis is more pronounced in water cured samples compare with sealed curing samples. The cavitation between P/P0 of 0.4 and 0.5 occurs in ink-bottle gel pores with neck of a layer space size (Scherer and Smith, 1995). The elevated curing temperature enforces few effects on the sorption of N_2 in fly ash blended pastes, inducing a minor reduction in the sorption above P/P0 of 0.9. However, it evidently reduces the N_2 sorption in slag blended paste above P/P0 of 0.8 but increases the sorption below this point.

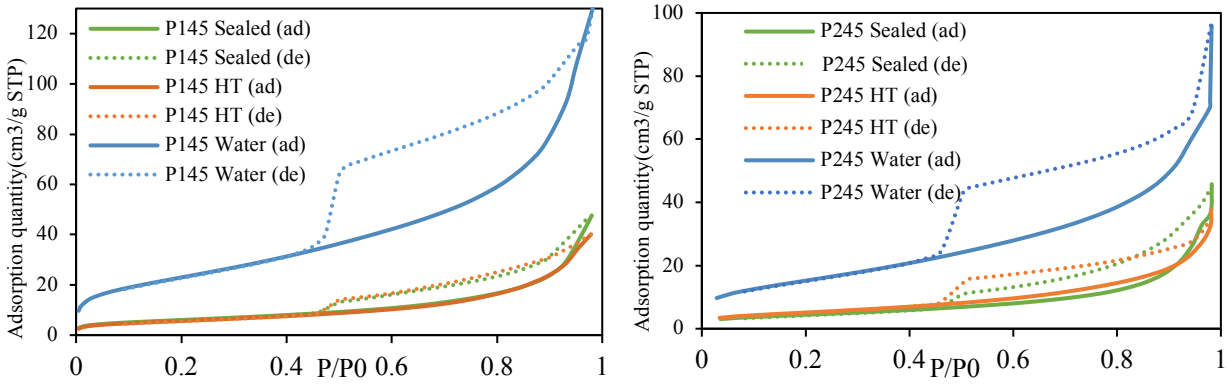

Figure 3. Adsorption and desorption of N_2 in fly ash and slag blended pastes after a long-term curing.

3.3 Inner RH

Figure 4 shows the equilibrium process between the RH meter and the crushed samples. The equilibrium reached after about 5 days. It shows that the inner RH of fly ash paste with sealed curing at 20 ℃ is about 74.5%, so water only exists in pore with a diameter of 7.33 nm after 600 days of hydration, according to Kelvin equation. An increase in temperature to 50 ℃ promotes the hydration to consume water in pores larger than 6.2 nm. After 600 days of hydration at 20 ℃, the water confined in slag-blended paste was in pores smaller than about 5.17. A curing at 50 ℃ after 390 days will consume the water in pores larger than 4.29 nm.

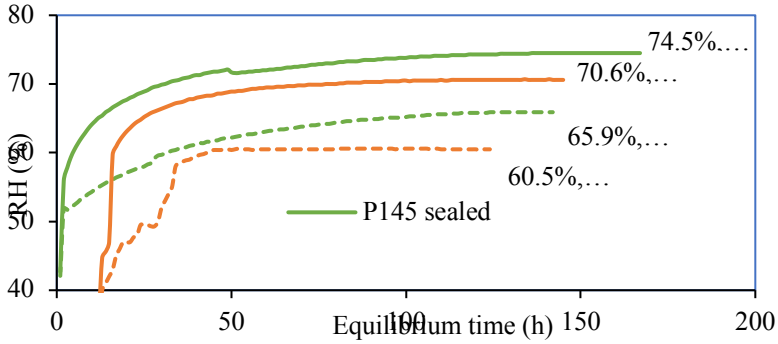

Figure 4. The inner RH of the hardened paste under sealed curing.

According to the classical nucleation theory, the nucleation rate J depends on the free energy change ΔG involved in the formation of a nucleus with a critical size as shown in equation (1).

$$J = \mathrm{P}\exp\left(-\frac{\Delta G}{kT}\right) \quad (1)$$

The fine single pores in hardened paste can be considered as a crystallization chamber, so the pore size can be used as the 'relevant' volume in equation (2) (Kashchiev and van Rosmalen, 2003; Prieto, 2014).

$$t_i = 1/JV \quad (2)$$

where V is the solution volume, and t_i is the induction time for nucleation in the small pores. By referring to an assigned pore shape and size (cylinder pore with radii of *r0*), the relative induction time, log(ti/t0), for nucleation in small pores can be calculated with the thermodynamic parameter in (Garrault-Gauffinet and Nonat, 1999). Figure 5 shows the effect of temperature and pore size on the nucleation of C-S-H in pores. As the water is confined in small pores with 10% (r/r0=0.1) of the reference size, the induction time will be increased largely by more than two magnitudes. An increase of temperature from 25 to 50 ℃ decreases the induction time with a factor of about 1000.

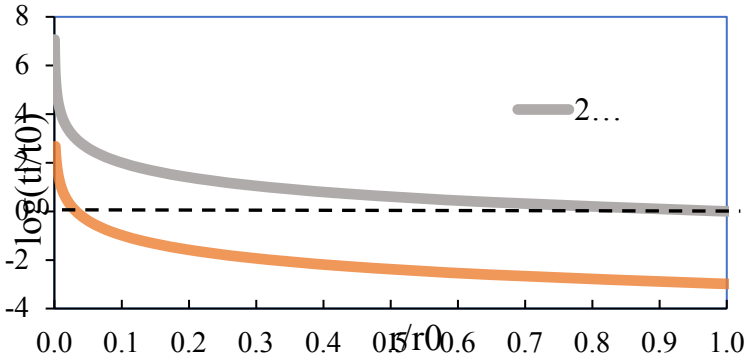

Figure 5. The effect of temperature and pore size on the nucleation of C-S-H in pores.

4. Conclusions

The water availability will impact the later age hydration of the fly ash and slag. Paste cured in water has much higher chemically bound water compared with the sealed curing even with an elevated temperature. Hence, the water cured paste has the highest specific surface area. An increase in the curing temperature after 390 d minorly increases the hydration of fly ash to reduce the inner RH. It has a pronounced effect on the hydration of slag to increase the volume of gel pores and decrease the inner RH. Water is only accessible in nanosized pores of the sealed curing samples. the limited size of pore solution will inhibit the nucleation of C-S-H, and an increase in temperature will reduce the induction time of nucleation.

Acknowledgements

Authors appreciate financial supports from Swedish Research Council for Sustainable Development FORMAS (2018-01430), Thomas Concrete Group, SBUF and Cementa AB.

References

Monteiro, P.J.M., Miller, S.A., Horvath, A., (2017) Towards sustainable concrete. Nature Mater 16, 698–699. https://doi.org/10.1038/nmat4930

Scrivener, K.L., Juilland, P., Monteiro, P.J.M., (2015) Advances in understanding hydration of Portland cement. Cement and Concrete Research 78, 38–56. https://doi.org/10.1016/j.cemconres.2015.05.025

Scrivener, K., et al., (2019) Advances in understanding cement hydration mechanisms. Cement and Concrete Research 16.

Huang, L., 2022. Water and alkali salts in the hydrating and hardened green cement-based materials: Hydration process, moisture content and transport (Licentiate thesis). Chalmers Tekniska Hogskola (Sweden), Gothenburg, Sweden.

Scrivener, K., Snellings, R., Lothenbach, B., (2018) A practical guide to microstructural analysis of cementitious materials. Crc Press.

Scherer, G.W., Smith, D.M., (1995) Cavitation during drying of a gel. Journal of Non-Crystalline Solids 189, 197–211. https://doi.org/10.1016/0022-3093(95)00222-7
Garrault-Gauffinet, S., Nonat, A., (1999) Experimental investigation of calcium silicate hydrate (C-S-H) nucleation. Journal of Crystal Growth 200, 565–574. https://doi.org/10.1016/S0022-0248(99)00051-2

The 16th International Congress on the Chemistry of Cement 2023 (ICCC2023)
"Further Reduction of CO_2 -Emissions and Circularity in the Cement and Concrete Industry"
September 18–22, 2023, Bangkok, Thailand

Activation of prehydrated CAC during curing at 20 ℃ using micro-sized $CaCO_3$

S. Chu[1], Y. Mu[2], Z. Zhang[3], J. Zeng[4], X. Xiong[5] and G. Ye[6*]

[1] *School of Materials Science and Engineering, Zhengzhou University, Zhengzhou 450001, China*
Email: 1220732384@qq.com
[2] *School of Materials Science and Engineering, Zhengzhou University, Zhengzhou 450001, China*
Email: myd1228@zzu.edu.cn
[3] *School of Materials Science and Engineering, Zhengzhou University, Zhengzhou 450001, China*
Email: 1345183859@qq.com
[4] *National Engineering Research Center for Advanced Polymer Processing Technology, Zhengzhou University, Zhengzhou 450001, China*
Email: zengjinyan0811@163.com
[5] *AdTech Metallurgical Materials Co., Ltd., Jiaozuo 454000, China*
Email: 1321899203@qq.com
[6] *School of Materials Science and Engineering, Zhengzhou University, Zhengzhou 450001, China*
Email: gtye@zzu.edu.cn

ABSTRACT

Calcium aluminate cement (CAC) is liable to prehydration in moist environment during production, transportation and storage. The prehydration reduces the hydration reactivity of CAC and leads to insufficient demoulding strength of CAC-bonded castables within the normal curing duration of 24 h. Therefore, how to use prehydrated CAC is of interest to cement manufacturers and users. In this work, CAC is exposed in the air atmosphere at 50% RH and 10 ± 2 ℃ temperature for 60 days to obtain the prehydrated CAC. The influence of prehydration on the hydration rate of CAC is evaluated in this study. Moreover, the effect of micro-sized $CaCO_3$ on hydration rate and hydration products of the fresh CAC and prehydrated CAC is comparatively investigated. The influence of addition of micro-sized $CaCO_3$ powder on the demoulding strength of prehydrated CAC-bonded castables cured at 20 ℃ is examined and the hydration activation effect of micro-sized $CaCO_3$ on prehydrated CAC during curing at 20 ℃ is explored.

KEYWORDS: *CAC, prehydration, micro-sized $CaCO_3$, demoulding strength*

1. Introduction

Cements interact with water vapor and CO_2 if they are exposed to ambient air, so that the hydration reactivity of cement is changed during storage (Valentin et al (2017)). It has been reported that the main consequences of prehydration of ordinary Portland cement (OPC) include delayed setting time, reduced heat of hydration, reduced mechanical properties and so on (Sprung et al (1978), Schmidt et al (2007)). It is known that the hydration rate of calcium aluminate cement (CAC) is faster than that of OPC (Dubina et al (2011)), so the prehydration degree of CAC is higher under the same conditions. Therefore, the problems caused by prehydration of CAC will be more serious. And in industrial practice, prehydration of CAC can even lead to waste of CAC during storage. How to reactivate the hydration reactivity of P-CAC is an urgent problem to be solved.

The previous study has shown that micro-sized $CaCO_3$ can promote hydration rate of fresh CAC to obtain cement blocks with high mechanical strength at 37 ℃ (Luz et al (2012)). So, whether micro-sized $CaCO_3$ can activate the hydration reactivity of P-CAC is a significative question to be explored. The purpose of this paper is to study the reaction process of prehydration of CAC in ambient air, and the influence of prehydration on the hydration reactivity of CAC is investigated. Furthermore, the effect of micro-sized $CaCO_3$ addition on the hydration reactivity of the P-CAC and the development of demoulding properties of castables is examined.

2. Experimental

The raw materials in Tables 1 and 2 are used to prepare castable samples and CAC paste specimens respectively, including tabular corundum aggregate (6-3 mm, 3-1 mm, 1-0.5 mm,0.5-0 mm, ≤ 0.045 mm), α-Al_2O_3 (CM370, purity Al2O3 ⩾ 99.56 wt.%, Cemat, China), micro-sized $CaCO_3$ (Xinrong Industry, China), fresh CAC (Secar 71, Kerneos, China), prehydrated CAC, and dispersing agents (ADW1 and ADS3, Almatis, China).

Table 1. Formulations of castables

Raw materials	Particle size	wt.%	
		PA0	PA10
Tabular corundum	6-3 mm	30	30
	3-1 mm	20	20
	1-0.5 mm	13	13
	0.5-0 mm	13	13
	≤0.045 mm	9	8
Micro-sized α-Al_2O_3	D_{50} = 2.14 μm	10	10
Micro-sized $CaCO_3$	D_{50} = 1.69 μm	0	1
Prehydrated CAC (P-CAC)	-	5	5
Dispersing additives	D_{50}= 2.6 μm	+1	+1
Deionized water	-	+4.2	+4.2

Table 2. Formulations of paste samples

Raw materials	Particle size	wt.%		
		FB0	PB0	PB10
Fresh CAC (F-CAC)	-	100	-	-
Prehydrated CAC (P-CAC)	-	-	100	100
Micro-sized $CaCO_3$	d_{50} = 1.69 μm	+0	+0	+10
Deionized water	-	+100	+100	+100

To prepare prehydrated CAC (P-CAC), the fresh CAC (F-CAC) were spread on a plate with a thickness of 2-3 mm, and the plate was placed in the air atmosphere at 50 %RH and 10 ± 2 ℃ for 60 days. The P-CAC was then collected and sealed for storage.

To investigate the influence of micro-sized $CaCO_3$ on the strength of prehydrated CAC bonded castables, the CAC-bonded castables using two different kinds of cements were prepared in the light of the formula in Table 1. Firstly, the raw materials were dry-mixed for 60 s and then wet-mixed for 120 s with water addition of 4.2 wt.% in a laboratory-scale mixer. The homogenized mixtures were poured into a mold with size of 40 × 40 × 160 mm and then cured at 20 ℃ for different periods of time. Then, the castable samples were demoulded for mechanical strength tests.

The of CAC paste samples were prepared in the light of Table 2, and the temperature evolution curves of hydration reaction of CAC pastes were drawn. A vacuum freeze drier was used to halt further hydration of CAC pastes, and then the phase compositions and microstructures of the hydration products of CAC paste samples were detected.

Mechanical properties of the castables including the cold modulus of rupture (CMOR) and cold crushing strength (CCS) were tested after curing for different periods of time. The temperature evolution curves of the CAC paste samples were drawn to identify their hydration behaviors at 20 ℃ by means of real-time temperature recording system used a heat of hydration instrument (PTS-12S, PTS, China). The phase compositions of pastes were identified by X-ray diffraction (XRD, D8 advance, Bruker, Germany).

3. Results and Discussion

Fig. 1 shows the temperature evolution curves of the F-CAC and P-CAC pastes curing at 20 ℃. As shown in Fig. 1, the hydration heat release of the PB0 sample (P-CAC pure paste) after curing for 27.8 h reaches the highest value, and the highest heat release temperature of the system is only 45 ℃. For the FB0 sample (F-CAC pure paste), the hydration heat release peak is reached after curing for 15 h, and the maximum heat release temperature could reach 100 ℃. These results indicate that prehydration of CAC particles significantly reduces the reactivity of CAC and delays the hydration time. This is not conducive to the development of mechanical properties of castables in actual industrial production.

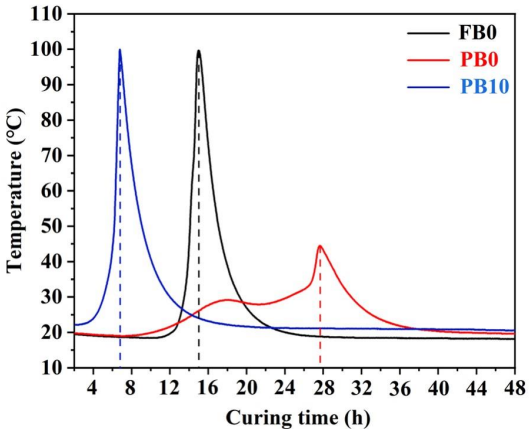

Fig. 1. The temperature evolution curves of CAC pastes cured at 20 ℃

To investigate the activation effect of micro-sized $CaCO_3$ on hydration of P-CAC, Fig. 1 compares the temperature evolution curves of PB0 (F-CAC pure paste) and PB10 (P-CAC paste with 1 wt.% $CaCO_3$) samples. After curing for 6.3 h, the hydration heat release of the PB10 sample reaches the highest value, and the highest heat release temperature of the system is 100 ℃. It is obvious that the addition of micro-sized $CaCO_3$ can significantly activate the hydration reactivity of the P-CAC, and even trigger the hydration reaction earlier than for fresh CAC (F-CAC).

To explore the influence of micro-sized $CaCO_3$ on the hydration products of the P-CAC, the phase compositions of the P-CAC pastes with and without micro-sized $CaCO_3$ cured at 20 ℃ are observed, as shown in Fig. 2. Fig. 2(a) shows that the PB0 sample (P-CAC pure paste) contains strong diffraction peaks of unhydrated CA and CA_2 after curing at 20 ℃ for 60 h. With the extension of curing time to 72 h, the strong diffraction peaks of the hydration products CAH_{10} appear. Fig. 2(b) shows that high-intensity diffraction peaks of CAH_{10} and $C_4A\bar{C}H_{11}$ have appeared in the PB10 sample (P-CAC pastes with 1 wt.% $CaCO_3$) cured only 24 h. These hydration products can provide demoulding strength for P-CAC bonded castables. By comparing XRD results of PB0 and PB10 pastes, it can be seen that micro-sized $CaCO_3$ can significantly activate the hydration reactivity of the P-CAC.

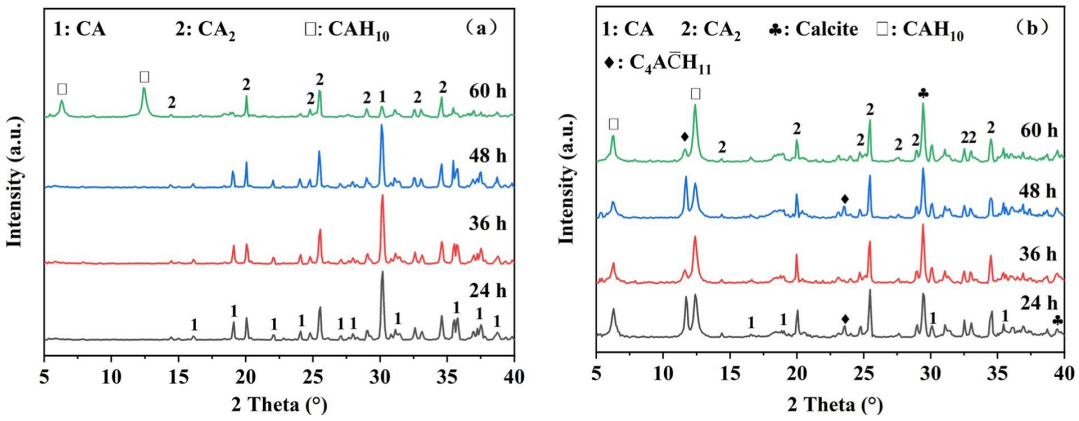

Fig. 2. XRD patterns of P-CAC pastes cured at 20 ℃ for different durations: (a) PB0 paste (b) PB10 paste

To further confirm the significant activation effect of micro-sized $CaCO_3$ on the P-CAC, Fig. 3 shows the demoulding strength of P-CAC bonded castables with and without micro-sized $CaCO_3$ after curing at 20 ℃ for different durations. As shown in Fig. 3, the demoulding strength of PA0 castables (without micro-sized $CaCO_3$ addition) develop very slowly with the extension of curing time. After curing for 48 h,

the CMOR of PA0 castables are only 1.32 MPa, which has not yet reached the requirement for demoulding (usually > 1.5 MPa). However, in the presence of micro-sized $CaCO_3$, the CMOR and CCS of PA10 castables are substantially higher than those of PA0 castables. Especially, the CMOR of PA10 castables after curing for 24 h obviously exceed 1.5 MPa in Fig. 3(a). And with the further extension of curing time, the CMOR and CCS of PA10 castables are still increasing slowly. By comparing the mechanical strength of the two kinds of CAC samples after curing at 20 ℃ for 24 h, it is found that the CMOR of the castables increases from 0.16 MPa (PA0) to 5.44 MPa (PA10) and CCS increases from 3.86 MPa (PA0) to 43.86 MPa (PA10) due to the activation of $CaCO_3$. This is very meaningful for the re-activation and reuse of expired cement in engineering.

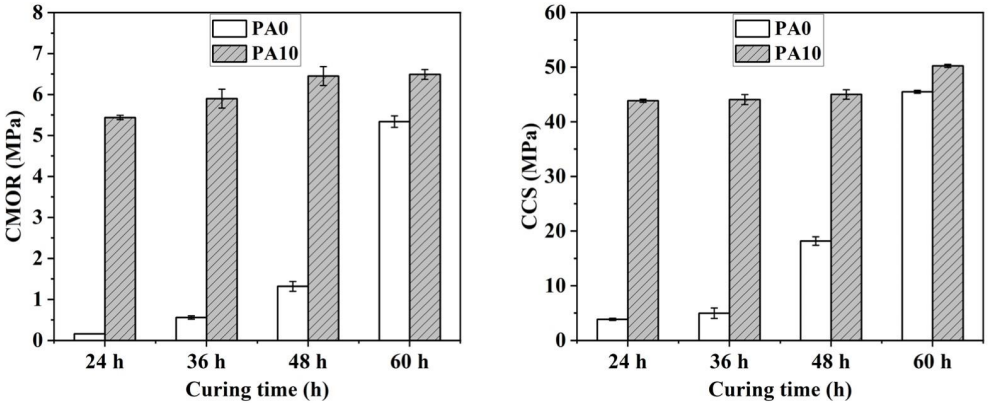

Fig. 3. The CMOR (a) and CCS (b) of P-CAC bonded castables with and without micro-sized $CaCO_3$ after curing at 20 ℃ for different durations

4. Conclusions

In this study, F-CAC was placed in the environment with relative humidity of 50% and temperature of 10 ℃ for 60 days to simulate the prehydration of CAC at the real storage condition. The hydration rates of F-CAC and P-CAC were compared. Moreover, the hydration reactivity activation effect of micro-sized $CaCO_3$ on the P-CAC was investigated. It is found that the hydration heat release of P-CAC is significantly postponed and mitigated compared to F-CAC, indicating the prehydration strongly reduces the hydration reactivity of CAC. When 1 wt.% micro-sized $CaCO_3$ is added, the peak time of the hydration exothermic curve of P-CAC is effectively shortened, demonstrating that micro-sized $CaCO_3$ can activate the hydration properties of P-CAC. Micro-sized $CaCO_3$ participates in the formation of hydration products of P-CAC to obtain $C_4A\bar{C}H_{11}$ phase, providing early strength for castables. Owing to the activation of micro-sized $CaCO_3$, the demoulding CCS of the P-CAC bonded castables at 24 h is sharply elevated from 3.86 MPa to 43.86 MPa. The outcome of this research provides a new approach of the reusing of prehydrated CAC.

Acknowledgements

The authors acknowledge the National Natural Science Foundation of China (52172030 and 52108258) for the financial support.

References

Dubina, E., Plank, J., Wadso, L. and Black, L. (2011) "The effects of prehydration of a combination of cubic C_3A with b-hemihydrate on adsorption of BNS superplasticizer", *Proceedings of the XIII ICCC International Congress on the Chemistry of Cement*, Madrid/ Spain, p. 250.

Luz, A.P. and Pandolfelli, V.C. (2012) "$CaCO_3$ addition effect on the hydration and mechanical strength evolution of calcium aluminate cement for endodontic applications", *Ceramics International*, 38(2): 1417-1425.

Schmidt, G., Bier, T.A., Wutz, K. and Maier, M. (2007) "Characterization of the ageing behavior of premixed dry mortars and its effect on their workability properties", *ZKG International*, 60(6): 94-103.

Sprung, V.S. (1978) "Effect of storage conditions on the properties of cements", *ZKG Int*, 30(6): 305–9.

Valentin, A., Jadvyga, K. and Edmundas, S. (2017) "Investigation of ageing of alumina cement-based mixtures using thermal analysis and calorimetry", *Journal of Thermal Analysis and Calorimetry*, 130: 35-44.

The 16th International Congress on the Chemistry of Cement 2023 (ICCC2023)
"Further Reduction of CO_2 -Emissions and Circularity in the Cement and Concrete Industry"
September 18–22, 2023, Bangkok, Thailand

Effect of Zn retention in alite on the hydration of cementitious systems

A. Teixeira[1*] and K. Scrivener[1]

[1] *École Polytechnique de Lausanne, Lausanne, Switzerland*
andrea.teixeirapita@epfl.ch, karen.scrivener@epfl.ch

ABSTRACT

The replacement of cement with supplementary cementitious materials (SCMs) represents one of the most feasible solutions to reduce the environmental impact of this industry. However, the replacement is limited, given the slow reactivity of these materials compared to cement. The incorporation of minor elements, particularly zinc, in the raw materials for C_3S production has shown the potential to increase cement reactivity. Results indicate that zinc incorporates into the C-S-H structure and changes its growth rate, as longer needles are observed. The same effect is seen in alite, an impure phase of C_3S, but not in polyclinker systems composed of alite-C_3A and alite-ferrite, due to different zinc repartition. This research investigates different approaches to incorporate Zn in the alite phase to enhance the hydration of more realistic systems. Different cooling rates, compositions, and the quantity of interstitial material were studied. The results evidenced that slow cooling promotes more Zn in the alite for the alite-C_3A polyclinker and enhances the hydration of these systems. The concentration of Zn in the alite for alite-ferrite polyclinker was higher but without an enhancement in the hydration. Longer induction periods were reported in this case and associated with the free ZnO and amorphous content. Even when the hydration is retarded, the height of the alite peak was increased, similarly to alite and C_3S.

KEYWORDS: *clinker, cooling, amorphous, reactivity, zinc oxide.*

1. Introduction

Minor amounts of zinc in the C_3S structure have shown potential to increase the reactivity of cement. Previous studies by Bazzoni et al. (2014) concluded that 1.16% of ZnO enhances the heat released by double when incorporated into the structure of the C_3S during the calcination process. This effect was attributed to the incorporation of zinc into the C-S-H structure, increasing its needle length. Similarly, Li and Scrivener (2022) demonstrated that the incorporation of Zn in C_3S has a significant effect on the early strength. However, this effect is not observed in more complex systems where doping with ZnO delays the reaction. Barbarulo et al. (2007) suggested that this delay can be related to the presence of Zn ions in solution, comparable to when ZnO is mixed directly with cement. Odler and Schmidt (1980) found ZnO retained by the silicate phases, but primarily in the interstitial phase. They also noticed an increase in the set time with ZnO additions higher than 1%, affecting the final mechanical properties. This research explores strategies for zinc incorporation into the alite phase of more complex systems, as it showed an enhancement in reactivity for the alite single phase. These strategies involve variations in the interstitial material composition, quantity, and cooling rate.

2. Materials and Methods

Three polyclinkers (polyphase clinkers) were synthesized: C_3A-polyclinker, ferrite-polyclinker and 5ferrite-polyclinker, with 90% alite and 10% C_3A, 90% alite and 10% ferrite phase, and 95% alite and 5% ferrite phase, respectively. The synthesis followed the method by Li et al. (2018) for the C_3S production,

the alite and the C_3A composition was taken from Taylor (1997) and for the ferrite the A/F was 0.64 (Teixeira (2022)). The C_3A-polyclinker was doped with 3 and 5% ZnO in the raw materials and calcination was at 1600 °C for 3 hours. The ferrite-Polyclinker and 5ferrite-Polyclinker were doped with 3% ZnO and the calcination temperature was at 1450 °C with a retention time of 3 hours. After calcination, the samples were cooled down by air with a fan. For a slow cooling, the samples were kept inside the furnace until 1250 °C. The hydration behaviour was followed by isothermal calorimetry at 20 °C, in where the samples were mixed with a stirrer at 1600 rpm, with a water to cement ratio of 0.5 and 5% of gypsum was added to the C_3A-polyclinker. X-ray diffraction (XRD) was used for phase quantification and scanning electron microscopy (SEM) coupled with EDX to study the microstructure and quantify the amount of zinc in the alite phase by point analysis. For SEM the powder was directly mixed with the resin, then polished and coated with carbon. Edxia was used to treat the mapping data.

3. Results and Discussion

The addition of zinc oxide in the C_3A-polyclinker system does not enhances the hydration. On the contrary, an increase in the quantity of ZnO in the raw materials results in prolonged induction periods (figure 1).

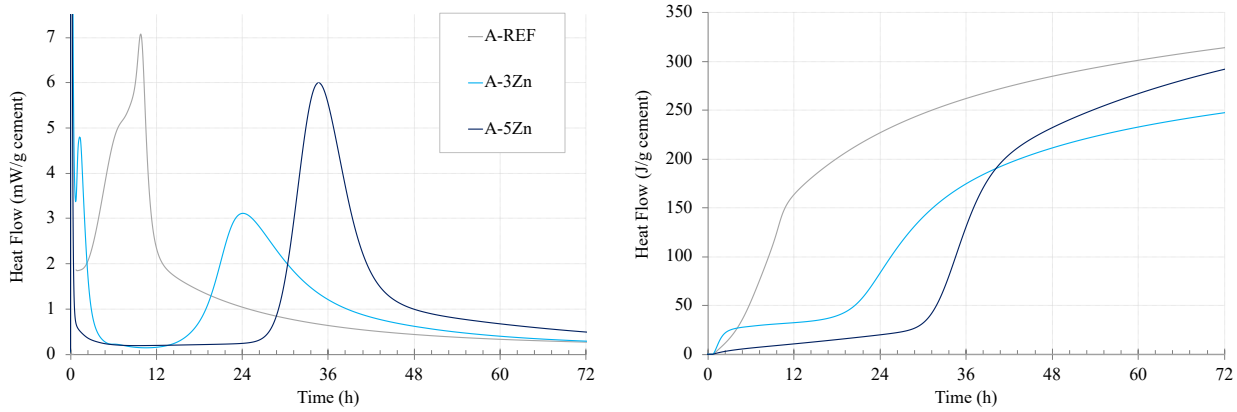

Figure 1. Calorimetric curves of C_3A-polyclinker system REF = 0% ZnO, 3Z = 3%ZnO and 5Z = 5% ZnO.

The phase quantification by XRD analysis indicates an increase in the amorphous content and the presence of free ZnO with the rise of the zinc dosage (table 1). Previous studies concluded that ZnO acts as a retarder when mixed with cement, hence the uncombined ZnO in the polyclinker may result in prolonged induction periods. However, even when the reaction is retarded, the alite peak height is enhanced for the sample with 5% ZnO dosage. This can be attributed to the increase of Zn in the alite with higher dosage. The zinc repartition is different in these systems from that of single alite, as other phases are involved, and it has a preference to remain in the interstitial material (figure 2). Point analysis revealed a concentration of 6.09 at%.

Table 1. Amorphous and free ZnO content obtained by XRD, and the amount of Zn in the alite obtained by SEM point analysis.

	Amorphous (%)	Free ZnO (%)	Zn in alite (at%)
A-REF	5.60	-	0.06
A-3Zn	18.70	0.50	0.39
A-5Zn	27.70	1.00	0.55

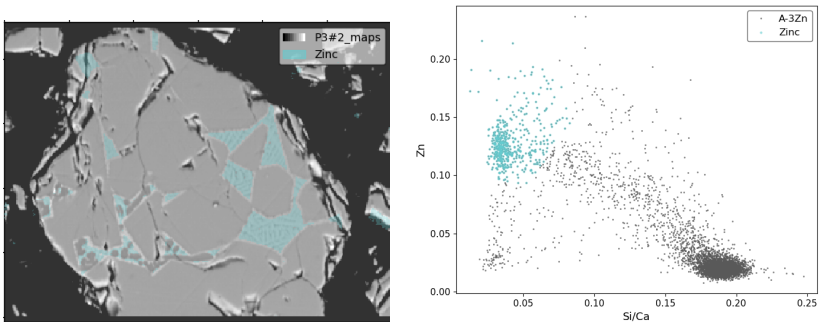

Figure 2. Polyclinker doped with 3%ZnO, a) BSE – overlap b) zinc repartition.

Three strategies were investigated to promote the Zn retention in the alite phase and evaluate its hydration behaviour. The first strategy focused on the C_3A-polyclinker systems, with a different cooling rate for its synthesis. At sintering temperatures, the interstitial material is liquid and crystallizes during cooling. However, a fraction of this material may remain in its amorphous state and retain more zinc than the crystalline material. A slow cooling process can promote the crystallization of the interstitial material, consequently, reduce the amorphous content, and probably increase the zinc retention in the alite. The second strategy was related to the composition of the interstitial material. A ferrite polyclinker was chosen as the solubility of zinc could be lower in this phase, promoting retention by the alite phase. And the third strategy involved a reduction of the interstitial material. Given the tendency of zinc to preferentially remain in this material, decreasing its amount would lead to an increase in the concentration of Zn in the alite.

Slow cooling of C_3A-polyclinker doped with 5%ZnO resulted in a reduction of the amorphous content to 16%, and a decrease in the free ZnO to 0.52%. The amount of Zn in alite increased to 0.67 at% and the concentration in the interstitial material decreased to 5.42 at%. As shown in figure 3, the hydration behavior improved, as the induction period is shortened and the alite peak height is increased. This result is consistent with the hypothesis that Zn in alite enhances its reactivity.

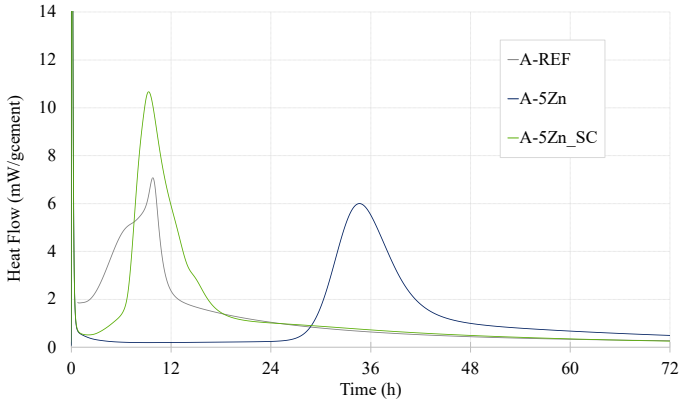

Figure 3. Calorimetric curves of C_3A-polyclinker system and the effect of slow cooling (A-REF = reference, A-5Zn = doped with 5% ZnO, A-5Zn_SC = doped with 5%ZnO and slow cooled)

By changing the composition of the interstitial material to ferrite and doping with 3%ZnO, the amorphous fraction resulted 9.10%, lower compared to the C_3A-polyclinker. The amount of Zn in alite and the free ZnO gave similar values, 0.40 at% and 0.50% respectively, which can explain the increase of the alite peak height and the retardation observed in figure 4a. A reduction in the amount of the interstitial material did not show an enhancement (figure 4b). In this case, a higher amorphous content of 12.70% and a lower quantity of free ZnO at 0.25% were observed. Moreover, the concentration of Zn in alite was found to be 0.47 at%, which is higher compared to the ferrite-polyclinker system. Nevertheless, the induction period is prolonged. The microstructure reveals the presence of white spots in the interstitial material similar to those observed by Barbarulo et al. (2007), which corresponds to the free ZnO (figure 5). While increasing the Zn concentration in the alite is desirable, it is essential to optimize other factors such as the ZnO dosage in the raw materials, to minimize the free ZnO and amorphous content to prevent retardation.

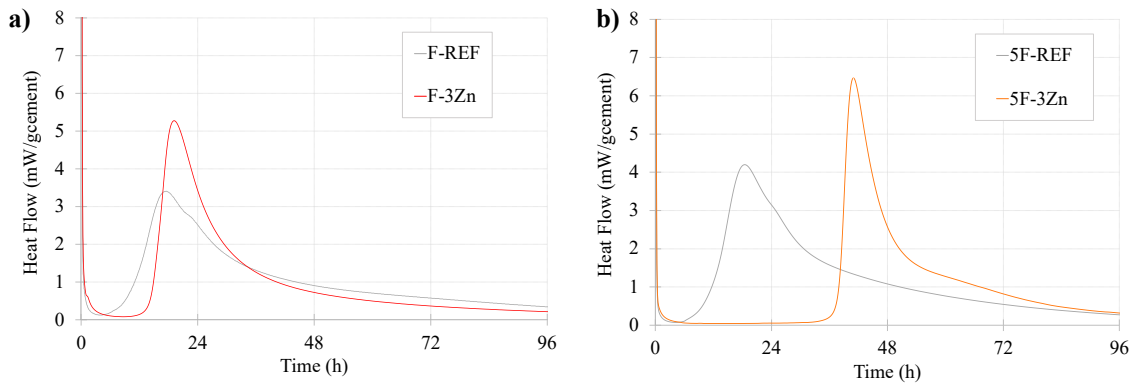

Figure 4. Calorimetric curves of a) the ferrite - polyclinker system (F-REF = reference, F-3Zn = doped with 3% ZnO), and b) 5% of ferrite- polyclinker system (5F-REF = reference, 5F-3Zn = doped with 3% ZnO).

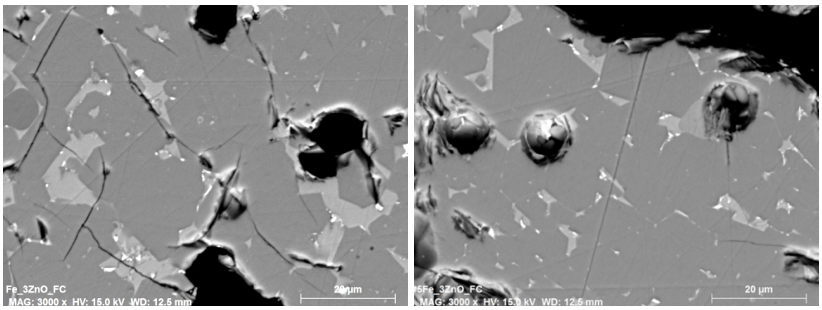

Figure 5. "White spots" microstructure in the doped samples: F-3Zn (left); and 5F-3Zn (right).

4. Conclusions

Three strategies were investigated to retain more Zn in the alite phase in polyclinker systems. A slow cooling process was found to promote greater retention of Zn by the alite phase, while reducing the amorphous fraction and the free ZnO content, resulted in a more reactive C_3A-polyclinker. A decrease of the ferrite interstitial material from 10% to 5%, also led to increased Zn content in the alite phase. However, retardation was observed in both ferrite systems, and it was related to the presence of amorphous and free ZnO content, seen as white spots in the microstructure. Although increasing the Zn retention in the alite phase is desirable, it is necessary to optimize other factors as the ZnO dosage in the raw materials to minimize the negative effects of amorphous content and uncombined ZnO.

Acknowledgements

The Swiss Federal Commission for Scholarship for foreign students (FCS) is acknowledged for the financial with the scholarship 2018.0706. Our gratitude to Dr. Alexander Pisch for his valuable feedback.

References

Bazzoni, A., Ma, S., Wang, Q., Shen, X., Cantoni, M., Scrivener, K. (2014) "The Effect of Magnesium and Zinc Ions on the Hydration Kinetics of C_3S", *The American Ceramic Society*, 97(1): 3684-3693

Barbarulo, R., Sorrentino, F., Sing, C., (2007) "Impact of ZnO on Clinker Composition and Reactivity Coupling with MgO", article ICCC

Li, X. and Scrivener, K. (2022) "Impact of ZnO on C3S Hydration and C-S-H Morphology at Early Ages", *Cement and Concrete Research,* 154(2022) article 106488

Li, X., Ouzia, A., Scrivener, K. (2018) "Laboratory Synthesis of C_3S on the Kilogram Scale", *Cement and Concrete Research,* 108(2018): 201-207

Odler, I. and Schmidt, O., (1980) «Structure and Properties of Portland Cement Clinker Doped with Zinc Oxide", *The Ametican Ceramic Society,* 63(1-2): 13-16

Teixeira, A. (2022) "Effect of ZnO on the reactivity of cementitious systems", Doctoral thesis, École Polytechnique de Lausanne

The 16th International Congress on the Chemistry of Cement 2023 (ICCC2023)
"Further Reduction of CO_2 -Emissions and Circularity in the Cement and Concrete Industry"
September 18–22, 2023, Bangkok, Thailand

Organic additive´s influence on M-S-H formation

C.R. Ruiz-Agudo[1*] and M. Marsiske[1]

[1] *Department of Chemistry, University of Konstanz, 78467 Konstanz, Germany*

Email: cristina.ruiz-agudo@uni-konstanz.de

ABSTRACT

One of the most promising strategies to reduce the CO_2 footprint of the cement industry is the replacement of Portland cement (PC) with alternative low-carbon binders. In that respect, magnesium-silicate-hydrate binders ($(MgO)x–SiO_2–(H_2O)y$, M-S-H), which can be produced by the hydration of MgO in the presence of silica, have caught strong attention lately. However, investigations of M-S-H cement paste evidence significant disadvantages compared with PC (e.g., high water demand, long setting times, and low compressive strengths). These drawbacks must be resolved to develop a competitive binding material that can be used as a PC surrogate. Polymeric additives are widely used in the cement industry to enhance the workability of the paste and regulate the setting. Among those, polycarboxylate ethers (PCEs) are widely used since they reduce the water demand, enhancing the flowability of cement paste. Nevertheless, the existing PCEs do not work as efficiently as for PC, and thus, novel admixtures must be explicitly developed for MgO-based binders. Since the commercial PCEs structures are complex and polydisperse, here, we investigated the influence of different anionic (acrylic acid, methacrylic acid, and maleic acid) and non-ionic (ethylene glycol) components of PCEs in the monomeric and polymeric form to uncover the effects on the formation of synthetic M-S-H. Titration experiments and complementary ex-situ characterization techniques were used to monitor the evolution of different physicochemical parameters of the reaction media (i.e., pH, conductivity, and transmittance) and the characteristics of the precipitates. Acrylic acid and methacrylic acid monomers caused a slight delay in M-S-H nucleation, whereas maleic acid and ethylene glycol did not affect the nucleation. Regarding the polymers, we identified a delay in M-S-H nucleation when all anionic polymers were in the media and no effect of polyethylene glycol. Polyacrylic acid caused the most prominent retardation among the anionic polymers.

KEYWORDS: *M-S-H, alternative binders, polymeric additives, titration.*

1. Introduction

MgO-based cements from magnesium silicate rocks have the largest potential for CO_2 savings, however, they are still in the research and development phase (Gartner and Sui, 2018; Scrivener et al., 2018). They use MgO instead of CaO as the main building block, which presents some challenges since the chemistry is very different from that of CaO. Therefore, the technology available for PC cannot be used in the case of MgO to produce a competitive binder (Bernard et al., 2017). One of the significant drawbacks of MgO cements is the high-water demand which can be tackled using dispersant agents (PCEs). PCEs are comb copolymers with an adsorbing backbone (anionic) and nonadsorbing side chains (non-ionic). However, the existing PCEs must be added in high doses in Mg-based blends (Winnefeld et al., 2019), and thus, it is urgent to develop new admixtures to facilitate their implementation in the construction industry. Herein, we focused specifically on M-S-H binders and investigated the influence of polymeric additives on its early formation. The complexity of PCEs architectures could result in complicated alterations of the crystallization of M-S-H. Thus, the effect of the different components of PCEs will be assessed in this first study to develop new PCEs structures adapted for the M-S-H system. First, monomeric units (acrylic acid, methacrylic acid, maleic acid, and ethylene glycol) were investigated, and following, homopolymers of those monomers (poly(acrylic acid), poly(methacrylic acid), poly(maleic acid), and poly(ethylene glycol)) were tested.

2. Methodology

2.1 Chemical synthesis of M-S-H

Double-titration experiments were conducted to investigate the early stages of M-S-H formation in the presence of different organic additives similar to those used in our previous works (Marsiske et al., 2021; Marsiske et al., 2023). See complete experimental details there. The evolution of pH, conductivity, and turbidity was recorded during the experiments. For a typical experiment, 50 mL of MilliQ water were stored in a Teflon beaker. Salt solutions (50 mM $MgCl_2$, 50 mM Na_2SiO_3) were added simultaneously by two computer-controlled dosing units at a constant rate of 50 µL/min into the beaker, under stirring. Experiments in which no additives were used are referred to as 'reference' runs. These salts were selected t prepare the solutions due to their high solubility ambient conditions ($MgCl_2$ = 54.3 g/100 mL , Na_2SiO_3= 22.2 g/100 mL). First, the effect on M-S-H crystallization of the monomeric units and, later, the homopolymers were examined. The amount was ´normed´ to the carboxyl group content of 1 ppm (wt.%) of acrylic acid to guarantee comparison between the investigated polymers. Before titration, the pH value was set to 6 using 0.1M NaOH or 0.1M HCl, respectively. Experiments have been performed, like the titration experiments for the 'reference' runs. After the experiments, the precipitates were centrifuged, washed with EtOH, and dried at 50°C. The obtained product was analyzed ex-situ via Fourier-transform infrared spectroscopy (FTIR), X-ray diffraction (XRD), Thermogravimetric Analysis (TGA), and electron microscopy (SEM, TEM).

3. Results

PCEs architectures are complex, and to differentiate effects caused by different segments, the ´individual´ components of PCEs were investigated. Acrylic (AA), methacrylic (MA), maleic acid (Maleic), and ethylene glycol (EG) monomeric units, as well as their homopolymers, were screened to investigate their influence on M-S-H crystallization. The experimental approach used here serves as a fingerprinting technique to distinguish the effect of additives on the crystallization of various substances (Ruiz-Agudo et al., 2016; Verch et al., 2011). With this approach, quantitative information about alterations of the nucleation by the additives can be obtained, such as the nucleation time of the solid phase. The solution's pH, conductivity, and transmittance were monitored during the formation of M-S-H, and the crystallization (nucleation) onset was determined independently (Figure 1).

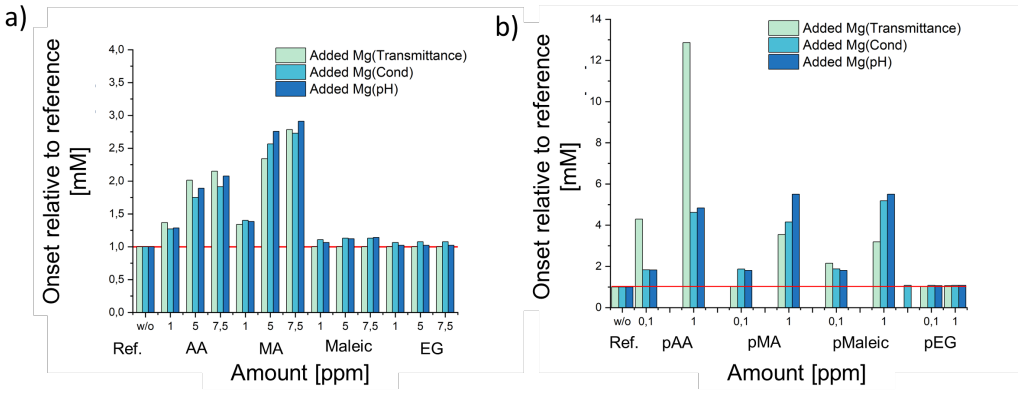

Figure 1. Summary of onset of the nucleation determined by the pH, conductivity, and transmittance probes for: a) monomeric additives (1, 5, and 7.5 ppm) and b) polymeric additives (0.1 and 1 ppm).

Monomeric additives were investigated first to see the direct effect of the functional groups on M-S-H nucleation. Concerning their development on nucleation, the monomeric units can be divided into nucleation-inhibiting additives and additives without effect (Figure 1a). For EG, no significant impact on the nucleation was observable for any amount, which agrees with the expectations for EG since it does not bear any complexation group. When EG is a building unit of the PCEs, it is a side chain that mainly acts as a steric stabilizer of the cement particles. Therefore, effects on M-S-H formation, either in the monomer (EG) or the polymer structure (pEG), are not expected. In the case of AA and MA, a significant effect on the nucleation was observed, which was more prominent when higher concentrations were used

(Figure 1b). The nucleation is delayed for both systems, with MA inhibiting more than AA. In contrast to the other carboxylic acids, the effect of maleic acid on nucleation is weaker than it was expected since it bears two carboxylic units, and the number of monomeric units is kept constant for all monomers, meaning the amount of carboxylic groups in the solution is doubled.

M-S-H formation in the presence of polymeric additives (homopolymers of the monomeric additives previously investigated) was studied to check the differences when the monomers are polymerized. The more substantial impact on the nucleation time is why using lower polymer concentration than the monomer experiments. A summary of the effect of the four polymers (pAA, pMA, pMaleic, and pEG) relative to the reference experiments where no additive was used is shown in Figure 1b. Compared to the reference experiments, the carboxylic-based polymers delay nucleation. This effect is enhanced by increasing the polymer concentration. In the case of the pEG, no effect was observed. The case of the pAA was interesting since inhibition of M-S-H nucleation was significantly increased compared with the pMA and pMaleic. Due to the limitations in space, only transmittance curves versus added magnesium concentration in solution are presented here for the tested polymers (Figure 2). The plots represent the averaged values of transmittance measurements from at least three independent experiments. As can be seen from the broadening of the error bars of the different transmittance graphs (Figure 2), the influence of polymers is complex, making the system less reproducible. Nevertheless, the general trend of nucleation delay can be seen in all titrations containing carboxylic-based polymers.

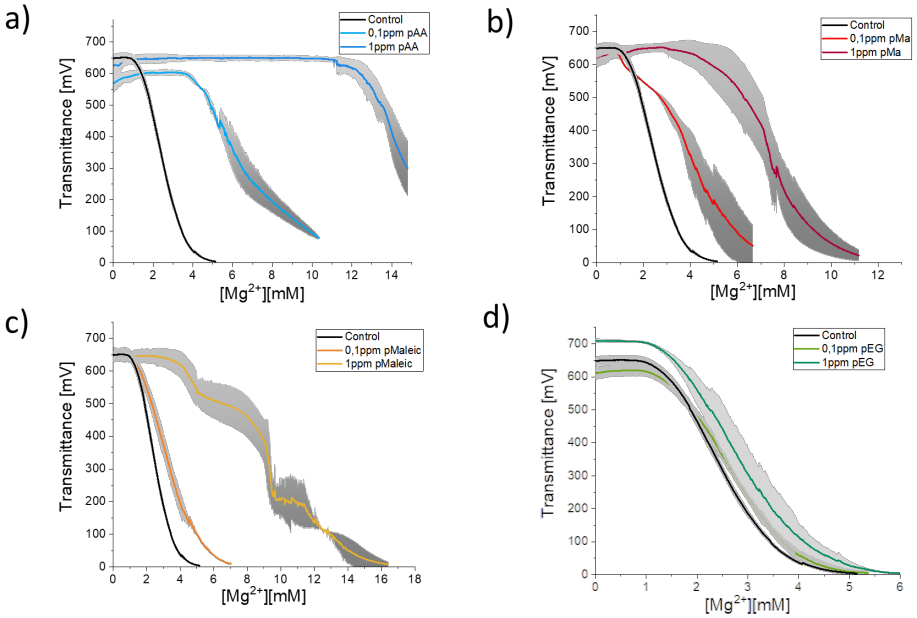

Figure 2. Transmittance curves obtained for the different homopolymers: a) polyacrylic acid, b) polymethacrylic acid (pMA), c) polymaleic acid (pMaleic), and d) polyethylene glycol (pEG). Black curves correspond to the control runs.

For the case of the pAA, the transmittance curves (Figure 2a) show a significant delay for the onset of nucleation even at the low concentration (0.1 ppm) and a slightly more downward slope in the signal decrease compared with the references. The fall in transmittance occurred 12 times later than in the reference (Figure 2b and 3a) when 1 ppm of pAA was used. This could be due to the stabilization of small M-S-H particles by pAA. In the case of pMA, transmittance data show that for low concentrations of additive, no delay in the onset can be observed, but the overall growth seems to be inhibited by the polymer (Figure 2b). At 1 ppm, nucleation shifted to a higher ion concentration with significant retardation of the transmittance drop. For the case of pMaleic (Figure 2c), no delay in nucleation for 0.1 ppm of additive was observed, whereas, for 1 ppm, the transmittance drop is delayed. Here, two plateaus appeared that could be due to polymer-stabilized phases. Concerning pEG, no significant changes in transmittance curves can be detected compared to the reference (Figure 2d).

Regarding the ex-situ characterization of the precipitates, Figure 3a shows the XRD pattern for M-S-H obtained in the presence of 1 ppm of the four polymers. The main reflexes correspond to M-S-H and do not show significant shifts compared to the reference M-S-H. The IR spectra of the 1 ppm polymeric samples (Figure 3b) showed the typical bands for M-S-H observed in the references. In the

case of pAA M-S-H samples, the polymer incorporates into the material as the bands appearing from 1500 to 1100 cm^{-1} are characteristic of $COOH^-$ vibrations. Also, a shift related to Q^3 Si-O stretching vibrations from 1000 to 990 cm^{-1} can result from a change in structural motifs of the silica-tetrahedra. The TGA profile for pEG and pMaleic samples is similar to the reference, indicating no polymer was incorporated into the material. For pAA and pMA, an additional mass loss of ca. 2% around 450°C can be assigned to the decomposition of the polymer (Figure 3c), hinting at its incorporation. No changes were observed concerning the morphology of the precipitates studied by SEM and TEM (results not shown).

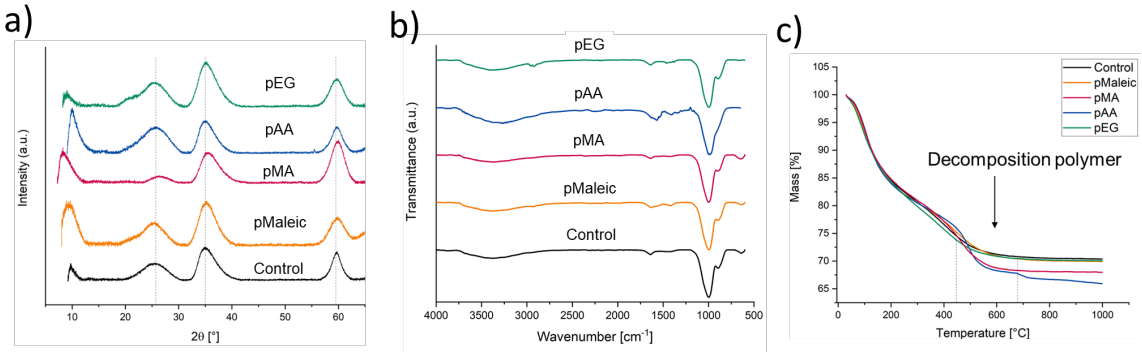

Figure 3. Analysis of the precipitates obtained in the presence of 1 ppm of polymer. a) XRD, b) FTIR and c) TGA.

4. Conclusions

This work presents a first glimpse into the crystallization mechanism of M-S-H from solution in the presence of different building units of PCEs. As expected, the non-ionic additives (EG and pEG) showed little or no influence, whereas additives from the carboxylic polymers' class delayed M-S-H's nucleation. Poly(acrylic acid) is particularly noteworthy. It influenced the nucleation strongly and showed unusual behavior compared to the other tested relatives. While most measured parameters (pH, conductivity) indicated the beginning of nucleation, the optical sensor showed contrary results, meaning most likely that stabilized M-S-H precursor species formed during the experiment. A clear answer on the precise nature of this precursor is an ongoing work. Nevertheless, the current results presented here show that if pAA-bearing PCEs are used as superplasticizers for M-S-H binders, a significant retardation effect in the setting is expected.

Acknowledgments

We thank the German Research Foundation (DFG) Project number: RU 2368/11-PI: C. Ruiz-Agudo.
C. Ruiz-Agudo thanks the Zukunftskolleg (University of Konstanz) for financial support.

References

Bernard, E., Lothenbach, B., Rentsch, D., Pochard, I., and Dauzères, A. (2017) "Formation of magnesium silicate hydrates (MSH) ", *Physics and Chemistry of the Earth, Parts A/B/C*, 99: 142-157.

Gartner, E., and Sui, T., 2018, "Alternative cement clinkers" *Cement and Concrete Research*, 114, 27–39.

Marsiske, M. R., Debus, C., Di Lorenzo, F., Bernard, E., Churakov, S. V., and Ruiz-Agudo, C. (2021) "Immobilization of (Aqueous) Cations in Low pH M-S-H Cement", *Applied Sciences*, 11(7): 2968.

Marsiske, M. R., Köser, R., Bäumle, B., and Ruiz-Agudo, C. (2023) "Uncovering the Early Stages of Magnesium Silicate Hydrate Formation: A Nonclassical Multistep Pathway", *ACS Applied Engineering Materials*, 1(1), 696-707.

Ruiz-Agudo, C., Ruiz-Agudo, E., Burgos-Cara, A., Putnis, C. V., Ibáñez-Velasco, A., Rodriguez-Navarro, C., and Putnis, A. (2016) "Exploring the effect of poly (acrylic acid) on pre-and post-nucleation $BaSO_4$ species: new insights into the mechanisms of crystallization control by polyelectrolytes", *CrystEngComm*, 18(16): 2830-2842.

Scrivener, K. L., John, V. M., and Gartner, E. M. (2018) "Eco-efficient cements: Potential economically viable solutions for a low-CO_2 cement-based materials industry", *Cement and Concrete Research*, 114: 2–26.

Verch, A., Gebauer, D., Antonietti, M., and Cölfen, H. (2011) "How to control the scaling of $CaCO_3$: A "fingerprinting technique" to classify additives", *Physical Chemistry Chemical Physics*, 13(37): 16811-16820.

Winnefeld, F., Epifania, E., Montagnaro, F., and Gartner, E. M. (2019) “Further studies of the hydration of MgO-hydromagnesite blends”, *Cement and Concrete Research*, 126: 105912.

The 16th International Congress on the Chemistry of Cement 2023 (ICCC2023)
"Further Reduction of CO_2 -Emissions and Circularity in the Cement and Concrete Industry"
September 18–22, 2023, Bangkok, Thailand

Modifications on the early hydration stages of a Portland cement paste induced by polydimethylsiloxane (PDMS)

N. Husillos-Rodriguez[1], M.T Blanco-Varela[1], S. Martinez-Ramirez[2]and I. Garcia-Lodeiro [(1, *)]

[1] *Eduardo Torroja Institute for Construction Science (IETcc-CSIC), Madrid, Spain*
2 Institute of Structure of Matter (IEM-CSIC), Madrid, Spain

** Corresponding Author: iglodeiro@ietcc.csic.es*

ABSTRACT

The objective of the present work is to study the influence of incorporating polydimethylsiloxane (PDMS) into fresh cementitious pastes and in particular to analyse its effect on the kinetic of hydration and in the mineralogy (after 7 days of hydration). The effects of silanes on cement hydration have been widely studied in the literature, however, there is some controversy about its effect at short ages. The PDMS interacts with the cement phases (C_3S, C_2S, C_3A or CSH) making the pastes obtained hydrophobic, due to the methyl groups that it presents in its structure. For this purpose, three cement pastes (BL 52.5R) were prepared using a water/cement ratio of 0.35 and 0, 3 and 6% (wt.) PDMS was incorporated during the mixing process. The heat flow and the total heat were monitored for 7 days by isothermal calorimetry. After this time, pastes were characterized by XRD, FTIR, TG/DTG, and TEM/EDX. The incorporation of 3 and 6% of PDMS affects the kinetic of hydration, delaying the precipitation of reaction products, and slightly declining the total heat released. Ettringite and portlandite were observed, although there was a loss in the crystallinity of the later. TEM results confirm the loss of crystallinity of portlandite, after the addition of PDMS.

KEYWORDS: *Hydrophobicity, PDMS (Polydimethylsiloxane), PC hydration, isothermal calorimetry, mineralogy*

1. Introduction

The development of superhydrophobic mortars and concretes, by the incorporation of different admixtures during the mixing, would avoid later stages of waterproofing for their protection (Muhammad et al (2015)). These admixtures should confer mass hydrophobicity without compromising other technological properties. Polydimethylsiloxane (PDMS) is the most widely used silicon-based organic polymer and has many advantages compared to small molecule silanes such as: transparency, harmless, non-flammable, generally inert, non-volatile and high cost-effectiveness (low cost). However, the literature on PDMS as a water-repellent admixture in concrete is exiguous, resulting in knowledge gaps around the impact of such applications on cement hydration kinetics, concrete mechanical properties and microstructure and, naturally, on its hydric properties (Eduok et al. (2017), Wang et al (2020)).
The aim of the present work is to analyse the effect of incorporating PDMS on the kinetic of hydration of cement pastes during the first reaction stages (up to 7days), as well as to explore the possible changes in their mineralogy and composition.

2. Experimental

2.1. Samples preparation, analysis details and instrumentation

Three cement pastes were prepared, with a w/c = 0.35 (standard consistency). The reference (PS) was mixed with only water, whereas the other two pastes contained 3% and 6% of PDMS (by weight of cement) labelled respectively as PS-3% and PS-6%. The mixing sequence was 90 seconds at 168 rpm followed by a 60 seconds rest and remixing for a further 90 seconds at 168 rpm. The PDMS (liquid) was added in the last 90 seconds. Hydration was monitored in 5 g aliquots of each mix, placed in the calorimeter immediately after preparation. Upon conclusion of the calorimetric test (7 days) the samples were removed, ground to a particle size of <45 µm and soaked in isopropanol to detain hydration. These samples were then characterized with XRD, FTIR, TG/DTG and TEM/EDX.

XRD analyses were performed on a Bruker D8 Advance diffractometer consisting in a 2.2 kW generator and a copper anode X-ray tube (CuKα1 radiation: 1.5406 Å and CuKα2: 1.5444 Å) operating at 40 kV and 30 mA and fitted with a 0.5° fixed divergence slit and a non-monochromatic Lynxeye super speed detector bearing a 3 mm anti-scatter slit, a 2.5° secondary Soller slit and a 0.5% Ni K-beta filter. Readings were taken for approximately 1 h per diffractogram over a 2θ angular range of 5°–60° with a 0.02° step size.Samples pressed into KBr pellets were scanned (10 scans per sample) to record their infrared spectra with a Nicolet 6700 spectrometer in the 400 cm^{-1} range at a spectral resolution of 4 cm^{-1}. Thermogravimetric heat flow was determined on a TA SDT Q600 analyser with platinum crucibles (empties were used as a reference). The samples were heated to 1050 °C at a 10 °C/min rate in a nitrogen atmosphere. TEM/EDX analysis was performed on a JEOL 2100 HT microscope, with an accelerating voltage of 200kV. EDX were made on an INCA microanalysis system, from Oxford Instruments. For this, two samples were selected, PS and PS-6%, after 7d of hydration, the powder of each of the samples was dispersed in an isopropanol solution, and a drop of the previous suspensions was deposited on a grid of Cu covered with carbon, it is allowed to dry under an IR lamp and the TEM holder is inserted.

3. Results and discussion

3.1 Changes in the kinetic of hydration

Figure 1 shows the calorimetric curves of cement mixed exclusively with water (PS) (reference system) and with water in the presence of 3% (PS-3%) and 6% (PS-6%) of PDMS.

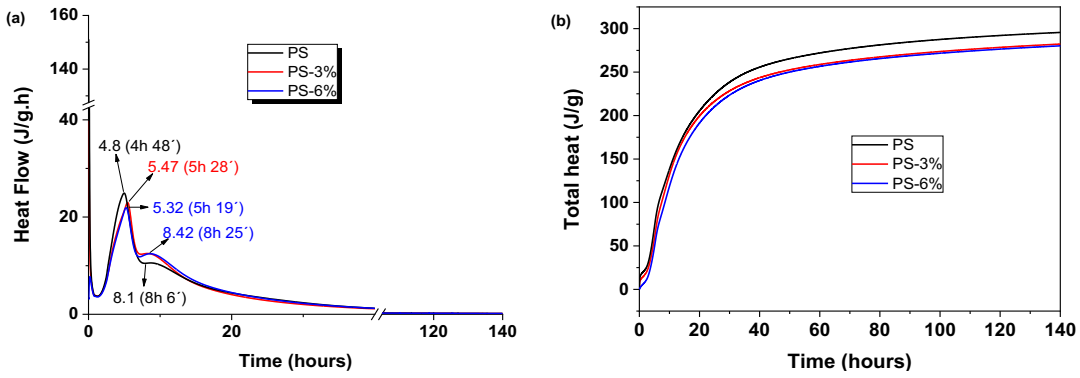

Fig. 1. (a) Heat flow and (b) Total heat in PC pastes with 0 % (PS), 3 % (PS-3%) and 6 % (PS-6%) PDMS

As can be seen in Fig. 1(a), the kinetic of hydration, at early reaction ages, was slightly delayed in presence of the PDMS. The maximum, corresponding to the acceleration/deceleration peak, associated with the precipitation of the hydration products, shifts from 4.8h in the reference to 5.32h and 5.47 h respectively when 3 and 6% of PDMS is added. The total heat at 7 days (Fig.1 (b)) was very similar in the two samples containing PDMS, being approximately 5% lower than the reference (PS).

3.2 Mineralogical and compositional analysis after 7 days of hydration

Fig. 2(a) shows the XRD patters, after 7 days of hydration, of the reference paste (PS) and those with 3 and 6% PDMS (PS-3% and PS-6%). All samples show peaks corresponding to the typical hydration products: ettringite (e) and portlandite (p). Signals corresponding to remains of anhydrous phases, mainly alite (A) and belite (B), were also detected. It is to notice that the intensity of the peaks corresponding to portlandite, considerably decreases with the incorporation of PDMS. This effect is much more significant in sample with the highest proportion of PDMS (PS-6%).

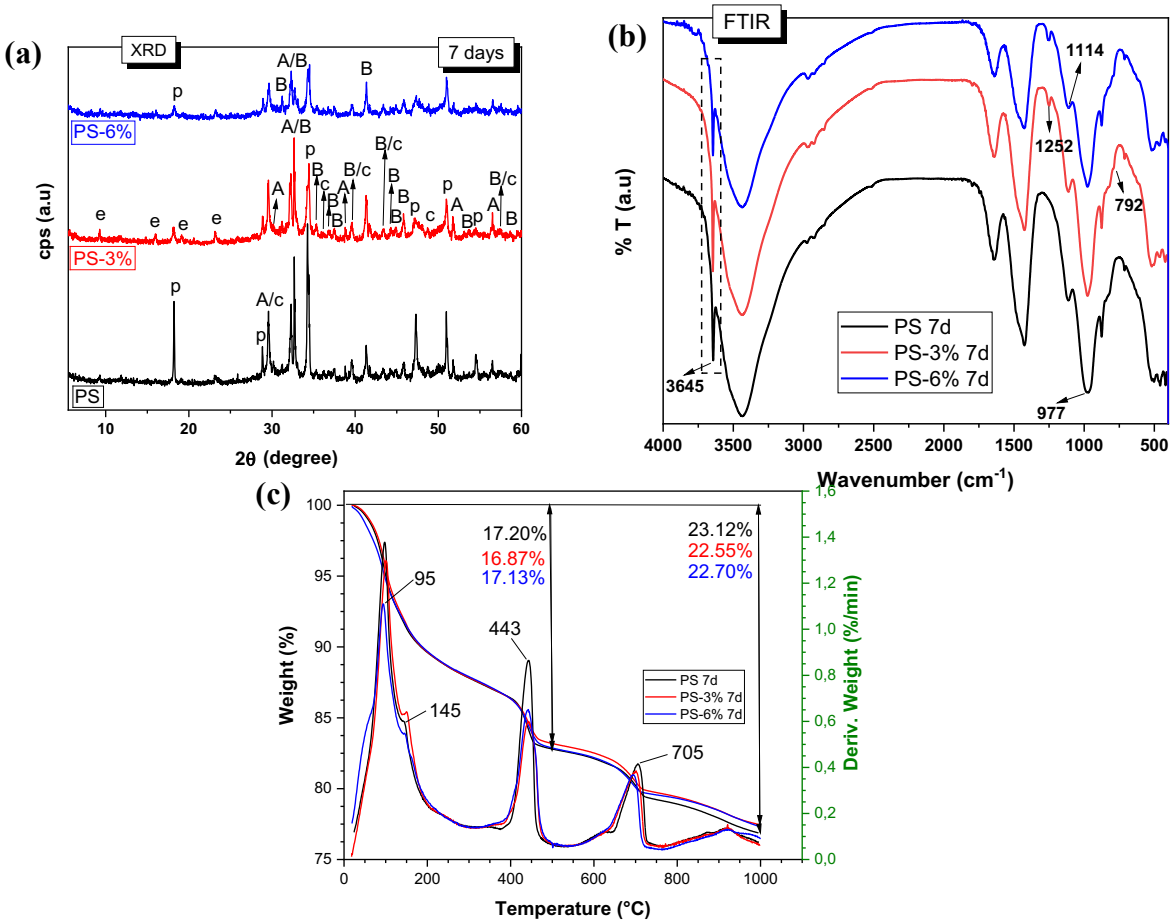

Fig. 2. **(a)** XRD patterns (Legend: A: alite (C_3S) (COD 1540704); B: belite (C_2S) (COD 9012789); c: calcite ($CaCO_3$) (COD 9016022); p: portlandite ($Ca(OH)_2$ (COD 1008781); e: ettringite (COD7020139) **(b)** FTIR spectra and **c)** TG/DTG curves of PS, PS-3% PDMS, and PS-6% PDMS

Fig. 2(b) shows the FTIR spectra of the same PS, PS-3% and PS-6% pastes after 7 days of hydration (4000-400 cm^{-1} region). In all spectra, the asymmetric stretching vibration O-H band (3645 cm^{-1}) assigned to portlandite can be distinguished. Contrary to observed by XRD, the intensity of this band was similar in both the reference (PS) and in presence of PDMS (3 and 6% PDMS). This fact could suggest that the presence of the PDMS is somehow affecting the degree of crystallinity of the portlandite. In samples containing the PDMS, the presence of bands at 1252 cm^{-1} and 792 cm^{-1} assigned respectively to Si-CH_3 symmetric tension vibrations and Si-CH_3 rocking, are observed. The rest of the bands, assigned to the precipitation of C-S-H (main band 970 cm^{-1}) and the formation of ettringite (main band at 1114 cm^{-1}) are practically the same. Fig. 2(c) shows the TG/DTG curves of the previous systems. All curves show different mass losses due to the decomposition of the different hydration products; ettringite (70-100 ºC) and C-S-H gel (90-100ºC), AFm phases (145ºC), portlandite (395-500ºC) and carbonates (500-750ºC). In the interval between 290º to 400 ºC, PDMS would thermally decompose, so the loss of mass in this area would correspond with the overlapping of portlandite and PDMS. In order to try to explore the possible amorphization of the portlandite in presence of the PDMS, selected samples (PS and PS-6% PDMS) were analysed by TEM/EDX. Fig. 3(a) and (b) shows respectively a micrograph corresponding to a portlandite particle analysed in the reference sample and in sample containing the PDMS.

Along with these micrographs, the corresponding electron diffraction pattern and the EDX analysis are depicted. In the reference sample, a clearly crystalline portlandite is observed (Fig. 3(a)), while in PS6% sample Fig. 3(b), the electron diffraction pattern shows a clear loss of crystallinity of portlandite. The EDX analysis shows the presence of silicon, that could correspond with the presence of a PDMS particle coating the portlandite, and therefore amorphizing it to some extent. Further studies are required to clarify this point.

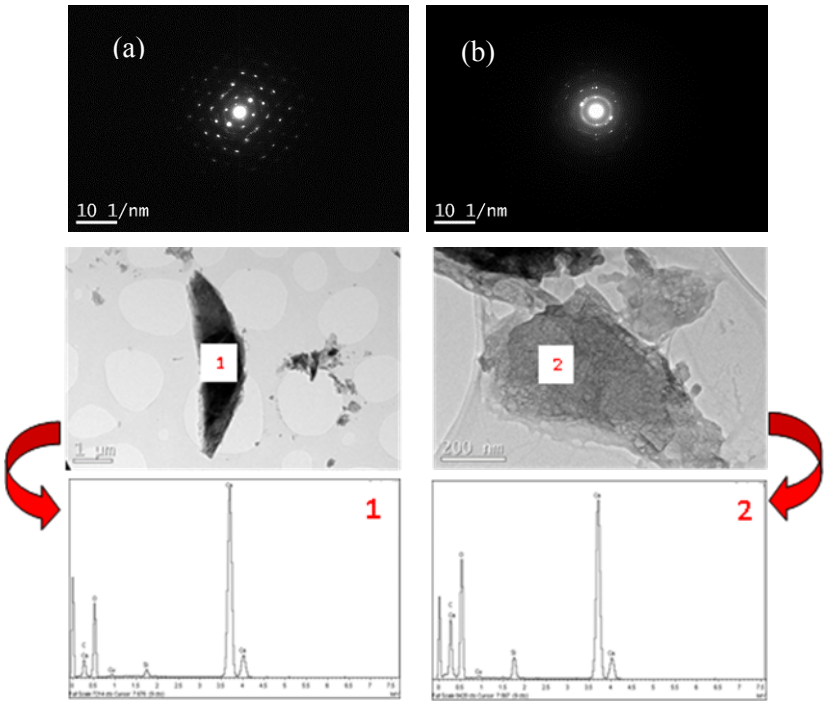

Fig. 3. TEM analysis of **(a)** PS (reference) and **(b)** PS-6%PDMS after 7d of hydration

4. Conclusions

1- The incorporation of PDMS to cement pastes causes a slightly delay in kinetic of hydration, as well as a decrease in the total heat (5% lower than sample without PDMS).
2- At 7 days of hydration and in presence of PDMS, XRD patterns showed a substantial decrease in the intensity of peaks of portlandite, which could be considered as an alteration in the normal hydration process. However, FTIR and TG/DTG analysis did not reveal an important reduction in the amount of portlandite. TEM/EDX suggest that the presence of PDMS could affect the crystallinity of portlandite, favoring its amorphization.

Acknowledgement

The authors thank TOP HERITAGE CM (S2018/NMT_4372) and the JIN project for their support in this research (PID2020-116738RJ-10) funded by the Ministry of Science and Innovation (R+D+I Projects 2020) and from CSIC Interdisciplinary Platform “Open Heritage: Research and Society” (PTI-PAIS).

References

Muhammad N.Z., Keyvanfar A., Abd M. Z. Majid, Shafaghat A., Mirza J., (2015) “Warterproof performance of concrete: a critical review on implemented approaches,” Constr. Build. Mater. 101, 80-90.
Eduok U., Faye O., Szpunar J. (2017) “Recent development and applications of protective silicone coatings: A review PDMS functional materials”, Prog. Org. Coating 111 124-163
Wang F., Lei S., Ou J., Li W., (2020) Effect of PDMS on the waterproofing performance and corrosion resistance of cement mortar, Applied Surface Science 507 145016.

The 16th International Congress on the Chemistry of Cement 2023 (ICCC2023)
"Further Reduction of CO_2 -Emissions and Circularity in the Cement and Concrete Industry"
September 18–22, 2023, Bangkok, Thailand

Challenges and opportunities of limestone calcined clays cements with less than 50% clinker

Franco Zunino[1*], Jinfeng Sun[2], and Karen Scrivener[3]

[1] *Laboratory of Construction Materials, EPFL STI IMX LMC, Station 12, CH-1015 Lausanne, Switzerland*

Current address: Physical Chemistry of Building Materials, Institute for Building Materials (IfB), ETH Zürich, CH-8093 Zürich, Switzerland

Email: franco.zunino@ifb.baug.ethz.ch

[2] *Laboratory of Construction Materials, EPFL STI IMX LMC, Station 12, CH-1015 Lausanne, Switzerland*

Email: jinfeng.sun@epfl.ch

[3] *Laboratory of Construction Materials, EPFL STI IMX LMC, Station 12, CH-1015 Lausanne, Switzerland*

Email: karen.scrivener@epfl.ch

ABSTRACT

The adoption of blended cements is the most feasible short-to-mid term strategy to achieve a more sustainable cement and concrete industry. In this regard, reducing the clinker factor, while retaining performance, is the key parameter to address. Limestone calcined clays are a promising technology as they offer similar performance to PC from 7 days onwards, while enabling a reduction of the clinker content of 50%. In many regions of the world, like in South America, pozzolanic cements (i.e., blended cements that combine clinker with natural pozzolans) have been used successfully for decades. Their clinker factors range from 80 down to 65%. However, their mechanical properties are considerably lower as compared to PC. The challenge arises then at the concrete mixture design stage, where low w/b ratios are needed to achieve medium-to-high strength concretes. For a given slump requirement, this limitation in general imply the requirement of increasing the cement content per cubic meter of concrete. In this study, we show that by using LC^3-type formulations, cements with the same performance as commercial pozzolanic cements can be produced with clinker contents significantly below 50%. These formulations were compared with commercial pozzolanic cements from the Chilean industry, and clinker savings of 40% were achieved for equivalent strength classes. This is explained by the high reactivity of calcined clays and the synergetic reaction of metakaolin and limestone that allows offsetting the clinker reduction. In a second stage, minor additions of calcium hydroxide (CH) were used to increase the threshold of MK reaction. Beyond the increased metakaolin reaction degree and carboaluminates precipitation, the addition of CH was also effective to reduce the carbonation rate of low clinker formulations. Moreover, we show that these additions can be sensible from an environmental point of view.

KEYWORDS: *sustainability, clinker factor, pozzolans, carboaluminates, strength*

1. Introduction

Reducing the carbon emissions associated with cement production is driving the industry to find solutions that are, technically and economically feasible. The most effective strategy to tackle this challenge in a global scale is to reduce the clinker factor (K. L. Scrivener et al., 2016). This has promoted the adoption of blended cements, which incorporate supplementary cementitious materials (SCMs) replacing part of

the clinker (Lothenbach et al., 2011; Schneider et al., 2011). Today, blended cements are more common than traditional Portland cements (PC).

Limestone calcined clay cements (LC^3) are a family of blended cements that incorporate limestone and calcined clays replacing part of the clinker Limestone and calcined clay are the only SCMs available in the quantities required for a reduction of the clinker factor on a global-scale (K. L. Scrivener et al., 2016). They allow reducing the clinker factor down to 50%, while retaining the same performance as PC from 7 days onwards (K. Scrivener et al., 2019; Zunino, 2020). The clinker reduction allows to save about 400 Mt of CO_2 per year, equivalent to 1% of the total manmade CO_2 emissions (Pillai et al., 2019; Zunino et al., 2021).

In regions where volcanic ash deposits are available, like in Chile and the rest of the pacific coast of South America, pozzolanic cements have been used since the 1960s. Pozzolanic cements are mixtures of clinker, natural pozzolans (volcanic ashes) and gypsum. The clinker factors of pozzolanic cements usually range from 80 to 50% (I.N.N., 1968), depending on the strength class required. Natural pozzolans are in general less reactive than calcined clays (Li et al., 2018). Consequently, the strength achieved by pozzolanic cements is in most cases lower than PC, particularly between 1 and 28 days.

This study explores the feasibility of producing LC^3-type cements with clinker contents lower that 50%, namely 35 and 25%. This conceptual approach shows that we can push the boundaries towards sustainable, low-carbon cements even further when highly reactive SCMs such as metakaolin are used. The performance of these cement formulations is compared with commercial pozzolanic cements from the Chilean market. The addition of CH is explored as a mean to boost the pozzolanic reaction.

2. Materials and methods

A commercial PC conforming to EN 197-1 as CEM I 42.5N was used in this study as a reference to benchmark the commercial pozzolanic cements against a classic European PC. The LC^3 systems were prepared using a natural kaolinitic clay with a kaolinite content of about 47%. Limestone from Omya (Betoflow D) was used. The clinker factors selected for this study were 35% and 25% (in terms of PC, 40 and 30% respectively, considering 5% gypsum), and a clay-to-limestone ratio of 1-to-1 was selected. In all cases, the sulfate content was adjusted by means of isothermal calorimetry (Zunino & Scrivener, 2019), Table 1. The w/b ratio was fixed at 0.4. Paste samples were prepared using a high-shear vertical mixer at 1600 rpm for 2 minutes. Mortar samples were prepared with each cement confirming to EN 196 standard. Samples were sealed-cured until the time of testing in an environmentally controlled chamber. An LC^3-50 with a clay to limestone ratio 2/1 was also prepared as a comparison. The effect of CH addition was explored in LC^3-35 and LC^3-25 by replacing 50% of the limestone by CH.

Table 1: Mixture design of the low clinker LC^3 systems explored in this study.

System	Label	OPC	CC	LS	Gypsum	CH	LS:CH
PC	PC	100	0	0	0	-	-
LC^3-50	LC^3-50-2:1	54.4	35.0	15.0	0.6	-	-
LC^3-35	LC^3-35-1:1	39.3	30.0	30.0	0.7	-	-
	LC^3-35-1:1-CH	39.8	30.0	15.0	0.2	15	1:1
LC^3-25	LC^3-25-1:1	29.2	35.0	35.0	0.8	-	-
	LC^3-25-1:1-CH	29.6	35.0	17.5	0.4	17.5	1:1

Strength measurements were conducted in mortar samples at 1, 2, 3, 7, 28 and 90 days of hydration, using a 300 kN load cell with a 100 N resolution and a loading rate of 2.4 kN/s. Discs of cement paste were

used at the same ages to conduct XRD measurements to determine the phase assemblage of the systems. Rietveld refinement was conducted using the HighScore Plus v4.8 software.

3. Results and discussion

Figure 1 shows the compressive strength of PC, LC^3-50 and LC^3-35 systems (a) and LC^3-25 (b) with and without the addition of CH. LC^3-50 achieves the same strength as PC at 7 days. In the case of low-clinker formulations, the strength is lower than PC at all ages. Still, it should be noted that LC^3-35 fulfils the strength requirements of high-strength grade in the Chilean standard NCh148 adapted for blends incorporating (volcanic) natural pozzolans (I.N.N., 1968), while LC^3-25 meet the general use grade (in both cases without the need of adding CH). Considering that the clinker factor of such pozzolanic cements is 80 and 65% respectively, low-clinker LC^3 would represent a solution to save an additional 40-45% clinker for the same strength class. This highlights that the reactivity of the SCMs matters, not only in term of performance, but opening new possibilities to reduce the clinker factor further for applications where PC-level strength is not required/expected.

The addition of CH has minor effect on the strength of LC^3-35 up to 7 days and LC^3-25 up to 3 days. This is linked with the availability of CH from clinker hydration. As the clinker content goes down, CH is depleted earlier from the system and quickly becomes the limiting factor to sustain the pozzolanic reactions of metakaolin. From there on, a substantial increase in strength is observed for systems incorporating CH, associated with a promoted metakaolin reactivity and consequent reduction in porosity (Zunino & Scrivener, 2021, 2022).

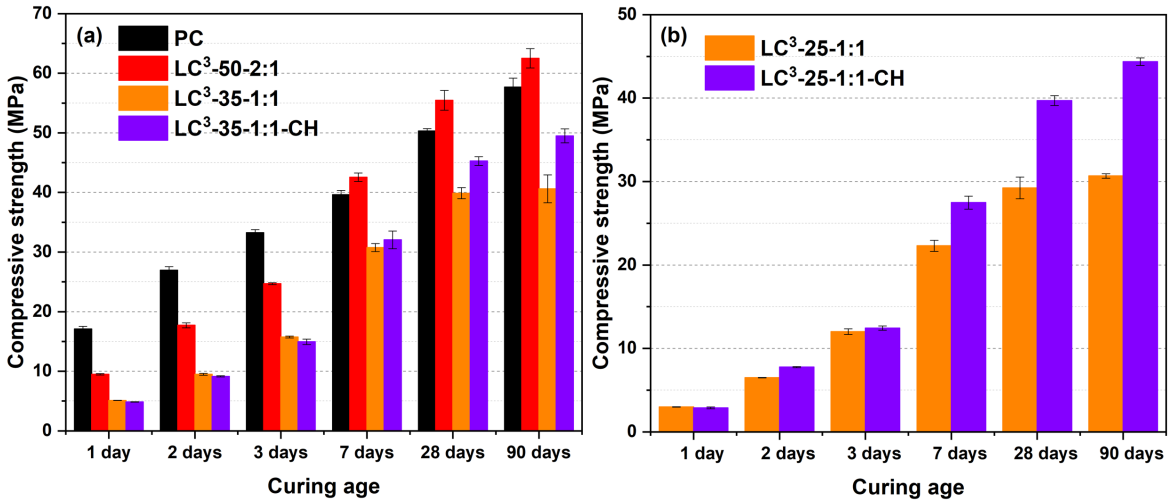

Figure 1: Compressive strength of low clinker LC^3 mortars with clinker factors 50/35 (a) and 25 (b).

Figure 2 shows the evolution of carboaluminates (Mc + Hc) in the systems studied. As shown in previous studies, carboaluminates play a key role in the development of mechanical properties of LC^3 (Zunino & Scrivener, 2021). As seen, a slightly higher amount of carboaluminates is observed in the LC^3-35 system with CH, while in the case of LC^3-25 this is more dramatic from 7 days onwards, in agreement with compressive strength results shown in Figure 1. In both cases, the low-clinker systems incorporating CH exhibit carboaluminate contents like the ones observed in LC^3-50 (benchmark system) at 28 and 90 days. This result not only confirms the close relationship between the precipitation of carboaluminates and compressive strength in LC^3 systems, but also highlights the potential of exploring minor CH additions as doping/accelerating agents in low-clinker (<50%) cement formulations. In addition to strength, further experiments showed that addition of CH also improves the carbonation resistance of these systems dramatically, in proportion to the increase in reactive CaO content (i.e., following a similar trend of carbonation coefficient vs reactive CaO as proposed in previous studies (Leemann & Moro, 2017)). While it is beyond of the scope of this article to address if this should be a concern in every scenario, it could certainly enable the application of these low-carbon cements in additional applications.

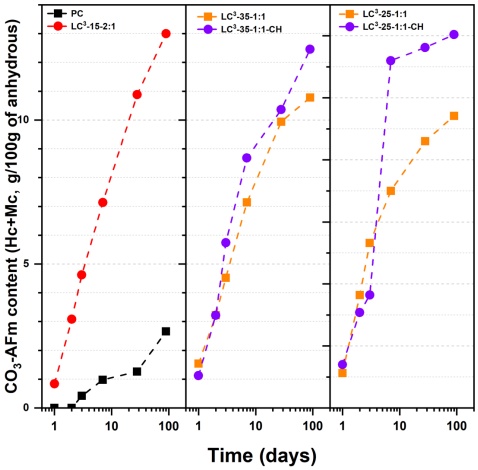

Figure 2: Evolution of carboaluminate content in low clinker LC^3 systems. Higher amounts are seen in systems incorporating CH additions.

An important aspect that cannot be neglected is the effect of CH additions on the overall CO_2 footprint of LC^3 formulations. CH does not occur in nature and in principle is produced by decarbonation of calcium carbonate. The CaO content in CH is higher (75.7%) than the average CaO amount in PC (64-68%). Assuming that no additional measures are taken, 1 gram of CH has a higher embodied CO_2 content than 1 g of PC (hereafter assumed as 0.96 and 0.82 $kgCO_2eq/kg$, respectively). As seen in Figure 3, adding CH always increase the carbon footprint respect to the corresponding baseline. Compressive strength also increases with the addition of CH, and thus results should be analysed on a performance per unit CO_2 basis. Based on this approach, none of the systems with CH presented here is as efficient as LC^3-50. However, further studies on samples with lower replacements of LS by CH showed similar mechanical behaviour, indicating that this is a parameter that can be optimized.

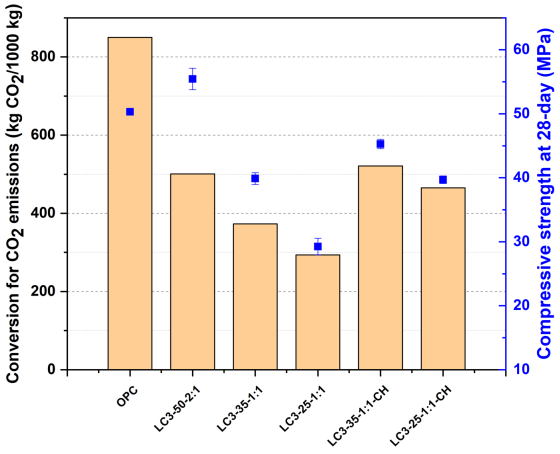

Figure 2: Carbon footprint and compressive strength of the LC^3 systems studied.

4. Conclusions

Based on the results presented on low-clinker LC^3 formulations, the following conclusions can be drawn:

- There is an enormous potential for LC^3 formulations with less than 50% clinker, particularly to take the place of other blended cements with performance below PC, but at a significantly lower clinker factor.
- CH additions are effective to promote the pozzolanic reaction in low-clinker LC^3 systems. Any strategy and technology that enables the production of CH at a lower CO_2 footprint is considered particularly interesting within the perspectives of this study.

Acknowledgements

Dr. Zunino and Prof. Scrivener acknowledge the financial support provided by the Swiss Agency of Development and Cooperation (SDC), grant 81026665. Dr. Zunino is supported by the Swiss National Science Foundation (SNSF) through an Ambizione fellowship (grant 208719).

References

I.N.N. (1968). *NCh148.Of68: Cemento – Terminología , clasificación y especificaciones generales*.

Leemann, A., & Moro, F. (2017). Carbonation of concrete: The role of CO2 concentration, relative humidity and CO2 buffer capacity. *Materials and Structures*, *50*(1), 30. https://doi.org/10.1617/s11527-016-0917-2

Li, X., Snellings, R., Antoni, M., Alderete, N. M., Ben Haha, M., Bishnoi, S., Cizer, Ö., Cyr, M., De Weerdt, K., Dhandapani, Y., Duchesne, J., Haufe, J., Hooton, D., Juenger, M., Kamali-Bernard, S., Kramar, S., Marroccoli, M., Joseph, A. M., Parashar, A., … Scrivener, K. L. (2018). Reactivity tests for supplementary cementitious materials: RILEM TC 267-TRM phase 1. *Materials and Structures*, *51*(6), 151. https://doi.org/10.1617/s11527-018-1269-x

Lothenbach, B., Scrivener, K., & Hooton, R. D. (2011). Supplementary cementitious materials. *Cement and Concrete Research*, *41*(12), 1244–1256. https://doi.org/10.1016/j.cemconres.2010.12.001

Pillai, R. G., Gettu, R., Santhanam, M., Rengaraju, S., Dhandapani, Y., Rathnarajan, S., & Basavaraj, A. S. (2019). Service life and life cycle assessment of reinforced concrete systems with limestone calcined clay cement (LC3). *Cement and Concrete Research*, *118*, 111–119. https://doi.org/10.1016/j.cemconres.2018.11.019

Schneider, M., Romer, M., Tschudin, M., & Bolio, H. (2011). Sustainable cement production—Present and future. *Cement and Concrete Research*, *41*(7), 642–650. https://doi.org/10.1016/j.cemconres.2011.03.019

Scrivener, K., Avet, F., Maraghechi, H., Zunino, F., Ston, J., Hanpongpun, W., & Favier, A. (2019). Impacting factors and properties of limestone calcined clay cements (LC ^{3}). *Green Materials*, *7*(1), 3–14. https://doi.org/10.1680/jgrma.18.00029

Scrivener, K. L., John, V., & Gartner, E. M. (2016). *Eco-efficient cements: Potential, economically viable solutions for a low-CO2, cement-based materials industry*. United Nations Environmental Programme (UNEP).

Zunino, F. (2020). *Limestone calcined clay cements (LC3): Raw material processing, sulfate balance and hydration kinetics*. EPFL Thesis 8173.

Zunino, F., Martirena, F., & Scrivener, K. (2021). Limestone calcined clay cements (LC3). *ACI Materials Journal*, *118*(3), 49–60. https://doi.org/10.14359/51730422

Zunino, F., & Scrivener, K. (2019). The influence of the filler effect on the sulfate requirement of blended cements. *Cement and Concrete Research*, *126*, 105918. https://doi.org/10.1016/j.cemconres.2019.105918

Zunino, F., & Scrivener, K. (2021). The reaction between metakaolin and limestone and its effect in porosity refinement and mechanical properties. *Cement and Concrete Research*, *140*. https://doi.org/10.1016/j.cemconres.2020.106307

Zunino, F., & Scrivener, K. (2022). Microstructural developments of limestone calcined clay cement (LC3) pastes after long-term (3 years) hydration. *Cement and Concrete Research*, *153*, 106693. https://doi.org/10.1016/j.cemconres.2021.106693

Monitoring The Impact Of Accelerators On The Reactivity Of Model Blended Cements

L. Gonzalez-Panicello[1], I. Sobrados[2], J.-B.- d´Espinose de Lacaillerie[3], P. Bowen[4], F. Puertas[5], R. J. Flatt[6], M. Palacios[7*]

[1] *Eduardo Torroja Institute for Construction Science (IETcc-CSIC), Madrid, Spain*
Email: laura.gonzalez@ietcc.csic.es
[2] *Materials Science Institute of Madrid (ICMM-CSIC), Madrid, Spain*
Email: isobrado@icmm.csic.es
[3] *Soft Matter Science and Engineering Laboratory, UMR CNRS 7615, ESPCI Paris, PSL Research University, Paris, France*
Email: jean-baptiste.despinose@espci.fr
[4] *Materials Institute, École Polytechnique Fédérale de Lausanne (EPFL), Lausanne, Switzerland*
Email: paul.bowen@epfl.ch
[5] *Eduardo Torroja Institute for Construction Science (IETcc-CSIC), Madrid, Spain*
Email: puertasf@ietcc.csic.es
[6] *Institute for Building Materials, ETH Zürich, Switzerland*
Email: flattr@ethz.ch
[7] *Eduardo Torroja Institute for Construction Science (IETcc-CSIC), Madrid, Spain*
Email: marta.palacios@ietcc.csic.es

ABSTRACT

In this work, a multi-technique approach that involves NMR, TGA and XRD was applied to gain unique insights into the reaction paths of C_3S and a model blended cement containing a slag-type synthetic glass in presence and absence of an accelerating admixture ($Na_2S_2O_3$). The preparation of isotopically enriched C_3S enabled us to track in-situ by NMR the reactivity of C_3S while the reactivity of the synthetic glass in blends was monitored by in-situ ^{27}Al MAS NMR measurements. Results concluded that the addition of 3% $Na_2S_2O_3$ enhanced the degree of reaction of the C_3S by 35 % and 23 % at 1 and 14 days of hydration, respectively, with respect to plain blends. Furthermore, $Na_2S_2O_3$ promoted the precipitation of S(II)-AFm that could lead to the undersaturation in Al of the pore solution and consequently a further dissolution of the glass. As a result, the degree of reaction of the glass increased up to 90 % and 27 %, at 1 d and 14 days, respectively, with respect to non-admixed model pastes.

KEYWORDS: *accelerator, supplementary cementitious materials, C_3S, reactivity, NMR*

1. Introduction

Over the last years, the level of clinker replacement by supplementary cementitious materials (SCMs) has reached a limit of 20 - 25 %. In addition to the availability of adequate SCMs, the decrease of the early mechanical strength due to the slow reactivity of the SCMs is one of the most relevant reasons that restrains the level of clinker substitution (Skibsted and Snellings, 2019). It is well-known that accelerating admixtures enhance the mechanical properties and hydration kinetics of blended cements (Cheung et al., 2011), (Boscaro et al., 2021), although more effective activators of the SCMs reactivity are needed to push down the clinker content in blends. The main limitation is that the applied experimental approaches do not distinguish between the reactivity of the clinker phases, the SCMs and the complex coupling of their reactive paths. Previous studies have shown that isotopic labelling of cementitious phases can provide unique information about their reactivity (Pustovgar et al., 2016), (Brough et al., 1995, 1994). In this study, the hydration of C_3S in blends was studied by ^{29}Si MAS NMR by selectively labelling this phase in ^{29}Si

while the early reactivity of the synthetic glass was be monitored by ^{27}Al MAS NMR (Nie et al., 2020). Further characterization of the hydrates was done by XRD.

2. Materials and Methods

2.1. Synthesis the C_3S and aluminosilicates

Two batches of C_3S, non-enriched and ^{29}Si-enriched C_3S, were synthesized according to the protocol described in the literature using a thermal treatment of 1600 ºC (Gonzalez-Panicello et al., 2023; Pustovgar et al., 2016). Thermal treatment was repeated until no reflections of free lime were observed in the XRD pattern. Two batches of aluminosilicate glass (G-SL), with the chemical composition shown in Table 1**,** were prepared using the methodology described in (Gonzalez-Panicello et al., 2022). In the preparation of these synthetic phases, $CaCO_3$ (Calcium carbonate, reagent grade, Scharlau) and Al_2O_3 (Aluminium oxide anhydrous, Merck KGaA). SiO_2, white quartz (sand, 99.995%, Aldrich), previously ground, and $^{29}SiO_2$ (99.9% enriched in ^{29}Si, Cortecnet) were used to synthesize non-enriched and ^{29}Si-enriched C_3S, respectively. The synthetic phases were carefully ground in a planetary ball mill reaching a specific surface area (SSA_{BET}) of around 1.1 m^2/g.

Table 1. Chemical composition (% mol) of the synthetic aluminosilicate glass.

Model glass	CaO	SiO_2	Al_2O_3
G-SL	47.29	41.62	11.09

2.2. Addition Impact of $Na_2S_2O_3$ on the reaction kinetics on model pastes.

Blends containing 50%wt C_3S and 50%wt G-SL were homogenized in a mixer (Turbula System Schatz, Switzerland) for 2 h. Pastes with a liquid/solid= 0.5 were firstly mixed for 30 s at 200 rpm and afterwards at 840 rpm for 3 min. 3%wt $Na_2S_2O_3$ (Acros Organics) by mass of solid was added into the mixing ultrapure water. Hydration kinetics were measured by isothermal calorimetry (TAM AIR) at 25 ºC.

2.3. Nuclear Magnetic Resonance experiments. Impact of $Na_2S_2O_3$

0.5 g of model blend (0.25 g of C_3S and 0.25 g of G-SL) was mixed with ultrapure water (liquid/solid=0.5) in a 7 ml LDPE vial for 3 min 30 s using a vortex mixer (Vortex 3, IKA) at 2500 rpm. The sample was introduced in a 4 mm ZrO_2 rotor. After 5 h and 7 h of hydration, the pastes without and with 3%wt $Na_2S_2O_3$, respectively, were exchanged to avoid its hardening inside the rotor.

^{29}Si and ^{27}Al MAS NMR measurements were done using a BRUKER AVANCE 400 spectrometer. Temperature was set at 25 ºC by a Bruker BVT 3000. ^{29}Si MAS NMR spectra of non-enriched and ^{29}Si enriched C_3S were acquired applying a pulse length of 4 μs, a recycle delay of 300 s and 8 scans. Resonance frequencies of 79.49 MHz were applied in the ^{29}Si MAS NMR spectra and the chemical shift values were referenced to tetramethylsilane (TMS). Resonance frequencies of 104.26 MHz were applied in ^{27}Al MAS NMR spectra and 1 M $AlCl_3$ aqueous solution was used as a reference for the chemical shift values. ^{27}Al MAS NMR spectra were obtained using a pulse length of 2 μs, a recycle delay of 5 s and 400 scans.

3. Results and discussion

3.1. Impact of the $Na_2S_2O_3$ dosage on the reaction kinetics of model pastes

Figure 1 illustrates the influence of the 3%wt $Na_2S_2O_3$ on the hydration of the blends. The addition of $Na_2S_2O_3$ accelerated by 5 h the time of appearance of the main peak; increasing its intensity and the cumulative heat of hydration during the first 15 h of reaction with respect to the non-admixed blend.

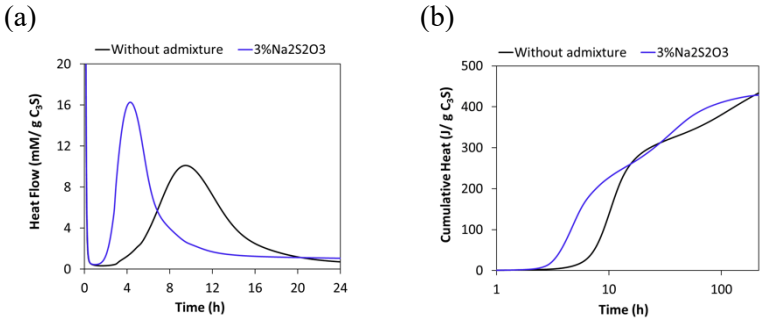

Figure 1. (a) Heat flow and (b) cumulative heat of 50C_3S-50glass blends without admixture (in black) and with 3%wt $Na_2S_2O_3$ (in blue).

3.2. Monitoring of the C_3S and glass reactivity in model blended cements.

Figure 2a shows an example of the ^{29}Si MAS NMR spectra of blends with C_3S enriched in ^{29}Si. The intensities of the ^{29}Si resonances of Q^1, Q^{2B} and Q^2 species from C-S-H, at -79.0, -81.4 and -85.0 ppm, respectively, increased with the evolution of the hydration time, while the isolated silicate (Q^0) species, between -68 ppm and -75 ppm, associated with non-hydrated C_3S, decreased. The incorporation of 3%wt $Na_2S_2O_3$ enhanced the polymerization of C-S-H (Table 2), as it can be inferred by the higher amount of Q^1 and Q^{2T} species with respect to non-admixed blends at the same hydration times. As shown in Table 2, $Na_2S_2O_3$ increased around 35 % and 23 % the degree of hydration of C_3S at 1 and 14 days, respectively.

Figure 2b shows the typical ^{27}Al MAS NMR spectra of the blends. The resonance at 71 ppm is assigned to the 4-fold Al of the non-reacted glass. The signals at around 73 - 61 ppm, 40 ppm and 5 ppm are associated to the 4, 5, and 6-fold Al of C-A-S-H, respectively (Kunhi Mohamed et al., 2020), (Andersen et al., 2006). In addition, a resonance is observed at around 10 ppm that it is assigned to the 6-fold Al of an AFm phase. The addition of $Na_2S_2O_3$ decreased the intensity of the resonances of Al assigned to C-A-S-H while it accelerated the time of appearance of the signal assigned to the AFm phase. It also played a key role on the amount and type of AFm precipitated. While small amounts of strätlingite and monocarboaluminate were formed in plain-blends, the admixture promoted the formation of S(II)-AFm as shown in the XRD patterns (Figure 2c) (Nedyalkova et al., 2019). The higher amount of the AFm phase formed in presence of admixtures, could lead to a higher Al undersaturation of the solution and the consequent increase of the glass reactivity as shown in Table 2, which enhances it to 90 % and 27 % at 1 and 14 days, respectively (see Table 3).

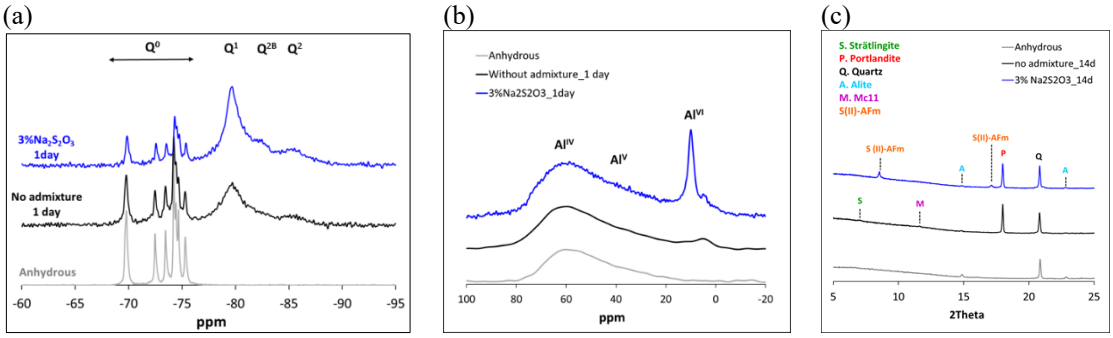

Figure 2. (a) One pulse ^{29}Si MAS NMR spectra, (b) ^{27}Al MAS NMR spectra and (c) XRD patterns for anhydrous and hydrated blends with and without 3%wt $Na_2S_2O_3$.

Table 2. Evolution of the silicon species and degree of hydration of C_3S for the model blends without admixture and with 3%wt $Na_2S_2O_3$ up to 14 days of hydration ($Q^{2T} = Q^2 + Q^{2B}$).

	No admixture				3%$Na_2S_2O_3$			
Time (h)	Q^0	Q^1	Q^{2T}	DoH C_3S (%)	Q^0	Q^1	Q^{2T}	DoH C_3S (%)
0	100	0.0	0.0	0.0	100	0.0	0.0	0.0
24	40.7	46.1	13.2	59.3	19.8	53.3	27.0	80.4
168	37.3	42.2	21.6	62.7	18.0	53.4	28.7	82.0
336	32.9	38.8	28.3	67.1	17.2	50.5	32.3	82.8

Table 3. Evolution of Al units of the synthetic glass in model blends without admixture and 3%wt $Na_2S_2O_3$

Time(h)/ Accelerator	*Al(IV) 71ppm*		*Al(IV) 73.8-61ppm*		*Al(VI) 10ppm*		*Al(VI) 5ppm*		*Al(V) 40ppm*		*Glass DoR (%)*	
	0%	**3%**	**0%**	**3%**	**0%**	**3%**	**0%**	**3%**	**0%**	**3%**	**0%**	**3%**
0	99.7	99.7	0.0	0.0	0.0	0.0	0.0	0.0	0.0	0.0	0.0	0.0
24	90.2	81.4	3.2	2.3	5.6	15.4	0.7	0.4	0.2	0.5	9.8	18.6
168	76.8	69.8	4.3	3.9	14.5	24.2	3.1	0.8	1.3	1.1	23.2	29.0
336	73.8	66.8	5.4	4.2	15.4	26.7	3.9	1.1	1.5	1.2	26.2	33.3

4. Conclusions

This study has proven the viability of the proposed methodology to monitor in situ, without stopping the hydration, the reactivity of the different components of synthetic blended cements. This has enabled us for the first time, to resolve on which phases, when the accelerator works and the main hydrates that each phase formed. Results conclude that C_3S is the main phase reacting in the blend over the first 24 h and the addition of $Na_2S_2O_3$ increases around 35 % its degree of hydration. In contrast, at 24 h, only 10 % of the glass has reacted but in the presence of $Na_2S_2O_3$ an enhancement of 90 % of the degree of reaction is observed. The positive effect of the accelerator on the glass reaction could be related to the formation of a high amount of S(II)-AFm that would increase the Al undersaturation of the pore solution and favor the glass dissolution. Furthermore, the lower concentration of aluminates in solution would decrease the passivation that they induce on silicate surfaces (Pustovgar et al., 2017) and consequently increase the C_3S dissolution in admixed samples.

5. Acknowledgements

NANOCEM is thanked for funding the internal project “SCMs reactivity: New methods and insights”.

6. References

Andersen, M.D., Jakobsen, H.J., Skibsted, J., 2006. A new aluminium-hydrate species in hydrated Portland cements characterized by 27Al and 29Si MAS NMR spectroscopy. Cem. Concr. Res. 36, 3–17.

Boscaro, F., Palacios, M., Flatt, R.J., 2021. Formulation of low clinker blended cements and concrete with enhanced fresh and hardened properties. Cem. Concr. Res. 150, 106605.

Brough, A.R., Dobson, C.M., Richardson, I.G., Groves, G.W., 1995. A study of the pozzolanic reaction by solid-state 29Si nuclear magnetic resonance using selective isotopic enrichment. J. Mater. Sci. 30, 1671–1678.

Brough, A.R., Dobson, C.M., Richardson, I.G., Groves, G.W., 1994. In situ solid-state NMR studies of Ca3SiO5: hydration at room temperature and at elevated temperatures using 29Si enrichment. J. Mater. Sci. 29, 3926–3940.

Cheung, J., Jeknavorian, A., Roberts, L., Silva, D., 2011. Impact of admixtures on the hydration kinetics of Portland cement. Cem. Concr. Res., Conferences Special: Cement Hydration Kinetics and Modeling, Quebec City, 2009 & CONMOD10, Lausanne, 2010 41, 1289–1309.

Gonzalez-Panicello, L., De la Torre, A.G., Palacios, M., 2023. Reactivity of C3S and model cement in presence of Na2S2O3 and NaSCN. Mater. Struct. 56, 23.

Gonzalez-Panicello, L., Garcia-Lodeiro, I., Puertas, F., Palacios, M., 2022. Influence of Accelerating Admixtures on the Reactivity of Synthetic Aluminosilicate Glasses. Materials 15, 818.

Kunhi Mohamed, A., Moutzouri, P., Berruyer, P., Walder, B.J., Siramanont, J., Harris, M., Negroni, M., Galmarini, S.C., Parker, S.C., Scrivener, K.L., Emsley, L., Bowen, P., 2020. The Atomic-Level Structure of Cementitious Calcium Aluminate Silicate Hydrate. J. Am. Chem. Soc. 142, 11060–11071.

Nedyalkova, L., Lothenbach, B., Renaudin, G., Mäder, U., Tits, J., 2019. Effect of redox conditions on the structure and solubility of sulfur- and selenium-AFm phases. Cem. Concr. Res. 123, 105803.

Nie, S., Thomsen, R.M., Skibsted, J., 2020. Impact of Mg substitution on the structure and pozzolanic reactivity of calcium aluminosilicate (CaO-Al2O3-SiO2) glasses. Cem. Concr. Res. 138, 106231.

Pustovgar, E., Mishra, R.K., Palacios, M., d’Espinose de Lacaillerie, J.-B., Matschei, T., Andreev, A.S., Heinz, H., Verel, R., Flatt, R.J., 2017. Influence of aluminates on the hydration kinetics of tricalcium silicate. Cem. Concr. Res. 100, 245–262.

Pustovgar, E., Sangodkar, R.P., Andreev, A.S., Palacios, M., Chmelka, B.F., Flatt, R.J., d’Espinose de Lacaillerie, J.-B., 2016. Understanding silicate hydration from quantitative analyses of hydrating tricalcium silicates. Nat. Commun. 7, 10952.

Skibsted, J., Snellings, R., 2019. Reactivity of supplementary cementitious materials (SCMs) in cement blends. Cem. Concr. Res. 124, 105799.

The 16th International Congress on the Chemistry of Cement 2023 (ICCC2023)
"Further Reduction of CO_2 -Emissions and Circularity in the Cement and Concrete Industry"
September 18–22, 2023, Bangkok, Thailand

Using Calcined Clay and Calcium Chloride to Enable Aluminium Reinforced Concrete

H. Justnes[1*], T. Danner[2], K.F. Kleinau[3], I. Westermann[4] and T. Furu[5, 6]

[1] *SINTEF Community, Trondheim, Norway*
Email: harald.justnes@sintef.no
[2] *SINTEF Community, Trondheim, Norway*
Email: tobias.danner@sintef.no
[3] *Department of Materials Science and Engineering, NTNU, Trondheim, Norway*
Email: Karlfk@stud.ntnu.no
[4] *Department of Materials Science and Engineering, NTNU, Trondheim, Norway*
Email: ida.westermann@ntnu.no
[5] *Department of Materials Science and Engineering, NTNU, Trondheim, Norway*
Email: trond.furu@ntnu.no
[6] *Norsk Hydro, Sunndalsøra, Norway*
Email: trond.furu@hydro.com

ABSTRACT

Concrete can be reinforced with alloys of aluminium metal providing the Portland cement in the binder is replaced with > 50% calcined clay. Even though the long-term stability of the aluminium metal embedded in such a binder is not disputed since pH is reduced to < 10 over time, there is an early time window just after setting where the portland cement is producing calcium hydroxide faster than the pozzolan can react away. In this period of less than 24 h there can be some hydrogen gas evolution from the hydroxides reacting with the aluminium. The amount of etching is only corresponding to a few microns on the aluminium bar and will not affect its mechanical strength, but the gas voids along the bar may reduce the adhesion between the bar and the binder. Adding 4% calcium chloride to a binder consisting of 45% Portland cement and 55% calcined kaolinitic clay (45% kaolin) with a water-to-powder ratio of 0.5 has been shown to drastically reduce the hydrogen gas evolution from embedded aluminium. This is also visually verified on split samples after gas monitoring for 24 h. The two common aluminium alloys used have good chloride resistance, but the chlorides end up as Friedel's salt taking most of the chlorides out of solution and lead to additional bound water. Adding calcium chloride has positive impact on the compressive strength of concrete with corresponding binder yielding a 1-day strength > 10 MPa and a 3-day strength of 36 MPa. The 28-day strength was 53.5 MPa fulfilling the criterion for a C35 concrete. Such a concrete will resist the common degradation mechanisms for regular reinforced concrete resulting in an extremely long service life without maintenance. Furthermore, a C35 concrete will in terms of strength cover about 80% of the concrete market.

KEYWORDS: *Aluminium reinforcement, Calcined clay, calcium chloride, concrete, hydrogen gas.*

1. Introduction

Cement-based concrete is the third largest CO_2 emitter of the world due its versatility and dominating use in construction. The shortest route to reduce its carbon footprint is to replace some of the Portland cement clinker with supplementary cementitious materials (SCMs) like calcined clay. Another important way to reduce CO_2 emissions from concrete structures is to make them last longer without maintenance. The most common deterioration of reinforced concrete is the corrosion of steel either caused by chloride

ingress or carbonation. As an answer to both these challenges, the concept of DARE2C (Durable Aluminium Reinforced Environmentally-friendly Concrete Construction) was described (Justnes, 2017). Since aluminium cannot withstand the high pH of regular concrete, the concept was based on replacing a high amount (> 50%) of the cement in concrete with a rapid reacting and "cheap" pozzolana like calcined natural clay. Since common aluminium alloys can withstand chlorides, it was postulated (Justnes, 2017) that the accelerator calcium chloride could be used, as well as seawater as mixing water. This was later documented (Justnes et al., 2022) to be true. Even though the long-term stability of the aluminium metal embedded in such a binder is not disputed since pH is reduced to < 10 over time (Justnes et al., 2022), there is an early time window just after setting where the portland cement is producing calcium hydroxide faster than the pozzolan can react away. In this period of less than 24 h there can be some hydrogen gas evolution from the hydroxides reacting with the aluminium. The amount of etching is only corresponding to a few microns on the aluminium bar and will not affect its mechanical strength, but the gas voids along the bar may reduce the adhesion between the bar and the binder. As shown in this paper, the addition of calcium chloride not only increase the early strength of concrete, but also contribute to reduce the initial aluminium etching shown by hydrogen gas measurements.

2. Experimental

The cement was a CEM I 42,5 N – SR3 according to EN 197-1 (Norcem, Norway). The chemical compositions of the cement and the clay (Leca International) before calcination in a rotary kiln of 10 min retention time at 850°C are listed in Table 1. The cement had a Blaine of 355 m^2/kg with 4.1% limestone interground giving a loss on ignition to 950°C of 2.0%. The calcined clay contained roughly 50% metakaolin and the major other materials was feldspar. The $CaCl_2$ used was anhydrous laboratory grade.

Table 1 - The chemical composition of cement and kaolinitic clay before calcination

Oxide	Cement	Raw clay
CaO	60.66	0.1
SiO_2	20.45	60.6
Al_2O_3	3.36	30.0
Fe_2O_3	4.28	3.4
MgO	1.90	0.4
K_2O	0.45	3.2
Na_2O	0.28	-
SO_3	2.67	-

Paste was made with cement / calcined clay 45/55 and water-to-powder ratio 0.50. 4% (weight% of solids) laboratory grade calcium chloride ($CaCl_2$) was dissolved in water prior to mixing. Two different commercial aluminium alloys; 6082 and 4xxxA, in the form of Ø10 mm bars were submersed in the pastes in a cup that was immediately placed in a 6-litre chamber from where gas was sampled as function of time and analysed for hydrogen gas by an Agilent 990 Micro Gas Chromatograph using column MS5A SS 10MX0.25MMX. Pastes with aluminium bar inserts were also cured in cups within closed plastic bags with additional water for 28 days. Thereafter they were chiselled open to inspect the bars for potential formation of gibbsite as white corrosion product. The compositions of the alloys are given in Table 2.

Table 2 – Chemical composition of the aluminium alloys 6082 and 4xxxA

Alloy	Al	Si	Mg	Mn	Fe	Cr	Ti	Ga	V	Zn	Ni
6082	97.232	1.0818	0.6451	0.5557	0.2576	0.1588	0.0299	0.0124	0.0103	0.0096	0.0054
4xxxA	87.478	9.1818	0.2795	0.1128	0.4094	0.1171	0.0205	0.0100	0.0086	0.2169	0.0037
Alloy	Cu	B	Zr	Sn	Ca	Co	Sb	P	Sr	Pb	Cd
6082	0.0029	0.0023	0.0016	-	-	-	-	-	-	-	-
4xxxA	2.1494	0.0023	0.0016	0.0031	0.0009	0.0005	0.0012	0.0009	0.0001	0.0012	0.0006

Concrete was made according to the following recipe per m^3: 186.9 kg cement, 228.4 kg calcined clay, 178.5 kg water, 974.8 kg granite sand, 676.7 kg crushed granite gravel, 8.3 kg Sika Viscocrete 6225, 2.1 kg SIKA Airpro V5 1:9 and 16.6 kg $CaCl_2$. The recipe corresponds to a water-to-powder ratio of 0.43. Several 100 mm cubes and Ø100·200 mm cylinders were cast for mechanical characterizations.

3. Results and discussion

The hydrogen gas evolution curves for bars of the 6082-alloy embedded in paste with 4% calcium chloride and without are plotted in Fig. 1. Next to the graph is a picture of paste with 4% $CaCl_2$ chiselled open after 28 days moist curing without any signs of white corrosion products. Fig. 2 shows similar results for the 4xxx (Cu)-alloy.

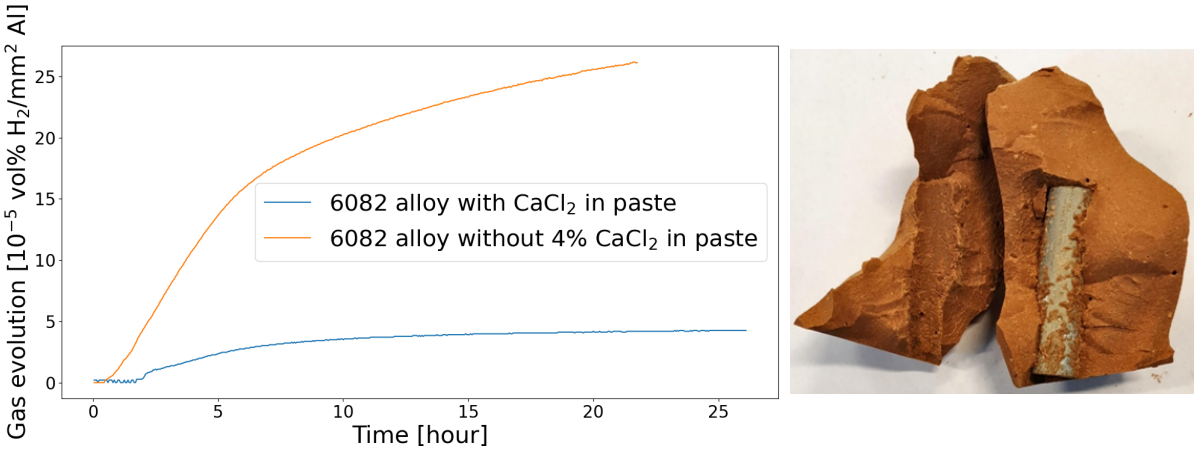

Fig. 1 - Hydrogen evolution (vol% H_2/mm^2 Al) versus time (h) for alloy 6082 embedded in paste where 4% $CaCl_2$ is dissolved in the mixing water (blue curve) and with pure water (orange curve). The picture to the right of the graphs shows 6082 embedded in paste with 4% $CaCl_2$ after 28 days moist curing.

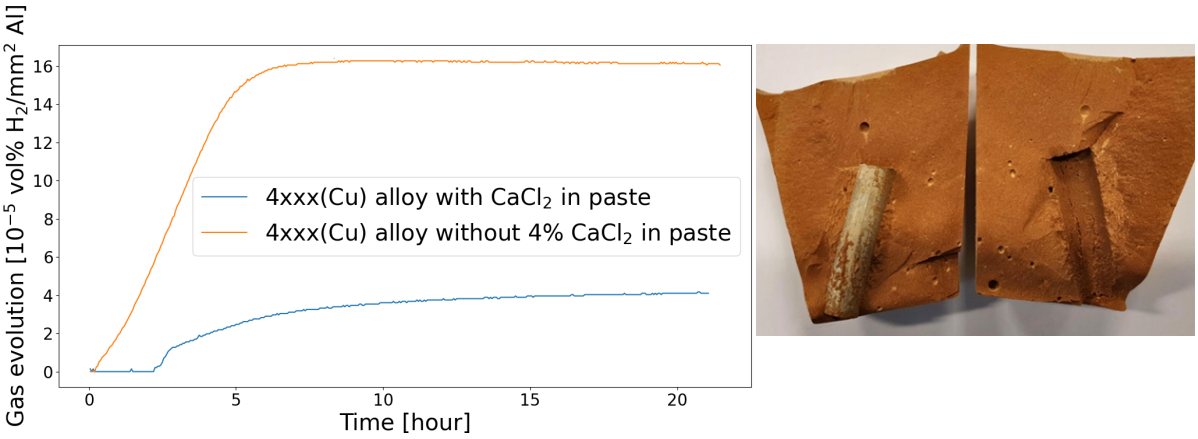

Fig. 2 - Hydrogen evolution (vol% H_2/mm^2 Al) versus time (h) for alloy 4xxx (Cu) embedded in paste where 4% $CaCl_2$ is dissolved in mixing water (blue curve) and with pure water (orange curve). The picture to the right of the graphs shows 4xxx embedded in paste with 4% $CaCl_2$ after 28 days moist curing.

The calcium chloride addition reduces the gas evolution by a factor of 6.2 from 26 to $4.2 \cdot 10^{-5}$ vol% H_2/mm^2 Al the first 24 h for alloy 6082 (Fig. 1), while the reduction factor is 3.9, for alloy 4xxx (Fig. 2) mostly because the hydrogen gas evolution without calcium chloride is lower for 4xxx ($16 \cdot 10^{-5}$ vol% H_2/mm^2 Al) than for 6082 ($26 \cdot 10^{-5}$ vol% H_2/mm^2 Al). The curve with calcium chloride flattens out rapidly for both alloys (at about 10 h), meaning that the gas evolution has stopped.

The reason why the hydrogen gas evolution without calcium chloride starts immediately compared to delayed when calcium chloride is included, is that the cement contains some alkali hydroxides that gives an immediate pH increase. When calcium salts are included, the pH is reduced by precipitation of calcium hydroxide and further depressed by excessive calcium by the common ion effect.

The X-ray diffractograms of the paste without and with calcium chloride are shown in Fig. 3 after 28 days curing. Since the calcined clay consumes all calcium hydroxide, strätlingite ($Ca_2Al_2SiO_7 \cdot 8H_2O$) is

stabilized without calcium chloride. With calcium chloride strätlingite is destabilized and Friedel's salt ($Ca_3Al_2O_6{\cdot}CaCl_2{\cdot}11H_2O$) formed instead, leading to increased water binding and thereby densification and contribution to increased strength.

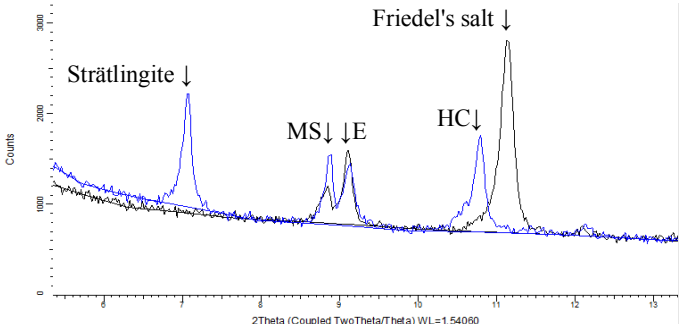

Fig. 3 – X-ray diffraction profiles of paste without (blue) and with calcium chloride (black). MS = calcium monosulphoaluminate hydrate, E = ettringite and HC = calcium hemicarboaluminate hydrate.

The properties of the cast concrete are listed in Tables 3-5. A third reason of including 4% calcium chloride ($CaCl_2$) in the concrete recipe was to ensure sufficient strength for removal of formwork in practice at 1 day, and this was achieved by a 10 cm cube strength > 10 MPa.

Table 3 – Fresh properties of the concrete.

Slump (mm)	Spread (mm)	Air (vol%)	Density (kg/m^3)	Temperature (°C)
245	500	4.8	2268	22.6

Table 4 – Compressive strength evolution for the concrete for 100 mm cubes.

1 day	3 days	7 days	28 days
10.6±0.1 MPa	35.7±1.0 MPa	43.8±0.9 MPa	53.5±0.4

Table 5 – Density and mechanical properties for 3 parallel Ø100·200 mm cylinders after 28 days.

Density, ρ (kg/m^3)	E-modulus		Compressive Strength, σ_c (MPa)	Splitting tensile Strength, σ_{spl} (MPa)
	E_0 (GPa)	E_C (GPa)		
2323±6	23.5±0.2	25.6±0.2	47.6±0.7	3.90±0.04

The compressive strength at 28 days should at least be sufficient for a C35 concrete.

3. Conclusions

A concrete recipe replacing 55% cement with calcined clay suitable for aluminium reinforcement has been presented that achieves compressive strength for a C35 concrete with sufficient early strength for 1 day formwork removal. The inclusion of 4% calcium chloride in the recipe is beneficial for 3 reasons: 1) reduces early hydrogen gas evolution by a factor of 4-6 depending on alloy. 2) Converting otherwise formed strätlingite to Friedel's salt leading to extra bound water. 3) Acceleration of cement hydration.

Acknowledgements

Grant no. 327863 from the Research Council of Norway supporting DARE2C2 is greatly appreciated.

References

Justnes, H.: "Durable Aluminum Reinforced Environmentally-friendly Concrete Construction – DARE2C", *Nordic Concrete Research*, Publication no. 56, 1/2017, pp. 71-81 (ISBN 978-82-8208-055-2).

Justnes H., Danner, T. and Sletnes, M.: Aluminium reinforced concrete enabled by calcined clay", *Proceedings of the 6th fib International Congress*, Eds. S. Stokkeland and H.C. Braarud, June 12-16, 2022, Oslo, Norway, pp. 705-714. ISBN Proceedings (Online) 978-2-940643-15-8.

The 16th International Congress on the Chemistry of Cement 2023 (ICCC2023)
"Further Reduction of CO_2 -Emissions and Circularity in the Cement and Concrete Industry"
September 18–22, 2023, Bangkok, Thailand

Critical Investigations on Two-Stage Mixing to Increase Early Strength of Cements with Slag and Limestone

J. Herrmann[1*] and J. Rickert[2]

[1] *VDZ Technology gGmbH, Duesseldorf, Germany*
Email: jens.herrmann@vdz-online.de
[*] corresponding author
[2] *VDZ Technology gGmbH, Duesseldorf, Germany*
Email: joerg.rickert@vdz-online.de

ABSTRACT
Clinker- and resource-efficient composite cements with their great variety of concrete technology advantages suffer mostly from early compressive strength. Literature postulates that the early reaction of cement can be increased by more intensive two-stage mixing.
To which extent various two-stage mixing processes can increase the early hydration reactions and thus accelerate the compressive strength development of ternary cements with granulated blast furnace slag and limestone was systematically investigated up to 56 days. Additionally, influences of a reduced w/c ratio were determined.
Results show that reducing the w/c ratio increases both early and late compressive strength much more significantly than energy-intensive and more complex two-stage mixing processes.

KEYWORDS: *Composite cement, two-stage mixing, compressive strength, w/c ratio*

1. Introduction

To achieve climate neutrality and to conserve natural resources, there is no alternative to the use of cements with several main constituents (so-called composite cements or blended cements) with their significantly reduced clinker content. However, with reducing the clinker content the early strength of concrete decreases, which is often considered as a disadvantage in construction practice.
It was therefore investigated whether the early strength can be increased by an amplified conversion of cement constituents into reaction products via application of intensive two-stage mixing, as described for example in Baumert and Garrecht (2010). According to this, in the first mixing stage, a suspension of water and cement and sometimes admixtures is produced at very high rotational speeds of the mixing tools of up to e.g. 10,000 rotations per minute (rpm). With such highly intensive mixed suspension, the aggregate is mixed at usual tool speeds in the second mixing stage.
If a so-called suspension mixer is used to produce the suspension, the particles are subjected to greater mechanical stress due to large centrifugal and shear forces as a result of the much higher tool speeds than in so-called intensive mixers, or especially in ordinary forced mixers. According to Reschke (1998), this deagglomerates the particles and distributes them more homogeneously in the suspension. As a result, cement suspensions are more reactive, since the particles, which are more isolated, thereby have a larger surface area and are wetted with water on all sides (Houlsby 1990). As per Juilland (2012), ions detaching from the cement particles' surfaces are shifted to a greater extent into the bulk aqueous solution due to the stronger mechanical stress. The interface therefore remains undersaturated for a longer time and more ions go into the solution. The stronger mechanical cement particle contacts could promote the conversion into reaction products, since crystal nuclei and/or first hydrates are dissolved from the surface and are distributed more regularly in the suspension, and the interfaces are then once more available for water influx or further

reaction (Kravetz 1959). In composite cements, softer limestone particles could be refined by harder constituents, such as granulated blast furnace slag. The same may apply to all cement constituents as a result of the higher tool speeds, and the refined cement would then be more reactive.

2. Materials and methods

To classify the influences of two-stage mixing processes, the compressive strength development of conventionally, i.e. single-stage mixed standard mortars acc. EN 196-1 was first determined. For this purpose, fresh mortar with 1350 g CEN standard sand, 450 g cement (c) and 225 g deionised water (w), i.e. w/c ratio = 0.50 ("050"), was produced in a commercial mortar mixer ("MM"). A commercial Portland cement CEM I 52,5 R ("PZ") served as reference. A CEM II/B-M (S-LL) 52,5 N ("PZ-20S-10LL") was used as clinker-efficient composite cement. The PZ-20S-10LL was produced in the laboratory from ≈ 70 mass % PZ, ≈ 20 mass % blast furnace slag ("S"), ≈ 10 mass % limestone ("LL") and some anhydrite dotation to optimise setting and hardening. Properties of the cements are given in Table 1.

Table 1. Cement properties.

	Blaine[1)]	x' [2)]	n[3)]	IST[4)]	compressive strength[5)], MPa	
	cm²/g	µm	-	min	2 days	28 days
PZ	4530	13.0	0.93	110	47.5 ± 0.7	69.4 ± 0.7
PZ-20S-10LL	4540	13.6	0.89	115	32.8 ± 0.4	63.7 ± 0.6

[1] Blaine fineness acc. EN 196-6; [2] position parameter and [3] slope of RRSB particle size distribution; [4] initial setting time acc. EN 196-3; [5] compressive strength acc. EN 196-1

The cements' clinker consisted of ≈ 75 mass % alite, ≈ 8 mass % belite, ≈ 10 mass % aluminate and ≈ 5 mass % ferrite. The glass content of S was ≈ 98 % and its fineness 3580 cm²/g acc. EN 196-6. The calcite content of LL was ≈ 89 mass %. The remains consisted mainly of quartz with some feldspars and mica. The LL fineness was 4390 cm²/g acc. EN 196-6.

For comparison, the compressive strength development of single-stage mixed mortar with a w/c ratio of 0.35 ("035"), 500 g cement and 1350 g CEN standard sand was determined. A commercially available PCE-based superplasticiser was added to the suspension so that its consistency was fluid and the mortars had a comparable spread of (150 ± 20) mm according to EN 1015-3. The water contained in the superplasticizer was deducted from the water added.

In the first stage of the two-stage mixing processes an intensive mixer ("IM") EL5 from Gustav Eirich with a star agitator as mixing tool or a suspension mixer ("SM") Ultra-Turrax T50 from IKA were used. As mixing tools for the suspension mixer, either a high-intensive dispersing head ("DK") G 45 M or a cutting head ("SK") W 65 were used. The rotational speeds of the mixing tools of the suspension mixer were up to approx. 9000 rpm ("9000") and those of the intensive mixer approx. 1644 rpm ("1644"). Standard mixing times were 30, 60 or 120 s ("30", "60" or "120"). In supplementary tests it was investigated whether the compressive strength of the mortar could be increased by mixing the suspension for a significantly longer time in the first mixing stage of up to 360 s ("360"). In order to be able to mix 360 s and to limit the temperature of the suspension to a maximum of 45 °C, the water to be added ("W") was cooled to around 5 °C ("5°C"). Otherwise, the materials and equipment were kept at a temperature of 20 °C. After the first mixing stage, 675 g of suspension were transferred to the mortar mixer and mixed in the second mixing stage with 1350 g of standard sand for 30 s at approx. 140 rpm (planetary motion: approx. 62 rpm) and afterwards for 60 s at approx. 285 rpm (planetary motion: approx. 125 rpm). The two-stage mixing regimes for the w/c ratios of 0.5 and 0.35 are given in Table 2.

Table 2. Two-stage mixing regimes.

w/c ratio = 0.5		w/c ratio = 0.35	
action	duration	action	duration
Pre-mixing of c and w in MM	60	Pre-mixing of c and w in MM	30
mixing in IM or SM with DK or SK	see text	adding PCE and mixing	30
mixing with sand in MM	90	mixing in IM or SM with DK or SK	see text
		mixing with sand in MM	90

It was also investigated whether the particles of the PZ-20S-10LL were refined by the more intensive mixing. To exclude influences of hydration reactions, the cement was mixed with a non-aqueous medium (isopropanol) instead of water at equal volume. After mixing, the suspension was diluted with approximately

three times the amount of isopropanol. Via vacuum filtration with a Büchner funnel and a Blauband filter the cement was separated. After drying and sieving over a 125 µm sieve to deagglomerate the particles, the particle size distribution after and before mixing was determined with a laser diffractometer 1190 from Cilas (dispersed in ethanol, 60 s ultra-sonic, triple determination) and evaluated according to the Fraunhofer theory.

3. Results

The compressive strength developments of the single-stage mixed mortars (MM) with Portland cement (PZ) or composite cement (PZ-20S-10LL) at a w/c ratio of 0.50 (050) or 0.35 (035) are shown in Figure 1.

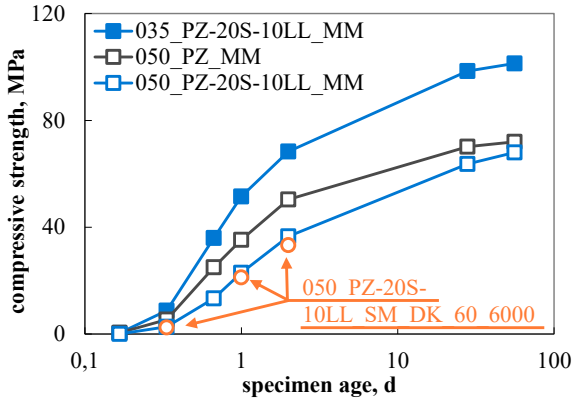

Figure 1. Compressive strength development of mortar with Portland cement PZ or composite cement PZ-20S-10LL depending on the w/c ratio of 0.5 or 0.35 and the mixing procedure.

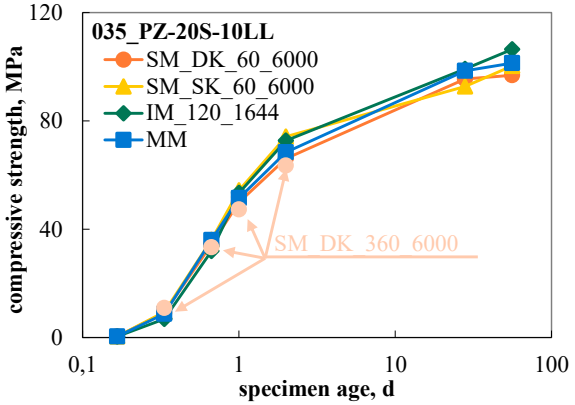

Figure 2. Compressive strength development of two-stage mixed mortar with composite cement PZ-20S-10LL at w/c ratio of 0.35 compared to single-stage mixed mortar.

As expected, the compressive strength of the single-stage mixed mortars with PZ-20S-10LL with a reduced clinker content to 70 mass % was around 30 % lower than that of the PZ mortars up to the age of two days (Figure 1). With increasing age, the compressive strength of the mortars with composite cement approached the compressive strength of the Portland cement mortars due to the latent hydraulic reaction of the blast furnace slag.

Figure 1 also shows the compressive strengths of mortars with PZ-20S-10LL at the age of 8, 24 and 48 h, which were mixed in two stages (open orange symbols). These results show by way of example for the different two-stage mixing processes tested (Chapter 2) that the compressive strength of mortar with composite cement at a w/c ratio of 0.50 could not be improved by the two-stage mixing processes applied in this project.

The lower early strength of resource-efficient composite cements with significantly reduced clinker contents and therefore significantly reduced specific CO_2 emissions can be increased relatively easily by reducing the w/c ratio. Figure 1 shows that as expected, the compressive strengths of the single-stage mixed mortars with PZ-20S-10LL at a w/c ratio of 0.35 were significantly higher at all test ages than those of the reference mortars with PZ at the w/c ratio of 0.50.

The development of the compressive strength of two-stage mixed mortar with composite cement PZ-20S-10LL at the w/c-ratio of 0.35 is shown in Figure 2 compared to the single-stage mixed mortar. Also, at the w/c ratio of 0.35 the mortar compressive strength could not be significantly increased by the applied two-stage mixing processes. Even the considerably longer mixing of the suspension of up to 360 s (360, filled light orange symbols) did not increase the mortar compressive strength.

The bulk densities of the hardened mortars with PZ-20S-LL10 at w/c = 0.35 ranged from 2270 to 2290 g/dm³. The comparatively uniform bulk densities, despite the clearly different mixing processes, show that the perhaps different amounts of air voids introduced via the various intensive mixing processes were able to be released during the compaction process of the mortars.

The mean values of the particle size distributions of PZ-20S-10LL before and after mixing in isopropanol are shown in Figure 3.

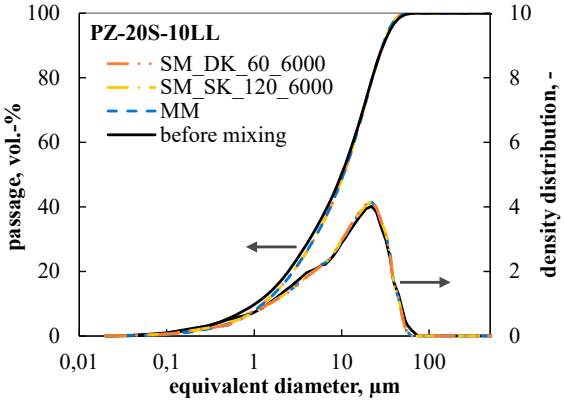

Figure 3. Particle size distributions of composite cement PZ-20S-10LL before and after mixing in isopropanol with different mixing procedure.

The particle size distributions show that PZ-20S-10LL was not measurably refined even by the suspension mixer with the high-intensity dispersing head (DK). In consequence, all the results presented show no indication for significantly increased conversion of the cement constituents into more strength-forming hydrates due to the applied two-stage mixing processes.

4. Conclusions

Based on the above-mentioned results on the use of two-stage mixing to increase the early compressive strength of clinker- and resource-efficient composite cements, the following conclusions can be drawn:
- two-stage mixing did not increase the early compressive strength of cements tested with w/c 0.5 and 0.35 and did not show any advantages in comparison to ordinary forced mixing
- in contrast to the two-stage mixing, the compressive strength of low-clinker cements could be increased more efficiently by reducing the w/c ratio and the application of a superplasticizer

Acknowledgements

The IGF project 21320 N of the research association VDZ Technology gGmbH is funded by the Federal Ministry of Economics and Climate Protection via the AiF in the programme for the promotion of joint industrial research (IGF) on the basis of a resolution of the German Bundestag.

References

Baumert, Chr. and Garrecht, H. (2010) "The Mixing Process of High Performance Concrete" (in German with English abstract) *Beton- und Stahlbetonbau*, 105(6): 371-378

Houlsby, A.C. (1990) "*Construction and design of cement grouting*" New York: John Wiley and Sons, 10-28

Juilland, P. et al. (2012) "Effect of mixing on the early hydration of alite and OPC systems" *Cement and Concrete Research*, 42(9): 1175-1188

Kravetz, G.A. (1959) "Cement and clay grouting of foundations" *ASCE Journal of Soil Mechanics and Foundation Devision*, 85: 109-114

Reschke, A.E. (1998) "The development of colloidal mixer based CRF systems" In: Bloss, M. (ed) *Proceedings of the Sixth International Symposium on Mining with Backfill*, Brisbane, Australia, 14-16 April, 65-70

The 16th International Congress on the Chemistry of Cement 2023 (ICCC2023)
"Further Reduction of CO_2 -Emissions and Circularity in the Cement and Concrete Industry"
September 18–22, 2023, Bangkok, Thailand

Using blast furnace slag from iron ore "green briquette" on cements – Part 1: chemical and mineralogical characterization

F. F. Chotoli[1*], M. F. L De Menezes[2], M. Longhi[3], F. V. Pimenta[4], V. G. De Resende[4], F. V. Parreira[4], R.F.C. Santos[5]

1, 5 Instituto de Pesquisas Tecnológicas do Estado de São Paulo (IPT) - Laboratório de Materiais para Produtos de Construção Civil, São Paulo, Brazil - fchotoli@ipt.br and rafaelfci@ipt.br

2 Co-log, Minas Gerais, Brazil – mariana.menezes@cologcoprodutos.com

3 Circlua, Minas Gerais, Brazil – Marlon.longhui@circlua.com.br

4- Centro de Tecnologia de Ferrosos, Vale S.A, Minas Gerais, Brazil. –felipe.pimenta@vale.com, valdirene.resende@vale.com and fabricio.parreira@vale.com

ABSTRACT

Green briquette is an iron ore agglomerate produced by cold agglomeration process for use as metallic burden in blast furnaces and direct reduction reactors, creating flexibility for the steel market. This product benefits CO_2 reduction at mining and steel mills. The presence of sodium in the composition of the green briquette, and, therefore, in the slag motivated the study. This work compares the characterization of high sodium blast furnace slags by using "green briquette" on the metallic burden with a reference slag. Chemical analysis, X-ray diffraction and reactivity and/or hydration analysis were applied in slags and slag cements characterization.

The combination of various characterization techniques represents an effective contribution to understand the behavior of these slags and the cements made from it and show producers that the high sodium blast furnace slag can be used in the ordinary slag cement, without any additional quality control from the currently applied by cement manufacturers and users.

KEYWORDS: *blast furnace, slags, sodium, green briquette, reactivity, hydration, slag cements.*

1. Introduction

The seek for products and technologies with lower greenhouse gas emission is of fundamental importance for the steelmaking industry to take into account new investments in the future. In this sense, the cold agglomeration process of iron ore has appeal to obtain products with lower greenhouse gas emission. In 2019, a cold agglomeration process was patented to produce iron ore briquettes to be applied in blast furnace and direct reduction reactors (Patent application BR102019023195-5, 2019). Considering the cold agglomeration process and the no use of solid fuel in its composition, this agglomerate was then name as "green briquettes" to be used as metallic burden. This kind of product must comply some physical properties at high temperatures. To warranty high physical property of the briquette at high temperatures, an inorganic binder, combined with other materials, is used to agglomerate the iron ore particles, which is the sodium silicate. However, this binder incorporates sodium into the product and, consequently, after the use of the briquette in the blast furnaces, the slag that comes out from these processes contains sodium.

Furthermore, it is well known that the hydraulic activity of slag is affected by the chemical composition of the main and minor chemical constituents, glass content and their combination. The quality control of slag

by the current standards is effective in avoiding noticeable quality fluctuation in blended slag cement production. However, since slag is no longer an admixture but a main ingredient, the quality of this kind of cement is much more sensitive to the quality of slag, and therefore, the methods of slag quality evaluation are important (Wang S. et al, 1994). Therefore, Part I of this work is devoted to compare the characterization of high sodium blast furnace slags obtained with the use of "green briquettes" as metallic burden with a reference slag. On the other hand, Part II of the work is focused on the study of the slag cements produced by adding high sodium blast furnace slags.

2. Experimental study

2.1 Materials and experimental process

High sodium blast furnace slags were obtained from an industrial trial performed in a small blast furnace (< 200 m^3), by using "green briquette" on the metallic burden and cooling down at ambient temperature. In the industrial trial, "green briquettes" gradually replaced lump ore. Slag samples were collected before (Slag reference SR) and two times (SGBA and SGBB) after the introduction of the briquettes into the furnace.

2.2. Analytical methods

The chemical composition was obtained by X-Ray Fluorescence (XRF) using a Panalytical Minipal Cement, and fused beads were produced in Claisse M4 fusion machine. This equipment was calibrated using commercial standard materials (BS, BAS, CANMET, ECRM, IPT, NHKG, NIST, SLOVAK and CECA). FeO was characterized by dichromate titrimetry (ASTM E 246-10) and metallic iron according (Xu Z. et al., 2003). Iron trioxide was calculated by difference of total iron, iron oxide and metallic iron. Free lime (CaOf) were analyzed by Brazilian Standard Methods which procedures are analogous to ASTM C 114/08. Slags reactivity was estimated by empirical formulas linked to the chemical composition and index requirements for good performance according to several authors (Kocaba V., 2009; Pal S. C. et al., 2003; Shi C. et al, 2005; Smolczyk H. G., 1980; Krüger J. E. and Smit M. S., 1969; Lang E., 2002; Wang S. et al, 1994; Dron R., 1986).

X-ray diffraction (XRD) was applied for mineralogical composition analysis. Powder samples were manually pressed into a 27 mm diameter sample holder and performed in a Panalytical Empyrean X-Ray powder Diffractometer, in a rotating sample stage, employing CuKα radiation, 45 kV, 40 mA, step size of 2º 2Θ per minute, 1/2º divergence slit. The minerals identification and phases quantification by Rietveld method was performed in X-Pert HighScore version 4.9 and based on standard diffraction data provided by ICDD (International Center For Diffraction Data). Minerals found: Åkermanite-Gehlenite, $Al_{1.3}Ca_2Mg_{0.35}O_7Si_{1.35}$ (ICSD 98-016-0338); Åkermanite, $Al_{0.41}Ca_{1.53}Fe_{0.16}Mg_{0.39}Na_{0.51}O_7Si_2$ (ICSD 98-002-0391); Quartz low, SiO_2 (ICSD 98-003-1228).

3. Results and Discussion

According to chemical compositions (Table 1), it is observed that slags from iron ore "green briquette" (SGBA and SGBB) showed content of elements similar to conventional blast furnace slags.

Table 1: Chemical compositions of slags /%, mass

Slags	Fe_2O_3	FeO	Fe^o	CaO	SiO_2	Al_2O_3	MgO	TiO_2	MnO	P_2O_5	Na_2O	K_2O	Na_2O eq	LOI
SR	0.53	1.55	0.03	35.8	40.9	10.5	5.30	0.69	0.88	0.07	0.48	1.48	1.45	0.26
SGBA	0.84	1.85	0.02	33.5	42.0	10.3	5.26	0.85	1.22	0.10	1.37	1.51	2.36	0.10
SGBB	0.72	1.01	0.01	34.0	40.8	11.9	5.88	0.88	1.28	0.06	1.27	1.55	2.29	0.30

Na_2O eq: equivalent alkali content, $\%Na_2O + 0.658 \times \%K_2O$

Mineralogical composition of slags from iron ore "green briquette" (Table 2) showed absent of RO phase (CaO–FeO–MnO–MgO solid solution). This fact indicates the possibility to apply this index in a quick evaluation of slags through chemical and/or mineralogical results. However, this method should be used with caution because of other chemical elements influence in the slag reactivity.

Table 2: Mineralogical compositions of slags /%, mass

Slags	Åkermanite – Gehlenite $[Ca_2 (Al_{0.65} Mg_{0.35}) ((Al_{0.65} Si_{1.35}) O_7)]$ + Åkermanite $[(Ca_{1.53} Na_{0.51}) (Mg_{0.39} Al_{0.41} Fe_{0.16}) Si_{2.0} O_7)]$	Quartz (SiO_2)	Amorphous phase
SR	58.1	0.4	41.5
SGBA	62.7	0.6	36.8
SGBB	76.6	1.6	21.8

Table 3: Evaluation of characteristic moduli of slags /%

Moduli	SR	SGBA	SGBB
$M_1 = CaO/SiO_2$	0.88	0.80	0.83
M_1 is the basicity index. When it increases, the solubility and thus the reactivity of slag increases (Krüger J. E. and Smit M. S., 1969)	low solubility and reactivity	low solubility and reactivity	low solubility and reactivity
$1.3 \leq M_1 \leq 1.4$ (Pal, S. C. et al., 2003)			
$1.5 \leq M_1 \leq 2.7$ (Shi C., 2005)			
$M_2 = (CaO+MgO)/SiO_2$	1.00	0.92	0.98
$M_3 = (CaO+MgO)/(SiO_2+Al_2O_3)$ Basicity Coefficient, Melting conditions of the slag (Smolczyk, H. G., 1980)	0.80	0.74	0.76
$M_2 \geq 1$ (EN 197-1)			
$0.7 \leq M_2 \leq 1.2$ and $1.0 \leq M_3 \leq 1.3$ (Shi C. et al, 2005)	favorable	Favorable	favorable
$M_4 = Al_2O_3/SiO_2$ Evaluate slags for cement application, where $0.55 \leq M_4 \leq 0.53$ indicate good performance in blended cements	0.26 "low" performance in blended cements	0.25 "low" performance in blended cements	0.29 "low" performance in blended cements
$M_5 = (CaO+MgO+Al_2O_3)/SiO_2$	1.26	1.17	1.27
Quality evaluation (Lang, E., 2002): $M_{5\ modified} = (CaO+MgO+Al_2O_3)/(SiO_2+TiO_2+(P_2O_5+F+MnO)$			
Quality coefficient (Lang, E., 2002; Wang, S. et al, 1994):	1.21	1.11	1.20
$1.5 < M_5$: poor hydraulic properties; $1.5 \leq M_5 \leq 1.9$: good hydraulic properties; $M_5 > 1.9$: quality is very good	poor hydraulic properties	poor hydraulic properties	poor hydraulic properties
$1.4 < M_5$ in Japanese standards (Shi C. 2005)			
$M_6 = (CaO*Al_2O_3)/(SiO_2+Al_2O_3)^2$	0.14	0.13	0.15
Dron R. (1986) defined an index of reactivity: slag with a suitable quality should have $M_6 \geq 0.18$.	low quality	low quality	low quality

The crystalline phases are those typically found in slags (Kashiwaya Y. et al., 2007; Gan L. et al., 2012; Mostafa N.Y. et al., 2001). It was observed a decrease of amorphous phase content as a function of the addition of iron ore "green briquette". The tendency of amorphous phase stabilization can be caused by a lower basicity of the green briquettes slag, though, this lower moduli probably comes from other not controlled parameters on the trial batch and are in acceptable ranges (Ryu H. G. et al., 2010). Furthermore, it can be observed a absent of CaO free, RO phase was eliminated and MgO was stabilized in phases with lower CaO/SiO_2 ratio. Akermanite-Gehlenite composition was $[Ca_2 (Al_{0.65} Mg_{0.35}) ((Al_{0.65} Si_{1.35}) O_7))$ but substitution between Ca and Na, between Mg and Al-Fe occurred to form $(Ca_{1.53}Na_{0.51}) (Mg_{0.39}Al_{0.41}Fe_{0.16}) Si_{2.0}O_7$ during reduction and cooling process (Table 2).

The moduli of the slags are shown in Table 3. Smolczyk (1980) explain that M_1, M_2 and M_3 basicity ratios of blast furnace slags were the starting-point for most of the hydraulic identification values, however, are not very suitable as hydraulic factor because the alumina is not taken into account in the proper way.

Furthermore, M1<1 in acid slag is not a limiting value if the lower CaO-content is compensated by corresponding higher content of MgO and Al_2O_3. Also, M4 index should be adopted carefully because high aluminum content in slags could decrease compressive strength in Portland Slag Cements in old ages. In case of SGBA and SGBB, they showed same hydraulic properties capacity that SR. According to Kocaba V. (2009), all the moduli are convenient tools to rapidly estimate the quality of slag, nevertheless some studies reported that in practice, the modulus ratios do not always correlate with strength, particularly at early ages.

4. Conclusions

The three slags analyzed are mostly crystalline, showing typical phases of slags under slow cooling. Higher silica and alumina plus lower iron oxides in the slags contributed to the glassy phase formation, absent RO phase absent as well as MgO stabilization in calcium and magnesium silicates (åkermanite phases) despite slow cooling process applied. Comparing SGBA and SGBB with SR, some differences were noted: the higher alkali content on the slags from the briquettes; similar basicity index and moduli; and the lower amorphous phase. The alkali content on these slags is expected, once the briquettes has high alkalis content that on the metallurgical process it ends up on the slag. Despite the result of the amorphous phase content apparently having reduced due to the addition of the briquette in the process, we suppose that the amorphous phase may have been harmed by slow cooling, typical of the process adopted in this study. The mechanical performance, as demonstrated in Part 2 of this work, was satisfactory. The use of green briquettes slags as a supplementary cementitious material without any change on the cement production and application process is an important tool to leverage the green briquettes use, considering the relevance to keep producing low environmental impact cement, with slag as raw materials.
It is recommended to apply other studies focusing process optimization, durability and performance of these cements, as well as increasing the reactivity of the three slags, the reference and the green briquettes ones.

References

- Dron R. Structure and reactivity of glassy slags, Proceedings of the 8th International Congress on the Chemistry of Cement, Rio de Janeiro, Brazil, IV, 3 81-85, 1986.
- Gan L., Zhang C., Shangguan F., Hagguan, F., Li X. A Differential Scanning Calorimetry Method for Construction of Continuous Cooling Transformation Diagram of Blast Furnace Slag, Mater. Trans. B. Process Metall. Mater. Process. Sci, 43 460–467 (2012).
- Kashiwaya Y., Nakauchi T., Pham K.S., Akiyama S., Ishii K. Crystallization Behaviors Concerned with TTT and CCT Diagrams of Blast Furnace Slag Using Hot Thermocouple Technique. ISIJ International, 47 (1) 44-52 (2007).
- Kocaba V. Development and Evaluation of Methods to Follow Microstructural Development of Cementitious Systems Including Slags, PhD Thesis, EPFL, 2009.
- Krüger J. E., Smit M. S. Endothermal DTA peak preceding exothermal devitrification peak for vitreous blast-furnace slag, Cement and Lime Manufacture, 42 (4), 77-80, 1969.
- Lang E. Chapter 12: Blast furnace cements, in Structure and performance of cements, 2nd edition, J. Bensted & P. Barnes (ed), Spon Press, 310-325, 2002.
- Mostafa N.Y., El-Hemaly S.A.S., Al-Wakeel E.I., El-Korashy S.A., Brown, P.W. Characterization and Evaluation of the Hydraulic Activity of Water-Cooled Slag and Air-Cooled slag, Cement and Concrete Research, 31 899-904 (2001).
- Pal S. C., Mukherjee A., Pathak S.R. Investigation of hydraulic activity of ground granulated blast furnace slag in concrete. Cement and Concrete Research, 33 (2003) 1481–1486.
- Ryu H. G., Zhang Z.T., Cho J.W., Wen G.H., Sridhar S. Crystallization Behaviors of Slags through a Heat Flux Simulator. ISIJ International, 50 (8) 1142-1150 (2010).
- Shi C, Roy D., Krivenko P. V. Alkali-Activated Cements and Concretes. CRC Press, 2005 [ISBN 9780415700047].
- Shi C. Steel Slag – Its Production, Processing, Characteristics and Cementitious Properties. Journal of Materials in Civil Engineering, 16 230-236 (2004).
- Smolczyk H. G. Slag structure and identification of slags, Proceedings of the 7th International Congress on the Chemistry of Cement, Paris, France, I, III 1/4-1/17, 1980.
- TAYLOR, H.F.W. 1998. The chemistry of cements. 2. ed London: Thomas Telford. 1v, 476p.
- Xu Z. et al: Journal of Minerals & Materials Characterization & Engineering, v. 2, n° 1, p. 65-70, 2003.
-Wang S., Scrivener K. L., Pratt, P. L. Factors affecting the strength of alkali-activated slag. Cement and Concrete Research, vol:24, iss:6, pg:1033 -1043, 1994.

The 16th International Congress on the Chemistry of Cement 2023 (ICCC2023)
"Further Reduction of CO_2 -Emissions and Circularity in the Cement and Concrete Industry"
September 18–22, 2023, Bangkok, Thailand

On the synergies among supplementary cementitious materials

D. Gastaldi[1]*, V. Merlo[1], F. Canonico[1], E. Boccaleri[2], G. Paul[3]

[1] *Built – Buzzi Unicem Innovation Lab and Technology, Vercelli, Italy*
Email: : dgastaldi@buzziunicem.it; vmerlo@buzziunicem.it; fcanonico@buzziunicem.it
[2] *UPO – Università del Piemonte Orientale; DISSTE Department for Sustainable Development and Ecological Transition, Vercelli, Italy*
Email: enrico.boccaleri@uniupo.it
[3] *UPO – Università del Piemonte Orientale; DISIT Department of Science and Technological Innovation, Alessandria, Italy*
Email: geo.paul@uniupo.it

ABSTRACT
In the framework of improved sustainability of cementitious binders, a key role is played by supplementary cementitious materials (SCMs). Recent studies demonstrated that an interaction among different SCMs effectively takes place resulting in the development of "non-conventional" hydrated phases, partly crystalline and partly amorphous, able to confer peculiar features in terms of both strength development and durability, Scrivener et al (2018), Adu-Amankwah et al (2017).
Our contribution describes a deep investigation on the hydration behavior of composite cements containing at least two different SCMs focusing the attention on the hydrated phase assemblage and the undergoing chemical reactions. For this purpose, a multi-technique approach has been used, combining X-ray diffraction for quantification of crystalline phases and ^{27}Al solid-state nuclear magnetic resonance for the determination of both crystalline and amorphous phases. Additional information were also gathered, such as the amount of bound water and calcium carbonate by means of thermogravimetric analysis (TGA). The results of the study revealed that: (i) there is no a priori optimal ratio between the different SCMs, but it must be optimized on case by case basis; (ii) the performances of the final binders are influenced by the clinker factor at a different extent for each formulation; (iii) a comprehensive knowledge of the type, composition and properties of the resulting phases needs to consider both crystalline, amorphous and transient species; (iv) a fundamental contribution in the hydration process is given by the sort and amount of ions released in the pore solution by the different SCMs.

KEYWORDS: *Low clinker factor cements, supplementary cementitious materials, cement hydration study, X-Ray diffraction, Thermogravimetric analysis.*

1. Introduction

Clinker replacement through supplementary cementitious materials is a promising strategy for reducing CO_2 emission associated to cement production, Gartner (2004), Gartner and Hirao (2015). SCMs such as pozzolan or slag are already widely used in cement production, while other materials such as calcined clay became more and more important in the last 5-10 years as new viable routes to produce sustainable binders. In this framework, one of the most innovative developments is a ternary system based on clinker, calcined clay and limestone (plus gypsum), in which for the first time the synergy between two different SCMs was experimentally verified, Scrivener et al (2018).
In this paper the study of the effect of the combination of different supplementary cementitious material on strength development and hydration behaviour has been extended to other SCM. Different cements have been prepared using pozzolan, slag and calcined clay in combination with limestone. The formulations have been chosen to comply the new EN 197/5:2021 as cements type II/C-M (50% clinker, 5% anhydrite and 45% of SCM). The ratio between SCM and limestone was set 1:1 and 2:1.

2. Materials and methods

The formulations of the cements are reported in Table 1 (% in weight of each component). Clinker, pozzolan, slag and anhydrite have been supplied by Buzzi Unicem SpA. Pozzolan comes from a quarry in central Italy, is amorphous by 45% and contains diopside ($CaMgSi_2O_6$) 25%, leucite ($K(AlSi_2O_6)$) 13%, analcime ($Na(AlSi_2O_6)•(H_2O)$) 12% and magnetite (Fe_3O_4) 5%. Slag is a ground granulated blast furnace slag deriving from an iron production plant in south Italy and is amorphous for more than 99%. Limestone is a natural material constituted by calcite and low amount (less than 2%) of dolomite. Calcined clay was supplied by Goerg and Schneider (Germany), the original clay contained kaolinite 34%, illite 27% and quartz 37%. In Table 2 the percentile values (from particle size distribution) of the SCM are reported, showing that different SCMs have similar particle size, while limestone is much finer.

Table 1 Compositions of the investigated binders

	Clinker (K)	Calcined clay (Q)	Pozzolan (P)	Blast furnace slag (S)	Limestone (LL)	Anhydrite
CEM II/C-M(Q-LL) 1	50	22,5	-	-	22,5	5
CEM II/C-M(Q-LL) 2	50	30	-	-	15	5
CEM II/C-M(P-LL) 1	50	-	22,5	-	22,5	5
CEM II/C-M(P-LL) 2	50	-	30	-	15	5
CEM II/C-M(S-LL) 1	50	-	-	22,5	22,5	5
CEM II/C-M(S-LL) 2	50	-	-	30	15	5

Table 2 Percentile values of supplementary cementitious materials from particle size distribution

	Calcined clay (Q)	Pozzolan (P)	Blast furnace slag (S)	Limestone (LL)
Dx (10) µm	1,173	1,078	1,785	0,727
Dx (50) µm	12,895	13,916	16,386	5,536
Dx (90) µm	75,903	65,543	54,912	32,436

Compressive strengths were determined in accordance with EN 196–1: prisms of dimensions 4 × 4 × 16 cm were cast using water, cement and sand in 0.5:1:3 mass ratio and stored for 24 h at 20 °C and 95 % RH in their moulds. After demoulding, they were cured in water until the compressive strength tests were performed at the desired ages (1, 2, 7, 28, 60 and 90 days).

For the hydration study, water-to-cement = 0.5 cement pastes were prepared and poured in plastic containers, sealed, and stored for 1, 2, 7, 28, 60 and 90 days. At the desired ageing time, the pastes were removed from the plastic holder and crushed in a laboratory jaw crusher (8, 5 and 2 mm), then put in a desiccator under nitrogen and placed in oven at 40 °C overnight to remove the unbound water.

For X-Ray Diffraction analyses (XRD) a Bruker AXS D4 Endeavor diffractometer (Bragg-Brentano geometry, ceramic X-ray tube KFF -Cu Kα radiation, "Linx Eye" dispersive detector) was used. EVA and Topas softwares were applied for mineral phase identification and Rietveld refinement. For the quantification of the amorphous phase content, 5% w/w of TiO_2 (Titanium(IV)-oxide Merck, anatase 98.6%, rutile 0.8% and brookite 0.6%) was mixed to the dried pastes as internal standard and the results from Rietveld analysis were further processed according to Gastaldi et al (2016).

TG/DSC measurements were performed on hydrated paste fragments by means of a TG/DSC 1 Mettler Toledo: thermal ramp was set from 35 to 950 °C at 20 °C/min in 80 mL/min air flow; 90 µl alumina pan were used. Combined water was calculated by measuring the weight loss between 35 and 500 °C, corresponding to the loss of water from hydrated phases, Gastaldi et al (2016), calcite content was derived from the weight loss between 650 and 950 °C.

^{27}Al Solid-state NMR spectra were acquired on a Bruker Avance III 500 spectrometer, using a wide bore 11.7 Tesla magnet with operational frequencies for 130.33 MHz. All experiments were conducted using a 4 mm triple resonance probe, in double resonance mode, with Magic Angle Spin (MAS). Samples were packed on a Zirconia rotor and spun at a MAS rate of 10–15 kHz. Chemical shifts are reported using δ scale and are externally referenced to $Al(H_2O)_6^{3+}$ ion in 1.0 M $AlCl_3$ solution to 0 ppm. DMFIT functions for quantitative deconvolution of overlapping peaks were applied to all NMR spectra, Massiot et al (2002). The line shape of the ^{27}Al peaks associated with crystalline phases were described by a Gaussian/Lorentzian function, while the amorphous/disordered phases by Czjzek model, Gastaldi et al (2016), Paul et al (2015).

3. Results

Compressive strength on mortars are summarized in Figure 1, showing that all formulations comply strength class 32.5. Q-LL cements show higher strength at early ages, after 2 days of hydration, then overcome by P-LL and S-LL between 7-28 and 60-90 days. The effect of a different ratio between SCM and limestone is generally less than 1 MPa, except for CEM II/C-M(Q-LL) and CEM II/C-M(S-LL) at 28 days, where a ratio 2:1 gives significantly better strength.

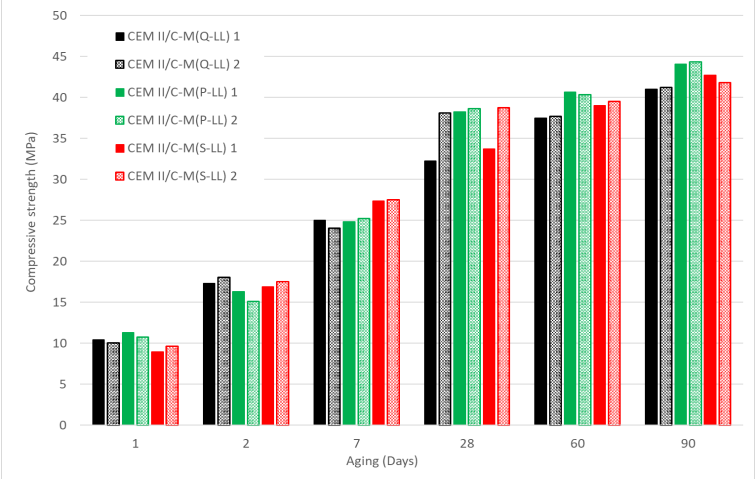

Figure 1 Compressive strengths on mortars according to EN 196-1

The comparison of XRD patterns of the cements having SCM:limestone ratio = 2:1 at 28 days (Figure 2), suggests that: (I) ettringite formation upon hydration of aluminates in clinker is boosted by aluminium bearing minerals in pozzolan and calcined clay, as its amount is lower in CEM II/C-M(S-LL); (II) AFm phases forms from aluminate species after depletion of sulfate in the paste or from ettringite modification; (III) in cements containing pozzolan and calcined clay, Monocarboaluminate (Mc) forms from the reaction between aluminate species and carbonate ions from limestone dissolution; (IV) Hydrotalcite (Ht) is observed in CEM II/C-M(S-LL) – it is typically formed in slag cements due to the high Mg content, Gastaldi et al (2021); (V) Portlandite is formed in all the cements from the hydration of silicate phases in Portland clinker, but in CEM II/C-M(Q-LL) and CEM II/C-M(P-LL) it is consumed by the pozzolanic reaction of calcined clay and pozzolan.

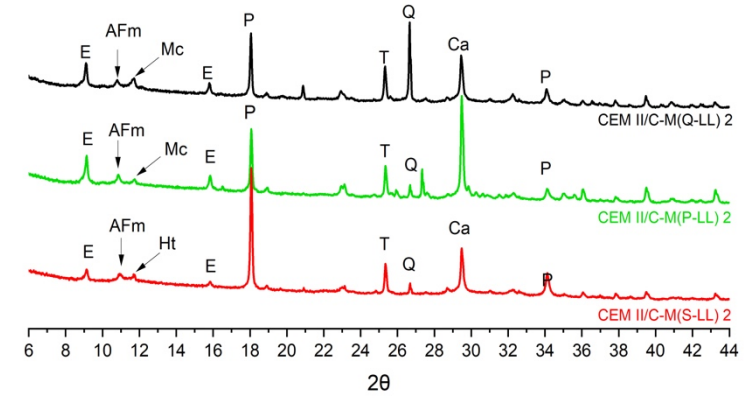

Figure 2 XRD patterns of 28 days aged cement pastes having SCM:limestone = 2:1 (E = ettringite; Mc = monocarboaluminate; P = portlandite; T = anatase; Q = quartz; Ca = calcite)

From TG/DSC measurements the amount of bound water can be derived, see Figure 3A. Calcined clay cements show the highest amount of bound water since the very early stage of hydration, a higher amount of calcined clay results in an increased bound water quantity and slightly higher strength. A reverse behavior is observed in presence of slag: the higher is the amount of slag, the lower is the water bound in the paste.

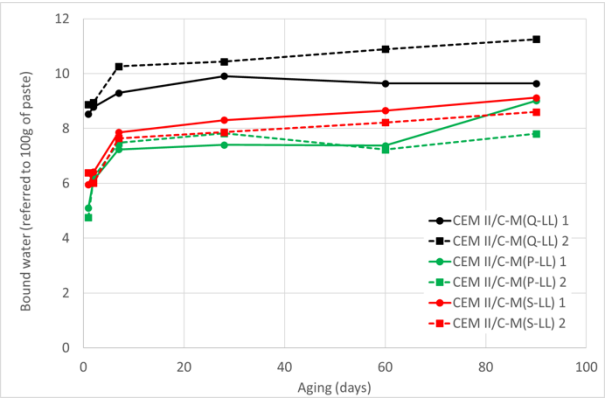

Figure 3A Amount of bound water in the hydrated paste derived from TG/DSC analysis

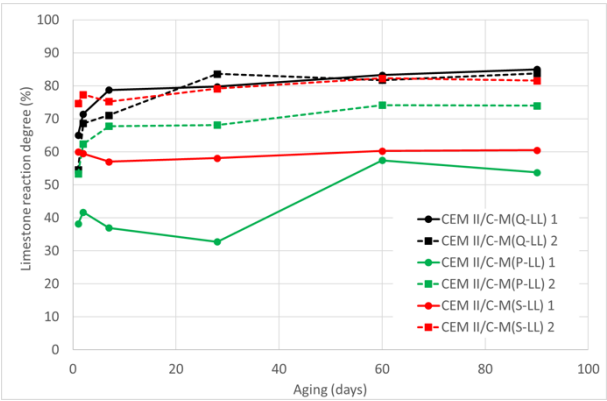

Figure 3B Limestone reaction degree in the hydrated cement pastes derived from TG/DSC analysis

In the pozzolan containing binders, larger amount of bound water is found only at late age when the lower amount of SCM is used.
From the TG measurements of decarbonation step, a limestone reaction degree can be quantified (Figure 3B). For the calcined clay-based binders, both the SCM:limestone different ratios show that at 90 days around 85% of limestone has reacted. Relevant differences are instead observed when pozzolan or slag are used, as a lower dosage of limestone (CEM II/C-M(P-LL)2 and CEM II/C-M(S-LL)2) show a higher reaction degree of calcite, probably because of the easier dissolution of carbonate in the paste (less ions in the pore solution).
^{27}Al Solid-state NMR investigation allowed to identify the different aluminium containing species and to quantify them regardless the crystallinity. Selected spectra are shown in Figure 4, main statements are: (I) amorphous aluminates hydrates are formed (third aluminate hydrates, TAH) in all the samples beyond crystalline phases ettringite and AFm; (II) reaction of SCM is confirmed by the reduction of tetrahedral coordinated aluminium nuclei (present in unhydrated phases, UP) from 1 to 28 days, quantified around 30% in all the samples.

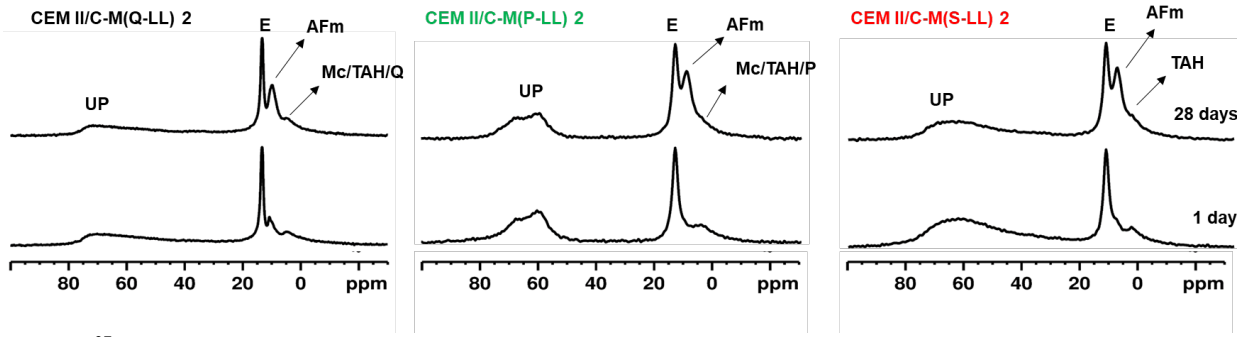

Figure 4 ^{27}Al SS NMR spectra of 1 and 28 days aged pastes having SCM:limestone = 2:1 (UP = unhydrated phases; E = ettringite; Mc = monocarboaluminate; TAH = third aluminate hydrates)

4. Conclusions

Combining different supplementary cementitious materials in cement formulations opens the route towards a wide family of innovative sustainable binders, exploiting synergistic effects among the various components and a possible further reduction of the clinker factor. The combination of limestone with calcined clay, pozzolan or slag gave similar results in terms of compressive strength development: calcined clay performed better at early ages, while pozzolan reached higher strength at later ages, i.e. from 28 days on, when pozzolanic consumption of portlandite becomes relevant. For P-LL and Q-LL formulations, the presence of monocarboaluminate among aluminate hydrated phases suggests the active contribution of calcite in the hydration process. ^{27}Al NMR measurements reveal that all supplementary cementitious materials react forming amorphous hydrates beyond crystalline phases ettringite and AFm. For slag-based systems, the role of limestone during hydration reaction is less clear, though for CEM II/C-M(S-LL)2 limestone consumption reaches 80%. Finally, it can be stated that the SCM:limestone ratio is scarcely relevant on strength development: the only significant difference is observed for CEM II/C-M(Q-LL) and CEM II/C-M(S-LL), having a large gain in strength between 7 and 28 days when the limestone amount is lower.

References

Scrivener, K., Martirena, F., Bishnoi, S. and Maity, S. (2018) "Calcined clay limestone cements (LC^3)", *Cement and Concrete Research*, 114: 49-56

Adu-Amankwah, S., Zajac, M., Stabler, C., Lothenbach, B., Black, L. (2017) "Influence of limestone on the hydration of ternary slag cements", *Cement and Concrete Research*, 100, 96-109

Gartner, E., (2004) "Industrially interesting approaches to "low-CO_2" cements", *Cement and Concrete Research*, 34: 1489-1498

Gartner, E., Hirao, H. (2015) "A review of alternative approaches to the reduction of CO_2 emissions associated with the manufacture of the binder phase in concrete", *Cement and Concrete Research,* 78:126-142

Gastaldi, D., Paul, G., Marchese, L., Irico, S., Boccaleri, E., Mutke, S., Buzzi, L., Canonico, F. (2016) “Hydration products in sulfoaluminate cements: evaluation of amorphous phases by XRD/solid-state NMR”, *Cement and Concrete Research, 90:162-173*

Paul, G., Boccaleri, E., Buzzi, L., Canonico, F., Gastaldi, D. (2015) “Friedel’s salt formation in sulfoaluminate cements: a combined XRD and ^{27}Al MAS NMR study, *Cement and Concrete Research, 67:93-102*

Gastaldi, D., Bertola, F., Irico, S., Paul, G., Canonico, F. (2021) “Hydration behavior of cements with reduced clinker factor in mixture with sulfoaluminate binder”, *Cement and Concrete Research*, 139:106261-106276

The 16th International Congress on the Chemistry of Cement 2023 (ICCC2023)
"Further Reduction of CO_2 -Emissions and Circularity in the Cement and Concrete Industry"
September 18–22, 2023, Bangkok, Thailand

Comparison of composite cements with limestone filler, fly ash, and calcined clays

L. Montani; A. Tironi; V. Bonavetti, E. F. Irassar*

Facultad de Ingeniería - CIFICEN (UNCPBA-CONICET-CIC) - Universidad Nacional del Centro de la Provincia de Buenos Aires, Olavarría, Argentina
Email: [1]lumontani2@gmail.com; atironi@fio.unicen.edu.ar; vbonavet@fio.unicen.edu.ar; firassar@fio.unicen.edu.ar

ABSTRACT

This paper explores the flow and the compressive strength mortar of composite cement containing portland cement (50 to 95%), limestone filler (5 to 20%), and variable percentages (0 to 45%) of calcined kaolinitic clay, calcined illite clay, and fly ash. An experimental design where the variables were LF and pozzolan content was used to evaluate the flow and compressive strength at 2, 7, 28, and 90 days. Results show that mortar flow was significantly affected by the incorporation of calcined kaolinite clay, to a lesser extent by calcined illite clay, and favored by fly ash, while small proportions of limestone filler improved it. When the sum of SCM was up to 35%, the compressive strength at an early age was greater than 10 MPa, greater than 30 MPa at 28 days, and greater than 35 MPa at 90 days. Composite cement with 20% LF and 30% calcined kaolinitic clay reached 47 MPa. Finally, the paths to developing cements with a low clinker factor are discussed.

KEYWORDS: *composite cements, limestone filler, calcined clay, Clinker factor, compressive strength*

1. Introduction

Several paths have been proposed to reach net zero emissions in the cement industry. Among this, the reduction of clinker factor to 50% for the next decade. Composite cements with two supplementary cementitious materials (SCMs) appear highly likely. For example, blended cements combining limestone filler (LF) with calcined kaolinitic clays appear as an opportunity from the compressive strength, but they present a high-water demand. The EN 197-5 standard recently established CEM II/C-M composite cements in which up to 50% of the clinker can be replaced with two SCMs.

For this level of SCMs replacement, the CO_2 reduction to mitigate climate change is possible when the SCMs are regionally available, with low-cost and low embodied energy materials. In the center of Buenos Aires province (Argentina), limestone and calcined illite clays are the main materials that meet these requirements. The research aims to analyze the flow and compressive strength of standard mortar made with blended cement containing portland cement (50 to 95%), LF (5 to 20%), and pozzolans (P = 0 to 45%) with different alumina content: low grade calcined kaolinitic clay (CKC), calcined illite clay (CIC) and siliceous fly ash (FA).

2. Materials

Portland cement (PC - CEMI/42.5 according to EN 197), limestone filler (LF), and three pozzolans were used. The mineralogical composition was 58% C_3S, 16% C_2S, 4% C_3A, and 11% C_4AF, with 5% LF as a minor component. The particle size distribution (PSD) obtained by laser granulometry (Figure 1a) shows a bimodal distribution with a d_{50} = 18.30μm. LF contains 85% $CaCO_3$ -as calcite- and quartz is the main impurity. LF presents a bimodal particle size distribution curve with a d_{50} = 4.25 μm, too finer than that corresponding to PC.

Pozzolans were: calcined illite clay (CIC), siliceous fly ash (FA) and calcined kaolinitic clay (CKC). CKC has a high Al_2O_3 content (23.9%), followed by FA (21.2%) and CIC (15.7%). The PSD and the XRD patterns of pozzolans are shown in Figure 1. As reported previously, CIC and CKC have 2% and 10% mortar water requirements compared to the PC (Cordoba et al., 2020). FA reduced the water requirement of the mortar due to the spherical shape and smooth surface of the particles. Pozzolanicity measured with Frattini's test was positive after 7 days for FA and CKC and after 14 days for CIC.

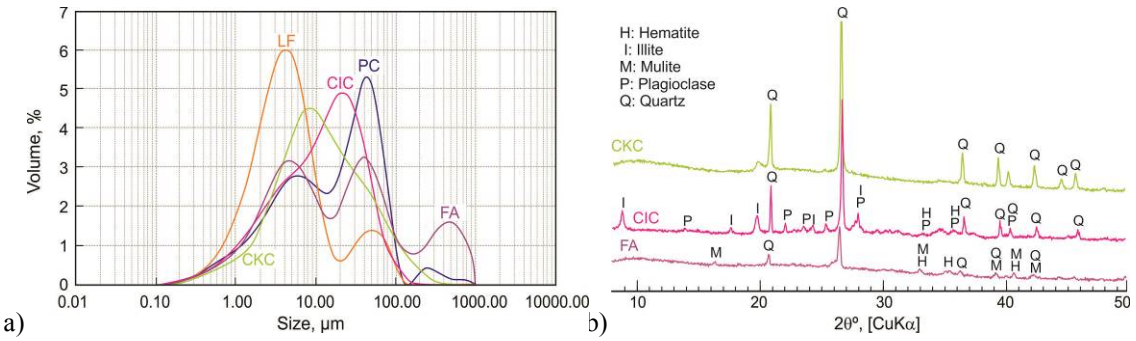

Figure 1: a) Particle size distribution of used materials. b) X-ray diffraction patterns of the pozzolans

3. Testing methodology

Eight blended cements were proportionated using an experimental design where LF-content and P-content (% by mass) are the variables. The studied domain (Figure 2) involves binary and ternary blended cements containing between 5 and 50% P+LF identifying with the pozzolan (P) and LF content (LF). The cementing materials were previously homogenized in dry state using a turbula.

Mortar proportions (sand/cm = 3; w/cm = 0.50), mixing, molding and curing of prisms, and compressive strength (CS) were carried out according to EN 196-1 at 2, 7, 28, and 90 days. Mortar flow was determined on the flow table by applying 25 blows in 15 seconds. The CS reported is the average of six values.

4. Results and discussion

4.1. Mortar flow: Figure 3 shows the flow for blended cement grouped by their composition (P+LF) ordering by increasing P-content. Both calcined clays showed a reduction in mortar flow when increasing the P-content (15 to 45%). It can be attributed to the finer particles in P compared with PC (see Fig. 1a), especially for CKC, with a high specific surface area (708 m^2/kg) and a high agglomeration tendency (Cordoba et al., 2020).

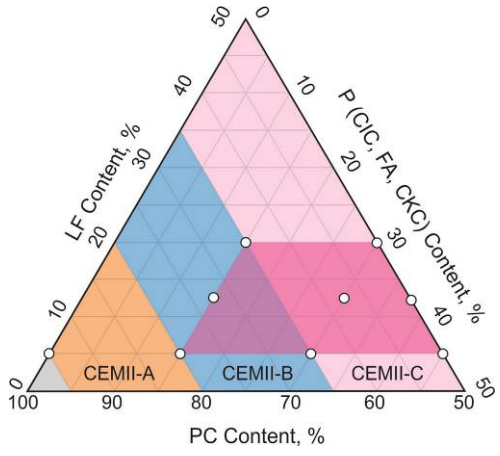

Figure 2: Identification of studied blended cements.

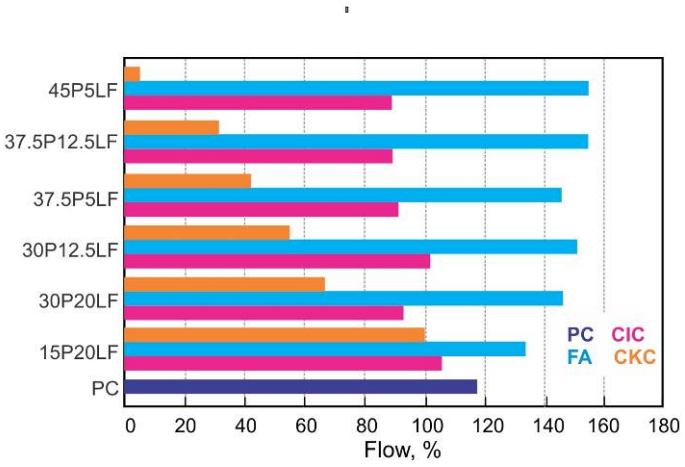

Figure 3: Mortar flow for the three studied systems.

On the contrary, FA replacement increases mortar flow when its content increases from 15 to 45%. The flow improvement can be attributed to a greater volume of paste due to the low density of FA (2.3 g/cm^3); the adsorption-dispersion caused by the same surface charge of particles adsorbed on the surface of the cement grains with opposite charge; a wider PSD; and the smooth surface and rounded shape of particles leading to high packing of cementitious materials (Thomas et al., 2013). For ternary cements with CIC or FA, LF slightly reduces the mortar flow. For low P-content (15%), LF reduces the mortar flow due to the decrease in the water film thickness surrounding the LF-particle with a high specific surface instead of the increase in packing density (Di Salvo Barsi et al., 2020). The water film surrounding the particles is thicker for large FA and CIC particles, providing high mobility to the mortar. Conversely, LF increases the mortar flow for blended cements with high CKC content (>30%). In this case, the water demand caused by the high specific surface area of CKC could be mitigated by the electrostatic effects between metakaolin and LF particles improving the particle space (Vance et al., 2013). However, LF reduced the mortar spread for low CKC content (15%) as occurs with CIC and FA, which also have a larger particle size than LF.

4.2. Compressive strength (CS): Figure 4 shows the evolution of CS for each system up to 90 days. For CIC+LF cements (Figure 4a), CS was lower than PC at all ages. Blended cements with CIC<15% with or without LF showed a CS >10 MPa at early ages, but it was smaller for 20%LF. Blended cements with CIC+LF >35% showed lower strengths than PC. The FA+LF system (Figure 4b) behaves similarly to the CIC+LF system with higher CS after 28 days. At 90 days, the CS of blended cements with FA+LF < 35% reach equal to or greater than that of PC, but the FA+LF > 50% is considerably lower than PC. For the CKC+LF system (Figure 4c), the 2 days' CS of blended cements was lower and higher after 7 days than those obtained in other systems, except for 45CKC5LF (low flow causes poor compaction and high porosity). High CS is attributed to the high reactivity of CKC, and it was improved by the LF (12.5 to 20%) for high CKC content (> 30%).

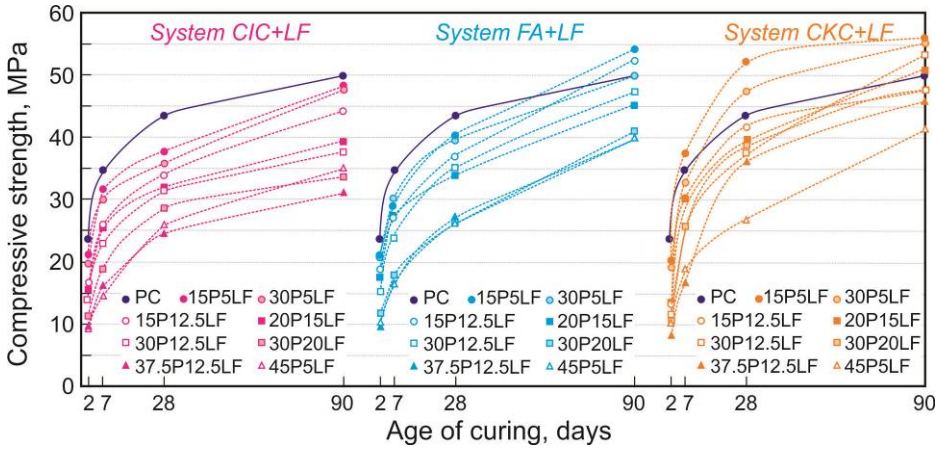

Figure 4: Compressive strength of blended cements: a) CIC+LF; b) FA+LF, and c) CKC+LF.

Figure 5 shows the CS as a function of the total SCM content for all systems. A dotted line indicates the CS achieved by the PC fraction. At 2 days (Figure 5a), CS of blended cements containing up to 30% SCM was higher than that of PC fraction, indicating that SCM stimulates the early hydration of cement, while the dilution effect is predominant for high replacement levels (>35%). The stimulation effect was more significant for LF due to their finer particles (performance filler) and possibly the favorable surface structure of limestone, which provides a substrate for C-S-H precipitation (Berodier & Scrivener, 2014). Low CS of CKC+LF can be attributed to the high amount of reactive alumina of the CKC rapidly consumes the calcium sulfate of PC, affecting the CS. However, this still needs to be analyzed.

At 7 days (Figure 5b), the CS of blended cements increases proportionally to the PC fraction computing the initial filler effect. Among the pozzolans, CKC showed a high CS due to the early reactivity with the CH released by the PC hydration (Tironi et al., 2012).

At 28 days (Figure 5c), the pozzolanic effect became predominant. High LF content does not improve CS, and the dilution effect is evident using non-pozzolanic SCM. The CS of cements containing pozzolan is above the proportional line of PC fraction and close to the line for those with high P-content. However,

their reactivity is differentiated: CS is highest by CKC, followed by FA, and lowest by CIC, and it was more significant for high replacements (50%). CKC combined with LF improves the CS, while FA and CIC have no significant differences. The high CS of FA+LF compared with LF+CIC cements is attributed to the high aluminum content of FA increasing its reactivity (ACI 232, 1998). At 90 days (Figure 5d), high P-content cements points are too far from the PC fraction line. LF binary cements did not contribute to the CS; they have an equivalent CS to the PC fraction. The pozzolan reactivity became more critical for high replacement (50%).

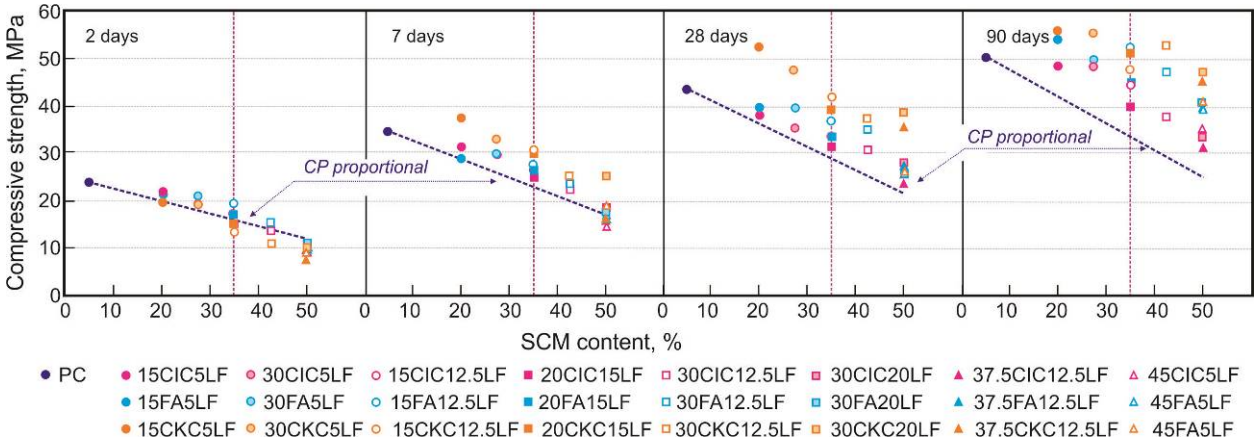

Figure 5: Compressive strength of blended cements as a function of SCM content: a) 2 days, b) 7 days, c) 28 days, and d) 90 days.

5. Conclusions:

The increased percentages of calcined clays, especially CKC, reduce the mortar flow. Contrary, mortar flow increases when FA content increases. Finer LF only improved the mortar flow when it had a low percentage. This LF combined with low replacements of FA or CIC reduces the mortar flow. However, this LF improved the mortar flow with high CKC replacements. Flow depends on the characteristics (density, particle size, specific surface, shape and surface charge) and the proportion in the blended cement.

For blended cements with LF+P content >35%, early compressive strength is lower than that PC fraction due to the dilution effect. Later compressive strength depends on the reactivity of the pozzolan (CKC > FA > CIC). The main shortcoming of LF+CKC is the low flowability which can affect the strength due to the poor compactness. The design age extension to achieve the required CS of blended cements can be competitive with LF+FA.

The chemical activation combined with a clinker grinding design that allows greater early hydration should be evaluated for high CIC and FA replacements.

6. References:

ACI 232, "Fly ash in concrete", ACI Manual of Concrete Practice, Part 1, Materials and General Properties of Concrete, (1998), 9.

Berodier, E., & Scrivener, K. (2014). Understanding the Filler Effect on the Nucleation and Growth of C-S-H. *Journal of the American Ceramic Society*, *97*(12), 3764-3773. https://doi.org/10.1111/jace.13177

Cordoba, G. P., Zito, S. V., Sposito, R., Rahhal, V. F., Tironi, A., Thienel, C., & Irassar, E. F. (2020). Concretes with Calcined Clay and Calcined Shale: Workability, Mechanical, and Transport Properties. *Journal of Materials in Civil Engineering*, *32*(8), 04020224. https://doi.org/10.1061/(ASCE)MT.1943-5533.0003296

Di Salvo Barsi, A., Marchetti, G., Trezza, M. A., & Irassar, E. F. (2020). Carbonate rocks as fillers in blended cements: Physical and mechanical properties. *Construction and Building Materials*, *248*, 118697. https://doi.org/10.1016/j.conbuildmat.2020.118697

Tironi, A., Trezza, M. A., Scian, A. N., & Irassar, E. F. (2012). Kaolinitic calcined clays: Factors affecting its performance as pozzolans. *Construction and Building Materials*, *28*(1), 276-281. https://doi.org/10.1016/j.conbuildmat.2011.08.064

Thomas, M. "Supplementary Cementing Materials in Concrete", CRC Press Taylor & Francis Group 6000 Broken Sound Park, (2013), 59-60.

Vance, K., Kumar, A., Sant, G., & Neithalath, N. (2013). The rheological properties of ternary binders containing Portland cement, limestone, and metakaolin or fly ash. Cement and Concrete Research, 52, 196-207. https://doi.org/10.1016/j.cemconres.2013.07.007

The 16th International Congress on the Chemistry of Cement 2023 (ICCC2023)
"Further Reduction of CO_2 -Emissions and Circularity in the Cement and Concrete Industry"
September 18–22, 2023, Bangkok, Thailand

Using blast furnace slag from iron ore "green briquette" on cements - Part 2: physical-mechanical characterization

Santos RFC[1*]. De Menezes MFL[2]. Longhi M[3]. Pimenta. FV[4]. de Resende VG[4]. Parreira FP[4]. Chotoli FC [5]

1, 5 Instituto de Pesquisas Tecnológicas do Estado de São Paulo (IPT) - Laboratório de Materiais para Produtos de Construção Civil, São Paulo, Brazil - rafaelfci@ipt.br and fchotoli@ipt.br

2 Co-log. Minas Gerais. Brazil - mariana.menezes@cologcoprodutos.com

3 Circlua. Minas Gerais. Brazil - marlon.longhui@circlua.com.br

4- Centro de Tecnologia de Ferrosos. Vale S.A. Minas Gerais. Brazil.- felipe.pimenta@vale.com, valdirene.resende@vale.com and fabricio.parreira@vale.com

ABSTRACT

Green briquette is an iron ore agglomerate produced by cold agglomeration process for use as metallic burden in blast furnaces and direct reduction reactors, creating flexibility for the steel market. This product benefits CO2 reduction at mining and steel mills. The presence of sodium in the composition of the green briquette and, therefore, in the slag motivated the study. This work presents the characterization of slag cements produced by adding high sodium blast furnaces slags. Chemical analysis and mineralogical characterization are presented in Part 1 of this Congress. The physical-mechanical and rheological characterizations of the cements and mortars were made after the addition of slag in common Portland cement and through tests to determine the setting times, axial compressive strength, flexural tensile, dimensional variation, mitigation of the expansion of the alkali-aggregate reaction and rheological tests. The physical, rheological and mechanical parameters indicate the feasibility of application as a supplementary cement material without significant alteration in the evaluated properties.

KEYWORDS: *Blast furnace; slag; sodium; SCM; physical and mechanical properties.*

1. Introduction

The cement hydration in presence of minerals additions, as steel slag, involves a great deal of complexity due to the incorporation of different components, which are competitive within clinker-gypsum-water system resulting in changes of cement phases dissolution rate, in ionic balance and hence in evolution and precipitation of hydrated phases.

The present work is another part of project which studies high sodium blast furnace slags obtained with the use of "green briquettes" as metallic burden with a reference slag, as described in CHOTOLI et al. (2023), whose purpose is obtain "green briquettes" steel slag with satisfactory cementitious performance. This paper presents mechanical and physical characterizations results of Portland Cements Slags (PSC) mixed with these "green briquettes" slags.

2. Experimental study

2.1 Materials and experimental process

Blast furnace slags from iron ore "green briquette" as presented in Chotoli F.F. *et al.* (2023) was ground in ball mill to 0.075mm. Part of samples and Ordinary Portland Cement were used to produce Portland Slag Cements (PSC. similar to CEM II/B-S) in a proportion of 30%/70% (slag/Portland cement). Cement mixtures composed of slag with 0% briquette (PSC-SR), 10% briquette (PSC-SGBA) and 15% briquette (PSC-SGBB) were submitted to the tests.

2.2. Characterization methods

The chemical and mineralogical properties are also presented in Chotoli F.F. et al. (2023). The compressive strength, normal consistency, setting time, soundness test by Le Chatelier method of PSC were tested according Brazilian Standard NBR 11578 (analogous to European Standards EN 197-1. ISO EN 196-1 and ISO EN 196-3). Other test such potential alkali-aggregate reactivity by the accelerated method (ABNT NBR-15577-4:2008) and mitigation of alkali-aggregate reactivity (ABNT NBR 15577-5:2018) was performed. Mortars were developed to carry out tensile strength tests (ABNT NBR 16738:2019) and dimensional variation (retraction or linear expansion) (ABNT NBR 15261: 2005).

PSC reactivity was investigated by measuring the liberated heat during hydration for 72h. The experiments were carried out using a Thermometric Tam Air isothermal calorimeter at a measurement temperature of 25°C. The cement paste with a 0.5 w/c ratio for each sample was mixed with a small ladle for 3 minutes at 1000 rpm and 15 grams were weighted into a flask; the flask was capped and placed into the calorimeter. The initial heat peak was not recorded because the mixing was done externally. The TA Instruments TGA/DSC SDT 2960 was used for thermogravimetric measurements in part of heat of hydration samples. with a heating rate of 10ºC/min from room temperature to 1000ºC. An argon flux was used in the heating chamber.

The rheological profile (stress x shear rate) of the cement pastes (water/cement ratio equal to 0.45) was determined by means of rotational rheometry using parallel plates with two hysteresis cycles. being an acceleration ramp with a rate of increasing shear from 0 to 100 s-1 for 120 seconds and a deceleration ramp from 100 to 0 s-1 for a further 120 seconds. This acceleration and deceleration ramp was measured twice. because in the first cycle. the paste may be influenced by possible heterogeneities.

The mini slump method was developed by Kantro (1980) and adopted for determining the consistency of cement pastes. This method consists of a truncated-conical acrylic mold and a glass plate.
Under the glass plate, a sheet of paper is positioned, used to measure two orthogonal diameters of the paste after removal from the mold. The objective of this test is to verify the loss of slump with the various cementitious compositions studied.

3. Results and Discussion

The compressive strength, tensile strength, and dimensional variation presented results close to each other, which shows little influence of the briquette on these parameters (Table 1). The values of compressive and flexural tensile strength show that the materials can be used in cementitious composites. The test for determining the potential attenuation of expansions by alkali-aggregate reaction shows that the three compositions are also effective as attenuating materials for this phenomenon, in addition to not increasing the expansion, even though the "green briquettes" slags had a higher alkali content.

Tab. 1 Mechanical and physical test of cements/%

Slags	Compressive strength (MPa) [(a)]		Flexural tensile strength (MPa)		Dimensional variation (mm/m)	Reduction of expansion by alkali aggregate reaction (%)	
	7d	28d	7d	28d	28d	Reactive Aggregate 1	Reactive Aggregate 2
PSC-SR	22.8	30.3	4.9	6.9	-0.98	23.8	15.6
PSC-SGBA	21.2	28.9	4.3	6.7	-1.02	28.5	12.5
PSC-SGBB	21.4	26.5	5.3	5.7	-0.62	19.0	6.3

(a): The limits specified in NBR 11578 (class 32) for ages 7 and 28 days are ≥20.0 and ≥32.0 MPa, respectively.

Tab. 2 Physical test of cements (fresh paste)

Slags	Apparent viscosity	Plastic viscosity	Yield stress	Mini slump	Setting time (min) [(b)]		Total hydration heat (3d)
	(Pa.s)	(Pa.s)	(Pa)	(mm)	Start	Final	($J.g^{-1}$)
PSC-SR	2.064	1.30	76.43	51	*n.t.*	*n.t.*	256.5
PSC-SGBA	1.082	0.66	47.62	49	210	285	260.4
PSC-SGBB	1.452	0.93	46.94	25	195	285	255.5

n.t.: it was not possible to determine the paste of normal consistency after 9 attempts.

(b): The limits specified in NBR 11578 (class 32) start and final setting time are ≥ 60 and ≤ 600 min, respectively.

The plastic viscosity of PSC-SGBA and PSC-SGBB decreased in relation of PSC-SR, indicating a better packing of particles in the mixture may have occurred, leaving more water in the system and thus requiring a lower yield stress. However, it is possible that there was an influence caused by the difference in specific area between the slags, causing higher water demand (BET, m²/g: SR=0.74; SGBA=0.98; SGBB=1.10). Although it was not possible to carry out the setting time test on the PSC-SR sample, the results of the other cementitious compositions show little variation and are within the limits of the standard (Table 2).
Regarding the heat of hydration of PSC-SGBA and PSC-SGBB cements showed low induction period, followed by increase during the acceleration. It is believed that this phenomenon is due to the increased availability of alkalis. About the cumulative heat in the first three days (72 hours), PSC-SGBA and PSC-SGBB showed values similar PSC-SR cement. It was observed in most folders forming a secondary shoulder after the acceleration period. This second shoulder is typical reactions from slag which has lower reactivity than the clinker (Figure 1).

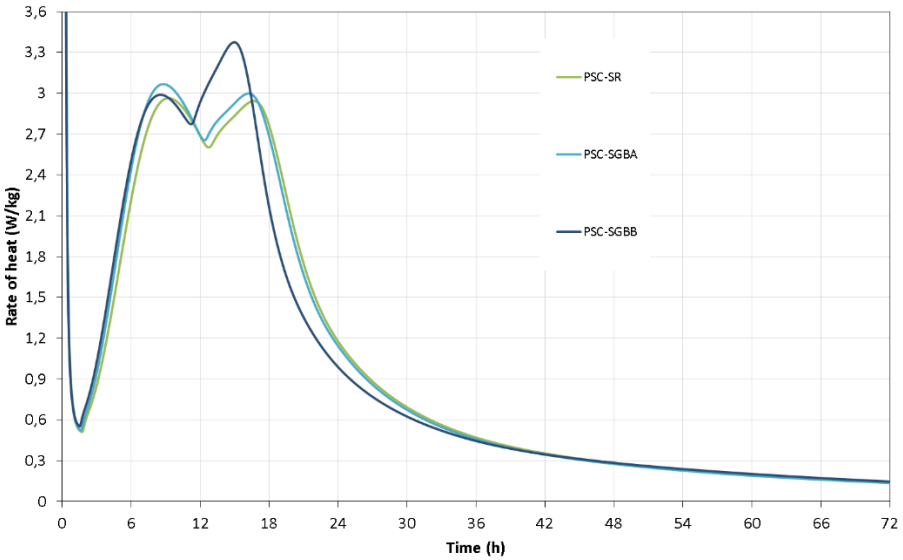

Figure 1 Calorimetry curves of the OPC and PSC cements

In general, the PSC cement pastes has typical Portland cement profile, and shape variations, time and rate of induction periods, acceleration and deceleration consistent with the PSC-BFS behavior. It is possible that these variations can be compensated according to the amount of slag and optimal SO_3 content in cements in function of mechanical performance. According Wang Q. *et al.* (2011) some researches showed that the setting time of cement and concrete became longer by replacing part of cement with steel slag, and the more the replacement the longer the setting time, and that one of the main reason for the long setting time of cement steel slag complex binder is its long dormant period.

According XRD (Figure 2) and TG/DTG (Figure 3) results of samples submitted to heat of hydration, there was formation of portlandite [$Ca(OH)_2$], ettringite [$Ca_6Al_2(OH)_{12}(SO_4)_3.26H_2O$], monocarboaluminate ($Ca_4Al_2O_6(CO_3).11H_2O$), which are common in Porland cement pastes. Part of non-hydrated mineral phases such belite (C_2S), brownmillerite (C_4AF), Åkermanite – Gehlenite [$Ca_2\ (Al_{0.65}\ Mg_{0.35})\ ((Al_{0.65}\ Si_{1.35})\ O_7$) and Åkermanite [$(Ca_{1.53}\ Na_{0.51})\ (Mg_{0.39}\ Al_{0.41}\ Fe_{0.16})\ Si_{2.0}\ O_7$)] was found by XRD.

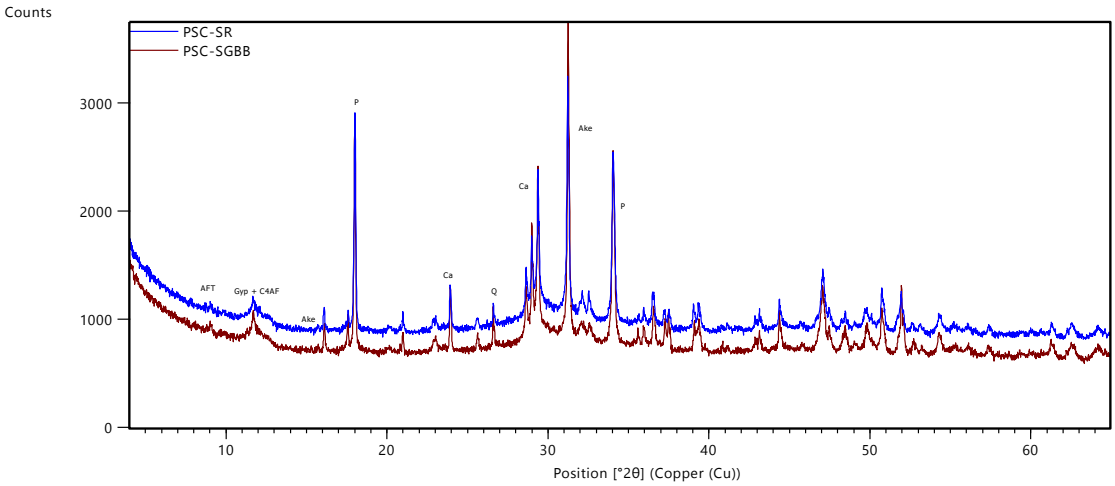

Figure 2 XRD patterns of the PSC pastes, where: AFT: ettringite; Gyp: Gypsum; C4AF: brownmillerite; P: portlandite; C: calcite; Ake: Åkermanite.

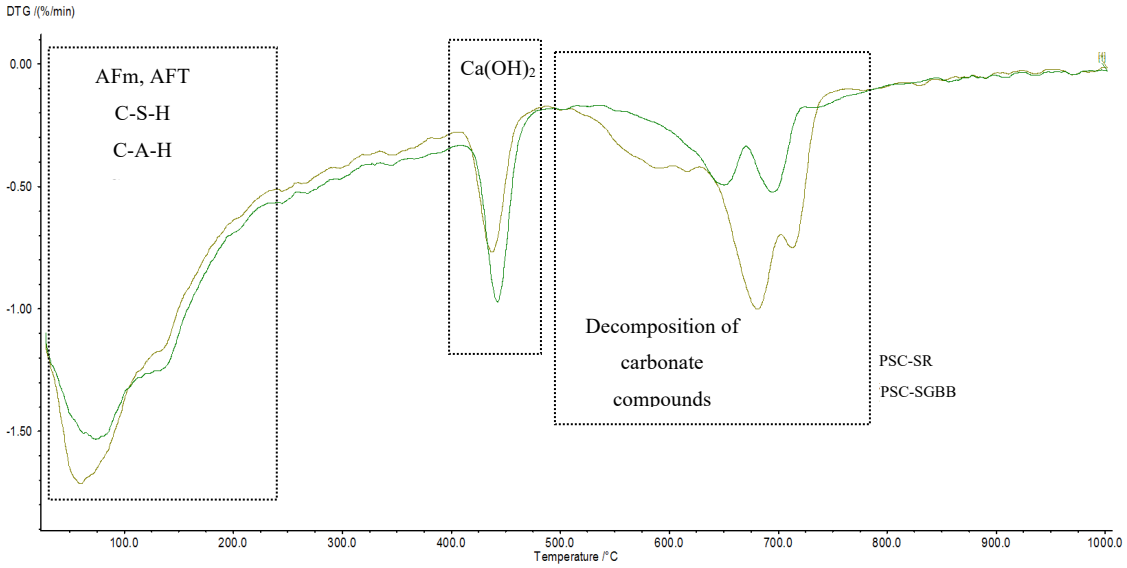

Figure 3 DTG curves of the PSC pastes

In terms of hydrated phases generation of mineral phases present in PSC´s and $Ca(OH)_2$ and hydration phases generation, the performance was following: PSC-SGSB > PSC-SGSA > PSC-SR. Slags contained

akermanite phases as principal phases who present low hydraulic reactivity (Shi C. et al., 2005). TGA curve presented a slight weight increase starting at 550ºC, associate to the recrystallization phenomena of amorphous phase (Ramachandran, V. S. et al., 2002) and decomposition of carbonate compounds.

4. Conclusions

Results of compressive, tensile strength and dimensional variation of PSC contained slags from iron ore "green briquette" indicate application viability, without significant variations between exemplary. Although the "green briquerttes" slags present a higher amount of alkali than the reference slag, the test for the determination of the mitigation potential of expansions by alkali-aggregate reaction demonstrates that the materials can also be used for this purpose.
Concretes were developed from the same cement mixtures discussed in this work, which were submitted to characterization and durability tests. The results follow the trend of those presented in this work, and will be part of a new article.
The mineralogical modification in steelmaking slag is a potential tool to produce a kind of supplementary cementitious material to obtain durable concretes with requirements of long service life, considering the relevance to use low environmental impact cement, produced with non-conventional raw materials.
It's recommended to apply other studies focusing process optimization, durability and performance of these PSC cements, as well for increases the reactivity of the reference and "green briquettes" slags.

References

- KANTRO, D. L. Influence of water-reducing admixtures on properties of cement paste: a miniature slump test. Cement, Concrete and Aggregates, Orlando, v. 2, 1980.
- Ramachandran, V. S. et al. Handbook of Thermal Analysis of Construction Materials. IRC-NRCC. Noyes Publications, New York, 2002, 691p.
- Wang, Q.; Yan, P.; Han, S. The influence of steel slag on the hydration of cement during hydration process of complex binder. Science China Technological Sciences, v. 54, n° 2, p. 388-394, 2011.

The 16th International Congress on the Chemistry of Cement 2023 (ICCC2023)
"Further Reduction of CO_2 -Emissions and Circularity in the Cement and Concrete Industry"
September 18–22, 2023, Bangkok, Thailand

Microstructure characterization of (A/F) H_3 phases with different alkali concentrations based on calcium sulfoaluminate cement

Jiangchuan Li[1], Jun Chang[2*]

[1,2]*School of Civil Engineering, Dalian University of Technology, Dalian, 116024, China*
[1]*E-mail: jclidut@163.com,* [2*]*E-mail: mlchang@dlut.edu.cn*

ABSTRACT

The effect of different pH on the formation of the synthesized (A/F) H_3 phase was characterized and investigatied based on calcium sulfoaluminate cement. The results show that the (A/F) H_3 phases with different Al/(Fe+Al) ratios at different pH have a crystalline structure and leads to a transition between microcrystalline and well-crystalline structures of the (A/F) H_3 phases. Low pH is not conducive to the formation of good crystals, while high pH is beneficial. At the same time, the higher Al/(Fe+Al) ratios leads to the precipitation of AH_3 phase crystals in an alkaline. In addition, the microscopic morphology of the (A/F)H_3 phase changes from a microcrystalline nano-granular to a good needle-like crystal structure at pH=6-12.5. The substitution of Al leads to a significant change in the particle morphology and agglomeration structure of the (A/F) H_3 phase, and the aspect ratio was significantly reduced.

KEYWORDS: *Calcium sulfoaluminate cement, (A/F) H_3 phase, Crystal, Microstructure*

1. Introduction

Calcium sulfoaluminate cement (CSA) has attracted widespread attention due to its potential in terms of low-carbon, early strength, quick-setting and anti-seawater erosion properties (Subramanian et al. 2018), which is closely related to the hydration products in CSA. In past studies, it was found that the AH_3 phase has a filling and compacting effect in the hydration products of CSA(Huang et al. 2019), and that higher contents of AH_3 are favourable for obtaining higher elastic modulus and hardness to cement pastes (Hu et al. 2017). The FH_3 phase is inevitably generated by the hydration of the CSA cement, although this is in small amounts. The variation in Fe/Al ratio forms different types of ferrite phase minerals, which provides the potential for the formation of more FH_3 phases and offers further potential for improved CSA properties. However, it has been reported that the gel produced by the hydration of the iron phase is an Fe-containing oxide or hydroxide (A,F)H_3 (Buenfeld 2003). At the same time, a recent study showed that the Al in the hydrated product of the vitrified C_4AF enters the Fe-containing gel (FH_3), and flake crystals appear on the surface of the FH_3 gel (Zhang et al. 2021). As the study progressed, it was not fully understood whether Al in the hydration products substituted for Fe in whole or in part, or whether (A,F)H_3 was formed, although the formation of (A,F)H_3 in the hydration products had been detected. In previous studies, it was found that alkalinity affects the microstructure of the AH_3 phase, and AH_3 is converted from microcrystalline to good crystal by adjusting the pH (Zhang et al. 2018). In addition, (A/F)H_3 has a good crystal structure under high pH (pH=12.5) (Li et al. 2022). Therefore, the study of the effect of different pH on the (A/F)H_3 phase contributes to a comprehensive understanding of the microstructure of the hydration products of CSA cements. Therefore, the purpose of this research was to characterize the microstructure of (A/F)H_3 phases at different pH to gain a comprehensive understanding of the evolution of (A/F)H_3 phases.

2. Experimental procedure

2.1 Materials and preparation of (A/F)H_3 phase The chemicals used in the experiments were AR grade $AlCl_3{\cdot}6H_2O$ (≥99%), $FeCl_3{\cdot}6H_2O$ (≥98%) and NaOH (≥99%) produced by Sinopharm and no further purification was required before use. The procedure for sample preparation is shown in Figure 1.

Fig. 1 Procedure for the preparation of Al-substituted ferric hydroxide

2.2 Characterization method XRD data of dried powder samples were acquired in an X-ray diffractometer (Bruker D8 advanced) equipped with Cu Kα radiation in steps of 0.02° at 5°-80° with a single dwell time of 0.5 seconds. SEM images of the synthetic samples were viewed through a FEI NOVA Nano SEM 450 scanning electron microscope. TEM images of samples prepared on copper grids

after ultrasonic dispersion with anhydrous ethanol were observed with a JEM-F200 field emission transmission electron microscope. High resolution transmission electron microscopy (HRTEM), selected area electron diffraction (SAED) and energy dispersive X-ray spectroscopy (EDS) were also viewed and analysed.

3. Results and discussion

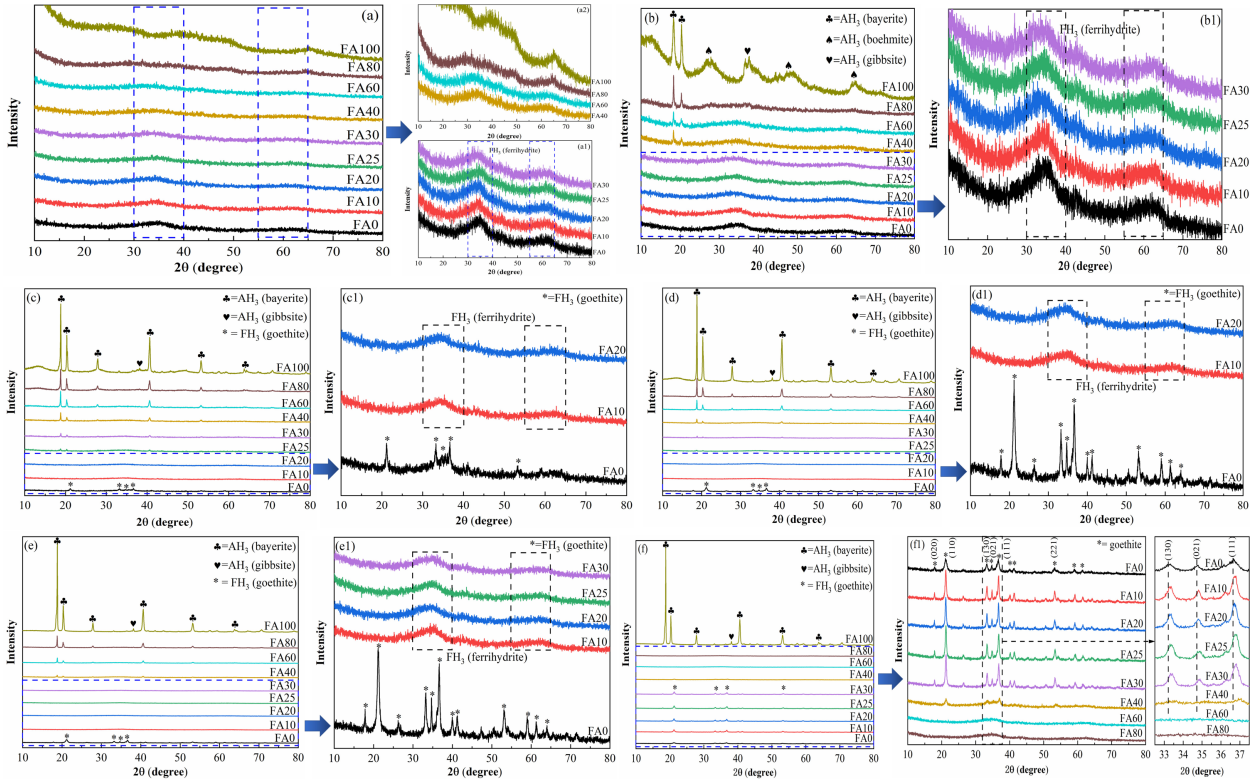

Fig 2. XRD patterns of (A/F)H_3 at different pH: (a) pH=6; (b) pH=8; (c) pH=10; (d) pH=11; (e) pH=12; (f) pH=12.5

Figure 2 shows the XRD patterns of the (A/F)H_3 phases at different pH. It can be clearly observed that at pH=6,8 the sample FA0 (FH_3) has two broad diffraction peaks at ~34°(2θ) and ~60°(2θ) respectively, which is found to be consistent with a typical ferrihydrite patterns by qualitative XRD analysis. This suggests that the FH_3 phase is a microcrystal with poor crystallinity at pH=6, 8. It is reported that ferrihydrite is a typical weakly crystallized iron hydroxide with a particle size of 2~6 nm, and is one of the most common metastable initial precipitated phases (Michel 2007). When Al is substituted for Fe in $Fe(OH)_3$, samples with different Al/(Fe+Al) ratios (FA10, FA20, FA25, FA30) have diffraction peaks consistent with ferrihydrite, and no other evidence of diffraction peaks for the Fe or Al phases is observed. This demonstrates that Al and $Fe(OH)_3$ form mixed Al-containing ferrihydrite crystals ((A/F)H_3). As the Al/(Fe+Al) ratios increases, the diffraction peaks become gradually broader and less symmetrical, the crystallinity of the sample decreases and the crystallisation of ferrihydrite is hindered, which implies defects and disorders in the crystal structure. More importantly, the relative intensity of the diffraction peaks decreases and 2θ is shifted towards a higher angle, and the Al content causing a more significant shift in the diffraction peaks. This information indicates that Al enters the ferrihydrite lattice leading to lattice distortion and a reduction in the interplanar spacing (d-spacing). Furthermore, the difference is that at pH=8, 40 mol% Al or higher content results in precipitation of AH_3 phase crystal. FA0(FH_3) at pH=10,11,12,12.5 gradually appear the diffraction peaks of goethite in XRD, which indicates that the increase of pH is beneficial to increase the nucleation rate and formation of good crystals of FH_3. In contrast, samples with different Al/(Fe+Al) ratios (FA10, FA20, FA30) show broad diffraction peaks of ferrihydrite at pH=10,11,12, which may be due to Al delaying the mineral dissolution dynamics on the surface of ferrihydrite (Jentzsch et al. 2006). This suggests that the increase in Al content decreases crystal growth nucleation and is unfavourable for the formation of goethite. At Al/(Fe+Al) ratios of 30 mol% or higher, diffraction peaks of AH_3 phase crystals appear in the XRD patterns at pH=10,11,12. This is due to the high content of Al not being able to form further stable precipitates with Fe, resulting in the precipitation of $Al(OH)_3$ crystals. This indicates that the increase in Al content at

pH=10,11,12 is not conducive to the formation of $(A/F)H_3$ phase crystals, but rather to the precipitation of AH_3 phase crystals. At pH=12.5, samples with different Al/(Fe+Al) ratios (FA10, FA20, FA25, FA30, FA40) were shown as the diffraction peaks of goethite in XRD, which indicated that Al and $Fe(OH)_3$ formed well mixed crystals of Al-containing goethite ($(A/F)H_3$). In addition, with the increase of the Al/(Fe+Al) ratios, the 2θ of Al-containing goethite shifts to a higher angle, which is caused by the decrease in the interplanar spacing (d-spacing). More detailed information about this change has been discovered by our research (Li et al. 2022), which means the possibility of the fact that Al substitutes for Fe to form $(A/F)H_3$ phase.

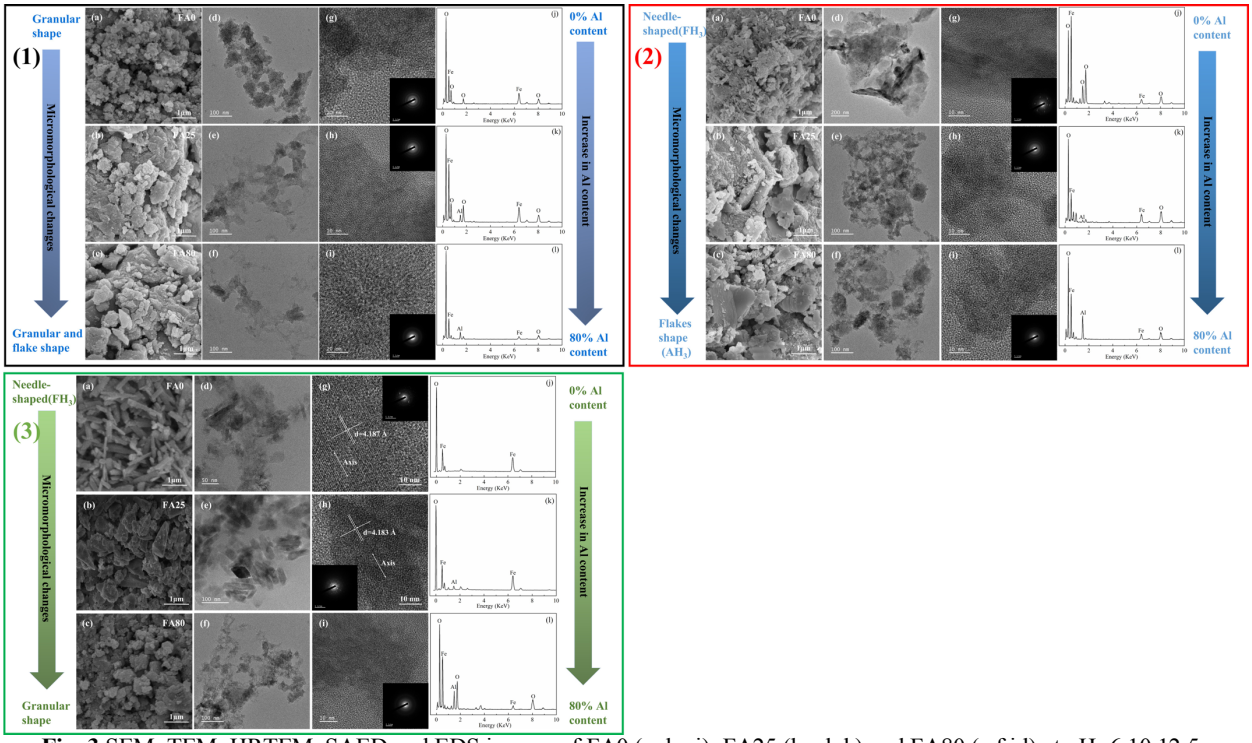

Fig. 3 SEM, TEM, HRTEM, SAED and EDS images of FA0 (a,d,g,j), FA25 (b,e,h,k) and FA80 (c,f,i,l) at pH=6,10,12.5

Scanning electron microscopy and transmission electron microscopy images of samples FA0, FA25, FA80 associated with 0 mol%, 25 mol%, 80 mol% Al at pH=6,10,12.5 are shown in Figure 3. The microscopic morphology of the $FA0(FH_3)$ sample without Al was observed to be granular (Fig. 3(1)a) and agglomerated in tiny particles (Fig. 3(1)d), which are clearly visible in profile and have an average particle size of approximately 2-3 nm. In addition, lattice streaks exist but are not clear (Fig. 3(1)g), and clear and regular diffraction rings are revealed through SAED, which indicate that the sample was nano-granular and was crystalline with a microcrystalline structure. As the Al content increases, the particle shape of the sample (FA25, FA80) is similar to FA0. The difference is that the particles become larger and the flakes are observed (Fig. 3(1)b, c), and the agglomeration structure is also significantly changed (Fig. 3(1)e, f), the average particle size is approximately 3-4nm, 4-5nm, respectively, which is related to the increase in Al content (Fig. 3(1)j, k, l) and the aggregation of smaller size nano-particles in $(A/F)H_3$ particles. The diffraction ring and unclear lattice stripes were observed in FA25 and FA80, and the diffraction ring of FA80 became diffuse (Fig. 3(1)h, i), which means that the Al-containing samples FA25 and FA80 are microcrystals and the crystallinity gradually weakens. At pH=10 (Fig. 3(2)), sample FA0 shows a typical needle-like structure of goethite (Fig. 3(2)a, d), which has an average particle size (length) of approximately 230 nm. HRTEM and SAED show clearly visible lattice streaks and diffraction spots, respectively (Fig. 3(2)g), which obviously indicate a good crystal structure of FA0 at pH=10. Samples FA25, FA80 were associated with 25 mol% and 80 mol% Al, respectively, and their microstructures were significantly different compared to FA0. The microstructures of FA25, FA80 shifted to a flake structure (Fig. 3(2)b, c) and FA25 and FA80 had distinctly different agglomerate structures (Fig. 3(2)e, f). HRTEM and SAED revealed clear lattice streaks and diffraction rings respectively (Fig. 3(2) h, i), and the SAED image of FA80 showed a more crystalline structure compared to FA25. This is attributed to the difference in Al content (Fig. 3(2) j, k, l), and corresponds to the XRD results, which

indicate that FA25, FA80 are microcrystalline structures at pH=10. The author believes that the crystalline phase associated with AlOOH perhaps exists as a separate phase inside or on the surface of the (A/F)H_3 particles, rather than as distinct $Al(OH)_3$ particles. At pH=12.5 (Fig. 3(3)), the sample FA0 has a distinct needle-like structure of goethite (Fig. 3(3) a, d), and the average particle size (length) is about 375 nm. Compared with FA0 at pH=10, the needle-like structure of FA0 at pH=12.5 is clearer and more regular, and the average particle size is larger. HRTEM and SAED display clear lattice streaks and diffraction spots, respectively, which indicate that FA0 has a distinct crystal structure. As the Al/(Fe+Al) ratios increases, the substitution of Al interferes with the growth of the typical needle-like structure of goethite, specifically, the width of the needle-like structure gradually increases and the aspect ratio gradually decreases. Compared with FA0, the morphology of FA25 and FA80 was transformed into rod-shaped and granular (Fig. 3(3) b, c), and have significantly different aggregate structures (Fig. 3(3) e, f). Meanwhile, FA25 in HRTEM and SAED showed clear lattice streaks and diffraction spots (Fig. 3(3) h), while the lattice stripes of FA80 became unclear, and SAED was shown as a diffraction ring (Fig. 3(3) i), which indicates that the crystallinity becomes weaker. The lattice spacing (d-spacing) of FA0, FA25 was analysed and measured by DigitalMicrograph software to be 4.187 Å, 4.183 Å respectively, which can be indexed to the 110 crystal surface of the goethite crystal. These variations imply that the microstructural changes of the (A/F)H_3 phase are related to the Al content (Fig. 3(3) j,k,l) and that the crystal structure changes with Al substitution.

4. Conclusions

The (A/F) H_3 phase changes from the microcrystalline structure of Al-containing ferrihydrite to a good crystal structure of Al-containing goethite at pH=6-12.5, and the increase in Al substitution affects the crystallinity and crystal structure of the (A/F) H_3 phase. At pH=6, the (A/F) H_3 phase is Al-containing ferrihydrite with a microcrystalline structure, and the increase in the Al/(Fe+Al) ratio reduces the crystallinity. At pH=8,10,11,12, the incorporation of Al tends to form microcrystals of Al-containing ferrihydrite, and the excessive Al/(Fe+Al) ratio leads to the precipitation of Al $(OH)_3$ crystals. At pH=12.5, the incorporation of Al formed good crystals of Al-containing goethite, while high Al/(Fe+Al) ratios (>40 mol%) resulted in reduced crystallinity and altered crystal structure.

The microscopic morphology of the (A/F) H_3 phase changes from a microcrystalline nano-particle shape to a good needle-like crystal structure at pH=6-12.5. The incorporation of Al causes the particle size, agglomeration structure and aspect ratio of the (A/F) H_3 phase to be altered. At pH=6, the (A/F) H_3 phase is a microcrystalline nano-granular structure, and the increase in Al substitution causes the particles to become larger and flaky. At pH=10, the increase in Al substitution resulted in the (A/F) H_3 phase to change from a good needle-like crystal structure to a flake-like microcrystalline structure. At pH=12.5, the (A/F) H_3 phase grows preferentially into good needle-like crystals. The increase in Al substitution leads to a decrease in particle length and a transition to granular shape. At the same time, the crystallinity decreases and the aspect ratio increases.

Acknowledgements

This research was supported by the National Natural Science Foundation of China (52172015). In addition, the authors acknowledge the assistance of DUT Instrumental Analysis Center.

References

Buenfeld, N. R. (2003) "Structure and performance of cements, 2nd edition", *Engineering Structures*, 25 (1):127.

Huang, G., Pudasainee, D. (2019) "Hydration reaction and strength development of calcium sulfoaluminate cement-based mortar cured at cold temperatures", *Construction and Building Materials*, 224:493-503.

Hu, C., Hou, D., Li, Z. (2017) "Micro-mechanical properties of calcium sulfoaluminate cement and the correlation with microstructures". *Cement and Concrete Composites*, 80:10–16.

Jentzsch, T. L., Penn, R. L. (2006) "Influence of aluminum doping on ferrihydrite nanoparticle reactivity", *The Journal of Physical Chemistry B*, 110 (24): 11746-11750.

Li, J., Chang, J. (2022) "Characterization of (A/F) H_3 phase microstructure with different Al/(Fe+Al) ratios based on calcium sulfoaluminate cement", *Journal of Materials in Civil Engineering*.

Michel, F. M. (2007) "The structure of ferrihydrite, a nanocrystalline material", *Science*, 316 (5832) 1726-1729.

Subramanian, S., Moon, S. W., et al. (2018) "CSA-Treated Sand for Geotechnical Application: Microstructure Analysis and Rapid Strength Development", *Journal of Materials in Civil Engineering*, 30 (12): 04018313.

Zhang, G., Ren, Q., He, J., et al. (2021) "New understanding of early hydration of C4AF under surface vitrification", *Powder Technology*, 377:372-378.

Zhang, Y., Chang, J. (2018) "Microstructural evolution of aluminum hydroxide gel during the hydration of calcium sulfoaluminate under different alkali concentrations", Construction and Building Materials, 180: 655-664.

The 16th International Congress on the Chemistry of Cement 2023 (ICCC2023)
"Further Reduction of CO_2 -Emissions and Circularity in the Cement and Concrete Industry"
September 18–22, 2023, Bangkok, Thailand

PCE Superplasticizers for a Green Binder Containing Calcined Clay

R. Li[1], J. Shi[2], T.B. Sui[3], K.-C. Thienel[4], and J. Plank[5] *

[1] *Technische Universität München, Munich, Germany*
Email: ran.li@tum.de
[2] *Technische Universität München, Munich, Germany*
Email:jie.shi@tum.de
[3] *Sinoma International Engineering Co., Ltd, Beijing, China*
Email: suitongbo@sinoma.com.cn
[4]*Universität der Bundeswehr München, Neubiberg, Germany*
Email: christian.thienel@unibw.de
[5] *Technische Universität München, Munich, Germany*
Email: johann.plank@tum.de

ABSTRACT

Calcined clays have attracted significant attention as a low-carbon supplementary cementitious material. In this study, the dispersing performance of three PCE superplasticizers varying in chemical structure (MPEG, HPEG and IPEG based polymers) were investigated in composite cements containing two different calcined clays. These two calcined clays were obtained from different regions and differ significantly in their metakaolin contents (~ 23 wt.% vs. ~ 51 wt.%). They were blended with Ordinary Portland cement (OPC) at a clinker substitution ratio of 30 wt.%.

It was found that as compared to OPC, both calcined clays decrease workability and substantially increase the water demand due to their higher fineness. Furthermore, the results differ depending on the mineral composition of the calcined clay (Sposito, 2022). For example, an increase in superplasticizer dosage of ~ 400 % as compared to neat OPC was recorded for the sample holding 51 wt.% metakaolin, while it was only ~ 60 % for that containing 23 wt.% metakaolin. In addition, among all the PCE samples tested, the HPEG PCEs disperse these composite cements best, followed by IPEG PCEs while MPEG PCEs performed the least.

It is concluded that the workability of calcined clay blended cements significantly depends on their specific mineral composition. High metakaolin content present in a calcined clay decreases the workability of the composite cement considerably.

KEYWORDS: *Common Clay, Calcined Clay, Metakaolin, Polycarboxylate Superplasticizer, Workability*

1. Introduction

Supplementary cementitious materials (SCMs) which exhibit pozzolanic reactivity attract substantial interest (Scrivener et al., 2018; Shi et al., 2019). Among all SCMs, calcined clay is drawing more and more attention due to its global ubiquitous availability and its high pozzolanic reactivity (He et al., 1995). Generally, the thermal activation of clay is carried out at temperatures ranging from 600 to 1100°C. In the process of calcination, dehydroxylation of the clay associated with structural changes occurs resulting in partially amorphous phases exhibiting pozzolanic reactivity. According to those studies (He et al., 1995), metakaolin (calcined kaolinite) possesses much superior pozzolanic reactivity as compared to metamontmorillonite or metaillite. Its high pozzolanic reactivity is attributed to the easier release of Si and

Al and further promoted by a disordered structure (Tironi et al., 2014). In cement, metakaolin reacts with calcium hydroxide and produces calcium silicate hydrate (C-S-H) and alumina-containing hydrate phases including C_4AH_{13}, C_3AH_6 and C_2ASH_8. Thus, metakaolin presents a valuable component in calcined clays used in composite cements as it provides higher early strength (Tironi et al., 2014). Besides, metakaolin can also improve other concrete properties such as reduced chloride ingress (Batis et al., 2005) and shrinkage reduction at early ages (Brooks and Megat Johari, 2001). Unfortunately, a high metakaolin content present in the composite cement results in decreased workability, as was reported in some previous publications (Li et al., 2021; Schmid and Plank, 2020). In addition to the metakaolin contents, also the calcination conditions (flash calciner vs. rotary kiln, calcination temperature), particle size and specific surface area influence the workability of such composites cement. Yet, the mineralogical composition of a calcined clay (especially for metakaolin contents) presents a prominent factor with respect to its properties (Li et al., 2022).

Therefore, in this study, two calcined clays exhibiting different metakaolin contents were sourced from different regions. At first, three PCE superplasticizers of different chemical composition (MPEG, HPEG and IPEG precast type products) were synthesized and characterized. Their high quality was confirmed using gel permeation chromatography. Then, the impact of the different calcined clays on PCE dosage requirements in composite cements holding 30 wt% of the calcined clays was investigated. From the results, it is found that HPCE PCE works particularly well in such calcined clay blended cements as compared to others.

2. Materials and Methods

2.1 Cement and calcined clays

The cement used in this study was an ordinary Portland cement CEM I 42.5 R provided by Schwenk company (Allmendingen plant, Germany). Its Blaine value was 3130 cm^2/g while its d_{50} value was18.1 µm (laser granulometer). Two calcined clay samples with different metakaolin contents (23% and 51%) were used in this study. Based on their metakaolin content, they were named as CC23 (BET SSA=3.9 m^2/g, d_{50}=13.2 µm) and CC51 (BET SSA=13.2 m^2/g, d_{50}=10.4 µm) respectively. The mineral compositions of calcined clay samples are listed in **Table 1**.

Table 1 Mineral composition of calcined clay samples

Phase	Illite-Smectite	Muscovite	Chlorite	Quartz	Feldspars	Calcite	Sulfates	Silicates	Hematite	Pyrite	Rutile	Amorphous
CC23	4.6	2.2	0.4	16.2	6.0	0.6	1.6	6.3	0.6	1.1	-	60.8
CC51	-	23.8	-	13.8	-	-	-	-	-	-	0.3	62.2

2.2 PCE superplasticizers

A series of chemically diverse PCEs prepared from ω-methoxy poly(ethylene glycol) methacrylate ester (MPEG), methallyl poly(ethylene glycol) ether (HPEG) and isoprenyl oxy poly(ethylene glycol) ether (IPEG) macromonomers were utilized. These PCEs are characterized by high anionicity and relatively long PEG side chains which identifies them as PCEs providing high initial fluidity (precast concrete type PCEs). The PCE samples were deployed to gel permeation chromatography (GPC) in order to determine their molecular properties (M_w, M_n, PDI).

2.3 Dispersing performance

The dispersing performance of the PCE samples was determined using a modified “mini slump” test according to DIN EN 1015. A fixed water-to-binder ratio of 0.5 was applied. At this w/b ratio, the dosages of the superplasticizer samples to reach a spread flow of 26 ± 0.5 cm were determined. The modified “mini slump” test was carried out as follows: 300 g of binder were added to 150 ml of deionized water contained in a porcelain cup and stirred manually for 10 s with a spoon. Then PCE solution was added to the mixture

and homogenized for 50 s. After 1 min of rest the suspension was mixed again for another minute. The amount of water contained in the PCE solution was subtracted from the total amount of mixing water to maintain a constant w/b ratio.

3. Results

At first, the PCE samples used in this study were characterized by GPC. The respective spectra are shown in **Figure 1** while **Table 1** lists their molecular properties.

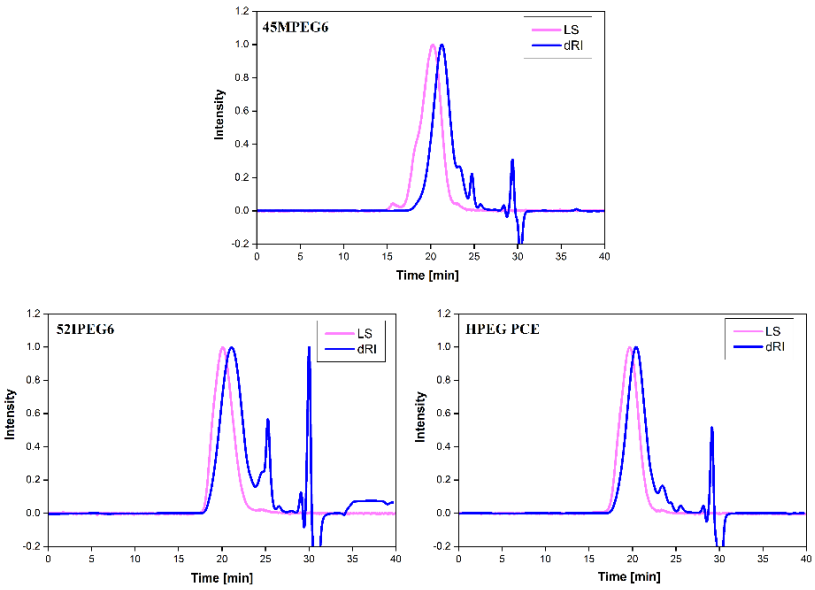

Figure 1. GPC spectra of the PCE samples tested (45MPEG6, 52IPEG6 and HPEG PCE)

According to these data, all PCE samples exhibit properties which are characteristic for high quality PCE polymers, namely relatively low polydispersity index (PDI) values (1.8 - 2.4) and high rates for macromonomer conversion (86 - 95 %). The detailed molecular parameters of the PCE polymers are shown in **Table 1**.

Table 1 Molecular properties of the PCE polymers used in this work.

Polymer sample	M_w [Da]	M_n [Da]	PDI	MM conversion
45MPEG6	25,180	10,610	2.37	95%
52IPEG6	31,500	13,700	2.30	86%
HPEG PCE	35,340	19,490	1.81	92%

Next, the dispersing ability of the three commonly used precast type PCE samples (high-range water-reducing type) in pastes prepared from neat OPC and OPC/CC blends at a clinker substitution rate of 30 wt% was assessed.

According to the results presented in **Figure 2** it becomes clear that the addition of calcined clay generally prompts higher PCE dosages. It also increases with the increase of metakaolin content. For example, an increase in HPEG PCE dosage of ~ 400 % as compared to neat OPC was recorded for the sample CC51, while it was only ~ 60 % for CC23.

On the other hand, different PCEs exhibited different dispersing effectiveness. The HPEG PCE provided the best dispersing ability, in both OPC and calcined clay composite cement, followed by the 52IPEG6 while the 45MPEG6 consistently required the highest dosages. Thus, the effectiveness of the PCE superplasticizers in the calcined clay blended cements correlated with their performance in neat OPC.

It suggests that PCEs which work well in neat OPC presumably will also exhibit a good performance in calcined clay composite cements.

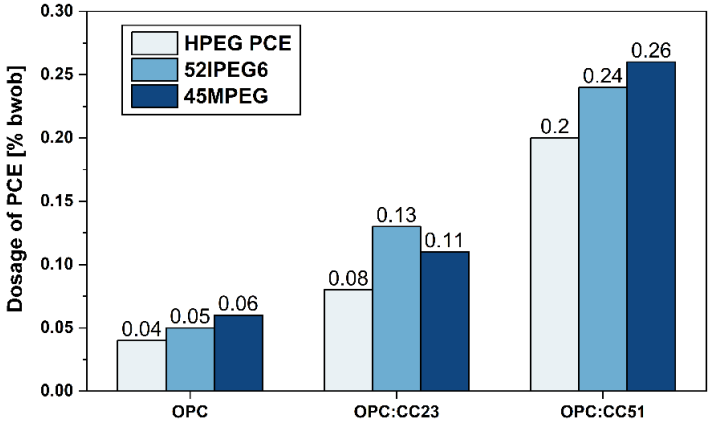

Figure 2. PCE dosages required in cement pastes prepared from OPC and a calcined clay blend cement (OPC:CC 70:30) to achieve a spread flow of 26 ± 0.5 cm; w/b ratio = 0.5.

4. Conclusions

In this study it was found that the presence of a calcined clay in a composite cement makes it more difficult to achieve proper workability, especially when the metakaolin content in the calcined clay is high. On the other hand, among all the PCE superplasticizer samples tested (MPEG, IPEG and HPEG), the HPEG PCE produced superior dispersing performance in the calcined clay blended cements.

Acknowledgements

The authors thank Jilin Zhongxin Chemical Group Co. Ltd. for providing the HPEG PCE, Schwenk Cement Co. for supplying the CEM I 42.5 R sample and Clariant Produkte (Deutschland) GmbH for providing the MPEG macromonomer for this study.

References

Batis, G., Pantazopoulou, P., Tsivilis, S., and Badogiannis, E. (2005). "The effect of metakaolin on the corrosion behavior of cement mortars". *Cem Concr Compos* 27, 125-130.

Brooks, J.J., and Megat Johari, M.A. (2001). "Effect of metakaolin on creep and shrinkage of concrete". *Cem Concr Compos* 23, 495-502.

He, C., Osbæck, B. and Makovicky, E., Pozzolanic reactions of six principal clay minerals: activation, reactivity assessments and technological effects. *Cem Concr Res*, 1995. 25 (8): pp. 1691-1702.

Li, R., Lei, L., Sui, T., and Plank, J. (2021). "Effectiveness of PCE superplasticizers in calcined clay blended cements". *Cem Concr Res* 141, 106334.

Li, R., Lei, L., and Plank, J. (2022). " Impact of metakaolin content and fineness on the behavior of calcined clay blended cements admixed with HPEG PCE superplasticizer". *Cem Concr Compos* 133, 104654.

Schmid, M., and Plank, J. (2020). "Dispersing performance of different kinds of polycarboxylate (PCE) superplasticizers in cement blended with a calcined clay". *Constr Build Mater* 258, 119576.

Scrivener, K., Martirena, F., Bishnoi, S., and Maity, S. (2018). "Calcined clay limestone cements (LC3)". *Cem Concr Res* 114, 49-56.

Sposito, R. (2022). *Investigations on the impact of metaphyllosilicates and calcined common clays on the rheology and early hydration of cements admixed with different superplasticizer.* (Dr.-Ing. Cummulative thesis). Universität der Bundeswehr München, Neubiberg, 280.

Shi, C., Qu, B., and Provis, J.L. (2019). "Recent progress in low-carbon binders". *Cem Concr Res* 122, 227-250.

Tironi, A., Trezza, M.A., Scian, A.N., and Irassar, E.F. (2014). "Potential use of Argentine kaolinitic clays as pozzolanic material". *Applied Clay Science* 101, 468-476.

The 16th International Congress on the Chemistry of Cement 2023 (ICCC2023)
"Further Reduction of CO_2 -Emissions and Circularity in the Cement and Concrete Industry"
September 18–22, 2023, Bangkok, Thailand

Impact of C-S-H seeding on hydration and strength of slag blended cement

Xuerun Li* **and Christoph Hesse**

BASF Construction Additives GmbH, 83308 Trostberg, Germany

Email: xuerun.li@basf.com

ABSTRACT

Ground granulated blast furnace slag (GGBFS) blended cements are widely investigated and used. Two different approaches are mostly used to promote the reaction of slag in classic slag blended cement: mechanical activation or chemical activation. Using C-S-H seeding (calcium silicate hydrates seeds) can be attributed to the chemical activation category and is one of the most effective ways to activate slag blended cements.

The impact of C-S-H seeding on the hydration of 50 wt.% slag blended cement was systematically investigated, trying to understand and explore the potential of C-S-H seeding. Compressive strength, calorimetry, in-situ XRD, MIP experiments were carried out. The pore structure of hardened blended cement paste was investigated using mercury intrusion porosimetry.

Results show that C-S-H seeding improves the performance of slag blended cement significantly with regards to strength at early and later stage. Quantitative XRD analyses show how C-S-H seeding influences the clinker hydration kinetics. C-S-H seeding altered the microstructure dramatically by refining the porosity. It was found that the C-S-H seeding promoted the hydration of slag as early as the first measured ages – 1 day according to selective dissolution method. Correlation of strength to heat release and pore structure indicates that there is structural impact of C-S-H seeding besides the impact on kinetics in the hardened samples

KEYWORDS: *slag, C-S-H seeding, microstructure, hydration kinetics, slag reaction*

1. Introduction

Ground granulated blast furnace slag (GGBFS, slag through this paper refers to GGBFS) blended cements are widely investigated and used. The main reasons for using slag in blended cement are: 1) improve the performances of the cement by increasing late strength and durability; 2) reduce the amount of ordinary Portland cement (PC) clinker. The main drawback of using large amounts of slag in blended cement is the reduction of early strength. This is mainly due to the slow reaction of the latent hydraulic slag compared to clinker phases (Kocaba, Gallucci et al. 2012, Durdziński, Ben Haha et al. 2017).
Mechanical activation or chemical activation can be used to enhance the strength of slag blended cement.
Mechanical activation – increase the fineness by grinding: the fineness of the slag is one of the parameters which was investigated Increasing fineness of non-ferrous metallurgy slag could play a role in the enhancement of early strength, nevertheless the improvement was limited (Hallet, De Belie et al. 2020).
Chemical activation - such as Na_2SO_4 and NaOH combined with sodium gluconate could enhance early strength of the blended cement made of white cement and slag to some extent according to Mota et al. (Mota, Matschei et al. 2019).
C-S-H seeding was used to accelerate the cement hydration was applied in cement and pure C_3S by Thomas et al. (Thomas, Jennings et al. 2009).

In this paper, the impact of a commercial C-S-H seeding product (HyCon® S) on 50 wt.% of slag blended cement was investigated.

2. Materials and Methods

Ground granulated blast furnace slag (GGBFS) from EcoCem France was used. With a 7-day heat release of 542.3 J/g slag from R^3 test. The reactivity is comparable to slags reported in the literature(Li, Snellings et al. 2018).
Portland cement (CEM I 52.5 R "Milke Premium") produced by HeidelbergCement AG was used. The powder form of C-S-H seeding (HyCon® S 7042 F) produced by BASF Construction Additives GmbH was used. HyCon® S is based on C-S-H nano particles dispersed by polycarboxylates.
XRD measurements were carried out using Bruker D8 Advance diffractometers. In-situ experiments were carried out on freshly mixed paste covered with a Kapton® film. Rietveld analysis was carried out using Bruker Diffrac.Suite TOPAS version 6.
Mercury intrusion porosimetry (MIP) was carried out using MicroActive AutoPore V 9600. Approximate 1.5 g of 2-3 mm diameter pieces from crushed binder paste slices (after hydration stoppage) were loaded into the measuring chamber.
The mortar sample preparation for strength test were carried out according to the EN 196-1 except the temperature setting and vibration setup. Curing temperature was set to 23 °C (room temperature).
The content of anhydrous slag in the hydrated paste was measured by the selective dissolution technique described by Lumley et al. (Lumley, Gollop et al. 1996) using EDTA and diethylamine.

3. Results

The 1-day strength was particularly enhanced compared to the reference sample without C-S-H seeding: the increments for samples with 3 wt.-% seeding compared to the reference were 159% (see Figure 1(a)). 1.5 wt.-% C-S-H seeding could also improve the strength by more than 100 % at 1 day. Later age strength (28 days) was also enhanced. At the age of 56 and 180 days, 3 wt.-% C-S-H seeding enables slag blended cements with 50 % PC replacement level to perform even better than the pure PC with respect to compressive strength
Hydration kinetics of the cement clinker phases were accelerated significantly, especially at the early hydration period (before 1 day), see Figure 1 (b) and (c). Compared to neat PC reference, the overall heat release of slag blended cement is much reduced even though C-S-H seeding promoted the heat release. The total heat at 1 day of these samples was 169 J/g binder for slag blended cement, much lower than the neat PC reference sample (231 J/g binder).

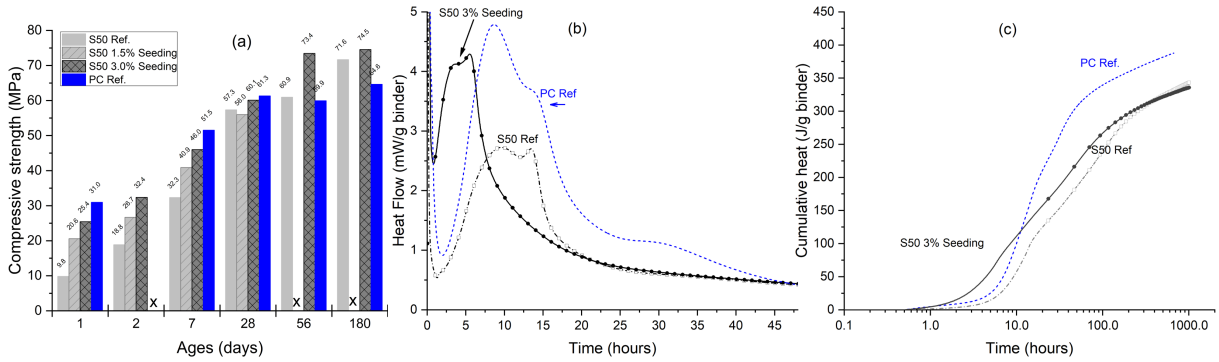

Figure 1 Mortar strength (a), heat flow (b) and cumulative heat release (c)

C-S-H seeding accelerates the hydration of C_3S and C_3A after about 1 hour of hydration as seen in Figure 2. More portlandite was formed with C-S-H seeding during the first 24 hours. The accuracy of the amount of portlandite is quite low due to the Kapton® film which introduces preferred orientation at the interface of the cement paste and the film. A more reliable portlandite content is obtained from the XRD analyses of the fresh disc samples and it is presented in the next sections.

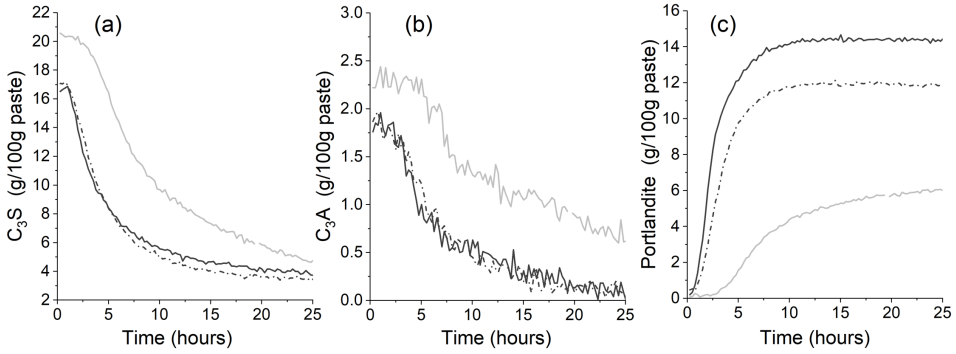

Figure 2 Quantitative in-situ XRD of sample with 50% slag (S50), C-S-H seeding promoted the reaction of the main clinker phases: C_3S, C_2S and C_3A

The degree of reaction (DoR) of slag was significantly enhanced at 1 day with 3% seeding, as is shown in Table 1. At later age, the enhancement of the reaction is less pronounced. The enhanced hydration kinetics in the first days improve not only the early strength, but also the late strength.

Table 1 Degree of reaction (DoR) of slag detected by selective dissolution

Sample	DoR of slag (%)		
Ages	1d	7d	28d
S50 ref	4.3	20.8	28.0
S50 3% C-S-H seeding	10.6	21.9	34.6

The critical pore sizes (values are labelled in the figure) are significantly lower at 1 day with 3% seeding. At later ages (data at 28 days), the critical pore size is still lower when seeding is used, however the difference is not as huge as those at early ages. The improved packing of the hardened cement paste is due to 1) the C-S-H seeding promoting the hydrates nucleation throughout the porous matrix at the very beginning of the hydration process, 2) accelerated clinker reaction during the first day forming large amounts of homogenously distributed C-S-H in the hardened cement paste, 3) the accelerated reaction of slag further densifying the microstructure of the hardened paste.

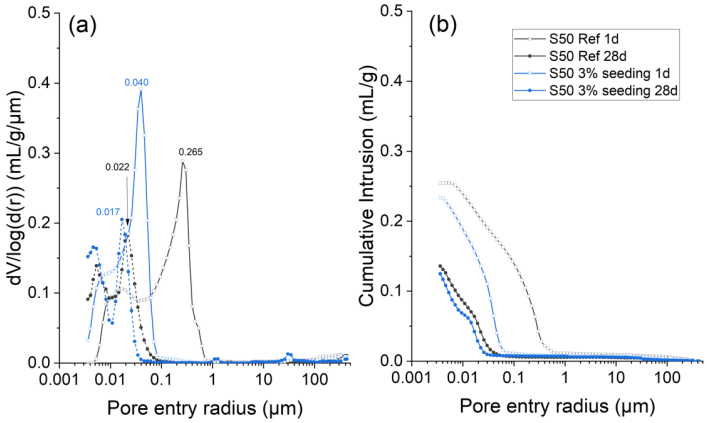

Figure 3 MIP porosimetry analyses of the hydrated paste. The values next to the peaks in (d) to (f) are the critical pore entry sizes in μm.

There is a constant shift of the correlation plot of strength and heat release when 3% C-S-H seeding was used (see Figure 4 (a))). The correlation of the MIP total porosity and critical pore entry size to the strength shows that the strength is correlated to the porosity regardless the mix design and the presence of C-S-H seeding (see Figure 4 (b,c))

Even though the compressive strength generated per heat release for the C-S-H seeded samples are higher than the references as is shown in Figure 4 (a), the overall good correlation of strength to MIP critical pore entry size indicates that the C-S-H seeding refines the pore structure of the hydrated samples thus producing higher strengths (see Figure 4 (b, c)). These two different correlation behaviors of strength to heat release and pore structure indicate that the C-S-H seeding not only enhances the hydration kinetics of the blended binders but also contributes directly to the formation of a finer microstructure of the hardened samples mostly probably by alter the C-S-H density by forming more outer C-S-H.

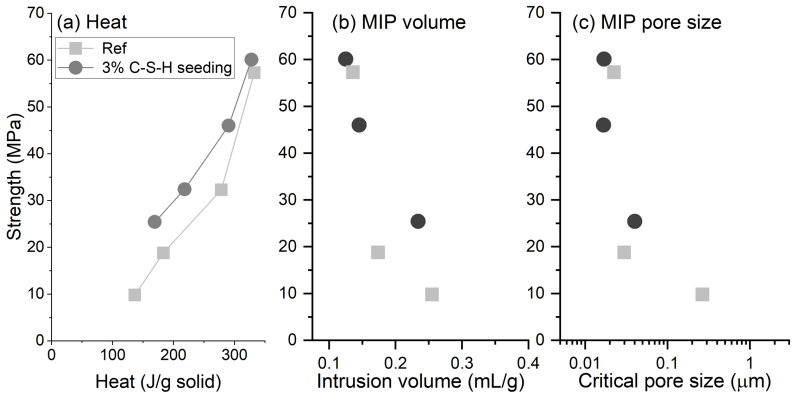

Figure 4 Compressive strength plotted against cumulative heat (a), intrusion volume of MIP (b) and critical pore entry size of MIP (c)

4. Conclusions

C-S-H seeding enhanced the reaction of clinker phases at early ages (<1 day) and slag reaction through the hydration process (up to 180 days as investigated in this paper).

- C-S-H seeding enhanced the strength development of the slag blended cement significantly from early ages to late ages (1 to 180 days).
- C-S-H seeding accelerates the hydration of the clinker phases (C_3A, C_3S) in the blended cement during early age (until a few days). C-S-H seeding accelerates the slag reaction from the beginning of hydration until later ages, at least until the measured age – 28 days.
- Correlation of strength to heat release and pore structure indicates that there is structural impact of C-S-H seeding besides the impact on kinetics in the hardened samples

References

Durdziński, P. T., M. Ben Haha, M. Zajac and K. L. Scrivener (2017). "Phase assemblage of composite cements." Cement and Concrete Research **99**: 172-182.
Hallet, V., N. De Belie and Y. Pontikes (2020). "The impact of slag fineness on the reactivity of blended cements with high-volume non-ferrous metallurgy slag." Construction and Building Materials **257**: 119400.
Kocaba, V., E. Gallucci and K. L. Scrivener (2012). "Methods for determination of degree of reaction of slag in blended cement pastes." Cement and Concrete Research **42**(3): 511-525.
Li, X., R. Snellings, M. Antoni, N. M. Alderete, M. Ben Haha, S. Bishnoi, Ö. Cizer, M. Cyr, K. De Weerdt, Y. Dhandapani, J. Duchesne, J. Haufe, D. Hooton, M. Juenger, S. Kamali-Bernard, S. Kramar, M. Marroccoli, A. M. Joseph, A. Parashar, C. Patapy, J. L. Provis, S. Sabio, M. Santhanam, L. Steger, T. Sui, A. Telesca, A. Vollpracht, F. Vargas, B. Walkley, F. Winnefeld, G. Ye, M. Zajac, S. Zhang and K. L. Scrivener (2018). "Reactivity tests for supplementary cementitious materials: RILEM TC 267-TRM phase 1." Materials and Structures **51**(6): 151.
Lumley, J. S., R. S. Gollop, G. K. Moir and H. F. W. Taylor (1996). "Degrees of reaction of the slag in some blends with Portland cements." Cement and Concrete Research **26**(1): 139-151.
Mota, B., T. Matschei and K. Scrivener (2019). "Impact of sodium gluconate on white cement-slag systems with Na2SO4." Cement and Concrete Research **122**: 59-71.
Thomas, J. J., H. M. Jennings and J. J. Chen (2009). "Influence of Nucleation Seeding on the Hydration Mechanisms of Tricalcium Silicate and Cement." The Journal of Physical Chemistry C **113**(11): 4327-4334.

The 16th International Congress on the Chemistry of Cement 2023 (ICCC2023)
"Further Reduction of CO_2 -Emissions and Circularity in the Cement and Concrete Industry"
September 18–22, 2023, Bangkok, Thailand

Comparison and optimization of calcination processes towards using clays as Supplementary Cementitious Materials

A. Koutsouradi[1*], A.J. Damø[1], M. Canut[2], W.R. Leal da Silva[2], and P.A. Jensen[1]

[1] *Technical University of Denmark, Department of Chemical Engineering, 2800 Kongens Lyngby, Denmark*
Email:anakou@kt.dtu.dk
[2] *FLSmidth A/S, 2650 Valby, Denmark*
Email: mariana.canut@flsmidth.com

ABSTRACT

Clays are abundant materials worldwide, have high pozzolanicity after thermal treatment (calcination), and can substantially contribute towards decreasing the CO_2 emissions associated with the cement industry by reducing the clinker factor in cement. Although many investigations have focused on this technology, not many are emphasizing calcination processes and how these affect the properties of calcined clays. The present study investigates two of the most commonly found clay minerals: Kaolinite and Montmorillonite, including calcination studies of those in a laboratory scale oven, a pilot-scale rotary kiln, and a pilot-scale flash calciner with a residence time of about 1 second, operated at different temperatures. The results show static calcinations deliver similar results, with the optimal dehydroxylation degree and reactivity observed at 750°C for both clays. Flash calcination in the system used for the present investigation delivers equally satisfactory results at higher temperatures, of 1050°C and 950°C for Kaolinite and Montmorillonite respectively, while agglomeration and deposit formation observed during the experiments are assessed.

KEYWORDS: *calcined clay, flash calcination, kaolinite, montmorillonite, pozzolanic reactivity*

1. Introduction

The cement industry is responsible for 5-8% of the worldwide CO_2 emissions, making it the second-largest source of anthropogenic CO_2 emissions, while the constantly developing urban structure causes the cement demand to continuously increase. To overcome that, Supplementary Cementitious Materials (SCMs) were introduced to enhance clinker substitution, with clays representing a widely available candidate (Scrivener et al., 2018). When thermally treated, clays acquire pozzolanic reactivity and to date, clinker replacement of up to 40% is reported and successfully implemented (Sharma et al., 2021). Industrially, rotary kilns and flash calciners are currently used to produce calcined clays (Hanein et al., 2021). However, limited studies focus on comparing these technologies. The present work emphasizes both static and flash calcination methods on Kaolinite and Montmorillonite while varying the calcination temperature. A thorough characterization of the calcination products follows, leading to a broad overview of how clay calcination conditions affect the properties of the two clay minerals.

2. Materials and methods

The two raw laboratory-grade clay minerals were characterized by X-ray fluorescence (XRF) and by X-Ray diffraction (XRD) analysis. Additionally, Thermogravimetric Analysis (TGA) was used to characterize raw and calcined clays, with a heating rate of 10°C/min from 25 to 1000°C and a nitrogen flux employed to avoid carbonation. Moreover, raw and calcined clays underwent Particle Size Distribution (PSD) using a Malvern Mastersizer 3000 laser diffractometer with ethanol as solvent to assess agglomeration after calcination. Finally, the R^3 bound water method (ASTM C1897-20) was used to assess the pozzolanic reactivity of all calcined samples.

For static calcinations, a programmable laboratory muffle furnace (Nabertherm) and a pilot-scale rotary kiln were used. The rotary kiln is electrically heated by a furnace surrounding it, and the rotating drum has a diameter of 0.30m, a length of 0.45m and a rotation speed of 20 rpm. For flash calcination, the investigations are carried out in a pilot-scale entrained flow reactor, where the material falls through a 1.50m long ceramic tube that is electrically heated by four heating elements. The residence time in the reactor is approximately 1 second. The tested clays were first calcined under static conditions in both the muffle furnace and the rotary kiln at 450, 750, and 950°C, while maintaining a stable heating rate (2°C/min) and residence time (30 min.). For flash calcinations, and due to clay fineness causing excessive agglomeration, the samples were pre-dried for 24 h at 150°C in a laboratory oven and passed through a 90µm sieve to break the agglomerates. Due to the short residence time in the reactor used for flash calcinations, the temperatures chosen for the flash calcinations are slightly higher than these of the static calcinations, at 950, 1050, and 1150°C. However, previous investigations concerning the flash calcination of kaolinite show that higher temperatures are needed to achieve full dehydroxylation (Inocente et al., 2021).

3. Results and discussion

3.1 Characterization of raw clays

Table 1 presents the chemical compositions as given by XRF, while Figure 1a,b shows the TGA and XRD curves of the Kaolinite and Montmorillonite used in the study. In Figure 1a, the mass loss of up to 250°C is associated with the removal of the adsorbed water, typically observed more intensely in 2:1 clays as Montmorillonite. The temperature range of 400-600°C is mainly dominated by the dehydroxylation of 1:1 clays as Kaolinite, while temperatures above that represent weight loss associated with 2:1 clays (Alujas et al., 2015). The XRD patterns presented in Figure 1b indicate the purity of the samples, with Kaolinite and Montmorillonite being the main phases identified, with small amounts of quartz, albite, and cristobalite being present – similar observations are reported by (Fernandez et al., 2011).

Table 1 – Chemical composition of Kaolinite and Montmorillonite used in the study as given by XRF.

% Weight	SiO_2	Al_2O_3	Fe_2O_3	CaO	MgO	SO_3	K_2O	Na_2O	Other	LOI
Kaolinite	47.27	36.98	0.77	0.07	0.28	0.03	1.82	0.03	0.66	12.25
Montmorillonite	74.21	13.39	2.40	0.34	1.13	0.03	1.69	0.34	0.62	5.40

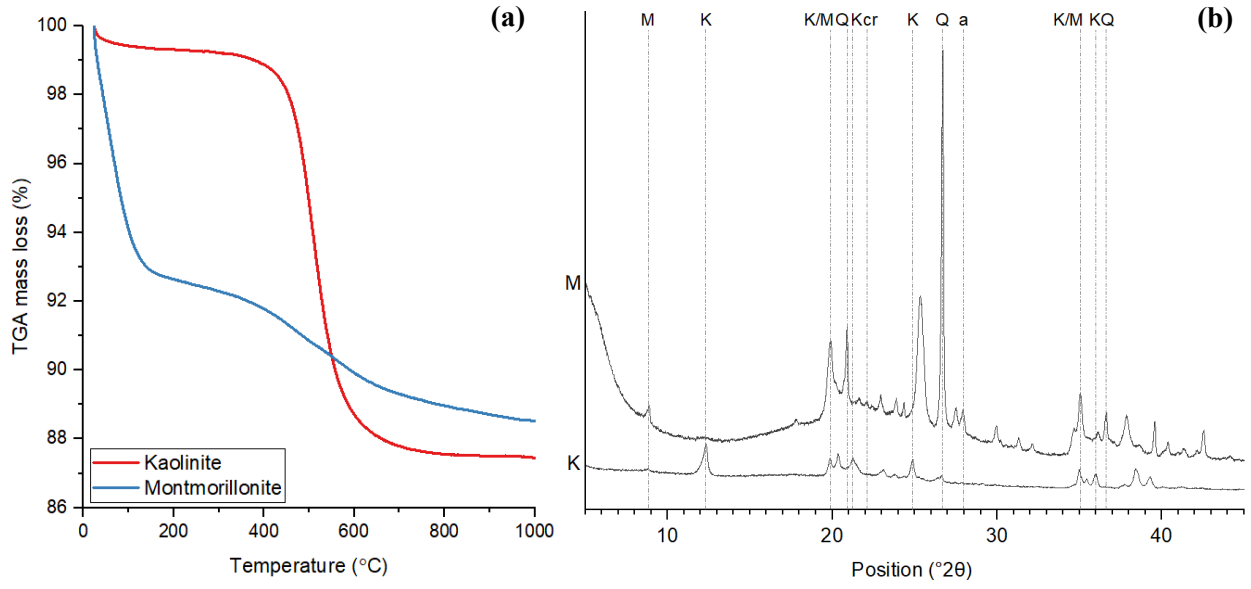

Figure 1 – (a) TGA and (b) XRD patterns of investigated clay minerals (K: kaolinite, M: montmorillonite, a: albite, cr: cristobalite, Q: quartz).

3.2 Characterization of calcined clays at different temperatures

The dehydroxylation degrees deriving from the TGA mass loss for the temperature interval of 350-900°C are presented in Table 2, while pozzolanic reactivity results are presented in Figure 2 for all calcined samples. Both clays represent very similar behaviour when comparing the two static calcination methods, muffle furnace and rotary kiln, with the only exception concerning Kaolinite calcined at 950°C, which seems to be delayed entering the recrystallization stage when calcined in the rotary kiln. Moreover, optimal static calcination temperature for both clay minerals is at 750°C.

As for the flash calcined samples, optimal calcination temperature for Kaolinite is at 1050°C, while for Montmorillonite at 950°C. The latter showcases a drop in reactivity already at 1050°C, while Kaolinite enters the recrystallization stage at 1150°C, indicating that Kaolinite can handle the highest operating temperatures that are occasionally occurring in flash calcination, although the actual reached temperature of the particle is not known. Note that in Table 2 (Montmorillonite) and Figure 2b, no results are presented for the highest flash calcination temperature of 1150°C. This is because the material could not be collected in the reactor's collection chamber.

Table 2 – Calcined samples dehydroxylation degrees (MF: Muffle Furnace; RK: Rotary Kiln; F: Flash).

Kaolinite				**Montmorillonite**			
Calcination temperature (°C)	**Dehydroxylation degree (%)**			**Calcination temperature (°C)**	**Dehydroxylation degree (%)**		
	MF	**RK**	**F**		**MF**	**RK**	**F**
550	82.29	87.79	-	**550**	45.27	49.41	-
750	96.65	97.08	-	**750**	77.51	79.29	-
950	99.66	100	86.24	**950**	98.52	95.86	87.87
1050	-	-	94.84	**1050**	-	-	94.38
1150	-	-	100	**1150**	-	-	-

Table 3 lists the collection efficiency for both samples (including mass loss by calcination) during the flash calcination experiments. Although there were no problems with Kaolinite, Montmorillonite exhibited excessive deposit formation (Figure 2b) that led to no material collection at 1150°C, with the collection efficiency already at 1050°C being very limited. It should be noted that the samples used in the present study are very fine (see PSD in Figure 3) and this could be enhancing the deposit formation. Moreover, the PSD results of the calcined samples in Figure 3 display that Kaolinite at 1050°C and 1150°C exhibit noticeable agglomeration, which could also be associated to the very fine starting material. In any case, if this agglomeration is observed when employing coarser feed particle sizes, Kaolinite might require special handling, since excessive agglomeration is likely to require greater energy towards after-grinding. Lastly, Montmorillonite shows no agglomeration tendency even at higher temperatures, opposed to the deposit issues described earlier.

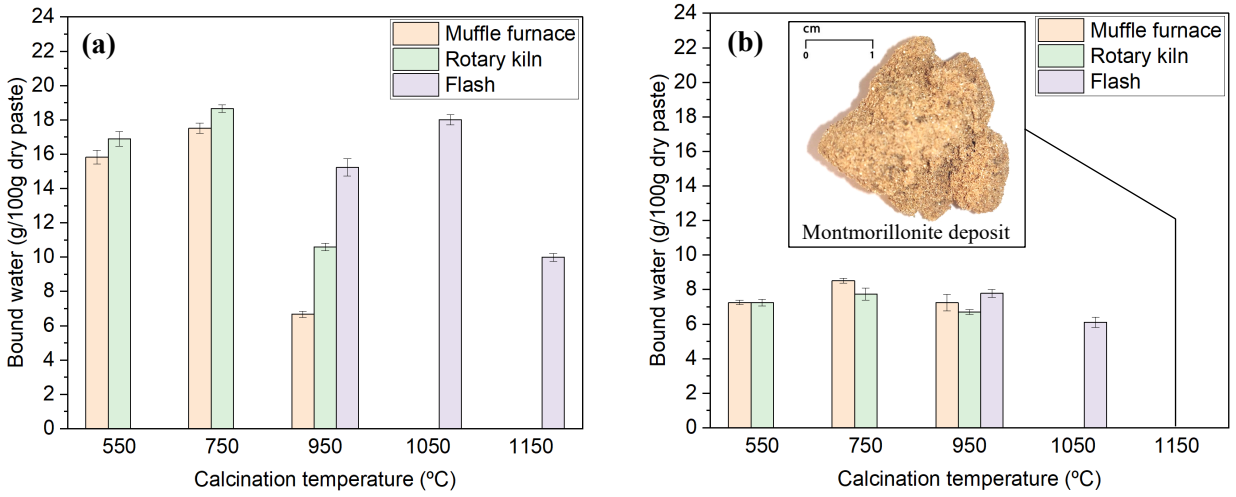

Figure 2 – R^3 bound water reactivity of all calcined samples: (a) Kaolinite and (b) Montmorillonite.

Table 3 – Collection efficiency of flash calcined samples.

Calcination temperature (°C)	Collection efficiency (%)	
	Kaolinite	Montmorillonite
950	82.9	87.8
1050	80.5	2.1
1150	80.3	0

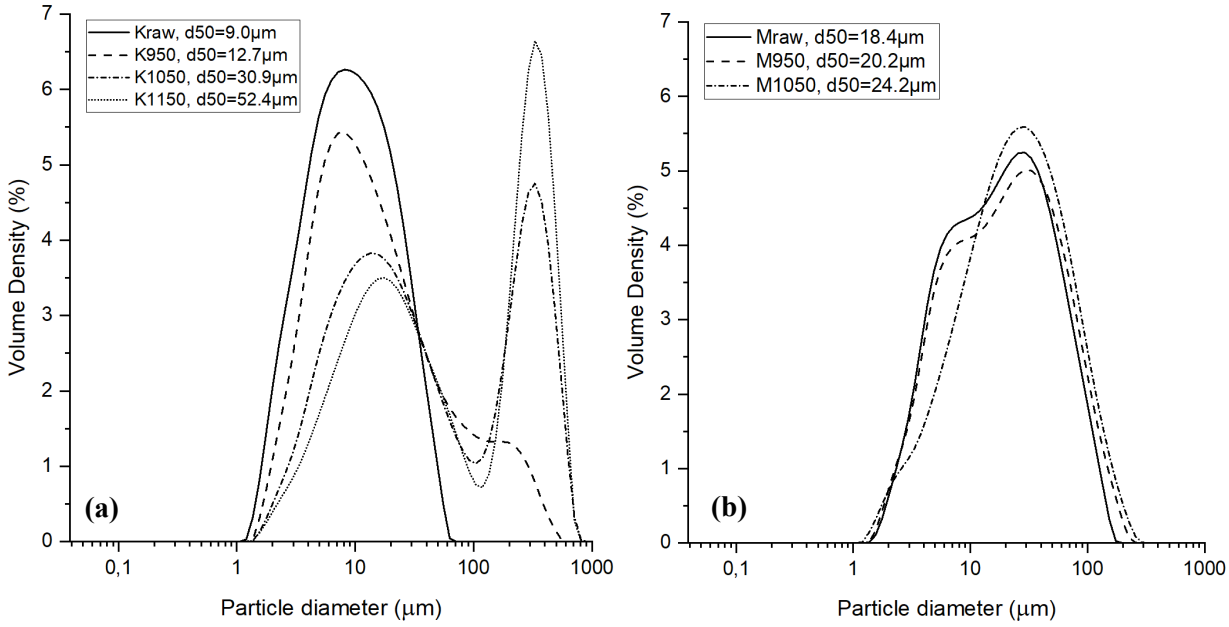

Figure 3 – PSD of raw clays and their flash calcination products: (a) Kaolinite and (b) Montmorillonite.

4. Conclusions

Calcination technologies such as static and flash methods can be applied to successfully activate Kaolinite and Montmorillonite clays. The optimal static calcination temperature for both clays was found to be at 750°C. Flash calcination, on the other hand, required higher operational temperatures to achieve optimal dehydroxylation of both clay minerals due to the short residence time (1s), with the optimal temperature for Kaolinite and Montmorillonite standing at 1050°C and 950°C. The highest temperature of the flash calcination is accompanied by agglomeration tendency observed for Kaolinite and deposit formation for Montmorillonite. These behaviours are likely associated with the highest temperatures needed due to the short residence time in the system or with the fine particle size of the clays. Complementary research is in progress in order to clarify these aspects and will be published elsewhere.

References

Alujas, A., Fernández, R., Quintana, R., Scrivener, K. L., & Martirena, F. (2015). Pozzolanic reactivity of low-grade kaolinitic clays: Influence of calcination temperature and impact of calcination products on OPC hydration. Applied Clay Science, 108, 94–101.

Fernandez, R., Martirena, F., & Scrivener, K. L. (2011). The origin of the pozzolanic activity of calcined clay minerals: A comparison between kaolinite, illite and montmorillonite. Cement and Concrete Research, 41(1), 113–122.

Hanein, T., Thienel, K. C., Zunino, F., et al. (2021). Clay calcination technology: state-of-the-art review by the RILEM TC 282-CCL. Materials and Structures 2023 55:1, 55(1), 1–29.

Inocente, J. M., Elyseu, F., Jaramillo Nieves, L. J., Jiusti, J., Cargnin, M., & Peterson, M. (2021). Production and characterization of high-reactivity metakaolins calcined in flash reactor. Applied Clay Science, 213, 106247.

Scrivener, K., Martirena, F., Bishnoi, S., & Maity, S. (2018). Calcined clay limestone cements (LC3). Cement and Concrete Research, 114, 49–56.

Sharma, M., Bishnoi, S., Martirena, F., & Scrivener, K. (2021). Limestone calcined clay cement and concrete: A state of-the-art review. Cement and Concrete Research, 149.

The 16th International Congress on the Chemistry of Cement 2023 (ICCC2023)
"Further Reduction of CO_2 -Emissions and Circularity in the Cement and Concrete Industry"
September 18–22, 2023, Bangkok, Thailand

Electrification of Calcined Clay Systems in the Cement Industry – Technical, Economic and Environmental Potentials

M. Nakhaei[1], L. Hu[1*], W. R. Leal da Silva[1], B. Laurini[2], Y. Zong[2], and C. Træholt[2]

[1] *FLSmidth A/S, Copenhagen, Denmark*
**Email: lohu@flsmidth.com*
[2] *Technical University of Denmark, Kgs. Lyngby, Denmark*
Email: yizo@dtu.dk

ABSTRACT

Clay is a naturally occurring material that is widely available around the globe and is a potential candidate to be used as a Supplementary Cementitious Material (SCM) in cement production. Properly activated clay can substitute 30-40% of clinker according to EU standards, and thereby directly reduce CO_2 emissions. Electrifying the clay calcination process using green electricity from renewables will further lower the CO_2 emissions up to a total of 50% reduction per ton of cement produced. Despite existing technical challenges, electrical activation of clays enables better control over the calcination temperature and thus improved material activation and product quality. FLSmidth and several industrial partners established a demonstration project on electric calcination of clay. A pilot plant will be built in Denmark within the next 2-3 years. The renewable energy prices have been declining considerably over the past decades and are expected to further decline over the next 5-10 years. Therefore, it is expected that commercialization of such a concept will become viable in a near future. In the current study, an outlook on electrification of clay calcination systems is presented, considering technical, economic, and environmental aspects.

KEYWORDS: *calcined clay, cement, CO_2 emission, electrification, Supplementary* Cementitious *Materials*

1. Introduction

The cement industry is a hard-to-abate sector that contributes to around 8.0% of the world's CO_2 emission (Monteiro et al. 2017). In the production process of ordinary Portland cement, OPC, (i.e., CEM I – EN197-1), the emission of CO_2 originates from limestone calcination and fuel combustion, with a total of 0.79-0.81 $[t_{CO_2}/t_{cement}]$, assuming a coal fired system. The cement industry has been experimenting with complementary technologies to help reduce its CO_2 emissions, e.g., use of alternative fuels, Carbon Capture and Storage, electrification, improvement of energy efficiency, and utilisation of SCMs to replace clinker. Among these, the latter is one of the most feasible solutions to decarbonize the cement industry today. This is because the technology is already a common practice in many countries, and there is a great capacity to deliver an immediate CO_2 reduction from the current global clinker-to-cement ratio of ca. 75%.
Driven by population growth and urbanization, the cement production is expected to reach 5.0 $[Gt/year]$ in 2050. With the current production rate of cement stagnating at 70%, there is enough clinker production capacity (3.0 $[Gt_{clinker}/year]$) to meet future urbanization needs. Thus, the current industrial effort to deliver a more sustainable cement is towards using more SCMs in composite cements, while reducing emissions from fossil fuels utilisation. To that end, calcined clay is gaining popularity as SCM due to its worldwide availability, excellent pozzolanic properties, and low cost (Jaskulski et al. 2020).
The main aim of the clay calcination process, i.e., thermal activation, is to remove hydroxyl groups from the clay structure, leading to activation of alumina and silica oxides in the clay. The mainstream industrial solutions for clay calcination comprise either a rotary kiln or a flash suspension calciner, each with their own particularities (Maia et al. 2021; Lien et al. 2021). In most cases, these solutions rely on the use of fossil fuels. Hence, the replacement of fuel combustion with full electrification in the clay calcination

processes will further reduce the CO_2 footprint of the produced composite cements. In this article, we elaborate on the technical, economic, and environmental aspects of the electrification of clay calcination, with focus on flash calcination as the baseline process.

2. Electrification of Clay Calcination: Technical Challenges & Benefits

The use of electricity in a flash clay calcination system enables recovery of the thermal energy of the gases leaving the preheating tower by incorporating a closed loop for the hot gas flow string. This involves using an electrical hot gas generator to heat the exhaust gas from the preheating cyclones to the desired temperature for the calciner. Besides the enhanced thermal efficiency of the process and lower operation cost, in principle, electrification of clay calcination provides improved control over the calciner temperature and thereby, the dehydroxylation process and product quality, especially with respect to presence of hot spot regions which may exist in fuel-fired calciners. Also, it is possible to reduce the volume and thereby, total height of the calciner since the retention time in this unit is mainly decided based on completion of the fuel combustion. For clays that require a long retention time for proper thermal activation, the material retention time is provided in the color control unit downstream of the calciner.

One of the important technical challenges corresponding to this process concept is inevitable presence of fine particles suspended in the gas entering the electric hot gas generator, even if a dedusting unit is used downstream of the preheating cyclones. This may result in melting and deposition of dust particles on the heating elements, and in long term, build-ups and declined efficiency and response time of the electric hot gas generator. Increased operating temperature of the electrical hot gas generator can intensify this issue, especially at a low gas to clay feed ratios.

Another complication that may arise with having a closed hot gas string is accumulation of corrosive gas species, such as water vapor (40-60 [vol.%]), CO, SO_2, and HCl, which can increase the corrosion tendency in the whole hot gas string. Besides, high water vapor levels may impact the quality of activated clay. The levels of these gases can be controlled, to a limited extent, by purging a fraction of the main gas stream as well as partial intake of fresh air. On the other hand, for some clays with high organic carbon content, a reducing environment may form during the dehydroxylation process. This would reduce the amount of reduction agent needed for controlling the color of the product and in an ideal case, removes the necessity of having a color control unit in the system.

Integration of the electrified process with the power grid presents technical and economic challenges as well. To accommodate the increased electricity demand, investments in the electrical infrastructure are required (Wei et al., 2019). As renewable energy sources (RES) penetrate the power system, market signals may become more volatile as they depend on high-cost thermal power plants as balancing agents (Kyritsis et al., 2017). This represents a challenge and opportunity for innovation, such as the adoption of demand side management measures in electrified plants (Golmohamadi, 2022; Zhang et al., 2018). In particular, the use of energy management systems to control flexible loads and storage can help reducing operational costs. Additionally, provision of ancillary services like frequency response can support system operators to handle the intermittence of RES and maintain power systems stability.

3. Electrification of Clay Calcination: Environmental Impact

The use of SCM in limestone-calcined clay cement (LC3) reduces the CO_2 footprint of the cement by around 40%, i.e., from 0.79 – 0.81 [t_{CO_2}/t_{OPC}] to 0.47-0.49 [t_{CO_2}/t_{LC3}], of which around 6% derives from lower fuel consumption (see details in FLSmidth, 2021). Electrification of the clay calcination process replaces the fuel consumption in this process, which reduces the CO_2 footprint further down to 50%, i.e., 0.40-0.42 [t_{CO_2}/t_{cement}], if renewable electricity sources are used. Another important environmental benefit of electrified clay calcination process is reduced amount of hot flue gases out of the system by up to around 75-90%, and thereby easier removal of harmful gases and dust from this stream as well as reduced capital and operational costs of the emission abatement equipment.

4. Electrification of Clay Calcination: Economic Impact

The worldwide lack of commercial electrified calcined clay installations in the cement industry makes it difficult to perform a detailed cost analysis of full electrification versus fuel firing in a flash calciner

solution. Therefore, this analysis relies on technical assumptions and considers a range of CO_2 prices as well as fuel and electricity costs, to provide a nomogram that helps identifying where the electrification would have lower operating expenses (OPEX) than the standard flash calcination.
It is safe to assume that the expected maintenance costs of an electrified clay calcination solution are in similar range compared to the traditional pyro lines. To compare the energy costs, which make up a significant portion of OPEX, a cost analysis is carried out assuming an annual production of 200 [kt] of calcined clay. The analysis compares the yearly energy-related expenditures of a fossil fuel-fired flash calcination system against an electrified process concept on an industrial scale, with assumed energy consumption inputs summarized in Table 1. Coal and natural gas are considered as fuel for the base scenarios with CO_2 emission factors of 0.05 [kg_{CO2}/MJ] and 0.09 [kg_{CO2}/MJ] (EIA, 2022), respectively, resulting in yearly emissions of around 38 [kt_{CO2}] when firing coal and 21 [kt_{CO2}] when firing natural gas. The yearly OPEX cost function is calculated as follows:

$$OPEX_{Energy}\,[USD] = D_{el} \cdot p_{el} + D_{fuel} \cdot p_{fuel} + E_{CO2} \cdot p_{CO2} \quad (1)$$

where D_{el} [kWh] and D_{fuel} [MJ] are the electricity and fuel demand, $E_{CO2}[t_{CO_2}]$ is the fuel combustion emission, and p_{el} [USD/kWh], p_{fuel} [USD/MJ] and p_{CO2} [USD/t_{CO_2}] are the average electricity, fuel and carbon prices, respectively.
Figure 1 presents the required electricity price, as a function of fossil fuel and CO_2 prices, so that the yearly OPEX of both scenarios would be the same. For a specific set of fossil fuel and CO_2 prices, if the current electricity price is lower than the identified value in Figure 1, the electrified flash calcination scenario would offer a financial advantage over the conventional fuel-fired process. Fossil fuel prices showed high volatility in the last years due to the energy crisis. For natural gas, industrial prices were in the range of 0.003-0.024 [USD/MJ] for different countries in 2019 (IEA, 2019). Meanwhile, international thermal coal prices were fluctuating in the range of 0.003-0.016 [USD/MJ] during 2021-2022 (IEA, 2022).

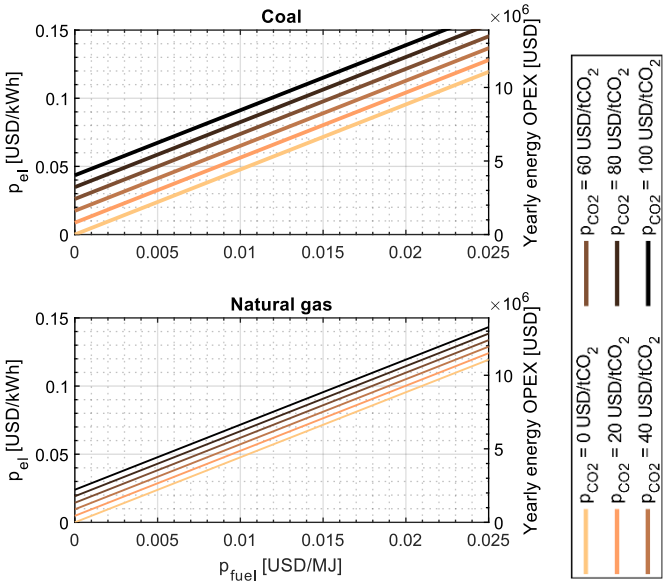

Figure 1: Required p_{el} as a function of p_{fuel} and p_{CO2} providing equal yearly energy OPEX for fuel-fired and electrified scenarios.

Table 1: Expected fuel and electricity consumptions of fuel-fired and electrified flash calciner solutions with yearly production of 200 [kt] of calcined clay.

Scenario	*Fuel Consumption [MJ/kgCC]*	*Electricity Consumption [kWh/tCC]*	*Total Energy Input [MJ/kgCC]*
Fuel-fired	2.09	25	2.18
Electrified	-	463	1.67

Examples of average industrial electricity prices for different countries: 0.11 USD/kWh for France, 0.141 USD/kWh for Spain, 0.081 USD/kWh for Turkey and 0.078 USD/kWh for Norway (BEIS, 2022).

Figure 1 also shows the impact of carbon pricing on electricity prices needed for equal energy costs of the two scenarios. When the electricity prices are prohibitive, higher carbon prices can improve the attractiveness of the electrified clay calcination solutions. While it is difficult to predict with certainty whether carbon prices will increase over the next years, there has been a trend towards more strict environmental regulations and greater action on climate change, which could result in an increase in carbon prices in the future. Many countries are implementing carbon pricing instruments, e.g., carbon taxes or emissions trading systems, in an effort to reach their climate goals (Dolphin and Xiahou, 2022). Some countries have seen an increase in carbon prices in recent years. For example, prices have risen sharply in the EU ETS since 2011, reaching nearly 70 [USD/t_{CO_2}] in 2021 (World Bank, 2022).

5. Conclusions

Utilization of limestone calcined-clay cement is a promising solution to reduce the carbon footprint of the cement industry by up to 40% in comparison to the OPC, type I, when fossil fuels are utilized. When the clay calcination process is electrified using renewable sources, the composite cement carbon footprint is reduced by up to 50% compared to the OPC.

A concept of an electrified flash clay calcination system with recirculating hot gas in a closed loop, to improve the thermal energy efficiency, is introduced in this paper. The gas in the hot string is reheated using an electrical hot gas generator. Electrification of clay calcination improves control over the calciner temperature and thereby, the clay dehydroxylation process and its quality as a SCM. Also, it is possible to reduce the volume and, thus, the total height of the calciner as no fuel combustion takes place in the calciner. The key challenges that may arise with this concept are the risk of clay dust deposition in the electric hot gas generator, as well as accumulation of corrosive gasses in the system, which may impose durability issues for the electric hot gas generator. Operating the system in open loop will eliminate such risks, however, it increases the energy consumption since the suspension air needs be heated from a lower inlet temperature and the exhaust air flow, that potentially needs abatement, will increase by a factor of 3-10. Lastly, the integration of the electrified process with the power grid can be optimized by applying demand side management strategies and providing ancillary services, which would contribute to lower operational costs and at the same time, support power system operators.

Based on expected energy costs of fuel-fired and electrified flash clay calciner solutions with 200 [kt] yearly production, a preliminary nomogram is presented to identify how CO_2 and fuel/electricity prices determine the economic advantage of the electrified clay calcination concept over the fuel-fired flash calciner. In general, higher carbon prices can improve the attractiveness of electrified clay calcination solutions, and there has been a trend towards more strict environmental regulations that may lead to an increase in carbon prices in the future.

Acknowledgements

The authors would like to thank the support from The Energy Technology Development and Demonstration Programme (EUDP) for providing financing for the project 64021-7009.

References

Department for Business, Energy & Industrial Strategy (BEIS), Industrial electricity prices in the IEA (2022). https://www.gov.uk/government/statistical-data-sets/international-industrial-energy-prices

Dolphin, G., & Xiahou, Q. (2022). World Carbon Pricing Database.

EN 197-1:2011. Cement - Part 1: Composition, specifications and conformity criteria for common cements

FLSmidth. Revealing the numbers behind calcined clay, 2021, https://www.flsmidth.com/en-gb/discover/cement-2021/revealing-the-numbers-behind-calcined-clay

IEA (2019), Natural gas prices for the industrial sector in selected countries, 2019, IEA, Paris https://www.iea.org/data-and-statistics/charts/natural-gas-prices-for-the-industrial-sector-in-selected-countries-2019, IEA. Licence: CC BY 4.0

IEA (2022), Coal Market Update – July 2022, IEA, Paris, https://www.iea.org/reports/coal-market-update-july-2022, License: CC BY 4.0

Jaskulski, R., Jóźwiak-Niedźwiedzka, D., and Yakymechko, Y. Calcined clay as Supplementary Cementitious Material. Materials, 13(21), 4734 (2020).

Kyritsis, E., Andersson, J., & Serletis, A. (2017). Electricity prices, large-scale renewable integration, and policy implications. *Energy Policy*, *101*, 550-560. https://doi.org/10.1016/j.enpol.2016.11.014

Lien, P. and Sons, Inc. Pilot scale kiln and flash calcination of shale. Pilot test report (2022).

Maia, J., and Ladeira, P. Clay calcining technologies: the rotary kiln approach. International cement review (2021).

Monteiro, P., Miller, S., and Horvath, A. Nature Materials 16, 698–699 (2017).

United States (2010). *U.S. Energy Information Administration EIA*. United States. https://www.eia.gov/environment/emissions/co2_vol_mass.php

Wei, M., McMillan, C.A. & de la Rue du Can, S. Electrification of Industry: Potential, Challenges and Outlook. *Curr Sustainable Renewable Energy Rep* **6**, 140–148 (2019). https://doi.org/10.1007/s40518-019-00136-1

World Bank. 2022. State and Trends of Carbon Pricing 2022, Washington, DC: WorldBank. © World Bank. https://openknowledge.worldbank.org/handle/10986/37455 License: CC BY 3.0 IGO.

The 16th International Congress on the Chemistry of Cement 2023 (ICCC2023)
"Further Reduction of CO_2 -Emissions and Circularity in the Cement and Concrete Industry"
September 18–22, 2023, Bangkok, Thailand

Modelling of clay calcination: Rotary kiln versus flash calciner

S.E. Schulze[1], K. Fleiger[2], M. Feiss[3] and J. Rickert[4]

[1, 2, 4] *VDZ gGmbH, Duesseldorf, Germany*

Email: simone.schulze@vdz-online.de

[3] *KHD Humboldt Wedag International AG, Koeln, Germany*

ABSTRACT

The worldwide availability of suitable clays makes calcined clays a very promising pozzolanic supplementary cementitious material (SCM) for further lowering the clinker content in cements. Thus, CO_2 emissions from fuel combustion and decarbonation of limestone during clinker production can partially be saved, but must be assessed against respective CO_2 emissions from the calcination process of the clay.

With regard to the future increase in demand for calcined clays in the context of decarbonization, significantly more rotary kilns and flash calciners will be built or retrofitted for clay calcination. In this study the energy demand and CO_2 emissions of both technologies were simulated for a clay production rate of 500 t/d depending on the clay's mineralogy and moisture. The CO_2 emissions for a calcination at around 800 °C range between 0.1 and 0.3 kg CO_2/kg calcined clay, depending on the type of calcination and the mineralogy and moisture of the clay.

It can however be stated that calcination in a flash calciner appears to be more efficient than calcination in a rotary kiln, both in terms of energy and CO_2 emissions.

KEYWORDS: *calcined clay, cement, rotary kiln, flash calcination, modelling*

1. Introduction

The ecological assessment of common composite cements is possible due to sufficient data on the CO_2 emission of their main components like slag and others. For the calcination of clays of different compositions, these data are lacking so far. They are required for assessing the CO_2-emissions and -savings of the production of clay-containing cements.

For example, Vizcaino et al (2015) indicate a CO_2 saving potential of 30 % for the use of calcined clays in composite cements with 55% clinker compared to an OPC. Hernandez and Scrivener (2015) and Sanchez Beriell et al (2015) derive saving potentials of 15 to 20 % from demonstration projects in Cuba. Scrivener (2014 and 2016) considers savings of up to 300 to 350 kg CO_2/t cement to be achievable. The values correspond approximately to the data given in ECRA (2017), where CO_2 saving potentials are estimated for the use of calcined clays in composite cements with clinker contents of 65 wt.%. Compared to cements commonly used today with an average clinker content of 75 wt.%, the saving potential is about 70 kg CO_2/t cement, and in relation to OPC slightly more than 200 kg CO_2/t cement. More detailed specifications taking into account the clay composition and the production process are mostly not available, but necessary.

2. Experimental work and simulation

The calcination of two different Calcite containing clays (cf. Table 1) in a rotary kiln and in a flash calciner was simulated. In order to be able to compare the results, the same initial parameters (moisture, fuel, phase composition, calcination temperature, etc.) were used in each case. The production rate was assumed to be 500 t/d for both simulated plants.

Table 1: Phase composition of the used clays W1 and W2, wt.%

Clay	Kaolinite	Illite	Chlorite	Calcite	Others (Quartz etc.)
W1	10	40	8	7	35
W2	4	18	4	30	44

Based on the composition of the clays (cf. Table 1), the interlayer water content of the individual clay minerals (Kaolinite: 12 wt.%, Illite: 8 wt.%, Chlorite: 15 wt.%), was calculated. This water content was related to the water content and the theoretical heat of formation of Kaolinite (H_R= 418 kJ/kg Kaolinite), so that all clay minerals were treated as Kaolinite in the simulation. Thus, the theoretical heat input for the dehydroxylation of all clay minerals at the respective temperature could be calculated in a simplified way.

The theoretical heat input for the decomposition of the carbonates was determined from the reaction of $CaCO_3$ to CaO and CO_2 at the respective temperature and the theoretical decomposition enthalpy of Calcite (H_R= 1780 kJ/kg $CaCO_3$). From the heat input for dehydroxylation and decomposition, the total theoretical heat requirement for calcination of the clays could be calculated (cf. Table 2). Via the specific energy content and CO_2 contribution of the fuel (in this case coal with 26300 kJ/kg and 66,90 wt.% C), it is possible to determine the specific CO_2 emissions for the calcination of the respective clay and also for the production of corresponding clay-containing cements with 20 wt.% calcined clay.

Table 2: Theoretical heat input for the calcination of the clays (dehydroxylation of the clay minerals and decomposition of the carbonates) depending on the temperature, kJ/kg product

Clay	Dehydroxylation of clay minerals			Decomposition of carbonates			Total		
	600 °C	800 °C	1000 °C	600 °C	800 °C	1000 °C	600 °C	800 °C	1000 °C
W1	125	151	178	0	15	129	125	166	307
W2	55	66	77	0	65	615	55	131	692

3. Results

The calculated CO_2 emissions caused by the calcination of the two clays consist of combustion-related and raw material-related CO_2. Therefore, the different Calcite contents of the clays have a particularly large influence on the amount of CO_2 emitted as soon as the respective clay is calcined at the temperature level of 800 °C or higher, which leads to the decomposition of the Calcite (cf. Figure 1).

At the temperature level of 600 °C, the CO_2 emissions are only combustion-related because $CaCO_3$ decomposition has not yet started and therefore the emissions correspond to the fuel-related CO_2 emissions. Depending on the calcination technology for a raw clay with 20 wt.% moisture the emissions were between about 0.12 and 0.17 kg CO_2/kg calcined clay. With increasing temperature and carbonate content, the CO_2 emissions increase caused by the decomposition of the Calcite and the higher fuel input. When calcining at 800 °C, the CO_2 emissions ranged between about 0.14 and 0.22 kg CO_2/kg calcined clay, depending on the technology. At 1000 °C, the decomposition of the Calcite is completely finished and the entire material-bound CO_2 is emitted. For clays containing carbonates, a firing temperature of more than 800 °C is therefore not recommended due to higher CO_2 emissions.

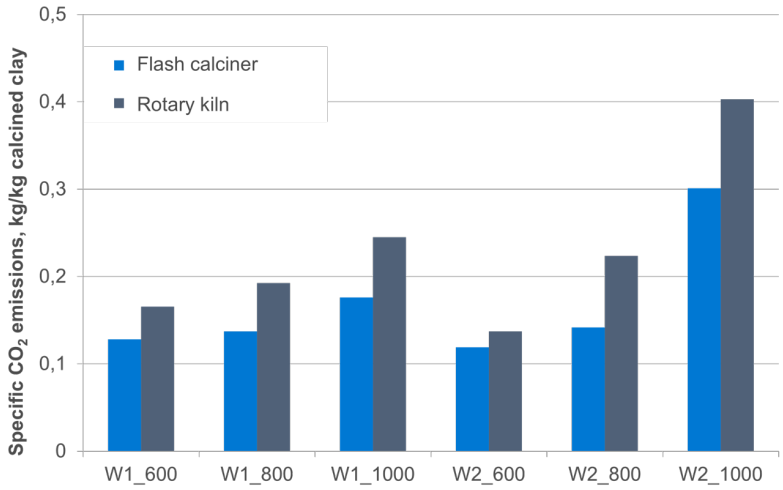

Figure 1: Specific CO_2 emissions of the calcination of clay W1 and W2 at different temperatures (600, 800 and 1000 °C); order of designation: clay_temperature

According to the simulation, the calcination in the flash calciner was more efficient than the calcination in the rotary kiln, both in terms of energy and CO_2 emissions. A fundamental advantage of the flash calciner is the improved energy exchange between gas and material, among other things due to the good mixing of the flows in the cyclone stages compared to the heat transfer through the material bed in the rotary kiln.

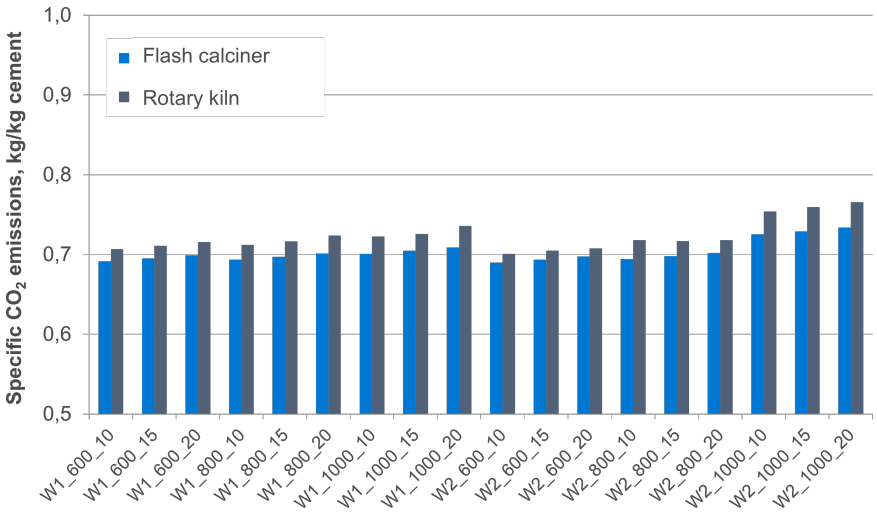

Figure 2: Specific CO_2 emissions of the production of composite cements with 20 % calcined clay depending on the calcination temperature (600, 800 and 1000 °C) and different raw material moisture (10, 15 and 20 wt.%), order of designation: clay_temperature_moisture

Taking into account the specific CO_2 emissions of 0.842 kg/kg Portland cement clinker (ECRA (2017)), the specific CO_2 emissions for the production of a composite cement with 20 wt.% calcined clay were calculated (cf. Figure 2) for raw clays with 10, 15 and 20 wt.% moisture. The specific CO_2 emissions of the production of such a cement are therefore around 0.7 kg/kg cement. Due to the high CO_2 contribution of the clinker compared to the clay used, the influence of the clay composition, moisture and calcination temperature is almost negligible. The influence of the selected calcination technology also moves into the background.

The differences between the simulated calcination technologies became more apparent with increasing calcined clay proportion in cement. The CO_2 emissions of the production of a cement with for example 40

wt.% calcined clay were between about 0.5 and 0.6 kg CO_2/kg cement at a calcination temperature up to 800 °C, depending on the calcination technology and raw material moisture.

4. Conclusions

The calcination of two different Calcite containing clays in a rotary kiln and in a flash calciner was simulated. The following conclusions can be stated:

- As the CO_2 emissions caused by the calcination of clays consist of combustion-related and raw material-related CO_2, different Calcite contents of the clays have a particularly large influence on the amount of CO_2 emitted at temperatures higher than 800 °C. Therefore, for materials containing carbonate, a firing temperature of more than 800 °C is not recommended with regard to CO_2 emissions.
- Depending on the calcination technology the emissions for both clays were between about 0.12 and 0.17 kg CO_2/kg calcined clay for calcination at 600 °C and between about 0.14 and 0.22 kg CO_2/kg for calcination at 800 °C.
- Under the assumptions made, the calcination process in the flash calciner is more efficient than calcination in the rotary kiln, both in terms of energy and CO_2 emissions. Beside other factors a significant difference is made by the waste heat losses, which are higher in the rotary kiln. Taking into account a more intensive use of waste heat or integration of clay calcination into the clinker production process, the disadvantages of the rotary kiln shown in the model can be significantly reduced.
- For the production of cements with 20 wt.% calcined clay the influences of clay mineralogy, moisture and calcination temperature as well as the calcination technology used are neglectable due to the high CO_2 footprint of Portland cement clinker. The specific CO_2 emissions of such a cement are about 0.7 kg/kg cement.

Acknowledgements

The Industrial Collective Research (IGF) project no. 19744 N of Verein Deutscher Zementwerke e.V., Research Institute of the German Cement Industry, is founded by the German Federation of Industrial Research Associations within the framework of IGF of the Federal Ministry for Economic Affairs and Climate Action based on a decision by the German Bundestag.

References

European Cement Research Academy; Cement Sustainability Initiative, Ed. Development of State of the Art-Techniques in Cement Manufacturing: Trying to Look Ahead; CSI/ECRA Technology Papers 2017. Duesseldorf, Geneva, 2017

Hernandez, J.F.M.; Scrivener, K.: Development and Introduction of a Low Clinker, Low Carbon, Ternary Blend Cement in Cuba. In: Proceedings of the 1st Int. Conf. on Calcined Clays for Sustainable Concrete (Lausanne). Heidelberg: Springer, 2015 (RILEM Bookseries 10), pp. 323-330

Sanchez Berriel, S.; Diaz, Y.C.; Hernandez, J.F.; Habert, G.: Assessment of Sustainability of Low Carbon Cement in Cuba. Cement Pilot Production and Prospective Case. In: Proceedings of the 1st Int. Conf. on Calcined Clays for Sustainable Concrete (Lausanne). Heidelberg: Springer, 2015 (RILEM Bookseries 10), pp. 189-194

Schulze, S.E.; Rickert, J.: Pozzolanic materials from calcination of calcareous and doped clays - studies on their hydration behaviour in cement: Reporting period: 01.01.2018-31.12.2019. Duesseldorf: VDZ gGmbH, 2020 (IGF-research project 19744 N)

Scrivener, K.: Options for the Future of Cement. Technical Paper in: The Indian Concrete Journal, July 2014, pp. 11-21

Scrivener, K., Fielding, R.: Reducing CO_2 Emissions: The Next Steps; World Cement, 2016, 4, pp. 9-14

Vizcaino, J.; Antoni, M.; Aluja, A.; Martirena, F.; Scrivener, K.: Industrial Manufacture of a Low-Clinker Blended Cement Using Low-Grade Calcined Clays and Limestone as SCM: The Cuban Experience. In: Proceedings of the 1st Int. Conf. on Calcined Clays for Sustainable Concrete (Lausanne). Heidelberg: Springer, 2015 (RILEM Bookseries 10), pp: 347-358

The 16th International Congress on the Chemistry of Cement 2023 (ICCC2023)
"Further Reduction of CO_2 -Emissions and Circularity in the Cement and Concrete Industry"
September 18–22, 2023, Bangkok, Thailand

ASSESSING THE VIABILITY OF INCOPERATING GRANITE DUST AS A PARTIAL CEMENT REPLACEMENT IN CONCRETE

Janina P Kanjee [1*], Thompho Netshivhera [2], Yunus Ballim [1] and Claudia Polese[2]

[1] *School of Civil and Environmental Engineering, University of the Witwatersrand, Johannesburg, South Africa Email: janina.kanjee@wits.ac.za*
[2] *School of Mechanical, Industrial and Aeronautical Engineering, University of the Witwatersrand, Johannesburg, South Africa. Email: 1610940@students.wits.ac.za*
[1] *School of Civil and Environmental Engineering, University of the Witwatersrand, Johannesburg, South Africa Email: yunus.ballim@wits.ac.za*
[2] *School of Mechanical, Industrial and Aeronautical Engineering, University of the Witwatersrand, Johannesburg, South Africa. Email: Claudia.Polese@wits.ac.za*

ABSTRACT

Granite is a highly durable material that is widely used in construction due to its resistance to weathering, thermal fluctuations and heavy loads. However, the process of cutting and preparing granite for commercial use generates a significant amount of dust powder that is typically discarded. This research explores the potential of utilising locally-sourced granite dust powder from South Africa as a partial replacement for Portland cement in concrete. The study aims to reduce waste and promote sustainable building practices. The project evaluated three different concrete mixtures, with a water-to-binder (w/b) ratio of 0.60. One of the mixtures was a control with 100% Portland cement (PC), while the other two mixtures replaced 30% of the Portland cement with either fly ash or granite dust powder. The heat of hydration and compressive strength of each mixture was assessed. The results showed that the concrete mixture containing 30% granite powder as a replacement for PC liberated more heat than the concrete made with 70/30% PC/fly ash. Additionally, the compressive strength of the concrete containing 30% granite powder was similar to that of the concrete containing 30% fly ash at 3, 7 and 28 days. These findings suggest that that the granite powder shows pozzolanic behaviour and may be considered as a supplementary cementitious material.

KEYWORDS: *granite dust powder, construction and demolition waste, pozzolan, cement replacement*

1. Introduction

Population growth, along with rapid urbanization and migration, has resulted in a significant increase in construction activities such as the development of housing, commercial buildings, and infrastructure projects. However, the generation of construction and demolition waste from these activities, which includes materials such as bricks, concrete, metal, timber, plasterboard, asphalt, glass, rock, and soil, is a growing concern. Unfortunately, due to the lack of knowledge and proper implementation of waste management legislation in South Africa, a considerable portion of this waste is disposed of in landfills or is illegally dumped [1]. This situation calls for urgent action to mitigate the negative environmental impacts of construction waste and has led to an increase in research focusing on the reuse of waste materials.

Granite dust powder is one such waste product generated from industrial activities, specifically the cutting and processing of granite blocks, extracted from parent rock, into slabs. Often, the excess granite powder and off-cuts are discarded in waste sites nearby. To explore more sustainable materials usage, this study examined the potential for using locally-sourced granite powder from South Africa as a supplementary cementitious material. The aim was to partially replace Portland cement (PC) in concrete, thus reducing both the amount of waste generated as well as the environmental impact of cement production [2]. Waste granite powder was obtained from a local manufacturing facility and used to replace PC in a concrete mixture. The adiabatic heat of hydration and compressive strength of the resulting concrete was determined. The results were compared with that of reference concretes made with a plain PC and one

with an equivalent replacement of fly ash as cement extender to provide an indication of the possible pozzolanicity of the granite dust.

2. Materials and test methods

2.1 Granite powder as a cement replacement

Granite dust was obtained from one of the large suppliers of thick granite slabs in the Southern African region. The grading profile of the as-received material was determined in accordance with SANS 201: 2008 [3] and is shown in Figure 1.

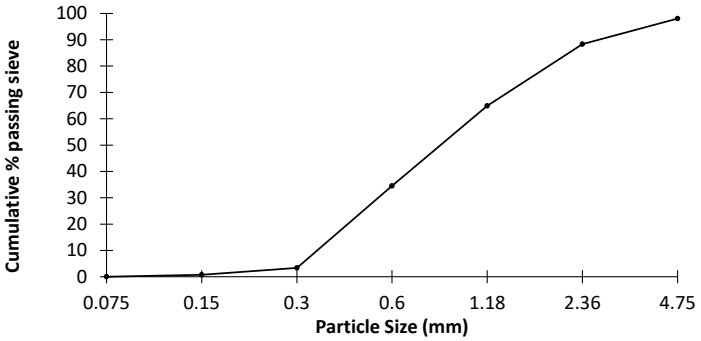

Figure 1 Grading profile for as-received granite dust powder

The material was milled in a laboratory-scale mill so that the entire sample passed a 75 μm sieve. X-ray fluorescence was used to determine the oxide composition of the granite powder and the results are shown in Table 1.

Table 1: Oxide composition of granite powder

Chemical composition (wt%)	Granite powder
SiO_2	50.9
Al_2O_3	15.6
CaO	11.8
FeO	8.92
MgO	8.32
Na_2O	2.01
K_2O	0.24

2.2 Concrete mix design

Table 2 provides a summary of the three concrete mixes used in this study. The mixes were designed using a water-to-binder (w/b) ratio of 0.6. One mixture served as the control, containing 0% replacement of PC while the other two mixes were replaced with either 30% fly ash (FA) or 30% granite powder (GP). The FA and PC were obtained from local commercial suppliers and are commonly used in concrete manufacture.

Table 2: Concrete proportions in kg/m^3

Material	Quantity (kg/m^3)		
	PC	PC-FA	PC-GP
CEM II 52.5 N (PC)	358	251	251
Water	215	215	215
Fly ash (FA)	0	107	0
Granite powder (GP)	0	0	107
Sand (Crushed Andesite)	873	873	873
Stone (19 mm Andesite)	1050	1050	1050

2.3 Testing approach

i. Determining heat of hydration

The heat of hydration test was conducted to determine the total heat evolved from the concrete with granite powder in comparison with the concrete mixtures containing PC and PC/FA as binders. The tests were carried out using an adiabatic calorimeter as described by Ballim *et al* [4, 5]. The temperature measurements were recorded over 100 hours. For each concrete mixture, both the total heat and the maturity heat rate were determined.

ii. Compressive strength tests

100 mm concrete cubes samples were prepared, water cured and tested in accordance with SANS:5863 [6]. The cubes were loaded using a cube machine which had a maximum loading capacity of 2 000 KN. The compressive strength of the concretes was determined at 3, 7 and 28 days after casting.

3. Results and discussion

3.1 Heat of hydration

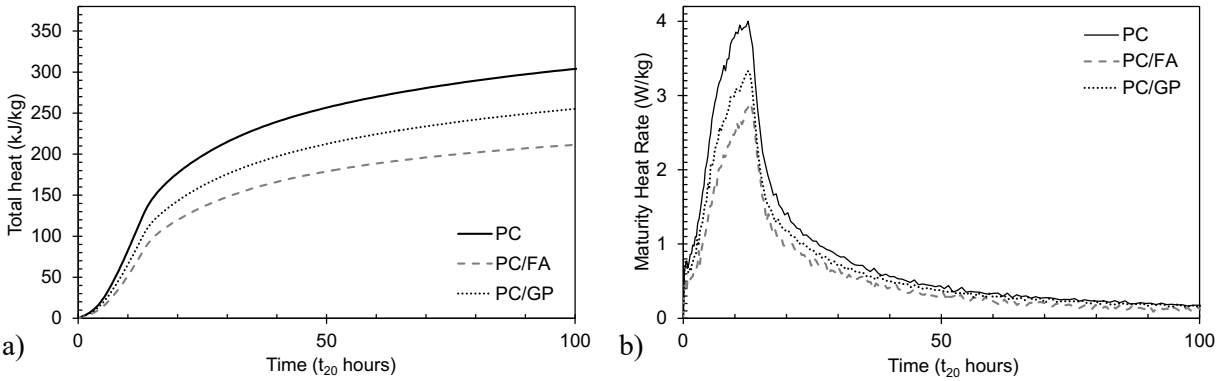

Figure 2: a) Total heat of hydration versus time b) Rate of heat release versus time.

Figure 2a illustrates the total heat liberated by the three concrete mixes over the first 100 t_{20} hours of testing. At this point, the total heat liberated was found to be approximately 303 kJ/kg for PC mix, compared to approximately 255 kJ/kg and 211 kJ/kg for PC/GP and PC/FA respectively. Given that the PC/GP curve falls between the PC and FA/PC curve, this indicates higher hydration activity in the GP concrete than in the FA concrete.

Figure 2b shows the maturity heat rates for all three concrete mixes with respect to the maturity time of hydration [7, 8]. The figure shows the heat rates over the first 100 t_{20} hours. Thereafter, the curves cluster close to each other, slowly tending towards the zero heat rate line. The important feature of Figure 2b is the peak heat rate that occurs between 4 and 18 t_{20} hours. The maximum measured heat rates for the concrete mixes are 4.00 W/kg for PC, 3.3 W/kg for PC/GP, to 2.85 W/kg for PC/FA. Based on the classification used by Ballim and Graham [8], cements PC and PC/GP fall in the category of high heat cements while PC/FA blend falls in the medium heat category. Nevertheless, the higher amount and rate of heat evolution from the GP concrete in comparison with that of the FA concrete indicates that the GP is either stimulating the hydration of the PC through the "fine-filler" effect or may well be reactive itself, resulting in greater amount and rate of heat evolution than the corresponding FA concrete.

3.2 Compressive strength

Figure 3 shows that as expected, over the 28-day testing period, replacing Portland cement (PC) with fly ash (FA) and granite powder generally leads to a decrease in compressive strength. Importantly, the compressive strength results of concrete incorporating GP were similar to those of concrete incorporating FA at 3 and 7 days. However, after 28 days, the compressive strength of the FA concrete was slightly greater, measuring 33 MPa compared to 30 MPa for the GP concrete. This again indicates that the GP may cause some stimulation in the hydration of the PC or that the GP has a pozzolanic reactivity that is at least as high as that of the FA used in this study.

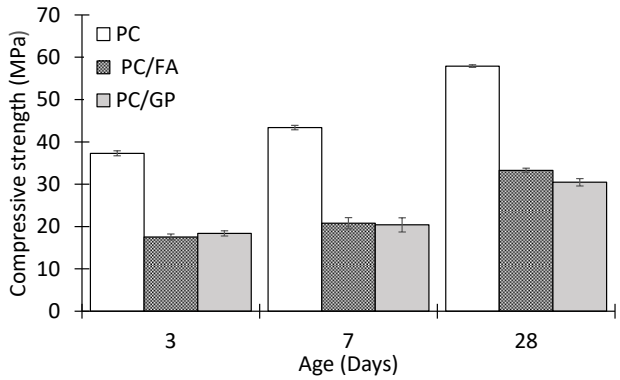

Figure 3: Compressive strength of concrete made using 100% PC, 70/30% PC/FA and 70/30% PC/GP as binders composition at 3, 7 and 28 days

4. Conclusions

The results of this study indicate that:

- The heat liberated from the concrete containing granite powder was greater than that of the concrete containing FA. This result indicates that granite powder may be pozzolanic in nature;
- The results indicate that, up to 28 days, the compressive strengths of concrete incorporating granite powder were lower than those of concrete containing 100% PC, as expected, but were similar to those of the concrete containing FA

In summary, the results suggest that granite powder may exhibit pozzolanic behavior and has the potential to be used as a viable supplementary cementitious material. However, further testing is necessary to assess the long-term compressive strength of the concrete, particularly in regard to a possible 'fine-filler' effect of the granite powder in stimulating the hydration of the PC in the composite binder.

Acknowledgements

The authors would like to acknowledge the support of Minaco (Pty) Ltd, from the Finstone Group for supplying the material for testing and for their agreement in publishing this paper.

References

1. Blengini, G.A., 2009. Life cycle of buildings, demolition and recycling potential: A case study in Turin, Italy. Building and environment, 44(2), pp.319-330.
2. Alexandru, T., Marinela, B., Laura, D. and Irina, B., 2019. Mechanical and Environmental Performances of Concrete Using Recycled Materials. Procedia Manufacturing, 32, pp.253-258.
3. SANS 201:2008., 2002. Sieve analysis, fines content and dust content of aggregates, Pretoria: South African Bureau of Standards.
4. Ballim, Y. (2004), A numerical model and associated calorimeter for predicting temperature profiles in mass concrete, Cement and Concrete Composites, Vol. 26, pp. 695-703
5. Gibbon, G.J., Ballim, Y. and Grieve, G.R.H. (1997), A low-cost, computer controlled adiabatic calorimeter for determining the heat of hydration of concrete. ASTM J Test Evaluation, 5(2), 261–266.
6. SANS 5863:2006., 2006. Concrete tests – compressive strength of hardened concrete, Pretoria: South African Bureau of Standards.
7. Ballim, Y. and Graham, P.C. (2003), A maturity approach to the rate of heat evolution in concrete. Magazine of Concrete Research 2003, 55(3): 249–256. 6.
8. Ballim, Y. and Graham, P.C. (2004), Early-age heat evolution of clinker cements in relation to microstructure and composition: implications for temperature development in large concrete elements, Cement & Concrete Composites, 26, 417–426

The 16th International Congress on the Chemistry of Cement 2023 (ICCC2023)
"Further Reduction of CO_2 -Emissions and Circularity in the Cement and Concrete Industry"
September 18–22, 2023, Bangkok, Thailand

Performance Evaluation and Beneficiation of Fly Ash Co-mingled with Flue Gas Desulfurization Products for Use in Concrete

G. Kaladharan[1*] and F. Rajabipour[2]
[1] *Senior Researcher, USG Corporation, Libertyville, Illinois, United States of America*
Email: gopakumarkaladharan@gmail.com
[2] *Professor, The Pennsylvania State University, University Park, Pennsylvania, United States of America*
Email: farshad@psu.edu

ABSTRACT
Fly ash co-mingled with flue gas desulfurization (FGD) products is often discarded as off-specification materials due to exceeding the 5.0%wt. SO_3 limit in ASTM C618. As such, it is expected that a sizeable fraction of fly ash harvested from landfills and ponds will have high SO_3 content. The composition of these materials differs significantly depending on the power plant boiler type and FGD process used and can include calcium sulfite, calcium sulfate, calcium oxide, calcium carbonate, sodium sulfate, and sodium carbonate. Consequently, the performance of these materials in concrete varies significantly and cannot be captured by the single SO_3 content limit specified. To investigate their use as alternative supplementary cementitious materials (SCM), four fly ashes co-mingled with FGD products were identified and tested. Their impact on workability, setting time, pore solution pH, compressive strength, and risk of volume expansion in lime water was investigated following standard protocols. Further, the early age hydration behavior of blended cement pastes incorporating these ashes was investigated using X-ray diffraction and isothermal calorimetry. Beneficiation options for the valorized use of these materials in concrete were identified based on the results.

KEYWORDS: *Off-specification fly ash, Setting time, Pore solution, Ettringite, X-ray diffraction*

1. Introduction
With the persistent shortage in the supply of fresh fly ash in the United States and many other countries (ACAA 2020), there is a need to identify suitable alternative SCMs for use in concrete. Fly ash contaminated with FGD products are a promising alternative that are currently discarded as off-specification materials due to exceeding the 5.0% SO_3 content limit in ASTM C618. This limit was put in place to prevent the risk of deleterious expansion caused by excessive ettringite formation. However, recent studies have shown that the SO_3 present in a majority of such fly ashes may not be in the form of calcium sulfate and thus may not cause deleterious expansion (Kaladharan and Rajabipour 2022; Sharifi et al. 2019). Other FGD contaminants present in the fly ash can include calcium sulfite, calcium oxide, calcium carbonate, sodium sulfate, and sodium carbonate (Miller 2011). Further, the authors have shown in a previous study that it may be more appropriate to restrict the SO_3 content of the total binder to 5.0%, rather than the fly ash, to prevent deleterious expansion when calcium sulfate is present (Kaladharan and Rajabipour 2022). Given that a sizeable fraction of fly ash harvested from landfills and ponds are expected to have a high SO_3 content (due to them being discarded in the past) (ACI PRC-232.5 2021), it is essential to evaluate these materials and beneficiate them for valorized used in concrete mixtures.

2. Materials and methods
A type I ordinary portland cement (OPC) was used in this study to evaluate the performance of five fly ashes. Among the fly ashes, one satisfied the ASTM C618 specifications and was referred to as the control fly ash (CFA). Two fly ashes contained hannebachite (calcium sulfite hemihydrate) as the primary FGD contaminant, resulting in high SO_3 contents. These high sulfur fly ashes were labelled HSFA1 and HSFA2. One fly ash had a high SO_3 content and high alkali content and was labelled as TFA (trona-impacted fly ash). The primary FGD contaminants in TFA were sodium sulfate and sodium carbonate. Finally, one fluidized bed combustion (FBC) fly ash was included with the primary FGD contaminant being anhydrite. The oxide composition of the cement and the five fly ashes are shown in Table 1. A detailed characterization of these materials can be found in the previous studies (Kaladharan et al. 2023; Kaladharan and Rajabipour 2022).

Table 1 – Oxide composition of cement and fly ashes

Material	SiO_2	Al_2O_3	Fe_2O_3	CaO	MgO	K_2O	Na_2O	SO_3	LOI
OPC	19.90	4.46	2.32	62.90	2.95	1.00	0.38	3.94	1.00
CFA	46.57	21.41	20.06	3.43	0.87	1.91	0.60	0.82	2.27
FBC	42.97	16.96	8.64	14.36	1.26	2.21	0.29	7.98	3.44
HSFA1	29.11	15.41	4.67	25.48	3.49	0.48	1.09	13.25	2.63
HSFA2	28.77	14.84	4.72	27.16	3.63	0.50	1.01	11.79	2.28
TFA	30.68	15.81	4.53	25.39	4.85	0.37	6.28	6.14	2.60

The fly ashes were tested in paste and mortar mixtures at 20% replacement level by mass of OPC. The tests performed includes normal consistency (ASTM C187), setting time (ASTM C191), and pore solution pH (Barneyback and Diamond 1981) at 0.45 w/cm using paste mixtures. The mortar mixture (at 0.485 w/cm) tests include flow (ASTM C1437), compressive strength of cubes (ASTM C109), and expansion in lime water test (ASTM C1038). An ASTM C33 concrete sand was used for the mortar mixtures with oven dry specific gravity of 2.62, absorption capacity of 1.66%, and fineness modulus of 3.00. Characterization studies such as quantitative x-ray diffraction (QXRD) and isothermal calorimetry (IC) were also conducted on paste mixtures at 0.45 w/cm and 20% replacement level by mass to understand the impact of these fly ashes on early age performance. The full procedure for these tests can be found in the previous study (Kaladharan et al. 2023). The effect of some additives was also evaluated. This includes the addition of the pH reducing admixture (Kaladharan et al. 2021) calcium acetate (CAc) to the mixtures with TFA ash and the addition of fine and coarse hannebachite powders to CFA ash to compare the performance to HSFAs.

3. Results and Discussion

The performance of the five fly ashes in selected standardized tests is reported in Table 2. The rest of the results can be found in the previous study (Kaladharan and Rajabipour 2022).

Table 2 – Performance of the five fly ashes in paste and mortar tests

Performance tests	OPC	CFA	HSFA1	HSFA2	FBC	TFA
Normal consistency (%)	29.4	27.2	28.2	28.2	31.5	26.2
Initial setting time (mins)	139	140	417	433	219	15
Final setting time (mins)	270	300	540	495	405	165
Pore solution pH (28-day, -)	13.97	13.88	-	-	-	14.16
Flow (%)	114	120	112	125	96	130
Compressive strength (1-day, MPa)	23.8	15.2	10.1	13.4	15.3	21.1
Compressive strength (91-day, MPa)	51.3	53.2	60.7	52.5	59.9	45.2
Expansion in lime water (14-day, %)	0.002	0.001	0.009	0.010	0.014	0.009

HSFA1 and HSFA2 were found to significantly delay the setting time of the paste. This is consistent with the literature on HSFA with hannebachite and the potential cause is discussed later. It has been shown in previous studies that the setting time can be accelerated either using chemical accelerators or using fine limestone powder (Kaladharan and Rajabipour 2022; Zunino et al. 2018). They also reduced the 1-day strength. However, the 91-day strength was similar or exceeded the performance of plain OPC and CFA mixtures. The 14-day expansion in lime water was less than the ASTM C595 limit of 0.02% for blended cements despite the high SO_3 content of the fly ashes due to lack of calcium sulfate phases.

In the case of TFA, flash setting was observed. This was due to sodium carbonate in the fly ash that is typically used as a shotcrete accelerator to encourage flash setting (Myrdal 2007). The flash setting was prevented by substituting 5% of the cementitious binder with calcium acetate. This increased the initial setting time from 15 to 94 minutes and final setting time from 165 to 285 minutes. The calcium acetate was initially added for its pH reducing effect, and as such it reduced the 28-day pore solution pH to 13.47; that was less than the 13.50 pH limit suggested in a previous study for mitigating ASR (Kaladharan et al. 2021). TFA increased the early age strength likely due to the excess alkalis accelerating the cement hydration. Finally, the expansion in lime water at 14 days was less than the ASTM C595 limit at 14 days despite the presence of sulfates. This is due to the lower SO_3 content of the overall binder (4.4%) and destabilization of ettringite at high pH (Alahrache et al. 2016).

Finally, FBC fly ash slightly delayed the setting time of the cementitious paste. However, this is likely due to the high w/cm required to achieve normal consistency. The morphology of the aluminosilicate phases in FBC ash is significantly different due to the differences in the combustion technology. As such, the aluminosilicates present in FBC fly ash are dehydroxylated phases that are similar to calcined clays and thus increase the water demand of the mix (also reduces the mortar flow value). The compressive strengths are comparable to or exceed the CFA mix. Finally, the expansion in lime water is higher than the other mixtures but still less than the ASTM C595 limit of 0.02% at 14 days. The total binder SO_3 content needs to be greater than 5.0% to exceed the 14-day expansion limit and the total SO_3 content of the binder with 20% FBC ash by mass was 4.75%.

The effect of HSFA1, HSFA2, TFA, FBC, and TFA+5%CAc on early age performance was further characterized using QXRD and IC analysis. The results are shown in Figure 1. It was observed that HSFA1 and HSFA2 delayed the dissolution of C_3S and C_3A (at 24 hours) phase based on the IC and QXRD results. It was also observed that the hannebachite content of the paste showed a slight negative slope indicating slow dissolution. The 24 h mass % was lower than the 10 min mass % and it was significant given the representative d2s value. It has been observed in previous studies that calcium sulfite can slowly dissolve over time in cement paste and prevent flash setting by controlling C_3A hydration similarly to calcium sulfate. However, it produces an Afm phase and no Aft phase and as such does not cause the deleterious expansion observed with ettringite production (Lagosz and Malolepszy 2003).

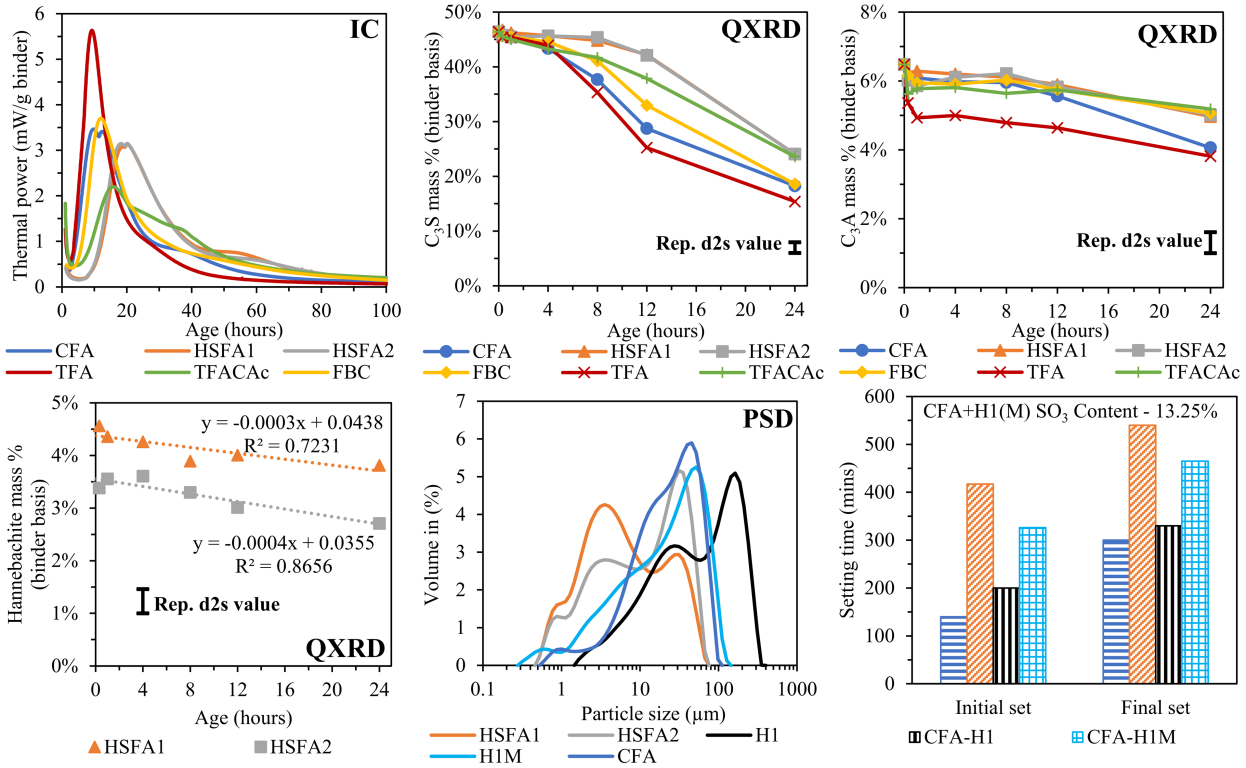

Figure 1 – Results from QXRD, isothermal calorimetry (IC), particle size distribution (PSD), and time of setting measurements of cement pastes containing the five fly ashes

HSFA1 and HSFA2 are significantly finer than CFA and this is consistent with the observations in literature (Sharifi et al. 2019; Zunino et al. 2018). Given the slow dissolution rate of hannebachite, the particle size distribution (PSD) of this FGD product may have a significant impact on the setting time performance. To replicate the performance of the HSFAs, CFA was combined with two hannebachite powders H1 and H1M such that the SO_3 content of this new "doped" fly ash matched the two HSFAs. H1M was much finer than H1 and was produced by milling H1. It was observed that the PSD of hannebachite plays a key role in setting time performance with the finer hannebachite (H1M) causing a more significant setting time delay as seen in Figure 1 (only "doped" fly ash corresponding to HSFA1 are shown). Further, it was shown in a previous study (Kaladharan et al. 2023) that sodium sulfite also causes setting time retardation suggesting that sulfite ions may be the cause of the observed early age behavior.

TFA caused a rapid dissolution of the C_3A phase as expected due to the presence of sodium carbonate. This resulted in a significant peak in the thermal power graph from IC since the primary (corresponding to silicate hydration) and secondary peaks (corresponding to gypsum depletion and renewed aluminate hydration) overlap. These observations are further substantiated by pore solution analysis using inductively coupled plasma atomic emission (ICP-AES) spectroscopy as shown in the previous study (Kaladharan et al. 2023). The addition of calcium acetate (CAc) significantly reduces the dissolution rate of C_3A phase and thus controls the flash set. It is expected that calcium acetate provides a highly soluble source of calcium ions that can react with the carbonate ions and precipitate it as calcium carbonate, thus preventing flash set. These observations were further substantiated using ICP-AES analysis of the pore solution as shown in the previous study (Kaladharan et al. 2023). Calcium acetate is also expected to precipitate out the sulfate ions supplied by the sodium sulfate phase as gypsum and this allows for good separation of the primary and secondary peaks as seen in the IC results of TFACAc.

FBC ash was also found to reduce the dissolution rate of C_3S slightly as seen in the QXRD results. However, the retardation effect observed at equal w/cm ratios in the characterization studies is roughly 20-30% and is much lower than the 56% delay observed in the vicat setting time study that is performed at normal consistency. Further, it was observed that FBC ash delays the dissolution of C_3A and the secondary peak in IC as expected due to the significant increase in the available sulfate content that delays depletion.

4. Conclusions

The performance of fly ash contaminated with FGD products varies significantly based on the contaminants present. In the case of HSFA with hannebachite, a significant setting time delay was observed likely due to the presence of fine (< 10 μm) hannebachite particles that can provide a constant supply of sulfite ions despite low solubility. This can be mitigated using chemical accelerators or fine limestone powder. TFA was found to cause flash setting of cement due to the presence of sodium carbonate. However, the pH reducing admixture, calcium acetate can mitigate the flash setting observed in addition to reducing the pore solution pH. Finally, FBC ash increases the water demand of the mix due to the differences in the particle morphology when compared to a traditional pulverized coal fly ash. In all cases, the expansion when submerged in lime water observed was less than the ASTM C595 limit of 0.02% at 14 days for blended cements. Since high SO_3 content is expected to be a significant challenge with harvested fly ash, it is essential to conduct further studies on these materials to encourage their valorized used in concrete.

Acknowledgments

Funding for this project was provided by the United States Dept. of Energy, under award# DE-AR0001143 granted to a team of researchers from Oregon State (lead), Penn State, Texas, and Purdue universities.

References

ACAA "American Coal Ash Association (ACAA) Production and Use Reports 2000-2020." Accessed Feb 27, 2023. https://acaa-usa.org/wp-content/uploads/coal-combustion-products-use/Coal-Ash-Production-and-Use.pdf.

ACI PRC-232.5-21: Harvested Fly Ash as a Supplementary Cementitious Material - TechNote. 2021.

Alahrache, S., F. Winnefeld, J.-B. Champenois, F. Hesselbarth, and B. Lothenbach. 2016. "Chemical activation of hybrid binders based on siliceous fly ash and Portland cement." *Cem Concr Compos*, 66: 10–23. Elsevier.

Barneyback Jr, R. S., and S. Diamond. 1981. "Expression and analysis of pore fluids from hardened cement pastes and mortars." *Cem Concr Res*, 11 (2): 279–285. Elsevier.

Kaladharan, G., R. M. Ghantous, and F. Rajabipour. 2023. "Early age hydration behavior of portland cement-based binders incorporating fly ash contaminated with FGD Products (Under Review)." *Cem Concr Compos*.

Kaladharan, G., and F. Rajabipour. 2022. "Evaluation and beneficiation of high sulfur and high alkali fly ashes for use as supplementary cementitious materials in concrete." *Constr Build Mater*, 339: 127672. Elsevier.

Kaladharan, G., T. Szeles, S. M. Stoffels, and F. Rajabipour. 2021. "Novel admixtures for mitigation of alkali-silica reaction in concrete." *Cem Concr Compos*, 104028.

Lagosz, A., and J. Malolepszy. 2003. "Tricalcium aluminate hydration in the presence of calcium sulfite hemihydrate." *Cem Concr Res*, 33 (3): 333–339. https://doi.org/https://doi.org/10.1016/S0008-8846(02)00957-2.

Miller, B. G. 2011. "Clean coal engineering technology." *Elsevier Inc.*

Myrdal, R. 2007. *Accelerating admixtures for concrete - State of the art, SINTEF Buiding and Infrastructure*.

Sharifi, N. P., R. B. Jewell, T. Duvallet, A. Oberlink, T. Robl, K. C. Mahboub, and K. J. Ladwig. 2019. "The utilization of sulfite-rich Spray Dryer Absorber Material in portland cement concrete." *Constr Build Mater*, 213: 306–312.

Zunino, F., D. P. Bentz, and J. Castro. 2018. "Reducing setting time of blended cement paste containing high-SO3 fly ash (HSFA) using chemical/physical accelerators and by fly ash pre-washing." *Cem Concr Compos*, 90: 14–26.

The 16th International Congress on the Chemistry of Cement 2023 (ICCC2023)
"Further Reduction of CO_2 -Emissions and Circularity in the Cement and Concrete Industry"
September 18–22, 2023, Bangkok, Thailand

Pozzolanic Reactivity and Characterization of Natural Pozzolans

K.S.T. Chopperla[1], K. Bharadwaj[2], G. Kaladharan[3*], S. Ramanathan[4], O.B. Isgor[5] and W.J. Weiss[6]

[1] *Postdoctoral Scholar, Oregon State University, Corvallis, USA*
Email: krishna.chopperla@oregonstate.edu
[2] *Postdoctoral Scholar, Oregon State University, Corvallis, USA*
Email: keshav.bharadwaj@oregonstate.edu
[3] *Postdoctoral Scholar, Oregon State University, Corvallis, USA*
Email: gopakumarkaladharan@gmail.com
[4] *Postdoctoral Scholar, Oregon State University, Corvallis, USA*
Email: sivakumar.ramanathan@oregonstate.edu
[5] *Professor, Oregon State University, Corvallis, USA*
Email: burkan.isgor@oregonstate.edu
[6] *Professor, Oregon State University, Corvallis, USA*
Email: jason.weiss@oregonstate.edu

ABSTRACT

Alternative supplementary cementitious materials (SCMs) such as natural pozzolans (NPs) have been gaining increasing interest as there is pressure to replace more of the clinker volume of concrete and concerns about the supply of conventional SCMs increase. This study demonstrates a framework for evaluating NPs for performance-engineered concrete. Four NPs were characterized for their physical and chemical properties. The reactivity of the NPs was quantified using the Pozzolanic Reactivity Test (PRT). The Reactive Pozzolanic Oxide (RPO) fractions of the NPs, which are calculated using the product of the oxide composition and PRT results, are useful defining the performance of the concrete mixtures. Thermodynamic and pore partitioning model calculations showed that NPs with similar RPOs as conventional SCMs can be used to produce concrete with similar properties as concrete made with conventional SCMs like Class F fly ash.

KEYWORDS: *Natural pozzolans, pozzolanic reactivity, reactive pozzolanic oxides, thermodynamic modeling, performance-engineered concrete*

1. Introduction

As the demand for supplementary cementitious materials (SCMs) has risen, and many commonly used SCMs are in short supply (American Coal Ash Association 2020), the interest in the use of natural pozzolans (NPs) has been increasing over the recent years (Natural Pozzolan Association 2019). In particular, volcanic ashes, tuffs, perlites, pumicites, and zeolites with high amorphous silica and alumina contents have been receiving significant attention as potential SCMs (Dedeloudis et al. 2018). However, NPs are reported to have a large variability in their composition and pozzolanic reactivity, and some NPs have been shown to increase the water demand of the mixtures as they may result in high water absorption from high internal porosity and specific surface area (Kastis et al. 2006, Seraj et al. 2016). Therefore, the use of these NPs in performance-engineered concrete mixtures requires careful characterization of their properties.

The goal of this paper is to demonstrate a process to evaluate NPs for their appropriate use in concrete. This paper focuses on characterizing NPs for their physical (e.g., fineness, specific gravity) and chemical properties (oxide composition), and determining their pozzolanic reactivity (DOR*) using the Pozzolanic Reactivity Test (PRT) (Bharadwaj et al. 2022). With the determined properties as inputs to thermodynamic and pore partitioning models (Azad et al. 2017, Bharadwaj et al. 2019), the performance of NPs in cementitious systems was predicted and compared to class F fly ashes (FA-F; data from (Weiss et al. 2022)) with corresponding mixture proportions (i.e., with similar water-to-binder ratio (w/b), age,

and SCM replacement amount). The used approach (outlined in Figure 1) allows for the prediction of paste specific properties such as gel and capillary pore volumes, and concrete properties such as total porosity, compressive strength, and formation factor (Bharadwaj et al. 2019, Bharadwaj et al. 2021). In this paper, the sum of capillary porosity and chemical shrinkage was chosen as the property to compare as it can be directly related to other mechanical and durability performance measures of concrete (Bharadwaj et al. 2019, Bharadwaj et al. 2021). This process is intended to provide a deeper understanding of the performance of cementitious mixtures with NPs when compared to traditional SCMs.

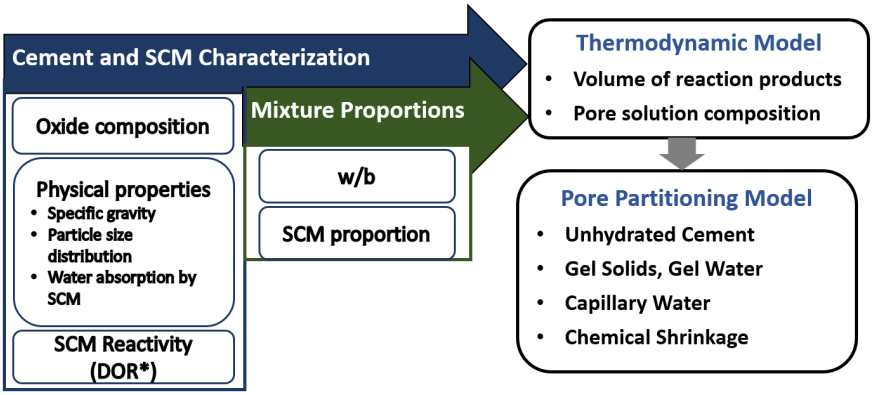

Figure 1: Illustration of the approach used to predict the performance of cementitious materials with SCMs

2. Materials and Methods

Four natural pozzolans (labelled as NP1 to NP4) were evaluated in this study as a partial replacement of a portland limestone cement (PLC, ASTM C595 IL). The PLC+NP systems had a constant w/b of 0.40, and the systems were studied at 56-days of reaction. The chemical compositions, specific gravity, particle size (d_{50}), and reactivity (DOR*) of the materials are given in Table 1. The DOR* is determined using PRT (Bharadwaj et al. 2022). In the PRT, the NP is reacted with an excess of calcium hydroxide (CH) (CH:SCM=3 by mass) and 0.5 N KOH (liquid:(CH+SCM)=0.9 by mass) at 50°C for 240 hours. The cumulative heat released by the reaction (Q) is measured using isothermal calorimetry. The DOR* is computed as Q divided by the maximum potential heat that can be released (theoretically calculated; e.g., 804 J/g_{SCM} for siliceous SCMs used in this study (Bharadwaj et al. 2022)). From the oxide compositions and DOR*, the reactive pozzolanic oxide (RPO) fraction of the SCM is calculated as the product of the DOR* and the sum of SiO_2 and Al_2O_3 in the SCM (Bharadwaj et al. 2023), shown in equation 1 (values for SCMs shown in Table 1).

Table 1: Composition (weight %), specific gravity, DOR*, RPO, and d50 of the materials used in the study

Oxide/property	PLC	NP1	NP2	NP3	NP4	FA-F Mean ± St. Dev.
Na_2O	0.10%	2.71%	1.64%	5.33%	0.15%	1.88%±2.17%
MgO	2.40%	0.15%	0.95%	0.98%	0.09%	2.27%±1.33%
Al_2O_3	3.69%	11.68%	10.28%	19.13%	24.64%	21.47%±2.57%
SiO_2	18.57%	72.39%	54.50%	63.33%	65.72%	51.97%±7.43%
SO_3	2.04%	0.08%	0.15%	0.03%	0.07%	1.05%±1.33%
K_2O	0.46%	5.75%	3.04%	1.58%	0.20%	1.34%±0.78%
CaO	62.68%	0.92%	16.40%	5.07%	0.18%	9.94%±5.61%
Fe_2O_3	3.71%	1.98%	2.76%	2.73%	0.80%	7.01%±3.37%
Loss on ignition	6.00%	4.06%	10.05%	1.27%	5.88%	2.89%±5.09%
Specific gravity	3.09	2.25	2.36	2.47	2.38	2.55±0.19
DOR*	-	32%	20%	21%	70%	42%±12%
RPO	-	27%	13%	18%	63%	33%±9%
d_{50} (µm)	14.5	14.6	11.3	22.6	9.3	-

$$RPO = DOR^* \times (SiO_2 + Al_2O_3) \quad (1)$$

Thermodynamic modeling can predict the reaction products that form when PLC+SCM binders react (Lothenbach et al. 2019). In this work, the GEMS3K software (Kulik et al. 2013) was coupled with the default PSI/Nagra and CemData v18.01 (Lothenbach et al. 2019) thermodynamic databases to perform thermodynamic calculations. The modified Parrott-Killoh model (Glosser et al. 2020) was used to generate the time-dependent input for thermodynamic calculations to predict reaction products at a given age. The outputs of thermodynamic modelling were used in a pore partitioning model for paste (Azad et al. 2017, Bharadwaj et al. 2019).

3. Results and Discussion

Figure 2(a) shows the distribution of RPOs of North American Class-F FAs, and the NPs tested in this study. The RPO is related to the performance of concrete made with the SCM as it is an indicator of the pozzolanic properties of the SCMs, in other words, their ability to react with CH to produce reaction products such as calcium-silica-hydrates. The tested NPs have RPOs between 13% and 63%, which in a similar range of the RPOs of conventional Class F fly ash (FA-F); the average RPO of FA-F is reported to be 33%±9% (Bharadwaj et al. 2023).
Figure 2(b) shows the sum of capillary porosity and chemical shrinkage of pastes made with PLC as a function of the replacement of PLC with SCM. The black solid line shows the dilution line (replacement of PLC with an SCM with RPO=0%, i.e., an inert filler). Increasing the replacement of PLC with an inert material increases the porosity due to dilution of reactive clinker with an unreactive material. The shaded region shows the performance of conventional FA-F. Increasing the replacement of PLC with FA-F by 10% increases the porosity by ~2% due to dilution of reactive clinker with less reactive FA-F. As the RPO of FA-Fs are typically 24-42%, the sum of capillary porosity and chemical shrinkage of the SCM system is slightly higher than that of the plain PLC system. The dashed lines indicate the sum of capillary porosity and chemical shrinkage vs. replacement for NP1-4. At a given replacement level, NPs with higher RPO (NP4) have a lower porosity than NPs with a lower RPO (NP2). This shows that RPO is an indicator of NPs potential for producing space-filling reaction products in concrete. Therefore, NPs with higher RPOs produce more pozzolanic reaction products that fill space and lower porosity.

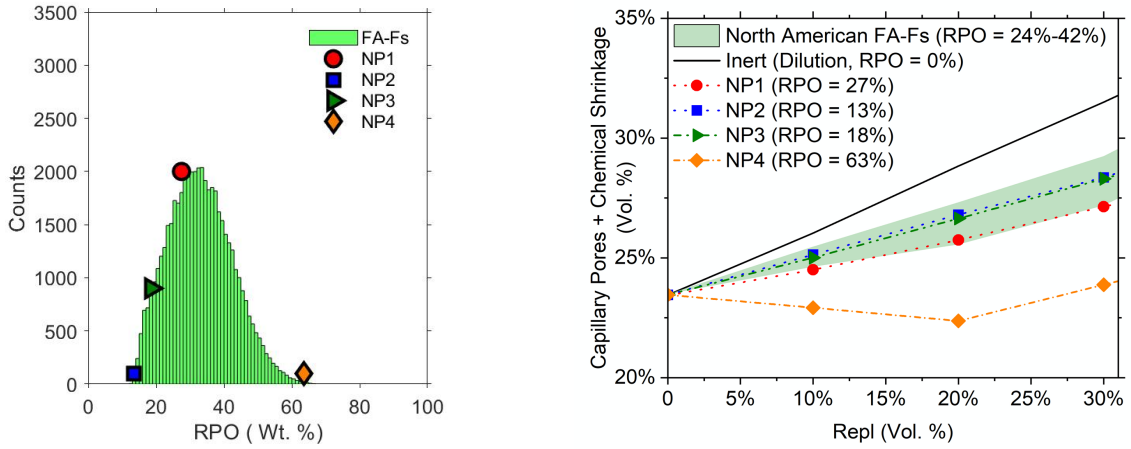

Figure 2: (a) Distribution of RPO of FA-Fs and NPs studied (b) predicted performance of PLC+Inert, PLC+FA-Fs, and PLC+NPs studied.

From Figure 2(b), for a target paste capillary porosity + chemical shrinkage of 27%, the volume replacement determined for NP1, NP2, NP3, and NP4 are 30%, 22%, 23%, and 50%, respectively. Therefore, the results of Figure 2 can be used to assess the potential use of NP1-4 in concrete and proportion them for concrete for a target performance, along with particle size and water demand information (the role of particle size and water demand are not discussed here).

4. Conclusions

This paper discusses a framework for evaluating NPs for use in performance-engineered concrete. The framework includes characterization of the cementitious materials, determination of SCM reactivity using

the pozzolanic reactivity test (PRT), and the use of thermodynamics-based modeling to predict the concrete performance. The results of the chemical analysis and PRT are used to calculated Reactive Pozzolanic Oxide (RPO) fraction, which is a simple index to describe the pozzolanic properties of SCMs. The comparison of the NPs with different RPOs with FA-F ashes show that NPs with similar RPOs as FA-Fs have similar performance (the sum of capillary porosity and chemical shrinkage was chosen as the performance indicator in this paper).

5. Acknowledgements

The authors would like to acknowledge California Department of Transportation (CALTRANS) for funding the study (Agreement Number 65A0974).

6. References

American Coal Ash Association (2020) “Ash at work: Applications, Science, and Sustainability of Coal Ash”, T. Adams. Farmington Hills, MI, American Coal Ash Association: 199.

Azad, V. J., Suraneni, P., Isgor, O. and Weiss, W. (2017) "Interpreting the pore structure of hydrating cement phases through a synergistic use of the Powers-Brownyard model, hydration kinetics, and thermodynamic calculations", *Advances in Civil Engineering Materials,* 6(1): 1-16

Bharadwaj, K., Glosser, D., Moradllo, M.K., Isgor, B.O. and Weiss, J. (2019). "Toward the Prediction of Pore Volumes and Freeze-Thaw Performance of Concrete Using Thermodynamic Modelling", *Cement and Concrete Research*, 124: 105820.

Bharadwaj, K., Ghantous, R.M., Sahan, F.N., Isgor, B.O. and Weiss, J. (2021) "Predicting Pore Volume, Compressive Strength, Pore Connectivity, and Formation Factor in Cementitious Pastes Containing Fly Ash", *Cement and Concrete Composites,* 122: 104113

Bharadwaj, K., Isgor, B.O. and Weiss, J. (2022) "A Simplified Approach to determine the Pozzolanic Reactivity of Commercial Supplementary Cementitious Materials", *Concrete International*, 44(1): 27-32

Bharadwaj, K., Weiss, W.J. and Isgor, B.O. (2023) "Towards Performance-Based Specifications for Fly Ash and Natural Pozzolans – Insights from a Monte-Carlo based Thermodynamic Modeling Framework." *Cement and Concrete Research*, In Review.

Dedeloudis, C., Zervaki, M., Sideris, K., Juenger, M., Alderete, N., Kamali-Bernard, S., Villagrán, Y. and Snellings, R. (2018) "Natural pozzolans." Properties of Fresh and Hardened Concrete Containing Supplementary Cementitious Materials: State-of-the-Art Report of the RILEM Technical Committee 238-SCM, Working Group 4: 181-231.

Glosser, D., P. Suraneni, O. B. Isgor and W. J. Weiss (2020) "Estimating reaction kinetics of cementitious pastes containing fly ash", *Cement and Concrete Composites,* 112: 103655

Juenger, M.C., Snellings, R. and Bernal, S.A. (2019) "Supplementary cementitious materials: New sources, characterization, and performance insights", *Cement and Concrete Research,* 122: 257-273

Kalina, R.D., Al-Shmaisani, S., Ferron, R.D. and Juenger, M.C. (2019) "False positives in ASTM C618 specifications for natural pozzolans", *ACI Materials Journal,* 116(1): 165-172

Kastis, D., Kakali, G., Tsivilis, S. and Stamatakis, M. (2006) "Properties and hydration of blended cements with calcareous diatomite", *Cement and Concrete Research,* 36(10): 1821-1826

Kulik, D. A., Wagner, T., Dmytrieva, S.V., Kosakowski, G., Hingerl, F.F., Chudnenko, K.V. and Berner, U.R. (2013) "GEM-Selektor geochemical modeling package: revised algorithm and GEMS3K numerical kernel for coupled simulation codes", *Computational Geosciences,* 17(1): 1-24

Lothenbach, B., Kulik, D. A., Matschei, T., Balonis, M., Baquerizo, L., Dilnesa, B., Miron, G. D. and Myers R. J. (2019) "Cemdata 18: A chemical thermodynamic database for hydrated Portland cements and alkali-activated materials", *Cement and Concrete Research,* 115: 472-506

Lothenbach, B. and Zajac, M. (2019). "Application of thermodynamic modelling to hydrated cements”, *Cement and Concrete Research*, 123: 105779

Natural Pozzolan Association, (n.d.). http://pozzolan.org/ (accessed February 25, 2023)

Seraj, S., Ferron, R.D. and Juenger, M.C. (2016) "Calcining natural zeolites to improve their effect on cementitious mixture workability." *Cement and Concrete Research,* 85: 102-110

Weiss, J. W., Isgor, B.O., Ideker, J.H., Bharadwaj, K., Ghantous, R.M., Rajabipour, F., Gomez, E., Kaladharan, G., Lan, Y.-C., Juenger, M.C.G., Katz, L., Zhu, T., Zavattieri, P., Wang, Y. and Innis, A. (2022) “Development of Thermodynamic and Kinetic Simulation Tools and Testing Procedures for Enhanced Durability of Concrete Containing Industrial By-Products”, Corvallis, Oregon, Oregon State University. Award No. DE-AR0001143

The 16th International Congress on the Chemistry of Cement 2023 (ICCC2023)
"Further Reduction of CO_2 -Emissions and Circularity in the Cement and Concrete Industry"
September 18–22, 2023, Bangkok, Thailand

Transformation of Bauxite Residue into a Reactive Supplementary Cementitious Material

Michiel Giels[1*], Tobias Hertel[2], and Yiannis Pontikes[3]

[1] *KU Leuven, Department of Materials Engineering, Leuven, Belgium*

Email: tobias.hertel@kuleuven.be
[2] *KU Leuven, Department of Materials Engineering, Leuven, Belgium*

Email: yiannis.pontikes@kuleuven.be
[3] *KU Leuven, Department of Materials Engineering, Leuven, Belgium*

Email: michiel.giels@kuleuven.be

ABSTRACT

In recent years, a new supplementary cementitious material (SCM) has been developed as a solution for the disposal of bauxite residue (BR), the alkaline residue generated by the alumina industry. This material is known as vitrified bauxite residue (VBR) and involves melting a mix of BR, and some minor fluxes at a temperature of 1200 °C followed by quenching. The purpose of this study was to investigate the reactivity and hydration of ground VBR in binary blends (with Portland cement (PC)) and ternary blends (with PC and limestone) for the production of pastes and mortars. Results indicate that VBR is actually a highly reactive SCM in the range of class C fly ash and ground granulated blast furnace slag, and its reactivity is significantly enhanced by the use of the grinding aid Triisopropanolamine (TIPA). An important synergy between limestone and VBR was identified, due to a difference in hydration products, allowing a strength activity index >80 % at 7 and 28 days, respectively, with only 53 wt% of PC.

KEYWORDS: *Alternative SCM, Bauxite residue, Reactivity, Hydration, Upscaling.*

1. Introduction

One of the main strategies pursued to decarbonize the cement industry is to replace a large amount of Portland cement (PC) clinker with locally produced SCMs. One such option is the use of bauxite residue (BR), the alkaline residue of alumina production, with a production of >150 Mt/y and a total disposed volume >4 Gt. The use of BR is currently still limited to less than 3%, and is generally considered an unsuitable SCM due to its negative impact on hydration, rheology, and mechanical performance, possibly also durability (Hertel & Pontikes, 2020). Figure 1 illustrates a new process that has been developed for transforming BR (>70 wt%) into a potential SCM suitable for blended and alkali-activated cement. This process involves partially melting a mixture of BR with SiO_2, CaO, and C-containing fluxes at 1200 °C, followed by quenching. The addition of SiO_2 as flux increases the quantity of the amorphous phase, CaO enhances SCM reactivity, and C reduces Fe^{3+} to Fe^{2+}, thereby lowering the liquidus temperature (Giels et al., 2022). It has been tested at pilot scale and shows promising results (Giels et al., 2021). This route results in the so-called vitrified bauxite residue, VBR, composed of an iron-depleted, reactive Al_2O_3-SiO_2-CaO-FeO-TiO_2-Na_2O amorphous phase, along with Fe-rich crystalline phases (Giels et al., 2022; Hertel et al., 2022). The current work aims to assess the reactivity of VBR as SCM, the resulting hydration products and the compressive strength of mortars in binary (with PC) and ternary (with PC and limestone) blends.

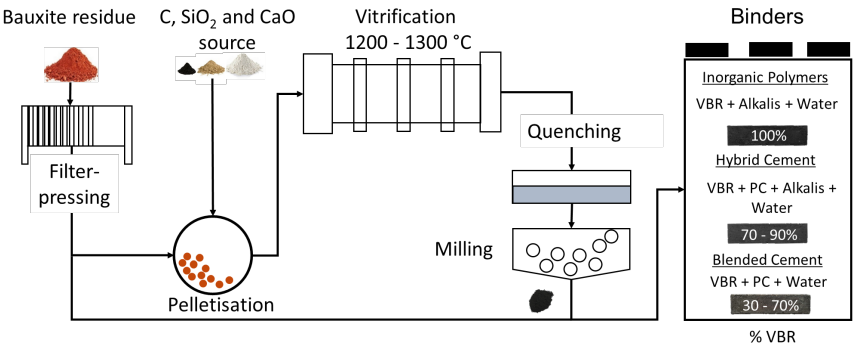

Figure 1: Simplified flowsheet showing the unit operations to obtain a milled VBR and its potential binders.

2. Methodology

VBR, produced at pilot scale (Giels et al., 2021), was dried at 105 °C and milled with and without the grinding aid Triisopropanolamine (TIPA) to a Blaine fineness of 4000 ± 300 cm²/g according to EN 196-6. VBR was chemically characterised on glass beads through XRF (S8 Tiger, Bruker). The mineralogy of VBR was analysed on powder through XRD (Bruker D2 Phaser). Samples were measured using a CuKα radiation of 30 kV, 10 mA from 5 to 70 ° 2 Θ, with a step size of 0.02°. Quantification of VBR was carried out using 10 wt% of an internal zincite standard. The reactivity of VBR was tested in a simulated cementitious pore solution with the rapid, relevant and reliable (R^3) test according to ASTM C1897-20. Table 1 shows the mortar mixes and cured according to EN 196-1. The compressive and flexural strength of the mortar prisms were tested using an Instron 5985 with a load rate of 2 and 0.5 mm/min, respectively. Paste samples were prepared using solely the components of the binder in Table 1 with hydration stoppage as described in Scrivener et al., 2016. The powdered pastes were measured with XRD with the settings mentioned for VBR. Thermogravimetric analysis (TGA; SDT Q600) of the powdered paste was conducted from 30 - 980 °C, in inert N_2 atmosphere, with a heating rate of 10 °C/min.

Table 1: Mix design of mortars according to EN 196-1.

[g]	PC	VBR	Gypsum (G)	Limestone (LS)	TIPA	Sand
PC	100	-	-	-	-	300
PC-VBR	68	29	3	-	-	300
PC-VBR-LS	53	29	3	15	-	300
PC-VBR-LS-T	53	29	3	15	0.02	300

3. Results and discussion

Table 2 shows that VBR is characterised by high FeO content and elevated Na_2O, which can be attributed to the presence of high volumes of BR.

[wt%]	Fe2O3	FeO	Al2O3	SiO2	CaO	Na2O	TiO2	Others	LOI
BR	49.2 ± 0.5	-	21.4 ± 0.5	13.3 ± 0.2	4.7 ± 0.1	7.3 ± 0.2	3.8 ± 0.1	0.2 ± 0	12.4 ± 1.4
VBR	-	34.7	18.7	18	17.5	7.0	2.8	1.3	-

Table 3 shows that Fe is mainly present in spinels within the solid solution $Fe(Fe, Al, Ti)_2O_3$, These spinels are of much interest as they are insoluble in alkaline conditions and immobilize hazardous element such as Cr and V (Giels et al., 2022; Hertel et al., 2022). The other elements are mainly enriched in the amorphous/glass phase.

Table 2: XRF of BR (10 samples) and VBR. VBR with Fe expressed as Fe^{2+} oxide, although also present as Fe^{3+}. LOI indicates loss on ignition (1000 °C).

[wt%]	Fe_2O_3	FeO	Al_2O_3	SiO_2	CaO	Na_2O	TiO_2	Others	LOI
BR	49.2 ± 0.5	-	21.4 ± 0.5	13.3 ± 0.2	4.7 ± 0.1	7.3 ± 0.2	3.8 ± 0.1	0.2 ± 0	12.4 ± 1.4
VBR	-	34.7	18.7	18	17.5	7.0	2.8	1.3	-

Table 3: Quantitative XRD of VBR, measurement on 3 independent samples.

Phase [wt%]	Amorphous	Spinel	Wüstite	Other
VBR	65 ± 4	32 ± 4	1 ± 1	2 ± 2

3.1 Reactivity test (R^3 test) and mortar strength

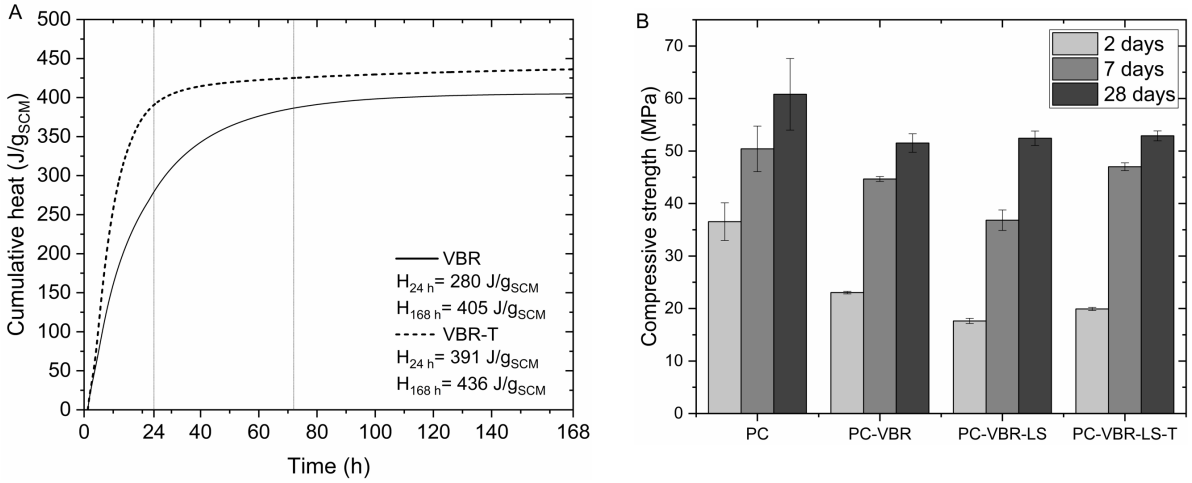

Figure 2A shows the cumulative R^3 heat up to 168 h for VBR milled without and with TIPA (0.02 wt%) to a Blaine fineness of 4300 ± 200 cm²/g. The reactivity of VBR milled with TIPA and without is in the range of class C-fly ashes and close to ground granules blast furnace slag (GGBFS), classifying VBR as a reactive SCM. The use of TIPA resulted in a significant effect on the heat release, particularly in the first 24 h compared to the one without TIPA. Overall, the results point to the likelihood of a high contribution of the VBR to the mechanical properties at about 7 d (24 h), which would even increase with the grinding aid TIPA.

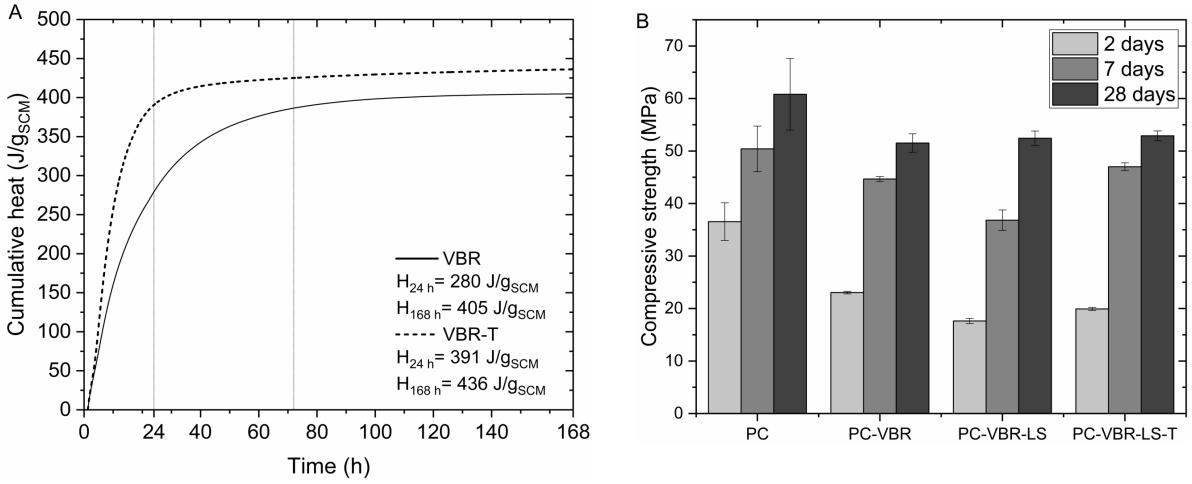

Figure 2B shows the compressive strength of the mortar bars. The strength for the mixes with VBR at 28d is all similar, with a strength activity index (SAI) of 86%. However, replacement of 15 wt% PC with LS did not affect the 28 d strength, indicating a possible synergy with carbonates. The use of TIPA increased significantly the 7 d strength up to a SAI of 93%. The beneficial effect of TIPA is most likely related to the increased dissolution rate of VBR, through complexation of Fe and Al and increased formation of AFm (Gartner & Myers, 1993; Hallet, 2022).

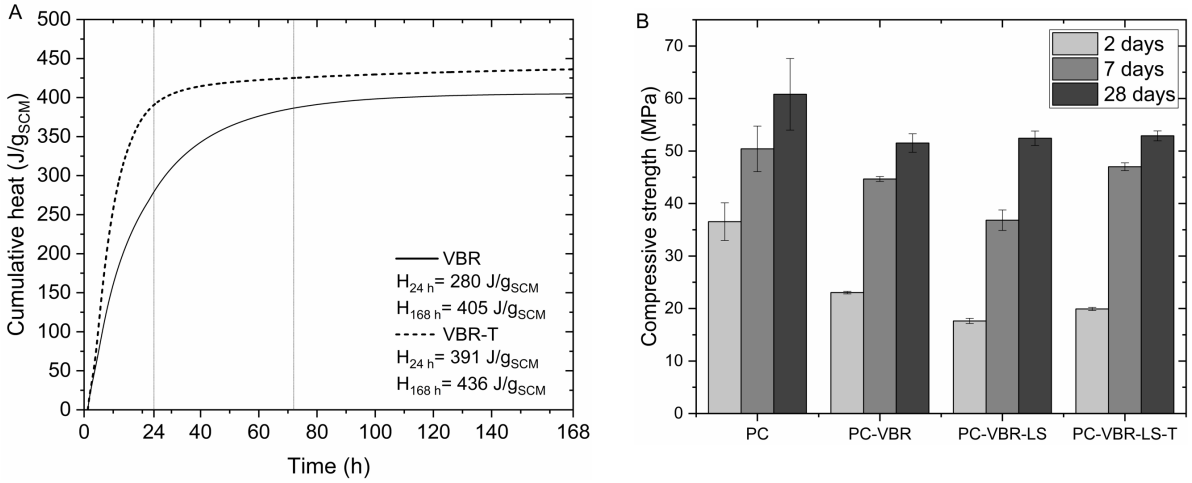

Figure 2: A) Cumulative R³ heat and comparison to other established SCMs according to (Li et al., 2018). B) 2, 7 and 28 d compressive strength of mortars.

3.3 Phase identification

The differential weight loss of the hydrated pastes measured by TGA for 2 and 28 d is shown in Figure 3A for PC-VBR and PC-VBR-LS. Several peaks can be observed due to AFt, AFm, CH and carbonates at 90, 140-160, 350, 440 and 600-800 °C. C-(A)-S-H can be identified as background between 100 and 600 °C (Scrivener et al., 2016). The AFt intensity is for PC-VBR significantly lower with respect to PC-VBR-LS and even decreases at 28 d. For both samples, increased AFm formation is observed, however the highest intensity was observed for PC-VBR-LS. The small hump at approximately 600 °C, indicates AFm-CO_3 is most likely present for PC-VBR-LS. Figure 3B shows the XRD of the hydrated pastes and indicates that the AFt phase is ettringite (Et) and the AFm phases are monosulfate (Ms), (carbonated) hemicarboaluminate (Hc), monocarboaluminate (Mc) and a AFm solid solution (Ss). For PC-VBR, , Ss is present, next to Et, at 2 d, while Et is transformed to Ms at 28 d with silicious hydrogarnet (Hg) formation also observed. For PC-VBR-LS Et, Hc and Mc are present, at 2 d, however, no Ms is formed. At 28 d, Et is not transformed to Ms, but is stabilized and an increased formation of Mc is observed. The presence of

LS improved the stability of Et as observed in LC³ systems (Antoni et al., 2012). The stabilization of Et also explains the similar compressive strength results in

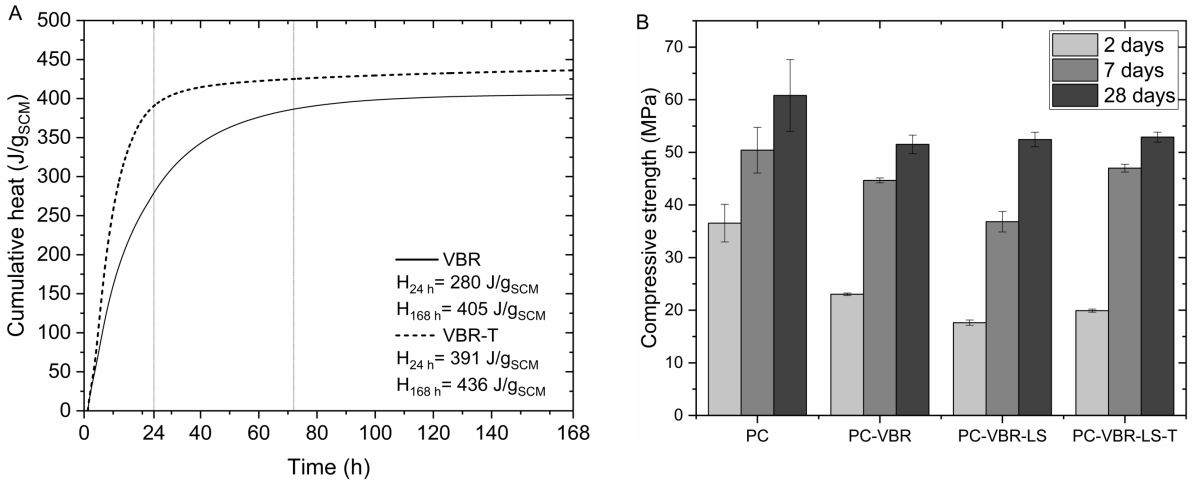

Figure 2B when 15% PC is substituted by LS.

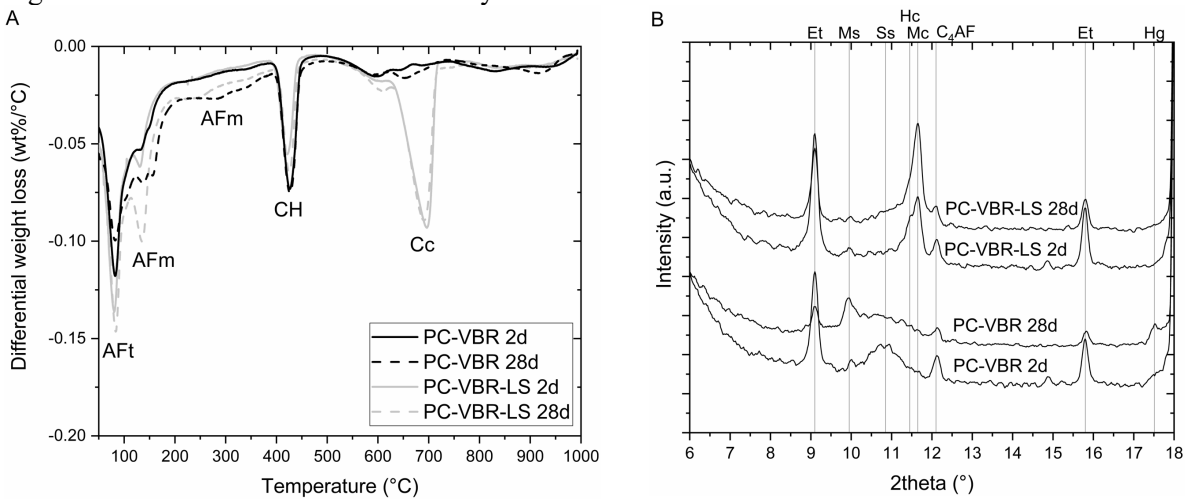

Figure 3: A) DTG B) XRD of paste mixes after 2 and 28 d.

4. Conclusions

This study revealed that VBR is a highly reactive SCM, in the range of class C fly ash and GGBFS, and that its reactivity is significantly enhanced with the use of the grinding aid TIPA. VBR and limestone showed a synergistic effect in ternary mixes on the formation of carboaluminates and the stabilization of ettringite in the binder. This resulted in a strength activity index of over 85% at 7 and 28 days, respectively, with only 53 wt% of PC in the mix. Various efforts are ongoing with the alumina and cement industry to investigate the durability of such binders, including the installation of products in a demo house (Removal project), as the process is further optimized with regard to cost and environmental impact.

Acknowledgements

The research leading to these results has been performed within the REMOVAL and REACTIV project, which received funding from the European Community's Horizon 2020 Programme under grant agreement n° 776469 and 958208.

References

Antoni, M., Rossen, J., Martirena, F., & Scrivener, K. (2012). Cement substitution by a combination of metakaolin

and limestone. *Cement and Concrete Research*, *42*(12), 1579–1589.
Gartner, E., & Myers, D. (1993). Influence of Tertiary Alkanolamines on Portland Cement Hydration. *Journal of the American Ceramic Society*, *76*(6), 1521–1530.
Giels, M., Hertel, T., Gijbels, K., Schroeyers, W., & Pontikes, Y. (2022). High performance mortars from vitrified bauxite residue; the quest for the optimal chemistry and processing conditions. *Cement and Concrete Research*, *155*, 106739.
Giels, M., Hertel, T., & Pontikes, Y. (2021). Transforming Bauxite Residue into an Alternative Cement via Vitrification, a Scalable Solution? *Proceedings of the 39th International ICSOBA Conference*, *50*, 401–407.
Hallet, V. (2022). High-volume replacement of cement by non-ferrous metallurgy slag and impact of limestone , fineness and grinding aids. In *Thesis KU Leuven*.
Hertel, T., & Pontikes, Y. (2020). Geopolymers, inorganic polymers, alkali-activated materials and hybrid binders from bauxite residue (red mud) – Putting things in perspective. *Journal of Cleaner Production*, *258*, 120610.
Hertel, T., Van den Bulck, A., Blanpain, B., & Pontikes, Y. (2022). Correlating the amorphous phase structure of vitrified bauxite residue (red mud) to the initial reactivity in binder systems. *Cement and Concrete Composites*, *127*(March 2021), 104410.
Li, X., Snellings, R., Antoni, M., Alderete, N. M., et al. (2018). Reactivity tests for supplementary cementitious materials: RILEM TC 267-TRM phase 1. *Materials and Structures/Materiaux et Constructions*, *51*(6).
Scrivener, K., Snellings, R., & Lothenbach, B. (2016). A Practical Guide to Microstructural Analysis of Cementitious Materials. In *Taylor & Francis Group* (Vol. 1).

The 16th International Congress on the Chemistry of Cement 2023 (ICCC2023)
"Further Reduction of CO_2 -Emissions and Circularity in the Cement and Concrete Industry"
September 18–22, 2023, Bangkok, Thailand

Reducing the clinker factor in vitrified bauxite residue-containing ternary blended cements

T. Hertel[1*], M. Giels[2], A. Muhammad[3], and Y. Pontikes[4]

[1] *KU Leuven, Department of Materials Engineering, Leuven, Belgium*
Email: tobias.hertel@kuleuven.be
[2] *KU Leuven, Department of Materials Engineering, Leuven, Belgium*
Email: michiel.giels@kuleuven.be
[3] *KU Leuven, Department of Materials Engineering, Leuven, Belgium*
Email: afsar.muhammad@kuleuven.be
[4] *KU Leuven, Department of Materials Engineering, Leuven, Belgium*
Email: yiannis.pontikes@kuleuven.be

ABSTRACT

In the present study, we investigated the potential of high volume incorporation of vitrified bauxite residue (VBR, produced via the partial vitrification of the Bayer's process alumina digestion residue) in ternary blends with limestone, mimicking systems that would classify as CEM II/B-M (70 wt% OPC), CEM II/C-M (55 wt% OPC) and CEM VI (40 and 35 wt% of OPC), according to EN197-5. With increasing contents of VBR, the early-age strength of mortars decreased from 25 to 7 MPa; however, more than 40 MPa were reached after 28 d for all systems. This strength gain over time demonstrates the high reactivity of VBR, a notable synergy between limestone and VBR, and ultimately, the possibility to significantly reduce the OPC content to as low as 35 wt% without compromising in late strength. Even with the lowest OPC content, a remarkable strength activity index (SAI) of >70 % was reached after 28 d. Sulfate optimisation led to an increase in early strength and approximately 20 MPa (SAI of 60 %) was reached in a CEM VI-type system with 35 wt% OPC, 15 wt% limestone and 50 wt% of VBR.

KEYWORDS: *ternary cements, bauxite residue, SCM, clinker factor, CO_2*

1. Introduction

Reducing the clinker factor in cement is one of the strategies, but also one of the challenges, towards carbon neutrality in the construction sector. In view of the envisaged energy transition and shifts in industrial production processes, well-established SCMs, such as coal combustion fly ash and ground granulated blast furnace slag, will become scarce. Alternative SCM systems are widely researched and several demonstrated their potential, some of them being at the implementation stage. A likely scenario for the future is a multitude of SCMs produced and used locally depending on the availability and where a synergy with other industries exists. Likely also, unexploited industrial wastes will play a crucial role. One of these candidates is vitrified bauxite residue (VBR), which is produced (to date at laboratory and pilot scale) via a reductive partial melting of the per se unreactive alumina digestion waste (bauxite residue) together with common additives, such as $CaCO_3$ and SiO_2 at temperatures of about 1200 °C, leading after quenching to a semi-vitrified, reactive SCM (Giels et al., 2021). The vitrification has been upscaled to 2 t and studies on the environmental and economic viability are currently ongoing. In the present study, we investigated the potential of high volume VBR incorporation in ternary blends with limestone, mimicking systems that would classify as CEM II/B-M, CEM II/C-M and CEM VI systems.

2. Materials and methods

Vitrified bauxite residue was produced at pilot scale (2 tonnes) by a partial vitrification process of bauxite residue together with minor contents of carbon as well as limestone and quartz using a top-blown rotary convertor at the pilot facilities of the RWTH Aachen University (Giels et al., 2021). An X-ray diffractogram was recorded, scanning a 2Theta range between 10 and 65° using a step size of 0.02° on a Bruker D2 (CuK_α radiation; 30 kV and 10 mA). Quantification was carried out using TiO_2 as an external standard. Electron microprobe analysis was carried out in order to determine the chemical composition of the amorphous as well as the crystalline phases present.
VBR was ground to a specific surface area (Blaine method, EN196-6) of about 4300 cm^2/g using triisopropanolamine (TIPA) (0.02 wt%) and was used as one of the constituents of the binder, next to OPC 52.5N from Holcim (France) and fine limestone from Carmeuse (Belgium), for producing mortar prisms according to EN196-1. Cement mortars were prepared increasing the fraction of vitrified bauxite residue in ternary blends with limestone to simulate CEM II/B-M, CEM II/C-M and CEM VI systems (Table 1). For some mixes, sulfate optimisation was carried out by adding gypsum in varying amounts and by assessing the effect on the mechanical properties, notably at early age. The consistency of the mortars was determined according to EN1015-3. Compressive strengths of the prisms were tested using an Instron testing device and a displacement speed of 2 mm/min. The strength activity index (SAI) was calculated based on a OPC 52.5N reference.

Table 1: Mortar mix designs.

Mix	Type	OPC (wt% of binder)	VBR (wt% of binder	Limestone (wt% of binder)	Gypsum (wt% of binder)
OPC-N	CEM I	100	-	-	-
70LVBRC	CEM II/B-M	70	15	15	-
55LVBRC	CEM II/C-M	53	29	15	3
40LVBRC	CEM VI	40	40	20	-
40LVBRC2G	CEM VI	39	39	20	2
35LVBRC	CEM VI	35	50	15	-
35LVBRC2G	CEM VI	34	49	15	2
35LVBRC4G	CEM VI	34	48	14	4
35L20VBRC	CEM VI	35	45	20	-
35L20VBRC2G	CEM VI	34	44	20	2

3. Results

X-ray diffraction quantification revealed an amorphous content of about 70 wt%, next to Fe-dominating crystalline phases, mainly spinel solid solutions $Fe(Fe,Al,Ti)_2O_4$.

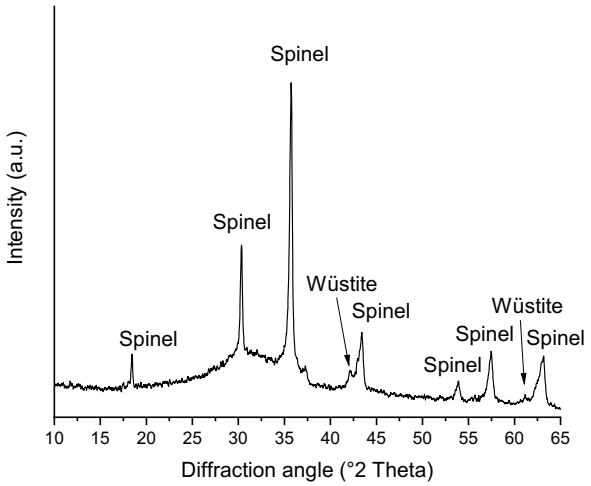

Figure 1: X-ray diffractogram of VBR.

The averaged chemistry of the amorphous phase (about 50 measurement points) was dominated in a descending order (expressed as oxides) by silica, alumina, calcium oxide and ferrous iron oxide (Table 2). Fe is in particular enriched in VBR compared to traditional SCMs, as well as the level of sodium oxide is elevated. Potential contaminants, such as Cr and V from bauxite residue, are present in spinel solid solutions and previous research has shown the immobility due to the encapsulation in the crystal lattice (Hertel et al., 2022; Giels et al., 2022). In contrast to LC^3 cements in which very often additives are required for controlling the rheology (Scrivener et al., 2018), the VBR-containing mixes reached without plasticiser a similar or better flow as the reference mortar (Table 3).

Table 2: Averaged composition of amorphous phase and spinel solid solution.

Phase	Amorphous phase wt%	Spinel solid solution wt%
SiO_2	27.0 ± 2.9	3.6 ± 2.0
Al_2O_3	21.9 ± 2.2	30.0 ± 3.6
CaO	21.8 ± 1.9	2.1 ± 2.0
FeO	16.8 ± 4.9	58.7 ± 4.9
Na_2O	6.1 ± 0.8	1.1 ± 0.8
TiO_2	3.2 ± 0.3	2.4 ± 1.1
MgO	0.1 ± 0.1	1.3 ± 0.9
V_2O_3	0.1 ± 0.0	0.2 ± 0.1
Cr_2O_3	0.0	0.6 ± 0.3

Table 3: Fresh mortar consistency.

Mix	Slump (mm)
OPC-N	190
70LVBRC	195
55LVBRC	190
40LVBRC	190
40LVBRC2G	190
35LVBRC	195
35LVBRC2G	205
35LVBRC4G	190
35L20VBRC	205
35L20VBRC2G	205

Results showed that with decreasing contents of OPC, the strengths decreased, in particular at early age. All prepared cement mortars reached, however, more than 42.5 MPa at late age and strength activity indices exceeded 70 % after 28 d, even for the system with less than 35 wt% OPC. For 55LVBRC, remarkable SAIs of >80 % were reached given the relatively low cement content, a result comparable to ground granulated blast furnace slag. These results demonstrated the high reactivity of the VBR and a notable synergy with limestone, also when comparing to a binary system of OPC and VBR (Giels and Hertel et al., 2023).
While low early age strengths were reached for mortars prepared with less than 40 wt% OPC and without sulfates, an increase in gypsum led to significantly higher early strengths and a 2 d compressive strength of 18 MPa, corresponding to an SAI of 60 %, was achieved in 35LVBRC4G. All investigated systems classify after gypsum optimisation as 42.5N according to EN 197-1 and are from a strength perspective comparable to GGBFS-containing cements in the market.

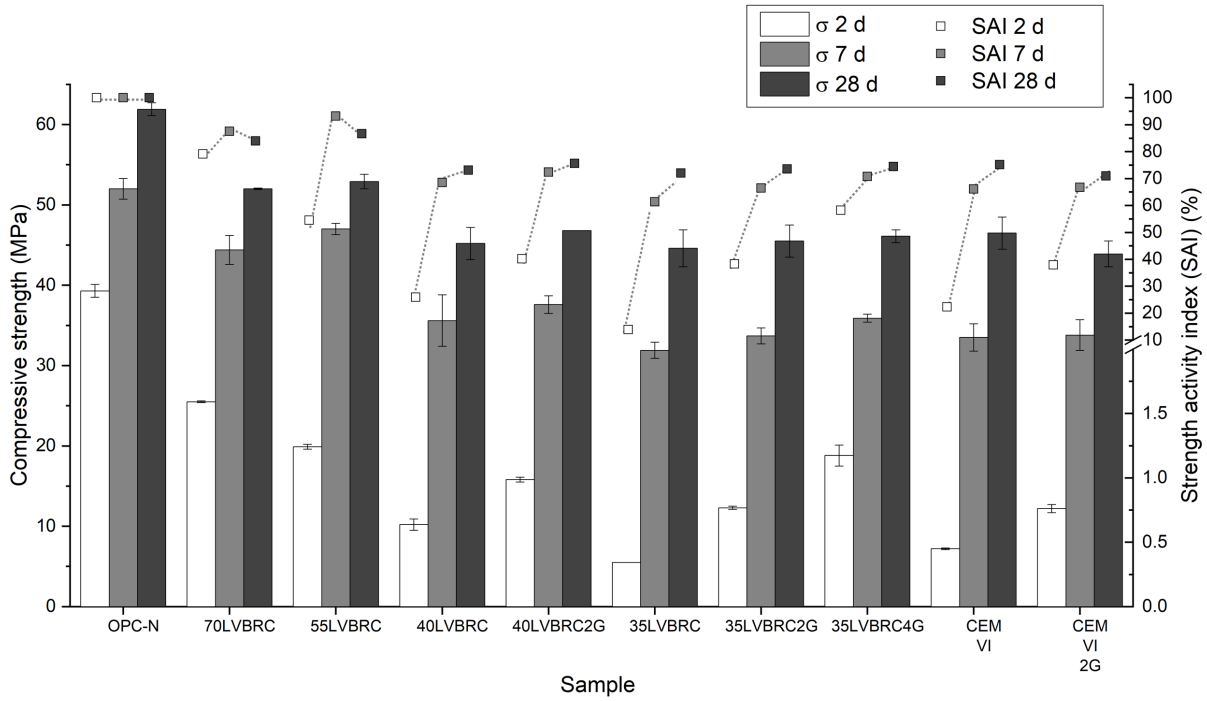

Figure 2: Compressive strength of investigated mortars.

4. Conclusions

In our study, we investigated ternary blends incorporating a high volume of VBR, OPC and limestone. The results highlighted the high reactivity of the VBR and a notable synergy with limestone, even at high replacement levels and low OPC contents. With an optimum gypsum content the systems classify as 42.5N according to EN 197-1. Our work has demonstrated that from a mechanical performance point of view VBR is a suitable alternative to GGBFS even with low clinker factors. Further research is currently ongoing to study the influence on other aspects, such as the long-term durability.

Acknowledgements

The research leading to these results has been performed within the REACTIV project and received funding from the European Community's Horizon 2020 Programme (H2020/2014-2020) under grant agreement n° 958208

References

Giels, M., Hertel, T., & Pontikes, Y. (2021). Transforming Bauxite Residue into an Alternative Cement via Vitrification, a Scalable Solution? *Proceedings of the 39th International ICSOBA Conference*, *50*, 401–407.

Giels, M., Hertel, T., Gijbels, K., Schroeyers, W., & Pontikes, Y. (2022). High performance mortars from vitrified bauxite residue; the quest for the optimal chemistry and processing conditions. *Cement and Concrete Research*, *155*, 106739.

Giels M. and Hertel T., Nguyen, T.N., Pontikes, Y. (2023) Vitrified bauxite residue as novel supplementary cementitious material, submitted to *Cement and Concrete Research*.

Hertel, T., Van den Bulck, A., Blanpain, B., & Pontikes, Y. (2022). Correlating the amorphous phase structure of vitrified bauxite residue (red mud) to the initial reactivity in binder systems. *Cement and Concrete Composites*, *127*, 104410.

Scrivener, K., Fernando, M., Shashank, B., Maity, S. (2018), Calcined clay limestone cements (LC3), *Cement and Concrete Research, 114*, 49–56.

The 16th International Congress on the Chemistry of Cement 2023 (ICCC2023)
"Further Reduction of CO_2 -Emissions and Circularity in the Cement and Concrete Industry"
September 18–22, 2023, Bangkok, Thailand

Use of synthetic-SCMs in blended cements and hybrid alkaline cements

A. Fernández-Jiménez[1*], P. Martín-Rodríguez [1], L. Fernández-Carrasco[2], A. Palomo[1], I. Garcia-Lodeiro[1]

[1] *Eduardo Torroja Institute for Construction Science (IETcc-CSIC), Madrid, Spain*

[2] *Escola de Camins, Canals i Ports de Barcelona, Universitat Politècnica de Catalunya, Barcelona, Spain*

Email: anafj@ietcc.csic.es

ABSTRACT

This work is part of a research project whose main objective is the elaboration of synthetic glassy/amorphous aluminosilicates to be used as supplementary cementitious materials (SCMs) in blended cements (BC) and in hybrid alkaline cements (HAC). Laboratory reagents (SiO_2, Al_2O_3 and CaO) were used to make a glassy/amorphous precursor with a chemical composition similar to a type C fly ash. To reduce the melting point, Na_2CO_3 was used as flux. Thermal treatment temperatures were 1000 ºC and 1100 ºC. With these Synthetic-SCMs (S-SCMs) two kind of cements were prepared: Blended Cements (BC=70% PC + 30% S-SCMs); and Hybrid Alkaline Cements (HAC=27.5% PC + 67.5% S-SCMs + 5% solid activator). Hydration kinetic were analyses by isothermal conduction calorimetry. The compressive strengths in cementitious pastes (cubes of 1*1*1 cm^3) were determined after 2 and 28 days of curing (Climatic Chamber at 21 ºC and 95% RH). Finally, the hydration products were characterized by XRD and the microstructure was explored by BSEM/EDX. Results indicate the viability of using this S-SCMs as a precursor in the elaboration of both blended and hybrid alkaline cements.

KEYWORDS: Synthetic-SCMs, blended- cement, hybrid alkaline cement

1. Introduction

Around 60% of the CO_2 generated by Portland cement (PC) manufacture is attributable to the decarbonation of the raw materials used to make portland clinker, 30% to the fuel used in the kiln and the remaining 10 % to the electric power consumption and transport. The most significant measures adopted to date by the cement industry include enhancing kiln efficiency; using alternative fuels and reducing the clinker factor, via replacement with supplementary cementitious materials (SCMs). Concerning this last approach, authors of this work, together with other research groups, are developing blended cements (BC) [Skibsted et al 2019], alkaline hybrid cements (HYC) [García-Lodeiro 2013) and/or alkaline cements (AC) [Palomo et al 2021].

The precursors used in these environmentally sustainable binders (BC, HYC and AC), comprise either natural products (pozzolans, thermally treated clays) or industrial wastes (such as blast furnace slag, fly ash or silica fume). SCMs were originally deployed to lower costs and to improve certain technological properties of cements or concretes (they may enhance late-age cement strengths, reduce the heat of hydration, improve the material durability and so on [Skibsted et al 2019].

Although the use of SCMs is technologically, economically and environmentally beneficial, their application is limited due to uncertainties around their quality, security on supply in sufficient quantities and geographic availability. Regarding blast furnace slag in recent years, higher growth in demand for cement than for steel and more intense steel recycling have led to a drastic decline in the proportion of slag relative to cement [Schneider 2019] Also, changing iron production technology from blast furnace to

electric arc furnace has decreased slag supply. Nowadays, worldwide BFS production covers just 8 % of cement industry demand, a trend that is bound to continue: in fact, in some countries, a tonne of slag is already more expensive than a tonne of clinker. FA supply poses problems of uniformity, with a composition varying with the type of coal and power plant operating conditions. Furthermore, coal fired plants are highly polluting and set to be closed in the years to come in many countries. The security on the fly ash (FA) supply in viable quantities is consequently disputable. Calcined pozzolans (Q) such as clays need to be thermally (750 °C to 900 ºC) or mechanically activated, and they are used less in Europe than BFS or FA because their lower reactivity, renders them less competitive. That may change in future, however, in light of the declining availability of slags and fly ashes, Scrivener et al. [2018] proved that low quality, thermally treated clays have potential for use in LC^3 (limestone-bearing ternary) cements.

For all these reasons, authors of this paper consider it is crucial to ensure a steady flow of viable quantities of SCMs. These innovative precursors could be used to manufacture binders such as BC, HYC and AC, which are cheaper and more sustainable cements than PC and perform as well as the latter. This project aims to develop glassy materials similar in composition to BFS and FA, and determine the effectiveness of such synthetic glass, as a replacement for substantial fractions of PC clinker in blended cements (BC) and hybrid alkaline cements (HAC).The specific objective of this work is to analyse the effect of the thermal treatment temperature (set at 1000 ºC and 1100 ºC) on the reactivity of a synthetic precursor, prepared with a chemical composition similar to a C-type fly ash (~ 20% CaO by weight, and SiO_2/Al_2O_3 =3).

2. Experimental

Laboratory reagents have been used to prepare the synthetic precursor (SP) with a chemical composition close to a C-type fly ash (54% SiO_2, 18%Al_2O_3, 18% CaO, 10% Na_2O weight %). The Na_2O content (added as Na_2CO_3) was incorporated as a flux, in order to lower the vitrification temperature. The synthesis processes were: SP1= 3 hours at 1000ºC; SP11=3 hours at 1100ºC. Subsequently, a quenching and a grinding were carried out to obtain a material with a particle size average smaller than 45 microns.

Figure 1 shows the XRD patterns of the SP synthesised under the two conditions (SP1 and SP11) , using BRUKER-AXS equipment. In both diffractograms wollastonite ($CaSiO_3$), pseudowollastonite ($Ca_3Si_3O_9$) and other calcium silicates (polymorphs of wollastonite) were identified as crystalline phases. Nepheline ($AlSiO_4$-Na) or albite ($Na(AlSi_3O_8)$ were also detected. Together with these cystalline phases, a hump for 2Θ values between 20º- 35º associated with an amorphous phase, was observed.

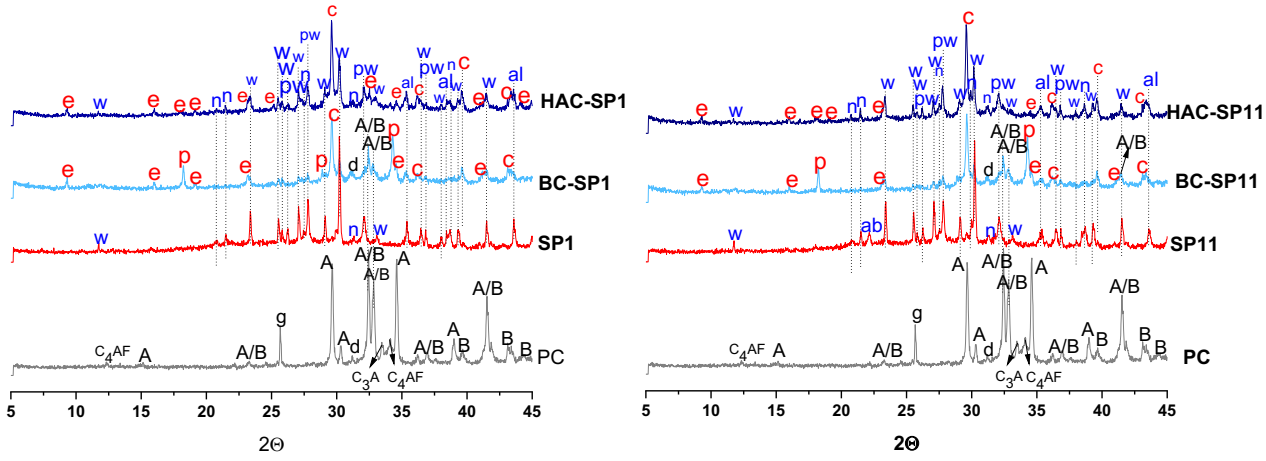

Fig. 1- XRD patterns of SP1, SP11, and Cem1 and hydrated cements at 28 days (BC-SP1, HAC-SP1, BC-SP11, HAC-SP11). Legend: g=gypsum; A=alite; B=Belite; w= wollastonite; pw=pseudowollastonite; n= nepheline; a=albite; e= ettringite; p=portlandite; c=calcite.

With these SP powders two types of cements were prepared: Blended Cements (BC-SP1=70% PC + 30% SP1; BC-SP11= 70% PC + 30% SP11); and Hybrid Alkaline Cements (HAC-SP1=27.5% PC + 67.5%

SP1 + 5% solid Activator; HAC-SP11=27.5% PC + 67.5% SP11 + 5% solid Activator). A CEM I 52.5N cement (61.47% CaO, 18.13 SiO_2 and 4.29% Al_2O_3) was used in the preparation of these cements (BC and HAC). Aditionally a reference system made of CEM I 52.5 was also studied.
With these pastes, cubes of 1*1*1 cm^3 were prepared and cured for 20h in a climatic chamber (at 22 ± 2 ºC, relative humidity > 95%) using a water/binder ratio (w/b)=0.3. The specimens were kept in the chamber until they reached the 2d. and 28d, (curing time); then the compressive strength was determined

Hydration kinetics (at 25ºC for a water/binder ratio= 0.3) was determined by isothermal conduction calorimetry (TAM Air isothermal calorimeter). Hydration products were characterized after 28 days, by XRD (Bruker D8 ADVANCE diffractometer), and BSEM/EDX (scanning electron microscope S-4800, HITACHI), more information about the recording conditions in reference Millán-Corrales et al (2020).

3. Results and discussion

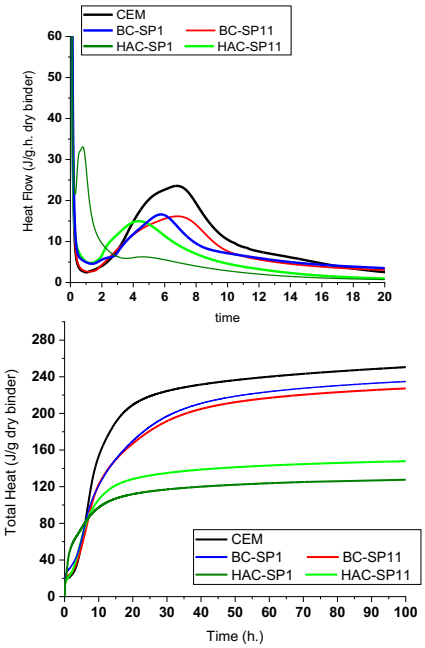

Fig. 2. Heat Flow and Total Heat

Fig. 2 show the heat flow (J/g.h) and total heat release curves (J/g). The heat flow curves were relatively similar for all the systems, with a first signal, very difficult to detect, followed by a brief induction period and then a second peak, much more wider than the first one. In PC system, the second peak is associated with the formation and precipitation of reaction products (C-S-H+$Ca(OH)_2$). The small shoulder detected on this peak, is attributed to sulfate depletion. The substitution of PC by SP (SP1 and SP11) hastened the hydration, although the intensity of the calorimetric peak declined, suggesting less heat of hydration.

Some differenceswere observed between BC and HAC; in BC, a delay in the kinetics of hydration was observed, and a higher heat of hydration is realesed. However in HAC, where the amount of SP added was higher (70%), an initial acceleration of the process and a lower total heat were observed. The acceleration detected in HAC is associated with the sum of several factors: the dilution effect, the filler effect and the accelerating effect of the alkaline activator**.**

Table 1 shows the compressive strengths of all the cementitious systems. All the pastes set and harden giving adequate mechanical strengths. Portland cement (CEM), exceeds 66 MPa at 2 days. Blended cement (BC) has lower initial strengths than the 100% cement system, although at 28 days the values tend to be similar. Hybrid alkaline cements (HAC) show lower initial and final strengths than the former, although they exceed 50 MPa at the age of 28 days. It is notice that the PC content in these systems is only 30%. No significant differences are observed between using SP1 (obtained at 1000 ºC) or SP11 (obtained at 1100 ºC).

Table 1. Compressive strengths (Mpa) in paste specimes (1*1*1 cm^3)

Cement	Precursor	w/b	2d	14d	28d
CEM I	**--------**	**0.3**	66.77±3.49	No data	70.49±7.59
BC	**SP1=1000ºC**	**0.3**	49.64 ± 6.39	70.88± 1.99	73.09±6.97
	SP11=1100ºC	**0.3**	48.97 ± 3.52	70.58±1.09	70.73±1.66
HAC	**SP1=1000ºC**	**0.3**	24.18 ± 0.80	44.63±3.36	52.67±1.08
	SP11= 1100ºC	**0.3**	26.41±1.03	44.55±7.16	56.21±3.09

XRD patterns corresponding to the pastes at 28 days are also shown in Fig. 1. It can be observed that the main clinker phases present in the PC (Alite, Belite,…) have reacted; however, the crystalline phases

detected in the original SP remain unaltered. As new crystalline phases in the hydrated material, ettringite and portlandite, are detected. The intensity of the peaks associated with portlandite is higher in BC than in HAC. It is also observed that the hump corresponding to the amorphous phase detected on SP1 and SP11 (2Θ = 20-30º) disappears or shifts towards higher values (2Θ=30-35º), indicating the formation of new amorphous reaction products, possibly a mixture of gels. From the mineralogical point of view, no relevant differences are observed between using SP1 or SP11.

Fig. 3 shows micrographs corresponding to BC-SP1-28d and HAC-SP1-28d pastes. EDX results show that the cementitious matrix consists mainly on Ca, Si and Al, however the proportion of each element varies throughout the matrix, suggesting the precipitation of a mixture of cementitious gels as main binding phases. C-A-S-H-like gels, with high calcium content (points 3 and 4) are formed near the cement particles, while (N,C)-A-S-H-like gels, low in Ca and high in Al (points 5) are detected around the SP particles. The proportion of C-A-S-H gels is apparently higher in the BC type cement, while a higher mixture of both gels (C-A-S-H + (N,C)-A-S-H) is observed in the HAC type cement .

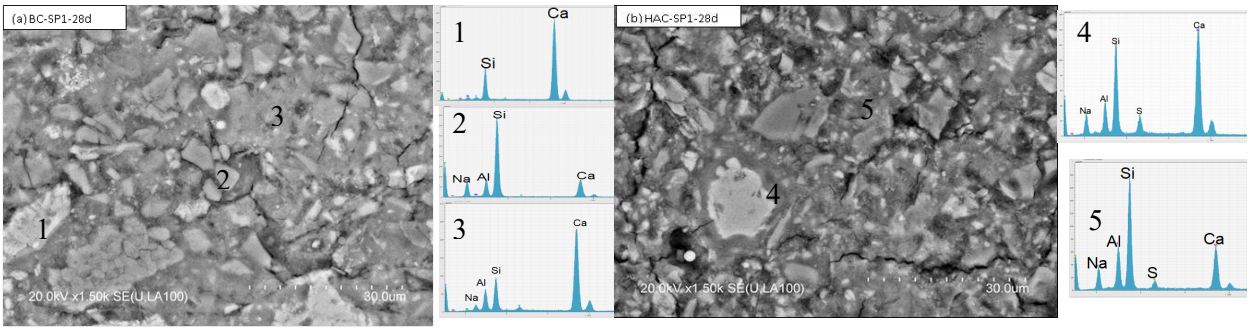

Fig. 3. BEM micrographs of cement pastes (a) BC-SP1-28 days; (b) HAC-SP1-28 days 1-particle of PC; 2 particle SP1; 3 Gel C-A-S-H; 4, GelC-A-S-H; 5-Gel (N,C)-A-S-H

3. Conclusions

The reaction mechanism of the SPs used as SCMs is complex and is associated with the overlapping of several mechanisms: filling effect, nucleation effect, dilution effect and chemical effect (the latter is more relevant in HACs). No significant differences were observed between using SP1 or SP11, the major differences observed are associated with the different levels of substitution (30% in BC and 70% in HAC).

The manufacture of Synthetic-SCMs would avoid the problems of geographical availability, compositional variability and product quality (purity). PC is produced in the temperature range of 1400-1500 ◦C while SP used in this work is obtained at temperatures around 1000 ◦C. The CaO content is low, therefore, the carbon footprint would be reduced compared with CEM I.

Acknowledgements

Authors wish to thank the Spanish Ministry of Science and Innovation, the Spanish State Agency for Research (AEI), and the FEDER funds for the award of the research project "Synthesis of low-temperature glassy supplementary cementitious materials (GlassyMat)" (PID2019-11464RB-100) and the award of the FPI pre-doctoral grant (PRE2020-091909).

Reference

Skibsted, J. Snellings, R. (2019) “Reactivity of supplementary cementitious materials (SCMs) in cement blends” *Cem. Concr. Res. 124, 105799.*

García-Lodeiro, I. Fernández-Jiménez, A. Palomo, A. (2013) “Variation in hybrid cements over time. Alkaline activation of fly ash-portland cement blends”, *Cem. Concr. Res*. 52, 112–122.

Palomo, A. Maltseva, O. Garcia-Lodeiro, I. and Fernández-Jiménez, A. (2021) “Portland Versus Alkaline Cement: Continuity or Clean Break: A Key Decision for Global Sustainability”. Front. Chem. 9:705475.

Schneider M. (2019), “The cement industry on the way to a low-carbon future” Cem. Concr. Res. 124, 105792.

Scrivener K., Martirena F., Bishnoi S., Maity S., (2018) “Calcined clay limestone cements (LC3)” *Cem. Concr. Res.* 114, 49-56.

Millán-Corrales, G. González-López, J.R. Palomo, A. Fernandez-Jiménez, A. (2020) "Replacing fly ash with limestone dust in hybrid cements” Construction and Building Materials 243, 118169

The 16th International Congress on the Chemistry of Cement 2023 (ICCC2023)
"Further Reduction of CO_2 -Emissions and Circularity in the Cement and Concrete Industry"
September 18–22, 2023, Bangkok, Thailand

Influence of burning level on calcined clay reactivity - Experience from a rotary field trial up to RMX application

C.P. Rodriguez[1*], C.A. Orozco[2], and A.C. Gómez[3]

[1] *Cementos Argos, Medellín, Colombia*
Email: crodriguro@argos.com.co
[2] *Cementos Argos, Medellín, Colombia*
Email: corozco@argos.com.co
[3] *Cementos Argos, Medellín, Colombia*
Email: acgomezgo@argos.com.co

ABSTRACT

Today's construction industry faces challenges in reducing carbon emissions through the use of alternative materials such as calcined clays that are widely abundant. To better understand and improve the experiences gained in the laboratory, a field trial in a rotary kiln (120-300 tpd) was carried out to produce calcined clays at different calcination levels as well as different fineness in the final product using an industrial ball mill (15 tph). The hypothesis is that high calcination temperatures, above the optimum, combined with proper grinding, could produce a calcined clay suitable for use as an SCM stand-alone in the RMX. Description of the calcined clay features such as LoI, XRD, density, BET, and residue on mesh 325, are linked to strength development and water demand up to mortar scale, and comparative results with Fly ash in concrete at lab scale are also shown. At mortar scale, the results indicate that overcalcination of clays, expressed as mullite formation (2-40%) could indeed reduce water requirement by up to 10%, with the natural consequence of decreasing compressive strengths (-10% SAI). Slight improvement in water demand was found when fineness is varied but some modest enhancement in compressive strength could be obtained. On concrete, straight replacement of fly ash by calcined clay could be done, gaining cementitious efficiency at 28 days (from 0.12 MPa/kg with fly ash up to 0.19 MPa/kg with calcined clay) with a 10% increase in the water required to achieve same slump. Finally, calcined clay could be implemented in RMX applications, but more education and a shift in the mindset of designers and engineers are needed to make calcined a reality.

KEYWORDS: *Calcined clays, burning level, calcined clay grinding, water requirement & RMX field application.*

1. Introduction

The use of calcined clays as pozzolanic materials has attracted interest in recent years as an alternative to reduce the carbon footprint of the construction industry. On the cement side, it involves reducing the clinker to cement ratio, i.e. LC3 cement (Scrivener, 2014), (Sharma et al., 2021), while on the concrete side it could be considered as a suplementary cementitious material, i.e. fly ash (Sabir et al., 2001). Despite the extensive experience of using metakaolin in concrete applications (Siddique & Klaus, 2009) such as high-performance concrete and precast concrete, calcined clays have not attracted the same interest as SCM, although benefits such as increased compressive and flexural strength, reduced permeability, and reduced alkali-silica reactivity (ASR) have been highlighted for this product (Sharma et al., 2021). Conversely, the additional water requirement is the Achilles heel of both metakaolin and calcined clay. In this regard, a 10% substitution of metakaolin can increase water requirements by 105-118%, while 20% substitution can account for 116-149%, with the small particle size considered the main reason for the water demand (Siddique & Klaus, 2009). With this in mind, it's proposed that the level of calcination and fineness be studied with respect to the water demand of the calcined clay. The premise is that a slight over-calcination may result in a more workable calcined clay.

2. Materials and Methods

2.1 Clay calcination and grinding

Calcination was carried out in an industrial rotary kiln (3.2 m diameter x 48.8 m length) equipped with a flame burner fueled by natural gas. Raw clay with moisture content of 20-24% was fed into the kiln, and a steady production of 12 t/h (approximately 50% of capacity) was achieved with an average heat consumption of 650 kcal/kg. The calcination level of the clay was linked to the loss on ignition (LoI) (ASTM C114 2007), which was used to adjust the calcination temperature, ranging from 750°C to 870°C. Following calcination, the clays were ground in a single-chamber ball mill (3 m diameter x 6 m length) at 15 tons per hour. Differential fineness was measured as residue on mesh 325 (R325) using the ASTM C 430 standard (ASTM, 2017). Calcined clays were identified according to their burning level (LoI) and fineness (R325), and are summarized in Table 1 along with the main variations in their quality features.

Table 1. Properties of calcined clays

	CC-1.6%	CC-1.3%	CC-1.1%	CC-0.3%	CC-R30%	CC-R15%	CC-R1%
Aim	Level of burning				Fineness		
LoI (%)	1.6	1.3	1.1	≈0.3		≈0.3	≈0.3
R325 (%)	26	29	33	32		13	1

2.2 Characterization of materials

A clay with a high kaolinite content (70%) was selected for testing. X-ray diffraction (XRD) was used to identify mineral companions (Figure 1). The raw clay contained kaolinite (K), quartz (Q), gibbsite (Gi), and minerals from the mica group, while the calcined clays contained quartz, cristobalite (Cr), magnetite/maghemite (not shown), and mullite (Mu).

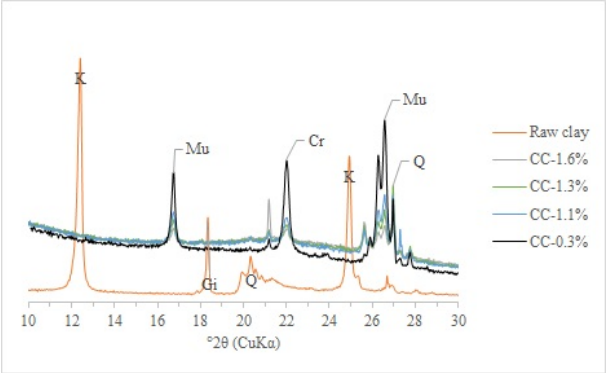

Figure 1. XRD of raw and calcined clay

3. Results and discussion

3.1 Clay calcination and grinding-physical qualities

The level of burning was evaluated by measuring mullite as a high-temperature phase and amorphous phase through XRD analysis, as well as physical parameters such as specific surface area (BET) and specific density (Table 2). The XRD patterns in Figure 1 show the formation of mullite as the LoI is decreased, consistent with the quantities estimated in Table 1. The hump seen in the patterns (15-30° 2θ) is flattened in the sample with 44% mullite (black line). Overcalcination increases the specific density but decreases the specific surface area.

Table 2. Mullite, amorphous, BET and density of calcined clays

	CC-1.6%	CC-1.3%	CC-1.1%	CC-0.3%/CC-R30%	CC-R15%	CC-R1%
Mullite (%)	1.7	6.6	15.7	44		
Amorphous (%)	94.5	87.1	75.5	45		
BET (m^2/g)	25.2	20.6	16.6	3.8	3.4	4.0
Specific density (g/cm^3)	2.80	2.83	2.85	2.92	2.93	2.96

Figure 2 shows the particle size of the calcined clays when they are calcined to a moderate level (a) and a high level of calcination (b). The level of calcination appears to increase the particle size of the calcined clay as well as its hardness. In a separate grinding test at the laboratory scale (not shown), both samples were ground under the same conditions, and it took 4 to 5 times longer to grind the calcined clay with a high level of calcination (b) to the same target fineness. This suggests that other considerations, such as refractory, conveyor equipment, and mill capacity, could be impacted when high calcination levels are desired.

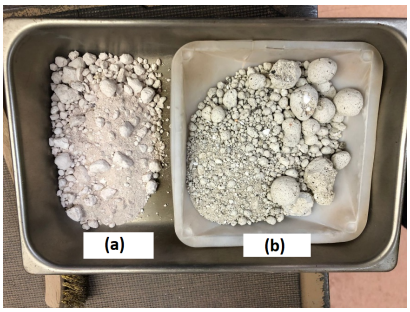

Figure 2. Calcined clay at moderate (a) and high level of calcination (b)

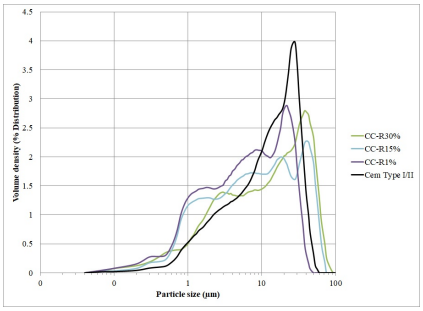

Figure 3. Particle size distribution of Cem Type I/II and calcined clays

Figure 3 presents the particle size distribution of three types of calcined clay obtained by varying the speed of the classifier. Cem Type I/II is included as a reference. Compared to OPC, the particle size distribution of the calcined clays is wider in range, with three modes seen in the curves. When producing a finer product, the trend suggests a significant increase in the finer portion of the curve (particles < 10 µm)."

3.2 Water demand and compressive strengths

The compressive strengths of mortars containing 20% calcined clay and 80% Ordinary Portland Cement (Type I/II) were assessed, and the strength activity index (SAI) was calculated following ASTM C618 (ASTM, 2019). Results are presented in Table 3. Regarding to the level of burning, water demand appears to be more controlled as the clay is more calcined. For instance, CC-0.3% did not require more water, while the highest water requirement was obtained with CC-1.3%, which was moderately calcined. In terms of the SAI, the trend is the opposite: more burning affects the synergy of the calcined clay, resulting in lower SAI values for the highly burnt (CC-0.3%). It appears that a proper balance between SAI and water demand should be found for each process and clay source. As for the milling process, little improvement is obtained even with higher fineness when the calcined clay is highly burnt. It seems that the high quantity of mullite (>40%) compromises clay reactivity. Even without a water requirement, no improvement in compressive strength is seen.

Table 3. Compressive strength

	w/b	Water requirement (%)	SAI 7d (%)	SAI 28d (%)
Cem Type I/II - 20% CC-1.6%	0.525	108%	83%	92%
Cem Type I/II - 20% CC-1.3%	0.535	110%	85%	90%
Cem Type I/II - 20% CC-1.1%	0.525	108%	79%	94%
Cem Type I/II - 20% CC-0.3% (CC-R30%)	0.485	100%	74%	80%
Cem Type I/II - 20% CC-R15%	0.485	100%	74%	80%
Cem Type I/II - 20% CC-R1%	0.485	100%	77%	81%

3.3 Concrete application

In Figure 4 is shown the results for a concrete application using FA and CC-1.3% at the same substitution and a total powder content about 240 kg to get a slump 12.5 +/- 2.5 cm (5 +/- 1 inch). As calcined clay requires more water, two types of concrete were produced to compare. The first concrete with CC tested by adding the water to achieve the desired slump, while the second one mix was produced with the same amount of water like Fly ash system and adding a high water reducer admixture (HWRA) to get the same slump. The mix with 20% CC requires 15% more additional water compared to the F ash system. In the third scenario, HWRA was added at a dose of 120 mL (4 ounces) per cementitious material. Results show that compressive strengths were higher with calcined clay than with F ash at boths scenarios tested. The water requirement did not impact the strength evolution after 7 and 28 days and further improvement could be obtained when HWRA are added into the system. The powder efficiency, expresssed as psi/lb at 28 days were 0.12 MPa/kg (8.27 psi/lb) for the F-ash, 0.14 MPa/kg (9.51 psi/lb) for the CC-1.3%, and 0.19 MPa/kg (12.4 psi/lb) for CC-1.3% with admixture added. These results show that calcined clay could replace the F-ash in mix designs not restricted by water content.

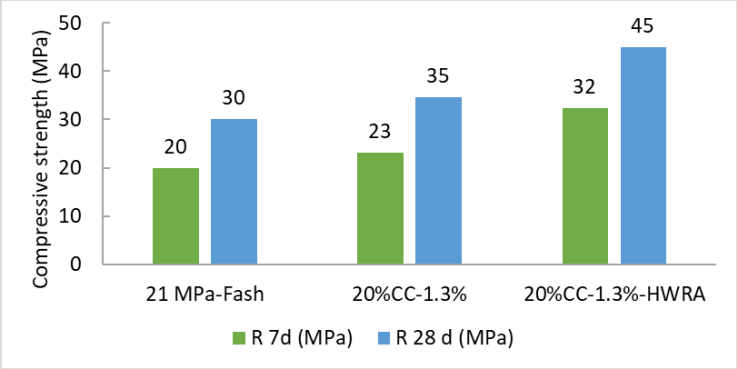

Figure 4. Compressive strength of concrete produced with CC-1.3%

3. Conclusions

- LoI measurements in calcined clay offer a limited indication of the level of calcination. However, complementary measurements such as XRD are needed to fine-tune the calcination process and maintain operations near their limits.
- Clay overburning, expressed as mullite presence, has a positive effect on water demand and still provides good performance as SCM. For clays with high kaolinite content (70%), a mullite content of 15% in the final product results in a water requirement of + 8-10%.
- Calcined clays can be used as substitute for fly ash as SCM in concrete., Higher powder efficiency (10-25%) can be achieved by balancing water requirements and admixture dosages to achieve same slump.

References

Astm. (2019). Standard Specification for Coal Fly Ash and Raw or Calcined Natural Pozzolan for Use. *Annual Book of ASTM Standards*, *C*, 3–6. https://doi.org/10.1520/C0618-19.2

ASTM. (2007). Standard Test Methods for Chemical Analysis of Hydraulic Cement. *Annual Book of ASTM Standards*, *March*, 1–8. https://doi.org/10.1520/C0114-10.

ASTM. (2017). *Standard Test Method for Fineness of Hydraulic Cement by the 45-μm (No. 325) sieve* (p. 3).

Sabir, B., Wild, S., & Bai, J. (2001). Metakaolin and calcined clays as pozzolans for concrete: A review. *Cement and Concrete Composites*, *23*(6), 441–454. https://doi.org/10.1016/S0958-9465(00)00092-5

Scrivener, K. (2014). Options for the future of cements. *The Indian Concrete Journal*, *88*(7), 11–21.

Sharma, M., Bishnoi, S., Martirena, F., & Scrivener, K. (2021). Limestone calcined clay cement and concrete: A state-of-the-art review. *Cement and Concrete Research*, *149*(July), 106564. https://doi.org/10.1016/j.cemconres.2021.106564

Siddique, R., & Klaus, J. (2009). Influence of metakaolin on the properties of mortar and concrete: A review. *Applied Clay Science*, *43*(3–4), 392–400. https://doi.org/10.1016/j.clay.2008.11.007

The 16th International Congress on the Chemistry of Cement 2023 (ICCC2023)
"Further Reduction of CO_2 -Emissions and Circularity in the Cement and Concrete Industry"
September 18–22, 2023, Bangkok, Thailand

A tailored supplementary cementitious material based on Calcined Clay technology for Ready Mix production

A.C Gómez[1*], C.P. Rodriguez[2], C.A. Orozco[3], W.E. Echeverri[4]

[1] *Cementos Argos, Medellin, Colombia*
Email: agomezgo@argos.com.co

[2]*Cementos Argos, Medellín, Colombia*
Email: crodriguro@argos.com.co
[3]*Cementos Argos, Medellín, Colombia*
Email: corozco@argos.com.co
[4] *Cementos Argos, Medellin, Colombia*
Email: wecheverri@argos.com.co

ABSTRACT

The low availability of common Supplementary Cementitious Materials (SCM) like Fly ash, Slag for cement and concrete production is creating the opportunity to explore new SCMs to reduce the overall embodied carbon of concrete while providing an economical way to achieve desired mechanical and durability attributes. Calcined clay (CC) technology is gaining more attention due to its broad availability, low temperature for material production, and higher reactivity than other SCM, among other benefits. On the other hand, CC tends to require more water and more admixture dosage to get the same consistency if compared with traditional SCMs such as fly ash (FA) and slag; setting time tends to be shorter than regular mixes, and strength evolution is lower mainly at early ages.

A comparative study was performed among straight cement, fly ash (FA), Calcined clay (CC), and a tailored SCM based on CC - Pozzolanic Mix (PM) technology to control water demand and extra admixture at paste, mortar, and concrete. All SCM were tested using particle size distribution PSD, BET, X-Ray Fluorescence XRF, and retained on 325 mesh. The main result suggests that the behavior of CC and PM depends mainly on their PSD and composition (Al_2O_3) and kaolinite content, having a direct connection with plastic behavior. Furthermore, the slump test and compressive strength were evaluated at 3 days, 7 days, and 28 days to compare addition performance with similar strengths at all ages between PM, FA, and CC. Also, durability tests on mortar such as alkali-silica reaction (ASTM C 1567), and concrete tests like rapid chloride rapid test permeability (ASTM C 1202) and water permeability (NTC 4483) were run at 28 days and 56 days to compare the microstructure development for each system. Similar durability results were obtained between Calcined Clay (CC) and Fly ash (FA). At the same time, the Pozzolanic mix (PM) depends on the amount of CC used to tailor the PM to improve concrete performance.

KEYWORDS: *Calcined Clay, Pozzolanic Mix, Filler, Supplementary Cementitious materials, Durability*

1. Introduction

Calcined clay is an interesting supplementary cementitious material that can be manufactured with medium and low kaolinite (60 %-40 %) content which is common and abundant in tropical and subtropical areas (Alujas *et al.,* 2018) resulting in a pozzolanic material comparable to or higher reactivity than other supplementary cementitious material. Fly ash and slag, the most widely used SCMs globally, are becoming harder to obtain and are limiting supply in certain regions, experiencing greater variability, and experiencing increases in cost (Benkeser *et al.,* 2022). The use of calcined clays as SCM usually decreases the workability of mortars and concretes and water demand at a set consistency varies depending on the type of the dominant clay mineral (Schulze and Rickert, 2019), as well as the fineness of the calcined clay what is identified are some improvements on strength mainly at 7 days and 28 days (Gmür et al., 2016). Calcined clay in cement or SCM not only influences the fresh-state properties mechanical properties but also improves durability (Cao *et al*., 2021)

Calcined clay typically needs more water to reach the desired consistency and the water-to-cement ratio is fixed, the amount of admixture dosage also tends to increase and impact the mix aspect, rheology, and cost

limiting the introduction of this technology into the market. A tailored supplementary cementitious material based on calcined clay technology was developed by combining calcined clay with a calcareous filler and gypsum focusing on mitigating water demand and keeping admixture dosage under regular values and tested on durability performance testing to identify its benefits and challenges.

2. Materials and method

The materials and techniques proposed in this study aimed to characterize the different supplementary cementitious materials such as FA (Fly ash), CC (Calcined clay), and PM (Pozzolanic mix), The XRF oxide components were evaluated using Axios Panalytical. PSD for each material was assessed via wet dispersion with laser detection (CILAS). The specific surface area was estimated using Brunauer–Emmett–Teller (BET). Isothermal calorimetry at 24°C and at a water/cementitious ratio of 0.45 for 50 hours was performed by TA instruments equipment.

Standard mortar according to ASTM C 618 to determine the water demand, and compressive strength after 7 days and 28 days. For the concrete mixtures measured slump, admixture dosage, and compressive strength at 1,3,7,28,56 days. A local aggregate source was used to conduct an alkali-silica reaction according to ASTM C 1260 and 20 % and 30 % substitutions of FA, CC, and PM were made in accordance with ASTM C 1567. Rapid test chloride was measured using ASTM C 1202. The resistance to water permeability of concrete was evaluated according to the standard NTC 4483 evaluated after 28, and 56 days of curing.

3. Results and discussion

Table 1 displays the chemical composition of the cement, FA, CC, and PM. CC material has a high amount of aluminum content and iron oxide that could be related to a brownish aspect that potentially impacts the color of the concrete. Finally, PM has lower percentages of silicon oxide, aluminum oxide, and iron oxide that produce a material more greyish aspect with a high amount of calcium oxides as a product of other material that is part of the PM recipe.

Table 1. XRF, BET, and retain mesh 325 for cement, FA, CC, and PM

	SiO_2	Al_2O_3	Fe_2O_3	MgO	CaO	Na_2O	K_2O	SO_3	LOI	Specific surface area (m2/g)	Retain mesh 325 (%)
Cement	19.7	4.24	3.1	2.1	63.1	0.3	0.1	2.9	3.8	2.05	1.97
FA	53.9	23.3	6.5	0.8	3.2	0.5	1.3	0.4	8.5	4.95	31.48
CC	62.2	19.3	9.4	0.6	0.8	0.15	2.6	0.05	3.5	18.58	6.57
PM	30.8	7.2	3.3	1.5	29.3	0.22	0.3	2.4	24.3	7.81	7.68

Cement has a specific surface area and is retained on mesh 325 which are the lowest values relative to all materials examined. CC material had the highest specific surface area and medium retain on mesh 325. FA and PM had distinct specific surface area and fineness values, indicating that PM might contain more fine particles that improve SCM reactivity at early ages but a medium-specific surface area in contrast to CC, which could request less water and admixture dose.

Particle size distribution for all materials is shown in Figure 1a. The cement has a fine curve with a good amount of particle sizes of around 30 microns. A bimodal curve with two primary peaks, one in 30 microns and 50 microns close to the cement curve could be seen on the PM material. The coarser SCM examined were evident in FA and CC where the main frequency peak was 90 microns and 100 microns, respectively. The heat flow curve for pastes run at 0.45 water to cementitious ratio and a 20 % SCM replacement is shown in Figure 1b. FA and CC reduce the maximum heat flow and with CC, a modest acceleration of the heat curve has the tendency to shorter the setting times. PM at the same substitution had less heat flow than cement mix but higher than FA and CC.

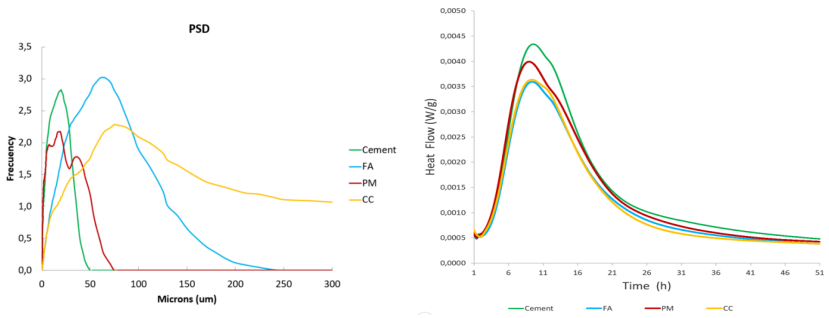

Figure 1. 1a. PSD for Cement, FA, PM and CC. 1 b. Isothermal Calorimetry for pastes at 20% SCM.

Data from ASTM C 618 is summarized in Table 2. While CC needs 10 % more water than PM to get a similar flow as the straight cement mix. This additional water had no significant impact on compressive strength values for CC at both ages, while PM showed interesting behavior at 7 and 28 days compared to FA which corresponds to an 82% pozzolanic activity index at 7 days and slightly higher at 28 days.

Table 2. Pozzolanic activity index (PAI) values at 7 days and 28 days

	w/cm	% Substitution	Water requirement	Flow	7 d PAI (%)	28 d PAI (%)
Cement	0.47	0		110		
FA	0.50	20	106%	110	71%	74%
CC	0.53	20	112%	108	86%	89%
PM	0.48	20	102%	108	82%	77%

Concrete tests with the amount of powder and fixed water adjust the superplasticizer dosage to get the same initial slump. Figure 2a shows the cylinders made with Cement, 16 % FA, 16 % CC, and 16 % PM does not show any significant impact on concrete color due to PM composition. Figure 2b presents the compressive strength at 1,3,7,28,56 days and CC has a better strength gain like fly ash based on its reactivity but with a 20 % increase in admixture dosage. PM needs the same amount of dosage of admixture of FA obtaining a slight reduction in strength values at all ages.

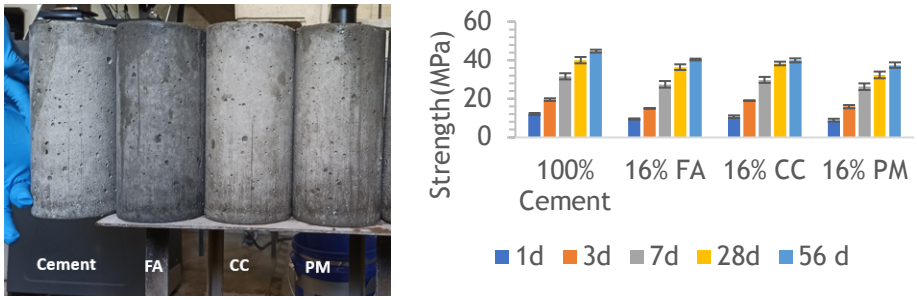

Figure 2. 2a. Cylinders at 16% SCM substitution. 2 b. Compressive Strength Results

Figure 3a shows that SCM that mitigates an aggregate that qualifies as potentially reactive is FA at 30 % of substitution which falls below 0.1 % of the expansion at 16 days. CC at 30% could reduce the expansion from 0.46 % to 0.17 % with respect to the straight cement mix. On the other hand, PM material at 20 % and 30 % of substitution had a poor performance because both values are higher than 0.2 %.

Figure 3b provides measurements of chloride rapid test and water permeability at 28 days and 56 days, respectively. According to ASTM C 1202 qualification, cement mix could be defined as a moderate chloride permeability at both ages, while the FA system, is moderate at 28 days but low at 56 days. The same outcomes with different numbers occurred with the CC system at 16 % of substitution, where CC can react with other minerals to improve the resistance of concrete to chloride penetration by generating additional gel phases, filling the pores and cracks of the cement matrix, which effectively prevents concrete deterioration under aggressive environments (Cao *et al.*, 2021).

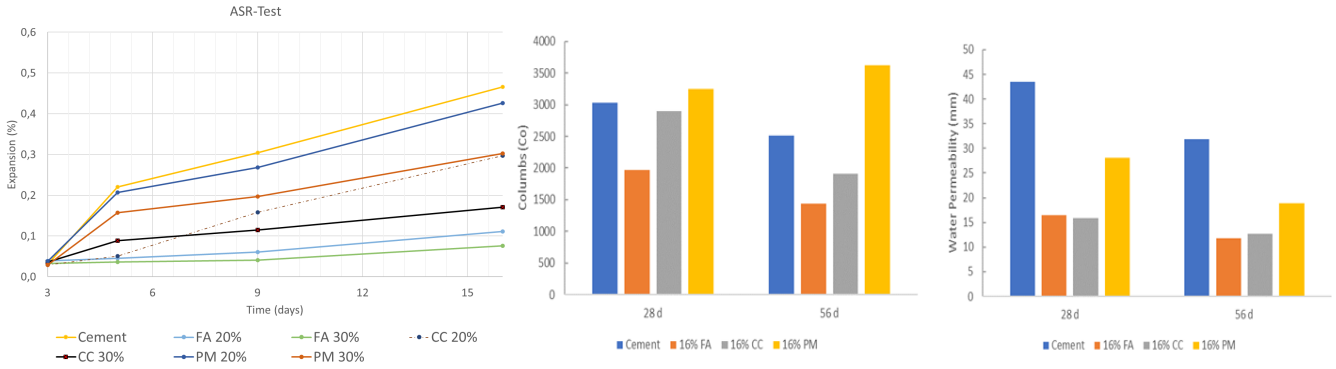

Figure 3. 3a.ASR test for mortar bars at different SCM substitutions. 3b. Chloride Permeability, Water Permeability

The same results were found for water permeability for cement, FA, and CC, where at 56 days for FA and CC had a low permeability (Below 30 mm). On the other hand, PM classifies the concrete as a low permeability mixture according to the results in Figure 3 b, where at 28 days and 56 days the length of water that break through the cylinder when the head of pressure above the cylinder surface is below 30 mm.

Conclusions

- A tailored SCM based on CC technology is a promising concept to mitigate water demand and admixture dosages and depends on the type of raw clay available and the calcination process, mainly iron oxide content to prevent a noticeable change in the color of the concrete.
- For a fixed water system, PM with a particle size distribution close to the cement distribution, reduces by 20 % admixture requirement compared to the CC system. However, despite this advantage, the low amount of aluminum phases present in the tailored SCM based on CC technology, alkali-silica reaction, and chloride permeability are not improved suggesting that to get a SCM that fully satisfies fresh state requirements, compressive strength performance and durability targets, the amount of CC should be increased.

Acknowledgments

To Cementos Argos R&D team to support and finance this study and use their expertise to identify new opportunities for calcined clay technologies.

References

Alujas, A., Almenares, R., Arcial, F., Martinera, F. "Proposal of a Methodology for the Preliminary Assessment of Kaolinitic Clay Deposits as a Source of SCMs " in Calcined Clays for Sustainable Concrete, RILEM series, 2018, pp 29-34.
ASTM C 618-22. Standard Specification for Coal Fly Ash and Raw or Calcined Natural Pozzolan for Use in Concrete
ASTM C 1260-22. Standard Test Method for Potential Alkali Reactivity of Aggregates (Mortar-Bar Method).
ASTM C 1567-21. Standard Test Method for Determining the Potential Alkali-Silica Reactivity of Combinations of Cementitious Materials and Aggregate (Accelerated Mortar-Bar Method).
ASTM 1202-19. Standard Test Method for Electrical Indication of Concrete's Ability to Resist Chloride Ion Penetration.
Benkeser,D., Hernandez, K., Lolli, F., Kurtis, K. (2022). Influence of calcined clay morphology on flow in blended cementitious systems, Cement and Concrete Research, Volume 160,106927.
Cao, Y., Wang, Y., Zhang, Z., Ma, Y., Wang, H. (2021). Recent progress of utilization of activated kaolinitic clay in cementitious construction materials, Composites Part B: Engineering,
Volume 211,108636.
Gmür, R., Thienel, K., Beuntner, N. (2016). Influence of aging conditions upon the properties of calcined clay and its performance as supplementary cementitious material, Cement and Concrete Composites, Volume 72, Pages 114-124.
Schulze, S. Rickert, J. (2019). Suitability of natural calcined clays as supplementary cementitious material, Cement and Concrete Composites, Volume 95, Pages 92-97.
NTC 4483-98. Método de ensayo para determinar la permeabilidad del concreto al agua.

The 16th International Congress on the Chemistry of Cement 2023 (ICCC2023)
"Further Reduction of CO_2 -Emissions and Circularity in the Cement and Concrete Industry"
September 18–22, 2023, Bangkok, Thailand

Influence of dregs and grits on the hydration of Portland cement pastes

Y.S. Oliveira[1], E.B.C. Costa[2]

1 Faculty of Civil Engineering, Federal University of Uberlandia, Uberlandia, Brazil
Email: yasminesimoes@gmail.com
[2] Faculty of Civil Engineering, Federal University of Uberlandia, Uberlandia, Brazil
Email: elianebetania@ufu.br

ABSTRACT

Lime slakers grits (grits) and green liquor dregs (dregs) are solid wastes generated in the kraft pulp mills, mainly composed of calcium carbonate. In addition to contributing to the reduction of CO_2 emission from cement production, the use of these wastes as supplementary cementitious material (SCM's) can be an alternative to supply the limited demand for some additives and reduce virgin resource consumption, minimizing the environmental impact originating from the cellulose pulp and cement industries. In this paper, the impact of use of grits and dregs on hydration kinetics and the degree of hydration of cement pastes was investigated using isothermal calorimetry, X-ray diffraction (XRD) and thermogravimetric analysis (DTA/TGA). Grits and dregs with particle sizes bellow to 75 μm were used. Pastes were produced with water/binder ratio of 0.48, replacing cement by grits or dregs at 0 (reference); 5; 10; 20; and 30% by weight of cement. Polycarboxylate ether superplasticizer was added all to the mixes by weight of cement with 0.40%, without altering the water/cement ratio. The replacement of cement at levels of 5% and 10% by dregs lead to an increase in the acceleration rate compared to the reference paste. For contents of 20% and 30% by dregs, the dilution effect was predominant increasing the dormancy period. At 28 days, magnesium silicate hydrate phase (M-S-H) appears in pastes with contents up to 20% of dregs; and calcium monocarboaluminate for pastes with 20% and 30% of grits. Furthermore, the results showed that dregs were more effective than grits in enhancing cement hydration.

KEYWORDS: *Supplementary cementitious materials. Pulp kraft process waste. Hydration. Calcium carbonate.*

1. Introduction

The kraft process is the most widely used method for pulp production worldwide, accounting for over 80% of the total pulp production (Mathew et al, 2018). Although, this process has excellent performance in relation to energy and chemical recovery, it generates many wastes, such as dregs and grits (Campos, Foelkel, 2016) produced during the clarification stage of green liquor and lime preparation. In 2021, worldwide pulp production was 189 million tons (FAO, 2022). According to Quina and Pinheiro (2020), it can be estimated that 2.8 million tons of dregs and 945,000 tons of grits were generated.

The use of supplementary cementitious materials (SCM's) is one of the most promising large-scale measures adopted by cement industry to mitigating CO_2 emissions. Due to the limited availability of some established materials, some alternative materials have been investigated. Therefore, the physical and chemical characteristics of dregs and grits, especially their calcium carbonate content, indicate a significant potential for use in partial replacement of cement (Quina and Pinheiro, 2020). Although some research has been conducted on the use of these residues in cementitious materials (Carvalho et al, 2019; Martinez-Lage et al, 2016; Torres, 2020), there are still gaps in the preparation, physical and chemical characterization, and appropriate content of these wastes. Moreover, little attention has been given to the interaction of these materials with the kinetics of hydration in terms of particle size and content, making it challenging to use them in cementitious materials. Therefore, this study aims to evaluate the influence of

content of grits and dregs as a partial replacement for cement on the hydration kinetics of cementitious paste.

2. Materials and methods

The dregs and grits were obtained from the company Suzano S.A, a company located in Três Lagoas-MS. They were dried at 100°C for 24 hours and subjected to a griding process using a Los Angeles abrasion mill (Contenco model C-3021) with 13 steel spheres of approximately 48 mm in diameter rotating at a speed of 30 rpm. The mass of wastes was kept constant at 5 kg. Previous studies were used to determine the griding time, which was 150 min for dregs and 180 min for grits, in order to obtain a greater quantity of particles below to 75 µm. After griding, the waste was manually sieved through a 200-mesh sieve and homogenized. A commercial Portland cement V type complying with Brazilian NBR 16697 Standard was used in this study. The chemical composition of cement, dregs and grits is shown in Table 1. Particle size distribution of powders determined by dynamic image analyses using *QicPic (Sympatec) with dispersion system* is plotted in Fig. 1.

Table 1. Chemical composition of all powders (wt.%).

	CaO	SiO_2	Al_2O_3	Fe_2O_3	SO_3	MgO	Na_2O	K_2O	P_2O_5	Others	L.O. I
Cement	62.22	15.24	3.46	2.62	5.22	1.90	0.51	1.03	0.21	0.72	6.87
Dregs	58.68	7.75	2.53	2.18	4.29	15.74	3.01	0.31	0.45	5.06	38.13
Grits	84.43	4.95	0.34	0.37	2.11	1.23	4.63	0.21	0.98	0.75	39.20

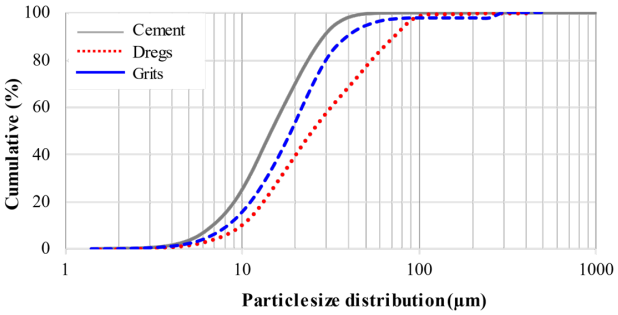

Fig. 1. Particle size distribution for all powders.

Table 2. Physical properties for all powders.

	Cement	Dregs	Grits
Density (g/cm³)	3.08	2.45	2.61
SSA BET (m²/g)[a]	2.38	20.95	2.44
Dv,10 (µm)	5.75	8.26	7.00
Dv,50 (µm)	12.41	21.02	16.03
Dv,90 (µm)	24.66	60.76	33.53
Particle shape factor[b]	0.69	0.68	0.69

[a] Determined by nitrogen adsorption.
[b] Determined by dynamic image analyses.

Five pastes were prepared by replacing cement with dregs or grits at levels of 0% (reference), 5%, 10%, 20%, and 30% by weight of cement. The water-to-fines ratios of 0.48 was kept constant. In all mixtures, a superplasticizer admixture based on polycarboxylate ether was used at a content of 0.40% by weight of fines to reduce the agglomeration of the particles.

The heat evolution was measured in an isothermal calorimeter (Calmetrix model ICAL 800HPC) at 23°C for up to 72 hours. The dry materials were homogenized before mixing. For paste mixes, a high-shear mixer (IKA labortechnik) was used at 1270 rpm for 1 min. The resulting mixture was then placed in a plastic cylinder, sealed, and introduced into the calorimeter.

To perform X-Ray Diffraction (XRD) and thermogravimetric (DTA/TGA) analyses, pastes were prepared using a mixer (Lennox turbo 600 w) at high speed for five minutes. After 28 days, paste samples was dried at 40°C until constant mass. A solvent exchange method with isopropanol was used to stop the hydration following the procedure described by Scrivener et al (2016). The samples were dried in an oven at 40°C for 60 min and, subsequently ground using oscillating disc mills (Herzog). The ground samples were sieved using sieves of 150 and 75 µm, and the fraction retained on the 75 µm sieve was used for analysis. XRD analysis were performed using a Shimadzu X-ray diffractometer, model XRD 6000, at room temperature. The experimental conditions consisted of Cu-Kα radiation (λ = 1,4187 Å), 30 kV and 30 mA, with a 2θ angle range of 4 to 70° and a step of 0.02° 2θ. The identification of crystalline phases was performed using HighScore 3.0 software. TGA/DTG curves were obtained using a TA instruments TGA-55 model thermal analysis instrument under an inert atmosphere, with heating from 25°C to 925°C at a rate of 5ºC/min. Platinum crucibles were used for the determination.

3. Results and discussions

The heat flow curves of the pastes mixed with different contents of dregs and grits are shown in Fig. 2a and Fig. 2b, respectively. As shown in Fig. 2a, the replacement of cement by 5% and 10% of dregs results in an increase in the initial peak related to the wetting and dissolution of solid materials, as well as a slightly earlier onset of the main peak. This can be explained by higher surface area of dregs compared to cement particles. An increase in specific surface area implies a higher acceleration rate due to the additional surface provided for the nucleation and growth of hydration product (Lothenbach et al., 2008; Brik et al. 2021). However, for high replacement levels of cement by dregs, such as 20% and 30%, a reduction in the acceleration rate and an increase in the dormancy period can be observed. In these cases, the dilution effect possibly prevailed over the nucleation effect. As for grits, it can be seen in Fig. 2b that the use of 5% and 10% did not affect the duration of dormancy period and acceleration rate compared to reference mixture. In contrast to dregs, the replacement of cement at levels of 20% and 30% by grits reduced the dormancy period and improve the acceleration rate. The average size of grits particles is similar to the cement used, and they have a high calcium oxide content in their composition (Table 1). The greater availability of calcium can promote faster attainment of the lime saturation point in the system (Berodier and Scrivener 2014).

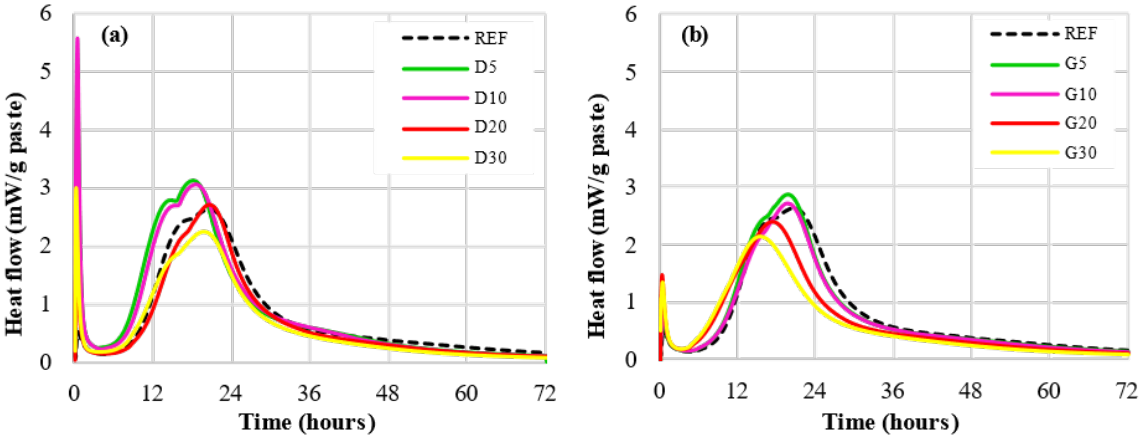

Fig.2. Isothermal calorimetry curves for pastes with, 0,5, 10, 20 and 30% of dregs (a) or grits (b).

Three peaks were identified in the TG/DTG curves of all the pastes studied at temperatures of approximately 60°C, 380°C and 630°C. These peaks are related to the loss chemically combined water up to 150°C, the dehydration of portlandite at approximately 460°C, and the decomposition of CO_2 between 600°C and 800°C (Scrivener et al 2016). The content of chemically combined water (H) and portlandite (CH) in the pastes was obtained from the mass loss and molar mass of the chemical compounds. The results of the H and CH content as a function of the replacement of cement by dregs and grits are shown in Fig. 3a and 3b, respectively.

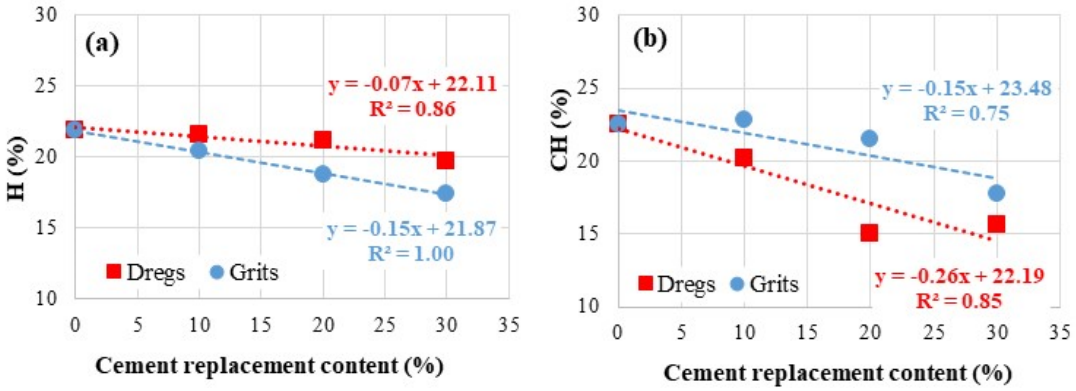

Fig.3. The content of H (a) and CH (b) in non-volatile base, as a function of the replacement of cement by dregs or grits in the pastes at 28 days.

The H refers to the loss of water associated with the dehydration of aluminates, C-S-H, and magnesium compounds. The results showed that the amount of H decreases with increasing levels of cements replacement. Dregs showed a higher amount of H than grits at all levels of replacement analyzed. In grits, a greater formation of calcium hydroxide is observed compared to dregs. This is due to the higher amount of calcium oxide as can be seen Table 1.

XRD patterns of the pastes studied at different levels of cement replacement are presented in Fig. 4. Typical cement hydration compounds were observed in all studied pastes: C-S-H; portlandite, ettringite, AFm phases and calcium carbonate. At replacement levels greater than 5% of cement by dregs, the presence of pyrssonite ($Na_2CO_3.CaCO_3.2H_2O$) and hydrate magnesium silicate (M-S-H) was observed. Pyrssonite is a byproduct of industrial process of cellulose production (Martins 2007). The presence of M-S-H in these pastes can be explained by the high MgO content in the dregs, which promotes the formation of this hydrated compound (Bernard et al 2017). In the pastes containing grits, the formation of calcium hemicarboaluminate was observed in mixtures with replacement levels of 10%, 20% and 30% of cement; and at levels above 10%, the presence of calcium monocarboaluminate was noticed. This could be attributed to the calcium carbonate content in the pastes, with increased as the cement replacement was replaced by grits. As the calcium carbonate content increased, so did the formation of calcium hemicarboaluminate, leading to its transformation into calcium monocarboaluminate (Matchei et al 2006).

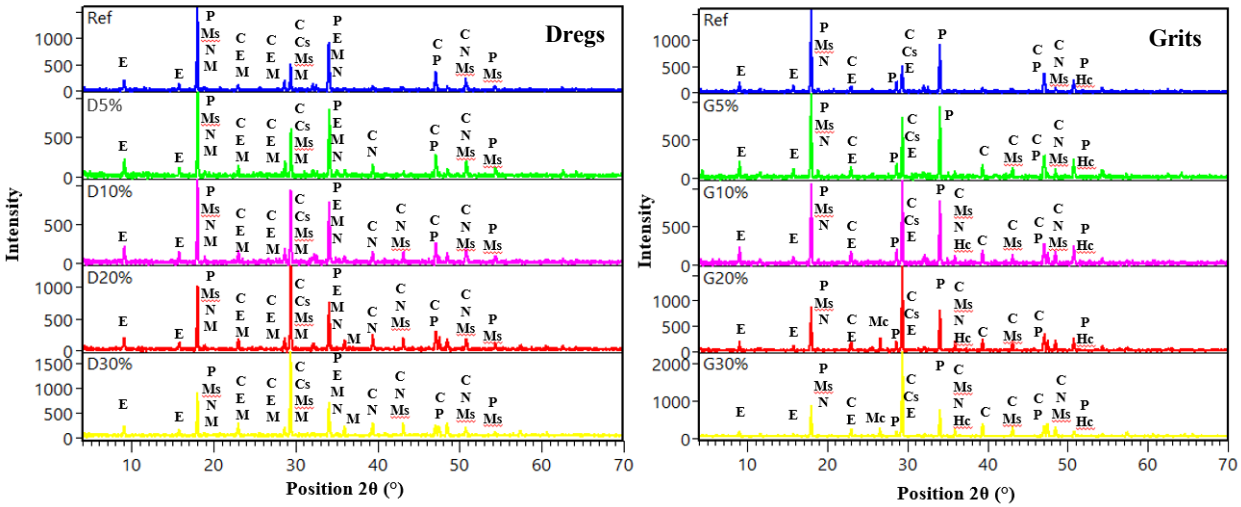

Legend: C – Calcite (005-0586); Cs – C-S-H (033-0306); E – Ettringite (041-1451); Hc – Hemicarboaluminate (041-0219); M – M-S-H (083-1768); Mc – Monocarboaluminate (036-0129); Ms – Monossulfoaluminate (083-1289); N – Pirssonite (072-0038); P – Portlandite (044-1481).

Figure 4: XRD curves of pastes with 0, 5, 10, 20 and 30% by dregs or grits after 28 days of hydration.

3. Conclusions

This study investigated the effect of using dregs and grits as a partial replacement of cement in paste mixtures with replacement level of 5%; 10%; 20% and 30%. Up to 10% cement replacement by dregs increased the acceleration rate compared to the reference mixture. For grits mixtures, this occurred at higher levels of cement replacement (20% and 30%). The higher replacement ratio of cement leads to the low chemical bound water content for both wastes. Dregs pastes chemically combined a larger volume of water than grits in all replacement contents evaluated. The XRD patterns revealed the formation of typical cement hydration compounds, as well as pyrssonite and hydrate magnesium silicate in dregs-containing pastes (D10, D20, and D30), and calcium hemicarboaluminate (G10, G20, and G30) and calcium monocarboaluminate in (G20 and G30) grits-containing pastes.

Acknowledgements

The authors would like to grateful to Suzano S.A. company for the donating the dregs and grits, to the Laboratory of Microstructure and Eco-Efficiency of Materials at the University of São Paulo, and to the

Multi-User Laboratories of the Institute of Chemistry and Pontal at the Federal University of Uberlandia for providing the necessary equipment and technical support for the isothermal calorimetry tests, X-ray diffraction, and thermogravimetric analysis.

References

Berodier, E., Scrivener, K. Understanding the filler effect on the nucleation and growth of C-S-H. Journal of the American Ceramic Society, 97, 12, 3764–3773, 2014.

Brazilian Association of Technical Standards. NBR 16697: Portland Cement - Requirements. 1. Ed. Rio de Janeiro: ABNT, 2018. 16 p.

Briki, Y.; Zajac, M.; Haha, M. B.; Scrivener, K. Impact of limestone fineness on cement hydration. Cement and Concrete Research, 147, 106515, 2021.

Campos, E. S; Foelkel, C. The technological evolution of the paper cellulose sector in Brazil. 1st edition. São Paulo.: Brazilian Pulp and Paper Technical Association, 2016. 228 p.

Carvalho, J. M. F.; Campos, P. A. M.; Defáveri, K.; Brigolini, G. J.; Pedroti, L. G.; Peixoto, R. A. F. Low Environmental Impact Cement Produced Entirely from Industrial and Mining Waste. Journal of Materials in Civil Engineering, v. 31, n. 2, p. 4018391, 2019.

FAO. Forestry Production and trade in the world in 2021. www.fao.org/faostat/en/#data/FO. Acess in 09 fev. 2023.

Lothenbach, B.; Le Saout, G.; Gallucci, E.; Scrivener, K. Influence of limestone on the hydration of Portland cements. Cement and Concrete Research, 38,6, p. 848-860, 2008.

Martins, F. M.; Martins, J. M.; Ferracin, L. C.; Da Cunha, C. J.. Mineral phases of green liquor dregs, slaker grits, lime mud and wood ash of a Kraft pulp and paper mill. Journal of hazardous materials, v. 147, 1-2, p. 610-617, 2007.

Martínez, I. L.; Lizancos, M. V.; Brugo, P. V.; Fernándes, M. R.; Herrero, C. V.; Rodríguez, A. R.; Cano, M. M. Concrete and mortars with wastepaper industry: Biomass ash and dregs. Journal of environmental management, 181, p. 863- 873, 2016.

Mathew, A. K.; Abraham, A.; Mallapureddy, K. K.; Sukumaran, R. K. Lignocellulosic biorefinery wastes, or Resources? Waste Biorefinery, p. 267–297, 2018.

Oey, T.; Kumar, A.; Bullard, J. W.; Neithalath, N.; Sant, G. The Filler Effect: The Influence of Filler Content and Surface Area on Cementitious Reaction Rates. Journal of the American Ceramic Society, v. 96, n. 6, p. 1978-1990.

Quina, M. J.; Pinheiro, C. T. Inorganic waste generated in kraft pulp mills: the transition from landfill to industrial application. Applied Sciences, v. 10, 2020.

Scrivener, K.; Snellings, R.; Lothenbach, B. A practical guide to microstructural analysis of cementitious materials. 1st. Boca Raton: CRC Press, 2016. 540p.

Torres, C. M. M. E. Dregs and grits from kraft pulp mills incorporated to Portland cement clinker. Journal of Materials Cycles and Waste Management, 22, p. 851-861, 2020.

Zheng, L.; Xuehua, C.; Mingshu, T. Hydration and setting time of MgO-type expansive cement. Cement and Concrete Research. 22, p. 1-5, 1992.

The 16th International Congress on the Chemistry of Cement 2023 (ICCC2023)
"Further Reduction of CO_2 -Emissions and Circularity in the Cement and Concrete Industry"
September 18–22, 2023, Bangkok, Thailand

The Assessment of SCMs Reactivity in Thailand

S. Chanatippakorn[1*], K. Faisadcha[2], S. Vangrattanachai[3]

[1] *SCG CEMENT CO.,LTD., Saraburi, Thailand*
Email: sutthinc@scg.com
[2] *SCG CEMENT CO.,LTD., Saraburi, Thailand*
Email: kunruetf@scg.com
[3] *SCG CEMENT CO.,LTD., Saraburi, Thailand*
Email: surachav@scg.com

ABSTRACT

In Thailand, there are various types of supplementary cementitious materials (SCMs) located in different areas, including coal ash, agricultural ash and also filler materials. Twelve SCMs samples, which have different characters and sources are selected for the reactivity tests with conventional (ASTM C311) and modified methods. As reported by many works, the misinterpretation of SCMs reactivity was occasionally encountered by the conventional method indicating the misleading of the actual reactivity of materials. Thus, the modified testing methods were developed and implemented to increase the precision of the SCMs reactivity. In this research, the SCMs reactivity is studied by modified methods in two systems. Firstly, in the binary cement-SCMs system, the modified strength activity index test and the bulk electrical resistivity test are demonstrated. The SCMs reactivity is quantified indirectly by monitoring the strength development of mortar at 25% replacement of cement with SCMs from 7 days to 90 days. Secondly, in the ternary calcite-lime-SCMs system, the modified R^3 test and the lime reactivity test are studied. The SCMs reactivity is measured directly on the pozzolanic reaction between SCMs and $Ca(OH)_2$. The former system demonstrates a preferable assessment of the reactivity of SCMs and can grade the SCMs into three groups regarding their reactivity which are highly reactive, slow reactive and inert materials. Moreover, bulk electrical resistivity is a non-destructive test method, testing can be continuously monitored without causing damage. The latter system promises to be an effective method to screen out inert materials. Measurements of cumulative heat release and calcium hydroxide consumption of hydrated paste in modified R^3 test are used to distinguish between hydraulic and pozzolanic reactivity of materials. Both modified systems are benefits based on the availability of machines and the application of users.

KEYWORDS: *Supplementary cementitious materials, Reactivity, Strength activity index, Electrical resistivity, R^3 test*

1. Introduction

Supplementary cementitious materials (SCMs) were widely used in cement or concrete by taking advantage of their hydraulic or pozzolanic properties. The situation of good quality coal fly ash (the most extensively used SCMs in Thailand) has been a concern because of the decline of coal-fired consumption in power generation plants and the increase of fly ash demand in both cement and concrete production, leading to the supply shortages in Thailand. Therefore non coal ash is studied, including agricultural ash, co-firing coal ash and other filler materials. However, SCMs verified by standard test methods, such as ASTM C311 can mislead in determining the actual reactivity of materials. In recent years, there are many research focusing on how to assess of SCMs reactivity to screen new SCMs for use in cement.
In this study, modified test methods were selected to test and screen SCMs samples in Thailand. Two test systems were performed. Firstly, in the binary cement-SCMs system, the modified strength activity index test and the bulk electrical resistivity test are demonstrated. Secondly, in the ternary calcite-lime-SCMs system, the modified R^3 test and the lime reactivity test are studied.

2. Materials and methods

Table 1 shows the designations and details of SCMs samples used in this research. All samples were size-controlled to be d50 of 20 μm by grinding (except the SCMs that original size was smaller than 20 μm)

Table 1 Designations and details of SCMs materials

Abbreviation	Full name	Detail
OPC	Ordinary Portland Cement	Hydraulic material (without pozzolanic)
S	Sand	Inert material
L	Limestone	Inert material
CF-C (L)	Coal fly ash class C (lower %CaO)	Coal fly ash with pozzolanic and hydraulic properties
CF-C (H)	Coal fly ash class C (higher %CaO)	Coal fly ash with pozzolanic and hydraulic properties
CB	Coal bottom ash	Bottom ash from coal
CF-F	Coal fly ash class F	Fly ash from coal that has pozzolanic properties
CoF	Co-fired blended fly ash	Fly ash from co-firing coal and biomass
BGA	Bagasse ash	Mixed ash from bagasse (Agricultural ash)
RHA	Rice husk ash	Mixed ash from rice husk (Agricultural ash)
WB	Wood chip bottom ash	Bottom ash from wood chip (Agricultural ash)
SF	Silica fume	Highly reactive material with 100%Si Amorphous

2.1 Modified strength activity index (SAI)

The mortar was cast at a constant w/b of 0.485. The cement was replaced by 25% of SCMs. Sand to binder ratio was 2.75. A water reducer additive was added to improve workability to reach the target flow which is ± 5 of the controlled mixture. The compressive strength was tested for 90 days. SAI strength requirement must be at least 85% compared with the controlled sample.

2.2 Bulk electrical resistivity

Bulk electrical resistivity was the measurement of the resistance of mortar to the flow of electrical charge when an electrical field was applied. The mortar specimen with the same proportion of the modified SAI method was used. The specimen was cast into a 100 x 200 mm cylindrical mold and then placed under the control room for 24 hours. After removing the mold, the specimen was immersed in calcium hydroxide ($Ca(OH)_2$) saturated solution until the date of testing.

2.3 Modified R^3 test

The proportioning and mixing of the paste mixture followed by ASTM C1897.

Method A: The heat of reaction was monitored up to 14 days by isothermal calorimetry controlled at 40±5°C.

Method B: $Ca(OH)_2$ consumption was measured by thermogravimetric analysis (TGA). The 14-day curing paste specimens were crushed to small particles and then water-free by replacement of alcohol. The $Ca(OH)_2$ consumption was calculated by weight loss at 400-550°C.

2.4 Lime reactivity test

Lime reactivity test was the measurement of SCMs reactivity in the mortar of which binder composed of 1:2 ratio of $Ca(OH)_2$:SCMs, 1:15 ratio of calcium carbonate ($CaCO_3$):binder, water to binder of 0.65 (potassium sulfate solution was used) and 1:2.5 ratio of binder:sand. The specimen was cured in distilled water in airtight containers at 40°C. Testing age was 7 days after mixing and compressive strength was performed.

3. Results and discussion

Table 2 shows the particle size distribution and oxide compositions of each materials.

Table 2 Particle sizes, main oxide compositions of materials

	OPC	S	L	CF-C (L)	CF-C (H)	CB	CF-F	CoF	BGA	RHA	WB	SF
d50 (μm)	15.9	20.1	19.8	18.1	8.20	19.9	14.0	16.4	21	20.1	19.4	9.03
SiO_2 (%)	20.5	98	0.9	33.4	20	31.3	69.7	44.9	56.3	89.4	56.6	96.5
Al_2O_3 (%)	4.7	N/A	0.3	16.7	9.8	14.4	19.9	14.1	6.1	0.4	7.4	0.1
Fe_2O_3 (%)	3.2	1.4	0.2	14.2	18.5	14.3	3.7	9.2	3	0.3	3.1	0.1
CaO (%)	64.8	0.3	53.6	24.3	32.3	26.3	1.1	14.8	9.1	0.7	16.5	0.4

3.1 Binary cement-SCMs system

3.1.1 Modified strength activity index test

For the conventional SAI method (ASTM C311), the misinterpretation of SCMs reactivity has occurred because of compressive strength results mostly depend on the water requirement instead of reactivity from SCMs. For example, coal fly ash which mostly has round shape particles can reduce the amount of water used and also increase compressive strength. On the other hand, when SCMs samples were tested by the modified SAI method of which w/b was fixed to constant, the compressive strength levels of these SCMs were changed (Fig.1). The analysis focus only on the chemical reaction of SCMs. From the results shown in Fig.1, the SCMs samples were graded into three groups regarding their reactivity, as shown below. Interestingly, alternative materials, such as CoF, RHA and BGA can quickly gain high SAI at 7 days and showed better SAI than conventional materials, such as CF-C and CF-F. Furthermore, the modified SAI method can effectively screen out inert materials. S and L did not pass the SAI requirement.

Highly reactive (SAI > 85% at 7 days): CoF > SF > RHA > CF-C (H) > OPC > BGA > CF-C (L)

Slow reactive (SAI > 85% at 28 or 90 days): CF-F > CB > WB

Inert material (SAI was not pass 85% at all ages): S, L

3.1.2 Bulk electrical resistivity test

A bulk electrical resistivity test can be used for assessing hydraulic or pozzolanic properties of SCMs because their reaction products reduce pore connectivity of mortar and therefore increase resistivity. The reactivity level of SCMs arranged by bulk electrical resistivity test and modified SAI test was similar. The materials provided highly reactive since 7 days were RHA, BGA and CoF. The materials provided late reaction and the resistivity highly developed after 28 days were CF-F and CF-C (L) (Fig.2). However, there was no precise criteria for grouping SCMs by resistivity values. Bulk electrical resistivity showed an advantage for reactivity tests because it is a non-destructive test method, testing can be continuously monitored from 7 to 90 days without causing damage.

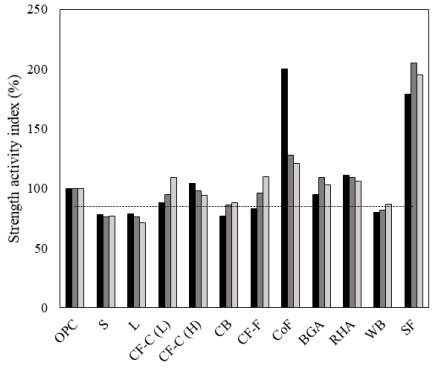

Fig. 1 SAI (%) of mortars by the modified SAI test. The dash line showed strength requirement at 85%.

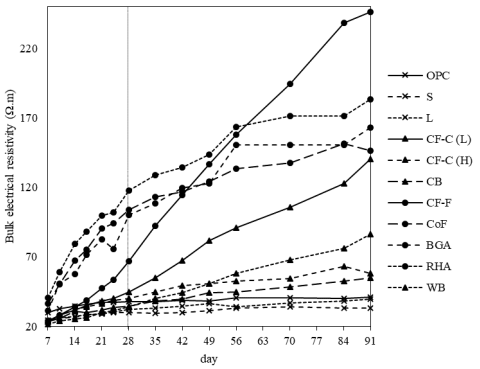

Fig. 2 Bulk electrical resistivity (Ω.m) monitored from 7 to 90 days of mortars.

3.2 Ternary calcite-lime-SCMs system

3.2.1 Modified R^3 test

R^3 test was the newly published ASTM standard in 2020 mentioning the methods of measuring the reactivity of SCMs by isothermal calorimetry and bound water. Beside classified SCMs by ASTM method, many research works also proposed the modified R^3 test by using isothermal calorimetry together with $Ca(OH)_2$ consumption to distinguish the hydraulic and pozzolanic properties of the SCMs (Suraneni et al (2019)). In this study, the analysis time was extended from 7 to 14 days to consider the SCMs which has slow reactivity. Fig.3 shows the scatter chart plotted between cumulative heat and $Ca(OH)_2$ consumption of twelve SCMs samples and the zoning based on hydraulic/pozzolanic reactivity. Almost all SCMs in Thailand provided $Ca(OH)_2$ consumption more than 100 g/100 g SCMs indicating the high degree of pozzolanic properties. According to cumulative heat values, it was found that CF-F and CF-C (L) still release the heat of reaction after 7 days meaning that there were still the pozzolanic reaction. Regarding the results, the potential of modified R^3 test as a method to differentiate between inert and reactive materials was observed.

3.2.2 Lime reactivity test

In the same system as the R^3 test, the mortar specimens composed of SCMs-$Ca(OH)_2$-$CaCO_3$ were prepared. Mortar compressive strengths are presented in Fig.4. This method effectively specifies the inert materials since they did not have any reaction in the system and the mortar specimens was not hardened. Referring to Al-Shmaisani (2022), CoF and BGA were defined as highly reactive materials (100-200 ksc). CB, CF-F and WB were graded to be low-reactive materials (30-50 ksc). However, the reactivity of CF-F when defined by other methods shows high reactivity but a slow reaction. It is indicated that the lime reactivity test may not be suitable to the SCMs which slowly react because the sample was done only until 7 day.

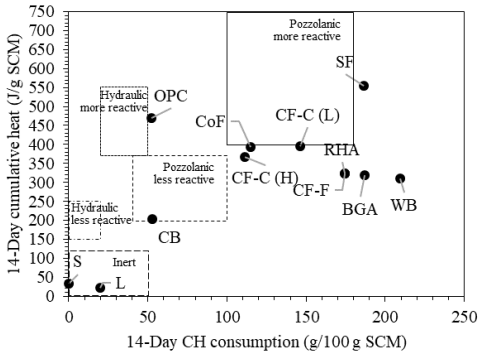

Fig. 3 Scatter plot between cumulative heat release and $Ca(OH)_2$ consumption of paste at 14 days

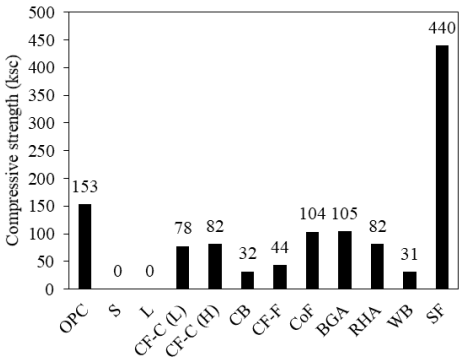

Fig. 4 Compressive strength (ksc) of mortar in the lime reactivity test

4. Conclusions

In this research, modified testing methods, such as modified strength activity index, bulk electrical resistivity, modified R^3 test and the lime reactivity test, were applied to assess the reactivity of SCMs in Thailand. From the study, the key points of each method were concluded below. However, these conventional and modified methods were only screening assessments of SCMs in the first stage. For the application of SCMs in construction, the performance of concrete and durability tests must be considered and further investigated.

	Advantages	Disadvantages
ASTM C311 SAI	▪ Conventional method	▪ Water requirement impact mortar strength ▪ Inert materials can pass SAI test
ASTM C1897 R^3 test	▪ Rapid testing-7 days ▪ Testing in small batch of specimen	▪ Insufficient analysis time for slow reactive material ▪ Cannot distinguish hydraulic and pozzolanic properties
Modified SAI	▪ Inert materials screen out ▪ Prevent false analysis of SAI test	▪ Time consuming: Experiment may require up to 90 days
Bulk electrical resistivity	▪ Inert materials screen out ▪ Non-destructive test	▪ Time consuming: Experiment may require up to 90 days
Modified R^3 test	▪ Inert materials screen out ▪ Rapid testing-14 days ▪ Differentiate hydraulic and pozzolanic properties	▪ Advanced instrument was required
Lime reactivity test	▪ Inert materials screen out ▪ Rapid testing-7 days	▪ Consumption of chemical reagent for 1 batch analysis

5. References

Al-Shmaisani, S., Kalina, R. D., Ferron, R. D., & Juenger, M. C. G. (2022). Critical assessment of rapid methods to qualify supplementary cementitious materials for use in concrete. *Cement and Concrete Research*, *153*, 106709.

Standard test methods for measuring the reactivity of supplementary cementitious materials by isothermal calorimetry and bound water measurements. ASTM International - Standards Worldwide.

Standard test methods for sampling and testing fly ash or natural pozzolans for use in Portland-cement concrete. ASTM International - Standards Worldwide.

Suraneni, P., Hajibabaee, A., Ramanathan, S., Wang, Y., & Weiss, J. (2019). New insights from reactivity testing of supplementary cementitious materials. *Cement and Concrete Composites*, *103*, 331–338.

The 16th International Congress on the Chemistry of Cement 2023 (ICCC2023)
"Further Reduction of CO_2 -Emissions and Circularity in the Cement and Concrete Industry"
September 18–22, 2023, Bangkok, Thailand

Performance of concretes with ternary blended cements containing limestone filler and calcined illitic clay

E.F. Irassar[1], V. L. Bonavetti[2], G. Cordoba[3], C. C. Castellano[4], H. Donza[5] & V. Rahhal[6]

Facultad de Ingeniería - CIFICEN (UNCPBA-CONICET-CIC) - Universidad Nacional del Centro de la Provincia de Buenos Aires, Olavarría , Argentina

Email: [1] firassar@fio.unicen.edu.ar, [2]vbonavet@fio.unicen.edu.ar, [3]gcordoba@fio.unicen.edu.ar, [4]ccastellano@fio.unicen.edu.ar, [5]hdonza@fio.unicen.edu.ar, [6]vrahhal@fio.unicen.edu.ar

ABSTRACT

Reducing the clinker factor using supplementary cementitious materials (SCM) is a potential cement and concrete decarbonization solution. Common clays (CIC) are widely available at low cost to produce SCM and, combined with limestone filler (LF), contribute to reaching net-zero emissions. This paper explores the properties of concretes made with composite cements with CIC+LF and compares the target properties with the embodied CO_2 of concretes. Five blended cements containing LF (10-25% by mass) and CIC (10-25% by mass) were used. The fresh properties (slump, flow, workability loss, and setting time), mechanical properties up to one year (compressive and flexural strength), and water penetration by pressure and capillary sorption were studied. Concrete eco-efficiency was evaluated as kg of embodied CO_2 per m^3 of concrete (ECO_2). Fresh concrete showed good workability (slump=15±3.5 cm; flow=45.5±6.5 cm) without segregation or water crown, no bleeding, and exceptional surface finish. The slump loss was similar for all concretes independent of SCM content. The initial and final setting time was prolonged for the highest substitution level (T25CIC25LF) concerning the lowest one (T10CIC10LF). At early ages, compressive strength was reduced according to the replacement level. Concretes with 35% of SCM reached a similar strength at 2 and 7 days (11.4±1.0 and 22.0±0.7 MPa, respectively). After 28 days, the compressive strength of concretes with 35% of SCM increased for higher CIC content due to the pozzolanic reaction. Flexural strength has a linear relationship with compressive strength. Water penetration parameters are improved after 28 days, indicating the need for longer curing times for these types of concretes. Low clinker factor reduces the ECO_2, but the eco-efficiency of concrete is limited by the age at which the designer establishes the strength-conformity. The eco-efficiency of concretes with CIC and LF is higher for later ages.

KEYWORDS: *calcined clay, limestone filler, concrete, strength, water penetration*

1. Introduction

Building environment requires a large volume of materials (aggregates, cement, ceramic, lime, gypsum, glass, wood, steel, aluminum, and plastic) with appropriate engineering properties, long service life, low embodied energy, low greenhouse emission, and local availability to satisfy the increase of the urban population (Habert et al., 2020). Concrete and masonry require a large volume of cement made with a Portland clinker, a great contributor to greenhouses gases emission. For this reason, the clinker factor should be reduced with appropriate proportions of supplementary cementitious materials (SCMs), and calcined clays appear as a potential solution (Scrivener et al., 2018; Maier et al., 2021). Common clays with low cost, high availability, and large proportions of impurities can be used to produce SCM that can be introduced with the limestone filler to contribute to the net-zero emission of cement and concrete. Ternary blended cements combining LF and an active SCM have been the best option for concrete production, such as slag-limestone filler (Menéndez et al., 2003; Fernandez et al., 2018), fly ash-limestone filler (De Weerdt et al., 2011; Bonavetti et al., 2022) and calcined kaolinite clay and limestone filler (Scrivener et al., 2018; Zunino et al., 2021).

This paper explores the fresh and mechanical properties of concretes made with ternary blended cements composed of calcined illitic clay (CIC = 10 to 25%) and limestone filler (LF =10 to 20%) and compares the target properties with the low embodied CO_2 of concrete.

2. Materials and Methods

Ordinary Portland cement (PC- CEM I 42.5), calcined illitic clay (CIC), and limestone filler (LF) were used. PC has low C_3A content (2.8%), natural gypsum as a sulfate source, and limestone filler as a minor component. Calcined clay was produced in a rotary kiln at 950 °C using illitic claystone (also called illitic shale) from a quarry near Olavarría, Buenos Aires, Argentina. Characteristics of raw clay, thermal treatment, grinding processes, and properties of CIC have been previously reported (Irassar et al., 2023). For 25% by mass replacement, CIC has a positive pozzolanicity at 7 days in the Frattini test (EN 197-5), and the strength activity index with cement at 20 °C (EN 450) was 0.88, 0.92, and 1.00 at 7, 28 and 90 days. Limestone filler has 88.2% of calcite and quartz as the main impurity.

Five ternary blended cement containing LF (10 to 25%) and CIC (10 to 25%) were formulated: T10CIC10LF, T17.5CIC17.5LF, T25CIC10LF, T10CIC25LF, and T25CIC25LF. Irassar et al. (2023) have also reported the mechanical characterization of mortars.

The five ternary blended cements, natural silica sand (fineness modulus = 2.02 and density = 2.636), granitic crushed stone (maximum size = 19 mm and density = 2.717) and a high-water reduction range chemical admixture (density =1.1 g/cm^3) were used for concrete production. Concrete mixtures (w/cm = 0.45 and UCC=350 kg/m^3; fine/coarse aggregate ratio = 43% - see Table 1) were designed to the same consistency (S3), and the fresh (slump, flow, workability loss, and setting time) and mechanical (compressive and flexural strength after 2, 7, 28, 90 and 365 days of water curing) properties were determined. Compressive strength was obtained on five 100 × 200 mm cylindrical specimens, and the flexural strength on two prismatic specimens using the three-point disposition. At 28 and 90 days, the water penetration under pressure (IRAM 1554) was determined on three 150 mm cubes, and the initial capillary water absorption rate (ASTM C1585) was measured on three slices of cylinders (h = 50 mm).

The eco-efficiency of concretes was evaluated in terms of kg of embodied CO_2 per ton of cement (ECO_2), considering an emission factor of 895 kgCO_2/t for PC (Cordoba et al., 2020), 253 kgCO_2/t for CIC (Cordoba et al., 2020), and 8 kgCO_2/t for LF (Miller et al., 2018).

3. Results and discussion

Table 1 reports the results of the fresh properties of concretes. The initial slump was 15±3.5 cm, and the initial flow was 45.5±6.5 cm without segregation or water crown. All mixtures showed good workability, excellent cohesion, no bleeding, and exceptional surface finish. The slump loss of T10CIC10LF was 18% and 43% at 15 and 45 minutes, respectively, while it was 68±9% at 45 minutes for the rest of the concretes. The flow loss (in %) was lower than that recorded for the slump and less dependent on the SCM content in the mixture. The initial and the final setting time were the shortest for T10CIC25LF and the longest for T25CIC25LF. The setting duration was similar (140 and 175 min) for all the concretes except for T25CIC25LF, which exhibited a slightly longer duration (210 min). Ternary CIC+LF cements can produce workable concretes without excessive slump loss or changes in the setting time.

Table 1: Concrete mixture proportions and fresh properties of concretes

Concrete	**Mixture proportions**, kg/m^3						**Slump**, cm	**Flow**, cm	**Setting time**, min	
	PC	CIC	LF	Water	Fine Agg	Coarse Agg			Initial	Final
T10CIC10LF	280	35	35	158	810	1075	14.0	46.9	420	630
T17CIC17LF	228	61	61	158	802	1075	16.0	39.5	470	645
T25CIC10LF	228	88	35	158	801	1075	11.0	38.0	430	615
T10CIC25LF	228	35	88	158	803	1075	12.0	34.0	390	555
T25CIC25LF	175	88	88	158	794	1075	18.5	44.0	550	760

Fig. 1a shows the compressive strength of ternary blended concretes. At 2 and 7 days, the compressive strength of T10CIC10LF was 14.6 and 27.0 MPa, respectively. The increase of 30% of SCM in T25CIC25LF reduced the compressive strength by 47 and 38% at 2 and 7 days, respectively. Concretes with 35% of SCM reached a similar strength, 11.4 ± 1.0 and 22.0 ± 0.7 MPa at 2 and 7 days, respectively. At 28, 90, and 365 days, the compressive strength of T25CIC25LF was lower (24 to 12%) than that of T10CIC10LF. The compressive strength of concretes with 35% of SCM increased more for higher CIC content. After 90 days, T25CIC10LF reached similar compressive strength to T10CIC10LF. At later ages, the pozzolanic reaction of CIC offsets the dilution effect caused by the non-reactive portion of the calcined clay (52%) and the LF. Flexural strength (f_{fl}) has a linear relationship with the compressive strength (f_c) for all concretes ($f_{fl} = 0.12\, f_c$; $R^2 = 0.998$).

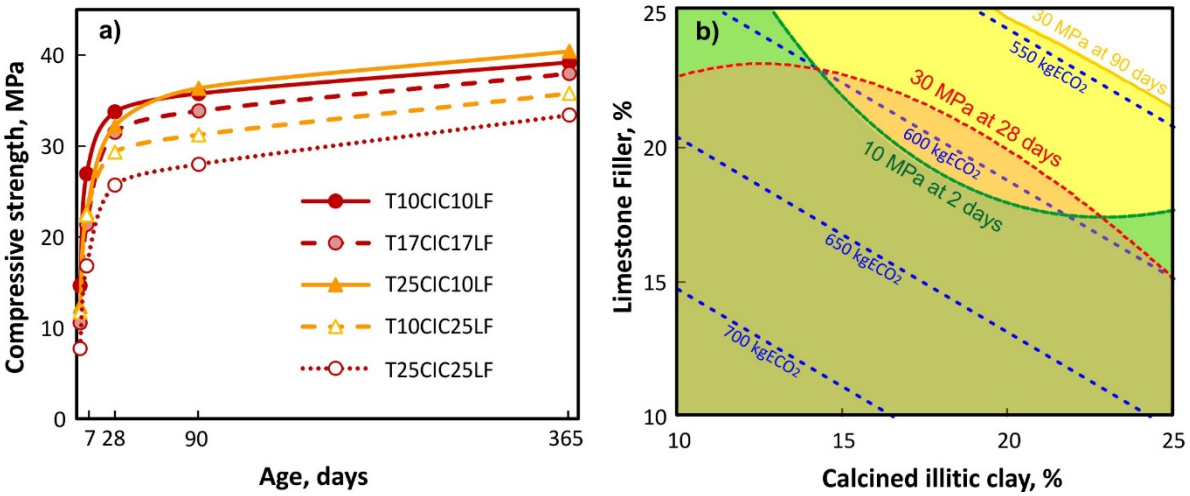

Figure 1: a) Compressive strength and b) Embodied CO_2 for concrete design

The average of water penetration under pressure and the initial capillary absorption rate of concretes at 28 and 90 days is reported in Table 2. The C10LF10CIC has the lowest at both test ages, and C25LF25CIC has the highest water penetration. For concretes with 35% SCM, the water penetration was similar at 28 days (20.5 ± 0.7 mm) and 90 days (17.8 ± 0.8 mm). Results indicate that the SCM replacement level is the main factor for the water penetration in this ternary concretes with constant w/cm.

Table 2: Water penetration under pressure and initial capillary absorption rate at 28 and 90 days

	Water penetration under pressure, mm		**Initial capillary absorption rate,** $g/m^2\ s^{1/2}$	
Concrete	28 days	90 days	28 days	90 days
T10CIC10LF	13.6	11.9	3.0	2.6
T17CIC17LF	19.8	17.6	3.9	3.0
T25CIC10LF	21.4	17.1	3.3	2.7
T10CIC25LF	20.4	18.6	4.9	3.3
T25CIC25LF	26.2	23.9	4.2	3.5

The initial capillary absorption rate of T10CIC10LF was the lowest at 28 and 90 days. This property appears to be dependent on the LF content in the ternary blended cement. For T10CIC25LF and T25CIC25LF, the initial rate was greater than 4.0 and 3.0 $g/m^2\ s^{1/2}$ at 28 and 90 days, respectively, had a mean value for T17CIC17LF and a closer value to the minimum for T25CIC10LF. For all concretes, the initial rate decreased from 28 to 90 days, indicating the importance of curing time to reduce the connectivity in the pore structure due to the progress of the pozzolanic reaction of CIC.

Regarding the ECO_2 of concrete, calculated as the sum of ECO_2 of each concrete component, Figure 1b shows the isolines from 700 to 550 $kgCO_2/t$ of cement when the clinker factor is reduced in the blended cement (sum of CIC+LF). For different strength levels of concrete (10 MPa at 2 days -green line-, 30MPa at 28 days -red line- or 90 days -yellow line-), the eco-efficiency of concrete is limited by the SCM replacement level that requires a given curing age at which the designer establishes the strength conformity. Namely, the later age of conformity, the higher CIC and LF content makes it possible to achieve the required compressive strength with lower ECO_2.

4. Conclusions

Ternary blended cements (PC+CIC+LF) can be used eco-efficiently to produce structural concrete with equivalent mechanical and water transport properties using different combinations. Concretes had good workability (without segregation or water crown, no bleeding, and exceptional surface finish) without significant doses of suplespastizicer. The slump loss was similar for all concretes, independent of SCM content, and the setting time was not significantly affected.

Compressive strength was reduced at 2 and 7 days with the increase in replacement level. After 28 days, among concretes with 35% of SCM, the compressive strength increased more for those with higher CIC content due to its pozzolanic reaction. Flexural strength has a linear relationship with compressive strength.

Water penetration under pressure depended primarily on the replacement level and was reduced after 28 days of curing, indicating the need for prolonged curing to ensure porosity disconnection. The initial absorption rate appears to depend more on the LF content, but it is also improved with curing time extension due to the slow pozzolanic reaction of CIC.

The design for later strength conformity age improves the eco-efficiency of concretes.

References

De Weerdt, K.; Ben Haha, M.; Le Saout, G.; Kjellsen, KO; Justnes, H.; Lothenbach, B. (2011) Hydration mechanisms of ternary portland cements containing limestone powder and fly ash. *Cement and Concrete Research*. 41,279–291.

Cordoba, G., S.V. Zito, R. Sposito, V.F. Rahhal, A. Tironi, K.-C. Thienel, E.F. Irassar. (2020). Concretes with calcined clay and calcined shale: Workability, mechanical, and transport properties. *Journal of Materials in Civil Engineering* 32(8): 4020224.

Fernández, Á.; Lothenbach, B.; Alonso, M.C.; García Calvo, J.L. (2018) Thermodynamic modelling of short and long term hydration of ternary binders. Influence of Portland Cement Composition and Blast Furnace Slag Content. *Construction & Building Materials*, 166, 510–521.

Habert, G., Miller, S. A., John, V. M., Provis, J. L., Favier, A., Horvath, A., Scrivener, K. L. (2020). Environmental impacts and decarbonization strategies in the cement and concrete industries. *Nature Reviews Earth & Environment*, *1*(11). https://doi.org/10.1038/s43017-020-0093-3

Irassar, E.F., Tironi, A., Bonavetti, V. L., Trezza, M., Castellano, C., Rahhal, V., Donza, H., Scian, A. (2019). Thermal treatment and pozzolanic activity of calcined clay and shale. *ACI Materials Journal*, *116* (4), 133–143.

Irassar, E.F.; Bonavetti, V.L.; Cordoba, G.P.; Rahhal, V.F.; Castellano, C.C.; Donza, H.A. (2023) Performance of composite portland cements with calcined illite clay and limestone filler produced by industrial intergrinding. *Minerals*, *13*, 240.

Maier, M., Beuntner, N., Thienel, K. C. (2021). Mineralogical characterization and reactivity test of common clays suitable as supplementary cementitious material. *Applied Clay Science*, *202*(January), 105990.

Marchetti, G.; Castellano, C.; Bonavetti, V.; Irassar, E.F. (2022) Tools for designing the early-age properties of fly ash and limestone filler ternary systems. *Construction & Building Materials*, 347, 128552.

Menéndez, G.; Bonavetti, V.; Irassar, E.F. (2003) Strength development of ternary blended cement with limestone filler and blast-furnace slag. *Cement and Concrete Composite*. 25 (1), 61-67

Miller, S.A., John, V.M., Pacca, S.A., Horvath, A., (2018). Carbon dioxide reduction potential in the global cement industry by 2050. *Cement Concrete Research,* 114, 115–124.

Scrivener, K. L., John, V. M., Gartner, E. M. (2018). Eco-efficient cements: Potential economically viable solutions for a low-CO_2 cement-based materials industry. *Cement and Concrete Research*, *114* (February), 2–26.

Scrivener, K.; Martirena, F.; Bishnoi, S.; Maity, S. (2018) Calcined Clay Limestone Cements (LC^3). *Cement Concrete Research*. 114, 49–56.

Zunino, F.; Martirena, F.; Scrivener, K. (2021) Limestone Calcined Clay Cements (LC^3). *ACI Materials Journal*, 118, 49–60.

The 16th International Congress on the Chemistry of Cement 2023 (ICCC2023)
"Further Reduction of CO_2 -Emissions and Circularity in the Cement and Concrete Industry"
September 18–22, 2023, Bangkok, Thailand

Determination of calcined clay minerals impact on strength and carbonation of Portland cement mortars using k-value concept

J. Szydłowski[1*], Ł. Kotwica[2]

[1] *AGH University of Science and Technology, Kraków, Poland*

szydlows@agh.edu.pl

[2] *AGH University of Science and Technology, Kraków, Poland*

lkotwica@agh.edu.pl

ABSTRACT

The paper focuses on replacing Portland clinker with thermally activated clay minerals. The thermal activation temperature depends on the particular mineral but, in general, it is much lower compared to the temperature used for the production of Portland clinker. The incorporation of calcined clays as SCMs significantly reduces the energy required for cement production, as well as the carbon footprint. The clay minerals used in the present study: montmorillonite and kaolinite differ in their nature and therefore in their properties during and after calcination. Quantitative determination of the influence of investigated calcined clay minerals on the hydration and strength of cement-based composites was made. The concept of k-value based on the EN 206-1 standard was used for a qualitative comparison of the influence of calcined kaolinite and montmorillonite on mortar strength. After 28 days of hydration, the k-values of calcined kaolinite and montmorillonite were 2.8 and 1.1 respectively, indicating their superior activity. On the other hand, both SCMs reduce the resistance to carbonation as a result of a reduction in the calcium oxide content. The tests were performed not only for different carbonation periods but also after different hydration times. In general, one can conclude that both calcined clays worsen carbonation resistance, and their influence is similar to the influence of ground quartz sand, used as a neutral filler. The results indicate an improved corrosion resistance for longer maturation times. It may be of importance in the attempt to construct a carbonation model and ultimately lead to a longer estimated lifetime of the structure.

KEYWORDS: *carbon footprint, calcined clays, Portland cement, pozzolanas, SCM, k-value*

1. Introduction

Clay minerals are hydrated layered aluminosilicates of aluminium, magnesium, and iron. They consist of tetrahedral and octahedral layers. Depending on the mutual arrangement of these layers, construction type 1:1 and construction type 2:1 can be distinguished. Kaolinite is typical member of the 1:1 (two layers) clay minerals group, while montmorillonite belongs to the 2:1 (three layer) group (Brigatti et al., 2013). The type of structure determines the properties and applicability of clays as a part of a binder and is closely related to its characteristic calcination temperature (Wolters and Emmerich, 2007).
LC^3 group cements have been of great interest to researchers over the past several years. In addition to Portland clinker, these cements consist of calcined clay, ground limestone, and gypsum (Scrivener et al., 2018). Usually, naturally occurring clays are used as raw materials for such cements. The number of works considering the properties of individual clay minerals is limited (Rodrigo et al. 2011). The present work is devoted to the determination of the influence of calcined montmorillonite and calcined kaolinite on the strength and durability of blended cements. Quantitative determination of the influence of calcined kaolinite using the concept of k-value (according to EN 206 standard) was performed (Badogiannis et al., 2004); however, there is a lack of such data for calcined montmorillonite.

2. Materials, methods and sample preparation

Ordinary Portland Cement (OPC) CEM I 42,5R, complying with EN 197-1 standard, kaolinite (Surmin-Kaolin S.A., Poland), montmorillonite (Zębiec® S.A., Poland) and standard quartz sand conforming to EN 196-1 were used. The chemical composition of the materials is shown in Table 1. The estimated purity of the kaolinite is >92 %, whereas no defects in the kaolinite structure were assumed for the calculations. The quartz content is estimated at 4 % and other impurities, including other clay minerals (muscovite, illite), at 4 %. Thermogravimetric analysis of montmorillonite allows to determine its purity to a minimum of 82 %, with the presence of muscovite, quartz and calcite.

Table 1. Chemical composition of kaolinite, montmorillonite and OPC used in experiments

	SiO_2	CaO	Al_2O_3	MgO	K_2O	Na_2O	TiO_2	Fe_2O_3
Kaolinite	58.02	0.11	38.31	0.27	0.93	0.11	0.73	0.77
Montmorillonite	60.50	9.39	22.13	3.83	0.16	0.17	0.37	2.86
OPC	16.70	66.49	4.64	1.26	0.78	0.18	0.37	4.43

Kaolinite and montmorillonite were calcined in ceramic muffles at the temperatures of 600°C and 870°C (rate of heating equal to 5°C/min) respectively, for 3 hours. Metakaolinite was then ready to use, whereas metamontmorillonite was ground in a ball mill (polyamide chamber, corundum grinding elements), to disintegrate agglomerates and to increase the specific surface of calcined montmorillonite. Fig. 1 presents the grain size distribution of both calcined minerals. Table 2 presents the parameters that characterise the grain size distribution of both calcined minerals. It can be assumed that the grain size distribution of both calcined clay minerals is similar, and the differences will not influence the activity of materials to a great extent.

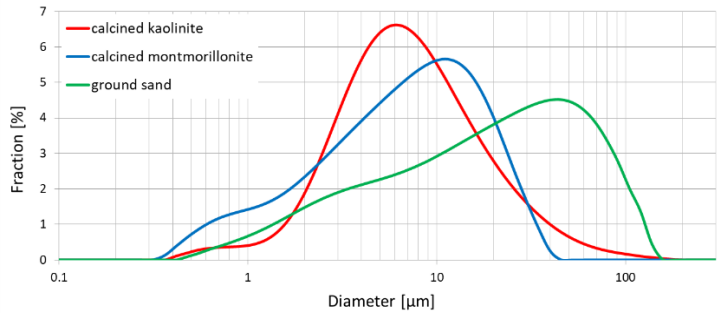

Figure 1. Grain size distribution of calcined kaolinite and montmorillonite (Malvern Mastersizer 2000, isopropyl alcohol as a carrier liquid)

Table 2. Parameters of grain size distribution of calcined kaolinite (CK), calcined montmorillonite (CB) and ground sand (CP)

	CK	CB	CP
	% by mass		
>5 µm	67.9	64.0	81.0
>10 µm	35.9	39.1	68.6
>32 µm	5.3	1.1	35.9
>45 µm	3.0	0	27.0
>90 µm	0.6	0	6.6

Four series of mortars were prepared. Table 3 presents the composition and designation of these mortars. The CP series of mortars contained 15% ground quartz sand, used as an inert filler to compare the properties of mortars with the same effective water / clinker ratio. Mortars were mixed in a laboratory mixer, cast in steel forms, and stored at 20°C and RH ≥ 95% for 40 hours, and then demoulded and kept in water at 20°C. Prior to the carbonation tests, samples were stored at 20°C and RH = 50% in order to dry and equilibrate.

Table 3. Mix proportions of mortars used for strength and carbonation tests

Series	OPC	Ground sand	Calcined-kaolinite	Calcined montmo-rillonite	Standard sand	Water/binder ratios
CC	100	-	-	-	300	0.50, 0.56, 0.59, 0.63, 0.70
CP	85	15	-	-	300	0.50, 0.56, 0.59, 0.63, 0.70
CK	85	-	15	-	300	0.50, 0.55, 0.60, 0.65
CM	85	-	-	15	300	0.50, 0.55, 0.60, 0.65

The compressive strength measurements were carried out on 25×25×100 mm mortar bars after 7, 14 and 28 days of curing. Samples were examined using a hydraulic press with a force increase rate of 500 N/s. Each value is the average of four to six measurements (in mostly six samples were measurement).
Carbonation test was conducted in carbonation chamber complying with EN 12390-12 at 3% CO_2 concentration and RH of 57% ± 3% using 40×40×160 mm mortar bars, after 7, 14 and 28 days of curing. Phenolphthalein was used as the indicator. Carbonation depth was measured using digital images of stained fractures. ImageJ software was used for image analysis and calculating unreacted area and carbonation depth according to method proposed by one of the authors (Szydłowski, 2023).
K-value concept is used to quantify the impact of a given supplementary cementitious material (SCM) on the strength of the cement-based composites. In present work, the methodology proposed by Łagosz et al. (2021), which is based on the concept of the k-value given in EN 206 standard was used. The values obtained are the mean of k-values for mortars of various water/binder ratios.

3. Results and discussion

3.1. Compressive strength

Compressive strength of mortars of water/binder ratio equal to 0.50 are shown in Fig. 2. It can be seen, that the influence of calcined clays is much dependent on its type. This relationship was also found for other water/binder ration investigated. Compressive strength values obtained in a whole experiment were used to calculate the k-values for calcined clay minerals and ground sand used as a reference material. In Fig. 3 the k-values are presented for mortars after 7, 14 and 28 days of hydration.
The results obtained showed that although the activity of calcined montmorillonite is significantly lower than that of metakaolinite, it is still very good, and after 28 days is comparable to that of Portland cement. This is represented by a k-value of 1.1. Further research is needed to determine the main reasons for such a significant difference with activity in relation to strength. It is worth mentioning that, in both cases, calcination was carried out at a carefully chosen optimum temperature that allowed the material to fully decompose. In addition, the grain size distribution was normalised.

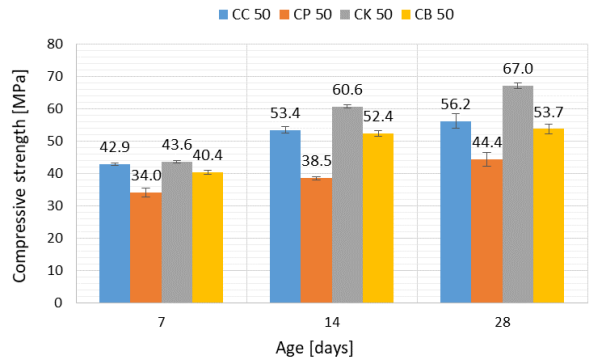

Figure 2. Compressive strength of mortars with 15% replacement of cement with ground quartz sand (CP), calcined kaolinite (CK) and calcined montmorillonite (CB) compared to neat OPC mortar (CC). Water/binder ratio 0.50

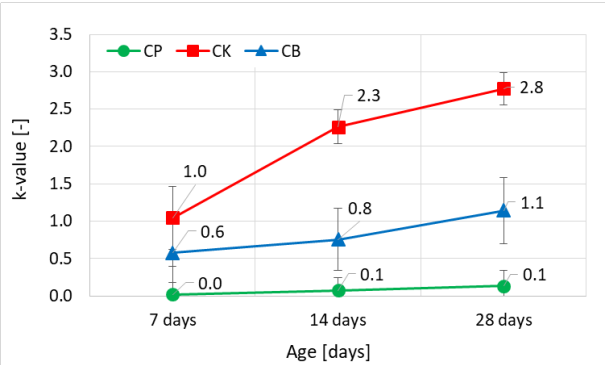

Figure 3. K-values for calcined kaolinite (CK), calcined montmorillonite (CB) and ground sand (CP) after 7, 14 and 28 days of curing. Error bars represents the confidence interval (α=0.05) determined using t-Student statistics

3.2. Carbonation

Figure 4 shows the depth of carbonation in the mortars tested. It can be seen that with increasing carbonation time (time in the carbonation chamber), the differences between OPC mortars and mortars made from blended cements increase. After 28 days in the carbonation chamber, all blended mortars show a similar depth of carbonation, regardless of the activity (quantified by the k value) of the additive.
By comparing the effects of both calcined clay minerals on strength and durability against carbonation, it can be concluded that the reactivity of a given SCM does not play a significant role from the point of view of carbonation progress, as measured by changes in carbonation depth. It is in line with conclusions of

Papadakis (2000) and Shah et al. (2020). They showed that the depth of carbonation is connected with the total content of calcium oxide available for carbonation. Since all SCMs used in the present study contain very low amount of calcium, thus their impact is also similar.

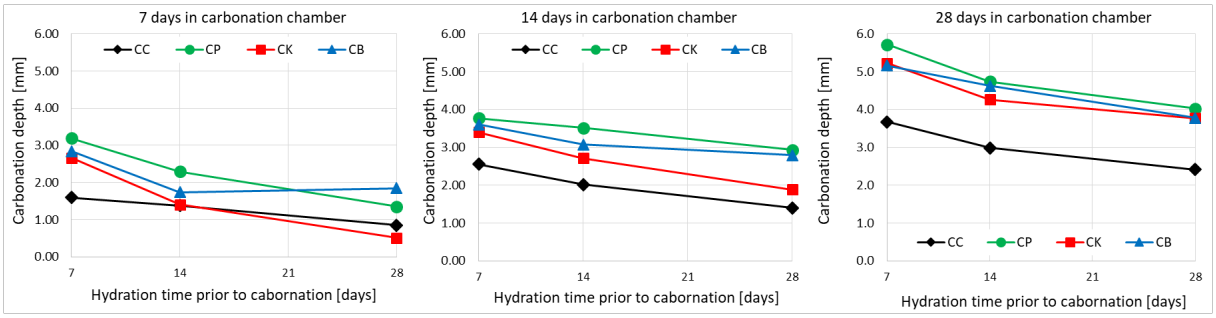

Figure 4. Depth of carbonation of neat OPC mortar (CC) and mortars with 15% replacement of OPC by calcined kaolinite (CK), calcined montmorillonite (CB) and ground quartz sand (CP). Water/cement ratio equal to 0.50

4. Conclusions

The present study confirmed the very high activity of calcined kaolinite. Obtained results are very close to those obtained by Badogiannis et al. (2004). On the other hand, the activity of calcined montmorillonite is significantly lower but still very high, comparable to Portland cement. The k-value obtained for calcined montmorillonite is 2 to 3 times lower than for metakaolinite, depending on the curing time.
Both calcined clay minerals tested were found to have a negative effect on the resistance of the mortars to carbonation. It was observed that as the degree of carbonation increased, that is, with longer time in the carbonation chamber, the differences between mortars with 15% cement replacement calcined clay and the reference sample (OPC) increased. After 28 days of testing in the carbonation chamber, the carbonation depth for the mortars with both calcined clays was practically the same as for the mortar with the inert additive, ground quartz sand.

Acknowledgements

The work was supported by the AGH University of Science and Technology, Project Excellence Initiative – Research University (IDUB), project no. 4176 „Research on calcined clay minerals as components of low-carbon mineral binders for use in sustainable construction“ (16.16.160.7998).

References

Badogiannis, E., Papadakis V.G., Chaniotakis, E., Tsivilisa S. (2004) “Exploitation of poor Greek kaolins: Strength development of metakaolin concrete and evaluation by means of k-value” Cement and Concrete Research 34: 1035-1041

Brigatti, M.F., Galán, E., Theng, B.K.G. (2013) “Structure and Mineralogy of Clay Minerals”, Developments in Clay Science 5: 21–81

Łagosz, A., Olszowski, D., Pichór, W., Kotwica, Ł. (2021) „Quantitative determination of processed waste expanded perlite performance as a supplementary cementitious material in low emission blended cement composites” Journal of Building Engineering, 40: 102335

Papadakis, V.G. (2000) “Effect of supplementary cementing materials on concrete resistance against carbonation and chloride ingress” Cement and Concrete Research 30:291-299

Szydłowski, J. (2023) “New method of cement mortars carbonation depth determination based on image analysis”, [Manuscript in preparation]

Scrivener, K., Martirena, F., Shashank, B., Soumen, M. (2018) “Calcined clay limestone cements (LC^3)” Cement and Concrete Research 114: 49-56

Shah, V., Parashar, A., Medepalli, S., Bishnoi, S. (2020) “Prediction of carbonation using reactivity test methods for pozzolanic materials” Advances in Cement Research 32(7): 297-306

Wolters, F., Emmerich, K. (2007) “Thermal reactions of smectites-Relation of dehydroxylation temperature to octahedral structure” Thermochim. Acta. 462: 80–88

The 16th International Congress on the Chemistry of Cement 2023 (ICCC2023)
"Further Reduction of CO_2 -Emissions and Circularity in the Cement and Concrete Industry"
September 18–22, 2023, Bangkok, Thailand

A preliminary study on pozzolanic activity and reaction kinetics of coal gasification slag

K.Z. FANG[1], D.M. WANG[2*], F.Y. LI[3]

China University of Mining and Technology (Beijing), Beijing, China
[1] *fangkuizhen@163.com*
[2*] *wangdongmin@cumtb.edu.cn*
[3] *lifangyuan2021@126.com*

ABSTRACT

The pozzolanic reactivity of coal gasification slag (GS) is a key factor in cement-based materials. In this study, a simplified GS powder-$Ca(OH)_2$-H_2O binding system was used. The chemical undissolved amount and reaction rate of GS powder were measured by the acid dissolution method, a pozzolanic reaction kinetics model was established, and the relationship between the degree of GS reaction and the strength of the system was analyzed. The results show that with the increase of CaO content and specific surface area of the powder, the reaction rate of GS powder increased, and it conformed to a first-order kinetics model. Among them, when CaO/GS exceeded 0.25, the strength of the system continued to increase. GS without participation of CaO did not possess hydraulic properties by itself. The degree of reaction of GS powder exhibited a good e-index relationship with the strength of the binding system, and when the reaction rate was approximately above 10%, the strength of the paste significantly increased.

KEYWORDS: *Coal gasification slag; $Ca(OH)_2$; Reaction degree; Pozzolanic reactivity*

1. Introduction

Gasification slag is a by-product of the coal gasification process and has become a subject of increasing research in recent years as a typical coal-based solid waste (Xin et al (2022)). Its high carbon content and high water content make it difficult to apply in practical engineering. From a theoretical research perspective, the low reactivity of gasification slag in the field of building materials is another challenge, which is related to the conditions of the gasification process and the composition of the coal. At present, the main research directions of gasification slag in the field of building materials include the preparation of aggregates, cementitious materials (Luo et al (2020)), wall materials (Yuan et al (2020)), and non-fired bricks. Due to its silica-alumina composition and pozzolanic activity, research on the use of gasification slag as a supplementary cementitious material (SCM)has been increasing (Blaisi et al (2018)).
As a SCM, the pozzolanic activity of gasification slag in powder form after ball milling is an important research foundation for the utilization of gasification slag in building materials (Li et al (2019)). When mixed with Portland cement, the active SiO_2 and Al_2O_3 in gasification slag partially dissolve and form hydration products with $Ca(OH)_2$, similar to the hydration products of ordinary Portland cement (Mazurkiewicz et al (2012)). To gain a deeper understanding and evaluate the reactivity of gasification slag, it is necessary to determine its ability to participate in pozzolanic reactions in a cementitious alkaline environment. Considering that the products of cement clinker and gasification slag coexist, accurately measuring the reaction degree is challenging. Therefore, the reaction degree of gasification slag in a $Ca(OH)_2$-H_2O system is used to evaluate its reactivity in cement paste, providing a theoretical basis for the study of gasification slag reactivity in cementitious composite materials.

2. Materials and Experiments

The gasification slag used in this study is a low-carbon gasification coarse slag (GS), originating from the dry coal powder gasification furnace in the coal-to-oil process in the Ningdong region of Ningxia. It is

rich in elements such as Ca, Si, and Al. The chemical composition obtained through XRF testing is shown in Table 1. The mineralogical composition analyzed by XRD mainly consists of a silicoaluminate glass phase and a small amount of SiO2, as shown in Figure 1. The powder prepared by ball milling the gasification slag for 50 minutes is denoted as GS50. The powder prepared by ball milling GS for 1 hour and then planetary milling for 20 minutes is denoted as GS80. The raw material obtained after decarbonization and iron removal, milled with a ball mill for 1h and then a planetary mill for 20 min, is denoted as MGS80. Due to the poor grindability and low pozzolanic activity of gasification slag, this study selects gasification slag with different milling times for comparison. Moreover, although the carbon and iron content in the gasification slag are not high, preliminary research has found that there are many magnetic particles and surface floating carbon particles in the gasification slag. Therefore, pretreated gasification slag is chosen for comparison. CaO is chemically pure reagent with a purity of ⩾98.0%.

Coal gasification slag with different specific surface areas is mixed with CaO at a mass ratio of 4:1, with a water/solid ratio of 0.70. At the same time, the powder MGS80 after decarbonization and iron removal grinding was used as the research object, and mixed with CaO at a mass ratio of 0, 1:4, 1.5:4, and 2:4 to prepare samples with different CaO/GS (C/G). The reaction degree of coal gasification slag is tested by acid dissolution method.

Table 1 Chemical compositions (%) of GS

composition	SiO_2	Al_2O_3	Fe_2O_3	CaO	MgO	SO_3	Loss
GS	53.77	17.04	10.45	9.31	1.92	2.84	2.90

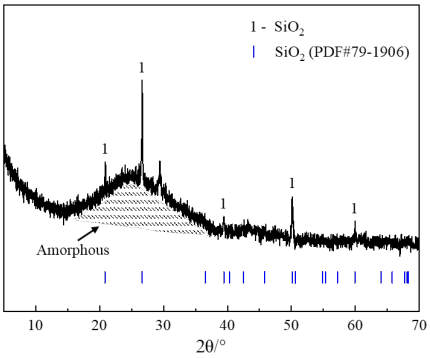

Fig. 1 XRD analysis of GS.

3. Results and Discussion

Figure 2(a) shows the measured reaction rates of the coal gasification slag-$Ca(OH)_2$-H_2O system at various curing ages under standard curing conditions. The results indicate that the pozzolanic reaction rate of coal gasification slag gradually increases with the extension of the curing period. In the early stage (within 7 days), the pozzolanic activity of coal gasification slag is relatively low. After 7 days, the pozzolanic activity gradually becomes apparent, and the hydration activity growth slows down after 28 days. Even at the 90-day curing age, the reaction rate of coal gasification slag is still about 20%, indicating that there are still some unhydrated particles in the coal gasification slag, which only serve as physical fillers. The pozzolanic activity of coal gasification slag is closely related to the amount of $Ca(OH)_2$ generated in the system. The observation results show that the reaction rate of coal gasification slag after decarbonization, iron removal, and sufficient grinding is higher than that of the other two types of coal gasification slag, indicating that the physical modification methods of decarbonization, iron removal, and increasing effective grinding time have a better promoting effect on the improvement of the pozzolanic activity of coal gasification slag.

Assuming the chemical insoluble content of the samples at each curing age is w_β, and w represents the content of the inactive components in the coal gasification slag that have not dissolved in acid, then w_β-w represents the residual concentration of the active components in the coal gasification slag at a certain curing age. Therefore, the reaction rate equation of coal gasification slag can be written as:

$$v=-d(w_\beta-w)/dt=k(w_\beta-w)^n \quad (1)$$

In this equation, k represents the reaction rate constant, and its unit depends on the reaction kinetics model; n represents the reaction order. Assuming the reaction order n of coal gasification slag pozzolanic reaction is 1, the integral form of the above equation can be transformed into:

$$\ln(w_\beta - w) = \ln(w_{\beta 0} - w) - kt \qquad (2)$$

Under the standard curing at 20°C, according to the values of wβ and w, plot $\ln(w_\beta - w)$ as the vertical coordinate and t as the horizontal coordinate (as shown in Figure 2(b)). The effective reaction rate constant k values are obtained based on the correlation coefficient R^2 of the fitted curve, as shown in Table 2.

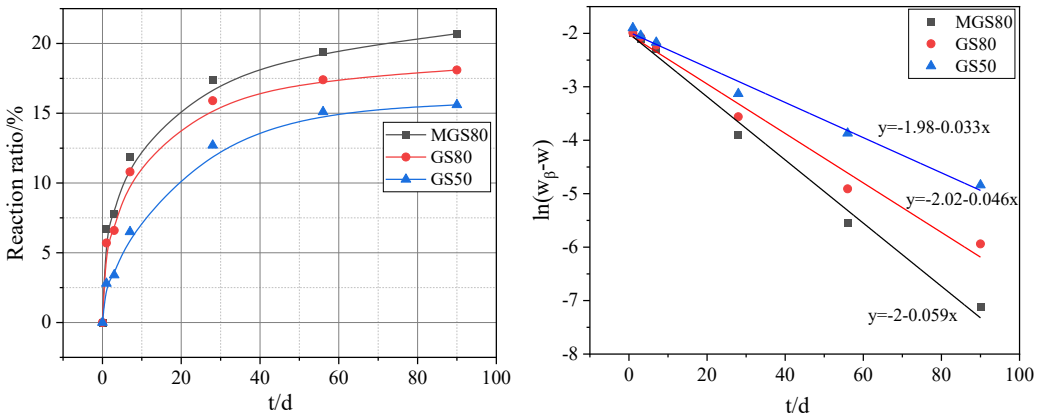

Fig. 2(a) Reaction rate of GS-$Ca(OH)_2$-H_2O system (b) The relationship between $\ln(w_\beta - w)$ and t

Table 2 Reaction rate constant k and line relation coefficient R^2 of pozzolanic reaction of GS at 20°C

GS	k/h^{-1}	R^2
GS50	0.033	0.988
GS80	0.046	0.982
MGS80	0.059	0.990

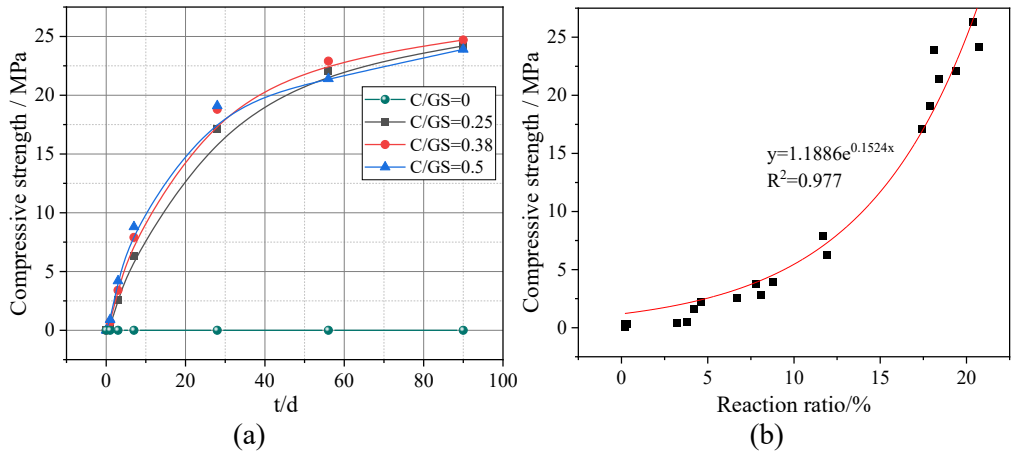

Fig. 3 (a) The development of system strength (b) The relationship between strength and GS reaction rate.

Figure 2 and Table 2 show that the pozzolanic reactions of different modified coal gasification slags conform to the first-order reaction kinetics model. The magnitude of the reaction rate constant k reflects the reaction rate of the pozzolanic reaction, i.e., the higher the k value, the faster the pozzolanic reaction rate, and the higher the activity. The results show that the pozzolanic activity of MGS80 (k=0.059) is higher than that of GS50 (k=0.033) and GS80 (k=0.056), which is consistent with the previous results of the degree of pozzolanic reaction of coal gasification slag. This is because the activity of the pozzolanic material is not only related to its glass content but also has a significant relationship with particle fineness,

mineral composition, and structural characteristics. Therefore, the physicochemical modification of coal gasification slag is necessary.

Figure 3(a) shows that as the C/GS ratio increases, the strength of the coal gasification slag-$Ca(OH)_2$-H_2O system gradually increases. At a C/GS ratio of 0.25, the compressive strength can reach a relatively high level. As the CaO content continues to increase, the increase in compressive strength is not significant. At 1 day, the system strength increases with the increase in CaO content, and after 3 days, the samples with a C/GS ratio of 0.25 show higher compressive strength. This is because a low CaO content is insufficient to fully stimulate the coal gasification slag, while excessive CaO content can lead to the formation of f-CaO, which in turn causes $Ca(OH)_2$ to form large crystals that are mixed with the hydrated particles of coal gasification slag, resulting in system expansion and strength reduction. The pure coal gasification slag system without CaO addition has no strength within 90 days, further indicating that the coal gasification slag itself has no self-hardening property and can only exhibit pozzolanic activity under the action of activators.

From the curve fitting results in Figure 3(b), the strength and reaction amount of coal gasification slag systems with different C/GS ratios show an approximate exponential relationship, with a correlation coefficient R^2 of 0.977, indicating that there is a good correlation between the system strength and the chemical reaction amount of coal gasification slag under different CaO content conditions. When the reaction rate of coal gasification slag is less than 10%, the contribution of the pozzolanic reaction of the coal gasification slag-$Ca(OH)_2$-H_2O system to strength is minimal (<5 MPa); when the reaction rate is greater than 10%, the contribution of the pozzolanic reaction to strength increases with the increase in the degree of reaction. This is consistent with the pattern presented in the previous study of the coal gasification slag- $Ca(OH)_2$-H_2O system.

4. Conclusions

(1) In the coal gasification slag-$Ca(OH)_2$-H_2O system, the pozzolanic reactivity of different fineness coal gasification slag under normal temperature all conform to the first-order reaction kinetics model;
(2) The physical modification method of decarbonization, deironing, and increasing effective grinding time has a good promoting effect on the enhancement of pozzolanic reactivity in coal gasification slag;
(3) The strength of the system with different CaO content presents a good exponential relationship with the degree of reaction of coal gasification slag. When the reaction rate of coal gasification slag exceeds about 10%, the strength of the paste increases significantly as the reaction degree increases.

Acknowledgements

This work was supported by the National Key Research and Development Program of China (2019YFC1904302).

References

Blaisi, N.I., Roessler, J.G. and Watts, B.E. (2018) "Construction material properties of high temperature arc gasification slag as a portland cement replacement", *Journal of Cleaner Production*, 196: 1266–1272.

Li, Z., Zhang, Y. and Zhao, H. (2019) "Structure characteristics and composition of hydration products of coal gasification slag mixed cement and lime", *Construction and Building Materials*, 213: 265–274.

Luo, F., Jiang, Y. and Wei, C. (2020) "Potential of decarbonized coal gasification residues as the mineral admixture of cement-based material", *Construction and Building Materials*, 269: 121259.

Mazurkiewicz, M., Tkaczewska, E. and Pomykala, R.(2012) "Preliminary determination of the suitability of slags resulting from coal gasification as a pozzolanic raw material", *Gospodarka Surowcami Mineralnymi-Mineral Resources Management*, 28: 5–14.

Yuan H., Yin H. and Tang Y. (2020) "Fabrication and characterization of a novel foam ceramic material based on coal gasification slags", *Journal of Ceramic Processing Research*, 21: 640–646.

Xin J., Liu L. and Xu L. (2022) "A preliminary study of aeolian sand-cement-modified gasification slag-paste backfill: Fluidity, microstructure, and leaching risks", *Science of The Total Environment*, 830: 154766.

The 16th International Congress on the Chemistry of Cement 2023 (ICCC2023)
"Further Reduction of CO_2 -Emissions and Circularity in the Cement and Concrete Industry"
September 18–22, 2023, Bangkok, Thailand

Low-Cost and Reliable Contact Angle Goniometry for Cementitious Materials

H. Kabir and N. Garg*

Department of Civil and Environmental Engineering, University of Illinois Urbana-Champaign, Urbana, United States

Email: hkabir2@illinois.edu, nishantg@illinois.edu

ABSTRACT

The wettability of cementitious materials is a critical aspect that affects their durability, particularly in resisting moisture and chemical attack. However, conventional goniometers that characterize surface wettability via fitting algorithms are expensive ($35-60k) and do not offer precise estimates of the wetting properties of cementitious materials with hydrophilic surfaces (due to the rapid change in the focal distance of absorbing drops on porous surfaces). Thus, this study aims to develop a low-cost (<$200) and robust setup that utilizes Convolutional Neural Networks (CNN) coupled with an orthogonally aligned camera goniometer to reliably determine the contact angle (CA) of non-spherical drops on heterogeneous cementitious surfaces. The proposed approach was trained on 3375 images and remains stable if subjected to higher optical noises, surpassing existing goniometers, especially after 10 seconds of solid-liquid interaction. Therefore, this study presents an inexpensive and reliable way of characterizing the surface wettability of cementitious materials aiding in predicting their durability and performance.

KEYWORDS: *Wettability, contact angle (CA), convolutional neural networks (CNN), heterogeneous surfaces, durability properties.*

1. Introduction

Wettability refers to a liquid's tendency to adhere to a solid surface, determined by surface energy in a solid-liquid-gas system. Adhesive forces promote drop spreading, while cohesive forces limit it. This property is measured by contact angle (CA), i.e., the angle between the interface of the solid-liquid and liquid-vapor phases. Surfaces with CAs greater than 90° are hydrophobic while those with CAs less than 90° are considered hydrophilic, and this property is widely characterized by the sessile-drop technique (Law (2014)). However, the fitting-based sessile-drop method has limitations in measuring CA, including difficulty in detecting flat drops, identifying drop boundaries with optical noises, and analyzing dynamic CAs (Srinivasan et al. (2011)). This means that a multi-layer neural network-based method is necessary to overcome these limitations, independent of the skills of the user, and less susceptible to camera variations (Kabir & Garg (2023)).

Therefore, this study presents an effective setup coupled with CNN (trained on 3,375 images) for reliable wettability assessment of both hydrophobic and hydrophilic surfaces. In particular, we have developed a simple and low-cost setup (< $200) comprising two USB microscope cameras with front-lit LEDs and a Z-axis manual mechanical stage that can provide two independent views of drops dispensed on heterogeneous surfaces. It should be noted that the use of conventional goniometers, which rely on fitting algorithms, cannot provide precise measurements of the wetting properties of cementitious materials with hydrophilic surfaces. This is due to the rapid focal distance change of absorbing drops on porous cementitious surfaces, especially after 10 seconds of solid-liquid interaction, in which the discrepancy between the CAs predicted by the existing and proposed methods can be ~ 60 degrees. Therefore, our proposed CNN-enabled goniometer offers significantly improved accuracy for the analysis of non-spherical drops dispensed on heterogenous cementitious materials.

2. Methods

2.1 Proposed Orthogonal Camera Goniometry (setup and operation)

Fig. 1c shows our CA measurement setup, which includes a leveled and adjustable XYZ mechanical stage and two orthogonally aligned digital microscope cameras. Each camera has a 10 μm spatial resolution and eight built-in LED light sources. The cameras' adjustable height allows for capturing the drop and its reflection in both directions and characterizing surface wettability on cementitious materials via two independent viewpoints, unlike existing commercial goniometers with only one viewpoint.

2.2 Existing Commercial Goniometer

Ramé-Hart 250-F1 Contact Angle instrument, equipped with a leveled mechanical base and a single external light source, was used to measure surface wettability. The goniometer's camera has a 10 μm spatial resolution and uses commercial DROPiA software, which relies on a contour-based fitting algorithm to detect the boundaries of drops. Moreover, the camera must be manually focused, tuned, and calibrated on the Region of Interest (ROI) for each CA measurement.

2.3 Convolutional Neural Networks (CNN)

The CNN model (shown in Fig. 1b), utilizes PyTorch with ResNet50 architecture to analyze both symmetrical and non-symmetrical drops by leveraging the uniqueness and overall geometry of the binarized images. Hyperparameters are fine-tuned (i.e. learning = 0.001, batch size = 16, and 200 epochs) for optimal performance. The Rectified Linear Unit (ReLU) activation function and dropout regularization rate of 0.2 are also used to facilitate complex pattern learning and reduce over-fitting. Besides, max-pooling layers are applied to decrease feature map dimensions and computational load. Moreover, image augmentations, such as random cropping, rotation, and noise injection, are applied to improve the performance of our model.

2.4 Drop Placement on Solid Surfaces

To estimate CAs via the sessile drop method, the syringe needle was fixed 1.5-2.5 mm away from the solid surface. The capillary length $\lambda = \sqrt{(\gamma/[\rho. g])}$ was considered to eliminate gravity effects, where γ is surface tension, ρ is liquid density and g is gravity. Therefore, at 23°C and 50% RH, the liquid volume should be less than ~10.7 μL. Also, if the volume is less than 3 μL, the kinetic energy dissipation of small-sized liquid results is rapid, which cannot be captured by our low frame rate cameras. Thus, a 5 ± 0.2 μL sessile deionized water drop is gently placed on the vibration-free surface of cement pastes. Besides, to avoid drop evaporation from the solid surface, measurements are limited to 30s from the beginning of solid-liquid interaction. Additionally, each drop is applied to a single virgin and dry surface that is vacuum dried for 72 hours (over silica gel) at room temperature with zero residual water content.

3. Results and Discussion

3.1 Training our Machine Learning (CNN) Model

Reliable and reproducible wettability measurements require proper selection of the illumination source. For naturally illuminated drops, however, the light transition is not sharp enough to outline drop boundaries, see Fig. 1a. Additionally, the use of a back-lit illuminated setup (Fig. 1a) which is commonly used for improved boundary detection, only works to analyze drops in a single direction, hence adding a perpendicular light source imposes false boundaries to the edge of the drops (Kabir & Garg (2023)). Subsequently, for the first time, we implemented front-lit illumination in a dark room (Figs. 1a and 1c) to clearly capture the surface heterogeneity of cementitious systems via two independent viewpoints. In the next step, a fully automated image-based technique is needed to be coupled with proper illumination conditions. For this purpose, we propose a unique procedure using feature extraction (rightmost column of Fig. 1a) and training stages (Fig. 1b) to autonomously measure the CAs of drops on both hydrophobic and hydrophilic surfaces. During feature extraction, front-lit drop images are noise-reduced, binarized, and fed into our CNN model. Binarizing natural images reduces Kolmogorov complexity, helping PyTorch with ResNet50 converge faster with fewer images (Fig. 1d). Moreover, binarizing the natural

images decreases the training time from 67 to 4 minutes (if implemented by NVIDIA Tesla T4 GPU). As a result, more precise, consistent, and speedy estimates are made when our CNN model is trained on binarized images.

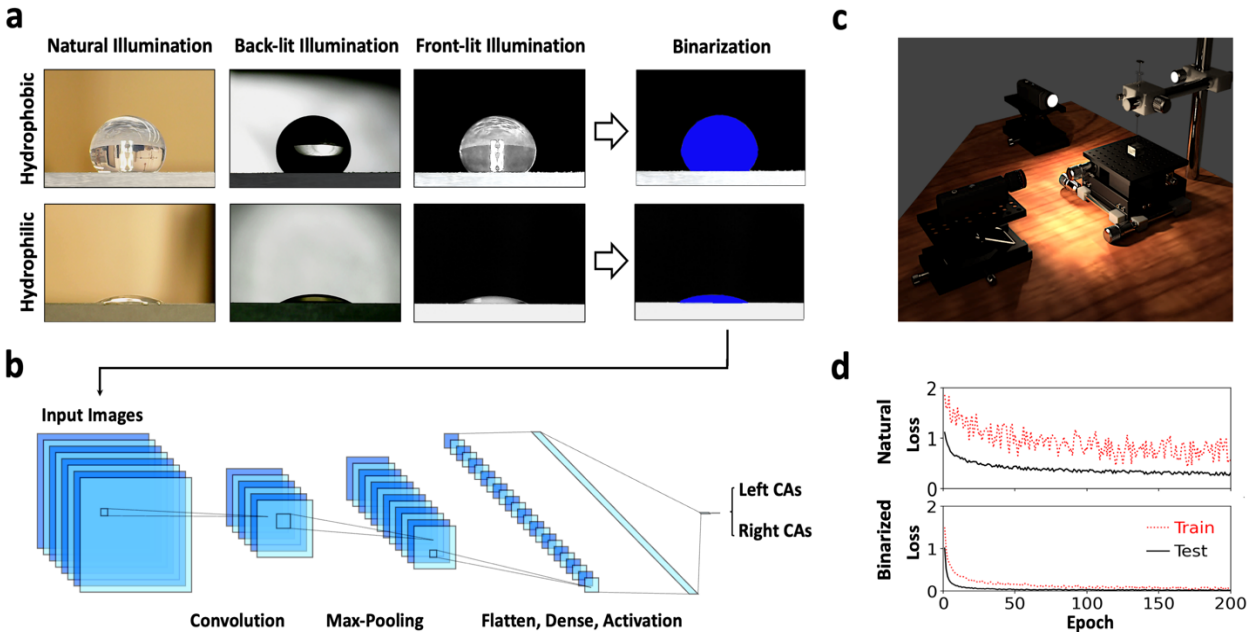

Figure 1. (a) Different ways of illuminating drops dispensed on cementitious materials, and extracting features from the front-lit illuminated drop images prior to being fed into the CNN model, (b) importing the binarized images to train the CNN model for estimating the left and right CAs of each image, (c) 3D schematic of the proposed dual camera goniometry placed in a dark room, and (d) pinpointing the performance of the CNN model trained on natural or binarized drop images.

3.2 Multi-Angle Simultaneous CA Measurements

The proposed goniometer has a key advantage in that it can simultaneously determine the tangent angles of a drop at different angles. Due to the presence of local surface heterogeneity of cement-based systems, the measured contact angles (CAs) along the ternary phase contact line can vary from point to point. As a result, the current setup increases the number of wettability measurements compared to traditional goniometers (with only one camera). In particular, Fig. 2a (top rows) shows the imagery of an absorbing drop on a porous cement paste captured via two separate cameras. In the next step, the natural images are binarized (Fig. 2a, bottom rows) and analyzed by our CNN model. Fig. 2b confirms a discrepancy between the left and right CAs measured by each camera suggesting that the surface heterogeneity of cementitious systems impacts the wettability properties measured at different angles. In the next step, the signal-to-noise ratio (SNR) of the drop, expressed in decibels (dB) is reported in Fig. 2c, which is calculated as SNR = 20 log10 (A_{signal}/A_{noise}), where A refers to the signal's root mean square amplitude. Fig. 2c confirms that the SNR of an absorbing drop (measured based on the first derivative of the grayscale values along the drop boundary) reduces with time because the focal distance of the moving drops (dispensed on porous cementitious systems) changes with time, reducing the acutance of drop images. Finally, Fig. 2d confirms that the stability of the existing fitting algorithm is notably impacted by camera focus, particularly after 10 seconds from the beginning of solid-liquid interaction as the algorithm cannot delineate the unfocused ROI (due to low SNR at the drop boundary). In contrast, the CAs estimated by our proposed CNN algorithm remain reliable proving its superior stability for analyzing optically distorted images.

4. Conclusions

The present study proposes a low-cost and reliable goniometer for measuring the surface wettability of cementitious materials using a combination of two USB cameras, a mechanical stage, and a strong CNN model. The proposed goniometer was trained on 3,375 binary images eliminating the need for manual

adjustment and is capable of fast bulk processing of focused/unfocused drop images. Moreover, it is inexpensive (< $200) and outperformed the existing commercial setup in its ability to analyze drops on porous cementitious substrates. Particularly in scenarios where solid-liquid interaction lasts for more than 10 seconds, the CAs estimated by the proposed goniometers remain reliable. Also, the presence of two cameras (in our proposed setup) facilitated the characterization of surface heterogeneity and boosted the number of wettability measurements for a more reliable analysis. Overall, this study presents powerful insights into characterizing the durability of heterogeneous cementitious surfaces.

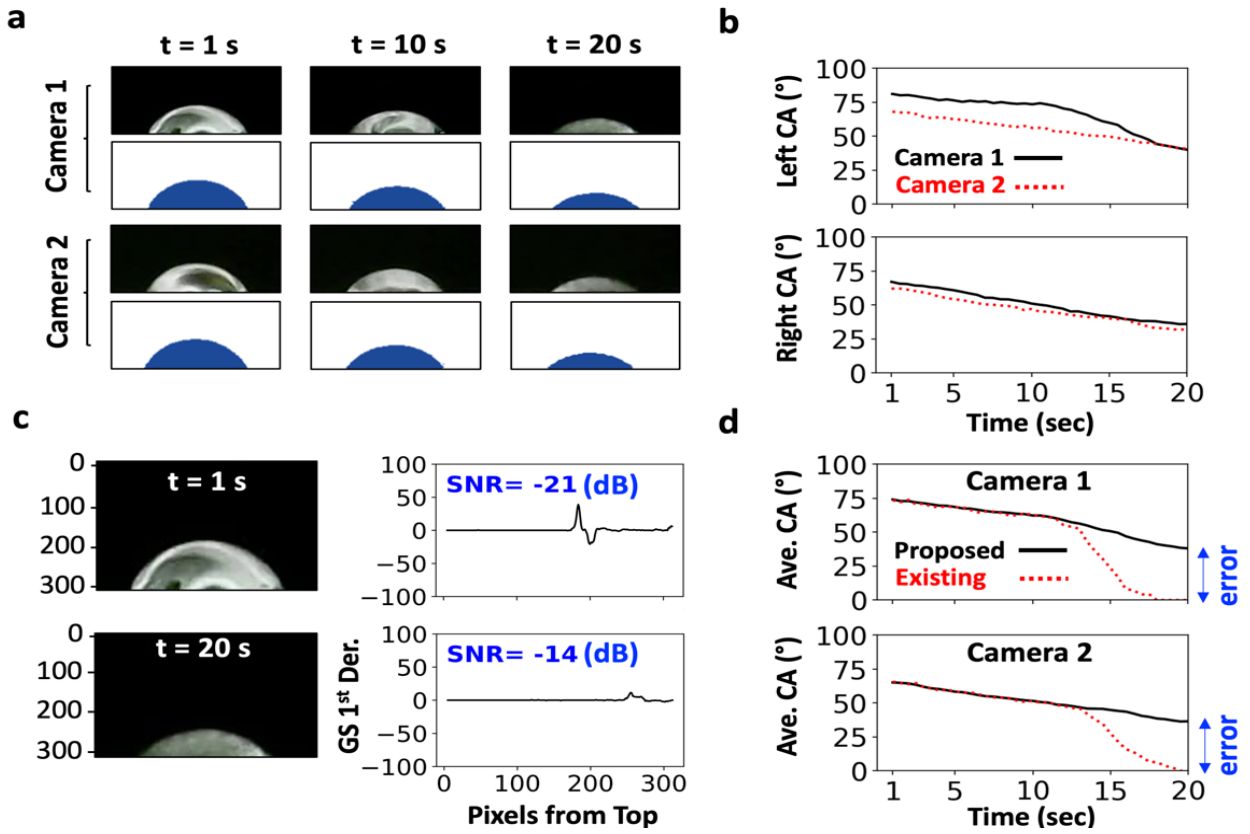

Figure 2. a) Ability of the proposed orthogonal goniometry to characterize surface heterogeneity of cementitious materials from various angles, i.e., via cameras 1 and 2, (b) marking the differences between the left and right CAs of drop captured by cameras 1 and 2, (c) marking the SNR at the drop boundaries at 1 and 20 seconds from the beginning of solid-liquid interaction, and (d) comparing the performance of the proposed over the existing model to analyze an absorbing (moving) drop on the surface of cement pastes. Particularly, this subplot confirms that at 20 seconds, the error (i.e., the difference between the CAs estimated by the proposed and existing goniometers) is around 60 degrees.

Acknowledgments

H. K. acknowledges partial support from the Department of Civil and Environmental Engineering at the University of Illinois Urbana–Champaign.

References

Kabir, H., & Garg, N. (2023). Machine learning enabled orthogonal camera goniometry for accurate and robust contact angle measurements. Scientific Reports, 13(1), 1497.

Law, K. Y. (2014). Definitions for hydrophilicity, hydrophobicity, and superhydrophobicity: getting the basics right. The Journal of Physical Chemistry Letters, 5(4), 686-688.

Srinivasan, S., McKinley, G. H., & Cohen, R. E. (2011). Assessing the accuracy of contact angle measurements for sessile drops on liquid-repellent surfaces. Langmuir, 27(22), 13582-13589.

The 16th International Congress on the Chemistry of Cement 2023 (ICCC2023)
"Further Reduction of CO_2 -Emissions and Circularity in the Cement and Concrete Industry"
September 18–22, 2023, Bangkok, Thailand

C-S-H sorption under temperature and relative humidity changes

F. Masara[1*], T. Honorio[1], and F. Benboudjema[1]

[1] *Université Paris-Saclay, CentraleSupélec, ENS Paris-Saclay, CNRS, LMPS - Laboratoire de Mécanique Paris-Saclay, 91190, Gif-sur-Yvette, France.*
Email: fatima.masara@ens-paris-saclay.fr
[2] *Université Paris-Saclay, CentraleSupélec, ENS Paris-Saclay, CNRS, LMPS - Laboratoire de Mécanique Paris-Saclay, 91190, Gif-sur-Yvette, France.*
Email: tulio.honorio@ens-paris-saclay.fr
[3] *Université Paris-Saclay, CentraleSupélec, ENS Paris-Saclay, CNRS, LMPS - Laboratoire de Mécanique Paris-Saclay, 91190, Gif-sur-Yvette, France.*
Email: farid.benboudjema@ens-paris-saclay.fr

ABSTRACT

Water vapor sorption measurements have positively contributed to the understanding of various phenomena affecting the durability and performance of cement-based materials. The temperature can have a great influence on these measurements. An in-depth research on the effect of temperature on sorption processes in cement-based materials informed by the molecular scale may offer new physical insights into understanding the phenomena. In this work, we aim to study water sorption in C-S-H. Specifically, we focus on the effect of temperature on water desorption in C-S-H at the molecular scale. Effective interactions and desorption isotherms are interpreted. Other features like water cavitation and stability under sorption are also analyzed. All these properties and features are investigated for temperatures between 27 and 150 °C through molecular simulation techniques. The influence of the pore size on the behavior of C-S-H under desorption is investigated. The effect of the temperature on the cohesion in C-S-H is also discussed. Cavitation shows a strong correlation with the temperature and the C-S-H pore size. The cohesion between the C-S-H layers increases with the temperature. These data can serve as valuable inputs for multi-scale models.

KEYWORDS: *C-S-H, Desorption, Temperature, Cavitation, Molecular simulations.*

1. Introduction

Moisture is a key factor in the durability of cement-based materials, as many processes affecting the durability of cement-based materials are moisture dependent (e.g., cracking, drying and autogeneous shrinkage, creep, and fire spalling). Water vapor sorption isotherms describe the variation of the moisture content with the relative humidity (RH). The temperature can have a significant impact on the water sorption behavior of cement-based materials, which can consequently affect the shape of the sorption isotherm (Poyet (2009)). C-S-H (calcium silicate hydrate), is the primary porous element of Portland cement concrete contributing to sorption in the material. The effect of temperature on sorption in C-S-H at the molecular scale is not yet fully addressed, especially in what concerns the interplay between temperature and RH changes.
In this study, we investigate water sorption in C-S-H at different temperatures (27, 100, and 150 °C) and relative humidities (from 100 to 0 %) using molecular simulations. We consider C-S-H pores of sizes between 10 and 26 Å (i.e., in the domain of interlayer pores and small gel pores). We analyse the effective interactions, water desorption isotherms, cavitation, and stability under sorption. We also study cohesion in C-S-H and the effects of temperature and relative humidity on this property. The observables of this study can be used to develop a model of the behavior of cement-based materials at different scales.

2. Models and Methods

2.1. C-S-H atomic details and force field

This study uses the atomistic C-S-H model of Kunhi Mohamed et al. (Kunhi Mohamed et al (2018)), which features an orthogonal structure with two micropores of 13.7 Å interlayer distance each. In this work, one of the micropores has a constant size (13.7 Å interlayer distance), while the other one varies in size between 10 and 26 Å. $Ca_{1.67}SiO_{3.7}$. nH_2O is the molecular formula of C-S-H. The interactions between atoms are elucidated using the ClayFF force field (Cygan et al (2004)) and the SPC/E water model (Berendsen & Grigera (1987)). Further details regarding the model can be found in (Honorio et al (2021), (2022); Masara et al (2023)). Figure 1 shows an atomic representation of one of the C-S-H pore sizes.

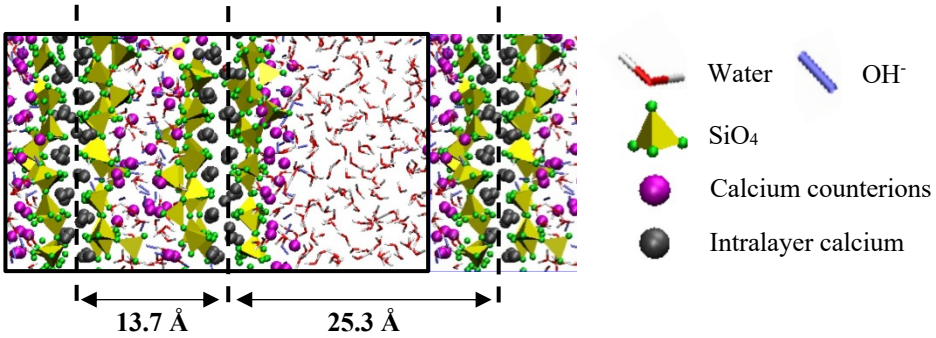

Figure 1: Atomic structure of the 25.3 Å interlayer distance pore at a T =27°C and RH =100 %.

2.2. Simulation steps

In this study, LAMMPS (Plimpton (1995)) is used to conduct hybrid Grand Canonical Monte Carlo (GCMC)-Molecular Dynamics (MD) simulations in two different ensembles: μVT ensemble for water and NVT ensemble for all the remaining particles. The first ensemble implies that the number of water molecules can flucuate (depending on the setted temperature and relative humidity). The second ensemble implies that the number of solid particles, calcium counterions and hydroxides is constant. Interlayer water molecules exchange with an infinite bulk water reservoir of a constant chemical potential μ and temperature T. The chemical potential of the water reservoir, which depends on the temperature and relative humidity, is given as $\mu \approx \mu_0\ (T) + k_B T \ln(\mathrm{RH})$, where μ_0 is the chemical potential when the system is saturated, k_B is the Boltzmann constant and RH is the relative humidity. The relationship between the temperature and vapor pressure (or the temperature and relative humidity) is expressed using the Clausius-Clapeyron equation (Fugel & Weiss (2017)). Periodic boundary conditions are used and the solid layers are immobilized to minimize the simulations time.

2.3. Effective interactions

The thermodynamic potential or the potential of mean force (PMF), describing the effective interactions in C-S-H, is calculated as a function of the interlayer distance using:

$$\Lambda(d) = \Lambda_0(d_0, \mu, T) - S_s \int_{d_0}^{d} P d(d) \tag{1}$$

where S_s is the surface area (constant), P is the confining pressure, and d is the imposed interlayer distance.

3. Results and discussion

3.1. Effective interactions

Figure 1 shows the evolution of the PMF with the interlayer distance from 100 to 0% relative humidity at 27, 100 and 150 °C.

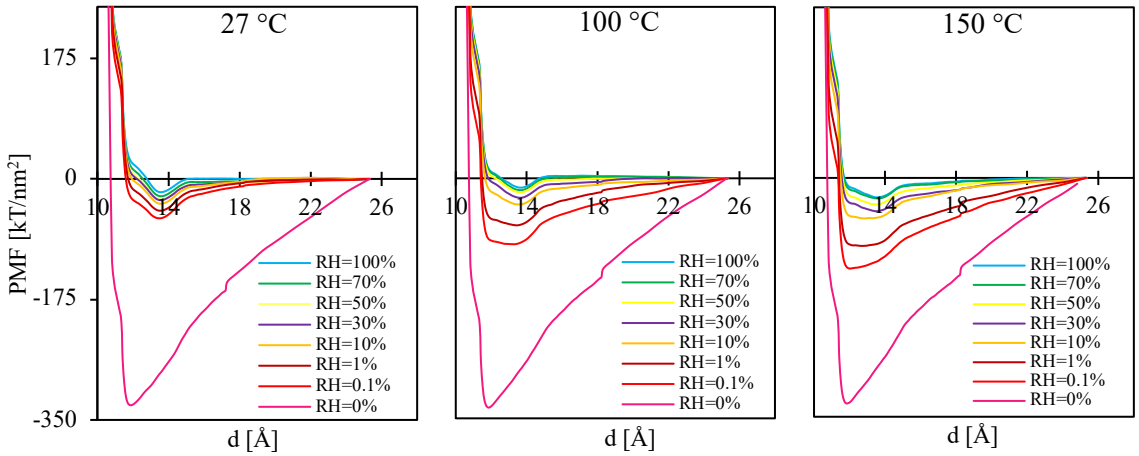

Figure 2: PMF versus the interlayer distance for various RH upon desorption at 27, 100 and 150 °C.

As shown in the figure, the shape of the PMF curve and the depth of the PMF well change with the relative humidity and the temperature. The minimum in the well refers to the most stable interlayer distance or the basal distance. At a given temperature, the basal distance decreases with the decreasing relative humidity. This implies the shrinkage of the pores upon desorption. The deepness of the PMF well increases when the relative humidity decreases with a jump occuring between 0.1 and 0 % relative humidity. The effect of the temperature on the depth of the PMF well is similar to that of relative humidity. At a constant relative humdity (range of relative humidities between 100 and 0.1%), the depth of the PMF well increases with the increasing temperature. For 0% relative humidity, the PMF well is independent of the temperature since water is totally desorbed at all the temperatures and the solid layers remain stable even when heated (the alteration of the solid layers upon heating is not simulated). The mobility of calcium counterions and hydroxides does not affect the PMF at this RH, which is an indication of the stability of microportlandinte clusters with temperature increase. The observed increase in the PMF well depth with the increasing temperature or decreasing relative humidity indicates a greater level of cohesion in C-S-H.

3.2. Desorption isotherms

Figure 1 shows the desorption isotherms of C-S-H interlayer distances between 25.3 and 13.7 Å at 27, 100 and 150 °C.

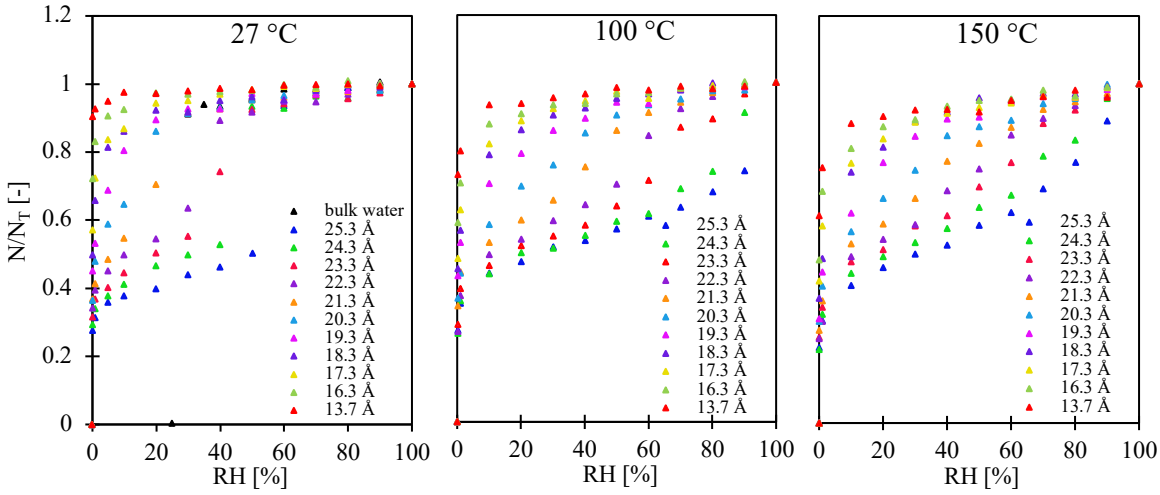

Figure 3: The water content evolution during desorption in C-S-H interlayer distances between 13.7 and 25.3 Å at 27, 100 and 150 °C.

In all the examined pore sizes, the desorption isotherms demonstrate a noticeable dependency on the temperature. At 27 °C, the desorption isotherms for the interlayer distances ≥ 20.3 Å exhibit a discontinuous pattern, where the sudden decay in the water content reflects cavitation. With an increase in the temperature to 100 °C, the cavitation relative humidity increases. As the temperature increases more (case of 150°C), the desorption isotherms display decreased discontinuity. For interlayer distances < 20.3 Å, the desorption isotherms show a continuous behavior at the three temperature values. The effect of temperature on the desorption behavior in these pore sizes can be seen as an increased water desorption (or decreased water content) at higher temperatures. The sensitivity of desorption isotherm to the temperature was also found in the work of Maruyama et al. (Maruyama et al (2018)). The authors of this work observed an increase in the cavitation relative humidity with the temperature for all the materials they tested (including concrete). The desorption isotherms in this work show as well a sensitivity to the pore size. This appears as a decrease in the cavitation relative humidity with the decrease in the pore size. The study of Rasmussen et al. (Rasmussen et al (2010)) on another microporous material reported a similar relationship.

4. Conclusion

This study aims to understand the combined effect of the temperature and relative humidity on sorption in C-S-H interlayer micropores with the help of molecular simulations. The effective interactions show an elevated cohesion upon water desorption, either due to the increased temperature or decreased relative humidity. This implies an increase in the strength of concrete due to the higher cohesion in C-S-H upon heating. The desorption isotherms show a large dependence on the temperature and the pore size. Cavitation appears in small mesopores (≥ 20.3 Å) and disappears in smaller pore sizes. For pores ≥ 20.3 Å, the cavitation RH increases with the temperature. The observations of this study gives important physical insights into predicting the drying shrinkage and creep of cement-based materials through the understanding of the molecular processes at the level of C-S-H leading to these phenomena.

Acknowledgment

The funding of the French National Research Agency (ANR) via the project THEDESCO (ANR-19-CE22-0004-01) is highly appreciated.

References

Berendsen, H. J. C., & Grigera, J. R. (n.d.) (1987). The Missing Term in Effective Pair Potentialst. *Journal of Physical Chemistry, 91*, 24.

Cygan, R. T., Liang, J.-J., & Kalinichev, A. G. (2004). Molecular Models of Hydroxide, Oxyhydroxide, and Clay Phases and the Development of a General Force Field. *The Journal of Physical Chemistry B*, *108*(4), 1255–1266.

Fugel, M., & Weiss, V. C. (2017). A corresponding-states analysis of the liquid-vapor equilibrium properties of common water models. *The Journal of Chemical Physics*, *146*(6), 064505.

Honorio, T., Masara, F., & Benboudjema, F. (2021). Heat capacity, isothermal compressibility, isosteric heat of adsorption and thermal expansion of water confined in C-S-H. *Cement*, *6*, 100015.

Honorio, T., Masara, F., Poyet, S., & Benboudjema, F. (2022). Surface Water in C-S-H: Effect of the Temperature on (De)Sorption. *SSRN Electronic Journal*.

Kunhi Mohamed, A., Parker, S. C., Bowen, P., & Galmarini, S. (2018). An atomistic building block description of C-S-H - Towards a realistic C-S-H model. *Cement and Concrete Research*, *107*, 221–235.

Maruyama, I., Rymeš, J., Vandamme, M., & Coasne, B. (2018). Cavitation of water in hardened cement paste under short-term desorption measurements. *Materials and Structures*, *51*(6), 159.

Masara, F., Honorio, T., & Benboudjema, F. (2023). Sorption in C-S-H at the molecular level: Disjoining pressures, effective interactions, hysteresis, and cavitation. *Cement and Concrete Research*, *164*, 107047.

Plimpton, S. (1995). Fast Parallel Algorithms for Short-Range Molecular Dynamics. *Journal of Computational Physics*, *117*(1), 1–19.

Poyet, S. (2009). Experimental investigation of the effect of temperature on the first desorption isotherm of concrete. *Cement and Concrete Research*, *39*(11), 1052–1059.

Rasmussen, C. J., Vishnyakov, A., Thommes, M., Smarsly, B. M., Kleitz, F., & Neimark, A. V. (2010). Cavitation in Metastable Liquid Nitrogen Confined to Nanoscale Pores. *Langmuir*, *26*(12), 10147–10157.

The 16th International Congress on the Chemistry of Cement 2023 (ICCC2023)
"Further Reduction of CO_2 -Emissions and Circularity in the Cement and Concrete Industry"
September 18–22, 2023, Bangkok, Thailand

Behavior of water in C-S-H

T. Honorio[1*], F. Masara[2], and F. Benboudjema[3]

[1]*Université Paris-Saclay, CentraleSupélec, ENS Paris-Saclay, CNRS, LMPS - Laboratoire de Mécanique Paris-Saclay, 91190, Gif-sur-Yvette, France.*
Email: tulio.honorio-de-faria@ens-paris-saclay.fr
[2]*Université Paris-Saclay, CentraleSupélec, ENS Paris-Saclay, CNRS, LMPS - Laboratoire de Mécanique Paris-Saclay, 91190, Gif-sur-Yvette, France.*
Email:fatima.masara@ens-paris-saclay.fr
[3]*Université Paris-Saclay, CentraleSupélec, ENS Paris-Saclay, CNRS, LMPS - Laboratoire de Mécanique Paris-Saclay, 91190, Gif-sur-Yvette, France.*
Email: farid.benboudjema@ens-paris-saclay.fr

ABSTRACT

The behavior of confined and surface water in hydrophilic systems is known to differ from bulk behavior. C-S-H is a hydrophilic micro/meso-porous phase with a large surface area. Understanding how water behaves in C-S-H is crucial to elucidate phenomena associated with water sorption and dynamics, which includes mass transport properties and durability, sorption-induced volume changes, thermal properties, and viscoelastic response. Molecular simulations are a powerful tool to quantify water behavior on the atomic level. In this work, these simulations are deployed to quantify the changes in the main physical properties – namely, density, self-diffusion, viscosity, bulk modulus, thermal expansion, heat capacity, and heat of adsorption – of liquid water confined in C-S-H as a function of the pore size under osmotic equilibrium. Then, we focus on surface water and how the properties of water change as a function of the distance from the C-S-H surface. For (slit) pores smaller than about 3-5 nm, the properties of water exhibit a transition from liquid-like to a more solid-like behavior. Surface water behavior differs from bulk behavior up to the fourth adsorbed layer. The results provided are critical inputs for multiscale modeling concerning the properties of confined and bound water. Also, they provide new physical insights to revisit sorption models and understand drying processes.

KEYWORDS: *Confined water, Surface water, Adsorption, Molecular simulations, Properties.*

1. Introduction

The interactions of water with pore surfaces are a crucial factor in determining how water will behave. In hydrophilic phases such as C-S-H, the water adsorbed onto the surface is less mobile, is more compact, and exhibits different energetics from bulk water (Abdolhosseini Qomi et al. (2021), Honorio et al. (2023)). When the pore is small enough so that the effects of two opposing surface walls superpose, the behavior of the adsorbed fluid deviates even further from its bulk form (Abdolhosseini Qomi et al. (2021)). In C-S-H, interlayer water is precisely in this strongly confined situation. Understanding how water behaves in C-S-H is crucial to elucidate the mechanisms associated with water sorption and dynamics, which includes mass transport properties and durability, sorption-induced volume changes, electromagnetic response (for non-destructive evaluation), thermal properties, and viscoelastic response.
Here, molecular simulations are deployed to quantify the changes in the main physical properties – namely, density, self-diffusion, permeability, viscosity, bulk modulus, thermal expansion, heat capacity, and heat of adsorption – of liquid water confined in C-S-H as a function of the pore size under osmotic equilibrium. Molecular simulation is the well-suited technique for this task because it allows computing properties under well-controlled thermodynamic conditions in the relevant scale (often difficult to assess

experimentally properly). Then, we focus on surface water and how the properties of water change as a function of the distance from the C-S-H surface.

2. Molecular Models and Methods

Molecular simulations are performed using the C-S-H atomic structure proposed by Kunhi Mohamed et al. (2018) with structural formula $1.67CaO.SiO_2.nH_2O$. ClayFF (Cygan et al. (2021)) is adopted as a force field. Extensive validation of the structural features of the atomistic model in comparison with experimental data is provided by Honorio et al. (2021). Various pore sizes are constructed by increasing the interlayer distance for one of the pores present in this C-S-H model. Grand canonical Monte Carlo simulations are performed to get the equilibrium water content for each pore size under ambient conditions (temperature of 300 K and 100% RH (Honorio et al. (2021)). Simulations for surface water are performed for a single pore size that is big enough so that superposing effects of the opposing pore surfaces are negligible and a significant portion of the pore behaves like bulk water (see details in Honorio et al. (2023)). Properties are computed using the appropriate fluctuation formula as detailed in each study.

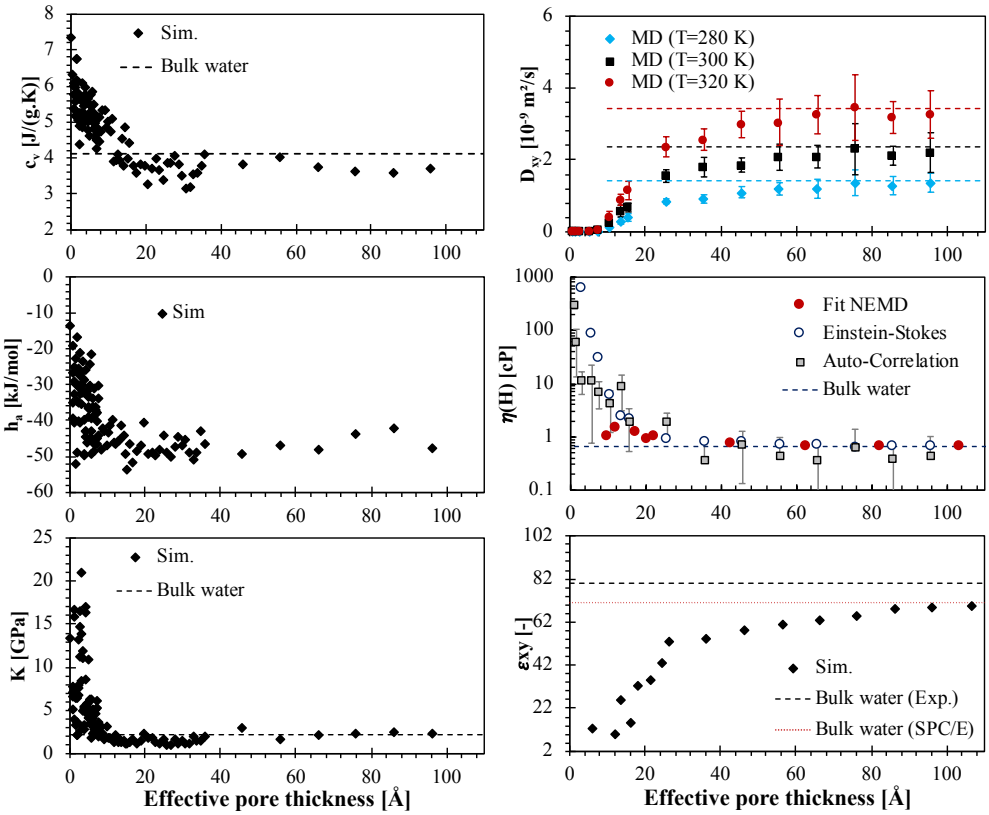

Figure 1: Properties of water confined in C-S-H as a function of the effective pore size (as defined in Honorio (2022)): isochoric heat capacity c_v, molar incremental enthalpy of adsorption h_a, bulk modulus K, self-diffusion D_{yx} (parallel to the pore plane), shear viscosity η, and dielectric constant ε.

3. Results and Discussion

Figure 1 shows the evolution of various properties as a function of the interlayer distance in C-S-H under ambient conditions. The isochoric heat capacity c_v, molar incremental enthalpy of adsorption h_a, and bulk modulus K of water increase with the confinement. Regarding transport properties, self-diffusion increases with confinement with a change in the dynamical regime for interlayer pores below 3 nm thick (Honorio et al. (2022)). The shear viscosity of water strongly increases with confinement, which is in agreement with experimental observations on various nanoporous systems (Honorio (2022)). For pores above 5-7 nm thick, water retrieves its bulk behavior overall. This means that larger portions of water have a bulk-like behavior, so that the contribution of surface water to the total behavior is less

pronounced. Properties like self-diffusion and dielectric permittivity are markedly anisotropic: the response perpendicular to the pore plan is strongly reduced in the case of self-diffusion (Honorio et al. (2022)) and vanishes in the case of dielectric permittivity (Ait Hamadouche et al. (2023)). Figure 2 shows how the isochoric heat capacity c_v, molar incremental enthalpy of adsorption h_a, and bulk modulus K of surface water vary as a function of the layer position. Two poromechanical conditions are considered: liquid water-saturated (RH = 100%) and constant partial fluid pressure (P_r = 1 atm). The first layer is closer to the C-S-H surface. Each layer is 2.4 Å thick based on the analysis of water oxygen profiles, as detailed in Honorio et al. (2023a). Layers 1-3 are within the interphase defined by the C-S-H rough surface and microportlandite clusters adsorbed. The heat capacity peaks are close to the phase boundary between surface water and bulk water. The analysis of enthalpy of adsorption confirms the high hydrophilicity of the surface, with the position closer to the surface being energetically more favorable than the bulk portion of the pore (layer 5 and above). The bulk modulus of the first layers is significantly larger, corroborating the picture in which surface water exhibits a more rigid, solid-like behavior.

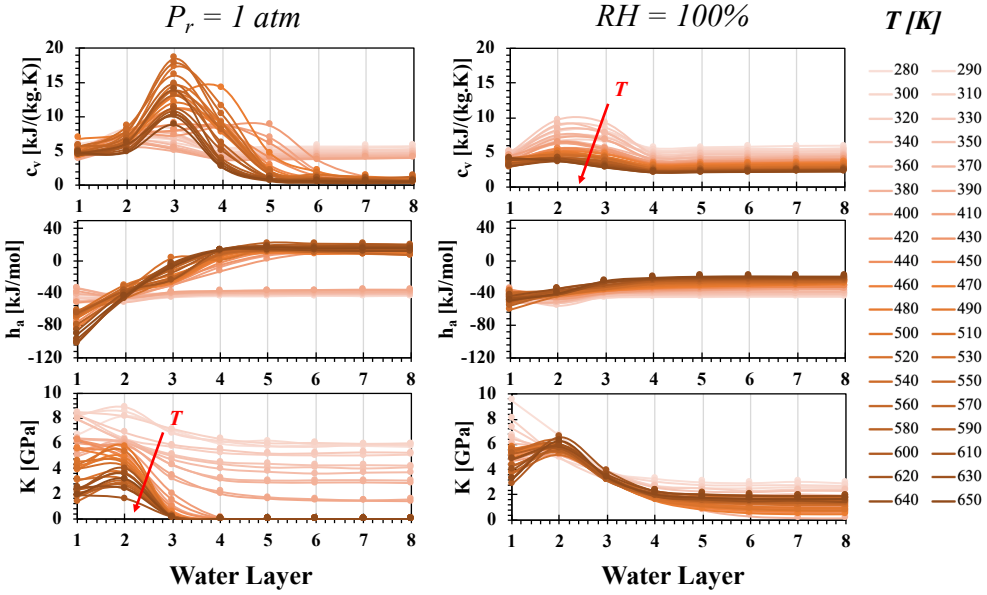

Figure 2: Properties of surface water per layer (layer 1 being closer to the surface; layers 5 and above being in the bulk zone of the pore): isochoric heat capacity c_v, enthalpy of adsorption h_a, and bulk modulus K.

The results above enable revisiting the classes of pore water required to fully explain the pore water behavior in cement-based materials. Only three classes of pore water are needed:

1. **Interlayer water**: it is the water confined in pores smaller than 3-4 nm. Due to the cohesion forces, the most prevalent interlayer distance is associated with the basal distance (the most stable one). Pores smaller than the ones associated with the basal distance are energetically unfavorable due to steric repulsion. The analysis of disjoining pressure profiles shows that mechanical instabilities may arise for some pore size immediately above (in the range of interlayer distance of 1.5 to 1.6 nm) the basal distance, which means that the distribution of interlayer pore size should be very narrow. Interlayer water can be seen as *pore* water since it diffuses, and (ii) the interlayer water molecules can exchange with neighboring pores reversibly under hydro-thermal variations (i.e. water can be dried out or readsorbed in the interlayer under the right RH and temperature conditions). The collapse of the interlayer space only occurs at extremely low RH (< 1%), which is not relevant for most of the applications. Property change under confinement is accompanied by changes in water molecules arrangements and H-bond network structure (Honorio et al. (2021)).
2. **Surface (or interfacial) water**: it is the water adsorbed onto the C-S-H surface in pores with interlayer distance above about 5-7 nm, so that the effects of opposing C-S-H do not superpose. Most of surface water is located within the interphase containing C-S-H surface roughness, calcium counterions and hydroxides adsorbed on the surface. The total thickness of this interphase is about 7.5 Å according to density profiles (of water, silica, and adsorbed ions) (Honorio et al. (2023a)) and also according to the slip length determined from the analysis of hydrodynamics in C-S-H channels (Honorio (2022)). The first 3 to 4 water layers (defined according to the density profiles of water oxygen) adsorbed on the C-S-H surface have a distinct behavior from bulk water and should be

considered as surface water. Each water layer is 2.4 Å thick up to temperatures exceeding around 300°C (Honorio et al. (2023a)).

3. **Bulk water**: water in the central portion of pores larger than 5-7 nm shows already bulk-like behavior. Properties strongly affected by anisotropic effects, such as diffusion, permeability and dielectric permittivity, also show bulk-like behavior in the direction parallel to the pore surface. For these properties, the behavior in the direction perpendicular to the pore surface is roughly suppressed (Honorio et al (2022), Ait Hamadouche et al. (2023), Honorio et al. (2023a)).

With this classification, gel and capillary pores are a mix of both surface and bulk water, with the latter dominating in the case of large gel and capillary pores.

3. Conclusions

The behavior of confined and surface water was quantified using molecular simulations, which is a well-suited technique enabling to assess the nanoscale under controlled conditions. Both surface and interlayer water exhibit reduced dynamics with an intermediary behavior between liquid and solid. The physical phenomena at the origins of the changes in the behavior of interlayer and surface water are water molecules arrangements, H-bond network structure, and changes in the system's local energetics. Only three distinct classes of water are needed to explain pore water in C-S-H: (i) interlayer water (pores smaller than 3-4 nm), (ii) surface water (water adsorbed onto C-S-H surface up to 1 nm distance from the surface in pores with interlayer distance above about 5-7 nm), and (iii) bulk water (water in the central portion of pores larger than 5-7 nm). These results are helpful inputs for multiscale modeling concerning confined and surface water properties. Also, they provide new physical insights to revisit sorption models and understand drying processes.

Acknowledgements

The financial support of the French National Research Agency (ANR) through the project THEDESCO (ANR-19-CE22-0004-01) is gratefully acknowledged.

References

Abdolhosseini Qomi, M.J., Brochard, L., Honorio, T., Maruyama, I., Vandamme, M., (2021). "Advances in atomistic modeling and understanding of drying shrinkage in cementitious materials". *Cement and Concrete Research,* 148: 106536.

Ait Hamadouche, S., Honorio, T., Bore, T., Benboudjema, F., Daout, F., Vourc'h, E. (2023) "Dielectric permittivity of C-S-H". Preprint at *SSRN*: https://doi.org/10.2139/ssrn.4310512

Cygan, R.T., Greathouse, J.A., Kalinichev, A.G., (2021) "Advances in Clayff Molecular Simulation of Layered and Nanoporous Materials and Their Aqueous Interfaces". *Journal of Physical Chemistry C*, 125: 17573–17589.

Honorio, T., Masara, F., Benboudjema, F., (2021) "Heat capacity, isothermal compressibility, isosteric heat of adsorption and thermal expansion of water confined in C-S-H". *Cement*, 6: 100015.

Honorio, T., Carasek, H., Cascudo, O., (2022) "Water self-diffusion in C-S-H: Effect of confinement and temperature studied by molecular dynamics". *Cement and Concrete Research,* 155: 106775.

Honorio, T. (2022) "Permeability of C-S-H". *SSRN*. https://doi.org/10.2139/ssrn.4132286

Honorio, T., Masara, F., Poyet, S., Benboudjema, F., (2023) "Surface water in C-S-H: effect of the temperature on (de)sorption". Preprint available at https://doi.org/10.13140/RG.2.2.15399.83369

Kunhi Mohamed, A., Parker, S.C., Bowen, P., Galmarini, S., 2018. "An atomistic building block description of C-S-H - Towards a realistic C-S-H model". *Cement and Concrete Research,* 107: 221–235.

Masara, F., Honorio, T., Benboudjema, F., (2023) "Sorption in C-S-H at the molecular level: Disjoining pressures, effective interactions, hysteresis, and cavitation". *Cement and Concrete Research,* 164: 107047.

Youssef, M., Pellenq, R.J.-M., Yildiz, B., (2011) "Glassy Nature of Water in an Ultraconfining Disordered Material: The Case of Calcium−Silicate−Hydrate". *Journal of the American Chemical Society*, 133: 2499–2510.

The 16th International Congress on the Chemistry of Cement 2023 (ICCC2023)
"Further Reduction of CO_2 -Emissions and Circularity in the Cement and Concrete Industry"
September 18–22, 2023, Bangkok, Thailand

Determination of amorphous silica and alumina fractions in metakaolin using X-ray diffraction and PONKCS method.

C. Rosero-Chicaiza[1*], D. Londono-Zuluaga[2,3], and J.I. Tobon[1]
[1] *Universidad Nacional de Colombia, Medellin, Colombia*
Email: dcroseroc@unal.edu.co; jitobon@unal.edu.co
[2] *Laboratory of Construction Materials (LMC), EPFL, Lausanne, Switzerland*
[3] *Research and Quality Center, Cementir Holding, Aalborg, Denmark*
Email: diana.londono@cementirholding.it

ABSTRACT

The main method to determine the reactive metakaolin fraction of a calcined kaolinitic clay depends on a thermogravimetric analysis. This approach is considered a reliable method. But, when this method is applied to low-grade clays, it assumes the dehydroxylated minerals are activated in the same way that kaolinite and this is not necessarily true. An alternative method has used an X-ray diffraction technic named Partial or Not Known Crystal Structure (PONKCS). This method relates the reactivity with the amorphous fractions. However, this method has been underestimated especially when there are small fractions of metakaolin. Nevertheless, maybe PONKCS is not inaccurate by itself under those conditions, perhaps its inaccuracy falls into the basic assumption that any reactive fraction, which in this method means the amorphous fraction, looks like a miniature version of the metakaolin amorphous but this must not be necessarily true, especially in low-grade clays where the ratio between amorphous silica and alumina could be different. For that reason, this work proposes a first approach to use the PONKCS method, using two amorphous fractions instead of one, trying to solve the problem of the ratio between amorphous phases. The two reactive fractions used as reference are silica fume and amorphous alumina synthesized from L-lactate of aluminum. Since what is reacting in the calcined clays are silica and alumina.

The proposed method showed to be an adequate alternative to determine different proportions of amorphous phases alumina and silica inside of metakaolin and artificial mixtures.

KEYWORDS: *PONKCS, XRD, metakaolin, dehydroxylation, amorphous phases.*

1 Introduction

Calcined kaolinitic clays as a metakaolin source have been proposed to reduce emissions of CO_2 in the cement industry, but pure kaolinitic clays are scarce and expensive. Therefore, the industry starts to use clays with a lower kaolinite content [1][2][3][4][5]. However, determining how much material is reactive in these cases is not so simple [6]. On the other hand, it has been shown that clays with a low kaolinite content can also be reactive and even increase the compressive strength of cement that uses them [7]. This may be because other clays when calcined also undergo changes or dehydroxylations that can activate the clays, however, the proportions between activated silica and alumina are not necessarily the same as those of a pure metakaolin, what is common to all these clays is that the amorphous fraction in XRD is proportional to the reactive material [1][8][9].

On the other hand, Snellings et al. [9], show that it is possible to accurately quantify how much amorphous supplementary cementing material there is, in mixtures of C-S-H with Fly ash or slag. This application indicates that not all amorphous are the same, so there must be a set of characteristics that make one amorphous material different from another and can be quantified. In this sense, Garg et al. show for different calcined clays [10][11][12], that the reactive fractions of silica present mainly are Q3 chemical environments, while alumina is usually in Al(V) coordination. So, these characteristics could be used to differentiate different types of amorphous.

Another application of the PONKCS method is shown by Avet, and et al. [13][14], they try to determine reactive fractions of different clays. For this, they build an *hkl* phase by the PONKCS method that represents the amorphous fraction of the purest kaolinite clay sample available. This work concludes that the method

is not very precise, mainly due to variability with samples that have very small metakaolin fractions. However, perhaps the assumption that a single *hkl* phase can represent any amorphous and reactive phase might not be the most appropriate. Because, there is no reason to think that the ratio between silica and alumina does not vary in the different clays, and since the method only varies the scale factor of the reference amorphous phases, clays with amorphous fractions whose proportion is different from pure metakaolin, would not be counted accurately.

For this reason, it is important to develop an approximation where the reference amorphous is not a single *hkl* phase of a pure metakaolin, but that the reference amorphous for any clay are amorphous silica and alumina. Therefore, the objective of this work is to determine the amorphous fractions of silica and alumina in metakaolin by the PONKCS method. This is the first step in determining reactive fractions in different clays.

2 Materials and Methods

In the PONKCS method, it is emphasized the need to have pure amorphous phases to apply the method [9][15]. For example, Snellings et al. used fly ash, blast furnace slag, or C-S-H as pure *hkl* phases to quantify their blends [9]. In the case of metakaolin, the silica and alumina phases are present in the remaining phyllosilicate structures of the kaolinite, after dehydroxylation. For this reason, it is difficult to obtain pure phases of silica and alumina from metakaolin, since no physical or chemical method guarantees that the structures responsible for the reactivity remain intact. For this reason, the use of phases that emulate the characteristics of silica and alumina in metakaolin is proposed. To achieve this, it is assumed that what is perceived as amorphous of structural origin in X-ray diffraction is caused by the presence of different chemical environments and coordination. For example, if it has a sample with silica in a Q4 chemical environment, the corresponding XRD scan shows characteristic quartz peaks, or if there is Al(VI) coordinated alumina, the corresponding XRD scan of that sample is the α-alumina peaks. In this way, since it has been shown that metakaolin silica is a mixture of Q2, Q3, and Q4 environments where the dominant environment is Q3 [12], Silica fume was chosen to be the reference amorphous silica, which has been reported to have this same configuration [16]. While the alumina coordinations in metakaolin have been reported to be a mixture of Al(IV), Al(V) y Al(VI) [12], for which amorphous alumina was synthesized, which has the same configuration of coordinations [17], this from aluminum L-lactate (98% Sigma Aldrich ref. 430633) by a sol-gel method at a pH of 7 controlled with ammonia and nitric acid and calcined at 600 ^{o}C. Finally, for the metakaolin, natural Kaolinite (Sigma-Aldrich ref. 03584) was used, calcined at 800 ^{o}C for 2h.

On the other hand, this kaolinite was evaluated by thermogravimetric analysis to determine the metakaolin content [14][13], and it was determined that the dehydroxylated water in the process was 10.83% of the sample, and therefore it has a 74.87% of metakaolin. From the stoichiometry of the dehydroxylation of kaolinite to metakaolin, it was determined that there were 40.5% SiO_2 and 34.37% Al_2O_3 reactants in the metakaolin. While it was determined that all the samples were through 325 mesh.

XRD scans were collected using a CuKα radiation PANalytical X'Pert Pro diffractometer in a flat-plate Bragg–Brentano θ–2θ geometry. The tension and current were set at 45 kV and 40 mA, respectively. Programmable divergence and anti-scatter slits were used in automatic mode at 10 mm to reduce the background scattering from the metal holder. Scans were collected in the 5–70 2θ range with a step size of 0.017 2θ and a step time of 59.69 s per step. Also, samples were rotated at 7 r min $^{-1}$.

The PONKCS method was applied as proposed by Stetsko et al. [15]. To create the *hkl* phases of the reference amorphous, cubic crystal systems were selected in all cases to reduce the number of parameters that must be fitted by the PONKCS method. For the reference amorphous phases of silica, alumina, and the mixture 50% silica and 50% alumina, space groups 225, 227, and 230 were selected respectively.

Results and Analysis

The results of the proposed method are presented in table 1. Each row represents a quantification and its respective error, made by the PONKCS method. However, all the samples include 20% by mass of rutile as an internal standard, so the composition blends will be discussed without including the rutile and the fractions will be normalized to 100%. On the other hand, rows 1 and 2 summarize the settings obtained for

the hkl phases of amorphous silica fume and alumina, which are used as a reference and are called Si_hkl and Al_hkl. In addition, rows 3 to 6 show the results of the phase quantification, using the hkl phases from rows 1 and 2. While rows 3, 4, and 5 are samples where it was weighed 20, 50, and 80% fumed silica, and the complementary fraction of each percentage is amorphous alumina. Furthermore, row 6 corresponds to a calcined kaolinitic clay at 800 ºC. Finally, rows 8 and 9 correspond to the same diffractograms of rows 4 and 5, but in this case, they are no longer evaluated using the hkl phases of fumed silica and amorphous alumina but are evaluated with a single hkl phase built from the diffractogram of the 50/50 mixture.

Table 1. Results of the quantification of the samples by PONKCS.

Row	Sample	Used Phases	$W_{si,norm}$	$W_{si,Teo}$	%error	$W_{al,norm}$	$W_{al,Teo}$	%error	W_{rutilo}	$W_{amor,norm}$
1	Si_Ref	Si_hkl	100,00	100,00	0,00	0,00	0,00	-	20,00	0,00
2	Al_Ref	Al_hkl	0,00	0,00	-	100,00	100,00	0,00	20,00	0,00
3	50/50 Si_Ref/Al_ref	Si_hkl + Al_hkl	49,63	50,00	0,75	50,38	50,00	-0,75	20,00	0,00
4	80/20 Si_Ref/Al_ref	Si_hkl + Al_hkl	76,50	80,00	4,38	19,13	20,00	4,38	20,00	4,25
5	20/80 Si_Ref/Al_ref	Si_hkl + Al_hkl	20,00	20,00	0,00	79,13	80,00	1,09	20,00	0,75
6	Mk800	Si_hkl + Al_hkl	39,50	40,50	2,47	31,75	34,37	7,62	20,00	11,60
7	50/50 Si_Ref/Al_ref	50Si/50Al_hkl	50,00	50,00	0,00	50,00	50,00	0,00	20,00	0,00
8	80/20 Si_Ref/Al_ref	50Si/50Al_hkl	27,88	20,00	-39,38	27,88	80,00	65,16	20,00	44,25
9	20/80 Si_Ref/Al_ref	50Si/50Al_hkl	50,00	80,00	37,50	50,00	20,00	-150,00	20,00	0,00

In the results of the pure phases of rows 1, 2, and 7, the errors are equal to zero, since they were the hkl phases that were expected to be built to be used as reference. On the other hand, when the hkl phases of the silica fume and alumina are used for rows 3, 4, and 5, the trends of all the amorphous mixtures fit quite well to the theoretical values, while the errors oscillate between 0.75% and 4.38%. This indicates that the pure amorphous chosen to be used as reference presents amorphous humps on XRD, different enough to quantify blends in the range between 20 to 80% with minimal error.

To evaluate the calcined clay sample at 800 ºC, an amorphous fraction of 11.6 % was initially determined by XRD and internal standard. While the non-kaolinitic crystalline phases of the uncalcined material were identified, they are quartz ICSD code 201362, orthoclase ICSD 30650, muscovite ICSD 68548, and rutile 51935. So, for the sample calcined at 800 ºC, initially, the scale factors of the selected crystalline phases are adjusted, using a background that does not take into account the amorphous fraction of the sample. Once the scale factors were determined, they were all fixed and the background included the contribution of the amorphous. The criteria for selecting the background was to select the background that allows obtaining 20% rutile. With this, 11.6% amorphous was found and the normalized crystalline fractions were Quartz with 5.8% Orthoclase 7%, muscovite 4.25%, and rutile 20% without normalizing. However, the normalized fractions of reference silica and alumina in calcined kaolinite at 800 ºC were 39.5 and 34.37%, which are very similar values to those determined from the thermogravimetric analysis.

Therefore, given the similarity of the results obtained by the PONKCS method concerning the theoretical values, it can be considered that the use of reference amorphous phases, such as silica fume and amorphous alumina synthesized from aluminum L-Lactate, is suitable for the determination of reactive fractions of silica and alumina in metakaolin. To better understand the quantification of the amorphous phases of silica and alumina using the PONKCS method, figure 1 indicates the results of the quantification of calcined kaolinite at 800 ºC, in this case, 20% rutile is included for understanding. the ratio between phases. In this figure, it is relevant to note the Si_hkl phase is in green, while the Al_hkl phase is in gray.

Another point to highlight is that until now the PONKCS method had been dependent on the use of pure phases of the mixture to be analyzed. [9] [13][14] [15]. However, given the difficulty of separating the silica and alumina phases from metakaolin without affecting its structure, phases that have chemical environments and coordinations similar to those found in metakaolin were chosen. This seems to be enough to obtain amorphous phases in XRD that emulate the behavior of the reactive phases of metakaolin.

On the other hand, the last two rows were evaluated from a single hkl phase, called 50Si/50Al_hkl, in this case, the calculation of the fractions of silica and amorphous alumina is done by dividing by two the fraction

obtained after completing the refinement since it is assumed that this phase is composed of a 50/50 mixture of these phases.

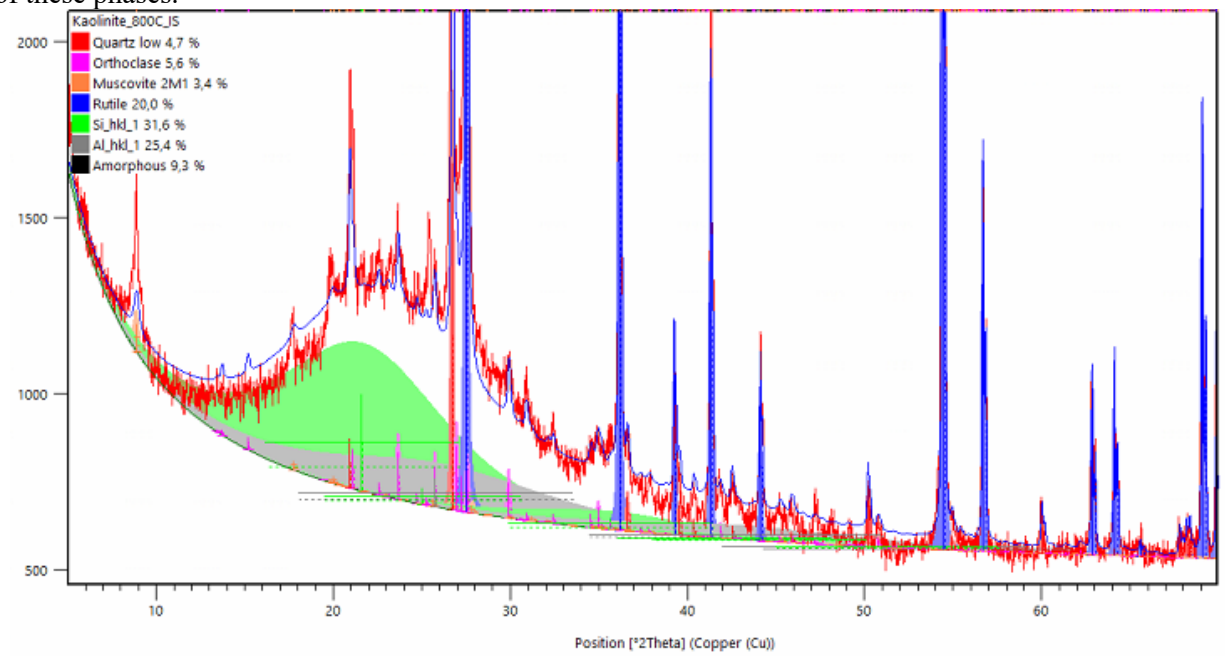

Figure 1. Representation of the refinement by PONKCS of the calcined kaolinite sample at 800 ºC.

For this reason, the quantifications of the 20/80 and 80/20 mixtures of fumed silica and amorphous alumina show much larger errors than when the Si_hkl and Al_hkl phases are used, and in general, the trends are notoriously different from the theoretical values. This demonstrates the conceptual error that is made when trying to evaluate clays where the amorphous fraction may have different proportions of reactive silica and alumina than the clay used as reference.

3 Conclusions

Silica fume and amorphous alumina that was chosen to be used as a reference, present amorphous humps in DRX, different enough to quantify the mixtures in the range between 20 to 80% with a minimum error.

It can be considered that the use of silica fume and amorphous alumina whose chemical environments and coordinations emulate those of metakaolin is enough to obtain amorphous phases in x-ray diffraction that allow a suitable determination of reactive fractions of silica and alumina in metakaolin by the PONKCS method.

There is a conceptual error that is made when trying to evaluate amorphous mixtures, from a single reference hkl phase. This will have to be considered in clays where the proportion of reactive phases of silica and alumina is not necessarily the same as that of pure kaolinitic clay. As well as, to determine the degree of reaction of calcined clays, since the rate of consumption of both phases does not have to maintain the same proportion throughout the hydration. For all this, the quantification of the reactive fractions of metakaolin should be done as proposed here, that is, using each reactive fraction that must be considered.

References

[1] J. Skibsted and R. Snellings, “Reactivity of supplementary cementitious materials (SCMs) in cement blends,” *Cem. Concr. Res.*, vol. 124, no. May, p. 105799, 2019.
[2] J. Rodríguez, M. Frías, and J. I. Tobón, “Eco-efficient cement based on activated coal washing rejects with low content of kaolinite,” *Constr. Build. Mater.*, vol. 274, 2021.
[3] O. O. Vásquez-Torres, F. D. Cabrera-Poloche, and J. I. Tobón, “Performance of Low-Grade Calcined Clays as Supplementary Cementitious Material in Relation to their Geological Characteristics,” *Clays Clay Miner.*, vol. 70, no. 2, pp. 233–251, 2022.
[4] C. Rodriguez and J. I. Tobon, “Influence of calcined clay/limestone, sulfate and clinker proportions on cement performance,” *Constr. Build. Mater.*, vol. 251, 2020.
[5] H. Yanguatin, J. H. Ramírez, A. Tironi, and J. I. Tobón, “Effect of thermal treatment on pozzolanic activity of excavated waste clays,” *Constr. Build. Mater.*, vol. 211, pp. 814–823, 2019.

[6] A. Tironi, M. A. Trezza, A. N. Scian, and E. F. Irassar, “Assessment of pozzolanic activity of different calcined clays,” *Cem. Concr. Compos.*, vol. 37, pp. 319–327, 2013.
[7] A. Alujas, R. Fernández, R. Quintana, K. L. Scrivener, and F. Martirena, “Pozzolanic reactivity of low grade kaolinitic clays: Influence of calcination temperature and impact of calcination products on OPC hydration,” *Appl. Clay Sci.*, vol. 108, pp. 94–101, 2015.
[8] A. Á. Barreto Maia, A. Rômulo Simões, R. de Freitas Neves, H. Pöllmann, C. Straub, and K. Saalwächter, “Use of 29Si and 27Al MAS NMR to study thermal activation of kaolinites from Brazilian Amazon kaolin wastes,” *Appl. Clay Sci.*, vol. 87, pp. 189–196, 2014.
[9] R. Snellings, A. Salze, and K. L. Scrivener, “Use of X-ray diffraction to quantify amorphous supplementary cementitious materials in anhydrous and hydrated blended cements,” *Cem. Concr. Res.*, vol. 64, pp. 89–98, 2014.
[10] N. Garg and J. Skibsted, “Thermal activation of a pure montmorillonite clay and its reactivity in cementitious systems,” *J. Phys. Chem. C*, vol. 118, no. 21, pp. 11464–11477, 2014.
[11] N. Garg and J. Skibsted, “Pozzolanic reactivity of a calcined interstratified illite/smectite (70/30) clay,” *Cem. Concr. Res.*, vol. 79, pp. 101–111, Jan. 2016.
[12] N. Garg and J. Skibsted, “Dissolution kinetics of calcined kaolinite and montmorillonite in alkaline conditions: Evidence for reactive Al(V) sites,” *J. Am. Ceram. Soc.*, vol. 102, no. 12, pp. 7720–7734, Dec. 2019.
[13] F. Avet and K. Scrivener, “Investigation of the calcined kaolinite content on the hydration of Limestone Calcined Clay Cement (LC3),” *Cem. Concr. Res.*, vol. 107, no. August 2017, pp. 124–135, 2018.
[14] F. Avet, X. Li, and K. Scrivener, “Determination of the amount of reacted metakaolin in calcined clay blends,” *Cem. Concr. Res.*, vol. 106, no. August 2017, pp. 40–48, 2018.
[15] Y. P. Stetsko, N. Shanahan, H. Deford, and A. Zayed, “Quantification of supplementary cementitious content in blended Portland cement using an iterative Rietveld-PONKCS technique,” *J. Appl. Crystallogr.*, vol. 50, pp. 498–507, 2017.
[16] C. C. Liu and G. E. Maciel, “The fumed silica surface: A study by NMR,” *J. Am. Chem. Soc.*, vol. 118, no. 21, pp. 5103–5119, 1996.
[17] J. He, D. Avnir, and L. Zhang, “Sol-gel derived alumina glass: Mechanistic study of its structural evolution,” *Acta Mater.*, vol. 174, pp. 418–426, 2019.

The 16th International Congress on the Chemistry of Cement 2023 (ICCC2023)
"Further Reduction of CO_2 -Emissions and Circularity in the Cement and Concrete Industry"
September 18–22, 2023, Bangkok, Thailand

Luminescent-based method for monitoring pH and chloride ingress in cementitious systems

I. Galan[1*], C. Grengg[1], I. Zögl[1], M. Sakoparnig[2], F. Mittermayr[2], J. Juhart[2], B. Müller[3], K. L. Sterz[3] and T. Mayr[3]

[1] *Institute of Applied Geosciences, Graz University of Technology, Graz, Austria*
igalangarcia@tugraz.at; cyrill.grengg@tugraz.at; iris.zoegl@student.tugraz.at

[2] *Institute of Technology and Testing of Building Materials, Graz University of Technology, Graz, Austria*
m.sakoparnig@tugraz.at; f.mittermayr@tugraz.at; joachim.juhart@tugraz.at

[3] *Institute of Analytical Chemistry and Food Chemistry, Graz University of Technology, Graz, Austria*
bernhard.mueller@tugraz.at; k.l.sterz@tugraz.at; torsten.mayr@tugraz.at

ABSTRACT
High quality data and easy-to-apply methods are crucial to make advancements in the field of concrete durability. In this contribution the authors propose the use of luminescent-based sensors to monitor pH and Cl ingress in cementitious systems. The presented method is based on the excitation of pH- and Cl-sensitive dyes applied to concrete and the measurement of the emitted signal. The pH sensors have been successfully used both for point measurements and to obtain high-resolution pH imaging maps of cementitious materials. The latter has shown the influence of the composition on the actual pH values in the 'carbonated' and 'not carbonated' zones of hardened mortars/concretes. Miniaturized sensor probes have been recently applied to study the pH development in cement pastes containing supplementary cementitious materials (SCMs), showing clear trends in terms of replacement percentages. Moreover, a new lucigenin-based sensor has been developed to measure the Cl content of powdered samples. The results are very promising and show the potential of these optical sensors to contribute to a better understanding of the hydration, carbonation and chloride penetration processes as well as to a better assessment of the state of concrete structures exposed to the environment.

KEYWORDS: *pH, Cl ingress, optical sensor, hydration, carbonation*

1. Introduction

Enhancing the durability of concrete is key to reduce the environmental impact and the associated costs. Service life models help to plan and design durable structures by predicting their behavior when exposed to the corresponding environment. For calibration and validation, the models need to be fed with experimental data obtained at laboratory and/or real conditions. The data quality is thus crucial to achieve accurate modelling results. Currently, the most commonly used methods to assess the state of concrete structures in terms of carbonation and chloride penetration are the phenolphthalein coloration approach and silver nitrate titration, respectively. The procedures are relatively easy and included in international standards. However, the accuracy of the methods and the correlation of the obtained results with the actual state of the considered structure in terms of potential damage are constantly being questioned. In this contribution the authors propose the use of luminescent-based sensors to quantify and monitor pH and Cl ingress in cementitious systems.

2. pH measurements

The sensors used to measure pH contain a fluorescent aza-BODIPY pH indicator dye (Staudinger, Breininger, et al., 2019) combined with a phosphorescent reference material made of chromium(III)-

activated gadolinium borate (Cr-GAB) which are both immobilized in a polymer matrix. The measurement principle is based on the excitation of the pH-sensitive dye and the reference compound and the subsequent measurement of the combined emitted light (Staudinger, Breininger, et al., 2019; Staudinger, Strobl, et al., 2019).
The versatility of the sensors allows for optical pH imaging on smooth, hardened samples (Grengg et al., 2019; Müller et al., 2018), as well as for continuous monitoring of pH during hydration of cementitious materials (Briendl et al., 2022; Galan et al., 2021), as well as for surface point measurements on hardened materials and slurries of powdered samples. Figure 1 shows the different measurement set-ups.
The measurements are in all cases luminescence life-time-based; however, depending on the application format, the referencing method varies: (i) in the case of imaging, intensity differences over time are measured, whereas (ii) for miniaturized sensor probe measurements (point measurements), phase angle differences in the signal frequency are considered.

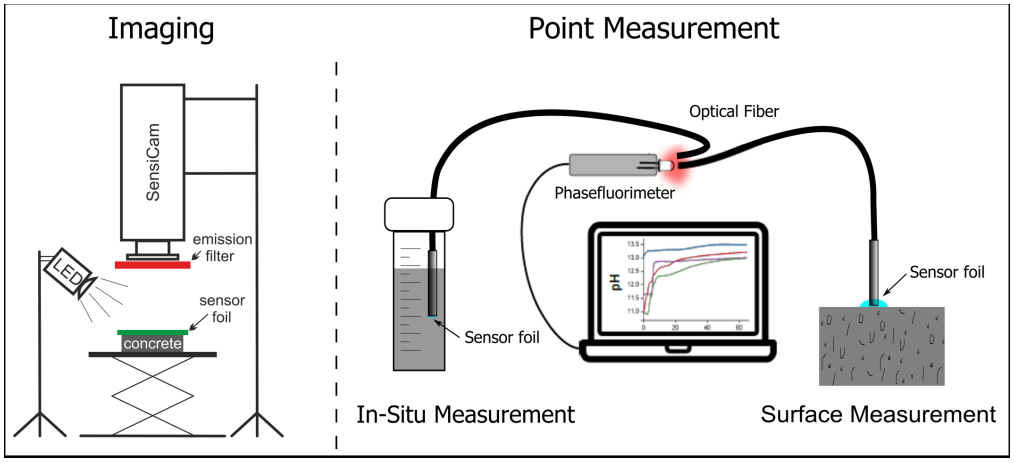

Figure 1. Measurement set-ups: imaging (left) and point measurements inside and on surface (right).

2-D mapping of surface pH

Recently, high-resolution pH imaging carried out on hardened mortar and concrete has shown the influence of the binder composition on the actual pH values in the 'carbonated' and 'not carbonated' regions (Sakoparnig et al., 2023). Figure 2 shows an example of a concrete sample exposed to natural carbonation in which the carbonated and not carbonated regions (as well as the aggregates) can be clearly differentiated (see left image with pH scale). The mean pH values from the areas indicated with red, blue and green boxes on the left image in Figure 2 result in actual depth profiles, and were plotted together with the carbonation depth according to phenolphthalein (see right image in Figure 2). In this specific sample, the average pH in the 'carbonated region', as indicated by phenolphthalein (colorless region), was above 10 and the phenolphthalein color transition (purple region) took place at a pH of ~11. However, the pH at the 'carbonated region' and at the phenolphthalein transition varied quite significantly in all analyzed concrete samples (over 100), showing values between 8 and 11, and 10.5 and 12, respectively.

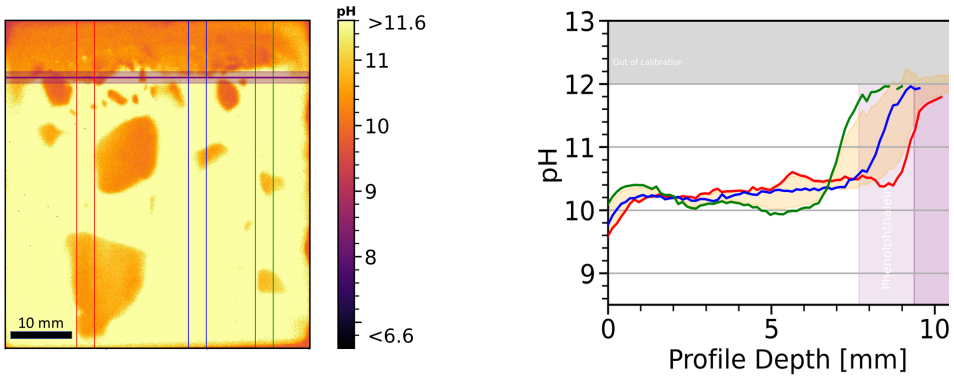

Figure 2. pH map of a concrete sample exposed to natural carbonation (left) and pH values along the profiles indicated in the pH map (right). Note the three regions in the right image (according to phenolphthalein coloration): colorless (carbonated), light purple (transition), dark purple (not carbonated).

Surface point measurements with sensor probes

Sensor probes were recently also applied to study the pH development in cement pastes containing supplementary cementitious materials (SCMs). Replacement of cement by SCMs is restricted due to the resulting low pH matrices produced because (i) they may not be suitable for steel reinforced structures and (ii) some of the hydrated phases may become unstable. To assess the exact replacement boundaries a combination between experimental data and thermodynamic modelling is needed. Among the existing methods currently used to measure pH in hardened materials, pore solution extraction and subsequent titration or measurement with standard electrode are the most accepted procedures. However, because the method is time and labor intensive, easier and faster alternatives, such as the use of the described optical sensors, are highly welcomed.

Cement pastes prepared with silica fume, metakaolin, granulated blast furnace slag and fly ash were cured in humid chambers for 90 days, after which the pH was measured by placing the miniaturized optical sensors on the surface where 10 µl of milli-Q water had been previously applied. Preliminary results show a clear dependency of the pH with the replacement % of SCMs and in some cases, the water/binder ratio (see

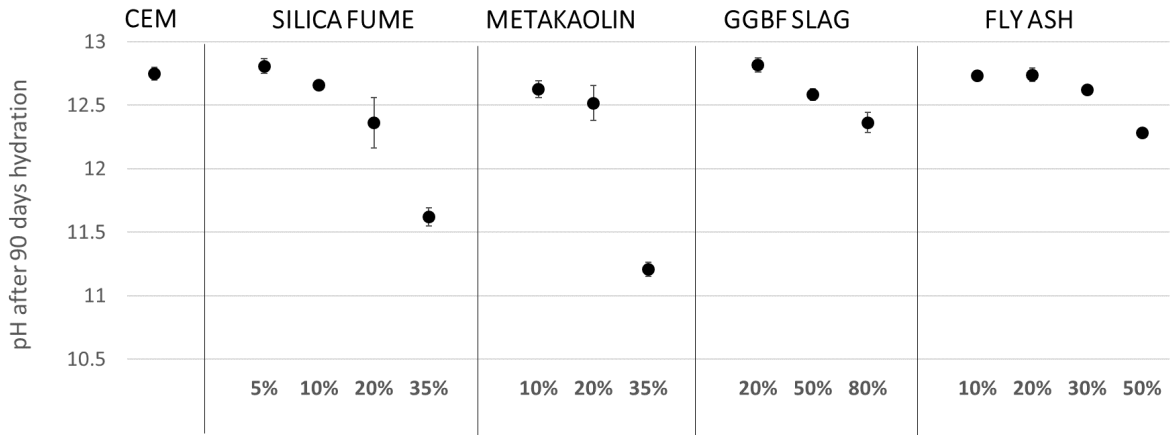

Figure 3 after 90 days hydration). Note all pastes were made with water/binder ratio of 0.5 except for those with 35% silica fume, 35% metakaolin and 50% fly ash (prepared with 0.7). The results indicate that, for example, replacements of metakaolin above 35% would lead to pH values below 11.5 after 90 days of hydration.

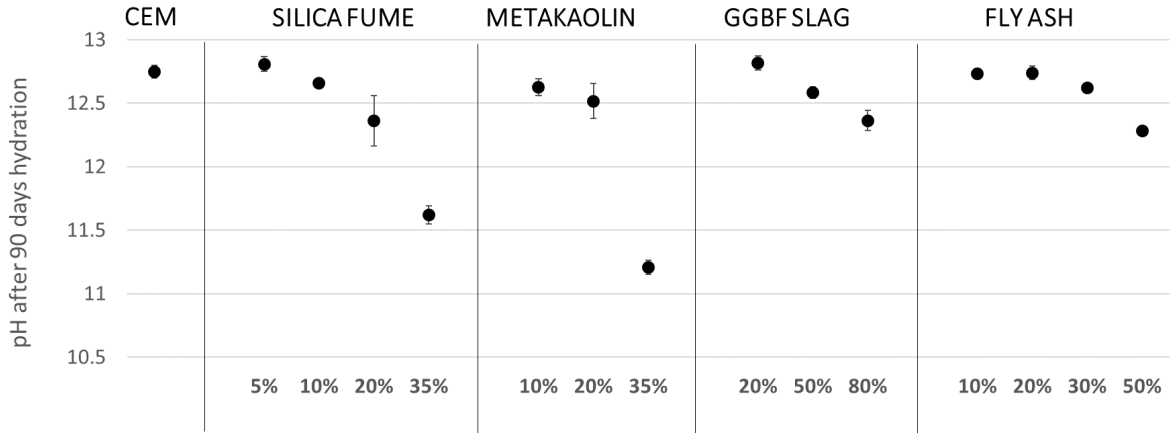

Figure 3. pH measured on the surface of the SCMs-containing pastes after 90 days hydration.

3. Chloride measurements

An optical sensor has been recently developed to measure the Cl^- content of powdered concrete samples. The fluorescent, chloride sensitive dye lucigenin and a phosphorescent, ruthenium-based reference compound were immobilized in a partially hydrolized polyacrylonitrile (PAN). Again, phase angle differences in the signal frequency of the combined emitted light (500 – 800 nm) to the excitation light (430 to 470 nm) are measured in order to determine the Cl^- content.
Calibration was done with MOPS buffered solutions of pH 7 containing different levels of NaCl, which were also adjusted with $NaNO_3$ to a constant electrical conductivity of 10.0 mS/cm^2. The measured phase angles were recalculated to intensity ratios (I_0/I), plotted against the corresponding Cl^- concentration and fitted with the two-site model of the Stern-Volmer equation. A calibration, with the corresponding errors, is shown in Figure 4.

In a first test, free chloride of powdered concrete samples, containing different chloride levels was determined. The samples were mixed with water (powder to water mass ratio 1:4), shaken for 10 minutes, centrifuged and filtered. The filtrate was buffered with 10 mM MOPS, adjusted to pH 7 with HNO_3 and its electrical conductivity brought to 10.0 mS/cm^2 by adding $NaNO_3$ prior to the optical measurement. Diluted samples of the filtrate were also analyzed via ion chromatography (IC) as reference (analytical error <3%). For better visualization of the found chloride levels, the concentration in the filtrate was converted to mass % in concrete powder samples (Table 1). The results of our method are in very good agreement with the reference method, confirming the suitability of the new method to measure free chloride under such conditions. In future work we will investigate (i) the influence of sample preparation (powder/water ratio, equilibration time), (ii) the effect of pH and ionic strength, and (iii) the accuracy for samples with low Cl^- concentration.

Figure 4. Calibration curve of lucigenin-based sensor for Cl measurements in concrete.

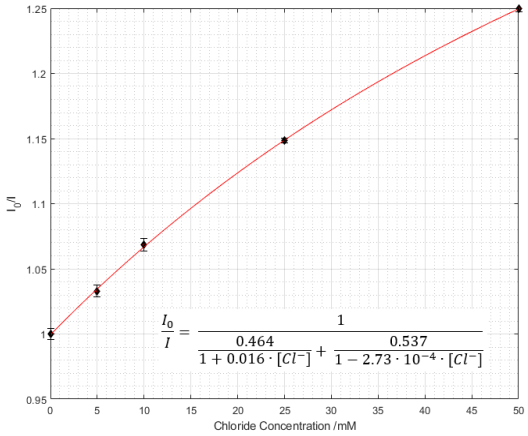

Table 1. Chloride concentration in powdered samples measured by optical sensor and ion chromatography.

Sample	Ionic Chromatography		Optical sensor	
	[mM]	[% concrete]	[mM]	[% concrete]
1	28.27	0.40	28.3	0.40
2	11.84	0.17	11.7	0.17
3	30.98	0.44	32.0	0.45
4	11.92	0.17	13.4	0.19
5	15.15	0.21	15.4	0.22
6	7.09	0.10	7.2	0.10

4. Conclusions

Recently the application of luminescence-based optical sensors has been expanded to pH surface measurements on SCMs-containing samples and to Cl concentration measurements on equilibrated water-powder samples. The promising results show that the application of this novel methodology will allow for a better assessment of the concrete structures' state and for a better understanding of the processes taking place in cementitious matrices during hydration and exposure to the environment.

Acknowledgements

The authors gratefully acknowledge the funding by the Austrian Research Promotion Agency FFG (LumAConM Project-No. 879008), the Austrian Society for Construction Technology ÖBV and the industry partners.

References

Briendl, L. G., Grengg, C., Müller, B., Koraimann, G., Mittermayr, F., Steiner, P., & Galan, I. (2022). In situ pH monitoring in accelerated cement pastes. *Cement and Concrete Research*, *157*.

Galan, I., Müller, B., Briendl, L. G., Mittermayr, F., Mayr, T., Dietzel, M., & Grengg, C. (2021). Continuous optical in-situ pH monitoring during early hydration of cementitious materials. *Cement and Concrete Research*, *150*.

Grengg, C., Müller, B., Staudinger, C., Mittermayr, F., Breininger, J., Ungerböck, B., Borisov, S. M., Mayr, T., & Dietzel, M. (2019). High-resolution optical pH imaging of concrete exposed to chemically corrosive environments. *Cement and Concrete Research*, *116*, 231–237.

Müller, B., Grengg, C., Schallert, V., Sakoparnig, M., Staudinger, C., Breininger, J., Mittermayr, F., Ungerböck, B., Borisov, S. M., Dietzel, M., & Mayr, T. (2018). Wide-range optical pH imaging of cementitious materials exposed to chemically corrosive environments. *RILEM Technical Letters*, *3*(0 SE-Articles).

Sakoparnig, M., Galan, I., Müller, B., Zögl, I., Juhart, J., Mittermayr, F., Autischer, M., & Grengg, C. (2023). New insights into the carbonation process of mortars and concretes. *SynerCrete'23*.

Staudinger, C., Breininger, J., Klimant, I., & Borisov, S. M. (2019). Near-infrared fluorescent aza-BODIPY dyes for sensing and imaging of pH from the neutral to highly alkaline range. *Analyst*, *144*(7), 2393–2402.

Staudinger, C., Strobl, M., Breininger, J., Klimant, I., & Borisov, S. M. (2019). Fast and stable optical pH sensor materials for oceanographic applications. *Sensors and Actuators, B: Chemical*, *282*, 204–217.

The 16th International Congress on the Chemistry of Cement 2023 (ICCC2023)
"Further Reduction of CO_2 -Emissions and Circularity in the Cement and Concrete Industry"
September 18–22, 2023, Bangkok, Thailand

Alkaline materials based on pulverized recycled concrete and waste glass.

J. Rodríguez-Morales[1], O. Burciaga-Diaz[2], and J. I. Escalante-Garcia[3*]

[1] *Cinvestav Saltillo, Ramos Arizpe Coahuila, México*
Email: juliana.rodriguez@cinvestav.mx
[2] *Tecnológico Nacional de México, Instituto Tecnológico de Saltillo, Saltillo Coahuila, México*
Email: oswaldo.bd@saltillo.tecnm.mx
[3] *Cinvestav Saltillo, Ramos Arizpe Coahuila, México*
Email: ivan.escalante@cinvestav.edu.mx

ABSTRACT

Alternative alkaline cements were synthesized using composite precursors of pulverized recycled concrete (PRC) and waste glass (WG) activated with sodium silicates. The experimental design was based on the Response Surface Methodology with a Central Composite Design; the experimental factors were: the PRC:WG ratios from 1:0 to 0:1, %Na_2O from 8 to 12% relative to the mass of the precursor and the modulus of the silicate Ms from 1 to 2. 15 formulations of pastes and mortars were initially cured at 60°C for 24h and then isothermally at 20°C. The compressive strength development was monitored for up to 900 days. A paste with 25%PRC-75%WG activated with 9%Na_2O using a Ms=1.25 reached strengths that evolved from 40.2 to 52.4 MPa from 1 to 900 days; while a mortar with 50%WG-50%PRC activated with 8%Na_2O and Ms=1.5 resulted in a strength evolution from 18.9 to 32.2 MPa from 1 to 900 days. X-ray diffraction and scanning electron microscopy, indicated that the cementitious reaction products included silica gel, C-S-H and (C,N)-S-H, indicating that Ca was released from the components of the recycled concrete, which reacted with the species from the alkaline activator and those liberated from the waste glass. The mechanical properties indicated that the composite cements are a promising sustainable alternative to reduce the environmental impacts associated to the cement industry.

KEYWORDS: *recycled Portland cement concrete, waste glass, sodium silicate, sustainable cements, alkaline cements.*

1. Introduction

Portland cement (PC) is the most used binder to make concrete, which is in turn the most commercialized material worlwide. After reaching the end of its service life, concrete constructions turn into an environmental passive after demolition operations (C&DW), which amount to about 10,000 Mt/year and 35% are landfilled Chen et al., (2021). On the other hand, it is estimated that ~ 40% of the C&DW correspond to concrete Borrachero et al., (2022). Alternative cements have been recently developed to phase the environmental challenges resulting from the demographic growth; among these are the alkaline cements, using precursors like metakaolin Pérez-Cortés and Escalante-García, (2020), pumice López-Salas and Escalante-García, (2019), waste glass (WG) Menchaca-Ballinas, et al,. (2021), among others. Limestone (LS) has also been reported as a precursor in alkaline cements Ortega-Zavala et al., (2019), which lead to preliminary tests and a number of patent applications at our lab using pulverized concrete with calcareous LS based aggregates as a precursor; these results indicate that recycled concrete can have more added value beyond its use as aggregates for new concrete.

In this research, alkaline cements were prepared using composite precursors combining pulverized concrete and waste glass, activated with sodium silicates, as an additional strategy towards the massive revalorization of the two wastes which are readily available worldwide.

2. Experimental details

One precursor was a pulverized recycled concrete (PRC) formulated in the laboratory with 400 kg/m3 of a commercial PC (CPC30 as per Mexican standards (NMX-C-414-ONNCCE, 2017) and cured for more than 1 year; the second one was a SiO_2-Na_2O-CaO waste glass (WG) from urban wastes. Both precursors were ground to a Blaine Surface area of 600m^2/kg (ASTM C204-2018). Figure 1 shows the DRX patterns of PRC of different particle size fractions, which show predominance of calcite peaks, while the WG appeared WG completely amorphous. The alkaline activators were commercial sodium silicates (SS); powdered anhydrous SS of modulus Ms=1 and 2 for pastes, while for mortars a liquid SS of Ms= 2.07 was used. The sand used for the latter was a commercial LS product with a maximum particle size of 4.75mm. The Ms in the activators was modified by incorporating industrial grade NaOH.

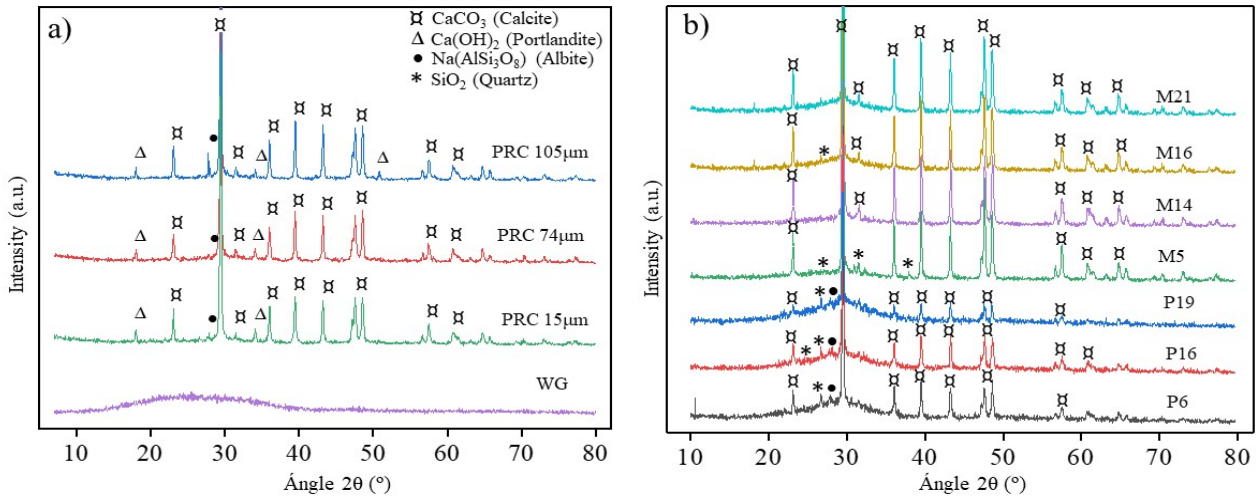

Figure 1. XRD patterns of a) the used precursors of recycled Portland cement concrete and waste glass. b) pastes and mortars dry cured at 900 days.

2.1 Design of Experiments

The experimental matrix was designed using the response surface methodology (RSM) using a randomized central compound design (CCD) that allowed evaluating the effect of three factors (the PRC:WG ratios from 1:0 to 0:1, 8%<%Na_2O<12% relative to the mass of the precursor and 1<Ms<2, each at 5 levels (as indicated in Table 1); the response variable was the compressive strength in pastes and mortars for up to 900 days. The formulations are shown in the first columns ot Table 2 along with the results of compressive stregth.

Table 1. Factors and levels in the experimental design according to the CCD

Factors	Levels				
PRC:WG	0	25	50	75	100
%Na_2O	8	9	10	11	12
Ms	1	1.25	1.5	1.75	2

2.2 Alkali activated binders synthesis of PRC:WG

The Ms of the activators for the pastes were modified by blending the powdered SS of Ms= 1 and 2 in the proportions described in Table 2; these were homogenized with the pulverized preecursors in a ball mill with a 10:1 material:ball ratio, for 10 minutes. The pastes were prepared as the one-part cements type. A 1.5% of a superplasticizer (SP) relative to the mass of the precursors was incorporated. Water was added at a water/binder (w/b) of 0.32. The pastes were mixed for 10 minutes added in a laboratory mixter with planetary movement. For the mortars, the Ms of the SS solutions were modified mixing the liquid SS (Ms=2.07) with a solution of NaOH; the w/b ratio, %SP and mixing time were the same as for the pastes. The pastes and mortar specimens were cast in cubic molds of 2.5 cm per side, which once filled were vibrated for 10 s to eliminate trapped air and were covered with plastic films and wet flannels to prevent water evaporation; both types of specimens were cured at 60ºC for the first 24 h to accelerate the reactions during setting, and cured to 20±3ºC afterwards.

Table 2. Experimental design matrix and experimental compressive strength data.

Full experimental design				Paste formulation (P)					Mortar formulation (M)				
Exp Nº	PRC:WG (%)	Na_2O (%)	Ms (a.u.)	Ms=1 (%)	Ms=2 (%)	Compressive strength (MPa)			Ms=2.07 (%)	NaOH (%)	Compressive strength (MPa)		
						1d	28d	900d			1d	28d	900d
1	50:50	10	1	100	0	4.3	7.0	6.6	92.11	7.89	17.2	25.3	34
2	50:50	10	1.5	35	65	14.2	22.7	25.7	97.05	2.95	20.2	30.4	25.7
3	50:50	10	1.5	35	65	14.6	17.4	22.9	97.05	2.95	18.4	30.3	24.6
4	75:25	11	1.75	16	84	5.8	8.2	14.2	98.56	1.44	13.7	21.4	22.2
5	0:100	10	1.5	35	65	8.7	9.0	13.1	97.05	2.95	27.5	52.1	43.2
6	25:75	9	1.25	61	39	40.2	54.9	52.4	95.01	4.99	22.9	43.4	33.9
7	75:25	9	1.25	61	39	33.3	35.6	n.a.	95.01	4.99	8.6	17.5	12.4
8	50:50	10	1.5	35	65	16.2	19.1	22.1	97.05	2.95	19.8	32.5	30.9
9	25:75	9	1.75	16	84	24.9	36.1	n.a.	98.56	1.44	18.4	42.6	32.4
10	100:0	10	1.5	35	65	2.2	3.0	10.8	97.05	2.95	5.1	7.5	15.1
11	50:50	12	1.5	35	65	16.3	21.1	30.3	97.05	2.95	24.1	35.7	37.5
12	50:50	10	2	2	98	23.7	36.5	51.5	99.72	0.28	17.2	30.8	26.9
13	50:50	10	1.5	35	65	12.7	25.0	27.4	97.05	2.95	22.9	36.8	27.2
14	25:75	11	1.75	16	84	26.9	47.1	47.5	98.56	1.44	22.6	48.3	41.8
15	75:25	9	1.75	16	84	7.9	11.9	25.9	98.56	1.44	8.1	9.9	12.1
16	50:50	8	1.5	35	65	12.8	20.4	36.7	97.05	2.95	18.9	31.6	32.3
17	50:50	10	1.5	35	65	14.8	25.1	29.2	97.05	2.95	20.9	31.5	27.9
18	50:50	10	1.5	35	65	19.2	24.8	28.4	97.05	2.95	20.1	32.2	28.8
19	25:75	11	1.25	61	39	7.8	46.2	57	95.01	4.99	23.9	39.3	42.5
20	75:25	11	1.25	61	39	8.6	7.1	7.5	95.01	4.99	8.3	17.7	28.4

n.a. = data not available

2.3 Characterization of samples

For each age of curing 3 specimens were mechanically tested using an automated hydraulic (cell of 250 kN). Fragments of the tested paste specimens were vaccum oven dried at 40ºC for 48 h to eliminate the water; these were then hand ground to pass the #200 sieve. The powders were characterized by X-ray diffraction (XRD; Phillips, model XPert 3040) in a range of 10-80º 2θ with a step of 0.025º every 3 seconds using Ka radiation from Cu at 40 keV and 30mA. For scanning electron microscopy (SEM), untested paste fractions were mounted in epoxy resin, these were ground with silicon carbide sandpaper and polished with diamont paste up to 0.25 microns; the surfaces were then carbon coated to make them conductive under the microscope operated 25 keV using backscattered electron images.

3. Results and discussion

The strength results (Table 2) for mortars and pastes showed that high WG contents were favorable. The paste 6 (25:75, 9% Na_2O and Ms=1.25) with a low %Na_2O had strengths 1 and 900 days strengths of 40.2 and 52.4 MPa, respectively, while mortar 16 (50:50, 8% Na_2O and Ms=1.5), with the lowest %Na_2O and high %PCR had 1 and 900 days strengths of 18.9 a 32.3 MPa, respectively; this suggests that low %Na_2O and high %PCR can results in useful properties, which in turn reduces CO_2 emissions and costs, while avoiding the landfilling of C&DW. A statistical optimization analysis indicated a formulation 70.7:23.9, 10.7%Na_2O and Ms=1.7 indicated predicted and experimentally corroborated strengths of 44 and 36.9 MPa, respectively, after 28 days, as well as 36.8 and 44 MPa, respectively, after 900 days. The latter indicated that the model was adecuate to describe the experimental data.

Figura 1b shows the DRX resutls for pastes and mortars. Although the calcite peaks dominated the patterns, there was a slight reduction of its peaks after the alkaline activation, which in agreement with previous works Ortega-Zavala et al., (2019), indicates that the LS from the PRC participated in the reactions with the SiO_2 species from the WG and SS forming amorphous cementitious products possibly of the type of silica gel, C-S-H and/or (C,N)-S-H. The components of the fraction of reacted PC from the PRC, like $Ca(OH)_2$ or carbonated calcium hydrates Santana-Carrillo et al., (2022) could have also participated in such reactions, but more research is needed to elucidate this. Figure 2 shows that the microstructures of paste 6 cured for up to 900 days. The matrix of reaction products was dense, although

some cracking was noted due to the drying of the silica gel formed. Particles of PCR and WG were distributed in the microstructure, both dissolved towards the formation of cementitious reaction products.

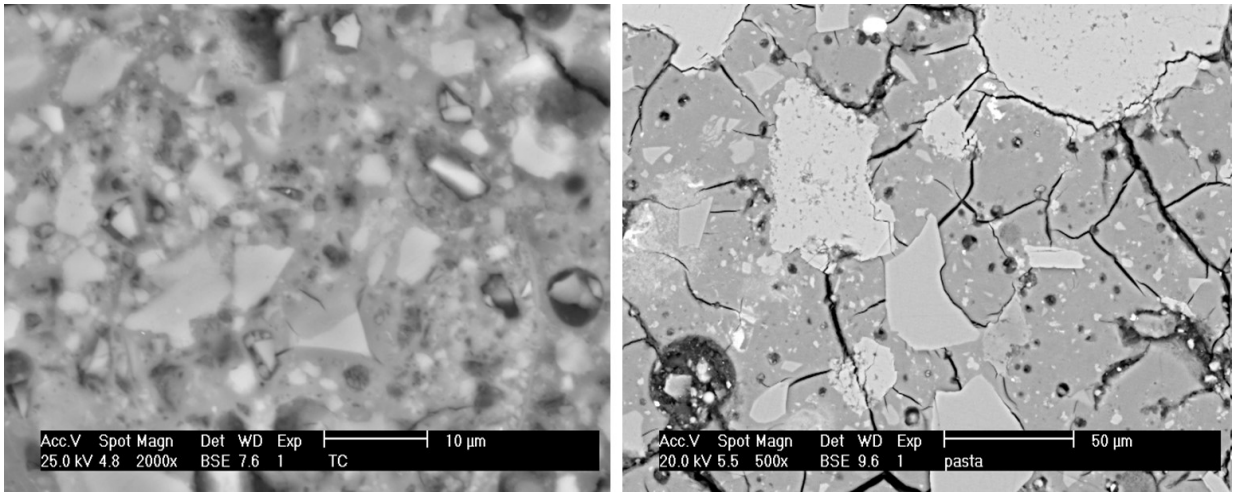

Figure 2. Backscattered electron images of the microstructures of paste 6 (25:75, 9%Na_2O and Ms=1.25) a) 1day (b) 900 days.

3. Conclusions

The strength evolution of pastes and mortars, as well as their characterization by XRD and SEM, indicated that after the alkaline activation, the waste glass and the ingredients of the recycled concrete (i.e. limestone, portlandite, etc.) released species that recondensed forming amorphous cementitious products, like silica gel, C-S-H and /or (C,N)-S-H. More research is needed to understand the role of the hydration products and anhydrous phases from the portland cement of the concrete. The results indicate that the pulverized recycled concrete is a promising precursor in combination with waste glass to formulate sustainable alkali activated construction materials.

Acknowledgements. Rodríguez-Morales acknowledges the scholarship Nº 1011798 Conacyt México.

References

Borrachero, M, Payá J, Brito S, Segura Y, Soriano L, Tashima M, and Monzó J.M. 2022. "Reusing Construction and Demolition Waste to Prepare Alkali-Activated Cement." *Materials*. https://doi.org/10.3390/ma15103437.

Chen, K, Wang J, Yu B, Wu H, and Zhang J. 2020. "Critical Evaluation of Construction and Demolition Waste and Associated Environmental Impacts: A Scientometric Analysis." *Journal of Cleaner Production* 287. https://doi.org/10.1016/j.jclepro.2020.125071.

López-Salas, J, and Escalante-García J.I. 2019. "Cementos de Bajo Impacto Ambiental Por Activación Híbrida de Material Volcánico." *Conpat Chiapas 2019* 1: 1–10. https://doi.org/10.21041/CONPAT2019/V1CC147.

Menchaca-Ballinas, L, Gorokhovsky A, and Escalante-García J.I. 2021. "Waste Glass as a Precursor in Sustainable Hydraulic Cements Activated with CaO-NaOH-Na_2CO_3." *Construction and Building Materials*. https://doi.org/10.1016/j.conbuildmat.2021.124099.

NMX-C-414-ONNCCE. 2014. *Especificaciones y Métodos de Ensayo*. *Organismo Nacional de Normalización y Certificación Para La Construcción y Edificación*.

Ortega-Zavala, D, Santana-Carrillo J.L, Burciaga-Díaz O, and Escalante-García J.I. 2019. "An Initial Study on Alkali Activated Limestone Binders." *Cement and Concrete Research*, 267–78. https://doi.org/10.1016/j.cemconres.2019.04.002.

Pérez-Cortés, P, and Escalante-García J.I. 2020. "Alkali Activated Metakaolin with High Limestone Contents – Statistical Modeling of Strength and Environmental and Cost Analyses." *Cement and Concrete Composites*. https://doi.org/10.1016/j.cemconcomp.2019.103450.

Santana-Carrillo, J. L., Burciaga-Díaz O, and Escalante-García J.I. 2022. "Blended Limestone-Portland Cement Binders Enhanced by Waste Glass Based and Commercial Sodium Silicate - Effect on Properties and CO_2 Emissions." *Cement and Concrete Composites* 126: 104364. https://doi.org/10.1016/j.cemconcomp.2021.104364.

The 16th International Congress on the Chemistry of Cement 2023 (ICCC2023)
"Further Reduction of CO_2 -Emissions and Circularity in the Cement and Concrete Industry"
September 18–22, 2023, Bangkok, Thailand

Microstructural modifications of alkali-activated fly ash cement pastes by the presence of calcium hydroxide

Ary A. Hoyos-Montilla[1] , Jorge I. Tobón[2], Francisca Puertas[3*]

[1] Construction School at Universidad Nacional de Colombia, Medellín, Colombia
Email: aahoyosm@unal.edu.co
[2] Cement and Construction Materials Group, Department of Materials and Minerals at Universidad Nacional de Colombia, Medellín, Colombia
Email: jitobon@unal.edu.co

[3]Eduardo Torroja Institute for Construction Sciences (IETcc, CSIC), Madrid, Spain*
Email: puertasf@ietcc.csic.es

ABSTRACT

Portland cement is a material with many excellent technical features but its vast production and consumption, expected to grow substantially in the decades to come, have very adverse energy and environmental impacts. Alkaline cements (also known as geopolymers) are products closely aligned with sustainability principles and can be considered alternative materials to Portland cement. In last decades, the behaviour and properties of these alkaline cements and their concretes have been studied in depth. However, there are still important aspects, both in fresh and hardened stated, to be elucidated and necessary for the final implementation of these products in the market. This research explores the influence of calcium hydroxide on the alkaline activation of a class F coal fly ash. The pastes of these alkaline cements were assessed for their compressive strength at 3 (RH 95% and 45 °C) and 28 (RH 95% and 25 °C) curing days. The sample characterization was carried out using XRD, FTIR, MAS NMR and BSEM/EDX. The presence of calcium hydroxide increased the compressive strength of the pastes at 28 days from 4.5 MPa to 25.6 MPa. Calcium hydroxide modifies the microstructure of the pastes due to the formation of (N,C)-A-S-H and C-(A)-S-H type gels and zeolite-type crystalline structures.

KEYWORDS: *Alkaline cements, geopolymers, calcium hydroxide, fly ash, microstructure*

1. Introduction

The construction sector is seeking to reduce the environmental impact because of the manufacturing and use of Portland cement. It is estimated that its production by 2050 will show an annual increase of 50% compared to the current amount produced [1]. The use of alternative cements (or geopolymers) can help reduce such environmental impacts. The most used precursors to produce such activated cements are fly ashes generated from coal combustion. One of the most influential variable for selecting them is the presence of calcium. Low calcium content in the ash implies a better durability response, while a high content of it is equivalent to better mechanical performance [2]. The presence of calcium hydroxide, during the alkaline activation, guarantees a greater quantity and speed of the reactions during the formation of the new cementing gels [3]. The objective of this research work is to explore and understand the microstructural modifications induced in an alkali-activated fly ash cement by the presence of calcium hydroxide.

2. Materials and methods

The used employed fly ash (FA) is a by-product of power generation from coal combustion. Calcium hydroxide (CH) has an industrial origin with a purity degree of 96.6% and sodium hydroxide (SH) is analytical grade (caustic soda flake) with a purity of 99-100%. Pastes with 0, 10 and 20% CH (wt% FA) were prepared. FA and CH were mixed dry for two hours. SH diluted in water to a concentration of 8 M was prepared. The solids and liquids were mixed using a liquid/solid (l/s) ratio of 0.44. The pastes were cured for three days (RH 95% and 45 °C) and then, they were exposed to room temperature (RH 95% and 25 °C). The samples were tested by compressive strengths at 3 and 28 curing days. A mineralogical and microstructural characterization of the 3-day-cured pastes was performed using XRD, FTIR, MAS NMR and BSEM/EDX. The chemical composition of fly ash and calcium hydroxide are presented in Table 1. The chemical constituents involved in alkaline activation reactions are divided into network-forming elements (Si and Al) and network-modifying elements (Ca and Na) [4].

Table 1. Chemical composition (wt%) of fly ash and calcium hydroxide.

Materials	SiO_2	Al_2O_3	CaO	Fe_2O_3	MgO	Na_2O	K_2O	TiO_2	Other	LOI [750°C]
FA	55.26	26.95	1.00	5.66	1.78	0.44	0.75	2.28	1.51	4.37
CH	0.14	0.06	73.42	0.07	0.37	-	-	-	0.34	25.60

LOI, Loss on Ignition

3. Results and discussion

3.1 Compressive strength

Fig. 1 summarizes the pastes' compressive strength results at 3 and 28 curing days based on the CH content's function. Once the curing process was completed after three days, it was observed how the compressive strength increased with a greater addition of CH. Average values from 4.5 MPa to 18.2 MPa were obtained. At 28 days, the resistances reached values of 25.65 MPa when the amount of CH added was maximum (20% wt).

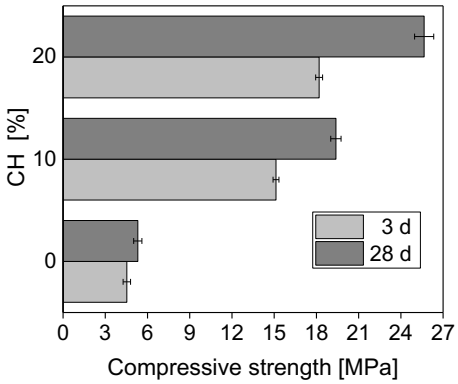

Fig. 1. Compressive strength of alkaline cement pastes. Effect of CH.

3.2 FTIR - XRD analysis

Once the curing process is finished, the IR spectra performed on the pastes (Fig. 2a) showed the transformation suffered by the ash in the presence of SH and CH, comparing the band corresponding to the T-O groups (1346 cm^{-1} to 650 cm^{-1}). The maximum value of such band (T-O) moves towards lower vibration frequencies during the alkaline activation process. For 0% CH, a maximum was observed at 1010 cm^{-1}, which is typical of N-A-S-H gels [5] and for 20% CH the maximum was detected at 991 cm^{-1}, typical of C-S-H/C-A-S-H gels. Figure 2b presents a loss in the area of the T-O groups and a displacement of the maximum towards lower frequencies; this confirms the ash's depolymerization process and the formation

of new cementing phases. Fig. 2c presents the diffraction patterns for the cement pastes under study (0 and 20% CH). When CH, in the form of a complex ($CaOH^+$), is part of the mixtures, it modifies the intensity and moves the amorphous halo towards higher values. In cements with 20% CH, the formation of zeolite-like crystalline phases accelerates. The results show that, a mixture of amorphous materials ((N,C)-A-S-H and C-(A)-S-H type gels) and crystalline structures (zeolites type) would generate.

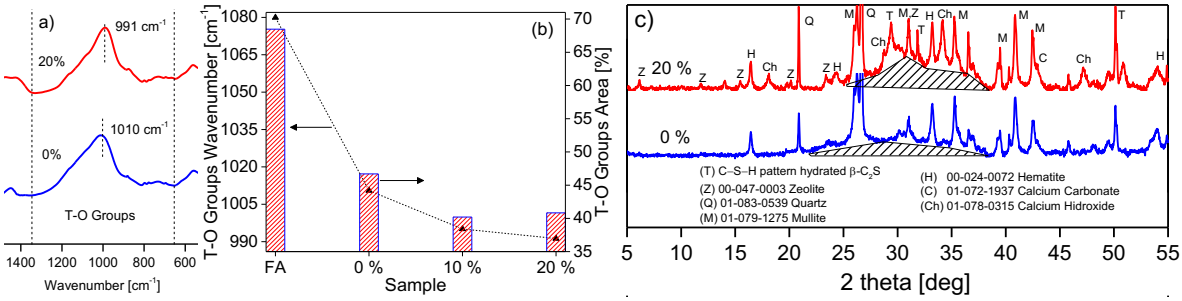

Fig. 2. IR spectra of the cements pastes with 0 and 20% CH at 3 days of curing (a). An effect of adding CH on the wavelength and on the T−O groups' area (b). XRD patterns for cement pastes with 0 and 20% CH (c).

3.3 NMR Analysis

Fig. 3a shows the ^{29}Si MAS NMR spectra for the cement pastes under study. The presence of CH in the activated fly ash pastes makes the main signals displace to the left. This indicates that changes are generated in the structure of the reaction products. As shown in Fig. 3b, when quantifying the variations of the areas that correlate with the network-forming elements (Si), the presence of the activator and an increase in CH in the mixtures contribute to increase of Q_1/Q_2 units in cementing gels [6]. The analysis of the NMR spectra confirms the presence of C-S-H and N-A-S-H type gels modified with the presence of aluminum, sodium, and calcium.

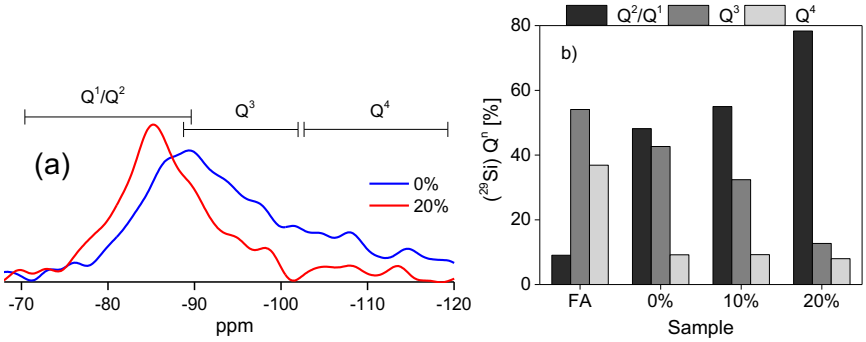

Fig. 3. ^{29}Si MAS NMR spectra (a) and unit area variation (b) for the mixtures with 0 and 20% CH.

3.4 BSEM/EDX Analysis

Fig. 4 shows the morphology of the cementing pastes. When comparing the micrographs in the paste with 0% CH (Fig. 4a), it is noted that the spherical shape of some ashes is preserved, while the paste containing a 20% CH (Fig. 4c) presents environments with a greater presence of precipitates. The ternary diagram for the mixtures analyzed via EDX shows that the N-A-S-H type gels are located along the line of silicon and aluminum oxides. As the amount of CH increases, the composition of the gels shifts towards the MeO (Me: Ca, Na) vertex; it indicates an enrichment in the mixtures of C-S-H/ C-(A)-S-H gels.

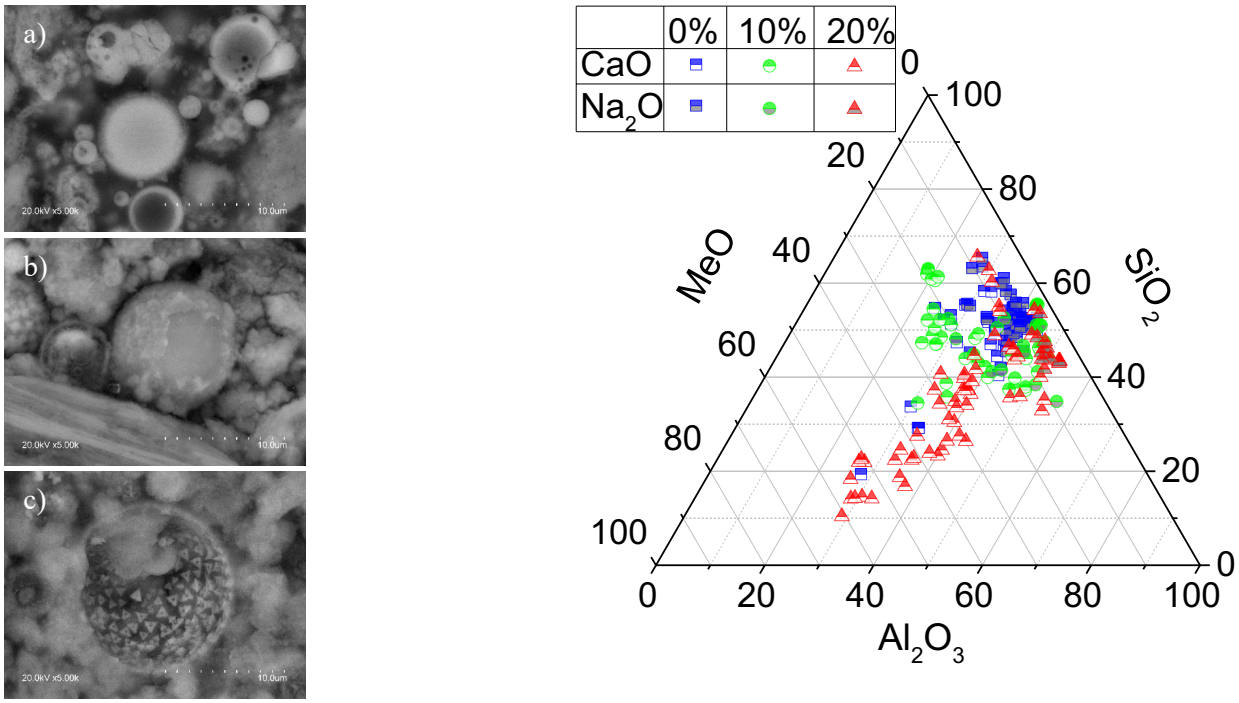

Fig. 4. BSEM micrographs for the pastes with (a) 0%, (b) 10% and (c) 20% CH. Representation of the pastes' composition in the MeO−Al_2O_3−SiO_2 (Me:Ca, Na) diagram from the EDX analysis.

4. Conclusions

The effect of calcium hydroxide on the composition and microstructure of sodium hydroxide alkali-activated fly ash cement has been presented. Calcium hydroxide affects the alkaline activation process; it intervenes in the depolymerization of the ash and the subsequent molecular restructuring. CH modifies the compressive strength of the pastes due to the formation of C-S-H/C-(A)-S-H and (C)-A-S-H/N-A-S-H type cementing gels; they densify the structure of the cementing material.

References

[1] M. Amran, S. Debbarma, and T. Ozbakkaloglu, "Fly ash-based eco-friendly geopolymer concrete: A critical review of the long-term durability properties," *Constr. Build. Mater.*, vol. 270, p. 121857, 2021.

[2] S. França, M. V. de Moura Solar Silva, P. H. Ribeiro Borges, and A. C. da Silva Bezerra, "A review on some properties of alkali-activated materials," *Innov. Infrastruct. Solut.*, vol. 7, no. 2, 2022.

[3] A. A. Hoyos-Montilla, F. Puertas, and J. I. Tobón, "Microcalorimetric study of the effect of calcium hydroxide and temperature on the alkaline activation of coal fly ash," *J. Therm. Anal. Calorim.*, vol. 131, pp. 2395–2410, 2018.

[4] Z. Li, G. Xu, and X. Shi, "Reactivity of coal fly ash used in cementitious binder systems: A state-of-the-art overview," *Fuel*, vol. 301, no. May, p. 121031, 2021.

[5] Y. Zhang, W. Sun, and Z. Li, "Infrared spectroscopy study of structural nature of geopolymeric products," *J. Wuhan Univ. Technol. Mater. Sci. Ed.*, vol. 23, no. 4, pp. 522–527, 2008.

[6] A. A. Hoyos-montilla, J. I. Tobón, and F. Puertas, "Role of calcium hydroxide in the alkaline activation of coal fly ash," *Cem. Concr. Compos.*, vol. 137, no. 104925, pp. 1–10, 2023.

The 16th International Congress on the Chemistry of Cement 2023 (ICCC2023)
"Further Reduction of CO_2 -Emissions and Circularity in the Cement and Concrete Industry"
September 18–22, 2023, Bangkok, Thailand

High-performance eco-cement synthesized from municipal solid waste incineration bottom ash and recycled concrete fine

Shipeng Zhang[1, 2, a *], Hanxiong Lyu[1, 2, b], Chi-sun Poon[1, 2, c]

[1] *Department of Civil and Environmental Engineering, The Hong Kong Polytechnic University, Hong Kong*
[2] *Research Centre for Resources Engineering towards Carbon Neutrality, The Hong Kong Polytechnic University, Hong Kong*

[a] *Email: shipeng.zhang@polyu.edu.hk*
[b] *Email: hanxiong.lyu@polyu.edu.hk*
[c] *Email: chi-sun.poon@polyu.edu.hk*

ABSTRACT

With rapid urbanization and modernization, there are two major solid waste streams in modern society: incineration bottom ash (IBA) generated from the sintering of municipal solid waste, and recycled concrete fine (RCF) from the demolition of out-serviced infrastructures. Thus, the recycling and reusing of IBA and RCF are of great significance. A sustainable high-performance eco-cement was developed by this study exclusively from IBA and RCF. β-C_2S is the main mineral phase in this novel eco-cement system sintered at 1100 ℃, possessing good reactivity when exposed to greenhouse gas CO_2. This eco-cement was able to achieve a CO_2 uptake of 12.5%, consequently leading to a compressive strength of 113.7 MPa after 1-day carbonation curing, which is far higher than that of reference OPC (45.4 MPa). Subsequent hydration behavior of β-C_2S ensured the increment of compressive strength up to 136.9 MPa at 28 days. Calcium carbonate and low Ca/Si C-S-H are the main carbonization products that densified the microstructure of cement pastes, ultimately leading to high strength. The heavy metals leaching test proves that this eco-cement satisfies the US EPA standard without detrimental environmental impact. This study demonstrated the feasibility of using IBA and RCF to produce high-performance clinker, while the CO_2 emission could be significantly reduced from three aspects: 1. Lower clinkering temperature; 2. Low embodied carbon raw materials; 3. CO_2 sequestration through carbonation curing.

KEYWORDS: Incineration bottom ash, Recycled concrete fine, Sustainable cement, Carbonation curing, Low-carbon concrete

1. Introduction

The intensive emission of anthropogenic CO_2 has caused serious global environmental threats to human beings, among which cement production is one of the biggest contributors to this risk, accounting for 8% of the total global anthropogenic CO_2 emission (Olivier, J G et al., 2012). Furthermore, the formation of solid waste is another threat to humanity, of which municipal solid waste (MSW) and construction/demolition waste (C&D-W) are the two main streams (Abdel-Shafy, H I and Mansour, M S M, 2018; Hassan, S H et al., 2022). Incineration is a popular MSW disposal method compared to traditional landfilling, but it is not a fully circular solution due to the residues generated, particularly incineration bottom ash (IBA) that accounts for about 20% of original MSW waste by mass (Yan, K et al., 2020). For C&D-W, its recycling process could produce a considerable amount (20%) of recycled concrete fine (RCF), which has few chances of being applied to concrete due to its poor binding capability to the new paste matrix (Jiang, Y et al., 2022), which could lead to a decrease in the mechanical and durability properties of the subjected concrete. Therefore, the common destination for IBA and RCF remains the landfill.
On the other hand, from a chemical compositional point of view, both IBA and RCF are mainly

composed of Ca, Si, Al, and Fe, which might qualify them to be the raw feed in cement production. Several studies have been conducted to re-use either IBA or RCF in conventional OPC production, while the reported clinkering temperatures exceeded 1400 ℃ to mineralize the primary OPC clinker phase - C_3S(Clavier, K A et al., 2020; Shih, P-H et al., 2003). Compared to C_3S, C_2S requires less lime and a lower clinkering temperature of 1200 ℃, which has obvious benefits for CO_2 emission reduction. Although C_2S only possesses latent hydraulic properties, this phase has a strong carbonation reactivity (Wang, D et al., 2019). It is reasonable to target C_2S as the primary mineral phase in the clinker, which can develop satisfactory macroscopic strength and produce chemically stable carbonates.
This study explored the feasibility of synthesizing a novel low-carbon eco-cement by re-utilizing IBA and RCF as raw ingredients, in which C_2S was the target clinker phase. Characterizations were conducted, including mechanical performance, mineralogical analysis, morphology observation, and leaching behavior. The embodied carbon of the cement clinker was significantly reduced from three aspects: low clinkering temperature, low-carbon embodied solid wastes as raw feeds and active CO_2 sequestration.

2. Methods

IBA and RCF were locally collected, and CaO was additive. The D50 particle size of IBA, RCF, and CaO was 16.7 μm, 29.9 μm, and 17.5 μm, respectively. These three raw materials were mixed homogeneously using a V-shape blender before sintering. The raw feed of them by weight was 37.5/48.0/15.5. The raw mixture was respectively heated at 1000 °C, 1100 °C, and 1200 °C for 1 hour, labeled as EC1000, EC1100, and EC1200. The cylindrical cement pastes with a water/cement ratio of 0.12 (20 mm in diameter and 15 mm in height) were taken pure CO_2 carbonation curing for 1 day under 2 bars, followed by taking normal hydration curing in a water tank at 25 ℃ till the testing age of 28 days (28D). OPC pastes were the reference. The carbonation and hydration curing methods were abbreviated as C and H, respectively. The compressive strength was evaluated by Testometric X500-50, which was averaged by three values. CO_2 uptake capability was assessed by the mass gain method (Monkman, S and Shao, Y (2006)). The mineralogical analysis of the clinker was detected by quantitative X-ray diffraction (QXRD) coupled with the Rietveld method (20 wt% ZnO as the internal standard). The micromorphology of samples was observed by scanning electron microscope (SEM, Tescan VEGA 3) with an energy-dispersive X-ray (EDX) spectrometer. The Toxicity Characteristic Leaching Potential (TCLP) Method 1311 was conducted to monitor the regulated heavy metals leaching behavior of raw and cured clinkers.

3. Results and discussion

3.1 Mechanical performance and CO_2 uptake

In Table 1, all eco-cement pastes rapidly gained strength under carbonation curing for 1 day and obtained noteworthy strength increments at the age of 28 days, proving the strong carbonation reactivity and latent hydraulic behavior. EC1100 had the highest compressive strength at all testing ages, inferring that 1100 ℃ was the optimal sintering temperature. The CO_2 sequestration capacity of all eco-cement pastes was stronger than OPC, indicated by higher CO_2 uptake value for eco-cements marked in Table 1. However, CO_2 uptake decreased along with the temperature increase. The unmatched strength vs. CO_2 uptake could be related to considerable mineralogical variations between eco-cement batches listed in the next section.

Table 1 Compressive strength and CO_2 uptake of eco-cements pastes with OPC reference

	EC1000C	EC1100C	EC1200C	OPC-C	OPC-H
1 day (MPa)	75.0	113.7	59.2	45.4	30.5
28 days (MPa)	96.5	136.9	72.9	55.9	44.1
CO_2 uptake (%)	15.4	12.5	10.2	8.4	

3.2 Mineralogical analysis

Table 2 shows the mineralogical composition of raw and cured eco-cements. For raw clinker, besides the unidentified amorphous phase, β-C_2S was the primary mineral phase for all eco-cements, which content approaching a maximum of 44.9% for EC1100. γ-C_2S detected in EC1000 and EC1100 had a decreased content with the temperature increase. A lower sintering temperature would be difficult to form the solid

solutions of CaO and SiO_2 with more minor elements (such as Na, Mg, and K in used solid wastes), inhibiting the stabilization effect of minor elements on the polymorphism transformation from β-C_2S to γ-C_2S (Kurdowski, W, 2014). Therefore, more γ-C_2S existed at a lower temperature. The existence of this mineral might also be beneficial, as orthorhombic γ-C_2S could be substantially reacted with CO_2 and has a more robust CO_2 sequestration capability than β-C_2S (Fang, Y et al., 2020). When the sintering temperature was raised to 1200 ℃, rankinite (24.7%) was the new main phase, which has no hydraulic properties, while CO_2 can activate it to take a carbonation reaction.

After taking carbonation curing, the amounts of calcium silicates (such as C_2S and rankinite) were significantly decreased, and calcium carbonates (calcite and/or vaterite) were detected with the increased content of the "amorphous" phase. EC1100C1D (meaning that EC1100 with carbonation curing for 1 day) had the largest consumption rate of β-C_2S (69.9%) compared to other batches. The co-existence of different types of calcium silicates in other batches inevitably diluted the consumption of β-C_2S, which is the phase that can contribute to the highest strength. The differences in mineral consumption combined with different carbonization reactivity led to the vast gap of 1-day strength between batches shown in Table 1. Vaterite was the production of γ-C_2S, and the calcite was generated as the typical product of carbonated β-C_2S and rankinite (Chang, J et al., 2016; Wang, X et al., 2022).

Table 2 Mineralogical analysis of raw and cured clinkers

Phase	Raw			Carbonation curing		
	EC1000	EC1100	EC1200	EC1000	EC1100	EC1200
β-C_2S	44.4	44.9	19.8	17.4	13.5	9.5
γ-C_2S	7.0	1.1	0	0.3	0.4	0
Gehlenite	6.4	6.7	20.1	4.9	6.2	17.6
Diopside	4.3	3.3	2.5	1.3	2.7	0.3
Quartz	1.9	0.7	2.1	1.5	0.8	2.4
Rankinite	0	0	24.7	0	0	12.8
Amorphous	36.0	43.3	30.8	51.6	59.3	42.1
Calcite	0	0	0	16.2	17	15.2
Vaterite	0	0	0	6.7	0	0
Total	100.0	100.0	100.0	99.9	99.9	99.9

3.3 Micromorphology observation

Fig. 1 (a) exhibits the micrographs for fractured EC1100C1D, where small cube-like crystalline calcium carbonates (calcite) intermixed with an amorphous phase (C-S-H gel) could be detected. Only EC1100C1D was chosen in all carbonating batches due to the similar carbonation products (calcium carbonates and C-S-H/silica gel). Ca/Si ratio in the gel matrix was obtained through EDX analysis, followed by drawing its relationship with strength. Fig. 1 (b) shows a good linear correlation of the Ca/Si ratio vs. strength, demonstrating the essential influence of gel property on the mechanical performance of the eco-cement. At the optimal sintering temperature of 1100 ℃, β-C_2S-based eco-cement produced C-S-H gel with the largest Ca/Si ratio, ensuring a good binding capacity.

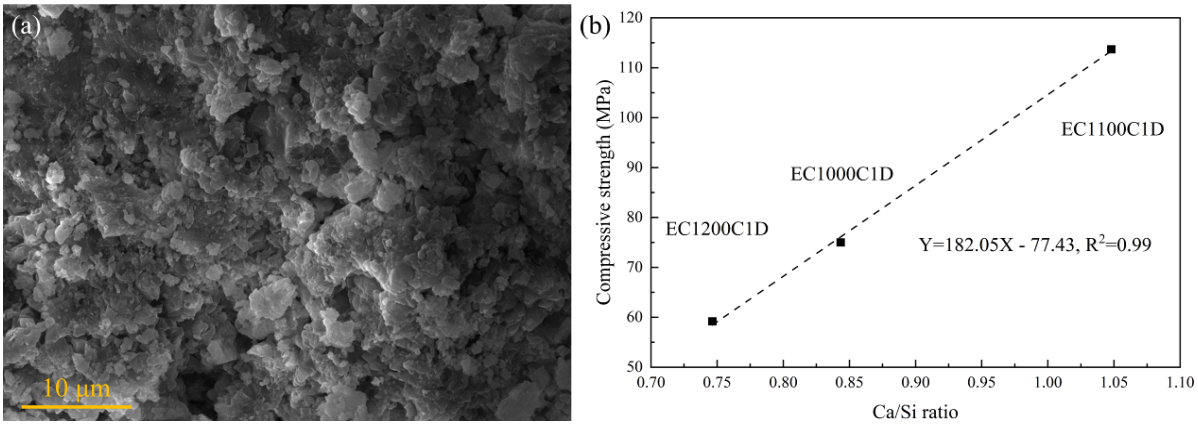

Fig. 1 (a) SEM observation of EC1100C1D; (b) Correlations between Ca/Si ratio and compressive strength

3.4 Leaching behavior

The criteria marked in Table 3 corresponded to the maximum concentration of targeted ions specified in TCLP (US, EPA, 2004). All eco-cements and cured samples had lower concentrations of heavy metals than the criteria thresholds, so these cements were called eco-cements. These results inferred that the eco-cements synthesized by solid wastes have few environmental detriments.

Table 3 Heavy metal ion concentrations of eco-cement leachates (mg/L)

	Cd	Se	As	Ag	Pb	Cr	Ba
Criteria	1	1	5	5	5	5	100
EC1000 raw	0.0181	0.133	0.129	0.141	0.109	2.795	1.307
EC1100 raw	0.0181	0.129	0.135	0.143	0.108	2.563	1.342
EC1200 raw	0.0182	0.134	0.147	0.14	0.11	1.658	2.863
EC1000 C1D	0.0182	0.126	0.122	0.136	0.111	1.133	0.577
EC1100 C1D	0.0187	0.138	0.13	0.138	0.111	1.533	0.953
EC1200 C1D	0.0186	0.135	0.13	0.137	0.112	0.562	2.203

4. Conclusions

This study demonstrated the feasibility of preparing high-strength ecological clinker by reusing IBA and RCF as main raw feeds. At the optimal incineration temperature of 1100 ℃, the eco-cement with the most β-C_2S content (44.9%) was obtained. EC1100 achieved the largest 1-day compressive strength of 113.7 MPa within 1-day carbonation curing, which value increased to 136.9 MPa at 28 days by subsequent hydraulic scenario. This clinker had no environmental leaching concern. The extensive usage of solid wastes (up to 85.5%) in the cement clinkering process could not only provide a new solution for waste management but also reduce the natural resource consumption in the cement industry.

Acknowledgements

We gratefully acknowledge the financial support of ITF and Everbright Environment Ltd. The equipment support from the UCEA at the Hong Kong Polytechnic University is also acknowledged.

References

Abdel-Shafy, H.I., Mansour, M.S.M., (2018). Solid waste issue: Sources, composition, disposal, recycling, and valorization. Egypt. J. Pet. 27(4), 1275-1290.

Chang, J., Fang, Y., Shang, X., (2016). The role of β-C2S and γ-C2S in carbon capture and strength development. Mater. Struct. 49(10), 4417-4424.

Clavier, K.A., Paris, J.M., Ferraro, C.C., et al., (2020). Opportunities and challenges associated with using municipal waste incineration ash as a raw ingredient in cement production – a review. Resour. Conserv. Recycl. 160.

Fang, Y., Liu, Z., Wang, Q., et al., (2020). Strength Development and Products Evolution of β-C2S and γ-C3S Induced by Accelerated Carbonation Curing. Journal of Wuhan University of Technology-Mater. Sci. Ed. 35(6), 1053-1060.

Hassan, S.H., Aziz, H.A., Johari, I., et al., 2022. Construction and Demolition (C&D) Waste Management and Disposal, in: Wang, L.K., Wang, M.-H.S., Hung, Y.-T. (Eds.), Solid Waste Engineering and Management: Volume 2. Springer International Publishing, Cham, pp. 165-216.

Jiang, Y., Shen, P., Poon, C.S., (2022). Improving the bonding capacity of recycled concrete aggregate by creating a reactive shell with aqueous carbonation. Constr. Build. Mater. 315, 125733.

Kurdowski, W., 2014. Cement and concrete chemistry. Springer Science & Business.

Monkman, S., Shao, Y., (2006). Assessing the Carbonation Behavior of Cementitious Materials. J. Mater. Civ. Eng. 18(6), 768-776.

Olivier, J.G., Peters, J.A., Janssens-Maenhout, G., (2012). Trends in global CO2 emissions. 2012 report.

Shih, P.-H., Chang, J.-E., Chiang, L.-C., (2003). Replacement of raw mix in cement production by municipal solid waste incineration ash. Cem. Concr. Res. 33(11), 1831-1836.

US, EPA., (2004). Test methods for evaluating solid waste, Physical/Chemical Methods (SW 846).

Wang, D., Fang, Y., Zhang, Y., et al., (2019). Changes in mineral composition, growth of calcite crystal, and promotion of physico-chemical properties induced by carbonation of β-C2S. J. CO2 Util. 34, 149-162.

Wang, X., Guo, M.-Z., Ling, T.-C., (2022). Review on CO2 curing of non-hydraulic calcium silicates cements: Mechanism, carbonation and performance. Cem. Concr. Compos. 133, 104641.

Yan, K., Sun, H., Gao, F., et al., (2020). Assessment and mechanism analysis of municipal solid waste incineration bottom ash as aggregate in cement stabilized macadam. J. Clean. Prod. 244, 118750.

The 16th International Congress on the Chemistry of Cement 2023 (ICCC2023)
"Further Reduction of CO_2 -Emissions and Circularity in the Cement and Concrete Industry"
September 18–22, 2023, Bangkok, Thailand

VALORIZATION OF A LOW-GRADE MAGNESIA AS A PRECURSOR IN THE PREPARATION OF MKPCs

I.Garcia-Lodeiro[1*], N. Husillos-Rodriguez[1], A. Palomo[1] and H. Kinoshita[2]

[1] *Eduardo Torroja Institute for Construction Science (IETcc-CSIC), Madrid, Spain*
[2] *University of Sheffield-Department of Material Science and Engineering, Sheffield, UK*
(*)Corresponding author Email: iglodeiro@ietcc.csic.es

ABSTRACT

This research explores the possibility of preparing MKPCs, as candidate to immobilise LL-IL radioactive waste, using a low-grade MgO (as a source of MgO), KH_2PO_4 (source of phosphates) and boric acid (as a retarder). Several MgO/KH_2PO_4 molar ratios (1, 2, 3 and 4) were tested. The effect of curing conditions, in a climatic chamber (21ºC, 99 % RH) or in the laboratory (21ºC, 52% RH) was also explored (up to 90 days). Mechanical strengths, changes in the porosity and the mineralogy of pastes were determined. The volume stability of mortars was also evaluated. The M/P ratio and the type curing highly affects the mechanical strengths and the stability of volume. For M/P ratios lower than 2, in addition to K-Struvite, different types of phosphates were identified. The curing in the climatic chamber, favours the fast dissolution of the phosphates and efflorescence were detected. For the lowest M/P ratio (M/P=1), when samples are cured in presence of high RH, the mechanical strengths declined with time and the specimens underwent expansion. However, MKPC cements prepared with M/P ratios ≥2, showed in general, good behaviour.

KEYWORDS: *Low-grade MgO; immobilisation; nuclear waste; magnesium phosphate cements; K-Struvite.*

1. Introduction

Magnesium phosphate cements (MKPCs) are produced through acid-base reaction commonly between phosphates and dead burnt magnesia, (Aminul et al. (2019)). Due to its low pH value and its low porosity, these cements are good candidates to immobilise specific nuclear wastes containing reactive metals, e.g. Al, Mg and U, (Gardner et al. (2021)). However this kind of cements, show some disadvantages; *i)* dead burnt MgO, used as basic precursor, is obtained after a calcination process of pure $MgCO_3$, at temperatures between 1600-2000ºC, which involves a very high energetic cost, not to mention additional cost such as separating the $MgCO_3$ from other impurities (i.e SiO_2, Fe_2O_3) that may be in the quarry as well *ii)* availability issues to ensure an adequate supply of raw material and *iii)* MPC are relatively new cements (the scientific literature on the chemical specifics of MPCs did not emerge until the early 1980s) and therefore additional studies are still required in relation to assess its durability.

The objective of the current work is to explore the possibility of using a low-grade magnesia (MgO ~58%), for the preparation of MKPCs and to analyse the effect of the curing conditions and the M/P molar ratio, on the mechanical properties, microstructure, mineralogy and volume stability.

2. Experimental

2.1 Materials

A low grade MgO, provided by MAGNESITAS NAVARRAS S.A, was used as a source of MgO. The mineralogical analysis (XRD, Rietveld analysis RWp 7.62) revealed that the main crystalline phase was periclase (MgO 57.62%). Some minor components, such as magnesite ($MgCO_3$, 25.77%), hematite (Fe_2O_3 2.30%), calcite ($CaCO_3$, 0.70%), dolomite ($MgCa(CO_3)_2$, 5.41%) , anhydrite ($CaSO_4$, 3.97%) and

quartz (SiO_2, 1.93%) were also detected. The particle size (measured by laser granulometry) showed a D90, D50 and D10 of 6.07 μm, 23.2 μm and 59.90 μm respectively, and the surface area (BET analysis) was 186.06 m^2/g. As source of phosphate, a KH_2PO_4 soluble salt (sold as fertilizer) with a purity >98 wt. % was used. A laboratory-grade boric acid (H_3BO_3) with a purity >99.5 wt. % was added as retarder.

2.2 Preparation of pastes and mortars

Table 1 shows the dosification of the pastes prepared. All systems were produced with the same w/b ratio, but with different MgO/KH_2PO_4 (M/P) molar ratio. With pastes, primatic specimens (1*1*6 cm^3) (See Fig.1) were prepared and cured under two types of curing; *i)* in the climatic chamber (CC) at 21ºC, 99% RH and *ii)* in the laboratory (LAB) (at 21ºC, 52 % RH). After 1d, 7d , 28d and 90d the mechanical strengths were tested. Selected samples were chracterised from the mineralogical (XRD) and microstructural (MIP) point of view.

Table 1 . Dosification of the pastes prepared.

PASTES		
M/P molar	**Boric ac./ (KH_2PO_4+ MgO) (mass)**	**w/b* mass**
1	0.025	0.25
2	0.025	0.25
3	0.025	0.25
4	0.025	0.25

**b=Binder: Low grade MgO+ KH_2PO_4*

Fig. 1 Physical aspect of MKPCs pastes prepared with different M/P ratios (efflorescences are detected at M/P=1)

Additionally, mortars (prismatic specimens of 2.5*2.5*28.5 cm^3) of MKPC with the same sand/binder mass ratio of 1 and water/binder mass ratio of 0.3, but with different M/P molar ratios (1,2,3 and 4) were prepared and cured under the same conditions than pastes (CC and LAB). The stability of volume was recorder during 90 d. Samples were storage in the CC and in the LAB and the length change was periodicallly measured duing this 90d.

3. Results and discussion

Fig. 2 shows the compressive mechanical strengths with time of the different pastes, when are cured in the climatic chamber (CC) (Fig. 2(a)) and in the laboratory (LAB) (Fig. 2(b)). In general term, the compressive strengths increase with the increasing of the M/P ratio, but up to 3. Above this value the strengths remains practically in the same order than systems prepared with M/P =3. For the same M/P ratio, the initial strengths developed in the systems cured at the laboratory (21ºC, 50 % RH) are higher than those cured in the chamber, which agrees with previous studies described in the literature (Linlin Chong et al (2017)). What is more, the strengths corresponding to the system prepared with the lowest M/P ratio (M/P=1) decrease with time in samples cured in the climatic chamber. The relative humidity plays a substantial role on the early reaction stages, favouring the rapid dissolution of the phosphates, which would induce the formation of efflorescences (see Fig. 1). The rapid dissolution of phosphates would induce changes in the microstructure, which will affect the mechanical development (see Fig. 2(a)).

(a)

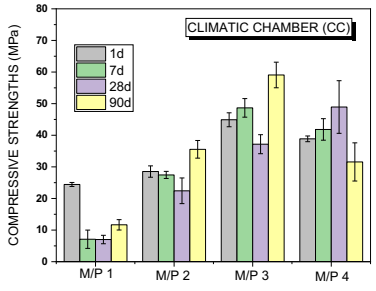

(b)

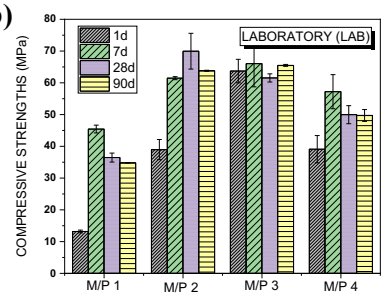

Fig. 2 Compressive strengths of the MKPCs pastes cured in (a) Climatic chamber (21ºC, 99% RH) (b) Laboratory (21ºC, 52% RH)

Fig. 3 shows the MIP results (total porosity and pore size distribution) after 28 days, of systems cured both media (CC and LAB). In general term, there was a decrease in the total porosity with the increasing of the M/P ratio, especially up to M/P =3. Samples cured in the CC show higher porosities than those cured in the laboratory, and this is much more notable in sample prepared with the lowest M/P (M/P 1), which is in agreement with the mechanical strengths (see Fig. 2). The high content of water during the curing (99% RH) would promote the fast dissolution of phosphates, which will be reflected in an important increase in the total porosity and therefore in the drop of the strengths. Pore size distribution is also slightly different depending on the type of curing; the more representative pores in samples cured in the LAB are range between 1-10 μm and 01-1 μm, while bigger pores (≥ 10 microns) are observed in systems cured in the CC.

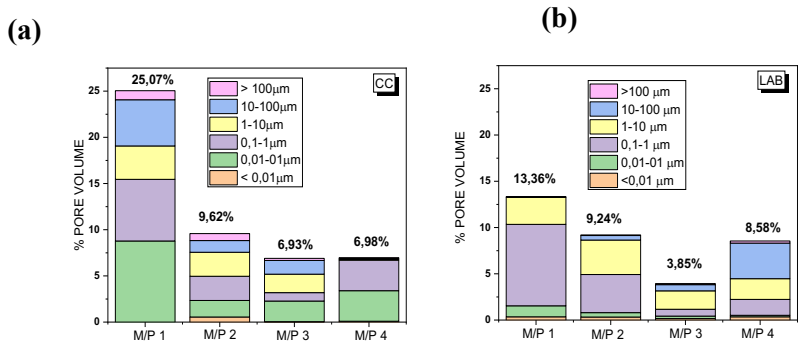

Fig. 3 Total Porosity and Pore Size Distribution of MKPC pastes cured at **(a)** Climatic chamber (CC) **(b)** Laboratory (LAB)

Fig. 4 (a) and (b) show respectively the XRD pattern of the different MKPCs systems cured in the CC and in the LAB (after 28 days). In all the systems, regardless the type of curing or the M/P ratio, the main reaction product is the K-Struvite. Unreacted particles of periclase were detected in all the samples (obviously, its intensity is higher in samples prepared with higher initial M/P ratios). The minor phases, present in the low- grade MgO (such as magnesite, dolomite, anhydrite…etc) were also detected in all the samples and seems not to affect to K-Struvite formation. Samples prepared with the lowest M/P ratio (M/P=1), additionally shows peaks associated with secondary phosphate salts, such as $Mg_2KH(PO_4)_2(H_2O)_{15}$, especially in those samples cured in the LAB. In general term, at M/P=1, K-Struvite is better crystallised in systems cured in the CC than in the LAB. The high relative humidity of this environment would favour the dissolution of phosphates promoting a better crystallization.

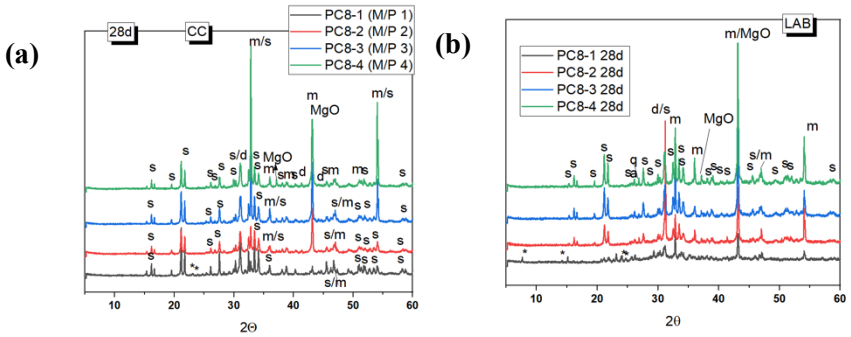

Fig. 4 XRD patterns of MKPCs prepared with different M/P ratios (a) cured in the CC (b) in the LAB (legend: S. K-Struvite $KMgPO_4.6H_2O$; MgO; m: magnesite ($MgCO_3$), d; dolomite; *: $Mg_2KH(PO_4)_2(H_2O)_{15}$)

Finally, the volume stability of the mortars was analysed. Fig. 5(a) and (b) shows respectively changes in the volume of the mortars prepared with different M/P ratio, when are storage in the CC (99 %RH, 21ºC) and when are maintained in the LAB (52%RH, 21ºC). As can be seen in this figure, volume stability is highly dependent on both the M/P ratio and the curing conditions. Samples cured in the CC (Fig. 5(a)), show good volume stability all systems, with the exception of the one prepared with M/P=1, where a clear expansion (up to 0.4 %) was observed. Samples with M/P of 2 and 3, cured, and storage in the LAB show a slightly shrinkage, while this shrinkage is much more significant in samples M/P= 1 and 4, even achieving in the first one around 0.8% shrinkage after 90 days. Further studies are needed to clarify this point. Future research will also include the evaluation of the durability of these cements under different kind of attacks (chemical attacks, freeze-thaw, carbonation....) and their role as a confining matrix of LL radioactive waste such as spent ion exchange resins).

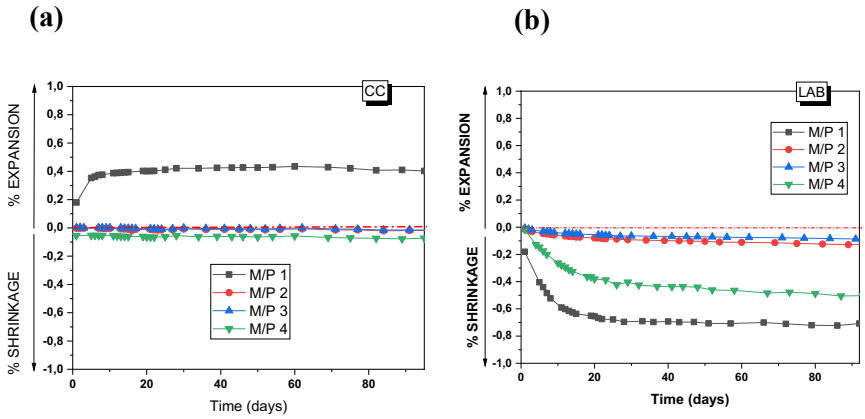

Fig. 5 Volume stability of MKPC mortars during 90d when are stored in **(a)** CC **(b)** LAB

4. Conclusions

Based on the previous results it can be concluded that; *i)* Low grade MgO (~ 58% MgO) can be used to produce MKPC cements. The presence of minor phases seems not to affect to the formation of the main reaction product which is the K-Struvite; *ii)* Mechanical Strengths, total porosity, pore size distribution and volume stability are going to be highly dependent on the M/P ratio used and *iii)* Systems with better performance correspond with M/P ratios of 2 and 3.

Acknowledgements

This work is part of a JIN project of the National Plan (PID PID2020−116738RJ−100), financed by the Spanish Ministry of Science and Innovation.

References

Aminul Haque M. , Bing Chen (2019) "Research progresses on magnesium phosphate cement: A review" , *Construction and Building Materials* 211 885–898

Gardner, L.J.; Corkhill, C.L.; Walling, S.A.; Vigor, J.E.; Murray, C.A.; Tang, C.C.; Provis, J.L.; Hyatt, N.C. (2021) "Early Age Hydration and Application of Blended Magnesium Potassium Phosphate Cements for Reduced Corrosion of Reactive Metals", *Cement and Concrete Research* 143, doi:10.1016/j.cemconres.2021.106375.

Linlin Chong , Jianming Yang , Caijun Shi (2017), "Effect of curing regime on water resistance of magnesium–potassium phosphate cement" *Construction and Building Materials* 151 43–51

The 16th International Congress on the Chemistry of Cement 2023 (ICCC2023)
"Further Reduction of CO_2 -Emissions and Circularity in the Cement and Concrete Industry"
September 18–22, 2023, Bangkok, Thailand

Effect of organic ligands in AAM binders

J. Yliniemi[1*], R. Ramaswamy[1], S. Bagheri[1], M. Akbarzadeh Khoei[1]

[1] *University of Oulu, Oulu, Finland*

**Email: juho.yliniemi@oulu.fi*

ABSTRACT

The sufficient rate and extent of dissolution of aluminosilicate precursors are crucial when preparing alkaline activated materials (AAMs). Traditional approach to achieve the needed reactivity is to use highly concentrated alkaline solutions – typically a mixture of sodium hydroxide and sodium silicate solutions. However, their use is not preferred as alkaline solutions are causing most of the environmental impact of AAMs; they are not user friendly due to the high alkalinity; they are the most expensive component of the mix; and cause efflorescence and instability of the binder. Instead, it could be possible to use small amounts of metal complexing ligands to improve the dissolution of the solid precursors without the need for high concentrated aggressive alkaline media. This work presents the effect of various conjugate bases of organic and inorganic acids (called as 'ligands' here) on the extent of dissolution of multi-oxide silicate materials, and on the fresh and hardened properties of the prepared AAM binders. The results show that extent of dissolution is increased by formation of various Al-, Mg-, Ca-, and Fe-complexes. Furthermore, in the presentation we will show how certain ligands can accelerate the reaction kinetics and improve the 1-day strength of typical Na_2CO_3-activated BFS from 4 MPa (without ligand) to 16 MPa (0.1 wt.% ligand dosage). We also present how ligands affect the surface properties of the precursors as analyzed by X-ray Photoelectron Spectroscopy and zeta potential measurements.

KEYWORDS: *alkaline activated materials, reactivity, ligands, dissolution, aqueous speciation*

1. Introduction

Alkaline activated materials (AAMs) are intensively investigated by cement science community due to their lower CO_2 emissions and lower energy requirements in production compared to Portland cement (Provis 2018). AAMs are produced by combining two main raw materials: natural or artificial aluminosilicates as solid powder precursor, and an alkaline activator.

While the most common solid precursors are ground granulated blast furnace slag (BFS) and coal fly ash, various other aluminosilicates could be potential AAM precursors as well, such as steel slags (Sun et al. 2020), biomass ashes (Shearer et al. 2016), and synthetic glasses (Alzeer et al. 2022). Alkaline activator is often mix of sodium silicate and NaOH solutions, which initiates the dissolution of the solid aluminosilicate precursor and provides suitable pH for cementitious phases to precipitate. However, using highly alkaline solutions has several downsides since they cause most of the environmental impact of AAMs; they are user non-friendly due to the high alkalinity; they are the most expensive component of the mix; and excess Na may cause efflorescence and instability of the binder. (Özçelik and White 2016; Luukkonen et al. 2018)

The performance of solid precursor depends largely on their extent and rate of dissolution i.e., reactivity in alkaline environment. Overall, reactivity of solid precursor is a complex process and depends on factors such as chemical composition, mineralogy, and surface area, and solution properties such as pH and activator properties (anionic group and concentration) (Kucharczyk et al. 2019).

During dissolution, reactions between H^+, H_2O, and OH^--ions and elements on the solid precursor surface occurs. In general, dissolution rate of silicate minerals decreases by increasing the amount of tetrahedral [SiO_4] units in their structure (Oelkers, Schott, and Devidal 1994; Chave et al. 2011). However, dissolution is also affected by adsorption and precipitation of ions on the surface (Maraghechi et al. 2016; Bagheri et

al. 2022). For example, Al adsorption and precipitation on the solid surface has been observed to significantly slow down dissolution rate of silicate materials at acidic, neutral, and alkaline conditions (Bagheri et al. 2022; Yliniemi 2022). In general, each positively charged metal ion can potentially neutralize negatively charged aluminosilicate surface, thus stabilizing the surface, and slow down the dissolution, depending on the silicate surface and solution properties.
Metal complexing ligands could potentially decrease the concentration of metal ions on silicate surface, consequently increasing the extent and rate of dissolution of aluminosilicates (Yliniemi 2022). In order to form a soluble complex, the affinity between the ligand and metal ion should be strong enough to have interaction between them, but not too strong so that the metal-ligand complex would precipitate and consequently decreasing metal ion participation in later cementitious phase forming reactions. Furthermore, ligands can also compete with OH-ions for metal ions under alkaline conditions, thereby reducing the extent of precipitation of $Ca(OH)_2$ and $Mg(OH)_2$, for instance.
This work investigated the effect of various ligands on dissolution of basalt glass. The chemical composition of basalt glass is similar to that of BFS, but with lower Ca content and higher Fe content, thus providing sufficient concentration of various metals for complex formation reactions. Batch dissolution experiment results are presented with short discussion about surface precipitation reactions. In the conference presentation, these results are extended to also present the effect of ligands on hardening kinetics of alkaline activated BFS.

2. Materials and methods

Batch dissolution tests were conducted by mixing basalt glass (Table 1) and 0.1 M NaOH solution with liquid-to-solid ratio 1000 in a glove box under N_2 atmosphere for 24 h at 23 °C. Ligand dosage was 4.6 mmol/L. Ligands studied were oxalate, salicylate, catecholate, acetate, tannate, humate, 3,4-dihydroxybenzoate (DHBA), 2,3-dihydroxynaphthalene (DHNP), and tetrapotassium pyrophosphate (TKPP). After each specific reaction time, bottles were removed from the glove box and the suspension was first filtered using 2–5-µm pore diameter Whatman filter paper and then the filtrate was passed through a 0.45-µm pore filter syringe. The filtered solution was then acidified with 2 % HNO_3 solution and stored at 4 °C until ICP-MS analysis. Solids were washed with cold isopropanol to stop further dissolution, then air-dried and stored in a desiccator for further analysis.
Zeiss Sigma field emission scanning electron microscope and JEOL JEM-2200FS scanning transmission electron microscope (STEM) equipped with EDS with an acceleration voltage of 200 kV and working depth of 1–2 µm were used for surface characterization of basalt glass after dissolution tests.

Table 1. Basalt glass composition as determined by XRF.

	CaO	**SiO_2**	**Al_2O_3**	**Fe_2O_3**	**Na_2O**	**K_2O**	**MgO**	**TiO_2**	**SO_3**
Basalt glass	21.9	41.1	15.2	4.0	2.7	0.7	9.0	1.8	0.3

3. Results

Figure 1 presents concentration of Si, Al, Ca, Mg, and Fe in leachate solution after dissolution experiments. All the ligands increased the concentration of elements in solution, except for acetate. Higher concentration of Si in solution indicates higher extent of dissolution. However, due to possible precipitation of cementitious phases such as calcium silicate hydrates (C-S-H) during dissolution experiments, the extent of dissolution cannot be concluded solely based on the Si concentration in solution.
Tannate increased Si concentration over 5 times compared to reference sample, also providing high concentrations of soluble Mg and Fe, which were absent in reference sample. Tannate is a big molecule with numerous phenol groups which can complex high number of cations. Also, humate has various functional groups such as amino, carboxylic, sulfhydryl, phenolic groups, however its effectiveness in providing aqueous elements to leachate solution was not as good as that of tannate.
Other ligands that provided soluble Mg and Fe, were catecholate, 3,4-dihydroxybenzoate, and 2,3-dihydroxynaphthalene. The fact that salicylate and 3,4-dihydroxybenzoate had significantly different dissolution results, despite they have similar molecular structure, shows that the position and number of functional groups of the ligand has a big impact on their effectivity as dissolution accelerating reagent.

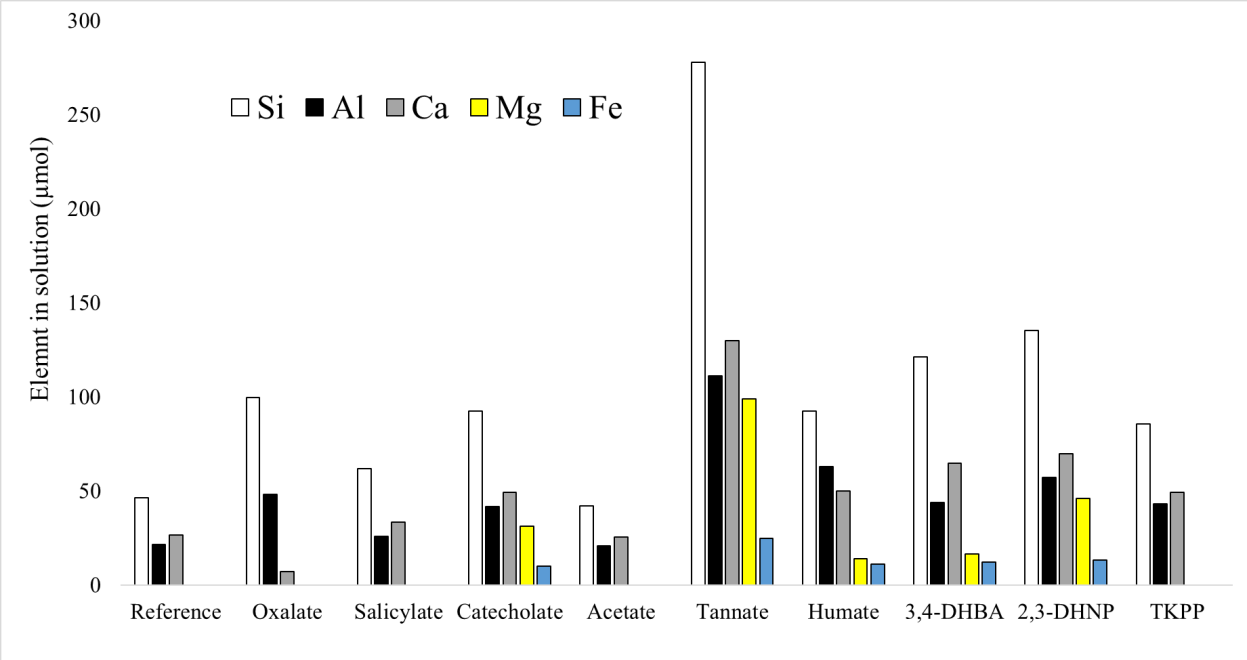

Figure 1. Batch dissolution experiments of basalt glass with various ligands. Experimental conditions: 0.1 M NaOH solution, L/S 1000, ligand dosage 4.6 mmol/L, mixing time 24 h, temp. 23 °C.

Figure 2 shows formation of Mg-Al/Fe layered double hydroxides and possibly some C-S-H on the surface of the reference sample (i.e., sample with no ligand), consistent with earlier research (Ramaswamy, Yliniemi, and Illikainen 2022). As an example of the effect of the ligand, in the presence of catecholate (Fig. 2c) Mg-Al/Fe layered double hydroxides are absent, although some surface precipitates are still observable. This demonstrates that ligand prevents the formation of surface precipitates and provides increased concentration of those elements to solution as seen in Fig. 1.

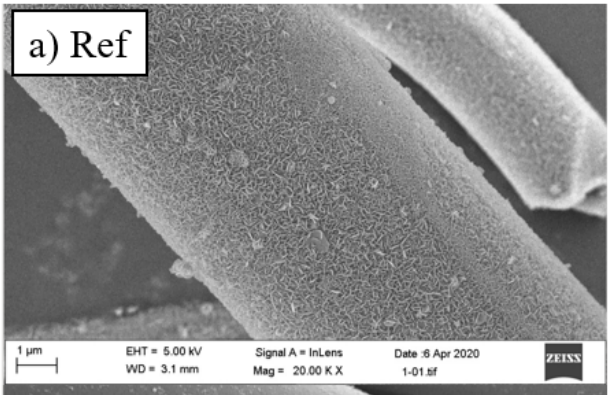

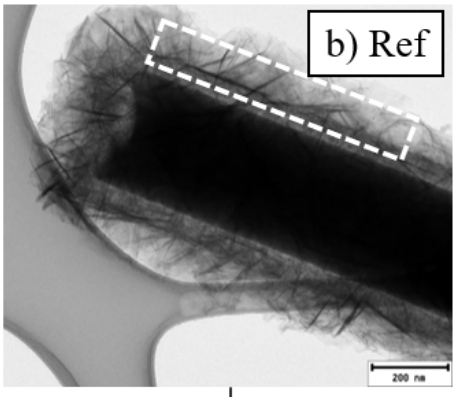

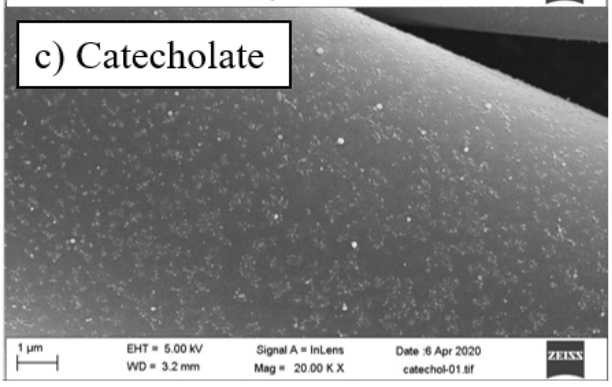

Element	At.%
Mg	21.4
Al	3.7
Si	8.3
Ca	2.6
Ti	1.7
Fe	6.4
C	5.1
Na	0.9

Figure 2. SEM-image of a) surface of basalt glass after dissolution experiments; b) STEM-image of reference sample and EDS-analysis of the marked rectangular area; c) SEM-image of basalt glass surface after dissolution experiments in the presence of catecholate.

3. Conclusions

Low reactivity of aluminosilicate precursors decreases their utilization potential for alkaline activated materials. Here, the effect of various ligands on multi-oxide silicate glass dissolution was investigated with batch dissolution experiments. Ligands increased the extent of dissolution, the effect being dependent on the molecular structure: type of ligand functional groups, number of functional groups, and position of functional groups. Ligands can prevent formation of common surface precipitates such as Mg-Al layered double hydroxides, consequently providing increased concentrations of soluble Al, Mg and Fe to pore solution. This work acts as a starting point for development of new chemical admixtures for alkaline activated materials.

Acknowledgements

This work was funded by Academy of Finland (grant # 322786). Techniques for the characterization of materials were conducted with the support of the Centre of Material Analysis, University of Oulu, Finland.

References

Al-Zeer, M. I. M., Nguyen, H., Fabritius, T., Sreenivasan, H., Telkki, V-V., Kantola, A. M., Cheeseman, C., Illikainen, M., and Kinnunen, P. 2022. "On the Hydration of Synthetic Aluminosilicate Glass as a Sole Cement Precursor." *Cement and Concrete Research* 159 (September): 106859. https://doi.org/10.1016/j.cemconres.2022.106859.

Bagheri, M., B. Lothenbach, M. Shakoorioskooie, and K. Scrivener. 2022. "Effect of Different Ions on Dissolution Rates of Silica and Feldspars at High PH." *Cement and Concrete Research* 152 (February): 106644. https://doi.org/10.1016/j.cemconres.2021.106644.

Chave, T., Frugier, P., Gin, S., and Ayral, A., 2011. "Glass–Water Interphase Reactivity with Calcium Rich Solutions." *Geochimica et Cosmochimica Acta* 75 (15): 4125–39.

Kucharczyk, S., Zajac, M., Stabler, C., Thomsen, R. M., Ben Haha, M., Skibsted, J., and Deja, J. 2019. "Structure and Reactivity of Synthetic CaO-Al2O3-SiO2 Glasses." *Cement and Concrete Research* 120 (June): 77–91. https://doi.org/10.1016/j.cemconres.2019.03.004.

Luukkonen, T., Abdollahnejad, Z., Yliniemi, J., Kinnunen, P., and Illikainen, M. 2018. "One-Part Alkali-Activated Materials: A Review." *Cement and Concrete Research* 103 (January): 21–23. https://doi.org/10.1016/j.cemconres.2017.10.001.

Maraghechi, H., Rajabipour, F., Pantano, C. G., and Burgos, W. D. 2016. "Effect of Calcium on Dissolution and Precipitation Reactions of Amorphous Silica at High Alkalinity." *Cement and Concrete Research* 87 (September): 1–13. https://doi.org/10.1016/j.cemconres.2016.05.004.

Oelkers, E. H., Schott, J., and Devidal, J-L., 1994. "The Effect of Aluminum, pH, and Chemical Affinity on the Rates of Aluminosilicate Dissolution Reactions." *Geochimica et Cosmochimica Acta* 58 (9): 2011–24.

Özçelik, V. O. and White, C. E., 2016. "Nanoscale Charge-Balancing Mechanism in Alkali-Substituted Calcium–Silicate–Hydrate Gels." *The Journal of Physical Chemistry Letters* 7 (24): 5266–72. https://doi.org/10.1021/acs.jpclett.6b02233.

Provis, J. L. 2018. "Alkali-Activated Materials." *Cement and Concrete Research* 114: 40–48. https://doi.org/10.1016/j.cemconres.2017.02.009.

Ramaswamy, R., Yliniemi, J., and Illikainen, M. 2022. "Dissolution-Precipitation Reactions of Silicate Mineral Fibers at Alkaline PH." *Cement and Concrete Research* 160 (October): 106922. https://doi.org/10.1016/j.cemconres.2022.106922.

Shearer, C. R., Provis, J. L., Bernal, S. A., and Kurtis, K. E. 2016. "Alkali-Activation Potential of Biomass-Coal Co-Fired Fly Ash." *Cement and Concrete Composites* 73 (October): 62–74. https://doi.org/10.1016/j.cemconcomp.2016.06.014.

Sun, J., Zhang, Z., Zhuang, S., and He, W. 2020. "Hydration Properties and Microstructure Characteristics of Alkali–Activated Steel Slag." *Construction and Building Materials* 241 (April): 118141. https://doi.org/10.1016/j.conbuildmat.2020.118141.

Yliniemi, J. 2022. "Surface Layer Alteration of Multi-Oxide Silicate Glasses at a Near-Neutral pH in the Presence of Citric and Tartaric Acid." *Langmuir* 38 (3): 987–1000. https://doi.org/10.1021/acs.langmuir.1c02378.

The 16th International Congress on the Chemistry of Cement 2023 (ICCC2023)
"Further Reduction of CO_2 -Emissions and Circularity in the Cement and Concrete Industry"
September 18–22, 2023, Bangkok, Thailand

Utilization of carbonated steel slag powder in cementitious materials

N. Li[1], C. Unluer[2*]

[1] *Department of Mechanical, Aerospace and Civil Engineering, University of Manchester, M13 9PL Manchester, United Kingdom*
Email: ning.li-3@manchester.ac.uk
[2] *Department of Mechanical, Aerospace and Civil Engineering, University of Manchester, M13 9PL Manchester, United Kingdom*
Email: cise.unluer@manchester.ac.uk

ABSTRACT

Steel slag is produced in large quantities as a by-product of primary steel-making, which is mainly landfilled or used as an aggregate. The high reactivity of steel slag with CO_2 makes it an ideal material for CO_2 capture, resulting in the formation of calcite, even at ambient temperatures and pressures. In this study, the direct carbonation of steel slag under 10% CO_2, 25ºC, and ambient pressure was investigated. The carbonated steel slag was then used in the preparation of cement paste samples, where 20% (by mass) of cement was replaced by carbonated steel slag. The prepared samples were cured under ambient conditions for up to 28 days. Results revealed that the carbonation of steel slag mainly occurred in the first 6 hours, enabling an increased CO_2 uptake by 5.2%. Carbonation reaction reduced the content of free calcium oxide in steel slag, resulting in the formation of calcite composed of non-uniform particles. Compared with cement paste samples containing uncarbonated steel slag, those involving steel slag carbonated for 3 hours achieved 22% higher 28-day compressive strengths. However, a decline in strength was observed with an increase in the carbonation duration, which was linked with the carbonation of the silicate phase in steel slag. Overall, this study highlighted the carbon sequestration capacity of steel slag and the potential benefits of this process in enhancing the mechanical and microstructural properties of resulting cement formulations.

KEYWORDS: *Steel slag, carbonation, compressive strength, microstructure, calcite*

1. Introduction

Cement manufacture is responsible for around 8% of global carbon dioxide (CO_2) emissions. A solution to address the reduction of the carbon footprint of construction materials involves the reduction of the cement content by substituting it with a more sustainable alternative (Mahasenan et al., 2003). Over 400 million tonnes of steel slag are produced globally each year from steel and iron production, according to the World Steel Association (Pan et al., 2017). The disposal of industrial wastes to landfill is a waste of resources and can cause significant pollution to farmland and freshwater due to the leaching of heavy metals.
Steel slag is abundant in highly CO_2-reactive minerals, such as α-C_2S, β-C_2S, and free MgO/CaO (Song et al., 2021). The CO_2 uptake capacity of steel slag could range from 200 to 400 g CO_2/kg, depending on carbonation conditions (Humbert and Castro-Gomes, 2019). However, the treatment of steel slag under low CO_2 concentrations and ambient temperature and pressure has not been widely investigated due to the slow carbonation kinetics (Li et al., 2022). The aim of this paper is to develop carbonated steel slag powder (SSP) as a supplementary cementitious material (SCM) in cement pastes. The carbonation kinetics and products of SSP at 10% CO_2 concentrations were investigated via gas-solid carbonation. The carbonated SSP was incorporated into the cement paste at a content of 20% (by mass of binder), followed by an evaluation of the mechanical and microstructural properties of the developed mixes.

2. Materials and Methodology

2.1 Materials

The steel slag was ground in a ball mill grinder to produce a fine powder with particles passing through a sieve size of 125 μm. A high strength Portland cement (PC) CEM I 52.5R with density and specific surface area of 3.15 g/cm^3 and 4200 cm^2/g, respectively, was used to prepare cement paste. The cement and steel slag had the same fineness, thereby the latter could be used as a direct replacement in the prepared mixes. The chemical compositions of the cement and steel slag, determined by X-ray fluorescence (XRF), are provided in Table 1.

Table 1. Chemical composition of cement and steel slag (wt.%)

	SiO_2	Al_2O_3	Fe_2O_3	CaO	MgO	SO_3	K_2O	Na_2O	LOI
Cement	19.38	4.94	2.87	62.89	3.4	3.29	0.35	0.35	0.99
Steel slag	13.88	8.66	22.15	35.95	9.83	0.28	0.06	0.31	3.13

2.2 Carbonation of SSP and sample preparation

The dried SSP was placed in a carbonation incubator under 20°C, 60% RH and 10% CO_2 concentration for 1, 3, 6, 24, 72, 168, 480 and 672 hours (C1h, C3h, C6h, C1d, C3d, C7d, C20d and C28d). Then 20% carbonated SSP by mass of cement was mixed with cement to produce cement paste with a water-to-binder (cement + steel slag) ratio of 0.5. The SSP and cement were added in mixing pot, and then mixed for 90 s until uniform. Then the solution was added, and stirred for the next 3 min. The paste mixes were cast into 20 × 20 × 20 mm^3 cubic moulds and compacted by a vibrating table. After being cured in the laboratory for 24 hours, the specimens were cured under 20°C and 95% RH for 3 and 28 days.

2.3 Experimental methods

The compressive strength of samples was measured using a compression machine, with a loading rate of 0.5 ± 0.1 MPa/s. The tests were carried out on three specimens for each mix and average strengths were taken as results. Thermogravimetric analysis (TGA) was conducted to evaluate the weight loss and corresponding peaks within each sample. 10 mg of each sample in powder form was heated from 30°C to 1000°C under a nitrogen atmosphere at rate of 10 °C/min in a TGA instrument (TGA8000, PerkinElmer). The TGA data was used to estimate the CO_2 uptake during the curing process of each sample, following Eq. (1).

$$CO_2Uptake_{wt.\%} = \text{mass loss between 500 and 950°C/mass at 1000°C} \times 100\% \quad (1)$$

Scanning electron microscopy (SEM) imaging was carried out by a Carl Zeiss Sigma for the microstructural analysis of the hydrate and carbonate phases in each sample. The dried samples were coated with gold before the SEM observation.

3. Results and Discussion

3.1 Carbonation of SSP

Fig. 1 shows the TGA curves and CO_2 uptake development of SSP with different carbonation duration. The mass loss occurred in the range of 30-200°C represent the water loss during the dehydration of reaction products (main C-S-H gel phases), which implies that the SSP presents in the samples experienced some form of hydration reaction. The mass loss occurred in the range of 400-500°C corresponding to dehydration of uncarbonated $Ca(OH)_2$ (Dung and Unluer, 2018), which suggests that uncarbonated calcium and magnesium was still present in the samples following carbonation. The mass loss occurred in the range of 500-800°C represent the decarbonation of magnesium and calcium carbonates (Li et al., 2017). As the carbonation duration increased, the mass loss in this interval gradually increased, indicating that more carbonate was generated. Steel slag has a low hydration reactivity, possessing highly CO_2-reactive minerals such as α-C_2S, β-C_2S, and free MgO/CaO. At a 10% CO_2 concentration, the carbonation of the SSP occurred predominantly within the first 6 hours, when the CO_2 uptake increased from 2.1% to 5.2%. Increasing the carbonation duration to 672 hours resulted in only a 7.7% CO_2 uptake. This is due to the available calcium content of the SSP, and the carbonation was further constrained by the produced calcium carbonate adhering to the surface of the SSP particles. At such a low

CO_2 concentration and atmospheric pressure, it was challenging for CO_2 to penetrate the dense carbonation layer on the particle surface and continue to react with the slag.

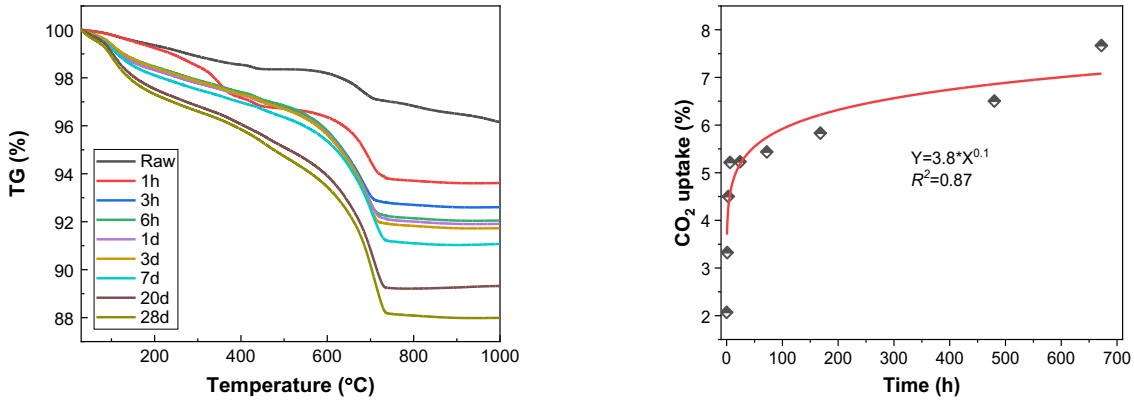

(a) TGA curves (b) CO_2 uptake development

Fig. 1. (a) TGA curves and (b) CO_2 uptake development of SSP with different carbonation duration

3.2 Compressive strength

Compressive strength of cement paste samples involving 20% carbonated SSP at 28 days is shown in Fig. 2. The addition of 20% uncarbonated and carbonated SSP significantly reduced the compressive strength of the cement paste. As an example of the 28-day strength, the addition of 20% uncarbonated SSP, C3h, C1d, C7d and C28d SSP reduced the strength of the cement paste by 27.3%, 11.6%, 21.3%, 27.8% and 34.1% respectively. This suggests that shorter carbonation treatment duration (within 3 hours) of the SSP improved the compressive strength of the specimens, whereas longer carbonation treatment durations of the SSP decreased the compressive strength. The prolonged carbonation duration could have, on the one hand, reduced the hydraulic mineral phases in the SSP and, on the other, promoted the transformation of calcium carbonate to the more stable crystalline form of calcite. Shen et al. (Shen et al., 2022) demonstrated that the needle-like whiskers characteristic of aragonite could strengthen cement and significantly improve its mechanical properties. It is worth noting that a longer carbonation duration was more beneficial for early strength. As shown in the Fig. 2, a maximum 3-day compressive strength of 59.2 MPa was achieved with the addition of 20% C7d SSP. The mechanism behind needs to be further explored.

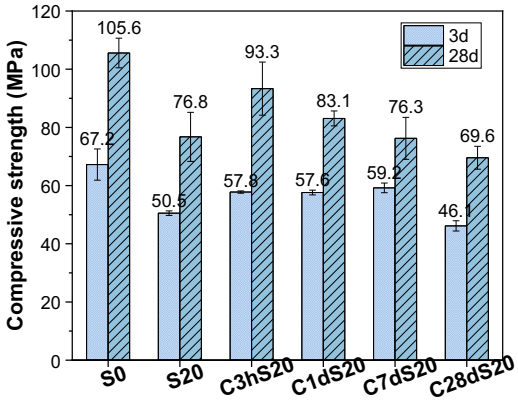

Fig. 2. Compressive strength of cement paste samples involving 20% carbonated SSP at 28 days

3.3 SEM observation

The SEM images of SSP after 3 hours and 28 days of carbonation are presented in Fig. 3. After 3 hours of carbonation, aragonite whisker-rich materials were generated with a length of approximately 200 nm and a diameter of approximately 20 nm. These whiskers acted as microfibres within the cement paste and contributed to the mechanical properties of sample (Shen et al., 2022). After 28 days of carbonation, the SSP consisted primarily of granular calcite crystals with particle sizes between 30 and 50 nm.

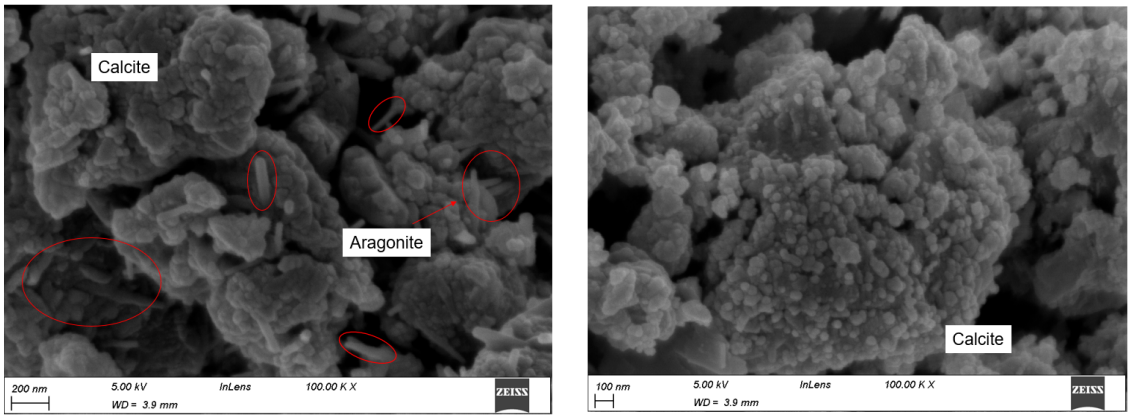

(a) C3h (b) C28d

Fig. 3. SEM pictures of SSP with (a) 3 hours and (b) 28 days carbonation

4. Conclusions

This study investigated the carbonation kinetics and microstructure of SSP under 10% CO_2, 25ºC, and ambient pressure. The use of carbonated SSP in cement pastes at 20% by mass of cement was evaluated via the assessment of mechanical and microstructural properties. Carbonation of SSP occurred mainly in the first 6 hours, with a CO_2 uptake of 5.2%. The rate of CO_2 uptake reduced over carbonation duration. The carbonated products were mainly aragonite whisker and granular calcite. The formation of aragonite and calcite contributed to the strength of the cement pastes, resulting in a 22% increase in the strength of the samples when compared to samples with uncarbonated SSP.

Acknowledgements

The authors acknowledge the financial support from The Royal Society (project ref: ICA\R1\201310).

References

Dung, N.T., Unluer, C. (2018) "Development of MgO concrete with enhanced hydration and carbonation mechanisms", *Cement and Concrete Research*, 103: 160-169

Humbert, P.S., Castro-Gomes, J. (2019) "CO2 activated steel slag-based materials: A review", *Journal of Cleaner Production*, 208: 448-457

Li, N., Farzadnia, N., Shi, C. (2017) "Microstructural changes in alkali-activated slag mortars induced by accelerated carbonation", *Cement and Concrete Research*, 100: 214-226

Li, N., Mo, L., Unluer, C. (2022) "Emerging CO2 utilization technologies for construction materials: A review", *Journal of CO2 Utilization*, 65: 102237

Mahasenan, N., Smith, S., Humphreys, K. (2003) "The Cement Industry and Global Climate Change: Current and Potential Future Cement Industry CO2 Emissions", in: Gale, J., Kaya, Y. (Eds.), *Greenhouse Gas Control Technologies - 6th International Conference*, Pergamon, Oxford, pp. 995-1000

Pan, S.-Y., Chung, T.-C., Ho, C.-C., Hou, C.-J., Chen, Y.-H., Chiang, P.-C. (2017) "CO2 Mineralization and Utilization using Steel Slag for Establishing a Waste-to-Resource Supply Chain", *Scientific Reports*, 7(1): 17227

Shen, P., Lu, J., Zhang, Y., Jiang, Y., Zhang, S., Poon, C.S. (2022) "Preparation aragonite whisker-rich materials by wet carbonation of cement: Towards yielding micro-fiber reinforced cement and sequestrating CO2", *Cement and Concrete Research*, 159: 106891

Song, Q., Guo, M.-Z., Wang, L., Ling, T.-C. (2021) "Use of steel slag as sustainable construction materials: A review of accelerated carbonation treatment", *Resources, Conservation and Recycling*, 173: 105740

The 16th International Congress on the Chemistry of Cement 2023 (ICCC2023)
"Further Reduction of CO_2 -Emissions and Circularity in the Cement and Concrete Industry"
September 18–22, 2023, Bangkok, Thailand

Evolution of products in CO_2 surface treated cement

Pingping He[1,2,3], Xiang Hu[1,2,3], Caijun Shi[1,2,3,4*]

[1]Key Laboratory for Green & Advanced Civil Engineering Materials and Application Technology of Hunan Province，College of Civil Engineering, Hunan University, Changsha 410082, P. R. China

[2]International Science Innovation Collaboration Base for Green & Advanced Civil Engineering Materials of Hunan Province, Hunan University, Changsha 410082, P. R. China

[3]Key Laboratory of Building Safety and Energy Efficiency of the Ministry of Education, Hunan University, Changsha 410082, P. R. China

[4]Department of Civil Engineering, The University of British Columbia, 6250 Applied Science Lane, Vancouver, BC Canada V6T 1Z4, Canada

Email:cshi@hnu.edu.cn

ABSTRACT

This study aims to investigate the characteristics and evolution of carbonation products and hydration products at different depth of cement subjected to CO_2 curing and further hydration. The characteristics of products were determined by various methods including X-ray diffraction (XRD), nanoindentation, and backscattered electron imaging (BSE). The results showed that the crystal size of calcite increased, and its content decreased with the increase of depth and post hydration. But the calcite content at the depth of 3.2mm increased after further hydration. And the calcite in the middle section showed the highest increase of crystal size. During further hydration, the content of $Ca(OH)_2$ at the depth less than 1.4 mm was negligible. But its content in the deeper sample increased more obviously. The micro elastic modulus of silica gel and calcium carbonate on the surface section was around 31.5GPa and 60GPa, respectively, and it increased with the depth and further water curing age. The porosity on the surface of CO_2 treated cement was much lower than that of the core sample, but the latter showed similar porosity after post hydration.

KEYWORDS: *Cement, Carbonation, Surface treatment, Post hydration, Microstructure*

1. Introduction

Accelerate carbonation of concrete is an effective means to the sequestration of CO_2 and production of construction materials with high early strength and low permeability(Wang, Fang et al.). Recently, this technique has been used for surface treatment of concrete. For example, Pan et al.(Pan, Shi et al. 2017) found the water absorption coefficients and chloride migration coefficient of concrete decreased by 33% and 16% respectively when it was subjected to CO_2 treatment for 6h. After 90d of further lime-saturated water curing, the water absorption and chloride migration were further decreased (Pan, Shi et al. 2019). Previous studies investigated the properties of surface of concrete after accelerate carbonation and further hydration. However, the microstructure of concrete and the characteristics of products were not systematically studied. The aim of this study is to investigate the characteristics development of carbonation and hydration products, and the fraction of each carbonation products at different depth of cement subjected to different CO_2 curing time and further hydration time.

2. Materials and methods

The cement pastes were prepared by mixing pure cement and tap water for 3 min in a high-speed agitator at a water/cement ratio of 0.35. The freshly prepared mixtures were introduced in a steel cylinder mould.

The samples were demoulded after 24h and put in the lab for 18h until the water/cement ratio was 0.18. Then they were coated with epoxy resin except for the top surface and put in a steel chamber for CO_2 curing for 3h. The gas pressure of CO_2 was kept at 0.2MPa and the humidity was controlled at about 60%. After accelerate carbonation, all samples were put in lime-saturated water for 90d of further hydration.

The XRD test of dry sample powders was conducted on Rigaku R-axis Spider working with Cu Kα radiation within the range of 5-65 °2θ using step size of 0.02 °2θ and a rate of 1.2°/min. 20% of rutile was used as the internal standard. Cement paste slices were dried, epoxy stabilized, grinded, polished with 5, 2.5, and 1μm diamond paste and carbon-coated before BSE analysis using Phenom LE SEM. Paste slices were also used for nanoindentation test, which was conducted on NanoTest Vantage (MML). 100 individual indentations were performed on a grid of 10×10 with a space of 10μm on each sample.

3. Results and discussions

3.1. XRD

Fig. 1 shows the phase content development along the depth of concrete. The calcium carbonate content decreased with the increase of the depth, which agreed with previous study(Pan, Shi et al. 2017). The whole area of carbonated cement can be divided into three areas according to the portlandite content: (I)surface section (within 1.4mm). In this area, portlandite content was negligible, which means carbonation was the main reaction in this area. But the cement particles were not fully carbonated as some unreacted cement clinkers were detected. This is due to the coating of carbonation products inhibiting further carbonation. (II) middle section (1.4-4.4mm). In this area, the carbonation and hydration reactions occurred at the same time. Calcium carbonate content decreased and the portlandite content increased along the depth. The content of unreacted cement was higher than that in area (I). (III) core section (> 4.4mm). The calcium carbonate content was very low and portlandite reached the maximum content (14%). The portlandite content kept a constant value in this area. After further hydration for 90d, unreacted cement clinker content decreased and portlandite content increased indicating the further hydration of cement particles. Meanwhile, the calcite content decreased for the area deeper than 1.4mm due to the reaction of C_3A and $CaCO_3$ forming Hc and Mc. In area (I), portlandite content was negligible. The C_3S content and C_2S content decreased slightly. The increase of portlandite content and the decease of cement clinker contents in area (II) was much higher than that in area (I) due to the less inhibiting effect of carbonation product coat. The content of portlandite at 3.2mm was similar to that deeper than 3.2mm, which means the product coating deeper than 3.2mm had no negative effect on the hydration reaction.

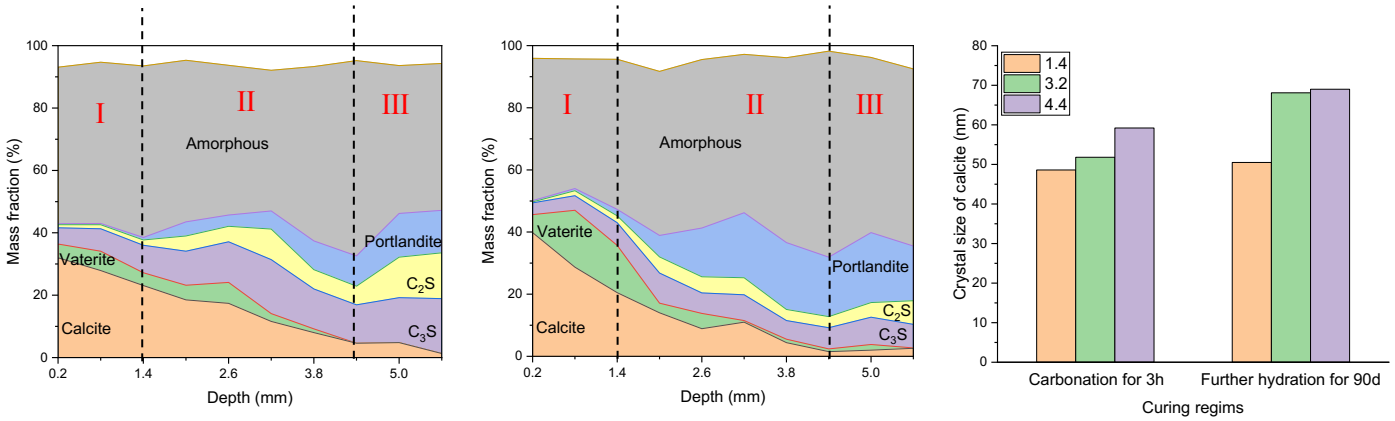

(a) Carbonation for 3h **(b) Further hydration for 90d** **(c) Crystal size of calcite**

Fig. 1 Phase assemblage along depth of concrete subjected to carbonation and further hydration.

Based on the XRD pattern, the crystal size of calcite can be calculated as shown in Fig. 1(c). The calcite content after 4.4 mm was very low. Therefore, the crystal size of calcite deeper than 4.4mm was not calculated. The crystal size of calcite increased with the increase of depth. This is because the reaction rate in deep area was slow, and the calcite was well crystallized. Further hydration promoted the development of crystal size of calcite. The increase of crystal size at 3.2mm was the highest. Fig. 1(b) shows the calcite content at 3.2mm was slightly higher than that at 2.8mm, which might be due to the transformation of amorphous calcium carbonate to calcite. This transformation may also result in the increase of calcite crystal size.

3.2. Nanoindentation modulus

Table. 1 Elastic modulus analysis results of carbonated samples and post hydrated samples.

	Peak center *							
0.8mm-carbonation	31.5(13)	45.5(22)	59.5(11)	73.5(4)	108.5(3)	143.5(3)	164.5(3)	
0.8mm-further hydration	38.5(24)	52.5(3)	66.5(3)	80.5(2)	115.5(3)	129.5(3)	153(7)	
3.2mm-carbonation	30(13)	52(27)	66.5(12)	83.5(2)	108.0(3)		122.5(1)	
3.2mm-further hydration	38.5(5)	52.5(18)		73.5(20)	101.5(4)	129.5(1)	178.5(1)	206.5(1)

*The values in the bracket are the intensity of these peaks.

From nanoindentation test result analysis, the frequency distribution of the elastic modulus was determined using a bin size of 7 GPa and the peak center of peaks is shown in Table 1. The mean elastic modulus of unreacted cement grains carbonated sample at 0.8mm was found to be higher than 80GPa (Han, Pan et al. 2012). The modulus of calcium carbonate formed on the surface of carbonated sample centered around 59.5GPa and 73.5GPa (Lee, Kim et al. 2016). The peak centered at 31.5GPa was corresponding to the silica gel, while the one at 45.5 might be the composites of silica gel and calcium carbonate. After 90 days of further hydration, all the peak center was shifted to the higher modulus, which might be due the continuously formation of calcium carbonate and the increase of crystallinity. For the carbonated sample at 3.2mm, the main modulus centered around 30GPa. It might be the composites of C-S-H gel and silica gel(Zhan, Xuan et al. 2021). The elastic modulus of portlandite was around 31-48 GPa(Han, Pan et al. 2012). However, it was not detected on the modulus patterns, which might be because it intermixed with C-S-H gel. The modulus of calcium carbonate was from 60 GPa -90 GPa, which was much higher than that at 0.8mm. This indicates the higher crystallinity of calcium carbonate in the deeper sample than that on the surface. After 90 days of further hydration, the content of products with modulus ranging from 50-80 GPa increased, which agreed with the XRD results that calcium carbonate was formed at 3.2mm during further hydration due to the exist of CO_2 dissolved in pore solution.

3.3. BSE

BSE images of carbonated and post hydrated samples were shown in Fig. 2. According to the image analysis, the porosity of the sample from (a) to (c) were 2.87%, 7.53%, 5.59%. The porosity of carbonated samples increased from 0.8mm to 3.2mm as the decease of carbonation degree. Then it decreased from 3.2mm to 5.6mm due to the hydration. After further hydration, these values decreased to 2.04%, 5.24%, 1.60% respectively. The sample in deeper location showed more obvious decrease as the surface sample were covered by dense carbonation products that inhibited the further hydration. The porosity of sample in core after 90d of hydration was similar to that on the surface after 3h of carbonation. Therefore, carbonation could rapidly establish dense surface and decease the permeability as shown in previous study(Pan, Shi et al. 2017).

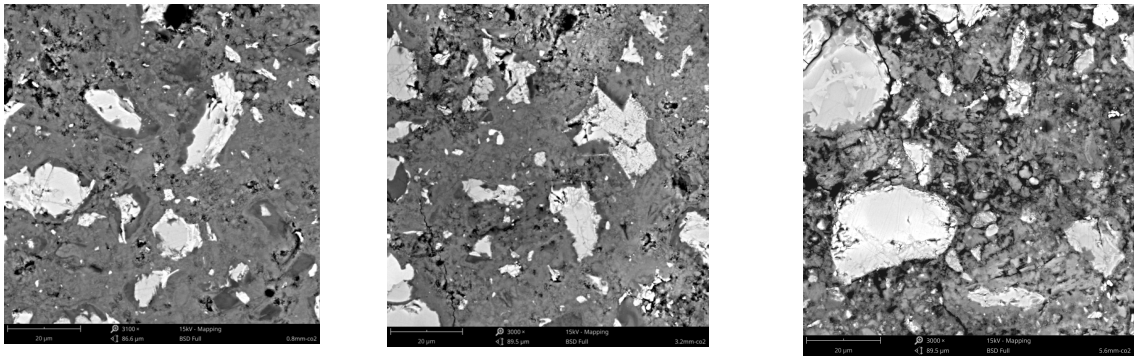

(a)0.8mm-carbonation for 3h **(b)3.2mm-carbonation for 3h** **(c)5.6mm-carbonation for 3h**

Fig. 2 BSE images of carbonated sample at different depth

4. Conclusions

Carbonation is an effective and economic way to improve the permeability of concrete. Previous study showed carbonation treatment could decrease the water permeability, water-vapor transmission, and chloride migration of the concrete. However, the development of products and microstructure of carbonation treated cement has not been well presented. In this study, carbonated cement paste was divided into three sections, i.e., surface section, middle section, and core section. The surface section has the highest carbonation product content and lowest porosity. The porosity of surface of carbonated sample was close to the core section subjected to 90d of hydration, which was the reason that the cement showed low permeability after carbonation for short period. But the crystallinity of calcite was lower than other sections due to the rapid reaction. The main reaction occurred in centre section was hydration. The elastic modulus of amorphous silica gel and the crystallinity of calcium carbonate was increased during further hydration. The porosity was decreased as well, but the centre section showed the most obvious decline.

Acknowledgement

The authors would like to acknowledge the financial support from National Natural Science Foundation of China grant numbers 52050410333, 52078204 and National Natural Science Foundation of Hunan province grant number 2021RC2063.

References

Han, J., G. Pan, W. Sun, C. Wang and D. Cui (2012). "Application of nanoindentation to investigate chemomechanical properties change of cement paste in the carbonation reaction." *Science China Technological Sciences,* **55**: 616-622.

Lee, S.-W., Y.-J. Kim, Y.-H. Lee, H. Guim and S. M. Han (2016). "Behavior and characteristics of amorphous calcium carbonate and calcite using $CaCO_3$ film synthesis." *Materials & Design,* **112**: 367-373.

Pan, X., C. Shi, N. Farzadnia, X. Hu and J. Zheng (2019). "Properties and microstructure of CO_2 surface treated cement mortars with subsequent lime-saturated water curing." *Cement and Concrete Composites,* **99**: 89-99.

Pan, X., C. Shi, X. Hu and Z. Ou (2017). "Effects of CO_2 surface treatment on strength and permeability of one-day-aged cement mortar." *Construction and Building Materials,* **154**: 1087-1095.

Wang, D., Y. Fang, Y. Zhang and J. J. J. o. C. U. Chang (2019). "Changes in mineral composition, growth of calcite crystal, and promotion of physico-chemical properties induced by carbonation of β-C_2S." *Journal of CO_2 Utilization,* **34**: 149-162.

Zhan, B. J., D. X. Xuan, C. S. Poon and K. L. Scrivener (2021). "Multi-scale investigation on mechanical behavior and microstructural alteration of CSH in carbonated Alite paste." *Cement and Concrete Research,* **144**: 106448.

The 16th International Congress on the Chemistry of Cement 2023 (ICCC2023)
"Further Reduction of CO_2 -Emissions and Circularity in the Cement and Concrete Industry"
September 18–22, 2023, Bangkok, Thailand

CO_2 utilization for ready mixed concrete production: development, challenges and scale up

S. Monkman[1*], Igor de la Varga[1]

[1] *CarbonCure Technologies, Halifax, Canada*
Email: smonkman@carboncure.com

ABSTRACT

A novel CO_2 utilization approach was developed and industrialized for ready mixed concrete production. Liquid carbon dioxide is used as an admixture for the in-situ development of nanoscale carbonate reaction products that can improve the compressive strength of the concrete and allow producers to unlock improved cement efficiencies and reduce the embodied carbon of their mixes. The technology evolved from a high dose manual gas injection using a lance to a commercialized optimal dose liquid injection system that is integrated into the concrete batching as described. The impacts on the concrete were examined to ensure that it was acceptable/performance-enhanced. Pilot work focused on the fresh properties (slump and air), compressive strength up to 56 days and compatibility with conventional cementing materials (Portland cement, slag, fly ash). Durability and mechanistic questions were examined as the technology was scaled industrially. The technology has resulted in concrete with improved compressive strength and no negative effects on durability thereby allowing producers to make more sustainable concrete.

KEYWORDS: *CO_2 Utilization, durability, mechanism, sustainability, case study*

1. Introduction

CO_2 utilization is an aspect of concrete sustainability road mapping (Global Cement and Concrete Association 2021) whereupon carbon dioxide is mineralized as part of concrete production. The mechanism of CO_2 activation of cement involves a reaction with the main calcium silicate phases in the presence of water to form both calcium carbonate and calcium silicate hydrate gel (Berger et al. 1972). The chemical reactions are exothermic and spontaneous.

$$3\ CaO{\cdot}SiO_2 + (3-x)\ CO_2 + y\ H_2O \rightarrow x\ CaO{\cdot}SiO_2 \cdot y\ H_2O + (3-x)\ CaCO_3 \quad (1)$$

$$2\ CaO{\cdot}SiO_2 + (2-x\ )CO_2 + y\ H_2O \rightarrow x\ CaO{\cdot}SiO_2 \cdot y\ H_2O + (2-x)\ CaCO_3 \quad (2)$$

Cement is the main concrete component driving its carbon footprint. Readily implementable approaches that allow for more efficient use of cement are meeting the challenge of addressing a high demand for concrete while simultaneously reducing its environmental impact. Adding CO_2 into fresh concrete as an admixture can yield sustainability benefits in the form of cement reductions without compromising concrete performance (Monkman et al. 2023). The approach has been industrialized whereby a retrofit CO_2 injection system is integrated into the concrete batching at hundreds of plants around the world. The technology evolved from a pilot proof of concept to a scalable CO_2 utilization solution.

2. Technology Development

The industrial approach pursued three variations of using CO_2 in ready mixed concrete production. In the first, a supply of gaseous CO_2 was injected into a ready mixed concrete truck after the mixing was completed. The intention was high doses of CO_2 to achieve sequestration. A second iteration used a liquid CO_2 dosing system with CO_2 added to truck mixed concrete and the target to improve the concrete

performance. The approach was piloted at more than a dozen different concrete plants and was applied to a range of concrete with varying mix designs. In the final iteration, a liquid CO_2 injection system was retrofitted in concrete operations (both central mix and truck mix) to deliver a performance-enhancing dose of CO_2 as an integrated part of the concrete batch process.

3. Results

3.1 Initial pilot with high doses

The mix design in the initial pilot was a standard 30 MPa mix with a target 100 mm slump. The unit mix design (1 m^3) contained 300 kg cement, 60 kg Class F fly ash, 980 kg fine aggregate, 900 kg of coarse aggregate, 160 kg water. Four loads were produced: a reference followed by three batches with three increasing dosages of CO_2. The pilot study demonstrated the CO_2 addition, quantified through analysis of sieved and dried cement paste using an Eltra CS 800 elemental analyzer, fixed from 0.43 to 0.64% CO_2 per unit of cement. The results from the first study are presented in Figure 1.

It was observed that the three doses of CO_2 caused the slump of the concrete to decline at an accelerated rate whereby the batches had less than half the slump of the control when measured at about 35 minutes after the mixing started (Monkman 2014). The compressive strength of the two higher doses were observed to slow down the hydration. They were about 70% of the control strength at 3 days before increasing to match/exceed the control at 56 days. The lowest dose was 9% lower strength at 3 days and 102% at 7 days before showing a +11% and +9% strength gain at 28 and 56 days. The mineralization did not impact the 28-day flexural strength or the RCP testing at 56 days.

The work concluded that a sufficiently high dose of CO_2 could compromise workability even if the CO_2 was bound and long-term strength development was acceptable. While this would be addressable through increased water or chemical admixtures it was concluded to be a non-viable approach.

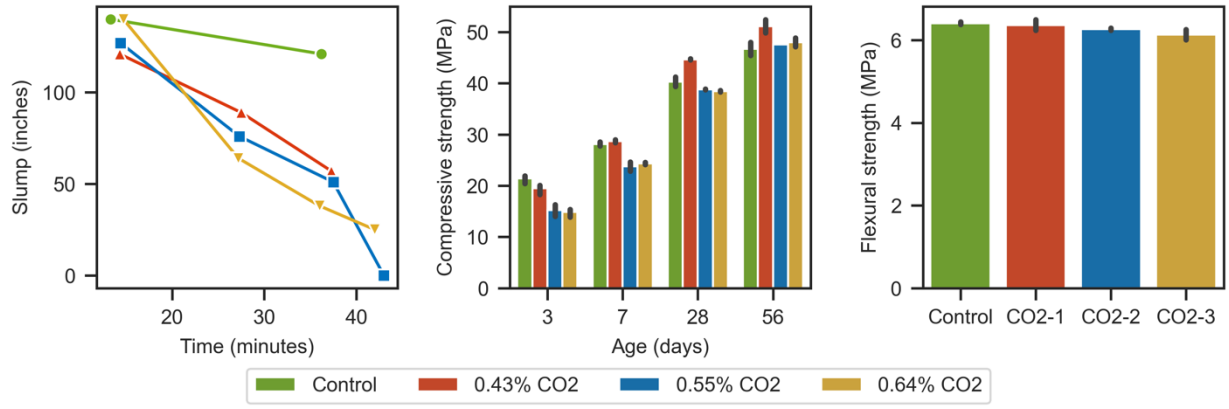

Figure 1: Slump, compressive strength development and 28 day flexural strength of the CO_2 activated concrete produced in the initial trial

3.2 Optimal dose pilots with liquid CO_2

Additional lab and industrial trials supported a pivot using lower dosages intended to avoid decreasing workability but potentially access the strength benefits identified in the original industrial trial. The technology shifted to the metering of liquid CO_2 since it was a simpler approach both practically (it is the primary mode of industrial gas transportation) and technologically (can avoid a heat exchanger/evaporator that would be used to convert liquid to gas on site). A range of CO_2 doses were examined through sequential addition to single load of concrete starting a few minutes after mixing was completed. The best outcome from each of 19 pilot cases is summarized in Table 1.

The pilot testing demonstrated a compatibility across a range of concrete binder compositions (plain cement, Class F fly ash, Class C fly ash, ternary blends) and strength classes (21 MPa to 69 MPa). The average results showed potential strength improvements at 1, 7 and 28 days of 10% or more. The fresh properties (slump and air content) were measured and no adverse impacts on the concrete were recorded at the dosages tested.

The advantage of eliminating batch-to-batch variation by using a single batch came with the disadvantage of the CO_2 mixes receiving more mixing prior to testing and creation of specimens. Additionally, the dosing

after mixing, at a wash rack, for example, was a process modification that would be difficult to scale if not otherwise unacceptable in practice. Nevertheless, the performance benefit observed prompted further investigation, refinement, and evolution of the concept.

Table 1: Pilot results reporting compressive strength at 1, 7 and 28 days relative to the control

Binder	CO_2 Dose	Target Strength (MPa)	Rel. 1 day strength	Rel. 7 day strength	Rel. 28 day strength
25% slag	0.15%	21	105%	106%	106%
25% Class F FA	0.05%	21	113%	108%	106%
20% slag	0.30%	25	122%	116%	115%
20% slag	0.30%	25	108%	115%	107%
20% slag	0.15%	25	114%	121%	115%
25% Class F FA	0.05%	28	98%	102%	102%
25% Class F FA	0.30%	28	112%	115%	108%
29% slag, 21% Class F FA	0.05%	28	131%	143%	122%
17.5% Class C FA	0.30%	28	106%	110%	116%
25% Class C FA	0.25%	28	124%	123%	119%
15% Class F FA	0.05%	28	100%	115%	110%
15% Class F FA	0.15%	28	108%	109%	118%
OPC	0.05%	35	106%	103%	111%
25% slag	0.05%	35	189%	139%	120%
20% slag	0.05%	35	114%	110%	101%
20% Class F FA	0.30%	35	111%	114%	108%
OPC	0.05%	35	109%	103%	105%
16% Class F FA	0.05%	41	116%	117%	107%
24% slag, 23% Class C FA	0.30%	69	110%	104%	97%
Average			116%	114%	110%

3.3 Technology deployment

The pilot work concluded in the development of a scalable retrofit system where liquid CO_2 was dosed like an admixture, as part of the concrete batching process (both in dry batch and wet batch operations). A tank of liquid CO_2 is installed near the concrete mixer. A dosing system delivers CO_2 to the concrete in communication with the concrete batching system. Industrial implementation established that the optimal dose of CO_2, added during concrete batching and mixing, could increase the compressive strength of the concrete (Figure 2) without impacting the fresh properties. It was demonstrated that enhanced strength further supported mix design modifications to use less cement yet maintaining performance (Monkman and MacDonald 2017). The binder efficiency (kg CO_2 m^{-3} MPa^{-1}) was improved 6%.

Fundamental work in C_3S systems have characterized the carbonate reaction products that are formed and the relevant chemical pathways (Monkman et al. 2022). The CO_2 addition impacted the solution phase composition of an activated paste in the first minutes of hydration. Thermodynamic modeling revealed that the presence of CO_2 resulted in stronger undersaturation with respect to the binder phases, which implies a strong driving force for their dissolution.

The impact of CO_2 mineralization on concrete durability was studied (Monkman et al. 2016, 2023). The carbon dioxide did not have any impacts on durability as tested in both the field- and laboratory-produced concrete. The pore solution alkalinity and reinforcing steel corrosion were not negatively impacted by the CO addition. Similarly, rapid chloride penetrability testing (RCPT) performance, surface resistivity, flexural strength, drying shrinkage, and freezing-and-thawing performance were assured.

Life cycle analyses have been completed (Monkman 2018, Monkman et al. 2023). Where the CO_2 addition can be leveraged to improve compressive strength and then save virgin cement the environmental impacts include energy required for CO_2 processing and transport, CO_2 removal through mineralization, and avoided CO_2 through the cement reduction. A typically industrial cement reduction of 5% can be achieved and the technology is compatible with other sustainability strategies such as SCM use.

The increasing usage of Portland limestone cements has caused the optimal dosing of the technology to expand. Whereas the piloting and initial commercialization unlocked compressive strength benefits with doses from 0.05% to 0.3% CO_2 by weight of cement, the maximum dosages have increased (as high as 0.7%). Technical similarities are found with other chemical admixtures where increased limestone contents in cements have resulted in increased dosages to maintain effectiveness.

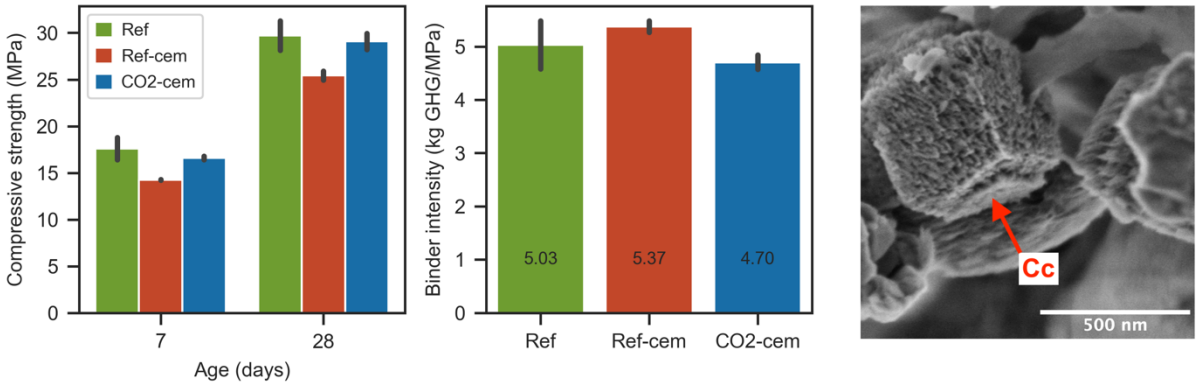

Figure 2: Compressive strength and binder intensity of industrially produced concrete. Ref is default mix with 320 kg/m^3 binder (160 kg cement, 71 kg fly ash, 89 kg of slag). Ref-cem has the binder reduced to 295 kg/m^3 while CO2-cem has the reduced binder and dose of 0.1% CO_2 by weight of cement. SEM image of in-situ produced calcium carbonate CO_2-activated tricalcium silicate

4. Conclusions

A CO_2 utilization solution was developed for ready mixed concrete production. CO_2 was added as an admixture to concrete; at higher dosages the concrete had a reduced workability and a retarded strength development while at lower, optimal, doses the concrete compressive strength was improved without any change to fresh properties. The technology evolved to become a scalable retrofit system. Concrete durability is not impacted by the use of CO_2 while the GHG efficiency of the binder can be improved 6%.

Acknowledgements

The technology development received the support of Sustainable Technology Development Canada (SDTC), and the National Research Council of Canada Industrial Research Assistance Program (NRC IRAP). Technical support was received from Doug Hooton, Larry Sutter and the late Mike Thomas.

References

Berger RL, Young JF and Leung K (1972). *Acceleration of Hydration of Calcium Silicates by Carbon-Dioxide Treatment*. Nature: Physical Science, Volume 240, pp 16–18.

Global Cement and Concrete Association (2021). *Concrete Future - The GCCA 2050 Cement and Concrete Industry Roadmap for Net Zero Concrete*. London.

Monkman S (2014). *Investigating Carbon Dioxide Sequestration in Fresh Ready Mixed Concrete*. In: *Proceedings of the International Symposium on Eco-Crete*. Reykjavik, Iceland. pp. 69–77.

Monkman S (2018). *Sustainable Ready Mixed Concrete Production Using Waste CO2: A Case Study*. In: *SP-330 Proceedings Fourteenth International Conference: Recent Advances in Concrete Technology and Sustainability Issues*. American Concrete Institute: Beijing, China. pp. 163–174.

Monkman S, Cialdella R and Pacheco J (2023). *Performance, Durability, and Life Cycle Impacts of Concrete Produced with CO2 as Admixture*. ACI Materials Journal, Volume 120, pp 53–62.

Monkman S and MacDonald M (2017). *On carbon dioxide utilization as a means to improve the sustainability of ready-mixed concrete*. Journal of Cleaner Production, Volume 167, pp 365–375.

Monkman S, MacDonald M, Hooton RD and Sandberg P (2016). *Properties and durability of concrete produced using CO2 as an accelerating admixture*. Cement and Concrete Composites, Volume 74, pp 218–224.

Monkman S, Sargam Y, Naboka O and Lothenbach B (2022). *Early age impacts of CO2 activation on the tricalcium silicate and cement systems*. Journal of CO2 Utilization, Volume 65, pp 102254.

The 16th International Congress on the Chemistry of Cement 2023 (ICCC2023)
"Further Reduction of CO_2 -Emissions and Circularity in the Cement and Concrete Industry"
September 18–22, 2023, Bangkok, Thailand

Amine-CO_2 Treatment of Cement Slurry and its Effect on Portland Cement-Fly Ash-Slag Ternary System

Z.A.S. Bairq[1,2], P. He[1,2], C. Shi[1,2,*]

[1] *Affiliation, City, Country1 Key Laboratory for Green & Advanced Civil Engineering Materials and Application Technology of Hunan Province, College of Civil Engineering, Hunan University, Changsha 410082, P. R. China*

[2] *International Science Innovation Collaboration Base for Green & Advanced Civil Engineering Materials of Hunan Province, Hunan University, Changsha 410082, P. R.*

ABSTRACT

The dual need to reach neutrality of carbon dioxide (CO_2) emission and reuse the industrial residues encourage the proposition of innovative pathways to sequestrate CO_2 and convert industrial residues into valuable chemicals concurrently. Carbonation of concrete slurry waste (CSW) is an efficient and effective approach to overcome these challenges. Also, to address the challenges of CO_2 slow carbonation and enhance the CO_2 sequestrate in CSW during the carbonation process, this study suggests the wet carbonation method as an efficient and effective approach to overcome the slow carbonation rate and to increase the sequestration of CO_2 in such systems. Different curing temperatures (20ºC and 60ºC) and curing times were investigated to evaluate the impact of the carbonation process. Results showed that wet carbonation increased CO_2 uptake by about 33%. Furthermore, the wet carbonation process in the CO_2-CSW system enhanced the crystallization of calcium carbonate by 60% compared to the dry carbonation method. Thus, these innovative approaches elucidate the feasibility of direct sequestration of CO_2 in CSW and producing calcium carbonate and demonstrate techniques for co-utilizing waste material.

KEYWORDS: *Slurry waste, Dry carbonation, CO_2 sequestration, Strength properties, Wet carbonation*

1. Introduction

Carbon dioxide (CO_2) emissions from human activities, such as burning fossil fuels, have been identified as a leading cause of climate change. One way to mitigate these emissions is through carbon capture and sequestration (CCS), which involves capturing CO_2 and storing it in a secure location, such as underground geological formations. Concrete production is one industry that contributes significantly to global CO_2 emissions. Cement production, a key component of concrete, is responsible for about 7% of global CO_2 emissions, according to the International Energy Agency. However, research has shown that CO_2 can be captured and stored in concrete during the curing process, resulting in what is known as CO_2 sequestration concrete. This process involves using CO_2 as a curing agent, which reacts with calcium ions in the concrete to form calcium carbonate, a stable mineral that permanently captures the CO_2. Several studies have investigated the feasibility of CO_2 sequestration in concrete, including its potential environmental and economic benefits [1]. A related study by Han et al.; concluded that using CO_2 as a curing agent in concrete could reduce CO_2 emissions by up to 50% while also increasing the compressive strength of the concrete [2]. Another study by Li et al.; found that the cost of producing CO_2-sequestration concrete was comparable to that of traditional concrete [3].

Waste concrete slurry is generated while washing concrete trucks and equipment and typically contains a high concentration of calcium ions. This waste stream presents an opportunity for CO_2 capture and storage through a process known as wet carbonation, in which CO_2 is dissolved in water and reacted with the calcium ions in the slurry to form calcium carbonate. Research has shown that wet carbonation of waste concrete slurry can significantly enhance CO_2 uptake and storage [4,5]. A previous study found that wet carbonation of waste concrete slurry could capture up to 0.75 tonnes of CO_2 per tonne of slurry, which is significantly higher than other carbonation processes [6]. Another study by Han et al.; demonstrated that

wet carbonation of waste concrete slurry could reduce the leaching of heavy metals from the slurry, producing a stable product that could be used as a soil amendment.
Furthermore, wet carbonation of waste concrete slurry represents a potential solution for the environmental challenges associated with waste concrete disposal [7]. By capturing and storing CO_2 in the slurry, this process can reduce the construction industry's carbon footprint while minimizing the need for landfills and other disposal methods. Overall, CO_2 sequestration in concrete represents a promising approach to reducing CO_2 emissions from the concrete industry. Wet carbonation of waste concrete slurry attracts significant attention from researchers as a practical approach to enhancing CO_2 uptake and storage while addressing environmental challenges associated with waste concrete disposal. Further research is needed to optimize the process and ensure its scalability and cost-effectiveness.
This study aims to assess the potential of concrete slurry waste (CSW) as a CO_2 sequester and to explore its performance as a supplementary cementitious material (SCM). The study has specific objectives, including the characterization of the physicochemical properties of fresh and carbonated WCS using various analytical methods and evaluating the effect of the applied parameters, such as water/binder (w/b) ratio and carbonation temperature, on the CO_2 uptake of CSW.

2. Materials and Methods

2.1 Carbonation of CSW

To overcome the complexity and heterogeneity of CSW from the cement plant, a synthetic CSW has been simulated in the lab. The slurry was produced using 60% Portland cement, 20% Fly Ash, 20% Slag and a different w/b ratio. A sealed stainless-steel chamber was used to cure the CSW powders with CO_2. To provide sufficient CO_2 for the curing process, a commercially sourced CO_2 gas with a purity of >99.99% was injected at a flow rate of 2L/min. Prior to the CO_2 injection, the chamber was vacuumed to -0.1MPa. When the pressure reached 0.35M in the chamber, the CO_2 injection was stopped. During the CO_2 carbonation process, the pressure was kept at 0.35M and kept supplying extra CO_2. not insert page numbers. Do not write in headers and footers or change them.

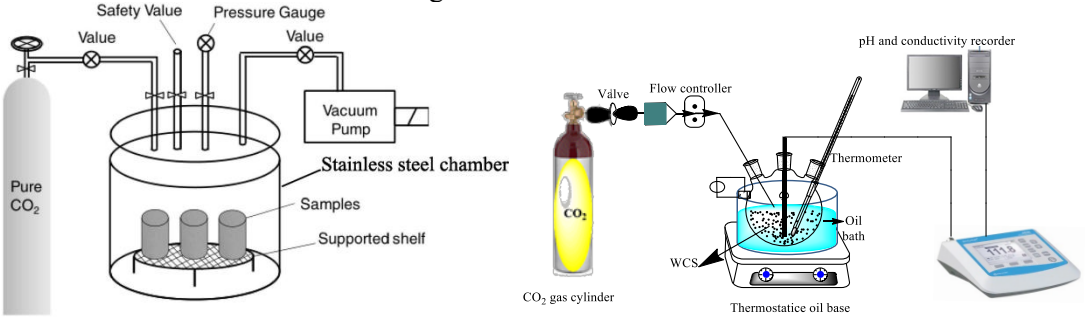

(a) **(b)**

Fig.1. Schematic setup of CO_2 curing chambers a) dry carbonation and b) wet carbonation chamber.

The wet carbonation process was conducted by mixing 50-100g Portland cement-FA-slag with the exact amount of deionized water. The mixture was heated and mechanically stirred to reach the desired temperature with a laboratory magnetic field stirrer at 250rpm for 10min at room temperature. A series of experiments were conducted using OPC, FA, and slag ternary system to investigate the carbonation behaviour using at different temperatures of 20˚C, 40˚C, 60, and 80˚C for different reaction times, different w/b ratios, and at atmospheric partial pressure and a stirring rate of 250 rpm (±5rpm). The experiment was systematically designed to explore the effects of carbonation curing on the CSW, determine the mechanical properties of the obtained cement paste, and changes in the physicochemical properties induced by carbonation curing.

2.2 Materials Characterization

Before each test, the selected samples were dried at 40°C for 24h in a vacuum oven. The oxide composition of WCS was determined using a PANalytical Axios X-ray fluorescence analyzer (XRF). Table 1 summarises the chemical compositions of CSW components. Thermo Scientific Nicolet IS10 with Cu Ka radiation and scan angles (2θ) ranged from 5˚ to 60˚ with a rate of 5˚/min, and a step size of 0.02˚ was performed to determine the crystalline composition of the carbonated concrete slurry waste (CCSW) samples. The scan was conducted in the range of 400cm^{-1}- 4000cm^{-1} with a resolution of 2cm^{-1}, averaging

64 scans for each measurement. A Phenom LE SEM was used to examine the morphology of the carbonated CSW samples. The reaction products were quantified using an SEM equipped with energy dispersive spectroscopy (EDS). The thermogravimetric and differential thermogravimetric (TG-DTG) analyses were performed to test the CO_2 uptake of the CCSW using the PerkinElmer TG instrument. The particle size distribution of carbonated WCS under different carbonation regimes was determined using a Laser particle size analyzer S3500.

3. Results and Analysis

Figs.2a and 2b exhibit the SEM images of CCSW, both dry and wet carbonation. The photos indicated the distinct differences in the morphology between the carbonation method and the carbonated CSW system. The surface morphology of carbonated CSW became less porous and denser and exhibited solid rhombohedral calcite ($CaCO_3$) morphology. This should be attributed to the formation, precipitation, and coverage of fine calcite particles on the surface of carbonated CSW due to the carbonation of the hydrated products. The carbonated slurry's calcium carbonate and CO_2 uptake were quantified using thermal gravimetric analysis (TGA). Before conducting the analysis, the samples of carbonated concrete slurry waste (CCSW) were subjected to vacuum oven drying for one day.

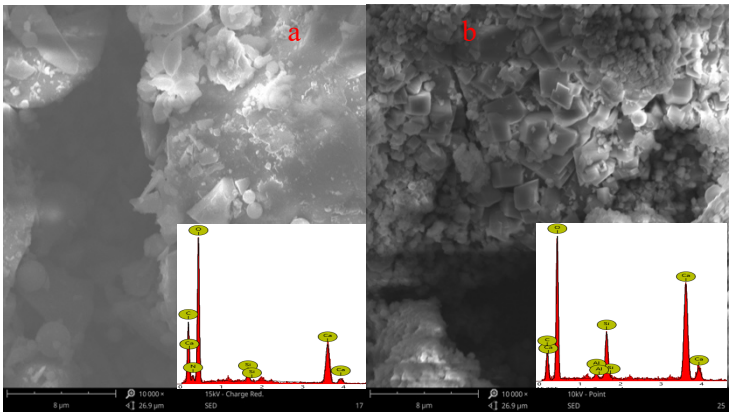

Fig. 2. The morphologies of carbonated CSW a) dry carbonated and b) wet carbonated samples.

Before conducting the analysis, the samples of carbonated concrete slurry waste (CCSW) were subjected to vacuum oven drying for one day. The peak typically indicates the presence of hydrates at 100°C. The decomposition of calcium carbonate is indicated by the second peak in the DTG curve and the mass loss between 450°C and 800°C, as shown in Fig.3. Around 12mg of the samples was heated with a heating rate of 10°C/min, using a thermogravimetric analyzer PerkinElmer TG instrument, under N_2 striping gas, from 30°C to 1000°C. Conversely, $Ca(OH)_2$ levels decreased and disappeared by the end of the curing time.

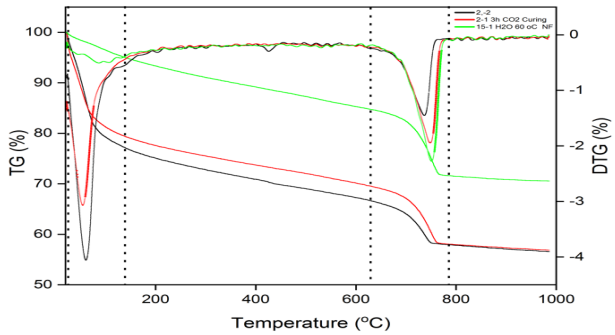

Fig.3 shows no peaks between 200°C-450°C that may be attributed to (C-S-H) or $Ca(OH)_2$, while there is a distinct peak with high intensity between 700°C and 800°C, corresponding to $CaCO_3$. Therefore, peaks related to $Ca(OH)_2$ and C-S-H are absent after carbonation, and all $Ca(OH)_2$ transforms to $CaCO_3$, as confirmed by a strong peak visible at around 750°C. Fig.4 illustrates the particle size distribution of carbonated CSW, with samples indicating particle sizes ranging from 65µm to larger sizes of 100µm.

Fig. 3. Thermal analysis of CSW samples after dry and wet carbonation.

This study confirms the formation of calcite particles, consistent with our observations from SEM analyses in Fig.2. The carbon mineralization of CSW is responsible for the construction of larger particles. However, the mean diameter is not the sole parameter that reflects the changes in the particle size distribution because carbon mineralization results in multi-modal particle size distributions. Our particle size analyses, and SEM images reveal that the newly formed calcium carbonate phases precipitate on the surface of the existing particles rather than creating discrete particle size distributions.

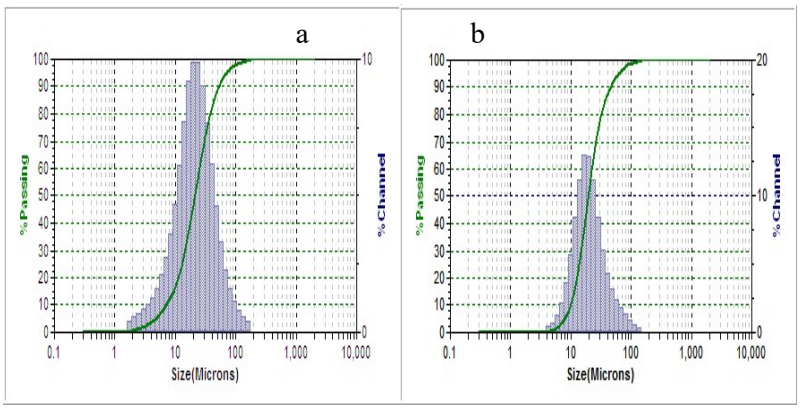

Fig. 4. Particle size distribution carbonated concrete slurry waste (CCSW) a) dry carbonated CSW and b) wet carbonated CSW.

The results reveal that carbonated WCS obtained from wet carbonation with water have particle size ranges of 100μm. This implies that wet carbonation led to the formation of calcite and vaterite with larger particle sizes within the 100μm range, potentially due to agglomeration effects. Following carbonation, the particles were bound together through the chemical reaction of calcite crystallization in the pore space between grains.

4. Conclusions

The research explored the potential of concrete slurry waste (CSW) as a supplementary cementitious material (SCM) and a carbon dioxide sequester in cement composites. The findings indicated that wet carbonation was more effective than dry carbonation in achieving the highest CO_2 uptake by the CSW. The study revealed that the CSW's pH was neutralized after carbonation, reducing the leachability of certain heavy metals, and all measured values remained below the hazardous landfill limits. The optimal conditions for achieving the highest CO_2 uptake were identified as a 10:1 w/b ratio and 60min of carbonation, resulting in a CO_2 uptake capacity of up to 330g CO_2/kg WCS. The study also found that wet carbonation stimulated the crystallization of calcium carbonate phases, particularly calcite and vaterite. The physical and chemical properties of WCS were significantly altered by accelerated carbonation, leading to increased particle size distribution and density due to agglomeration and calcite polymorphous formation.

Acknowledgements

The authors would like to acknowledge the financial support from the National Natural Science Foundation of China, grant number 52050410333, 52078204.

References

Chen, Y., Liu, X., Shen, L., and Wang, X. (2019) "Wet carbonation of waste concrete slurry for CO_2 capture and utilization", Journal of CO_2 Utilization, 31, 148-156.

Gartner, E. M., and Sui, T. S. (2019) "CO_2 sequestration in concrete", Materials Today Sustainability, 2, 100008.

Han, B., Li, Z., and Li, W. (2017) "Enhanced CO_2 uptake and heavy metal immobilization by wet carbonation of cementitious waste slurry", Journal of Environmental Management, 196, 388-394.

Han, B., Zhou, X., Li, Z., and Chen, G. (2018) "Carbonation curing for concrete with carbon dioxide: A review", Journal of Cleaner Production, 171, 601-611.

Li, Q., Li, H., Huang, Y., and Chen, G. (2018) "Cost-effective CO_2 sequestration in concrete by accelerating carbonation with carbon dioxide", Energy Conversion and Management, 167, 262-269.

Yang, X., Cui, X., Hou, L., Wang, Y., and Zhang, H. (2021) "Environmental and economic evaluation of CO_2 capture and utilization from waste concrete slurry", Journal of Cleaner Production, 296, 126563.

Zhang, Q., Chen, Y., and Li, J. (2021). Wet carbonation of waste concrete: A review of CO_2 capture and utilization", Journal of Environmental Sciences, 101, 287-296.

The 16th International Congress on the Chemistry of Cement 2023 (ICCC2023)
"Further Reduction of CO_2 -Emissions and Circularity in the Cement and Concrete Industry"
September 18–22, 2023, Bangkok, Thailand

Synthesis of Giorgiosite [$Mg_5(CO_3)_4(OH)_2 \cdot 5–6H_2O$], further light on a new hydrated magnesium carbonate for MgO-based cement

H. Nguyen[1,2*], E. Bernard[2], F. Winnefeld[2], B. Lothenbach[2], and P. Kinnunen[1]

[1] *Fibre and Particle Engineering Research Unit, University of Oulu, Pentti Kaiteran katu 1, 90014 Oulu, Finland*

[2] *Empa, Swiss Federal Laboratories for Materials Science and Technology, Überlandstrasse 129, 8600 Dübendorf, Switzerland*

Emails: Hoang.Nguyen@oulu.fi; Ellina.Bernard@empa.ch; Frank.Winnefeld@empa.ch; Barbara.Lothenbach@empa.ch; Paivo.Kinnunen@oulu.fi

ABSTRACT

Giorgiosite is a relatively unknown hydrated magnesium carbonate (HMC) without a clear understanding of its characteristics and synthesis pathway. The phase has a nano-wire morphology with high surface area, and hence, attracts immediate interests for various applications including as early-strength-giving phase in HMC-based binder. However, there had been no clear and successful pathway in the past to synthesize the phase. The present work addresses this research gap and reports an effective protocol to obtain giorgiosite in high purity. We found that giorgiosite can be synthesized via the conversion of pure nesquehonite [$MgCO_3 \cdot 3H_2O$] in a 1M Mg-acetate solution at 50 °C. In contrast, nesquehonite converted to dypingite [$Mg_5(CO_3)_4(OH)_2 \cdot 5H_2O$] in the absence of acetate. Here, the characteristics of giorgiosite as determined by XRD, TGA/FTIR, SEM, and Raman spectroscopy are reported. The better understanding of the characteristics of giorgiosite will contribute to the development of HMC-based binders, which have the potential to be a carbon-negative construction material. Further work is needed to shed light on the conversion pathway in the presence of organic ligand (e.g., acetate) and to determine the thermodynamic properties of giorgiosite.

KEYWORDS: *carbonation; giorgiosite; hydrated magnesium carbonate; MgO-based cement*

1. Introduction

MgO-based cements have been attracting increased interests due to their potential as a major binding system. Hydrated magnesium carbonate (HMC)-based binders show the ability to utilize carbon as a precursor in producing the binder. Thus, they can potentially reach net carbon-negative emission, if the source of MgO comes from non-carbonate sources such as Mg-silicates (Scott et al., 2021; Zevenhoven et al., 2017). Mg-silicates are abundant on Earth's crust and widely distributed worldwide, as well as Mg-containing brines (Badjatya et al., 2022). However, little is known about the formation, stability, and the role of different HMCs in the binder. In our previous work (Nguyen et al., 2022), when acetate (CH_3COO^-) ligand was present in the system, giorgiosite [$Mg_5(CO_3)_4(OH)_2 \cdot 5–6H_2O$] was formed by conversion from nesquehonite [$MgCO_3 \cdot 3H_2O$]. It is a relatively unknown phase (no single crystal structure and thermodynamic data available in literature) and with only scattering information from X-ray diffraction available in literature (Canterford et al., 1984; Friedel, 1975). The phase was mentioned for the first time by Friedel (1975) with a relatively low synthesis yield (~50%) and unclear formation route. Hence, in this work we provide a clear pathway to synthesize giorgiosite, a detailed characterization as well as an outlook to shed further light on the crystal.

2. Synthesis of giorgiosite

The synthesis of giorgiosite was based on the conversion of nesquehonite in a 1 M Mg-acetate solution. First, nesquehonite was synthesized via wet carbonation of brucite (VWR Finland, purity 99.7%, CAS number: 1309-42-8) at 20 °C. Brucite was used as a source of magnesium at 0.7 mol $Mg(OH)_2$ per liter of solution. The CO_2 gas was bubbled into the suspension with a flow rate of 100 cm^3/min. During the synthesis, the pH was measured in-situ. The pH value stabilized at around 7 when the carbonation of brucite was completed.
One part of the suspension was vacuum filtrated (filter size: 1 µm) after carbonation. The solid was washed twice with isopropanol and once with diethyl ether and then dried in an oven at 40 °C for 1 hour before completing the drying process at ambient conditions for 2 days. The solid was then characterized by X-ray diffraction (XRD) analyses, and the formation of high purity nesquehonite (with about 1 mass-% brucite remaining) was confirmed.
To obtain giorgiosite, a part of the nesquehonite suspension was sealed with 1M Mg-acetate after wet carbonation and oven-cured at 50 °C for 14 days. After the curing period, the solid was collected following the above-mentioned procedure prior to further analyses. Note that although the conditions of synthesis (e.g., duration, acetate concentration, and temperature) can be further optimized, the present work intends to report the route for giorgiosite synthesis, and the optimization will be the focus in future study.

3. Characterization

The XRD measurements were performed with a PANalytical X'Pert Pro using with a Co X-ray source at 45 mV voltage and 40 mA intensity and an X'Celerator detector. Prior to the measurement, samples were sieved through a 63-µm sieve, and back-loading was used for sample preparation. The measurement was performed from 5 to 90° 2θ with a scanning step of 0.017° 2θ and step time 66 seconds; this leads to a total time for a measurement around 45 mins. Data were further analyzed using X'pert Highscore Plus software version 5.1 coupled with PDF-4+ 2022.
The morphology of synthesized giorgiosite was observed via scanning electron microscopy (SEM) using a FEI Quanta 650 (ThermoFisher Scientific). The instrument was set at an accelerating voltage of 10 kV and a working distance of 10 mm using a secondary electron detector. Prior to SEM analyses, the samples were stored in sealed conditions and coated with Pt prior to the measurement.
Thermogravimetric analyses were performed under nitrogen atmosphere (flow rate 20 cm^3/min) using a Netzsch STA 449 F3 Jupiter coupled with a Fourier Transform Infrared (FT-IR) spectrometer (IR Alpha detector, Bruker AG, Germany) for gas analysis. Weight changes were measured on 50–70 mg sample during heating s from 30 to 1000 °C with a heating rate of 10 K /min in alumina crucibles.
Raman spectroscopy was performed using a laser confocal micro-Raman spectrometer from B&W Tek. The calibration was done using pure silicon as a reference sample. The scan was set at 20% laser intensity with a total 10 seconds of scanning for an average of 10 scans.

4. Results and discussion

Pure giorgiosite was obtained by the conversion of nesquehonite in the presence of acetate in the suspension within 14 days at 50 °C (Figure 1). However, the exact kinetics of this conversion remains unclear, particularly the influence of temperature. Since nesquehonite is known to convert to either dypingite [$Mg_5(CO_3)_4(OH)_2 \cdot 5H_2O$] or hydromagnesite [$Mg_5(CO_3)_4(OH)_2 \cdot 4H_2O$], depending on the temperature (Hopkinson et al., 2008), the role of temperature coupled with the presence of additives e.g., other organic ligands, will be of interest for further studies. Giorgiosite has a clearly distinguishable morphology compared to other HMCs such as nesquehonite (Figure 2), dypingite or hydromagnesite (Raade, 1970). As shown in Figure 2, giorgiosite has a needle-like shape with very high aspect ratio, which could be beneficial to provide early strength for the HMC-based binder.

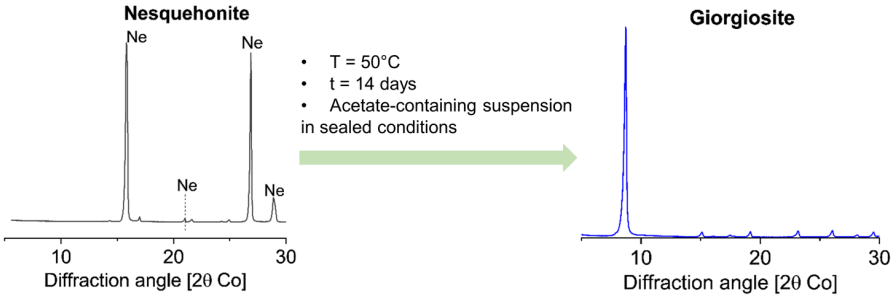

Figure 1. XRD patterns of synthesized nesquehonite and giorgiosite

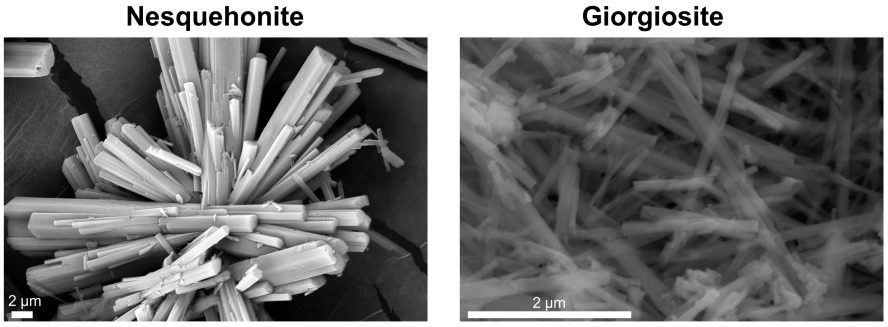

Figure 2. Morphology of nesquehonite and giorgiosite as determined by SEM

The thermal decomposition of giorgiosite confirms the phase as a hydrated carbonate with both FT-IR signals for H_2O and CO_2 present (Figure 3a). The dehydration started during 60–200 °C and the dehydroxylation and decarbonation appeared simultaneously in an identical range of temperature from 300 °C to 500 °C. Furthermore, Raman spectroscopy indicates the presence of acetate with the C–C stretching, and CH_3 deformation signals at 940 cm^{-1} and 1356 cm^{-1}, respectively [q.v. (Wang et al., 2005)]. The peak at 1114 cm^{-1} is assigned to the antisymmetric stretching vibration ν_1 of CO_3^{2-}, while there is a hump around 900–700 cm^{-1} which may be due to the antisymmetric stretching vibration ν_4 of CO_3^{2-} [q.v. (Frost, 2011; Skliros et al., 2020)]. Since giorgiosite was formed in the presence of acetate at relatively high concentration (i.e., 1 M), there is high possibility that giorgiosite in addition to carbonate either absorbs or incorporates some acetate in its structure, as indicated by the trace of acetate in the Raman spectroscopy. Further investigation is needed to verify the potential uptake of acetate in giorgiosite and to confirm the chemical formula of this phase. In addition, the thermodynamic data of giorgiosite and its crystal structure will be beneficial to enable better prediction in thermodynamic modelling and the quantification of HMC-based binders with the presence of giorgiosite.

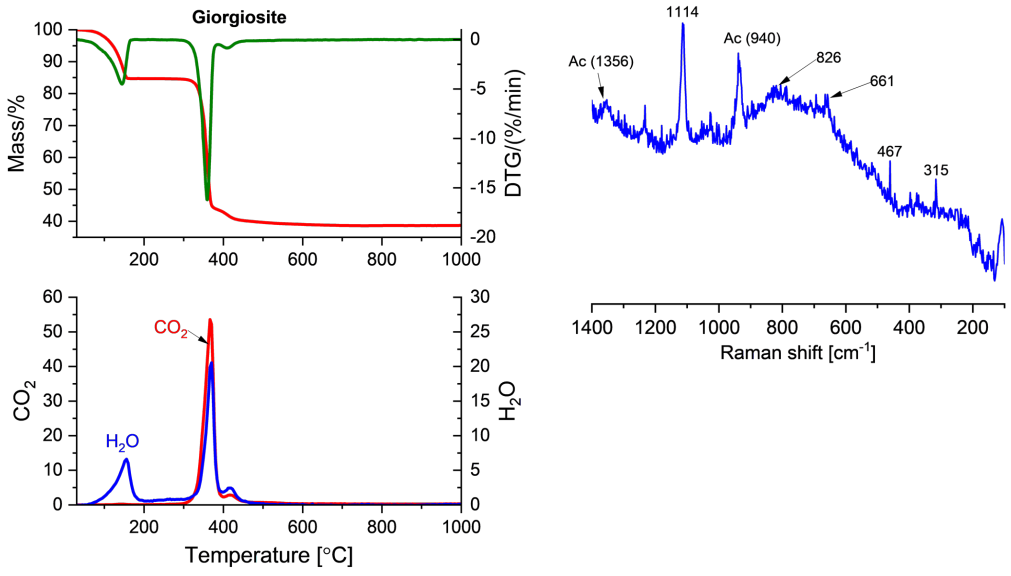

(a) (b)

Figure 3. (a) Thermal properties of giorgiosite and its correspondence of mass loss to CO_2 and H_2O signals from FT-IR, (b) Raman spectroscopy of the giorgiosite showing the trace of acetate (Ac) in the giorgiosite

5. Conclusions and outlook

In this work, we suggested a pathway to synthesize giorgiosite based on the conversion of nesquehonite in an acetate-containing suspension. The synthesis route yields a full conversion to giorgiosite in a relatively short curing time (i.e., 14 days). The giorgiosite contains a trace of acetate as seen via Raman spectroscopy. Thus, there may be the possibility that acetate is incorporated in the crystal leading to the need to redefine whether giorgiosite is an organo-HMC or not. Therefore, further work is needed to confirm and shed further light on the nature of giorgiosite phase that was synthesized in this work. The phase will also be beneficial to further investigate the role of organic ligand in the formation of HMC towards the utilization of HMC-based binder in construction when the properties and characteristics of this phase are fuller understood.

Acknowledgements

P.K. and H.N. are grateful for the financial support from the University of Oulu & The Academy of Finland Profi5 326291, as well as the Academy of Finland project 329477. H.N. thanks the Faculty of Technology, University of Oulu for financial support during mobility activities. The authors thanks Dr. Andreas Leemann for the help with SEM observation. Part of the work was carried out with the support of the Centre for Material Analysis, University of Oulu, Finland.

References

Badjatya, P., Akca, A.H., Fraga Alvarez, D.V., Chang, B., Ma, S., Pang, X., Wang, E., van Hinsberg, Q., Esposito, D.V., Kawashima, S., 2022. Carbon-negative cement manufacturing from seawater-derived magnesium feedstocks. Proceedings of the National Academy of Sciences 119, e2114680119. https://doi.org/10.1073/pnas.2114680119

Canterford, J.H., Tsambourakis, G., Lambert, B., 1984. Some observations on the properties of dypingite, Mg5(CO3)4(OH)2·5H2O, and related minerals. Mineralogical Magazine 48, 437–442. https://doi.org/10.1180/minmag.1984.048.348.15

Friedel, B., 1975. Synthetischer Giorgiosit. Neues Jahrb Mineral Monatsh 1975, 196–208.

Frost, R.L., 2011. Raman spectroscopic study of the magnesium carbonate mineral hydromagnesite (Mg5[(CO3)4(OH)2]· 4H2O). Journal of Raman Spectroscopy 42, 1690–1694. https://doi.org/10.1002/jrs.2917

Hopkinson, L., Rutt, K., Cressey, G., 2008. The Transformation of Nesquehonite to Hydromagnesite in the System CaO-MgO-H2O-CO2 CaO - MgO - H 2 O - C O 2 : An Experimental Spectroscopic Study. The Journal of Geology 116, 387–400. https://doi.org/10.1086/588834

Nguyen, H., Santos, H., Sreenivasan, H., Kunther, W., Carvelli, V., Illikainen, M., Kinnunen, P., 2022. On the carbonation of brucite: Effects of Mg-acetate on the precipitation of hydrated magnesium carbonates in aqueous environment. Cement and Concrete Research 153, 106696. https://doi.org/10.1016/j.cemconres.2021.106696

Raade, G., 1970. Dypingite, a new hydrous basic carbonate of magnesium, from Norway. Am. Mineral. 55, 1457–1465.

Scott, A., Oze, C., Shah, V., Yang, N., Shanks, B., Cheeseman, C., Marshall, A., Watson, M., 2021. Transformation of abundant magnesium silicate minerals for enhanced CO 2 sequestration. Communications Earth & Environment 2, 1–6. https://doi.org/10.1038/s43247-021-00099-6

Skliros, V., Tsakiridis, P., Perraki, M., 2020. A combined Raman, Fourier transform infrared, and X-ray diffraction study of thermally treated nesquehonite. Journal of Raman Spectroscopy 51, 1445–1453. https://doi.org/10.1002/jrs.5768

Wang, L.-Y., Zhang, Y.-H., Zhao, L.-J., 2005. Raman Spectroscopic Studies on Single Supersaturated Droplets of Sodium and Magnesium Acetate. J. Phys. Chem. A 109, 609–614. https://doi.org/10.1021/jp0458811

Zevenhoven, R., Slotte, M., Koivisto, E., Erlund, R., 2017. Serpentinite Carbonation Process Routes using Ammonium Sulfate and Integration in Industry. Energy Technology 5, 945–954. https://doi.org/10.1002/ente.201600702

The 16th International Congress on the Chemistry of Cement 2023 (ICCC2023)
"Further Reduction of CO_2 -Emissions and Circularity in the Cement and Concrete Industry"
September 18–22, 2023, Bangkok, Thailand

Limitations of isothermal calorimetry for sulfate optimization of Limestone Calcined Clay Cements (LC^3)

M. R.C. Silva[a,b*], J.S. Andrade Neto[a], B. Walkley[b], and A.P. Kirchheim[a*]

[a] *Department of Civil Engineering, Universidade Federal do Rio Grande do Sul, Av. Osvaldo Aranha, 99/706, Zip Code: 90035-190, Porto Alegre, RS, Brazil.*

[b] *Department of Chemical and Biological Engineering, The University of Sheffield, Sir Robert Hadfield Building, Mappin Street, S1 3J, Sheffield, United Kingdom.*

*Corresponding authors. *Email:* mrcardosodasilva1@sheffield.ac.uk (M.R.C. Silva). anapaula.k@gmail.com (APK)

ABSTRACT

Compared to Portland cement, LC^3 has accelerated sulfate depletion during hydration, leading to subsulfated systems where an extra amount of calcium sulfate is needed to ensure proper interval between the reactions of the silicate and aluminate phases. This study assessed the sulfate optimization by isothermal calorimetry (within 72 hours), in terms of $SO_{3,\ total}$, in two LC^3-based pastes mixes (with kaolinite or montmorillonite calcined clays). Quartz powder in place of calcined clay was used as a reference LC^3. The qualitative observation of isothermal calorimetry results for sulfate optimization is very empirical. Therefore, using solely isothermal calorimetry is insufficient and more tests should be performed to help define this parameter. This work provides important insight into methods for assessing sulfate optimization in LC^3, information that is critical to enable widespread implementation of these low-carbon cements.

KEYWORDS: *metakaolin; bentonite, sulfate balance, optimal sulfate, SO_3*

1. Introduction

Sulfate optimization is essential to balance the early and later reactions occurring during the hydration of Portland cement (PC). It consists of adding calcium sulfate into cement (more than added during clinker grinding) to ensure proper sulfated cements. Otherwise, sub-sulfated or super-sulfated cements may occur, impairing the kinetics of silicate and aluminate phases at early ages or bringing durability problems at longer ages, respectively (Andrade Neto, De la Torre and Kirchheim, 2021). This is a common problem with LC^3-type cements, and further studies on the effectiveness and limitations of analytical techniques on cements are needed.

Isothermal calorimetry has been performed to assess the sulfate balance in LC^3. It is unknown if this would be a suitable approach, particularly if one would go a step further by using other calcined clays, such as calcined Na-bentonite clay, in which montmorillonite is the main clay mineral. This study investigated the limitations of the isolated use of isothermal calorimetry in determining the optimal sulfate content in LC^3 cements. The work discusses the need for further studies on possibilities and approaches to correct sulfate balancing, estimating the greater use of blended cements with lower environmental impact.

2. Materials and methods

2.1 Materials characterization and mix proportions

This study used a natural clay (kaolinite clay, CK) and commercial sodium bentonite (Na-montmorillonite main clay mineral, CM), obtained from Pantano Grande, southern Brazil, and Buschle & Lepper S.A., respectively. In a static oven, both clays were calcined at 800 °C at 1h. Mineral gypsum ($CaSO_4.2H_2O$) (GYP) as calcium sulfate, Portland clinker (PC) and limestone (LS) were provided by the cement industry. A commercial quartz powder (QP) was used as inert material. The materials' PSD was measured by laser granulometry in triplicate with 60 seconds of ultrasound/each repetition and dispersion in isopropanol or water. The specific surface area was measured using BET method (SSA_{BET}), heating rate 20 °C/min with gas nitrogen atmosphere. The chemical composition was assessed by X-ray fluorescence (XRF) in a sequential X-ray fluorescence spectrometer between 400 and 4000 cm-1 wavelengths. Key material characteristics are presented in Table 1.

Table 1 Materials characteristics

Characterization	Portland Cement (PC)	Quartz powder (QP)	Calcined kaolinite (CK)	Calcined montmorillonite (CM)	Limestone (LS)	Gypsum (GYP)
D_{v90} (μm)	27.79	13.01	37.85	39.83	37.18	34.83
SSA_{BET} (m^2/g)	2.51	2.71	12.00	15.35	1.02	5.11
Oxide compositions (wt.%) as determined by X-ray fluorescence analysis						
SiO_2	19.97	96.98	45.70	61.93	0.23	0.72
Al_2O_3	3.96	2.22	38.20	19.73	0.08	0.21
Fe_2O_3	3.11	-	0.65	5.02	0.05	0.11
CaO	60.43	-	0.31	1.30	55.06	33.27
MgO	7.64	-	-	3.01	0.44	0.59
SO_3	1.21	0.34	-	1.28	0.07	43.48
K_2O	1.39	0.10	0.39	0.45	0.01	0.05
P_2O_5	0.08	-	-	0.09	0.09	-
MnO	0.15	-	-	0.02	0.01	0.03
ZnO	-	0.09	-	-	-	-
SrO	0.04	-	-	0.02	0.23	0.18
Na_2O	0.20	-	-	2.92	0.05	-
TiO_2	0.20	0.06	0.13	0.51	-	0.01
LOI	1.37	14.62	10.54	3.53	43.61	21.62
%Total	99.8	100	95.92	99.8	99.9	100

The blended cements were prepared based on the mix proportions of LC^3-50 (Antoni *et al.*, 2012). Clinker and gypsum proportions were adjusted based on 5 levels of $SO_{3,\ total}$ (2.0-4.0 wt.%), while calcined clay (or quartz) and LS were fixed. The $SO_{3,\ total}$ was calculated by Equation 1(ASTM, 2018). Where $M_{calcium\ sulfate}$ = mass of calcium sulfate (gypsum); M_{cement} = mass of cement; $SO_{3\text{-}calcium\ sulfate}$ = mass percentage of SO_3 in the calcium sulfate; and $SO_{3\text{-}cement}$ = mass percentage of SO_3 in the cement. The water:cement (w:c) ratio at 0.5.

$$SO_{3total} = \frac{M_{calcium\ sulfate}}{M_{calcium\ sulfate} + M_{cement}} x\ SO_{3-calcium\ sulfate} + \frac{M_{cement}}{M_{calcium\ sulfate} + M_{cement}} x\ SO_{3-cement} \quad (1)$$

Table 2 Mix proportions used to prepare the cement samples in this study

Cement	PC	GYP	LS	QP	CK	CM	$SO_{3,\ total}$
LC^3-QP_2.0%$\bar{S}$	52.11	2.89	15.00	30.00	-	-	2
LC^3-QP_2.5%$\bar{S}$	50.93	4.07	15.00	30.00	-	-	2.5
LC^3-QP_3.0%$\bar{S}$	49.74	5.26	15.00	30.00	-	-	3
LC^3-QP_3.5%$\bar{S}$	48.56	6.44	15.00	30.00	-	-	3.5
LC^3-QP_4.5%$\bar{S}$	47.38	7.62	15.00	30.00	-	-	4
LC^3-CK_2.0%$\bar{S}$	51.87	3.13	15.00	-	30.00	-	2
LC^3-CK_2.5%$\bar{S}$	50.68	4.32	15.00	-	30.00	-	2.5
LC^3-CK_3.0%$\bar{S}$	49.50	5.50	15.00	-	30.00	-	3
LC^3-CK_3.5%$\bar{S}$	48.32	6.68	15.00	-	30.00	-	3.5
LC^3-CK_4.0%$\bar{S}$	47.14	7.86	15.00	-	30.00	-	4
LC^3-CM_2.0%$\bar{S}$	52.78	2.22	15.00	-	-	30.00	2
LC^3-CM_2.5%$\bar{S}$	51.59	3.41	15.00	-	-	30.00	2.5
LC^3-CM_3.0 %$\bar{S}$	50.41	4.59	15.00	-	-	30.00	3
LC^3-CM_3.5%$\bar{S}$	49.23	5.77	15.00	-	-	30.00	3.5
LC^3-CM_4.0%$\bar{S}$	48,04	6.96	15.00	-	-	30.00	4

2.3 Isothermal calorimetry

The test was performed on a TA instruments TAM Air calorimeter. 100 grams of dry material was placed in a stainless-steel container and mixed with deionized water at 0.5 w/c (wt.%). The pastes were manually mixed with a threaded rod for 30 seconds, after 20 seconds of resting, then the paste was mechanically mixed for 70 seconds in a 10,000-rpm mixer. About 5 grams of paste was added to the equipment for monitoring hydration for 72 hours. Deionized water was used as a reference sample.

3. Results and discussion

Figure 1 shows the calorimetry results of the cements with calcined clays (or quartz powder as reference material) for different levels of total SO_3, normalized per gram of clinker.

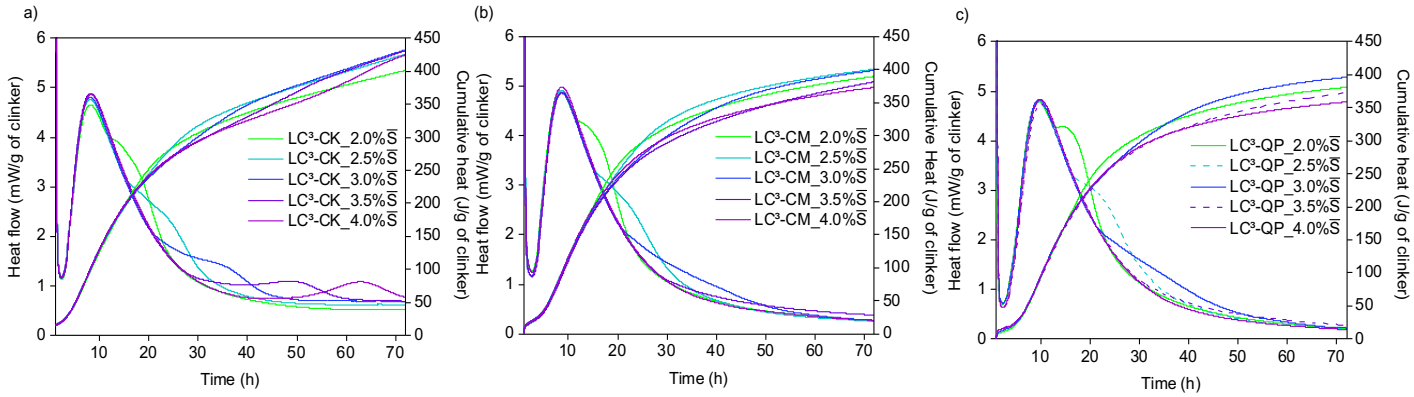

Figure 1 Materials characterization

Sulfate optimization using isothermal calorimetry in LC^3 has been mainly based on two approaches. The first one, used by a group of authors, adds extra amounts of gypsum to the cement (beyond that added in the clinker grind) until the aluminate heat flow peak is distinct from the silicate heat peak (Avet and Scrivener, 2018, 2020; Avet, Boehm-Courjault and Scrivener, 2019). Increasing the gypsum content (here as $SO_{3,\,total}$) lead to a smaller, broader, and delayed second heat flow peak in LC^3, as well as observed by previous study (Zunino and Scrivener, 2019). This simple criterion would include all SO_3 levels observed within 72h in the LC^3-CK and only the 2-3% SO_3 levels in -QP and -CM cements.

However, many reasons can suggest that this is not the most suitable approach for determining the optimum sulfate content in blended cements. First, the simple criterion based on an extra addition of gypsum to cement can result in higher SO_3 contents in cement. High levels of calcium sulfate can affect the durability of concrete structures due to the increase likelihood of delayed ettringite formation (DEF), according to (Mohammed and Safiullah, 2018). Instead, the optimum sulfate content should be determined by SO_3 content as describe by cement standards. The Brazilian standard (ABNT, 2018) limits this total value to 4.5% (SO_3) and the European standard (EN 197-1, 2018) limits to 3.5-4 % (SO_3), while the American standard (ASTM, 2018) only request a limited expansion. The second reason is due to the substitution of cement clinker by gypsum (to change the SO_3 levels), as the compressive strength can also reduce. The third reason is that high additions of gypsum into cement delay the start of the reactions and the onset of the aluminates peak, which can affect the kinetics of reactions due to the time for the proper reactions of C_3A with gypsum. It is important to think carefully how to define an upper bound for optimum sulfate content – the lower bound is easy to define using isothermal calorimetry, but the upper bound is more challenging.

The second sulfate optimization approach is defined by the mix of the highest total 72h cumulative heat (or just total heat) released between all the SO_3 levels assessed (ASTM, 2018). As shown in Figure 2, the SO_3 level which presented the highest total heat was 3% for all the cements, indicating the optimum SO_3 level. However, note that this determination based only on total heat released leads to a determination of the mixes with longer reaction times between aluminate and silicate peaks among all cements.

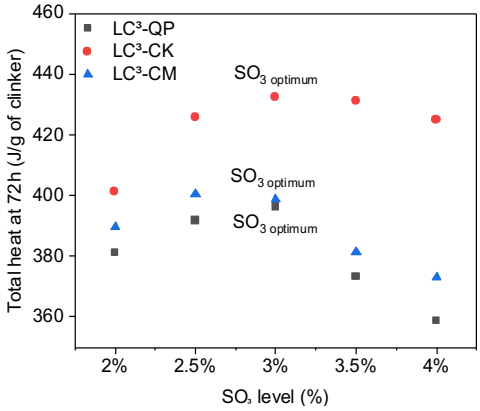

Figure 2 total heat at 72 hours vs. the $SO_{3,\,total}$ levels

4. Conclusions

Sulfate optimization based on isothermal calorimetry data is an empirical approach. The visual determination of the heat flow peaks must be used carefully as higher amounts of gypsum leads to delay the kinetics reaction, especially for low reactivity calcined clays, such as montmorillonite clays. Higher total heat does not necessarily mean in a proper sulfate content. Sulfate optimization in terms of $SO_{3,\,total}$ level, over addition of gypsum (wt.%) is encouraged.

Therefore, using solely isothermal calorimetry is insufficient to determine the optimum $SO_{3,\,total}$ level and more tests should be performed to help define this parameter. Quantitative approaches can be useful in this matter (modelling, compressive strength tests, etc). However, it is worth pointing out that the proper sulfate content should be based on criteria established by the decision maker.

Acknowledgements

Intercement Participações S.A supported the participation of MRCS. The participation of JSAN was supported by the fellowship DAI/CNPq/Brazil. The participation of BW was sponsored by The Department of Chemical and Biological Engineering, The University of Sheffield. APK was sponsored by CNPq/Brazil. We thank the cement industry for the supplied materials.

References

ABNT (2018) *NBR 16697: Cimento Portland-Requisitos*. Available at: www.abnt.org.br.

Andrade Neto, J. da S., De la Torre, A.G. and Kirchheim, A.P. (2021) 'Effects of sulfates on the hydration of Portland cement – A review', *Construction and Building Materials*, 279. Available at: https://doi.org/10.1016/j.conbuildmat.2021.122428.

Antoni, M. *et al.* (2012) 'Cement substitution by a combination of metakaolin and limestone', *Cement and Concrete Research*, 42(12), pp. 1579–1589. Available at: https://doi.org/10.1016/j.cemconres.2012.09.006.

ASTM (2018) 'C563:18 - Standard Guide for Approximation of Optimum SO_3 in Hydraulic Cement 1'. Available at: https://doi.org/10.1520/C0563-19.

Avet, F., Boehm-Courjault, E. and Scrivener, K. (2019) 'Investigation of C-A-S-H composition, morphology and density in Limestone Calcined Clay Cement (LC^3)', *Cement and Concrete Research*, 115, pp. 70–79. Available at: https://doi.org/10.1016/j.cemconres.2018.10.011.

Avet, F. and Scrivener, K. (2018) 'Investigation of the calcined kaolinite content on the hydration of Limestone Calcined Clay Cement (LC^3)', *Cement and Concrete Research*, 107, pp. 124–135. Available at: https://doi.org/10.1016/j.cemconres.2018.02.016.

Avet, F. and Scrivener, K. (2020) 'Study of Concrete Made of Limestone Calcined Clay Cements (LC^3)', pp. 257–261. Available at: https://doi.org/10.1007/978-981-15-2806-4_29.

EN 197-1 (2018) *EN 197-1 Cement-Part 1: Composition, specifications and conformity criteria for common cements*. Available at: www.mbsmw.org (Accessed: 5 July 2021).

Mohammed, S. and Safiullah, O. (2018) 'Optimization of the SO_3 content of an Algerian Portland cement: Study on the effect of various amounts of gypsum on cement properties', *Construction and Building Materials*, 165, pp. 362–370. Available at: https://doi.org/10.1016/j.conbuildmat.2017.12.218.

Zunino, F. and Scrivener, K. (2019) 'The influence of the filler effect on the sulfate requirement of blended cements', *Cement and Concrete Research*, 126. Available at: https://doi.org/10.1016/j.cemconres.2019.105918.

The 16th International Congress on the Chemistry of Cement 2023 (ICCC2023)
"Further Reduction of CO_2 -Emissions and Circularity in the Cement and Concrete Industry"
September 18–22, 2023, Bangkok, Thailand

Chemical and structural evolution of magnesium silicate hydrate

Marco Simoni[1], Chun Long Woo[2], Han Zhao[2], Dinu Iuga[3], Petr Svora[4], Theodore Hanein[2], Hajime Kinoshita[2], and Brant Walkley[1]

[1] Department of Chemical and Biological Engineering, University of Sheffield, S1 3JD, United Kingdom
[2] Department of Materials Science & Engineering, University of Sheffield, S1 3JD, United Kingdom
[3]Department of Physics, University of Warwick, Coventry, UK
[4]Department of Materials Engineering and Chemistry, Czech Technical University in Prague, Prague, Czech Republic

ABSTRACT

Magnesium silicate hydrate (M-S-H) is a binder phase that is of interest for construction and radioactive waste immobilisation applications, due to its low-energy production process and chemical durability. Given the higher availability of $Mg(OH)_2$ in comparison to the limited sources of natural $MgCO_3$, $Mg(OH)_2$ was used as a precursor for the synthesis of M-S-H. This study investigates the compositional and nano-structural development of M-S-H gels over time. M-S-H samples cured at 35°C for 7, 14, 28, 56, and 112 days were studied using high field nuclear magnetic resonance experiments probing ^{25}Mg and ^{29}Si nuclei, as well as X-ray diffraction, scanning electron microscopy, and thermogravimetric analysis. M-S-H gels were formed and observed to exhibit nanostructural rearrangement over time. The gel-like structure appeared exhibit a metastable state after 56 days of curing, when the average Mg/Si ratio was assessed between 0.5 and 1.0; beyond that, a further dissolution of brucite led to a higher Mg/Si ratio (0.8 – 1.0) within the M-S-H. The M-S-H exhibited structural similarity to the serpentine-group mineral lizardite, and modelling of the kinetics of dissolution of silica fume and brucite indicated that the mechanism of the formation of M-S-H was controlled by nucleation reactions. M-S-H silicate chains are more hydrated than the endmembers or crosslinking members. Increased gel crosslinking and polymerisation is also observed at later ages providing crucial information on the durability of M-S-H cements. The evolution of the M-S-H was studied in terms of Mg/Si molar ratio, which was observed to continue to change over time even after complete reaction of the solid precursors.

KEYWORDS: *Magnesium silicate hydrate; reaction mechanisms, kinetics; nanostructure*

1. Introduction

Magnesium-based cements comprising magnesium silicate hydrate (M-S-H) gels are alternative low-carbon cements comprising predominantly a (M-S-H) gel (Gartner and Sui 2018). M-S-H gels do not exhibit long range order, and are believed to be composed of tetrahedral and octahedral sheets containing mainly Si^{4+} and Mg^{2+}, respectively, and often compared to talc ($Mg_3Si_4O_{10}(OH)_2$) or serpentine-group minerals ($Mg_3(Si_2O_5)(OH)_4$) (Brew and Glasser 2005, Roosz, Grangeon et al. 2015, Bernard, Lothenbach et al. 2019). However, there remains some debate around the most appropriate structural model for M-S-H (Walkley and Provis 2019), and the chemical composition of M-S-H changes over its lifetime (Bernard, Lothenbach et al. 2017) and depends on factors such as chemical composition of the precursors and reaction mixture, temperature, pressure, and activity of water. Here, we synthesise M-S-H gels via reaction of $Mg(OH)_2$ and silica fume, and examine their chemical and nanostructural evolution over time.

2. Magnesium silicate hydrate synthesis and characterisation

Samples were prepared in a single batch using solid, powdered, reagent grade chemicals magnesium hydroxide $Mg(OH)_2$ (brucite, Sigma-Aldrich, ≥95%) and silica fume (SiO_2, Elkem microsilica 940-U). $Mg(OH)_2$, rather than the more commonly used solid precursor MgO, was used as a precursor for the synthesis of M-S-H gel for two reasons: 1) the use of $Mg(OH)_2$ would be beneficial for commercialisation of M-S-H cements, given the alternative production routes cited above which would mitigate the limited availability of natural $MgCO_3$ required for production of MgO, and 2) $Mg(OH)_2$ powder facilitates faster dissolution of the solid precursor than MgO, and hence greater availability of soluble Mg^{2+} during the

early stages of reaction. The oxide (wt.%) chemical composition of silica fume, as determined by X-ray fluorescence (XRF) analysis, is reported in Table 1, and the purity of silica fume is 94.4% wt.% SiO_2. Particle size distribution (PSD) analysis was performed using a Malvern Mastersizer, and revealed average diameter sizes (D_{50}) of 83.0 and 6.0 μm for the silica fume and brucite, respectively (Supplementary Information Figure S1).

Table 1. *Oxide composition (wt.%) of silica fume as determined by X-ray fluorescence analysis, together with the Loss On Ignition (LOI) at 1000°C.*

Oxide	**SiO_2**	**K_2O**	**MgO**	**Fe_2O_3**	**Al_2O_3**	**Na_2O**	**CaO**	**ZnO**	**Others**	**LOI (%)**
Wt.%	*94.4*	*1.1*	*0.7*	*0.6*	*0.5*	*0.3*	*0.2*	*0.2*	*2.0*	1.82

***only compounds with >0.1 wt.% are presented**

Samples were prepared in a single batch with mass ratios of $Mg(OH)_2$:silica fume:H_2O equivalent to 1:1:2, with excess distilled water provided to ensure a workable viscosity and complete hydration. Considering the purity of both $Mg(OH)_2$ and silica fume, this formulation resulted in a Mg/Si molar ratio of 1.05 for all samples. The batch was mixed using a Kenwood mixer by first adding the distilled water to the brucite powder, and then adding silica fume slowly over a few minutes to avoid dusting and mass loss. Once all the silica fume was added, the batch was mixed for further five minutes to produce a homogeneous paste. The paste was then divided into five 50 mL centrifuge tubes (each approximately 30 mL filled) which were sealed and cured at 35°C for 7, 14, 28, 56, and 112 days.

Samples were characterised by X-ray diffraction, scanning electron microscopy (SEM) with energy dispersive X-ray spectroscopy (EDS), thermogravimetry, and solid state nuclear magnetic resonance (NMR) spectroscopy experiments probing ^{29}Si and ^{25}Mg. Finally, the mechanisms and kinetics of dissolution of SiO_2 and $Mg(OH)_2$ to form M-S-H was analysed using three solid-state kinetic models often used for solid state reactions (Khawam and Flanagan 2006), specifically the Avrami-Erofeyev nucleation model, contracting volume model, and 3D diffusion model.

3. Results and Discussion

M-S-H gels were synthesised via reaction of $Mg(OH)_2$ with silica fume, and ^{25}Mg and ^{29}Si MAS NMR and ^{1}H–^{29}Si CP MAS NMR experiments, complemented by X-ray diffraction, scanning electron microscopy (SEM), and thermogravimetric (TG) measurements, were used to examine and quantify 1) the dissolution of brucite and silica fume during reaction, 2) the chemical and nanostructural evolution of the M-S-H gels over time, and 3) model the reaction kinetics and mechanism of M-S-H formation.

In each sample, a M-S-H gel was formed after curing for 7 days, with no additional reaction products observed at any curing age examined (up to 112 days). The M-S-H gel exhibited a microstructure with a gel-like morphology, with globular chains (Figure 1). During the early stages of reaction (<56 days curing), the gels exhibited significant variations in chemical composition (with a broad distribution of molar Mg/Si values of between 0.5 and 1.0), however after curing for 112 days, two distinct M-S-H gels were formed, each with minimal variation in chemical composition: a Si-rich M-S-H gel with molar Mg/Si = 0.55 (±0.2), and a Mg-rich M-S-H gel with molar Mg/Si = 0.80 (±0.5). This appeared to result from the spatial distribution of silica fume and brucite particles, which caused kinetic limitations on mass transport of Si and Mg ions, creating regions rich in either Si or Mg ions. For all samples, multinuclear solid-state NMR spectroscopy experiments probing ^{25}Mg and ^{29}Si nuclei (Figure 1), including measurements at high field, showed unambiguously the formation of a M-S-H gel with structural similarity to the thermodynamically stable serpentine-group mineral lizardite, suggesting that a thermodynamically stable M-S-H is formed within 112 days in these samples. The M-S-H gel at each curing time exhibited a high degree of Q^3 Si sites relative to Q^2 and Q^1 Si sites, indicating a significant degree of polymerisation. After 56 days curing, ^{25}Mg and ^{29}Si MAS NMR and ^{1}H–^{29}Si CP MAS NMR spectroscopy and SEM-EDX data showed continued incorporation of Mg into the M-S-H gel and subsequent preferential formation of the Mg-rich M-S-H phase in the sample.

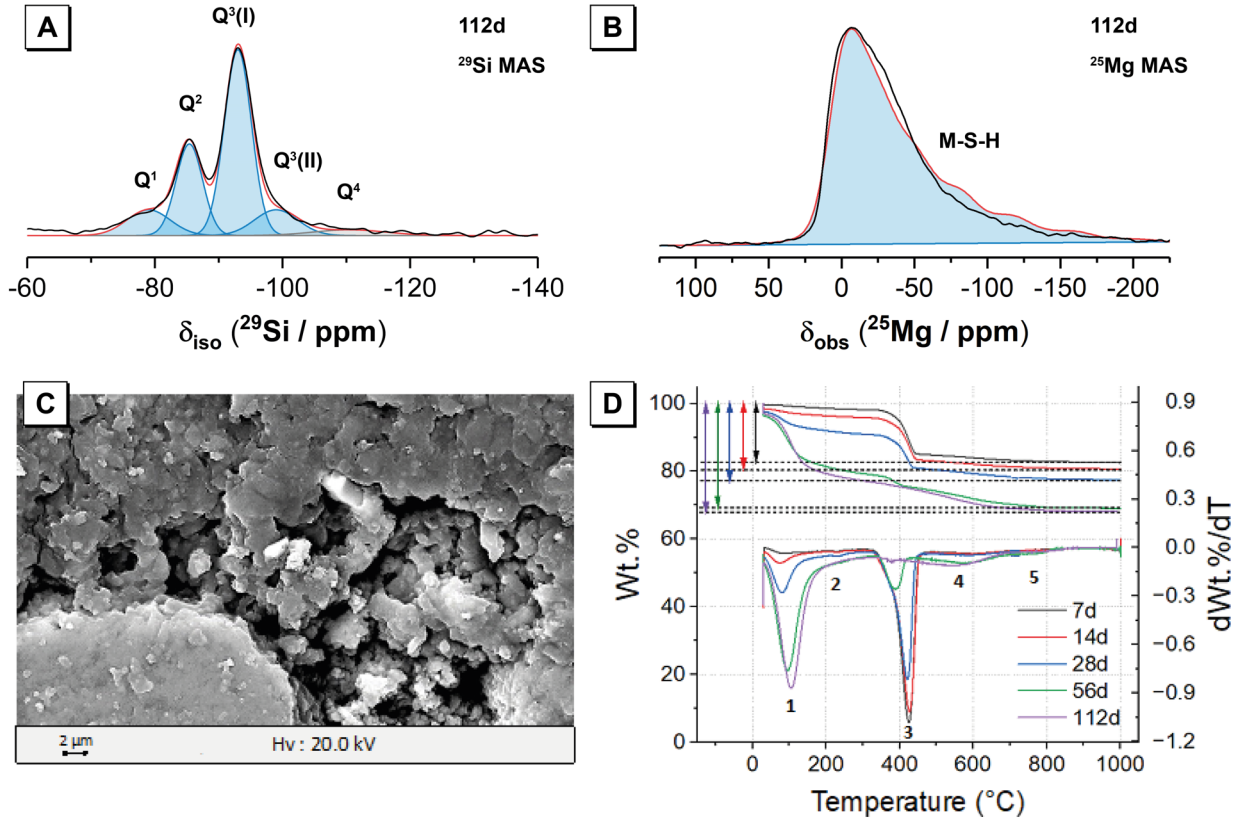

Figure 1: a) ^{29}Si MAS (B_0 = 11.7 T, ν_R = 12.5 kHz) and b) ^{25}Mg MAS (B_0 = 20.0 T, ν_R = 14 kHz) NMR data and associated deconvolutions for the gel cured for 112 days. Data are shown in black; the fit (red) is the sum of the deconvoluted peaks; peaks attributed to Si or Mg sites in M-S-H are shaded blue; those attributed to sites within remnant anhydrous silica fume or brucite are shaded grey; c) Secondary electron SEM images of the gel cured for 112 days; d) TG/dTG data for gels cured for 7, 14, 28, 56, and 112 days. Mass loss event 1, 4, and 5 are attributed to M-S-H, and mass loss events 2 and 3 are attributed to brucite.

Quantification of data from ^{25}Mg and ^{29}Si MAS NMR and ^{1}H–^{29}Si CP MAS NMR spectroscopy experiments, electron microscopy, and thermogravimetric measurements (Figure 1) showed that upon mixing of brucite, silica fume, and water, dissolution of brucite and silica fume both occurred approximately linearly with time up to 56 days curing, correlating with the subsequent formation of M-S-H that occurred approximately linearly with time up to 56 days. The data were fit with and showed strong correlation with the Avrami-Erofeyev nucleation solid-state kinetic model, indicating that the mechanism behind the formation of M-S-H in these samples was governed by nucleation reactions. After this time, the consumption of silica fume and brucite and their incorporation of Si and Mg into M-S-H plateaus, but the nanostructural rearrangement of the M-S-H gel continues, with an increase in crosslinking and polymerisation of M-S-H as the gel ages. Furthermore, rearrangement in the local hydration (i.e. clustering of water molecules) surrounding each Si site occurs as the gel age, with M-S-H silicate chains becoming more hydrated than the endmembers or crosslinking members.

Through quantification of the thermogravimetric and NMR data and associated spectral deconvolutions, and fitting data regarding dissolution and extent of reaction over time with the appropriate solid-state kinetic models, this study reveals mechanisms and kinetics of M-S-H formation, and the chemical composition, nanostructure, and local hydration of these M-S-H gels. This has significant implications for the application of binders comprising M-S-H gels in construction and contaminant and radioactive waste immobilisation applications, particular regarding chemical durability and immobilisation capability. Furthermore, this study highlighted the limitations of using solely XRD data to identify formation of M-

S-H gels, and the necessary use of both spectroscopic and thermogravimetric characterisation techniques to identify and quantify this phase conclusively.

3. Conclusions

M-S-H gels were synthesised via reaction of $Mg(OH)_2$ and silica fume, and use ^{25}Mg and ^{29}Si MAS NMR and ^{1}H–^{29}Si CP MAS NMR spectroscopy experiments, complemented by X-ray diffraction (XRD), electron microscopy, and thermogravimetric measurements, to examine the chemical and nanostructural evolution of the M-S-H gels over time.

In each sample, a M-S-H gel was formed after curing for 7 days, with no additional reaction products observed at any curing age examined (up to 112 days). After curing for 112 days, two distinct M-S-H gels were formed, each with minimal variation in chemical composition: a Si-rich M-S-H gel with molar Mg/Si = 0.55 (±0.2), and a Mg-rich M-S-H gel with molar Mg/Si = 0.80 (±0.5). This appeared to result from the spatial distribution of silica fume and brucite particles, which caused kinetic limitations on mass transport of Si and Mg ions, creating regions rich in either Si or Mg ions.

Upon mixing of brucite, silica fume, and water, dissolution of brucite and silica fume both occurred approximately linearly with time up to 56 days curing, correlating with the subsequent formation of M-S-H that occurred approximately linearly with time up to 56 days. The data showed strong correlation with the Avrami-Erofeyev nucleation solid-state kinetic model, indicating that the mechanism behind the formation of M-S-H in these samples was governed by nucleation reactions.

Acknowledgements

We are grateful to the Engineering and Physical Science Research Council (EP/R025959/1), the UK 850 MHz solid-state NMR Facility, itself funded by EPSRC and BBSRC (EP/T015063/1), the University of Warwick, Birmingham Science City Advanced Materials Projects 1 and 2, supported by Advantage West Midlands (AWM) and European Regional Development Fund.

References

Bernard, E., B. Lothenbach, C. Chlique, M. Wyrzykowski, A. Dauzeres, I. Pochard and C. Cau-Dit-Coumes (2019). "Characterization of magnesium silicate hydrate (MSH)." Cement and concrete research **116**: 309-330.

Bernard, E., B. Lothenbach, D. Rentsch, I. Pochard and A. Dauzères (2017). "Formation of magnesium silicate hydrates (MSH)." Physics and Chemistry of the Earth, Parts A/B/C **99**: 142-157.

Brew, D. R. M. and F. P. Glasser (2005). "Synthesis and characterisation of magnesium silicate hydrate gels." Cement and Concrete Research **35**(1): 85-98.

Gartner, E. and T. Sui (2018). "Alternative cement clinkers." Cement and Concrete Research **114**: 27-39.

Khawam, A. and D. R. Flanagan (2006). "Solid-state kinetic models: basics and mathematical fundamentals." The journal of physical chemistry B **110**(35): 17315-17328.

Roosz, C., S. Grangeon, P. Blanc, V. Montouillout, B. Lothenbach, P. Henocq, E. Giffaut, P. Vieillard and S. Gaboreau (2015). "Crystal structure of magnesium silicate hydrates (MSH): The relation with 2: 1 Mg–Si phyllosilicates." Cement and Concrete Research **73**: 228-237.

Walkley, B. and J. L. Provis (2019). "Solid-state nuclear magnetic resonance spectroscopy of cements." Materials Today Advances **1**: 100007.

The 16th International Congress on the Chemistry of Cement 2023 (ICCC2023)
"Further Reduction of CO_2 -Emissions and Circularity in the Cement and Concrete Industry"
September 18–22, 2023, Bangkok, Thailand

Utilization of biochar as a carbon sink in low carbon concrete

Atthapol Kasemsuknimit[1], Benjaluk Na Lampang[2], Nipat Puthipad[3], and Sakprayut Sinthupinyo[4]

[1] *SCG, Bangkok, Thailand*
Email: atthapok@scg.com
[2] *SCG, Bangkok, Thailand*
Email: benjalun@scg.com
[3] *SCG, Bangkok, Thailand*
Email: nipaputh@scg.com
[4] *SCG, Bangkok, Thailand*
Email: sakprays@scg.com

ABSTRACT

Biochar production is a potential approach for capturing and storing atmospheric carbon dioxide. Agricultural waste, such as rice straw and sugarcane leaves, is one of the main greenhouse gas (GHG) sources in Thailand. After cultivation, these straw and leaves are left in the field and decomposed into methane gas. The production of biochar from these wastes can store carbon in the organic part as a solid carbon form. The produced biochar can be used to partially replace cement in concrete, which is widely used material, in order to permanently sink this carbon. In this paper, an experimental study has been conducted to investigate effects of biochar addition on concrete fundamental fresh and hardened properties. The study has suggested that compositions of the biochar are essential for concrete properties, while burning temperature in the process of biochar production can influence biochar properties itself. The biochar is shown to have amorphous silica and fixed carbon as main compositions. Amorphous silica has pozzolanic reaction with cement hydration products and improve compressive strength whereas carbon has negative affect on fresh concrete properties. Total embodied carbon in normal concrete can be reduced around 79kgCO_2e/m^3 or 32%.

KEYWORDS: *Biochar, Low carbon Concrete, Carbon sink*

1. Introduction

Concrete has been widely used for centuries, as one of the building materials, due to its versatility and performance. According to Global Cement and Concrete Association (GCCA), volume of the concrete being produced is forecasted to increase from current 14 billion m^3 to around 20 billion m^3 in 2050. This equals to 3.8Gt CO_2 emitted to the atmosphere. One of the main causes to this high amount of embodied CO_2 in concrete is cement due to high energy consumption in its manufacturing process. Therefore, various supplementary cementitious materials (SCM) have been widely studied to be used for cement replacement in concrete (Fantilli and Jóźwiak-Niedźwiedzka, 2021).
Fly ash is a common SCM in Thailand (Tangtermsirikul, 2003), but its availability is decreasing due to the move towards renewable energy. Calcined clay is being studied as an alternative but it requires higher superplasticizer dosage and can lead to faster loss in workability (Antoni et al, 2012 and Sharma et al, 2021). A novel admixture is needed, which adds to the cost of the concrete (Bhattacherjee et al, 2022).
Recently, biochar has been introduced as a SCM in concrete (Li et al, 2021, Aneja et al, 2022, Khan et al, 2022 and Sirico et al 2022). Since the production of biochar includes thermochemical conversion process (e.g. pyrolysis and gasification) of hydrocarbons from various sources, such as biomass and agricultural waste, stable form of carbon can be obtained (Sun et al, 2017). Typically, biochar can retain 50% of the initial carbon from its production (Kurniawa et al, 2023). Hence, embodied carbon in concrete can be significantly reduced by incorporating biochar as an SCM and permanently sink the retained carbon. However, no research has been found to investigate the effects of biochar from sugarcane leaves, which, according to the Ministry of Energy (Thailand), are one of the main available agricultural waste in Thailand,

on the concrete properties. Therefore, in this study, the impacts of biochar produced from sugarcane leaves in Thailand on properties of concrete, in terms of water demand, slump retention and compressive strength, are investigated. Also, the potential of using biochar as SCM on reducing embodied carbon in concrete has been analyzed.

2. Materials and Testing Method

2.1 Materials and sample preparation

The properties of fundamental materials used in this study include Ordinary Portland cement (OPC), according to ASTM C150, river sand as fine aggregate (FA), coarse limestone, with maximum size of 20mm as coarse aggregate (CA), conforming to ASTM C33, with the specific gravity of 3.15, 2.65 and 2.70 g/cm^3, respectively. A carbohydrate-based mid-range water reducer (WR), corresponding to ASTM C494, was used. Two size ranges of biochar used were prepared in the laboratory by stimulating the thermochemical conversion of sugarcane leaves. These include biochar with the median particle diameter (D50) of 5µm and 13µm called B5 and B13, respectively, with chemical composition shown in Table 1.
A concrete pan mixer was used for all concrete mixes. The batch size of each concrete mix was 20 litres. After the concrete mixing was finished, slump testing was conducted, according to ASTM C143, at 0, 30, 60 and 90 minutes. Moreover, the concrete compressive strength at the age of 3, 7 and 28days was tested by using 3 samples, with the size of 10cm x 10cm x10cm, from each concrete mix per 1 age. Mixture proportions of tested concrete are presented in Table 2. The dosage of water reducer was fixed constant, while water content of each concrete mix was altered to obtain targeted initial slump of 15±1cm.

Table 1
Chemical composition of biochar

Material	Chemical composition (%)														LOI (%)	
	SiO_2	Al_2O_3	Fe_2O_3	CaO	MgO	SO_3	K_2O	P_2O_5	MnO	ZnO	NiO	TiO_2	SrO	Rb_2O	Fixed carbon	Other LOI
Biochar	25.16	2.93	1.27	13.34	0.77	0.44	1.63	0.32	0.07	0.01	0.01	0.24	0.03	0.01	29.58	24.18

Table 2
Concrete mixture proportions

Mix	Mix proportion (kg/m^3)								Admixture (cc/m^3)	Initial slump
	Cement	B5	B13	FA	CA	Designed water	Actual water	W/B	WR	(cm)
C1	275	-	-	850	1150	200	200	0.73	1375	15.0
C2	247	28	-	850	1150	200	210	0.76	1375	14.5
C3	234	41	-	850	1150	200	220	0.80	1375	14.5
C4	247	-	28	850	1150	200	220	0.80	1375	15.0
C5	234	-	41	850	1150	200	215	0.78	1375	15.0

2.2 Concrete embodied CO_2 analysis

In this research work, the potential effect of biochar on the reduction in embodied carbon of concrete were investigated. In order to study this effect, the embodied carbon of each concrete mixture proportion was calculated by using equations from BRE (2018) and emission factors of OPC, FA and CA and WR, and power, of 874, 8.106 and 6.531 $kgCO_2eq/t$ and 0.201 $kgCO_2eq/l$ and 1.029 $kgCO_2eq/m^3$, respectively, according to Thailand Greenhouse Gas Management Organization (TGO). In the case of biochar, the emission factor was calculated based on the assumption that fixed carbon in the biochar can be permanently sunk inside the concrete and CO_2 from the atmosphere can be reduced, which turns out to be -1,084 $kgCO_2eq/t$ (EBC, 2020).

3. Results, Analysis and Discussions

3.1 Effects of Biochar on Concrete Water Demand, Slump Retention and Compressive Strength

In this investigation, the water demand of concrete was used to evaluate the effects of biochar on the workability of the concrete. The results have indicated that the concrete with biochar requires higher amount of water to achieve the same workability as that without biochar replacement (Fig. 1). Besides, the water demand of concrete tends to increase with higher replacement ratio of biochar B5. These results are similar to the findings from Sirico et al (2022) and Gupta and Kua (2018), in which can be explained by the porous structure of the biochar that can absorb high amount of water.

The workability retention of the concrete with biochar has also been measured in terms of decrease in slump over a period of time. Fig. 1 indicates that concrete with biochar tends to have longer workable time as the results show slower loss in slump over time. This may be attributed to the reduction in degree of hydration as the cement has been replaced with biochar.

In addition to the fresh properties of concrete, the compressive strength of all concrete mixture proportions was tested at the age of 3 days, 7 days and 28 days. The results show that the compressive strength of concrete tends to be reduced when cement is replaced by biochar (Fig. 1). The concrete compressive strength decreases as higher replacement ratio of biochar, both B5 and B13, is employed. Besides, concrete with larger biochar particle, B13, tends to have lower compressive strength than that with smaller biochar particle, B5. This can be attributed to the increase in water to binder ratio used and less cement content available for hydration process when incorporating biochar into the concrete, as well as lower reactivity of biochar with larger particle size (Sirico et al, 2022). However, although with higher water content, compressive strength of concrete, at the age of 28day, with 10% replacement of biochar, B5, tends to be slightly lower than that without biochar. Additionally, the results indicate that the concrete with biochar tends to have larger development, with the value of more than 13%, in strength from the age of 7day to 28day, as compared to that without biochar, with the value of around 9%. Aneja et al (2022) have notified similar findings and suggested that this can be due to the potential pozzolanic reactivity of the biochar.

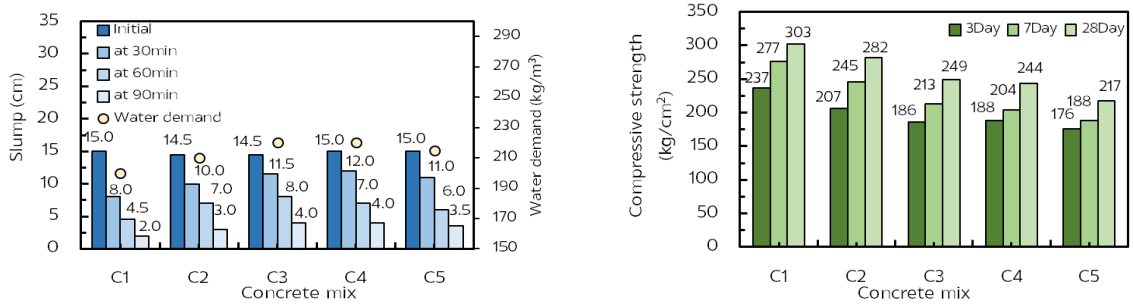

Fig. 1 Influences of biochar on slump retention (left) and compressive strength of concrete (right)

3.2 Potential of Biochar in Reducing Embodied Carbon of Concrete

This study has analyzed the effects of biochar on the embodied carbon of concrete by using equations and assumptions explained in section 2.2. The analysis suggests that, with biochar replacement ratio of 10% and 15%, the embodied carbon of concrete can be reduced by 22% and 32%, respectively, despite the particle size of biochar (Fig. 2). Although, with large particle size of biochar, the concrete compressive strength tends to be significantly reduced, concrete with only 10% replacement ratio of smaller particle size biochar tends to have slightly lower 28day compressive strength, while the embodied carbon can be reduced for 22%, when comparing with that without biochar.

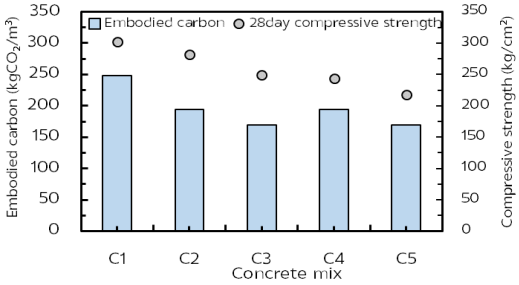

Fig. 2 Embodied carbon and 28day compressive strength of concrete with and without biochar

4. Conclusions

One of the main approaches to reduce embodied carbon of concrete is the use of SCM. The availability of the most commonly used SCM, which is fly ash, is decreasing. Recently, some research works have suggested the utilization of biochar as SCM in concrete. However, no research has been found to consider the biochar from sugarcane leave that is one of most available agricultural waste in Thailand. In order to close down this gap, this study has investigated the influences of biochar from sugarcane leaves in terms of water demand, workability retention, compressive strength and reduction in embodied carbon has also been analyzed. These effects can be concluded as follows:

(1) Employment of biochar leads to higher water demand but slower loss in workability. This can be attributed to high porosity of biochar, which can absorb high amount of water and less cement content in the matrix available for hydration process.
(2) Concrete with biochar was found to have lower compressive strength than that without biochar. This may be attributed to higher water to binder ratio required and less cement content in concrete with biochar.
(3) Concrete with biochar tends to have larger development in strength from 7day to 28day from potential pozzolanic reactivity of the employed biochar.
(4) Based on the assumption that the fixed carbon in biochar can be permanently sunk when being employed in concrete, 10% and 15% replacement ratio of biochar can reduce embodied carbon of concrete for 22% and 32%, respectively.

Although the biochar tends to reduce concrete compressive strength, with 10% replacement ratio of small particle size biochar, the concrete compressive strength is only slightly reduced while the embodied carbon diminished by 22%. Apparently, the concluded findings suggest high potential of biochar from sugarcane leaves to be utilized as SCM in concrete, as well as decreasing the concrete embodied carbon by reducing the cement content used and sinking fixed carbon from agricultural waste.

References

Aneja, A., Sharma, R.L. and Singh, H. (2022) Mechanical and durability properties of biochar concrete. *Materials Today: Proceedings*. 65: 3724-3730.

Antoni, M., Rossen, J., Martirena, F. and Scrivener, K. (2012) Cement substitution by a combination of metakaolin and limestone. *Cement and Concrete Research*. 42: 1579-1589.

Bhattacherjee, S., Jain, S. and Santhanam, M. (2022) A method to increase the workability retention of concrete with limestone calcined clay based cementitious system using a dispersing agent containing sodium hexametaphosphate. *Cement and Concrete Composite*. 132

BRE (2018) Methodology for LCA of buildings using EN 15978:2011. *BRE Global*.

EBC (2020) *Certification of the carbon sink potential of biochar*. Ithaka Institute, Arbaz, Switzerland.

Fantilli, A.P. and Jóźwiak-Niedźwiedzka, D. (2021) Special issue: Supplementary cementitious materials in concrete, part I. *Materials*. 14(9).

Gupta, S. and Kua, H.W. (2018) Effect of water entrainment by pre-soaked biochar particles on strength and permeability of cement mortar. *Construction and Building materials*. 159: 107-125.

Khan, K., Aziz, M.A., Zubair, M. and Amin, M. (2022) Biochar produced from Saudi agriculture waste as a cement additive for improved mechanical and durability properties-SWOT analysis and techno-economic assessment. *Materials*. 15(15).

Kurniawa, T.A., Othman, M.H.D., Liang, X., Goh, H.H., Gikas, P., Chong, K.K. and Chew, K.W. (2023) Challenges and opportunities for biochar to promote circular economy and carbon neutrality. *Journal of Environmental Management*. 332.

Li, J., Spanu, L., Heo, J., Zhang, W., Gardner, D.W., Carraro, C., Maboudian, R. and Monteiro, P.J.M. (2021) Sequestration of solid carbon in concrete: A large-scale enabler of lower-carbon intensity hydrogen from natural gas. *MRS Bulletin*. 46.

Sharma, M., Bishnoi, S., Martirena, F. and Scrivener, K. (2021) Limestone calcined clay cement and concrete: A state-of-art review. *Cement and Concrete Research*. 149.

Sirico, A., Belletti, B., Bernardi, P., Malcevschi, A., Pagliari, F., Fornoni, P. and Moretti, E. (2022) Effects of biochar addition on long-term behavior of concrete. *Theoretical and Applied Fracture Mechanics*. 122.

Sun, J., He, F., Pan, Y. and Zhang, Z. (2017) Effects of pyrolysis temperature and residence time on physiochemical properties of different biochar types. *Soil and Plant Science*. 67 (1): 12-22.

Tangtermsirikul, S. (2003) *Durability and mix design of concrete*. Printing House of Thammasat, Thailand.

The 16th International Congress on the Chemistry of Cement 2023 (ICCC2023)
"Further Reduction of CO_2 -Emissions and Circularity in the Cement and Concrete Industry"
September 18–22, 2023, Bangkok, Thailand

Effect of Carbonated Phases on the Performance of Different MgO-based Formulations

S. Sai Krishna Dinakar[1*], and G.V.P. Bhagath Singh[2]

[1]*Research Scholar, Department of Civil Engineering, SRM University, AP-Andhra Pradesh, Andhra Pradesh, India*
Email: saikrishnadinakar_s@srmap.edu.
[2]*Assistant Professor, Department of Civil Engineering, SRM University, AP, Andhra Pradesh, India*
Email bhagathsingh.g@srmap.edu.in:

ABSTRACT

The current study investigates the strength and phase formation of magnesium cement formulations such as MgO, MgO-MS and MgO-RHA cured in a sealed and carbonated atmosphere. XRD was used to determine the phase formation in these mixes. In the case of MgO-MS binders, carbonated samples attained higher compressive strength than under sealed conditions. Increasing the MgO dosage beyond 50% increases the strength of the mix in case of the sealed condition. Whereas in carbonation, different phenomena were observed. Strength is directly associated with phase information, and Brucite is responsible for strength development in samples that are cured under sealed conditions. Magnesium silicate hydrate (M-S-H) is the major hydration product formed in the case of MgO-MS formulations. The strength depends on the quantity of M-S-H formation and reacted silica content. The level of replacement MgO with microsilica and rice husk ash depends on the reactive silica content. The effect of carbonation in MgO and MgO-RHA mixes are nominal.

KEYWORDS: *Carbonated phases, MgO, Rice husk ash, Microsilica, M-S-H.*

1. Introduction

Reactive magnesium oxide (MgO)-based binders have obtained significant attention due to their potential to be an alternative to ordinary Portland cement (OPC) in certain applications (Walling and Provis (2016)). Researchers are examined various MgO and MgO-microsilica (MS) based binders. Hydration of MgO, which results in the formation of brucite, provides very limited strength in formulations (Liska et al (2008)). At the same time, carbonation improves the strength of the product by forming various hydrated magnesium carbonates (HMCs) (Liska and Al-Tabbaa (2014)). MgO-SiO_2 based binders have the potential to be used as a cementitious binder in building applications due to their satisfactory fresh and hardened properties (Tran and Scott, (2017)). M-S-H is the major hydration product formed during MgO-MS blends, and strength depends on the product quantity (Jia et. al (2016)). Lower M-S-H concentrations and a change in its structure were connected to the drop in strength (Fruhwirth et. al (1985)). Variations in M-S-H formation within different samples could be attributed to variations in the properties and the dissolution rates of various silica sources (Zhang et al., (2011)). Samples with crystalline RHA showed the lowest strength due to the lack of any reaction between crystalline silica and Mg-phases (Sonat et al., (2018)).

So far, studies are focused on strength development by using various MgO-based blends. The link between the formation of different phases and strength gain in MgO and MgO-SiO_2 systems needs to be established. The current study focuses on the properties of MgO and MgO-SiO_2 based binder systems cured at carbonated and ambient conditions. Rice husk ash (RHA) and microsilica were used as sources of SiO_2. The link between the formation of different phases and strength development was established via a detailed microstructural analysis involving various qualitative and quantitative techniques. The quantification of the contents of the hydrate and carbonate phases was performed via X-ray diffraction.

2. Materials and Methods

The raw material used in this study was collected from southern India. Reactive MgO and micro silica (MS) were supplied by Vishnu Priya Chemicals Pvt Ltd, and Rice Husk Ash (RHA) was collected from Sri Varalakshmi Agro Tech Industries. The d_{50} size of the MgO, MS, and RHA are 18.87 µm, 23.87 µm, and 45.72 µm. The oxide composition of these materials is listed in Table 1. Coarse aggregates with a 4.7-9.5 mm particle size were used to prepare concrete samples. The reactive SiO_2 content present in MS and RHA are determined using combined XRF and XRD techniques, and the values are 81.5% and 73.8%.

Table 1 Oxide composition of raw materials (% by mass)

Composition	Na_2O	MgO	Al_2O_3	SiO_2	P_2O_5	SO_3	Cl	K_2O	CaO	MnO	Fe_2O_3	ZnO
MgO	4.05	93.56	0	0.49	0.86	0.56	0	0.42	0	0	0	0
Microsilica	2.85	2.77	2.43	81.5	2.17	0.93	1.15	4.17	1.25	0.04	0.71	0.01
RHA	4.04	2.98	2.11	73.8	0.98	3.46	1.78	6.06	1.54	0.1	2.04	0.37

Three sets of binders were prepared to consist of MgO, MgO-MS, and MgO-RHA. The detailed binder compositions used to prepare samples are listed in Table 2. In all the mixes, the water-to-binder (w/b) ratio was fixed at 0.46. 1.2% of Sodium hexametaphosphate (SHMP) was used as an admixture to improve the workability of the mixes. Concrete samples are prepared with 40% binder and 60% aggregates using pan mixes. After preparation of the mix, concrete was poured into 50X50X50 mm cube moulds, then placed at curing temperature 27±1 ºC with a relative humidity of 95±2%. Two conditions were used: (i) sealed curing and (ii) accelerated curing at 10% CO_2 concentration.

Table 2 Mix proportions of binders (mass proportions)

Label	MgO	MS	RHA
MgO	100	0	0
50MgO-50MS	50	50	0
60MgO-40MS	60	40	0
50MgO-50RHA	50	0	50
60MgO-40RHA	60	0	40

Compressive strength was determined at 3,7,14, and 28 days. After testing the specimens, fragments were collected for microstructural analysis at 7, and 28 days. Coarse aggregates were removed from the fragments to avoid contamination, and Isopropanol solvent exchange was carried out to stop the hydration process. The D8 phaser (Bruker) XRD was used to determine the spectrum of the samples. The diffraction measurements were performed between the 2θ angles from 10 to 70º with a 0.02º increment. The total measurement time is about 30 minutes. Quantification was performed using TOPAS 5 software using an external standard (Corundum) approach (Bhagath Singh et al., 2020)

3. Results and Discussion

3.1 Compressive strength

The strength development of MgO, MgO-MS, and MgO-RHA cured under sealed conditions is shown in Figure 1(a). A steady increase in strength was observed in all mixes with age, and MgO-MS mixes showed higher strengths than the other mixes. An increase in the MgO content from 50% to 60% increases the compressive strength of the MgO-MS mixes at all ages. At an early age (i.e., 3-day), all the mixes strength is similar. The MgO-MS mix attained strength from 7 days onwards. Whereas, MgO-RHA blends showed lower strength compared to other mixes. Increasing the RHA dosage from 40 to 50% does not show improvement in strength at any particular age. Both the MgO-RHA blends showed similar strength at any particular age. Overall, MgO-MS mixes reached 28-day strengths of 34 MPa (60MgO-40MS) and 31 MPa (50MgO-50MS).

A different scenario was observed when carbonation curing, as shown in Figure 1(b). A steady increase in strength was observed in all mixes with age, although carbonation slowed down after the first 7 days of curing. The use of carbonation curing had the highest influence on MgO and MgO-MS mixes, which experienced a 145-171% increase in their 28-day strengths via the use of 10% CO_2 during the curing process. In the case of MgO mixes, the carbonation is influenced after 14 days. Alternatively, carbonation was less influential in the strength development of MgO-RHA mixes, whose performance mainly depended on forming hydrate phases such as M-S-H. Within these samples, very little difference in early and 28-day

strength was observed under both curing conditions. On the other hand, carbonated MgO-MS samples achieved a rapid increase in strength at early ages (i.e. 7 days). Accordingly, this translated into a 177 % increase in the 7-day strength of 50MgO-50MS compared to uncarbonated samples (43.17 Vs. 24.32 MPa). A similar trend was observed in the longer period at 28 days of curing. These samples revealed strengths of up to 53.67 MPa, compared to 31.39 MPa observed in the corresponding samples cured under uncarbonated/sealed conditions. Overall, these results highlighted the critical role of carbonation curing in the strength development of MgO, MgO-MS, and MgO-RHA mixes. Alternatively, MgO-MS and RHA mixes achieved strength via the formation of M-S-H. This could indicate the potential use of Mg-based binders in certain applications.

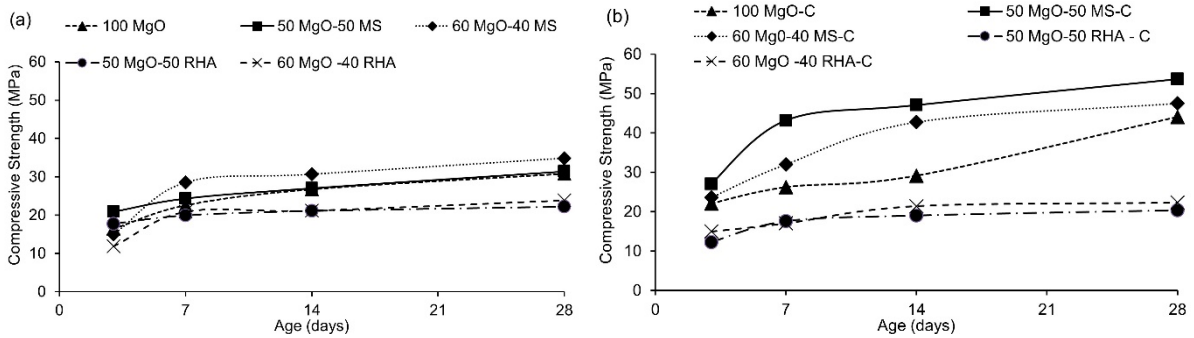

Figure 1 Compressive strength of mixes with age cured at (a) sealed and (b) carbonation.

3.2 Phase quantification

The XRD spectra of MgO and MgO-MS samples cured under sealed and carbonated conditions for 7 and 28 days are shown in Figure 2. Samples cured under sealed conditions revealed brucite periclase and magnesite Samples subjected to carbonation consist of hydromagnesite, nesquehonite, artinite, and dypingite. Brucite was reported as the main hydrate phase under sealed conditions, and the formation of HMCs under carbonation conditions. The obtained phase quantities within each sample are listed in Table 2. A reduction in the periclase content over time was an indication of the continuation of hydration/carbonation within the prepared samples. An increase in the brucite content with curing duration under both curing conditions accompanied this. The use of carbonation curing led to a lower periclase content in MgO samples, which could be partially ascribed to the formation of carbonate phases over time. All samples relatively fixed magnesite content indicated its presence as undecomposed parent material within the original MgO powder. The M-S-H quantification was performed as outlined in bhagath Singh et al. (2020). The obtained phase quantities within each MgO-MS sample are listed in Table 3. Compared to MgO samples, lower periclase contents were observed in MgO-MS samples, which was associated with the increased hydration/carbonation reactions and the latter's lower initial MgO content. A steady decline in the periclase content with age in all the mixes represented the progress of hydration (i.e. under sealed conditions) and carbonation (i.e. under carbonated conditions). Minor formations of HMC phases such as hydromagnesite, dypingite and nesquehonite were observed in carbonated samples, contributing to the strength development of MgO-MS samples over time. The decline in the unreacted glassy content was accompanied by an increase in M-S-H quantity with age under both curing conditions, indicating the progress of hydration. These findings clearly indicated the role of M-S-H in providing strength. Nevertheless, a considerable amount of unreacted glass and periclase was present in these samples even after 28 days, indicating that the continued progress of hydration enabled via the availability of these phases could result in an even better performance in the longer term.

Table 3 Quantities of various compounds with age (% by mass).

Compound name/mix	MgO				50MgO-50MS			
	Sealed		Carbonation		Sealed		Carbonation	
Age (days)	7 days	28 days	7 days	28 days	7 days	28 days	7 days	28 days
Periclase	15.89	6.96	16.19	6.69	7.15	5.45	6.85	4.89
Magnesite	12.45	14.83	11.56	18.59	6.02	7.42	6.15	9.45
Brucite	45.65	77.31	50.12	73.17	2.15	3.21	1.24	2.12
Hydromagnesite	0.24	0.17	0.20	0.16	0.52	0.23	0.61	0.15
Dypingite		0	0	0.09	0	0	0.53	0.21
Unreacted Glass					34.87	14.85	33.65	13.15
M-S-H					45.89	65.54	44.97	70.89

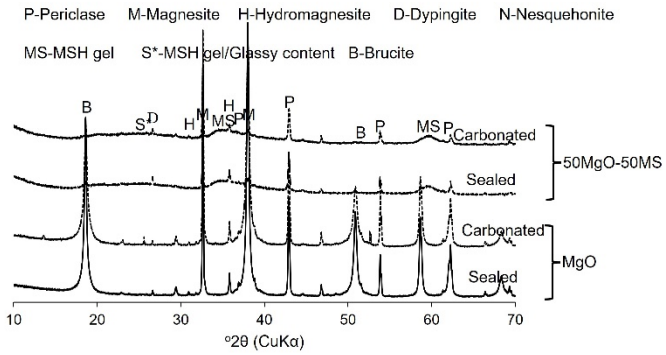

Figure 2 XRD signature of MgO and 50MgO-50MS samples at 28 days.

4. Conclusions

The study investigated the performance and microstructural development of MgO, MgO-MS and MgO-RHA systems cured under two different curing conditions. The use of carbonation curing led to the formation of carbonate phases, along with the major hydrate phases observed under sealed conditions. MgO systems mainly relied on the conversion of brucite into HMCs such as hydromagnesite and nesquehonite for strength development, while the formation of M-S-H was the main source of strength in MgO-MS systems. Increasing the MgO content beyond 50% increases the strength of the concrete cured under sealed conditions, whereas carbonation reduces the strength. MgO-RHA mixes are shown in similar strength irrespective of time and curing, and they attained lower strength compared to MgO and MgO-MS mixes. The increase in strength is associated with M-S-H formation in the MgO-MS mixes. The results indicated a direct link between strength development and M-S-H content in these samples, whereas the unreacted silica and periclase contents were revealed to be inversely proportional to performance.

References

G.V.P. Bhagath Singh, C. Sonat, Y. En-Hua and C. Unluer (2020). "Performance of MgO and MgO-SiO_2 systems containing seeds under different curing conditions," *Cement and Concrete Composites*,108, 103543.

H. Tran, A. Scott, Strength and workability of magnesium silicate hydrate binder systems, *Constr. Build. Mater*. 131 (2017) 526-535.

M. Liska, A. Al-Tabbaa, Ultra-green construction: reactive magnesia masonry products, Waste and Resource Management 162 (2009) 185-196.

M. Liska, L.J. Vandeperre, A. Al-Tabbaa, Influence of carbonation on the properties of reactive magnesia cement-based pressed masonry units*, Adv. Cem. Res*. 20 (2008) 53-64.

S.A. Walling, J.L. Provis, Magnesia-based cements: a journey of 150 years, and cements for the future?, *Chem. Rev*., 116 (2016) 4170-4204.

Y. Jia, B. Wang, Z. Wu, J. Han, T. Zhang, L.J. Vandeperre, C.R. Cheeseman, Role of sodium hexametaphosphate in MgO/SiO2 cement pastes, *Cement Concr. Res.* 89 (2016) 63–71.

O. Fruhwirth, G.W. Herzog, I. Hollerer, A. Rachetti, Dissolution and hydration kinetics of MgO, *Surf. Technol*. 24 (3) (1985) 301–317.

J. Wei, Q. Yu, W. Zhang, H. Zhang, Reaction products of MgO and micro silica cementitious materials at different temperatures, *J. Wuhan Univ. Technol. Mater. Sci. Ed.* 26 (4) (2011) 745–748.

C. Sonat, C. Unluer, Development of magnesium-silicate-hydrate (M-S-H) cement with rice husk ash, *Journal of Cleaner Production* (2018), doi: 10.1016/j.jclepro. 2018.11.246.

The 16th International Congress on the Chemistry of Cement 2023 (ICCC2023)
"Further Reduction of CO_2 -Emissions and Circularity in the Cement and Concrete Industry"
September 18–22, 2023, Bangkok, Thailand

Phase formation and CO_2 absorption of reactive magnesium oxide (MgO) cement (RMC) with additive under various curing regimes

R. Hay[1], L. Gkoura[2], A. Equbal[3], and K. Celik[4*]

[1] *Division of Engineering, New York University Abu Dhabi, Abu Dhabi, P.O. Box 129188, United Arab Emirates*

Email: rh137@nyu.edu
[2] *Division of Science, New York University Abu Dhabi, Abu Dhabi, P.O. Box 129188, United Arab Emirates*

Email l.gkoura@nyu.edu
[3] *Division of Science, New York University Abu Dhabi, Abu Dhabi, P.O. Box 129188, United Arab Emirates*

Email: ae2589@nyu.edu
[4] *Division of Engineering, New York University Abu Dhabi, Abu Dhabi, P.O. Box 129188, United Arab Emirates*

Email: kemal.celik@nyu.edu

ABSTRACT

Reactive magnesium oxide (MgO) cement (RMC) is one of the emerging sustainable alternatives to Portland cement (PC). RMC hydrates to form brucite, which further transforms into carbonates under carbonation. It has been claimed that the formation of crystalline hydrated magnesium carbonates (HMCs) contributes to the strength development of RMC-based composites. However, the relationship between the mechanical performance, content of the crystalline phases, and carbonation level has been contentious. This study offers further insights into the carbonation products of RMC under two curing regimes (20% CO_2 and supercritical CO_2 ($scCO_2$)) with and without calcium oxide (CaO), a common impurity in RMC produced from the dry-route process with magnesite. A series of testing techniques, including X-ray diffraction (XRD), thermal gravimetric analyses (TGA), acid digestion to quantify the CO_2 absorption level, scanning electron microscopy (SEM), and ^{13}C nuclear magnetic resonance (NMR), were performed. XRD data revealed that the peak intensities for the crystalline HMCs did not significantly change between air curing and the two carbonation conditions. A rightward shift of the main decomposition peak from 385 ^oC (assigned to brucite) to 405-415 ^oC was observed for the carbonated samples. To match the CO_2 content obtained from acid digestion, this new peak had to be assigned to CO_2 arising from the decomposition of amorphous carbonation phases. While the exterior regions were dominated by hydromagnesite under 20% CO_2 and nesquehonite under $scCO_2$, the interior regions were concentrated with amorphous carbonates of a fused platelet morphology. The presence of CaO formed smaller-size brucite, leading to faster carbonation. The amorphicity of the carbonates was also confirmed by ^{13}C NMR, which clearly demonstrated C=O peaks.

KEYWORDS: *Reactive magnesium oxide cement, hydration, carbonation, carbonates, CO_2 sequestration*

1. Introduction

Upon contact with water, magnesium oxide (MgO) in reactive MgO cement (RMC) is converted to brucite ($Mg(OH)_2$), which under a carbon dioxide (CO_2) environment undergoes carbonation to form hydrated magnesium carbonates (HMCs) (Dung and Unluer 2017, Dung, Lesimple et al. 2019). It is commonly believed that the carbonation phases include nesquehonite ($MgCO_3.3H_2O$), dypingite ($Mg_5(CO_3)_4(OH)_2.5H_2O$), hydromagnesite ($Mg_5(CO_3)_4(OH)_2.4H_2O$), and artinite ($Mg_2(OH)_2CO_3.3H_2O$) whose formations are governed by **Eqs. 1-4** (Liska and Al-Tabbaa 2008, Liska, Al-Tabbaa et al. 2012, Pu and Unluer 2016, Sonat, Lim et al. 2017). The equations demonstrate the incorporation of CO_2 and H_2O

into the reaction products, leading to a net volume increase (Dung, Lesimple, et al. 2019). The associated pore refinement, together with the interlocking property of the reaction products (Dung and Unluer 2016, Pu and Unluer 2016, Ruan, Liu, et al. 2017), contributes to the strength development of RMC-based composites (Dung and Unluer 2016).

$$Mg(OH)_2 + CO_2 + 2H_2O \rightarrow MgCO_3 \cdot 3H_2O \text{ (nesquehonite)} \quad (1)$$
$$5Mg(OH)_2 + 4CO_2 + H_2O \rightarrow Mg_5(CO_3)_4(OH)_2 \cdot 5H_2O \text{ (dypingite)} \quad (2)$$
$$5Mg(OH)_2 + 4CO_2 \rightarrow Mg_5(CO_3)_4(OH)_2 \cdot 4H_2O \text{ (hydromagnesite)} \quad (3)$$
$$Mg(OH)_2 + CO_2 + 2H_2O \rightarrow Mg_2(CO_3)(OH)_2 \cdot 3H_2O \text{ (artinite)} \quad (4)$$

However, the relationship between the mechanical performance, the content of the crystalline phases and the carbonation level has been contentious. Despite achieving a similar strength level, RMC-based composites were shown to have an effective CO_2 content of about 3 times under supercritical CO_2 ($scCO_2$) conditions compared with a 20%-CO_2 environment (Hay and Celik 2020). The decomposition of HMCs has been reported over a wide temperature spectrum (360-950 ^oC) (Sawada, Uematsu, et al. 1978, Frost, Bahfenne, et al. 2008, Hollingbery and Hull 2010, Jauffret, Morrison et al. 2015), with peak centers assigned at approximately 460, 510, 560 and 650 ^oC. Based on previous works (Hay and Celik 2020, Hay and Celik 2020), the decarbonation at 560 and 650 ^oC was associated with inherent HMCs and $MgCO_3$ of the raw materials. It has been found that a new temperature range of 400-440 ^oC had to be associated with decarbonation to achieve a matching CO_2 content obtained from TGA and acid digestion (Singh, Hay, et al. 2022). The findings indicated that the carbonation products are unknown new phases rather than the crystalline HMCs. Recent studies revealed that the hydration of RMC in the presence of hydromagnesite produced an amorphous phase composed of brucite, hydromagnesite, and water to provide strength to the composite (Kuenzel, Zhang, et al. 2018). Thermogravity confirmed that more water is bound into the new amorphous phase (Winnefeld, Epifania, et al. 2019). It is hypothesized that amorphous phases of similar characteristics also form in RMC under carbonation. The objective of this study is thus to unravel and elucidate the presence of the amorphous phases. Insights into its nature, strength contribution, and morphology will be discussed based on data obtained from compressive strength, CO_2 content from acid digestion, TGA, XRD, SEM, and NMR.

2. Materials and methodology

Reactive magnesium oxide (MgO) cement (RMC) with a mean particle size of 21.2 μm was used as the main binder. Quick lime (CaO) derived from the calcination of limestone ($CaCO_3$) powder with a mean particle size of 5.5 μm and purity of 98.6% was used to replace RMC at 5 and 10 wt.%. The coexistence of $MgCO_3$ and limestone ($CaCO_3$) or dolomite ($CaMg(CO_3)_2$) (Howie, Zussman, et al. 1992, Tang, Yin, et al. 2020) in nature means a consequential presence of CaO in the final RMC. The oxide composition based on X-ray fluorescence (XRF) is given in **Table 1** for RMC. Magnesium acetate $(CH_3COO)_2Mg$, shown to be effective in enhancing the hydration of RMC (Dung and Unluer 2017), was used as a hydration agent (HA) at a concentration of 0.1 M.

Table 1: Oxide composition of RMC

	SiO_2	Al_2O_3	Fe_2O_3	CaO	MgO	SO_3	Na_2O	K_2O	TiO_2	P_2O_5
Reactive MgO	1.20	0.42	0.71	1.31	96.00	0.18	-	0.04	0.01	0.02

Ø25 mm × 25 mm paste and mortar samples were produced for chemical and mechanical testing, respectively. A water-to-binder ratio of 0.55 was adopted to achieve workable mixes. In the mortar preparation, a sand-to-binder ratio of 2.75 was adopted as stipulated in ASTM C109 (American Society for Testing and Materials (ASTM) 2016). The CaO powder was used to replace RMC at 0, 5, and 10 wt.%, and the corresponding samples were designated as M100L0, M95L5, and M90L10, respectively. The samples were first cured in the laboratory air at 22 ± 2 ^oC. After 3 days, they were exposed to a concentrated CO_2 environment of 20% CO_2 and 80% RH at 30 ^oC for a total period of 28 days (annotated as M100L0C, M95L5C, and M90L10C). M100 was also subjected to $scCO_2$ for 4 h (M100S)

At the designated curing ages, compression testing was performed on the samples at a loading rate of 1.2 mm/min with a 100 kN MTS universal testing machine. Concurrently, the interior 10 mm regions of the paste samples were extracted and prepared for chemical analyses. X-ray diffraction (XRD) was measured with PANalytical Empyrean of a Cu Kα radiation source set at 40 mA, 40 kV with a step of 0.013 ^{o} and an acquisition time of 350 s. Thermal gravimetric analysis (TGA) was also performed with SQ600 TG/DTA series by ramping the temperature from 25 ^{o}C to 1000 ^{o}C at 10 ^{o}C/min. The experiment was performed under a nitrogen gas environment at a flow rate of 100 ml/min. ASTM D4373 method (American Society for Testing and Materials (ASTM) 2021) was also implemented to assess the carbonation content. The samples were dried in an oven at 105 ^{o}C for 24 h, ground, and subsequently digested in 3 N HCl solution in a sealed reactor (Model 4501, Karol-Warner). The pressure build-up was recorded at 10 min, and calibration was performed with reagent grade $CaCO_3$ powder at 0.2, 0.4, 0.6, 0.8, and 1 g also in 3 N HCl. Scanning electron microscopy (SEM) and selected samples were investigated using 1H → ^{13}C Cross-Polarization Magic-Angle-Spinning (CPMAS) NMR at a sample spin rate (νR) of 14 kHz and a magnetic field strength of 14 T, providing valuable insights into the nature of the carbonation products.

3. Results and discussion

The average compressive strengths of M100L0, M95L5, and M90L10 samples under the different curing conditions are given in

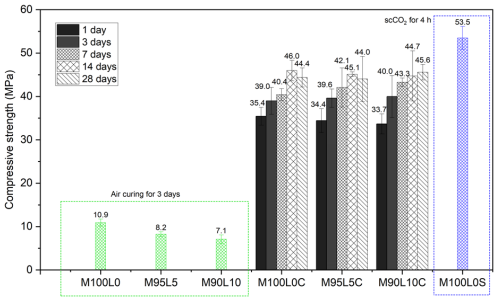

Fig. 1. Compressive strength development

Fig. 1. The samples achieved a strength level of 10.9 MPa, 8.2 MPa (-24.8%) and 7.1 MPa (-34.8%), respectively, at 3 days under air curing. The incorporation of the calcined limestone generally led to a strength reduction, attributed to: (i) reduced hydration of RMC as a result of the increased pore solution pH, (ii) formation of $Mg(OH)_2$ of smaller morphology (**Fig. 2**), and (iii) a poorer binding action of $Ca(OH)_2$ in comparison to $Mg(OH)_2$. Carbonation led to a remarkable strength enhancement of the composites. At 1 day under 20% CO_2, the strengths of M100L0C, M95L5C, and M90L10C increased by 3.2, 4.2, and 4.7 folds in comparison to their respective strengths at 3 days under air curing. The fast strength development demonstrated that carbonation of RMC with and without the calcined limestone is a relatively fast process. Under carbonation, there was no noticeable strength reduction with the incorporation of the calcined limestone. The phenomenon was attributed to improved CO_2 dissolution induced by a higher pore solution pH and nucleation effects provided by the calcined limestone. $scCO_2$ led to a rapid strength gain of the RMC-based composite, which achieved a strength of 53.5 MPa at 4 h of exposure. The carbonation products were characterized by hydromagnesite under 20% CO_2 and nesquehonite under $scCO_2$ for the exterior region and fused phases for the interior under both the curing conditions (**Fig. 2**). These phases interlocked and filled pores to provide strength to the composites.

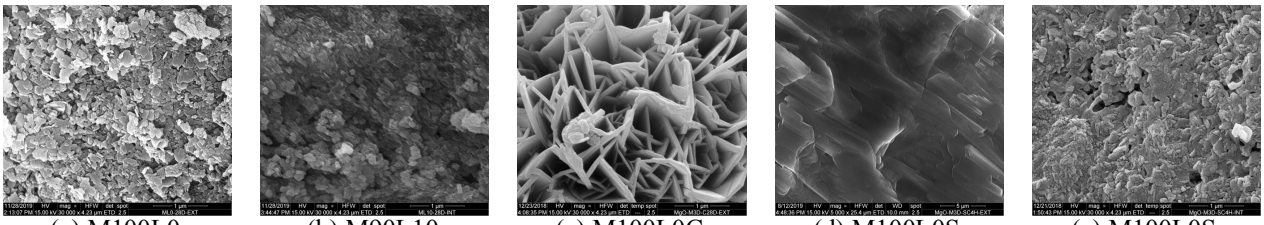

(a) M100L0 (b) M90L10 (c) M100L0C (exterior) (d) M100L0S (exterior) (e) M100L0S (interior)

Fig. 2. Morphologies of reactions products at 28 days of curing (a-c) and 4 h under scCO₂ (d-e)

XRD results in **Fig. 3 (a)** confirmed that the peak intensities for brucite at 3 days under air curing were reduced in M95L5-3D and M90L10-3D as compared with M100L0-3D. However, at 28 days under 20% CO_2, the reduction in the peak intensity of brucite became more prominent in the samples with the calcined limestone. The incorporation of the calcined limestone increased the pore solution pH, which impeded the hydration of MgO but improved CO_2 dissolution and carbonation afterward. This contributed to the improved strength development of M95L5C and L90L10C. A slight increase in the peak intensities of nesquehonite, hydromagnesite, and artinite was observed in the carbonated samples.

In M95L5C-28D and M90L10C-28D, peaks for calcite transformed from portlandite were also observed. More apparent peaks for HMCs were noted in M100L0S relative to M100L0C-28 due to its higher carbonation degree under scCO₂. TGA data in **Fig. 3 (b)** reveal narrower decomposition peaks for brucite in M95L5-3D and M90L10-3D, arising from its smaller size under an increased pH environment induced by the calcined limestone. Endothermic peaks at 560 and 650 °C were attributed to the decomposition of $MgCO_3$ and other forms of HMCs inherent in the raw RMC. Under carbonation, dehydration of water from carbonates led to noticeable weight losses up to 200 °C. Shoulder peaks at approximately 455 and 500 °C appeared from the decarbonation of HMCs. An increase in the intensity of endothermic peaks at approximately 750 °C was observed in M95L5C and M90L10C due to $CaCO_3$ decarbonation, which occurs at 550-900 °C (Borges, Silva, et al. 2014, Grist, Paine, et al. 2015).

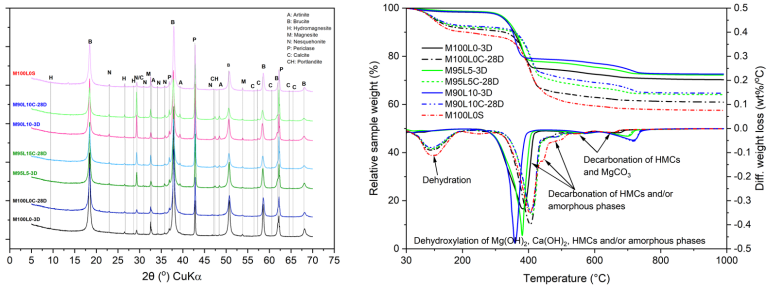

(a) XRD (b)TGA

Fig. 3. XRD and TGA results of selected samples: (a) XRD, and (b) TGA

Table 2 provides the effective CO_2 sequestration factors ($S_{CO2, effective}$) in terms of RMC weight, as derived from the deconvolution of the TGA curves and acid digestion according to ASTM D4373. In the analysis, the peak centers for HMCs were assigned at approximately 460 and 510 °C (Hay and Celik 2020, Hay and Celik 2020). A new peak in the range of 410-420 °C had to be assigned to a new amorphous phase in order to achieve consistent CO_2 sequestration values against ASTM D4375. It is noted that despite the lower initial contents of brucite in the samples incorporated with the calcined limestone at early ages, their carbonation contents were greater than the levels observed in M100L0C. CPMAS experiments confirmed strong C=O resonance peaks in M100L0C-28DC, M100L0S, and M90L10C-28D at ≈163-165 ppm and ≈ 171 ppm (**Fig. 4**). Given the low intensities observed in XRD for HMCs (hydromagnesite, nesquehonite, and artinite), it is justifiable to attribute the C=O peaks to the existence of amorphous carbonate phases. This conclusion is reinforced by the broad line width observed in the C=O NMR peaks, which indicates the presence of amorphicity in the sample.

Table 2: Effective CO_2 sequestration factors for carbonated samples (MgO wt.%) according to TGA and ASTM D4373 method

Method	Sample	Carbonation age (day)				
		1	3	7	14	28
TGA	M100L0C	4.77	8.02	9.86	10.57	15.80
	M95L5C	5.62	9.11	13.99	14.18	15.72
	M90L10C	6.71	11.90	14.35	17.16	16.00
ASTM D4373	M100L0C	8.44	8.84	11.83	11.11	15.10
	M95L5C	10.19	11.41	11.74	12.39	15.01
	M90L10C	9.68	11.93	12.87	13.12	15.44

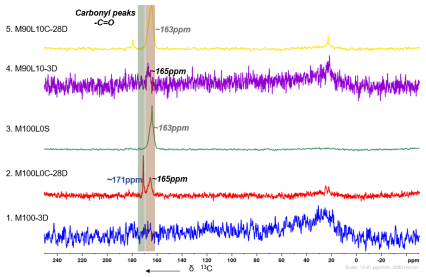

Fig. 4. CPMAS spectra of selected samples

4. Conclusions

The study confirms a rapid strength development of RMC under carbonation due to the formation of carbonates that interlocked and filled pores. Traces of hydromagnesite, nesquehonite, and artinite were formed as crystalline HMCs. However, the carbonation products were dominated by amorphous carbonate phases, as confirmed by the presence of C=O peaks with a decomposition temperature of around 410-420 °C. The long-term CO_2 sequestration factor was estimated at 15-16%. Also, the incorporation of calcined limestone slowed down the hydration and formed small-size brucite susceptible to decomposition and carbonation.

References

American Society for Testing and Materials (ASTM) (2016). ASTM C109/C109M-16a: Standard Test Method for Compressive Strength of Hydraulic Cement Mortar. ASTM Standards. 100 Barr Harbor Dr., PO box C-700, West Conshohocken, Pennsylvania, ASTM International.

American Society for Testing and Materials (ASTM) (2021). ASTM D4373-21: Standard Test Method for Rapid Determination of Carbonate Content of Soils. 100 Barr Harbor Dr., PO box C-700, West Conshohocken, Pennsylvania ASTM International

Borges, C., A. S. Silva and R. Veiga (2014). "Durability of ancient lime mortars in humid environment." *Construction and Building Materials* **66**: 606-620.

Dung, N. T., A. Lesimple, R. Hay, K. Celik and C. Unluer (2019). "Formation of carbonate phases and their effect on the performance of reactive MgO cement formulations." *Cement and Concrete Research* **125**: 105894.

Dung, N. T. and C. Unluer (2016). "Improving the performance of reactive MgO cement-based concrete mixes." *Construction and Building Materials* **126**: 747-758.

Dung, N. T. and C. Unluer (2017). "Carbonated MgO concrete with improved performance: The influence of temperature and hydration agent on hydration, carbonation and strength gain." *Cement and Concrete Composites* **82**(Supplement C): 152-164.

Dung, N. T. and C. Unluer (2017). "Sequestration of CO_2 in reactive MgO cement-based mixes with enhanced hydration mechanisms." *Construction and Building Materials* **143**: 71-82.

Frost, R. L., S. Bahfenne, J. Graham and W. N. Martens (2008). "Thermal stability of artinite, dypingite and brugnatellite—Implications for the geosequestration of green house gases." *Thermochimica Acta* **475**(1): 39-43.

Grist, E. R., K. A. Paine, A. Heath, J. Norman and H. Pinder (2015). "The environmental credentials of hydraulic lime-pozzolan concretes." *Journal of Cleaner production* **93**: 26-37.

Hay, R. and K. Celik (2020). "Accelerated carbonation of reactive magnesium oxide cement (RMC)-based composite with supercritical carbon dioxide (scCO2)." *Journal of Cleaner Production* **248**: 119282.

Hay, R. and K. Celik (2020). "Hydration, carbonation, strength development and corrosion resistance of reactive MgO cement-based composites." *Cement and Concrete Research* **128**: 105941.

Hollingbery, L. A. and T. R. Hull (2010). "The thermal decomposition of huntite and hydromagnesite—a review." *Thermochimica Acta* **509**(1-2): 1-11.
Howie, R. A., J. Zussman and W. Deer (1992). An introduction to the rock-forming minerals, Longman.
Jauffret, G., J. Morrison and F. P. Glasser (2015). "On the thermal decomposition of nesquehonite." *Journal of Thermal Analysis and Calorimetry* **122**(2): 601-609.
Kuenzel, C., F. Zhang, V. Ferrándiz-Mas, C. R. Cheeseman and E. M. Gartner (2018). "The mechanism of hydration of MgO-hydromagnesite blends." *Cement and Concrete Research* **103**: 123-129.
Liska, M. and A. Al-Tabbaa (2008). "Ultra-green construction: reactive magnesia masonry products." *Waste and Resource Management* **162**: 185-196.
Liska, M., A. Al-Tabbaa, K. Carter and J. Fifield (2012). "Scaled-up commercial production of reactive magnesia cement pressed masonry units. Part II: Performance." *Proceedings of the Institution of Civil Engineers-Construction Materials* **165**(4): 225-243.
Pu, L. and C. Unluer (2016). "Investigation of carbonation depth and its influence on the performance and microstructure of MgO cement and PC mixes." *Construction and Building Materials* **120**: 349-363.
Ruan, S., J. Liu, E.-H. Yang and C. Unluer (2017). "Performance and microstructure of calcined dolomite and reactive magnesia-based concrete samples." *Journal of Materials in Civil Engineering* **29**(12): 04017236.
Sawada, Y., K. Uematsu, N. Mizutani and M. Kato (1978). "Thermal decomposition of hydromagnesite $4MgCO_3 \cdot Mg(OH)_2 \cdot 4H_2O$ under different partial pressures of carbon dioxide." *Thermochimica Acta* **27**(1-3): 45-59.
Singh, I., R. Hay and K. Celik (2022). "Recovery and direct carbonation of brucite from desalination reject brine for use as a construction material." *Cement and Concrete Research* **152**: 106673.
Sonat, C., C. H. Lim, M. Liska and C. Unluer (2017). "Recycling and reuse of reactive MgO cements–A feasibility study." *Construction and Building Materials* **157**: 172-181.
Tang, Y., W. Yin and S. Kelebek (2020). "Magnesite-dolomite separation using potassium cetyl phosphate as a novel flotation collector and related surface chemistry." *Applied Surface Science* **508**: 145191.
Winnefeld, F., E. Epifania, F. Montagnaro and E. M. Gartner (2019). "Further studies of the hydration of MgO-hydromagnesite blends." *Cement and Concrete Research* **126**: 105912.

The 16th International Congress on the Chemistry of Cement 2023 (ICCC2023)
"Further Reduction of CO_2 -Emissions and Circularity in the Cement and Concrete Industry"
September 18–22, 2023, Bangkok, Thailand

Development of Calcium Sulfoaluminate-Belite Cement Using Low-Grade Limestone

Bipina Thaivalappil[1*] and Piyush Chaunsali[1]

[1] *Department of Civil Engineering, IIT Madras, Chennai, India*

Email:ce20d700@smail.iitm.ac.in, pchaunsali@civil.iitm.ac.in

[*]**Corresponding Author**

ABSTRACT

Calcium Sulfoaluminate-Belite (CSAB) cement has been drawing research and industry interest in the past decade as a technically and environmentally advantageous binder compared to conventional Portland Cement (PC). Limestone, clay, bauxite, and calcium sulfate are used as raw materials for producing CSAB cement. Lower clinkering temperature, lesser clinker grinding energy requirement, and higher sulfate addition in CSAB cement result in a considerable reduction of CO_2 emission associated with the cement production. CSAB cement does not require a high-purity limestone for its production as the lime requirement in the raw meal is lower than PC due to the absence of alite phase. This paper investigates the feasibility of using low-grade limestone – with siliceous and clayey impurities – for CSAB cement development. The influence of low-grade limestone on the sintering and formation of CSAB cement was studied. The cement pastes were hydrated and characterized to understand the effect of using low-grade limestone on their reactivity using X-ray diffraction and thermogravimetric analysis. The characteristics of CSAB cement synthesized using low-grade limestone were compared against the CSAB cement synthesized using cement-grade limestone, and also with a commercially available CSAB cement having similar phase assemblage. The utilization of low-grade limestone up to 20% in the raw meal could produce CSAB cement of similar phase composition and hydration reactivity. The requirement of pure limestone and bauxite in CSAB raw mix could be reduced by partial replacement using low-grade limestone.

KEYWORDS: *Calcium Sulfoaluminate-Belite Cement, Synthesis, Low-grade Limestone*

1. Introduction

The precursor to the development of Calcium Sulfoaluminate-Belite (CSAB) cement is ye'elimite ($4CaO.3Al_2O_3.SO_3$), first developed at the University of California at Berkeley as an expansive additive to OPC in the 1960s (Alexander and Calif (1966)). Further, it led to the development of CSAB cements in China under the name 'Third Cement Series' in the early 1970s (Zhang et al. (1999).) The ye'elimite phase is responsible for the expansion characteristics of CSAB cement and has significantly less carbon footprint than the alite and belite phases in the Portland cement (PC) (Gartner 2004). The other essential phases in CSAB cement are belite, ferrite, and calcium sulphate, which can be present in varying proportions. CSAB cement is conventionally produced using limestone, bauxite, clay, and gypsum as raw materials. Similar to the PC manufacturing process, the raw materials are heated in a rotary kiln to form clinker, which is further cooled to room temperature and ground with calcium sulphate to obtain the cement.

As alite is the main constituent in PC, which is crucial for the early age strength development, high purity limestone is required for PC production. Whereas in CSAB cement, lime requirement in the raw meal is reduced due to the absence of alite phase. Ye'elimite is the principal strength-giving phase in CSAB cement at early ages (Ben Haha et al. 2019). Hence, the low-grade limestone (limestone that is unsuitable for PC production) may be utilized for CSAB cement production. Huge quantities of limestone are being rejected from cement plants due to the presence of various impurities and are left unused. Its usage in CSAB cement manufacturing would help in reducing the over-exploitation of limestone reserves for cement production.

Researchers have successfully produced CSAB cement from alternative raw materials, including a few industrial wastes, without compensating mechanical performance, when compared to the CSAB cement produced with natural raw materials (Canbek et al. 2020; Chen and Juenger 2012; Li et al. 2021). However, these cements were observed to have different hydration characteristics depending on the chemical composition and proportions of the raw materials used. In this study, similar CSAB phase assemblages were synthesized with incorporating different amounts of low-grade limestone in the raw mix. The synthesized clinkers were studied for the effect of raw mix on sintering and formation of phases and cement's early age hydration reactions. Further, a commercially available CSAB cement was also used to compare the performance of laboratory-synthesized cements.

2. Materials and methodology

A commercially available CSAB cement and CSAB cements developed in laboratory scale were used for the study. Bauxite (B), limestone (LS), and reagent grade calcium sulfate ($C\hat{S}$) (purity > 96%) were used for the CSAB clinker synthesis. Two types of limestone:1) cement grade (CG), and 2)low-grade (LG) – due to silicious and clayey impurities, were collected from Ariyalur district of Tamil Nadu, India. The major oxide composition of the raw materials, determined using X-ray fluorescence spectroscopy (XRF), is shown in Table 1. The raw mix proportioning for CSAB clinkering was performed using modified Bogue equations (Iacobescu et al. 2013), such that the target phase compositions are almost similar to that of the commercial CSAB cement. An additional 5% $C\hat{S}$ was added to the raw mix to compensate for the possible sulfur volatilization during the clinkering process. In order to adjust the sulfate content in the cement, additional 15% gypsum was added to the CSAB clinkers developed in the laboratory. The raw mix proportions used for the synthesis are shown in Table 2.

Table 1: Major oxide composition of raw materials determined using XRF

(wt%)	CaO	Al_2O_3	SiO_2	SO_3	Fe_2O_3	TiO_2	MgO	P_2O_5	Na_2O	K_2O	MnO	LOI
B	0.73	88.35	2.64	0.13	2.74	3.15	0.35	-	0.12	0.28	0.06	-
LS-CG	46.04	1.92	13.94	0.08	4.82	-	0.39	0.16	-	0.41	0.10	37.26
LS-LG	36.31	7.24	23.82	0.04	3.59	0.38	1.89	0.06	0.35	0.81	0.07	25.30

Table 2: Raw mix proportions used for CSAB cement synthesis

(wt%)	B	LS-CG	LS-LG	$C\hat{S}$
CSAB_0LG	22	68	0	10
CSAB_10LG	19	61	10	10
CSAB_15LG	17	59	15	9
CSAB_20LG	17	54	20	9

The clinkering was done in a high-temperature muffle furnace at a maximum temperature of 1300 °C with 5 °C/min heating rate and 1 hour retention time. The clinkers were allowed for fast cooling under air and further ground to similar fineness (D_{50} ~10 µm) in a planetary ball mill. The developed clinkers and hydrated pastes were characterized using X-ray diffraction (XRD) and thermogravimetry (TG) for the formation of phases and their hydration reactivity. The samples hydrated for 3 days were preserved in a vacuum desiccator after hydration stoppage using isopropyl alcohol. The samples were ground using mortar and pestle to pass through 75 µm for the tests. Using the Rietveld refinement method, XRD quantification was performed with PANalytical Xpert High Score Plus Software V.3.

3. Results and discussion

3.1 Clinker mineralogy and phase distribution in cements

Figure 1 shows the XRD of the synthesized CSAB clinkers along with that of the commercial CSAB cement. The major phases in the synthesized clinkers were observed as ye'elimite and belite, along with anhydrite and a few secondary phases. The synthesized CSAB clinkers were ground with 15% gypsum to provide CSAB cements having phase compositions as shown in Figure 2. Though slight variations were noticed, the overall phase distribution were almost similar in all the cements, except for the type of sulfates. The calcium sulfate in the commercial CSAB cement was mainly in the form of anhydrite,

whereas, in the synthesized cements, amount of anhydrite was comparatively smaller as sulfates were added in form of gypsum. However, in all the cements, the calcium sulfate to ye'elimite molar ratio were maintained above 2 (amount of calcium sulfate required for complete ye'elimite hydration to form ettringite). The amount of ye'elimite varied between 40-45% in the synthesized cement against 49% in the commercial cement. The belite content in commercial CSAB was 22%, whereas it varied between 25-28% in the synthesized cements. Even with the incorporation of low-grade limestone in the raw mix by up to 20%, the target phase composition was successfully achieved without compromising on any major phases. In addition to CaO, the aluminous contents in low-grade limestone has also contributed to the formation of ye'elimite and thus the proportion of bauxite could be reduced from 22% to 17% (by ~23%). The low-grade limestone also contributed to the formation of belite by providing SiO_2 to the system.

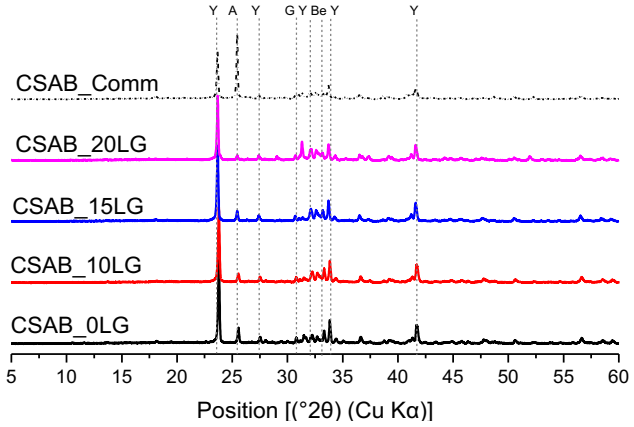

Figure 1: XRD of commercial CSAB cement and synethsiszd CSAB clinkers (*Y: Ye'elimite, A: Anhydrite, G: Gyspum, Be: Belite*)

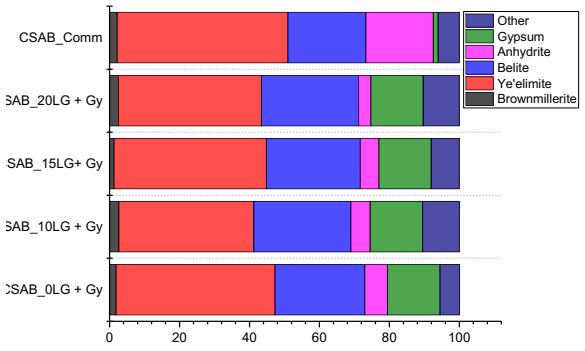

Figure 2: Phase composition of commercial and synethsized CSAB cements

3.2 Hydration products

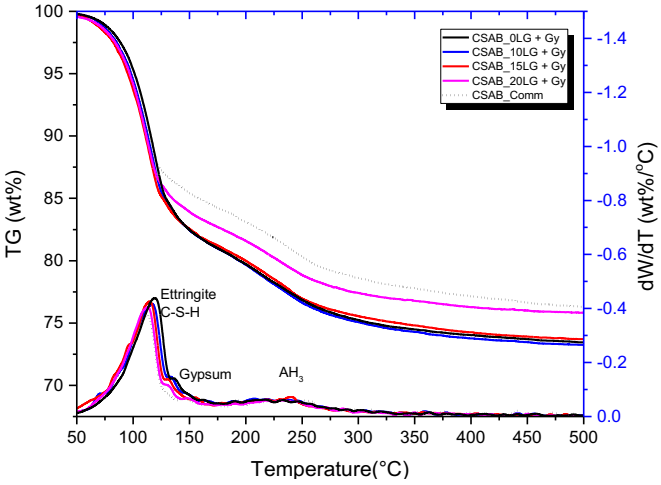

Figure 3: Thermogravimetry of 3-day hydrated commercial and synthesized CSAB cements

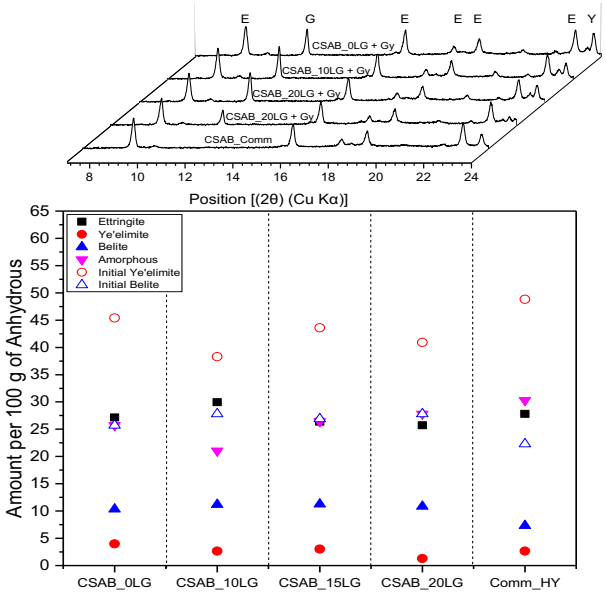

Figure 4: Ettringite evolution (XRD) and major hydration products at 3-day quantified against initial ye'elimite and belite (*E: Ettringite, G: Gyspum, Y: Ye'elimite*)

The hydration reactions and evolution of hydrate phases in the cement pastes (w/b = 0.5) at 3 days were studied using XRD and TG (
Figure 3 and

Figure 4). The major hydration products in all the pastes were ettringite, along with some amorphous content. The QXRD results (

Figure 4) showed that some part of the belite reacted in 3 days. There is a possibility of C-S-H gel formation in the system, though it could not be distinguished in TG or XRD plots. Hence, the amorphous content should be C-S-H from belite hydration and aluminium hydroxide formed as a secondary product during ye'elimite hydration (V.Kasselouri and P.Tsakiridis 1995). As observed from

Figure 4, the amount of unreacted ye'elimite and the initial amount of ye'elimite in the cement follows the same trend in all the cement pastes, indicating that the reactivity of ye'elimite is not affected due to the use of low-grade limestone in producing CSAB cement. Similarly, the hydrates developed in the commercial CSAB cement and the CSAB cement developed without low-grade limestone are almost the same, showing that the synthesis procedure used produced cement of comparable reactivity. Both the TG and XRD results showed similar ettringite content in the 3-day hydrated pastes. Additionally, gypsum peaks could be observed in the synthesized cements as they contained additional gypsum added during clinker grinding.

4. Conclusions

The low-grade limestone used in the study, rejected from cement plants due to silicious and clayey impurities, had chemical compatibility with the conventional CSAB raw materials. CSAB clinkers were prepared in a laboratory scale by incorporating 10-20% low-grade limestone, which could reduce cement-grade limestone by up to 20% and bauxite by up to 23% in the raw mix. It was proved that, with proper raw mix proportioning based on the oxide composition of the raw materials, it is possible to develop similar CSAB phase assemblages without compromising their hydration reactivity. This study was focused mainly on ye'elimite reactivity, and later age hydration from belite reactions was not addressed. A detailed investigation of later-age hydration, mechanical performance, and microstructure development of the developed cements and the effect of higher replacement levels of low-grade limestone in the raw mix could bring a comprehensive understanding about the possibility of developing CSAB cement from low-grade limestone, and should be considered in the future work.

Acknowledgements

The authors would like to acknowledge the Institute of Eminence Research Initiative grant on Technologies for Low Carbon and Lean Construction. The first author wishes to thank the Department of Civil Engineering of IIT Madras for providing the experimental facilities. The first author would also like to acknowledge Ministry of Education, India for the Prime Minister's Research Fellowship.

References

Alexander, K., and Calif, D. (1966). "Expansive and Shrinkage Compensated Cement." *United States Patent Office*.

Canbek, O., Shakouri, S., and Erdoğan, S. T. (2020). "Laboratory production of calcium sulfoaluminate cements with high industrial waste content." *Cement and Concrete Composites*.

Chen, I. A., and Juenger, M. C. G. (2012). "Incorporation of coal combustion residuals into calcium sulfoaluminate-belite cement clinkers." *Cement and Concrete Composites*, Elsevier Ltd, 34(8), 893–902.

Gartner, E. (2004). "Industrially interesting approaches to ' 'low-CO2 ' ' cements." *Cement and Concrete Research*, 34, 1489–1498 Industrially.

Ben Haha, M., Winnefeld, F., and Pisch, A. (2019). "Advances in understanding ye'elimite-rich cements." *Cement and Concrete Research*, Elsevier, 123(July), 105778.

Iacobescu, R. I., Pontikes, Y., Koumpouri, D., and Angelopoulos, G. N. (2013). "Synthesis, characterization and properties of calcium ferroaluminate belite cements produced with electric arc furnace steel slag as raw material." *Cement and Concrete Composites*, Elsevier Ltd, 44, 1–8.

Li, Z., Huang, L., Wang, S., Yang, Z., and Yu, L. (2021). "Using alumina-rich sludge and phosphogypsum manufactures low-CO2 cement."

V.Kasselouri, and P.Tsakiridis. (1995). "A study on the hydration products of a non-expansive sulfoaluminate cement V." *Cement and Concrete Research*, 25(8), 1726–1736.

Zhang, L., Su, M., and Wang, Y. (1999). "Development of the use of sulfo- and ferroaluminate cements in China." *Advances in Cement Research*, 11(1), 15–21.

The 16th International Congress on the Chemistry of Cement 2023 (ICCC2023)
"Further Reduction of CO_2 -Emissions and Circularity in the Cement and Concrete Industry"
September 18–22, 2023, Bangkok, Thailand

Composition-Reactivity Relationship of Indian Biomass Ash

M. Nilakanmani[1]*, Manu Santhanam[2], Piyush Chaunsali[3]

[1]PhD student, [2]Professor, [3]Assistant Professor

Department of Civil Engineering, Indian Institute of Technology Madras, Chennai, India

**Corresponding Author Email: nilakanmani@gmail.com*

ABSTRACT

Agro-based biomass ash which is rich in reactive silica can be used to produce cementitious binders with reduced CO_2 emissions. However, the compositional variability and the presence of unburnt carbon in the biomass ash affect its utilization potential. The standard reactivity assessment methods for supplementary cementitious materials (SCMs) have their own shortcomings. This study involves characterisation of ashes for reactivity using heat of hydration, thermogravimetry analysis, and dissolution of ash in alkaline medium. The study aims to understand the dissolution potential of Indian biomass ashes in low-molar alkaline medium with the addition of hydrated lime and reactive alumina in order to formulate a suitable binder. The influence of ash composition on reactivity was studied by measuring the cumulative heat release from the heat of hydration study, portlandite consumption from thermogravimetry analysis and the extent of silica dissolution in the alkaline medium, and characterizing the reaction products from the residues. Overall, composition-reactivity relationship of Indian biomass ashes was proposed in this study.

KEYWORDS: *Biomass ash, dissolution, reactive silica, reactivity assessment*

1. Introduction

Global electricity demand is expected to increase annually by 3–4 % from 2019 to 2050 and the power consumption is projected to get tripled by 2050 (McKinsey and Company (2022)). The negative environmental impacts of fossil fuel usage have motivated the countries to move towards renewable energy resources. Biomass is a widely used renewable energy resource and considered to be carbon neutral. Incinerating biomass for energy generation is quite common in developing countries like India because of its easy accessibility. Using biomass as energy resource in small-to-medium scale industries generates considerable amount of residual ash. The reactive silica in the residual ash and the high specific surface area of the ashes makes it a suitable candidate for producing cementitious binders. However, the variation in ash composition based on feedstock source, presence of unburnt carbon and crystalline phases due to inefficient burning, lack of availability data, and lack of processing routes affects the utilisation of biomass ash in cementitious binders (Athira et al. (2020)). Hence, the ashes are currently disposed of in nearby landfills leading to environmental disruption.

Also, the conventional reactivity assessment tests like strength activity index test, Chappelle test, Frattini test are not suitable for pozzolanic materials when used in alternative cementitious binders. The MR_3 test method recommends studying the heat of hydration and portlandite consumption to understand the pozzolanic reactivity of SCMs similar to R_3 test method proposed by RILEM TC 267 (Choudhary et al. (2022); Ramanathan et al. (2020)). Further, the dissolution of biomass ash in alkaline medium, responsible for its reactivity, is also not well explored (Uvegi et al. (2019)). The current study aims to understand the reactivity potential of Indian biomass ashes using heat of hydration study and dissolution of ash in alkaline medium of low molarity (<2 M) with addition of lime and alumina source to establish composition-reactivity relationship of Indian biomass ashes.

2. Experimental program

2.1 Material

Three agro-based biomass ashes were collected for the study. The collected ashes had high fraction of unburnt carbon. Hence, the ashes were sieved through 300 μm, to remove the unburnt carbon particles

greater than 300 µm and heated at 105 °C for 24 hours to remove the moisture content. The biomass ashes were labelled as BA1, BA2 and BA3. The feedstock sources of BA1 and BA2 were mixed, whereas BA3 was sugarcane bagasse ash.

2.2 Physio-chemical characterisation

The ashes were characterised for specific gravity, loss on ignition (LOI) values (ASTM C311), particle size distribution, oxide composition and mineralogical composition. The oxide composition and mineralogical composition of the ashes were studied using X-ray fluorescence (XRF) spectroscopy and X-ray diffraction (XRD) respectively. XRF was performed using Rigaku Supermini200 instrument operated at 50 kV. Pellets were prepared from the ashes using boric acid powder as a binding agent to perform XRF. XRD was performed with MiniFlex Rigaku benchtop powder X-ray diffraction instrument with CuKα radiation (1.5405 Å) generated at 45 kV and 15 mA. X'Pert HighScore plus software with Rietveld refinement was used for phase quantification. ZnO was used as an internal standard to quantify the amorphous content. Particle size analysis was performed with Malvern Mastersizer v3.81 using laser diffraction and isopropyl alcohol was used as the dispersing medium.

The physical properties and oxide composition of the ashes are presented in Table 1. The specific gravity of the ashes lies in the range of 2 to 2.2. The LOI values indicate sieving the ash through 300 µm did not completely remove the unburnt carbon fraction in BA1 and BA2. The D_{50} of all the ashes is reported in Table 1 and the particle size distribution graph is plotted in Figure 1(a). The sum of SiO_2 + Al_2O_3 + Fe_2O_3 is plotted in Figure 1(b) and it is seen to fulfil the oxide requirement as recommended by ASTM C618 (>50%) and IS 3812 (>70%). The X-ray diffractograms of the ashes are plotted in Figure 1(c). The amorphous content (including the carbon content) of BA1, BA2, BA3 were 87%, 93%, and 77%, respectively. BA3 showed the presence of cristobalite phase formed due to recrystallisation of silica which occurs at a relatively higher temperature (>700 °C) of incineration (Fernandes et al. 2016).

Table 1 Physical properties and oxide composition of the ashes

Properties measured	BA1	BA2	BA3
Specific gravity	2.10	2.07	2.20
D_{50} (µm)	166	171	141
LOI	8.7	13.7	2.7
Oxide Composition (wt%)			
SiO_2	79.9	73.1	66.6
Al_2O_2	1.8	1.0	4.1
Fe_2O_3	0.9	1.3	2.0
CaO	0.9	2.1	4.5
K_2O	3.8	3.8	11.6
Na_2O	0.3	0.2	0.5
P_2O_5	1.8	1.3	3.1
MgO	1.1	0.9	3.4

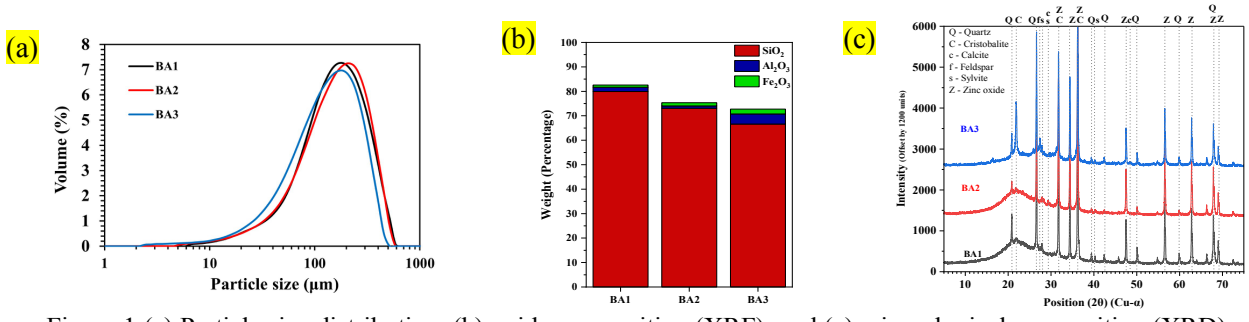

Figure 1 (a) Particle size distribution, (b) oxide composition (XRF), and (c) mineralogical composition (XRD) of the ashes

2.3 Reactivity assessment

Reactivity assessment was performed using heat of hydration study, thermogravimetry analysis, and dissolution of ash in alkaline medium. Heat of hydration and thermogravimetry analysis were performed as per MR_3 test method (Ramanathan et al. (2020)). Heat of hydration was determined by isothermal

calorimetry with a Calmetrix I-Cal 4000 instrument at a temperature of 50 °C for 10 days. The paste for heat of hydration study was prepared using a mini stirrer, mixed at 1600 rpm for 120 seconds. The binder for the study consisted of hydrated lime, ash (pozzolan to be tested) and 0.5 M KOH solution. Lime to pozzolan ratio of 3:1 and 0.9 liquid-to-solid ratio was used. The binder was placed in the calorimeter within 2-3 minutes of mixing without any delay. The materials were preconditioned at 50 °C for 24 hours before starting the heat of hydration study. On completion of the heat of hydration test, the hardened paste was taken for thermogravimetry analysis (TGA) after hydration stoppage. In TGA, the samples were heated from 30–1000 °C and the heating rate followed was 10 °C per minute in nitrogen atmosphere.

The dissolution of ash was carried out in 1M Sodium hydroxide solution. The presence of alumina may affect the silica dissolution in alkaline medium due to polycondensation reaction. So, dissolution was carried out with: 100% ash, 90% ash + 10% hydrated lime (addition of hydrated lime), 95% ash + 5% alumina (addition of reactive alumina), 85% ash + 10% hydrated lime + 5% alumina (addition of both hydrated lime and reactive alumina). The liquid-to-solid ratio maintained was 25 (2 grams of ash in 50 ml NaOH solution) to understand the maximum dissolution potential. The test was carried out at 25 °C for 24 hours. Then the solution was filtered using 0.22 µm nylon syringe filter and digested with nitric acid solution and taken for ICP-OES analysis. The residue was filtered using Whatman 42 grade filter paper and treated with isopropyl alcohol for hydration stoppage. The residue was taken for Fourier Transform Infrared (FTIR) spectroscopy analysis.

3. Results and discussion

3.1 Heat of hydration and thermogravimetry analysis

The cumulative heat release for three ashes is plotted in Figure 2. The cumulative heat released after 10 days is shown in Figure 2(a). The cumulative heat curves indicate the ashes are slow reacting pozzolanic material since the ashes continue to react after 10 days even at a relative higher temperature (50 °C). The cumulative heat release after 10 days for the ashes BA1, BA2 and BA3 was 444, 413, and 363 J/g, respectively. Compared to BA1 and BA2, BA3 showed a linear response from cumulative heat release. The initial reactivity of BA1 and BA2 was quite high compared to BA3. Though BA3 has a lower LOI value, the presence of crystalline phases in BA3 affected its reactivity compared to other ashes. Even if the D50 of BA3 is smaller, the irregular shape and porous structure of the BA1 and BA2 could have resulted in better reactivity of these ashes.

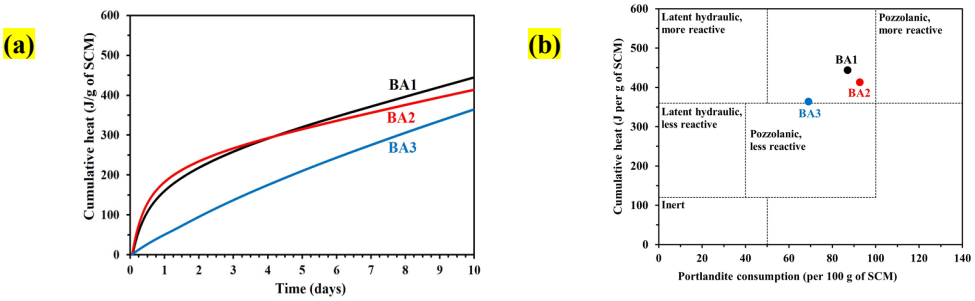

Figure 2 (a) Cumulative heat release after 10 days, (b) Cumulative heat Vs portlandite consumption (MR_3)

The TGA plot for the binders from heat of hydration study was analysed to quantify portlandite consumption. The mass loss between 350–450 °C can be attributed to decomposition of portlandite into CaO and H_2O. Portlandite consumed by the ashes was calculated from the initial mass of portlandite added and the final mass that remained unreacted after heat of hydration study. The cumulative heat release was plotted against the portlandite consumption as in Figure 2**Error! Reference source not found.**(b) to classify the ashes as specified in MR_3 test method (Ramanathan et al. (2020)). As per the classification, all the three ashes fall in the category of pozzolanic less reactive to pozzolanic more reactive.

3.2 Dissolution studies

The dissolution of Si from the ashes and ashes with the addition of hydrated lime and reactive alumina is shown in Figure 3(a). The dissolution of Si from BA2 is higher compared to BA1 and BA3. The high

amorphous content of BA2 could have resulted in the higher extent of dissolution. The addition of hydrated lime resulted in the formation of C–S–H/C–(A)–S–H as observed from the FTIR results reported in Figure 3(b). The formation of reaction products decreased Si concentration in the filtered solution. The addition of alumina showed a decrease in the dissolution extent of Si in alkaline medium; the dissolved Si might have reacted and precipitated to form reaction products, which requires further study into the dissolution mechanism of Si in presence of reactive alumina. The addition of both hydrated lime and reactive alumina resulted in the formation of reaction products; and alumina addition increased the fraction of hydrated lime reacted, which is evident from the FTIR results.

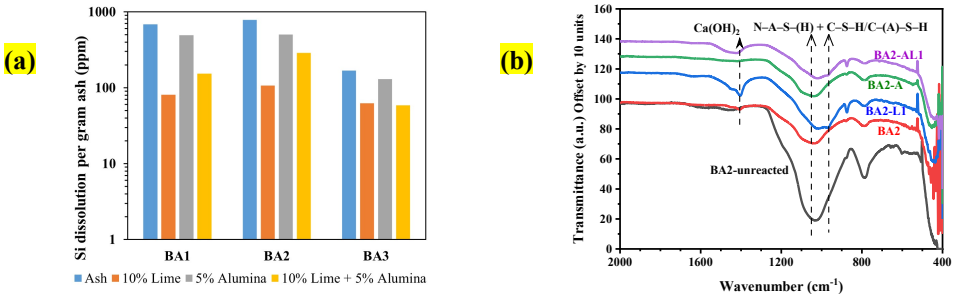

Figure 3 (a) Si dissolution from ICP-OES analysis, (b) FTIR spectra for the residue obtained from dissolution

3. Conclusions

This study analysed the reactivity of agro-based biomass ashes from India using heat of hydration study, thermogravimetry analysis and dissolution studies. The cumulative heat released is mainly affected by the amorphous content and crystalline phases than the unburnt carbon fraction. Sieving the ashes through 300 µm did not completely remove the unburnt carbon fraction. Though the D_{50} size of BA3 is smaller than BA1 and BA2, the irregular shape of the ashes could have played a significant role on the reactivity of ashes in addition to amorphous content. The role of reactive alumina on Si dissolution with and without addition of hydrated lime could be confirmed on analysing the reaction products. However, the dissolution mechanism of Si in presence of reactive alumina should be further investigated.

Acknowledgements

The first author would like to acknowledge the Ministry of Education for the financial support for her doctoral research. The first author would also like to acknowledge the Prime Minister's Research Fellowship granted by Government of India. The funding from the Centre of Excellence on Technologies for Low Carbon and Lean Construction (TLC2) at IIT Madras is gratefully acknowledged.

References

Athira, G., Bahurudeen, A., Sahu, P. K., Santhanam, M., Nanthagopalan, P., and Lalu, S. (2020). "Effective utilization of sugar industry waste in Indian construction sector: A geospatial approach." *Journal of Material Cycles and Waste Management*, Springer Japan, 22(3), 724–736.

Choudhary, A., Bharadwaj, K., Ghantous, R. M., Isgor, O. B., and Weiss, W. J. (2022). "Pozzolanic Reactivity Test of Supplementary Cementitious Materials." *ACI Materials Journal*, 119(2).

Fernandes, I. J., Calheiro, D., Kieling, A. G., Moraes, C. A. M., Rocha, T. L. A. C., Brehm, F. A., and Modolo, R. C. E. (2016). "Characterization of rice husk ash produced using different biomass combustion techniques for energy." *Fuel*, Elsevier Ltd, 165, 351–359.

McKinsey and Company. (2022). "Global Energy Perspective 2022 McKinsey ' s Global Energy Perspective is a collaboration between Energy Insights and adjacent practices." *Executive Summary*, (April).

Ramanathan, S., Kasaniya, M., Tuen, M., Thomas, M. D. A., and Suraneni, P. (2020). "Linking reactivity test outputs to properties of cementitious pastes made with supplementary cementitious materials." *Cement and Concrete Composites*, Elsevier Ltd, 114(May), 103742.

Uvegi, H., Chaunsali, P., Traynor, B., and Olivetti, E. (2019). "Reactivity of industrial wastes as measured through ICP-OES: A case study on siliceous Indian biomass ash." *Journal of the American Ceramic Society*.

The 16th International Congress on the Chemistry of Cement 2023 (ICCC2023)
"Further Reduction of CO_2 -Emissions and Circularity in the Cement and Concrete Industry"
September 18–22, 2023, Bangkok, Thailand

Transforming lignite fly ash into a carbon negative SCM through mineral carbonation

C. Felten[1*], H. Kruppa[1], A. Vollpracht[1] and T. Matschei[1]

[1] *Institute of Building Materials Research, RWTH Aachen University, Aachen, Germany*
Emails: felten@ibac.rwth-aachen.de, kruppa@ibac.rwth-aachen.de, vollpracht@ibac.rwth-aachen.de and matschei@ibac.rwth-aachen.de

ABSTRACT

The largest contributor in the CO_2 intensive cement manufacturing process is the clinkering process. Because of this, substituting clinker with supplementary cementitious materials (SCMs) is an important factor in developing sustainable cements. The currently most common SCMs will be available in decreasing amounts in the future, due to industrial transformation in Europe. This causes a need for alternative SCMs. Lignite fly ashes (LFA) are produced in a significant scale (5-10 Mio.t/a in Germany) to be of interest for the application as SCM. In the past LFAs have rarely been used as SCMs, due to the presence of free CaO and MgO and varying sulfate contents. During cement hydration CaO and MgO form their hydroxide species, which leads to an increase in volume, which may lead to stress induced cracking of the concrete. The new ERA-MIN 3 project called "CO2TREAT", addresses the aforementioned problems of LFAs in cementitious systems. The key to a non-expansive binder is the transformation of the critical oxides into their carbonates. The present study reveals a glimpse into the carbonation behavior of one lignite fly ash from eastern Germany. The carbonation process was conducted in a wet reactor and subsequently analysed with XRD and R^3 test.

KEYWORDS: *Lignite Fly Ash, Mineral Carbonation, use of waste materials*

1 Introduction

CO_2 utilization is one of the main focus areas to further reduce the environmental impact of cement production and a key enabler to achieve the 2050 climate neutrality targets. Enforced mineral carbonation approaches may not only help to sequester CO_2 in mineral products but also to produce novel SCM´s with higher reactivity due to CO_2 beneficiation. Zajac for example has shown that the carbonation of recycled concrete fines leads to the formation of an amorphous aluminosilicate gel which shows significant pozzolanic reactivity, thereby enabling the conversion of an initially inert filler into a reactive SCM which enables a reduction of the clinker factor of cement (Zajac (2020)).
As a consequence of enforced mineral carbonation new SCM´s become available and may counteract the projected decrease of fly ash and slag in the future due to stoppage of coal fired power plants and changes in the steel production process
In the past, e.g. in Greece significant volumes of lignite fly ashes (LFA) were used as SCMs in cement and concrete. Several technical problems due to high contents of CaO MgO and SO_3 and heavy metals (Tsimas (2005)). The free CaO and MgO in concrete react with water to hydroxides which causes a volume increase and can result in cracking of the concrete, if the reaction proceeds after hardening. In addition, care has to be taken to avoid excessive sulfate contents which may lead to oversulfatisation and secondary ettringite formation in concrete. Hazardous heavy metals could also be leached out of the binder containing the SCMs and infiltrate into the groundwater. Nevertheless, currently more than 0,8 Mrd t of lignite are still combusted annually and the waste is mainly deposited (DEBRIV (2017)). On average, 2-8 wt.% of ash remains after lignite combustion, up to a maximum of 20 %, which can be used

as SCM in concrete after a beneficiation process (Niemann-Delius (2008), DEBRIV (2015)). Hence a main objective of the current study is to assess the potential of treated LFA as SCM.

2 Experimental section

2.1 Material characterization

The chemical composition was determined according to EN 196-2:2013-10 by XRF. The results of the chemical characterization are shown in Table 1. CaO and SiO_2 are the most abundant with > 33 wt.%. The content of alkali metals and P_2O_5 are very low. The sulfate content is in the medium range of LFA.

Table 1: Elemental composition of lignite fly ash obtained by XRF (dry sample)

sample	unit	SiO_2	Al_2O_3	Fe_2O_3	Na_2O	K_2O	CaO	MgO	MnO	SO_3	P_2O_5
LFA	wt.%	35,30	11,20	7,13	0,50	0,48	33,7	2,82	0,16	6,98	0,33

Mineralogical characterization of the uncarbonated and carbonated LFA was performed using a Malvern Panalytical X'Pert Pro diffractometer in Bragg Brentano configuration with CuKα radiation and equipped with a Panalytical X'Celerator detector. The generator settings were 40 kV and 40 mA and the measurement range was 5 to 80 °2θ.
In accordance with ASTM 1897-20, the R³ test was performed on the uncarbonated and carbonated lignite fly ashes to determine the pozzolanic activity of the two samples. Here, a potential SCM is investigated in a controlled chemical environment and the heat development is analysed over 7 days with an isothermal heat flow calorimeter. A TAM Air by TA Instruments is used for this purpose. The samples and utensils were equilibrated at 40 °C for 24 hours and the mixture was mixed externally.

2.2 Carbonation process of the LFA

A lignite fly ash from eastern Germany was used. For the experiments, the ash was ground to cement fineness (< 125 µm) and dried at 105 °C until constant mass. The carbonation experiments were performed in a so-called wet reactor, shown in Figure 1. The reactor was placed in a glovebox in which a defined CO_2 concentration of 20 % up to 90 % ± 5 % by volume. In the following manuscript only the results of the highest and the lowest CO_2 concentration are shown. Gas was continuously pumped into the reaction medium via a bubbling stone fed from an air pump. The stirring rate was 750 rpm and the reaction medium consisted of pure water with a conductivity of 40 µS/cm.

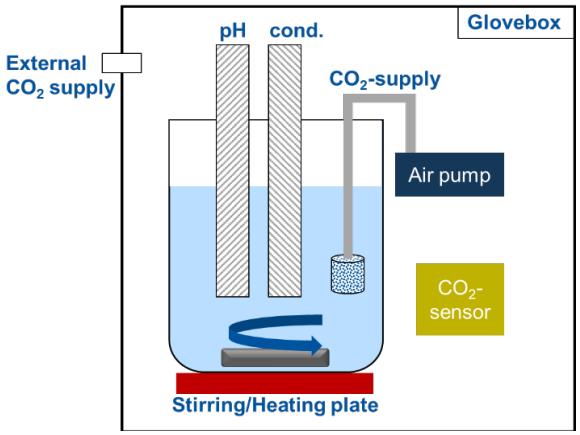

Figure 1: Chart of the carbonation reactor

The sample was added after pH equilibrium was reached. Continuous data recording of pH, conductivity and temperature was performed with a measurement interval of 1 s. The reaction time was 1300 min. After completion of the reaction, the carbonated sample was filtered with a blue-ribbon filter in a Büchner funnel and dried at 105 °C until mass constancy.

3 Results and discussion

During carbonation in the wet process, the pH and conductivity were continuously recorded in the reactors. The graphs of this recording are shown in Figure 2.
The progression of the curves is similar for the all the experiments with a CO_2 content from 20 vol.-% to 90 vol.-%. The pH value of the CO_2 saturated deionized water is in the acidic range. After the addition of the LFA, the pH value rises sharply within the first minute into the neutral to basic range and subsequently drops again in the next minutes and then remains stable in a neutral pH range. The conductivity increases after the addition of LFA over a period of 5 hours and then decreases afterwards.

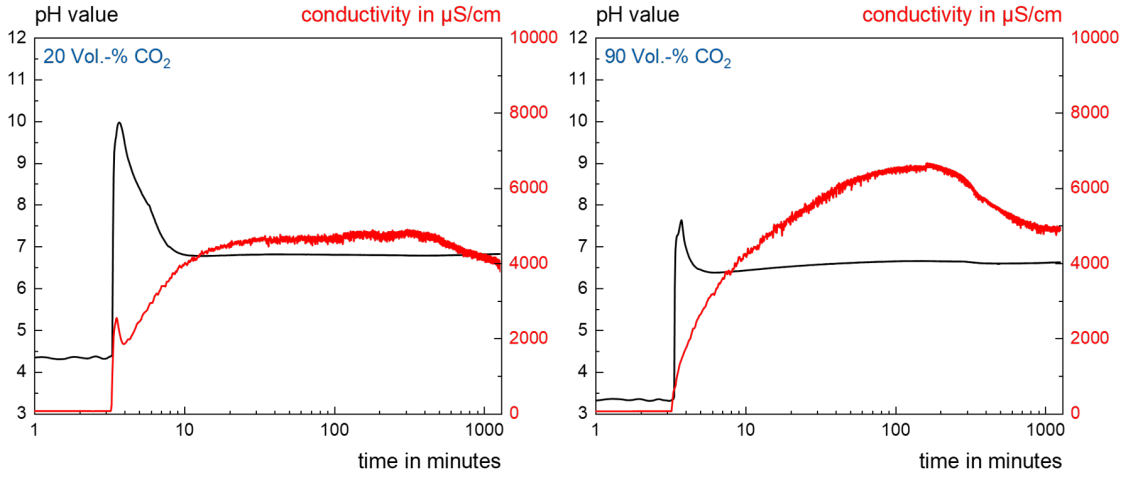

Figure 2: Evolution of pH and conductivity during the carbonation process

The results of the XRD investigations in Figure 3 show a clear formation of calcite, marked by the main reflex at 29.4 °2θ. Accordingly, it could be proven that the lignite fly ash is carbonated after the process. Portlandite could no longer be detected after carbonation. Furthermore, after carbonation, crystalline sulfate phases could be detected, which could not be detected before carbonation, and the decrease of the Akermanite-Gehlenite solid solution could be verified.

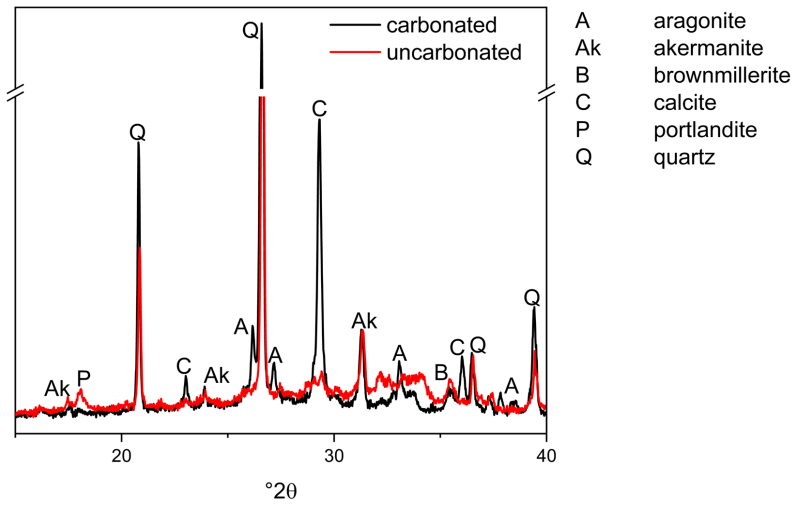

Figure 3: Extract of the XRD -pattern of LFA and carbonated LFA

Figure 4 shows the results of the R³-Test. The heat flux (left) as well as the cumulated heat (right) differ between the uncarbonated and the carbonated LFA. The uncarbonated sample has a low heat flux at the beginning of the reaction, which drops quite quickly and is subsequently quite steady. The carbonated sample has a higher heat flux at the beginning of the reaction, which decreases and after one day the level is below that of the uncarbonated sample.

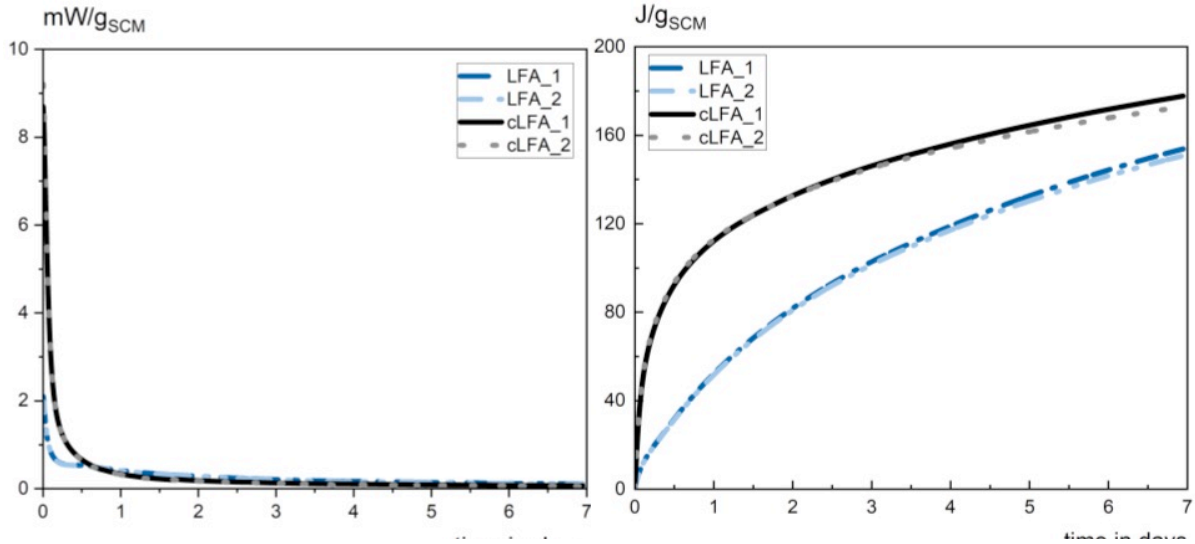

Figure 4: Heat flow in mW/g$_{SCM}$ (left) and cumulative heat in J/g$_{SCM}$ (right) of carbonated and uncarbonated LFA

The trend shown in the heat flow can also be seen in the cumulated heat. The plot of the carbonated sample rises rapidly and flattens out after some days. The plot of the uncarbonated sample rises more slowly, but still approaches the plot of the carbonated fly ash towards the end of the test. The cumulative heat after seven days is 150 J/g$_{SCM}$ for the uncarbonated sample and 180 J/g$_{SCM}$ for the carbonated sample. The investigations show that the LFA could be carbonated, but the amount of carbonates formed cannot have resulted from the carbonation of portlandite and other crystalline phases alone. This indicates a formation of carbonate phases from the X-ray amorphous phase. An indication of the carbonation of the X-ray amorphous phase may be the detected drop in conductivity after about 5 hours. The measurement of pH and conductivity indicates that the carbonation may take place in a two-step process. In the first minutes a rapid formation of calcite from the reactive phases such as portlandite takes place. Furthermore a longer lasting carbonation of X-ray amorphous phases and less reactive crystalline phases which are completed from the time the conductivity reaches equilibrium occur. The cumulative heat in the R³ test is lower than expected, but a change in the reaction kinetics is visible from a slow but steady reaction to a strong but shorter reaction.
To verify these assumptions, further studies will be performed to analyse the total CO_2 uptake.

4 Conclusions

- A CO_2 beneficiation process using the wet process was presented
- The in situ recording of pH value and electrical conductivity shows a complex, multi-step carbonation process which is strongly influenced by the CO_2 concentration
- An increased cumulative heat of the carbonated ash of 30 J/g$_{SCM}$ compared to the uncarbonated ash was achieved after 7 d.

References

DEBRIV (2015): "Braunkohle in Deutschland 2015 – Profil eines Industriezweiges" *Bundesverband Braunkohle* (DEBRIV). Stand: März 2015, Köln.

DEBRIV (2017): „Braunkohle in Deutschland 2017"; *Bundesverband Braunkohle (DEBRIV)*. Köln

Niemann-Delius, C., Stoll, R. D., Drebenstedt, C., & Müllensiefen, K. (2008). "Der Braunkohlentagebau. *Der Braunkohlentagebau: Bedeutung.*"

Zajac, M., Skocek, J, Durdzinski, P., Bullerjahn, F., Skiibsted, J. and Ben Haha, M. (2020) "Effect of carbonated cement paste on composite cement hydration and performance", *Cement and concrete research*, 134: 106090

Tsimas, S., Moutsatsou-Tsima, A. (2005): „High-calcium fly ash as the fourth constituent in concrete: problems, solutions and perspectives", *Cement & Concrete Composites*, 27, 231 - 237

The 16th International Congress on the Chemistry of Cement 2023 (ICCC2023)
"Further Reduction of CO_2 -Emissions and Circularity in the Cement and Concrete Industry"
September 18–22, 2023, Bangkok, Thailand

Synthesis of polycarboxylate ether (PCE) polymer superplasticizers and the study of their interaction with cement´s main clinker phases

A. Barquero[1*], A. Herranz[2], S. Beldarrain[1], I. Emaldi[1], E. Erkizia[3], J.S. Dolado[4] and J.R. Leiza[1]

[1] POLYMAT, Kimika Aplikatua saila, Kimika Fakultatea, University of the Basque Country UPV/EHU, Joxe Mari Korta zentroa, 20018 Donostia-San Sebastián (Spain).
Email: aitor.barquero@ehu.eus, sara.beldarrain@ehu.eus, inaki.emaldi@ehu.eus, jrleiza@ehu.eus
[2] POLYMAT, Polimero eta material aurreratuak: Fisika, Kimika eta Teknologia saila, Kimika Fakultatea, University of the Basque Country UPV/EHU, Joxe Mari Korta zentroa, 20018 Donostia-San Sebastián (Spain).
Email: alejandro.herranz@ehu.eus
[3] TECNALIA, Basque Research and Technology Alliance (BRTA), c/Astondo, Edificio 700, Parque Tecnológico de Bizkaia, Derio 48160, Spain
Email: edurne.erkizia@tecnalia.com
[4] Centro de Física de Materiales (CSIC, UPV/EHU) Materials Physics Center (MPC) Paseo Manuel de Lardizabal 5, 20018 Donostia-San Sebastián (Spain).
Email: j.dolado@ehu.eus

ABSTRACT

One of the most used superplasticizers in construction are polycarboxylate ether-based copolymers, PCEs. However, the effect that the microstructure of the PCEs has in the interaction with the OPC is not completely understood yet due to the complexity of the hydration of cement and the structural versatility of the PCEs. One of the reasons for the complexity of cement is that OPC is a multi-component material, which is formed by different crystal phases. In this regard, knowing and understanding the interaction of the PCEs on each of the individual crystal phases is important because these interactions can help understand their effect on the OPC and also on the cement of different compositions. In this work, the effect of a wide range of purposely synthesized PCEs in the adsorption and hydration of different crystal phases (such as C_3S and C_3A) has been studied. The PCEs have been synthesized by semi-batch aqueous free-radical copolymerization of methacrylic acid and polyethyleneglycol methacrylates and their microstructure (chain length, charge density, and side chain length) have been thoroughly characterized to study their effect on the different crystal phases.

KEYWORDS: *MPEG-type PCE, superplasticizers, free-radical copolymerization, OPC crystal phases, hydration of cement*

1. Introduction

Polycarboxylate ether-based PCE superplasticizers are a key component in the formulation of many cementitious materials. Despite their wide use, there is still a lack of understanding on the structure-property relationship. The first attempts to correlate the structure of PCEs with their performance using fundamental knowledge were done by Flatt et al. (2009), as they could reduce the structure of the complex comb-like polymer chain to three characteristic parameters: *n,* which represents the number of segments in the main polymer chain, *P,* the ethylene oxide (EO) units of grafted chains and *N*, that gives the number of monomers in each segment for the main chain. A schematic representation is shown in Figure 1. These three parameters could be used to predict the conformation of the polymers in aqueous phase (Flatt et al., 2009).
Later, the structural parameter of PCEs were correlated with the delay on the hydration of a custom made OPC (Marchon et al., 2017). They observed that the delay on the hydration was mostly controlled by the carboxylate dosage. Using PCEs with varying *n*, *P* and *N* values, they could fit all their results to a master curve. This relationship was later corroborated by Emaldi et al. (2022), but with an expanded range of PCEs. Not only that, they showed that the relationships proposed by Marchon et al. hold for PCEs

synthetized by free-radical copolymerization of methacrylic acid (MAA) and polyethylene glycol methacrylate (PEGMA) macromonomer, and in a commercial OPC.

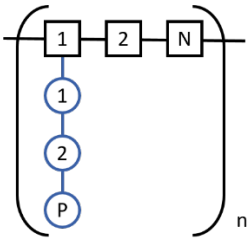

Figure 1. Schematic illustration of PCEs based on the parameters as proposed by Flatt et al. (2009).

Although these works shed some light on the effect of PCEs on hydration mechanism, there is still much to learn. The current work examines the impact of PCEs on the hydration of three of the most important clinker phases that compose the OPC, namely alite (C_3S), belite (C_2S) and calcium aluminate (C_3A).

2. Materials and methods

2.1 Materials and Synthesis of the PCEs

Methacrylic acid (MAA) was purchased from Across Organics, polyethylene glycol methyl ether methacrylates (PEGMA) with 22.5, 45 and 113 ethylene oxide (EO) units were kindly supplied by Evonik Industries. 3-Mercaptopropionic acid (3-MPA), potassium persulfate (KPS), sodium bicarbonate ($NaHCO_3$), sodium nitrate ($NaNO_3$), gypsum ($CaSO_4 \cdot 2H_2O$) and sodium hydroxide (NaOH) were purchased from Sigma-Aldrich and used as received. Deionized water was used as solvent. The clinker phases, alite (C_3S), belite (C_2S) and calcium aluminate (C_3A) were purchased in Bonding Chemicals with an average particle size of 4 µm, 1 µm and 10 µm, respectivelly.
The copolymerization reactions were carried out in aqueous solution in semibatch in a 250 mL glass jacketed reactor with a thermostatic water bath and a mechanical turbine stirrer at 200 rpm. To carry out the reactions, deionized water (100 g) was loaded to the reactor and heated to 80 °C. When the reaction temperature was achieved, the feeding started. The monomers (PEGMA and MAA), initiator (KPS), chain transfer agent (CTA, 3-MPA) and sodium bicarbonate dissolved in the rest of the water were fed in the same stream for three hours at 0.56 $g \cdot min^{-1}$. After, post polymerization was carried out for an hour, with the aim of reaching full conversion of the monomer. Table 1 summarizes the PEGMA type, MAA/PEGMA ratio, final solids content and CTA amount for each PCE that was synthetized.

Table 1. Sumary of the PCEs synthetized for this work.

PCE	Number of EO in PEGMA	MAA/PEGMA ratio (mol)
1/1-M	22.5	1/1
3/1-M		1/3
6/1 M		1/6
1/1-L	45	1/1
3/1-L		1/3
6/1-L		1/6
1/1-XL	113	1/1
3/1-XL		1/3
6/1-XL		1/6

2.2 Hydration kinetics of the OPC

The hydration kinetics were carried out using a TAM air conduction calorimeter at room temperature for 48 hours with water as reference material. Cement pastes with a total mass of 5 g were prepared with a 0.4

water to cement ratio. The mixing of the components was made by a vortex mixer with the following procedure: 90 seconds at 800 rpm, 60 seconds of pause and 90 seconds at 800 rpm. The PCE was added by direct addition (dissolved in the initial water).

3. Results and discussion

All polymers showed similar behavior, therefore, for Figure 2 one representative PCE was selected (1/1-XL) and only the effect of the PCE dosage is presented in each one of the three main clinker phases.

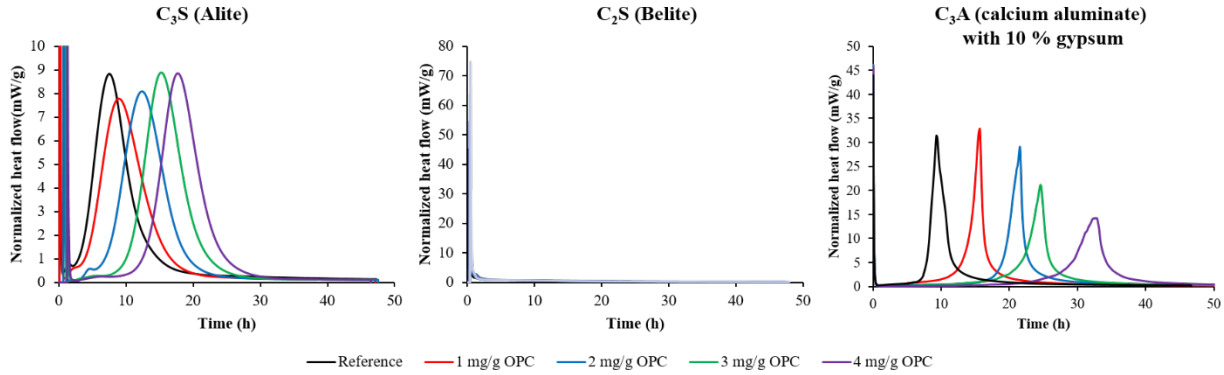

Figure 2. Effect of the concentration of a selected PCE (1/1-XL) on the hydration kinetics of the different clinker phases.

The results obtained are quite different, depending on the clinker phase. In the case of C_3S (alite), the hydration is delayed as the dosage of PCE increases. This is very similar to what Marchon and Emaldi and others have reported for OPC. In fact, C_3S is the most important component of the OPC, which explains the similarities.

The C_2S (belite) phase behaves very differently. There is no peak in the heat-flow curve, even though the hydration reaction is taking place, because it is very slow. Therefore, adding PCE does not make a difference in the time frame used for the calorimetric analysis.

Finally, the C_3A (calcium aluminate) phase was analyzed. Note that 10% by weight of gypsum (calcium sulfate dihydrate) was added to these samples, because without it the reaction was too fast to be monitored by calorimetry. In general, the behavior is very similar to the C_3S phase, as the hydration is retarded with increasing the concentration of PCE.

Following the work by Marchon et al., the retardation on the hydration was plotted over the carboxylate dose (expressed as $C_{PCE}((C/E)/M_{RU})$), as presented in Figure 3. Only the cases of C_3S and C_3A were plotted, as the C_2S phase could not be analyzed due to the absence of peaks. The retardation was measured as the time delay of the peak (in hours) with respect to the reference sample (with no PCE).

The results obtained here do not match with what they reported. In their work, for a given MAA/PEGMA ratio all curves would overlap no matter the number of EO units in the side chain, but in this case clearly each series (M, L or XL) shows a different slope. We do not understand yet why the proportionality that so well describes the effect of PCEs on the hydration of OPC does not hold when the phases are analyzed individually. For this reason, we did not plot the delay over the carboxylate dose.

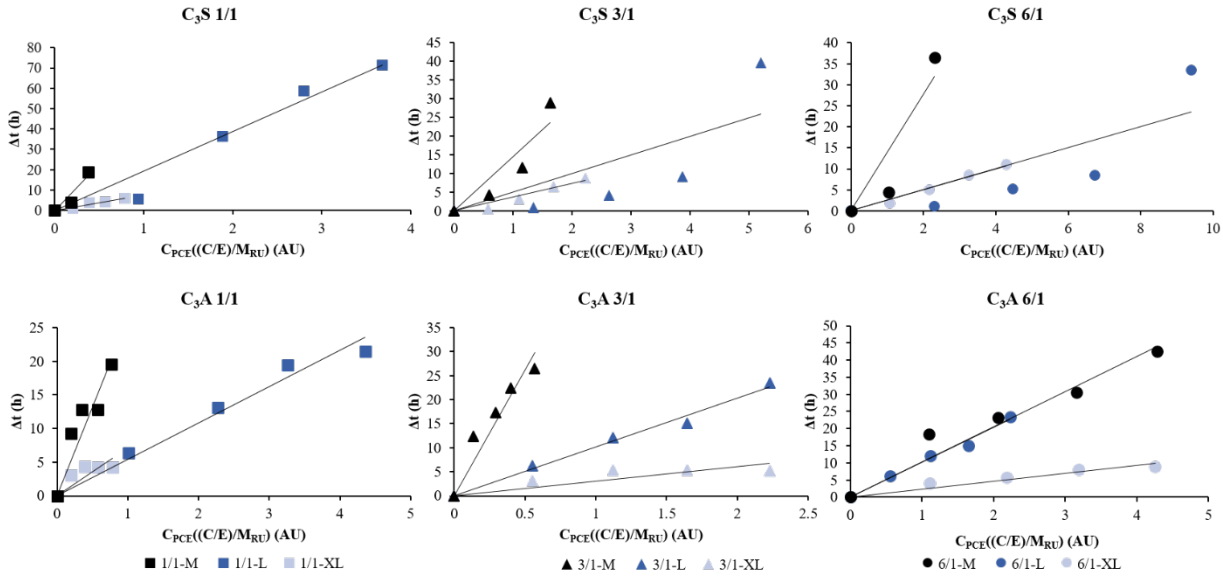

Figure 3. Retardation of the hydration peak of C_3S and C_3A over the carboxylate dose.

4. Conclusions

In this work, we studied the effect of different purposely synthesized PCEs on the hydration kinetics of three of the most important clinker phases of OPC: C_3S, C_2S and C_3A. C_2S did not show any peak in the calorimetry, and it could no be analyzed. C_3S and C_3A, on the other hand showed a clear hydration peak. There was a clear retardation in the hydration when PCEs were added, similarly to what was observed for OPC in previous works. However, when the retardation of the hydration was plotted over the carboxylate dose, the slope was dependant on the number of EO units in the side chain, unlike in the OPC, where all curves collapse to a single master curve. The reason for this different behavior is not clear yet, and further research will be carried out to elucidate the causes of the differences.

Acknowledgements

The financial support from Eusko Jaurlaritza (GV-IT-1512-22), Ministerio de Ciencia e Innovación (PID2021-123146OB-I00), Euskampus (Misiones 1.0) and LTC Green Concrete is gratefully acknowledged.

References

Emaldi, I., Erkizia, E., Leiza, J. R., & Dolado, J. S. (2022). Understanding the effect of MPEG-PCE's microstructure on the adsorption and hydration of OPC. *Journal of the American Ceramic Society*, *July 2022*, 2567–2579. https://doi.org/10.1111/jace.18912

Flatt, R. J., Schober, I., Raphael, E., Plassard, C., & Lesniewska, E. (2009). Conformation of adsorbed comb copolymer dispersants. *Langmuir*, *25*(2), 845–855. https://doi.org/10.1021/la801410e

Marchon, D., Juilland, P., Gallucci, E., Frunz, L., & Flatt, R. J. (2017). Molecular and submolecular scale effects of comb-copolymers on tri-calcium silicate reactivity: Toward molecular design. *Journal of the American Ceramic Society*, *100*(3), 817–841. https://doi.org/10.1111/jace.14695

The 16th International Congress on the Chemistry of Cement 2023 (ICCC2023)
"Further Reduction of CO_2 -Emissions and Circularity in the Cement and Concrete Industry"
September 18–22, 2023, Bangkok, Thailand

A New Class of Admixtures for Low Carbon Concrete

G. Ferrari[1*] and M. Squinzi[2]

[1] *Mapei S.p.A., Milan, Italy*
Email: g.ferrari@mapei.it
[2] *Mapei S.p.A., Milan, Italy*
Email: marcosquinzi@mapei.it

ABSTRACT

It is well known that almost never cement hydrates completely and a residual unreacted fraction may remain in concrete even after years from placement. This could be even more true for low embodied carbon concrete (LCC), where high fractions of less reactive supplementary cementitious materials (SCMs) can affect hydration and reduce the strength. As LCCs will play a major role in the future of concrete, it is crucial to find solutions for improving the reactivity of blended cements and SCMs in LCCs and in concrete as well. In the present paper a new class of Low Carbon Concrete admixtures (LCCAs), developed to optimize the hydration reactions of all cementitious materials involved in LCCs and to enhance their mechanical performance, is presented. Their characteristics are discussed based on both experimental data and the existing literature.

KEYWORDS: *Blended cements, gel porosity, hydration degree, low carbon concrete admixtures LCCA, supplementary cementitious materials SCM*

1. Introduction

Hydration is the fundamental reaction responsible for the hardening of cement paste and the final characteristics of mortar and concrete. Even if over the past decades the hydration mechanism of cement was deeply investigated, still there is a real paucity of knowledge on the mechanisms controlling hydration kinetics beyond one day, as outlined by Scrivener et al (2019). Indeed, it is well known that, even after curing for long time, a fraction of unreacted anhydrous cement always exists in the cement paste. Mills (1966) reported that when curing is limited, as is usually the case in service, 50 % or more of the original cement may never be hydrated. Beside obvious economic considerations, this has negative consequences on concrete sustainability, as higher dosage of cement is necessary for the designed final strength. This condition can even be made worse in the presence of supplementary cementitious materials (SCMs), which are increasingly replacing clinker or are added to concrete as fillers to produce concrete with reduced carbon foot-printing (Low Carbon Concrete, LCC) (Skibsted and Snellings, 2019).
In the present paper a new class of admixtures, developed to increase the degree of hydration (DoH) of cement and enhance the final mechanical performance of concrete, particularly of LCC based on SCMs, is presented.

2. The new Low Carbon Concrete Admixtures (LCCAs).

Compared to traditional admixtures (plasticizers and superplasticizers, retarders and accelerators), whose function is addressed to control specific properties of concrete in the period of hydration from initial mixing up to the main hydration peak, (periods I-II in Fig. 1), the new class of admixtures have been developed to increase the degree of hydration (DoH) after the main peak (period III in Fig. 1).

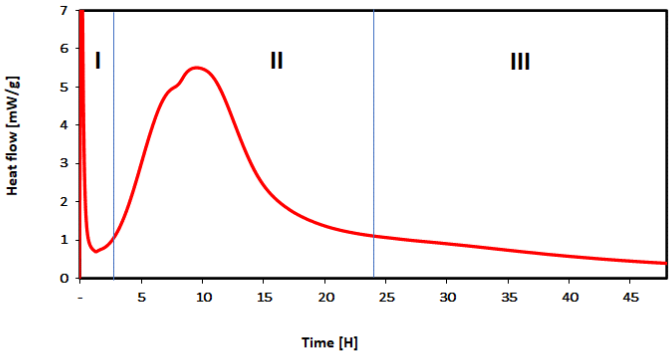

Fig. 1. Typical heat evolution curve of Portland cement, broken in 3 periods as discussed here.

Their function is to replace more clinker with SCMs or to reduce the cement dosage without losing mechanical performances. Both these options comply with the requirements of reducing the carbon footprint of concrete with the aim to reach the concrete carbon neutrality by 2050. For this reason, Ferrari (2022) suggested for this new class of admixtures the Low Carbon Concrete Admixtures (LCCAs), which has been adopted also in the present work. LCCAs are used at dosages ranging from 0.5 to 1 % bwb (by weight of binder), in addition to the proper amount of plasticizer or superplasticizer for attaining the selected flow.

3. Experimental

A LCCA admixture based on a formulation of synthetic nanocomposite of metal silicate hydrate (Me-S-H), synthetic nano-Aft, glucose syrup and alkanolamine was tested on blended limestone cement type CEM II/A-LL 42.5, according to European norm 197-1. Mortars tests with 0.7 and 1 % bwc LCCA were produced according to EN 196-1 norm. Compressive strength was measured on 4 x 4 x 16 cm prisms cured for different times at 20 °C and 95 % R.H. Reference mortar without LCCA at the same W/C = 0.60 was used for comparison. Commercial Dynamon Cube 805 superplasticizer produced by Mapei S.p.A. was used in both cases at a dosage of 1.3 % bwc, for an initial flow of 250 mm (flow table test, 15 drops).
In a second series of tests, cement pastes were prepared with the same blended limestone cement type CEM II/A-LL 42.5 at the same W/C = 0.60 with and without 1 % bwc LCCA and cured for 28 days at 20 °C and 95 % R.H. After this time, the hardened cement pastes (HCP) were crushed and quenched in isopropanol and the fractions from 600 µm to 1200 µm were analyzed by B.E.T., using N_2 and a Micromeritics Tristar II Plus instrument.

4. Results and discussion

Results of mortars compressive strength are shown in Table 1.

Table 1. Results of compressive strength of mortars with LCCA at different dosages.

Mix	LCCA	Cement	Normalized sand	W/C	Compressive strength (MPa)		
	% bwc	g	g		24h	7 days	28 days
LCCA 0.7	0.7	450	1350	0.60	12.2	41.4	45.3
LCCA 1.0	1.0	450	1350	0.60	11.5	42.1	46.7
Reference	-	450	1350	0.60	11.7	30.8	34.3

At 24 hours compressive strength was similar for all the mortars, but at 7 and 28 days the mortars with LCCA developed higher compressive strength than the reference, confirming that LCCA, even at the lower dosage of 0.7 % bwc, boosts up the final strength of cementitious mixtures.

The higher 28 days compressive strength of mortars with LCCA is explained by the B.E.T. experiments. B.E.T. measurements on HPCs indicated a higher value of specific surface of 24.89 m^2/g for the HCP containing 1.0 % bwc LCCA compared with a value of 16.12 m^2/g for the reference. The resulting normalized cumulative pore distribution for both HCPs is shown in Figure 2.

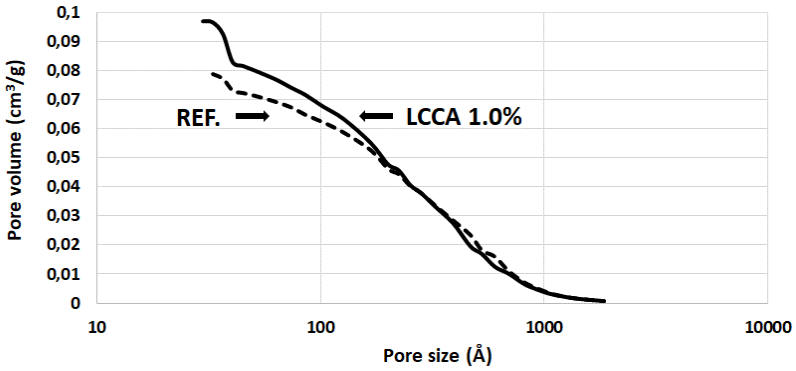

Figure 2. Cumulative pore size distribution of HCP after 28 days of curing (w/c = 0.60).
Solid line: 1 % bwc LCCA; Dotted line: Reference

Figure 2 indicates that the higher porosity of HCP containing LCCA is due to the fraction of pores smaller than 10 nm, which are directly related to the volume of C-S-H in HCPs, as reported by Collepardi (1991) and Muller et al (2013). Therefore, the DoH of the mortar with LCCA (Table 1) is higher compared with the reference mortar. As a consequence of the higher DoH, also compressive strength is enhanced, even both the mortars have the same W/C.
The capability of LCCA to increase DoH was exploited to reduce the carbon foot-printing of concrete. Two concretes were mixed by using the same cement (CEM II/A-LL 42.5) and superplasticizer (Dynamon Cube 805) used in the mortar tests of Table 1. The concrete with LCCA (1 % bwc) was designed with a lower dosage of cement compared to the reference concrete without LCCA (320 kg/m^3 vs 370 kg/m^3). Cubic specimens 15x15x15 cm were cured at 23 °C and 95 % R.H. for different times, before measuring compressive strength. Global Warming Potential (GWP_{100}) of the two concretes was calculated by Sphera software with Sphera and Ecoinvent databases based on about 50,000 process datasets from over 60 industries associations and certified by Dekra. The final GWP_{100} value of each concrete was calculated as the sum of the GWP_{100} of each ingredient multiplied by the relative amount in one cubic meter. Results are shown in Table 2.

Table 2. Characteristics of fresh and hardened concrete with and without 1 % bwc LCCA and different cement dosages.

Mix	LCCA	Dosage of Cement	W/C	Initial slump	Compressive strength (MPa)			GWP_{100}
	% bwc	kg/m^3		Mm	2days	7 days	28 days	kg CO_2 eq/m^3
LCCA	1.0	320	0.53	210	30.9	48.3	57.0	691
Reference	-	370	0.46	180	43.2	49.8	56.8	775

Max aggregate diam.: 20 mm

Due to the lower dosage of cement, concrete with LCCA is characterized by higher W/C compared to the reference. It is worth noting that only the early compressive strength at 2 days was affected, while compressive strength at 7 and 28 days were similar for both concretes, confirming that LCCA promoted the hydration of cement at longer times of curing and correspondingly enhanced the final strength of concrete. Moreover, as a result of the lower dosage of cement, the carbon foot-printing of concrete with LCCA was reduced by 11 % compared to the reference.
One essential feature of LCCAs is the combination of accelerating and retarding agents in the same formulation. Among accelerating agents, particularly effective are the latest generation accelerators, inducing secondary nucleation of cementitious hydrate products, like synthetic nano-C-S-H and nano-Aft,

beside other conventional accelerating agents. Valentini et al (2018) demonstrated that such secondary nucleating agents, beside showing an accelerating effect on hydration at very early ages, modify the microstructure of HCP at longer ages. The same compounds increased the final strength of blended cements, by promoting the pozzolanic reaction of fly ash, slag and metakaolin, as reported by Kanchanason et al (2018, 2019) and Sun (2021). Moreover, the effect of PCE/C-S-H nanocomposites can be boosted up to produce "cement free" concrete by combining secondary nucleation with alkaline activation, as demonstrated by Ferrari et al (2022). Gartner et al (1993) found that some alkanolamines form iron complexes which can increase the iron solubility by several order of magnitude and co-precipitate with aluminum ions at the growth sites of Afm and Aft phases. Among retarders, carbohydrates with different chemical structures can be conveniently used. Bouzouaid et al (2022) demonstrated that carbohydrates can form polynuclear complexes with silicates which resulted in significant increase in the silicate concentration in equilibrium with C-S-H.
Even if the aforementioned literature indicates that LCCA ingredients can modify the kinetic of hydration of cement phases and improve the reactivity of SCMs, presently there is no explanation how they are capable of increasing the DoH and the final strength.

5. Conclusions

LCCAs represent an innovative class of concrete admixtures which joins the existing superplasticizers, retarders and accelerators. Different from the other admixtures, whose function is to control specific properties of fresh concrete, LCCAs have been primarily developed for sustainability issues. LCCAs increase the hydration degree of cement and enhances the final strength of concrete, which are essential requirements to produce LCCs characterized by high compressive strength, particularly when high fraction of SCMs is used. It is necessary to deepen knowledge on the mechanism of action of this new class of admixture to optimize their formulation and develop LCCAs even more effective in reducing the carbon foot-printing of concrete.

References

Scrivener, K.L., Ouzia, A., Juilland, P. and Mohamed, A.K. (2019) "Advances in Understanding Cement Hydration Mechanism", *Cement and Concrete Research*, 124: 105823

Mills, R.H. (1966) "Factor Influencing Cessation of Hydration in Water Cured Cement Pastes", *Highway Research Board Special Report*, 90

Skibsted, J. and Snellings, R. (2019) "Reactivity of Supplementary Cementitious Materials (SCMs) in Cement Blends", *Cement and Concrete Research*, 124: 105799

Ferrari, G. (2022), "Where are Admixtures Going", Keynote at 13th International Conference on Superplasticizers and other chemical admixtures in concrete, Milan, July 13th, 2022, American Concrete Institute.

Collepardi, M. (1991) "Scienza e Tecnologia del Calcestruzzo", *U. Hoepli, ed., Milan*, Third Edition: 126 -135

Muller, A.C.A., Scrivener, K.L., Gajewicz, A.M. and McDonald, P.J. (2013), "Densification of C-S-H Measured by ^{1}H NRM Relaxometry", *Journal of Physical Chemistry*, 117: 403-412

Valentini, L., Ferrari, G., Russo, V., Stefancic, M., Serjun, V.Z. and Artioli, G. (2018), "Use of Nanocomposites as Permeability Reducing Admixtures", *Journal of American Ceramic Society*, 101 (9): 4275-4284

Kanchanason, V. and Plank J. (2018) "Effectiveness of a Calcium Silicate Hydrate – Polycarboxylate Ether Nanocomposite on early Strength development of fly ash cement", *Constr. Build. Mater*., 169: 20-27

Kanchanason, V. and Plank J. (2019) "Effect of Calcium Silicate Hydrate – Polycarboxylate Ether (C-S-H-PCE) Nanocomposite as Accelerating Admixture on Early Strength Enhancement of Slag and Calcined Clay Cements", *Cem. Concr. Res*., 119: 44-50

Sun, J., Dong, H., Wu, J., Jiang, J., Li, W., Shen, X. and Hou, G. (2021), "Properties Evolution of Cement-Metakaolin System with C-S-H/PCE nanocomposites", *Constr. Build. Mater*., 282: 122707

Ferrari, G., Brocchi, A., Castiglioni, F., Bravo, A., Moretti, E., Salvioni, D., Squinzi, M., Artioli, G., Dalconi, M.C., Valentini, L. and Dal sasso, G. (2022), "A New Multifunctional Additive for Blended Cements", Constr. Build. Mater., 354: 129086

Gartner, E. and Myers, D. (1993), "Influence of Tertiary Alkanolamines on Portland Cement Hydration", *J. Am. Ceram. Soc*., 6: 1521-1530

Bouzouaid, L., Lothenback, B., Fernandez-Martinez, A. and Labbez, C. (2022), "Gluconate and Hexitols Effect on C-S-H Solubility", *Cem. Concr. Res*., 160: 106894

The 16th International Congress on the Chemistry of Cement 2023 (ICCC2023)
"Further Reduction of CO_2 -Emissions and Circularity in the Cement and Concrete Industry"
September 18–22, 2023, Bangkok, Thailand

Chemical Admixtures Used in 3D Printing

J. Plank[1*], H. Chan[2]

[1]*Technische Universität München, Munich, Germany*

Email: johann.plank@tum.de

[2] *Technische Universität München, Munich, Germany*

*Email:*akingdom17@hotmail.com

ABSTRACT

Chemical admixtures are indispensable for the success of 3D printing. This paper highlights current technologies and provides an outlook into which products might be required in the future.
At this time, three kinds of 3D printing exist: extrusion, shotcrete and printing in particle bed. As of today, about 90 % of actual work is based on extrusion printing which therefore is the focus of this paper. It is noteworthy that current 3D printing technology only uses mortar, not concrete.
In extrusion printing, immediate stiffening of the mortar is required once it leaves the nozzle. To achieve such sudden structuration, liquid alumina cement slurry or crosslinking polymers are applied. To avoid the sag of printed mortar layers, thixotropic agents (e.g. nanoclays or attapulgite) are admixed. Additionally, adhesive polymers (latex copolymers) facilitate cohesion between individual layers printed and provide form stability. Early strength development can be achieved by seeding materials such as C-S-H-PCE nanocomposites.
A major problem is excessive shrinkage of 3D printed mortars. It derives from chemical shrinkage (most mortars exhibit very high cement content) as well as physical/dry shrinkage (no protection of the formwork from desiccation). Currently, no technically satisfying and economical solution has been found, which requires significant development work.
In the future, more effort will need to be devoted to print actual concrete. This, and not mortar, presents the large market potential for this technology. However, to print concrete with steel embedded presents a major challenge. To solve this problem, completely new approaches are required.

KEYWORDS: *Chemical admixture; Digital manufacturing; Extrusion printing; Structuration; Thixotropy; Early strength; Shrinkage.*

1. Introduction

Digital Manufacturing (often referred to as 3D printing) has become a standard process in numerous industries including the automotive and airline industry, in utility manufacturing or even in dentistry and pediatry. More recently, also the construction industry has developed significant interest, and several conferences have been held on this subject [1-3]. Prominent companies which are most active in this field include Baumit (Austria), Siam Cement Group (SCG, Thailand), Sika (Switzerland), ApisCore (Russia) as well as Huashang and WeiSunTengda (China).
The processes generally used in 3D construction include extrusion printing, shotcrete printing and printing in particle bed. As of today, extrusion printing has become the method of choice and is predominantly (~ 90 %) applied [4]. Therefore, in the following only this process will be addressed with respect to the use of chemical admixtures.
In extrusion printing, the requirements as follow exist: 1. printability: the mortar must be fluid enough to allow pumping and extrusion from the nozzle. 2. structuration: immediately when dispensed from the nozzle, the mortar must develop sufficient "green strength" to maintain the shape and to not soften and subside. 3. adhesion: individual layers of mortar need to adhere well to each other in order to form a larger construct. This requirement is particularly critical when printing objects with inclination. 4. acceleration: extremely fast early strength development is required in order to allow fast printing without collapse of the structure during the printing process or shortly thereafter.
In order to achieve all these properties, chemical admixtures are indispensable. Only with their help, 3D printing in construction became possible. This paper presents about key admixtures which are used in the digital manufacturing of building products and highlights their function.

2. Methods

At this moment, no industry standards exist which specifically address the requirements in 3D printing of building materials. For this reason, the methods commonly applied to test these admixtures include standard tests from the mortar industry, including DIN EN 1015-3 (spread flow), DIN EN 12004 (tile adhesives), DIN EN 196-3 (initial & final setting), DIN EN 196-1 (early strength development) and API RP 13B (10'' / 10' gel strengths).

3. Discussion of results

In the following, specific products, their functionality and characteristic properties to achieve the effects as follow will be discussed:
• pumpability of the ink
• providing structuration and shape stability of deposited ink
• thixotropy to avoid particle sag
• adhesion between individual deposited layers
• rapid strength development
• shrinkage control

3.1. PCE Superplasticizers for pumpability

Inks commonly used in digital manufacturing of building products are characterized by high cement contents (350 – 480 Kg/m3). As a result, such suspensions exhibit no fluidity and require superplasticizers to achieve pumpability. The most common kinds of fluidizers include polycarboxylate (PCE) superplasticizers (**Figure 1**) [5]. In Europe, the MPEG and VPEG type PCEs are most dominant whereas in Asia the HPEG and IPEG kind of PCEs are more widely used. In 3D printing, the so-called precast types of PCE (polymers of very high anionicity) provides best results because they develop high initial fluidity which quickly vanishes.

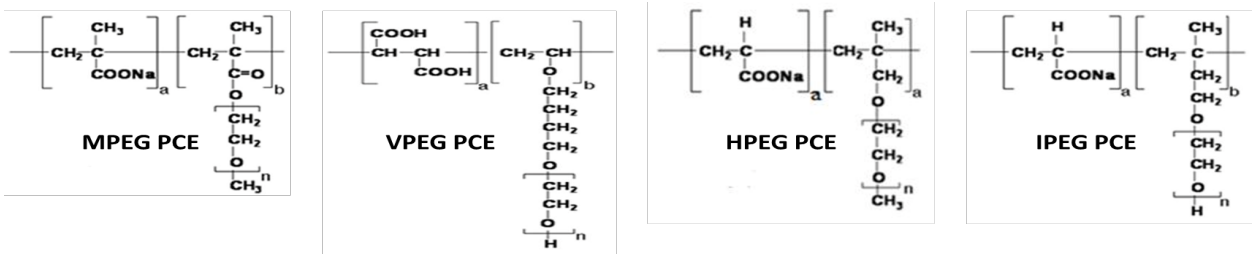

Figure 1. Chemical structures of the most widely used PCE superplasticizers.

3.2. Admixtures for structuration

Once the ink has left the nozzle, immediate stiffening is required in order to achieve shape stability. The most widely used product for this purpose comprises an aqueous slurry of calcium aluminate cement (CAC) which is injected just before the nozzle and results in immediate setting of the slurry [6]. The mechanism behind premature CAC hydration in the aqueous slurry is adjustment of a low pH value and coating of the CAC surfaces with inorganic particles which prevent the access of water. Once this slurry is brought in contact with OPC, then the high pH activates CAC hydration and induces instantaneous set.

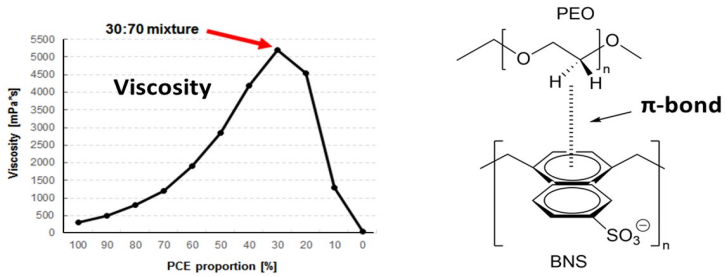

Figure 2. Formation of a π complex between BNS and PCE yielding a sharp increase in paste viscosity.

Another system providing immediate stiffening is based on a reaction between BNS superplasticizer and polyethylene oxide (PEO). When combined, these two polymers form a π complex (see **Figure 2**) which induces high viscosity into the slurry [7] and thus provides shape stability.

3.3. Thixotropy

Thixotropy describes the effect whereby a suspension which is fluid and exhibits low viscosity under shear becomes viscous (= stiffens) once the shear subsides. Such behavior is extremely desirable in 3D printing. Common thixotropic admixtures used in 3D printing are comprised of nano clays, in particular of nano-sized bentonite and attapulgite (see **Figure 3**). The advantage of attapulgite over bentonite is that it can provide higher thixotropy in the ion-loaded cementitious pore solution, however it requires intensive shearing to sufficiently activate the needle-like attapulgite particles to yield.

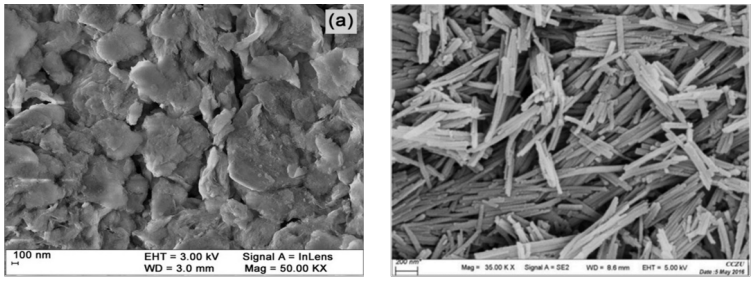

Figure 3. Morphology of platy bentonite particles (left) and of needle-like attapulgite particles (right) [8,9].

3.4. Admixtures for adhesion

The printed layers must exhibit sufficient adhesion between each other, otherwise the entire structure may collapse (see **Figure 4**). To avoid such mishap, aqueous latex polymer emulsions are applied based on e.g. styrene-butadiene (SBR), ethylene-vinylacetate (EVA) copolymers [10] or natural rubber latex [11]. Such latex dispersions contain micro-sized polymer particles which coalesce into consistent polymer films once the water in the ink is used up by cement hydration or desiccation (see **Figure 4**).

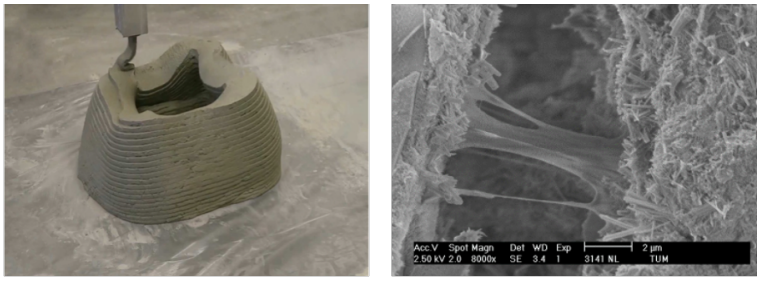

Figure 4. Example of a structure collapsed because of insufficient bonding between individual printed layers (left) [12]; SEM image of a latex polymer film between layers (right).

3.5. Rapid strength development

The build-up of layered structures mandates that within few minutes after extrusion the ink rapidly develops sufficient early strength to support the entire object. Ideally, once printed the ink should exhibit a right angle set and immediately harden. Accelerators are applied to achieve this. Common shotcrete accelerators (calcium formate, sodium silicate, sodium aluminate or aluminum hydroxy sulfate [13]) can induce high early strength, however, they are known for poor final strength (up to 50 % less).

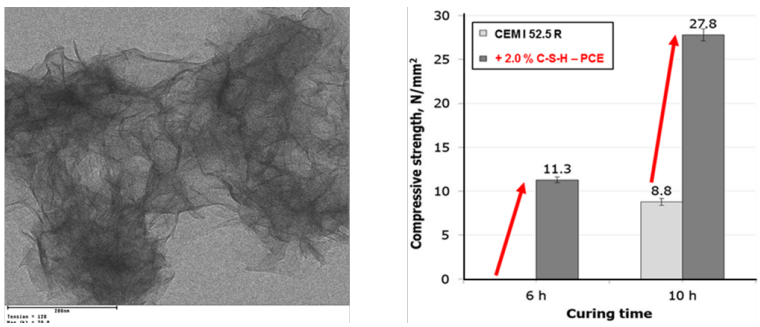

Figure 5. Foil-like nano-sized C-S-H-PCE particles (left, TEM image) and accelerating effect of such nanocomposite with respect to early strength development of OPC (right).

An alternative is presented by calcium silicate hydrate-polycarboxylate (C-S-H-PCE) admixtures (see **Figure 5**). These composites consist of nano-sized C-S-H foils (l < 100 nm) which act as seeding material for C-S-H formation [14]. They provide relatively high early strength already after ~ 5 hours, at no sacrifice in final strength.

3.6. Shrinkage control

Shrinkage still presents a major problem in digital manufacturing of cement-based materials. Autogenous shrinkage results from the high cement content commonly used in the inks and dry shrinkage occurs as there is no formwork which protects from desiccation by wind and sun.
To control autogenous shrinkage, shrinkage compensators such as monocalcium aluminate (CA) which works via C-A-H formation or shrinkage compensated binder systems (e.g. based on ternary binder systems like OPC/CAC/anhydrite) have been evaluated, yet results were mixed. Also, common admixtures to reduce dry shrinkage such as neopentyl glycol have not produced satisfying results. As a consequence, no practical solution exists as of today which provides proper control of autogenous (chemical) and dry (physical) shrinkage.

4. Conclusion

Compared to other industries, digital manufacturing in the construction industry still is in its infancy and is faced with numerous problems. However, it has been recognized and is generally accepted that, next to the printing hardware, admixtures play a pivotal role to achieve the properties which are indispensable for successful 3D printing. At the moment, much euphoria exists which – according to the famous "Gartner hype cycle" [15] – present the peak of inflated expectations. Unfortunately, so far all inks are based on mortar only which limits the objects printed to decorative products such as vases, tables, chairs, etc. Yet, to manufacture large concrete structures including multi-story houses, pillars, bridges and other objects of infrastructure would make this technology attractive indeed, but it requires to include steel reinforcement into the printing process.

References

[1] First RILEM International Conference on Concrete and Digital Fabrication – Digital Concrete 2018, Zürich, Switzerland
[2] Scaling Up 3D – the Interdisciplinary Symposium on Printable Mortars; 2019, drymix.info, Vienna, Austria
[3] Digital Concrete 2020 - 2nd RILEM International Conference on Concrete and Digital Fabrication, Eindhoven, Netherlands
[4] Buswell, R. A., De Silva, W. L., Jones, S. Z., Dirrenberger, J. (2018). 3D printing using concrete extrusion: A roadmap for research. Cement and Concrete Research, 112: 37-49.
[5] Plank, J., Sakai, E., Miao, C. W., Yu, C., Hong, J. X. (2015). Chemical admixtures—Chemistry, applications and their impact on concrete microstructure and durability. Cement and Concrete Research, 78: 81-99.
[6] Imerys, product information - Exalt®, Vaulx-Milieu, France.
[7] Pickelmann, J., Plank, J. (2012). A mechanistic study explaining the synergistic viscosity increase obtained from polyethylene oxide (PEO) and β-naphthalene sulfonate (BNS) in shotcrete. Cement and Concrete Research, 42: 1409-1416.
[8] Ravi, K., Krishnakumar, B., Swaminathan, M. (2012). An efficient protocol for the green and solvent-free synthesis of azine derivatives at room temperature using BiCl3-loaded montmorillonite K10 as a new recyclable heterogeneous catalyst. International Scholarly Research Notices, 2012.
[9] Li, Q., Ju, L., Lu, M., Zhang, Y., Xu, S., Li, Z. (2018). Significant improvement of styrene oxidation over mononuclear/binuclear carboxyl metal phthalocyanine-attapulgite composites. Fullerenes, Nanotubes and Carbon Nanostructures, 26(12): 791-798.
[10] Plank J. (2019). "Bauchemie" in: Zilch K., Diederichs C. J., Beckmann K. J., Gertz C., Malkwitz A., Moormann C., Urban W., Valentin F. (Eds), "Handbuch für Bauingenieure", Springer Verlag, p. 1 – 57.
[11] Vo, A.S. and Plank, J. (2018) Vo M L, Plank J. Evaluation of natural rubber latex as film forming additive in cementitious mortar. Construction and Building Materials, 169: 93-99.
[12] Suiker, A. S., Wolfs, R. J., Lucas, S. M., Salet, T. A. (2020). Elastic buckling and plastic collapse during 3D concrete printing. Cement and Concrete Research, 135: 106016.
[13] Prudencio Jr, L. R. (1998). Accelerating admixtures for shotcrete. Cement and Concrete Composites, 20(2-3): 213-219.
[14] Kanchanason, V., Plank, J. (2018). Effectiveness of a calcium silicate hydrate–Polycarboxylate ether (CSH–PCE) nanocomposite on early strength development of fly ash cement. Construction and Building Materials, 169: 20-27.
[15] Dedehayir, O., Steinert, M. (2016). The hype cycle model: A review and future directions. Technological Forecasting and Social Change, 108: 28-41.

The 16th International Congress on the Chemistry of Cement 2023 (ICCC2023)
"Further Reduction of CO_2 -Emissions and Circularity in the Cement and Concrete Industry"
September 18–22, 2023, Bangkok, Thailand

Novel PCE Superplasticizers for Low Carbon and Zero Clinker Binders

L. Lei[1], and J. Plank[2*]

[1] *Technische Universität München, Munich, Germany*

Email: lei.lei@tum.de

[2] *Technische Universität München, Munich, Germany*

Email: johann.plank@tum.de

ABSTRACT

Concrete is the most commonly used man-made material globally. Regrettably, cement - its major ingredient - has an extremely high CO_2 footprint. However, substituting cement clinker with supplementary cementitious materials (SCMs) that have a low carbon footprint can substantially decrease CO_2 emissions. A prominent example of such low carbon binder is LC^3 consisting of 50% clinker, 30% calcined kaolinitic clay, 15% limestone and 5% gypsum. More radical concepts include LC^2 (zero clinker, 60% calcined clay, 30% limestone powder and 10% gypsum) and alkali-activated slag cements comprising of 15% clinker, 82% slag and 3% alkali activator. Those binders allow to reduce the CO_2 emission from ~ 825 kg CO_2/ton of cement to 200 kg CO_2/ton of binder. Despite the remarkable progress achieved in reducing CO_2 emissions through the use of such low carbon materials as substitutes for cement clinker, these binders exhibit much inferior rheological properties. Consequently, substantial research and development efforts are necessary to to develop the suitable superplasticizers that can enhance the workability. This article explores the interaction between PCEs and low-carbon binders (such as calcined clay and alkali-activated materials). Appropriate PCE structures have been identified for achieving initial workability and maintaining slump retention of such low carbon binder systems.

KEYWORDS: *Climate Change, CO_2 Emission, Calcined Clay, Slag, PCE Superplasticizer.*

1. Introduction

Globally, construction presents by far the largest single source of CO_2 emission (~ 40% of total greenhouse gas release), cement alone accounts for ~ 8% of GHG emission, ~ 825 kg CO_2 are emitted per ton of clinker. Hence, major efforts are undertaken to design low carbon "green" binders with significantly lower clinker content (clinker substitution rates of 50 - 85%). Potential clinker replacements include calcined clays and slag as pozzolanic materials and limestone filler.

Experience with those binders suggest that mechanical properties comparable to those of OPC can be attained, albeit at very low water-to-binder ratios (typically ~ 0.3). However, the rheological properties of such green binders are much inferior to OPC. This prompts the use of highly effective PCE superplasticizers to achieve sufficient workability. Here, substantial innovation will be required to allow widespread application of such slag binders. Another problem includes slump retention in those systems. Current PCE technology is considered to be inadequate to successfully tackle this problem.

Large-scale field experience with those binders in Europe, India, Cuba and Columbia is now available which confirms that they present realistic "green" alternatives to OPC, with up to 80% less CO_2 release as

compared to Portland cement. However, their more widespread use demands a significant progress in admixture technology, in particular of polycarboxylate superplasticizers.

2. PCEs for Calcined Clay Blended Cements

Several recent studies have investigated the interaction between polycarboxylate superplasticizers (PCEs) and calcined clays or calcined clay blended cement. One earlier study conducted by Li et al (2021) investigated the dispersing performance of various structurally different precast-type PCEs, including MPEG, HPEG, and zwitterionic types, in a meta-kaolin rich calcined clay. The results revealed that increasing the calcined clay content in the mix generally resulted in higher PCE dosages, with the 60:40 mixture demonstrating a significant increase of six times in PCE dosage compared to the neat OPC system (**Fig. 1**). This effect was ascribed to the higher water demand of the calcined clay. Additionally, HPEG always required the lowest dosages compared to the other superplasticizer types.

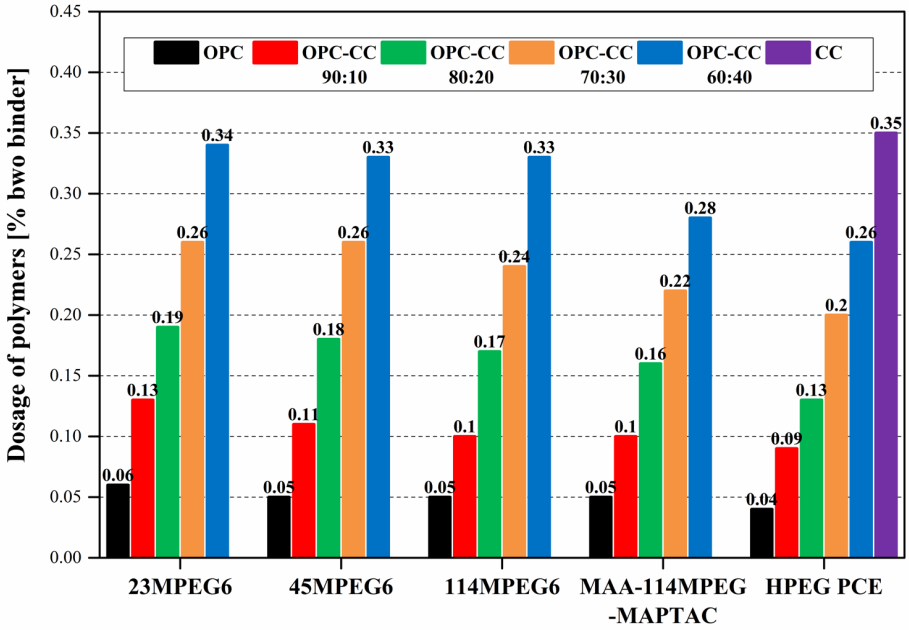

Fig. 1. Dosages of PCE polymers required to achieve a spread flow of 26 ± 0.5 cm in pastes from neat OPC and OPC/CC blends; w/b ratio = 0.5 for cements or 1.2 for neat CC.

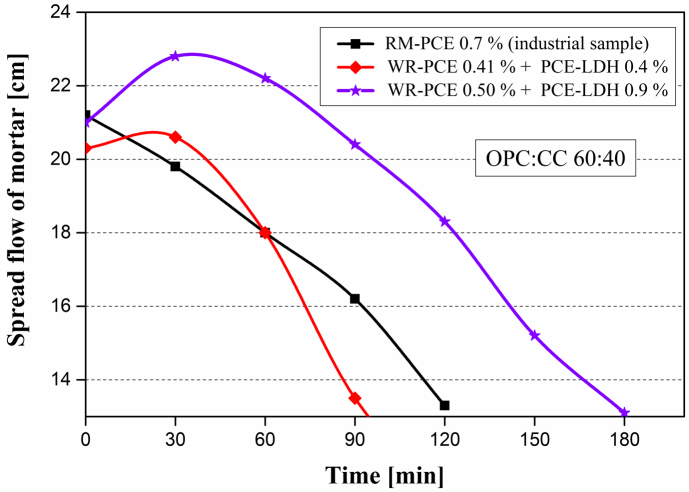

Fig. 2. Fluidity retention of mortars (w/b ratio = 0.4) achieved in the OPC:CC 60:40 blend when admixed with different PCE products.

In terms of slump retention, Li et al (2021) found that in calcined clay blended cements, conventional ready-mix HPEG PCEs based on hydrolyzing esters or the combination of precast PCE and sodium gluconate exhibited only limited effectiveness on slump retention. This is due to the high uptake/adsorption of PCE by the calcined clay. However, a novel PCE-LDH admixture was shown to achieve extended slump retention times by gradually releasing the superplasticizer via progressive anion exchange with sulfate anions present in the pore solution (**Fig. 2**). Overall, these findings suggest that careful selection of suitable PCE products for the calcined clay blended cements particularly with high meta kaolin content.

3. PCEs for Alkali-Activated Slag Binders

Alkali-activated slag (AAS) has proven to be a more environmentally friendly option than OPC in terms of its environmental impact. While AAS has demonstrated competitive engineering properties such as strength, durability, and shrinkage when compared to Portland cement. However, its limited workability has hindered its widespread use. Researchers have devoted tremendous effort into improving the rheological properties of AAS by designing specific polycarboxylate structures.
Conte et al (2019) successfully identified a maleic anhydride-APEG PCE copolymer with a short side chain and high molecular weight was very effective at dispersing AAS whereas conventional MPEG PCEs could not provide any dispersion. More recently, Lei et al (2020) synthesized a series of structurally different HPEG PCE polymers possessing different anionicity and side chain lengths. The authors investigated the effect of different HPEG PCEs on the rheological properties of NaOH-activated AAS and found that highly anionic HPEG PCEs with short side chains exhibited superior dispersing power in AAS (**Fig. 3**), in agreement with the solubility tests. The study also found that highly anionic HPEG PCEs adsorbed more strongly onto the surface of slag particles compared to OPC, which may contribute to their superior dispersing power.

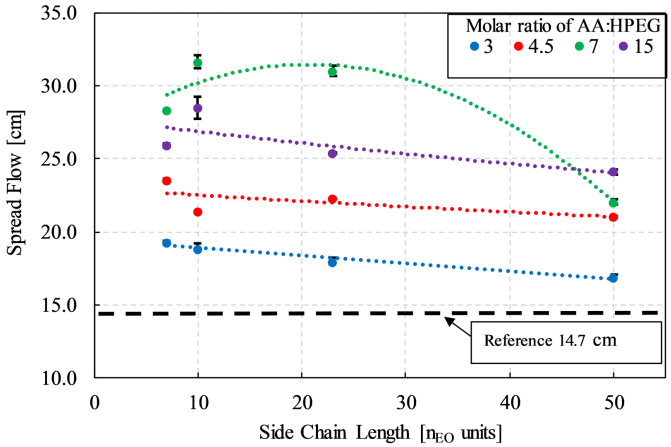

Fig. 3. Spread flow of NaOH-activated slag pastes admixed with 0.05 % of different HPEG PCE polymers; w/s ratio = 0.5; 4 % bwos NaOH activator.

In a subsequent study, Li et al (2023) investigated the effect of the molecular weight of isoprenol ether-based (IPEG) polycarboxylate superplasticizers on their ability to disperse NaOH activated slag binder and slag composite cement. First, a series of IPEG polycarboxylate ether (PCE) superplasticizers with the same anionicity and side chain length but varying molecular weights (ranging from 13,000 to 400,000 Da) were synthesized and subjected to application-related tests. The study found that the dispersing capacity of the PCE polymers in the AAS binder varied significantly, and that those with higher molecular weights were generally more effective. The study also revealed that the dispersing performance results were well-correlated with the adsorbed layer thickness, which increased with higher molecular weight of PCEs. Furthermore, PCEs with higher molecular weights preferentially adsorbed in "loop" or "tail" mode, leading to a stronger steric hindrance effect and enhanced dispersion (**Fig. 4**).

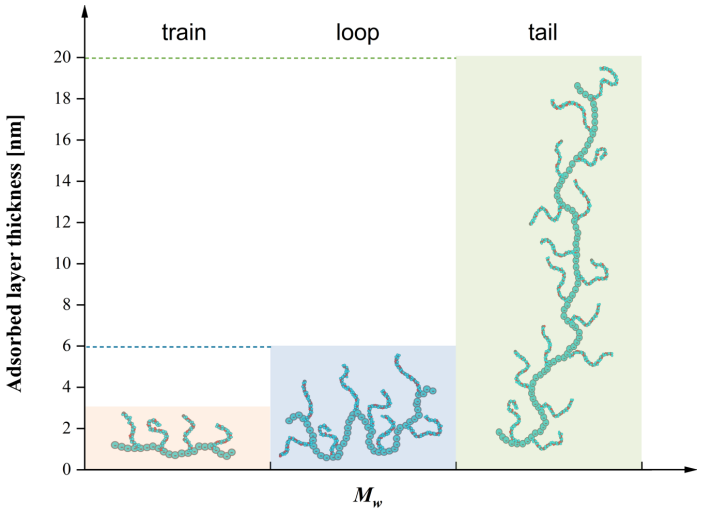

Fig. 4. Schematic illustration of the different adsorbed conformations attained by PCEs possessing different Mw on the surface of PS nanoparticles.

4. Conclusions

It can be assumed that over the next 20 years, a significant and irreversible shift away from cement with high clinker content to materials with lower carbon footprint will occur, especially in developed countries. These materials may include those made from waste products or those produced with low emissions. Calcined clays and alkali-activated binders are expected to be more prominent in this transformation. However, these binders are less compatible with conventional superplasticizers and retarders than ordinary Portland cement, posing a challenge for the admixture industry to develop new technology to facilitate their wide application.

References

Li, R., L. Lei, T. Sui and J. Plank (2021). "Effectiveness of PCE superplasticizers in calcined clay blended cements." Cement and Concrete Research 141: 106334.

Li, R., L. Lei, T. Sui and J. Plank (2021). "Approaches to achieve fluidity retention in low-carbon calcined clay blended cements." Journal of Cleaner Production 311: 127770.

Conte, T. and J. Plank (2019). "Impact of molecular structure and composition of polycarboxylate comb polymers on the flow properties of alkali-activated slag." Cement and Concrete Research 116: 95-101.

Lei, L. and H.-K. Chan (2020). "Investigation into the molecular design and plasticizing effectiveness of HPEG-based polycarboxylate superplasticizers in alkali-activated slag." Cement and Concrete Research 136: 106150.

Li, R., W.-C. Chen, L. Lei and J. Plank (2023). "Dispersing Efficacy of Tailored IPEG PCEs in AAS Binders: Elucidating the Impact of PCE Molecular Weight." Industrial & Engineering Chemistry Research.

The 16th International Congress on the Chemistry of Cement 2023 (ICCC2023)
"Further Reduction of CO_2 -Emissions and Circularity in the Cement and Concrete Industry"
September 18–22, 2023, Bangkok, Thailand

Investigation into A Novel Starch-based Superplasticizer for Alkali-activated Slag

N. Miao, Y. Zhang, L. Lei*, Johann Plank**

Technische Universität München, Garching, Germany
na.miao@tum.de
Technische Universität München, Garching, Germany
yue1.zhang@tum.de
Technische Universität München, Garching, Germany
lei.lei@tum.de
Technische Universität München, Garching, Germany
johann.plank@tum.de

ABSTRACT
In this work, a novel starch-based superplasticizer (designated as S-SP) synthesized via graft copolymerization was studied. The structure was characterized by size exclusion chromatography (SEC). Its dispersing effectiveness was tested in both AAS paste and mortar. In AAS paste, it was found that S-SP exhibited strong dispersion at relatively low dosage (0.12% bwos). Most surprising, it also maintained fluidity over 6 hours. In AAS mortar, 0.3% bwos of S-SP were required to reach an initial spread flow of 21 cm, and high fluidity was maintained over 6 hours. From the results it can be concluded that S-SP provides excellent dispersion and slump-retaining ability. To further study the interaction between the novel superplasticizer and AAS, adsorption measurements and adsorbed layer thickness measurements were carried out. It was found that S-SP molecules adsorb on slag particles following a Langmuir adsorption trend.

KEYWORDS: *low-carbon binder, alkali-activated slag, starch, superplasticizer, dispersion*

1. Introduction

Out of the concern for global warming Andrew (2019), researchers have come up with many solutions to reduce CO_2 emission in cement industry, for example, replacing OPC clinker with supplementary cementitious materials (SCMs), such as ground granulated blast furnace slag (GGBFS) Flower and Sanjayan (2007). Despite the latent hydraulic properties of slag, with the addition of alkaline activators (such as sodium hydroxide Shi and Day (1995) and sodium carbonate) Yuan, Yu et al. (2017) the concrete can possess high durability and resistance to acid attack and corrosion. However, the application of slag is facing several drawbacks, including poor workability, quick setting and high shrinkage after hydration Tong, Yuqi et al. (2021). Moreover, the superplasticizers (SP) commonly used in OPC fail to disperse the AAS systems. Thus, there is a strong need for the development of new superplasticizers, which could be applied in AAS binders. In cement industry, there have been a lot of superplasticizers invented and widely applied, ranging from lignosulfonates (LS), to polynaphthalene sulphonates (PNS), polymelamine sulphonates and polycarboxylate ethers (PCE) Pagé and Spiratos (2000, Javadi, Mehr et al. (2017, Breilly, Fadlallah et al. (2021). However, the synthetic raw materials of these superplasticizers are mostly from the petroleum industry. Due to the huge market of construction materials worldwide, the consumption of such PCEs would take up a lot of petroleum resources Wang, Zhou et al. (2022). Based on such concern, there emerges a need for SPs with greener sources, such as natural materials. In this work, a novel starch-based superplasticizer named as S-SP was studied, which was provided by China Academy of Building Research (CABR). Through structure characterization and performance tests, its potential application in AAS was investigated and discussed.

2. Experimental

2.1. Size exclusion chromatography (SEC)

Size exclusion chromatography (SEC), also referred to as gel permeation chromatography (GPC), was applied for the determination of weight averaged molecular weight (*Mw*), number averaged molecular weight (*Mn*), polydispersity index (PDI) and the macromonomer conversion of synthesized PCE polymers. The measurements were deployed by a Waters Alliance 2695 instrument (waters, Eschborn, Germany) equipped with three Ultrahydrogel™ columns (120, 250, 500) and an Ultrahydrogel™ Guard column. As eluent, 0.1 N $NaNO_3$ (pH = 12) was used with a flow rate of 1.0 mL/min. For the calculation of Mw and Mn, a dn/dc value of 0.135 mL/g (value for PEO) was utilized.

2.2. Anionic charge measurement

The specific anionic charge of S-SP samples was determined based on the method of titration. A particle charge detector (PCD 03 pH from Mütek Analytic, Herrsching, Germany) was utilized for the charge titration. A 100 mL sample solution was prepared containing 0.01 M NaOH and 0.1 g/L S-SP, and titrated against a 0.34 g/L aqueous poly-diallyl dimethyl ammonium chloride (polyDADMAC) until charge neutralization. The specific anionic charge of S-SP (amount of negative charge per gram) was calculated based on the volume of polyDADMAC consumed.

2.3. Dispersing performance in AAS paste and mortar

The spread flow of alkaline-activated slag pastes containing S-SP was determined by conducting a "mini-slump" test following a modified version of DIN EN 1015 standard. The slag mortar was prepared by mixing 450 g of slag, 202.5 g of DI water, 16 g of NaOH and 0.3% bwos of S-SP with 1350 g of CEN standard sand (slag to sand ratio of 1:3). Mixing of mortar was conducted according to DIN EN 196-1 using an eccentric agitator from Toni Technik (ToniMIX, Baustoffprüfsysteme, Berlin, Germany).

2.4. Adsorption via TOC

The adsorption of S-SP on the slag was determined by the depletion method based on total organic carbon (TOC) analysis. In this experiment, 16 g of slag was dispersed in 7.2 g DI water (w/s ratio of 0.45) with addition of 0.64 g NaOH and PCE. Firstly, a series of sample solutions were prepared with different polymer content, from 0 to 2% bwos at maximum. Then each solution was mixed with slag, DI water and NaOH on a vibrator for 2 min. Then, after centrifugation at 8500 rpm for 10 min, take the supernatant for analysis, and filtrate into a sample tube. A LiquiTOC analyzer (Elementar, Hanau, Germany) was utilized to detect the total organic carbon content in the collected supernatant.

2.5. Adsorbed layer thickness via zetasizer

The adsorbed layer thickness (ALT) of S-SP was determined in Ca^{2+} and Ca^{2+} free medium. 1% wt. S-SP was dissolved in 0.1 M aqueous NaOH and mixed with their charge equivalent amount of Ca^{2+} added as $CaCl_2 \cdot 2H_2O$. In a separate solution, 1% wt. PCE was dissolved in 0.1 M aqueous NaOH without any Ca^{2+} addition. Both stock solutions were then diluted to prepare a series of PCE concentrations from 0.1-1.5 g/L in a volume of 50 mL. Thereafter, 50 µL of polystyrene nanoparticle were added into the PCE solutions with various concentrations. The polystyrene nanoparticle was prepared according to the literature Stecher and Plank (2020). The opaque dispersions were subjected to ultrasonication for 15 min and remained at rest for 15 min before the diameter determination with dynamic light scattering on the ZetaSizer Nano ZS instrument. The corresponding diameters of polymer free polystyrene nanoparticles were measured before each sample measurement. The adsorbed layer thickness of PCE was calculated according to the following equation:

$$ALT = (D_1 - D_0)/2$$

where D_1 was defined as the particle diameter with adsorbed PCE, and D_0 was noted for the pristine particle diameter.

3. Results and Discussion

3.1. Characteristic properties of S-SP sample

The molecular properties of S-SP obtained from GPC were displayed in Table 1. The weight averaged molecular weight (*Mw*) of the S-SP sample was around 38,000 g/mol, and the number averaged molecular weight (*Mn*) was around 16,000 g/mol. The PDI value was 2.4 and the macromonomer conversion was 53.76%. Through the titration against polyDADMAC, the anionic charge of synthesized S-SP sample was measured to be 1544 μeq/g.

Table 1. Molecular properties of synthesized S-SP.

Mw [g/mol]	Mn [g/mol]	PDI	Conversion [%]	Anionic Charge [μeq/g]
3.794×10^4	1.573×10^4	2.4	53.8	1544

3.2. Dispersing effectiveness of S-SP in NaOH activated slag

The dispersing power and retaining ability of S-SP in both AAS paste and mortar were shown in Fig. 1. In AAS paste, the addition of 0.12% bwos of S-SP was able to increase the initial spread flow to 26 cm, and keep the spread flow above 23 cm within 6 h. Despite the lower dosage applied on the reference sample, 7IPEG4.5, to achieved the same initial spread flow, its dispersing power was lost much faster compared to S-SP. The spread flow yielded by reference sample dropped to 11 cm within 90 min. Such outstanding slump-retaining ability of S-SP was also observed in AAS mortar, where 7IPEG4.5 was no longer effective in dispersing. As shown in the figure, 0.3% bwos of S-SP provided the AAS mortar with an initial spread flow of 21 cm, which was still kept above 11 cm for 6 h.
These experiments clearly showed the dispersing power of S-SP in AAS paste and mortar, as well as the ability of maintaining the dispersion over long time. Compared with traditional PCEs, which mainly possess only the initial dispersing effectiveness, the dual ability of S-SP makes it more advantageous in the situations where retarders are needed.

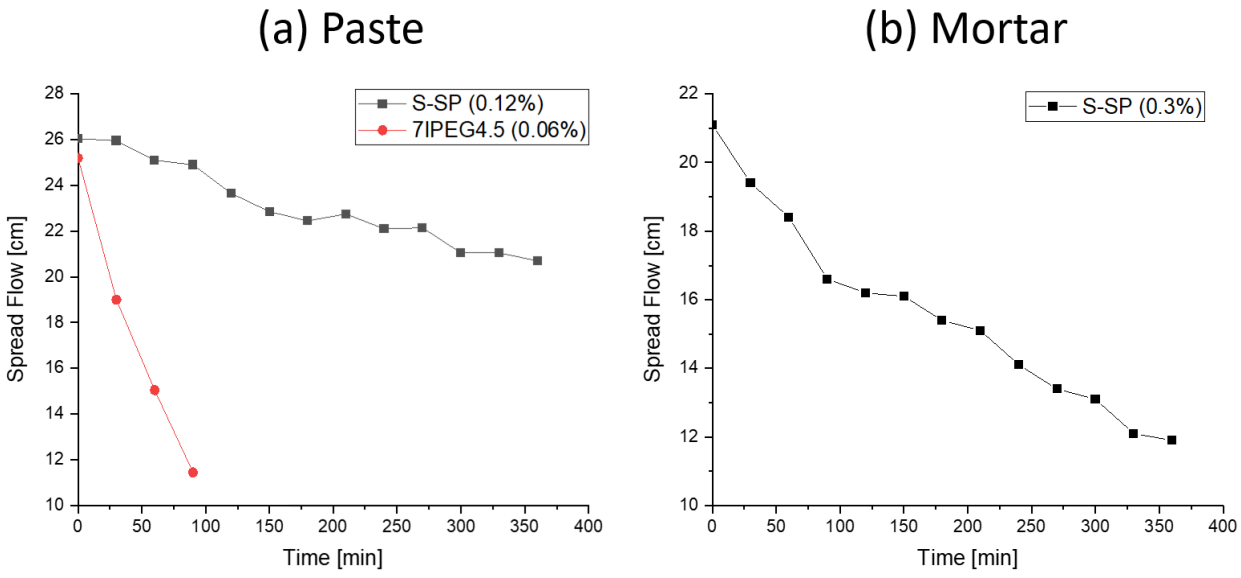

Fig. 1. The change in spread flow against time of (a) AAS paste with 0.12% bwos of S-SP and (b) AAS mortar with 0.3% bwos of S-SP.

3.3. Adsorption of S-SP on AAS

The result of TOC analysis was displayed in Fig. 2. With the polymer dosage increasing, the adsorption amount firstly raised within 1% bwos of addition, then the rate of growth gradually reached plateau until 2% bwos of addition, following a Langmuir adsorption model. S-SP exhibited a much higher adsorbed amount as compared to the 7IPEG4.5 polymer.

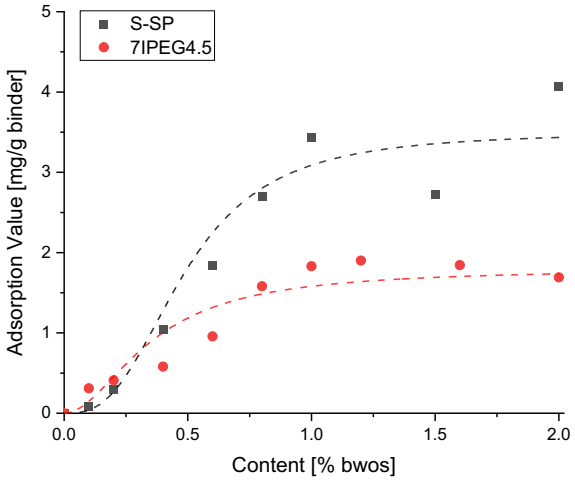

Fig. 2. Adsorption value curve of the synthesized S-SP on AAS, compared with 7IPEG4.5.

The measured adsorbed layer thickness was ~6.5 nm when the polymer concentration was over 600 mg/L.

4. Conclusion

In this work, the novel starch-based superplasticizer (S-SP) exhibited superior dispersing performance in AAS system compared with the IPEG PCE. In both slag paste and mortar, S-SP was effective in providing high initial spread flow with relatively low dosage, as well as maintaining the spread flow for much longer time than 7IPEG4.5. The strong adsorption of S-SP polymer onto slag particles results in its high dispersion efficiency.

5. References

Andrew, R. M. (2019) "Global CO2 emissions from cement production, 1928–2018", Earth System Science Data, 11(4): 1675-1710

Breilly, D., S. Fadlallah, V. Froidevaux, A. Colas and F. Allais (2021) "Origin and industrial applications of lignosulfonates with a focus on their use as superplasticizers in concrete", Construction and Building Materials, 301

Flower, D. J. M. and J. G. Sanjayan (2007) "Green house gas emissions due to concrete manufacture", The International Journal of Life Cycle Assessment, 12(5): 282-288

Javadi, A., H. S. Mehr and M. D. Soucek (2017) "(Meth)acrylated poly(ethylene glycol)s as precursors for rheology modifiers, superplasticizers and electrolyte membranes: a review", Polymer International, 66(12): 1765-1786

Pagé, M. and N. Spiratos (2000). "The role of superplasticizers in the development of environmentally-friendly concrete". CANMET/ACI International Symposium on Concrete Technology for Sustainable Development.''Canada.

Shi, C. and R. L. Day (1995) "A calorimetric study of early hydration of alkali-slag cements", Cement and concrete Research, 25(6): 1333-1346

Stecher, J. and J. Plank (2020) "Adsorbed layer thickness of polycarboxylate and polyphosphate superplasticizers on polystyrene nanoparticles measured via dynamic light scattering", Journal of colloid and interface science, 562: 204-212

Tong, S., Z. Yuqi and W. Qiang (2021) "Recent advances in chemical admixtures for improving the workability of alkali-activated slag-based material systems", Construction and Building Materials, 272

Wang, Z., C. Zhou, W. Liu, C. Pan, J. Yan, Z. Li, Z. Lei, S. Ren, X. Wang and H. Shui (2022) "A Low-Carbon and High-Efficiency Utilization of Lignite Based on the Preparation of Superplasticizer by Oxidative Depolymerization and Sulfomethylation", Available at SSRN 4176901,

Yuan, B., Q. Yu, E. Dainese and H. Brouwers (2017) "Autogenous and drying shrinkage of sodium carbonate activated slag altered by limestone powder incorporation", Construction and Building Materials, 153: 459-468

The 16th International Congress on the Chemistry of Cement 2023 (ICCC2023)
"Further Reduction of CO_2 -Emissions and Circularity in the Cement and Concrete Industry"
September 18–22, 2023, Bangkok, Thailand

Rheology of superplasticized limestone calcined clay cements

M. Palacios*[1], S. Real*[1], F. Puertas[1], A. Pachon-Montaño[1], M. Roig-Flores[2], M.C.Alonso[1], M. Lanzón[3]

[1] *Eduardo Torroja Institute for Construction Science (IETcc-CSIC), Spain*
marta.palacios@ietcc.csic.es; sergio.real@ietcc.csic.es; puertasf@ietcc.csic.es; apachon@ietcc.csic.es; mcalonso@ietcc.csic.es

[2]*Department of Mechanical Engineering and Construction. Universitat Jaume I, Spain*
roigma@uji.es

[3]*Departamento de Arquitectura y Tecnología de la Edificación, ETSAE, Universidad Politécnica de Cartagena, Spain*

Marcos.Lanzon@upct.es

ABSTRACT

Superplasticized LC^3 cements and concrete have been reported to exhibit a rapid loss of flowability, although the underlying mechanisms are still unknown. This study focuses on gaining a deeper scientific understanding on the evolution of the flow over time of superplastized LC^3 cements and its correlation with their hydration kinetics, polymer adsorption and hydrate formation over time. The results obtained showed that, in contrast to OPC pastes, in LC^3 pastes the flow loss starts before the onset of the acceleration period, independently of the molecular structure of the polymer added. In particular, flow loss is observed in pastes a few minutes after mixing and ettringite has been the only hydrate identified over the period of time when workability of superplasticized pastes is lost. Moreover, the amount of polymer adsorbed onto the solids remained almost constant over the studied time period.

KEYWORDS: *limestone calcined clay cements, superplasticizers, fluidity, reactivity, polymer adsorption*

1. Introduction

LC^3 cements and concrete have received a great interest from industry and scientific community because of their low environmental impact, vast availability of raw materials and good properties. The synergistic reactions among their three main components enable clinker replacements of 50% and beyond (Sharma et al., 2021) with a reduction of 40% of the CO_2 emissions with respect to Portland cement. However, the addition of calcined clays increases the water demand. In addition to the high specific surface area of the calcined clays, Hou et al. (Hou et al., 2021) reported the formation of agglomerates in these ternary cements that trapped water and reduced its fluidity. Superplasticizers are consequently essential components in LC^3 concrete to enhance their fluidity while reaching low water/binder ratios. Several studies in the literature have reported the lower efficiency of polycarboxylate-based superplasticizers (PCE) with respect to Portland cement (Lei et al., 2022). Methallyl ether (HPEG) superplasticizers have been pointed to be more effective and robust to the clay content than isoprenol ether (IPEG) and methacrylate ester (MPEG) polymers (Li et al., 2021), (Schmid and Plank, 2020). Furthermore, superplasticized LC^3 cements and concrete suffer from fast flow loss, although the underlying mechanisms are still unknown. This study aims at getting further insights into the flow loss and investigates the correlation of the quick flow loss in LC^3 systems with the polymer adsorption and phase assemblage overtime.

2. Experimental part

2.1. Materials

A CEM I 52.5R from Cementos Portland Valderrivas (Spain) (OPC), a natural clay from SAMCA with 47% of kaolinite (K) and a commercial limestone (LS) from Omya were used. Table 1 shows the chemical composition of the raw materials measured by XRF. Kaolinite was treated at 800 ºC for 2 h. Characteristic particle diameters (volume based, D_v) of the powders are reported in Table 1 measured using laser diffraction (MALVERN MASTERSIZER S). A ternary blend with 50% clinker content and a clay to limestone ratio of 2:1 were obtained by mixing 55% OPC, 12.75% limestone, 30.25% calcined clay and 2% of gypsum (to ensure the adequate sulfate balance) in a turbula over 20 h. Two non-commercial PCE polymers were synthesized by Sika AG by esterification on pre-formed backbones based on polymethacrylic acid (PMA). Table 2 shows the characteristics of the polymers.

Table 1. Chemical composition of the raw materials (XRF) and characteristic particle diameters

	CaO	*SiO_2*	*Al_2O_3*	*Fe_2O_3*	*MgO*	*Na_2O*	*K_2O*	*TiO_2*	*SO_3*	*L.O.I*	*D_{v10} μm*	*D_{v50} μm*	*D_{v90} μm*
OPC	64.5	20.3	5.7	2.3	0.84	0.11	0.97	0.24	2.9	2.9	2.3	9.0	26.2
K	0.6	54.0	27.6	1.2	1.1	-	1.3	0.3	-	12.2	5.7	22.5	65.5
LS	56.2	0.05	0.10	-	-	-	-	-	-	15.0	2.6	7.7	22.5

Table 2. Characteristics of the PCE used

	Carboxylate/ether (C/E)	*Side chain (g/mol)*	*# COO^- (mmol/g polymer)*
2PMA1000	2	1000	1.6
3PMA1000	3	1000	2.2

2.2. Pastes preparation and characterisation methods

One kilogram of the LC^3 binder was mixed with ultrapure water in a planetary mixer (30 s at 140 rpm plus 3 min at 285 rpm). The initial liquid/solid ratio was 0.4 and 0.15% of polymer by weight of binder (bwob) was added 10 minutes after the initial contact of the water and the binder and mixed for 3 additional minutes at 285 rpm. The paste was divided in sealed plastic containers with around 200 g of cement paste. At the selected time of rest, each batch was stirred for 1 minute at 800 rpm with a 4-bladed propeller stirrer and the following tests were done:

- *Rheological measurements*: Flow curves were obtained with a Haake Rheowin Pro RV1 rotational viscometer fitted with a grooved cylindrical rotor. The method consisted of an initial preshear at 100 s^{-1} during 1 min, a shear rate ramp from 0 to 100 s^{-1} over 1.5 minutes followed by a final reversed ramp from 100 s^{-1} to 0 s^{-1} over 2.5 min. Yield stress was obtained by fitting the curve to a Herschel-Bulkley model.
- *Hydration kinetics:* 5 g of LC^3 pastes were poured after mixing in plastic ampoules and inserted into an isothermal calorimeter TAM Air (TA Instruments and Waters) set at 25 ºC.
- ^{27}Al MAS NMR measurements were done using a BRUKER AVANCE 400 spectrometer. Resonance frequencies of 104.26 MHz were applied and 1 M $AlCl_3$ aqueous solution was used as a reference for the chemical shift values. ^{27}Al MAS NMR spectra were obtained using a pulse length of 2 μs, a recycle delay of 5 s and 720 scans. Hydration of pastes was previously stopped at different times by treatment with isopropanol in a solid:isopropanol ratio of 1:10.
- *Polymer adsorption*: Pore solution was obtained by filtering the pastes in a stainless-steel pressure filter holder with a nylon membrane filter with a 0.45 μm pore diameter. Pore solution was analyzed by using a SHIMADZU TOC-VCSH/CSN total organic carbon (TOC) analyser.

3. Results and discussion

Figure 1 shows the evolution of the yield stress and heat flow of the LC^3 pastes containing 0.15% 2PMA100 and 3PMA1000. Both pastes have an initial yield stress of 7 Pa that significantly increases over the dissolution period of the heat flow curve. In particular, yield stress increased and reached values

of 40-70 Pa at the onset of the acceleration period. This behaviour contrasts with the flow loss of admixed OPC pastes described by Mantellanto et al. (Mantellato et al., 2019). In particular, these authors reported that the yield stress of OPC pastes remained constant over the dissolution period and the onset of the flow loss occurred once the acceleration period started and the main nucleation and growth of hydrates occurred.

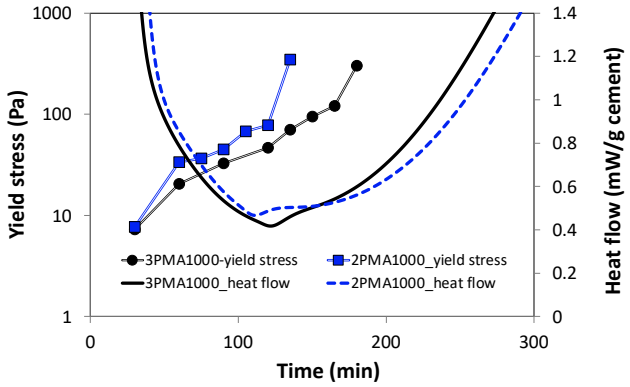

Figure 1. Evolution of the yield stress and heat flow of admixed LC^3 pastes

Hydrates formed over the period of flow loss were characterized by XRD (data not included here) and NMR techniques to understand the correlation of the evolution of the fluidity with the new surfaces formed. Ettringite was the only hydrate identified in the admixed LC^3 pastes by both techniques. In particular, ^{27}Al MAS NMR spectra (see Figure 2) show resonances at around 55, 28 and 3 ppm associated with the 4, 5 and 6-fold Al of the metakaolin while the intense peak at 13 ppm corresponds to the 6-fold Al of ettringite (Skibsted et al., 2017). As seen in Figure 2b, the major formation of ettringite occurs during the first 60 minutes of hydration while the intensity of the 6-fold peak remains almost constant afterwards. It is well-known that PCEs have a great affinity to adsorb onto the ettringite surfaces (Dalas et al., 2015; Marchon et al., 2017). However, the amount of polymer adsorbed on the studied LC^3 pastes remains almost constant over the studied 2-3 hours of hydration, with values of around 85 – 90% of the initially added PCE (see Table 3). This means that the added PCE would initially adsorb onto the binder components causing their dispersion. However, the fact that the amount of polymer does not change with time would indicate that the same amount of polymer would have to adsorb on anhydrous and hydrated surfaces. Polymer surface coverage would thus be lower with time as new surfaces form, that would lead to the agglomeration of particles and consequently to the observed flow loss. These results highlight the critical selection of the initial amount of polymer in the LC^3 binders to compensate for the new early-formed surfaces (ettringite). However, further studies are still required to fully understand the flow properties of admixed LC^3 binders. In particular, the interaction of the PCEs with the LC^3 components, mainly with the calcined clay, and the impact of the polymer on the interparticle forces in LC^3 systems should be better understood.

(a) (b)

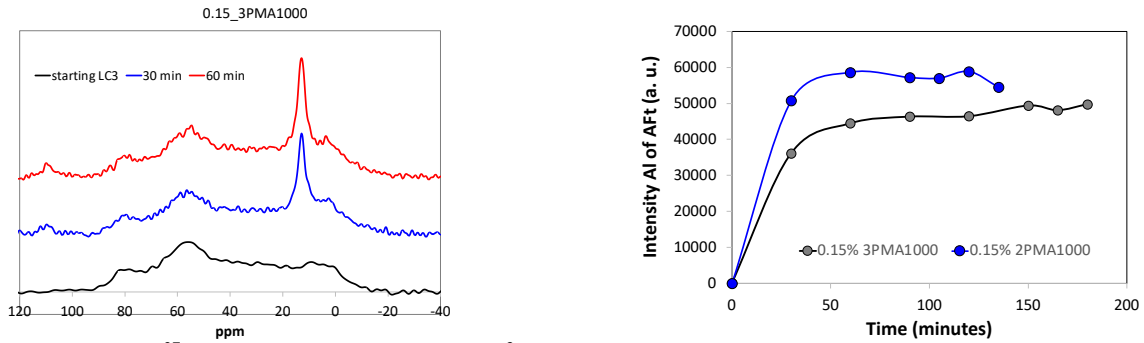

Figure 2. (a) ^{27}Al MAS NMR spectra of LC^3 pastes containing 3PMA1000 polymer; (b) evolution oft he intensity of the 6-fold Al signal (13 ppm) asssociated to ettringite.

Table 3. Polymer adsorption over time in admixed LC^3 pastes (initial added PCE = 0.15% bwob)

Time (minutes)	*2PMA1000 adsorbed*	*3PMA1000 adsorbed*
30	87 %	91 %
90	86 %	90 %
120	85 %	90 %

4. Conclusions

The rheology of LC^3 systems over time is a complex phenomenon that depends on several factors. This study has concluded that in contrast to OPC systems, admixed LC^3 binders' lose their fluidity before the onset of the acceleration period. The fast formation of ettringite, with a high affinity for PCEs might play a relevant role on this rheological behaviour, indicating extra amount of polymer should be initially added to compensate for the new early-formed surfaces. However, getting further insights into the interaction of the PCEs with the LC^3 components, mainly with the clay, and the impact of the polymer on the interparticle forces in LC^3 systems are required.

Acknowledgements

Authors thank PID2020-115797RB-I00 project funded by MCIU/AEI/FEDER, UE.

References

Dalas, F., Pourchet, S., Rinaldi, D., Nonat, A., Sabio, S., Mosquet, M., 2015. Modification of the rate of formation and surface area of ettringite by polycarboxylate ether superplasticizers during early C3A–CaSO4 hydration. Cem. Concr. Res. 69, 105–113. https://doi.org/10.1016/j.cemconres.2014.12.007

Hou, P., Muzenda, T.R., Li, Q., Chen, H., Kawashima, S., Sui, T., Yong, H., Xie, N., Cheng, X., 2021. Mechanisms dominating thixotropy in limestone calcined clay cement (LC3). Cem. Concr. Res. 140, 106316. https://doi.org/10.1016/j.cemconres.2020.106316

Lei, L., Palacios, M., Plank, J., Jeknavorian, A.A., 2022. Interaction between polycarboxylate superplasticizers and non-calcined clays and calcined clays: A review. Cem. Concr. Res. 154, 106717. https://doi.org/10.1016/j.cemconres.2022.106717

Li, R., Lei, L., Sui, T., Plank, J., 2021. Effectiveness of PCE superplasticizers in calcined clay blended cements. Cem. Concr. Res. 141, 106334. https://doi.org/10.1016/j.cemconres.2020.106334

Mantellato, S., Palacios, M., Flatt, R.J., 2019. Relating early hydration, specific surface and flow loss of cement pastes. Mater. Struct. 52, 5. https://doi.org/10.1617/s11527-018-1304-y

Marchon, D., Juilland, P., Gallucci, E., Frunz, L., Flatt, R.J., 2017. Molecular and submolecular scale effects of comb-copolymers on tri-calcium silicate reactivity: Toward molecular design. J. Am. Ceram. Soc. 100, 817–841. https://doi.org/10.1111/jace.14695

Schmid, M., Plank, J., 2020. Dispersing performance of different kinds of polycarboxylate (PCE) superplasticizers in cement blended with a calcined clay. Constr. Build. Mater. 258, 119576. https://doi.org/10.1016/j.conbuildmat.2020.119576

Sharma, M., Bishnoi, S., Martirena, F., Scrivener, K., 2021. Limestone calcined clay cement and concrete: A state-of-the-art review. Cem. Concr. Res. 149, 106564. https://doi.org/10.1016/j.cemconres.2021.106564

Skibsted, J., Pedersen, M.T., Holzinger, J., 2017. Resolution of the Two Aluminum Sites in Ettringite by 27Al MAS and MQMAS NMR at Very High Magnetic Field (22.3 T). J. Phys. Chem. C. https://doi.org/10.1021/acs.jpcc.6b11875

The 16th International Congress on the Chemistry of Cement 2023 (ICCC2023)
"Further Reduction of CO_2 -Emissions and Circularity in the Cement and Concrete Industry"
September 18–22, 2023, Bangkok, Thailand

Synergy effect of TEA as cement additive and PCE on rheological and hydration kinetics of limestone cementitious materials

A.C.R. Martho[1*], D. F. Ferraz[2], G.C.M. Carvalho [3], R.C.O. Romano[4] and R.G. Pileggi[5]

[1] *GCP Applied Technologies, Sorocaba, Brazil*
Email: ariane.martho@gcpat.com
[2] *GCP Applied Technologies, Sorocaba, Brazil*
Email: danila.f.ferraz@gcpat.com
[3] *GCP Applied Technologies, Sorocaba, Brazil*
Email: gustavo.carvalho@gcpat.com
[4] *University of São Paulo, São Paulo, Brazil*
Email:cesar.romano@lme.pcc.usp.br
[5] *University of São Paulo, São Paulo, Brazil*
Email:rafael.pileggi@lme.pcc.usp.br

ABSTRACT

Amines are usually used as activators in cement additives to accelerate setting or hardening, the effect of this additive can be modified based on the cement physical-chemical and mineralogical composition plus the interaction with polycarboxylates that are used as concrete admixtures. The amines activation is related to the hydration of specific cementitious phases, which can be induced by complexation mechanisms, in addition, the polycarboxylate dispersion effect can also influence the hydration as well as the rheological behaviour.

In this work, studies were conducted to evaluate the interaction of triethanolamine used as cement additive with polycarboxylate on limestone cement. The dispersion effect of polycarboxylate can expose more cement surface area to react, the presence of triethanolamine was evaluated based on the two scenarios, dispersed and non-dispersed state of the cementitious paste/mortar. The rheological behaviour, flow, apparent viscosity, yield stress and hysteresis loop of each paste at the fresh state were evaluated. The hydration kinetics obtained by calorimetric evaluation was evaluated too and the initial strengths using two different standards. The hydration kinetics showed intensification on aluminate peak on the paste with triethanolamine and the polycarboxylate. By combining the analysis of paste dispersion state and chemical reaction, this study allowed identifying the effect of triethanolamine in limestone blended cement with and without polycarboxylate.

KEYWORDS: *Cement, admixtures, rheology, triethanolamine, polycarboxylate*

1. Introduction

Cement additives are mixtures of chemical products applied during cement production that increase the efficiency of the grinding process and/or improve the performance generally aiming at reducing production costs. or meeting specific performance demands for each cement. Chemical products used in quality improvers additives have different mechanisms of action that can vary depending on the composition of each cement and when combined with other chemicals in the same formulation. Alkanolamines are one of the main classes of raw materials used in additives. These alkanolamines have different mechanisms of action and different synergies depending on the composition of the cement, some have higher or lower affinity for certain SCM (supplementary cementitious materials). In general, they act by catalyzing cement hydration, but the extent of hydration acceleration depends on many factors (JARDINI and CHEUNG, 2015). TEA is one of the alkanolamines widely used in cement additives.
The study carried out by Cheung et. al (2016) evaluated the impact of TEA on the hydration of an ordinary Portland cement (OPC) and a cement with fly ash (FA). The results indicated that TEA provided the highest early strength gain for the FA cement.

The admixtures are considered an essential component for the production of mortar and concrete, with cost and performance well suited to the required application (AÏTCIN et al., 2016). The best efficiency of each admixture depends on the synergy with the cement, since each binder is produced with different physical, chemical, mineralogical and surface characteristics. The rheological properties of concrete are influenced by the interaction between cement, aggregates and additives, in addition to the composition of the mix design (RAMACHADRAN, 1995; AÏTCIN et al., 2016). The interaction of these components, is determined by the chemical and mineralogical composition of the cement, surface area, particle size distribution, porosity, prehydration for example, as well as the composition of the cement additive and the structure of each polycarboxylate polymer.
Rheological properties, hydration kinetics and compressive strength in mortar were evaluated in this study. The objective was to demonstrate the synergy between cement and concrete additives to improve cement/mortar properties. In each experiment, the TEA dose was set at a usual level for cement additives and the PCE dose was determined through oscillatory rheometry testing.

2. Materials and cement preparation

A limestone blended cement without chemical additive was selected. Triethanolamine was used at a fixed dosage of 200g/ton as a cement additive and the admixture MiraFlow 965 at different dosages. The study was carried out comparing the cement without the addition of TEA (cement ref.) and the same cement with the addition of alkanolamine (cement TEA), both without and with admixture.
To prepare the cement sample, triethanolamine was sprinkled on cement and then homogenized in the laboratory. The admixture was dosed in the mixing water during the execution of the tests.

3. Methods

3.1 Cement characterization

Particle size distribution: equipment used: Malvern Instruments model Mastersizer 2000/2000E. The test was performed wet, in absolute ethyl alcohol (Figure 1).

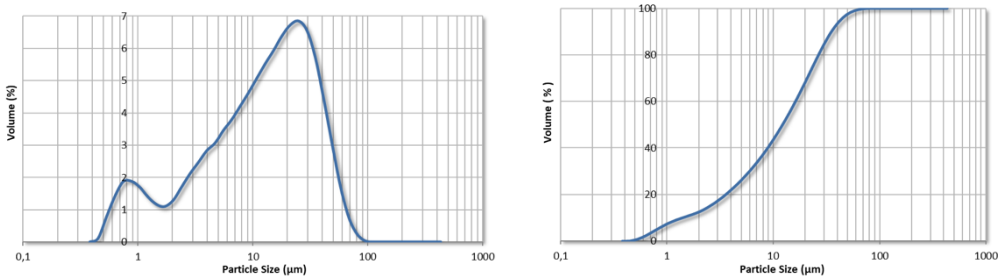

Figure 1: Particle size distribution of the cement sample

X-ray fluorescence (XRF): the fineness of the sample was checked in an agate mortar. After that, the sample was placed in an aluminum capsule and pressed (Herzog press), using 25 tons of force for 30 seconds. This "pebble" that formed was taken to the Rigaku X-ray spectrometry device, model ZSX Primus III+. Table 1 shows the chemical species of the cement obtained by X-ray fluorescence and also the mineralogical composition obtained from x-ray diffractometry.

X-ray diffraction (XRD): the sample was ground in an agate mortar, pressed manually and placed to carry out the analysis in an X-ray diffraction apparatus, Rigaku, model D/MAX.

Table 1: Chemical composition by fluorescence of X-ray and mineralogical composition by diffractometry of X-ray calculated by Rietveld

Analyte, %	Cement
SiO_2	16.6
Al_2O_3	4.4
Fe_2O_3	2.7
CaO	66.8
MgO	2.5
SO_3	4.2
Na_2O	0.2
K_2O	1.4
TiO_2	0.3
P_2O_5	0.5
V_2O_5	<0,1%
MnO	<0,1%
NiO	<0,1%
CuO	<0,1%
ZnO	<0,1%
SrO	<0,1%

Analyte, %	Cement
C_3S	53.0
C_2S	16.9
C_4AF	7.4
C_3A	3.0
Lime	0.4
Periclase	2.1
Portlandite	2.2
Calcite	12.9
Bassanite	0.4
Anhydrite	0.9
Quartz	0.8

4. Results and discussion

4.1 Kantro

The Kantro results showed a tendency of the Cement TEA to present lower flow, especially in the more dispersed system, with the higher dosage of admixture. This was an effect of the more dispersed system, with more particles exposed to react and because of the presence of TEA, that acts accelerating the initial hydration reactions (Figure 2).

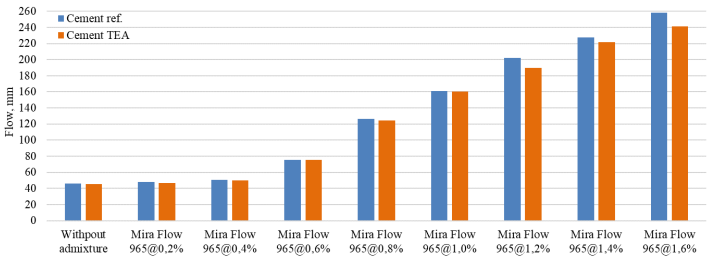

Figure 2: Flow (Kantro) for the different cements and admixture dosages

4.2 Rotational rheometry

Rotational rheometry did not show significant variation between Cement ref and Cement TEA. For both samples the higher the dosage of the admixture, showed lower the viscosity, yield stress and hysteresis loop. These results were used to define the dosage of 0.8% of the admixture, this dosage was selected to avoid segregation of the paste, in addition choice of the optimized admixture content was made with the stabilization of the viscosity, but also considered the yield stress, to be used in the other tests (Figure 3).

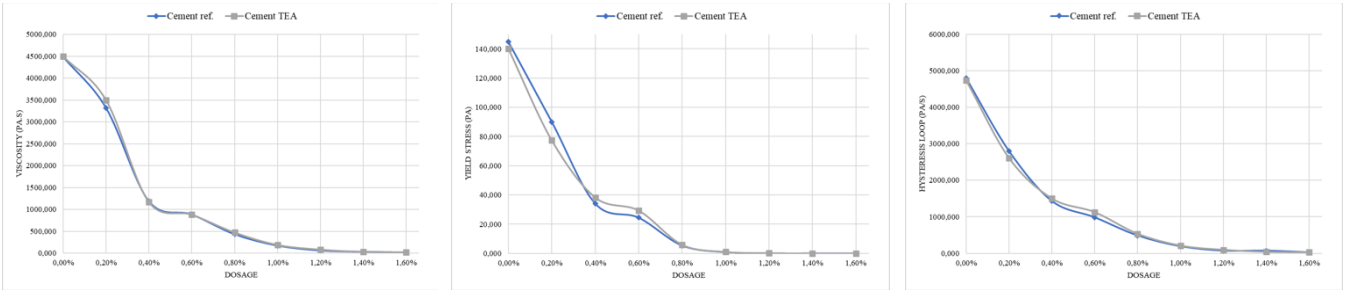

Figure 3: Apparent viscosity, yield stress and Hysteresis loop (rheometry) with and without admixture Mira Flow 965 (dosage curve)

4.3 Hydration kinetics evaluation

Isothermal calorimetry did not show significant variation between the cements without admixture, but in the dispersed system, an intensification of the hydration peak of silicates and aluminates was observed, indicating a greater degree of hydration of these phases in the presence of TEA (KAPELUSZNA and CHRABASZCZ, 2023) (Figure 4).

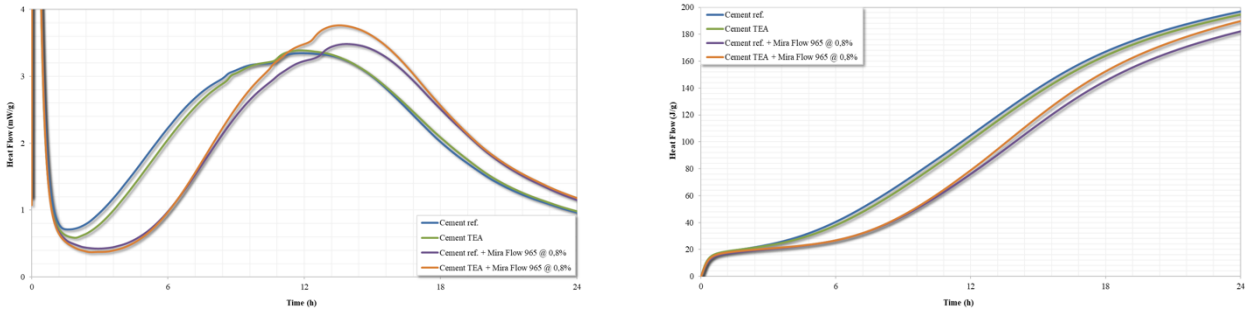

Figure 4: Heat flow and cumulative heat of the cements with and without admixture

4.4 Physical-mechanical properties evaluation

According to the results of the test carried out using EN 196-1 (Table 2), a standard that uses fixed w/c, it was possible to evidence the increase in resistance only after 1 day in cement with TEA without the admixture (~7% more resistance) and in higher proportion of the cement with TEA in the presence of the admixture (~9% more resistance) and an increase in resistance at 3 and 7 days was also seen. The mortar results with admixture are lower in comparison with without admixture because of the air incorporation in the mortar.

Table 2: Compressive strength results according to EN 196-1:2016

Admixture	Dosage, %	Cement	Air, %	1 day		3 days		7 days	
				MPa	δxi	MPa	δxi	MPa	δxi
Without admixture	-	Cement ref.	3,8%	**22.0**	0,7	**37.4**	0,3	**44.4**	0,7
Without admixture	-	Cement TEA	3,6%	**23.5**	0,8	**36.9**	0,5	**43.3**	0,2
Mira Flow 965	0.8	Cement ref.	9,8%	**15.4**	0,5	**26.9**	0,2	**31.6**	0,3
Mira Flow 965	0.8	Cement TEA	9,7%	**16.8**	0,6	**28.1**	0,6	**32.2**	0,5

In the results according to the ASTM C109, it was possible to observe a decrease in the w/c in the samples with the admixture, an effect expected by the dispersion and increment on the strength at 1 day in both systems, without admixture and in the dispersed system.

Table 3: Compressive strength results according to ASTM C109/C109M-20

Admixture	Dosage, %	Cement	w/c	Flow, %	Air, %	1 day		3 days		7 days	
						MPa	δxi	MPa	δxi	MPa	δxi
Without admixture	-	Cement ref.	0.51	114.8	2,3%	**21.4**	0,8	**36.4**	0,8	**43.9**	0,4
Without admixture	-	Cement TEA	0.51	113.7	2,2%	**23.3**	0,0	**36.9**	0,5	**43.3**	0,5
Mira Flow 965	0.8	Cement ref.	0.38	109.7	7,8%	**34.7**	0,4	**50.7**	0,6	**54.2**	0,2
Mira Flow 965	0.8	Cement TEA	0.38	114.7	7,9%	**35.5**	0,2	**51,0**	0,0	**54.9**	0,2

5. Conclusions

According to the tests carried out, the synergy between triethanolamine and admixture in the evaluated limestone cement is evident. In the dispersed system, it was possible to obtain the best degree of hydration of the cement particles and in the presence of TEA the hydration was enhanced due to acceleration of the initial reactions of cement hydration. The addition of superplasticizers results in the prolongation of the induction and acceleration periods; however, the presence of TEA reduces the delay effect of superplasticizers.

References

Aïtcin, P. C.; Flatt, R. J.; Science and Technology of Concrete Admixtures handbook .Elsevier, 2017.
Cheung, J., Sibbick, R., Nicolich, J., Detellis, J., Impact of Alkanolamines on Hydration of Portland and Fly Ash Cements, International Congress on the Chemistry of Cement, 2016.
Jardini, L., Cheung, J, Faster cement hydration, International Cement Review, 2015.
Kapeluszna, E., Chrabaszcz, K., Mutual compatibility of superplasticizers (PC, SNF), grinding aids (TEA, glycol) and C3A in Portland cement systems – Hydration, rheology, physical properties and air void characteristics. Construction Building Materials. pp 373, 2023.
Ramachandran, V.S . Concrete. Admixtures Handbook, Properties, Science and Technology. Institure of Research in Construction National Research Council Canadá, Ottawa. 2nd edition. pp 78-79, 1995.

The 16th International Congress on the Chemistry of Cement 2023 (ICCC2023)
"Further Reduction of CO_2 -Emissions and Circularity in the Cement and Concrete Industry"
September 18–22, 2023, Bangkok, Thailand

The Effect of Crystalline Morphology on the Rheology of Ettringite Suspensions in Presence of Admixtures

Anna Szabo[1]*, Julien Chapelat[1], Emmanuel Gallucci[1] and Patrick Juilland[1]

[1] *Sika Technology AG, Zurich, Switzerland*

[*] *Corresponding author: szabo.anna@ch.sika.com*

ABSTRACT

The interaction between ettringite and admixtures is a topic of interest to achieve robustness in construction. It is known that admixtures influence the ettringite morphology: in presence of PCEs, the size of ettringite crystals decreases, and the aspect ratio stays high, while with Na-Gluconate, ettringite crystals are small and exhibit lower aspect ratio than without admixtures. However, the impact of ettringite morphology on the rheology of suspensions and ultimately to concrete is not yet fully understood. In this study, ettringite suspensions were prepared either without admixtures or by co-precipitation with admixtures: PCE or Na-Gluconate. The suspensions were tested with a rheometer to obtain their yield stress and viscosity while the ettringite morphology was studied with BET and SEM. The results show that both ettringite morphology and the rheology of ettringite suspensions can be significantly impacted by the mixing energy at preparation and by the presence of admixtures. Na-gluconate co-precipitation and high mixing speed are preferential for achieving low yield stress with ettringite morphology, while PCE co-precipitation deteriorates the performance. The rheological tests provided a mean to quantify the impact of ettringite morphology on the flow and they are in good agreement with the qualitative microscopic assessment.

KEYWORDS: *Ettringite, Rheology, Organic admixtures, Shape, Crystal morphology*

1. Introduction

The rheological behavior of a suspension is strongly affected by its volume fraction and in the case of cement-based slurry, the first hydrate to precipitate and increase the volume fraction is ettringite. A link between the rheological properties and the ettringite formation was established by Jakob et al. (2019). In this paper, ettringite suspensions are studied as an analogy for ettringite in the pore solution around the concentrated suspension of relatively large cement particles. Previous studies address different synthetic ettringite suspension concentrations on rheology (Vladu et al., 2006) or the effect of PCEs on the specific surface area of ettringite, however the impact of this on the flow through admixture coverage of the surface is not studied (Mantellato et al., 2016). The aim of this paper is to advance the knowledge on how ettringite formation impacts rheology by the different crystal morphologies evolving due to the presence of admixtures or by different mixing protocols.

2. Materials and Methods

2.1 Material preparation and analytics

The ettringite suspensions were obtained by dissolving $Al_2SO_4 \cdot 15.6H_2O$ (VWR) in MilliQ water and optionally an admixture for co-precipitation, before $Ca(OH)_2$ (VWR) powder is added in stoichiometric proportions at 2.7 w% or 5.6% concentration. A week after preparation, the ettringite is dried and crushed under N_2 environment and XRD is used to assess the degree of conversion while the specific surface area is measured by BET (Mantellato et al., 2016).
Two admixtures, sodium gluconate and a PCE, were selected to assess their impact during the precipitation of ettringite but the variation of adsorption on ettringite with different morphologies and its impact on rheology will be the subject of another study. The impact of mixing energy on the ettringite morphology is introduced in this paper by testing different mixing protocols. All variations are summarized in Table 1.

Table 1: Protocol for ettringite preparation

Sample Name	Conc. (w%)	Mixing protocol (rpm)	Admix. dosage(mg/$g_{ettringite}$)
Aft_REF	2.7	500 (10min) + Shaking table (24h)	N/A
Aft_REF_2Xconc+shear	5.6	750 (3min) + rest	N/A
Aft_REF+shear	2.7	750 (3min) + rest	N/A
Aft_NaG_CoP	2.7	500 (10min) + Shaking table (24h)	30
Aft_PCE_CoP	2.7	500 (10min) + Shaking table (24h)	10.7

The ettringite suspensions were filtered, subsequently dried and stored under N_2 environment before their morphology was characterized by SEM. The SEM images were captured at 4kV acceleration voltage from 8.3-8.5mm working distance with the backscatter electron detector at 20K, 35K and 100K magnifications. The length and diameter of at least 25 crystals were measured on BSE images to characterize the crystal size and its related aspect ratio (Vladu et al., 2006).
For the rheological measurements, two additional suspensions were prepared by adding Na-gluconate and PCE to the already formed ettringite (AFt_REF) with the same dosages used for co-precipitation to assess the impact of morphology on rheological behaviour in presence of admixtures.

2.2 Rheological measurements

Rheological tests were performed on all suspensions with an Anton Paar MCR301 rheometer with a helical impeller. 100 s^{-1} pre-shear was applied for 30s before a logarithmic ramp between 100-0.01 s^{-1} shear rates with 10s data acquisition time for every step to record the respective shear stresses and apparent viscosities. The modified Bingham model was used to transform raw data into fundamental rheological units as it is widely accepted for the characterization of non-linear rheological behavior even when moderate shear thickening occurs at high shear rates (Feys et al., 2013):

$$\tau = \tau_0 + \mu \cdot \dot{\gamma} + c \cdot \dot{\gamma}^2 \qquad (1)$$

where τ is the shear stress, τ_0 is the yield stress, μ is the plastic viscosity, $\dot{\gamma}$ is the shear rate and c is coefficient of the second order correction term in shear rate indicating shear thinning or thickening.

3. Results and Discussion

3.1 Analytics

The SEM backscattered electron images in Figure 1 are obtained for the reference ettringite suspensions precipitated without admixtures at different mixing intensities and different concentrations. Large, fused ettringite needles were obtained for low initial shear mixing while short but high shear mixing yield significantly smaller needles see Figure 1). Furthermore, the concentration also impacts the ettringite morphology as thicker needles are obtained for the more concentrated suspension, although the mixing protocol remained the same.

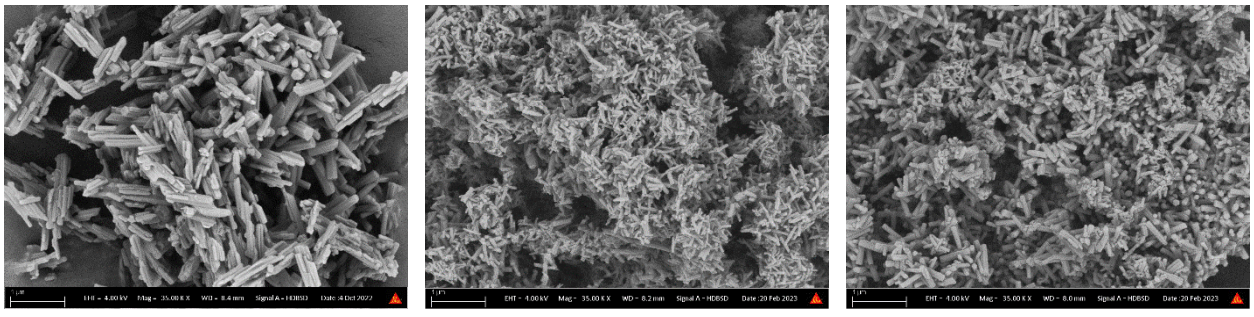

Figure 1: BSE images of the ettringite without admixtures at 35K magnification. Left: AFt_REF (SSA_{BET}=12.6 m^2/g); Middle: AFt_REF+shear (SSA_{BET}=23.9 m^2/g); Right: AFt_REF_2Xconc+shear (SSA_{BET}=20.2 m^2/g)

These qualitative observations are supported by image analysis summarized in Figure 2. For the non-admixed systems, dimensions are hard to extract as most crystals are fused and the reported data remain qualitative while in the other cases, a semi-quantitative description can be made. Nonetheless a doubling in SSA is measured due to the impact of mixing intensity which is in good agreement with the decrease in the average particle size extracted from the micrographs. Further, the slight decrease in SSA for the more concentrated suspension is also in line with the data obtained by image analysis.

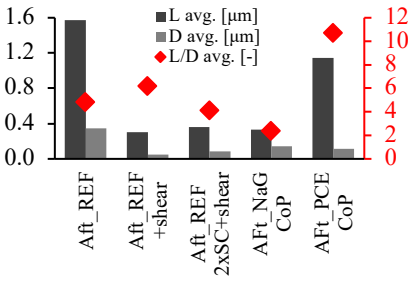

Figure 2: Results of the particle analysis based on the SEM images

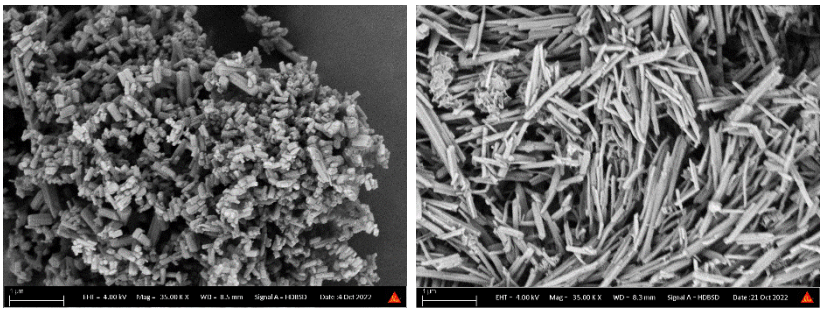

Figure 3: BSE images at 35K magnification. Left: AFt_NaG_CoP (SSA_{BET}=17.9 m^2/g); Right: AFt_PCE_CoP (SSA_{BET}=14.8 m^2/g)

Figure 3 represents the effect of admixtures on ettringite morphology, and as the admixtures were added before the precipitation occurred, these molecules could interact directly during the nucleation and growth of ettringite. The short needles of the Na-gluconate sample exhibit the smallest aspect ratio amongst all suspensions and a higher SSA compared to the reference ettringite which was prepared in the same way. The ettringite prepared with PCE exhibits the largest aspect ratio but only a moderate increase in surface area due to the moderate decrease in the particle size as well.

3.2 Rheological measurements

Numerous general observations can be made regarding the results of the rheological measurements. First, all samples exhibit shear thinning behaviour at low shear rates where the network of particle interactions are dominant and shear thickening at high shear rates where the hydrodynamic interactions govern the response (Roussel et al, 2010).
Table 1 presents differences in yield stress and plastic viscosity at a few orders of magnitude due to admixtures or preparation methodology. While 'c' coefficient, the expression of particle momentum transfer, indicates similar shear thickening response for all samples. The modified Bingham model is suitable to fit the data, only the scattered AFt_REF + PCE data show low coefficient of determination (R^2) as it was obtained close to the lower limit of the measuring range with the rheometer.
The reference ettringite without admixtures has the highest viscosity and yield stress when it is prepared in low shear conditions. The yield stresses and viscosities of the admixture-free high-shear suspensions with small particles are significantly lower, even when their solid fraction is doubled. This suggests that the packing of these small crystals is much better than the reference.

Table 2: Fitting parameters for the rheological data based on the modified Bingham model.

	τ_0	μ	c	R^2
Aft_REF	0.44	0.015	0.00010	0.9987
AFt_REF + NaG	0.10	0.012	0.00006	0.9773
AFt_NaG CoP	0.0011	0.002	0.00009	0.9011
AFt_REF + PCE	0.0006	0.001	0.00008	0.6661
AFt_PCE CoP	0.04	0.008	0.00009	0.9991
Aft_REF +shear	0.02	0.004	0.00006	0.9938
Aft_REF 2Xconc +shear	0.35	0.005	0.00010	0.9956

The rheological data are plotted as both obtained shear viscosities over shear rate in Figure 4-5. The sole effect of admixture is seen on measurements of the reference ettringite with and without admixtures. Both admixtures decreased the yield stress and viscosity of the suspension with the same reference ettringite morphology, however, Na-gluconate only moderately while the PCE significantly.

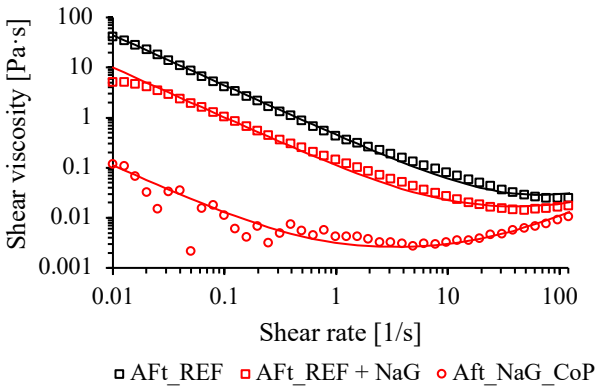

Figure 4: Flow curves showing AFt_REF and the effect of co-precipitation and late addition of NaG

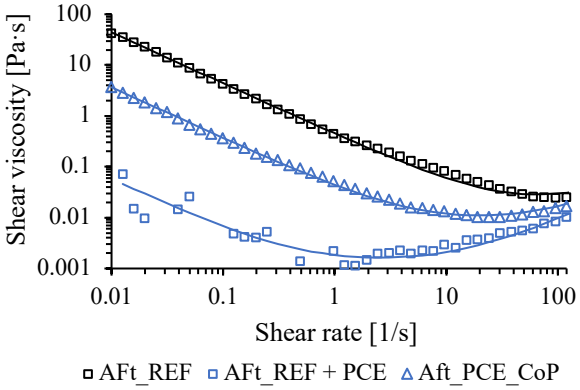

Figure 5: Flow curves showing AFt_REF and the effect of co-precipitation and late addition of PCE

The effect of shape is seen between suspensions with different ettringite morphologies containing the same amount of admixture: the co-precipitated suspensions AFt_NaG_CoP and AFt_PCE_CoP with the reference ettringite with late admixture additions AFt_REF + NaG and AFt_REF + PCE. With PCE, the delayed admixture addition to the reference ettringite results in lower yield stress and viscosity, the needle morphology of the co-precipitated ettringite with increased aspect ratio compromises the flow. In contrary, with Na-gluconate, the decreased aspect ratio and average particle size compared to the reference results in lower yield stress and viscosity. These results are in good agreement with the observations made based on SEM images and BET measurements.

4. Conclusions

In this study the rheological impact of different ettringite morphologies was investigated. It was found that the effect of mixing protocol of the suspensions has a significant impact on ettringite morphology. The mixing protocol affects mostly the particle size, the concentration the aspect ratio, and admixtures impact both. Higher mixing speed, enhancing the dissolution of raw materials, promotes the formation of shorter needles resulting in an order of magnitude lower yield stress and viscosity compared to the reference suspension. The effect of short needles on rheology was so pronounced that it dominates the yield stress response even at double solid fraction. In presence of admixtures two extremes were chosen with significant impact on rheology, however the adsorption conditions of both admixtures would be necessary to address to draw more definitive conclusions. Nevertheless, this preliminary investigation already suggests that Na-gluconate might improve the rheology of cement pastes through influencing the ettringite morphology.

References

Feys, D., Wallevik, J.E., Yahia, A., Khayat K.H. & Wallevik O.H. (2013) “Extension of the Reiner–Riwlin equation to determine modified Bingham parameters measured in coaxial cylinders rheometers” *Mat Struct* 46, 289–311.

Jakob, C., Jansen, D., Ukrainczyk, N., Koenders, E. a. B., Pott, U., Stephan, D., & Neubauer, J. (2019) “Relating Ettringite Formation and Rheological Changes during the Initial Cement Hydration: A Comparative Study Applying XRD Analysis, Rheological Measurements and Modeling”, *Materials*, 12(18), 2957.

Mantellato, S., Palacios, M., & Flatt, R. J. (2016) “Impact of sample preparation on the specific surface area of synthetic ettringite”, *Cement and Concrete Research*, 86, 20–28.

Roussel, N., Lemaître, A., Robert J. Flatt, R.J. & Coussot, P. (2010) “Steady state flow of cement suspensions: A micromechanical state of the art”, *Cement and Concrete Research*, 40, 77–84.

Tadros, T. (2013). *Encyclopedia of Colloid and Interface Science*. Springer.

Vladu, C. M., Hall, C., & Maitland, G. C. (2006) ”Flow properties of freshly prepared ettringite suspensions in water at 25 °C”, *Journal of Colloid and Interface Science*, 294(2), 466–472.

The 16th International Congress on the Chemistry of Cement 2023 (ICCC2023)
"Further Reduction of CO_2 -Emissions and Circularity in the Cement and Concrete Industry"
September 18–22, 2023, Bangkok, Thailand

A study on early strength development of fly ash-GGBS geopolymer concrete admixed with inhibiting admixtures

Shehnazdeep[1*], and Bulu Pradhan[2]

[1*] *Department of Civil Engineering, Indian Institute of Technology Guwahati, Guwahati, India*
Email: shehnazdeep_199@iitg.ac.in
[2] *Department of Civil Engineering, Indian Institute of Technology Guwahati, Guwahati, India*
Email: bulu@iitg.ac.in

ABSTRACT

Geopolymer concrete is gaining popularity in the construction industry as a result of its long-term viability, positive impact on the surrounding environment, and significant contribution to effective waste management practices. However, durability-related difficulties, in particular, the corrosion-related deterioration and degradation of civil infrastructures are unavoidable worldwide challenges that require attention. Concrete's resistance to degradation in corrosive conditions is directly correlated to its type and microstructure. The variations in the mechanical properties, which affect the denseness of the microstructure of concrete have significant influence on the resistance of concrete against durability problems. In this study, the effect of two distinct inhibiting admixtures (sodium molybdate (Mo) as inorganic inhibiting admixtures and sodium oleate (So) as organic inhibiting admixtures) on different properties of geopolymer concrete (GPC), such as workability, early age compressive strength and microstructure have been investigated. Two different combinations of fly ash (FA) and ground granulated blast furnace slag (GGBS) at proportions of 80%:20% and 60%:40% (by mass) were used in the production of GPC mixes. The properties of GPC mix in fresh state (workability), hardened state (early age compressive strength at 7 days), and microstructure (FESEM and XRD analyses) were evaluated. Results indicated a substantial early age strength development and denser microstructure in case of sodium molybdate (Mo) based GPC with increasing GGBS (%) content as well as molarity of NaOH solution when compared with control mix (without inhibiting admixture). However, the performance of sodium oleate (So) based GPC was lower in terms of workability and early age strength, which is consistent with the findings from the microstructure analysis.

KEYWORDS: Fly ash; Ground granulated blast furnace slag; Geopolymer concrete; Inhibiting admixtures; Microstructure.

1. Introduction

It is widely agreed that geopolymers represent the next technological advancement in the field of construction materials. They exhibit superior mechanical and physical properties with a minimal adverse environmental impact (Fouad et al. (2021)). The most often employed precursors for the synthesis of geopolymer include fly ash (FA), slag etc. For the synthesis of geopolymer, an aluminosilicate source material, such as fly ash, a strongly alkaline solution, such as NaOH, KOH, Na_2SiO_3, or K_2SiO_3 solutions, and adequate curing conditions are needed for the geopolymerization processes of dissolution, speciation, reorientation, and polycondensation ((Duxson et al. (2007), Yazdi et al. (2018)). When compared to traditional concrete, geopolymer concrete mixtures have reportedly demonstrated greater resilience to corrosion in marine environments (Reddy et al. (2013)).
In the case of traditional concrete, a wide range of inorganic and organic compounds have been explored as inhibiting admixtures, while the research is scanty in case of geopolymer concrete (GPC). Therefore, in this study, attention is given to the effect of inorganic and organic inhibiting admixtures on the fresh and hardened properties of geopolymer concrete. The inhibiting admixtures are generally used to minimize

the extent of corrosion of steel reinforcement in concrete. In addition to evaluating their efficiency against corrosion, there is also a need to investigate the effect of different inhibiting admixtures on fresh and different hardened properties of concrete. This may be attributed to the fact that the variations in the mechanical properties of concrete indicating the changes in its microstructures significantly influence the resistance of concrete against durability problems like corrosion of steel reinforcement in concrete. Keeping this in view, in the present research, the influence of sodium molybdate (Mo) as inorganic inhibiting admixtures and sodium oleate (So) as organic inhibiting admixtures on workability, early-age compressive strength, and microstructure of fly ash-GGBS blended GPC mixes at varied NaOH solution concentrations have been investigated. For this purpose, NaOH solution of 8 M and 12 M were employed for producing GPC mixes blended with FA/GGBS ratios by weight of 80%/20% and 60%/40%, respectively. Slump test for workability, compressive strength, and FESEM and XRD analyses for microstructure characterization of GPC mixes were carried out in this study.

2. Experimental program

2.1 Materials

In the present study, class F fly ash (FA) and ground granulated blast furnace slag (GGBS), both of which passed through a sieve with mesh size of 75µm, were employed as the precursor materials. Sodium silicate (SS) (Na_2O: 8 wt%, SiO_2: 26.5 wt%) solution, which is readily available, was used in conjunction with sodium hydroxide (NaOH, SH) solution (8 M and 12 M) to activate the aluminosilicates present in the precursor materials. In the current experimental study, the NaOH pellets were mixed in laboratory tap water to form an aqueous solution according to the requisite molarity 48 hours before GPC mix preparation. The sodium silicate (SS) solution was added to the NaOH solution 24 hours prior to casting. The mass ratio i.e., SS/SH was kept constant at 1.5 for all GPC combinations. Fine aggregate (sand) complying with Zone II as per IS 383: 2016 and coarse aggregates with maximum size 10 mm and 20 mm were used. The relative density of aggregates i.e., 20 mm coarse aggregate, 10 mm coarse aggregate, and river sand were 2.66, 2.67, and 2.65 respectively. Sodium molybdate (Mo) as inorganic inhibiting admixture and sodium oleate (So) as organic inhibiting admixture were added to the fly ash-GGBS blended GPC mixes at a dosage of 4% by mass of geopolymer solids. The quantities of ingredients of geopolymer concrete mixes are provided in Table 1.

Table 1 Quantities of ingredients of geopolymer concrete mixes

Mix details	Fly ash (kg/m^3)	GGBS (kg/m^3)	Sodium silicate solution (kg/m^3)	Sodium hydroxide solution (kg/m^3)	Coarse aggregate 20 mm maximum size (kg/m^3)	Coarse aggregate 10 mm maximum size (kg/m^3)	River sand (kg/m^3)
*FGS 80/20	368	92	138	92	577.36	472.39	565.25
FGS 60/40	276	184	138	92	577.36	472.39	565.25

*FGS 80/20 mix corresponds to GPC mix with Fly ash 80% and GGBS 20% by mass of total binder.

2.2 Test techniques

The workability of all freshly prepared fly ash-GGBS blended GPC mixes were investigated using the slump test. Following the slump test, concrete cubes measuring 150 mm in size were made. For each GPC mix, three replicate cubes were produced and assessed over the course of seven days in a compressive testing machine. By averaging the results of the three replicates, the strength of the corresponding GPC mix was determined. After the compressive strength test, the GPC cube fragments were ground and sieved through 75 µm sieve size to obtain the geopolymer concrete powder. The powder obtained from GPC mixes was assessed in X-ray Diffractometer (Rigaku SmartLab 9kW model) with CuKα radiation (λ = 1.5405 Å) from 5° 2θ to 60° 2θ at a step size of 0.03° 2θ to determine the crystalline phase composition of control and inhibiting compound admixed GPC mixes. FESEM analysis was conducted using FESEM (ZEISS Gemini) instrument in in-lens mode to investigate the changes in the morphology of control and inhibiting compound admixed GPC mixes.

3. Results and discussions

3.1 Workability of GPC mixes

The slump values of all GPC combinations with FGS80/20 and FGS60/40 added with and without inhibiting admixtures are presented in Figure 1a. At both molarities of NaOH solution (i.e., 8M and 12M), reduced flow values were observed in case GPC admixed sodium oleate (So) when compared with control GPC mixture. The lowest slump value was observed in case of 40% GGBS and 12M NaOH solution GPC mix added with sodium oleate (So). In case of inorganic inhibiting admixture, i.e., sodium molybdate (Mo) added GPC mixes, a less significant variation in slump value was observed when compared with control GPC mixes at both NaOH solution molarity. The lower consistency in case of inhibiting compound added GPC mixes when compared with control mixes may be attributed to the increase in viscosity of the mixes in the presence of inhibiting compounds. Further, the sodium molybdate added GPC mixes exhibited higher consistency when compared with that added with sodium oleate, which can be attributed to the effect of comparatively increased particle mobility in the GPC mixtures containing sodium molybdate.

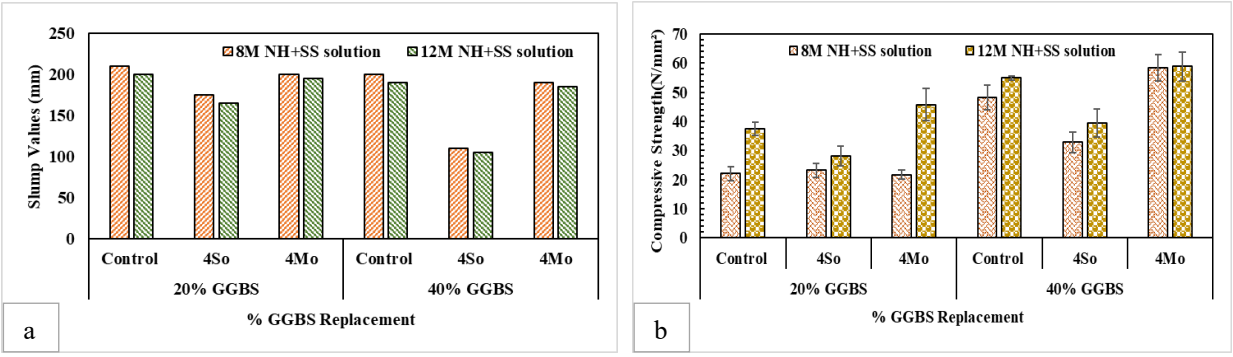

Figure 1 a) Slump value of all GPC mixes b) Compressive strength of all GPC mixes at 7 days .

3.2 Compressive strength of GPC mixes

The compressive strength values of GPC mixes added with and without inhibiting admixtures at 7 days of ambient curing are shown in Figure 1b. The results showed that increase in molarity of NaOH solution improved compressive strength in all GPC mixes, regardless of the inclusion of inhibiting admixtures. This is due to the effect of increased extent of polycondensation process in GPC mixtures made with higher molarity of NaOH solution. The control GPC mixes at both molarity of NaOH solution exhibited higher compressive strength than GPC mixes prepared with incorporation of organic inhibiting admixture i.e., sodium oleate (So). In contrast, considerable improvement in early age strength was observed in GPC mixes admixed with inorganic inhibiting admixture i.e., sodium molybdate (Mo) when compared with control mixes. This indicates that the presence of sodium oleate hindered the geopolymerization process whereas the presence of sodium molybdate enhanced the geopolymerization reaction in GPC mixes. There was significant increase in compressive strength with increase in GGBS content from 20% to 40% in GPC mixes as observed from Figure 1b. Although, there was increase in compressive strength with increase in molarity of NaOH solution, the increase was less significant in GPC mixes made with 40% GGBS in case of sodium molybdate when compared with all other mixes.

3.3. Microstructure analysis of GPC mixes

The XRD patterns of GPC mixes made with and without inhibiting admixtures at 7 days of ambient curing are presented in Figure 2. From the XRD patterns, it is observed that the crystalline peaks of quartz and mullite indicated the presence of unreacted fly ash particles in the GPC mixes. The compounds formed during the geopolymerization process were related to sodium (and calcium) aluminosilicate complex (N-(C)-A-S-H) such as albite ((Na, Ca)Al(Si Al)$_3$O$_8$) and anorthoclase ((Na$_{0.67}$ K$_{0.33}$)(AlSi$_3$O$_8$)), which were identified by their corresponding peaks in the XRD patterns. The albite peak at 28.0° 2θ and anorthoclase peaks at 27.5° 2θ and 27.8° 2θ were found in the XRD patterns of the GPC mixes at seven days of ambient curing (Figure 2(a)-(b)). A peak related to feldspar (K$_{0.94}$Na$_{0.06}$Al$_{1.01}$Si$_{2.99}$O$_8$) at 27.5º 2θ was identified in the XRD patterns of all GPC mixes irrespective of admixed inhibiting admixtures. A

less intense peak of muscovite ($(K_{0.82}Na_{0.18})$ $(Fe_{0.03}Al_{1.97})$ $(AlSi_3)O_{10}(OH)_2$) and Clinochlore ($(Mg_{2.96}Fe_{1.55}Fe_{0.136}Al_{1.275})(Si_{2.622}Al_{1.376}O_{10})(OH)_8$) were identified at 8.8° 2θ and 12.5° 2θ, respectively, in the XRD patterns of the GPC mixes as observed from Figure 2 (a)-(b). The presence of unreacted/ partly reacted fly ash and GGBS particles from the FESEM analysis is observed in case of sodium oleate (So) admixed GPC mixes while sodium molybdate (Mo) admixed GPC mixes exhibited slightly more homogeneous and denser microstructure in comparison to the control GPC mix as shown in Figure 3 (c)-(e).

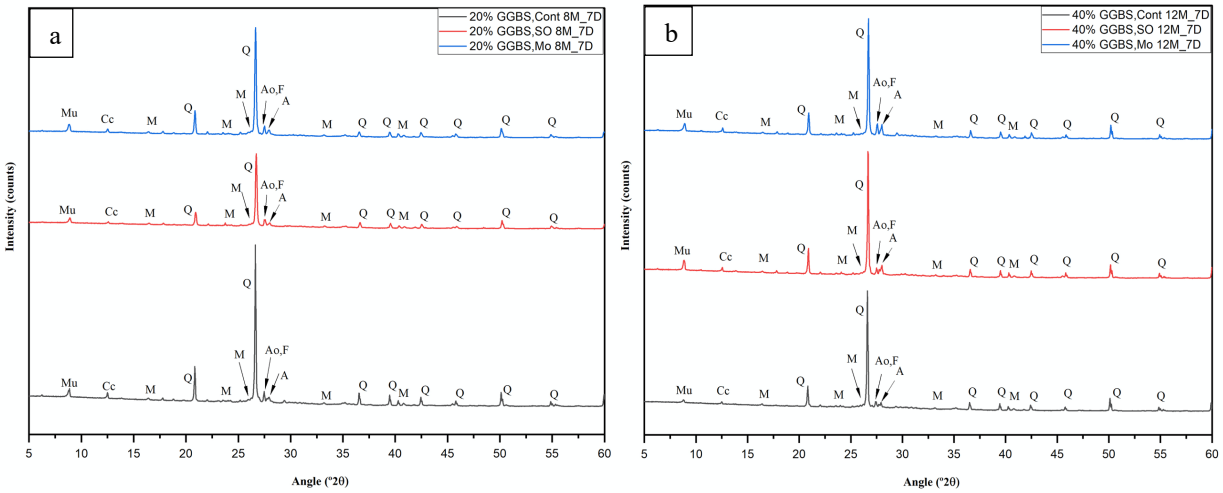

Figure 2. XRD diffractogram patterns of GPC mixes with and without inhibiting admixture at 7 days a) FGS 80/20 at 8M NaOH solution b) FGS 60/40 at 12M NaOH solution (Mu = muscovite; Cc = Clinochlore; M = mullite; Q = quartz; Ao = anorthoclase; F = Potassium Feldspar; A = albite)

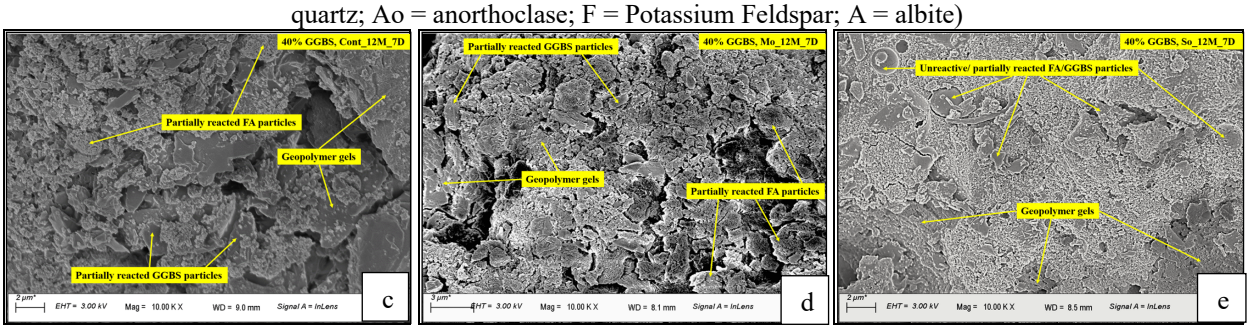

Figure 3. FESEM images (c)-(e) of control and inhibiting admixture admixed FGS 60/40 GPC mixes at 12M NaOH solution

4. Conclusions

The main findings from this research work are:

• The incorporation of inhibiting admixtures in the GPC mixes has resulted in lower consistency as compared to control GPC mixes. For all concentrations of NaOH solution and GGBS (%) content, GPC mixes admixed with inorganic inhibiting admixture i.e., sodium molybdate (Mo) exhibited higher slump value than GPC mixes admixed with organic inhibiting admixture i.e., sodium oleate (So).

• The compressive strength varied on addition of inorganic and organic inhibiting admixtures in GPC mixes. The organic inhibiting admixture (sodium oleate) led to reduction in compressive strength whereas the strength was significantly enhanced due to addition of inorganic inhibiting admixture (sodium molybdate) when compared with control GPC mixes. Increase in molarity of NaOH solution and GGBS (%) content enhanced the compressive strength development of all GPC mixes, i.e., with and without addition of inhibiting admixtures.

• The microstructure analysis showed higher peak intensity of albite (from XRD analysis) and slightly dense microstructure (from FESEM analysis) at higher molarity of NaOH solution and increasing GGBS (%) content in case of control and sodium molybdate admixed GPC mixes. This might have contributed toward higher early age strength development of control and sodium molybdate admixed GPC mixes. Further, poorly ordered microstructure is observed in case of sodium oleate admixed GPC mixes.

Acknowledgements

The authors would like to acknowledge the Central Instruments Facility (CIF) at IIT Guwahati for providing the scientific research facility required to conduct the XRD and FESEM analysis presented in this study. The authors are grateful to the Ministry of Education (MoE), Government of India (GoI), for granting Prime Minister's Research Fellowship (PMRF) to the author.

References

Duxson, P., Fernández-Jiménez, A., Provis, J.L., Lukey, G.C., Palomo, A. and Van Deventer, J.S.J. (2007) "Geopolymer technology: The current state of the art", *Journal of Materials Science*, 42(9): 2917–2933

Fouad, H.Z., Madkour, T.M. and Khedr, S.A. (2021) "Investigating the Geopolymerization Process of Aluminosilicates and Its Impact on the Compressive Strength of the Produced Geopolymers", *International Journal of Structural and Construction Engineering*, 15(12): 478–483

IS: 383-2016 (Reaffirmed 2021), Bureau of Indian Standards, New Delhi

Reddy, D. V., Edouard, J.-B. and Sobhan, K. (2013) "Durability of Fly Ash–Based Geopolymer Structural Concrete in the Marine Environment", *Journal of Materials in Civil Engineering*, 25(6): 781–787

Yazdi, M.A., Liebscher, M., Hempel, S., Yang, J. and Mechtcherine, V. (2018) "Correlation of microstructural and mechanical properties of geopolymers produced from fly ash and slag at room temperature", *Construction and Building Materials*, 191: 330–341

The 16th International Congress on the Chemistry of Cement 2023 (ICCC2023)
"Further Reduction of CO_2 -Emissions and Circularity in the Cement and Concrete Industry"
September 18–22, 2023, Bangkok, Thailand

PRELIMINARY STUDY OF CEMENTITIOUS COMPOSITE AS A SELF-HEALING MATERIAL IN CONCRETE STRUCTURES

M.E. UYANIK[1]* and H. DEMIR[2]

[1] *General Directorate of State Hydraulic Works / Technical Research and Quality Control Department, Concrete Laboratory, Ankara, Türkiye*
Email: meuyanik@dsi.gov.tr
[2] *General Directorate of State Hydraulic Works / Technical Research and Quality Control Department, Concrete Laboratory, Ankara, Türkiye*
Email: huseyindemir@dsi.gov.tr

Abstract

Cracks inevitably occur due to different causes in plane concrete and reinforced concrete structures during their service life. If some of these cracks are not intervened and repaired, the propagation of the cracks may continue by deepening and widening, negatively affecting the integrity of the concrete matrix and structural health, service life and maintenance costs. Scientific researches carried out in recent years have indicated that it is possible to produce concretes that can repair the cracks in its structure autonomously (self-healing) in the presence of water in the environment, without outside intervention. These products, which are produced by using bacteria and/or chemical-based additives called "self-healing concrete", are among the most up to current subjects on which the scientific world has researched. The primary aim of this research study is to investigate the producibility of conventional concrete in the form of self-healing concrete by using solid and liquid form of chemical additives. The main focus is to carry out performance analysis of the self-healing process in the produced concrete samples by examining the discontinuity, strength, waterproofing performances of the improvement in concrete, and to reveal the effect of the healing activity to concrete matrix and microstructure by using various tehcniques. The outcomes of the this prelimary study suggest that utilizing self-healing additives in concrete technology may be a potential option for hydraulic structures to extend service life and to reduce the inspection and maintenance costs of structure.
Keywords: *Cementitious composite, concrete, crack, hydraulic structures, self healing*

1 Introduction

Concrete is the most preferred building material for the construction of various types of civil structures because it is durable, inexpensive, easily workable, and placeable. It is a composite material produced by mixing aggregate, cement, water, mineral and chemical admixtures. It is an adaptable material, which can be readily mixed to meet different design and structural needs whilst it can easily be moulded in just about any shape. However, the most significant disadvantage of concrete is small, medium and large cracks which may be the result of excess load, dynamic displacement, aging, shrinkage, dusting, bleeding, improper design and so on. Especially, small, and medium ones may appear at an early age or throughout the service life of the structure. If some of these structural micro cracks are not repaired, they deepen and the water and harmful chemicals penetrating through these discontinuities cause the matrix to deteriorate in the concrete, causing corrosion of the elements such as the reinforcement that it may contain, especially by combining with the oxygen in the environment. Most importantly, the service lifetime of concrete may exponentially decrease when the cracks has not been detected and properly treated in time. In order to prevent this situation, scientists have been conducting research on the self-healing of concrete with cracks in its structure without any external intervention

The self-healing or repairing process in concrete can generally be grouped under two headings. These can be classified as autogenous recovery and autonomic recovery. While there is no additional additive material to the concrete mixture in the autogenous (natural healing tendency) healing mechanism, additional additives are added to the concrete mixture in autonomous healing (Roig-Flores et al (2021); Amran et al. (2022); Nair et al. (2022)).

In this study, it is targeted to investigate producibility of conventional concrete in the form of self-healing concrete by using two separate chemical additives. At the beginning of the research study, concrete samples representing C16/20 and C40/50 strength classes were produced to study ability of healing activity of

conventional concrete having low and high compressive strengths. To investigate the autogenous and autonomic healing abilities, control samples having no additives (S, control sample) and the specimens containing two separate healing additives (X and N) were produced. In other words, for each strength class three group of the samples were casted. The first group was occurred by control samples without any additives, the second and third groups were produced by using two separate healing additives which contained Portland cement, very finely treated silica sand and various chemicals which were hidden by manufacturers. The self-healing ability of the three concrete mixtures for each strength class was researched through the compressive strength, depth of water penetration under water pressure tests and crack and crystal analysis under optic microscope.

2 Experimental Program

Within the scope of the study, the self-healing performance of cracks in hardened concrete with chemical-based additives and without additives was planned to be subjected to microscopic examination in 7-day periods and recorded. For this purpose, 7 and 28 days cured hardened concrete specimens were damaged without any predefined crack number and position by applying compressive and splitting tensile forces. Widths and shapes of the cracks, on the surface of damaged samples, were measured and recorded by using microscope. After that, the damaged samples were submerged in 20 ± 2 °C water. At the end of each 7 days submersion or curing process, It was targeted to investigate the amount of healing activities of the pre-damaged samples having X and N chemicals and the cracked specimens having no chemicals.

2.1 Concrete mix design and preperation of specimens

CEM I 42.5 R type Portland cement, crushed stone sand, medium and coarse aggregates, which were between 0-5, 5-12 and 12-25 mm respectively were used. Additionally, 1.5% of the total amount of cement in the mix design, chemical additives X and N were separately used to investigate self-healing or autonomous healing property. The concrete mix amounts were presented in Table 1.

Table 1. Theoretical fresh concrete mix designs for 1 m^3

Compounds (kg)	C16/20			C40/50			
	Control Sample	Concrete X	Concrete N	Control Sample	Concrete X	Concrete N	Unit Weight (gr/m^3)
Cement	240	240	240	495	495	495	3.10
Water	205	205	205	230	230	230	1.00
Crushed Sand (0-5 mm)	853.18	849.23	849.23	722.93	714.77	714.77	2.67
Medium Aggregate (5-12 mm)	455.03	452.92	452.92	385.56	381.21	381.21	2.70
Coarse Aggregate (12-25 mm)	587.75	585.02	585.02	498.02	492.40	492.40	2.74
Chemical additive X	-	3.60	-	-	7.43	-	1.14
Chemical additive N	-	-	3.60	-	-	7.43	1.14

2.2 Compressive strength test

The fresh concrete mixtures were poured into 150 x 150 x 150 mm cubic molds. Specimens were prepared and cured according to TS EN 12390-2 standard conditions such as 20±2°C curing temperature. By depending on TS EN 12390-3 standard, compressive strengths of all designs in different ages which are 7 and 28 days were specified on 24 cubic samples. It was targeted to experience the effect of healing additives X and N on the compressive strength without concrete pre-damage.

2.3 Depth of water penetration test

In this part of the study, depth of water penetration under pressure was specified on 7 and 28 days of the hardened samples by applying TS EN 12390-8 standard. In order to assess effect of the self healing chemicals in terms of water penetration depth under 5 bar water pressure through 3 days, 24 cubic specimens having no pre-damage were prepared. After 7 and 28 days curing periods, the samples were

taken out of the water and then, water penetration test was applied after 1 day sample preparation processes which are drying at the room temperature and applying impermeable layer on the surface of specimens Eventhough TS EN 12390-8 standard included an obvious subject about the necessity of the sample age which was at least 28 days, the 7 day samples were also tested to observe possible early effects of the chemicals X and N on water penetration depth under pressure.

2.4 Crack and crystal analysis

The test samples were cured under standard curing conditions (20±2°C water). After this stage, the cured samples were left to dry for 7 days at 20±2°C and 50±5% humidity (according to customer statement). Then, cracks were formed by applying pressure and shear forces on the samples. These cracks were marked by using red and black color, numbered, and their initial state was recorded. Afterwards, these samples having cracks were completely immersed in water and removed from the water after a certain period, and the current microphotograph of the same crack was recorded again microscopically, then the samples were again immersed in water. Micro-photos obtained during the immersion process and closure of the cracks were recorded.

3 Experimental Results

Sample ID	MPa	MPa (avg)	Strength Change (%)	Sample ID	MPa	MPa (avg)	Strength Change (%)
C20S7	18.9	19.6		C20S28	23	22.7	
C20S7	20.4			C20S28	22.4		
C20N7	20.1	19.6	-0.1	C20N28	23.4	23.4	3.1
C20N7	19.2			C20N28	23.3		
C20X7	19.3	19.5	-0.7	C20X28	22.5	22.8	0.6
C20X7	19.7			C20X28	23.1		
C50S7	43.7	42.4		C50S28	51.2	50.7	
C50S7	41.1			C50S28	50.3		
C50N7	45.6	45.2	6.5	C50N28	49.9	51.1	0.7
C50N7	44.7			C50N28	52.3		
C50X7	49.1	48.9	15.4	C50X28	54.9	53.3	5.0
C50X7	48.8			C50X28	51.7		

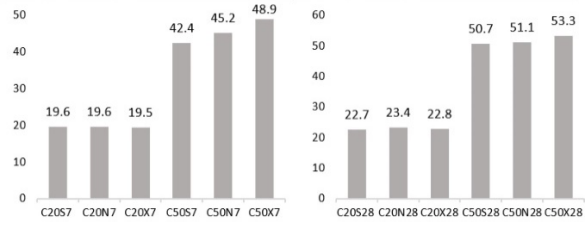

Fig.1. The compressive strength test results.

Sample ID	mm	mm (avg)	Penetration Change (%)	Sample ID	mm	mm (avg)	Penetration Change (%)
C20S7	115	125		C20S28	63	81.5	
C20S7	135			C20S28	100		
C20N7	135	135.5	8.4	C20N28	80	90	10.4
C20N7	136			C20N28	100		
C20X7	128	132	5.6	C20X28	75	75	-8.0
C20X7	136			C20X28	75		
C50S7	42	41		C50S28	15	20	
C50S7	40			C50S28	25		
C50N7	40	40	-2.4	C50N28	15	16	-20.0
C50N7	40			C50N28	17		
C50X7	25	23.5	-42.7	C50X28	13	15	-25.0
C50X7	22			C50X28	17		

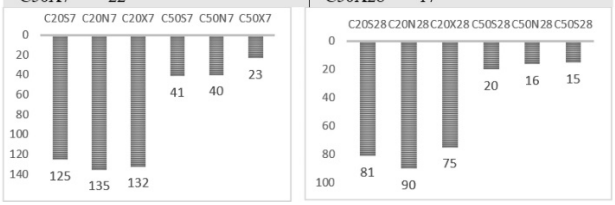

Fig. 2. The water penetration test results.

3.1 Compressive strength test

As can be seen from the figure 1, the 7 day compressive strength of C20 class with additives N and X decreased slightly compared to control samples. However, average percentages regains in compressive strength for class of C50 observed up to %15 compared to reference sample. In the 28-days specimens, recovery percentages are very close each other and slightly higher than the control samples (Fig. 1)

3.2 Depth of water penetration test

The results of the water penetration test demonstrated that, for all the C20 specimens, the permeability tended to increase compared to control samples except one 28-days sample with X additives. This behaviour shows the ability to seal for additives X for 28-days of the hardened samples in age. The permeability of C50 samples decreases for all samples is comporison with control samples. It is indicated that there is good agreement in the samples both X and N additives. Especially for the additives X, these changes have been observed up until %42 (Fig.2).

3.3 Crack and crystal analysis

Change in surface crack width has been investigated by using stereo microscope. Surface crack width and initiation of sealing material were recorded repeatedly almost over a period of two months. Crystallization

in the cracks wall function of time was observed as a function of time. The results then compared with the control samples. The results reveal that self-healing additives can seal static cracks efficiently especially when the crack widths are under 0.35 mm. Most of the healing phenomena occur in the first month and beyond that time there is no significant difference. Healing performance has been also observed for the control samples for the smaller surface cracks owing to ongoing hydration reactions. The main healing product occurred in the cracks is mostly microcrystalline phases in both cases. There is strong indication that the efficiency of the closure of cracks depend on the crack depth and its geometry. In other words, the effectiveness of the additives seems to be restricted with increasing depth.

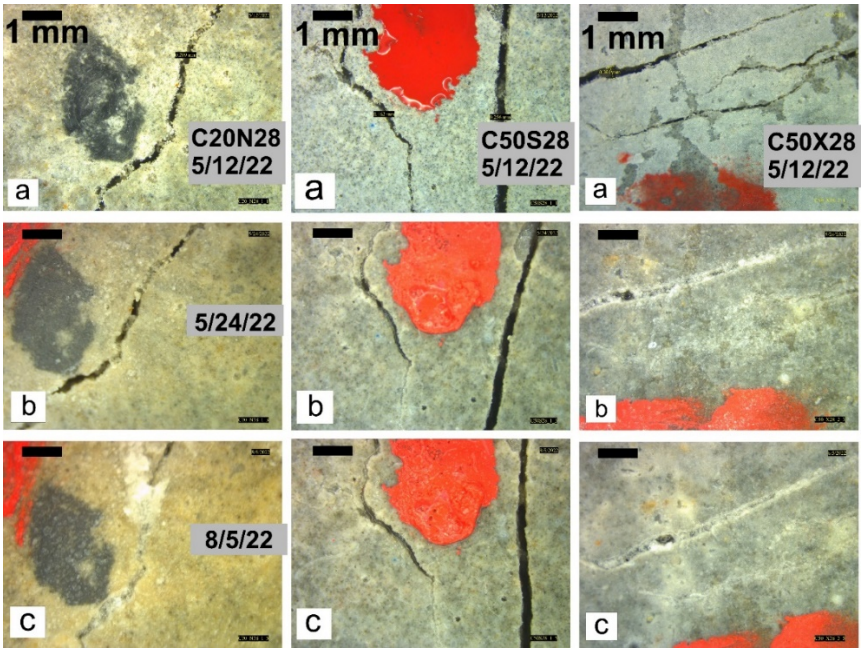

Fig. 3. Some of the microscopic images of cracked samples.

4. Conclusion

Self- healing concrete technology is still under development and has already promising results. The development of self-healing agents may be crucial for sustainable and environment-friendly concrete technology. For better understanding, the technology is going to be tested with big sample sizes and macro-scale concrete structures. Based on the preliminary data presented in this paper, the following conclusions can be drawn:

-The compressive strength of the concrete samples containing additives has slightly increased compared to the control samples.
-The water penetration tests for the C50 class with additives show significant reductions whereas C20 class happen to be more permeable compared to the control samples.
- Surface cracks up to 0.35 mm crack width in the samples including additives were closed in a short time. However, the efficiency of the additives seems to be restricted with increasing depth.
- Most of the healing phenomena occur in the first month and beyond that time there is no significant difference.

References

Roig-Flores, M., S. Formagini, and P. Serna. "Self-healing concrete-what is it good for?." *Materiales de Construcción* 71.341 (2021): e237-e237.

Amran, Mugahed, et al. "Self-healing concrete as a prospective construction material: a review." *Materials* 15.9 (2022): 3214.

Nair, Priya S., Rajesh Gupta, and Vinay Agrawal. "Self-healing concrete: a promising innovation for sustainability-a review." *Materials Today: Proceedings* (2022).

The 16th International Congress on the Chemistry of Cement 2023 (ICCC2023)
"Further Reduction of CO_2 -Emissions and Circularity in the Cement and Concrete Industry"
September 18–22, 2023, Bangkok, Thailand

Thermal stability of UHPC based on alkali-activated slag and metakaolin

A. Wetzel[1*], J. Link[1] and B. Middendorf[1]

[1] *Department of Structural Materials and Construction Chemistry, University of Kassel, Kassel, Germany*
Email: alexander.wetzel@uni-kassel.de

ABSTRACT

Ultra-high performance concrete is characterized by its high strength and high durability. This is due to the optimized packing density which is the result of the targeted use of reactive and non-reactive fines as well as a low water/binder ratio. UHPC is usually based on ordinary Portland cement (OPC), but UHPC can also be produced based on alkali-activated materials (AAM). Since the reaction products of AAMs differ from those of OPC, other properties in the solid state can also be derived. For example, some concretes based on AAMs have a higher thermal resistance compared to OPC-based concretes. For the application of aluminium casting moulds, a UHPC formulation based on alkali-activated ground granulated blast furnace slag was optimized by successively replacing the slag with metakaolin. This results in a reduction of the calcium content, which means a shift of the reaction products from C-A-S-H to N-A-S-(H) phases. Since the thermal stability of AAMs is due to the strength-forming N-A-S-(H) phases, the thermal stability could thus be increased. Furthermore, the thermal stability could be achieved by using cellulose based fibres in the range of 0.5 vol.%.

KEYWORDS: *alkali-activated materials, ultra-high performance concrete, metakaolin, thermal stability, die-casting*

1. Introduction

Ultra-high performance (UHPC) concrete is characterised by its high compressive strength and enhanced durability [1]. Due to the use of reactive fines like silica fume and a low water/binder-ratio (w/b), which in turn necessitates the use of high performance superplasticizers, these characteristics are reached. UHPC usually is based on Ordinary Portland Cement (OPC) as the mineral binder. Anyhow, based on alkali-activated materials UHPC can be achieved in terms of named characteristics as well [2, 3]. Alkali-activated materials are alumosilicatic precursors which form strength building phases after activating them with alkali solutions. Caused by the high alkalinity, superplasticizer are not effective [4], but it could be shown that by the combination of slag, silica fume and alkali-silicates a low w/b-ratio and a good workability could be achieved as well [2]. The alkalis might be provided by alkali-silicate or alkali-hydroxide solutions [5]. As alumosilicatic precursors fly ashes, ground granulated blast furnace slag (slag) and metakaolin are mainly used. In general, AAMs provide a higher thermal stability due to a lower amount of crystalline bound water [6]. The strength forming phases of AAM are C-A-S-H phases in case of Ca-rich precursors and N-A-S-(H)-phases in case of precursors poor in Calcium. The thermal stability rises with the content of N-A-S-(H)-phases as the water in brackets indicates, the water is present only in gel stadium and not in the final state of the hardened material. The used precursors of the UHPC based on AAM are slag and silica fume, and thus the Calcium content is rather high. Thus, the thermal stability should rise by substituting the slag by metakaolin. One disadvantage of AAM is the high shrinkage value. This might be decreased by this substitution with metakaolin, too [7].

UHPC fails suddenly at high temperatures due to its high packing density, as the release of the physically and chemically bound water creates an increased water vapour pressure. To increase the resistance of UHPC at higher thermal loads and to prevent spalling, the water vapour pressure inside the material must

be lowered. For this purpose, cellulose fibres can be added to the concrete mix. The fibres form a branched spatial network in the cured material and decompose under high thermal load. Scheffler et al. showed that the remaining fibre channels can dissipate the water vapour pressure to the outside without further damaging the binder matrix [8]. By combining AAM-based UHPC and regenerated cellulose fibres, heat resistance for temperatures >700°C could be achieved. Due to the very high surface quality of the fine concrete and the thermal stability of the AAM-UHPC, this material is suitable for the production of permanent moulds in the light metal casting process. However, the aim of the present investigation was to qualify first the basic AAM-mixture for higher performance in terms of thermal load in the range up to 700°C first without the use of cellulose fibres.

2. Materials and Methods

AAM-UHPC based on ground granulated blast furnace slag, silica fume and metakaolin, activated with potassium waterglass, was produced using an Eirich intensive mixer (Table 1). After mixing, the fresh material was poured into the pre-treated moulds while being vibrated at 50 Hz for two minutes. The concrete formworks were demoulded the day after production. More information about the mixing process can be found elsewhere [2, 3].

Table 1: Formulation of UHPC based on AAM, weights given for a 3 l mixture.

Component	**Ref. [kg]**	**Met1 [kg]**	**Met2 [kg]**
Potassium waterglass (molar ratio SiO_2:K_2O of 1)	1.4065	1.4065	1.4065
Ground granulated blast furnace slag	1.8900	1.6065	1.6065
Metakaolin 1		0.2835	
Metakaolin 2			0.2835
Silica fume	1.0500	1.0500	1.0500
Hydrophobic agent	0.0294	0.0294	0.0294
Quartz flour W3	0.5600	0.5600	0.5600
Quartz sand (0.125 mm/0.5 mm)	1.8910	1.8910	1.8910
Slump flow (mm)	340	315	305
Setting time (min)	116	128	140
Shrinkage after 14 days (mm/m)	2.706	1.997	1.915

Two different typed of metakaolin were used to substitute parts of the granulated blast furnace slag. The spread flow was determined and test specimens for compressive strength tests were carried out. Test specimen measuring 50 mm x 50 mm x 50 mm were produced for this purpose. After demoulding, these test specimen were stored in standard climate conditions (20 °C, 65% rel. hum.). On additional samples the porosity was measured using a mercury intrusion porosimeter. The shrinkage was measured directly after demoulding on prisms (40 mm x 40 mm x 160 mm) with a measuring gauge at least for 14 days. For the thermal load, the test specimens were heated up to a temperature of 700°C at the age of 7 days. Due to the aforementioned application of aluminium casting this maximum temperature was chosen. The heating rate was 5 K/min, the maximum temperature of 700°C was maintained for 30 min. After cool-down the specimen were also tested for compressive strength.

3. Results and Discussion

The substitution of the granulated blast furnace slag by metakaolin could be carried out up to a value of 25 wt.-%. Higher degrees of substitution led to a restriction of the workability. The spread flow in the

reference mixture amounted from 340 mm to 315 mm and successively decreased to 287 mm in the case of a 25 wt.-% substitution.

In general, a clear effect was observed with regard to the reduction of the shrinkage (Fig. 1). Although the base mixture generally shows a relatively high shrinkage compared to OPC-based UHPC, the shrinkage value could be reduced by approx. 35 %. Significant improvements were also observed at a lower substitution level of 15 % (Fig. 1). The porosity measured by mercury intrusion porosimetry showed a low porosity in the measured range of 0.003 µm to 100 µm of about 5 %. The capillary porosity (0.03-10 µm) has values of about 2.5 % and did not change much by substitution of slag by metakaolin (Fig. 2), which was different from prior investigations [2], where this porosity could be reduced.

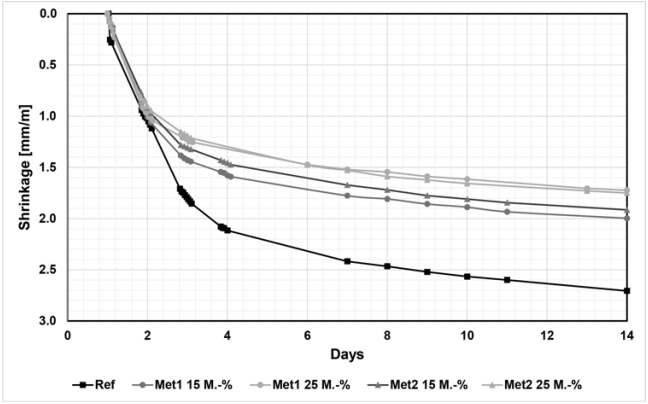

Figure 1: Shrinkage of UHPC based on slag and metakaolin.

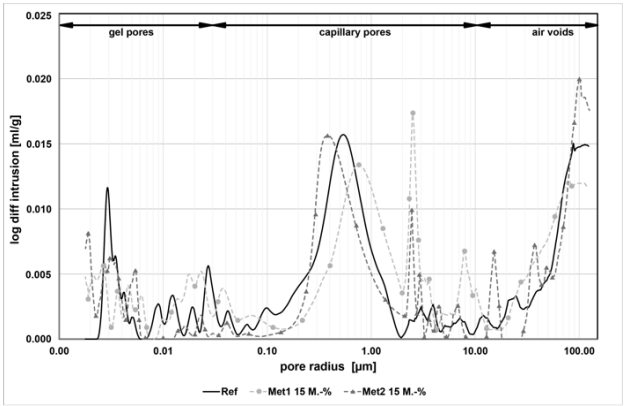

Figure 2: Porosity of AAM-UHPC with certain amounts of metakaolin in substitution for slag.

The compressive strength after 7 days is in the order of magnitude of the reference without metakaolin. After thermal loading, there was no spalling as usually occurs with OPC-UHPC of similar compressive strength and comparable porosities at temperatures above 250°C [8]. Nevertheless, the compressive strength was clearly reduced after thermal load. Anyhow, comparing the residual compressive strength of the reference with the samples in which 15 % of the slag was substituted by metakaolin, a clear increase is obvious (Fig. 3). This could be confirmed using different types of metakaolin, which results are not shown here. Using an AAM-UHPC without any metakaolin but an amount of 0.5 vol.% of organic fibres resulted in an increase of the residual compressive strength after thermal load compared to the reference, too (Fig 3). On prior investigations using OPC-UHPC these cellulose fibres exceeded the performance of polypropylene fibres, which are already used as standard in concretes to increase the thermal resistance [8].

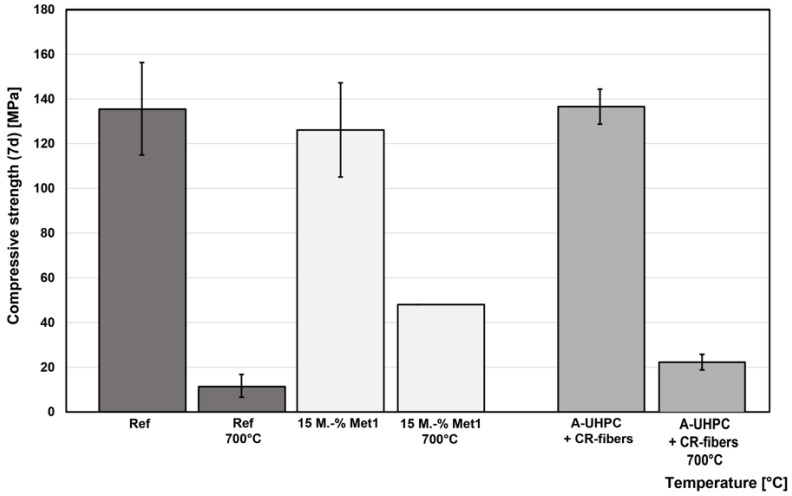

Figure 3: Compressive strength of cubes (50 mm x 50 mm x 50 mm) measured after storage at room temperature for 7 days and after thermal loading at 700°C.

The application of AAM-UHPC as a casting mould for aluminium casting could already been proven. In several tests, it was possible to realise multiple casts without damage or aluminium penetrating the concrete formwork. Fig. 4 shows a concrete formwork before (a) and after (b) casting aluminium 5 times.

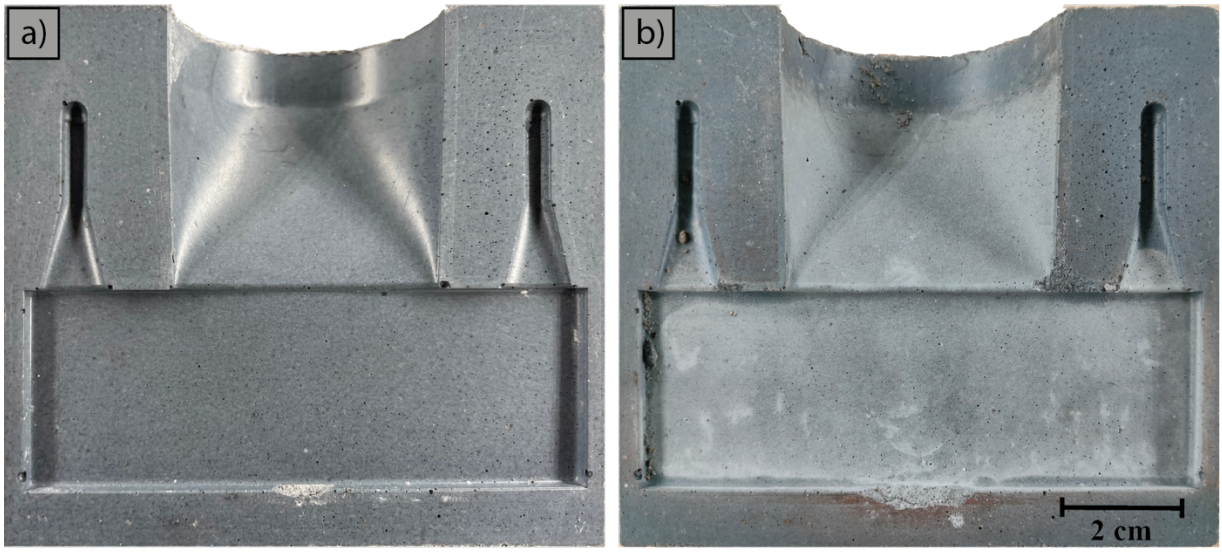

Figure 4: One casting form made of AAM-UHPC before (a) and after (b) aluminium casting.

4. Conclusions

Metakaolin increases the viscosity of the mixture and thus reduces the workability. Anyhow, a substitution of slag with metakaolin up to 25 wt.-% was possible without changing other parts of the formulation, for instance the w/b-ratio. The use of metakaolin leads to a delay in solidification, which is a positive side effect due to the relatively short processing time of these systems. By adding metakaolin, the shrinkage could be reduced by up to 35 %. The compressive strength remained in the same order of magnitude, especially for mixtures up to 15 wt.-%. With higher substitutions, there was a reduction, which is presumably due to lower compaction as a result of poorer workability. Anyhow, it could be shown that the substitution of slag with metakaolin lead to an increase of the residual compressive strength after thermal load at 700°C. This was the case as well for the use of cellulose fibres in the mixture without metakaolin. It is supposed that the combination will lead to an additional improvement, which need to be proved especially for the application of aluminium casting for which the mixtures of AAM-UHPC with cellulose fibres already showed a high stability during aluminium casting.

References

[1] Fehling, E., Schmidt, M., Walraven, J., Leutbecher, T., Fröhlich, S., 2014. Ultra-High Performance Concrete UHPC: Fundamentals, Design, Examples. Ernst, Wilhelm & Sohn

[2] Wetzel, A.; Middendorf, B. (2019): Influence of silica fume on properties of fresh and hardened ultra-high performance concrete based on alkali-activated slag. Cem. Concr. Comp. 100, 53-59.

[3] Wetzel, A.; Göbel, D.; Schleiting, M.; Wiemer, N.; Middendorf, B. (2022): Bonding Behaviour of Steel Fibres in UHPFRC Based on Alkali-Activated Slag. Materials 15, 1930.

[4] Wetzel, A., Link, J., Middendorf, B., 2022. Adsorption of PCE in alkali-activated materials analysed by fluorescence microscopy. Journal of microscopy 286, 79–84.

[5] J.L. Provis, J.S.J. van Deventer, " Alkali Activated Materials: State-of-the-Art Report", RILEM TC 224-AAM (2014)

[6] Bernal, S.A., Rodriguez, E.D., de Gutierrez, R.M., Gordillo, M., Provis, J.L. (2011). J Mater Sci 46

[7] Li, Z., Nedeljković, M., Chen, B., Ye, G, 2019, Mitigating the autogenous shrinkage of alkali-activated slag by metakaolin, Cement and Concrete Research (122), 30-41.

[8] Scheffler, B., Wetzel, A., Sälzer, P., Middendorf, B., 2019. Thermische Stabilität von UHPC. Beton- und Stahlbetonbau. 114, 674–82.

The 16th International Congress on the Chemistry of Cement 2023 (ICCC2023)
"Further Reduction of CO_2 -Emissions and Circularity in the Cement and Concrete Industry"
September 18–22, 2023, Bangkok, Thailand

Sprayable Glass Bubble Insulation for Sustainable and Energy Efficient Building Insulation

F. Scharfe[1*], T. Gerdes[2], A. Rosin[2], S. Zelder[2]

[1] *Calmix Company Ltd., Bangkok, Thailand*
Email: friedbert.scharfe@googlemail.com
[2] *University of Bayreuth, Keylab Glass Technology, Bayreuth, Germany*
Email: thorsten.gerdes@uni-bayreuth.de

ABSTRACT

An internal and external insulation based on micrometer-sized hollow glass beads as an alternative to existing thermal insulation composite systems is investigated, characterized by a special combination of open and closed pores. The so-called Ecosphere system is a sprayable insulation material with a volume fraction of approximately 90% micro hollow glass beads (glass microspheres) and 10% calciumsulfoaluminate (CSA) cement as a binder. Due to their hollow structure, glass beads have a very low thermal conductivity. In addition to the low thermal conductivity, the manufacturing process creates near-vacuum conditions inside these bubbles. This results in a very low overall thermal conductivity for the hollow glass beads. In addition, CSA cement is fast setting due to its ettringite formation, which helps the plaster to adhere to the wall without the need for additional support structures. In addition to the fast setting time, ettringite hydration forms needle-like structures that connect the glass bubbles intrinsically, thus increasing the mechanical strength of the plaster.

KEYWORDS: *building insulation, sprayable plaster, hollow glass beads, cement*

1. Introduction

In 2018, 117 Mt of CO_2 emissions in Germany came from the building sector. This corresponds to 14% of total greenhouse gas emissions. These emissions are mainly caused by the use of fossil fuels for heating. CO_2 emissions can therefore be reduced by improving building insulation to reduce heat losses through the building envelope (Dombaycı et al. 2006). As new buildings are generally well insulated, the impact of energy-efficient renovation of old buildings is even greater (Paiho et al. 2015). Apart from the general need to improve the insulation of old buildings, the rate of renovation needs to be accelerated to meet the European Union's 2030 targets. The current renovation rate is around 1% of the building stock per year, but it is estimated that this rate needs to be at least doubled in the near future (European Commission 2020).
Building insulation materials range from purely mineral insulation such as rock wool, to polymer foams such as expanded polystyrene (EPS) or extruded polystyrene (XPS) foam, to organic materials such as wood or straw based materials. EPS panels have a market share of around 80% in Europe (Heller and Flamme 2020) due to their low thermal conductivity of 0.035 to 0.049 $Wm^{-1}K^{-1}$ (Lakatos 2014), low density of 30 $kg \cdot m^{-3}$ (Ellouze 2020) and low cost. EPS panels are applied directly to the wall, which presents two challenges. Firstly, the flat panels have to be manually adjusted and fixed to the facade, which is labour- and time-intensive. Secondly, the EPS panels must cover the entire facade to avoid thermal bridging, which is problematic for some older buildings as their facades are often uneven, decorated and even listed. As EPS panels cover and hide any individual facade design, there is a growing interest in form following materials and new application techniques for facade renovation. And, due to its purely mineral composition, the insulation plaster is inherently fire resistant without addition of flame retardants.

2. Methods and Materials

The application tests for the sprayable plaster were performed with formulations containing hollow glass beads, cement binder, few additives, and water. These compounds were mixed in order to achieve a flowable plaster.

2.1 Materials

The hollow glass beads are thin-walled (0.3-2.0 µm), spherical but hollow glass particles with a range of diameters from 30 µm to 200 µm. The selected hollow glass beads of type K15 (3M, Germany) have a medium diameter of 65 µm, a compressive strength of 1.7 MPa, a thermal conductivity of 0,047 $W \cdot m^{-1}K^{-1}$, and a bulk density of 125 kg/m^3. The CSA cement (Buzzi Unicem, Italy) is added as binder to the dry plaster composition. The CO_2 footprint during production of CSA cement is reduced by about 50% compared to Portland cement (Hanein 2018).
The necessary water/cement ratio was determined by visual inspection. As soon as the mixture stopped absorbing water, excess water showed up on the surface, which is known as “bleeding”. The necessary water-cement ratio is in the range 1.5 to 2. The prepared mixtures were finally stirred for at least 1 min according to DIN EN 196-1.

2.2 Characterization

Wet specimens for testing were stored inside a sealed cabinet at 99% relative humidity and 20 °C for 14 days. The density of the raw materials was determined using a helium pycnometer (AccuPyc II 1340, Micromeritics, USA). The chamber was flushed 10 times by helium gas before measurement. The filling pressure was set to 134.45 kPa. The measurement started at equilibrium.
Mechanical testing was performed using a universal testing machine (Inspect 5 Table Blue, Hegewald & Peschke, Germany) according to DIN EN 196-1. The three-point bending tests were performed at a traverse speed of 2 mm/min. Termination was reached when the force decreased by 80%.
Thermal conductivity was measured using a surface probe (Isomet 2114, Applied Precision, Slovakia). Each specimen was dried in a drying chamber at 40 °C for 5 days before measurement. The measurement was conducted in an air-conditioned laboratory at 20 °C.

2.3 Application technique

The plaster insulation was applied with a state-of-art plastering machine from a bag or silo. This involved working "fresh in fresh" in several layers, i.e. in directly successive work steps up to the desired layer thickness without idle times. A commercially available insulation plaster equipment was used without adaptation.
In addition to workability, a high durability of the sprayable plaster system had to be ensured. For this purpose, test conditions and guidelines for testing the stability of the plaster and the insulating system against solvent attack as well as the freeze-thaw resistance were developed, based on the AKR performance and CIF tests. The conditions were chosen to be much more stringent than would be expected in the real system and include for example the stability of the hollow glass spheres by storage at 60 °C and pH 13.5 for 90 days. The stability of the insulating plaster was tested by storing it for several days in a drying oven at 40 °C, with one side in constant contact with downstream deionized water and the opposite side left free to evaporate, allowing dissolved constituents to crystallize on the free surface. Freeze-thaw resistance was tested by storing test specimens in water with subsequent temperature cycling from -20 to +20 °C.

3. Results and Discussion

The microstructure and the adhesion between hollow glass beads and CSA cement were investigated with SEM. Figure 1a shows needle-like structures surrounding the hollow glass beads. These crystals are characteristic for ettringite formation. Ettringite provided solid bonds between the cement phase and

hollow glass beads. The ettringite matrix contributed positively to the final porosity (seen Figure 1b). The thermal conductivity of the sprayed plaster-based insulation was 0.04 $W \cdot m^{-1}K^{-1}$.

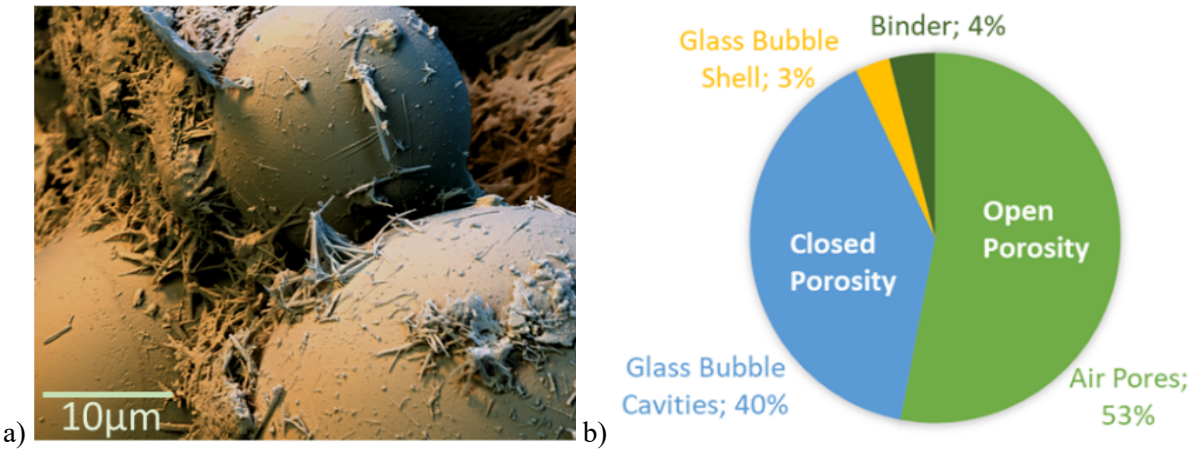

Figure 1. Sprayed Ecosphere insulation: a) SEM image of ettringite crystals forming solid bridges between the hollow glass beads, b) volume shares of the sprayed insulating plaster - 93% of the material's volume are spent on porosity, while only 7% are occupied by solids (either cement or glass).

By modifying the mineral binder system, it was possible to achieve high volume stability, good drying behavior and excellent workability. The spray application of the insulating plaster was done "fresh in fresh" in several layers as shown in Figure 2a. The layers were applied in directly successive work steps up to a layer thickness of 150 mm. One ton of dry mortar produced 7,500 liters of sprayable insulation. After hydration, the plaster has a compressive strength of about 0.55 MPa. In order to increase the protection against impacts like hail, a glass-fiber based reinforcing layer was applied (see Figure 2b). Finally, a surface cement-based plaster and a paint were applied for protective and decorative reasons.

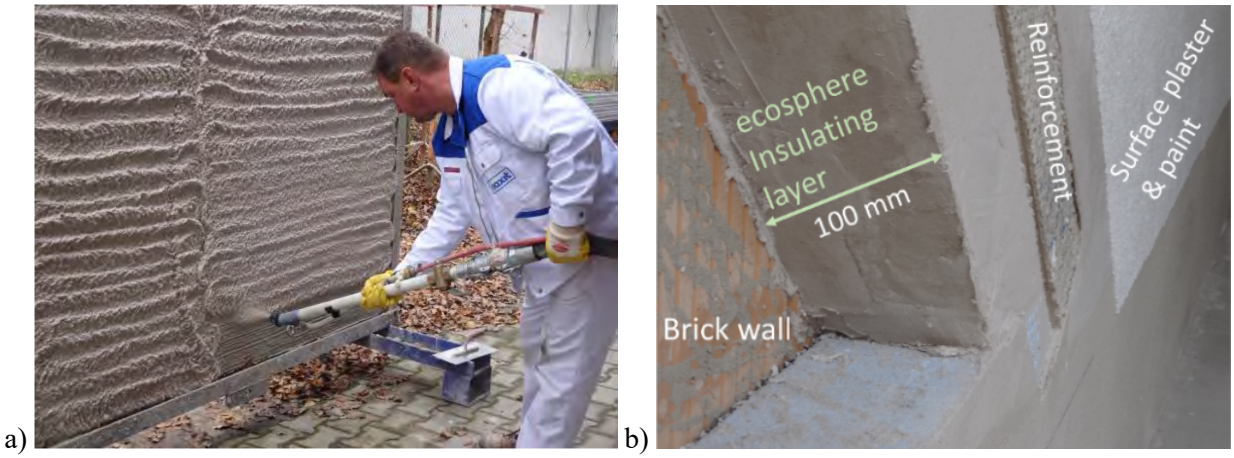

Figure 2. The insulating Ecosphere plaster: a) application of the plaster by spaying to a brick wall, b) cross-section after spraying with addition of a fibre-based reinforcement and surface plaster layer.

Installation errors, as can occur with panel systems, were virtually eliminated thanks to the sprayability of the plaster. The performed stability tests proved that the final plaster formulation exhibited high durability against dissolving attacks in solvents as well as very good freeze-thaw resistance as indicated in Figure 3.

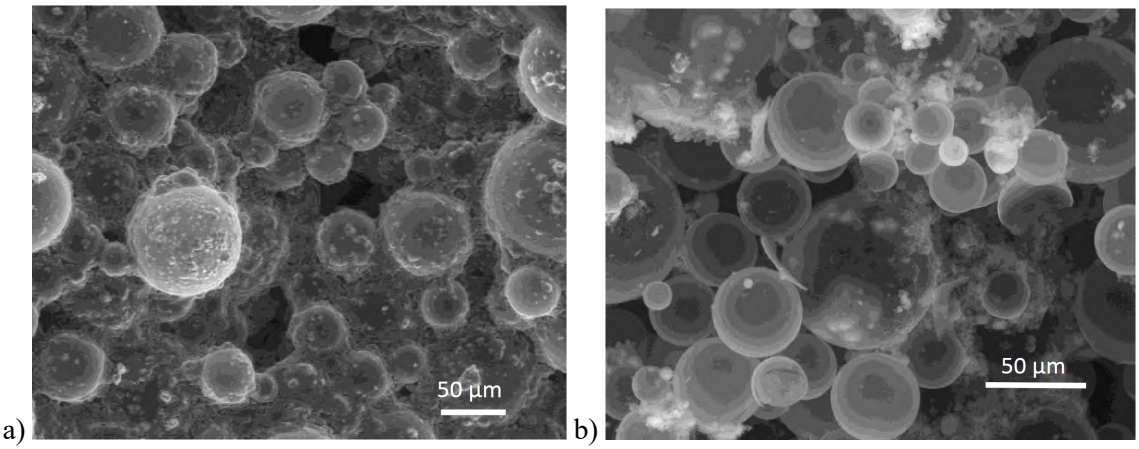

Figure 3. Results of stability tests: a) intact hollow glass beads after solvent attack, b) intact hollow glass beads after frost attack, each test performed on a plaster with 85 vol.% glass beads.

4. Conclusions

The application technology of the developed sprayable plaster made of CSA cement and micro hollow glass beads is crucial to the excellent performance of the insulation. By improving the existing plaster spraying technologies, it is possible to apply this composite material to facades as thick as 150 mm without damaging the delicate glass bubbles. The compressed air spraying process introduces additional porosity into the insulation, further reducing thermal conductivity. Due to the high porosity of 93%, the glass bubble insulation has a density of only 125 kg/m³ and a thermal conductivity of 0.04 $W \cdot m^{-1}K^{-1}$. After hydration, the plaster has a compressive strength of about 0.55 MPa. This is sufficient to form a self-supporting layer of plaster, but not sufficient to withstand environmental influences such as hail. Therefore, the insulation layer is reinforced with glass fibre fabric and a layer of cement. This provides sufficient mechanical strength without compromising the insulation properties. Overall, the properties of the purely mineral insulation plaster are comparable to the insulation properties of EPS boards, making this material a suitable purely mineral alternative. Furthermore, it is much easier to demolish and recycle it. After crushing and moderate heat treatment, the plaster can be reused as aggregate for hydraulically setting building materials.

Acknowledgements

The authors gratefully acknowledge the German Federal Ministry of Education and Research for funding (funding references 13N13186 to 13N13189).

References

Dombaycı, Ö.A., Gölcü, M. and Pancar, Y. (2006) "Optimization of insulation thickness for external walls using different energy-sources", *Journal of Applied Energy*, 83(9): 921-928, doi:10.1016/j.apenergy.2005.10.006

Paiho, S., Seppä, I.P. and Jimenez, C. (2015) "An energetic analysis of a multifunctional façade system for energy efficient retrofitting of residential buildings in cold climates of Finland and Russia", *Sustainable Cities and Society*, 15: 75-85, doi:10.1016/j.scs.2014.12.005

European Commission (2020) *In focus: Energy efficiency in buildings*, available online: https://ec.europa.eu/info/news/focus-energy-efficiency-buildings-2020-02-17_en (accessed on March 17th, 2023)

Heller, N. and Flamme, S. (2020) "Waste management of deconstructed external thermal insulation composite systems with expanded polystyrene in the future", *Waste Management Resources*, 38(4): 400-407

Lakatos, A. (2014) "Comparison of the Thermal Properties of Different Insulating Materials", *Advanced Materials Research*, 899: 381-386, doi:10.4028/www.scientific.net/AMR.899.381

Ellouze, A., Jesson, D. and Ben Cheikh, R. (2020) "The effect of thermal treatment on the properties of expanded polystyrene", *Polymer Engineering & Science*, 60(11): 2710-2723, doi:10.1002/pen.25502

Hanein, T., Galvez-Martos, J.-L. and Bannerman, M.N. (2018) "Carbon footprint of calcium sulfoaluminate clinker production", *Journal of Cleaner Production*, 172: 2287-2287, doi:10.1016/j.jclepro.2017.11.183

The 16th International Congress on the Chemistry of Cement 2023 (ICCC2023)
"Further Reduction of CO_2 -Emissions and Circularity in the Cement and Concrete Industry"
September 18–22, 2023, Bangkok, Thailand

Preparing energy conservation self-levelling mortar via fly ash cenospheres/paraffin using in floor radiant heating

Fei Wang [1], Wukui Zheng [1], Yujin Gou[1], Zhigang Qiao[1], Yongle Qi[1], Hui Li [1,2,*]

[1] *College of Materials Science and Engineering, Xi'an University of Architecture and Technology, Xi'an, Shaanxi, China, 710055*
[2] *Shaanxi Ecological Cement & Concrete Engineering Technology Research Center, Xi'an, Shaanxi, China, 710055*
* *Correspondence: sunshine_lihui@126.com*

ABSTRACT

Gypsum-based self-levelling mortar used for indoor backfilling and levelling has been widely studied. This paper investigated the feasibility of preparing self-levelling energy storage mortar by incorporating fly ash cenospheres/paraffin (FACP) into gypsum-based materials. A comprehensive experiment was designed to assess the effects of FACP on the flowability, mechanical and thermal properties of gypsum based self-leveling mortar. Result shows that the particle size, pre-treated method of FACP and sand replacement ratio affects many properties. Compared with untreated FACP and treated with silica fume, FACP treated with hardened cement could decrease the leakage of paraffin and increase the flowability of the mortar. A radiant floor system proved that the mortar with FACP has better indoor comfort. This study shows that FACP has good application potential in self-levelling mortar and could improve the thermal performance of self-levelling mortar.

KEYWORDS: *Gypsum, self-levelling mortar, fly ash cenospheres, phase change materials, floor radiant heating*

1. Introduction

With the development of economy and the improvement of people's living standard in our country, people require more and more comfort of life, which will inevitably increase the consumption of energy. Data show that building energy consumption has accounted for more than one third of the world's total energy consumption, in which nearly half of the energy consumption is used for space heating and cooling control. In the heating system, radiant floor heating system (RFHS) has the advantages of large heat exchange area, high space utilization efficiency, uniform indoor temperature distribution, etc., and has been widely used at home and abroad. However, RFHS contribute negatively to global energy consumption and greenhouse gas emissions, it is necessary to develop new energy-saving technologies to reduce the energy consumption caused by controlling the variation of cold and heat in space. Gypsum is a kind of green and environment-friendly cementitious material, which has excellent performance of ecology, low carbon, environmental protection and health. Gypsum-based self-leveling mortar made of gypsum is used as the ground leveling layer. After pouring on the ground, the ground will not produce cracks, drum and other phenomena. Gypsum-based self-leveling mortar has the social and economic benefits of energy saving and emission reduction, and can promote the comprehensive utilization of industrial solid waste. It is an environment-friendly green leveling mortar for the ground. In addition, phase change materials (PCM) are considered as potential candidates for RFHS because of their high enthalpy and relatively constant temperature during phase change as an effective heat storage technique. A growing literature has investigated RFHS integrated with PCMs in dry and wet construction. However, few scholars use gypsum self-leveling material and phase change material together for RFHS, so as to simplify the construction process and increase the heat storage capacity of the RFHS.

In this paper, the feasibility of preparing self-levelling energy storage mortar by incorporating fly ash cenospheres/paraffin (FACP) into gypsum-based materials. A comprehensive experiment was designed to assess the effects of FACP on the flowability, microstructure, mechanical and thermal properties of gypsum based self-leveling mortar. This provides a new way for building energy saving and is conducive to promoting the development and application of self-leveling materials.

2. Materials and Method

The main materials used in the experiment are gypsum, P.O. 42.5 cement, mineral power, fine aggregate. Gypsum comes from Jinjiu Co., Ltd., P.O. 42.5 cement is produced by Liquan Conch cement Co., Ltd. (China), mineral powder is provided by Delong Resources Comprehensive Utilization Co., Ltd., fine aggregate is consisted of local river sand and fly ash compounded with phase change materials (FACP). In addition, water-reducer is polycarboxylic water-reducer, when the temperature is 20 °C, the concentration is 2.0 wt.%. The viscosity of HPMC is 20000 mpa·s and sodium citrate are added as a retarder. The adsorbed PCM is paraffin, the phase transition temperature is 28.0 °C and the phase transition enthalpy is 228.3 J/g. The PCM is introduced into the cavity of fly ash cenospheres through vacuum adsorption method.
According to the Technical standard for Gypsum based self-leveling compound for floor (JC/T 1023-2021), the mix design is shown in Table 1. The proportion COPCM are added to replace the same volume of river sand, and the replacement rate is 25%, 50%, 75%, and 100%.

Table 1 Mix design of gypsum self-levelling

Sample	Gelling materials			Fine aggregate		Water reducer	HPMC	sodium citrate	W/C
	Gypsum	Cement	Mineral powder	River sand	COPCM				
A1-A5	80 wt.%	10 wt.%	10 wt.%	0-100 vol.%	100-0 vol.%	0.4%	0.08%	0.17%	0.38

Note: The mass ratio of Gelling materials and Fine aggregate is 6:4; The River sand and COPCM in fine aggregate are equal volume substitutions; The amount of admixture is in proportion to the Gelling materials.

3. Results and discussion

3.1 Effect of FAC particle size and pre-treated method

Three types of fly ashcenospheres are investigated in this study. The average particle densities, particle sizes, wall thickness and crush strength are shown in Table 2. FAC 1 and FAC 2 using adsorption can be selected through gravity separation method in water. FAC 3 has a glass-crystalline film covering surface which prevent the PCMs into inner cavity. It is necessary to pre-treat the surface using acid. Three different inorganic materials silica fume, CAS and 52.5 PO. Cement are chosen as the coating materials. In order to reduce the negative impact on thermal properties caused by coating material, the mass ratio of coating materials and FAC is 1:4. After vacuum adsorption, the thermal properties of the FAC/Paraffin are tested, and the results are shown in Fig. 1. All types of FAC/Paraffin have the same crystallization peak temperature at around 29 °C, however, the latent heat of FAC/Paraffin decreases with the decrease of particle size, as shown in Table 3. This is mainly due to the different pre-treated method. Although the use of acid etch fly ash can open up the passage of PCMs into the inner cavity, it also causes damage to the FAC and is more likely to leak in the cleaning.

Table 2 Properties of fly ash cenospheres used in this research

Sample	Materials	Particle size (μm)			Density (g/cm^3)	Crush strength (MPa)
		D_{10}	D_{50}	D_{90}		
FAC 1	Fly ash cenospheres	2.448	17.912	64.781	1.2	1.0-4.2
FAC 2		60.476	110.504	190.658	0.94	1.0-4.2
FAC 3		111.986	418.272	643.388	0.77	1.0-4.2

Table 3 DSC thermograms of the produced FAC/Paraffin with different particle sizes and coating materials

Sample	Peak temperature (°C)	Latent heat (J/g)			Density (g/cm^3)		
		Silica fume	CAS	52.5 Cement	Silica fume	CAS	52.5 Cement
FACP 1	29.2	64.86	67.63	66.21	1.92	1.87	1.98
FACP 2	29.1	84.57	80.22	83.54	1.54	1.49	1.47
FACP 3	29.4	91.39	90.28	94.15	1.35	1.43	1.46

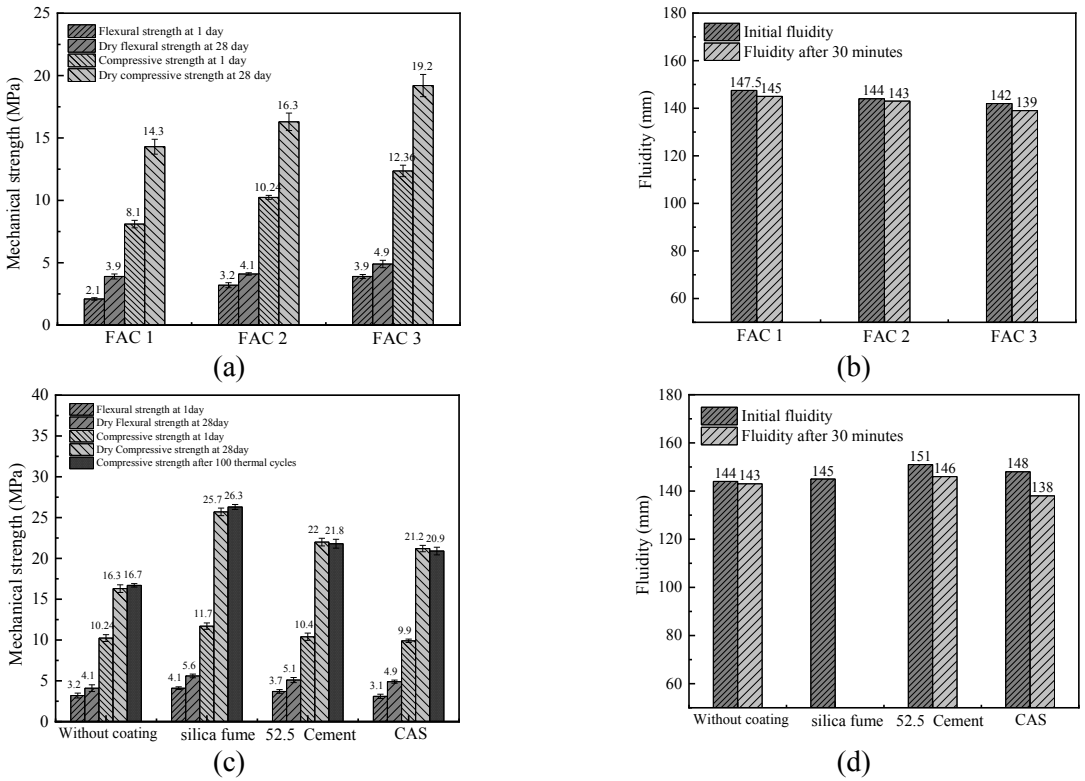

Fig. 2. Mechanical strength and Fluidity of specimens

3.1.1 Compressive strength and flowability

To examine the mechanical and fluidity performance of FAC in self-leveling mortar, the compressive and flexural strength and fluidity of mortar with different particle sizes and coating materials are shown in Figure 2. Figure 2 (a) and (b) show the influence of particle size on the properties of mortar, the volume fractions of river sand and FACP is 1:1. The results indicate that the mechanical strength of mortar increases gradually with the decrease of fly ash particle size. However, the fluidity presents the opposite development law, with the decrease of particle size, the fluidity also decreases. This is mainly because acid etching affects the sphericity of FAC, and small particles are more likely to gather which increase water absorption. Combination of strength, fluidity and thermal property as well as possible economic and environmental impacts, FAC 2 is considered to be a suitable particle size for making self-leveling mortar. Previous study has shown that gypsum specimens prepared by unencapsulated FAC could cause leakage of PCM. It is necessary to pre-treat. In this study, three kinds of inorganic materials (silica fume, 52.5 cement and CAS) are used to encapsulate FACP. As shown in Fig. 2 (c) and (d), inorganic coating could increase the mechanical performances of self-levelling mortar, this is mainly due to the improvement of the interface and increased shell strength. As an inorganic material with pozzolanic activity, silica fume will react in alkaline environment to improve the contact interface between FAC and mortar. 52.5 Cement and CAS provide a higher strength shell for FAC which could improve the mechanical performances of mortar. For fluidity of specimens, silica fume coating requires a large amount of water in the early stage, and loses fluidity after standing for 30 minutes, which does not meet the requirements of the specification. 52.5 Cement and CAS coatings can increase the fluidity of mortar, it is mainly due to the inorganic shell has been sufficiently hydrated with low water absorption. And when the shell is coated with pelleting machines, the smoothness of the fly ash shell is also increased. However, combined with mechanical properties, 52.5 hardened shell is the most suitable shell material.

3.2 Simulation analysis of temperature regulation performance

By pouring gypsum-based self-levelling mortar into a mold containing S-shaped copper tube, a heat-regulated composite gypsum base plate is obtained under natural curing condition, the process flow chart is shown in Figure 3 (a). The self-levelling mortar were made into 10 mm phase change plates, and then

they were installed in the electric floor heating system of the experimental room. The thermal performance of the experimental room was monitored under the condition of simulating the winter climate. As for the indoor temperature, it can be seen from Figure 3 (b) that when plate without PCMs is installed in the electric floor heating system, the indoor temperature reaches the maximum value of 17.1℃ at 120 min. When the phase change plate was installed, the maximum indoor temperature reached 17.6℃ in 213 min. Indoor temperatures spend significantly longer in the comfort range (Δt), resulting in higher thermal comfort. The results show that self-leveling energy storage mortar could improve building thermal comfort and demonstrate enormous energy-saving potential.

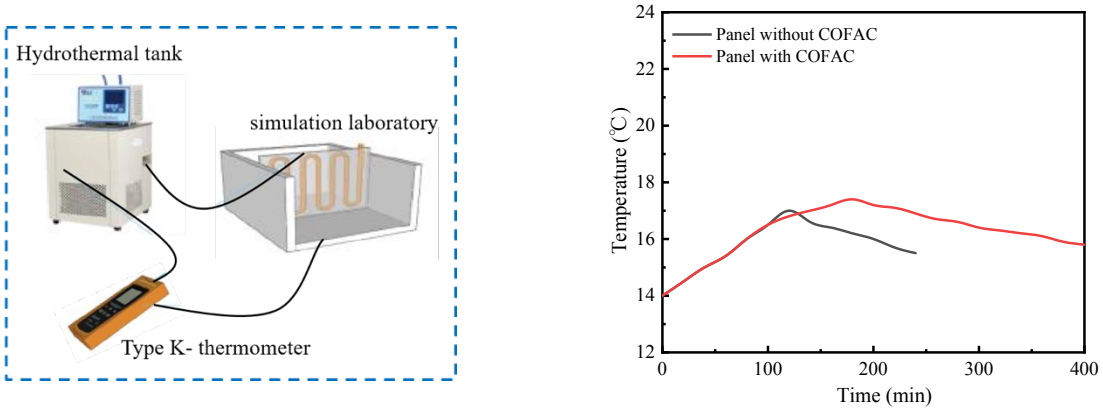

(a) (b)

Fig. 3. Instrument for testing heat transfer performance (a); Variation trend of the center temperature in the laboratory with time.

4. Conclusions

This paper investigated the feasibility of preparing self-levelling energy storage mortar by incorporating fly ash cenospheres/paraffin (FACP) into gypsum-based materials. The following conclusions were drawn from this study:

1. Combination of strength, fluidity and thermal property as well as possible economic and environmental impacts, FAC 2 is considered to be a suitable particle size for making self-leveling mortar.
2. 52.5 Cement coating can increase the mechanical strength and fluidity of mortar which is the most suitable shell material.
3. Self-leveling energy storage mortar can prolong the indoor temperature within the comfortable range and improve the thermal comfort.

In short, high performance, low cost FAC mixed phase change materials will be widely used in electric floor heating. In the application prospect, the research results provide a reference basis for using electricity to solve the problem of winter heating in hot summer and cold winter areas.

References

Li M, Wu Z, Tan J. Heat storage properties of the cement mortar incorporated with composite phase change material[J]. *Applied Energy*, 2013, 103(MAR.):393-399.

Liu Z, Hu D, Lv H, et al. Mixed mill-heating fabrication and thermal energy storage of diatomite/paraffin phase change composite incorporated gypsum-based materials[J]. *Applied Thermal Engineering*, 2017, 118(Complete):703-713.

Wan, K.T. and Leung, C.K.Y. (2007a) "Fiber Optic Sensor for the Monitoring of Mixed-Mode Cracks in Structures", *Sensors and Actuators*, 135(2): 370-380

Lachheb M, Karkri M, Nasrallah S B. Development and thermal characterization of an innovative gypsum-based composite incorporating phase change material as building energy storage system[J]. *Energy & Buildings*, 2015, 107(12):93-102.

The 16th International Congress on the Chemistry of Cement 2023 (ICCC2023)
"Further Reduction of CO_2 -Emissions and Circularity in the Cement and Concrete Industry"
September 18–22, 2023, Bangkok, Thailand

Experimental study on ion penetration in concrete under the condition of competitive adsorption

K. Yamada[1*], K. Himori[2], S. Tomita[3], H. Aihara[4], K. Shibuya[3] Y. Tojo[2], G. Igarashi[5], and I. Maruyama[6]

[1] *National Institute for Environmental Studies/Taiheiyo Cement, Miharu, Japan*
yamada.kazuo@nies.go.jp
[2] *Hokkaido University*
[3] *Taiheiyo Consultant, Co., Ltd, Sakura, Japan*
[4] *Japan Atomic Energy Agency, Tokai, Japan*
[5] *Nagoya University, Nagoya, Japan*
[6] *The University of Tokyo, Tokyo, Japan*
i.maruyama@bme.arch.t.u-tokyo.ac.jp

ABSTRACT

Prediction of Cs-137 and Sr-90 penetration is an important issue in radioactive waste disposal. The effects of concrete condition and solution composition on Cs and Sr penetration was investigated through experiments reproducing the contamination history of the underground turbine pit at TEPCO's Fukushima Daiichi Nuclear Power Station (1F), where the accident occurred. OPC mortar made of crushed river gravel, which irreversibly adsorbs Cs, used at 1F was used for the penetration experiment. Under water-saturated conditions, the apparent diffusion coefficient of Cs was six times higher in the contaminated water from the core mixed with seawater used as cooling water brought by the 1F accident than in a simple CsCl solution, but it was unchanged for Sr. This may indicate that K in seawater inhibited Cs adsorption and accelerated the penetration of Cs. The actual concrete had been several decades before the accident and was considered to be dry and carbonated. In addition, during the accident, the concrete was first submerged in seawater by the tsunami, and contaminated water mixed with seawater from the reactor core arrived one day later. In an experiment reproducing these conditions, the apparent diffusion coefficient evaluated at 330 days was 2×10^{-13} m^2/s for both Cs and Sr.

KEYWORDS: *Cs, Sr, penetration, competitive adsorption, carbonation*

1. Introduction

The Great East Japan Earthquake on March 11, 2011 triggered a massive tsunami that caused the core of TEPCO's Fukushima Daiichi Nuclear Power Station (1F) to melt down and contaminated water was discharged from the core into underground concrete structures. The amount of radioactive waste in the decommissioning phase could be reduced by predicting the penetration of radionuclides and decontaminating the concrete (CLADS 2022). Therefore, the authors focused on Cs-137 and Sr-90, which are important from the viewpoint of radiation exposure, and studied the prediction of penetration in the underground structure of turbine pits (Univ. Tokyo 2022). In reality, 38 years have passed since Unit 1 started operation in 1973 until 2011, and the inside of the turbine pit is considered to have dried out and carbonated. In addition, the concrete was submerged by the tsunami and contaminated water entered the concrete one day later due to the core meltdown; however, the contaminated water was a mixture with seawater, as seawater was injected to cool the core. When considering ion penetration into such concrete, it is necessary to consider water advection and competitive adsorption with ions in seawater, in addition to the interaction between ions and solid phase and the connectivity of pores, which are important for ion penetration into concrete in a saturated condition. Therefore, experiments were conducted to investigate

the advection and competitive adsorption between ions in ion penetration by considering the history of immersion of materials and contaminated water under conditions similar to those of real contamination.

2. Experiments

Aggregate samples were actually taken from the same collection site as the river gravel used on 1F and crushed to make mortar. The cement used was Ordinary Portland cement (OPC). The water cement ratio was 0.55 and the sand cement ratio was 3.0. After forming into larger shaped molds, 20 x 50 x 50 mm rectangles were cut out. Some specimens were resin coated except one surface and then accelerated carbonated at 40 °C 60 %RH CO_2 5%, and 3 mm were found to be neutralized by the coloration of phenolphthalein solution.

Specimens in a sound water saturated condition in a non-carbonated state and in a dry neutralized state were used for the immersion tests. The immersion solutions were set to a Cs concentration of 3.5 µM and a Sr concentration of 71 µM, considering the composition of the contaminated water immediately after the accident as shown in Table 1 (Univ. Tokyo 2022). Three immersion conditions were used: simple chloride solution, initially contaminated water mixed with seawater, and initially contaminated water after one day of immersion in artificial seawater (historical reproduction). To measure the permeation of Cs and Sr, we used solutions labeled with Cs-137 or Sr-90, and after the immersion period, samples were cut for measurement so that the penetration cross section could be obtained, and an imaging plate (IP) was used. The samples were cut to obtain a penetration surface after the immersion period and quantitatively analyzed by autoradiography using an imaging plate (IP) (Fig. 1, Yamada et al 20212). The reading resolution was 25 µm.

Table 1 Estimated chemical compositions of contaminated solution and seawater [Univ. Tokyo 2022]

Date	Na	K	Rb	Cs	Mg	Ca	Sr	Cl	SO_4	Ratio to sea water
Unit	**ppm**	**ppm**	**ppb**	**ppb**	**ppm**	**ppm**	**ppm**	**ppm**	**ppm**	**%**
Mar. 12, 2011	8,100	309	96.1	467	960	310	6.22	15,000	670	80
Mar. 1, 2017	150	5.57	1.73	6.0	19	43	0.109	270	110	1.5
*Seawater **	*10,780*	*399*	*20*	*0.306*	*1,280*	*412*	*7.8*	*19,350*	*530*	*100*
Atomic wt	23.0	39.1	85.5	132.9	24.3	40.1	87.6	35.5	96.0	-
Unit	**mM**	**mM**	**µM**	**µM**	**mM**	**mM**	**µM**	**mM**	**mM**	**%**
Mar. 12, 2011	352	7.90	1.12	3.51	39.5	7.73	71	423	6.98	80
Mar. 1, 2017	6.52	0.142	0.0202	0.045	0.782	1.07	1.24	7.61	1.15	1.5
Sea water	*469*	*10.2*	*0.234*	*0.00230*	*52.7*	*10.3*	*89.0*	*545*	*5.52*	*100*

*Nozaki 1997

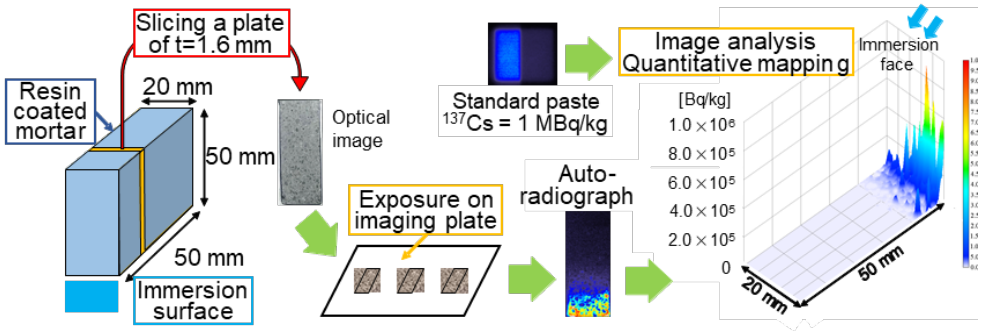

Fig. 1 Procedures of sample processing and auto-radiography using imaging plate [Yamada et al 2021].

3. Results and discussions

3.1 Elemental distribution on immersed surface

Fig. 2 shows the concentration distribution of Cs and Sr on the immersed surface after 7 days of immersion. The contrast in the upper and lower rows is adjusted separately to make the figures easier to

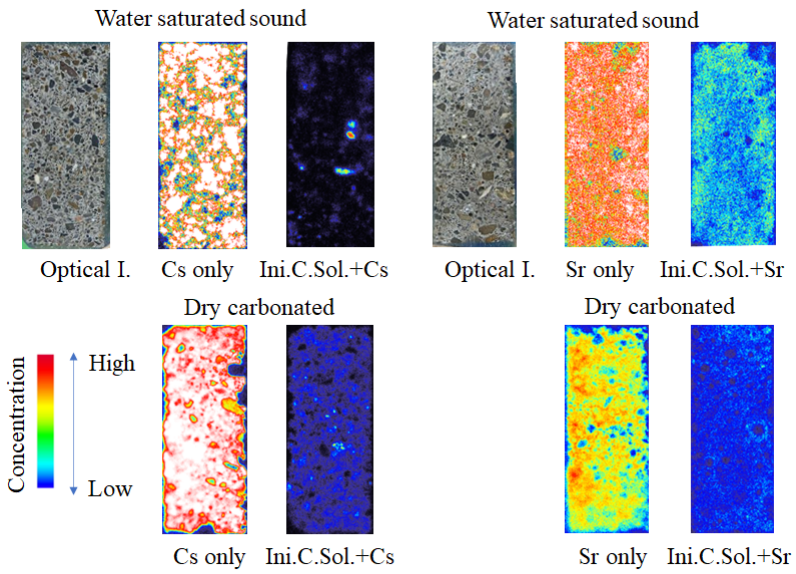

Fig. 2 Cs and Sr distributions on the exposedd surface by auto-radiography.

read, so the concentrations are not directly comparable. In the case of the saturated sound sample in the upper part of Fig. 2, Cs was not adsorbed on some aggregates but was significantly adsorbed on many aggregates, while Sr was mainly adsorbed on cement paste. When the immersion solution was set to the initial contaminated water composition, the adsorption of both Cs and Sr decreased, but was particularly pronounced for Cs. However, even under these conditions, some aggregates strongly adsorbed Cs. The carbonated sample is shown in the lower part of Fig. 2; both Cs and Sr were significantly adsorbed in the carbonated cement paste. The initial contaminated water composition reduced the adsorption of both Cs and Sr, probably because Cs adsorbs competitively with K at 2000 times the molar concentration in seawater and Sr adsorbs competitively with Ca at 1000 times the molar concentration.

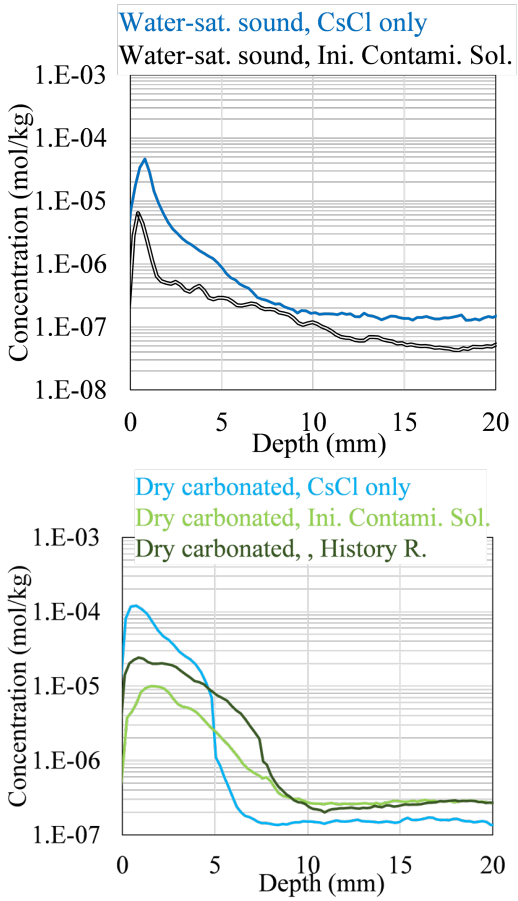

Fig. 3 Cs penetration profiles in various sample and solution conditions.

3.2 Penetration Profiles

Figs. 3 and 4 show the penetration profiles of Cs and Sr, respectively, under various conditions. The profiles show a peak near the immersion surface, but this is due to the low spatial resolution of the IP, which is affected by signals in the range of 1 mm for Cs and 2 mm for Sr. The signal is smaller at the edge than in the interior because there is no signal from one side.

Fig. 3 top shows water-saturated sound samples. Compared to the simple solution, the surface concentration decreased by one order of magnitude and the depth of penetration increased for the initial contaminated water. The apparent diffusion coefficient Da was obtained by fitting Fick's diffusion equation, and it was 1×10^{-13} m^2/s for the simple solution and 6×10^{-13} m^2/s for the initially contaminated water.

Fig. 3 bottom shows dry carbonated samples. The surface concentration doubled for the simple solution compared to the water-saturated sound sample, likely due to adsorption on the carbonation paste. However, the depth of penetration was smaller and Da was 5×10^{-14} m^2/s. In the initial contaminated water, the surface concentration was 1/5 and Da was 2×10^{-13} m^2/s. Under the historical reproduction conditions, the surface concentration was twice that of the initial contaminated water, but the Da was the same, 2×10^{-13} m^2/s. According to a previous study, Da was 3×10^{-12} m^2/s over a wide concentration range of 100 pM to 100 mM of Cs in OPC paste (Yamada et al 2021), and from the present results, it is considered that Da was decreased one order of magnitude smaller due to aggregate adsorption.

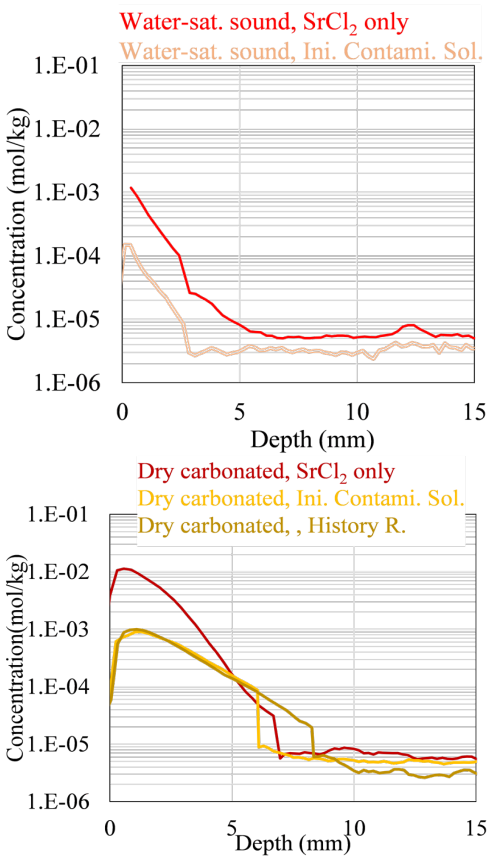

Fig. 4 Sr penetration profiles in various sample and solution conditions.

Fig. 4 left shows Sr penetration into water-saturated sound samples. Compared to the simple solution, the surface concentration decreased by one order of magnitude in the initial contaminated water, but the depth of penetration also decreased, with Da of 4×10^{-14} m^2/s in the simple solution and 3×10^{-14} m^2/s in the initial contaminated water. This was smaller than the 1×10^{-13} m^2/s in cement paste (Yamada et al 2021), but may be due to the effect of aggregates that are difficult to penetrate ionically.

Fig. 4 right shows Sr penetration into a dry carbonated sample. In the simple solution, the surface concentration increased by one order of magnitude and the depth of penetration was greater than that in the saturated solution, with a Da of 6×10^{-14} m^2/s. In the initial contaminated water and historical replication conditions, the surface concentration decreased by one order of magnitude from that in the simple solution. Penetration depth increased under the historical replicate condition, with Da of 2×10^{-13} m^2/s.

4. Conclusions

The contamination of the turbine pit basement after the accident at the Fukushima Daiichi NPP was reproduced and the following conclusions were obtained.

- The apparent diffusion coefficient Da of Cs is 3×10^{-12} m^2/s for cement paste, but 1×10^{-13} m^2/s for water-saturated sound mortar, which is more than one order of magnitude lower than that of Cs due to Cs adsorption by aggregates.
- The Da of Sr is 1×10^{-13} m^2/s in cement paste, which is more than one order of magnitude smaller than that of Cs, but 4×10^{-14} m^2/s in water-saturated sound mortar, which is smaller due to the low permeability of aggregate, and the difference with Da of Cs is reduced.
- The Da of Cs and Sr were the same 2×10^{-13} m^2/s in the real concrete condition, i.e., dry carbonation, and in the contamination history, i.e., 1-day immersion in seawater followed by immersion in initial contaminated water.
- The contamination history of the concrete and the actual concrete condition should be taken into account for the estimation of Cs and Sr penetration in real concrete.

Acknowledgements

This research was supported by the JAEA Nuclear Energy S&T and Human Resource Development Project through Concentrating Wisdom Grant Number JPJA20P20333545.

References

Collaborative Laboratories for Advanced Decommissioning Science (CLADS) (2022) “Decommissioning Science Diagram” https://clads.jaea.go.jp/en/rd/map/map.html

Nozai, Y. (1997) “Newest elemental composition of seawater (1996 version) and the interpretation”, *Bulletin of the Society of Sea Water Science, Japan*, 51: 302-308 (in Japanese)

The University of Tokyo (2022) “Quantitative Evaluation of Long-Term State Changes of Contaminated Reinforced Concrete Considering the Actual Environments for Rational Disposal － FY2021 Nuclear Energy Science & Technology and Human Resource Development Project －” (in Japanese).

Yamada, K., Igarashi, G., Osawa, N., Kiran, R., Haga, K, Tomita, S., Maruyama, I. (2021) “Experimental Study Investigating the Effects of Concrete Conditions onthe Penetration Behaviors of Cs and Sr at Low Concentration Ranges.” J. Advanced Concrete Technology, 19: 756-770.

The 16th International Congress on the Chemistry of Cement 2023 (ICCC2023)
"Further Reduction of CO_2 -Emissions and Circularity in the Cement and Concrete Industry"
September 18–22, 2023, Bangkok, Thailand

Crack reactivity of ultra-high performance fibre reinforced concrete under the flowing impact of geothermal water

M.C. Alonso[1*], M. Gimenez[1], M. Criado[1] and L. Ferrara[2]

[1] *Eduardo Torroja Institute for Construction Sciences (IETcc, CSIC), Madrid, Spain*
mcalonso@ietcc.csic.es, mercedes.gimenez@ietcc.csic.es, maria.criado@ietcc.csic.es
[2] *Politecnico di Milano, Milan, Italy*
liberato.ferrara@polimi.it

ABSTRACT

It is well-known that the formation of cracks in concrete affects the durability in aggressive media due to the cracks contributing to the transport processes. However, the interaction processes occurring inside a crack are not well known and depend on several parameters; such as the composition of the aggressive media or the type of concrete. Besides, the self-sealing phenomena in the crack cannot be ruled out that modify the interaction with the aggressive environment. In the present work, the chemical interactions processes inside the crack of an ultra-high performance fibre reinforced concrete (UHPFRC) containing 45% blast furnace slag (BFS) and a crystalline admixture (CA) additive to promote the self-healing has been analysed after 24 months of exposure to the impact of simulated geothermal water flow (sgw) that contains sulphate and chloride. The obtained results confirm the interaction of the aggressive environment inside the crack, which varies along the depth of the crack. Self-healing of the crack external part is mainly due to calcite precipitation, while phenomena of leaching of cement paste of the crack walls and precipitation of ettringite inside the crack has been observed.

KEYWORDS: *Concrete, Crack, Self-healing, Sulphates, Chlorides*

1. Introduction

The main cause for the loss of durability of concrete structures is related to the way they interact with the aggressive environment in service operating conditions. Advanced concretes employing UHPFRCs are undergoing continuous progress and development, Shi et al. (2015), Cuenca et al. (2022). High durability of UHPFRC in aggressive environments is considered, Wang et al. (2014), Son et al. (2020), El-Joukhada et al. (2021).
The damage expected from interaction with chloride-rich environments is mainly related to reinforcement corrosion, Song et al. (2020), El-Joukhada et al. (2021) but could also be due to the effect on steel fibres that affects the structural integrity of UHPFRC. The sulphates have a preferential interaction with cement paste forming new solid phases with higher volume causing expansions in the interior of the concrete.
The combined action of sulphates and chlorides has led to synergic interaction with cement paste. Some authors postulate reduction of chloride binding capacity with the preferential formation of ettringite, Alonso et al. (2017), while others found enhancement of chemical absorption of chlorides in presence of sulphates promoting the formation of Friedel's salt, Cheng et al. (2019).
The presence of a crack in concrete has been demonstrated to reduce the service life of concrete structures due to the preferential entrance of the aggressive, Li et al. (2019). The interaction of the crack with the environment can benefit from self-healing, which, by sealing the cracks, reduces the transport of aggressive agents and can result in a beneficial extension of service life, Maes et al. (2016), Van-Belleghem et al. (2017).
Most of the processes related to the consequence of the interaction of the crack with the environment are referred to what is observed on the surface of the same crack, including its self-healing, Cuenca et al. (2021), Van-Belleghem et al. (2017). However, the processes occurring in the crack and the consequence

of the interaction with the local chemical composition of the water filling the crack is not well addressed, Gimenez et al. (2021).
In present paper, a microstructural study has been carried out of the phenomena occurring on crack walls of UHPFRC exposed for 24 months to the flowing impact of simulated geothermal water rich in sulphates and chlorides, analysing the interaction inside the crack as a function of the distance from the surface.

2. Experimental programme

UHPFRC cylinders of Ø100x300 mm were casted with the mix design shown in Table 1. The binder used consisted of CEM I+45% and Blast Furnace Slag (BFS) with a w/b ratio equal to 0.18. A crystalline admixture (CA) was employed with the aim of stimulating the autogenous self-healing capacity.

Table 1. Mix composition of the investigated UHPFRC in kg/m^3

CEM I 52.5 R	BFS	Water	Steel fibres	Sand (0-2mm)	SP	CA
600	500	200	120	982	33	4.8

The samples were cured in a moist room at 20 °C and 95 %RH for at least 2 months. Slices of Ø100x50 were obtained for testing. A 5 mm deep notch was produced for crack generation, as shown in figure 1-left. Brazilian splitting tensile tests at a constant rate of 0.5 µm/s was used to generate the crack the crack.

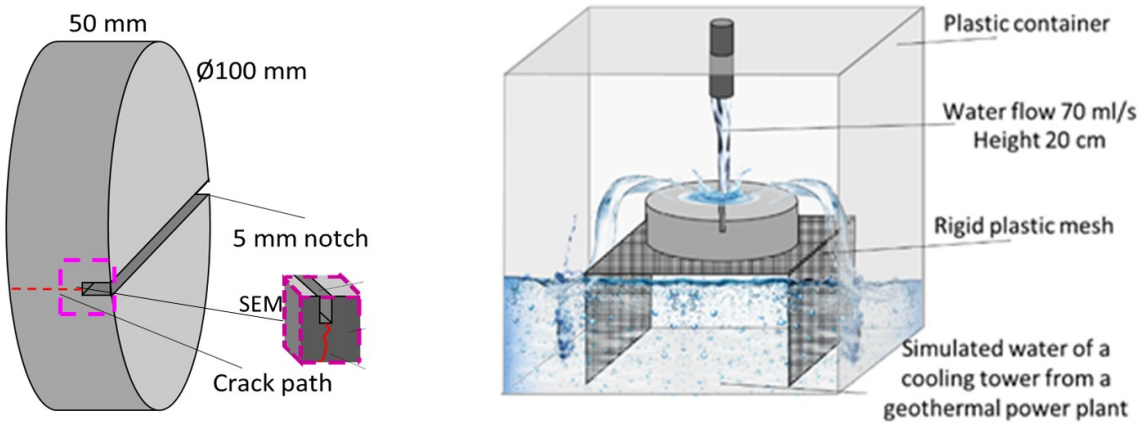

Figure 1. Left, Concrete sample geometry used for test showing notch and crack path and SEM sample location. Right, set-up for the sgw flow-impact test.

A water impact tests was carried out employing the set-up shown in figure 1-right. The test was specifically designed to simulate in the lab the real site interaction of a tank made with the investigated material with the flowing water in the cooling towers of a geothermal power plant. The test arrangement consisted of a plastic container in which one specimen was placed over a plastic mesh to avoid immersion in the water. A pump was connected to a rubber tube allowing the recirculation of the water and the impact of the flowing water on the specimen. The test conditions intend to replicate the physical impact through the water movement, which recirculates from the bottom of the plastic container to the top with a flow rate of 70 ml/s and hits the concrete surface from a height of 20 cm.
Sulphate and chloride polluted water simulating the cooling water of a geothermal plant (sgw) was used for the physical-chemical interaction with the UHPFRC. The sgw chemical composition was SO_4^{-2} (2300 ppm), Cl^- (300 ppm), Na^+ (1280 ppm). The pH was adjusted to three with HNO_3.
After 24 months of exposure, the specimens were removed and sampled for the SEM characterisation, as shown in figure 1-left. The samples for the microscopy were obtained from slices of the concrete sample cut transversely to the crack. Pieces of around 20 mm were taken from the region of the crack. To obtain the images, the pieces of UHPFRC were embedded into an epoxy resin, polished and coated with carbon. The samples were studied along the depth of the crack. For microstructure analysis, the SEM in backscattered mode (BSEM) was used. EDX analyses were also carried out to identify the element composition differences.

3. Results and Discussion

The aim of this study is focused on the characterisation of the interaction of the crack walls with the continuous impact of the sgw on the surface of the cracked concrete. The study has been done analysing a depth of 20 mm inside the walls of the crack. In Figure 2, the micrographs and mapping at two crack depths are shown.

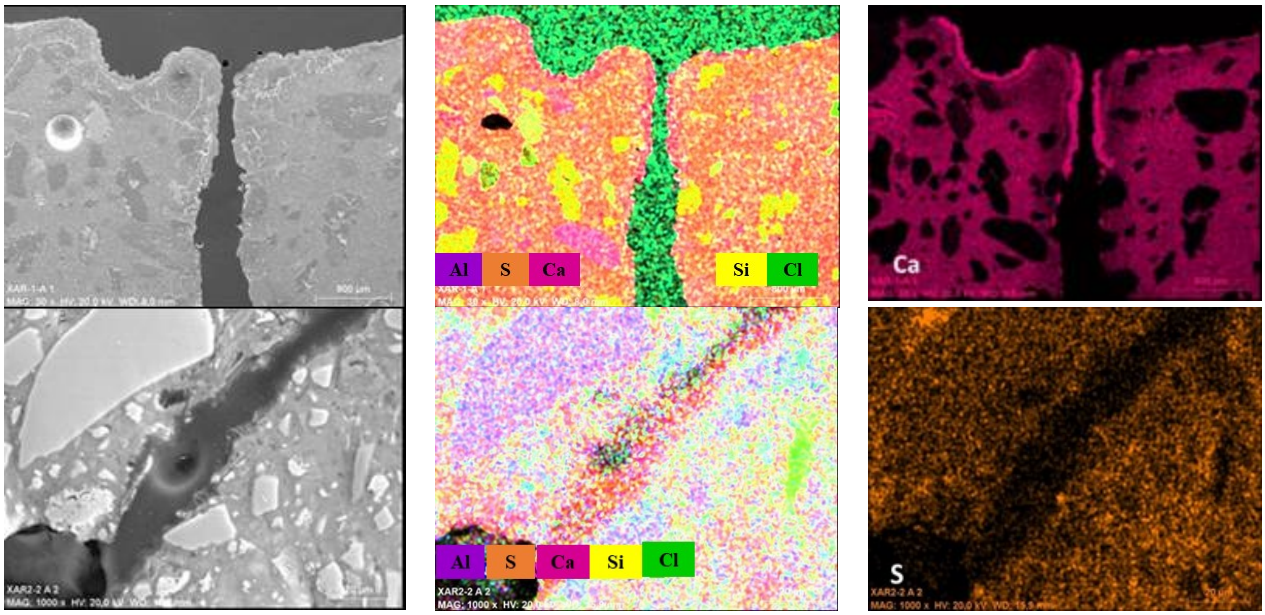

Figure 2. Micrographs and mapping showing the reactivity of walls of a crack of the UHPFRC with CA after 24 months of exposure to the impact of sgw.

On the figure 2-left-up, crack walls closest to the concrete surface are considered. A reduction of the crack width is attributed to the interaction of the crack wall with the external environment, identified as the self-healing of a crack observed from the surface, also observed by Cuenca et al (2022). In addition, the contribution to crack filling products are consequence of the interaction with the calcium ion leached from the cement paste of the internal walls of the crack, found in Gimenez et al (2021). This self-healing is appreciated to penetrate less than 1mm in the depth of the crack. The composition of the crack edges affected by the self-healing process is appreciated in the mapping of figure 2-middle-up that highlights the element distribution (Si, Ca, S and Cl). The composition of the external sealing product is rich in Ca, as shown in figure 2 right-up associated with the precipitation of calcite. The explanation found for this is related to the initial acid pH of the sgw, which favours the dissolution of cement paste, namely of C-S-H gel and portlandite, releasing Ca^{2+} ions to the sgw and increasing the pH, as demonstrated by Gimenez et al. (2021). Soon after, the Ca^{2+} ions are captured by the CO_2 dissolved in the sgw, facilitating in this way the calcite precipitation. Below this self-healing region, figure 2-left-up, the crack width remained scantly affected. Inside the crack, figure 2-left-down, more precipitated products occupy the inner part of the crack. The mapping of figure 2-middle-down and right shows the enrichment in S, Ca and Al.

Several types of processes drive the internal interaction of the concrete crack walls with the sgw that fills the crack. The alteration of the cement paste at the edge of the crack wall, shown in figure 3-left, with changes in SiO_2 and CaO content, appreciated in figure 3-right. The distance of cement paste showing chemical changes from the edge of the crack wall is around 20µm. This process is typically associated with a leaching process of concrete in contact with water, also observed in Alonso et al (2006).

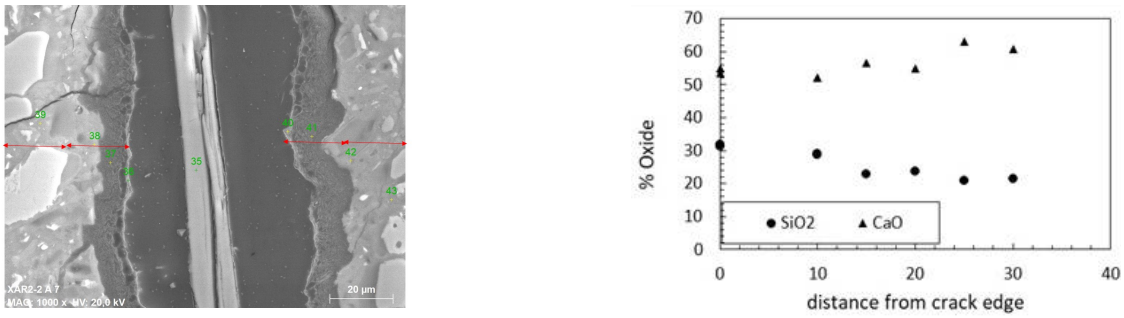

Figure 3. Left, microstructural alteration of cement paste from the crack edges. Right, variation of % of SiO_2 and CaO from the crack wall edge.

In addition to in crack leaching, crack-sealing regions with more precipitated product are observed, as shown in figure 4-left. This filling product is related to the precipitation of ettringite (figure 4-right), which confirms the penetration of sulphates from the sgw into the crack. The differences in the reactivity of the walls of the crack suggest changes in the ionic composition of the water that fills the inner part of the crack with the composition of the outer sgw as consequence of the crack reactivity process. Corrosion of the steel fibres of the concrete was only observed on the external surface directly exposed to the sgw, but no iron-rich product could be seen filling the crack.

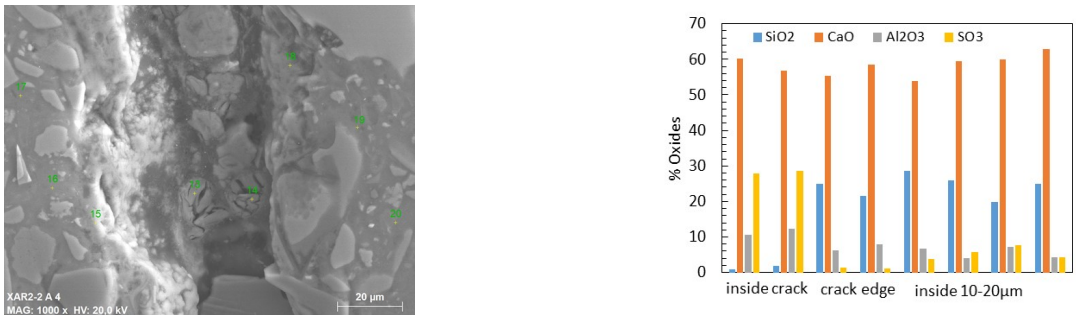

Figure 4. Left, microstructure of the internal filling of the crack. Right, Ettringite and C-S-H alteration.

4. Conclusions

The results observed in the analyses of the crack walls suggest different chemical processes that characterize the interaction of the simulated and flowing geothermal water inside the crack, which varies with the depth of the crack. Self-healing of the crack external part due to calcite precipitation, while leaching of C-S-H in the crack wall and precipitation of ettringite inside the crack.

Acknowledgments

The research activity reported in this paper was performed in the framework of the ReSHEALience project, which has received funding from the European Union's Horizon 2020 research and innovation program under grant agreement No. 760824. Also, MC Alonso, M Gimenez and M Criado acknowledge the help of the experimental work of J Carretero.

References

Alonso, M.C, García Calvo, J.L., Cuevas, J, Turrero, M.J., Fernández, R., Torres, E., Ruiz, A.I. (2017). "Interaction processes at the concrete-bentonite interface after 13 years of FEBEX-Plug operation. Part I: Concrete alteration. *Phys. and Chem. of the Earth,* 99: 38–48

Cheng, S., Shui, Z., Sun, T., Gao, X., Guo, C. (2019). "Effects of sulfate and magnesium ion on the chloride transportation behavior and binding capacity of Portland cement mortar". *Constr. Build. Mat*., 204, 265–275.

Cuenca, E., Criado, M., Gimenez, M., Alonso, M. and Ferrara, L. (2022), "Effects of alumina nanofibers and cellulose nanocrystals on durability and self-healing capacity of ultra-high performance fiber reinforced cementitious composites*". J. Mater. Civ. Eng. (ASCE),* 34. 8: 04022154.

El-Joukhadar, N. and Pantazopoulou, S. J. (2021). “Effectiveness of UHPFRC cover in delaying bar corrosion”. *Constr. and Build Mat*, 269: 121288.

Giménez, M., Alonso, M.C., Menéndez, E. and Criado M. (2021). “Durability of UHPFRC functionalised with nanoadditives due to synergies in the action of sulphate and chloride in cracked and un-cracked states”. *Materiales de Construccion,* 71 (344): e264.

Li, K. and Li, L. (2019). “Crack-altered durability properties and performance of structural concretes. *Cem and Conc. Re*s, 124(July), 1–11.

Shi, C., Wu, Z., Xiao, J., Wang, D., Huang, Z., & Fang, Z. (2015). “A review on ultra-high performance concrete: Part I. Raw materials and mixture design”. *Constr. Build. Mater.*, 101: 741-751.

Song, Q, Yu, R., Shui, Z., Rao, S., Fan, D. and Gao, X. (2020).”Macro/micro characteristics variation of ultra-high performance fibre reinforced concrete (UHPFRC) subjected to critical marine environments. *Constr. Build. Ma*t. 256, 119458.

Van-Belleghem, B., Van-den Heede, P., Van Tittelboom, K., and N. de Belie (2017). “Quantification of the service life extension and environmental benefit of chloride exposed self-healing concrete”. *Materials*, 10 (5), 1-22.

Wang, W., Liu, J., Agostini, F., Davy, C. A., Skoczylas, F. and Corvez, D. (2014). “Durability of an Ultra High Performance Fiber Reinforced Concrete (UHPFRC) under progressive aging. *Cem. and Conc. Res* 55, 1–13.

Alonso, M.C., Castellote, M., Llorente, I., Andrade, C. (2006). “Ground water leaching resistance of high and ultra-high performance concretes in relation to the testing convection regime”. *Cem. and Conc. Res*, 36(9), 1583–1594.

The 16th International Congress on the Chemistry of Cement 2023 (ICCC2023)
"Further Reduction of CO_2 -Emissions and Circularity in the Cement and Concrete Industry"
September 18–22, 2023, Bangkok, Thailand

Durability of concrete with low temperature belite binder (LTBB)

B. I.E. Kraft[1*], S. Unbehau[2], M. Mueller[3], and H.-M. Ludwig[4]

[1] *Bauhaus Universität Weimar, Weimar, Germany*
bettina.ines.elisabeth.kraft@uni-weimar.de
[2] *Bauhaus Universität Weimar, Weimar, Germany*
sophie.unbehau@uni-weimar.de
[3] *Bauhaus Universität Weimar, Weimar, Germany*
matthias.mueller@uni-weimar.de
[4] *Bauhaus Universität Weimar, Weimar, Germany*
horst-michael.ludwig@uni-weimar.de

ABSTRACT
As high CO_2 emissions result from the production of Ordinary Portland cement (OPC), alternative binder systems are increasingly gaining importance. A novel binder type is the low temperature belite binder (LTBB), which is produced in a two-step process. The first step is a hydrothermal treatment of a raw material containing CaO and SiO_2 in a ratio of 2:1. The resulting precursor consists mainly of alpha-dicalcium silicate hydrate (α-C_2SH). Annealing this precursor in a second step at relative low temperatures (<500°C) leads to the formation of high reactive belite polymorphs.
In order to evaluate the usability of LTBB in reinforced concrete, a basic understanding of the durability is crucial. Hence, the carbonation behavior, chloride migration resistance and freeze-thaw resistance with and without de-icing salt were investigated on concretes made with LTBB. In addition, phase composition and microstructure were analyzed using binder paste samples.
In air-entrained concrete, LTBB shows good frost resistance, while resistance to chloride migration still has potential for improvement. Surprisingly, the resistance to carbonation is very high, although only small amounts of portlandite are formed during hydration and the pore structure contains a high volume of cross-linked capillary pores. Overall, the durability of concrete with LTBB is satisfactory, but differs in some respects from that of OPC based concrete.

KEYWORDS: *belite binder, microstructure, carbonation, freeze-thaw, chloride migration*

1. Introduction

To reduce the CO_2 emissions in the cement industry, alternative binders with improved CO_2 footprint are gaining importance. One type are so-called C-S-H binders such as Celitement® (Möller (2017)) or NT-C_2S (Niedrig Temperatur-C_2S; engl. low temperature C_2S (Link 2017)), which are produced in a two-step process: Firstly, the crystalline C-S-H phase α-C_2SH (α-dicalcium silicate hydrate) is synthesized from raw materials by hydrothermal treatment. Secondly, the α-C_2SH is activated, either mechanochemically by grinding (Celitement® (Möller (2017)) or thermally by annealing (NT-C_2S (Link (2017)). As this paper deals with LTBB, a binder which was developed on the basis of NT-C_2S, the activation and reactivity of the latter will be discussed in more detail.
Link determined that the temperature range from 400 to 500°C is suitable for annealing NT-C_2S, with an optimum at 420°C. An annealing time of 1 h in the muffle furnace was sufficient to fully dehydrate α-C_2SH (Link (2017)). The resulting binder consisted mainly of x-C_2S (x-dicalcium silicate) and a highly reactive X-ray amorphous phase (Link et al. (2015)).
For both Celitement and NT-C_2S, the main hydration products are C-S-H phases and very small amounts of portlandite (NT-C_2S). Information on durability is only available for Celitement, but not for NT-C_2S. Celitement-based concrete was found to have a very high resistance to chloride penetration and carbonation (Achenbach et al. (2021), Kraft et al. (2022)).

2. Materials and Methods

Self-produced LTBB was used as material. For this purpose, $Ca(OH)_2$, SiO_2 in a CaO/SiO_2 ratio of 2, and α-C_2SH seeds were first hydrothermally treated at 200°C for a total of 36 h in an industrial autoclave at a sand-lime brick plant. The resulting precursor contained 92 % α-C_2SH. The material was then ground, granulated, and annealed at 490°C in a laboratory rotary kiln to completely dehydrate the material to obtain LTBB.
To determine the hydrated phase composition, LTBB paste samples were prepared with a w/b-ratio of 0.35 and stored for 28 d. Low temperature differential scanning calorimetry (LT-DSC) was performed to determine the pore structure of the paste samples in analogy to Sant et al. (2011). That method allows the testing of samples without prior drying, which might affect the pore structure. For QXRD analysis, the hydration was stopped by solvent exchange with isopropanol followed by drying at 40°C. More details are given in Kraft et al. (2022). Durability test were carried out on two types of concretes - one composition without (1) and one with air entrainment (2), see Table 1. As LTBB has a lower water-binding capacity than OPC, the relatively low w/b-ratio of 0.35 was chosen.

Table 1: Concrete Composition without/with air entrainment and resulting fresh concrete properties

Composition	Binder [kg/m³]	w/b	Super-plasticizer [kg/m³]	Air entrain. agent [kg/m³]	Aggregates 0/2 [kg/m³]	Aggregates 2/8 [kg/m³]	Aggregates 8/16 [kg/m³]	Air content [vol.%]	Spread rate [mm]
1	380	0.35	7.60	-	611.0	528.0	749.0	0.45	530
2	380	0.35	7.60	1.90	611.0	528.0	749.0	5.30	560

Composition 1 was used to determine the compressive strength as well as the resistance against carbonation (accelerated procedure), chloride migration and freeze-thaw exposure without de-icing salt. All specimens were demolded after one day and stored under water until the 7 th day. They were then stored at laboratory climate (20°C/65 % rel. humidity). The determination of compressive strength was performed on 15 x 15 x 15 cm³ cubes after 2, 7, 28 and 56 d (DIN EN 12390-3). Furthermore, 10 x 10 x 40 cm³ beams were stored at 1.0 vol.-% CO_2 to determine the carbonation resistance according to DIN EN 12390-12. Chloride migration resistance was measured analogous to DIN EN 12390-18. Frost resistance was tested with the CIF method. Analogous to DIN CEN/TR 15177, the internal damage was determined.
The air entrained mix (Composition 2) was used to determine the salt frost scaling resistance with the CDF method in accordance with DIN CEN/TS 12390-9. These samples were treated and stored in the same way as Composition 1. For comparison, the compressive strength after 28 d was also investigated on Composition 2.

3. Results

The composition of the hydrated LTBB paste, as determined by QXRD, shows only a slight change compared to the unhydrated LTBB, see Table 2. X-C_2S is completely converted during hydration and small amounts of portlandite are formed. The change in γ-C_2S can be considered as a measurement artefact in the context of determining the X-ray amorphous fraction. As γ-C_2S is inert, it is not expected to react during hydration. The X-ray amorphous fraction remains close to the same. Since the C-S-H phases formed by hydration are also X-ray amorphous, no conclusions about the degree of conversion of the reactive X-ray amorphous phase can be drawn from the amorphous content. Other techniques such as Si-MAS-NMR, thermal analysis or IR spectroscopy would be appropriate to make this differentiation.

Table 2: Phase composition of LTBB

	α-C_2SH [%]	x-C_2S [%]	X-ray amorph. [%]	γ-C_2S [%]	Calcite [%]	Dellaite [%]	Portlandite [%]
LTBB	0	5	50	34	7	4	0
LTBB 28 d hydr.	0	0	46	37	8	6	3

LT-DSC measurements allow to distinguish between different pore types by relating them to respective temperature ranges roughly following the classification of Sant et al (2011), which was slightly adjusted in Müller (2021). The amount of freezable water in the temperature range below -35°C is assigned to the gel pores. In the range between -35 and -20°C freezing occurs is isolated capillary pores and between -20 and 0°C in cross-linked capillary pores. As shown in Figure 1, LTBB paste has only a very small amount of freezable water in the gel pore range. No freezing peaks are evident in the region of the isolated capillary pores. The largest peak occurs in the range with cross-linked capillary pores. In summary, this means that the pore structure of LTBB consists mainly of capillary pores.

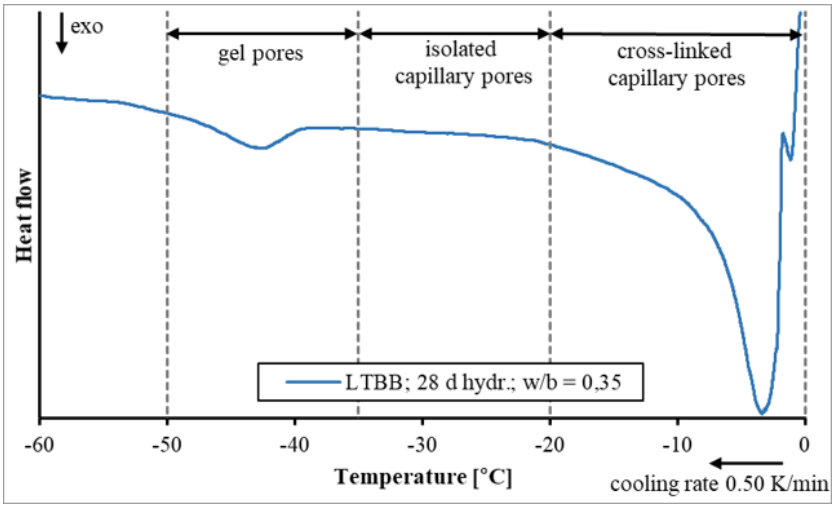

Figure 1: Freezing curve as heat flow to determine the pore structure following Sant et al. (2011)/Müller (2021)

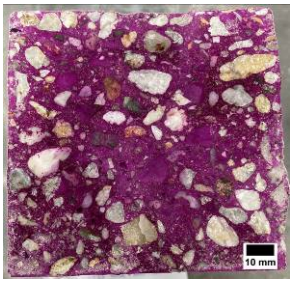

Figure 2: Carbonation after 98 d storage in 1 vol.% CO_2

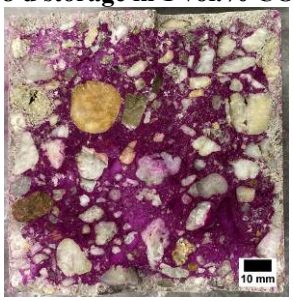

Figure 3: Carbonation after 800 d storage in 1 vol.% CO_2

The LTBB concrete achieves a compressive strength of 64.0 MPa after 28 d, which corresponds to a strength class of C45/55, according to DIN EN 206. With 47.9 MPa, the 2 d compressive strength already equals 70 % of the 28 d value. Despite the fast strength development at early ages, a further increase in strength can still be observed after 28 d, with 69.0 MPa after 56 d.

Carbonation tests on LTBB at a CO_2 concentration of 1.0 vol.-% showed that no significant carbonation occurs during 98 days of storage, see Figure 2. Thus, no carbonation coefficient can be determined for this period. Therefore, the CO_2-storage was prolonged. After 800 d the carbonation depth was measured again. This resulted in a carbonation depth of 5.85 mm, see Figure 3. Considering the lack of portlandite and the pore structure of the LTBB paste as described above, this value is remarkably low. The reasons for this have not yet been fundamentally investigated. A potential explanation is the specific carbonation behavior of γ-C_2S. Guan et al. (Guan (2016)) described that the carbonation of γ-C_2S results in the formation of calcite and silica gel, which also leads to an increase in strength. The carbonation products of γ-C_2S were further found to have a pore blocking effect (Fang (2020)). Similar to the densification of the pore structure by portlandite carbonation in OPC systems, this effect can potentially slow down carbonation attack. Investigations to resolve the underlying causes are ongoing.

The chloride migration coefficient D_{Cl} is calculated to be 25.20 x 10^{-12} m^2/s for the LTBB. According to BAW (2012a), the lowest requirement is 10.00 x 10^{-12} m^2/s. The relatively low chloride migration resistance of the LTBB is probably due to the lack of C_3A, since the chlorides are only physically bound by C-S-H phases. Thus, significantly lower amounts of chloride can be bound compared to OPC-based concrete. Another assumption is that the chloride-binding potential of the LTBB is likely to be quite low due to the relative small amount of C-S-H phases. Furthermore, the high volume of capillary pores should enable intensive transport processes.

In the CIF-test, the LTBB shows severe internal damage already after 6 freeze-thaw cycles, with a remaining relative E-modulus of 70 %. Below 75 %, the concrete is considered to be damaged according to BAW (2012b). With each subsequent freeze-thaw, cycle the damage increases. The strong internal damage is probably due to two effects: First, the LTBB showed a significant water absorption before and

during the measurement (end of pre-storage 1.31 %). This indicates micro cracks in the LTBB concrete, which increased the susceptibility to frost damage. On the other hand, the air content of the fresh concrete is very low with 0.45 vol.-%, due to the defoaming effect of the SP. For OPC based concrete, the air content of the fresh concrete is typically between 1.5 and 2.0 vol.-%.
For Composition 2 the use of air entraining agent increased the air content to 5.3 vol.-%, resulting in a decrease of the compressive strength after 28 d to 52.6 MPa. The concrete shows a very good salt frost scaling resistance. With an amount of 0.67 kg/m² after 28 cycles, the accumulated scaling is well below the acceptance criterion for the CDF test with 1.50 kg/m², acc. to BAW (2012b).

4. Conclusions

In this paper, the durability of LTBB-based concrete was investigated. Significant differences to OPC-based concrete were found in some respects. In a composition without air entrainment compressive strength C45/55, according to DIN EN 206, was achieved. Early compressive strength was notably higher than in OPC-based concretes, with already 70 % of the 28 d compressive strength after only 2 d. Thus, LTBB is characterized by a rapid strength development.
Furthermore, LTBB has a remarkably high resistance to carbonation, although only a very low amount of portlandite is formed during hydration. The specific effect of the carbonation of usually inert γ-C_2S was found to be a plausible cause for that behavior. Analyses of the pore structure have shown that the pore structure of LTBB consists mainly of cross-linked capillary pores with only a few isolated gel pores, indicating a rather coarse pore structure. This microstructure appears to be responsible for the low resistance to chloride migration, in addition to the absence of C_3A. Without air entrainment, LTBB concrete has a low frost resistance. With air entrainment, the salt frost resistance was very good. Accordingly, it can be assumed that a good frost resistance is given with a functioning air void system.
Despite the differences to OPC concrete, LTBB can be used for durable concrete. However, care must be taken to ensure that the composition and the choice of admixtures and additives is appropriate. E.g., an optimized durability with regard to chloride ingress might be achieved by partial substitution with GGBFS.

Acknowledgements

The authors thank A. Itul, M. BenHaha, W. Tian, E. Wagner (Heidelberg Materials) for their cooperation.

References

Möller, H., (2017) “Novel cements based on calcium hydrosilicates.” Presentation in *The Future Of Cement 200 years after Louis Vicat*, Paris, 2017

Link, T. (2017) “Entwicklung und Untersuchung von alternativen Dicalciumsilicat-Bindern auf der Basis von α-C_2SH”. Dissertation; *Fakultät Bauingenieurwesen; Bauhaus-Universität Weimar; F.A. Finger-Institut für Baustoffkunde*,

Link, T., Bellmann, F., Ludwig, H.M. and Ben Haha, M. (2015) “Reactivity and phase composition of Ca_2SiO_4 binders made by annealing of alpha-dicalcium silicate hydrate” *Cement and Concrete Research*, 67 (2015): 131–137

Achenbach, R., Kraft, B., Ludwig, H.-M. and Raupach, M. (2021) ”Dauerhaftigkeitseigenschaften von alternativen Bindemittel“ *Beton- und Stahlbetonbau* 116 (2021): 775-785

Kraft, B., Achenbach, R., Ludwig, H.-M. and Raupach, M (2022) “Hydration and Carbonation of Alternative Binders“ CMD 3 (2022): 19-15

Sant, G., Bentz, D. and Weiss, J. (2011) “Capillary porosity depercolation in cement-based materials: Measurement techniques and factors which influence their interpretation” *Cement and Concrete Research* 41 (2011): 854–864,

Müller, M. (2021) “Frost-Tausalz-Angriff auf Beton - Neue Erkenntnisse zum Schadensmechanismus”. Dissertation; *Fakultät Bauingenieurwesen; Bauhaus-Universität Weimar; F.A. Finger-Institut für Baustoffkunde*

Guan, X., Liu, S. Feng, C. and Qiu, M. (20416) “The hardening behavior of c -C 2 S binder using accelerated carbonation” Construction and Building Materials 114 (2016) 204–207

Fang, Y., Liu, Z., Wang, Q., Zhang, and Y. Zhang, M. (2020): „ Strength Development and Products Evolution of β-C_2S and γ-C_2S Induced by Accelerated Carbonation Curing” Journal of Wuhan University of Technology-Mater. Sci. Dec. 2020 (2020): 1053 - 1060

BAW (2012a) “BAW Code of Practice “Chloride Migration Resistance of Concrete (MCL)” *Bundesanstalt für Wasserbau (BAW)(Hrsg.) –Merkblätter und -Richtlinien*

BAW (2012b) “BAW Code of Practice “Frost Resistance Tests for Concrete (MBF)” *Bundesanstalt für Wasserbau (BAW) (Hrsg.) –Merkblätter und –Richtlinien*

The 16th International Congress on the Chemistry of Cement 2023 (ICCC2023)
"Further Reduction of CO_2 -Emissions and Circularity in the Cement and Concrete Industry"
September 18–22, 2023, Bangkok, Thailand

Insight on Chloride Ions Solidification Mechanism in Layered Double Hydroxides Designed with Different Cations both from First Principles Calculation and Experimental Work

Qianqian Wang[1,2*], Hu Zhao[1,2], Zhizong Tian[1,2], and Xiaodong Shen[1,2]

[1] *College of Materials Science and Engineering, Nanjing Tech University, Nanjing, P.R. China, 211816*
[2] *State Key Laboratory of Materials-Oriented Chemical Engineering, Nanjing Tech University, Nanjing, P.R. China, 211816*
Email: qqwang@njtech.edu.cn, h.zhao@njtech.edu.cn, zztian@njtech.edu.cn, xdshen@njtech.edu.cn

ABSTRACT

Layered double hydroxides (LDHs) could be an efficient chloride ion solidification agent in cementitious materials by exchanging their interlayer anions with chloride ions in Marine concrete structures. In this work, nine types of chloride-hydrotalcite crystal structures consisting of different cationic ions were designed based on first principles calculations. Chloride ions binding energy was calculated and indicated that CaAl-Cl-LDHs possess the strongest ability to bind chloride ions in structure and that in ZnFe-Cl-LDHs are the weakest. Four types of nitrate-hydrotalcite (CaAl-LDH, MgAl-LDH, MgFe-LDH, ZnAl-LDH) were synthesized by co-precipitation method and their chloride ion adsorption and desorption processes were compared in the simulated concrete pore solution. The results showed that CaAl-LDH has a faster adsorption rate, higher adsorption capacity, and strong solidification ability of chloride ions. This corresponds to the first principles calculation results that CaAl-LDH has the highest chloride ions binding energy.

KEYWORDS: *Layered Double Hydroxides, Co-precipitation Synthesis Method, Chloride ion adsorption, Desorption, First-principles calculation*

1. Introduction

Layered double hydroxides (LDHs) are new concrete additives enhancing chloride ions resistance(Mir et al., 2020). Furthermore, LDHs are well adapted to cement paste and can be used as an effective hydration hardener(Yang et al., 2021). The general chemical formula of LDH is described as $[M^{2+}_{1-x}M^{3+}_{x}(OH)_2]^{x+}(A^{n-})_{x/n}\cdot mH_2O$, where the M^{2+}, M^{3+}, and A^{n-} represent the divalent cation, trivalent cation, and interlayer anion respectively. Its atomic structure is like a sandwich where the $[M^{2+}_{1-x}M^{3+}_{x}(OH)_2]^{x+}$ constitute the cationic layer and the A^{n-} ions and water molecules are jammed in the two cationic layers(Chen et al., 2019).

Interestingly, density functional theory calculation results showed that the sequence of anion exchange in the anionic layer is $CO_3^{2-} > SO_4^{2-} > OH^- > F^- > Cl^- > Br^- > NO_3^-$ (Liu et al., 2020) in LDHs by calculating the binding energy. This can be the theoretical basis for the anion design of LDHs that NO3- intercalated types can be the most probable anion-controlled functional group for chloride ions sorption. Nevertheless, both SO_4^{2-} and Cl^- in seawater play a detrimental role in marine concrete. Especially, the affinity order of sulfate ions is before chloride ions and it has the potential to substitute the chloride ions between the LDHs cationic layers. Whether sulfate will react with LDHs and lead to the degradation of chloride ions sorption stability remains largely unknown.

Based on the above issues, nine types of chloride-hydrotalcite crystal structures were designed based on first principles calculations. Chloride ions binding energy was calculated in structure. Furthermore, four types of NO_3^-LDHs, namely, CaAl-LDH (CA), MgAl-LDH (MA), MgFe-LDH (MF), and ZnAl-LDH (ZA), trying to illustrate the influence of different types of cations on the ability of chloride ion solidification. A simple co-precipitation synthetic method with different drying methods was investigated

to improve their microstructure. Afterward, their chloride ions' solidification ability in simulated concrete pore solution (SCPS) was compared. This work attempted to illustrate the design mechanism of chemical composition and its chloride ions solidification mechanism of different types of LDHs.

2. Materials and methods

2.1 Model Construction

Based on the low-temperature phase (at 20℃) of Friedel's salt(Renaudin et al., 1999), 9 different types of $M^{II}M^{III}$-Cl-LDHs containing chloride ions (Cl-LDHs) were designed, and built in this work. M^{II} are Ca^{2+}, Mg^{2+}, Ni^{2+} and Zn^{2+}, and M^{III} are Al^{3+}, Cr^{3+}, Ga^{3+} and Fe^{3+} respectively. Firstly, the 2×2×1 supercell symmetry of Friedel's salt was established and that is CaAl-Cl-LDHs. Subsequently, the divalent and trivalent cations in CaAl-Cl-LDHs were substituted by Mg^{2+}, Ni^{2+}, Zn^{2+} and Cr^{3+}, Ga^{3+}, Fe^{3+} respectively, i.e., MgAl-Cl-LDHs, NiAl-Cl-LDHs, ZnAl-Cl-LDHs, CaCr-Cl-LDHs, CaGa-Cl-LDHs, CaFe-Cl-LDHs. In the same way, the divalent cation in CaFe-Cl-LDHs was replaced by Mg^{2+} and Zn^{2+}, thus MgFe-Cl-LDHs and ZnFe-Cl-LDHs are formed.

2.2 Computational methods

All these 9 structures were relaxed to find the minimum electronic energy using the first principles calculations method. The core-ion approximation and electrostatic interaction were dealt with ultrasoft pseudopotential during the geometry optimization process. Perdew-Burke-Ernzerhof function (PBE) and generalized gradient approximation (GGA) were selected to calculate the contribution of all many-bodies to the total energy. According to pseudopotential and atoms, the cut-off energy of plane wave basis was set up. Oxygen was set as 340 eV, calcium was set as 280 eV and aluminum was set as 140 eV, and so on. The k-point grid was set up by the Monkhorst-Pack method. The K-point grids of Ca/Mg/Zn/NiAl-Cl-LDHs and Mg/ZnFe-Cl-LDHs were set as 1×3×1. The other structures were set as 1×2×1. BFGS algorithm(Anglada and Bofill, 1998) was used to find the potential energy surface during optimization. the calculation parameters were set as: (1) the maximum energy tolerance: 1×10^{-5} eV/atom; (2) the maximum force tolerance: 0.03 eV/Å; (3) the maximum displacement: 1×10^{-3} Å; (4) the maximum stress tolerance: 0.05 GPa.

2.3 Synthesis process of LDHs and Chloride ions solidification process with LDHs

Different cation types of LDHs, namely $[Ca_4Al_2(OH)_{12}](NO_3)_2{\cdot}4H_2O$ (Ca-Al-NO_3-LDH, abbr. CA), $[Mg_4Al_2(OH)_{12}](NO_3)_2{\cdot}4H_2O$ (Mg-Al-NO_3-LDH, abbr. MA), $[Zn_4Al_2(OH)_{12}](NO_3)_2{\cdot}4H_2O$ (Zn-Al-NO_3-LDH, abbr. ZA), and $[Mg_4Fe_2(OH)_{12}](NO_3)_2{\cdot}4H_2O$ (Mg-Fe-NO_3-LDH, abbr. MF), were synthesized by the co-precipitation method.

2.4 Chloride ions solidification process with LDHs in different solutions

The variation of chloride ions concentration is an efficient way to evaluate the anion adsorption rate of different types of LDHs. First, the simulated concrete pore solution (SCPS) was prepared with 0.6 g NaOH, 1.4 g KOH and 0.037 g $Ca(OH)_2$ with 1 liter of distilled water according to Yang's(Yang et al., 2020) study. An ion meter (Lei-ci, PXSJ-216F), ion selective electrode (ISE, Lei-ci, PCl-1-01), and reference electrode (RE, Lei-ci, 217-01) were used to in-situ measure the concentration of chloride ions in the solution.

0.75 g of the synthesized four types of LDHs were added to this solution. The electrodes were put into the mixture to in-situ measure the chloride ions concentration every 2 minutes in the first ten minutes and then every 10 minutes after the reaction for 5 hours. Batch experiments were also conducted at the same time and then 0.284 g Na_2SO_4 was added to the solution for the anion exchange. Then the in-situ measurements with ion-selective electrodes were conducted. The numbers were recorded every 5 minutes in the first two hours and then every 10 minutes in the last three hours.

3. Results and Discussion

3.1 Crystal structures analysis

Crystal structures characteristics of MⅡMⅢ-Cl-LDHs was shown in Fig. 1. (a)-(d) are MⅡAl-Cl-LDHs, (e)-(g) are CaMⅢ-Cl-LDHs, (h) and (i) are Mg / ZnFe-Cl-LDHs. Various kinds of cations lead to a diverse atomic arrangement in the cationic layer and anionic layer. The calcium ions lie around in oxygen atoms of the cationic layer. However, the magnesium, nickel, and zinc ions lie around aluminum atoms. The chloride ions and water molecules in NiAl-Cl-LDHs, ZnAl-Cl-LDHs, and ZnFe-Cl-LDHs arrange irregularly. It is worth noting that the atomic configuration in ZnFe-Cl-LDHs is disorder. Meanwhile, the lattice parameters of LDHs differ from each other, especially for lattice c. Furthermore, the interlayer distance of CaAl-Cl-LDHs, MgAl-Cl-LDHs, NiAl-Cl-LDHs, and ZnAl-Cl-LDHs increases linearly in order as shown in Fig. 2. CaM^{3+}-Cl-LDHs is same as that, however, their interlayer distances are similar with each other. Among them, the interlayer distance of ZnAl-Cl-LDHs is the largest and the one of CaAl-Cl-LDHs is the smallest. In summary, divalent metal cations have a more prominent effect on crystal structures compared to trivalent metal cations.

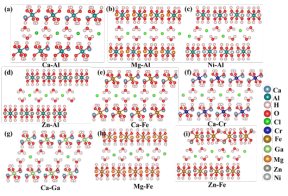

Figure 1 Crystal structures of chloride ions contained LDHs with different types of M^{2+} and M^{3+} ions. Different colored balls represent different types of atoms depicted in the figure.

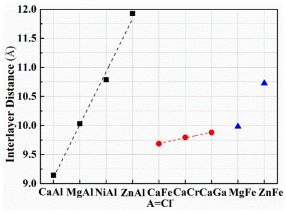

Figure 2 Interlayer distance between cationic layers in different LDHs (The dashed lines derived from linear fitting.)

3.2 Chloride ions binding energy and electrostatic interactions

The binding energy of an anion can reflect the ability of the anion to bind with LDHs. The average binding energies of anions in different LDHs are calculated according to this formula(Liu et al., 2020):

$$E_B = \frac{E_{LDH} - \langle N_{M^{2+}} E_{M^{2+}} \rangle - \langle N_{M^{3+}} E_{M^{3+}} \rangle - \langle N_{OH^-} E_{OH^-} \rangle - \langle N_{H_2O} E_{H_2O} \rangle - \langle N_{Cl^-} E_{Cl^-} \rangle}{N_{Cl^-}}$$

Where E_{LDH} means the total energy of LDHs; E_{M2+}, E_{M3+}, E_{OH-}, E_{H2O}, and E_{Cl-} are the energies of a single divalent cation, trivalent cation, hydroxyl, water molecule, and chloride ion; N_{M2+}, N_{M3+}, N_{OH-}, N_{H2O} and N_{Cl-} are the numbers of divalent cations, trivalent cations, hydroxyl, water molecules, and chloride ions in LDHs. The calculated results are shown in Tab. 1. All the values are negative. A more negative value means a stronger binding ability. The results indicate that the chloride ions in CaAl-Cl-LDHs possess the strongest ability to bind with structure and that in ZnFe-Cl-LDHs is the weakest. For LDHs with the same trivalent cations but different divalent cations, the absolute value of binding energy increases with the decrease in interlayer distance. While the absolute value of binding energies of LDHs with different trivalent cations does not increase linearly with interlayer distance. In other words, the types of divalent metal cations can influence the interlayer distance and binding energy of LDHs directly. As the interlayer distance is smaller, the chloride binding ability is stronger.

Table 1 Binding energies of different types of LDHs

LDHs	CaAl	MgAl	NiAl	ZnAl	CaFe	CaCr	CaGa	MgFe	ZnFe
Binding energy (eV)	-56.47	-53.56	-50.51	-47.22	-48.97	-48.90	-49.54	-46.13	-39.68

3.3 Chloride ion solidification in different types of LDHs

From the in-situ measurement by the ion selective electrode, the chloride ion concentration C_t can be read in real-time. Then the adsorption capacity (AC) is calculated as flows:

$$AC = \frac{(\frac{0.09mol}{L} - C_t) \times 0.07L}{0.75g}$$

The variation of chloride ion adsorption capacity with time is shown in Fig. 3. In the adsorption part (time <= 300 minutes), the adsorption rates of these four types of LDHs are different. The adsorption rate of CA was the fastest, followed by MA and ZA, and MF was the slowest. It can be seen from the above that all LDHs have a certain adsorption capacity, among which CA and ZA have certain advantages in adsorption capacity and adsorption rate. The maximum value of chloride ion adsorption capacity of CA (3.44 mmol/g) and ZA (2.62 mmol/g) was higher than those of MA (2.28 mmol/g) and MF (1.85 mmol/g) After the addition of Na2SO4 solutions (time > 300 minutes), chloride ion adsorption capacity decreased significantly. CA has the highest chloride ion desorption capacity, but the final chloride ion adsorption capacity of CA and ZA after sulfate addition is still higher than that of the other two types of LDHs. The chloride ion desorption ability of ZA (17.94%) is much lower than that of CA (44.48%), MA (33.97%), and MF (25.95%), indicating that ZA has excellent chloride ion solidification ability, while CA is the worst although it has the highest chloride ion capacity. The chloride ion adsorption and desorption mechanism in different types of LDHs will be discussed comprehensively thereinafter.

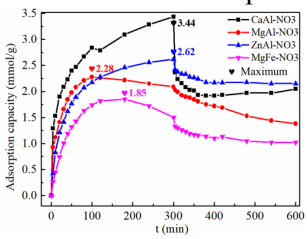

Figure 3 Chloride ion adsorption capacity of synthesized LDHs in different types of SCPSs

4. Conclusions

(1) Chloride ions binding energy of nine cationic types of $M^{II}M^{III}$-Cl-LDHs were calculated, indicating that CaAl-Cl-LDHs possess the strongest ability to bind chloride ions in structure and that in ZnFe-Cl-LDHs are the weakest.
(2) Four types of nitrate-hydrotalcite (CaAl-LDH, MgAl-LDH, MgFe-LDH, ZnAl-LDH) were synthesized by co-precipitation method and their chloride ion adsorption and desorption processes were compared in the simulated concrete pore solution. CaAl-LDH has the fastest adsorption rate, highest adsorption capacity, and strongest solidification ability of chloride ions. This corresponds to the first principles calculation results that CaAl-LDH has the highest chloride ions binding energy.

Acknowledgments

The authors thank the support of the projects Funded by the National Nature Science Foundation of China (No. 52072171), State Key Laboratory of High Performance Civil Engineering Materials (No. 2022CEM011), and the Priority Academic Program Development of Jiangsu Higher Education Institutions (PAPD). The computational resources generously provided by the High-Performance Computing Center of Nanjing Tech University are greatly appreciated.

References

Anglada, J.M. and Bofill, J.M. (1998) How good is a Broyden-Fletcher-Goldfarb-Shanno-like update Hessian formula to locate transition structures? Specific reformulation of Broyden-Fletcher-Goldfarb-Shanno for optimizing saddle points. Journal of Computational Chemistry 19, 349-362.
Chen, M., Wu, F., Yu, L., Cai, Y., Chen, H. and Zhang, M. (2019) Chloride binding capacity of LDHs with various divalent cations and divalent to trivalent cation ratios in different solutions. CrystEngComm 21, 6790-6800.
Liu, H.M., Zhao, X.J., Zhu, Y.Q. and Yan, H. (2020) DFT study on MgAl-layered double hydroxides with different interlayer anions: structure, anion exchange, host-guest interaction and basic sites. Phys Chem Chem Phys 22, 2521-2529.
Mir, Z.M., Bastos, A., Hoche, D. and Zheludkevich, M.L. (2020) Recent Advances on the Application of Layered Double Hydroxides in Concrete-A Review. Materials (Basel) 13.

Renaudin, G., Kubel, F., Rivera, J.P. and Francois, M. (1999) Structural phase transition and high temperature phase structure of Friedels salt, 3CaO center dot Al2O3 center dot CaCl2 center dot 10H(2)O. Cement and Concrete Research 29, 1937-1942.
Yang, L., Chen, M., Lu, Z., Huang, Y., Wang, J., Lu, L. and Cheng, X. (2020) Synthesis of CaFeAl layered double hydroxides 2D nanosheets and the adsorption behaviour of chloride in simulated marine concrete. Cement and Concrete Composites 114, 103817.
Yang, L., Zhao, P., Liang, C., Chen, M., Niu, L., Xu, J., Sun, D. and Lu, L. (2021) Characterization and adaptability of layered double hydroxides in cement paste. Applied Clay Science 211.

The 16th International Congress on the Chemistry of Cement 2023 (ICCC2023)
"Further Reduction of CO_2 -Emissions and Circularity in the Cement and Concrete Industry"
September 18–22, 2023, Bangkok, Thailand

Sulphate Attack of Concrete in Sewer System

H. Justnes[1*]

[1] *SINTEF Community, Trondheim, Norway*

Email: harald.justnes@sintef.no

ABSTRACT

Concrete in sewage systems is prone to sulphate attack in direct contact with sewage / waste waters due to the sulphate content, as well as indirectly above the water level due to oxidation of hydrogen sulphide by bacteria to hydrogen sulphate (sulphuric acid). The situation above the water level is considered worse due to simultaneous action of neutralization by the strong acid followed by sulphate attack forming expanding products like gypsum and ettringite as well as thaumasite at temperature < 15°.

The paper presents a case study of a concrete manhole that have been in operation since 2000. The microstructure of both mortars was studied by scanning electron microscopy and energy dispersive spectra of details for composition. The deterioration mechanism is oxidation of hydrogen sulphide to sulphuric acid as the concentration of H_2S was monitored in the manhole over some time (periodically 20-30 ppm). The outer layer was deteriorated 17-18 mm from the surface of today (neglecting former scaling). The deteriorated layer had large deposits of pure gypsum due to direct attack of sulphuric acid and it does not seem that ettringite was stable in this layer. Both ettringite and thaumasite was however found just below the layer of direct acid attack and often filling air voids to the rim. The mechanism of this sulphate attack is discussed.

KEYWORDS: *Sewage, sulphate attack, ettringite, thaumasite, gypsum*

1. Introduction

Sewer networks are critical urban infrastructures of modern societies, performing the safe transport of sewage from domestic and industrial sites to treatment facilities. However, concrete corrosion caused by the biogenic sulfuric acid, derived from the oxidation of gaseous hydrogen sulphide, is a major deteriorating process in sewer systems (Song et al., 2019). The U.S. Environmental Protection Agency (EPA) states that microbially induced concrete corrosion (MICC) can reduce the 50-100 year expected sewer service life to less than 10 years.
The reduction of sulphate (SO_4^{2-}) in the presence of waste organic matter (carbon) proceeds by desulfovibrio bacteria as follows:

$$2C\ (\text{organic matter}) + 2\ H_2O + SO_4^{2-} = H_2S + 2\ HCO_3^- \quad (1)$$

Sulphate-reducing bacteria thrive in the slime layer that coats the inner wet pipe wall. Oxygen cannot normally penetrate this layer, leading to the formation of an inert anaerobic zone next to the pipe wall where the sulphides are formed. Hydrogen sulphide in the atmosphere can be oxidized on moist surfaces by bacteria, producing sulfuric acid by the bacteria *Thiobacillus thiooxidans* according to the following reaction (Meyer 1980):

$$H_2S + 2\ O_2 = H_2SO_4 \quad (2)$$

This can lower the pH value on the surface to 1.0 or even lower and can cause a very strong acid attack.

2. Experimental

Concrete cores were drilled from a concrete manhole of a sewer system that had been in operation since 2000. The core was sawn along the axis, epoxy impregnated and 40x20 mm thin sections were made from the surface inwards. Such thin sections without covering glass are suitable for investigation both by optical and scanning electron microscopy (SEM). The paper focuses on the results from the SEM analyses which show compositional details and are verified by energy dispersive spectra (EDS).

3. Results and discussion

The investigated manhole has been in service since 2000 (22 years) and the last few months prior to the investigation a H_2S level of 20-30 ppm was measured in the air above the water level. Fig. 1 (left image) shows how porous and degraded the surface is, while the right image shows a pore where pure gypsum is growing inwards. There is otherwise a lot of light grey gypsum embedded in a dark binder which is now a silica gel nearly without calcium (decalcified) derived from the original C-S-H.

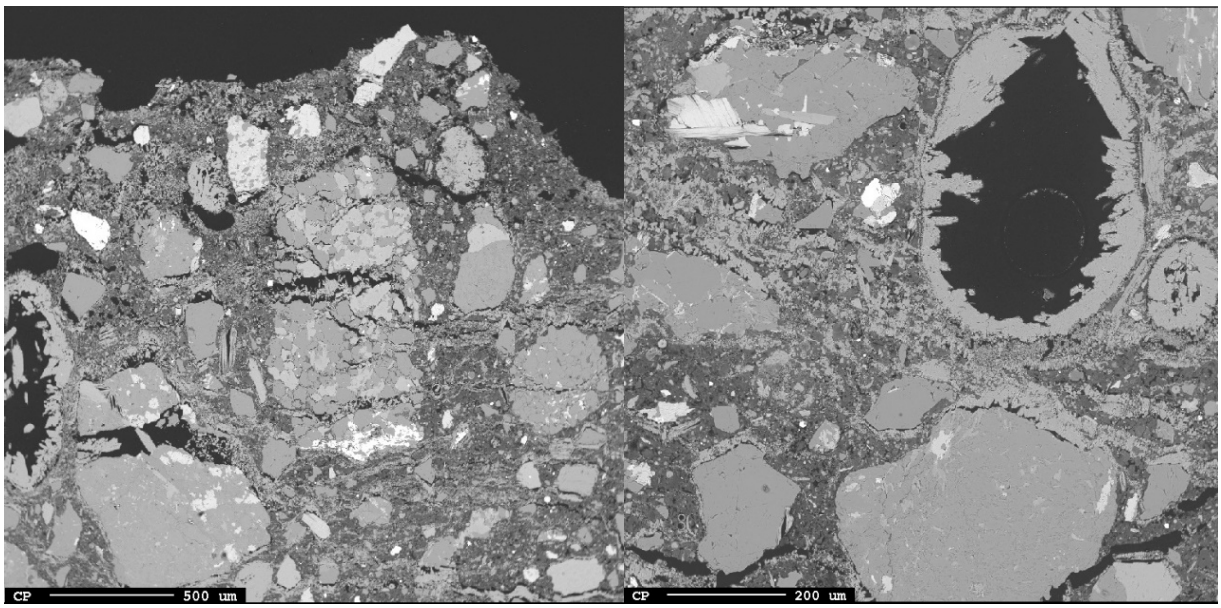

Fig. 1 – The concrete surface to the left showing how deteriorated the binder is, including splitting of sand grains. The light grey streaks in the dark binder is pure gypsum and the dark grey is C-S-H nearly totally decalcified by the sulphuric acid. The right image show a pore (black) in the upper right quadrant with light grey gypsum growing into the pore.

Fig. 2 indicates that the acid attack goes into about 17 mm from the surface seen as darker more porous zone next to a lighter grey denser zone. Two pores filled to the rim by thaumasite are pointed out by arrows along with the EDS confirming only Ca, Si and S (along with C and O) as proof of thaumasite; $Ca_3Si(OH)_6(CO_3)(SO_4)\cdot 12H_2O$. The calcium and silicon come from the C-S-H, sulphate from gypsum (or sulphuric acid) and the carbonate from either carbonation or added limestone filler. A higher magnification of the two pores with thaumasite is shown in Fig. 3.
The left image of Fig. 4 shows an apparently sound binder about 30 mm from the surface, while the image to the right shows a small air void of 60 µm diameter that is filled to the rim by a mixture of ettringite and thaumasite. This indicates that you can get a sulphate attack even at this depth. Even though the acid (H^+) does not influence at this depth, apparently the sulphate ions (SO_4^{2-}) can diffuse to this level. The sulphuric acid formed in Eq. 2 can form gypsum both in reaction with C-S-H and calcium hydroxide:

$$H_2SO_4 + Ca(OH)_2 = CaSO_4\cdot 2H_2O \quad (3)$$

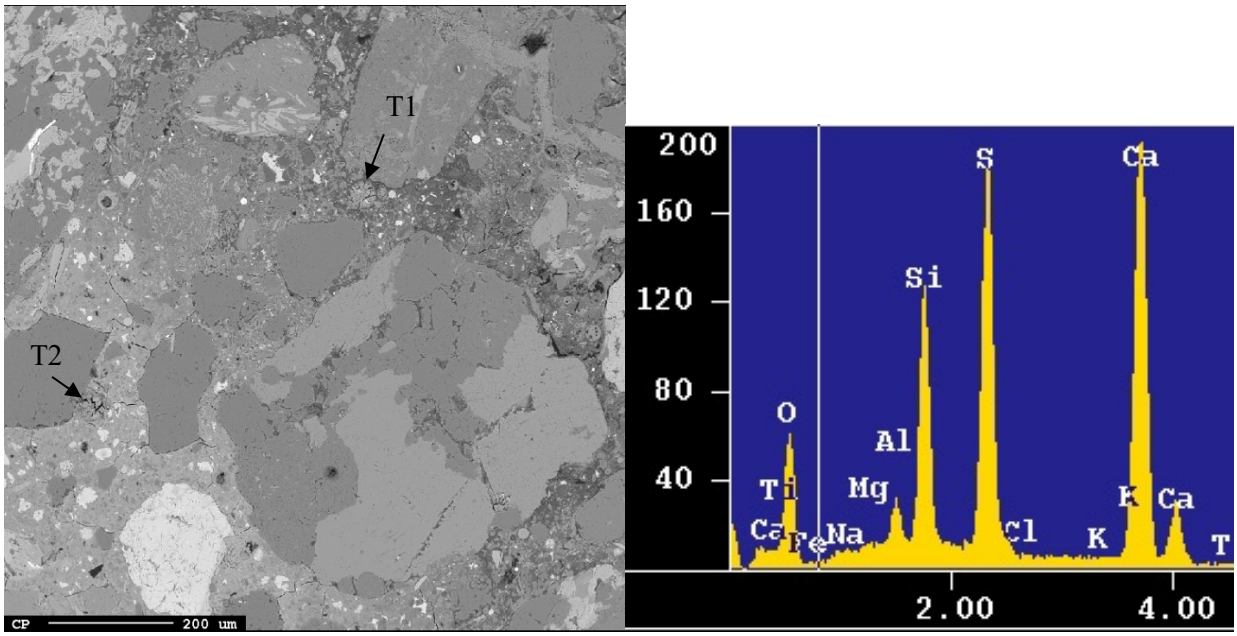

Fig. 2 – The left image shows the borderline between a darker, more porous binder and a lighter grey denser binder. The surface is about 17 mm from the top of the image. The arrows T1 and T2 are pointing at two pores filled with thaumasite and the image to the right shows the EDS from pore T2 proving thaumasite by Ca, Si and S along with nearly no Al. The weak carbon signal is to the left of oxygen peak.

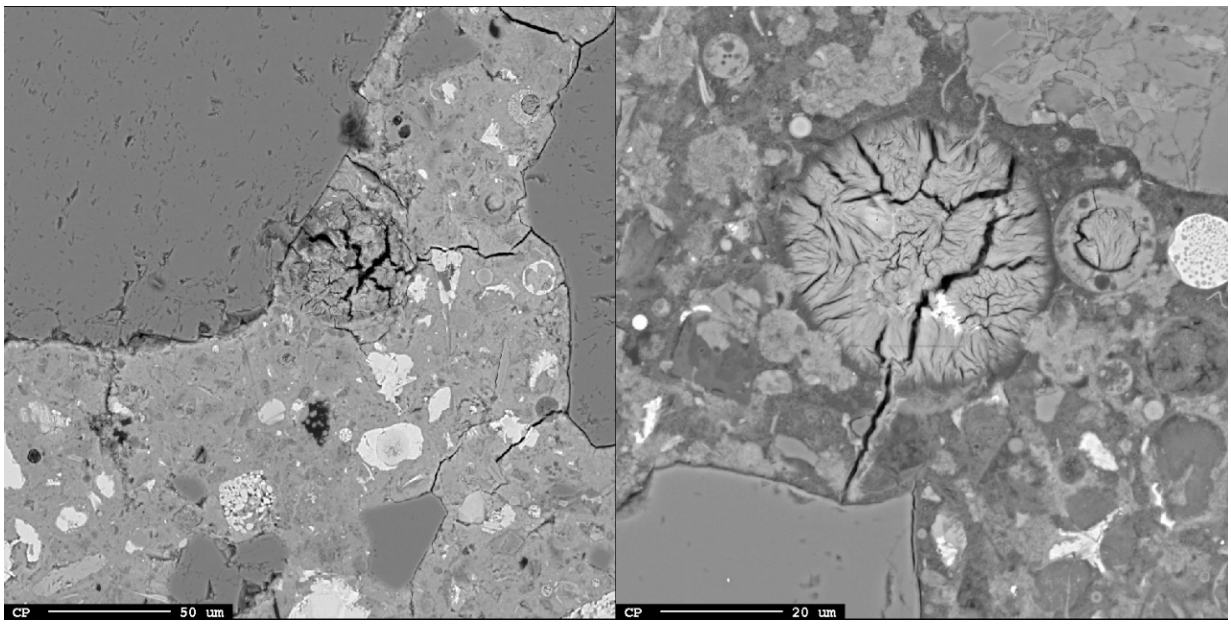

Fig. 3 – Enlargement of the two pores filled with thaumasite from Fig. 3 with the image of T2 to the left and T1 to the right. It is evident from the darker colour of the binder in the right image, that the C-S-H is partly de-calcified. The cross-section of spheres to the right of T2 shows that the cement used for the concrete was blended with fly ash.

After 22 years in serice the manhole concrete is deteriorated to a depth of 17-18 mm and sulphate affected to a depth of 32 mm. The manhole is still in service at the same conditions and the progress of deterioration will be followed up over time. Later the performance of this manhole will be compared to another manhole where the concrete has been added an admixture that should prevent MICC. It is also known that calcium aluminate cement (CAC) is more resistant to MICC than OPC (Grengg et al., 2018).

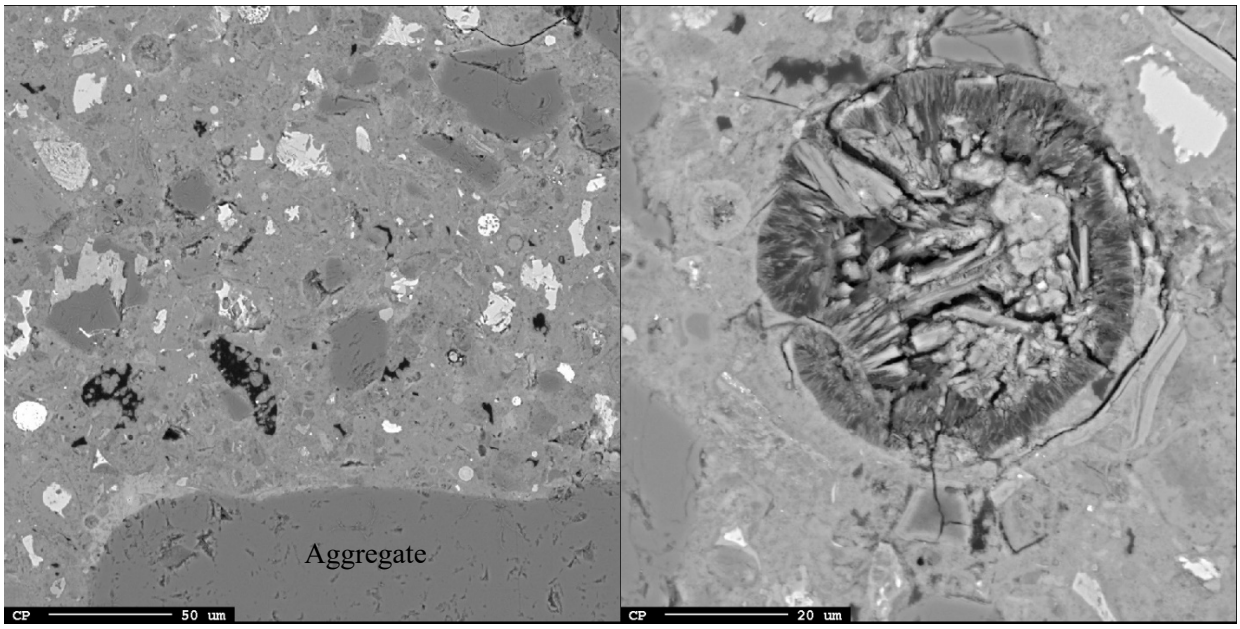

Fig. 4 – The left image shows an overview of a dense binder without microcracks at about 30 mm from the surface that seemingly is unaffected by sulphates. The right image, on the other hand, shows a pore about 32 mm from the surface that are filled to the rim with a mixture of thaumasite and ettringite indicating that the sulphate can influence even so far from the surface. Note the difference in scale bars in the lower left corner of the two images. The nearly white particles with ireggular shapes in the left images is mostly unreacted cement, while the circular ones are crossection of spherical fly ash grains.

4. Conclusions

Oxidation of hydrogen sulphide to sulphuric acid above water level in a sewer led to a strong acidic attack of the concrete surface of a manhole to a depth of 17-18 mm after 22 years in service. In the acid etched zone, only gypsum was stable as sulphate bearing compound and cracks were formed even splitting sand grains. Beyond the acid affected zone both ettringite and thaumasite could form since the temperature in Norway quite often is < 15°C, which is the limiting condition for formation of thaumasite (Justnes, 2003)).

References

Justnes, H. (2003) "Thaumasite f ormed by sulfate attack on mortar with limestone filler", *Cement and Concrete Composites*, 25; 955-959.

Grengg, C., Mittermayer, F., Ukrainczyk, N., Koraimann, G., Kienesberger, S. and Dietzel, M. (2018) "Advances in concrete materials for sewer systems affected by microbial induced concrete corrosion: A review." *Water Research*, 134; 341-352.

Meyer, W.J. (1980) "Case study of prediction of sulphide generation and corrosion in sewers." *Journal WPCF*, 52 (11); 2666-74.

Song, Y., Tian, Y., Li, X., Wei, J., Zhang, H., Bond, P.L., Yuan, Z. and Jiang, G. (2019) "Distinct microbially induced concrete corrosion at the tidal region of reinforced concrete sewers", *Water Research*, 150; 392-402.

The 16th International Congress on the Chemistry of Cement 2023 (ICCC2023)
"Further Reduction of CO_2 -Emissions and Circularity in the Cement and Concrete Industry"
September 18–22, 2023, Bangkok, Thailand

Effects of Mixed salt in Saline Soil on the Microstructural Evolution of Cement Paste

H.T. Liao, H.D. Wang, Y. Li*, T.J. Liu*

School of Civil and Environmental Engineering, Harbin Institute of Technology, Shenzhen, China

Email: 21b954010@stu.hit.edu.cn (H.T. Liao), 15818602282@163.com (H.D. Wang), liye@hit.edu.cn (Y. Li), liutiejun@hit.edu.cn (T.J. Liu)

ABSTRACT

This thesis investigates the effects of Cl^-, and Mg^{2+} ions in saline soil on the microstructural formation and evolution of early-age cement paste. Cement paste samples are exposed to aggressive salt solutions since the mixing stage or after 14 days of water curing. Several analytical techniques, including scanning electron microscopy (SEM), X-ray diffraction (XRD), thermogravimetry-derivative thermogravimetry (TG/DTG), and mercury intrusion porosimetry (MIP), are employed to examine the phase assemblage, morphology, porosity, and micromechanics of the cement paste after salt-affected hydration. The results suggest that exposure to Cl^- since the mixing stage leads to denser microstructures with reduced porosity. The presence of Mg^{2+} ions further enhances this reduction in porosity. The solutions containing Mg^{2+} ions cause the consumption of calcium hydroxide to form magnesium hydroxide. The Cl^- ions increase the degree of hydration of the cement paste, whereas the combined effect of Mg^{2+} ions leads to a delay in the hydration reaction of the cement.

KEYWORDS: *Salt attack, early-age, microstructure*

1. Introduction

Transportation projects in highland areas often rely on cast-in-place concrete for foundations, roads, and tunnels due to the difficulty of transporting precast concrete to remote construction sites. While cast-in-place concrete can be used anywhere, its early hydration stages are crucial and can be impacted by external environmental factors. Saline soils with high levels of chloride, sulfate, and magnesium ions are common in highland areas, and these ions can modify the microscopic components and microstructure of early-age cement mortars. This can lead to varying degrees of initial microstructural damage, posing a serious challenge to the safe service and durability of major transport projects.

While concrete is subject to salt attack by aggressive ions throughout its service life, existing literature has primarily focused on the long-term damage caused by chloride or sulfate attack (Ikumi et al., 2019). Although some studies have investigated the mechanisms of concrete deterioration under the combined effects of chloride and sulfate attack, most research has been conducted on precast cement samples (Maes et al., 2014). Consequently, there is a gap in research regarding the effects of Cl^-, Mg^{2+}, and their combined impact, which are present in saline soils, on cement hydration during cast-in-place concrete construction in remote areas.

This paper addresses this gap by developing corrosion conditions with different curing and corrosion days to examine the hydration and hardening process of early-age cast-in-place concrete in saline soil environments. The material's microstructure morphology, pore structure, and physical phase composition were analyzed using XRD, MIP, SEM, and TG/DTG to investigate the impact of the onset of corrosion time and multi-ion coupled corrosion on the early-age cement mortar.

2. Materials and experimental program

2.1 Materials and sample preparation

For this test, PII 52.5 Portland cement from Onoda Cement Co. was utilized. All salts used to prepare the solutions were analytically pure inorganic salts from Sinopharm. The cement mortar was prepared using a ratio of cement to water of 1:0.35. Distilled water, 7% $MgCl_2$ solution and 7% NaCl solution were used to mix the cement and immerse the cement paste specimens. The thickness of the cement mortar was controlled at 2 mm to circumvent the size effect. After pouring, the cement paste specimens were left to set at room temperature for 24 hours before being demolded and placed in the liquid for curing and corrosion for a total of 28 days. Table 1 shows the details of the specimens and solutions.

Table 1 The details of specimens and solutions.

Group	Mixing solution	Immersion condition
Plain	Distilled water	28 days of water curing
Mix-NaCl	7% NaCl solution	28 days in 7% NaCl solution
Mix-$MgCl_2$	7% $MgCl_2$ solution	28 days in 7% $MgCl_2$ solution
External-NaCl	Distilled water	14 days of water curing + 14 days in 7% NaCl solution
External -$MgCl_2$	Distilled water	14 days of water curing + 14 days in 7% $MgCl_2$ solution

2.3 Characterization methods

After 28 days of salt-affected hydration, an analysis of the phase assemblage, morphology, porosity, and micromechanics of the cement paste was conducted using various methods, including scanning electron microscopy (SEM), X-ray diffraction (XRD), thermogravimetry-derivative thermogravimetry (TG/DTG), and mercury intrusion porosimetry (MIP). Before conducting characterization methods, the cement mortar samples were soaked in isopropanol reagent for 24h to stop hydration, and then were dried in an oven at 40 °C for 24 h and lastly ground into powder. The details of these characterization methods can be found in our previous research (Zou et al., 2021).

3. Experimental results

3.1 Porosity and pore size distribution

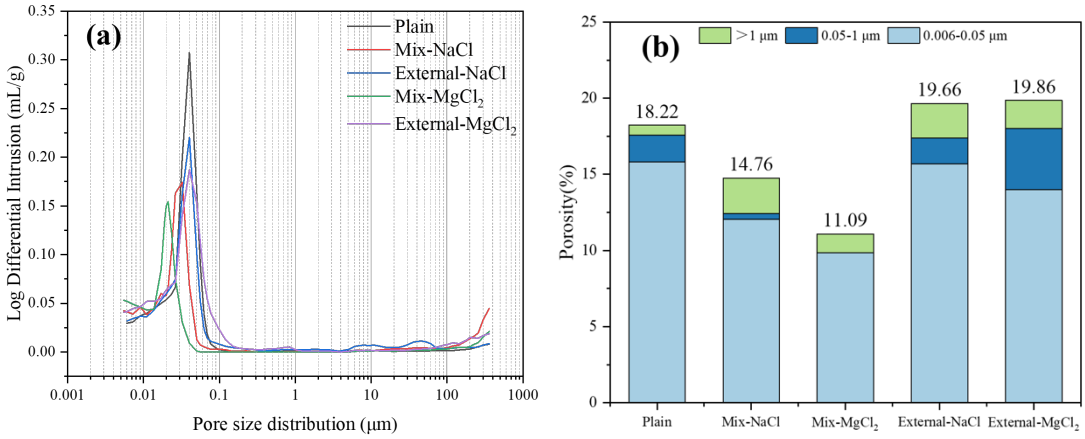

Fig. 1 (a) Pore size distribution and (b) porosity of the cement mortars.

Figure 1 presents the results of the MIP tests, showing the pore size distribution and porosity. As depicted in Figure 1(a), the pore sizes in all groups were predominantly below 0.1 μm, with Mix- $MgCl_2$ exhibiting the smallest peak pore size. Moreover, the addition of NaCl or $MgCl_2$ solutions during the mixing stage decreased the porosity of the cement paste after 28 days of hydration, resulting in a denser internal structure, as indicated in Figure 1(b). Notably, the use of $MgCl_2$ solution had a more pronounced effect on reducing porosity, with most of the pore sizes ranging from 0.006 to 0.05 μm in diameter, which may due to the production of $Mg(OH)_2$ and Friedel's salt. However, exposing the cement paste to NaCl or $MgCl_2$ solutions after 14 days of hydration did not significantly alter its porosity, with only a slight increase observed after

28 days of hydration. Furthermore, exposure to $MgCl_2$ increased the percentage of 0.05-1 μm pores from 9.62% to 20.64%, compared to the use of NaCl.

3.2 Microstructure observations

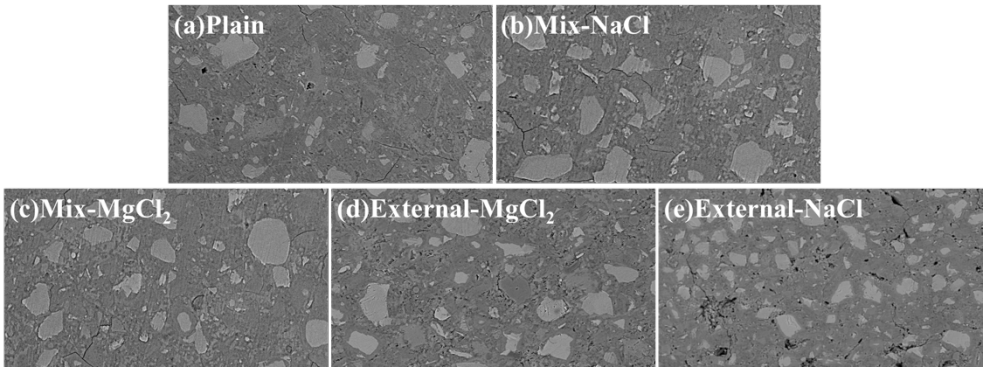

Fig. 1 The microstructure of the cement mortar

The SEM results in Fig. 2 demonstrate that exposing the net cement paste to NaCl and $MgCl_2$ solutions during the mixing stage results in a dense cement matrix, as observed in Fig. 2(b) and (c) compared to the other groups. However, as shown in Fig. 2(d) and (f), exposing the net cement paste to NaCl solution and $MgCl_2$ after 14 days of water curing causes a large number of pores and cracks in the cement matrix at 28 days of age, leading to an increase in initial damage. This observation is consistent with the MIP results.

3.3 Chemical composition

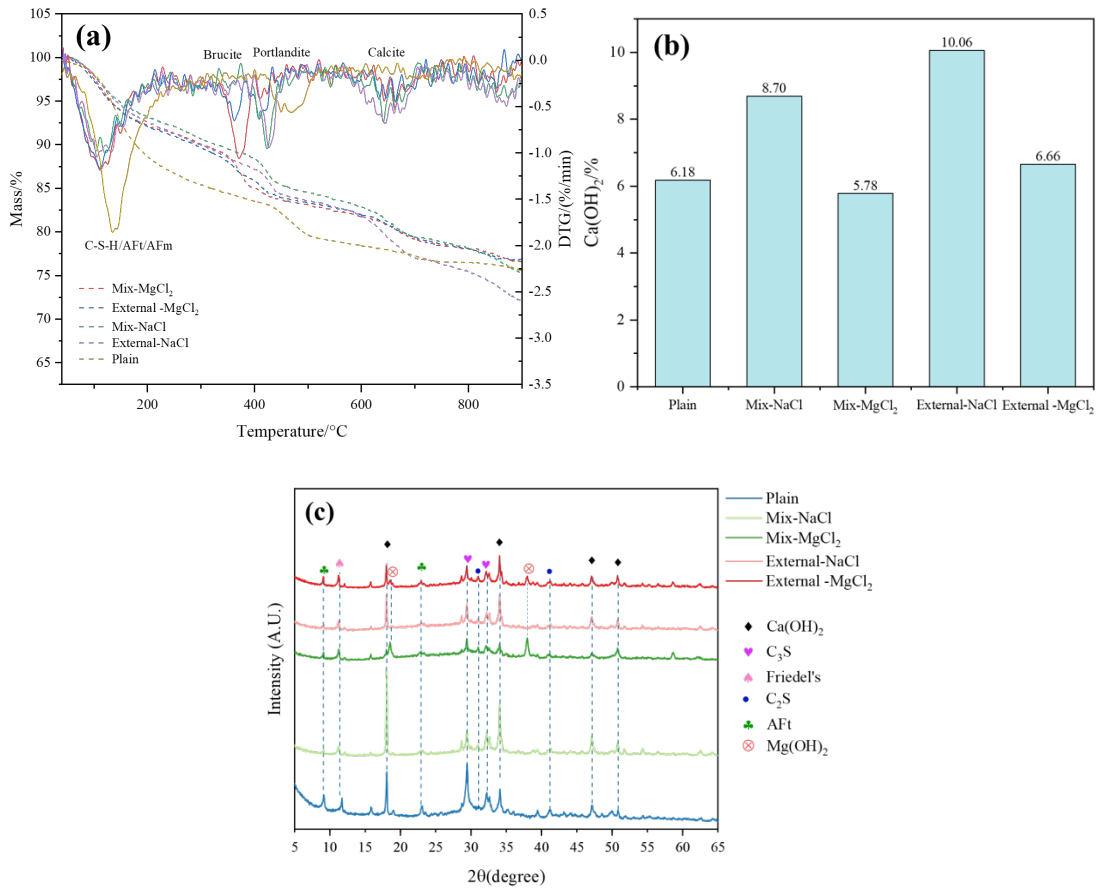

Fig. 3 The (a)TG results, (b)$Ca(OH)_2$ content and (c)XRD results of the cement paste

Fig. 3 presents the X-ray diffraction (XRD) and thermogravimetric (TG) results of the cement paste. The XRD data reveal that the salt-affected paste contains $Ca(OH)_2$, $Mg(OH)_2$, Aft, Friedel's salt, and unhydrated cement. Notably, the $Ca(OH)_2$ peaks around $2\theta=18°$ are markedly higher in the Mix-NaCl group than in the other groups, indicating that the involvement of Cl^- in the hydration reaction has a greater impact on the cement's hydration products than external corrosion. This effect generates a considerable amount of $Ca(OH)_2$. Given that $Ca(OH)_2$ formation positively correlates with the degree of hydration, it's suggested that exposure to Cl- ions during the mixing stage and after 14 days of hydration increase the degree of hydration (Mo et al., 2016). The XRD data also reveal that the earlier the onset of corrosion, the lower the $Ca(OH)_2$ content and the higher the $Mg(OH)_2$ content in the cement, as evidenced by the $Ca(OH)_2$ and $Mg(OH)_2$ peaks in Fig. 3(b).

In the TG results in Fig. 3(a), weight loss peaks for C-S-H, AFt, AFm, $Ca(OH)_2$, $Mg(OH)_2$, and $CaCO_3$ are evident. $Ca(OH)_2$ production was calculated from 400°C-500°C ($Ca(OH)_2$ decomposition) and 550°C-750°C ($CaCO_3$ decomposition), as $Ca(OH)_2$ was partly carbonized to form $CaCO_3$ (Kriskova et al., 2012). The $Ca(OH)_2$ content in Fig. 3(b) indicates that Cl- ion addition enhances hydration in both the case of salt mixed and external salt attack. However, when the cement paste is exposed to $MgCl_2$ during the mixing stage or after 14 days of hydration, the coupling effect of Mg^{2+} ions significantly inhibits $Ca(OH)_2$ production during early hydration, leading to a delay in the cement's hydration reaction and decreasing the degree of hydration. This finding is consistent with the XRD analysis in this study.

5. Conclusions

This study investigated the effects of Cl^- and Mg^{2+} ions in saline soil on the microstructural formation and evolution of early-age cement paste. The results indicated that exposure to Cl^- since the mixing stage leads to denser microstructures with reduced porosity, while the presence of Mg^{2+} ions further enhances this reduction because of the production of $Mg(OH)_2$ and Friedel's salt. The solutions containing Mg^{2+} ions cause the consumption of calcium hydroxide to form magnesium hydroxide. The Cl^- ions increase the degree of hydration of the cement paste, whereas the combined effect of Mg^{2+} ions leads to a delay in the hydration reaction of the cement. This study has important implications for cast-in-place concrete construction in remote areas with saline soils containing high concentrations of chloride and magnesium ions. By understanding the effects of these ions on cement hydration, appropriate measures can be taken to ensure the safe service and durability of transport projects in highland areas.

Acknowledgements

This work was supported by the National Key Research and Development Program of China (Grant No. 2021YFFO500801), the National Science Fund for Distinguished Young Scholars of China (Grant No.52025081), and the Shenzhen Science and Technology Innovation Program of China (Grant RCYX20200714114525013).

References

Ikumi, T., and Segura, I. (2019). "Numerical assessment of external sulfate attack in concrete structures. A review". *Cement and Concrete Research*, 121: 91-105.

Kriskova, L., Pontikes, Y., Cizer, Ö., Mertens, G., Veulemans, W., Geysen, D., and Blanpain, B. (2012). "Effect of mechanical activation on the hydraulic properties of stainless steel slags". *Cement and Concrete Research*, 42(6): 778-788.

Maes, M., and De Belie, N. (2014). "Resistance of concrete and mortar against combined attack of chloride and sodium sulphate". *Cement and Concrete Composites*, 53: 59-72.

Mo, L., Zhang, F., and Deng, M. (2016). "Mechanical performance and microstructure of the calcium carbonate binders produced by carbonating steel slag paste under CO2 curing". *Cement and Concrete Research*, 88: 217-226.

Zou, D.J., Qin, S.S., Liu, T.J., Jivkov, A. (2021) "Experimental and numerical study of the effects of solution concentration and temperature on concrete under external sulfate attack", *Cement and Concrete Research*, 139: 106284.

The 16th International Congress on the Chemistry of Cement 2023 (ICCC2023)
"Further Reduction of CO_2 -Emissions and Circularity in the Cement and Concrete Industry"
September 18–22, 2023, Bangkok, Thailand

Physicochemical stability of calcium aluminate cement and hemihydrate-based material exposed to deep sea

T. Akitou[1*], K. Takahashi[2]

[1] *Mitsubishi UBE Cement Corporation, Ube, Japan*
Email: Tetsu.akito@mu-cc.com
[2] *Mitsubishi UBE Cement Corporation, Ube, Japan*
Email: keisuke.takahashi@mu-cc.com

ABSTRACT

In recent years, ocean utilization such as construction of offshore wind power generation and tidal power generation and development of seabed mineral resource has attracted much attention. Cementitious materials can be used as one of the base materials for these applications. Previously the authors reported that deterioration behaviour of a Portland cement mortar under deep sea differed from shallow sea due to the low temperature and high hydraulic pressure. The focus of this study is to investigate the physicochemical stability of a hardened binary binder paste consisting of calcium aluminate cement and hemihydrate exposed to a depth of 1,882 meters. The specimen consisting mainly of ettringite were recovered after 295 days of exposure. The recovered specimen did not show any microstructural fracture as observed in the Portland system. However, compositional analysis of the cross section by EPMA showed that ettringite decomposed to form Mg-containing hydrates in the surface layer of the specimen. Interestingly, chlorine was only detected penetrating up to 9 mm from the surface layer. This binary binder system could be a new option for the use of cementitious materials in deep sea applications.

KEYWORDS: *Deep sea, calcium aluminate cement, hemihydrate, durability, sea water attack*

1. Introduction

In recent years, much attention has focused on the utilization of the ocean for the construction of floating wind and tidal power generation facilities and the development of offshore mineral resources. The authors are investigating the use of cementitious materials as base materials for the construction of these structures. The authors reported that long-term exposure of Portland cement (PC) materials to deep-sea floor, which is a special environment of low temperature and high pressure, resulted in significant deterioration compared to those exposed to shallow sea (Kobayashi et al. 2021). Furthermore, a ternary-binder system consisting of calcium aluminate cement (CAC), PC, and anhydrite prevented calcium leaching, but the penetration of chloride ions caused the formation of Friedel's salt from monosulfate, which also produced a lot of ettringite, resulting in extremely large expansion of the specimen (Kobayashi et al. 2022). In this paper, a binary cement paste specimen consisting of calcium aluminate cement and hemihydrate (HH), which was designed to mitigate chloride ion penetration and also decrease monosulfate formation owing to a sulfur-rich condition in the specimen, was exposed to a deep seafloor at a depth of 1,882 m. Specimens recovered after 295 days were analyzed to evaluate their physicochemical properties.

2. Experimental

2.1 Materials

A high alumina CAC consisting of $CaO\text{-}Al_2O_3$ and $2CaO\text{-}Al_2O_3$ was used. The paste contained CAC, HH (30 wt% of CAC), water, acrylic acid-based dispersant, gum-based viscosity modifying agent (VMA), and setting regulators (sodium tartrate and lithium sulfate). The main hydrates were ettringite, monosulfate and aluminium hydroxide (gibbsite). The water to cement ratio was 0.6. The size of the specimens was 40 mm × 40 mm × 160 mm. The specimens were cured for 91 d at 20 °C under sealed conditions before exposure.

2.2 Testing field and related conditions

Exposure tests on the deep seafloor were conducted at a depth of 1,882 m at Nankai Trough Kumano-nada, Japan for 295 days from January to Novenber 2021. Three paste specimens were set on the seafloor using a remote oparated vehicle KM-ROV. The temperature and salinity of seawater at the exposure site were 2.2 °C and 34.6 PSU, respectively. After 295 days of exposure, the specimens were salvaged by KM-ROV. The descension and acension speed of the vehicle was approximately 50 m/min and 30 m/min, respectively. Three paste specimens were immersed in a laboratory-scale seawater tank (216 L) at ambient pressure to investigate the effect of hydraulic pressure on the property changes of the hardened paste. The seawater temperature in the tank was maintained to 2 °C using a heat exchanger. Seawater in the tank was supplied from a shallow sea area near the laboratory and replaced approximately every 24 h.

2.3 Analytical methods for specimens

The length and weight of the specimens were measured according to JIS A 1129. Changes in the length and weight of the specimens immersed in the laboratory were measured at 44, 98, 160, and 295 days. Expansion was considered a positive change in length and the gauge length was 100 mm. The specimens were cut near the center and its cross-section was mapped for elemental distribution by electron probe micro analyzer (EPMA). The specimens were cut from the surface to the center into three areas (0-5mm, 5-10mm and 10-20mm), which were referred to as areas A, B and C. The specimens from the three areas were subjected to mineral identification by X-ray diffraction (XRD). All specimens were dried and stopped hydration with isopropanol prior to measurement.

3. Results

3.1 Visible specimen and dimensional changes

The specimen after retrieval is shown in Fig. 1. Although the specimens recovered from deep seafloor (referred to as “deep-sea specimens”) showed fine cracks on the surface, there was no significant mudding as observed in the Portland cement system. The specimens immersed in a seawater tank inside the laboratory (referred to as “laboratory specimens”) had no visible fine cracks.

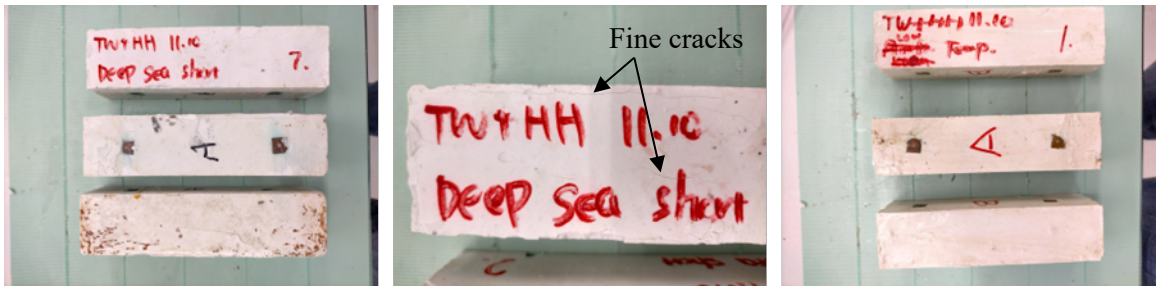

Fig. 1 View of the recovered specimens (*left*: deep-sea specimens, *right*: laboratory specimens). The specimen recovered from the deep sea had fine cracks on the surface (*center*).

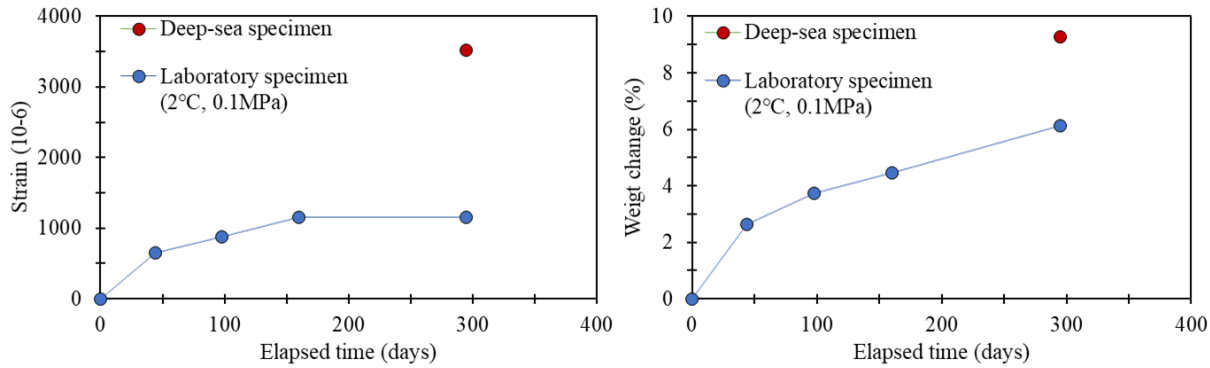

Fig. 2 The changes in the strain *(left)* and weight (*right*) of the specimens

Figure 2 shows the changes in the strain and weight of the specimens as a function of the exposure/immersion time. The deep-sea specimens showed a larger strain and higher weight gain than the laboratory specimens. The strain and weight gains of the laboratory specimen first increased quickly and then continued to increase slowly. These results indicate a good correlation between seawater uptake into the specimen and its expansion.

3.2 Chemical characterization

Figure 3 shows the EPMA results of the cross-section analysis for each element. Deep-sea specimens and laboratory specimens showed similar trends. Near the surface, the concentrations of calcium and sulfur decreased, while the concentrations of chlorine, sodium and magnesium increased. It is observed that the changes in elemental concentrations were more pronounced in the deep-sea specimens than in the laboratory specimens. Chlorine penetrated 9 mm from the surface in the deep-sea specimens and 5 mm from the surface in the laboratory specimens. Aluminum concentrations were constant regardless of depth. Figure 4 shows the XRD peak diagrams of the specimens. The deep-sea specimens showed a clear peak of Friedel's salt in area A (0-5mm), while the laboratory specimens showed a somewhat indistinct peak. This is consistent with the results of the EPMA elemental diagrams, and some of the monosulfate peaks around 10° may contain Kuzel's salt. No significant Friedel's salt peaks were identified in areas B (5-10 mm) and C (10-20 mm). At the superficial layers of both specimens, the calcium-containing hydrates that were originally present dissolved and decomposed, and products containing magnesium, sodium, aluminum, sulfur, and chlorine could be precipitated. Since gibbsite forming the binder phase was stable against the pH decrease (Gayer et al. 1958), the dissolution or decomposition of hydrates near the surface layer would not have affected the aluminum concentration. As a result of the gibbsite not being decomposed, there may have been no significant damage to the specimen's appearance.

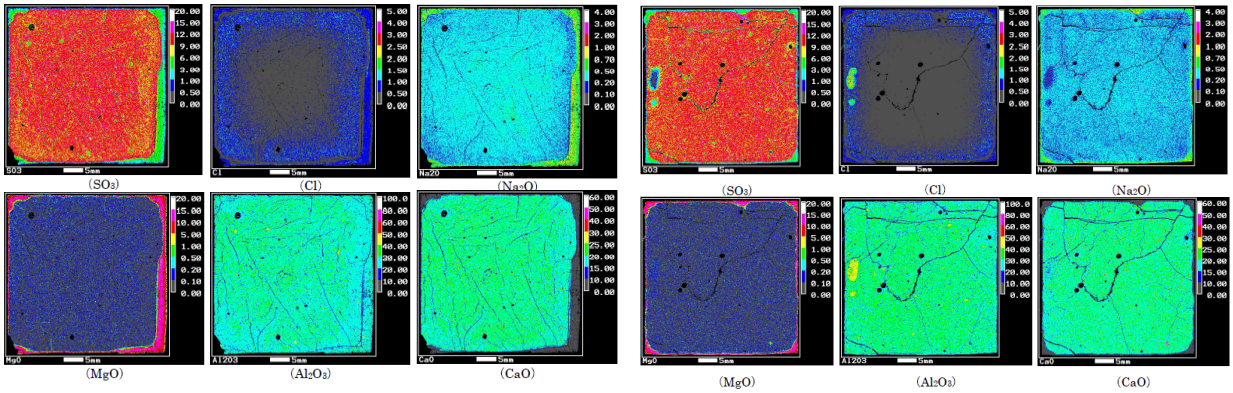

Fig. 3 The EPMA results of the cross-section analysis for each element (unit: mm). *left*: deep-sea specimen, *right*: laboratory specimen. SO_3, Cl, Na_2O, MgO, Al_2O_3 and CaO were analyzed for each specimen. The color bar presents the concentration range (unit: wt.%). Calcium was dissolved at 0.5-2.5 mm from the surface in the deep-sea specimens and at less than 1 mm in the corner of the laboratory specimens.

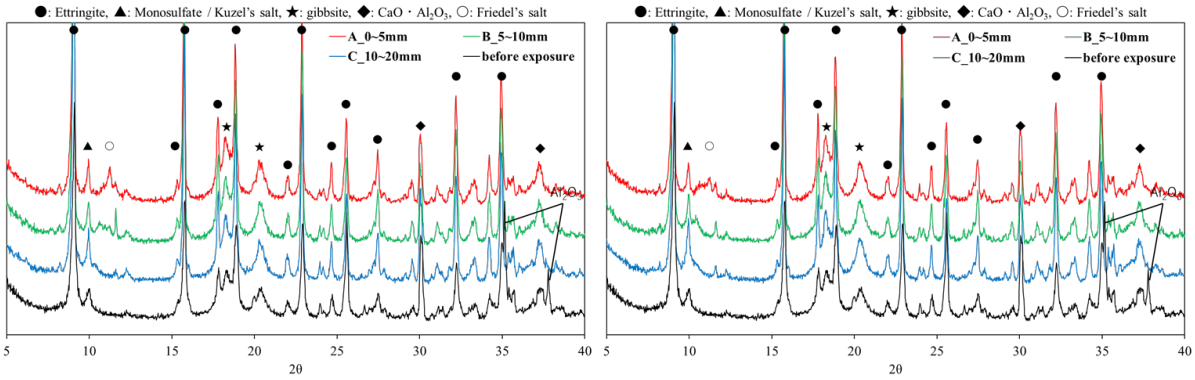

Fig. 4 The XRD patterns of the specimens. *left*: deep-sea specimen, *right*: laboratory specimen.

Further investigation of the relationship between changes in hydrate in the specimens and hardened physical properties is needed, taking into account the pore structure and other factors. At inner of the specimen, seawater penetration could decrease pH, and the unstable monosulfate and ettringite reacted with chloride ions in the seawater to form Friedel's salt and Kuzel's salt. Since liquid water penetration is enhanced under high hydraulic pressure conditions (Kawabata et al. 2022 and Takahashi et al. 2021), the deep-sea specimens were more strongly affected by seawater than the laboratory specimens. This may have resulted in the differences in element concentrations between the specimens shown in Figure 3. However, chlorine was fixed up to 9 mm from the surface layer, even in the deep-sea specimens, and the amount of chloride fixation was minimal. This suggests that the binary binder-based materials used in this study are more resistant to chloride ion penetration than the Portland and the ternary binder system.

3. Conclusions

Analysis of a binary binder paste specimens consisting of CAC and HH exposed to a deep seafloor at a depth of 1,882 m for 295 days showed that seawater penetration caused hydrate changes in the surface layer of the specimens. Chlorine was hardly fixed at depths deeper than 9 mm from the surface layer of the deep-sea specimens, and the appearance of the specimens showed no noticeable damage, although there were some fine surface cracks. This suggests that the binary-binder based material consisting of CAC and HH used in this study may be one candidate cementitious material for use on the deep seafloor. The effects of hydrate changes on the physicochemical properties of the hardened material should be studied continuously in the future.

Acknowledgements

We would like to thank Dr. Toshinori Kimura, Dr. Shuhei Nishida, Takashi Yokobiki and Dr. Eiichiro Araki from JAMSTEC for their assistance in conducting the deep-sea field tests and Dr. Yuichiro Kawabata from Port and Airport Research Institution for his assistance in conducting the laboratory tests.

References

Kobayashi, M., Takahashi, K., and Kawabata, Y. (2021) "Physicochemical properties of the Portland cement-based mortar exposed to deep seafloor conditions at a depth of 1680 m", *Cement and Concrete Research*, 142: 106335

Kobayashi, M., Takahashi, K., Kawabata, Y., and Bier, T.A. (2022) "Physicochemical properties of Portland cement/calcium aluminate cement/calcium sulfate ternary binder exposed to long-term deep-sea conditions", *Materials and Structures*, 55: 182

Gayer, K.H., Thompson, L.C., Zajicek, O.T., (1958) "The solubility of aluminum hydroxide in acidic and basic media at 25 ºC", *Canadian Journal of Chemistry*, 36, 9

Kawabata, Y., Takano, D., Takahashi, K. and Iwanami, M. (2022) "In situ observation for the influence of hydraulic pressure on internal damage of cement-based materials", *Materials & Design*, 216: 110556

Takahashi, K., Kawabata, Y., Kobayashi, M., Gotoh, S., Nomura, S., Kasaya, T., and Iwanami, M. (2021) "Action of hydraulic pressure on Portland cement mortars – current understanding and related progress of the first-ever in-situ deep sea tests at a 3515 m depth", *Journal of Advanced Concrete Technology*, 19: 226-239

The 16th International Congress on the Chemistry of Cement 2023 (ICCC2023)
"Further Reduction of CO_2 -Emissions and Circularity in the Cement and Concrete Industry"
September 18–22, 2023, Bangkok, Thailand

Influence of carbonation on chloride Resistance of low clinker cements

Bharati[1*], and Lupesh[2], and Shashank Bishnoi[3]

[1] *Indian Institute of Technology Delhi, New-Delhi, India*

Email: bharatithakur93@gmail.com
[2] *Indian Institute of Technology, New-Delhi, India*

Email: lupeshdudi@gmail.com

[3] *Indian Institute of Technology Delhi, New-Delhi, India*

Email: bishnoi@iitd.ac.in

ABSTRACT

Carbonation and presence of chlorides in concrete are the two major causes of reinforcement corrosion. Cement containing low clinker had been observed to have a higher degree of carbonation . Limestone calcined clay cement is one such cement with low clinker, which have high aluminate content. Owning to high aluminates and densified microstructure, LC^3 gives excellent resistance to chloride ingress In the proposed study, we aim to ascertain the effect of carbonation on chloride ingress resistance of concrete having low clinker content. Two types of cement namely Portland pozzolana cement (PPC) and limestone calcined clay cement (LC^3) has been used in this study. To compare the chloride ingress resistance, rapid chloride permeability test had been performed before and after carbonation of concrete prepared with both cements. Additionally, to measure the degree of carbonation in both blends, carbonation depth and pH has been determined. Results obtain showed that carbonation had a negative impact on the chloride ingress resistance, however trend between the blends remained the same, i.e. LC^3 having better resistance than PPC.

KEYWORDS: *Carbonation, chloride ingress, pH, RCPT*

1. Introduction

Considering high levels of carbon emission due to the production of clinker, opting to low carbon cements has become necessary and one of the best practices to reduce carbon emissions. LC^3 has emerged as a potential binder that seems promising in reducing the carbon emmisons and at the same time exhibits comparable or even better mechanical and durability performance than ordinary portland cement (OPC) after initial few days (Sharma et al., (2021)). However, durability of concrete is compromised with time due to various physical and chemical processes. Carbonation and chlorides ingress are the two major factors that pose risk of corrosion to reinforcement embedded in concrete, thus shortening the service life of reinforced concrete structures. The carbonation is governed by various parameters and the blended cements showed lower carbonation resistance compared to OPC (Shah & Bishnoi, 2018). As a result of carbonation, microstructure of the concrete gets altered and in case of blended cements porosity had been found to increase (Shah et al., (2018)). On the other hand, resistance of LC^3 against the transport of chlorides is high from early age (28 days) when compared to fly ash based concrete (Dhandapani et al., (2018)) which can be attributed to the combined effect of higher chloride binding and the refined pore structure. The higher resistivity observed in case of LC^3 concrete can also benefit to produce a durable concrete even if the threshold chloride content for such a low carbon cement is much lower than the portland cement (Pillai et al., 2019). Behaviour of low carbon concrete under chloride ingress after the carbonation would be intriguing to observe. Therefore, this study had been carried out in order to determine how carbonation can

influence the chloride ingress resistance of the low carbon cement concrete. The two low carbon cements i.e. portland pozzolana cement (PPC) and LC^3 had been comapred for their resistance against chloride after 90 days of carbonation. The RCPT results give insight into the resistance to transport of the chlorides in these two binders after carbonation.

2. Materials and Methods

2.1 Materials

Types of cements used in this study are Portland Pozzolanic cement (PPC-70%OPC + 30%FA), Limestone calcined clay cement (LC^3- 55%OPC + 30%Calcined clay + 15%Limestone). River sand has been used as fine aggregate and crushed stone as coarse aggregate with specific gravity 2.7. Table 1 shows the physical properties of the blends. Specific gravity of two blends was determined according to IS 4031 part 2. To find out the normal consistency of two blends IS 4031 part 4 has been followed. Initial setting and final setting time had been performed in compliance with IS 4031 part 5.

Table 1: Physical properties of blends

Sr. No	Cement Type	Specific Gravity	Normal Consistency (%)	Initial Setting time (min)	Final Setting time (min)
1	PPC	2.9	31.5	190	295
2	LC^3	2.9	34.5	151	229

2.2 Sample preparation

Cylinder specimens of diameter 100 mm and height 200 mm were cast and cured by submerging in water for 56 days. Two control specimens were left under extended curing and three samples of each blend were subjected to carbonation. Before subjecting to the carbonation , samples cylinders were sliced to obtain three discs having a diameter 100 mm and thickness 50 mm. Epoxy was applied on the curved surface of these disc samples and were left to dry. After 90 days carbonation, the effect of carbonation on chloride ingress in concrete was observed by performing RCPT experiment and for quantifying degree of carbonation in concrete, carbonation depth and pH was determined.

3. Experimental Program

3.1 Accelerated Carbonation

Concentration of CO_2 in the environment is approximately 0.03%, hence the rate of carbonation will be very slow. Therefore, in a laboratory the concentration of CO_2 had been increased to hundred folds to get faster results of carbonation. In this study CO_2 concentration of 3% was used. The plexiglass carbonation chamber had been used to keep the samples and relative humidity had been kept constant with help of a saturated sodium chloride solution.

3.2 Carbonation depth and pH

Carbonation front can be determined by spraying the phenolphthalein on freshly broken surface of concrete samples. pH of the pore solution of the carbonated and non-carbonated concrete had been determined using the potentiometric titration technique. Powder of concrete was obtained from the sample core using a drilling machine for carbonated and non carbonated zones. The powder is then collected and sieved through a 150µm sieve. A solution with solid to liquid ratio of 1:10 had been prepared using this powder and distilled water. Before pH measurements of the sample, electrode was cleaned and pH meter calibrated with the standard buffer solutions.

3.3 Rapid Chloride Permeability Test

Rapid chloride permeability test (RCPT) is performed in the lab to know the resistance to the penetration of chloride ions in concrete. This test was carried out in compliance with ASTM C1202.

4. Results and Discussion

4.1 Carbonation depth and pH

Carbonation depth test results show that after 90 days of carbonation at 3% carbon dioxide concentration LC^3 concrete exhibits higher carbonation depth than PPC. Carbonation front was visibly seen after spraying phenolphthalein in LC^3 (Fig. 1 (a)) and PPC (Fig. 1(b)). In case of LC^3 carbonation depth of 5.8mm had been observed, while in PPC 2.9mm carbonation depth was observed, shown in Fig. 2. LC^3 exhibits twice the carbonation depth than PPC for the same duration and under similar ambient conditions. Determination of the pH of the carbonated and non-carbonated samples had been done and shown in Fig. 3. pH of samples under 90 days of carbonation is lower than the non-carbonated samples as expected because of the reaction of CO_2 with portlandite leading to lowering of pH. It is apparent that in case of the carbonated sample, the pH of LC^3 is lower than the PPC whereas in non-carbonated samples pH of LC^3 and PPC is quite similar. Suggesting that degree of carbonation of calcium rich phases in LC^3 is more than in that of PPC.

Fig. 1(a): Carbonation depth front in LC^3

Fig. 1(b): Carbonation depth front in PPC

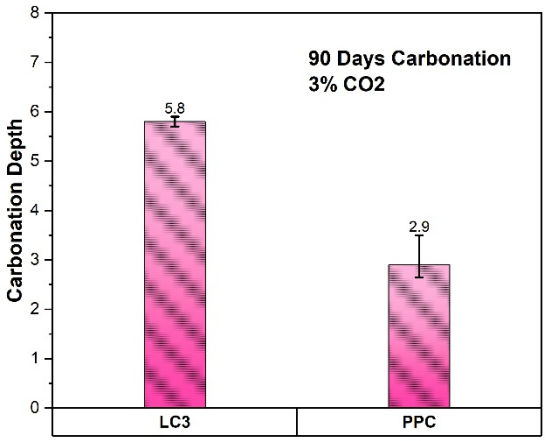

Fig. 2: Carbonation depth (mm)

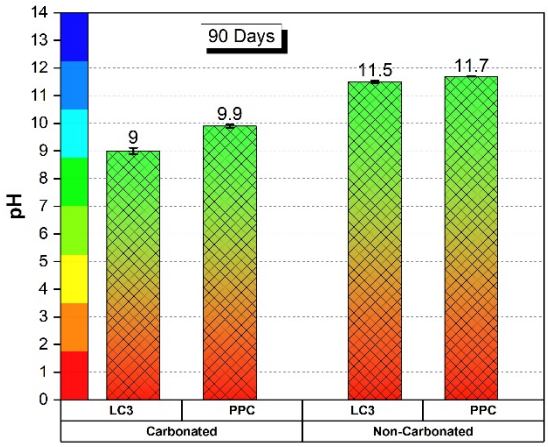

Fig. 3: pH in LC^3 and PPC

4.2 Rapid Chloride Permeability test

RCPT result had been presented in Fig. 4. It had been observed that after carbonation, the total charge passed for same duration increased in both the blends which can be attributed to the coarsening of pore structure and increase in total porosity on carbonation as reported by Shah et al. 2018. For the duration of carbonation used in this study, LC^3 had been observed to perform better than PPC in both carbonated and non-carbonated conditions. However, LC^3 has been observed to be more influenced by subjection to carbonation as compared to PPC, which can be attributed to higher fraction of aluminates phases in hydrated LC^3 as compared to PPC.

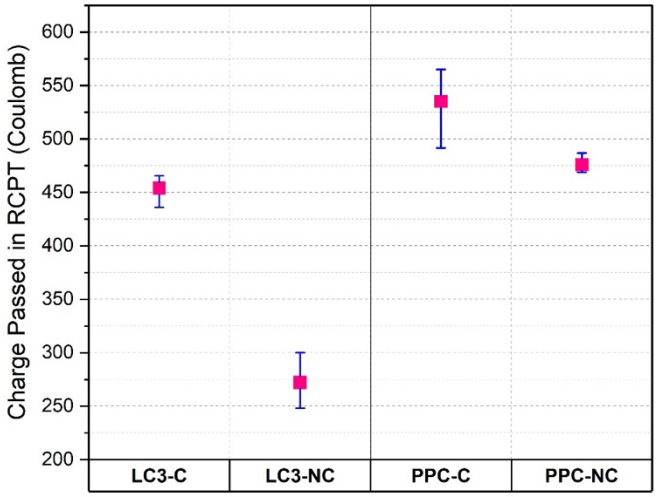

Fig. 4: Chloride penetration resistance by RCPT

5. Conclusions

Carbonation depth in LC^3 concrete has been observed to be almost twice than the PPC concrete. Moreover, pH reduces significantly after carbonation in LC^3 concrete than in PPC concrete. After subjecting carbonated and non-carbonated samples to RCPT following conclusions were drawn

- Resistance to chloride ingress in LC^3 as well as in PPC lowered as a result of carbonation
- Influence of carbonation on chloride ingress is more significant in LC^3 concrete than in PPC concrete.
- Even if LC^3 concrete carbonates more than the PPC, resistance against chloride ingress remains higher than PPC concrete after carbonation

References

Dhandapani, Y., Sakthivel, T., Santhanam, M., Gettu, R., & Pillai, R. G. (2018). Mechanical properties and durability performance of concretes with Limestone Calcined Clay Cement (LC3). *Cement and Concrete Research*, *107*, 136–151. https://doi.org/10.1016/j.cemconres.2018.02.005

Pillai, R. G., Gettu, R., Santhanam, M., Rengaraju, S., Dhandapani, Y., Rathnarajan, S., & Basavaraj, A. S. (2019). Service life and life cycle assessment of reinforced concrete systems with limestone calcined clay cement (LC3). *Cement and Concrete Research*, *118*, 111–119. https://doi.org/10.1016/j.cemconres.2018.11.019

Shah, V., & Bishnoi, S. (2018). Carbonation resistance of cements containing supplementary cementitious materials and its relation to various parameters of concrete. *Construction and Building Materials*, *178*, 219–232. https://doi.org/10.1016/j.conbuildmat.2018.05.162

Shah, V., Scrivener, K., Bhattacharjee, B., & Bishnoi, S. (2018). Changes in microstructure characteristics of cement paste on carbonation. *Cement and Concrete Research*, *109*, 184–197. https://doi.org/10.1016/j.cemconres.2018.04.016

Sharma, M., Bishnoi, S., Martirena, F., & Scrivener, K. (2021). Limestone calcined clay cement and concrete: A state-of-the-art review. *Cement and Concrete Research*, *149*, 106564. https://doi.org/10.1016/j.cemconres.2021.106564

The 16th International Congress on the Chemistry of Cement 2023 (ICCC2023)
"Further Reduction of CO_2 -Emissions and Circularity in the Cement and Concrete Industry"
September 18–22, 2023, Bangkok, Thailand

Towards the Development of Prescriptive-Based Specifications for Non-Traditional SCMs to Prevent Alkali-Silica Reaction

K.S.T. Chopperla[1*] and J.H. Ideker[2]

[1] *Oregon State University, Corvallis, OR, USA*
Email: krishna.chopperla@oregonstate.edu
[2] *Oregon State University, Corvallis, OR, USA*
Email: Jason.Ideker@oregonstate.edu

ABSTRACT

Current specifications in standard guides for preventing alkali-silica reaction (ASR) such as ASTM C1778 are limited to traditional supplementary cementitious materials (SCMs). As the availability of traditional SCMs is reducing, the use of non-traditional SCMs has increased and there is a need to develop prescriptive-based specifications to prevent ASR for them. In addition, the current specifications are based on only the chemical composition of the SCMs and do not consider the reactivity of SCMs. This paper discusses potential ways to improve the current prescriptive-based specification by including the reactivity of SCMs in addition to the chemical composition. Another approach based on proposing alkali loading limits of concrete and minimum SCM amounts required to prevent ASR in concrete mixtures with reactive aggregates for different alkali threshold values is discussed. Additional research that is needed to improve prescriptive-based specifications to prevent ASR using non-traditional SCMs is discussed.

KEYWORDS: *Alkali-silica reaction, Supplementary cementitious materials, Specifications, Pozzolanic reactivity, Alkali sensitivity.*

1. Introduction

Alkali-silica reaction (ASR) is a chemical reaction between alkali hydroxides in the pore solution of concrete and reactive silica of aggregates to form expansive products that may crack the concrete. Above a certain pore solution alkalinity (alkali threshold), reactive aggregates will cause expansion in concrete due to ASR (Thomas et al. 1996). Using supplementary cementitious materials (SCMs) in concrete with reactive aggregates is the most used strategy to prevent ASR. Using appropriate amount of SCM(s) can prevent ASR as their usage reduces alkalinity of concrete pore solution from dilution effects and alkali binding by pozzolanic reaction products (Thomas 2011). In addition, alumina in SCMs can reduce silica dissolution from aggregates and usage of SCMs can reduce transport of external alkalis and moisture thus limiting the reaction (Chappex and Scrivener 2013, Thomas 2011).
Standard guides such as ASTM C1778, "Standard Guide for Reducing the Risk of Deleterious Alkali-Aggregate Reaction in Concrete", includes specifications to prevent ASR using traditional SCMs such as coal ashes, slag, and silica fume. As there has been an increase in short supply of traditional SCMs such as coal ashes in the recent years, interest in the use of non-traditional SCMs such as natural pozzolans, harvested ashes, blended pozzolans, and ground glass has increased (Juenger et al. 2019). It is reported that non-traditional SCMs are reported to have a large variability in their composition and reactivity (Juenger et al. 2019). Therefore, it requires careful characterization of non-traditional SCMs for developing specifications for their use in concrete to prevent ASR.
The current prescriptive-based specifications recommend minimum amounts of SCMs to be used to prevent ASR are based on the chemical composition of the SCMs and not their reactivities. SCMs with similar oxide composition may have different reactivities as their amorphous contents may be different. SCMs with very low reactivity may not be able to form enough pozzolanic products (such as calcium-

silicate-hydrates) to bind alkalis and lower the pore solution alkalinity to prevent ASR. In addition, current guidelines specify prevention strategies based on the reactivity levels of aggregates (for example, R0, R1, R2, and R3 aggregate reactivity classes in ASTM C1778) and not on alkali threshold values.
The goal of this paper is to review recent research that showed that the reactivity of SCMs is related to their efficacy in preventing ASR and discuss potential ways to improve specifications by including the SCM reactivity measures. In addition, an approach to improve the specifications by recommending appropriate ASR prevention measures based on alkali sensitivity of reactive aggregates is discussed.

2. Potential approaches to improve the presciptive-based specifications

Two measures of SCM reactivity - calcium hydroxide consumed by SCMs in a model system and electrical resistivity measurement of binder systems were used as tools to determine the SCMs efficiency to prevent ASR. These approaches are discussed in sections 2.1. An approach to improve specifications regarding alkali sensitivity of reactive aggregates and alkali loading is discussed in section 2.2.

2.1 Determining SCM amount for ASR prevention based on SCM reactivity

SCM pozzolanic reactivity can be measured by determining the amount of CH consumed by SCM in a model system, where SCM and calcium hydroxide (CH) were mixed at 1 to 3 mass ratio, and then the blend was mixed with 0.5 M KOH solution at a liquid to solid ratio of 0.9 (Suraneni and Weiss 2017). The mixture was seal cured at 50 ºC for 10 days, and these conditions are expected to react the SCM entirely in most cases (Choudhary et al. 2022). CH consumed by SCM at the end of the test was determined by measuring the remaining CH in the system using thermogravimetric analysis (TGA). Recent research (Chopperla and Ideker 2022, Wang et al. 2022) showed that CH consumed as an SCM reactivity measure along with amount of SCM in the binder correlated well with the ASR expansion determined using the accelerated mortar bar test (AMBT; ASTM C1567) and the miniature concrete prism test (MCPT; AASHTO T 380). Figure 1a shows that higher the reactive SCM fractions in the binder, lower the expansion. The data shown in Figure 1a is for materials such as limestone (LS), slag (SL), pumice (PU), and glass powder (GP). Similar observations were made when SCMs such as fly ashes and silica fume are used; more details can be found in ref. (Chopperla and Ideker 2022). Figure 1b shows the correlation between the MCPT expansion and bulk electrical resistivity of concrete.

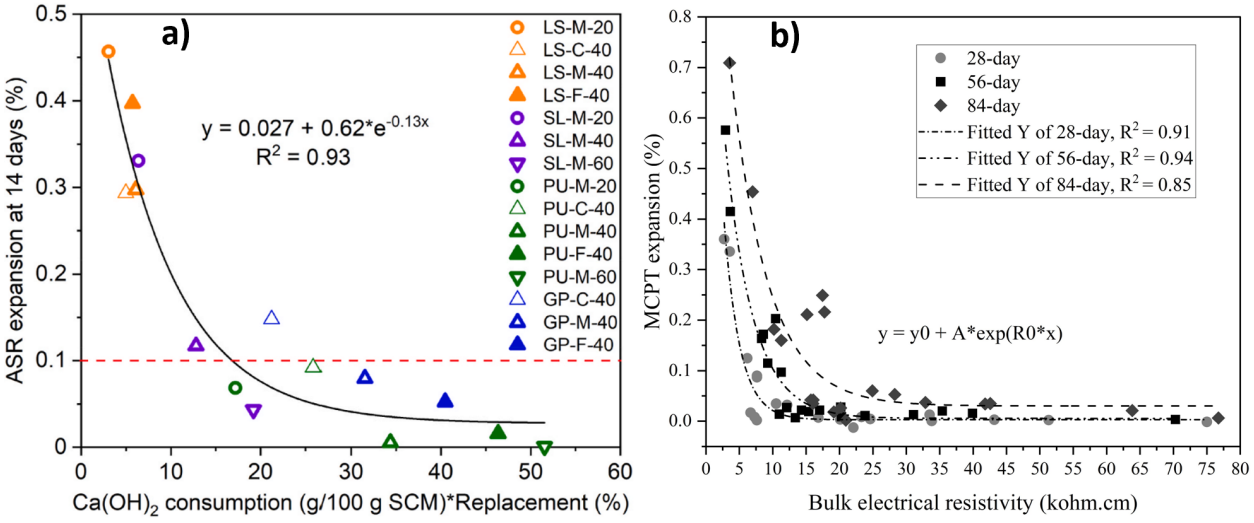

Figure 1. a) Correlation between AMBT expansion an the product of CH consumption and SCM amount (Wang et al. 2022); b) Correlation between MCPT expansion and bulk electrical resistivity (Chopperla and Ideker 2022)

It has been shown that electrical resistivity of cementitious binders can be used as an alternate method for evaluating SCMs with different reactivities (Wang et al. 2021), and it can also be used to evaluate SCMs efficiency to prevent ASR (Chopperla and Ideker 2022, Wang et al. 2022). This is because reaction of SCMs increase bulk resistivity by reducing pore connectivity and pore solution alkalinity. Therefore, cementitious systems with higher reactive SCM(s) will have higher electrical resistivity. As electrical

resistivity is a non-destructive and simple test, it could be used as an alternate test for SCM reactivity measurement (Wang et al. 2021), and specifications could be developed based on resistivity values.
Using the discussed approaches, SCM amounts can be specified based on their composition and reactivity for different levels of aggregate reactivities and alkali loadings to prevent ASR.

2.2 Alkali sensitivity of aggregates

Another approach that is being investigated by the authors is to develop information on the alkali sensitivity of specific aggregates or aggregate classes. That information could then be combined that with the available alkali in the total cementitious blend (e.g. portland cement or portland limestone cement + supplementary cementitious materials) as well as any alkalis that are releasable by the aggregates themselves (Menendez et al. 2021). Externally available alkalis may also be included in this calculation. The idea of this approach is summarized as a schematic shown in Figure 2.

The alkali content in the pore solution governs the pH and in turn will dictate when deleterious ASR occurs. Our standard accelerated mortar bar testing methods rely on an external soak solution of 1N which is often criticized for being overly aggressive. **Figure 3**a shows the impact of varying the alkali normality in the soak solution in the accelerated mortar bar test. For a very highly reactive aggregate a 0.265 N soak solution showed that the aggregate related expansion was suppressed at, or near this level. More work is underway to determine the exact alkali threshold needed to induce expansion in this aggregate. But this demonstrates an important proof of concept that limiting the alkali content can prevent deleterious ASR. This was well known and is shown in a 1996 publication by Thomas and co-workers as shown in **Figure 3**b. However, this approach was long considered too arduous to establish these relationships for all aggregates. It is proposed to start by establishing this for aggregate reactivity classes and/or mineralogies. Though, not much additional testing would be needed to run a normality series on each aggregate for consideration in concrete construction. To determine the total alkali available to the system the cold water extraction technique (CWE) proposed by Plusquellec et al. (2018), and later refined by Tuinukuafe et. al. (2022) could be used. An alternative approach called the alkali leaching test (ALT) outlined by Ghanizadeh and Thomas (2023) in this conference may also be possible.

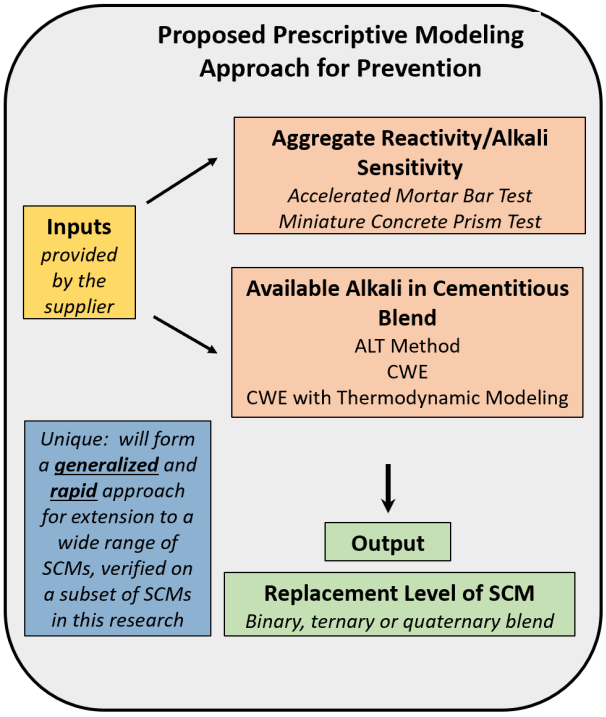

Figure 2: Proposed Approach For Assessing Alkali Sensitivity of Aggregates And Available Alkali Loading of the System For ASR Prevention

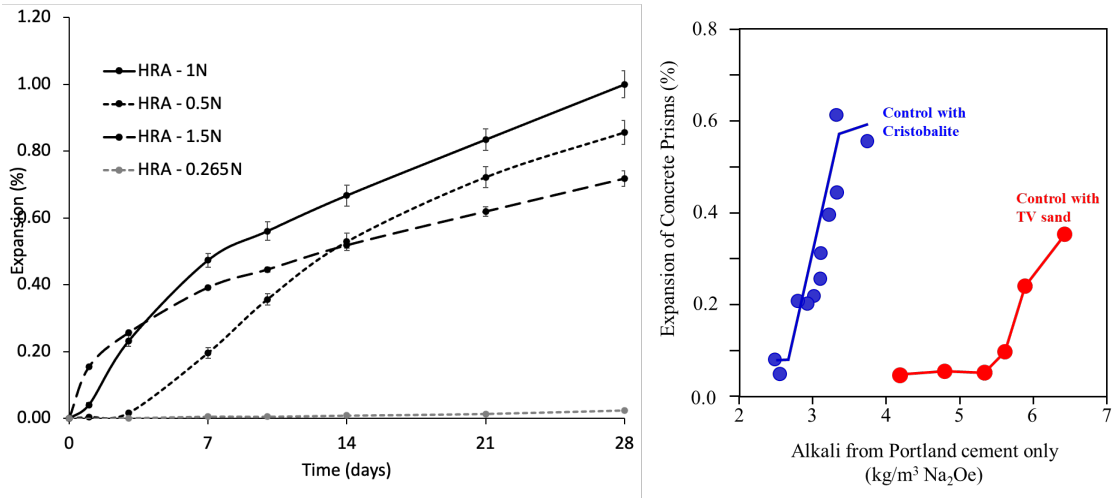

Figure 3: a) expansion of mortar bars (Parashar and Ideker unpublished data, 2023); b) expansion of concrete prisms (Thomas et al., 1996)

3. Conclusions

Two approaches to develop prescriptive specifications to prevent ASR using non-traditional SCMs are discussed in this paper. Both measures of SCM reactivity, calcium hydroxide consumed by SCM and electrical resistivity of binder, showed good correlation to the mortar and concrete expansions measured in mixtures with reactive aggregates. Considering SCM reactivity in addition to their composition could improve the specifications for ASR preventive measures. Also, a prescriptive approach of ASR prevention based on aggregative alkali sensitivity and alkali loading of concrete is discussed in this paper.

References

Chappex, T. and Scrivener, K.L. (2013) "The effect of aluminum in solution on the dissolution of amorphous silica and its relation to cementitious systems", *Journal of the American Ceramic Society*, 96 (2)

Chopperla, K.S.T. and Ideker, J.H. (2022) "Using electrical resistivity to determine the efficiency of supplementary cementitious materials to prevent alkali-silica reaction in concrete", *Cement and Concrete Composites*, 125: 104282

Choudhary, A., Bharadwaj, K., Ghantous, R.M., Isgor, O.B. and Weiss, W.J. (2022) "Pozzolanic Reactivity Test of Supplementary Cementitious Materials", *ACI Materials Journal*, 119(2): 255-268

Ghanizadeh, A. and Thomas, M.D.A. (2023) "Alternatives to pore solution extraction method to determine available alkalis of cement pastes", *The 16th International Congress on the Chemistry of Cement (ICCC)* (In Review)

Juenger, M.C., Snellings, R. and Bernal, S.A. (2019) "Supplementary cementitious materials: New sources, characterization, and performance insights", *Cement and Concrete Research,* 122: 257-273

Menendez, E., Silva, A.S. and Duchesne, J. (2021) "Recommendation of RILEM TC258-AAA: RILEM AAR-8: determination of potential releasable alkalis by aggregates in concrete*", Materials and Structures*, 54 (205)

Plusquellec, G., Geiker, M.R., Lindgard, J. and de Weerdt, K. (2018) "Determining the free alkali metal content in concrete - Case study of an ASR affected dam", *Cement and Concrete Research*, 105: 111-125

Suraneni, P. and Weiss, W.J. (2017) "Examining the pozzolanicity of supplementary cementitious materials using iso-thermal calorimetry and thermogravimetric analysis", *Cement and Concrete Composites*, 83: 273-278

Thomas, M.D.A., Blackwell, B.Q. and Nixon, P.J. (1996), "Estimating the Alkali Contribution from Fly Ash to Expansion due to Alkali-Aggregate Reaction in Concrete", *Magazine of Concrete Research*, 48 (177): 251-264

Thomas, M.D.A. (2011) "The effect of supplementary cementitious materials on alkali-silica reaction: A review", *Cement and Concrete Research*, 41 (12): 1224-1231

Tuinukuafe, A., K. S. T. Chopperla, J. Weiss, J. Ideker and B. Isgor (2022). "Estimating Na+ and K+ concentrations of the pore solution based on ex-situ leaching tests and thermodynamic modeling", *RILEM Technical Letters,* 7: 88-97

Wang, Y., Burris, L., Shearer, C.R., Hooton, D. and Suraneni, P. (2021) "Strength activity index and bulk resistivity index modifications that differentiate inert and reactive materials", *Cement and Concrete Composites*, 124: 10420

Wang, Y., Ramanathan, S., Chopperla, K.S.T., Ideker, J.H. and Suraneni, P. (2021) "Estimation of non-traditional supplementary cementitious materials potential to prevent alkali-silica reaction using pozzolanic reactivity and bulk resistivity", *Cement and Concrete Composites*, 133: 104723

The 16th International Congress on the Chemistry of Cement 2023 (ICCC2023)
"Further Reduction of CO_2 -Emissions and Circularity in the Cement and Concrete Industry"
September 18–22, 2023, Bangkok, Thailand

Influence of elevated environmental temperatures on passivation and corrosion risk of steel reinforcement

C.S. Das[1], H. Zheng[2], and J.G. Dai[3*]

[1] *PhD Student, The Hong Kong Polytechnic University, Hong Kong*

Email: chandrasekhar.das@connect.polyu.hk

[2] *Assistant Research Fellow, Henan Academy of Sciences, China*

Email: zhenghaibing.ln@163.com

[3*] *Professor, The Hong Kong Polytechnic University, Hong Kong*

Email: cejgdai@polyu.edu.hk

ABSTRACT

One of the major consequences of climate change is an increase in environmental temperature around the world. However, limited research has been conducted to understand its implications on the chloride-induced corrosion of embedded steel reinforcement. This paper aims to evaluate the effect of elevated environmental temperature on the passivation and chloride-induced corrosion process of reinforcing steel. Three different temperatures (i.e., 25˚C, 35˚C and 45˚C) were employed in the study, and the corrosion susceptibility of steel reinforcement was investigated in simulated pore solution using different electrochemical and surface characterization techniques. The study revealed that steel samples immersed in the solution with high-temperature initially exhibited a more negative open circuit potential, but the potential shifted to noble values within the first 12 hours of immersion. The increase in potential with immersion time was most significant at 45˚C, leading to the more noble stable potential among all the samples. However, the passive film formed at higher temperatures was comparatively thinner and offered less protection against chloride ions, as observed from electrochemical impedance spectroscopy results. Subsequently, this led to a lower chloride threshold value for corrosion initiation.

KEYWORDS: *Corrosion, climate change, steel reinforcement, durability, temperature*

1. Introduction

Reinforcing steel with concrete is typically shielded by a passive film generated as a result of the highly alkaline surroundings within the concrete. However, this film can deteriorate when aggressive ions are present or when the pH of the concrete pore solution decreases due to carbonation. The chloride threshold value (CTV) is the primary physical factor that determines chloride-induced corrosion. Most existing research has focused on improving the CTV by altering the steel type and improving the surrounding concrete properties. Nevertheless, comparatively little research has been done on the influence of different environmental factors on CTV in reinforced concrete. Laboratory tests are typically performed at standard temperature and humidity, which differs significantly from practical circumstances where reinforced concrete structures are exposed to diverse climatic conditions during their service life. Due to the impending threat of climate change and global warming, it is anticipated that various structures will be subjected to high temperatures and abrupt temperature variations, making it necessary to assess the temperature impact on chloride-induced corrosion in reinforced concrete structures. From a chemical perspective, the corrosion reaction rate is greatly influenced by temperature, as per the Arrhenius equation. The temperature also changes the equilibrium potential of both anodic and cathodic processes leading to significant changes in corrosion risk (Pour-Ghaz et al. (2009). The steel in reinforced concrete undergoes two chemical processes:

formation of oxide film (i.e., passivation) and passive film breakdown (i.e., depassivation). The exposed temperature significantly affects the concentration of individual ions in pore solution and the nature of hydration products (Lothenbach et al. (2007)). Further, a high-temperature environment has also been observed to result in a less protective passive film on the stainless steel surface and increases the corrosion current density during the passivation period (Liu et al. (2021)).

Previous studies indicate that the temperature of the environment significantly impacts the chemical environment, electrochemical properties, and ion transport, which are all factors that contribute to a structure's service life. Nevertheless, there is a lack of systematic research examining the passivation process and the progressive changes in corrosion susceptibility that occur with rising temperatures. Given the passive film's nanoscale thickness, any alterations in its properties resulting from an increase in temperature can have significant implications for its ability to protect against chloride ions. Therefore, a comprehensive investigation into the passive film's growth and characteristics during the exposure period is necessary.

2. Methodology

The exposure scheme consisted of exposing cross-section of polished steel samples (500B as per BS 4449:2005) in saturated $Ca(OH)_2$ solution, which was maintained in equilibrium at different temperatures (25 ˚C, 35 ˚C and 45 ˚C). After 14 days of exposing steel rebars to saturated $Ca(OH)_2$ solution, 0.2 M of NaCl was added every 12 hours to the solution to monitor the interaction between chloride ions and the steel surface. De-ionized water and analytical-grade chemicals were used throughout the experiments. The electrochemical setup was a three-electrode system consisting of a platinum plate (4 cm^2) as the counter electrode (CE), carbon steel as the working electrode (WE) and solid Ag/AgCl as the reference electrode (RE). Open circuit potential (OCP) were measured periodically to study the evolution passivation and depassivation behavior. The Electrochemical impedance spectroscopy (EIS) test was conducted at the end of passivation study using an excitation AC voltage of 10 mV at the OCP over a frequency range from 100kHz to 0.01Hz. Ten points per decade were recorded over the frequency range.

3. Results

3.1. Passivation behavior of steel in alkaline solution at different temperatures

The EIS response of the steel samples in chloride-free saturated $Ca(OH)_2$ solutions maintained at different temperatures are presented through Nyquist and Bode plots in Fig 1. It can be observed that the highest phase angle at low frequency and highest impedance was observed at 25 ˚C, followed by that at 35 ˚C and the lowest at 45 ˚C.

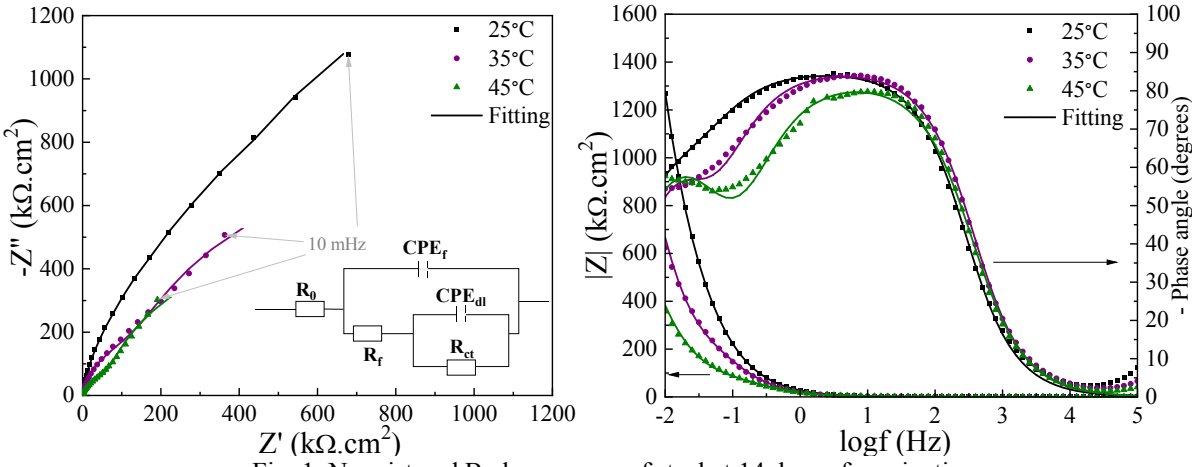

Fig. 1. Nyquist and Bode response of steel at 14 days of passivation

An equivalent circuit with two hierarchical parallel RC loops, R(QR(QR)) was adopted to fit the EIS data. The two-time constants consider the influence of exposed $Ca(OH)_2$ solution, passive film properties and steel solution interface. A constant phase element (Q) was used instead of an ideal capacitance to consider

the deviation from ideal capacitance properties due to surface inhomogeneities. Aligned with the EIS response plots, it was observed that the resistance of passive film for 25 ˚C (1053 kΩ.cm^2) was 7 times and 20 times higher than that for 35 ˚C (144 kΩ.cm^2) and 45 ˚C (57.5 kΩ.cm^2), respectively at 14 days. The development of a more protective passive film reduced the redox reactions on the steel surface. Subsequently, the charge transfer resistance at 25 ˚C was 3750 kΩ.cm^2 and decreased 57.5 kΩ.cm^2 for the samples at 45˚C. The effect of temperature was also evident in the capacitance values. The lowest capacitance values were observed for samples immersed at 25 ˚C suggesting the formation of a passive film with least amount of defects that can provide an easier pathway for chloride ions.

The variation of open circuit potential (OCP) of steel samples with exposure time for steel samples immersed in alkaline solution at different temperatures is provided in Fig. 2. It can be observed that the samples at 45 ˚C showed the most negative potential in the initial period of immersion (< 3 hours) similar to observations by Deus et al. (2012) in stainless steel. One reason could be the low dissolved oxygen (DO) content in alkaline solutions at high temperatures. The measured DO were 5.8 mg/L, 5.1 mg/L and 4.1 mg/L for 25 ˚C, 35 ˚C and 45 ˚C respectively. Some previous literature studies have reported that the steel potential varies with the nature and composition of the passive oxide film formed on the surface (Abd El Haleem et al. (2010)). A higher Fe(III)/Fe(II) ratio could shift the potentials to more positive values through the oxidation of magnetite to form Fe_2O_3 (Sánchez et al. (2007)). Thus, the observed steel potential resulted from the interplay between DO contents in the alkaline solution and Fe(III)/Fe(II) ratio in the passive film. While the DO levels played a dominating role at the early age, the oxidation of Fe(II) to Fe(III) during the ageing of passive film formed at 45 ˚C which increased Fe(III)/Fe(II) ratio, was primarily responsible for the positive shift in potential values at later periods.

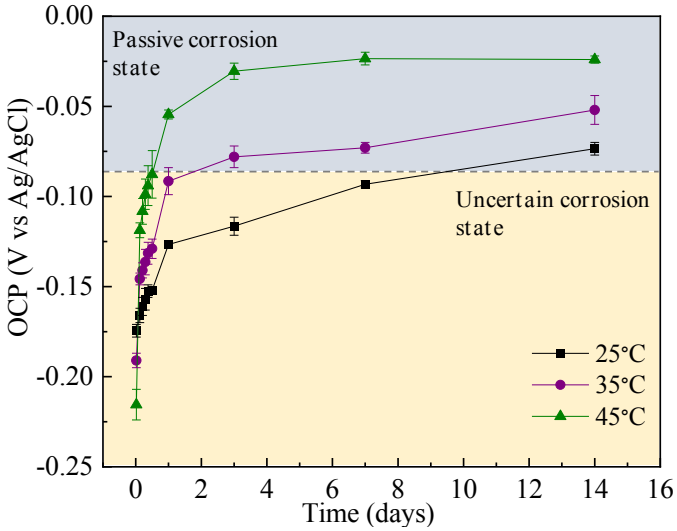

Fig 2. Evolution of open circuit potential (OCP) of steel at different temperatures.

3.2. Depassivation behavior and chloride threshold value

Another implication of this study was determining the chloride concentration required for corrosion initiation in steel samples at different temperatures. This was evaluated by measuring the open circuit potential (OCP) periodically after every chloride addition until the OCP dropped into the active corrosion zone (-0.232 V vs. Ag/AgCl based on ASTM C876-15). The chloride threshold value decreased with an increase in temperature, as shown in Fig 3. As observed earlier, the effect of temperature rise on the corrosion susceptibility of steel is not uniform. For samples at 25°C, the chloride threshold value was in the range of 3.4M and 3.6M chloride concentration. With an increase in temperature to 35°C, the chloride threshold value dropped significantly to about 1.8M, which means the corrosion resistance halved at just a 10°C temperature rise. With another 10°C temperature increase, the chloride threshold further dropped to about 1-1.2M of chloride concentration, which denotes a sharp decrease in corrosion resistance at 45°C to less than one-third of that at 25°C. This can be attributed to a combined effect of two factors which include: structural and chemical modification of the passive, which reduced the passive film's protectiveness; elevated temperature could have promoted the reaction between chlorides and passive oxide film and accelerated the oxide film dissolution, which is crucial for protectiveness.

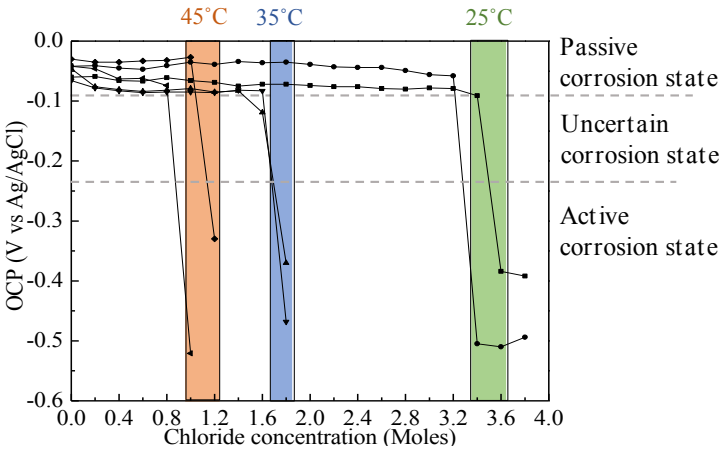

Fig 3. Evolution of OCP with chloride addition for steels at different temperatures.

4. Conclusions

This study aimed to investigate the effect of exposure temperature, specifically 25℃, 35℃, and 45℃, on the passivation ability of steel and its implications for the chloride threshold value using electrochemical measurements. The results indicated that the passive film resistance of samples at 25℃ was seven times greater than the passive film resistance at 35 ℃ and 20 times greater than that at 45 ℃. The lower impedance was found to be related to three factors: the decrease in passive film thickness with an increase in temperature, the higher concentration of defects in the passive film at high temperatures, and the promotion of higher oxidation of Fe (II) oxides to porous Fe (III) oxides, which provide less protection at high temperatures. The reduced protectiveness of the passive film had a significant impact on the chloride threshold value and, consequently, the risk of steel corrosion. Increasing the temperature from 25℃ to 35℃ resulted in a 50% drop in CTV compared to 25℃. Moreover, increasing the temperature to 45℃ further decreased the CTV to a value that was less than one-third of that observed at 25 ℃.

Acknowledgements

This research was supported by Guangdong Province R&D Plan for Key Areas (Project code: 2019B111107002) and the Research Institute for Sustainable Urban Development of the Hong Kong Polytechnic University (No.1-BBWE).

References

Pour-Ghaz, M., Isgor, O. B., and Ghods, P. (2009). "The effect of temperature on the corrosion of steel in concrete. Part 1: Simulated polarization resistance tests and model development." *Corrosion Science*, 51(2), 415-425.

Lothenbach, B., Winnefeld, F., Alder, C., Wieland, E., and Lunk, P. (2007). "Effect of temperature on the pore solution, microstructure and hydration products of Portland cement pastes." *Cement and Concrete Research*, 37(4), 483-491.

Liu, X., MacDonald, D. D., Wang, M., and Xu, Y. (2021). "Effect of dissolved oxygen, temperature, and pH on polarization behavior of carbon steel in simulated concrete pore solution." *Electrochimica Acta*, 366, 137437.

Deus, J., Freire, L., Montemor, M., and Nóvoa, X. (2012). "The corrosion potential of stainless steel rebars in concrete: Temperature effect." *Corrosion science*, 65, 556-560.

Abd El Haleem, S., Abd El Aal, E., Abd El Wanees, S., and Diab, A. (2010). "Environmental factors affecting the corrosion behaviour of reinforcing steel: I. The early stage of passive film formation in Ca (OH) 2 solutions." *Corrosion Science*, 52(12), 3875-3882.

Sánchez, M., Gregori, J., Alonso, C., García-Jareño, J., Takenouti, H., and Vicente, F. (2007). "Electrochemical impedance spectroscopy for studying passive layers on steel rebars immersed in alkaline solutions simulating concrete pores." *Electrochimica Acta*, 52(27), 7634-7641.

The 16th International Congress on the Chemistry of Cement 2023 (ICCC2023)
"Further Reduction of CO_2 -Emissions and Circularity in the Cement and Concrete Industry"
September 18–22, 2023, Bangkok, Thailand

Ultra-green concrete: a technological breakthrough to save 800 Mt of CO_2 per year

F. Zunino[1*], G. Habert[2] and R.J. Flatt[3]

[1] *Physical Chemistry of Building Materials, Institute for Building Materials (IfB), ETH Zürich, CH-8093 Zürich, Switzerland*

Email: franco.zunino@ifb.baug.ethz.ch
[2]*Institute of construction and infrastructure management, ETH Zürich, CH-8093 Zürich, Switzerland*

Email: habert@ibi.baug.ethz.ch

[3] *Physical Chemistry of Building Materials, Institute for Building Materials (IfB), ETH Zürich, CH-8093 Zürich, Switzerland*

Email: fflattr@ethz.ch

ABSTRACT

Concrete is the substance used in largest quantity by mass after water, with an anticipated demand that will continue to increase in decades to come. The ultra-green concrete project aims at developing a new family of concretes to radically reduce the CO_2 emissions related to this material, substantially beyond the CO_2 savings of any of the technologies currently available. Ultra-green concrete will therefore be the next breakthrough in sustainable technologies for decarbonization of the construction industry, saving at least 800 Mt of CO_2 per year. The project approaches the development of ultra-low carbon concrete with a novel and innovative two-fold strategy. First, to reduce the amount of clinker in cement substantially below 50%, maximizing the use of mineral additions such as calcined clay and limestone through a fundamental understanding of reaction kinetics and hydrate precipitation that contributes to reduce porosity. Second, to reduce the amount of binder (hydrated paste) below 250 kg/m^3 per cubic meter of concrete, bringing together the knowledge gained at the cement scale with the development of novel admixture formulations to tackle this challenge. A key aspect to materialize ultra-green concrete lies in chemical admixtures, in particular polymeric dispersants, to achieve a good rheological control (initial and over time) in systems where colloidal interactions are dominated by the mineral additions rather than clinker. While conceptually simple, the balance of flow, flow retention and hydration kinetics is a complex multivariate problem controlled by the fundamental physicochemical characteristics of the system.

KEYWORDS: *sustainability, hydration, admixtures, workability, slump*

1. Introduction

Portland cement (PC), a combination of clinker (95%) and gypsum (5%), is the product manufactured in largest on a mass basis, and it is the binder used to produce concrete. Concrete is the second most used substance by mankind after water (K. L. Scrivener et al., 2016). Due to this enormous utilization, PC is responsible for about 8% of manmade CO_2 emissions (Boden et al., 2017), so that addressing this situation is essential, but not trivial. Indeed, on the one hand we need concrete to sustain the development

of civil infrastructure, particularly in emerging economies, but on the other hand our future is founded on our ability to preserve our environmental integrity. Existing technologies, such as blended cements that incorporate mineral additions in combination with clinker, enable substantial CO_2 reductions compared to traditional PC (K. Scrivener et al., 2017; K. L. Scrivener et al., 2016). However, their contributions remain insufficient for global warming mitigation and more radical solutions are urgently needed.

Concrete is the only material on Earth that can be produced in the volume required to meet the current and future demand of construction. It is not only widely available, but it is also cheap, easy and safe to use, as well as versatile and durable. There is no other material that can replace it that satisfies all of these qualities and consequently, concrete will remain the cornerstone of human development for decades and centuries to come (K. L. Scrivener et al., 2016).

1.1 Low-carbon cements

Concrete was, is, and will remain, the choice to build our cities. Consequently, the most effective way to reduce the CO_2 footprint linked to this development is to reduce the clinker content in the concrete that will be used (K. L. Scrivener et al., 2016). This has oriented the industry towards an increasing adoption of blended cements, that incorporate supplementary cementitious materials (SCMs) replacing part of the clinker with a low carbon substitute (Lothenbach et al., 2011). The availability of commonly used SCMs such as fly ash (by-product of burning coal) and slag (by-product of iron production in blast furnaces) is limited and, especially in the case of fly ash, expected to decrease in the forthcoming decades (IEA & CSI, 2018). On the contrary, kaolinite and limestone are available in virtually unlimited quantities, and can enable a significant worldwide reduction in PC content (K. Scrivener et al., 2017; K. L. Scrivener et al., 2016).

Limestone calcined clay cements (LC^3), a project originated and developed mainly at EPFL in Switzerland, are a family of multi-component cements that incorporate limestone and calcined kaolinitic clays replacing up to 50% of clinker. They achieve similar strength to conventional PC from 7 days onwards (K. Scrivener et al., 2019). Overall, LC^3 cements can save between 30 to 40% of the CO_2 emissions per ton of cement produced compared to PC (Pillai et al., 2019). LC^3 technology enables substantial CO_2 reductions. Preliminary results show that the high reactivity of metakaolin and synergistic reaction between metakaolin and limestone (Zunino & Scrivener, 2021) enable to reduce the clinker content substantially below 50%, while still retaining good performance in terms of strength and durability.

2. The two-fold strategy: towards a definition of ultra-green concrete (UGC)

It is accepted that modern concrete contains more cement than is needed. The reasons behind this are diverse: some national standards prescribe the minimum binder content for different durability exposure classes, they can also be relatively arbitrarily specified on a project basis, importantly also there is often a lack of availability of multigranular aggregates to improve packing. As an example, the EN-206 standard for concrete prescribes minimum cement contents between 280-300 kg/m^3 for the most common exposure classes. In the US, a minimum binder content is not prescribed by standards but is commonly specified in projects, falsely believing that this will ensure high quality concrete. Conceptually, the binder volume (cement plus water) should be enough to fill the voids between the aggregates. This leads to values around 200 kg/m^3 for well graded (highly packed) aggregate size distributions at a standard (0.5) water to cement ratio. The minimum binder contents were originally specified to ensure workability when modern superplasticizers such as PCEs were not available. However, this technical limitation is not currently justified, and the massification of admixtures enables their use in a cost-effective manner. The contradiction is that, in many regions, lower cement contents are allowed and robust, industrialized concrete mixtures are produces daily (I.N.N., 2019). Rather than prescribing minimum cement contents, performance-based metrics to assess the robustness of concrete should be used instead.

From an environmental performance perspective, there has been a clear trend to focus solely on cement, for example, by targeting all efforts to clinker factor reduction. This is certainly an important step, as previously mentioned, particularly considering that more than 90% of the embodied CO_2 in 1 cubic meter of concrete correspond to cement. However, the environmental benefits can be easily lost with an inadequate concrete mixture design. Moreover, focusing solely on cement masks other relevant elements towards low-carbon concrete, such as performance and mixture design. As shown in Figure 1, reducing the clinker content in cement, and reducing the binder content in concrete have similar carbon saving potentials. This highlights the relevance of the problem and the need for tackling both challenges simultaneously, in what we define as the *two-fold strategy*. Ultra-green concrete (UGC) is then defined as a concrete mixture that incorporate a blended cement with less than 50% clinker content, and binder content below 250 kg/m^3.

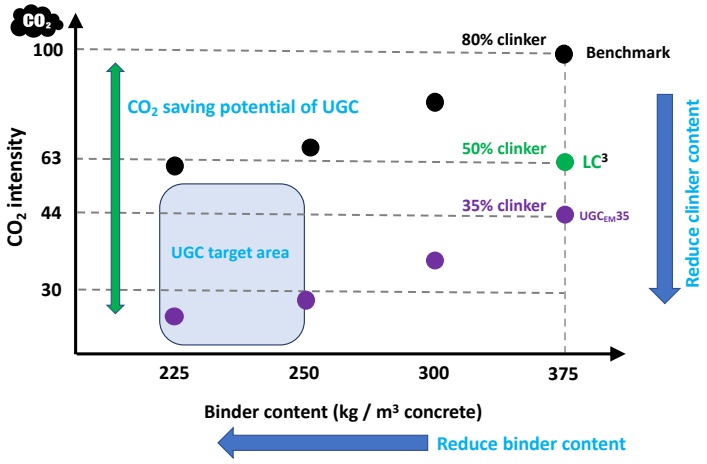

Figure 1: *Two-fold strategy scheme to save CO_2 with the UGC technology. Benchmark assumed is a concrete with CEM II/A-LL (80% clinker, 20% limestone + gypsum) cement and 375 kg/m^3 binder content in concrete.*

Increasing the replacement level of clinker by SCMs generally implies challenges in terms of workability, as replacement materials tend to have higher specific surface area than PC. Simultaneously, the reduction of binder content reduces the volume of paste and thus the lubrication between aggregate particles. In summary, both elements of the two-fold strategy pose significant challenges in terms of workability, and thus a key aspect towards the deployment of UGC will be the development of polymeric dispersant (superplasticizer) formulations tailor-made for low-carbon cements, bridging between the developments at the cement and the concrete scale. However, these compounds also have a tendency to retard the hydration of cement, and is much more problematic in low carbon concrete than in ordinary concrete (Schmid & Plank, 2021). It is then necessary to revisit the molecular structure of these superplasticizers with a view of delivering an optimum performance in UGC.

2.1 Chemical admixtures: the technological enables of UGC

Chemical admixtures can be described as the "spices of concrete" (Flatt, 2016). Added in very low amounts, they can massively impact concrete properties. For blended cements this is particularly valuable to help UGC achieve the same fresh-state behavior as ordinary concrete. Hydration activators or accelerators can help to increase early strength by promoting the hydration of clinker and the reaction of SCMs, while superplasticizers (SP) are additionally used to control rheology (flow and flow retention). Superplasticizers are polymeric dispersants used in cementitious materials to reduce yield stress at a constant solids content (Gelardi et al., 2016; *Science and Technology of Concrete Admixtures - 1st Edition*, n.d.). The latest SPs are polycarboxylate-ethers (PCEs) (Plank et al., 2015; Plank & Ilg, 2020). They offer versatile chemical structures and excellent water reduction capability and are the most used type of superplasticizer today with yearly productions estimated at 2-5 Mio tons (Marchon et al., 2016).

The underlying mechanisms of action of admixtures are complex, involving specific interactions between admixtures and cement (Abile et al., 2018; Dalas et al., 2015; Ezzat et al., 2019; Flatt et al., 2009; Gelardi & Flatt, 2016) as well as among admixtures themselves (Flatt et al., 1998; Marchon et al., 2013). In the case of UGC, particularly interesting are the interactions of these molecules with the surface of the SCMs, which will be dominant in the system as the clinker content goes down below 250 kg/m^3.

2.2 Benchmarking concrete environmental performance and definition of UGC

The environmental footprint of cementitious materials (cement, concrete) is traditionally assessed through different indicators to compare and highlight the potential of different technologies. During the last decade, special attention has been placed to reduce the clinker factor and thus in the embodied CO_2 per unit mass of cement (ton CO_2/ton cement). The problem with this parameter is that it does not reflect differences in performance achieved with different replacement materials. Moreover, it misses the focus to which is the actual construction material.

A better indicator is the CO_2 content per cubic meter of concrete, as this is the actual footprint of a unit volume of material with a certain set of properties (strength, durability class, slump). Some authors have systematically explored large datasets with this perspective (Damineli et al., 2010), showing a large dispersion in the data (i.e., very different CO_2 footprints for the same strength), further highlighting the need of optimization and consideration of these concepts.

Certainly, the best approach would be to refer to the CO_2 footprint per unit surface of building/infrastructure, since this is the actual input of CO_2 to the environment for a given project. Computing this parameter is challenging, as it involves architectural and structural design considerations. Nevertheless, the adoption of a unified CO_2/m^3 approach by the concrete industry to benchmark products should enable designers to quickly compute the CO_2/m^2 for a given project, verifying compliance with recent standards such as the RE2020 (France) which introduced limits in this regard.

3. Concluding remarks and perspectives

This concept article introduced the ultra-green concrete concept as a technologically feasible pathway to develop a new generation of low-carbon concrete formulations based on a two-fold strategy (reduce clinker, reduce binder). In this regard, two outstanding questions are identified as key players to materialize UGC, and therefore attention and research efforts should be placed to develop solutions towards resolving them:

1. Reactivity of the supplementary cementitious materials used, to enable a considerable reduction in clinker content without the need of increasing the binder content in concrete to achieve typical strength and durability classes.
2. Development of dispersants (chemical admixtures) to make low clinker/low binder concrete compatible with common applications in conventional concrete construction.

As shown, both component of the two-fold strategy have in principle similar potential to reduce the CO_2 footprint of concrete. In markets where reactive SCMs such as calcined clays are (still) not available, attention should be focused in optimizing the concrete mixture design (reduce binder) with the available cements, enabling a timely reduction of CO_2 while accounting for the reality of different scenarios of application.

Acknowledgements

The ultra-green concrete project is supported by the Swiss National Science Foundation (SNSF) through an Ambizione fellowship granted to Dr. Zunino (grant 208719).

References

Abile, R., Russo, A., Limone, C., & Montagnaro, F. (2018). Impact of the charge density on the behaviour of polycarboxylate ethers as cement dispersants. *Construction and Building Materials*, *180*, 477–490. https://doi.org/10.1016/j.conbuildmat.2018.05.276

Boden, T., Andres, B., & Marland, G. (2017). *Global CO2 Emissions from Fossil-Fuel Burning, Cement Manufacture, and Gas Flaring*. Carbon Dioxide Information Analysis Center, Oak Ridge National Laboratory. https://cdiac.ess-dive.lbl.gov/trends/emis/tre_glob.html

Dalas, F., Pourchet, S., Nonat, A., Rinaldi, D., Sabio, S., & Mosquet, M. (2015). Fluidizing efficiency of comb-like superplasticizers: The effect of the anionic function, the side chain length and the grafting degree. *Cement and Concrete Research*, *71*, 115–123. https://doi.org/10.1016/j.cemconres.2015.02.001

Damineli, B. L., Kemeid, F. M., Aguiar, P. S., & John, V. M. (2010). Measuring the eco-efficiency of cement use. *Cement and Concrete Composites*, *32*(8), 555–562. https://doi.org/10.1016/j.cemconcomp.2010.07.009

Ezzat, M., Xu, X., El Cheikh, K., Lesage, K., Hoogenboom, R., & De Schutter, G. (2019). Structure-property relationships for polycarboxylate ether superplasticizers by means of RAFT polymerization. *Journal of Colloid and Interface Science*, *553*, 788–797. https://doi.org/10.1016/j.jcis.2019.06.088

Flatt, R. J. (2016). 28—Conclusions and outlook on the future of concrete admixtures. In *Science and Technology of Concrete Admixtures* (pp. 527–530). Woodhead Publishing. http://www.sciencedirect.com/science/article/pii/B978008100693100028X

Flatt, R. J., Houst, Y. F., Bowen, P., Hofmann, H., Widmer, J., Sulser, U., Mäder, U., & Bürge, T. A. (1998). Effect of Superplasticizers in Highly AlKaline Model Suspensions Containing Silica Fume. *Proc. 6th CANMET/ACI Intern. Conf. on Fly-Ash, Silica Fume, Slag and Natural Pozzolans in Concrete*, *2*, 911–930.

Flatt, R. J., Schober, I., Raphael, E., Plassard, C., & Lesniewska, E. (2009). Conformation of Adsorbed Comb Copolymer Dispersants. *Langmuir*, *25*(2), 845–855. https://doi.org/10.1021/la801410e

Gelardi, G., & Flatt, R. J. (2016). 11—Working mechanisms of water reducers and superplasticizers. In *Science and Technology of Concrete Admixtures* (pp. 257–278). Woodhead Publishing. http://www.sciencedirect.com/science/article/pii/B9780081006931000114

Gelardi, G., Mantellato, S., Marchon, D., Palacios, M., Eberhardt, A. B., & Flatt, R. J. (2016). 9—Chemistry of chemical admixtures. In *Science and Technology of Concrete Admixtures* (pp. 149–218). Woodhead Publishing. http://www.sciencedirect.com/science/article/pii/B9780081006931000096

IEA, & CSI. (2018). *Technology Roadmap: Low-Carbon transition in the Cement Industry*. 10.1007/springerreference_7300

I.N.N. (2019). *NCh170-19: Hormigon—Requisitos generales*.

Lothenbach, B., Scrivener, K., & Hooton, R. D. (2011). Supplementary cementitious materials. *Cement and Concrete Research*, *41*(12), 1244–1256. https://doi.org/10.1016/j.cemconres.2010.12.001

Marchon, D., Mantellato, S., Eberhardt, A. B., & Flatt, R. J. (2016). 10—Adsorption of chemical admixtures. In *Science and Technology of Concrete Admixtures* (pp. 219–256). Woodhead Publishing. http://www.sciencedirect.com/science/article/pii/B9780081006931000102

Marchon, D., Sulser, U., Eberhardt, A., & Flatt, R. J. (2013). Molecular design of comb-shaped polycarboxylate dispersants for environmentally friendly concrete. *Soft Matter*, *9*(45), 10719–10728. https://doi.org/10.1039/C3SM51030A

Pillai, R. G., Gettu, R., Santhanam, M., Rengaraju, S., Dhandapani, Y., Rathnarajan, S., & Basavaraj, A. S. (2019). Service life and life cycle assessment of reinforced concrete systems with limestone calcined clay cement (LC3). *Cement and Concrete Research*, *118*, 111–119. https://doi.org/10.1016/j.cemconres.2018.11.019

Plank, J., & Ilg, M. (2020). The Role of Chemical Admixtures in the Formulation of Modern Advanced Concrete. In W. P. Boshoff, R. Combrinck, V. Mechtcherine, & M. Wyrzykowski (Eds.), *3rd International Conference on the Application of Superabsorbent Polymers (SAP) and Other New Admixtures Towards Smart Concrete* (pp. 143–157). Springer International Publishing. https://doi.org/10.1007/978-3-030-33342-3_16

Plank, J., Sakai, E., Miao, C. W., Yu, C., & Hong, J. X. (2015). Chemical admixtures—Chemistry, applications and their impact on concrete microstructure and durability. *Cement and Concrete Research*, *78, Part A*, 81–99. https://doi.org/10.1016/j.cemconres.2015.05.016

Schmid, M., & Plank, J. (2021). Interaction of individual meta clays with polycarboxylate (PCE) superplasticizers in cement investigated via dispersion, zeta potential and sorption measurements. *Applied Clay Science*, *207*, 106092. https://doi.org/10.1016/j.clay.2021.106092

Science and Technology of Concrete Admixtures—1st Edition. (n.d.). Retrieved September 8, 2020, from https://www.elsevier.com/books/science-and-technology-of-concrete-admixtures/aitcin/978-0-08-100693-1?countrycode=CH&format=print&utm_source=google_ads&utm_medium=paid_search&utm_campaign=switzerlandshopping&gclid=CjwKCAjw19z6BRAYEiwAmo64LeYS_hMjfZWvcbVa9pyz2UJzbWFIgdwXsuzDnnewtVmHMj-eTg3KXBoCCa4QAvD_BwE

Scrivener, K., Avet, F., Maraghechi, H., Zunino, F., Ston, J., Hanpongpun, W., & Favier, A. (2019). Impacting factors and properties of limestone calcined clay cements (LC ^{3}). *Green Materials*, *7*(1), 3–14. https://doi.org/10.1680/jgrma.18.00029

Scrivener, K. L., John, V., & Gartner, E. M. (2016). *Eco-efficient cements: Potential, economically viable solutions for a low-CO2, cement-based materials industry*. United Nations Environmental Programme (UNEP).

Scrivener, K., Martirena, F., Bishnoi, S., & Maity, S. (2017). Calcined clay limestone cements (LC3). *Cement and Concrete Research*, *August 2017*, 1–8. https://doi.org/10.1016/j.cemconres.2017.08.017

Zunino, F., & Scrivener, K. (2021). The reaction between metakaolin and limestone and its effect in porosity refinement and mechanical properties. *Cement and Concrete Research*, *140*. https://doi.org/10.1016/j.cemconres.2020.106307

The 16th International Congress on the Chemistry of Cement 2023 (ICCC2023)
"Further Reduction of CO_2 -Emissions and Circularity in the Cement and Concrete Industry"
September 18–22, 2023, Bangkok, Thailand

Cement-Based Radiative Coolers for Photovoltaics: Towards a Practical Design

M. Cagnoni[1,a*], P. Testa[1,b], J.S. Dolado[2,3,c], and F. Cappelluti[1,d]

[1] *Department of Electronics and Telecommunications, Politecnico di Torino, Corso Duca degli Abruzzi 24, Torino, 10129, Italy*

[2] *Centro de Física de Materiales, CSIC-UPV/EHU, Paseo Manuel de Lardizabal 5, San Sebastián, 20018, Spain*

[3] *Donostia International Physics Center, Paseo Manuel de Lardizabal 4, San Sebastián, 20018, Spain*

[a] *matteo.cagnoni@polito.it*

[b] *pietro.testa@polito.it*

[c] *j.dolado@ehu.eus*

[d] *federica.cappelluti@polito.it*

ABSTRACT

In 2014, the experimental realization of radiative coolers capable of reaching sub-ambient temperatures under direct sunlight has opened up new possibilities for the thermal management of solar cells. Radiative coolers eject excess heat by emitting thermal radiation within the so-called atmosphere transparency window. The completely passive nature of this process and its reliance on material properties only, make radiative coolers extremely attractive in terms of energy efficiency. Integrated with a photovoltaic cell, the radiative cooler can reduce the cell operating temperature, leading to high efficiency and lifetime gains. Yet, most radiative coolers in the literature are metamaterials with scarce elements or complex fabrications processes, or organic materials with potential UV instability, with questionable economic viability or reliability. To address this problem, we have recently proposed cement-based materials as a low-cost, scalable and stable solution for photovoltaics cooling, showing that their electromagnetic properties can be tuned to maximize their thermal emissivity by acting on their microstructure. In particular, using a detailed balance model, we have demonstrated that their cooling performance could increase the efficiency of silicon solar cells by up to 9% and extended their lifetime by up to 4 times. In this work, we take a further step towards the experimental realization of this attractive concept, by investigating possible approaches, requirements and prospects for the practical design of photovoltaic systems employing cement-based radiative coolers.

KEYWORDS: *cements and concretes, radiative cooling, solar cells, thermal simulations, electromagnetic simulations*

1. Introduction

In the last decade, radiative cooling has become a very attractive thermal management solution for buildings and solar cells (Zeyghami, Goswami, and Stefanakos 2018), after the experimental demonstration of sub-ambient temperatures under direct sunlight in 2014 (Raman et al. 2014). Radiative coolers are designed to emit a large amount of thermal radiation within the so-called atmosphere transparency window (AW). In this wavelength range between 8 and 13 μm, radiation propagates undisturbed toward outer space. By

ejecting energy through this channel, radiative coolers can get rid of excess heat permanently and reduce their own temperature (Li and Fan 2019). Radiative coolers can be thermally coupled to a solar cell in the planar configuration shown in Figure 1. The cooler slab captures the excess heat generated within the cell during operation and ejects it from the system, reducing the temperature of the cell. This provides the two-fold advantage of increasing the solar cell efficiency and extending its lifetime (Zhu et al. 2014).

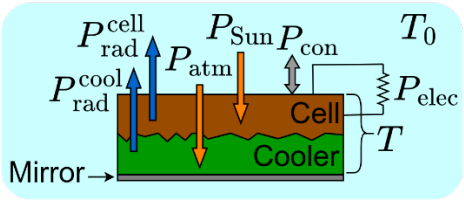

Figure 1. Solar cell with radiative cooler in planar configuration. The energy exchange terms entering the detailed-balance model used to determine the system operating temperature T are depicted. In particular, P_{Sun} is the power density absorbed by the cell from the Sun, P_{atm} is the one absorbed by the cooler from the atmosphere, $P_{\mathrm{rad}}^{\mathrm{cell}}$ and $P_{\mathrm{rad}}^{\mathrm{cool}}$ are the power densities emitted by the cell and the cooler, P_{elec} is the electrical power density delivered by the cell to the end user, P_{con} is the power density exchanged by the system with the environment by conduction/convection, and T_0 is ambient temperature.

Different kinds of radiative coolers have been proposed in the last few years (Hossain and Gu 2016), the most common ones being metamaterials made of stratified thin films or thick layers with a micro-patterned surface. Unfortunately, these technologies suffer from the use of scarce materials or expensive manufacturing processes, that might hinder scalability. Organic materials have been proposed as a low-cost alternative (Mandal et al. 2018), but their application might be jeopardized by UV-instability.

Looking for an alternative combining efficiency, low-cost and stability, we have recently proposed cementitious materials as extremely promising radiative coolers (Cagnoni, Tibaldi, Testa, et al. 2022; Cagnoni, Tibaldi, Dolado, et al. 2022), in the context of the EU-funded project MIRACLE (European Commission, n.d.). Not only cement-based solutions are cheap, scalable and robust, but also the complex nature of these materials, consisting of a heterogeneous porous matrix fillable with aggregates, provides many tuning knobs, from chemical to micro-structural modifications, to tailor their properties to fit radiative cooling applications. In our previous work, we have studied the interplay between microstructure and thermal radiation in slabs produced by alite hydration, used this knowledge to maximize their emissivity within the atmospheric window, and estimated their performance limit for the thermal management of solar cells, obtaining an impressive temperature reduction of 20 K for silicon-based devices, comparable with the more expensive metamaterials.

In this proceeding, we complement the aforementioned study focused on optimizing the cement-paste microstructure at fixed slab geometry (thickness = 100 µm, roughness = 0), by investigating the impact of thickness and roughness on the slab emission properties and cooling performance; this let us define geometric design rules for the cement slab.

2. Methodology

For this study, we have considered the cementitious material having the highest emissivity in the AW, characterized by (R_{CSH}, R_{CH}) = (0.6, 2.3) µm in our previous work (Cagnoni, Tibaldi, Dolado, et al. 2022); R_{CSH} and R_{CH} quantify the average size of the CSH and CH sub-domains forming the heterogeneous cement paste. The spectral directional absorbance/emissivity $A_{\Omega,\lambda}^{\mathrm{cool}}(\lambda,\theta)$ of a slab made of it has been determined as a function of thickness and roughness by inserting the previously determined complex permittivity into the transfer-matrix model (TMM) described in (Katsidis and Siapkas 2002), reformulated into scattering-matrix form to ensure numerical stability at large thickness and roughness.

Then, the calculated $A_{\Omega,\lambda}^{\mathrm{cool}}(\lambda,\theta)$ has been introduced into a detailed-balance model describing the energy exchange between cell, cooler, environment and end user as a function of the system temperature, by means of the power density terms introduced in Figure 1 and given by (Perrakis et al. 2021):

$$P_{\mathrm{Sun}} = \int_0^{hc/E_g} \mathrm{d}\lambda\, E_{e,\lambda}^{\mathrm{Sun}}(\lambda) \tag{1a}$$

$$P_{\mathrm{rad}}^{\mathrm{cell}} = \pi \int_0^{hc/E_g} \mathrm{d}\lambda\, L_{e,\Omega,\lambda}^{BB}\left(\lambda, T, V_{\mathrm{MPP}}\left(T, E_g\right)\right) \tag{1b}$$

$$P_{\text{elec}} = J_{\text{MPP}}(T, E_g)\, V_{\text{MPP}}(T, E_g) \tag{1c}$$

$$P_{\text{atm}} = \int_0^{2\pi} \mathrm{d}\Omega \int_0^{+\infty} \mathrm{d}\lambda \cos\theta\, A_{\Omega,\lambda}^{\text{atm}}(\lambda,\theta)\, A_{\Omega,\lambda}^{\text{cool}}(\lambda,\theta)\, L_{e,\Omega,\lambda}^{\text{BB}}(\lambda, T_0) \tag{1d}$$

$$P_{\text{rad}}^{\text{cool}} = \int_0^{2\pi} \mathrm{d}\Omega \int_0^{+\infty} \mathrm{d}\lambda \cos\theta\, A_{\Omega,\lambda}^{\text{cool}}(\lambda,\theta)\, L_{e,\Omega,\lambda}^{\text{BB}}(\lambda, T) \tag{1e}$$

$$P_{\text{con}} = h_c\,(T - T_0) \tag{1f}$$

where E_g is the solar cell band-gap, $E_{e,\lambda}^{\text{Sun}}$ is the Sun spectral irradiance, $L_{e,\Omega,\lambda}^{BB}$ is the black-body spectral radiance, J_{MPP} and V_{MPP} are the solar cell current density and voltage at maximum-power-point calculated according to the Shockley-Queisser model, $A_{\Omega,\lambda}^{\text{atm}}(\lambda,\theta)$ is the atmosphere spectral directional absorbance/emissivity, h_c is the conduction/convection coefficient, and Ω and θ are the solid and zenith angles. The solar cell temperature T is obtained by solving the equation:

$$P_{\text{rad}}^{\text{cell}} + P_{\text{rad}}^{\text{cool}} + P_{\text{elec}} - P_{\text{Sun}} - P_{\text{atm}} + P_{\text{con}} = P_{\text{net}}(T) = 0 \tag{2}$$

3. Results and Discussion

Figure 2 summarizes our findings. First, the spectral emissivity (angularly-averaged) of the cement-based slab as a function of thickness is depicted on the left for the case of a smooth surface. As expected, increasing the thickness enhances the emission properties and enables one to approach unit emissivity within the AW. Interestingly, one can obtain significant emission also for non-bulk thickness, even lower than the previously studied case of 100 µm. However, as a thickness of a few micrometers is approached, the layer starts to become transparent and the emission properties are lost. Although a very large thickness (~ cm) can be easily achieved for cementitious materials, sub-mm geometries can be an advantage for integrating the cement-based cooler into the photovoltaic system. Moreover, our results show that the emission loss due to a reduced thickness can be compensated for by a controlled surface roughness (Figure 2, center). For example, unit emissivity can be achieved with a 100 µm layer having approximately 2% roughness (RMS). Finally, the right image of Figure 2 shows the temperature reduction experienced by a solar cell when coupled to the cement-paste under study with the structural features reported in the legend. Clearly, a too much thin layer is unable to provide an appreciable cooling performance. On the other hand, little difference is found between the previously studied case of 100 µm and a much thicker layer (10 cm), which is encouraging concerning the possibility of integrating a cement-based radiative cooler with a solar cell. Remarkably, we observe that a realistic roughness (2%) enables one to reach the temperature reduction brought by an ideal solar cell radiative cooler (black-body in IR spectral range (Zhao et al. 2019)).

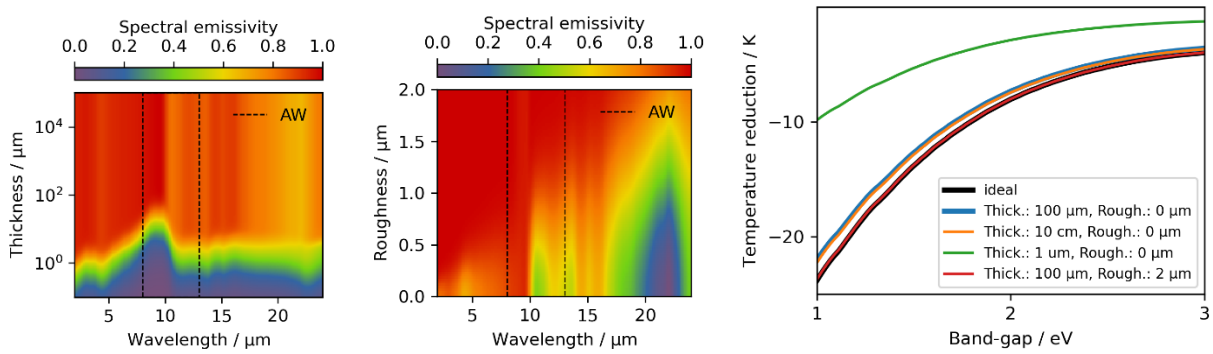

Figure 2. Spectral emissivity of cement-based radiative coolers vs thickness (left) and roughness (center, 100 µm thickness), and solar cell temperature reduction vs bandgap (right) for different thickness-roughness values. The atmospheric window (AW) is highlighted, as well as the temperature reduction brought by an ideal cooler.

4. Conclusions

Cement-based materials are a very attractive solution for realizing radiative coolers for the thermal management of solar cells because their thermal emissivity can be optimized by tuning their micro-structure. In this work, we have systematically studied the impact of the cement slab geometry on the cooling performance of a practical system consisting of a solar cell mounted on top of a cement slab. Interestingly, we have confirmed that satisfying cooling performance can be preserved by resorting to

relatively small thickness, which is encouraging in view of integration of cement-based radiative coolers into photovoltaic systems. Furthermore, we have shown that possible emissivity losses due to the reduced size of the cooler can be compensated for by introducing a controlled surface roughness, which leads to enhanced emission and enable us to approach ideal emissivity and significant solar cell temperature reduction. These findings bring us closer to the practical realization of this concept, by clarifying structural design requirements for the cement-based radiative cooler. Therefore, high efficiency and lifetime gains could be pursued by photovoltaic systems integrating radiative coolers relying on the cheap, scalable and robust class of cementitious materials.

Acknowledgements

This project has received funding from the European Union's Horizon 2020 research and innovation program under grant agreement No. 964450.

References

Bohnet, Matthias, and Fritz Ullmann, eds. 2003. *Ullmann's Encyclopedia of Industrial Chemistry*. Weinheim, DE: Wiley.

Cagnoni, Matteo, Alberto Tibaldi, Jorge S. Dolado, and Federica Cappelluti. 2022. "Cementitious Materials as Promising Radiative Coolers for Solar Cells." *IScience* 25 (11): 105320. https://doi.org/10.1016/j.isci.2022.105320.

Cagnoni, Matteo, Alberto Tibaldi, Pietro Testa, Jorge Sánchez Dolado, and Federica Cappelluti. 2022. "Passive Radiative Cooling of Solar Cells by Low-Cost and Scalable Metamaterials: Physical Simulation and Efficiency Limits." In *Physics, Simulation, and Photonic Engineering of Photovoltaic Devices XI*, 1199606. San Francisco, US-CA: SPIE. https://doi.org/10.1117/12.2607489.

Centurioni, Emanuele. 2005. "Generalized Matrix Method for Calculation of Internal Light Energy Flux in Mixed Coherent and Incoherent Multilayers." *Applied Optics* 44 (35): 7532. https://doi.org/10.1364/AO.44.007532.

European Commission. n.d. "Photonic Metaconcrete with Infrared Radiative Cooling Capacity for Large Energy Savings." CORDIS: EU Research Results. https://cordis.europa.eu/project/id/964450.

Hossain, Md. Muntasir, and Min Gu. 2016. "Radiative Cooling: Principles, Progress, and Potentials." *Advanced Science* 3 (7): 1500360. https://doi.org/10.1002/advs.201500360.

Katsidis, Charalambos C., and Dimitrios I. Siapkas. 2002. "General Transfer-Matrix Method for Optical Multilayer Systems with Coherent, Partially Coherent, and Incoherent Interference." *Applied Optics* 41 (19): 3978–87. https://doi.org/10.1364/AO.41.003978.

Li, Wei, and Shanhui Fan. 2019. "Radiative Cooling: Harvesting the Coldness of the Universe." *Optics and Photonics News* 30 (11): 32. https://doi.org/10.1364/OPN.30.11.000032.

Mandal, Jyotirmoy, Yanke Fu, Adam C. Overvig, Mingxin Jia, Kerui Sun, Norman N. Shi, Hua Zhou, Xianghui Xiao, Nanfang Yu, and Yuan Yang. 2018. "Hierarchically Porous Polymer Coatings for Highly Efficient Passive Daytime Radiative Cooling." *Science* 362 (6412): 315–19. https://doi.org/10.1126/science.aat9513.

Perrakis, George, Anna C. Tasolamprou, George Kenanakis, Eleftherios N. Economou, Stelios Tzortzakis, and Maria Kafesaki. 2021. "Combined Nano and Micro Structuring for Enhanced Radiative Cooling and Efficiency of Photovoltaic Cells." *Scientific Reports* 11 (1): 11552. https://doi.org/10.1038/s41598-021-91061-1.

Raman, Aaswath P., Marc A. Anoma, Linxiao Zhu, Eden Rephaeli, and Shanhui Fan. 2014. "Passive Radiative Cooling Below Ambient Air Temperature Under Direct Sunlight." *Nature* 515 (7528): 540–44. https://doi.org/10.1038/nature13883.

Safi, Taqiyyah S., and Jeremy N. Munday. 2015. "Improving Photovoltaic Performance Through Radiative Cooling in Both Terrestrial and Extraterrestrial Environments." *Optics Express* 23 (19): A1120. https://doi.org/10.1364/OE.23.0A1120.

Zeyghami, Mehdi, D. Yogi Goswami, and Elias Stefanakos. 2018. "A Review of Clear Sky Radiative Cooling Developments and Applications in Renewable Power Systems and Passive Building Cooling." *Solar Energy Materials and Solar Cells* 178 (May): 115–28. https://doi.org/10.1016/j.solmat.2018.01.015.

Zhao, Dongliang, Ablimit Aili, Yao Zhai, Shaoyu Xu, Gang Tan, Xiaobo Yin, and Ronggui Yang. 2019. "Radiative Sky Cooling: Fundamental Principles, Materials, and Applications." *Applied Physics Reviews* 6 (2): 021306. https://doi.org/10.1063/1.5087281.

Zhu, Linxiao, Aaswath Raman, Ken Xingze Wang, Marc Abou Anoma, and Shanhui Fan. 2014. "Radiative Cooling of Solar Cells." *Optica* 1 (1): 32. https://doi.org/10.1364/OPTICA.1.000032.

The 16th International Congress on the Chemistry of Cement 2023 (ICCC2023)
"Further Reduction of CO_2 -Emissions and Circularity in the Cement and Concrete Industry"
September 18–22, 2023, Bangkok, Thailand

Capability of traditional and geopolymer cementitious systems for the immobilization of a thermally treated ion exchange resin

P. Perez-Cortes[1], I. García-Lodeiro[1], E. Torres[2], M.C. Alonso[1]* and F. Puertas[1]

[1] *Eduardo Torroja Institute for Construction Sciences (IETcc, CSIC), Madrid, Spain*

pedro.perez@ietcc.csic.es; iglodeiro@ietcc.csic.es; mcalonso@ietcc.csic.es*; puertasf@ietccc.csic.es

[2] *CIEMAT, Madrid, Spain*

elena.torres@ciemat.es

ABSTRACT

This work explores the ability of cementitious systems of Portland cement and geopolymer for the immobilization of a surrogate radioactive waste from thermally treated resins (RI). The RI made up of ashes obtained from the thermal decomposition at 450°C of a Spent Ion Exchange Resin doped with B, Cs, Sr and metal traces (Cr, Co, Fe, Zn). As Portland cement systems, a CEM I (CEM I/42.5SR) and a CEM III (CEM III/B 32.5) were selected. The geopolymer was designed based on one-part geopolymer matrices, formulated with mixtures of metakaolin (MK) and blast furnace slag (BFS) as precursors, and Na_2SiO_3/NaOH powders as the solid activator. The effect of incorporating 0, 10, 20 and 30% of the surrogated RI (% relative to the weight of the cementitious binder) on the mechanical strength of cement pastes at 3, 7 and 28 days was studied. In addition, changes in the hydration kinetics, pore structure and microstructure were analyzed. According to the results, the compressive strength of all systems decreased with increasing the RI dosage; this was accompanied by an increase in the total porosity and changes in the pore size distribution. Furthermore, the acidic nature of the RI significantly delayed the hydration and strength gain of Portland cement systems, an effect that was more remarkable in CEM I. Despite the unfavorable effect of the RI, the CEM III and geopolymer matrices reached 28-day compressive strengths of 40 MPa and 45 MPa, respectively, when 20% of RI was incorporated, making the latter a promissory novel alternative cementitious system for the immobilization of radioactive wastes of type thermally-treated spent ion exchange resins.

KEYWORDS: *nuclear wastes; encapsulation; geopolymers; Spent Ion exchange resins, Portland cement.*

1. Introduction

Solid radioactive wastes of variable types and sources are generated by several nuclear applications. Low (LLW) and intermediate (ILW) levels of solid radioactive wastes represent about 99% of the total volume in the world (≈38 million m^3; IAEA, 2022) and large amounts correspond to the spent granular ion-exchange resins (SIERs), which are generated in the water purification systems of nuclear power plants. The SIERs are usually heat treated to reduce volume and then confined in a solid cementitious matrix (Ojovan et al., 2001). The stability of the reconditioned solid waste form depends to a large extent on the compatibility between the waste and cementitious matrix (Alonso et al., 2022). Portland cement (PC) - based systems have been for many years the preferred matrix for confining L&ILW. However, specific components in nuclear wastes can easily affect the hydration process of PC and hardening properties, leading to various durability issues because, in PC systems, the radionuclides are mainly immobilized by chemisorption and physical encapsulation (Zhu et al., 2022). Recently, geopolymer (GP) cementitious systems are emerging as promising binder materials for L&ILW encapsulation, due to their cationic binding sites and good durability properties. As a new technology, the capability of GP systems to confine thermally treated SIER remains to be demonstrated.

This study aims to evaluate the capability of PC and GP cementitious systems for the encapsulation of a thermally-treated SIER radioactive surrogate waste (RI), focusing on the influence of the RI on the mechanical properties, porosity and microstructure of the cementitious matrices.

2. Experimental

A CEM I/42.5SR and a CEM III/B32.5 were evaluated as PC systems. The one-part geopolymer (GP), systems consisted of a mixture of metakaolin (MK) and blast furnace slag (BFS), which were activated with blends of Na_2SiO_3 (49.16%SiO_2, 50.77%Na_2O, 2.61 density) and NaOH powders. Table 1 shows the chemical composition of the CEM I, CEM III, MK and BFS while the dosage of the studied PC and GP systems are shown in Table 2.

Table 1. Chemical composition (% wt. oxide, by XRF)

	SiO_2	Al_2O_3	Na_2O	MgO	CaO	K_2O	TiO_2	Fe_2O_3	SO_3	Others	LOI*
CEM I	17.4	4.7	0.2	1.8	60.3	0.3	-	5.0	3.2	2.9	4.2
CEM III	27.2	8.3	0.2	6.5	51.5	0.7	0.7	1.5	2.1	0.3	1.0
BFS	34.8	11.6	-	11.9	37.9	0.3	0.5	0.2	-	2.6	0.3
MK	55.9	38.9	-	0.1	0.1	0.5	1.6	1.2	-	0.3	1.4

*LOI: Loss of ignition 1000±5ºC

Table 2. Dosage of the studied PC and GP systems (weight %)

System ID	CEM I	CEM III	MK	BFS	Na_2SiO_3	NaOH	RI	w/s*
CEM I	100							0.4
CEM III		100						0.4
GP A			43	40	10	7		0.4
CEM I+10%RI	90						10	0.4
CEM III+10%RI		90					10	0.4
GP A+10%RI			38.7	36	9	6.3	10	0.4
CEM I+30%RI	70						30	0.4
CEM III+30%RI		70					30	0.4
CEM I	100							0.3
CEM III		100						0.3
GP B			42.5	42.5	15			0.3
CEM I+20%RI	80						20	0.3
CEM III+20%RI		80					20	0.3
GP B+20%RI			34	34	12		20	0.3

*Water/solid ratio

The RI consisted of ashes obtained from the thermal decomposition at 450°C of a Spent Ion Exchange Resin (mixture of Amberlite IRN-77 and IRN-78 in a 50/50 ratio) doped with B, Cs, Sr and metal traces of Cr, Co, Fe, Zn. The conditioned RI was granular, with a mean particle size of 300 μm, hygroscopic, with a water content of 3% and had a very acidic pH of 2.4. The RI was incorporated in PC and GP pastes in the proportions indicated in Table 2 and its effect on the compressive strength of prismatic specimens of 1x1x6 cm^3 at 3, 7 and 28 days was evaluated. In addition, changes in the hydration kinetics, pore structure and microstructure were analyzed in selected samples by isothermal calorimetry tests, mercury intrusion porosity (MIP) and backscattering electron microscopy (BSEM), respectively.

3. Results and discussion

Figure 1a shows that the incorporation of RI reduced the compressive strength in all systems. CEM III+10%RI and GP A+10%RI did not record mechanical strength in the first 3 days. After 28 days, CEM I+10%RI and CEM III+10%RI samples achieved similar compressive strength values, which were ≈62% lower than the systems without the RI, but in any case slightly overpassed the 10 MPa that is considered as the acceptable limit for the immobilization of the radioactive wastes (ENRESA, 2008). The 28-day compressive strength of GP A+10%RI was under the acceptable limit. It is noteworthy that the incorporation of 30% of RI inhibited the setting of CEM I and CEM III and therefore the PC samples did not record compressive strength during the evaluated period.

Considering the above and that the RI has a fluidizing effect on the fresh binders, it was decided to evaluate the incorporation of 20% of RI, and adjust the water/solid ratio (w/s) to 0.3 for the PC and GP systems, guaranteeing adequate fluidity of the fresh binders. In the case of GP, an optimization of the components was also carried out to improve its mechanical performance. As shown in Figure 1b, with this adjustment, all reference matrices (without the RI) underwent a better mechanical strength development, reaching 28-day compressive strength values higher than 60 MPa. As expected, the mechanical strengths reduced after the incorporation of 20% RI; this effect was more remarkable in CEM I (16 MPa after 28 days). CEM III had a better mechanical performance than CEM I, recording acceptable strengths after 7 days and reaching up to 40 MPa after 28 days. The GP B showed a more favorable response in mechanical performance reaching more than 30 and 45 MPa after 3 and 28 days, respectively. Despite the deleterious effects of the RI, both PC and GP matrices with 20% of RI far overpassed the acceptance criteria of compressive strength for encapsulating radioactive wastes (ENRESA, 2008).

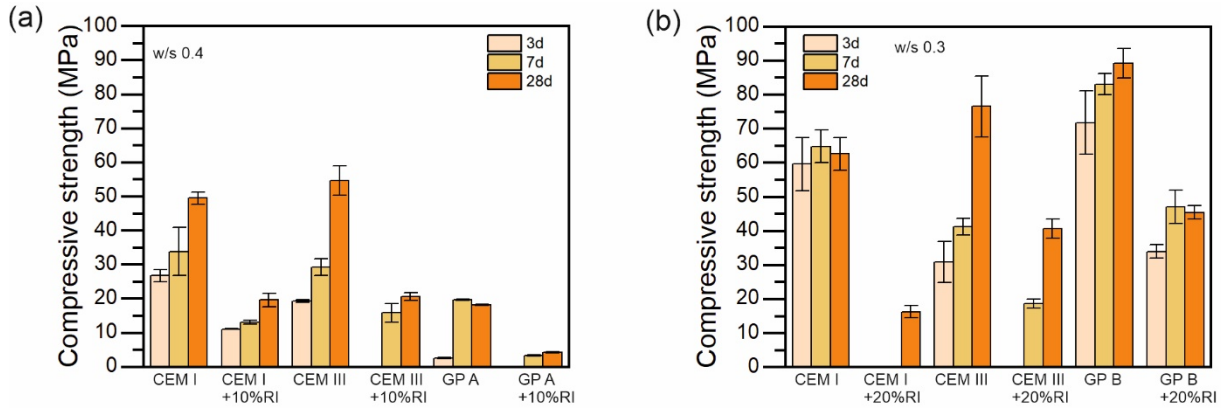

Figure 1. Compressive strenghts at 3, 7 and 28 days of PC and GP pastes of (a) w/s of 0.4, without and with 10% of RI, and (b) w/s of 0.3, without and with 20% of RI.

Isothermal calorimetry tests were performed on PC systems (w/s=0.4) to elucidate the effect of the RI on PC hydration. As shown in Figure 2, the cement hydration was delayed with 10% of RI and practically inhibited when 30% of RI was incorporated (Figure 2a). CEM III+10%RI underwent lower heat flow than CEM I+10%RI in the first 85h. In addition, the total heat reduced from 250-300 J/g to <50 J/g in both PC samples with 30% of RI (Figure 2b). The acidic character of the RI clearly delays and inhibits the PC hydration.

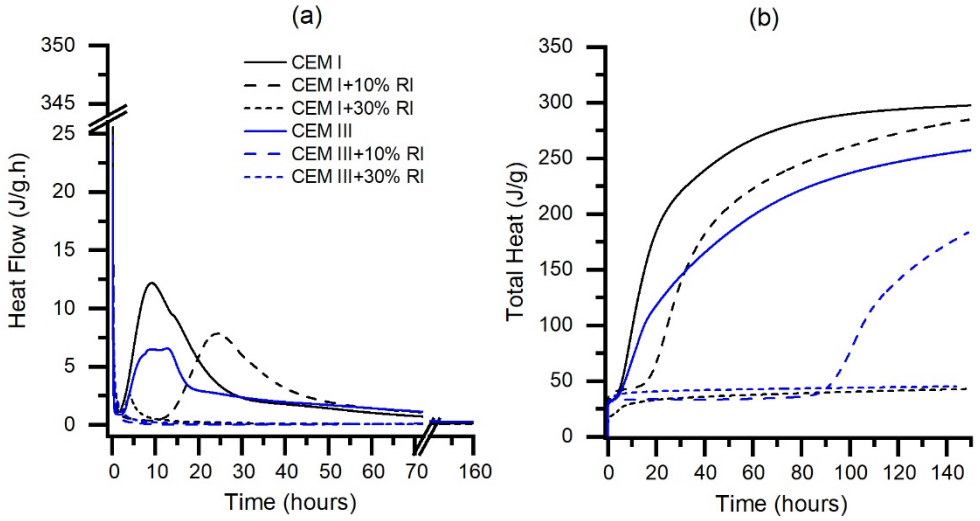

Figure 2. (a) Heat flow and (b) Total heat of CEM I (black lines) and CEM III (blue lines) without (solid lines) and with 10% (dash lines) and 30% (short dash lines) of RI.

The characterization of the pore structure and microstructure of the matrices agree well with the mechanical test results. As shown in Figure 3a, the incorporation of 20%RI increased the total porosity in all systems and shifted the pore size diameter towards higher values. The latter was more remarkable in CEM I+20%RI,

which also showed a more heterogeneous microstructure with an important number of anhydrous clinker phases. The RI particles (dark color) introduced pores in the cementitious matrices, where a porous interfacial zone can be identified in all systems (Figure 3b-d).

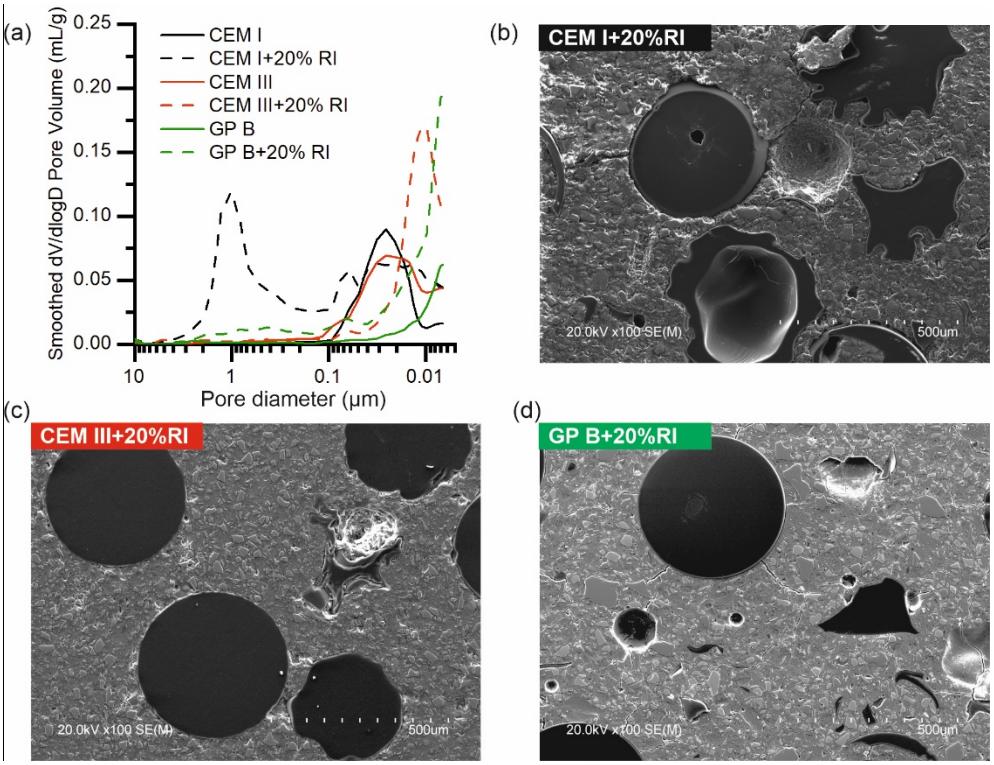

Figure 3. Pore structure and microstructure of PC and GP matrixes with 20% RI after 28 days (w/s=0.3).

4. Conclusions

The RI surrogate waste influences the microstructure and mechanical properties of both PC and GP-based systems. Its incorporation increases the total porosity and the pore size diameter, which significantly reduces the mechanical properties. In PC systems, the acid character of RI delays and inhibits the cement hydration phases, seriously affecting the early mechanical strengths. Despite the deleterious effects of the RI, both PC and GP matrices with 20% of RI far overpasses the acceptance criteria of compressive strength for encapsulating radioactive wastes. CEM III+20%RI and GP+20%RI achieve 40-45 MPa, making geopolymers promising matrices for the immobilization of thermally-treated SIERs.

Acknowledgments

Authors thank the EU project "PRE-DISposal management of radioactive waste". The project has received funding from the Euratom research and training programme 2019-2020 under grant agreement No. 945098. An author acknowledges the concession of the JIN project (Ref. PID2020-116738RJ-I0) funded by the Ministry of Science and Innovation (Projects I+D+I 2020).

References

Alonso, M.C., Puertas, F., Garcia-Lodeiro, I., Perez-Cortes, P. (2022) "Immobilization of the treatet wastes by geopolymer or cement-based materials encapsulation", *PREDIS Proceedings of April Workshop 2022*, Espoo, Finland.

ENRESA (2008) "Criterios de Aceptación de Unidades de Almacenamiento", *Referencia 031-ES-IN-0002* rev. 1. Julio 2008.

IAEA (2022) "Status and Trends in Spent Fuel and Radioactive Waste Management", IAEA Nuclear Energy Series No. NW-T-1.14 (Rev. 1), Vienna, 2022.

Ojovan, M.I., Petrov, G.A., Dmitriev, S.A., Trusov, B.G., Semenov, K.N. and Klimov, V.I. (2011) "Thermochemical Treatment of Spent Ion Exchange Resins", *IAEA-CSP—6/C,* paper 49, 2001.

Zhu, Y., Zheng, Z., Deng, Y., Shi, C., & Zhang, Z. (2022). Advances in immobilization of radionuclide wastes by alkali activated cement and related materials. *Cement and Concrete Composites*, 126, 104377.

The 16th International Congress on the Chemistry of Cement 2023 (ICCC2023)
"Further Reduction of CO_2 -Emissions and Circularity in the Cement and Concrete Industry"
September 18–22, 2023, Bangkok, Thailand

Influence of Waste Glass Powder and Silica Flour on Compressive Strength and Permeability of Cement Pastes at HTHP

C. Geng[1], C. Wang[1], Y. Ma[1], X. Yao[1*], D. Lu[1], J. Xu[1]

[1] *College of Materials Science and Engineering, Nanjing Tech University, Nanjing, China*

** Corresponding author. E-mail: htmpaper@sina.com (X. Yao).*

ABSTRACT

The strength stability of the cement sheath is critical for the long-term safe exploitation of high-temperature and high-pressure (HTHP) wells. This study discovered that oil well cement replaced by a mixture of waste glass powder (WGP) and silica flour (SF) has a higher compressive strength than that replaced by a single silicon-rich material at 260℃ and 21 MPa for up to 300 d. After 300-day curing at HTHP, the compressive strengths of HCPs incorporating 40 wt.% WGP, 35 wt.% SF and mixture of 25%WGP and 10%SF were 27.51 MPa, 30.61MPa and 34.68 MPa, respectively. Amorphous SiO_2 in WGP improved the early age compressive strength of HCPs due to its higher activity, while crystalline SiO_2 in SF was more effective at refining the pore structure of HCPs. The most probable pore diameter decreased with increasing dosage of SF, it caused the permeability of HCPs decreased. XRD results indicated that the xonotlite, which provided high compressive strength of HCPs, dominated the phase component of HCPs with the incorporation of SiO_2. Properly compounding SF and WGP and adjusting the dosage will be beneficial to the development of strength and permeability of HCPs. And it gives an assistance to the reduction of CO_2 emissions.

KEYWORDS: *Waste glass powder, Silica flour, High temperature and high pressure, Crystalline SiO_2, Amorphous SiO_2*

1. Introduction

Glass is one of the most commonly used materials in the world. And 10 million-tons waste glass powder (WGP) cannot be recycled every year, e.g. the recycling rate of waste glass is 13% in China and 27% in America (Dong et al., 2018). The glass contains ~70% amorphous SiO_2 that is used as an activity admixture for cement because of its pozzolanic activity. Silicon-rich materials are commonly used to improve strength stability by adjusting the Ca to Si ratio (C/S) of hardened cement pastes (HCPs). Geng et al (2022a) investigated the effect of WGP on compressive strength of HCPs at 260℃ and 21 MPa and the results confirmed the feasibility of WGP as a high-temperature stabilizer in deep-well cementing. However, Geng et al (2022b) reported the effect of crystalline state of SiO_2 on mechanical properties and results showed that crystalline SiO_2 had a better effect on the pore structure of HCPs than amorphous SiO_2 which was positive to the permeability. In this paper, the compressive strengths and permeability of HCPs incorporating different dosages of WGP and silica flour (SF) at 260℃ and 21 MPa were studied. Microstructure of HPCs was investigated by X-ray diffraction (XRD) and mercury intrusion porosimetry (MIP). This work gives an assistance for the design of the cement slurry formulation and reduction of CO_2 emissions by reducing the amount of cement used in cementing at HTHP.

2. Materials and methods

2.1 Materials

Class G oil well cement (OWC) was obtained from Gezhouba Enterprise Company (Changde, China). 325-mesh silica flour (SF325) was obtained from Fengyang Tengfei quartz sand factory (Anhui, China). The detailed physicochemical properties of materials was described in our previous study (Geng et al, 2022a). The waste glass was plate glass discarded by households and companies. Waste glass was ground fine with ethanol by using a planetary ball mill and the particle size of WGP was 325 mesh (WGP325).

2.2 Experimental methods

Cement slurries were prepared according to API standard and water to solid ratio was 0.44. The information of cement slurries is shown in Table1.

Table 1 Mix proportions of cement mixtures.

Samples	Mix proportions(wt.%)			W/S	ρ(g/cm^3)
	OWC	SF325	WGP325		
WGP40	60	0	40	0.44	1.85
WGP15	65	20	15	0.44	1.85
WGP25	65	10	25	0.44	1.86
SF35	65	35	0	0.44	1.86

Cylindrical molds (2.54 cm×φ2.54 cm) were used in pre-curing of cement slurries. HCPs were demoulded and pre-cured at 80℃ and 0.1 MPa for 48 h in water bath. After pre-curing, the HCPs were put into the pressure vessel. The temperature and pressure were preset for 260℃ and 21 MPa. The temperature was heated at a heating rate of 50 ℃/h. Pressure was controlled by pressure booster pump. When being cured for specific age, HCPs were cooled naturally and removed from the autoclave. The uniaxial compressive strengths of HCPs cured at HTHP were tested by an AEC-201 cement strength tester (Ruifeng, Shanghai) with a loading rate of 1.2 kN/s. The permeability of sample was tested by HLY-2 core flow meter. The confining pressure was 10±0.1 MPa and displacement pressure was 2.9±0.1 MPa. It was carried out at 25℃ and the test medium was water. The samples used for characterization analysis were submerged in anhydrous ethanol to remove the free water from HCPs in order to stop hydration. Before XRD and MIP tests, the samples were taken out of the ethanol, and then dried at 60℃±2℃ using a drying oven for 4 h.

3. Results and discussion

3.1 Compressive strength

The compressive strengths of HCPs cured at 260℃ and 21 MPa at different ages are shown in Fig. 1.

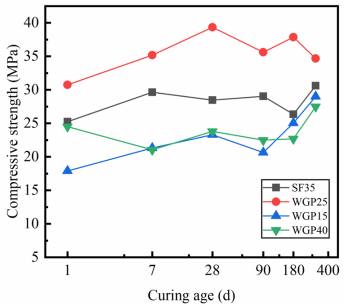

Fig. 1. Compressive strengths of HCPs cured at 260℃ and 21 MPa at different ages

Compared with neat cement pastes, WGP could stabilize the compressive strength of HCPs effectively at under long-term HTHP condition. It has been studied in our previous work (Geng et al., 2022a) and it will not be discussed in this work. There was no significant correlation between the dosage of WGP325 and the compressive strength of HCPs. When the dosage of WGP325 is highest, the compressive before 28 d is lowest. However, the compressive strength of WGP25 is highest at every curing age. After 300-day curing at HTHP, the compressive strengths of WGP40, SF325 and WGP25 were 27.51 MPa, 30.61 MPa and 34.68 MPa, respectively. Amorphous SiO_2 in WGP improves the early age compressive strengths of

HCPs due to its higher activity. The compressive strength of hardened cement paste at HTHP is related to its microstructure. The phase development and pore structure of HCPs will be discussed in related section.

3.2 Permeability

The permeability of HCPs cured at 260°C and 21 MPa at different ages are shown in Table 2. There was no significant difference in the order of magnitude of the permeability of all samples. To some extent, the permeability of HCPs increases with the increasing dosage of WGP325 before 300 d. And the permeability of HCPs incorporating both WGP325 and SF325 are close. It means that SF325 have more positive effect on the permeability of HCPs cured at HTHP than WGP325.

Table 2 Permeability of HCPs cured at 260°C and 21 MPa at different ages/mD

Samples	Curing age/d					
	1	7	28	90	180	300
WGP40	1.69×10^{-1}	6.15×10^{-2}	1.12×10^{-1}	1.15×10^{-1}	8.76×10^{-2}	3.54×10^{-2}
WGP15	3.08×10^{-2}	2.57×10^{-2}	2.04×10^{-2}	2.04×10^{-2}	1.54×10^{-2}	1.32×10^{-2}
WGP25	4.61×10^{-2}	4.61×10^{-2}	3.58×10^{-2}	3.54×10^{-2}	2.74×10^{-2}	1.03×10^{-2}
SF35	1.08×10^{-2}	1.20×10^{-2}	1.03×10^{-2}	8.96×10^{-3}	6.61×10^{-2}	1.03×10^{-2}

3.3 Phase development

The diffraction spectra of HCPs are displayed in Fig. 2a-d. The xonotlite dominates in all samples at every curing age, and this phase is the main skeleton of HCPs to provide the strength at HTHP. Unreacted α-SiO_2 can be observed after 300-day curing at HTHP in SF35. As shown in Fig. 2b and d, tobermorite that is indentified at 2θ≈7.8°, is observed in WGP15 and WGP40 at 1 d, but it disappears at 180 d and 300 d. That is caused by the transition from tobermorite to xonotlite at HTHP. Tobermorite only occurring in HCPs incorporating WGP325 indicated that the transformation from tobermorite to xonotlite is inhibited. And Geng et al (2022a) suggested that foreign ions in WGP325 caused it.

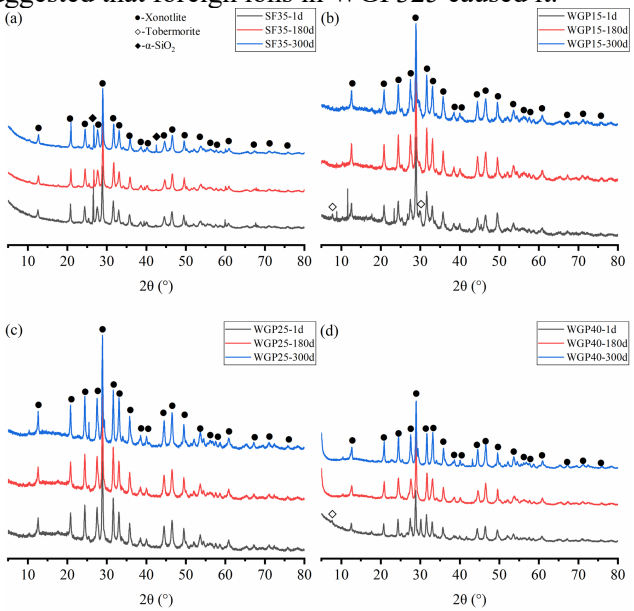

Fig. 2. XRD patterns of HCPs at 260°C and 21 MPa. Phase identified: Quartz alpha, SiO_2, PDF No. 89-8935; Tobermorite, $xCaO{\cdot}SiO_2{\cdot}zH_2O$, PDF No. 6-13; Xonotlite, $Ca_6Si_6O_{17}(OH)_2$, PDF No. 29-379.

3.4 Pore structure

The pore structure of HCPs is divided into three categories: large capillaries (>100 nm), medium capillaries (50~100 nm) and gel pores (10~50 nm), according to Mindess et al (2002). Fig. 3 shows the pore distribution of all samples. Živica et al (1997) proposed that the permeability of HCPs is related to the pore structure. In this work, the same relationship is observed. When the dosage of WGP325 increases,

the peak of pore distribution shifts regularly that the most probable pore size increases. And permeability increases with the increasing most probable pore size of HCPs. In addition, the denser pore structure of HCPs is positive to the compressive strength, e.g. SF35 and WGP25. However, the strength of HCPs is influenced by the phase composition, as well. It explains why the compressive strength of WGP15 is low, but the pore structure is dense as shown in Fig. 3b. However, detailed quantitative relationship between strength and microstructure is not clear and that will be studied in further work.

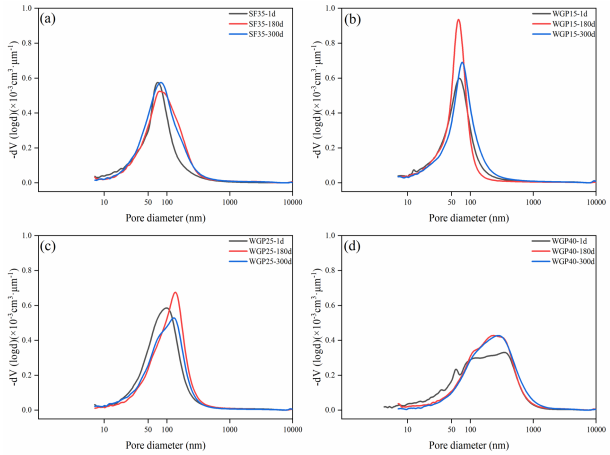

Fig. 3. Pore distribution of all samples curing at 260℃ and 21 MPa.

4. Conclusion

This study investigated the effect of WGP and/or SF on the compressive strength, permeability and microstructure of cement pastes at 260℃ and 21 MPa. The following conclusions were obtained according to the results:

(1) Silica flour and waste glass powder were positive to the compressive strength and permeability of cement pastes at HTHP. Cement pastes incorporating mixture of 10% silica flour and 25% waste glass powder had highest strengths at every curing age. Meanwhile the permeability was lowest after 300-day curing.

(2) Effects of silica flour and waste glass powder on the phase composition of HCPs at HTHP were similar, and xonotlite dominated in all samples. However, the tobermorite was only observed in HCPs incorporating waste glass powder and it may be caused by the foreign ions in waste glass powder.

(3) Incorporating of waste glass powder increased the most probable pore size which was negative to the pore structure and caused the permeability of HCPs to increase. Silica flour replacing suitable dosage of waste glass powder could decrease the permeability by densifying the pore structure of HCPs. The mixture of silica flour and waste glass powder could optimize the properties of HCPs at HTHP. However, the dosage need to be adjusted appropriately.

References

Dong, H. Geng, Y. Yu, X. Li, J. (2018) “Uncovering energy saving and carbon reduction potential from recycling wastes: a case of Shanghai in China”, *Journal of Cleaner Production*, 205: 27-35.

Geng, C. Wu, X. Yao, X. (2022a) “Reusing waste glass powder to improve the strength stability of cement at HTHP”, *Journal of Petroleum Science and Engineering*, 213: 110394.

Geng, C. Mei, Z. Yao, X. (2022b) “Effect of the crystalline state of SiO2 on the compressive strength of cement paste at HTHP”, *Construction and Building Materials*, 362: 129787.

S. Mindess. J.F. Young. D. Darein. (2002), “Concrete, Second ed.”, Prentice Hall.

V. Živica (1997) “Relationship between pore structure and permeability of hardened cement mortars: on the choice of effective pore structure parameter”, *Cement and Concrete Research*, 27(8): 1225-1235.

The 16th International Congress on the Chemistry of Cement 2023 (ICCC2023)
"Further Reduction of CO_2 -Emissions and Circularity in the Cement and Concrete Industry"
September 18–22, 2023, Bangkok, Thailand

Valorization of Calcium Sulfate Residues by Adding Accelerating Admixture in Portland cement

R. Pinto Costa[1*], M. H. Gomes de Medeiros[1], A. Machado Fagundes[1], F. Viero Silveira[1], S. Suzuki[2], A. P. Kirchheim[1]

[1] *Federal University of Rio Grande do Sul (UFRGS), Porto Alegre, RS, Brazil*
Email: rayarapintocosta@gmail.com
Email: matheus96h@gmail.com
Email: andre.mf.af@gmail.com
Email: fernando.v.silv@gmail.com
Email: anapaula.k@gmail.com
[2] *InterCement Brasil S.A., Brazil, São Paulo, SP*
Email: seiitis@intercement.com

ABSTRACT

Using residues from industrial processes has been a viable strategy to reduce greenhouse gas emissions and decrease the extraction of traditional raw materials. In recent years, there has been a growth in research related to alternative materials to replace natural gypsum (NG) in Portland cement production. Among these residues, phosphogypsum (PG) and flue gas desulfurization gypsum (FGD), industrial wastes generated annually in large quantities, stand out. PG is a waste product from the phosphate fertilizer industry, and FGD is a waste product from the flue gas desulfurization process released by thermal power plants. Their composition is mainly calcium sulfate, but impurities can be found in their constitution. These impurities can cause excessive delays in setting time and compromise the initial mechanical strength of cement. Accelerating admixtures can improve the lower reactivity of these types of cement, making their use feasible. Thus, this paper aims to evaluate the hydration behavior of Portland cement with NG, PG, and FGD as set regulators in the presence of triethanolamine (TEA). For this, an experimental program composed of two stages was carried out. The first stage consisted of the physical-chemical characterization of the materials by X-ray fluorescence, X-ray diffraction, laser granulometry, thermogravimetry, and hydrogen potential. The second step evaluated the hydration behavior of cement in the presence of TEA. Isothermal calorimetry (72h), X-ray diffraction, thermogravimetry, and paste compressive strength tests (1, 3, 28 days) were performed to evaluate cement microstructural development. The results suggest that TEA increased portlandite content in all samples and affected the cement sulfate consumption but did not significantly reduce delays in hydration.

KEYWORDS: *Phosphogypsum, desulfurization gypsum, accelerating admixture, hydration, cement*

1. Introduction

Phosphogypsum (PG) and flue gas desulfurization gypsum (FGD) are wastes from the phosphate fertilizer industry and the flue gas desulfurization process released by thermal power plants. These wastes consist mainly of calcium sulfate compounds ($CaSO_4$) and are a further alternative to the natural gypsum (NG) extracted from stockpiles. They replace NG as a setting regulator in the composition of Portland cement to control the hydration of tricalcium aluminate ($3CaO\text{-}Al_2O_3$), responsible for setting characteristics and workability of cement in a fresh state Andrade et al. (2021). However, due to impurities and acid pH, their cement tends to cause excessive delays in setting and compromising the mechanical strength Costa et al. (2022) and Caillahua and Moura (2018). Thus, using additive organic accelerators based on alkanolamines such as triethanolamine (TEA), which are employed as grinding aids, may improve the initial lower reactivity of these cements. TEA accelerates the dissolution of clinker aluminate phases, increasing the formation of aluminate hydrates and accelerating the transformation into C_3AH_6 Lu et al. (2020).

2. Methodology

Natural gypsum (NG), phosphogypsum (PG) and flue gas desulfurization gypsum (FGD), and clinker supplied by a Brazilian cement industry were used to produce the cement. Also, an alkanolamine called triethanolamine (TEA) was used as an accelerating admixture at 0.3% by cement mass. Cement was composed, meeting 4.5% $SO_{3\ total}$. Three cement of Portland clinker and different sources of calcium sulfate (NG, PG or FGD) were composed. The sample ID comprises two parts: first, it indicates the calcium sulfate source (NG, PG or FGD); second, the acronym represents the TEA content in cement (0,0 –0,3).
The physical-chemical, mineralogic, and thermal properties of clinker, NG, PG, FGD, and hydrated cement pastes (w/c 0.45) were evaluated. An X-ray fluorescence (XRF) analysis was performed using a Panalytical X-ray fluorescence sequential spectrometer, which operates from 400 to 4000 cm^{1}. The X-ray diffraction (XRD) was conducted using a Bruker D8 Advance diffractometer equipped with a CuK radiation source, a Ni filter, and a 0.020° step size. The 2θ scan range was set from 5° to 65°, with a scan speed of 1.7°/min, and the sample was rotated at 30 rpm speed. The thermogravimetric analysis (TGA) was conducted using the SDT Q600 TA Instruments. The samples were analysed in a 110 µL platinum crucible, under a nitrogen flow rate of 100 ml/min, with a heating rate of 10°C/min until it reached 1000°C. The combined water and portlandite were calculated between 40 to 500 °C. The hydration of pastes was stopped at the respective ages with isopropyl alcohol. The hydrogen ionic potential (pH) was measured with a mPA210 pH meter from MS TECHNOPON Instrumentation. The isothermal conduction calorimetry was performed using a TAM Air model at a constant temperature of 25 ± 0.01 º C. The cement was mixed with deionized water in an automatic mixer at 10.000 rpm for 2 min.
Furthermore, particle size distribution was determined using a CILAS 1180 laser granulometer, with isopropyl alcohol as the solvent, and scattered using ultrasound treatment for 60 s. Finally, cement paste compressive strength, at 1 and 28 d of curing, was measured in 2x2x2 cubes. Specimens were cured in a 99% relatively humid chamber for 24 h and then immersed in a lime-water solution. The equipment used was an EMIC DL20000 Press with a 200 kN load cell, 1 N accuracy, and a 0.2 mm/min pitch.

3. Results

Table 1, Figure 1 (a) and (b) show the chemical, mineralogic, physical, and thermal characterization of clinker, NG, PG, and FGD. PG has higher SO_3 content than FGD and NG. PG has approximately 5% more SO_3 compared to FGD and 1% compared to NG. In addition, it has contents of P_2O_5 (about 1%) and F, not observed in NG and FGD. These contents are commonly associated with residual phosphoric acid and undissolved phosphate rock from the PG process. The P_2O_5 and F content associated with the normal acid pH of PG may affect PG properties and performance in cement (Costa et al, 2022). FGD also has an acid pH, while NG has a basic pH. In combined water (cw), PG showed the highest content, 3.6% higher than FGD and 4.6% higher than NG. Between 100 and 250 °C thermal transformations are observed concerning the decomposition of calcium sulfate dihydrate, which occurs in two steps: dihydrate to hemihydrate ($CaSO_4$-½H_2O); and hemihydrate to anhydrite ($CaSO_4$). Also, a mass variation between 600 and 700 ˚C was observed, suggesting the oxidation of some carbon in the sample. In x-ray diffraction (XRD), it was possible to identify the phases with X'Pert High Score software and PDF (Powder Diffraction Files) sheets: FGD has calcium sulfate dihydrate (CaSO4*2H2O), and quartz (SiO_2); NG has calcium sulfate dihydrate ($CaSO_4$*2H_2O), and anhydrite ($CaSO_4$); PG has calcium sulfate dihydrate ($CaSO_4$*2H_2O), anhydrite ($CaSO_4$), and calcium phosphate silicate (Ca_2SiO_4-0.05$Ca_3(PO_4)_2$). Regarding physical properties, the mean diameter ($D_{Vaverage}$) is around 13-16 µm, a difference considered not to affect the study proposal.

Table 1 – Chemical, physical, and thermal characterization of raw materials

	SiO_2	Al_2O_3	Fe_2O_3	CaO	MgO	SO_3	Na_2O	K_2O	P_2O_5	F	TiO_2	SrO	MnO	FeO
FGD	4,30	0,74	0,46	31,18	0,97	40,32	0,13	0,08	0,02	-	0,04	0,06	0,01	-
PG	1,20	0,04	0,30	30,30	0,20	45,40	0,10	0,00	0,90	0,05	-	-	-	-
NG	0,8	0,2	0,3	31	0,8	44,5	0,1	0,0	0,1	0	-	-		-
CL	19,67	4,19	-	60,41	7,92	1,66	0,21	1,62	0,09	-	0,19	0,04	0,12	2,72

Granulometry (µm)				Thermal Analysis cw (%)	Hydrogen Ionic Potential pH	L.O.I (%)
D_{v10}	D_{v50}	D_{v90}	$D_{v\ average}$			

FGD	2,46	8,83	29,81	13,35	18,9	3,88	21,64
PG	3,23	11,56	34,67	16,34	22,5	3,08	21,40
NG	1,56	7,84	31,64	13,23	17,9	8,82	22,2
CL	1,14	7,91	21,53	11,07	0,1	-	1,13

(L.O.I.) loss of ignition at 1000 ºC

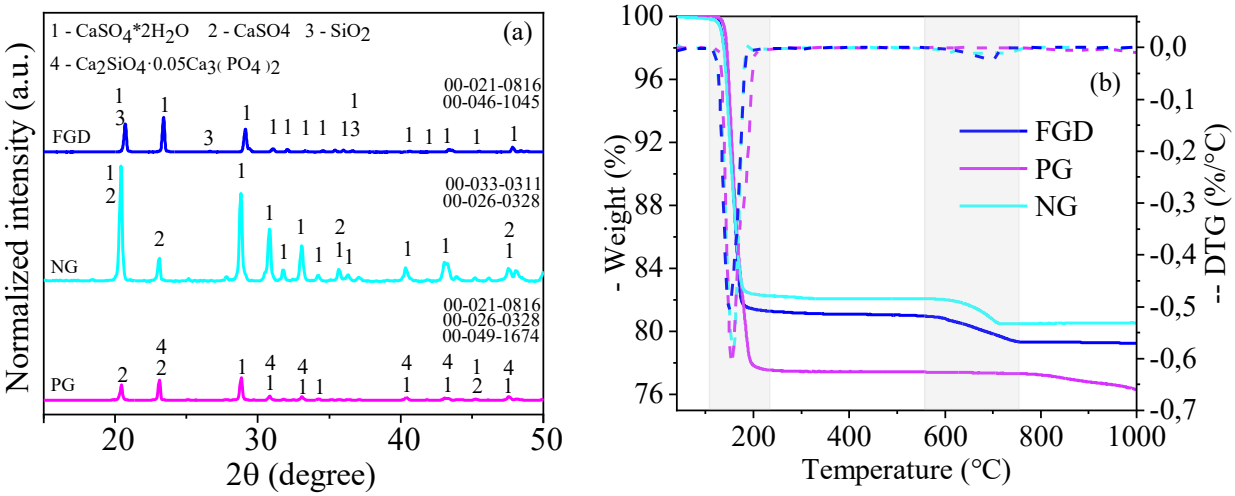

Figure 1 – Mineralogic and thermal characterization of NG, PG, and FGD.

In hydrated cement paste, it was identified through XRD and TGA, the hydration products at 1 day (Figure 2 (a) and (b)). The cement showed the presence of hydration products as ettringite (C_6ASH_{32} - PDF 00–042–0062 – identified as [3]), portlandite (CH – PDF 01–072–0156 - identified as [4]), and remaining anhydrous phases as alite (C_3S - PDF 01-086-0402 - identified as [1]), and belite (C_2S – PDF - 01-083-0461 - identified as [2]). No significant difference was observed in XRD when replacing NG for PG or FGD in cement and using TEA. In TGA, three significant mass losses were identified: 100 °C - corresponds to ettringite; 450 °C - related to the dihydroxylation of portlandite; and 650 °C - due to the decomposition of calcium carbonates.

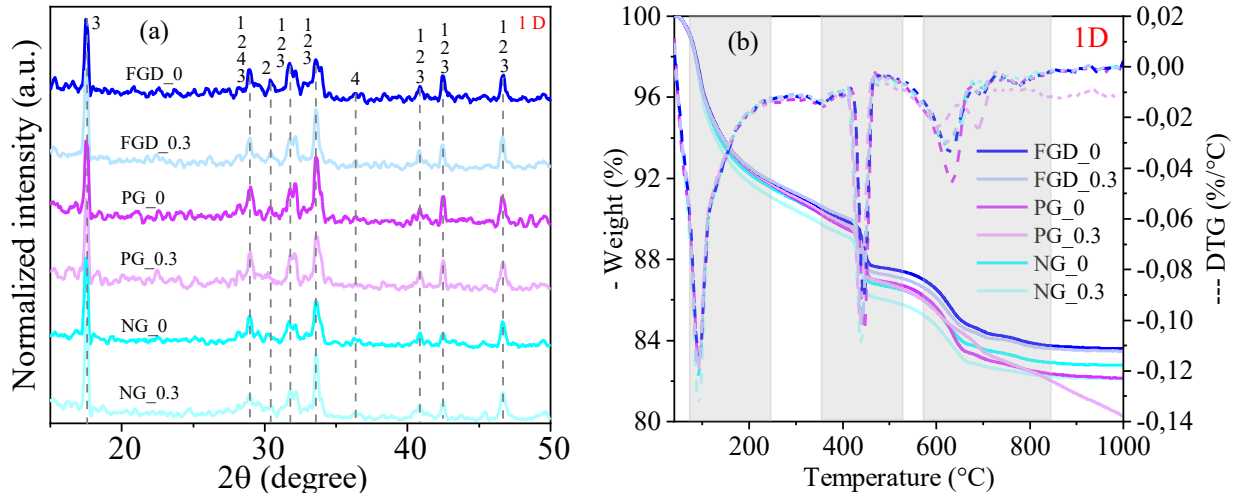

Figure 2 – Mineralogic and thermal characterization of hydrated cement paste with NG, PG, FGD, and TEA at 1 d.

Figure 3 exhibits the heat flow (a) and cumulative heat (b) curves during 72h, compressive strength at 1 and 28 days, and portlandite content at 1 day (b) of cement paste with NG, PG, FGD, and TEA. In calorimetry, PG caused delays in hydration compared to NG and FGD, approximately 1,43 h more than NG and 1 h more than FGD. This behaviour identified for PG was expected, according to literature which is suggested to be related to forming a protective barrier of calcium phosphate and calcium fluoride that reduces hydration (Tabikh et al, 1971). Furthermore, the cumulative heat at early ages (until 18h) is lower for PG than NG and FGD. At 24h and 72h, cumulative heat for NG cement is higher than PG and FGD

showing higher reaction rates. Also, there was no significant difference in the curve delays when using TEA in cement. Still, it affected the sulfate depletion point (E), which occurs earlier or is not identified at heat flow curves. Properly sulfated cement has a peak associated with sulfate depletion after alite main hydration pea (Andrade et al, 2021). Regarding portlandite content at 1 day, NG cement paste showed higher values while FGD exhibited lowers. In addition, all cement pastes showed higher CH content when using TEA, even though the compressive strength results did not present a clear trend.

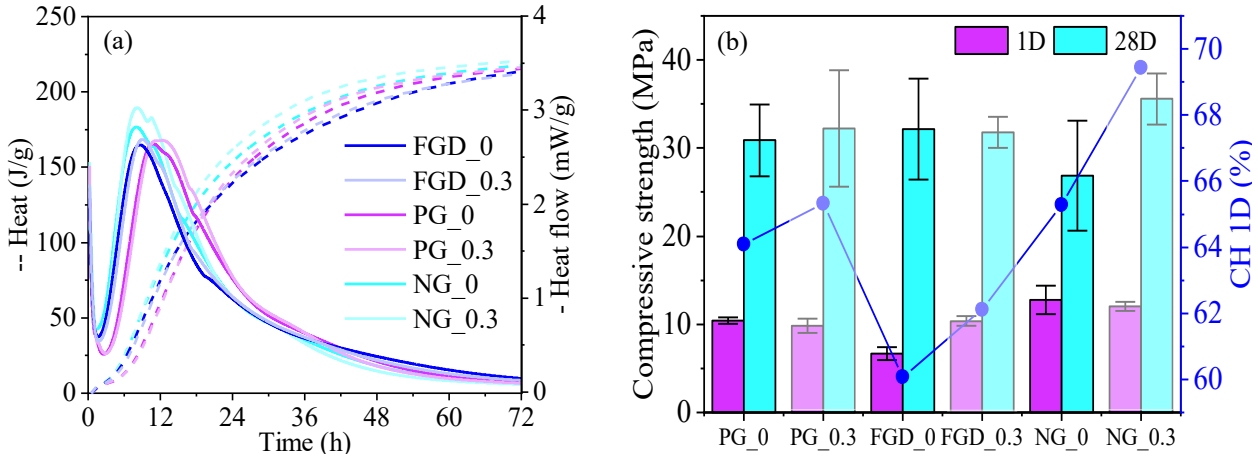

Figure 3 – Heat flow curves and cumulative heat (a), compressive strength at 1 and 28d, and portlandite content at 1day (b) of hydrated cement paste with NG, PG, FGD, and TEA.

3. Conclusions

The research's main novelty relies on assessing the TEA performance in cement as an option to overcome the drawbacks of using PG and PGD as setting regulators. TEA affected the cement sulfate consumption but did not reduce delays observed in PG heat flow curves at early ages. TEA increased the CH content in all samples. No significant difference was observed in hydration products mineralogy when replacing NG for PG or FGD in cement and using TEA. Thus, the results suggest that TEA can improve the performance of cement with PG and FGD as set regulators.

References

Andrade Neto, J. da S., de la Torre, A. G., & Kirchheim, A. P. (2021). "Effects of sulfates on the hydration of Portland cement – A review", *Construction and Building Materials*, 279: 122428. https://doi.org/10.1016/j.conbuildmat.2021.122428

Caillahua, M. C., and Moura, F. J. (2018). "Technical feasibility for use of FGD gypsum as an additive setting time retarder for Portland cement", *Journal of Materials Research and Technology*, *7*(2), 190–197. https://doi.org/10.1016/J.JMRT.2017.08.005

Costa, R. P., de Medeiros, M. H. G., Rodriguez Martinez, E. D., Quarcioni, V. A., Suzuki, S., & Kirchheim, A. P. (2022). "Effect of soluble phosphate, fluoride, and pH in Brazilian phosphogypsum used as setting retarder on Portland cement hydration", *Case Studies in Construction Materials*, 17: e01413. https://doi.org/10.1016/J.CSCM.2022.E01413

Lu, Z., Kong, X., Jansen, D., Zhang, C., Wang, J., Pang, X., and Yin, J. (2020). "Towards a further understanding of cement hydration in the presence of triethanolamine", *Cement and Concrete Research*, *132*. https://doi.org/10.1016/J.CEMCONRES.2020.106041

Tabikh, A. A., Miller, F. M., Cement, M., & Company, M. (1971). "The Nature of Phosphogypsum Impurities and their Influence on Cement Hydration", *Cement and Concrete Research*, *1*, 663–678.

The 16th International Congress on the Chemistry of Cement 2023 (ICCC2023)
"Further Reduction of CO_2 -Emissions and Circularity in the Cement and Concrete Industry"
September 18–22, 2023, Bangkok, Thailand

Effect of calcination temperature on paper mill lime sludge as an activator for GGBFS based cementless UHPC

Yanchen Oinam[1], Prabhat Vashistha[1], Mandip Dahal[2], and Sukhoon Pyo[1*]

[1] *Department of Urban and Environmental Engineering, Ulsan National Institute of Science and Technology (UNIST), Ulsan 44919, Republic of Korea*

[*] *Email: shpyo@unist.ac.kr*

[2] *Department of Civil & Environmental Engineering, University of Connecticut, 261 Glenbrook Road Unit 2037, Storrs, CT 06269-2037, USA*

ABSTRACT

This study proposes the utilization of paper mill lime sludge, a by-product, as an activator in cementless UHPC. The lime sludge is usually disposed in landfill, causing significant environmental issues. The chemical composition of the lime sludge generally consists of calcium carbonate. It is an already known procedure that upon heating at high temperature, calcium carbonate can be decomposed to calcium oxide (CaO). From previous study, it was found that inclusion of CaO as an activator can significantly improve the hydration and mechanical properties of ground granulated blast furnace slag based (GGBFS) based cementless UHPC. In this study, lime sludge was calcined at different temperatures and investigated its effect as an activator at 15% dosage for the GGBFS based cementless UHPC. It was revealed that the calcined lime sludge can significantly improve the mechanical, exceeding compressive strength of 150 MPa. The TGA results also indicated differences in the trend of the hydration products detected. The increase in temperature of calcination led to an increase in the formation of hydration products, which resulted in higher compressive strength. The results highlight the importance of the addition of calcined lime sludge to develop a sustainable cementless UHPC.

KEYWORDS: *lime sludge, calcium carbonate, cementless UHPC, morphology, hydration*

1. Introduction

The paper industry is responsible for producing 1.63 tons of lime sludge as a byproduct of the causticization process used to recycle alkali during the paper-making process (Vashistha et al., (2019), Simão et al., 2017). The amount of lime sludge generated has increased over time due to the growing demand for paper. However, the complexity of recycling lime sludge means that it is typically discarded in landfills (Maheswaran et al., 2015). Therefore, it is necessary to develop effective methods for the utilization of lime sludge.

In recent years, researchers have focused on finding ways to repurpose this industrial waste in the construction and building industries. Several studies have investigated the use of lime sludge as a replacement for ordinary Portland cement (OPC) in the manufacturing of concrete (Dong et al., 2022). It was found that using a large amount of lime sludge in the mixture led to a decrease in compressive strength, but that using it as a replacement for fine aggregates did not significantly affect the mechanical properties (Malaiskiene et al., 2018). The primary component of lime sludge is calcium carbonate ($CaCO_3$), which can be converted to calcium oxide (CaO) by heating at high temperatures. Frías et al., (2008) also reported that calcined lime sludge can be a potential source for metakaolin, depending on the raw material source. Regardless of the numerous studies conducted to utilize lime sludge in different ways, the influence of calcined lime sludge on the hydration and mechanical properties of cementless binders have not been investigated.

Ultra high performance concrete (UHPC) is renowned for its exceptional mechanical and durability properties, with compressive strength exceeding 150 MPa and tensile strength over 8 MPa (Pyo et al., 2016). Its high packing density is achieved through the inclusion of micron-sized particles such as silica powder, silica fume, and fine aggregates, as well as an extremely low water-binder ratio. Typically, UHPC requires three to four times more ordinary Portland cement (OPC) than regular concrete, resulting in significant carbon dioxide emissions and high energy consumption during production. To mitigate these drawbacks, researchers have explored alternative industrial by-products, such as ground granulated blast furnace slag (GGBFS). GGBFS has shown efficiency due to its cementitious properties, although it often requires the use of an alkali activator solution to achieve higher hydration products with inferior mechanical properties (Oinam et al., 2022). Recently, the authors developed a CaO-activated GGBFS-based cementless UHPC that utilized calcium formate as an accelerator to improve hydration and mechanical properties. Given that calcined lime sludge can be a source of CaO, this study aims to explore the use of calcined lime sludge as a replacement for CaO in this context and assess its impact on the properties of the resulting cementless UHPC.

2. Materials and specimen preparation

2.1 Materials

The study utilized lime sludge obtained from a local paper industry in South Korea as well as materials including commercial GGBFS, undensified silica fume as binder material. Meanwhile, silica powder, and two silica sands of different particle size were used as filler. Additionally, calcium formate was employed as an accelerator, and the workability of the mixture was regulated by using a polycarboxylate-based liquid superplasticizer. The mixture was further reinforced with brass coated steel fiber measuring 19.5 mm in length and having a tensile strength of 2450 MPa.

2.2 Specimen preparation

The lime sludge was calcined at different temperatures ranging from 550-850 °C with 100 °C increment. And using a planetary mixer, silica fume with two different types of quartz sands were dry mixed for 5 min. Later, GGBFS, calcined lime sludge, calcium formate and silica powder were added and mixed for another 5 min. And then, water and superplasticizer were added. After the mixture showed a certain consistency, steel fibers were added gradually to the mixture. The mixture was poured in the specified molds and were demolded after 24 h of curing in a humidity chamber and cured in a steam bath for 48 h at 90°C. Then the samples were subjected for different test methods. Specifically, the samples were labelled as dry (not calcined), 550°C, 650°C, 750°C, and 850°C. These designations were used in conjunction with LS, which refers to lime sludge, resulting in the sample names DLS, 550LS, 650LS, 750LS, and 850LS.

3. Results and discussion

The compressive strength results of the samples with 15 wt.% inclusions of the lime sludge are shown in Figure 1. It can be seen that the compressive strength gradually increases with the increase of calcination temperature of the lime sludge. DLS showed a compressive strength lower than 20 MPa, which indicates that the samples hardly went through any reaction to develop the compressive strength. In addition, 550LS showed nearly up to 100 MPa indicating the improvement in the hydration reaction with the calcined lime sludge. Meanwhile, 650LS, 750LS and 850LS had compressive strength more than 100 MPa.

The enhancement of compressive strength can be attributed to the reaction between ground granulated blast furnace slag (GGBFS), silica fume, and calcined lime sludge. An increase in heating temperature resulted in the decomposition of calcium carbonate into calcium oxide. Furthermore, the use of calcium oxide (CaO) as an activator has been reported to significantly improve compressive strength due to its ability to enhance the hydration properties, as has been previously reported by Kim et al., (2013). Overall,

only 850LS had shown superior compressive strength of more than 150 MPa. From this result, it can be said that the 850 °C is the preferred temperature for the calcination of lime sludge to achieve the desirable strength.

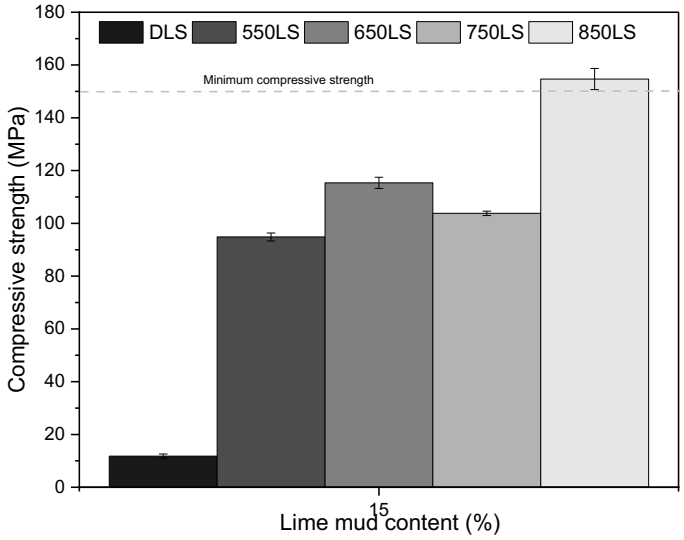

Figure 1. Compressive strength of the UHPC samples

The UHPC samples exhibited three peaks on the DTG curve as shown in Figure 2, with the first peak appearing around 100 ^{0}C. Typically, this peak corresponds to the presence of C-S-H and ettringite, but the inclusion of calcined lime sludge at higher temperatures caused a change in the appearance of this peak. The U850 sample exhibited the broadest peak, indicating an improvement in the hydration reaction products formed. The peak around 300-400 ^{0}C indicated the formation of C-A-H. The peak corresponding to the decomposition of portlandite at ~400 ^{0}C became duller with higher temperature of calcination, indicating that the portlandite had been consumed due to the pozzolanic reaction of the composites. Finally, the peak corresponding to the decarbonation of calcite was present at 600-700 ^{0}C. The amount of calcite decreases gradually in the UHPC matrix with the addition of lime sludge calcined at higher temperatures.

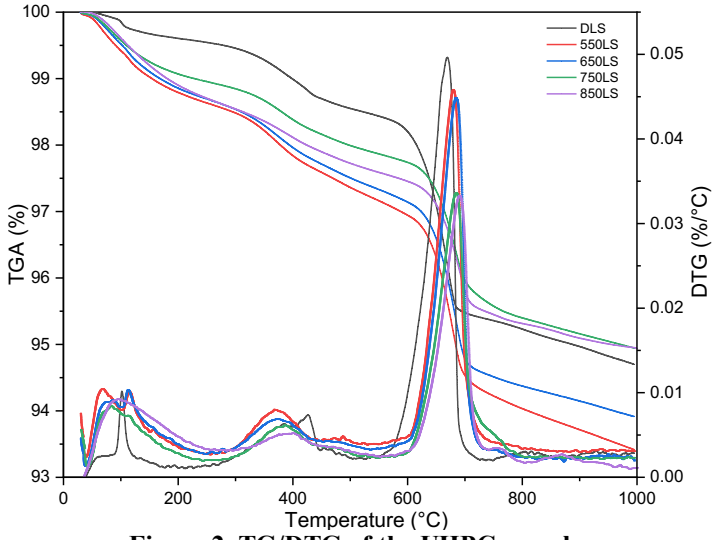

Figure 2. TG/DTG of the UHPC samples

3. Conclusions

In this study, the compressive strength and TGA/DTG tests of cementless UHPC incorporating calcined lime sludge as an activator were investigated. The strength of the UHPC was enhanced by incorporating calcined lime sludge that was processed at higher temperatures. The 850LS sample, demonstrated a

compressive strength exceeding 150 MPa. The improvement in strength was presumably due to a reaction between the calcined lime sludge and GGBFS. Additionally, it is worth mentioning that the 650LS and 750LS samples also exhibited a compressive strength exceeding 100 MPa. The TGA/DTG outcomes indicated that the formation of hydration products such as C-S-H, katoite, and portlandite was significantly improved by the addition of calcined lime sludge processed at higher temperatures.

Acknowledgements

This work was supported by the National Research Foundation of Korea (NRF) grant funded by the Korea government (MSIT) (No. 2021R1A4A1030867).

References

Dong, B., Chen, C., Fang, G., Wu, K., & Wang, Y. (2022). Positive roles of lime mud in blended Portland cement. *Construction and Building Materials*, *328*. https://doi.org/10.1016/j.conbuildmat.2022.127067

Frías, M., De Rojas, M. I. S., Rodríguez, O., García Jiménez, R., & De La Villa, R. V. (2008). Characterisation of calcined paper sludge as an environmentally friendly source of metakaolin for manufacture of cementitious materials. *Advances in Cement Research*, *20*(1), 23–30. https://doi.org/10.1680/adcr.2008.20.1.23

Kim, M. S., Jun, Y., Lee, C., & Oh, J. E. (2013). Use of CaO as an activator for producing a price-competitive non-cement structural binder using ground granulated blast furnace slag. *Cement and Concrete Research*, *54*, 208–214. https://doi.org/10.1016/j.cemconres.2013.09.011

Maheswaran, S., Kalaiselvam, S., Arunbalaji, S., Palani, G. S., & Iyer, N. R. (2015). Low-temperature preparation of belite from lime sludge and nanosilica through solid-state reaction. *Journal of Thermal Analysis and Calorimetry*, *119*(3), 1845–1852. https://doi.org/10.1007/s10973-014-4371-5

Malaiskiene, J., Kizinievic, O., Kizinievic, V., & Boris, R. (2018). The impact of primary sludge from paper industry on the properties of hardened cement paste and mortar. *Construction and Building Materials*, *172*, 553–561. https://doi.org/10.1016/j.conbuildmat.2018.04.011

Oinam, Y., Ju, S., Gwon, S., Shin, M., & Pyo, S. (2022). Characteristics of GGBFS-Based Pervious Concrete Considering Rheological Properties of the Binder. *International Journal of Concrete Structures and Materials*, *16*(1), 62. https://doi.org/10.1186/s40069-022-00551-7

Pyo, S., El-Tawil, S., & Naaman, A. E. (2016). Direct tensile behavior of ultra high performance fiber reinforced concrete (UHP-FRC) at high strain rates. *Cement and Concrete Research*, *88*, 144–156. https://doi.org/10.1016/j.cemconres.2016.07.003

Simão, L., Jiusti, J., Lóh, N. J., Hotza, D., Raupp-Pereira, F., Labrincha, J. A., & Montedo, O. R. K. (2017). Waste-containing clinkers: Valorization of alternative mineral sources from pulp and paper mills. *Process Safety and Environmental Protection*, *109*, 106–116. https://doi.org/10.1016/j.psep.2017.03.038

Vashistha, P., Kumar, V., Singh, S. K., Dutt, D., Tomar, G., & Yadav, P. (2019). Valorization of paper mill lime sludge via application in building construction materials: A review. In *Construction and Building Materials* (Vol. 211, pp. 371–382). Elsevier Ltd. https://doi.org/10.1016/j.conbuildmat.2019.03.085

The 16th International Congress on the Chemistry of Cement 2023 (ICCC2023)
"Further Reduction of CO_2 -Emissions and Circularity in the Cement and Concrete Industry"
September 18–22, 2023, Bangkok, Thailand

Utilizing paper mill lime mud as fine aggregate for sustainable high-strength mortar

A.M. Kebede, Sukhoon Pyo*

Department of Urban and Environmental Engineering, Ulsan National Institute of Science and Technology (UNIST), Ulsan, Korea

**Email: shpyo@unist.ac.kr*

ABSTRACT

Lime mud (LM) is a solid byproduct with high alkalinity and calcium carbonate ($CaCO_3$) content, which is produced during alkali recovery in the paper-making industry. In this work, a high replacement ratio (>50%) of sand with raw LM was investigated in a mortar mixture containing cement, silica fume (SF), and sand. Considering the agglomeration of LM and the fast hydration of SF. The mechanical and other properties were then studied using compressive strength, thermogravimetric analysis, and Mercury intrusion porosimetry (MIP). The experimental findings demonstrate that incorporating the LM with a high replacement ratio improves the strength by almost 40%. The reason is because of the small particle size of LM particles, which can act as a filler and refine the pore structure. In addition, the $CaCO_3$ offers additional nucleation sites for the precipitation of cement hydration products and contributes to the increment of compressive strength. The alkalinity of the LM also facilitated the secondary hydration of silica fume and enhanced the later age strength.

KEYWORDS: *Lime mud, High replacement ratio, Hydration kinetics, High strength mortar, Sustainability*

1. Introduction

Lime mud (LM) is a solid byproduct with high alkalinity and calcium carbonate ($CaCO_3$) content that results from alkali recovery during papermaking. Approximately 0.5 tons of LM are generated per ton of pulp (Modolo et al. 2014), but recycling LM is challenging due to the high energy needed to recover it at temperatures of 800 °C-900 °C. Consequently, many paper companies dispose of LM untreated, which raises alkalinity levels and causes damage to vegetation and groundwater. Therefore, it is crucial to find ways to reduce environmental pollution by using LM and benefiting from its constituent materials (Sthiannopkao and Sreesai 2009).

Various researchers have employed LM for different purposes, including construction materials. For instance, Modolo et al. (2014) created a mortar using LM in varying proportions (10%, 20%, and 30%) of the cement's dry weight, determining that 30% didn't affect strength but influenced rheological properties and flowability. Azevedo et al. (2018) investigated LM's sustainability in cement-based mortar for coating walls and ceilings, concluding that less than 10% LM was preferable for mechanical strength.

This study aimed to investigate the effect of high replacement of LM, and an LM replacement ratio of (>50%) in sand replacement was used. The compressive strength of the mortar was measured for various LM replacement ratios, and the pore size distribution of the samples was determined using the mercury intrusion test (MIP). The mortar hydration products were also investigated.

2. Materials and methods

2.1 Raw materials

The study used specimens made from cement (CEM I 52.5N), natural river sand, silica fume (SF), and LM. A polycarboxylate-based superplasticizer (SP) was used to compensate for the decrease in fresh mortar flowability caused by LM. The chemical composition of the binding materials, which was obtained with X-ray fluorescence analysis (XRF; T8 Tiger, USA), is shown in Table 1. Moreover, LM, SF, and cement have a mean particle size of 21.7 □m, 3.98 μm, and 10 □m. Additionally, the LM has a density of 2.7 g/cm^3

Table 1. Chemical composition of raw materials (wt. %).

	CaO	SiO_2	Al_2O_3	Fe_2O_3	MgO	SO_3	Na_2O	K_2O	Others	LOI
Cement	64.1	17.8	4.4	3.7	3.3	3.9	0.5	1.4	1.0	3.1
SF	0.1	97.3	0.1	0.2	0.4	0.9	-	-	1.0	2.0
LM	90.4	0.8	0.5	0.9	1.4	1.3	2.5	0.1	2.1	43.1

2.1 Sample preparation

The specimens were prepared using ASTM C305 (2020) with a water-to-binder ratio of 0.6 and a sand-to-binder ratio of 1 as shown in Table 2. The SP used was 2.5%–3.0%, the weight of the binder, to maintain the same flowability. After mixing the materials following the standard, the fresh paste was then poured into a 0.05 × 0.05 × 0.05 m^3 mold, which was sealed with a plastic bag and left at room temperature for 24 h. After 24 h, the samples were demolded and cured in steam curing for 48 h at (90 °C).

Table 2. Mix design for the mortar specimens (kg/m^3).

Mixture ID	Cement	Silica fume	Lime mud	Sand	Water	SP
REF	738.5	184.6	0.0	923.1	553.8	4.6
LM50			461.5	461.5		13.8
LM75			692.3	230.8		18.5
LM100			923.1	0.0		27.7

2.2 Testing methods

The compressive strength tests were performed using ASTM C109/109M-16a (2016) with a loading rate of 0.5 mm/min. The average of the three replicates was then used as a representative test result. For the quantification of hydration products thermogravimetric analysis (TGA; Q500, TA Instruments USA) was used. Mercury intrusion porosimetry (MIP) measurements were performed with Autopore VI 9620 (Micromeritics Instrument Corp., USA) at pressures ranging from 0.2 to 413.7 MPa to investigate the microstructure of the mortar samples.

3. Result and Discussion

3.1 Mechanical strength

The compressive strength of different specimens is shown in Figure 1. Compared to the reference sample, the LM50, LM75, and LM100 specimens exhibit varying degrees of increased compressive strength, with the LM100 sample showing the largest increase of 39.5%. This improvement is mainly due to the micro-aggregate effect of LM and SF, which fills the pores and improves the pore structure. More detailed information on this topic can be found in Section 3.3. Previous studies have also demonstrated that LM creates nucleation sites that enhance strength, contributing to the increase in strength observed (Goldman and Bentur 1993; Singh et al. 2015).

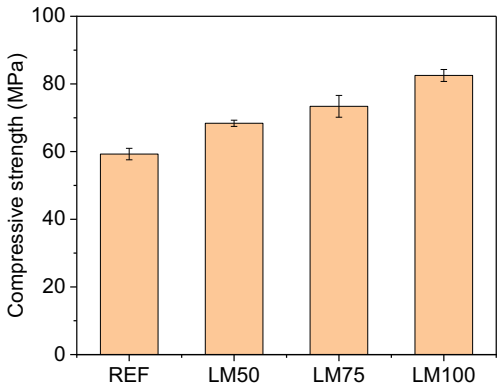

Figure 1. Compressive strength of different replacement ratios (LM50=50% replacement of sand with LM)

3.2 Thermogravimetric analysis

In Figure 2, the TG-DTG curves of various specimens indicate that they experienced notable mass loss at approximately 100 °C. However, this peak only suggests the presence of C-S-H rather than both C-S-H and ettringite. This is because ettringite decomposes above 70 °C (Taylor et al. 2001). Besides that, there are no visible portlandite peaks in the curves, which could be due to the high-temperature curing process causing SF to consume portlandite. The curves also reveal significant mass loss at approximately 700-750 °C, which is mainly attributed to the calcite present in the LM. This calcite acts as a filler, increasing strength along with the reaction products, thus confirming the results obtained from compressive strength tests.

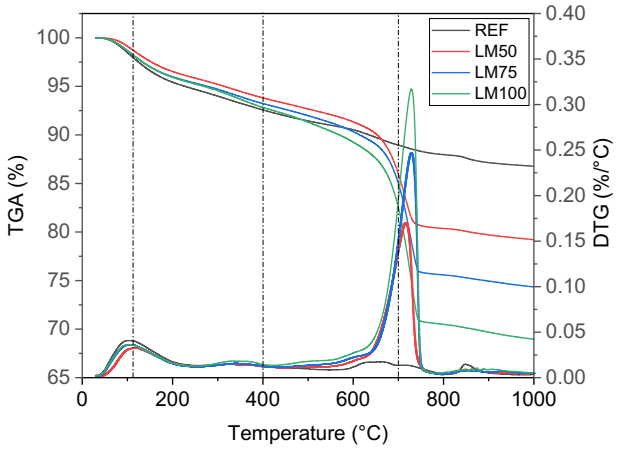

Figure 2. TG- DTG curves of different replacement ratios

3.3 Mercury intrusion porosimetry

Figure 3 illustrates the relationship between cumulative intrusion and pore size for different samples. The impact of using a high replacement ratio of LM is visible in the capillary pores, which range from 0.01 to 5 µm, as depicted in Figure 3. The addition of LM resulted in lower capillary pores for specimens with higher LM dosage, indicating the filler effect of LM. This finding is consistent with the compressive strength results. Furthermore, Figure 3(b) shows that the addition of LM led to an increase in gel pores for all specimens, which may be attributed to the limited reactivity of LM. However, this effect is not significant in terms of compressive strength, as it is related to shrinkage and creep (Meng & Khayat, 2018).

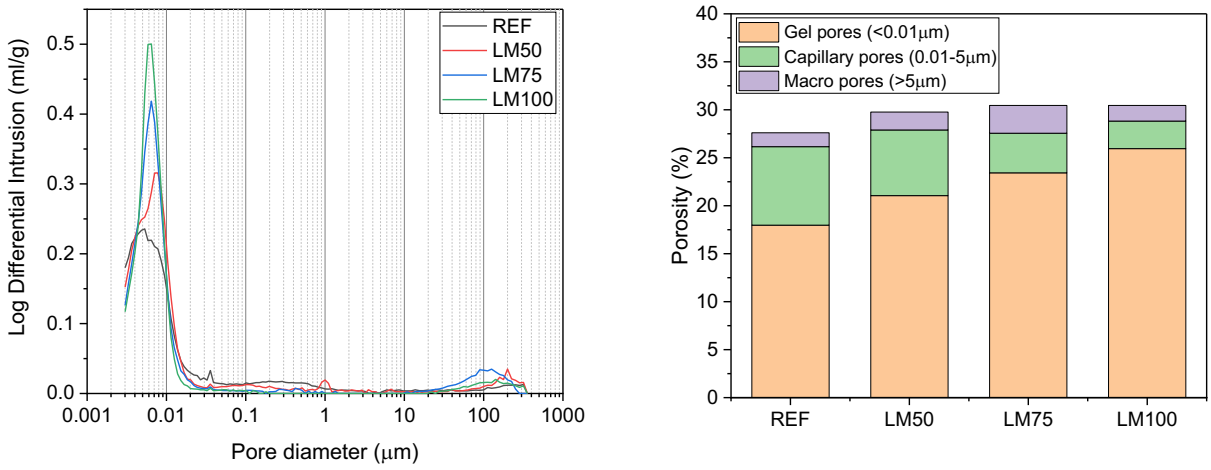

(a) (b)

Figure 3. Typical data from MIP: (a) cumulative intrusion graphs, and (b) pore size distribution of samples

4. Conclusions

In this study, the impact of increasing the amount of LM as a sand substitute on the mechanical properties was examined. Through various measurements such as compressive strength, TGA, and MIP, it was found that the addition of LM improved the strength of the material while enhancing the hydration process and refining the pore structure. To provide a reference point, a sample without LM was also tested. Additionally, the use of the LM-enhanced mix design improved the sustainability of the material in comparison to standard conventional mortar samples.

1. The alkaline environment created by LM promoted the secondary hydration of SF with cement, leading to more C-S-H formation and a dense microstructure.
2. The smaller LM particles acted as fillers during hydration, filling the pores and providing nucleation sites for hydration.
3. Using LM as a sand substitute did not alter total porosity, but it did affect capillary and macro pores due to the filler effect.

These findings suggested that LM utilization increased matrix densification by improving SF secondary hydration and by refining the pores. Moreover, the use of LM at a high replacement ratio increased the sustainability of the material.

Acknowledgments

This work was supported by the National Research Foundation of Korea (NRF) grant funded by the Korean government (MSIT) (No. RS-2023-00212366). The opinions expressed in this paper are those of the authors and do not necessarily reflect the views of the sponsors or their employers.

References

ASTM C109/109M-16a. (2016). Standard test method for compressive strength of hydraulic cement mortars (Using 2-in. or cube specimens). *Annual Book of ASTM Standards*, *04*, 1–10. https://doi.org/10.1520/C0109

ASTM C305-20. (1998). Standard Practice for Mechanical Mixing of Hydraulic Cement Pastes and Mortars of Plastic Consistency. *ASTM International*, *14*(2), 147. https://doi.org/10.1177/089033449801400218

de Azevedo, A. R. G., Alexandre, J., Xavier, G. de C., & Pedroti, L. G. (2018). Recycling paper industry effluent sludge for use in mortars: A sustainability perspective. *Journal of Cleaner Production*, *192*, 335–346. https://doi.org/10.1016/J.JCLEPRO.2018.05.011

Goldman, A., & Bentur, A. (1993). The influence of microfillers on enhancement of concrete strength. *Cement and Concrete Research*, *23*(4), 962–972. https://doi.org/10.1016/0008-8846(93)90050-J

Meng, W., & Khayat, K. H. (2018). Effect of graphite nanoplatelets and carbon nanofibers on rheology, hydration, shrinkage, mechanical properties, and microstructure of UHPC. *Cement and Concrete Research*, *105*(May

2017), 64–71. https://doi.org/10.1016/j.cemconres.2018.01.001
Modolo, R. C. E., Senff, L., Labrincha, J. A., Ferreira, V. M., & Tarelho, L. A. C. (2014). Lime mud from cellulose industry as raw material in cement mortars. *Materiales de Construccion*, *64*(316), 1–9. https://doi.org/10.3989/mc.2014.00214
Singh, N. B., Kalra, M., Kumar, M., & Rai, S. (2015). Hydration of ternary cementitious system: Portland cement, fly ash and silica fume. *Journal of Thermal Analysis and Calorimetry*, *119*(1), 381–389. https://doi.org/10.1007/s10973-014-4182-8
Sthiannopkao, S., & Sreesai, S. (2009). Utilization of pulp and paper industrial wastes to remove heavy metals from metal finishing wastewater. *Journal of Environmental Management*, *90*(11), 3283–3289. https://doi.org/10.1016/j.jenvman.2009.05.006
Taylor, H. F. W., Famy, C., & Scrivener, K. L. (2001). Delayed ettringite formation. *Cement and Concrete Research*, *31*(5), 683–693. https://doi.org/10.1016/S0008-8846(01)00466-5

The 16th International Congress on the Chemistry of Cement 2023 (ICCC2023)
"Further Reduction of CO_2 -Emissions and Circularity in the Cement and Concrete Industry"
September 18–22, 2023, Bangkok, Thailand

Relationship between the chemical composition of cementitious materials and their radioactivity

J.A. Súarez-Navarro[1*], A. Caño[2], F. Puertas[2] and M.M. Alonso[2]*

[1] *Centre of Energy, Environment and Technology Research (CIEMAT), Madrid, Spain*
Email: ja.suarez@ciemat.es
[2] *Eduardo Torroja Institute for Construction Sciences (IETcc-CSIC), Madrid, Spain*
Email: andres.cano@ietcc.csic.es; puertasf@ietcc.csic.es;
Corresponding author Email: mmalonso@ietcc.csic.es

ABSTRACT

In this study, the possible relationship between the chemical composition of different cements and fly ashes with their radiological activity has been studied using Principal Component Analysis (PCA). PCA allowed the cements to be grouped on the basis of two main factors, their CaO-SO_3 content and their Fe_2O_3-Al_2O_3-TiO_2 content. The latter factor was found to be the most correlated with the presence of natural radionuclides. The PCA showed a lower correlation for fly ash as the scores of the samples were centered showing a large scatter. However, the clustering shown by the PCA for the cements allowed to establish from multiple regression a model relating the activity concentration of ^{226}Ra, ^{232}Th (^{212}Pb) and ^{40}K with chemical composition.

KEYWORDS: *Cement, Supplementary Cementitious Materials, Chemical composition, Radioactiviy, Principal Component Analysis*

1. Introduction

The use of supplementary cementitious materials (SCM) to replace part of the cement clinker, is one of the main approaches to reduce the high energy and environmental costs of Portland cement manufacture. The use of these SCMs lead cement manufacture towards higher levels of sustainability and lower greenhouse gas (GHG) emissions. In many cases, these SCMs can be Naturally Occurring Radioactive Materials (NORM). In 2013, the European Union published Directive 2013/59/EURATOM (EU, 2013) that establishes in its Article 75 the limit for the excess effective dose (without taking into account the background absorbed dose of approximately 50 nGy·h-1) to be applied for outdoor exposure in enclosed areas in addition to outdoor exposure, which will be 1 mSv. The gamma activity concentration index (ACI) (Eq 1) is calculated from the activity concentration (Bq·kg^{-1}) of ^{226}Ra (^{238}U series), ^{232}Th and ^{40}K.

$$ACI = \frac{C_{226_{Ra}}}{300} + \frac{C_{232_{Th}}}{200} + \frac{C_{40_K}}{3000} \quad (1)$$

Annex XIII of this Directive lists those types of building materials to be taken into account in relation to the emitted gamma radiation (including several supplementary cementitious materials –SCMs). The methodology used to determine the activity concentration of these radionuclides is through gamma spectrometry.

Among the most commonly used SCMs are fly ash (FA) from coal-fired power plants. The physical and chemical characteristics of FA depend among other factors on the starting coal, the degree of pulverisation, combustion conditions, collection methods, etc (Ndahirwa, D. et al 2022), which ultimately determine FA reactivity. However, to date, it has not been possible to determine whether there is a clear relationship between such radioactivity and the chemical composition and characteristics of the FA.

The aim of this work is to determine whether there is a relationship between the chemical composition and the radiological content of cements and FA.

2. Materials and methodology

In this study, the following samples were used: i) 23 cements (CEM) of different types (17 CEM I, 1 CEM II/A-L, 5 CAC, 1 calcium sulfoaluminate cement and 2 belitic cements blended with fly ash); ii) 26 fly ash (FA). All samples were chemically characterised by XRF and their radionuclide activity concentration were determined by gamma spectrometry.
A statistical study was carried out using the Real Statistics Resource Pack software Release 7.6 (www.real-statistics.com), in order to obtain the models relating the sets of chemical analysis results and radionuclide activity concentration data for each type of sample (CEM and FA). The two sets of results were analysed using principal component analysis (PCA), iteratively eliminating variables until a Kaiser-Meyer-Olkin (KMO) fitness index value greater than 0.7 was reached (Coletti C et al 2020). The results obtained for the variables and the scores obtained from the samples were plotted in an HJ-Biplot, as seen in Figure 1.

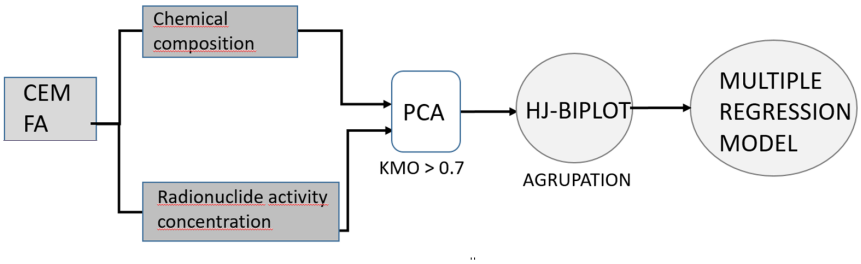

Figure 1. Scheme of the methodology used

The results obtained for both variables (chemical composition and radionuclide activity concentration) as well as the scores obtained from the samples were plotted on an HJ-Biplot, and no- orthogonally rotation was applied. In order to test viability of the proposed models, one new CEM (Test CEM), and one new FA (Test FA) were used afterwards, whose chemical composition was previously determined by XRF.
The activity concentrations of ^{226}Ra, ^{232}Th(^{212}Pb), and ^{40}K obtained using the proposed models with the chemical compositions were compared with the experimental values of the samples using Student's t-test of paired results for a significance level $\alpha = 0.05$. The estimated ACIs using calculated values from the proposed models were compared with those obtained with their experimental activity concentrations determined by gamma spectrometry using the relative standard deviation (RSD ≤30%.).

3. Results and discussion

The HJ-Biplot obtained for the cements studied (Figure 2) presents a KMO coefficient= 0.809, indicating adequate data sampling. The two factors found represented 79.4% of the variance of the factors analyzed. First factor (Fe_2O_3, Al_2O_3, TiO_2, CaO, SO_3, and radionuclides of the ^{238}U and ^{232}Th series) accounts for 50.9% of the variance, while second factor, that represents 29.1% of variance, was related to the amount of SiO_2, MnO, MgO, K_2O and 40^K. Figure 2 shows that increasing the Fe_2O_3, Al_2O_3, and TiO_2 content lead to an increased activity concentration of the radionuclides of the ^{238}U and ^{232}Th radioactive series. Cluster analysis identified 3 groups:

a) In blue, corresponding to CEM-I, CEM-II with limestone addition, white cements and calcium sulfoaluminate cement (C16)
b) In green, corresponding to CACs , with a higher concentration of natural radionuclide activity
c) In red, corresponding to samples two belite cements with a 30% FA addition with high amounts of SiO_2, K_2O, Na_2O, and natural radionuclides in both the uranium and thorium radioactive series and 40^K.

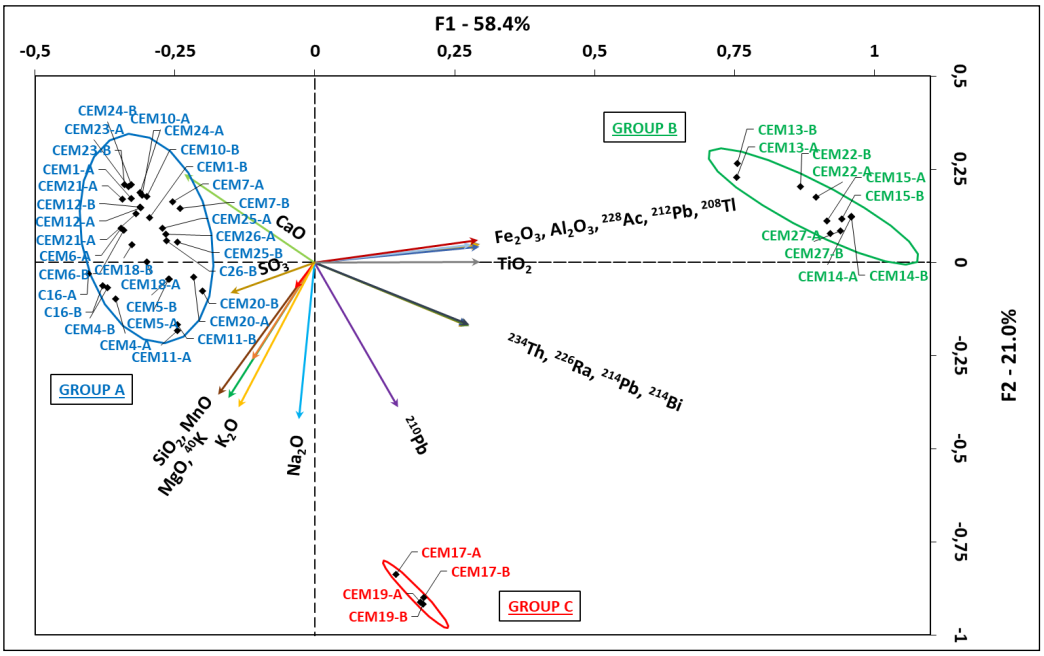

Figure 2. HJ-Biplot for the cements studied. The correlations between the studied variables were established from the cosine of the angle they form between them. The clusters were established by means of confidence ellipses determined at a significance level $\alpha = 0.05$.

With regard to FA samples, similar HJBiplot was obtained and two factors were founded that accounted for 67.6% of the variance, as well as KMO index of 0.709. First factor represented the amount of TiO_2, Al_2O_3, Na_2O, and radionuclides from the ^{235}U and ^{232}Th series, while second one was the amount of SiO_2, CaO, Fe_2O_3, MgO, K_2O, MnO, SO_3, and 40^K. In this case, six clusters were found which showed high variability as they were distributed in the four quadrants of the HJBiplot. Three of these clusters were in very close relation to each other, while the other three were within one FA each. Kovler et al (2005) and Puertas et al (2015), among others, determined the presence of natural radionuclides in FA, but until this study the existence of a relationship between radioactivity and the chemical composition of the FA had not been confirmed. Kovacs et al. (2017) held that the concentration of natural radionuclides in FA was due to the quantity of sulphur and heavy metals in the coal. However Sanjuán et al (2021) observed a dependence between the chemical composition and the content of natural radionuclides as a function of the type of coal burned.

From the two sets of data for CEM and FA, prediction models for the activity concentration of the different radionuclides were established. The models are presented in Figure 3.

CEM	FA
$A^e_{^{226}Ra} = (0.914\cdot[SiO_2]) - (1.974\cdot[Fe_2O_3]) + (19.899\cdot[MnO]) + \cdots$ $\cdots + (59.250\cdot[TiO_2])$	$A^e_{^{226}Ra} = (1.826\cdot[Al_2O_3]) + (2.707\cdot[Fe_2O_3]) - \cdots$ $\cdots - (11.414\cdot[MgO]) + (51.505\cdot[TiO_2])$
$A^e_{^{212}Pb} = (0.179\cdot[CaO]) + (2.258\cdot[Al_2O_3]) - (5.389\cdot[MgO]) + \cdots$ $\cdots + (9.267\cdot[K_2O]) + (20.412\cdot[TiO_2]) - (2.6075\cdot[SO_3])$	$A^e_{^{212}Pb} = (3.455\cdot[CaO]) + (5.007\cdot[Al_2O_3]) - \cdots$ $\cdots - (3.046\cdot[Fe_2O_3]) - (16.916\cdot[MgO])$
$A^e_{^{40}K} = (4.483\cdot[SiO_2]) - (0.629\cdot[CaO]) + (2.960\cdot[Al_2O_3]) - \cdots$ $\cdots - (34.967\cdot[Na_2O]) + (171.010\cdot[K_2O]) - (66.140\cdot[TiO_2])$	$A^e_{^{40}K} = (230.428\cdot[K_2O]) - (67.528\cdot[TiO_2])$

Figure 3. Models established to determine the activity concentration of ^{226}Ra, ^{212}Pb, and ^{40}K in CEM and FA from their chemical composition

Figure 4 shows the experimental values of activity concentration for ^{226}Ra, ^{212}Pb, and ^{40}K and those estimated from the proposed models for the samples Test-CEM and Test-FA used in the validation of the models. RSD % values are also presented.

The highest RSD% value obtained corresponds to the FA-V sample and its estimation of ^{40}K with an RSD of 27.8%, so it can be concluded that all the results obtained by estimation compared to the experimental value comply with the RSD value <30%.

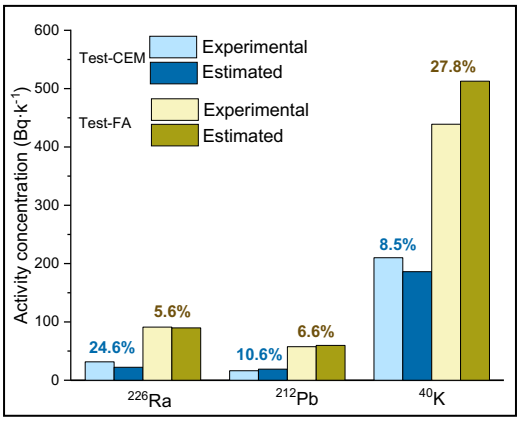

Figure 4. Validation of activity concentrations for ^{226}Ra, ^{212}Pb, and ^{40}K for Test-CEM and Test-FA experimentally determined by gamma spectrometry and those estimated by the proposed models (validation criterion for satisfactory results was an RSD(%) ≤30%)

These results indicate the suitability of the models to reliably estimate radionuclide activity values of cements and fly ashes from their chemical composition.

4. Conclusions

Through this study, models have been established that relate the chemical composition of cements and fly ashes to the activity concentration index of the different radionuclides. These models make it possible to predict the radiological content of the samples using statistical methods.

Acknowledgements

Authors wish to thank the support of Project PID2020-116002RB-100/AEI/10.13039/501100011033 (HORRADIONEX). The authors would also like to thank the MICINN for the pre-doctoral contract (PRE2021-098535) of Andrés Caño Blanes.

References

Coletti, C., Brattich, E., Cinelli, G., Cultrone, G., Maritan, L., Mazzoli, C., Mostacci, D., Tositti, L., Sassi, R (2020) Radionuclide concentration and radon exhalation in new mix design of bricks produced reusing NORM by-products: The influence of mineralogy and texture. *Construction and Building Materials* 260:119820.

EU (2013) Council Directive 2013/59/Euratom of 5 Dec. Laying down basic safety standards for protection against the dangers arising from exposure to ionising radiation, and repealing Directives 89/618/Euratom, 90/641/Euratom, 96/29/Euratom, 97/43/Euratom and 2003/122/Euratom, vol 57. L13, vol ISSN 1977-0677. European Commission,

Kovacs, T., Bator, G., Schroeyers, W., Labrincha, J., Puertas, F., Hegedus, M., Nicolaides, D., Sanjuán, MA., Krivenko, P., Grubeša, IN., Sas, Z., Michalik, B., Anagnostakis, M., Barisic, I., Nuccetelli, C., Trevisi, R., Croymans, T., Schreurs, S., Todorović, N., Vaiciukyniene, D., Bistrickaite, R., Tkaczyk, A., Kovler, K., Wiegers, R., Doherty, R. (2017) "From raw materials to NORM by-products". In: Schroeyers W (ed) *Naturally Occurring Radioactive Materials in Construction*. Woodhead Publishing, pp 135-182.

Kovler, K., Perevalov, A., Steiner, V., Metzger, LA (2005) "Radon exhalation of cementitious materials made with coal fly ash: Part 1--scientific background and testing of the cement and fly ash emanation". *J Environ Radioact* 82 (3):321-334.

Ndahirwa, D., Zmamou, H., Lenormand, H., Leblanc, N. (2022) The role of supplementary cementitious materials in hydration, durability and shrinkage of cement-based materials, their environmental and economic benefits: A review. *Cleaner Materials* 5:100123. doi:10.1016/j.clema.2022.100123

Puertas, F., Alonso, MM., Torres-Carrasco, M., Rivilla, P.,Gascó, C.,Yagüe, L., Suárez, JA., Navarro, N (2015) "Radiological characterization of anhydrous/hydrated cements and geopolymers". *Construction and Building Materials* 101, Part 1, 1105-1112.

Sanjuán, MÁ., Suarez-Navarro, JA., Argiz, C., Estévez, E (2021) "Radiation dose calculation of fine and coarse coal fly ash used for building purposes", *Journal of Radioanalytical and Nuclear Chemistry* 327 (2):1045-1054.

The 16th International Congress on the Chemistry of Cement 2023 (ICCC2023)
"Further Reduction of CO_2 -Emissions and Circularity in the Cement and Concrete Industry"
September 18–22, 2023, Bangkok, Thailand

Effects of post-fire water curing on strength recovery of thermally damaged mortar from 800 ℃

H.D. Wang, H.T. Liao, Y. Li*, T.J. Liu*

School of Civil and Environmental Engineering, Harbin Institute of Technology, Shenzhen, China

Email: wanghdhitsz@163.com (H.D. Wang), 21b954010@stu.hit.edu.cn (H.T. Liao), liye@hit.edu.cn (Y. Li), liutiejun@hit.edu.cn (T.J. Liu)

ABSTRACT

This study investigated the effects of post-fire water curing on the compressive strength recovery of thermally damaged mortars with different water-to-cement ratios (w/c). The mortar samples were exposed to 800°C and then underwent post-fire water curing after natural cooling. Multiple microscopic characterization methods, including scanning electron microscopy (SEM), mercury intrusion porosimetry (MIP), thermogravimetric analysis (TGA), and X-ray diffraction (XRD), were utilized to analyze the microstructure, pore distribution, and chemical composition of the mortar samples. The results indicated that mortar with low w/c consistently exhibits higher compressive strength than mortar with high w/c, whether tested before heating, after heating, or after post-fire water curing (W). After 800 ℃ exposure, the compressive strength of the two mixtures decreased to approximately 37% of their initial compressive strength before heating due to the decomposition of hydration products and the coarsened microstructure. After post-fire curing, the rehydration products of C_3S and β-C_2S healed most of the microcracks and large capillaries, leading to a remarkable recovery in compressive strength to over 128% of their initial values before heating.

KEYWORDS: *Post-fire curing, Thermally damaged mortar, Water-to-cement ratio, Microstructure changes*

1. Introduction

Concrete undergoes drastic deterioration of mechanical properties during fire exposure due to a series of physical and chemical changes. These changes include the evaporation of free water (at around 100 ℃) and chemically combined water (at around 180 ℃), the transformation from α-quartz to β-quartz (at 573 ℃), and the decomposition of ettringite (at above 60 ℃), calcium hydroxide ($Ca(OH)_2$, at around 500 ℃), and calcium-silicate-hydrate (C-S-H, at around 700 ℃). The complex procedures to rehabilitate damaged concrete is labor-intensive and costly. The idea of autogenous self-healing methods such as post-fire curing has been proposed as a promising approach for healing the thermally damaged concrete. The recovery of concrete correlates with the degree of thermal damage and the initial unhydrated cement paste. However, as the main effect factor for the above two, very few studies have been conducted on the effects of water-to-cement (w/c) ratio on the properties of concrete after post-fire curing.

The objective of the current study is to investigate the effects of post-fire water curing on the compressive strength recovery and the changes of microstructure and chemical composition of thermally damaged mortar with different w/c. The mortar specimens were heated to 800 ℃ and subsequently full immersed in lime-saturated water for post-fire curing. The compressive strength of mortar specimens before heating, after heating, and after post-fire water curing were tested. To discussed the healing process and mechanisms of compressive strength recovery during post-fire water curing, the changes in microstructure, pore distribution, and chemical composition of the mortar specimens were analyzed by using SEM, MIP, XRD, and TGA.

2. Materials and methodology

2.1 Materials and sample preparation

Table 1 shows the two mix proportions of used mortar specimens. The water-to-cement ratios are 0.18 and 0.36. CEM I 52.5 N Portland cement, fine aggregate with the maximum size of 1.18 mm, and silica sand with the median particle size of 125 μm were used as raw materials. The chemical composition of the cement is shown in **Error! Reference source not found.**. Polypropylene (PP) fibers, 12 mm in length and 31 μm in diameter, were incorporated to prevent explosive spalling during heating.

Table 1 Mix proportions of mortar.

Mix Design	PP fiber (kg/m^3)	Relative weight ratio to cement weight					
		Cement	Fine aggregate	Silica sand	Water	Superplasticizer	W/C
M-0.18	3.0	1.00	0.94	0.31	0.18	0.045	0.18
M-0.36	3.0	1.00	0.94	0.31	0.36	0.005	0.38

The preparation of mortar specimens and the heating regime were described in detail in our previous study (Li et al., 2023). After being cooled to ambient temperature, the mortar specimens were completely immersed in lime-saturated water for 30 days. Afterward, the specimens were removed from the lime-saturated water and dried in laboratory environment for 3 days before performance testing.

2.2 Characterization methods

The compression tests, scanning electron microscopy, mercury intrusion porosimetry, X-ray diffraction, and thermogravimetric analysis were conducted to characterize the changes in compressive strength, microstructure, pore distribution, and chemical composition of the mortar specimens before heating, after heating, and after post-fire water curing. The details of these characterization methods can be found in our previous research (Li et al., 2023).

3. Results and discussions

3.1 Compressive strength

Fig. 1 presents the changes of compressive strength of the specimens. Before heating, the mortar with 0.18 w/c ratio (M-0.18) showed 83.7 MPa of compressive strength, which is 14.3 MPa higher than that of the M-0.36 specimen. This observation confirems the previous findings that an increase in w/c leads to a reduction in mechanical stength. The compressive strength of the M-0.18 and M-0.36 specimens reduced to 30.9 and 25.8 MPa, respectively, after 800 ℃ exposure due to the decomposition of the hydration products, accompanied by the formation of microcracks and the coarsening of pore structure. After post-fire curing, the recovered compressive strength of the two mixtures even exceeded their respective original compressive strength before heating by 28.2% and 29.0%, respectively. The mechanism of compressive strength recovery is analyzed in the following sections.

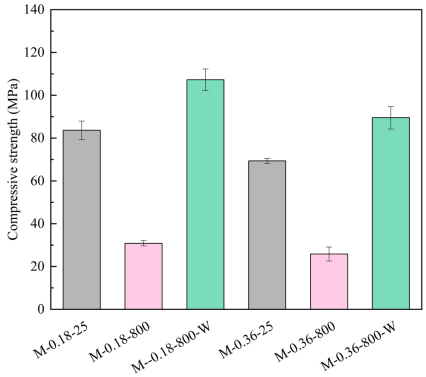

Fig. 1 Compressive strength of the mortar specimens before heating, after heating, and after post-fire water curing.

3.2 Microstructure observations

As shown in Fig. 2 (a) and (d), the microstructure of specimen M-0.18-25 is more compact than M-0.36-25 due to its low w/c. Specimen M-0.36-25 has relatively fewer unhydrated cement grains. After being exposed to 800 ℃, specimens M-0.18-800 and M-0.36-800 exhibit a highly loose and porous microstructure, and more microcracks were formed in specimen M-0.36-800 due to the extensive decomposition of hydration products. The damage of microstructure is the main reason for the significant reduction in compressive strength of mortar after heating. From Fig. 2 (c) and (f), post-fire water curing densifies the loose and porous microstructure due to the consolidated effect of the rehydration products formed inside coarsened pores and microcracks. The densification of microstructure is reflected in the macroscopic recovery of compressive strength. Additionally, specimen M-0.36-800-W still has partial unhealed microcracks, leading to the lower compressive strength compared to specimen M-0.18-800-W.

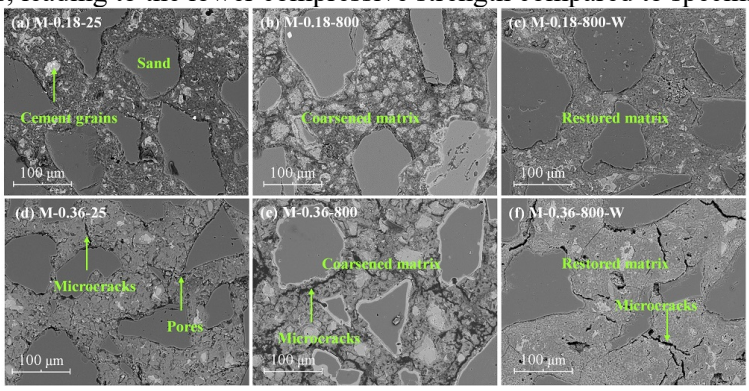

Fig. 2 The microstructure of the mortar specimens before heating, after heating, and after post-fire water curing.

3.3 Porosity and pore size distribution

The pore size distribution and porosity of the M-0.18 and M-0.36 specimens are shown in Fig. 3. From Fig. 3 (a), the pore size of the two specimens before heating were mostly less than 0.1 μm and their peak pore size centered around 0.03 and 0.05 μm, respectively. After 800 ℃ exposure, owing to the decomposition of hydration products and the coarsened microstructure, the overall porosity of the M-0.18 and M-0.36 specimens increased to 26.2% and 33.9%, respectively. The development of the microcracks (>1 μm) and large capillaries (0.05-1 μm), agreeing with the SEM observations shown as Fig. 2 (b) and (e), was the main reason for the significant decrease in compressive strength. After post-fire water curing, most of the microcracks and large capillaries were healed as the corresponding porosity reduced significantly. The overall porosity of the M-0.18 and M-0.36 specimens declined to 10.1% and 13.1%, respectively, leading to the recovery of compressive strength of the mortar specimens. This filling effect was caused by the rehydration of C_3S and β-C_2S, which is analyzed in section 3.4.

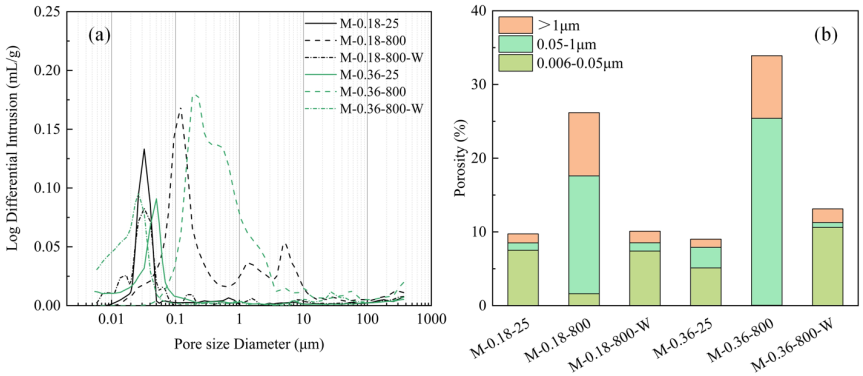

Fig. 3 (a) Pore size distribution of the mortar specimens before heating, after heating, and after post-fire curing; and (b) porosity of the mortar specimens divided into three ranges.

3.4 Chemical composition

Fig. 4 depicts the XRD patterns (a) and the thermogravimetric and differential thermogravimetric curves (b) of the mortar specimens before heating, after heating, and after post-fire water curing. From Fig. 4 (a), the unhydrated C_3S and β-C_2S remains, and $Ca(OH)_2$ (CH) and ettringite are the major crystalline

hydrated phases before heating. Ettringite may completely decompose during the drying test of the specimen powder. After 800 ℃ exposure, C_3S remained in specimens, and the amount of β-C_2S increased, corresponding to the increase of its peak intensity, due to the decomposition of C-S-H and solid state reaction between C_3S and the dehydration products of CH at elevated temperature. The decomposition of hydration products is related to the decrease in compressive strength. After post-fire water curing, from Fig. 4 (a) and (b), the new hydration products (CH, ettringite, and C-S-H) were formed due to the rehydration of C_3S and β-C_2S, which were obtained from unhydrated cement grains and decomposition products of initial hydrates. The thermally damaged mortar matrix was restored by the filling effect of the rehydration products (see Fig. 2 (c) and (f)), leading to the recovery of the compressive strength.

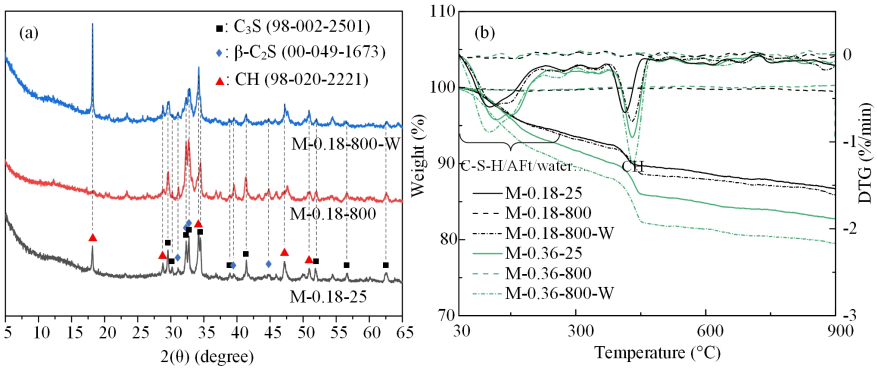

Fig. 4 The chemical composition of the mortar specimens before heating, after heating, and after post-fire curing.

4. Conclusions

This work investigated the effects of post-water curing on compressive strength recovery of mortar with different w/c subjected to 800 °C. After heating, the compressive strength of mortar decreased significantly due to the decomposition of hydration products, accompanied by the generation of microcracks and coarsening of pores. Post-fire water curing can effectively restore the compressive strength of thermally damaged mortar, even exceeding the initial value before heating, attributed to the rehydration products of C_3S and β-C_2S filling and healing the coarsened pores and microcracks. These findings suggest that post-fire water curing is an effective method for restoring fire-damaged mortar. Further research is needed to optimize the post-fire curing process and develop practical applications for fire-damaged structures.

Acknowledgements

This work was supported by the National Science Fund for Distinguished Young Scholars [No. 52025081], the National Natural Science Foundation of China [No. 52008136], and the Natural Science Foundation of Guangdong Province of China [No. 2023A1515012635].

References

Akca, A. H., and Özyurt, N. (2018). Effects of re-curing on residual mechanical properties of concrete after high temperature exposure. Construction and Building Materials, 159, 540-552.

Yim, H. J., Park, S. J. and, Jun, Y. (2019). Physicochemical and mechanical changes of thermally damaged cement pastes and concrete for re-curing conditions. Cement and Concrete Research, 125, 105831.

Li, Y., Wang, H., Shi, C., Zou, D., Zhou, A. and, Liu, T. (2023). Effect of post-fire lime-saturated water and water-CO_2 cyclic curing on strength recovery of thermally damaged high-performance concrete with different silica contents. Cement and Concrete Research, 164, 107050.

Li, L., Shi, L., Wang, Q., Liu, Y., Dong, J., Zhang, H., and Zhang, G. (2020). A review on the recovery of fire-damaged concrete with post-fire-curing. Construction and Building Materials, 237, 117564.

Nijland, T. G., and Larbi, J. A. (2001). Unraveling the temperature distribution in fire-damaged concrete by means of PFM microscopy: Outline of the approach and review of potentially useful reactions. Heron, 46(4), 253-264.

Poon, C. S., Azhar, S., Anson, M. and, Wong, Y. L. (2001). Strength and durability recovery of fire-damaged concrete after post-fire-curing. Cement and Concrete Research, 31(9), 1307-1318.

Schneider, U. (1988). Concrete at high temperatures—a general review. Fire Safety Journal, 13(1), 55-68.

The 16th International Congress on the Chemistry of Cement 2023 (ICCC2023)
"Further Reduction of CO_2 -Emissions and Circularity in the Cement and Concrete Industry"
September 18–22, 2023, Bangkok, Thailand

Strength performance of recycled aggregate concretes with different qualities of recycled aggregates

D. Garcia[1], C. Hazaree*[2], and A. Yacoub[3]

[1] *Holcim Innovation Center, Saint-Quentin-Fallavier, France*
Email: denis.garcia@holcim.com
[2] *Holcim Innovation Center, Saint-Quentin-Fallavier, France*
Email: chetan.hazaree@holcim.com
[3] *Holcim Innovation Center, Saint-Quentin-Fallavier, France*
Email: aiman.yacoub@holcim.com

Abstract

Compromised properties of recycled concrete aggregate (RCA) in terms of specific gravity, water absorption, mechanical properties, etc. often limit its use in concrete. These properties of RCA could degrade the performance of concrete in terms of workability, strength, and durability. To increase the substitution levels of virgin aggregates with RCA, to have equivalent to virgin aggregate concrete performance without letting the cost parameters get distorted, it is necessary to obtain better quality of RCA.

In this study, the effect of different concentrations of RCA from three different processes is reported. Both virgin coarse aggregate (VCA) and virgin fine aggregate (VFA) are respectively replaced with the coarse recycled aggregate (CRA) and fine recycled aggregate (FRA). Replacement levels of virgin aggregate include 0%, 50% and 100%. The effects of these replacement levels on admixture demand, workability, fresh concrete behavior and compressive strength are systematically reported. Based on these observations, a basis for a new system for classifying RCA and allowable replacement levels of virgin aggregates is proposed.

Keywords: *Circular Economy, Recycled concrete aggregate (RCA), Crushing, Workability, Strength*

1. Introduction

In each market, in addition to the feedstock quality, the quality of the recycled concrete aggregate (RCA) depends on the crushing process used for its production. With the basic crushing equipment used today, the RCA contains attached residual mortar, making it characteristically lower strength, porous, and highly absorbent (de Juan and Gutiérrez, 2009; Djerbi Tegguer, 2012; Kim, 2022). Concrete made with such RCA exhibits lower performance, higher variability, could be uneconomical and with shorter estimated life (Florea and Brouwers, 2013). The water absorption coefficient (WAC) of such RCA is directly proportional to the attached mortar. Higher the attached mortar, lower is the performance of concrete made with such RCA.

The objective of this research is to investigate the effect of three crushing techniques on the cleanliness of the RCA. The efficiency of the technique is determined at first by comparing the WAC of the RCAs and its cement paste content. Both coarse recycled aggregate (CRA) and fine recycled aggregate (FRA) are used for substituting virgin aggregate in the recycled aggregate concrete (RAC) mixtures. The RCA and RAC characterization will allow us to propose a basis for classification system based on quality of the aggregates.

2. Experimental Program

2.1 Crushing systems

Locally available and sorted concrete from the construction and demolition waste (CDW) is used as feedstock in producing RCA1, RCA2 and RCA3, respectively. Recycled aggregate obtained from three different crushing systems viz. C1, C2 & C3 were used in this experimental program. The RCA in C1 system is obtained by a two-stage crushing system consisting of a new crushing technology while that from C2 system is obtained from

a 3-stage conventional crushing line consisting of a Jaw-Horizontal shaft impactor-Vertical shaft impactor. RCA from the C3 system is the currently produced RCA using a horizontal shaft impactor.

2.2 Concrete materials & mixes

CEM II/A 42.5 R conforming to EN 197-1, one type of virgin aggregate and three types of recycled aggregates were used to produce concrete. Aggregates were characterized as per NF EN 1097-6 (NF EN 1097-6, 2022). A PC-type superplasticizer with 20% dry content and 1.06 density was used for achieving water reduction and targeted workability. Optimized C25/30 mixes for S4 (initial slump of 160 mm-210 mm.) class were designed at three substitution levels of CRA and FRA. The mixes are designated as 'C# - %CRA / %FRA'; for example, concrete made of 50% CRA and 50% FRA using RCA from crushing process 1 is dominated by C1-50/50. The concrete made with virgin aggregate is designated as Ref. A total volume substitution of the virgin aggregates by recycled concrete aggregates is used in these experiments. Accordingly, the following 10 mixtures are evaluated.

- Reference: Ref
- Crushing line - 1: C1-0/100, C1-50/100, C1-100/100
- Crushing line - 2: C2-0/100, C2-50/100, C2-100/100
- Crushing line - 3: C3-0/100, C3-50/100, C3-100/100

2.3 Test methods

The primary aggregate and RCA were characterized using NF EN 1097-6 (NF EN 1097-6, 2022). The cement paste content is obtained using method outlined in GranduBé (Arliguié et al., 2007). The cement paste volume in concrete mixtures were optimized for C25/30 grade and the initial workability was achieved by adjusting the admixture dosage. The workability was characterized with NF EN 206 (NF EN 206+A2/CN,2022) and the compressive strength of concrete was measured at 28 days in conformance with NF EN 206 (NF EN 206+A2/CN,2022).

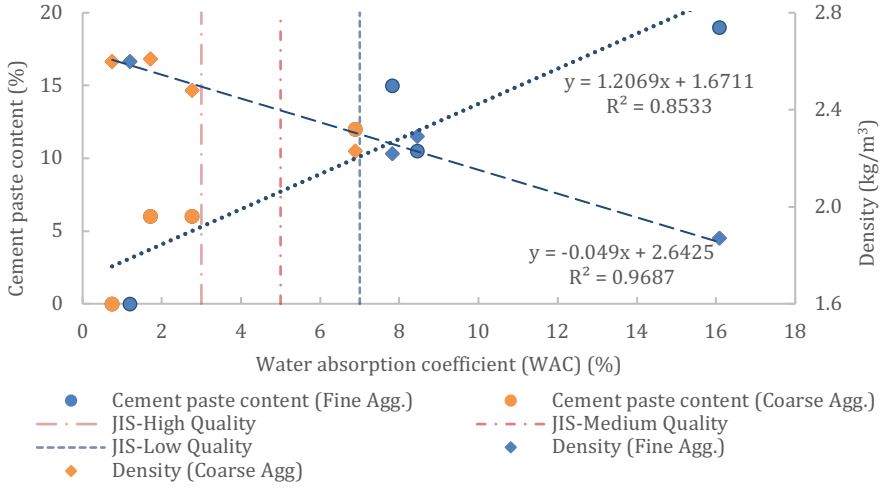

Figure 1 Linear correlation between the WAC, Density and Cement Paste Content

3. Typical Results and discussions

Typical results are described below, while complete results are discussed during the conference.

3.1 Effect of crushing process on residual cement paste and aggregate quality

The crushing process acts as a recovery process. Due to cleaning of coarse aggregate, the cement paste enters the recycled fine aggregate (0/4) fraction and enriches it. Hence it could be found that the cleaner the RCA, the richer the corresponding FRA. It can be seen from Figure 1 that the CRA cleaning effectiveness of the tested

crushing processes could be ranked as C1 > C2 > C3. It can be inferred that the better the crushing process, the lesser the cement paste content. On the other hand, the corresponding RFA shall have commensurate cement enriching effectiveness. Furthermore, Figure 1 shows linear correlation between the water absorption coefficient and cement paste content and that between cement paste content and density. From the graph, using the Japanese standard (JIS A 5021, JIS A 5022, JIS A 5023), the CRA1 could be classified High quality aggregates, CRA2 could be considered as marginally medium quality and CRA3 as low quality aggregate.

3.2 Concrete results

3.2.1 Example of Coarse & fine aggregate substitution

Figure 2 represents the effect of 100% replacement of virgin aggregates with recycled ones on concrete properties. Quite along the established inferences, the admixture demand and paste volume increase with increased RAC. In addition, we can see that the crushing process makes an impact on the cleanliness of RCA, which in-turn influences the WAC eventually impacting performance of RCA in concrete.

We can notice that the admixture demand of C1 and C2 increased three and four times, respectively compared to the reference concrete; this is due to the cement paste content in the Recycled aggregate. So, to achieve the desired properties, we had to increase the admixture demand and the paste volume; this conclusion is applicable for concrete made with good quality aggregates (C1) and medium quality aggregates (C2). Whereas for the concrete made with low quality aggregates (C3) and as shown below, the admixture demand is like C1 (1,5%), the cement paste is around 320l/m3 and the slump desired is around 230mm. Thus, we were obliged to increase the target value for the slump and optimize the relation paste volume and admixture demand to obtain a workable concrete as desired on construction sites. Otherwise, by only increasing the cement paste alone or the admixture demand alone, the concrete obtained was not workable. With lower WAC of the aggregate grading (high and medium quality of aggregates) we can compensate the loss of workability with an addition of the superplasticizer. As if for high WAC aggregate grading (low quality aggregates), we need to change the slump target value and compensate with higher addition of paste volume. This maneuver could be environmentally and economically costly.

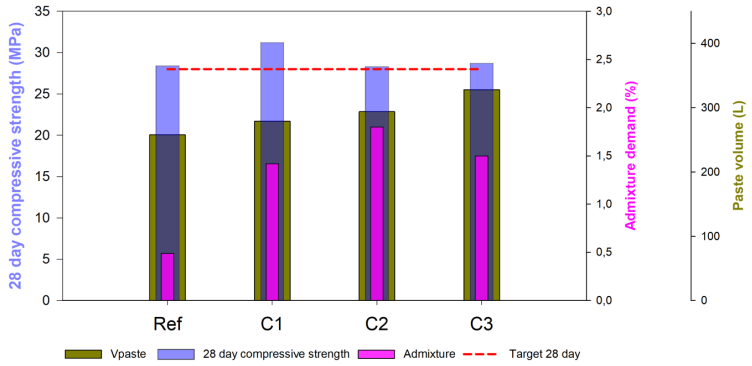

Figure 2 Effect of 100% replacement level with aggregate from different crushing lines on concrete properties

3.2.2 WAC of combined aggregate grading, Recycling ratio and paste efficiency

Figure 3 shows the correlation between the WAC of combined aggregate grading (weighted average of WAC) and the paste efficiency. The paste efficiency is defined as the ratio of 28-day compressive strength and paste volume, expressed in MPa/L/m^3. The paste efficiency depends on the cleaning efficiency of aggregate, the cleaner the RCA the higher is the efficiency; paste efficiency of C1 > C2 > C3. On the other hand, we can clearly notice that the introduction of 100% RFA creates an important impact of the paste efficiency; When 100% of RFA is used, the paste efficiency drops steeply compared to 0/100 substitution level.

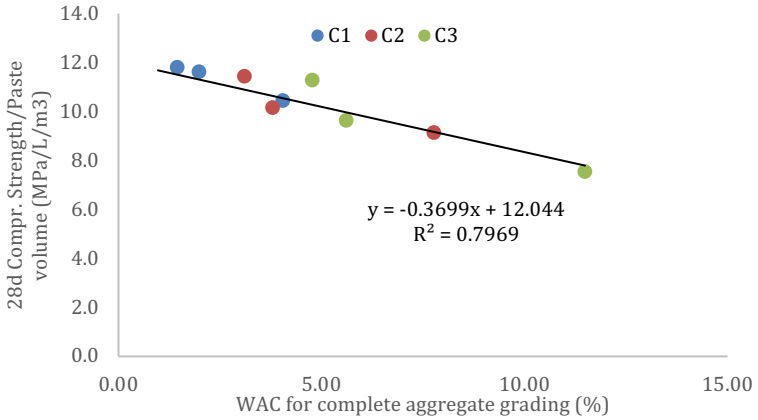

Figure 3 The correlation between the WAC and the paste efficiency

4. Summary

The following observations can be drawn from the results and discussion in this paper:

1. The quality of recycled aggregates produced depends on the crushing process. A better crushing process is a process with a high RCA cleaning efficiency. The cleanliness of aggregate, represented by cement paste content, correlates very well with the water absorption coefficient and density
2. The WAC of combined aggregate grading is a good indicator of modified aggregate skeleton with recycled aggregate. This WAC correlates well with most concrete properties. It can thus be used for defining a framework for classifying an aggregate system consisting of recycled aggregate

5. References

Arliguié, G.D. de publication P., Hornain, H., Coste, J.-F.P., Projet national GranDuBé, Association française de génie civil, Réseau Génie civil et urbain, 2007. GranDuBé: grandeurs associées à la durabilité des bétons. Presses de l'École nationale des ponts et chaussées, Paris, France.

de Juan, M.S., Gutiérrez, P.A., 2009. Study on the influence of attached mortar content on the properties of recycled concrete aggregate. Construction and Building Materials 23, 872–877. https://doi.org/10.1016/j.conbuildmat.2008.04.012

Djerbi Tegguer, A., 2012. Determining the water absorption of recycled aggregates utilizing hydrostatic weighing approach. Construction and Building Materials 27, 112–116. https://doi.org/10.1016/j.conbuildmat.2011.08.018

Florea, M.V.A., Brouwers, H.J.H., 2013. Properties of various size fractions of crushed concrete related to process conditions and re-use. Cement and Concrete Research 52, 11–21. https://doi.org/10.1016/j.cemconres.2013.05.005

JIS A 5021:2018 [WWW Document], n.d. . Normadoc. URL https://www.normadoc.com/english/jis-a-5021-2018.html (accessed 2.23.23).

JSA - JIS A 5022 - Recycled aggregate concrete-Class M | GlobalSpec [WWW Document], n.d. URL https://standards.globalspec.com/std/10385916/jis-a-5022 (accessed 2.23.23).

JSA - JIS A 5023 - Recycled aggregate concrete-Class L | GlobalSpec [WWW Document], n.d. URL https://standards.globalspec.com/std/10385917/JIS%20A%205023 (accessed 2.23.23).

Kim, J., 2022. Influence of quality of recycled aggregates on the mechanical properties of recycled aggregate concretes: An overview. Construction and Building Materials 328, 127071. https://doi.org/10.1016/j.conbuildmat.2022.127071

NF EN 206+A2/CN [WWW Document], n.d. . Afnor EDITIONS. URL https://www.boutique.afnor.org/en-gb/standard/nf-en-206-a2-cn/concrete-specification-performance-production-and-conformity-national-addit/fa203976/336018 (accessed 2.27.23).

NF EN 1097-6, 2022. Tests for mechanical and physical properties of aggregates.

The 16th International Congress on the Chemistry of Cement 2023 (ICCC2023)
"Further Reduction of CO_2 -Emissions and Circularity in the Cement and Concrete Industry"
September 18–22, 2023, Bangkok, Thailand

Study on the Deterioration Mechanism of Cementitious Waterproofing Membrane (Part II: Microstructural Evolution)

W.Y. Li[1], J. Wang[1], B. Peng[2], J.X. Liao[1], S.X. Wang[2], Z. Zeng[2], and X.M. Kong[1*]

[1] *Department of Civil Engineering, Tsinghua University, Beijing, 100084, China*

Email: kxm@mail.tsinghua.edu.cn

[2] *BASF Advanced Chemicals Co., Ltd., Shanghai 200137, China*

Email: bo.a.peng@basf.com

ABSTRACT

Understanding the deterioration mechanism is essential for improving the service life and durability as well as upgrading the formulation of cementitious waterproofing membranes (CWPM). This study discloses the correlation between deterioration process and evolution of microstructures, which is further divided into part I, the change of macroscopic performance including mechanical strength, adhesion and waterproofing performance; and part II, the evolution of microstructures and compositions including inorganic cementitious part, organic polymer film and the inorganic/organic interface. The synchronous latex polymer film formation and deterioration were tracked by time-domain NMR. The NMR results show that microscopically the organic part of the CWPM contains a hard polymer core and a water-sensitive polymer shell which plays an important role in the water migration process during film formation, and the inorganic/organic interface acts as extra channels during water re-absorption process and facilitates the unwanted cement hydration in CWPM. The hydration of cement at interface plus the promoted water uptake might be the microscopic explanation for CWPM deterioration under serve condition.

KEYWORDS: *waterproofing membrane, polymer latex, cement, deterioration mechanism, time-domain NMR.*

1. Introduction

Cementitious waterproofing membranes (CWPM) or polymer cement waterproof coating is widely used at construction scenarios such as roofing, swimming pool, bathrooms, wall protection and gap repair. The fundamental reason for the wide range of applications is that the addition of polymers not only increase the waterproof ability of cement, but also improves the tensile strength as well as extensibility and offers crack-bridging ability.

Despite the extensive application, only few studies (Waldvogel et al. (2020)) focused on the micro-structure evolution during the CWPM formation and deterioration process. Furthermore, the general microscopic CWPM characterization methods were limited to techniques such as X-ray diffraction (XRD) and scanning electron microscopy (SEM) which only provide information on the morphology and solid phases. However, water plays an important role in both film formation and deterioration process of CWPM. The investigations of the change of water content, the process of water migration and the role of interfaces are the critical part of studying CWPM deterioration mechanisms.
In this study, the importance of water migration and interface in the deterioration process is highlighted and investigated by time domain NMR (TD-NMR). The polymer film formation was studied *in-situ* and the CWPM deterioration is realized by immersing the membrane in water, which simulates the real service conditions of CWPM.

2. Materials and methods

The white Portland cement (WPC) was purchased from Yinshan White Cement Corporation and the mineral composition is shown in Table 1. The polymer emulsion (57% solid content) is a styrene propylene latex from BASF. The water-to-cement (w/c) ratio and the polymer-to-cement (p/c) ratio were controlled at 0.43 and 0.57, respectively. The specific mix proportion of the polymer-WPC films is shown in Table 2. The preparation of films was referred to the Chinese industry standard JC/T1017-2006.

Table 1 Mineral composition of white cement based on XRD-Rietveld results. (wt%)

C_3S	C_2S	Calcite	Dolomite	C_3A	CH	Hemihydrate	Periclase	C_4AF
68.05%	17.16%	5.19%	2.59%	2.13	2.12%	1.26%	1.23%	0.26%

Table 2 The specific mix proportion of the polymer-WPC films

Component	cement	emulsion	defoamer
Mass (g)	100.0	100.0	1.0

Hydration kinetics of the WPC was monitored *in-situ* by calorimetry and the heat flow curves were recorded by a Thermometric TAM Air isothermal microcalorimeter at 25 °C. The time-domain nuclear magnetic resonance (TD NMR) ^{1}H NMR measurements were performed on a Niumag (Suzhou, China) MicroMR12-025 spectrometer at 0.5 T. The samples were inserted into 25 mm glass tubes for NMR measurements. Carr-Purcell-Meiboom-Gill (CPMG) (Carr and Purcell (1954), Meiboom and Gill (1958)) and magic sandwich echo (MSE) (Maus et al., 2006) pulse sequences were used. The Butler-Reeds-Dawson (BRD) (Butler et al. (1981)) algorithm was used for inverse Laplace transform (ILT).
The obtained films were dried under Nitrogen atmosphere for two weeks until the weight change is smaller than 0.5%. The dried films were then immersed into deionized water to imitate the service condition of CWPM. During the water absorption process, the weight of films was measured on a METTLER TOLEDO XPR204S balance with a readability of 0.1 mg.

3. Result and Discussions

3.1 The retardation effect of polymer latex

From the heat flow curves (Figure 1), it can be seen that the polymer latex strongly retards cement hydration at dosages above 30 wt%. In addition, based on TG analysis (see PART I: MACROSCOPIC PERFORMANCE of this study) the induction period is beyond 3 days.

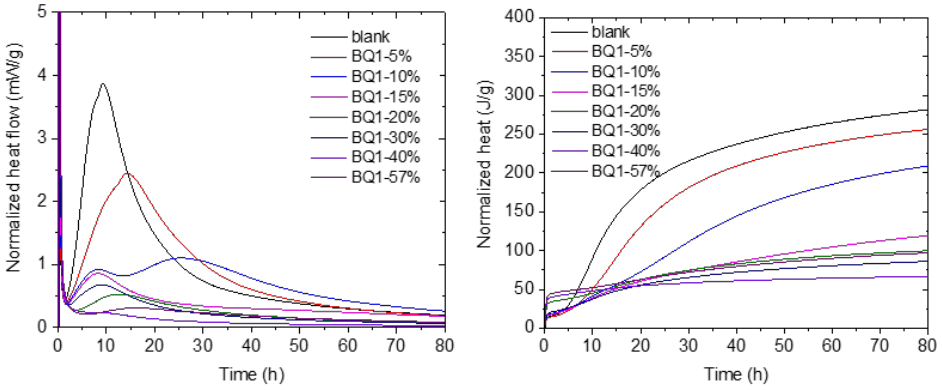

Figure 1. Calorimetry curves of the WPC in the presence of BQ1 at dosages of 0 (blank), 5, 10, 15, 20, 30, 40 and 57 wt%, (a) differential heat flow and (b) cumulative heat flow.

3.2 Film formation tracked by NMR

The *in-situ* NMR successfully characterized the film formation process of water-proofing membrane (Figure 2a). Three major signals are present in the T_2 profile (Figure 2b): 0.05 ms, 0.2 ms and 100–1000 ms, which correspond to the ^{1}H signals of the polymer core, polymer shell and free water, respectively.

As seen from Figure 2c, the sum of core and shell signals decreases during film formation, which indicates a water-sensitive feature of the polymer shell. The amount of free water drops due to evaporation, once the free water content approaching zero, the water further migrates out of the water sensitive polymer shell and the formation of film is completed. The core-shell speculation based on NMR results agrees well with a previous study (Caimi et al. (2018)) on polymer-cement waterproof mortars.

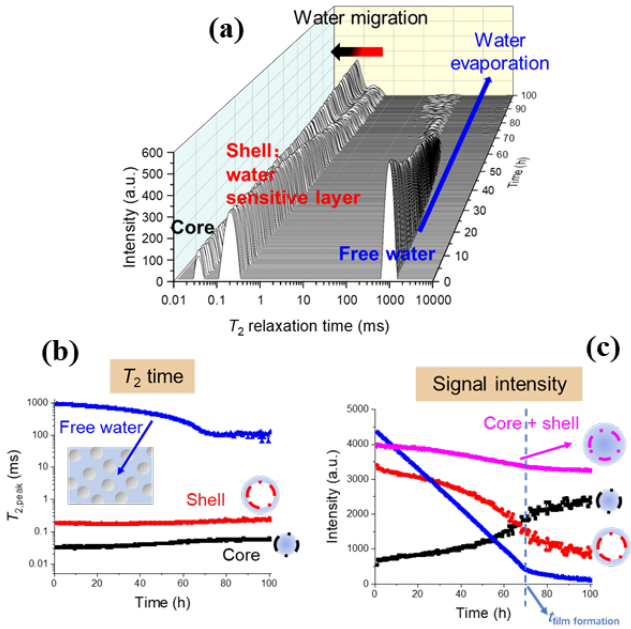

Figure 2. Relaxation profile and signal evolution of ^{1}H NMR during polymer film formation.

3.3 Water absorption process

The deterioration process of CWPM is essentially a water re-absorption process of dried films, which can be investigated by both weight change and NMR tests. The gained weight was normalized to initial weight of dry films and it can be seen from Figure 3 that the CWPM absorbed more water than PM.

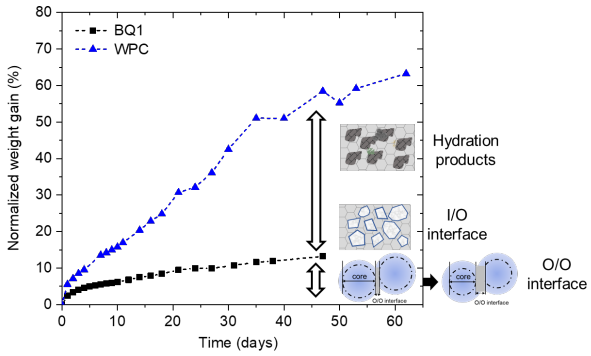

Figure 3. Normalized weight changes of the polymer and polymer-WPC films during the water absorption process.

The source of additional water uptake of CWPM than pure polymer film was investigated by TD-NMR. Figure 4 shows the T_2 relaxation profile and the signal evolution from CPMG measurements during at different days of water immersion. The ^{1}H reservoirs with T_2 relaxation time at approx. 0.1 ms, 1 ms, 10 ms and 100 ms relate to the polymer (but only partially due to the limit of CPMG method), the I/O interface, the I/O with hydration product interface and the free water, respectively. The first kind of I/O interface with T_2 of 1 ms shows negligible signal increase, which corresponds to a small amount of water filled between polymer and the embedded cement. The signal intensity of second interface with T_2 of 10 ms grows to reach a plateau, which is attributed to the hydration products growing at larger spaces. The

first I/O interface only act as channels during water migration but significantly promotes the uptake of free water inside the CWPM.

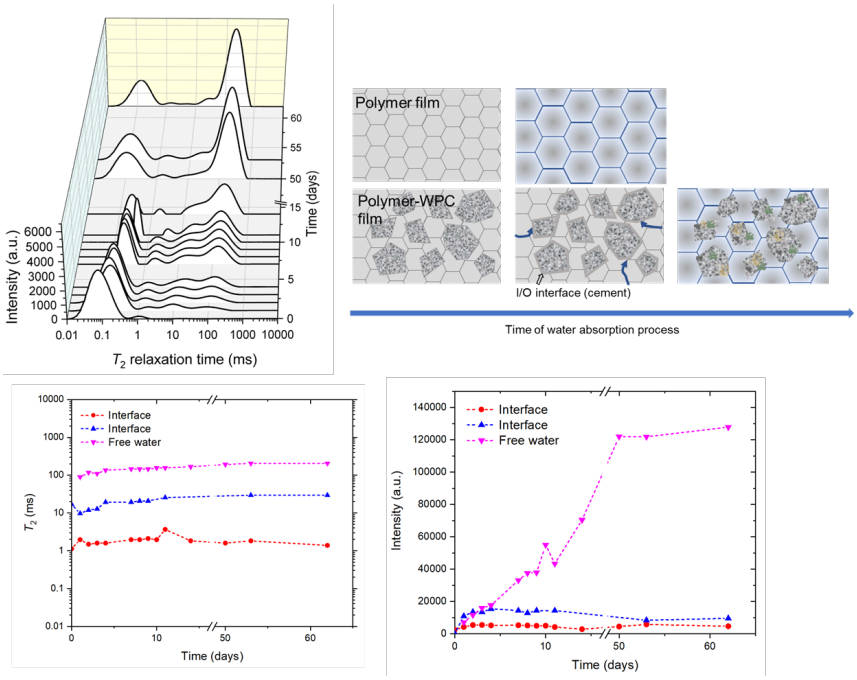

Figure 4. NMR of the polymer film during the water absorption process.

4. Conclusions

This study mainly focused on the microstructural evolution and water migration during CWPM formation as well as the deterioration process. TD-NMR was validated as an effective method to track microstructural evolution. Together with the thermogravimetry and mechanical tests (see PART I of this study), it is concluded that the deterioration process of CWPM can be described in four steps: 1) The migration of water at the inorganic/organic (I/O) interface, 2) the secondary hydration of cement and the growth of hydration products, 3) The de-bonding of I/O interface and 4) the breakdown of the waterproofing membrane. The secondary hydration of the unreacted cement in films is the main reason for the deterioration of CWPM. The key to durable CWPM is primarily the waterproofing property of the polymer film itself as water migration may occur through the channels between the fused polymer particles in the formed polymer films.

Acknowledgments

This work is supported by the collaboration project "Durability of cementitious waterproofing membrane" between Tsinghua University and BASF Advanced Chemicals Co., Ltd.

References

Butler, J.P., Reeds and J.A., Dawson, S.V. (1981). Estimating Solutions of First Kind Integral Equations with Nonnegative Constraints and Optimal Smoothing. *SIAM J. Numer. Anal.* 18, 381–397.

Caimi, S., Timmerer, E., Banfi, M., Storti and G., Morbidelli, M. (2018). Core-Shell Morphology of Redispersible Powders in Polymer-Cement Waterproof Mortars. *Polymers* 10, 1122.

Carr, H.Y. and Purcell, E.M. (1954). Effects of Diffusion on Free Precession in Nuclear Magnetic Resonance Experiments. *Phys. Rev.* 94, 630–638.

Maus, A., Hertlein, C. and Saalwächter, K. (2006). A Robust Proton NMR Method to Investigate Hard/Soft Ratios, Crystallinity, and Component Mobility in Polymers. *Macromol. Chem. Phys.* 207, 1150–1158.

Meiboom, S. and Gill, D. (1958). Modified Spin-Echo Method for Measuring Nuclear Relaxation Times. *Rev. Sci. Instrum.* 29, 688–691.

Waldvogel, M., Zurbriggen, R., Berger, A. and Herwegh, M. (2020). The microstructural evolution of cementitious, flexible waterproofing membranes during deformation with special focus on the role of crazing. *Cem. Concr. Compos.* 107, 103494.

The 16th International Congress on the Chemistry of Cement 2023 (ICCC2023)
"Further Reduction of CO_2 -Emissions and Circularity in the Cement and Concrete Industry"
September 18–22, 2023, Bangkok, Thailand

Influence of Hardened Cement Paste (HCP) Particle Size on Their Reuse in Fresh Cement Paste

S. R. Yahaya[1], H. Zhao[1], N. Vallo[1], T. Hanein[1], and H. Kinoshita[1*]

[1] *Department of Material Science and Engineering, The University of Sheffield, United Kingdom*
Email: h.kinoshita@sheffield.ac.uk

ABSTRACT

The recycling of hydrated cement fines from concrete wastes is challenging as they cause quality issues when used in the new products. To gain further understanding of recycling the fine particles of hardened cement in new products, the effects of different size ranges of hardened cement paste (HCP) particles were examined in the new cement pastes. The phase analysis of the products after 28 days of curing suggested an increased formation of mono-carbonate and reaction of C_3A. The HCP particle size did not show obvious trends on the microstructure of the new cement paste. Although the smaller size appeared to result in more homogeneous microstructure; finer HCP size resulted in reduced workability.

KEYWORDS: *Recycle, Reuse, Hydrated cement fines, Workability, Particle size*

1. Introduction

Recycling of waste cement is one of the potential routes to increase the sustainability of the relevant industry, through the reduction in the wastes and new cement consumption, leading to reduced carbon emission and sustainable use of natural resources. Concrete wastes are often ground and sieved into fractions, and the coarse fraction mainly composed of natural aggregates can be recycled as coarse aggregate for new products, while the finer fraction, the left over hydrated cement causes quality issues when used in the new products due to their lower density, higher water absorption, higher porosity and lower mechanical properties (Otsuki, Miyazato and Yodsudjai, 2003; Serpell and Lopez, 2013).

The aim of the present investigation is to further understand the impact of recycling the fine particles of hardened cement in new products. We used hardened cement paste (HCP) particles, as a simulant of the fine fractions of the concrete wastes, and the influence of HCP particle size was investigated when HCP was used as a part of new cement paste. It has been generally accepted that the particle size fractions of the raw materials used in the mortars have a significant impact on both the chemical and mechanical properties (Sugrañez *et al.*, 2013). Cement pastes were prepared mixing with 40 wt.% of HCP with 4 ranges of particle size and two different w/s ratios. Their hydration, microstructure and porosity were assessed, together with their workability.

2. Method

To simulate the fine fractions of the waste cement, HCP was prepared using Portland cement (PC) (Breedon Group Company) mixed with distilled water at water to cement (w/s ratio of 0.5. The HCP were moulded in 2 cm cubes and cured in open air at room temperature for over 1 year. HCP were crushed manually using percussion mortar and ground to 4 size ranges: (A) 1.00-0.50 mm, (B) 0.50-0.25 mm, (C) 0.25-0.15 mm, (D) 0.15-0.063 mm.

The crushed HCP were mixed with anhydrous PC powder to make a new cement pastes at 2 different water to solid (w/s) ratios; 0.50 and 0.35. The replacement of PC by HCP was 40 wt.% in all systems. PC and HCP were mixed manually for 3 minutes, then distilled water were added, and mixing continued for

another 3 minutes. Approximately 10g of sample were placed into a plastic centrifuge tube, sealed with parafilm and cured in the desiccator at room temperature. The cured sample were demoulded at 1, 7, 14 and 28 days, and their hydration arrested using acetone.

The product phases were analysed using X-ray diffraction (XRD) (Bruker D2 Phaser) and thermogravimetry (TG) (Perkin Elmer Pyris1) performed in nitrogen flow at 10°C/min up to 1000°C. Scanning electron microscopy (SEM) (Hitachi TM3030) was used to examine the microstructure of the products in the backscattered electron (BSE) mode. The samples mounted in the epoxy resin were polished to 1/4µm and carbon-coated. The porosity of the samples was studied using 3mm in diameter were taken from each of samples using Mercury Intrusion Porosimetry (MIP) (Micromeritics AutoPore V). Workability of the cement grouts were studied using mini-slump test. Sample were placed in the cone (a height of 57 mm, a 19 mmϕ at top and 38 mmϕ at base) and the cement paste left to flow by vertically lifting the cone from a base plate to recording the area covered by the grout on the base plate. A photograph was taken for the final slump and the area was calculated using ImageJ software.

3. Result and Discussion

3.1 Phase Analysis

XRD pattern of w/s=0.5 series cured for 28 days are shown in Fig. 1. Anhydrous cement phases i.e. alite, belite and aluminate phase can be found in all samples. The main hydration products common to all samples are portlandite (P) and ettringite (E). Reflection peaks that belong to mono-carbonate (Mc), and calcite (CC) are also detected. Peaks for rutile exist in the XRD pattern as it has been used as interntal standard. The XRD data of w/s= 0.35 series indicated similar trends, but the peaks for Mc and E appear to be more visible for the w/s=0.5 series in the comparation to the w/s=0.35 series while the peaks for aluminate (Al) phase looks more visible in w/s=0.35 series. This may suggest an enhanced reaction of Al phase to form E and Mc in w/s=0.5 series.

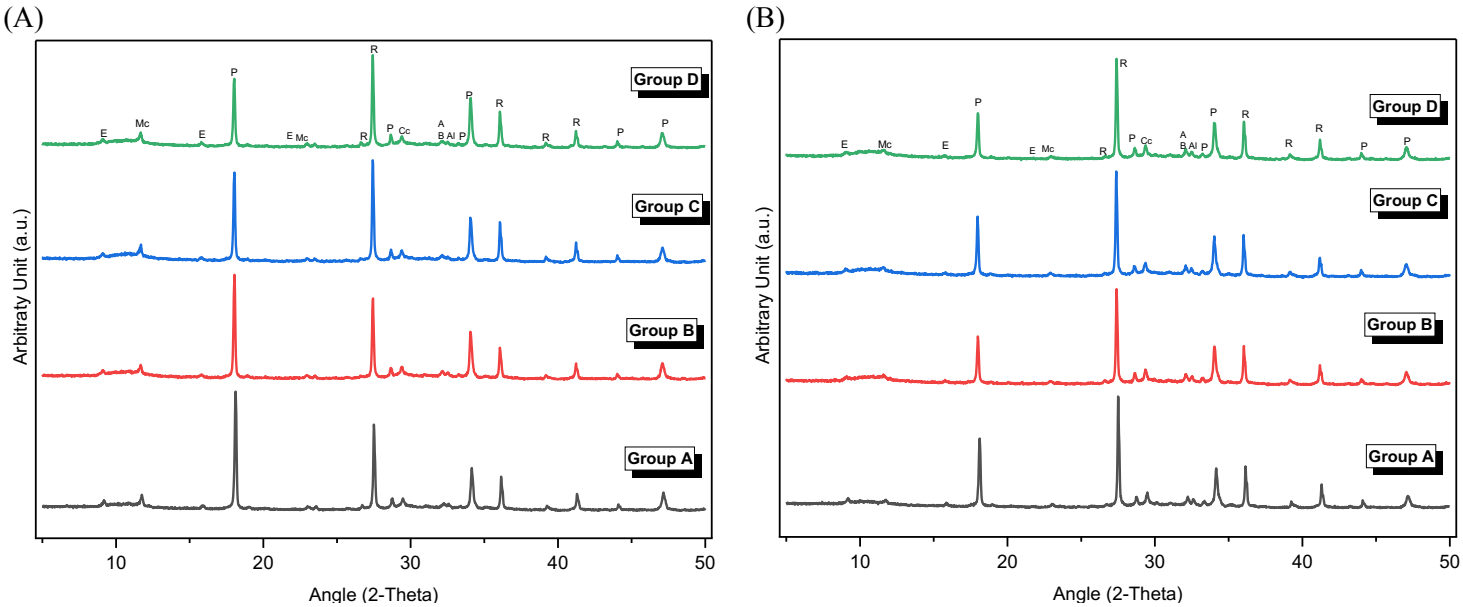

Fig. 1 XRD patterns of (a) w/s=0.5 and (b) w/c=0.35 series cured for 28 days. E-ettringite, Hc-hemi-carbonate, Mc-mono-carbonate, P-portlandite, Cc-calcite, A-alite, B-belite, Al-aluminate and R-rutile.

Fig. 2(a) and (b) shows the TG and DTG results of set of w/s=0.5 and 0.35, respectively. The effects of HCP were subtracted from the TG and DTG data in order to analyse the hydration reaction that took place following the creation of the new cement samples. Based on the proportion employed in the systems, the weight loss data for the HCP samples were subtracted from the weight loss data for the new cement samples.Three main weight loss events and associated peaks are observed in TG and DTG for all samples; ettringite loses its water content at temperature between 100 to 105 °C; a broad peak of water loss between 50 and 200 °C indicates the presence of C-S-H; dehydroxylation of portlandite can be

observed at 460°C; calcite decomposes at temperature from 500 to 800 °C. For the w/s=0.35 series shown in Fig. 2(b), peak of monocarbonate can be observed only for finer HCP (group C and D). Monocarbonate loses its water content at temperature between 60 to 200 °C and CO_2 at around 650 °C.

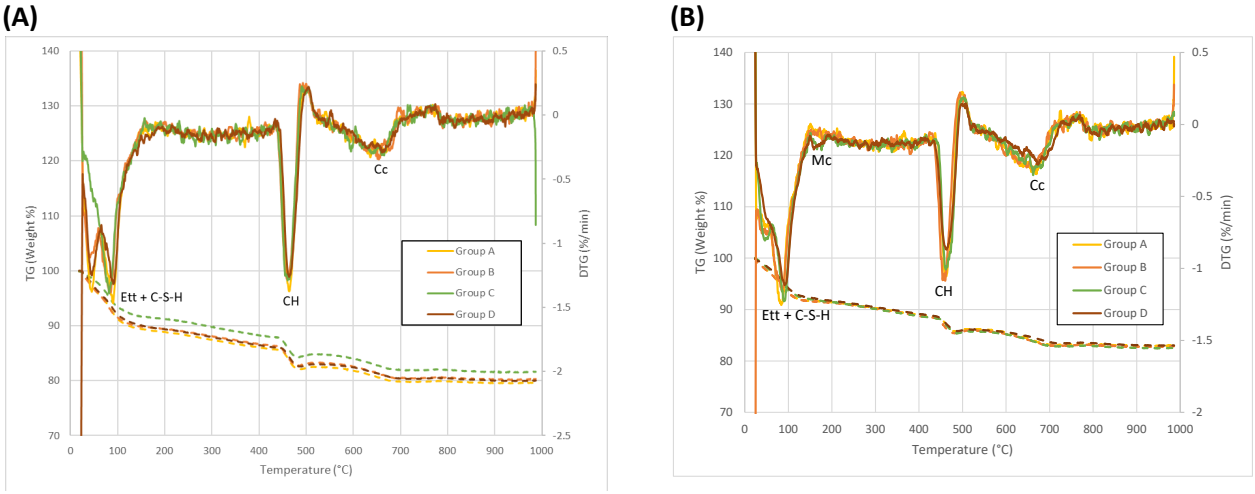

Fig. 2 TG and DTG curves of (a) w/s=0.5 and (b) w/s=0.35 series with 4 different HCP size ranges (A-D) cured for 28 days.

3.2 Microstructure Analysis

Figure 3 shows BSE image of w/s=0.35 series with different size of HCP particles cured for 28 days. Clincker phases are light grey in the BSE images, while hydration products are darker grey. All samples indicated similar microstructure, with denser particles, which appears to be the HCP particles, surrounded by the less dense structure. The HCP particles are expected to be denser as they had been hydrated for a much longer period (> 1 year). Among different HCP size ranges, the finest set (group D) appears to have more homogeneous microstructure. It is known that finer aggregates have a filling effects that allows a denser and more homogeneous matrix of the hydrated cement (Santos *et al.*, 2020).

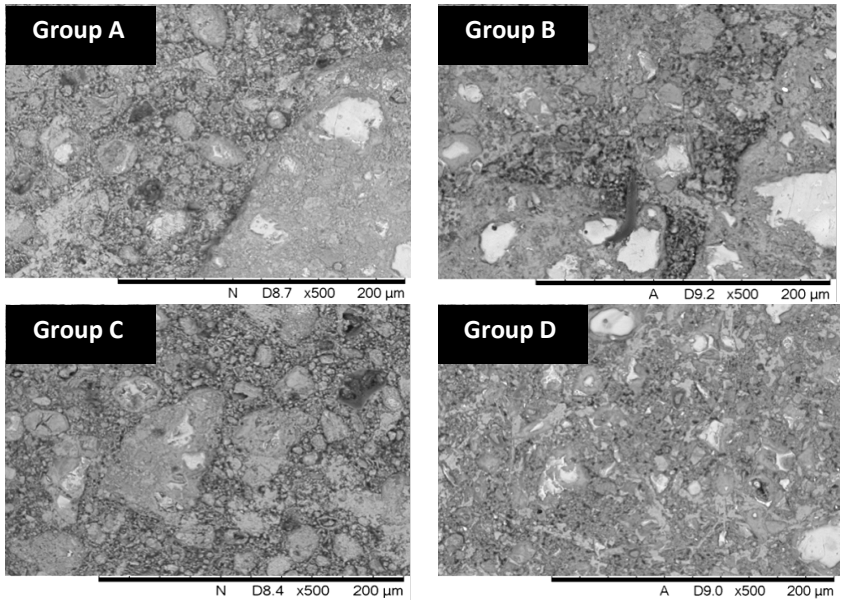

Fig. 3 BSE image of w/s=0.35 series with different size of HCP particles cured for 28 days.

As shown in Fig. 4(a), for the w/s=0.5 series, there is a general trend of increasing porosity with decreasing the HCP particle size from A to D. The w/s=0.35 series did not show clear trends with the HCP particle size. The effect of w/s ratio appears to become more significant when the HCP particle size becomes finer.

(A) (B)

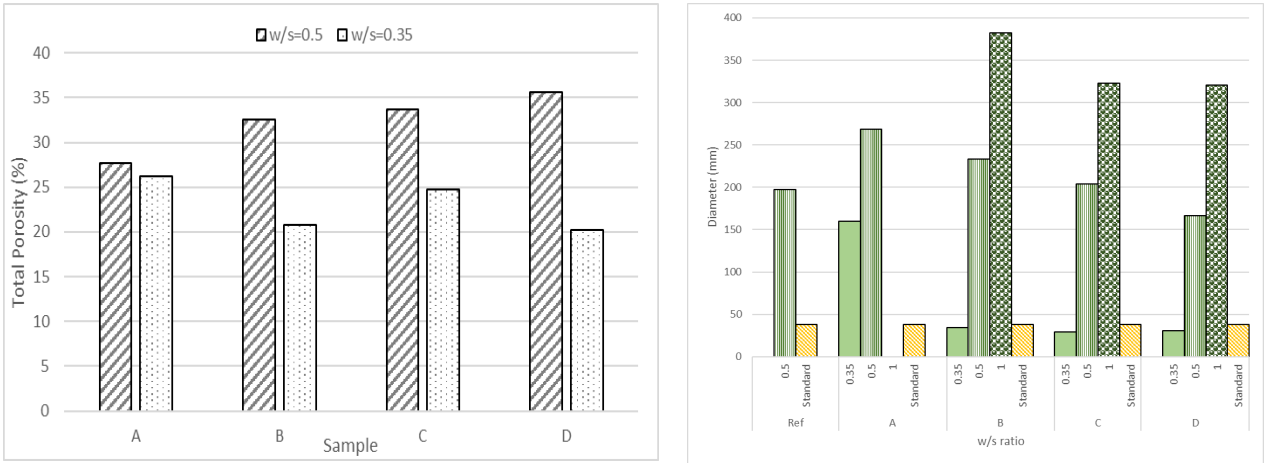

Fig. 4 (a) Total porosity of samples cured for 28 days, (b) slump area of pastes prior to curing. The slump test data for the neat PC paste without HCP inclusion is also shown as Ref. The data for w/s=1 are also included.

3.4 Workability

Figure 4(b) show the results of mini-slump tests. The slump area increases in the samples with larger HCP size range, indicating that the larger HCP particle provides a better workability. With w/s=0.5, the HCP size can be as small as Group C, to achieve the same level of workability to the neat PC. As expected, a lower w/s ratio creates a smaller slump area for ecah blend. For w/s=0.35, workability is very low, but significantly improved with Group A, the largest the HCP particle size range.

4. Conclusions

The blended cement systems, with finer particle size indicated responses towards natural carbonation in the present study. Finer particles exhibit fast reaction kinetics due to their higher surface area. It appears that more Mc were observed in finer particle compared to coarse grain. Microstructure of fine grain appear to be more homogeneous and denser as fine particles will arrange in such a way to fill voids and increase the pore structure; however, fine grains require more water to be more workability. Fluidity and workability of the cement grout is usually crucial and the present study suggests that w/s=0.5 is the optimum value for most of the particle sizes tested.

Acknowledgements

This research utilised the HADES/MIDAS facility at the University of Sheffield established with financial support from MARA.

References

Otsuki, N., Miyazato, S. and Yodsudjai, W. (2003) 'Influence of Recycled Aggregate on Interfacial Transition Zone, Strength, Chloride Penetration and Carbonation of Concrete', *Journal of Materials in Civil Engineering*, 15(5), pp. 443–451. Available at: https://doi.org/10.1061/(ASCE)0899-1561(2003)15:5(443).

Santos, A.R. *et al.* (2020) 'Microstructure as a critical factor of cement mortars' behaviour: The effect of aggregates' properties', *Cement and Concrete Composites*, 111, p. 103628. Available at: https://doi.org/10.1016/j.cemconcomp.2020.103628.

Serpell, R. and Lopez, M. (2013) 'Reactivated cementitious materials from hydrated cement paste wastes', *Cement and Concrete Composites*, 39, pp. 104–114. Available at: https://doi.org/10.1016/j.cemconcomp.2013.03.020.

Sugrañez, R. *et al.* (2013) 'Controlling microstructure in cement based mortars by adjusting the particle size distribution of the raw materials', *Construction and Building Materials*, 41, pp. 139–145. Available at: https://doi.org/10.1016/j.conbuildmat.2012.11.090.

The 16th International Congress on the Chemistry of Cement 2023 (ICCC2023)
"Further Reduction of CO_2 -Emissions and Circularity in the Cement and Concrete Industry"
September 18–22, 2023, Bangkok, Thailand

Investigation of Properties of Recycled Fine Aggregate Carbonated by Different Methods in Air or Water

H. Kadota[1*], Y. Ikeo[2], Y. Takeuchi[3], D. Atarashi[4]

[1] *Takenaka Corporation, Chiba, Japan*

Email: kadota.hiroshi@ takenaka.co.jp
[2] *Takenaka Corporation, Chiba, Japan*

Email: ikeo.yousaku@takenaka.co.jp
[3] *Takenaka Corporation, Chiba, Japan*

Email: takeuchi.yuuto@takenaka.co.jp
[4] *Shimane University, Shimane, Japan*

Email: atarashi@riko.shimane-u.ac.jp

ABSTRACT

In this study, wet (in water) or dry (in air) carbonation treatment of recycled fine aggregate was carried out, and the changes in physical properties of recycled fine aggregate were examined. In addition, physical properties of mortars made with recycled aggregate was investigated. Fine aggregates carbonated in air were found to have increased density and decreased water absorption. However, when the recycled fine aggregate was carbonated in water, it was confirmed that the water absorption increased. This is because the calcium from $Ca(OH)_2$ and C-S-H in the recycled fine aggregate dissolves in water, and the dissolved Ca^{2+} forms on the surface of the recycled fine aggregate as calcite. The Ca^{2+} leached from the surface layer of the cement paste, reducing the density of wet carbonated recycled fine aggregate, and precipitated as calcite on the surface. The increased water absorption could be attributed to reduce the weight of the sample and increased the size of the particles. The compressive strength of the mortar with dry carbonated recycled fine aggregate was higher than that of mortar with untreated one and wet carbonated one. In terms of drying shrinkage, mortar with wet carbonated recycled fine aggregate was larger than that with untreated one and dry carbonated one.

KEYWORDS: *CO_2 adsorption, Recycled fine powder, Low-quality recycled aggregate, Low carbon concrete, Carbonation in air or water*

1. Introduction

The Japanese concrete industry is also required to develop and establish technologies to reduce CO_2 emissions. In addition, it is also important to build a recycling-oriented society, and it is required to develop the technology for effectively utilizing waste discharged from concrete. In the field of concrete recycling in Japan, research and development of recycled aggregates is underway. Recycled aggregates cause recycled fine powder to be produced during manufacture. The generation of recycled fine powder is undesirable because of the limited number of applications for recycled fine powder. As a result, the production of recycled fine aggregate is limited in Japan. In Japan, recycled fine aggregate is classified into different types according to quality, such as water absorption and oven - dry density. Recycled aggregates of lower quality have less recycled fine powder produced during manufacture. The use of low-quality recycled fine aggregate is necessary to build a resource-recycling society.
On the other hand, concrete contains a large amount of the calcium component of cement, and it has been clarified that calcium fixes CO_2. For this reason, research and development aimed at fixing CO_2 in concrete are being actively carried out[1)]. It has been reported that CO_2 fixation by carbonation of recycled aggregate and recycled fines also improves the strength of recycled concrete by densifying the hardened cement through carbonation of calcium hydroxide and C-S-H in the hardened cement[2)]. If CO_2 can be fixed in low-

quality recycled fine aggregate and its quality can be improved, the use of recycled aggregate will be promoted, and CO_2 emissions from the concrete industry can be reduced.
In this study, recycled fine aggregate was carbonized in dry and wet processes to improve the quality of the recycled fine aggregate, and the effects of carbonization on the recycled fine aggregate and on the mortar were investigated.

2. Material

2.1 Formulation and Fabrication

(1) Recycled fine aggregate
Commercially available ordinary Portland cement (OPC,N) was used for concrete. Recycled fine aggregate was produced from two types of concrete (Concrete with target strength of 21 N/mm^2 and 30 N/mm^2; Fc21 and Fc30) with different water-cement ratios by dry crushing. Recycled fine aggregate is denoted as RS (Recycled Sand). Table 1 shows the properties of the concrete and recycled fine aggregate. The higher oven – dry density of Fc21 than Fc30 may be due to more advanced carbonation due to the higher calcium carbonate and silica gel content. Other effects may be due to micro voids where water could not penetrate the cement paste attached to the fine aggregate, but we do not know the details.
(2) Carbonation process
Two types of carbonation methods were performed: dry and wet. For the dry method (RS-d), the recycled fine aggregate was placed in a accelerated carbonation machine at a CO_2 concentration of 10%, a temperature of 293 K (20°C), and a humidity of 60 % (60 %RH) for 7 days.
For the wet method (RS-w), the recycled fine aggregat, 60 kg of recycled fine aggregate was added to 1800 L of water and stirred for 1 hour. CO_2 gas was then supplied at a flow rate of 100 l/min while stirring, and the solution was collected as soon as the pH of the solution reached 6.8.

2.2 Experimental

(1) Recycled fine aggregate
Recycled fine aggregate was subjected to oven - dry density, water absorption, identification of products by X-ray Diffraction (XRD), and surface analysis by Electron Probe Micro Analyzer (EPMA). Oven – dry density and water absorption were averaged in two measurements.
(2) Mortar using recycled fine aggregate
Compressive strength and drying shrinkage were tested in mortar tests. For mortar tests, the water to cement ratio was 50 %, the sand to cement ratio was 1.7, and admixture was used. Sand was RS, RS-d, and RS-w fine aggregate. Compressive strength specimens were demolded at 1 day of age, and standard cured until the test age. Drying shrinkage specimens were demolded at 1 day of age and standard cured until 1 week of age. The base length was measured at 1 week of age, and thereafter, measurements were conducted in a constant-temperature, constant-humidity room at 293 K and a humidity of 60 %. Compressive strength and drying shrinkage were averaged in three measurements.

3. Results

3.1. Recycled fine aggregate

(1) Oven - dry density and water absorption on recycled fine aggregate
Figure 1 shows the oven - dry density and water absorption results from the aggregate tests, with both Fc21 and Fc30 RS-d showing a decrease in water absorption and an increase in oven - dry density compared to

Table 1 Concrete and Recycled fine aggregate properties. (%)

Concrete type	Water/ Cement	Sand/ Aggregate	L.O.I.	insol.	Oven-dry density (g/cm^3)	Water absorption	$CaCO_3$	Silica gel
Fc21	60	47.8	3.69	85.9	2.42	3.44	3.41	0.50
Fc30	49	46.2	4.73	78.6	2.29	5.55	3.35	0.38

*1: Calculated from mass loss from 600 to 950°C using TG-DTA

RS. While RS-w was increased the water absorption and decreased the oven - dry density compared to RS. Previous findings and existing literature have reported that concrete and cement pastes densify and increase in oven - dry density through carbonation[3)], but a different trend was observed in the wet type.

(2) XRD and EPMA on recycled fine aggregate

Figure 2 shows the X-ray diffraction pattern. Portlandite (CH) were observed only in the RS and not in the RS-d and RS-w. Calcite (C) peaks were observed in all samples, with the RS-w having the highest peak. Vaterite (V) peaks were observed in RS-w. No Aragonite (A) was identified in any of the aggregates by XRD.

Figure 3 shows the results of reflection electron images (BSE) and color mapping (Ca) of the EPMA surface analysis. Comparison of the reflection electron images (BSE) shows that the RS and RS-d had a relatively cross-section with few shading differences. The RS-d was brighter, suggesting that carbonation increased its oven - dry density. On the other hand, a 1 μm layer of Calcite was formed on the surface of the RS-w. The Ca^{2+} leached from the surface layer of the cement paste, reducing the density of RS-w. The dissolved Ca^{2+} partly precipitated as Calcite ($CaCO_3$) on the surface and partly in water. The increased water absorption could be attributed to the leaching of calcium, which reduced the weight of the sample, and the precipitation of calcite, which increased the size of the particles. Figure 4 shows an image of wet carbonation.

3.2 Compressive Strength and Drying Shrinkage

(1) Compressive strength

Figure 5 shows the results of compressive strength tests. The compressive strength of the mortar with Fc21 was higher than that with Fc30 at each age. Compared to Fc21, Fc30 has higher compressive strength due to concrete with lower water cement ratio. The mortar's compressive strength was higher due to the lower water absorption of the Fc21 recycled fine aggregate, or due to the lower cement paste attachment, which has a lower strength than the aggregate. The compressive strength of the mortar with Fc21 and Fc 30 both showed higher compressive strength for mortar with RS-d than with RS, and lower compressive strength for mortar with RS-w than for mortar with RS. For both Fc21 and Fc30, RS-d increased in strength due to a decrease in water absorption because of carbonation.RS-w of Fc30 decreased in strength due to increased

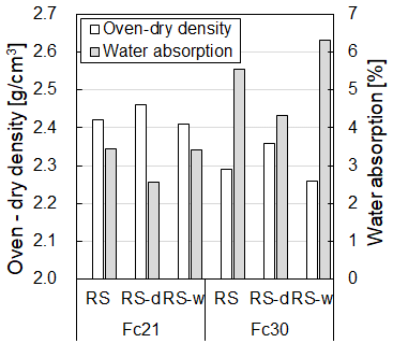

Fig. 1 Oven – dry density, water absorption on Fc21 and Fc30.

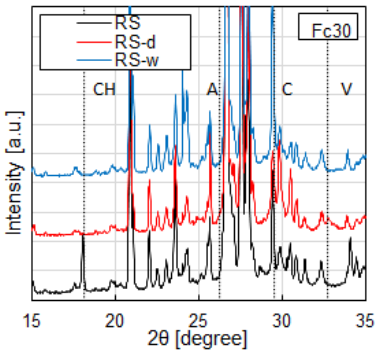

Fig. 2 XRD on Fc30.

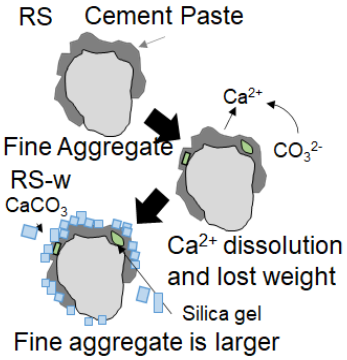

Fig. 4 Image of wet carbonation.

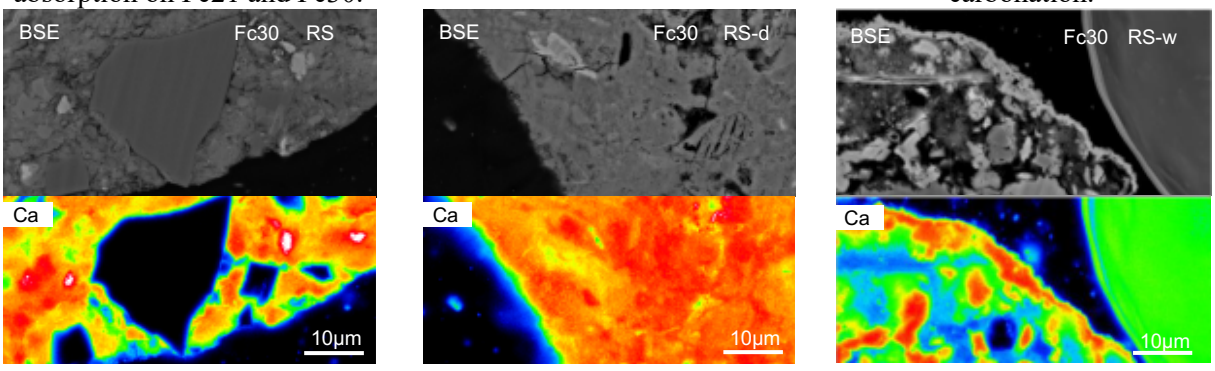

(a) RS (b) RS-d (c) RS-w

Fig. 3 BSE and color mapping (Ca) on Fc30.

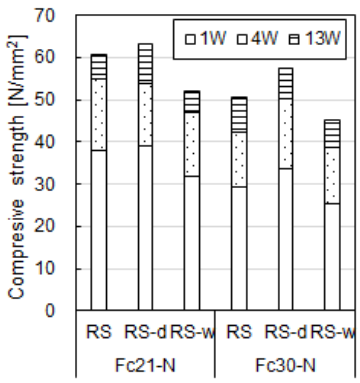

Fig. 5 Compressive strength on mortar.

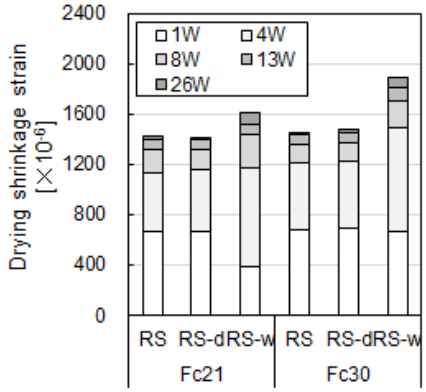

Fig. 6 Drying shrinkage on mortar.

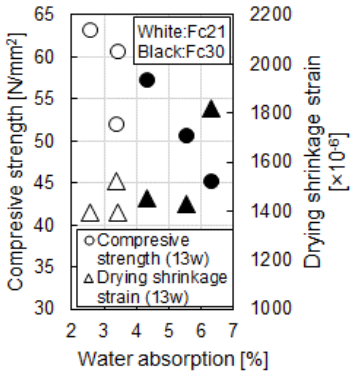

Fig. 7 Relationship between water absorption and compressive strength.

water absorption. However, no relationship between water absorption and compressive strength was observed for RS-w of Fc21.

(2) Drying shrinkage

Figure 6 shows the drying shrinkage. There was no significant difference between RS mortar and RS-d mortar, but a slightly larger shrinkage was observed when RS-w was used. A relationship between drying shrinkage and water absorption was observed in RS-d. However, no relationship between drying shrinkage and water absorption was identified in RS-w.

Figure 7 shows the relationship between water absorption and compressive strength or drying shrinkage of mortar. As mentioned above, no relationship was identified between water absorption and compressive strength and drying shrinkage of RS-w of Fc21, and water absorption and drying shrinkage of RS-w of Fc30. Wet carbonation treatment may have leached Ca^{2+} and made the surface layer of the cement paste weak areas. This altered areas are thought to be responsible for the reduced compressive strength and increased drying shrinkage.

4 Conclusions

The following conclusions were drawn from this study.

I. Dry carbonation treatment showed an increase in the compressive strength of the mortar, but wet carbonation treatment showed a decrease in the compressive strength.
II. The Ca^{2+} leached from the surface layer of the cement paste and areas of low C-S-H Ca/Si were observed. This altered area was responsible for the reduced compressive strength and increased drying shrinkage.

Acknowledgements

This paper is based on results of "Development of Materials, Manufacturing Methods and Quality Control System on Innovative Carbon Negative Concrete", JPNP21014, commissioned by the New Energy and Industrial Technology Development Organization (NEDO).

References

1). Shen, P. et al. (2021) "Synthesis of Amorphous Nano-silica from Recycled Concrete Fines by Two-step Wet Carbonation", *Cement and Concrete Research*, 147 : pp.1-11
2). Klemm, W. A., Berger, R. L. (1972) "Accelerated Curing of Cementitious Systems by Carbon Dioxide: Part I. Portland cement", *Cement and Concrete Research*, 2(5): 567-576
3). N. Matsuda and T. Iyoda, (2019) "Proposal of Low Quality Recycled Aggregate Improved by Carbonation Technology and Influence on the Improved Recycled Aggregate on Concrete", *Concrete Research and Technology*, 30: 66-76

The 16th International Congress on the Chemistry of Cement 2023 (ICCC2023)
"Further Reduction of CO_2 -Emissions and Circularity in the Cement and Concrete Industry"
September 18–22, 2023, Bangkok, Thailand

Develop new concepts of Two Stage Concretes (TSC) achieving carbon neutral society

T. Iyoda[1*], and Y.Kato[2]

[1] *Shibaura Institute of Technology, Tokyo, Japan*
Email: iyoda@shibaura-it.ac.jp
[2] *Tokyo University of Science, Chiba, Japan*
Email: katoyosh@rs.tus.co.jp

ABSTRACT

There are various efforts in the concrete industry to reduce the global environmental impact and achieve a carbon neutral society. It has been reported that demolished concrete blocks from structures have the potential to absorb and fix carbon dioxide. The development of Two-Stage Concrete (TSC) using these demolished concrete blocks as aggregate is expected to contribute to society in the future. Furthermore, it is important to develop a grouting material for TSC that can contribute to reducing the environmental impacts by using ground granulated blast furnace slag, etc. In this study, the influence of aggregate type on TSC will be sorted out, and the possibility of using demolished concrete blocks will be explored. In addition, the development of environmentally friendly grouting materials and their required performance will be organized. The objective is to evaluate how much environmental impact reduction can be achieved by these materials in the future.

KEYWORDS: *Carbon neutral society, Carbonated aggregate, Recycled Aggregate, Two Stage Concrete (TSC)*

1. Introduction

Many initiatives have been initiated to curb carbon emissions and build a recycling-oriented society in order to combat global warming worldwide. In the construction sector, such efforts are accelerating and becoming more active. On the other hand, structures are aging rapidly, structures built during the period of high economic growth in the 1960s are deteriorating rapidly in Japan, and now the time for renewal is approaching. The demolition of concrete structures generates many concrete blocks. So far right now this reuse rate has been over 96% as applied to roadbed materials. However, it has been pointed out that as road construction is scaled down in the future, the number of locations where it is used may decrease, and the reuse rate may decline. On the other hand, it has been pointed out that this concrete can absorb and fix the surrounding carbon dioxide and are expected to contribute to a carbon-neutral society. Then, it is being promoted to recycle these carbon dioxide-absorbing concrete blocks into recycled aggregate and reuse them in concrete.
Two-Stage Concrete (TSC) is also called Pre-Placed Aggregate Concrete and is made by placing the aggregate first and then injecting grout material to integrate it into the concrete. If the aggregate is made of the above carbon dioxide-absorbed concrete blocks and the grouting material is made of a material that emits as little carbon dioxide as possible, we believe we will be closer to realizing a carbon-neutral society. In this study, the effects of aggregate on the strength and mass transport resistance of TSCs were first examined. Then, grouting materials were developed to reduce carbon dioxide emissions.

2. Organize the influence of Coarse aggregate type on TSC

2.1 Outline of Experiment for influence of aggregate on TSC

In order to organize the influence of aggregate type used in TSC, TSC and comparison normal concrete were prepared using various aggregates. Aggregates were normal concrete aggregate (C-40) with a maximum size of 40 mm, roadbed aggregate (RC-40) made from concrete blocks, and waste ballast from railroad track (Ballast). Small coarse aggregates, less than 10 mm, were excluded to allow grout injection. The physical properties of the aggregate used are shown in Table 1 and the particle size distribution is shown in Figure 1. For the grout material, a premix no-shrink mortar with about 40% ground granulated blast furnace slag was used to reduce environmental load. A fine aggregate with a maximum diameter of 2.5 mm was used for filling. On the other hand, the normal concrete used the normal particle size distribution of coarse aggregate and fine aggregate. The sand aggregate ratio (s/a) was set at 0.48 and unit water is 170kg/m^3. The water to powder ratio of normal concrete and TSC was set to 0.45.
For the compressive strength test, three cylindrical specimens of 150 mm × 300 mm dia. were prepared and sealed for 7 days before testing. For the pressurized air permeability test, a 200 mm x 200 mm x 600 mm specimen was prepared and cored. After curing the samples in water for 7 days, the specimens were cut and dried for testing.

Table 1. Physical properties of coarse aggregate

	Surface drying density (g/cm^3)	Specific surface area (cm^2/g)	Grading	Absorption ratio (%)	Solid content (%)
C-40	2.56	3.11	Good	2.2	58.3
RC-40	2.39	2.69	Good	5.0	58.2
Ballast	2.68	1.63	Bad	1.2	58.1

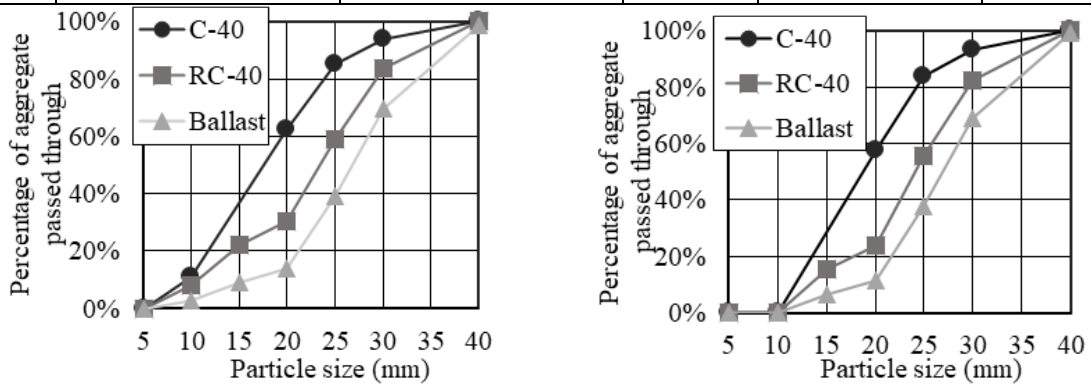

Figure 1 Particle size distribution on aggregate (left: normal concrete, right: TSC (cutting under 10mm)

2.2 Results and Discussions

Figure 2 show the compressive strength results for each aggregate type in normal concrete and TSC. It can be seen that the compressive strength of normal concrete differs depending on the type of aggregate. This is because it is clearly stated that the strength of concrete usually depends on the strength and hardness of aggregate, and it is assumed that the strength of the matrix is high in this W/C. Therefore, it is assumed that the strength of RC-40 is low, and the strength of normal aggregate (C-40) is high. On the other hand, a comparison of the strength of TSC showed that the strength development was almost the same regardless of the aggregate type. This is considered to be because the interfacial transition zone (ITZ) between the aggregate and the matrix is the weak point and determines the strength rather than the strength of the aggregate. Figure 3 shows the results of the air permeability test. There is no significant difference in the air permeability of normal concrete. On the other hand, in TSC, the air permeability is slightly lower for ballast. This is because when considering the gas pathway, it permeates through continuous voids, and similar to the compressive strength results, no difference is recognized in that continuous void in ordinary concrete because it permeates through the mortar matrix. On the other hand, in the case of TSC, the difference may be recognized due to the influence of the aggregate interface, depending on the shape and particle size of the coarse aggregate.

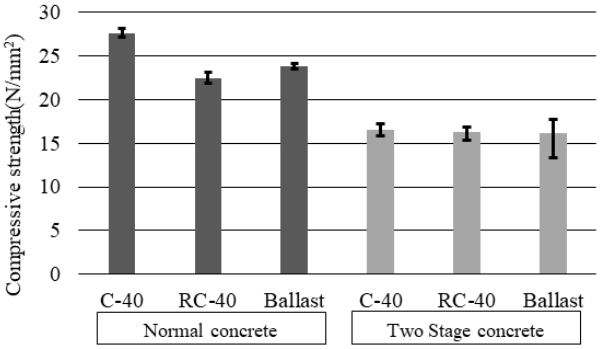

Figure 2 Results of compressive test

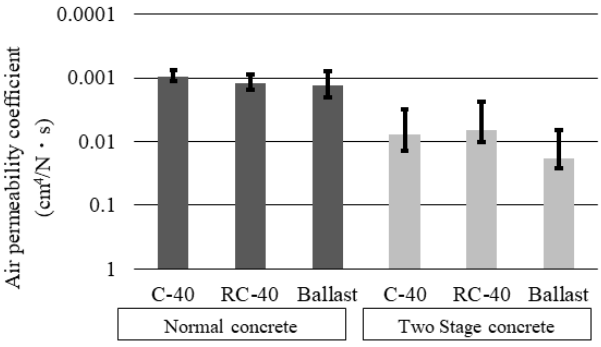

Figure 3 Results of Air permeability test

2.3 Improvement of TSCs physical properties

In order to examine the improvement of strength, addition of expansion materials to the grout material was attempted as filling ITZ. In this experiment, the maximum coarse aggregate dimension was 20 mm and the specimen was 100 x 200 mm. Table 2 shows the various expansion materials in the grout materials. Three types of materials were used: lime, ettringite, and their combinations. Figure 4 shows the relationship between strength and air permeability after the addition of expansion material. It was observed that the addition of lime-based expansive material increased the strength of the concrete, and that compressive strength similar to that of normal concrete could be obtained. This is because that the presence of aggregate contact points and the like in TSC creates an interface between the aggregate and the matrix, which is assumed to be gaps, but the expansion material can densify these gaps.

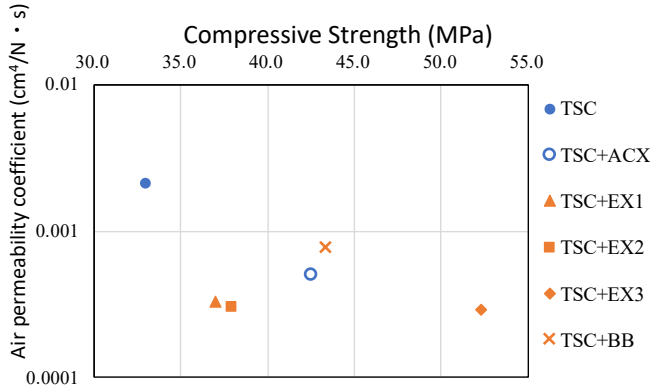

Figure 4 Relationship strength and air permeability using agent for TSC

Table 2 Various expansive material agents

Name	Agents
ACX	Accelerated harden Agent (5% of water mass)
EX1	Ettrigite (20kg/m^3)
EX2	Combination with Ett and Lime (20kg/m^3)
EX3	Lime (20kg/m^3)
BB	Slag cement typeB (20kg/m^3)

3. Development for environmentally friendly grouting materials

3.1 Outline of Experiments of development for grouts

To create environmentally friendly grouting materials, 46 blends of grouting materials were prepared by varying the cement as shown in Table 3. As fresh properties, a mini-slump flow test and a JP funnel test were conducted, as shown in Photo 1. In the slump flow test, the flow value and maximum flow arrival

Table 3 Testing grout materials

Kinds of cement	OPC, BB, BC
Water	Tap, Sludge water
W/C	0.45 – 0.70
S/C	0.2 – 1.0
SP	0 – 2 (C*%)
Powder thicker (ASK)	0 – 1 (C*%)
Expanding material (EX2)	0 – 20 (kg/m3)
Total	46 proportions

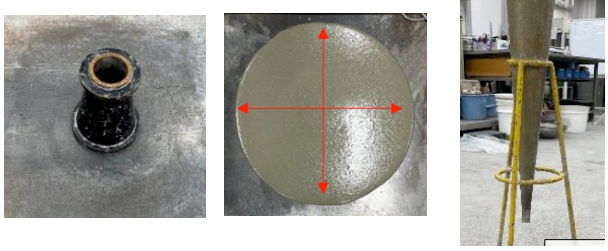

Photo1 Flow test and JP funnel test equipments

time were measured. In the JP funnel test, it was determined if all the material passed through the funnel.

3.2 Results of grout tests

Figure 5 shows the obtained experimental results as slump flow and JP funnel. Here, in the JP funnel test, many of the materials did not permeate or were separated. In the end, 4 blends passed in Table 4. Furthermore, they were confirmed to have a slump flow of more than 400 mm.

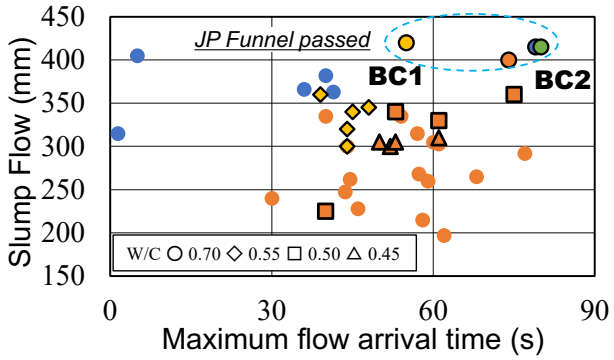

Figure 5 Results of fresh test and pasted grouts

Table 4 Passed grout mix proportions

Name	water	W/C	S/C	GGBS (%)	ASK (C × %)	SP (C × %)	EX2 (kg/m³)
N	Tap	0.55	1.0	0	0.25	1.0	20
BB				50			
BC1				70			
BC2	Sludge						

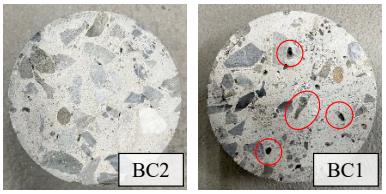

Photo 2 Observation for voids on coring samples

3.3 Testing for TSC samples

TSC was made with 300 mm x 450 mm x 200 mm specimens using the four mix proportions (N,BB,BC1 and BC2). As a result, no significant change in compressive strength was observed in all mix proportions, but a slight difference was observed in the air permeability test. Furthermore, observation of the cross section of the specimens showed that the space around the aggregate remained in BC1, as shown in Photo 2. On the other hand, almost no space was observed in BC2. Therefore, Figure 5 shows that BC1 results in a shorter maximum flow arrival time and lower viscosity than BC2. It is considered that grout with some viscosity is needed to fill the voids in TSC, and it is desirable to have more than 60s of arraival time.

4. Conclusions

In this study, we attempted to develop a new TSC aimed at reducing environmental impact. The following is a summary of the results obtained.

(1) TSC can be produced with various aggregates, and its compressive strength is not so much affected by aggregate type. To improve the strength of TSC, it is effective to fill the space at the aggregate interface by adding appropriate expansive materials.

(2) The development of grouting materials using ground granulated blast furnace slag and supernatant water has shown the possibility of realizing grouting materials with reduced environmental impact.

(3) Fresh performance is essential to meet the filling performance as TSC, and it is necessary to add a certain degree of viscosity in addition to fluidity.

References

Akari Shibuya, Takeshi Iyoda (2019) "A REVIEW OF PREPLACED-AGGREGATE CONCRETE USING RECYCLED AGGREGATE AND RAILWAY WASTED BALLAST", *The 16th East Asia-Pacific Conference on Structural Engineering & Construction (EASEC-16)*

Karen Midori Masunaga, Tomoki Nagoya, Takeshi Iyoda (2022) "Experimental Study to Improve Performance of Two-Stage Concrete without Injection Focusing on the Interfacial Transition Zone", *The 17th East Asia-Pacific Conference on Structural Engineering & Construction*

Esmaeili, M. and Amiri, H. (2022) "Laboratory Investigation into the Flexural Behavior of Embedded Concrete Sleepers in Two-Stage Concrete with Preplaced Ballast Aggregate", *International Journal of Concrete Structures and Materials*.

The 16th International Congress on the Chemistry of Cement 2023 (ICCC2023)
"Further Reduction of CO_2 -Emissions and Circularity in the Cement and Concrete Industry"
September 18–22, 2023, Bangkok, Thailand

The Cement Sector and Life Cycle Assessment: Insights from a Systematic Literature Review

M.C.S. Rihner[1*], J.W. Whittle[2], S.N. Mohamad[1], M.H.A. Gadelhaq[2], B. Walkley[1], and S.C.L. Koh[3]

[1] *Department of Chemical and Biological Engineering, University of Sheffield, United Kingdom*
Emails: mcsrihner1@sheffield.ac.uk; snmohamad1@sheffield.ac.uk; b.walkley@sheffield.ac.uk
[2] *Department of Mechanical Engineering, University of Sheffield, United Kingdom*
Email: jwwhittle1@sheffield.ac.uk , mhagadelhaq1@sheffield.ac.uk
[3] *Management School, University of Sheffield, United Kingdom*
Email: s.c.l.koh@sheffield.ac.uk

ABSTRACT

This paper describes a methodology for conducting a systematic literature review into Life Cycle Assessments (LCAs) which study the global cement industry, one of the largest contributors to CO_2 emissions. The studies collected have been analysed to understand the current implementation of LCA methodology. It has been found that the most common functional unit is mass based despite a significant number of studies performing a comparative LCA. All of the articles analysed selected a strict 'cradle to gate' system boundary due to supply chain complexities. Furthermore, a majority of studies utilised primary data sources but nearly all had to supplement this information with secondary data. The global nature of cement production means that studies were performed across the world with concentrations in China, Spain and Brazil. There are an innumerable number of assessment methodologies available despite the LCA technique being the subject of an ISO standard. A wide range of impact assessment methodologies were used, but the most common were CML, ReCiPe, and IMPACT, with a very few studies choosing to assess endpoint indicators. Due to this, it is often challenging to compare different studies which directly opposes the fundamental principles of LCA. This knowledge will be used to provide a key set of recommendations and guidelines for cement sector LCAs, which may prove useful in developing a consistent, comparable, and transparent approach to their implementation, thereby enhancing the insight gained.

KEYWORDS: *Systematic Literature Review, LCA, Cement Production, Foundation Industries*

1. Introduction

In 2021, the global industrial sector contributed roughly 25% of all CO_2 emissions (IEA, 2023). With countries pledging to reach Net Zero by 2050, decarbonisation of all industrial sectors on a national level has become a priority. In the United Kingdom (UK) six industrial sectors, including cement, were identified as the largest contributors to the country's CO_2 emissions output. The crucial role these energy intensive industries play in the UK's overall economic output has resulted UK Research & Innovation labelling these as key 'foundation industries'. Despite industrial and economic differences between countries, the concept of having an identified group of industries for which innovative and sustainable decarbonisation solutions can be applied is valid. The only standardised method for assessing a wide range of environmental impacts of a product is by conducting a Life Cycle Assessment (LCA) (BSI, 2020a, BSI, 2020b). It can also be described as a decision making tool where environmental changes and improvements can be prioritised to best optimise a system given current financial and technological resources (Jolliet et al., 2015). By assessing peer-reviewed LCA literature, current trends and practices employed for products on a sectoral level can be highlighted. The aim of this paper is to conduct a systematic literature review on journal articles containing cement LCAs to analyse the implementation of the standardised LCA methodology.

2. Methodology

A systematic literature review is a multistage process-based technique that evaluates peer-reviewed journal articles by employing a meticulous group of keywords. The first stage involves planning the review through the creation of a keyword string. The scope considered for this string includes English language peer-reviewed journal articles published between 2003 and 2023, that focus on addressing the environmental effect of cement production by conducting a LCA. The databases selected for this review were SCOPUS, EBSCO and WOS. Numerous strings were trialled and the final keyword string selected was *("Life Cycle Assessment" OR "Life Cycle Analysis" OR "LCA" OR "Life Cycle Impact Assessment") AND ("Portland Cement Production" OR "Portland Cement Manufactur*").*

The second stage assesses the collected papers through a descriptive and bibliometric analysis. A descriptive analysis involves the filtration of papers for further retrieval and study. Bibliometric analysis is a research method that was developed to assess the effectiveness of solitary research, research groups, journals, countries, or institutions (Atanasovska et al., 2022). For this study, VOSviewer was used to visually display and analyse the co-occurrence of author keywords.
The final stage is article evaluation. This study opted to evaluate each article based on the LCA methodology steps as defined in ISO 14040. This includes goal and scope (number of scenarios, functional unit, geographic location, system boundary, and allocation method), inventory analysis (data type and sources), impact assessment (method, indicators, and software type), and interpretation (sensitivity and uncertainty analysis). Data specific to cement LCAs was collected, including cement types (Portland cement [PC], blended cements utilising supplementary cementitious materials [SCMs], alkali-activated cements [AACs]), alternative input fuel types, and compressive strength.

3. Results and Discussion

A total of 128 studies were obtained through the process shown in Figure 1. For the purposes of this initial review, only 50 key studies have been considered.

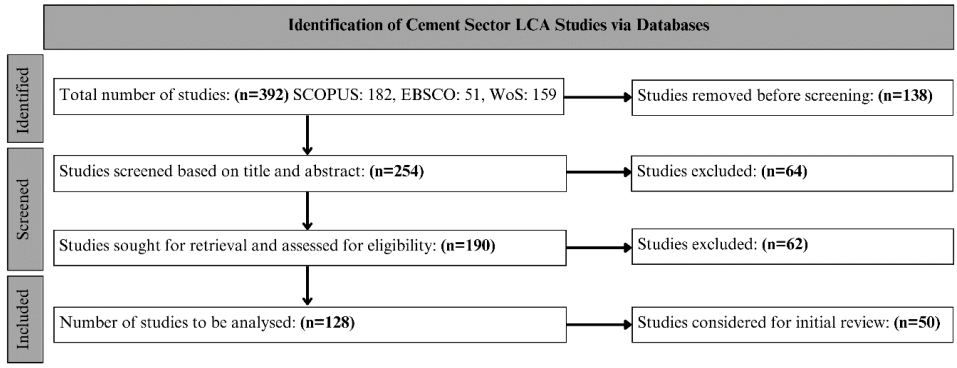

Figure 1: Cement Sector Systematic Literature Review Flow Diagram

In line with the developed systematic literature review process, a bibliometric analysis was performed on the retrieved articles to verify the accuracy of the methodology by identifying the most common keywords and how they relate to each other. The 'Author Keyword Co-occurrence' parameter was set to a minimum of 2 occurrences per keyword. Figure 2 shows the VOSviewer visualisation (Van Eck and Waltman, 2010). The outcome of this study would suggest that the taxonomy has a good alignment to the keywords utilised in the search strategy, including capturing several key terms related to LCA studies (e.g., 'environmental impact' and 'circular economy') and cement production (e.g. 'Portland cement' and 'blast furnace slag').
While 80% of all selected studies included a LCA on PC production, only 24% focused exclusively on PC manufacturing. These studies often evaluated the current "business as usual" PC production processes seen in a specific geographical region (Tun et al., 2021, Stafford et al., 2016). Several PC production studies opted to conduct a comparative LCA to assess the environmental impacts of utilising alternative fuel types (Khan et al., 2021, Holt and Berge, 2018). With the calcination process requiring the largest fuel input, most studies opted to only evaluate the production of clinker by considering 1kg of clinker as a functional unit (Valderrama et al., 2012, Georgiopoulou and Lyberatos, 2018).
The most commonly conducted comparative LCA compared traditional PC production to low carbon cement solutions such as blended cements, AACs, and LC^3. Approximately half of all studies in this initial sampling evaluated the environmental impacts of utilising SCMs such as ground granulated blast furnace slag (GGBFS) and fly ash at various substitution levels in blended PC. AACs were also considered in five of the retrieved studies, with sodium silicate being the most commonly assessed alkali activator. The compressive strength at 28 days was unspecified in roughly half of all studies considered, however when this value was reported, 42.9MPa was typically selected. While the retrieved publications were diverse in the geographical locations considered, cement production in China, Spain and Brazil were found to have the greatest number of evaluations.
In LCA, the functional unit relates all input and outputs through the defined function of the assessed material (BSI, 2020a). The most commonly selected functional unit type in cement LCA studies is a mass based unit. While a simple and straightforward selection, the mechanical performance of the material has not been taken into account. It is critical to assess the material's function when defining a functional unit, especially when performing a comparative LCA in which functional equivalency must be considered

(Panesar et al., 2017). Only eight of the 28 comparative LCA studies evaluating more than one cement type opted to consider strength grade.

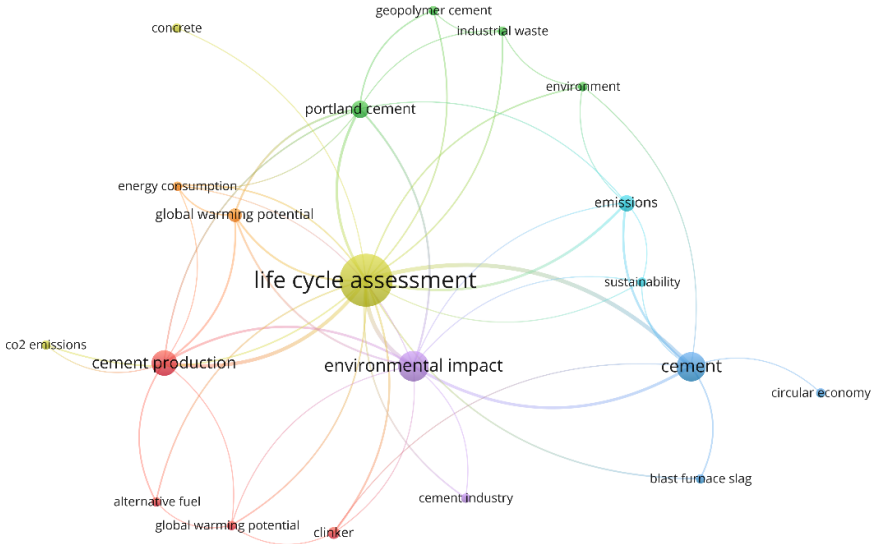

Figure 2: VOS Viewer: Author Keyword Co-occurrence for the Cement Sector. The larger the node, the higher the keyword co-occurrence is for that term. Each colour represents a cluster of related terms.

The system boundary in an LCA defines which aspects of a product's life cycle will be included and excluded in the analysis. In all selected papers, a 'cradle to gate' system boundary (raw material supply, transport, and manufacturing) was selected as these stages account for the greatest environmental impact in cement production (Colangelo et al., 2018). 'Cradle to grave' or 'cradle to cradle' are typically not considered due to the complexity of determining the use and end of life stages. However, a significant portion of the environmental impacts are not properly evaluated. This also includes benefits such as carbon uptake that occurs in concrete structures during the use and end of life stages.

In relation to allocation, most articles did not specify which procedure was implemented. It can be assumed however, that most utilised the cut off method. For blended cement LCAs that analyse the impacts of SCMs, careful consideration must be made for the allocation of these materials. This is particularly true for blended cements that utilise GGBFS, an iron industry waste product. In 2008, the European Union Directive reclassified the material as a by-product due to its increased demand in other sectors (EU, 2008). Since the material is no longer considered a waste product, the environmental impacts associated with the material's production must be considered when conducting an LCA. Of the 16 studies that analysed GGBFS as an SCM, only four considered either economic or mass allocation procedures, with the remaining opting for the cut off or avoided burden method.

Three of the retrieved papers relied solely on primary data. 60% of studies evaluated utilised primary data in addition to secondary data for either foreground or background processes. Despite the reliance on secondary data, only two studies performed a quantitative data quality assessment (Feiz et al., 2015, Vázquez-Rowe et al., 2019). Although this type of data quality assessment is not specified in the ISO standards, data quality requirements such as temporal, spatial, and technological coverage must be considered. The three most commonly utilised impact assessment methods are CML, ReCiPE, and IMPACT. While this is the case, many studies opted to only evaluate a select few midpoint environmental indicators, with only 16% of studies assessing endpoint environmental indicators. The reporting of impact assessment data varied widely which resulted in difficultly comparing values across publications. At the interpretation stage, it was found that less than 10% of all retrieved publications conducted an uncertainty analysis, whilst 56% of publications conducted a sensitivity analysis. Both are required practices in the ISO standards to ensure accurate and robust results.

3. Conclusions

A systematic literature review was conducted on existing cement sector LCA journal articles to evaluate how the current standardised methodology is applied. A string was created to retrieve the most relevant publications. After evaluating each paper retrieved based on a set of defined criteria, the final taxonomy yielded 128 studies with 50 key studies being considered for this initial review. VOSviewer was utilised to verify that the string used was accurate based on the co-occurrence of author keywords. Despite most papers

following the ISO 14040/44 LCA guidelines, there were several notable gaps in current cement production LCA implementation. The most commonly selected functional unit was mass based which fails to consider functional equivalence required in comparative cement LCAs. All studies opted for a 'cradle to gate' system boundary. Most studies that analysed SCMs in blended cements did not consider an allocation procedure which resulted in the impacts associated with the production of by-products such as GGBFS to not be properly accounted for. The impact assessment method selected varied between publications, however endpoint environmental indicators were often not evaluated. It was also found that nearly all publications did not include an uncertainty analysis with even fewer performing a quantitative data quality assessment. A sensitivity analysis was also found to be only be performed in roughly half of all retrieved publications. The results from this work will be used to develop a robust, consistent, and transparent framework for conducting LCAs related to both the global cement sector and other key industrial sectors.

Acknowledgements

M. S. C. Rihner, M. H. A. Gadelbaq and B. Walkley would like to thank the Energy Institute at The University of Sheffield for a DTP PhD Scholarship, and the Grantham Centre for Sustainable Futures. J. W. Whittle would like to thank EPSRC through the Advanced Metallic Systems Centre for Doctoral Training (EP/S022635/1). S. N. Mohamad would like to thank Majlis Amanah Rakyat Malaysia and GCSF.

References

ATANASOVSKA, I., CHOUDHARY, S., KOH, L., KETIKIDIS, P. H. & SOLOMON, A. 2022. Research gaps and future directions on social value stemming from circular economy practices in agri-food industrial parks: Insights from a systematic literature review. *Journal of Cleaner Production,* 354**,** 131753.

BSI 2020a. BS EN ISO 14040:2006+A1:2020 Environmental management- Life cycle assessment- Principles and framework.

BSI 2020b. BS EN ISO 14044:2006+A2:2020 Environmental management-Life cycle assessment- Requirements and guidelines. British Standards Online.

COLANGELO, F., FORCINA, A., FARINA, I. & PETRILLO, A. 2018. Life Cycle Assessment (LCA) of Different Kinds of Concrete Containing Waste for Sustainable Construction. *Buildings,* 8**,** 70.

EU 2008. European Union Directive 2008/98/EC of the European parliament and of the council on waste and repealing certain directives. European Union.

FEIZ, R., AMMENBERG, J., BAAS, L., EKLUND, M., HELGSTRAND, A. & MARSHALL, R. 2015. Improving the CO2 performance of cement, part I: utilizing life-cycle assessment and key performance indicators to assess development within the cement industry. *Journal of Cleaner Production,* 98**,** 272-281.

GEORGIOPOULOU, M. & LYBERATOS, G. 2018. Life cycle assessment of the use of alternative fuels in cement kilns: A case study. *Journal of Environmental Management,* 216**,** 224-234.

HOLT, S. P. & BERGE, N. D. 2018. Life-cycle assessment of using liquid hazardous waste as an alternative energy source during Portland cement manufacturing: A United States case study. *Journal of Cleaner Production,* 195**,** 1057-1068.

IEA. 2023. *Industry: Sectorial Overview* [Online]. Available: https://www.iea.org/reports/industry [Accessed].

JOLLIET, O., SAADE-SBEIH, M., SHAKED, S., JOLLIET, A. & CRETTAZ, P. 2015. Environmental Life Cycle Assessment.

KHAN, M. M. H., HAVUKAINEN, J. & HORTTANAINEN, M. 2021. Impact of utilizing solid recovered fuel on the global warming potential of cement production and waste management system: A life cycle assessment approach. *Waste Management & Research: The Journal for a Sustainable Circular Economy,* 39**,** 561-572.

PANESAR, D. K., SETO, K. E. & CHURCHILL, C. J. 2017. Impact of the selection of functional unit on the life cycle assessment of green concrete. *The International Journal of Life Cycle Assessment,* 22**,** 1969-1986.

STAFFORD, F. N., RAUPP-PEREIRA, F., LABRINCHA, J. A. & HOTZA, D. 2016. Life cycle assessment of the production of cement: A Brazilian case study. *Journal of Cleaner Production,* 137**,** 1293-1299.

TUN, T. Z., BONNET, S. & GHEEWALA, S. H. 2021. Emission reduction pathways for a sustainable cement industry in Myanmar. *Sustainable Production and Consumption,* 27**,** 449-461.

VALDERRAMA, C., GRANADOS, R., CORTINA, J. L., GASOL, C. M., GUILLEM, M. & JOSA, A. 2012. Implementation of best available techniques in cement manufacturing: a life-cycle assessment study. *Journal of Cleaner Production,* 25**,** 60-67.

VAN ECK, N. J. & WALTMAN, L. 2010. Software survey: VOSviewer, a computer program for bibliometric mapping. *Scientometrics,* 84**,** 523-538.

VÁZQUEZ-ROWE, I., ZIEGLER-RODRIGUEZ, K., LASO, J., QUISPE, I., ALDACO, R. & KAHHAT, R. 2019. Production of cement in Peru: Understanding carbon-related environmental impacts and their policy implications. *Resources, Conservation and Recycling,* 142**,** 283-292.

The 16th International Congress on the Chemistry of Cement 2023 (ICCC2023)
"Further Reduction of CO_2 -Emissions and Circularity in the Cement and Concrete Industry"
September 18–22, 2023, Bangkok, Thailand

Estimating carbon uptake at building level: insights from a bottom-up approach

Hessam AzariJafari[1*], Ipek Bensu Manav[2], Motahareh Rahimi[3], Elizabeth Moore[4], Bruno Huet[5] Christophe Levy[6], Chetan Hazaree[7] and Randolph Kirchain[8]

[1]*MIT, Cambridge, USA, Email: hessam@mit.com*

[2] *MIT, Cambridge, USA, Email: bensu@mit.com*

[3] *MIT, Cambridge, USA, Email: m.rahimi259@gmail.com*

[4] *MIT, USA, Email: eamoore@mit.com*

[5] *Holcim Innovation Center, Saint Quentin Fallavier, FRANCE, Email: bruno.m.huet@holcim.com*

[6] *Holcim Innovation Center, Saint Quentin Fallavier, FRANCE, Email: christophe.levy@holcim.com*

[7] *Holcim Innovation Center, Saint Quentin Fallavier, FRANCE, Email: chetan.hazaree@holcim.com*

[8] *MIT, Cambridge, USA, Email: kirchain@mit.com*

ABSTRACT

As the extent of carbon uptake varies dramatically from one cement-based product to another, it is essential to employ an approach that captures the context in the estimation of building carbon uptake. In this study, we propose a bottom-up framework for modeling the lifetime carbon uptake of concrete and mortar applications at the building level. The framework incorporates two major steps: 1) estimation of carbon uptake for each individual element of a building and 2) creation of archetypes to represent local practices of construction. The results of this study show that the total amount of uptake can vary significantly. The building use and end-of-life uptake can neutralize 21 – 46% of the cement calcination emissions. While underground and covered elements, such as footings and foundations, possess the lowest carbon uptake quantity, mortar applications such as masonry units and plastering can be fully carbonated within a decade of the building's lifetime. Therefore, in building archetypes with significant mortar use, such as those prevalent in Mexico, carbon uptake per unit of cement consumption is larger compared to the uptake in typical US single-family buildings. The carbon uptake range in different building types implies the importance of considering a bottom-up approach. Also, the results of our bottom-up approach provide new insights for understanding the importance of CO_2 uptake in the life cycle emissions of concrete buildings and in achieving carbon neutrality.

KEYWORDS: *Carbon uptake, Carbon neutrality, Bottom-up estimation, Commercial, Residential.*

1. Introduction

To achieve carbon neutrality, it is essential to reduce and neutralize greenhouse gas (GHG) emissions associated with the concrete life cycle. With concrete, the neutralization can occur through natural carbon uptake. Carbon uptake is a chemo-physical process that results in the permanent sequestration of CO_2 in cementitious matrices. Primarily motivated by its impact on rebar corrosion, carbon uptake has been studied for a long time by developing different experimental and analytical works. From the experimental perspective, it was observed that the rate and maximum quantity of CO_2 uptake for cement-based products (CBPs) such as mortar, blocks, and structural concrete, are influenced by regional factors such as cement type and content, use of supplementary cementitious materials, concrete porosity (water-to-binder ratio), compressive strength, temperature, relative humidity, exposure conditions, as well as the geometry of

structures and their individual elements. Based on these research observations, several semi-empirical models validated against experimental evidence were developed and used for estimating the amount of carbon uptake in design codes and guidelines (BSI 2017).
Recent momentum around the incorporation of life cycle thinking in the environmental impact assessment provided an opportunity to implement different carbon uptake empirical models. While these models can provide an acceptable amount of carbon uptake per surface area unit of CBPs, accounting for the type and surface areas (and corresponding exposure conditions) of CBPs in a given building needs further elaboration. Estimating carbon uptake in buildings is complicated since CBPs comprise elements with different shapes, thicknesses, and mechanical properties. One study (Sacchi et al. 2020) reported that the uptake fraction across elements (as a percentage of process emissions) can vary from 4 – 67% depending on the surface-to-volume ratio and mix design of the studied elements. This wide range implies the importance of variation accounting when calculating the carbon uptake of CBPs.
In this study, we propose a bottom-up approach to have a context-sensitive estimation of the carbon uptake in different CBPs used buildings. The approach was applied to two case studies of residential and commercial buildings in the US and Mexico. The proposed approach allows for accounting for type, concrete composition, exposure condition, mechanical properties (a proxy for the porosity of matrix), and geometry of building elements. The results of this study can provide a deeper understanding of carbon uptake strategies in different regions and assist concrete value chain stakeholders in making informed decisions about the potential neutralization capacity of CBPs in buildings.

2. Methodology

The modeling framework applied in this paper aims to provide a context-sensitive approach to estimate the amount of CO_2 sequestered into CBPs during product use and end-of-life. The use-phase uptake, $U_a^u(t)$, for a given archetype a in a given year of its service life, t (referred to as life-year), is estimated from the sum of the uptake of individual surfaces that form individual elements in that archetype. Formally, this is expressed as:

$$U_a^U(t) = \sum_{l \in L} \sum_{j \in J} U_{j,l,a}^U(t) = \sum_{l \in L} \sum_{j \in J} \left[\overleftarrow{U}_{j,l,a}^U(t) \cdot A_{j,l,a} \right] \quad (1)$$

where $\overleftarrow{U}_{j,l,a}^U(t)$ is the uptake per unit area of surface j on element l present within a in life-year t and $A_{j,l,a}$ is the surface area of the same.

Following the models described in (Andersson et al. 2019, Cao et al. 2020, Sacchi et al. 2020), $\overleftarrow{U}_{j,l,a}^U(t)$ is modeled as:

$$\overleftarrow{U}_j(t) = K_j \cdot \sqrt{t} \cdot \frac{M_{CO_2}}{M_{CaO}} \sum_{i \in I} \left(CaO_{i,j} \cdot B_{i,j} \right) \cdot DOC_j \quad (2)$$

where K ($mm/yr^{1/2}$) is the carbonation coefficient for surface j, $CaO_{i,j}\left(kg\,CaO/kg\,i\right)$ is the calcium-oxide content of binder component i (e.g., cement, fly ash, and slag) in j, and $B_{i,j}\left(kg\,i/m_j^3\right)$ is binder content for i in j, M_{CO_2}/M_{CaO} is the molar ratio of CO_2 to CaO, which converts CaO mass to the maximum theoretical uptake of CO_2, and finally, DOC_j is the degree of carbonation, a unitless fraction that represents the practical observed maximum uptake fraction. DOC is influenced by the exposure condition of a surface j.
The input data for carbonation rate and degree of carbonation were adopted from the EN 16757 standard (BSI 2017). For the end-of-life uptake modeling, the MIT CSHub tool was used and a 6-month stockpiling period was assumed (AzariJafari et al. 2021). The mix designs for the US case studies were extracted from

the national ready mix concrete association industry-average EPDs (NRMCA 2019) while for the Mexican concrete mixtures, the binder composition was extracted from the Global Cement and Concrete Association Statistics (GCCA 2020). Typical Mexican single-family and commercial prototypes in the country and contemporary styles were used to estimate the geometry and estimate the amount of carbon uptake (Ceballos Ruiz AM 2018). The binder content and the incorporation of slag and fly ash vary from one concrete compressive strength to another according to the NRMCA data. However, the amount of portland cement was fixed at 198 kg/m^3 for masonry block.

Table 1. Surface areas and corresponding exposure conditions for the building cases studies in the US and Mexico (Exposure conditions: A = indoor with cover, B = in-ground, C = sheltered from rain)

Country	USA				Mexico			
Building type	Single Family (232 m^2)		Commercial (3 stories – 1200 m^2)		Single Family (70 m^2)		Commercial (3 stories - 1200 m^2)	
Element name	Surface area (m^2)	Exposure condition	Surface area (m^2)	Exposure condition	Surface area (m^2)	Exposure condition	Surface area (m^2)	Exposure condition
Slab	232.3	A, B	2400.0	A	85.3	A, B	2400.0	A
Footing/Foundation	52.4	B	507.1	B	20.6	B	507.1	B
Frame (columns and beams)	-	-	342.7	A, C	21.3	A, C	342.7	A, C
Basement Wall*	206.3	A, B	912.0	A, B	-	-	912.0	A, B
Partitions (CMU/Mortar layers)	-	-	-	-	112.7	A, C	4128.0	A, C
Compressive strength (MPa)	15 – 20 MPa		25 – 35 MPa		CMUs = < 15 MPa, Rest: 15 – 20 MPa		Columns: 25-35 MPa, CMUs:<15 MPa, Rest: 15 – 20 MPa,	

*Commercial buildings' basement walls were assumed to be cast-in-place concrete, whereas the basement walls of US single-family residences were assumed to be made from CMU blocks.

3. Results and Discussion

Figure 1 shows the carbon uptake results for the four described buildings in the US and Mexico. When analyzing the fraction of calcination emission sequestered by carbon uptake, it is important to have a precise estimation of masonry and mortar applications and their geometry in buildings. For example, there is a significant difference between the calcination fraction sequestered by commercial buildings in the US and Mexico due to the extensive use of mortars in the Mexican cases. The use of CMU blocks as interior and exterior walls in the Mexican buildings majorly causes a carbon uptake equivalent to 33 – 46% calcination emission during the 60-year analysis period. According to this analysis (Figure 1.b and d), the CMU blocks are carbonated in less than a decade due to their porous nature and thin layers of mortars. In the US cases (Figure 1.a and c), although the masonry units were used for basement walls, the total amount of uptake was less significant as one side of the walls are in contact with the ground (and therefore insignificant carbon uptake happened).

The minimum amount of carbon sequestration percentage (15% of the calcination emissions) was observed in the US commercial archetype as generally, there are no mortar products used in these types of buildings. However, in the US residential building with basement walls made from masonry units (Figure 1.a), the amount of uptake from the basement walls is an order of magnitude larger than that happened in the other structural elements (frame and footing/foundation). Slabs in the single-family archetypes are thinner (10 cm in the single-family as opposed to 15 – 20 cm in commercial), which causes a more significant amount of carbon uptake in the single-family homes compared to the commercial buildings. The other influential factor is the compressive strength of slabs in the single-family buildings (15 – 20 MPa) which allows for a faster carbonation rate compared to the slabs in the commercial buildings.

The amount of end-of-life carbon uptake in the buildings depends on the quantity of structural concretes used in buildings as the majority of concrete blocks and mortars were already carbonated during the use phase. Comparing the commercial building in the US and Mexico (Figure 1.c and d), the end-of-life uptake in the US case is slightly higher as a proportion of basement walls remains uncarbonated after 60 years and will be carbonated at the end of life.

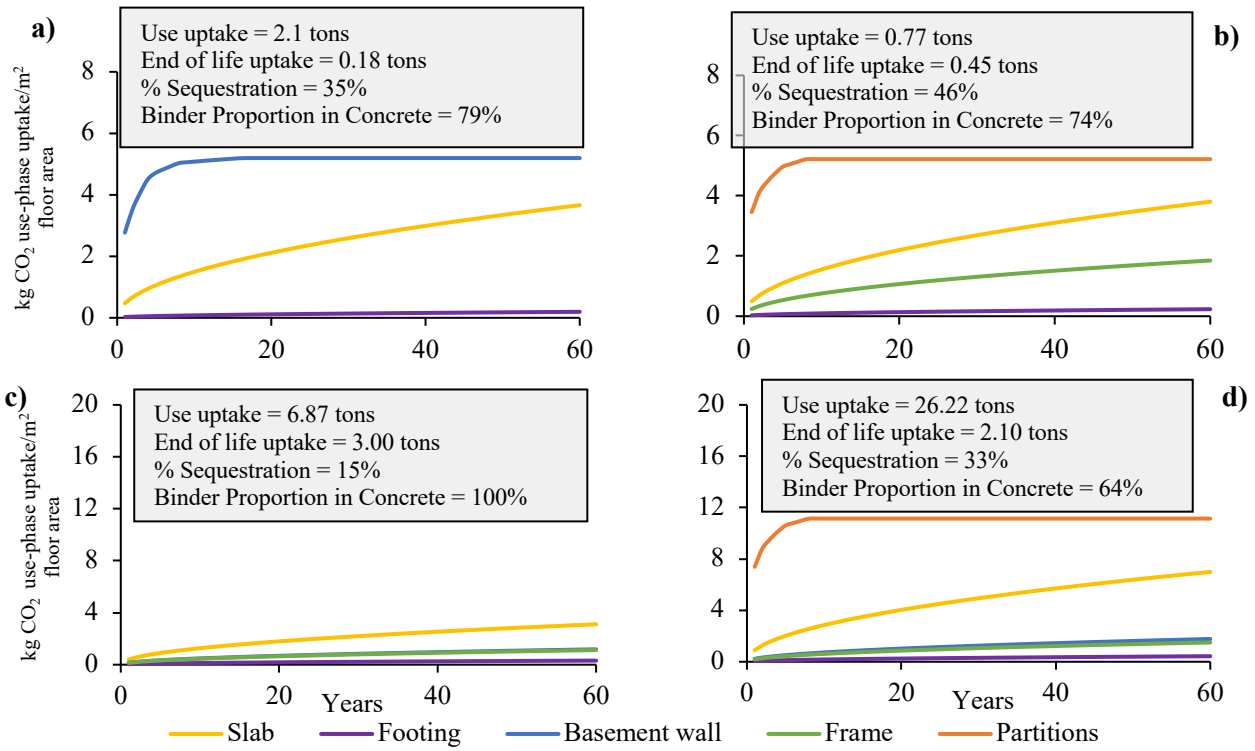

Figure 1. Total in-use and end-of-life phase carbon uptake, the sequestered fraction of calcination emission, and annual in-use (curves) carbon uptake of cement-based products per unit of the floor area of a) US single family, b) Mexican single family, c) US commercial and d) Mexican commercial buildings (Partitions = Concrete masonry unit walls, Frame = columns and beams) The proportion of binder materials used in concrete is shown as percentage.

4. Conclusions

This study evaluates the impact of building types and local construction on the amount of carbon uptake in buildings using a bottom-up approach. The carbon uptake was calculated at the element level for all the CBPs and then scales for a given building given the surface area and volume of CBPs used in buildings. The results show that 15 – 35% and 33 – 46% of the calcination emission of cement production can be sequestered in the US and Mexican commercial and residential buildings, respectively. The upper bound range belongs to the building cases that use CMUs as the inner and outer walls. CMUs are fully carbonated during the first decade of building lifetime. The results variations emphasized the importance of considering details accounting in carbon uptake estimation. The results of this study and the developed approach can be implemented to estimate the carbon uptake of CBPs in the regional scales to have an accurate estimation of the carbon uptake role in the carbon neutrality of nations.

References

Andersson, R., H. Stripple, T. Gustafsson and C. Ljungkrantz (2019). "Carbonation as a method to improve climate performance for cement based material." Cem. Concr. Res. **124**: 105819.https://doi.org/10.1016/j.cemconres.2019.105819

AzariJafari, H., F. Guo, J. Gregory and R. Kirchain (2021). "Carbon uptake of concrete in the US pavement network." Resour. Conserv. Recycl. **167**: 105397.https://doi.org/10.1016/j.resconrec.2021.105397

BSI (2017). BS EN 16757: Sustainability of construction works. Environmental product declarations. Product Category Rules for concrete and concrete elements. London UK, British Standards Institution.

Cao, Z., R. J. Myers, R. C. Lupton, H. Duan, R. Sacchi, N. Zhou, T. Reed Miller, J. M. Cullen, Q. Ge and G. Liu (2020). "The sponge effect and carbon emission mitigation potentials of the global cement cycle." Nature Communications **11**(1): 3777.10.1038/s41467-020-17583-w

Ceballos Ruiz AM. (2018). "30 Planos de casas prototipo: autoconstruya como arquitecto." Retrieved 12/21/2022, from https://www.librosarq.com/manual/30-planos-de-casas-prototipo-autoconstruya-como-arquitecto/#.Y6INBJ7MJD9.

GCCA. (2020). "Global Cement and Concrete Association. GNR 2.0 - GCCA in Numbers " Retrieved 12/21/2022, from https://www.bccresearch.com/market-research/advanced-materials/global-cement-market.html.

NRMCA (2019). Industry-Wide Environmental Product Declarations (EPDs) program. Silver Spring, MD, National Ready Mix Concrete Association.https://www.nrmca.org/wp-content/uploads/2020/02/EPD10080.pdf.

Sacchi, R. and C. Bauer (2020). "Should we neglect cement carbonation in life cycle inventory databases?" Int J Life Cycle Assess.10.1007/s11367-020-01776-y

The 16th International Congress on the Chemistry of Cement 2023 (ICCC2023)
"Further Reduction of CO_2 -Emissions and Circularity in the Cement and Concrete Industry"
September 18–22, 2023, Bangkok, Thailand

Calcium sulfoaluminate clinker production from sulfidic mine tailings

N. Pires-Martins[1,2*], R. Snellings[2,3,4], G. Habert[1]

Email: natalia.piresmartins@vito.be; ruben.snellings@kuleuven.be; habert@ibi.baug.ethz.ch
[1] *Institute of Construction and Infrastructure Management, Swiss Federal Institute of Technology (ETH Zurich), Zurich, Switzerland*
[2] *Sustainable Materials Management, Flemish Institute for Technological Research (VITO), Mol, Belgium*
[3] *Department of Earth and Environmental Sciences, KULeuven, Leuven, Belgium*
[4] *Department of Materials Engineering, KULeuven, Leuven, Belgium*

ABSTRACT

Mine tailings are the fine-grained mineral waste stream of mine processing plants. The management of such materials is a great challenge for the mining industry particularly given their massive annual production - estimated at 5–7 billion tonnes worldwide – and their potentially hazardous character. Parallel to that, tailings also constitute an abundant secondary resource for metals that are in high demand to support the transition from a fossil fuel-based to a renewable energy matrix. The re-mining of valuable metals from mine tailings in turn leaves behind a mineral fraction that could be used in the production of cement-based materials. In this study, highly sulfidic mine tailings containing pyrite (FeS_2) as a major mineral constituent are studied as an alternative raw material to produce calcium sulfoaluminate (CSA) clinkers in the laboratory. The chemical and mineral phase composition of the produced clinkers are characterized by XRD, XRF, and SEM-EDS. To better understand the hydration behavior of the phases formed during clinkering, the hydration kinetics and evolution of hydrate assemblages are characterized in clinker pastes by isothermal calorimetry, XRD, and TGA. Finally, the metal(loid) immobilization potential after clinkering and hydration is discussed based on the results of batch leaching tests performed on clinkers and hydrated clinker pastes.

KEYWORDS: *CSA clinkers, sulfidic mine tailings, waste valorization, mineralogy, hydration.*

1. Introduction

The development of alternative cements and binders is one of the approaches used to reduce CO_2 emissions in the production of the binder phase in Portland cement (PC) concrete. Among them, ye'elimite-rich cements are considered an attractive type of lower-CO_2 cements based on non-Portland clinker due to their lower limestone requirement and lower production temperatures - of about 1250°C, using a conventional cement kiln system (Shi, Qu and Provis, 2019). Ye'elimite, $C_4A_3\overline{S}$, is a hydraulic mineral phase that forms in major amounts in the production of this cement type. Under the name calcium sulfoaluminate cement (CSA), this cement type has been commercialized, primarily in China, since the 1970s (Zhang, Su and Wang, 1999), and, more recently, its mineralogy has been adapted to incorporate higher contents of PC clinker phases such as belite, C_2S, and ferrite, $C_4A_nF_{1-n}$, as in belite-ye'elimite-ferrite (BYF) clinkers.

The conventional raw materials for ye'elimite-rich clinkers such as CSA are bauxite or high-alumina clay, gypsum, and limestone. Relative to PC, ye'elimite-rich clinkers require moderate levels of SO_3 – sourced from gypsum – and tolerate higher levels of Fe_2O_3 in the raw materials. This shift in binder chemistry can be an opportunity for the utilization of iron and surfur-rich mineral residues that would not be suitable for PC clinker production. CSA cements are also known for their ability to immobilize heavy metals in their hydrated matrix (Peysson, Pera and Chabannet, 2005), which is attributed mainly to the formation of

ettringite as a main hydrated phase. This property is of interest for the valorization of potentially hazardous residues such as mine tailings.

Sulfidic mine tailings are high-volume waste streams from metal mining. They typically contain sulfidic minerals that oxidize when in contact with air, generating acid and leaching heavy metals into the environment. To prevent sulfide oxidation and the environmental impacts related to it, sulfidic tailings are commonly stored as a slurry in tailings storage facilities (Lottermoser, 2013). If remined, those materials could be re-sourced for their valuable metals and valorization routes would be necessary for the remaining mineral fraction. In the present article, sulfidic tailings are used as raw material for CSA clinker production. The clinkers are characterized and their hydration is investigated. Last, the environmental compatibility is assessed on clinkers and hydrated pastes by means of leaching tests.

2. Materials

The sulfidic tailings used in this study come from an operational Cu-Zn mine. They were received as a slurry and underwent drying (at 40 ºC) and homogenization prior to use. Their properties are shown in Table 1. The XRD pattern of the tailings is shown in Figure 1 (a). The other materials used in clinker making were reagent grade $CaCO_3$ (VWR), Al_2O_3 (Alteo), and $CaSO_4.2H_2O$ (VWR).

Table 1. Properties of sulfidic tailings.

Chemical composition (%)										
Na	Mg	Al	Si	S	K	Ca	Ti	Mn	Fe	Others
3.1	1.1	6.2	15.1	18.2	0.5	0.8	0.1	0.1	22.8	1.7
Mineral phase composition (%)										
Quartz	Pyrite	Siderite	Gypsum	Muscovite	Chlorite	Chalcopyrite		Dolomite	Biotite	
24.9	46.4	2.5	1.9	4.7	13.7	0.5		1.9	3.5	
SSA (m^2/g)		Density (g/cm^3)			d_{10} (µm)	d_{50} (µm)	d_{90} (µm)			
0.95		3.6			3.2	8.3	53.5			

3. Methods

The sulfidic tailings were incorporated in the raw meal for CSA clinker production. The raw meal consisted of 13.7 wt.% sulfidic tailings, 13.7 wt.% gypsum, 35.9 wt.% calcite, and 36.6 wt.% alumina. The powders were blended for 24 hours in a rolling bench and pelletized. The clinker was produced using Al_2O_3 crucibles in a LHT 16/R Nabertherm furnace at 1250 °C, with a retention time of 3 hours and heating/cooling rate of 180 °C/h. The clinker was characterized by X-ray diffraction (XRD) and scanning electron microscopy/energy dispersive X-ray spectroscopy (SEM-EDS). The SEM used was a JEOL JSM 6400 using (at 25 kV) equipped with a Ametek-EDAX EDX detector. EDS spectra was analyzed using EDAX TEAM™ EDS software package. The hydration kinetics and evolution of hydrate assemblages are characterized in clinker pastes by isothermal calorimetry (TAM Air calorimeter, 20 ºC), XRD (PANalytical Empyrean, Co source, 40 kV/45 mA), and thermogravimetric analysis (TGA; Netzsch STA 449C, under N_2). Clinker pastes (water:clinker 0.5) produced with distilled water using a high speed mixer were cast in cylindric containers that were sealed and kept at 20 ºC. The phase content was determined on hydration-stopped powder samples by XRD/Rietveld refinement using the Profex software package and rescaled to a common basis (g/100g anhydrous) using the values of chemically bound water determined by TGA (mass loss between 35 and 400 °C). The mobility of potentially hazardous metal(loid)s was evaluated based on batch leaching tests test (EN 12457-2).

3. Results

The XRD pattern of a clinker produced from a raw meal containing 13.7 wt.% of tailings is shown in Figure 1 (a). The tailings-based CSA clinker presents ye'elimite ($C_4A_3\overline{S}$), grossite (CA_2), and gehlenite (C_2AS) as major phases. Minor phases could be identified using a selective dissolution method using HCl. With the dissolution of $C_4A_3\overline{S}$ and partial dissolution of C_2AS, the peaks of a calcium-poor ferrite phase (silico-ferrite of calcium and alumina, SFCA, an analogue of the mineral khesinite) could be identified.

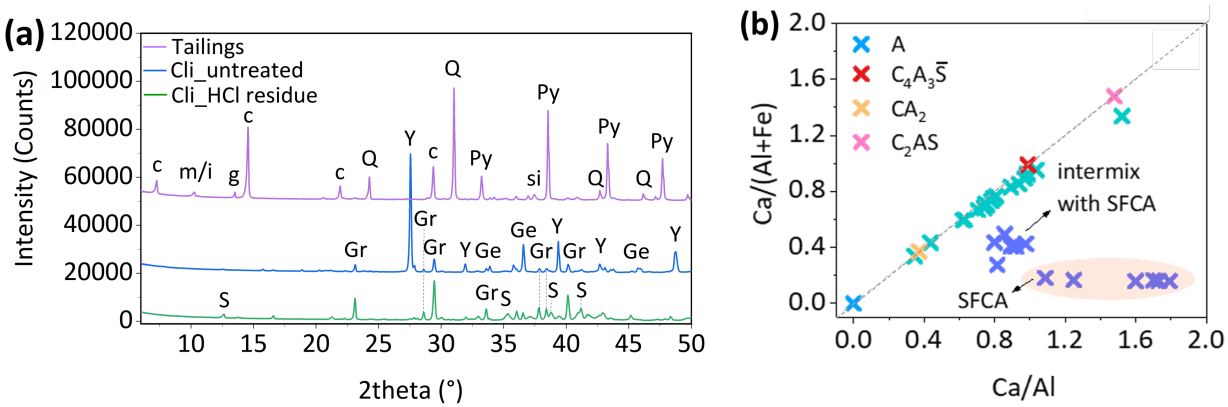

Figure 1. (a) XRD patterns (Co-Kα) of a clinker produced from a raw meal containing 13.7 wt.% of tailings and its solid residue after selective dissolution using HCl. The XRD pattern of the tailings is also shown. c: chlorite; m/i: muscovite/illite; g: gypsum; Q: quartz; Py: pyrite; si: siderite; Y: ye'elimite; Ge: gehlenite; Gr: grossite; S: SFCA. (b) Compositions obtained by EDS point analyses on a clinker pellet.

The compositions of points selected across the matrix of the clinker pellet were plotted in terms of their Ca/(Al+Fe) mass ratios and compared to the theoretical composition found in pure minerals (Figure 1 (b)). Intermediate compositions between $C_4A_3\bar{S}$ and CA_2 were detected, which can be explained by the formation of fine grains of both phases with a high intermix. The $C_4A_3\bar{S}$-CA_2 matrix presented a slight enrichment in Fe. However, most of the iron contributed by the tailings was accommodated by the formation of iron oxides and the SFCA phase. EDS also shows that the SFCA phase(s) have an average Ca/(Al+Fe) ratio of 0.17; far below the Ca/(Al+Fe) ratios of typical calcium ferrites present in clinkers, e.g., C_4AF, C_2F, C_6AF_2, C_6A_2F, which are in the 0.72-1.1 range. The linear arrangement of points in Figure 1 (b) indicate that the Al content varies at the expense of the Fe content in SFCA. Moreover, traces of Zn (0.62 wt.%), Cu (0.99 wt.%), Mg and Si (< 0.3 wt.%) were detected in SFCA.

The heat curve of the clinker is shown in Figure 2 (a). Without the addition of a sulfate source, the hydration of the clinker starts after a dormant period of 16 hours. However, the hydration kinetics can be regulated by the addition of a sulfate source, as in commercial CSA cement. The evolution of phase composition in the clinker was followed up to 90 days and is shown in Figure 2 (b). The hydration series of the clinker show a decrease in the content of $C_4A_3\bar{S}$ (within the first 3 days) and CA_2 (predominantly between 3 and 28 days). The following hydrates are observed: ettringite, AH_3 (crystalline and nanocrystalline), AFm phases ($C_4A\bar{S}H_{14}$, $C_4A\bar{S}H_{12}$, solid solutions), and CAH_{10}. The content of the latter continuously increases up to 90 days. It is suggested that CAH_{10} forms predominantly as a result of CA_2 hydration. However, this phase is metastable and may convert to more stable hydrates in the long-term. The absence of an additional sulfate source explains the predominance of AFm phases over ettringite. Poorly crystalline AFm and AH_3 are accounted for in the quantification of the expressive amorphous fraction of this hydrated clinker. The XRD/Rietveld results do not show a clear reduction on the content of SFCA with hydration time. In agreement with the expectations, SFCA and gehlenite remain inert.

The concentrations detected in the leachates of clinker powders (C) and 28-days hydrated pastes (P) are presented together with the values obtained for the tailings in Table 2. The total concentrations of metal(loid)s (measured by XRF) are also shown in Table 2. The analysis of total and leached concentrations indicates that, despite being present in the tailings-based clinker, the metal(loid)s are not mobile. The leached concentrations are comparable to those of a tailings-free clinker produced from lab-grade chemicals (CSA_Ref). Moreover, considering that the raw meal contained 13.7 wt.% of tailings, the total concentrations measured in the clinker indicate that volatilization of metal(loid)s, e.g., Pb, Zn, Cd, As, during clinkering was low, if any. Table 2 suggests that the clinkering process itself might contribute to the immobilization, which is further enhanced during the hydration process. It must the noted that the leaching test is performed in water for 24 hours, therefore clinkers were not fully anhydrous.

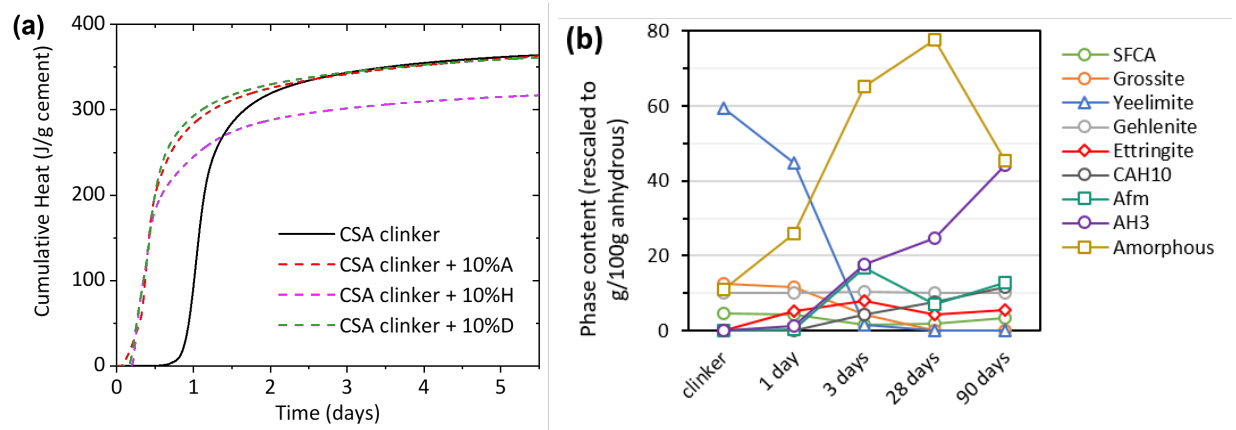

Figure 2. (a) Cumulative heat curves of CSA clinker and cement pastes produced using anhydrite (A), hemihydrate (H), and gypsum (D) as additional sulfate sources (w:c=0.5; 20°C; sulfate source is added as 10 wt.% of the clinker). (b) Phase content in the anhydrous clinker and pastes hydrated up to 90 days. The amorphous content was calculated considering gehlenite as an internal standard (this phase was inert over the duration of the hydration study).

Table 2. Total elemental concentrations (measured by XRF) and leached concentrations (measured by ICP, test EN 12457-2) of tailings, tailings-based CSA clinker (CSA_T) and a tailings-free CSA clinker (CSA_Ref). The values for the tailings are compared to legislation limits for inert waste (WILL) and non-hazardous waste (NHWLL).

	mg/kg	As	Cd	Cr	Cu	Ni	Pb	Sb	Zn
Tailings	Total (XRF)	3670	20.8	56.4	2940	<5	2440	218	6300
	Leached (ICP)	3.9	2.4	0.06	112.3	1.6	31	6.3	790
	IWLL	0.5	0.04	0.5	2	0.4	0.5	0.06	4
	NHWLL	2	1	10	50	10	10	0.7	50
CSA_T	Total (XRF)	666	<5	18.8	394	<5	256	29.3	1120
	Leached_C (ICP)	<0.15	0.003	<0.01	<0.03	<0.01	<0.08	0.14	<0.07
	Leached-P (ICP)	<0.15	<0.0028	<0.01	<0.03	<0.01	<0.08	<0.1	<0.07
CSA_Ref	Total (XRF)	<5	<5	<10	10.2	<5	8.3	<5	8.6
	Leached-C (ICP)	<0.15	<0.0028	<0.01	<0.03	<0.01	<0.08	0.47	<0.07
	Leached-P (ICP)	<0.15	<0.0028	<0.01	<0.03	<0.01	<0.08	<0.1	<0.07

4. Conclusions

Sulfidic tailings were incorporated in the raw meal of a CSA clinker. The hydration of the clinker relies on the reaction of $C_4A_3\overline{S}$ and, to a minor degree, CA_2. The slow kinetics can be adjusted by the addition of calcium sulfate. Immobilization of the metal(loid)s coming from the tailings was achieved on clinkers (after 24 hours of leaching test in water) and on clinker pastes hydrated for 28 days.

Acknowledgements

This work was supported by the European Union's Framework Programme for Research and Innovation Horizon 2020 (SULTAN Project, grant agreement #812580). The authors gratefully acknowledge Jillian Helser (KULeuven), the ScopeM, Lydia Zehnder, and Michael Plötze (ETHZ), and Myrjam Mertens, Willem Stuyck, and Dirk Vanhoyweghen (VITO) for their support & assistance in this work.

References

Shi C, Qu B, Provis JL. Recent progress in low-carbon binders. Cem Concr Res. 2019;122(May):227–50

Zhang L, Su M, Wang Y. Development of the use of sulfo- and ferroaluminate cements in China. Adv Cem Res. 1999;11(1):15–21.

Peysson S, Péra J, Chabannet M. Immobilization of heavy metals by calcium sulfoaluminate cement. Cem Concr Res. 2005;35(12):2261–70.

Lottermoser B. Sulfidic Mine Wastes. In: Mine Wastes. 2013. p. 31–82.

Winnefeld F, Lothenbach B, Frank Winnefeld, Barbara Lothenbach, Winnefeld F, Lothenbach B. Phase equilibria in the system Ca4Al6O12SO4 – Ca2SiO4 – CaSO4 – H2O referring to the hydration of calcium sulfoaluminate cements [Internet]. Vol. 1, RILEM Technical Letters. 2016. Available from: http://letters.rilem.net/index.php/rilem/article/view/5

The 16th International Congress on the Chemistry of Cement 2023 (ICCC2023)
"Further Reduction of CO_2 -Emissions and Circularity in the Cement and Concrete Industry"
September 18–22, 2023, Bangkok, Thailand

Recommendations of the French National project FastCarb about accelerated carbonation of recycled concrete

X. Guillot[1*], and J.-M Torrenti[2],

[1] *FastCarb WG3 convenor, Paris, France*
Email: xavier.guillot@lafarge.com
[2] *FastCarb Director, Paris, France*
Email: jean-michel.torrenti@univ-eiffel.fr

ABSTRACT

FastCarb is a French R&D collaborative project that has been conducted between 2018 and 2023 by 23 partners. The main objectives of the project were to understand the key parameters controlling accelerated carbonation of recycled concrete aggregates (RCA), demonstrate the industrial feasibility of the process and evaluate the impact of carbonated RCA on concrete properties. This paper presents the main recommendations of the project about the optimized parameters (water content, size of the aggregates, temperature, treatment duration…), industrial process, testing methods to determine the fixed CO2 content and conditions for successful implementation of this approach. During the project, two pre-industrial types of equipment have been installed in cement plants and about 80 Tons of recycled aggregates have been carbonated (~ 1 Ton/hour) using directly flue gas. The efficiency of the process has been demonstrated, and as such carbonated RCA can contribute to the overall reduction of the concrete carbon footprint. A very promising perspective lies at the level of the fine fraction which can be used also as a new cement constituent. FastCarb is a true example of a circular economy between concretes, cements and recycled aggregates.

KEYWORDS: *FastCarb, accelerated carbonation, recycled concrete aggregate, circularity*

1. Introduction

In the 2010s, France decided to set up R&D collaborative projects to increase the technical knowledge about the use of Recycled Concrete Aggregates (RCA) in concrete. The first National Project in that area was Recybéton (de Larrard & Colina (2019)) and this extensive research conducted to a better understanding of the impact of RCA in reinforced concrete (from design rules to concrete formulation and durability aspects). An important outcome was the revision of the French annexes of the European concrete standard and Eurocodes, specifying the rules on the use of RCA, increasing their content within concrete (till 60% for the coarse fraction in some exposure classes) but also including rules for the fine fraction (sand) excluded so far. After this first National Project, another significant one, focusing on the accelerated carbonation of RCA, emerged rapidly but it took several years before getting the budget. Eventually, thanks to the funding of the French Ministry of Ecological Transition and contributions from the partners, this second project named FastCarb was launched. The main objective of the National Project FastCarb (fastcarb.fr) was to study how to store CO_2 in recycled concrete aggregates to improve their quality by clogging the porosity, increase again their use in new concrete, and thus, reduce the concrete carbon footprint. The idea was to use recycled concrete aggregates from the demolition of concrete structures as a "carbon sink" by taking advantage of the spontaneous tendency of hydrated cement paste to fix atmospheric CO_2. At the international level, there is an increasing interest in this topic of accelerated carbonation of RCA, as evidenced by recent publications (Pu et al (2021), Li et al (2022), Xiao et al (2022) or Winnefeld et al (2022)). A large number of publications also show the potential interest of this technology but works were only conducted at the laboratory level (Zhan et al (2014), Tam et al (2020)). The project consisted of three main phases: laboratory R&D and modelling, carbonation at

the industrial scale and evaluation of the properties of concrete incorporating these carbonated RCA. Life cycle analyses (LCA) but also economic studies considering the whole production of carbonated RCA value chain were also performed. Compared to other studies, the originality of FastCarb stands in the findings about the identification of mechanisms and conditions to accelerate and increase the CO_2 captured in the RCA, directly at an industrial scale using the flue gas of cement plants but also on the optimal use of carbonated RCA in concrete. The added value of the project lies also in various recommendations issued, whether in terms of testing methods or prerequisites for the model viability, for the practical implementation of the use of carbonated RCA. A part of the results of the FastCarb project was already published (Sereng et al (2021), Torrenti et al (2022) and Izoret et al (2023)). This paper presents a synthesis of the main recommendations of the project gained from the results.

2. Results and recommendations

One of the main interest of such R&D collaborative projects, in particular for the industry, lies in the fact that results are capitalized into recommendations to enhance the standardization process when necessary and facilitate the implementation of the technology developed. This paper summarizes some of the recommendations of FastCarb.

2.1 Key parameters for accelerated carbonation of RCA

The optimization of CO_2 mineralization in recycled concrete aggregates depends on many parameters to be controlled. The results of laboratory studies and modelling distinguish two types of parameters:
Parameters linked to RCA such as the initial natural carbonation state of the aggregates which impacts the CO_2 storage potential. It is possible to qualitatively check whether potential carbonation is still possible by spraying a colored indicator such as phenolphthalein. The water content is another predominant factor. An optimum water content of recycled aggregates allowing maximum carbonation stands in the range of 65 to 85% of the 24-hour water absorption value of RCA**.** The aggregates' size has a significant impact on the quantity of CO_2 stored; for the sand fraction, it can be twice that of 12-20 mm gravel. The type of cement of the original concrete has also an influence on the CO_2 storage potential. For RCA containing Portland cement paste, the quantity of CO_2 stored can be triple of that captured in RCA with slag cement paste.
Parameters linked to the accelerated carbonation process such as the temperature (40°C and above) has a favorable effect on carbonation. The gain of a partial pressure greater than 15% of CO_2 in the gas is not significant. For these two reasons, gases at the cement kiln outlet (which have a CO_2 content close to 15% and a temperature between 70 and 90°C) are suitable for accelerated carbonation. The presence of other combustion products in the gas (SO_2, NO_2) can however significantly disturb the CO_2 mineralization kinetics. Granular agitation is more effective than carbonation in a fixed granular bed. Nevertheless, granular agitation also produces attrition with desirable or undesirable effects on the aggregate (creation of fine particles favorable to CO_2 storage, reduction in the angularity of the aggregates). The effect of forced gas flow in the aggregate bed improves the carbonation kinetics. The gas pressure also plays a significant role in increasing the storage rate. However, at a too high pressure gradient (> 1.5 bar), a condensation phase is observed, thus limiting the penetration of CO_2. A longer treatment duration logically increases the quantity of CO_2 stored. But this effect is limited by the porosity filling and the increase in the saturation of the medium which slows down the kinetics of carbonation.

2.2 Pilot facilities

Two pilot facilities (rotating drum and fluidized bed dryer) have been implemented on a full scale in two cement plants, namely the Vicat Créchy cement plant and the Lafarge Val d'Azergues cement plant. These experiments have demonstrated that the carbonation of RCA was possible at the industrial scale (directly in CO_2 emitting sites with the real flue gas) and not only on samples in the laboratory.
The main learnings gained from these trials are the following :

- The use of flue gas (CO_2 content of about 15%) from the cement plants is sufficient and satisfying to accelerate natural carbonation, with an optimal relative humidity between 50 and 70% and a temperature between 70 and 90°C.

- The amount of CO_2 stored in the RCA tested was between 31 and 39 kg CO_2/t for the fine fraction and between 5 et 12 kg for the coarse fraction; these typical values, which are in line with laboratory results, have been obtained after a 1 hour treatment (contact between the flue gas and the RCA) in the cement plant.
- In the pilot facilities, implemented in existing installations, the three main parameters to control to maximize the CO_2 captured are the CO_2 concentration, the humidity and the gas temperature.
- Additional results demonstrate that the combination of the main gas (N_2) with other gases (SO_2 et NO_x) does not lead to the precipitation of specific compounds but they can nevertheless impact the carbonation rate.

From the perspective of industrial developments, the control of the water content of RCA is also important in addition to the other key parameters already mentioned before. The site must also have a reliable method for determining the CO_2 captured to be able to take into account these values in the calculations of the Environmental Product Declarations (EPD) of the aggregates but also to valorise from the economical point of view the CO_2 that has not been not emitted. This is also the reason why the last activities of FastCarb have been dedicated to the evaluation of different testing methods described below.

2.3 Testing methods to determine CO_2 stored in RCA

The objective was to propose quantitative, representative and reproducible methods to precisely assess the quantity of CO_2 captured during the accelerated carbonation of coarse and fine RCA. Five methods have been evaluated: Thermogravimetric analysis (TGA), loss on ignition (LOI), calcimeters (Bernard or Carbonate Bomb) and Total carbon content.
Depending on the context in which it is necessary to determine the CO_2 stored, the interest of those methods differs. For example, the TGA can be used for a change of deposit, the loss on ignition (simple method with good reproducibility and repetability results) is adapted for the qualification of average batches before and after carbonation. The calcimetry (Bernard or carbonate bomb) can be used for quality control between 2 measurements of loss on ignition.

2.4 Conditions of the development of the use of carbonated RCA

Accelerated carbonation facilities will be implemented only if the environmental and economic benefits are demonstrated; limited transport and proximity between actors (recycling platforms, CO_2 sources and concrete facilities (RMX and precast)) are prerequisites for the viability of the model. Results from the project indicate that for 1 ton of carbonated RCA transported on a distance of 30 km between the recycling platform and the carbonation site then on a distance of 20 km between this site and the concrete production unit, the CO_2 emission is 11 kg. Taking into account the CO_2 stored, the average CO_2 balance in these conditions is -1 kg of CO_2 for 1 ton of coarse aggregates and -28 kg of CO_2 for 1 ton of sand.
For the production of RCA, it is recommended to optimize the location of recycling platforms to reduce the share of transport in the environmental balance, by promoting a modal shift (river, rail) when possible. It is important to continue operational works on the types of crushers to be used in the recycling of concrete to concentrate the cementitious fraction which can recarbonate compared to the granular fraction whose core is an aggregate with no potential for recarbonation.
Strengthening waste sorting at all stages of deconstruction (worksites, platforms, etc.) should promote the identification, tracking and marking of concrete so that it can be directed to recycling channels by increasing the volumes of RCA and ultimately those of carbonated RCA. For the economic viability of the projects, different paths can be followed depending on local legislation. In Europe, for companies under Emissions Trading System (ETS) like those of the cement industry, a ton of CO_2 captured in RCA could save a quota corresponding to the price of 1 ton of CO_2. For others, this reduction in emissions could make it possible to obtain Carbon Offset Credits which, like the unused CO_2 quotas, would contribute to the profitability of future CO_2 capture projects. All these economic instruments of regulation need to be adjusted or elaborated. When possible, the use of compressed CO_2 to carbonate RCA directly on the deconstruction site or on a recycling platform constitutes an alternative to reduce the CO_2 emissions corresponding to the transport.

3. Perspectives

FastCarb is a true example of the circular economy between concretes, cements and recycled aggregates. The project has demonstrated that the most attractive fraction for CO_2 mineralization is the fine fraction containing the highest cement paste content. The use of a significant amount of carbonated RCA in concrete is a lever to reduce its carbon footprint. An alternative interesting path, not studied in FastCarb, could be the use in cements of specially selected and prepared material coming from crushed carbonated RCA. Indeed, this will be possible with the new European cement standard NF EN 197-6 recently published. This standard specifies cements with a new constituent which is Recycled Concrete Fines. Some publications even indicate that the carbonation could enhance the reactivity of the material used as a Supplementary Cementitious Materials (SCM). Further investigations have to be conducted.

4. Conclusions

FastCarb has shown that accelerated carbonation is realistic at industrial scale with results consistent compared to laboratory experiments and with positive impacts when RCA transport is limited. The amount of CO_2 that could be mineralized will not solve the problem of CO_2 emissions from the concrete industry by itself but it is a possible and interesting contribution to fostering the circular economy. The LCA of the pilot facilities have confirmed that the sand fraction of RCA was the most interesting material for CO_2 capture and climate change impact when the carbonated RCA were used in new concrete. The carbonated sand has an initial negative weight in terms of CO_2. This is also interesting for a circular economy objective as the recycled concrete sand is more difficult to use in concretes made with RCA. Maybe the perspective of use as SCM in cement could be a promising path. Recent French regulatory evolutions (RE 2020 and REP for instance) demonstrate the relevance of collaborative projects as FastCarb and the importance to develop technical knowledge in that area. Finally, economic incentives have to be elaborated by regulators to develop widely the approach.

Acknowledgements

The FastCarb National Project was funded by the French Ministry of Ecological Transition and by the 23 academic and industrial partners for a total budget of 3 M€. IREX brought its support in the organization and the financial control of the project.

References

de Larrard, F., & Colina, H., (Eds.) (2019) "Concrete Recycling: Research and Practice." *CRC Press*

Pu, Y., Li, L., Wang, Q., Shi, X., Luan, C., Zhang, G., Fu, L., El-Fatah Abomohra, A. (2021) "Accelerated carbonation technology for enhanced treatment of recycled concrete aggregates: A state-of-the-art review". *Constr. Build. Mat.*, 282, 122671

Li, Liang, and Min Wu. (2022) "An overview of utilizing CO2 for accelerated carbonation treatment in the concrete industry." *Journal of CO2 Utilization* 60

Xiao, J., Zhang, H., Tang, Y., Deng, Q., Wang, D., & Poon, C. S. (2022). "Fully utilizing carbonated recycled aggregates in concrete: Strength, drying shrinkage and carbon emissions analysis." *Journal of Cleaner Production*, 377, 134520.

Winnefeld, F., Leemann, A., German, A., & Lothenbach, B. (2022). "CO2 storage in cement and concrete by mineral carbonation." *Current Opinion in Green and Sustainable Chemistry*, 100672

Zhan, B., Poon, C.S., Liu, Q., Kou, S.C., Shi, C. (2014) "Experimental study on CO2 curing for enhancement of recycled aggregate properties" *Constr. Build. Mat.*, 67, 3–7.

Tam, V.W., Butera, A., Le, K.N., Li, W. (2020) "Utilising CO2 technologies for recycled aggregate concrete: A critical review." *Constr. Build. Mater.,* 250, 118903

Sereng, M., Djerbi, A., Metalssi, O., Dangla, P., Torrenti, J.-M. (2021) " Improvement of recycled aggregates properties by means of CO2 uptake." *Appl. Sci.,* 11, 6571

Torrenti, J.M., Amiri, O., Barnes-Davin, L., Bougrain, F., Braymand, S., Cazacliu, B., Colin, J., Cudeville, A., Dangla, P., Djerbi, A., et al. (2022) "The FastCarb project: Taking advantage of the accelerated carbonation of recycled concrete aggregates." *Case Stud. Constr.Mater*., 17, e01349.

Izoret, L., Pernin, T., Potier, J.-M., Torrenti, J.-M. (2023) "Impact of Industrial Application of Fast Carbonation of Recycled Concrete Aggregates." *Appl. Sci*., 13, 849. https://doi.org/10.3390/app13020849

The 16th International Congress on the Chemistry of Cement 2023 (ICCC2023)
"Further Reduction of CO_2 -Emissions and Circularity in the Cement and Concrete Industry"
September 18–22, 2023, Bangkok, Thailand

Preparation and hydration of steel slag-based cementitious material

Y. Ma[1*], J. Wang[1], Z. Xu[1], X. Shen[1]

[1]College of Materials Science and Engineering, Nanjing Tech University, Nanjing 211816, China

Email: maying@njtech.edu.cn

ABSTRACT

The design and preparation of low-carbon cementitious materials by solid wastes have gradually become a research hotspot in recent years. Steel slag has been largely discharged but little utilized causing an environmental problem in China. In this paper, the design and experimental study of steel slag-based cementitious material were performed by analyzing hydration products, the development of compressive strength and volume stability. The results show that more AFt and less $Ca(OH)_2$ formed during the hydration of steel slag-based cementitious material. Less steel slag and high GBFS in cementitious material favor the 3 days' compressive strength. A higher compressive strength occurred in the binder with 47.5%-52.5% SS, 20%-25% GBFS, 12.5%-17.5% FGDG and 15% PC at 28 days. The 50% SS-20%GBFS-15%FGDG-15%PC binder presents high compressive strength reaching 58.2 MPa. There is no destructive effect on the volume stability of steel slag-based cementitious material with the amount of steel slag up to 50%.

KSYWORDS : *Steel slag, solid waste, volume stability, compressive strength*

1.Introduction

Steel slag (SS) is one of the main wastes produced in the steelmaking process. The annual emission of steel slag in China is about 160 million tons, and the accumulated stock is nearly 2 billion tons, but the comprehensive utilization rate is less than 30% (Shi (2002)). The mineral composition of SS contains C_3S, γ-C_2S, C_4AF, C_2F, RO phase (CaO–FeO–MnO–MgO solid solution), free-CaO and MgO. A great part of SS is randomly discarded resulting in land occupation and environmental pollution, the waste of resources. Aside from SS, the typical industrial wastes including granulated blast-furnace slag (GBFS), fly ash (FA), and flue gas desulfurization gypsum (FGDG) have been utilized as supplementary material and prepare solid waste based cementitious materials (Han et al (2020), Liu and Wang (2017), Wang et al (2012)) .

SS, GBFS and FA are rich in aluminate and silicate phases, which have a potential pozzolanic activity to prepare cementing materials. Typically, different types of binders such as alkali activated materials, supersulfated cement, non- or/and less-cement binders were developed, which favors the high utilization of solid wastes as well as low carbon emission (Zhang et al (2016), Rosales et al (2017)) . Practical studies on the preparation and hydration properties of steel slag-based cementitious material were performed (Xiang et al (2016)). Low compressive strength occurred in binders due to the low activity of steel slag (He et al (2021)). The rise of replacement of steel slag results in a decrease in strength, while the addition of GBFS can improve the compressive strength.

In this study, steel slag-based cementitious material was prepared by high volume SS along with GBFS, FGDG, FA and less or no Portland cement (PC) based on the activity matching between aluminosilicate phases and the calcium and sulfate phases. The hydration and hardening properties of steel slag-based

binders were discussed by hydration products, compressive strength and volume stability analyses.

2. Experimental

Steel slag powder from Jigang Group Co., Ltd., Shandong, GBFS powder from Jintaicheng Environmental Resources Co., Ltd., Hebei., Fly ash powder and PC-Ⅱ 525 Portland cement (PC), Jiangnan Onoda were used in the experiment. Flue gas desulfurization gypsum (FGDG) was through a 200 mesh sieve in size of 75 μm. The chemical compositions of raw materials were determined by X-ray fluorescence (XRF), as shown in Table 1. The amounts of 40%-60% SS, 15%-35% GBFS, 10%-30% FGDG, less than 15% PC and FA were used.

Table 1 Chemical composition of raw materials (wt. %).

	CaO	SiO_2	Al_2O_3	SO_3	MgO	Fe_2O_3	Na_2O	K_2O	MnO	P_2O_5	LOI
Steel slag	36.46	16.64	5.71	0.24	7.42	21.03	0.29	0.09	6.06	2.14	1.06
FGD	32.06	1.65	0.80	42.46	0.7	0.20	-	0.08	0.02	0.02	21.59
PC	53.66	36.70	3.83	2.52	-	3.30	0.23	0.47	0.05	0.12	2.22
GBFS	31.26	45.12	17.00	1.23	3.94	0.28	0.58	0.36	0.23	0.03	-
FA	7.95	46.41	31.18	1.91	1.30	4.97	0.60	0.86	0.08	0.60	-

The molds in sizes of 20 mm × 20 mm × 20 mm and 20 mm × 20 mm × 80 mm molds were used for compressive strength and length change tests respectively. The water to binder (w/b) of 0.3 was used. The paste was mixed by a mixer for 4 minutes. Then, the paste with the mold was vibrated by a vibrating machine. After casting, that was placed in a curing box (20 ± 2℃ and RH 95 ± 2%). The samples were demolded after 24 hours and cured in water at 20 ± 1℃ until certain periods. The values of compressive strength and linear expansion ratios were measured at certain periods. Part of the sample was broken into pieces and soaked in anhydrous ethanol for stopping the hydration of the binder. The sample pieces were dried at 40℃ for one day before XRD analysis.

The compressive strength was measured by an automatic strength testing instrument (AEC-201 type), and the strength value was calculated by the average of 6 cubes. The length change was measured with reference to GB/T 29417-2012. The linear expansion ratio was obtained by calculating the length value at specific periods corresponding to the initial length value. The hydration products of binders were identified by XRD methods. XRD analysis was performed by a Rigaku-Smart-lab 3000A X-ray diffractometer with Cu Kα radiation. The accelerating voltage and current were 40 kV and 35 mA, respectively. The scanning range is between 5^o and 70^o at 10^o per minute with the step of 0.01^o.

3. Results and discussion

3.1 Hydration products

The hydration products of steel slag-based cementitious materials at different times are analyzed by XRD as shown in Fig 1. The phases of AFt, $Ca(OH)_2$ and $CaCO_3$ were produced along with unhydrated RO and γ-C_2S phases as well as gypsum were observed in steel slag-based cementitious materials. A stronger intensity of AFt and a weaker intensity of $Ca(OH)_2$ are exhibited in steel slag-based cementitious materials while amorphous C-S-H cannot be detected. The hydration process of steel slag-based cementitious materials would be attributed to the following, as shown in Eq. (1) and (2).

$$Ca^{2+} + xSiO_4^{4-} + yH_2O \rightarrow CaO{\cdot}xSiO_2{\cdot}yH_2O \quad (1)$$

$$12Ca^{2+} + 2AlO_4^{5-} + 6SO_4^{2-} + 2OH^- + 61H_2O \rightarrow 2(3CaO{\cdot}Al_2O_3{\cdot}3CaSO_4{\cdot}32H_2O) \quad (2)$$

SS and GBFS particles decompose in an alkaline ($Ca(OH)_2$) environment producing Ca^{2+}, SiO_4^{4-} and AlO_4^{5-}, respectively. These ions can occur in hydrate reaction to form C-S-H gel and react with sulfate from FGDG to produce AFt. A small amount of $CaCO_3$ is a carbonization product of $Ca(OH)_2$. Furthermore, at 90 days, the diffraction peaks of γ-C_2S and RO phase remained nearly unchanged, indicating that the RO phase is stable in this system.

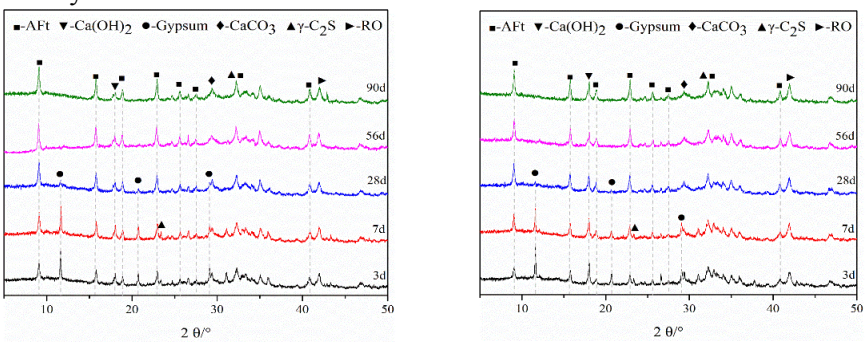

(a) SS40-GBFS20-FA12 (b) SS50-GBFS20-FA2

Fig. 1 XRD patterns of steel slag-based cementitious material with 13%FGDG and 15%PC.

3.2 Compressive strength

The compressive strength contour of the SS-GBFS-FGDG binder is shown in Fig 2. The compressive strength of binders increased with increasing hydration time. Less steel slag and high GBFS in cementitious material favor the 3 days' compressive strength. At 3 days, a higher compressive strength occurred in the binder with 40%-42.5% SS, 32.5%-35% GBFS, 10%-12.5% FGDG and 15% PC.

At 28 days, a higher compressive strength occurred in the binder with 47.5%-52.5% SS, 20%-25% GBFS, 12.5%-17.5% FGDG and 15% PC. The binder with 50% SS, 20% GBFS, 15% FGDG and 15% PC can obtain a strength value of 58.2 MPa at 28 days.

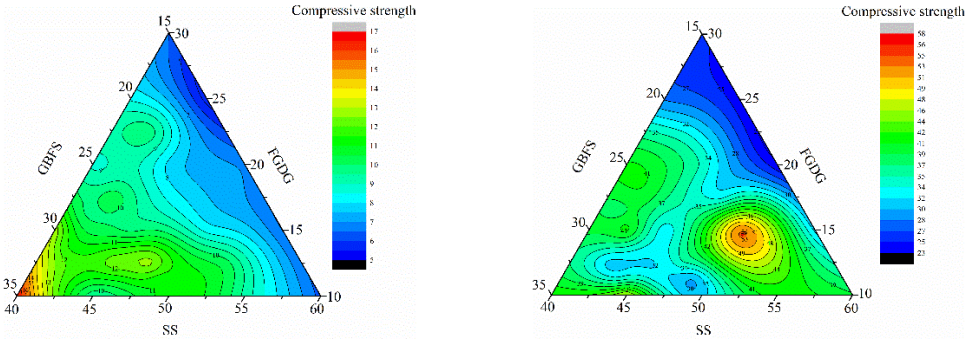

(a) (b)

Fig. 2 Compressive strength contour of SS-GBFS-FGD along with 15% PC cured at (a) 3 days and (b) 28 days.

3.3 Volume stability

Fig. 3 shows the linear expansion rate of steel slag-based cementitious materials. It can be seen that the expansion ratio is less than 0.46% cured in water for 360 days. Before 28 days, the linear expansion rate showed rapid growth and decreased after 150 days. Potential volume instability has been proposed because the reaction between water and f-CaO and f-MgO in steel slag produces $Ca(OH)_2$ and $Mg(OH)_2$ as a result of the expansion. There is no destructive effect on the volume stability of steel slag-based cementitious material with the amount of steel slag up to 50%. The linear expansion rate increases with the increase of fly ash content. The study has proposed that the expansion rate decreases with the increase of fly ash content, and the early expansion development was dominated by the formation of AFt (Duan et al (2020)).

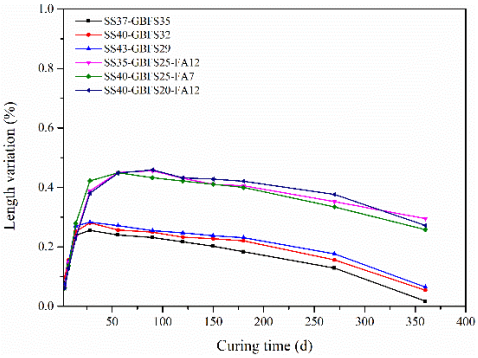

Fig. 3. Linear expansion ratio of steel slag-based cementitious materials with 13% FDGD and 15% PC.

4. Conclusion

Steel slag-based cementitious materials containing high volume steel slag were prepared by the chemical match (hydration reaction) between components of blended cement. Steel slag-based cementitious materials hydrate to produce more AFt, less $Ca(OH)_2$ and C-S-H, as well as the unhydrated RO phase and γ-C_2S. Less steel slag and high GBFS in cementitious material favor the 3 days' compressive strength. A higher compressive strength occurred in the binder with 47.5%-52.5% SS, 20%-25% GBFS, 12.5%-17.5% FGDG and 15% PC at 28 days. The 50% SS-20% GBFS-15% FGDG-15% PC binder presents high compressive strength reaching 58.2 MPa. There is no destructive effect on the volume stability of steel slag-based cementitious material with the amount of steel slag up to 50%.

References

Shi C.J. (2002) "Characteristics and cementitious properties of ladle slag fines from steel production", *Cement and Concrete Research*, 32:459-462.

Han X., Feng J.J., Shao Y.X. and Hong R.A. (2020) "Influence of a steel slag powder-ground fly ash composite supplementary cementitious material on the chloride and sulphate resistance of mass concrete", *Powder Technology*, 370:176-183.

Liu J. and Wang D.M. (2017) "Influence of steel slag-silica fume composite mineral admixture on the properties of concrete", *Powder Technology*, 320:230-238.

Wang Q., Yan P.Y. and Mi G.D. (2012) "Effect of blended steel slag-GBFS mineral admixture on hydration and strength of cement", *Construction and Building Materials*, 35:8-14.

Zhang Y.J., Pan F. and Wu R. (2016) "Study on the performance of FGD gypsum-metakaolin-cement composite cementitious system", *Construction and Building Materials*, 128:1-11.

Rosales J., Cabrera M. and Agrela F. (2017) "Effect of stainless steel slag waste as a replacement for cement in mortars. Mechanical and statistical study", *Construction and Building Materials*, 142:444-458.

Xiang X.D., Xi J.C., Li C. and Jiang X.W. (2016) "Preparation and application of the cement-free steel slag cementitious material", *Construction and Building Materials*, 114:874-879.

He W., Zhao J.H., Yang G.Q. and Liu Y.S. (2021) "Investigation on the Role of Steel Slag Powder in Blended Cement Based on Quartz Powder as Reference", *Advances in Civil Engineering*, 2021:1-15.

Duan S.Y., Liao H.Q., Cheng F.Q. and Tao M.J. (2020) "Effect of curing condition and carbonization enhancement on mechanical properties of fly ash - desulfurization gypsum - steel slag blocks", *Journal of CO2 Utilization*, 38:282-290.

The 16th International Congress on the Chemistry of Cement 2023 (ICCC2023)
"Further Reduction of CO_2 -Emissions and Circularity in the Cement and Concrete Industry"
September 18–22, 2023, Bangkok, Thailand

Recent advances on European cement standards prepared by CEN TC51 for more sustainable products

X. Guillot[1*], F. Van Rickstal[2], and M. Schneider[3]

[1] *CEN TC 51 Chairman, Paris, France*
Email: xavier.guillot@lafarge.com
[2] *CEN TC 51 Secretary, Brussels, Belgium*
Email: f.vanrickstal@cric-occn.be
[3] *CEN TC 51 / WG6 Convenor, Düsseldorf, Germany*
Email: martin.schneider@vdz-online.de

ABSTRACT

In Europe, the CEN (European Committee for Standardization) Technical Committee 51 (CEN/TC51) is in charge for the last 50 years of the standardization activities about cements, building limes and other hydraulic binders in an extensive framework including testing methods and conformity control. Benefits expected from the work of CEN/TC 51 are mainly to address major issues within the framework of the European Green Deal and more especially concerns about hydraulic binders' carbon footprint and circular economy. Significant progress has been made in recent years in that direction with the preparation of new standards: EN 197-5 about Portland-composite cement CEM II/C-M and composite cement CEM VI and also EN 197-6 Cement with Recycled Building Materials. Portland-composite cement CEM II/C-M are ternary cements containing clinker in the range of 50% to 64% and two other main constituents. Composite cement CEM VI are made with less than 50% clinker, blast-furnace slag and a third constituent. Cements specified in EN 197-6 contain a new constituent designated as Recycled Concrete Fines, specially selected and prepared mineral material coming from Construction and Demolition Wastes. The content of these two standards and the way they have been developed are detailed in this paper. These new cements are adapted for most of the applications and for structural concrete in particular, allowing a significant reduction of the concrete carbon footprint. In standardization, this momentum to extend solutions will continue and be reinforced in order to support the European Strategy to put standards back at the core of a resilient, green, and digital EU single market and to strengthen the global role of the European standardisation system.

KEYWORDS: *cement standards, sustainable products, European context, circularity*

1. Introduction

All decarbonisation roadmaps rely on several levers of the construction value chain and the development of new more sustainable cements constitute a significant one. Inevitably, standardization of these products is an essential path towards the reduction of the construction sector's carbon footprint. But the valorisation of the results obtained from technical works or fruitful collaborative research into specifications of a product in a standard has many pitfalls. Several aspects have to be considered: regulations, technical performances, intended uses, relationships with other standards, health and environmental assessments.... Even though their application is voluntary, European harmonized standards are part of the European law. In particular, activities conducted within CEN (European Committee for Standardization) Technical Committee 51 (CEN/TC51) are covered by the European Construction Products Regulation (CPR). So, requirements of cements, building limes and other hydraulic binders are specified in accordance with this specific framework.

To address major issues linked to consequences of the Climate change, European Commission has initiated end of 2019 the Green Deal initiative with a set of Regulations, Directives and Strategies prepared since that time. Among them, the CPR revision but also the communication on Standardization Strategy have been released. To support the European Strategy to put standards at the core of a resilient, green and digital EU single market, CEN/TC51 has undertaken several works.
This paper presents the main content of the two lasts cement standards EN 197-5 and EN 197-6 that have been published respectively in 2021 and 2023. Perspectives in terms of development of new standards are also mentioned.

2. Recent advances

2.1 Methodology

To standardize a new cement or a new hydraulic binder, the fitness for intended use has to be demonstrated. For that purpose, a few years ago, the CEN/TC51 has developed guidance CEN TR 16912 (2017) for the procedure to be followed to support this standardization. A categorization of new cements (Table 1) has been developed and a list of corresponding requirements to be assessed has been established.

Table 1. Categorization of new cements and the corresponding requirements

<table>
<tr><th>Category 1
Cement from a new combination of constituents according to EN 197-1</th><th>Category 2
Cement containing a minor amount of one or more new constituents</th><th>Category 3
Cement differing substantially from those types defined in existing standards</th></tr>
<tr><td colspan="3">Assessment of
mechanical, physical and chemical performances</td></tr>
<tr><td colspan="3">Assessment of
durability related characteristics</td></tr>
<tr><td rowspan="3"></td><td colspan="2">Assessment of influence on
environmental performance</td></tr>
<tr><td colspan="2">Assessment of
possible health impact</td></tr>
<tr><td colspan="2"></td><td>Relevant practical experience gained under approved conditions prior to European standardization</td></tr>
</table>

In order to prepare the two standards described hereafter, technical dossiers have been prepared according to these guidelines.

2.1 Ternary cements

During technical works, it has been demonstrated that some new combinations of well-known constituents with a limited amount of clinker were relevant for reducing the carbon footprint of cements while maintaining the required level of mechanical performance and durability necessary for current applications. As a consequence, EN 197-5 has been prepared then published in 2021. Portland-composite cement CEM II/C-M are ternary cements containing clinker in the range of 50% to 64% and two other main constituents (Table 2). Composite cement CEM VI are made with less than 50% clinker, blast-furnace slag and a third constituent. Another change about the requirements of limestone has been introduced into EN 197-5. As it has been demonstrated that dolomitic limestone was also suitable to be used into cement, the requirements have been extended accordingly. Cements covered by this standard shall fulfil the same mechanical, physical and chemical requirements as those specified into EN 197-1 for common cements. With such new cements, the carbon footprint can be significantly reduced, below 500 kg CO_{2eq}. / t for CEM II/C and below 400 kg CO_{2eq}. / t for CEM VI. Across Europe, National Annexes of concrete standard EN 206 are progressively introducing rules on the use of these cements depending the Exposure Classes.

Table 2. Portland-composite cement CEM II/C-M and Composite cement CEM VI

Main types	Notation of the products (types of cement)		Composition (percentage by mass a)										
			Main constituents										Minor additional constituents
			Clinker	Blast-furnace slag	Silica fume	Pozzolana		Fly ash		Burnt shale	Limestone		
						natural	natural calcined	siliceous	calcareous				
	Type name	Type notation	K	S	D [b]	P	Q	V	W	T	L [c]	LL [c]	
CEM II	Portland-composite cement [d]	CEM II/C-M	50-64	‹---------- 36-50 ----------›									0-5
CEM VI	Composite cement	CEM VI (S-P)	35-49	31-59	–	6-20	–	–	–	–	–	–	0-5
		CEM VI (S-V)	35-49	31-59	–	–	–	6-20	–	–	–	–	0-5
		CEM VI (S-L)	35-49	31-59	–	–	–	–	–	–	6-20	–	0-5
		CEM VI (S-LL)	35-49	31-59	–	–	–	–	–	–	–	6-20	0-5

[a] The values in the table refer to the sum of the main and minor additional constituents.

[b] In case of the use of silica fume, the proportion of silica fume is limited to 6-10 % by mass.

[c] In case of the use of limestone, the proportion of limestone (sum of L, LL) is limited to 6-20 % by mass.

[d] The number of main constituents other than clinker is limited to two and these main constituents shall be declared by designation of the cement (for examples, see Clause 6).

2.3 Cements with Recycled Building Materials

A new breakthrough has been achieved in 2023 with the publication of a new standard EN 197-6 Cement with Recycled Building Materials. To start with, the Recycled Building Materials specified are Concrete Recycled Fines (F) which are defined as a specially selected and prepared mineral material coming from plants or units producing recycled concrete aggregates (coarse and/or fine); it can be also reclaimed from concrete production operations. As Recycled Concrete Fines are mainly non-reactive, they can be treated as a limestone. The standard precisely states the requirements to be fulfilled on the Total Organic Carbon (TOC) content, sulfate content and clay content (Table 3).

Table 3. Requirements of Recycled Concrete Fines

Requirements	Limit
TOC content	≤ 0,8 % by mass
Sulfate content (as SO3)	≤ 2,0 % by mass
Assessment of fines determined by the methylene blue test	≤1,20 g/100 g

Possible compositions of cement containing Recycled Concrete Fines are indicated in Table 4.

Table 4. Cement with Recycled Concrete Fines

Main types	Notation of the products (types of cement)		Composition (percentage by mass) [a]											
			Main constituents											Minor additional constituents
			Clinker	Recycled concrete fines	Blast-furnace slag	Silica fume	Pozzolana		Fly ash		Burnt shale	Limestone		
							natural	natural calcined	siliceous	calcareous				
	Type name	Type notation	K	F	S	D [b]	P	Q	V	W	T	L [c]	LL [c]	
CEM II	Portland-recycled-fines cement	CEM II/A-F	80–94	6–20	—	—	—	—	—	—	—	—	—	0–5
		CEM II/B-F	65–79	21–35	—	—	—	—	—	—	—	—	—	0–5
	Portland-composite cement [d]	CEM II/A-M	80–88	6–14	‹---------- 6–14 ----------›									0–5
		CEM II/B-M	65–79	6–29	‹---------- 6–29 ----------›									0–5
		CEM II/C-M	50–64	6–20	‹---------- 16–44 ----------›									0–5
CEM VI	Composite cement	CEM VI	35–49	6–20	31–59	—	—	—	—	—	—	—	—	0–5

[a] The values in the table refer to the sum of the main and minor additional constituents.

[b] In case of the use of silica fume, the proportion of silica fume is limited to 6 % to 10 % by mass.

[c] In case of the use of limestone, the proportion of the sum of limestone and recycled concrete fines (sum of L, LL and F) is limited to 35 % by mass.

[d] The number of main constituents other than clinker is limited to two and these main constituents shall be declared by designation of the cement (for examples, see Clause 6). In case of the use of both F and (L or LL) in the composition, the number of main constituents other than clinker is limited to three and these main constituents shall be declared by designation of the cement.

Up to 35% of Recycled Concrete Fines are allowed in the composition of these cements, enabling a truly circular economy of Construction and Demolition Materials and reducing the use of natural resources. Despite the long process to elaborate new standards, it took only two years to prepare and publish it from the time CEN/TC51 received officially the request. In a near future, it will be also possible to introduce Recycled Concrete Fines into other hydraulic binders' standards such as Hydraulic Road Binders' ones. Investigations will also continue to identify additional promising materials coming from construction and demolition that could be considered suitable as cement constituents.

3. Perspectives

On the short term, the deployment of these new sustainable cements will be possible only by endorsement of EN 197-5 and EN 197-6 into application standards (concrete and mortar mainly). It will be beneficial for the construction sector to promote these new standards at international level in order to implement similar standards in other regions of the world.
Within CEN/TC51, a new momentum for the development of standards covering more sustainable hydraulic binders is given and different areas are investigated such as : identification of new promising construction and demolition materials and alternative Supplementary Cementitious Materials (SCMs), further investigations on CO_2-efficient cements and support in test methods development and validation.
It is worth to mention also that in the next two years and in the framework of the revision of the European Construction Product Regulation, a huge activity will be conducted between European Commission, Member States and CEN experts. The outcome will be a new Standardization Request from the European Commission, a binding document for CEN/TC51 on the basis of which experts will elaborate harmonized standards of tomorrow.

4. Conclusions

In the last two years, new standards specifying more sustainable cements have been published in Europe by CEN/TC51. This is the result of several years of work, based on a robust methodology and this despite some legal issues due to the complexity of the European law.
EN 197-5 specifies new combinations of constituents and a reduced amount of clinker and EN 197-6 introduces a new constituent coming from Construction and Demolition Materials. Both standards will be beneficial to reduce the carbon footprint of products and to promote circular economy.
Many considerations to transform a promising product from the technical point of view into specifications in a product standard have to be tackled: among others, regulations, technical performances, intended uses, relationships with other standards and building codes, health and environmental assessments, assessment and verification of constancy of performance, certification. Awareness of all stakeholders on these issues will shorten the time to market of more sustainable products necessary to achieve the net zero targets.
In a near future, additional paths to extend possibilities within hydraulic binders and building limes' standards will be followed once new solutions will be technically validated.

Acknowledgements

Authors acknowledge all CEN/TC51 experts for their valuable contributions in the development of standards.

References

CEN TR 16912 (2017) Guidelines for a procedure to support the European standardization of cements
EN 197-5 (2021) Cement - Part 5: Portland-composite cement CEM II/C-M and Composite cement CEM VI
EN 197-6 (2023) Cement - Part 6: Cement with recycled building materials